

AD-A070 950

ADVISORY GROUP FOR AEROSPACE RESEARCH AND DEVELOPMENT--ETC F/6 21/5
STRESSES, VIBRATIONS, STRUCTURAL INTEGRATION AND ENGINE INTEGRI--ETC(U)
APR 79

UNCLASSIFIED

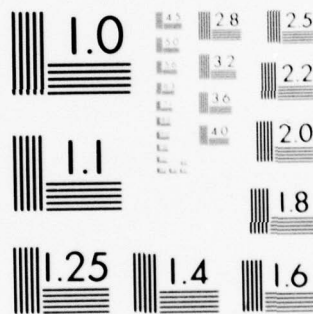
AGARD-CP-248

NL

1 of 6

AD
A070950





MICROCOPY RESOLUTION TEST CHART
NATIONAL BUREAU OF STANDARDS-1963-A

①

LEVEL II

AGARD-CP-248

DA 070950

DDC FILE COPY

AGARD

ADVISORY GROUP FOR AEROSPACE RESEARCH & DEVELOPMENT

7 RUE ANCELLE 92200 NEUILLY SUR SEINE FRANCE

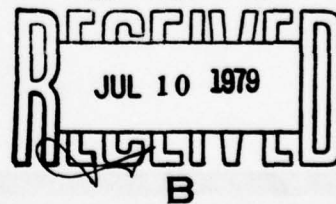
AGARD CONFERENCE PROCEEDINGS No. 248

Stresses, Vibrations, Structural Integration and Engine Integrity (Including Aeroelasticity and Flutter)

DISTRIBUTION STATEMENT A

Approved for public release;
Distribution Unlimited

DDC



NORTH ATLANTIC TREATY ORGANIZATION



DISTRIBUTION AND AVAILABILITY
ON BACK COVER

19 07 09 213

9 Conference Proceedings

14

AGARD-CP-248

NORTH ATLANTIC TREATY ORGANIZATION
ADVISORY GROUP FOR AEROSPACE RESEARCH AND DEVELOPMENT
(ORGANISATION DU TRAITE DE L'ATLANTIQUE NORD)

11 Apr 79

12 498P

6

AGARD Conference Proceedings No.248

STRESSES, VIBRATIONS, STRUCTURAL INTEGRATION
AND ENGINE INTEGRITY (INCLUDING AEROELASTICITY
AND FLUTTER)

DISTRIBUTION STATEMENT A

Approved for public release;
Distribution Unlimited

DDC
RECEIVED
JUL 10 1979
B

Copies of Papers and Discussions presented at the Propulsion and Energetics Panel's 52nd Meeting,
a Symposium held in Cleveland, Ohio, USA, 23-28 October 1978.

400 043

503

THE MISSION OF AGARD

The mission of AGARD is to bring together the leading personalities of the NATO nations in the fields of science and technology relating to aerospace for the following purposes:

- Exchanging of scientific and technical information;
- Continuously stimulating advances in the aerospace sciences relevant to strengthening the common defence posture;
- Improving the co-operation among member nations in aerospace research and development;
- Providing scientific and technical advice and assistance to the North Atlantic Military Committee in the field of aerospace research and development;
- Rendering scientific and technical assistance, as requested, to other NATO bodies and to member nations in connection with research and development problems in the aerospace field;
- Providing assistance to member nations for the purpose of increasing their scientific and technical potential;
- Recommending effective ways for the member nations to use their research and development capabilities for the common benefit of the NATO community.

The highest authority within AGARD is the National Delegates Board consisting of officially appointed senior representatives from each member nation. The mission of AGARD is carried out through the Panels which are composed of experts appointed by the National Delegates, the Consultant and Exchange Programme and the Aerospace Applications Studies Programme. The results of AGARD work are reported to the member nations and the NATO Authorities through the AGARD series of publications of which this is one.

Participation in AGARD activities is by invitation only and is normally limited to citizens of the NATO nations.

A large part of the content of this publication has been reproduced directly from material supplied by AGARD or the authors; the remainder has been set by Technical Editing and Reproduction Ltd.

Published April 1979

Copyright © AGARD 1979
All Rights Reserved

ISBN 92-835-0235-3



*Printed by Technical Editing and Reproduction Ltd
Harford House, 7-9 Charlotte St, London, W1P 1HD*

PROPULSION AND ENERGETICS PANEL

CHAIRMAN: Prof. Dr-Ing. G. Winterfeld, DFVLR, Institut für Antriebstechnik, 5000 Köln 90, Germany

DEPUTY CHAIRMAN: Dr J. Dunham, National Gas Turbine Establishment, Pyestock,
Farnborough, GU14 0LS, Hants, UK

PROGRAM COMMITTEE

Mr J. Acurio (Chairman)
US Army Research and Technology Labs
(AVRADCOM)
Cleveland, Ohio, 44135, USA

Prof. J. Chauvin
Institut de Mécanique des Fluides
13003 Marseille, France

Mr J. Fabri
ONERA
92320 Châtillon-sous-Bagneux, France

Dr D.K. Hennecke
Motoren und Turbinen Union GmbH
8000 München, 50, Germany

Mr A.J.B. Jackson
Rolls Royce Ltd
Aero Division
Derby DE2 8BJ, UK

Dr-Ing. G. Maoli
FIAT Divisione Aviazione
10100 Torino, Italy

HOST NATION COORDINATOR

Mr J. Acurio
US Army Research and Technology Labs (AVRADCOM)
Cleveland, Ohio, 44135, USA

PANEL EXECUTIVE

Dipl.-Ing. J.H. Kregel, DIC

ACKNOWLEDGEMENT

The Propulsion and Energetics Panel wishes to express its thanks to the US National Delegates to AGARD for the invitation to hold its 52nd Meeting at the Bond Court Hotel, Cleveland, Ohio, and for the facilities and personnel made available and for the welcome and support it received in Cleveland and at the NASA Lewis Research Center.

Accession For	
NTIS GRA&I	<input checked="checked" type="checkbox"/>
DDC TAB	<input type="checkbox"/>
Unannounced	<input type="checkbox"/>
Justification	
By	
Distribution/	
Availability Codes	
Dist.	Avail and/or special
A	

PREFACE

A Symposium on "Stresses, Vibrations, Structural Integration, and Engine Integrity (Including Aeroelasticity and Flutter)" was held in Cleveland, Ohio, during the week of 23 October 1978. This Symposium was the 52nd Meeting of the AGARD Propulsion and Energetics Panel (PEP). Except for an afternoon tour of the NASA-Lewis Research Center on 25 October, all other technical and administrative activities were conducted at the Bond Court Hotel.

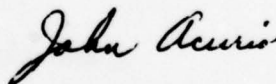
The Symposium was divided into eight sessions as follows:

- Session I – Experimental Stress Analysis
- Session II – Stress Analysis Techniques, Life Prediction
- Session III – Stress Analysis Techniques, Life Prediction
- Session IV – Engine Structural Integrity, Vibration, Containment
- Session V – Engine-Airframe Integration/Compatibility
- Session VI – Engine-Airframe Integration/Compatibility
- Session VII – Aeroelasticity and Flutter
- Session VIII – Aeroelasticity and Flutter

The Technical Evaluation Report (TER) on this Symposium has been prepared by Dr L. Beitch, Manager of Engineering Mechanics and Life Management, General Electric Company, Cincinnati, Ohio. The TER provides a very complete summary and understanding of the technical sessions and recommends topics to be covered in future activities. In particular, Dr Beitch's comments emphasize the need for better technical tools to be applied to life-prediction techniques.

Judging by the attendance at the Symposium and the discussions which followed most of the presentations, the meeting met its objectives and is regarded as a success. It is hoped that the activity provided a baseline to stimulate further work on the critical subjects covered.

The committee is pleased to have had the opportunity to conduct this Meeting. In addition, the effort by Dr Beitch in providing the TER is gratefully acknowledged. His work in support of the Panel will be a valuable assistance in preparing future AGARD programs.



JOHN ACURIO
Chairman,
52nd Meeting of PEP.

CONTENTS

	Page
PROPULSION AND ENERGETICS PANEL	iii
PREFACE	iv
	Reference
 <u>SESSION I – EXPERIMENTAL STRESS ANALYSIS</u>	
STRUCTURAL ANALYSIS OF A GAS TURBINE IMPELLER USING FINITE-ELEMENT AND HOLOGRAPHIC TECHNIQUES by P.S.Kuo and K.S.Collinge	1
ANALYSE DES VIBRATIONS DE MOTEUR par M.Lalanne, P.Trompette, R.Henry et G.Ferraris	2
AIRCRAFT ENGINE DESIGN USING EXPERIMENTAL STRESS ANALYSIS TECHNIQUES by B.L.Koff	3
CONTRIBUTION DE LA PHOTOELASTICIMETRIE A L'ETUDE DES PIECES DE TURBOMACHINES par J.L.Guillo	4
 <u>SESSION II – STRESS ANALYSIS TECHNIQUES, LIFE PREDICTION</u>	
Paper 5 Cancelled	
A CONTRIBUTION ON THERMAL FATIGUE IN COOLED TURBINE BLADING by W.Peschel and R.Schrieck	6
PREVISION DE LA DUREE DE VIE DES MOTEURS par D.Grandoulier	7
STRESS INTERPRETATION IN THE FINITE ELEMENT METHOD by P.Beckers	8
THREE-DIMENSIONAL FINITE-ELEMENT TECHNIQUES FOR GAS TURBINE BLADE LIFE PREDICTION by M.R.Peterson, R.G.Alderson, R.J.Stockton and D.J.Tree	9
 <u>SESSION III – STRESS ANALYSIS TECHNIQUES, LIFE PREDICTION</u>	
CALCUL DE CONCENTRATIONS DE CONTRAINTES DANS LES ALVEOLES DE DISQUES par M.Chaudonneret	10
SOME THEORETICAL AND EXPERIMENTAL INVESTIGATIONS OF STRESSES AND VIBRATIONS IN A RADIAL FLOW ROTOR by A.Grasso, J.J.Blech and G.Martinelli	11
PREDICTION OF AEROELASTIC INSTABILITIES IN ROTORCRAFT ENGINE DESIGN by D.Dini	12
APPLICATION OF ENGINE USAGE ANALYSIS TO COMPONENT LIFE UTILISATION by M.Holmes	13
BOUNDARY-INTEGRAL EQUATION ANALYSIS OF AN ADVANCED TURBINE DISK RIM SLOT by R.B.Wilson, R.G.Potter and J.K.Wong	14

SESSION IV – ENGINE STRUCTURAL INTEGRITY VIBRATION, CONTAINMENT

ENGINE ROTOR BURST CONTAINMENT/CONTROL STUDIES by E.A.Witmer, T.R.Stagliano and J.J.A.Rodal	15
PETITES TURBOMACHINES: EXPERIENCES SUR LA RUPTURE DES DISQUES par J.M.Foueillassar et A.R. Von Der Muhll	16
AN INVESTIGATION OF VIBRATION DAMPERS IN GAS-TURBINE ENGINES by R.Holmes and B.Humes	17
MODAL ANALYSIS OF COMPRESSOR BLADES BY MEANS OF IMPULSE EXCITATION by U.Bolleter, J.Eberl and E.Buehlmann	18
ROTOR BURST PROTECTION: DESIGN GUIDELINES FOR CONTAINMENT by J.T.Salvino, G.J.Mangano and R.A.Delucia	19

SESSION V – ENGINE-AIRFRAME INTEGRATION/COMPATIBILITY

ENGINE/AIRCRAFT STRUCTURAL INTEGRATION: AN OVERVIEW by T.E.Dunning, M.N.Aarnes and G.L.Bailey	20
DYNAMIC PRESSURE LOADS IN THE AIR INDUCTION SYSTEM OF THE TORNADO FIGHTER AIRCRAFT by K.W.Lotter and N.C.Bissinger	21
HANDLING PROBLEMS THROUGH COMPRESSOR DETERIORATION by J.P.K.Vleghert	22
SMALL TURBINE ENGINE INTEGRATION IN AIRCRAFT INSTALLATIONS by M.Botman and R.K.Blinco	23

SESSION VI – ENGINE-AIRFRAME INTEGRATION/COMPATIBILITY

DETERMINATION DES EFFORTS DYNAMIQUES DUS A UN BALOURD AUX ATTACHES D'UN MOTEUR MONTE EN PODE par B.Schneider	24
INTEGRATION OF AN AIRFRAME WITH A TURBOFAN AND AFTERBURNER SYSTEM by M.S.Wooding and H.Hurdis	25
A NEW FACILITY FOR STRUCTURAL ENGINE TESTING by R.L.B.Swain and J.G.Mitchell	26
INTEGRITE DES REACTEURS D'AVIONS SOUS IMPACTS DE CORPS ETRANGERS par D.Hedon et J.Barrere	27

Paper 28 Cancelled

SESSION VII – AEROELASTICITY AND FLUTTER

THE EFFECT OF INTAKE CONDITIONS ON SUPERSONIC FLUTTER IN TURBOFAN ENGINES by D.G.Halliwell	29
UNSTEADY ROTOR BLADE LOADING IN AN AXIAL COMPRESSOR WITH STEADY-STATE INLET DISTORTIONS by M.Lecht and H.B.Weyer	30
DISTORTIONS, ROTATING STALL AND MECHANICAL SOLICITATIONS by J.Colpin	31

ETUDES DES INSTABILITES AEROELASTIQUES DES COMPRESSEURS EN
SOUFFLERIE DE GRILLE RECTILIGNE D'AUBES
par E.Szechenyi, H.Loiseau et B.Maquennehan

32

SESSION VIII - AEROELASTICITY AND FLUTTER

REVIEW OF THE AGARD S & M PANEL EVALUATION PROGRAM OF THE NASA-LEWIS
"SRP" APPROACH TO HIGH-TEMPERATURE LCF LIFE PREDICTION
by M.H.Hirschberg

33

THE UNSTEADY AERODYNAMICS OF A CASCADE IN TRANSLATION
by S.Fleeter, R.E.Riffel, T.H.Lindsey and M.D.Rothrock

34

SUPERSONIC UNSTALLED FLUTTER
by J.J.Adamczyk, M.E.Goldstein and M.J.Hartmann

35

STRUCTURAL ANALYSIS OF A GAS TURBINE IMPELLER USING FINITE-ELEMENT AND HOLOGRAPHIC TECHNIQUES

by

Peter S. Kuo and Kenneth S. Collinge
AVCO LYCOMING DIVISION
Stratford, Connecticut

ABSTRACT

Centrifugal stiffening coupled with complex vibrating modes imposes a serious limit to the structural design of a gas turbine impeller for a more favorable aerodynamic geometry. This paper presents a rigorous finite-element structural analysis method which combined with Holographic technique deals with the highly stressed, curved vanes and the vibration of the flexible circular backplate so that the magnitude and the pattern of static, dynamic and thermal loadings can be improved. The method demonstrates a computerized procedure for the design of a modern centrifugal impeller. Holography which has been used as a means for determining the dynamic behavior of the engine component offers an accurate experimental measurement of natural frequencies and modes. The interference fringe pattern representing the contours of equal surface displacement provides a permanent record for vibration amplitude evaluation. Comparison between the theoretical and the experimental results is made.

INTRODUCTION

Finite element method for analyzing gas turbine engine components such as compressor/turbine blades (1)¹, disks(2), and shells, etc. has provided a powerful tool for design use. Continuing development by using a similar approach to deal with the more complex geometry of a centrifugal impeller has been undertaken. Due to vast variation in rigidity and a large number of flexible radial or nonradial vanes, various analytical requirements have to be met to ensure the integrity of the design. Dynamically, it must be capable of predicting the vibration behavior in rotating/nonrotating conditions and coupled/uncoupled modes in a large frequency range with good accuracy. From the static viewpoint, an iteration method to optimize the high bending stresses in the leanback vanes and to control the radial/axial disk growths are equally important.

The complexity of the analytical results has been explored in earlier work using finite element substructuring techniques (3), in which a unique segment model was used to evaluate the vibration modes. This paper presents a procedure that will achieve a greater overall degree of accuracy. Various mathematical models are formulated to cover the requirements needed in different analyses.

Holography has been utilized as a means for measuring the dynamic behavior of this engine component. The experimental measurements of natural frequencies and modes were used for verification of the theoretical analysis. Comparison between the results shows a good agreement.

FINITE ELEMENT ANALYSIS

Method of Analysis

In view of the multiple requirements for analyzing the impeller design, it is felt that a finite element technique which uses various types of models and elements will best suit the different needs for different analyses. This could provide a more effective tool for preliminary stress/dynamics assessments as well as in the final design. The approaches used are outlined as follows together with detailed illustrations given in the appropriate sections.

The overall impeller static stress pattern resulting from centrifugal and thermal loadings is determined by using a two-dimensional axisymmetric element model which combines the plate-like elements to represent the vane and disk geometry. This analysis offers a simple but accurate method of predicting the elastic as well as plastic deformations of the impeller disk.

The single full or split impeller vanes are essentially thin shell structures of complex geometry; structural modeling of a three-dimensional model using triangular/quadrilateral plate elements provides a logical tool for stress and vibration analyses. Differential stiffening effect and enforced root boundary conditions are included in the calculations through the NASTRAN program.

Rotational cyclic symmetry analysis, which uses a finite Fourier transformation method in NASTRAN, is employed to determine the impeller vane-disk coupled modes in the high frequency range, where the dynamic couplings are strong between the flexible back-plate and the blade trailing portion. The analysis needs to model only one identical segment of the impeller.

¹ Numbers in parenthesis designate references at the end of the paper.

Normal mode analysis will be performed to avoid occurrences of the impeller disk resonances, diametral or circumferential, in the operating range. An approach of using a model impeller sector including only the flexible back-plate and the exit of bladings has proved to be sufficient. The results compared with Holographic measurements are given herein.

IMPELLER STRESSES

Two-Dimensional Impeller Disk

The impeller disk stress analysis was performed by using a two-dimensional axisymmetric finite element computer program. The program has an ability to combine the axisymmetric elements with plate-like elements to calculate stress/temperature fields in the centrifugal impeller. The mechanical forces/displacements, thermal loads and normal stresses may be applied at nodes by specifying the corresponding values. The boundary-condition-string, a program optional feature, will automatically linearly interpolate the input values at the nodes along the boundary to save the input effort. For plastic analysis, an iterative procedure based on total deformation theory is used which allows the material to flow along the effective stress/strain curve until the applied loads are absorbed. This analysis permits the prediction of the stress/strain redistributions if the applied load exceeds the elastic limit of the material.

Figure 1 shows a two-dimensional mathematical impeller model which consists of a number of axisymmetric triangle / quadrilateral elements and the plane elements for a flat vane. The model uses relatively finer grid meshes in the region of anticipated high centrifugal stresses to achieve a good accuracy.

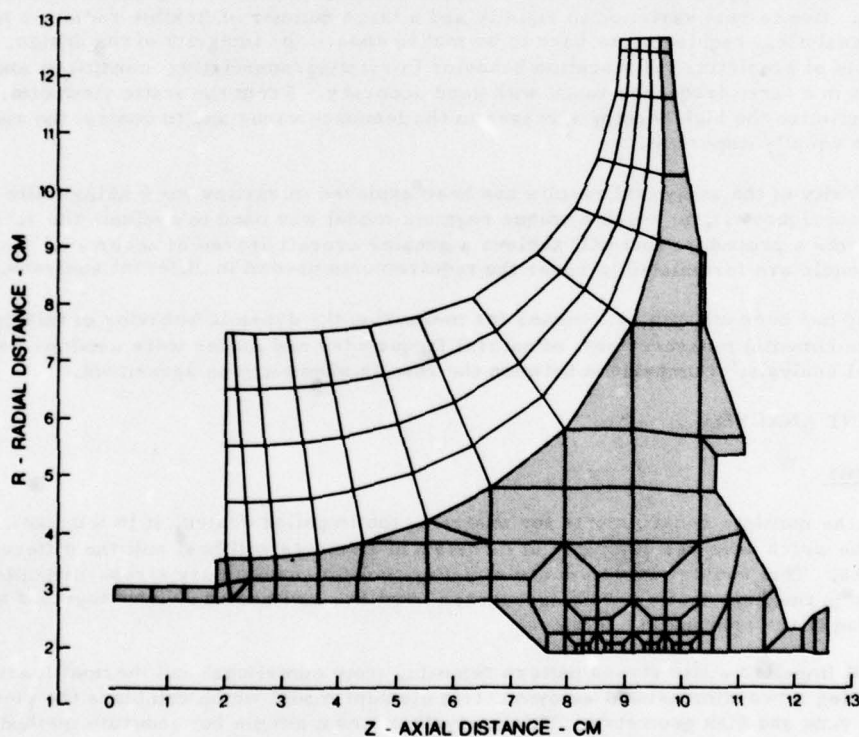


Figure 1. Impeller Structural Model (2-D)

The combined equivalent stress and in plane shear distribution of the given impeller are plotted in Figure 2. This is produced by a rotating speed of 48,000 rpm, and an overall temperature variation of 70° - 650°F on the disk. The noticeable disk radial growth and axial movement occurring on the impeller backplate are shown as solid lines in Figure 2.

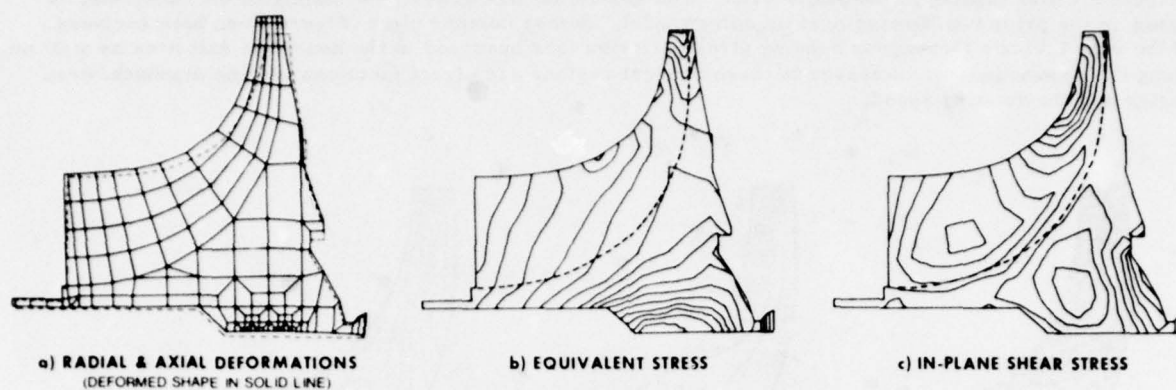


Figure 2. Impeller Deformed Shape and Stress Distribution

Three-Dimensional Single Vane

The success of an advanced impeller design becomes highly critical when the component contains nonradial and leanback vanes. Centrifugal stiffening and disk radial growth produce high bending stresses on the nonradial tip region and along the root boundary. The bending behavior of backward leaned impeller vanes cannot be accounted for by the preceding two-dimensional analysis since the finite element model considers the vane as a flat radial plate. To calculate the stresses accurately, it becomes necessary to formulate a separate three-dimensional single vane model including in and out of plane curvatures and finer meshes.

Figure 3 illustrates a finite plate element model adequately representing the complicated vane geometry. Modeling is accomplished by setting the grid points along the flow paths to represent the mid-surface of the structure and by interconnecting the grid points to form triangular finite plate elements. A three-dimensional cylindrical coordinate system is provided to define the rotational and translational degrees of freedom at each grid point.

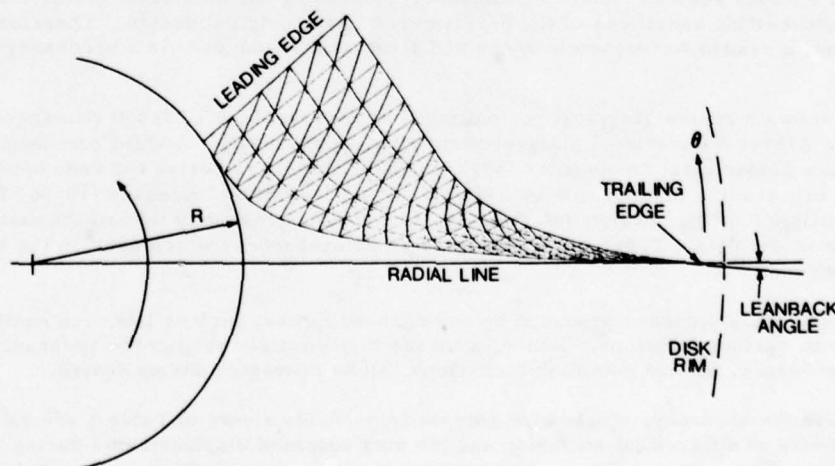
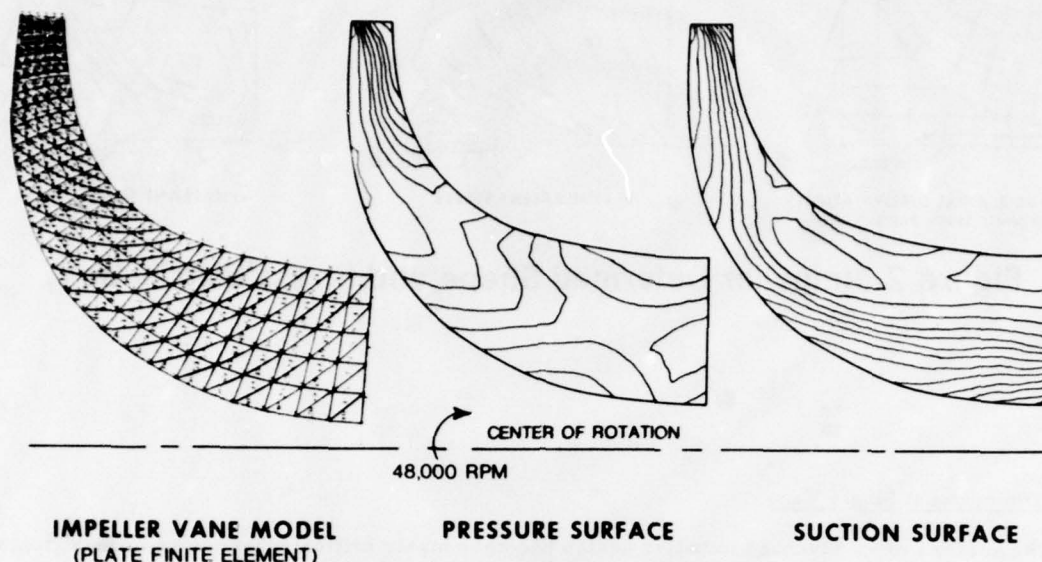


Figure 3. Axial View of a Single Vane Finite Element Model

The centrifugal stresses of the three-dimensional vane is performed using the NASTRAN program. The analysis includes the enforced deflections along the root boundary in the radial and axial directions to account for disk loading to the single vane. The amount of disk deflections mainly in the backplate, is based on the prior two-dimensional impeller model. Stress contour plots (Figure 4) on both surfaces of the vane indicate that higher bending stress distributions occurred in the nonradial exit area as well as along the root boundary. Stresses in these critical regions are direct functions of vane leanback/wrap angles and the rotating speed.



**Figure 4. Impeller Vane Steady Stress Distribution
Due to Centrifugal Load**

VIBRATION ANALYSIS

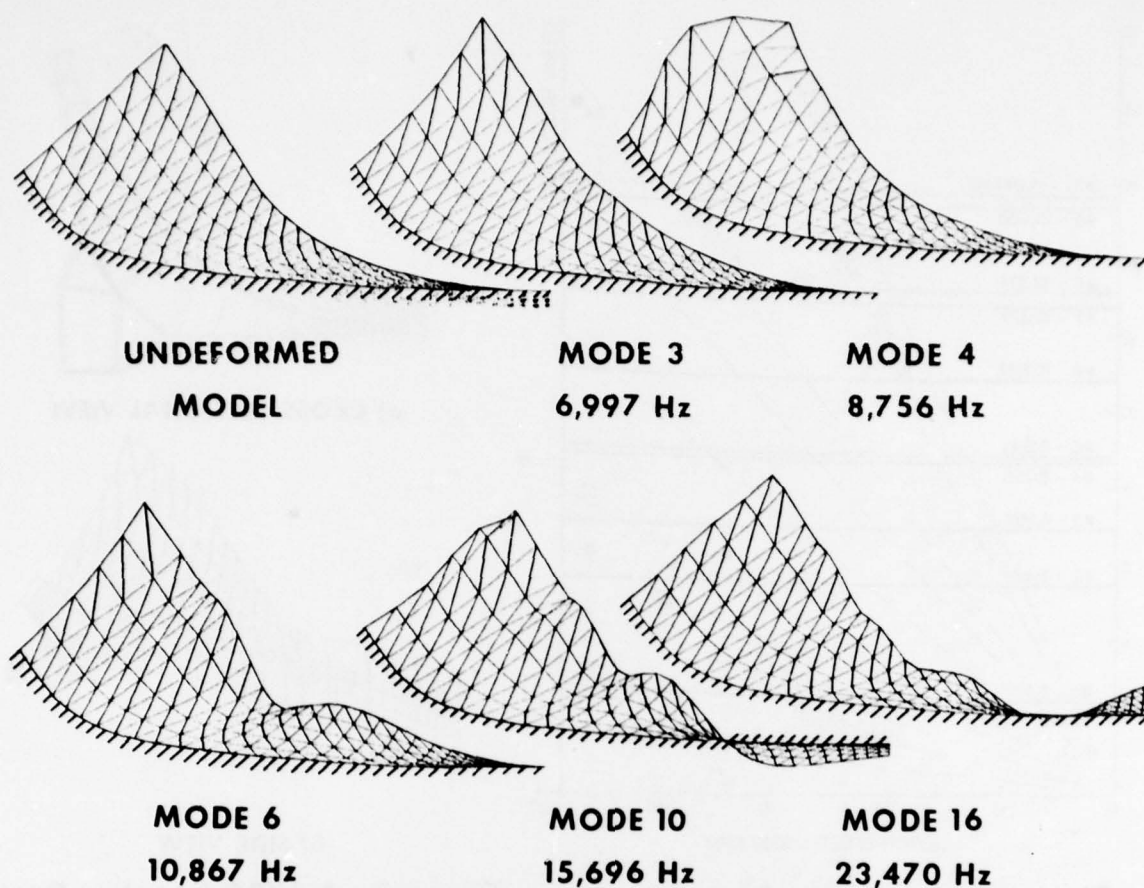
Single Vane Vibration

The flexible and nonlinear geometry of the impeller vanes have created numerous natural modes which can be excited by various sources of aerodynamic flow excitation in the operating range. Any structural modifications such as thickening the vane, decreasing the lean-back and/or the wrap angles are rarely without certain sacrifices of the performance of the original design. Therefore, an analytical method which optimizes the aerodynamic shape and structural soundness, is a necessary tool during the development.

Figure 5 shows a series of typical normal mode shapes (in the 0 - 23,500 Hz range) calculated by NASTRAN using a three-dimensional plate-element single vane model. A rigid root boundary is considered. The low fundamental frequencies (6997 Hz, 8756 Hz) characterize the vane bending modes of its leading tip, in a similar manner to a built-in plate. As frequency increases (10,867 Hz, 15,697 Hz, 23,470 Hz), multiple bending/torsion deformations advance progressively toward the exit of the vane as shown on higher mode plots. There are as many as 16 natural modes which exist in the specified range for a given long vane.

Any high vibratory stresses produced by any of these modes, high or low, can easily cause fatigue failures at various locations. Hence, a means to accurately predict the resonances at rotating conditions is necessary, so that potential excitations can be prevented during design.

To increase the accuracy, single vane natural frequencies shown in Table 1 are calculated by including the effects of differential stiffening and the disk enforced displacements during rotation. The percentage of frequency increase due to combined effects (case 3) is highest in the 1st bending (15.4%) but is less in higher modes (2 - 3%). When disk-enforced displacements are allowed in the axial and radial directions, stiffening effects are consistently greater than the vane with a rigid root boundary (case 2). The vane natural frequencies are also plotted in the excitation diagram (Figure 6) to show the rotating speed effect.



**TABLE 1 DIFFERENTIAL STIFFENING EFFECT
ON SINGLE VANE NATURAL FREQUENCIES
WITH/WITHOUT DISK DISPLACEMENT**

Mode No.	(1) $\Omega = 0$ RPM Rigid Vane Root	(2) $\Omega = 48,000$ RPM No Disk Displacement (Rigid Vane Root)	(2)/(1) %	(3) $\Omega = 48,000$ RPM With Disk Displacement Along Vane Root	(3)/(1) %
	Freq. - Hz	Freq. - Hz		Freq. - Hz	
1	2,494	2,869	15.0	2,878	15.4
2	5,487	5,689	3.7	5,735	4.5
3	6,997	7,118	1.7	7,213	3.0
4	8,756	8,822	0.7	9,009	2.9
5	8,841	9,139	3.4	9,156	3.6
6	10,867	10,870	0.	11,171	2.8
7	12,827	13,068	1.9	13,128	2.3
8	13,194	13,201	0.	13,607	3.1
9	15,420	15,623	1.3	15,748	2.1
10	15,696	15,750	0.3	16,206	3.3

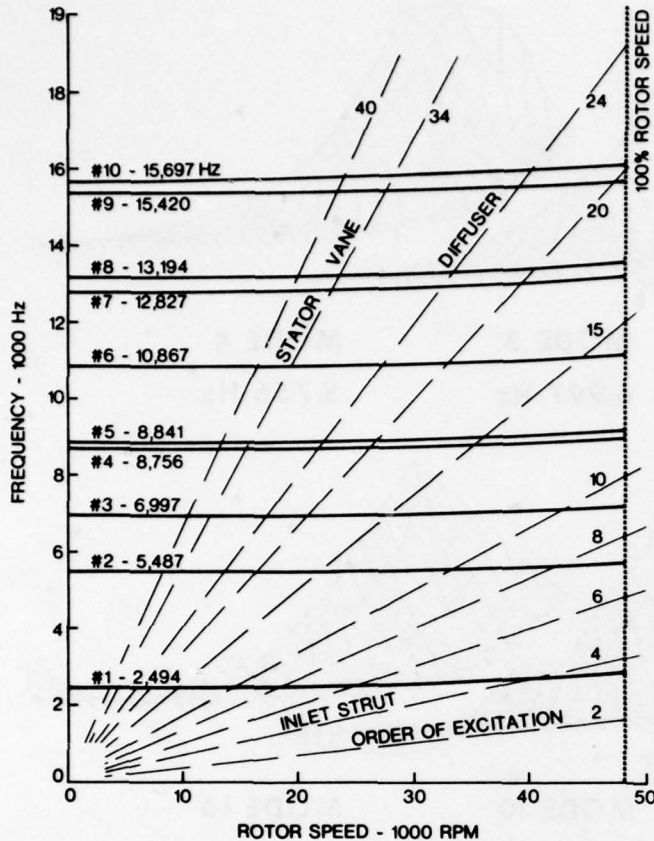
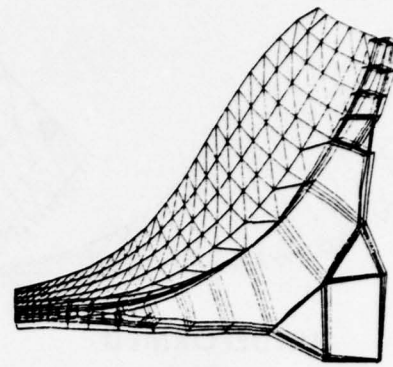
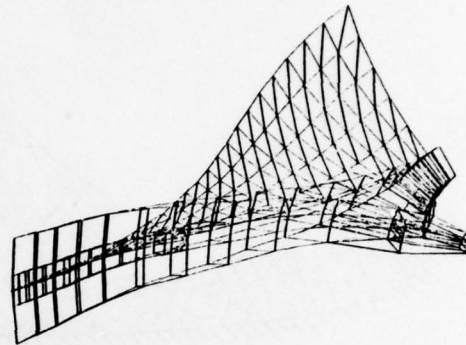


Figure 6. Excitation Diagram of Impeller Vane Showing Stiffening Effect



a) CROSS-SECTIONAL VIEW



b) SIDE VIEW

Figure 7. A 1/32 Impeller Sector Model Using Plate and Solid Elements

Vane-Disk Coupled Modes - Rotational Cyclic Symmetry Analysis

The centrifugal impeller is a rotating component composed of many identical vanes which are symmetrically arranged with respect to its rotational axis. To take advantage of this geometric feature, the capability of cyclic symmetry analysis in the NASTRAN can be utilized for static and dynamic analyses of the compressor. Since the application of the rotational symmetry will allow the analyst to model only one of the identical segment of the complex structure, it therefore becomes analytically feasible. The approach is demonstrated here for the impeller vibration problems.

The formulation of the cyclic symmetry analysis (4) is based on the mathematical treatment of the compatibility at the boundaries between segments. This is done by the "cyclic transformation", which linearly combines distortion effects into a single segment, so that it can be solved independently. The relationship of cyclic index (K) to the boundary constraints in a segment is illustrated in the Appendix by giving a numerical example.

A symmetrical model of 1/32 impeller segment (11.25°) was constructed. The chosen segment has the full vane centrally located with the finite element meshes connecting through the vane root and extending evenly by 5.625° on either side of the segment. Two different models were formed: one uses plate element for modeling the complete vane which is joined by the 6 and 8-node solid elements (Figure 7) as the impeller disk; the other uses plate elements throughout the segment (Figure 8). For simplicity the latter model is employed in the analysis. It contains a total of 360 grid points (180 on vane) and 1800 degrees of freedom. However, to reduce the computing effort, only those grid points on the vane trailing part and the corresponding backplate retain 5 degrees of freedom at each point; the remaining are all constrained.

The results of the cyclic symmetry analysis on the restrained model (Figure 8) are tabulated in Table 2. Among the seven (7) vane-disk modes generated, four (4) characterize disk vibration; three (3) are the vanes. The results obtained from separations of vane and disk (i.e., vane only; disk only) provide a confirmation for the cyclic symmetry analysis. The coupled modes, though not as strong, are plotted in Figure 8. Among the modes investigated, the 32 diametral (36,700 Hz) shows a high deflection around the disk rim, caused by sine-wave peak passing through each vane segment.

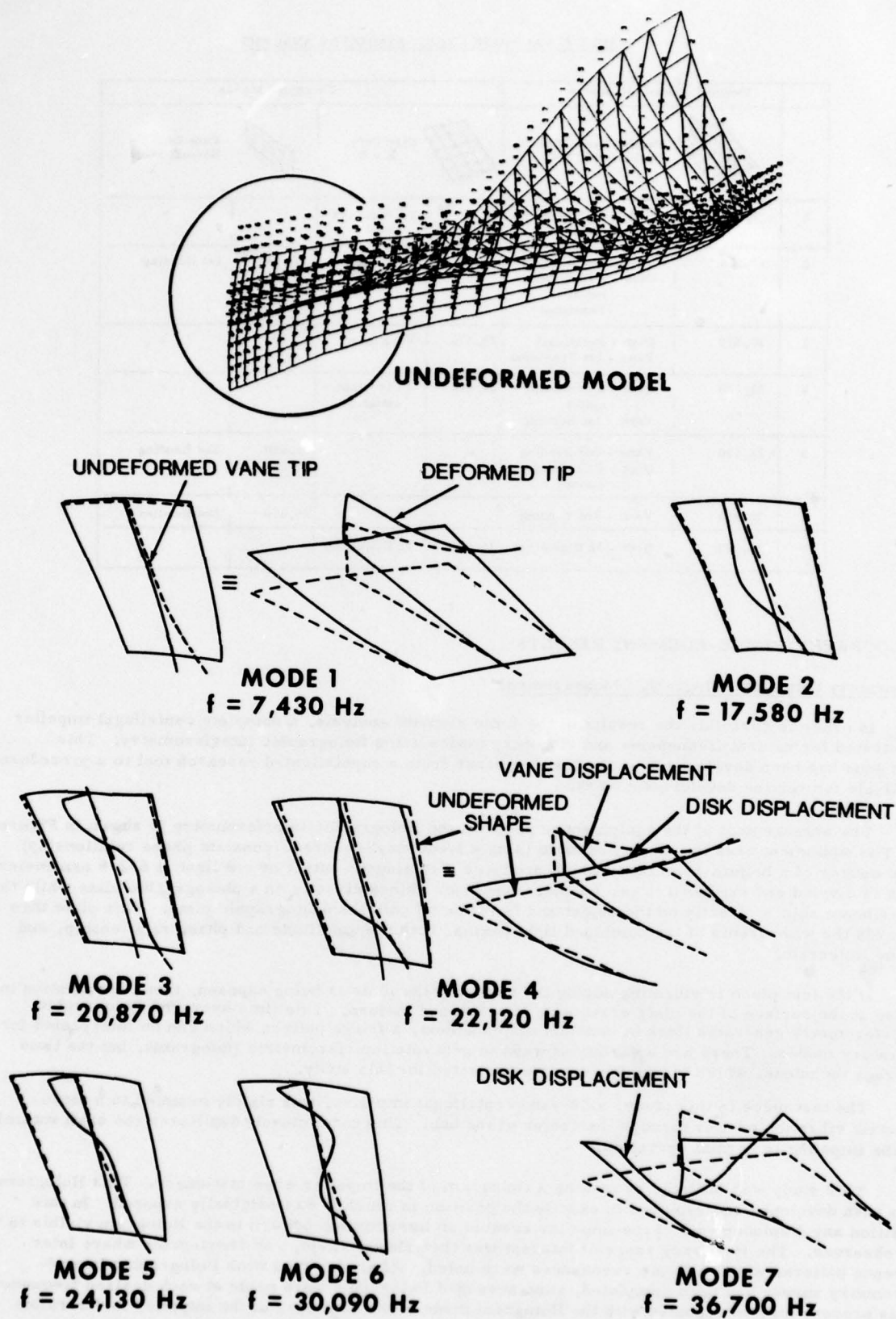
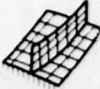
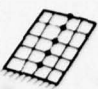
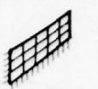


Figure 8. A 1/32 Impeller Sector Model Using Plate Elements and the Resulting Vane-Disk Modes

TABLE 2 VANE-DISK CYCLIC SYMMETRY ANALYSIS

	Coupled Vane-Disk Modes			Uncoupled Modes		
		Partial Vane-Disk Cyclic Index K=0		Disk Only K = 0		Vane Only Normal Mode
1	7,430 Hz	Disk - 1 Circumferential	7,460 Hz	1 Circumferential	-	-
2	17,580	Vane - 1st Bending Disk - 2 Circumferential + Torsional	-	-	18,930 Hz	1st Bending
3	20,870	Disk - Rotational Vane - 1st Torsional	20,970	Rotational	-	-
4	22,120	Disk - 2 Circumferential Vane - 1st Bending	22,010	2 Circumferential	-	-
5	24,130	Vane - 2nd Bending Disk - 2 Circumferential	-	-	23,550	2nd Bending
6	30,690	Vane - 3rd Bending	-	-	30,670	3rd Bending
7	36,700	Disk - 32 Diametral	36,600	32 Diametral	-	-

HOLOGRAPHY/FINITE-ELEMENT RESULTS

Laboratory Setup for Holographic Measurement

In order to correlate the results of the finite element analysis, a complete centrifugal impeller was tested for natural frequencies and vibratory modes using Holographic interferometry. This technique has been developed over the last ten years from a sophisticated research tool to a procedure available for routine development work.

The arrangement of the equipment to perform the Holographic interferometry is shown in Figure 9. The equipment uses the monochromatic (single frequency) coherent (constant phase relationship) light source of a helium-neon laser which produces a continuous output of red light at 632.8 nanometers. This is divided and expanded in two beams. One beam shines directly on a photographic plate while the other beam shines directly on the object and is reflected onto the photographic plate. This plate then records the wave fronts of the combined light beams, both the amplitude and phase relationship, and is the Hologram.

If the test piece is vibrating during the time that the plate is being exposed, then the variation in phase at the surface of the plate creates an interference pattern. This time averaged Holographic interferometry generates lines of constant displacement, a fringe pattern which can be interpreted for vibratory modes. There are a variety of ways to generate interferometric Holograms, but the time average technique, which is widely used, was selected for this study.

The test piece in this study, a 32-vane centrifugal impeller, was rigidly mounted to a piezo-electric vibration exciter through the center of the hub. This most closely duplicates the shaft mounting of the impeller in normal operation.

This study was initiated by making a Hologram of the impeller when stationary. This Hologram was then developed and replaced in exactly the position in which it was originally exposed. In this position any displacements of the impeller created an interference pattern in the Hologram visible to an observer. The frequency range of interest was then slowly swept, and frequencies where interference patterns which indicate resonances were noted. After this real time Holographic interferometry survey had been completed, time averaged Holograms were made at each desired frequency. This process may be repeated with the Hologram made of the rear face of the impeller to determine modes which include displacements of the rear face.

After all the desired Holograms were made, then each was illuminated with the laser and photographed by conventional means. These reconstructed Holograms are available for convenient study.

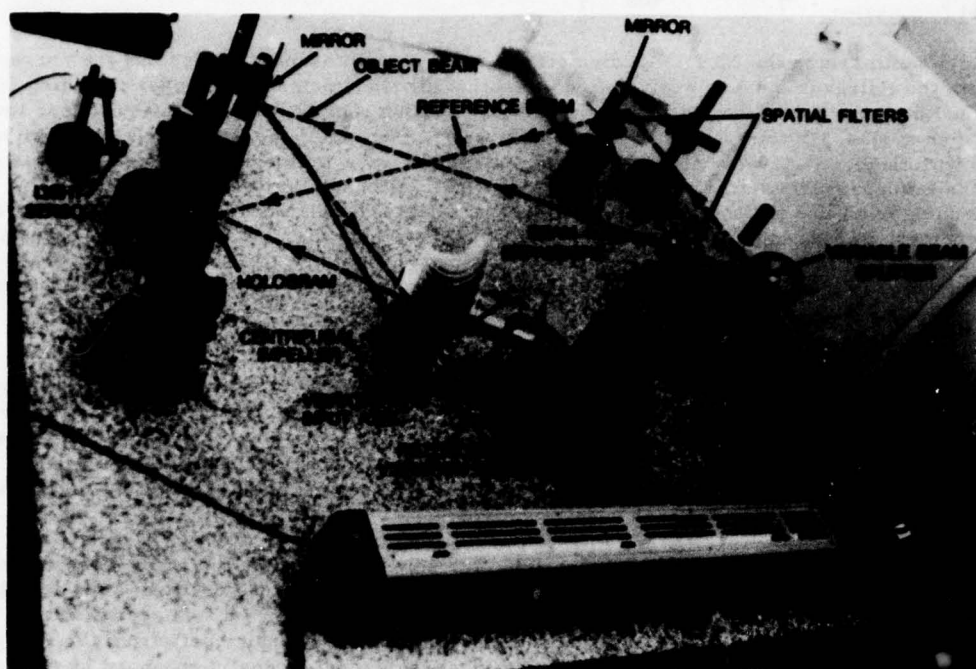


Figure 9. Set-up for Holographic Measurement

Impeller Sector Model

The impeller investigated has a geometry that consists of 32 thin, curved full vanes which are integrally cast with a relatively solid cylindrical hub and a flexible circular backplate. The average thickness at the disk rim (O.D. 22.352 cm) is approximately equal to that of the vanes at the trailing tip (.1524 cm). The primary objective of the analysis and the Holography measurement is to determine the various disk natural frequencies and modes of the flexible circular backplate where the vibration of the disk has potential coupling with the trailing tip of the connecting blades. This information is not available from the previous single vane calculations.

A simplified impeller disk model of a quarter sector (Figure 10) which consists of flexible backplate and approximately 1/3 of each full vane over the downstream side will suit the purpose for this investigation. The finite plate element model, referred to a cylindrical coordinate system (R, θ, Z), contains translational and rotational degrees of freedom at each grid point. The model considers a simply supported constraint around the disk's inner circle, and assumes a boundary condition along the disk radius such as $T_R = T_\theta = \theta_R = 0$, which forces the nodal lines to form at a desirable location. Previous analysis of flexible disks (2) yields good results by using similar assumptions.

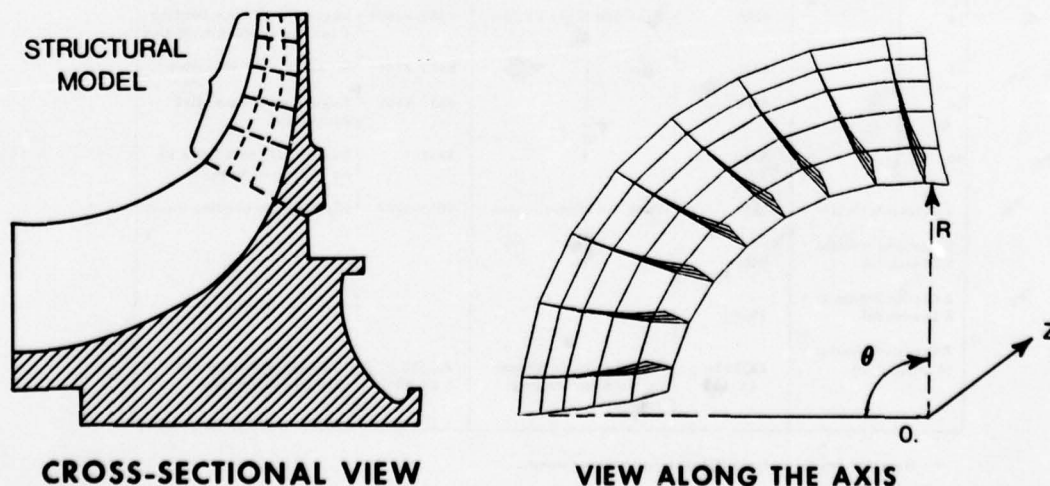


Figure 10. A 90° Impeller Sector Model with Backplate Included

Results and Discussions

Table 3 summarizes the NASTRAN diametral and/or circumferential modes and the corresponding results from the Holograms. The analysis indicates that all fundamental disk modes including 16 diametral and higher exist in the frequency range below 10,000 Hz. Figure 11 shows the four lowest analytical disk modes. In this region there are only a few low bending modes of the vane which may be coupled with them. Vane natural modes shown in Table 3 were previously analyzed; they correlate well with the Hologram fringe patterns of a vibrating disk. Although the association of the vane motions (leading part) are visible from the fundamental disk modes in the majority of the Holograms, the close numerical agreement between the two analyses suggests that the strength of coupling is really insignificant in the frequency range. The variation shown on the measured frequencies is believed attributed to the variation of mechanical tolerances among the bladings and the high sensitivity of the Holography. Holographic modal patterns of 6 diametral and complex modes are shown in Figures 12 and 13 respectively.

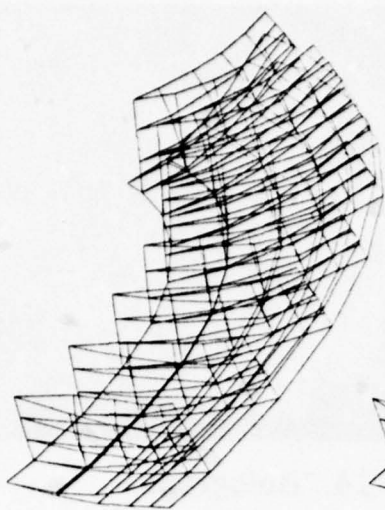
Complex modes, which begin at frequencies beyond 20,000 Hz with the periodic traveling wave around the disk rim, produced by multiple diametral modes, have strong association with the vane trailing tip. Figure 14 illustrates multiple modes of this nature. The strong coupling can impose additional vibratory stresses on the statically already critical region of a leanback vane design. The effect of full vane grouping could cause variations among the analyses, since theoretical modeling includes only the trailing portion of each vane.

An analysis covering a small sector of an impeller helps to minimize the occurrence of multiple modes over a finite frequency range. The confusion of the multiple modes resulting from the vibration of the flexible blading at the upstream side is avoided in the analytical model to a great extent. The calculated results have also been used as a guide to sorting out the extensive data from the Holographic measurements. The interpretation of the measured frequencies and modes is enhanced by the comparison with analytical results which are mainly the disk modes, and by the experience gained from the single vane analysis. The investigation could provide a useful baseline for further rotational symmetry analysis of an impeller as demonstrated above.

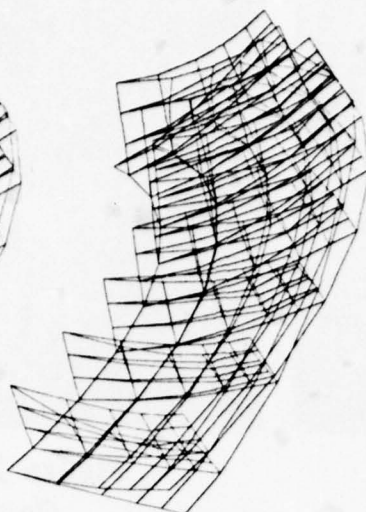
TABLE 3 THEORETICAL/EXPERIMENTAL NATURAL MODES COMPARISONS

Basic Disk Modes	Finite Element (NASTRAN)		Holography Measurement	
	Freq. - Hz	Primary Vane Mode	Freq. - Hz	Associated Vane Motion
1 Circumferential	5370	Vane 1st Mode Region	5444	Vane (L. E.) moving with disk
1 Diametral	5410	↓	- *	
2	5440	Vane 2nd Mode Region	5252	Coupled vane corner bending
3	5500	↓	5317-5326	Coupled vane corner bending
4	5625	↓	-	
5	5860	↓	-	
6	6220	↓	6167	Strong disk mode; no vane motion
12	8220	Vane 3rd Mode Region	8288-8360	Beginning of vane bending - torsion coupled with disk
13	8490	↓	8379-8349	Stronger vane vibration
14	8700	↓	8535-8606	Beginning of vane-disk decoupling
16	8890	↓	8852	Disk mode; with little or no motion of vane
2 Circumferential	9350	Vane 4th Mode Region	9258-9273	Higher vane bending mode
2 Circumferential + 1 Diametral	9460	↓	-	
2 Circumferential + 2 Diametral	9540	↓	-	
2 Circumferential + 16 Diametral	22,500-23,100	Complex mode shown on the vane trailing region	20,530-24,500	Complex deformations throughout the vane

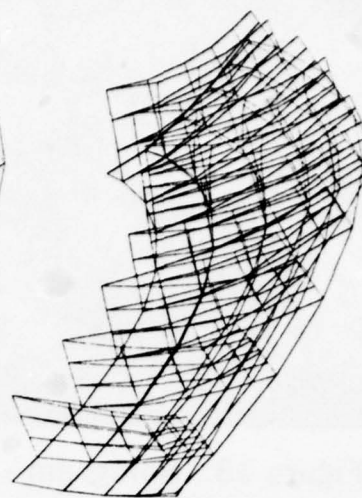
* - Data not available from Holographic measurement.



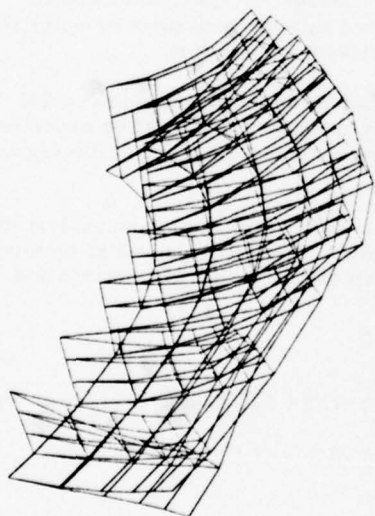
MODE 1 - 5,370 Hz
1 CIRCUMFERENTIAL



MODE 2 - 5,410 Hz
1 DIAMETRAL



MODE 3 - 5,440 Hz
2 DIAMETRAL



MODE 4 - 5,500 Hz
3 DIAMETRAL

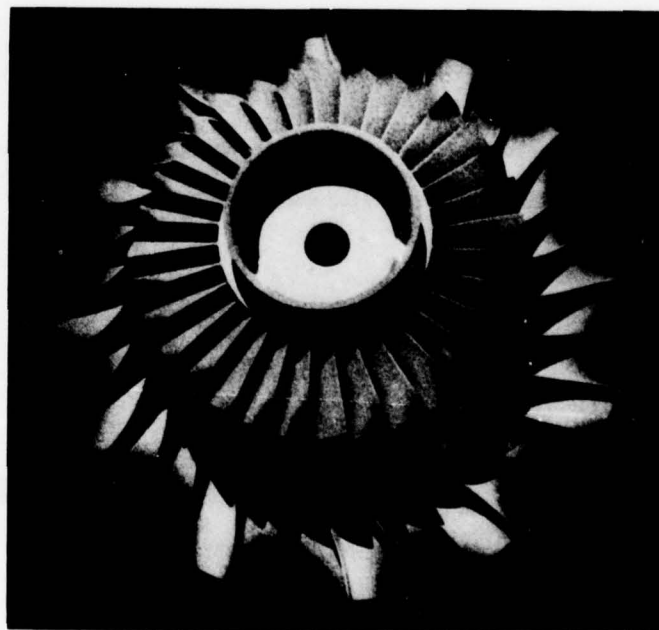
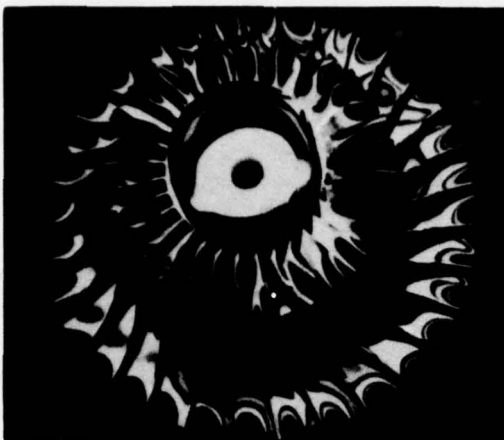


Figure 12. Hologram -
6 Diametral, 6167 Hz

Figure 11. Basic Modes of
the 90° Impeller Sector Model



**Figure 13. Hologram -
Complex Mode
(16 Diam + 2 Circ + Vane)
20,535 Hz**



**Figure 14. Hologram -
Complex Mode
(16 Diam + 2 Circ + Vane)
20,517 Hz**

CONCLUDING REMARKS

Various finite-element structural analysis techniques have been demonstrated in this paper for improving the overall analytical accuracies in the design of advanced impellers. Correlation between theoretical and experimental results has been established to be good.

The single vane modeling approach has provided an effective means for static and dynamic analyses with good accuracy. The same model can simply be joined by additional plate or solid elements to formulate an impeller segment for cyclic symmetry analysis without much effort.

Any partial frequency range selection, by specifying the order of cyclic index in the cyclic symmetry analysis, can result in elimination of pertinent dynamic modes. Care must be exercised to avoid this pitfall. An understanding of the mathematical treatment on the boundary of the segment due to different indices is helpful.

Complex coupled modes recorded in the Hologram provide a valuable image for an analyst to visualize the structural characteristics in various frequency ranges. Theoretical results, however, establish the baselines for sorting out the multiple modes shown up during the measurements and provide a valuable design tool.

REFERENCES

1. Kuo, P. S., "Blade Dynamics Analysis Using NASTRAN", NASA TM X2893, September 1973.
2. Kuo, P. S., "Finite Element Approach to the Vibration Analysis of Elastic Disks on a Flexible Shaft", ASME 75-GT-57, December 1975.
3. Mak, S. W., Botman M., "Substructures Analysis of Impeller Vibration Modes", ASME 75-DET-112, June 1975.
4. MacNeal, R. H., Harder, R. L., Mason, J. B., "NASTRAN Cyclic Symmetry Capability", NASA TM X-2893, September 1973.

APPENDIX

Theoretical Background

Rotational Transformation (4) between the structural segments is governed by the equation:

$$u^n = \bar{u}^0 + \sum_{k=1}^{K_L} \bar{u}^{kc} \cos (n-1) ka + \bar{u}^{ks} \sin (n-1) ka + (-1)^{n-1} \bar{u}^{N/2}$$

Where:

$n = 1, 2, \dots, N = \text{number of segment}$

$K = \text{Cyclic index; } K_L \ll \frac{N}{2}$ is the limit of K

$u^n = \text{A physical variable (displacement, load, stress, etc.) in the } n\text{th segment}$

$$\left. \begin{array}{l} \bar{u}^0 \\ \bar{u}^{kc} \\ \bar{u}^{ks} \end{array} \right\} = \text{Symmetrical components (cyclic coefficients) used in the solution which define the entire structure}$$

$a = 2\pi/N = \text{circumferential angle for each segment}$

Note: Dynamics analysis is performed individually for each harmonic index K ; for static analysis the calculation proceeds as a summation of every value of K index from zero to K_L .

In the rotational symmetry analysis, the dependent displacements (side 2 of the model) are related to the independent displacements (side 1) by the following equations of constraint.

$$\left. \begin{array}{l} \bar{u}_2^0 = \bar{u}_1^0 \\ \bar{u}_2^{kc} = \bar{u}_1^{kc} \cos ka + \bar{u}_1^{ks} \sin ka \\ \bar{u}_2^{ks} = -\bar{u}_1^{kc} \sin ka + \bar{u}_1^{ks} \cos ka \\ \bar{u}_2^{N/2} = \bar{u}_1^{N/2} \end{array} \right\} K = 1, \dots, K_L$$

Equations above are the equations of boundary constraint for the symmetrical components. The only symmetrical components coupled by the compatibility constraints are 1c and 1s, 2c and 2s, etc. Thus, for a 90° segment model ($N = 4$, $a = \pi/2$), the compatibility constraints for each cyclic index are:

$$\begin{array}{ll} K = 0, & \bar{u}_2 = \bar{u}_1 \\ K = 1, & \begin{array}{l} \bar{u}_2^{1c} = \bar{u}_1^{1s} \\ \bar{u}_2^{1s} = -\bar{u}_1^{1c} \end{array} \\ K = 2, & \begin{array}{l} \bar{u}_2^{2c} = -\bar{u}_1^{2c} \\ \bar{u}_2^{2s} = -\bar{u}_1^{2s} \end{array} \\ K = 3, & \begin{array}{l} \bar{u}_2^{3c} = -\bar{u}_1^{3s} \\ \bar{u}_2^{3s} = \bar{u}_1^{3c} \end{array} \end{array}$$

$K = 4$, is identical to $K = 0$ since $Ka = 2\pi = 0$.

From the compatibility constraint relations, it can be seen that the selection of each K index pre-determines the vibration modes which may occur in the entire structural model. This is illustrated in the numerical examples given below.









Numerical Example

A 90° segment model of a circular flat plate was investigated using Rotational Cyclic Symmetry Method (NASTRAN RIGID FORMAT 15). In this demonstration problem, normal modes were obtained in the frequency range 0 to 7,000 Hz for each cyclic index $K = 0, 1$ and 2. The model was restrained against radial and rotational displacements to limit the solution to the 'diametral' and 'circumferential' modes only.

The results are summarized in Table 1 together with displacement plots in Figure 1 for $K = 0$.

TABLE 1. SUMMARY OF CYCLIC SYMMETRY NORMAL MODES
A 90° SEGMENT MODEL

$a = \frac{\pi}{2}$, N (SEG) = 4, K (INDEX) = 1,2,3, F (FREQ) = 0.~7000 Hz

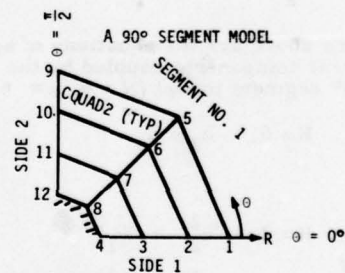
MODE NO. & SHAPE	f (Hz)	K (INDEX)	CIRC MODE	DIAM MODE
1 	939	0	1st	NONE
2 	1017	1	1st	1st
3 	1226	2	1st	2nd
4 	1744	1	1st	3rd
5 	2308	0	1st	4th
6 	5388	0	2nd	NONE
7 	5756	1	2nd	1st
8 	6615	2	2nd	2nd

NOTE: NO MODES EXIST FOR KINDEX = 3 IN THE 90° MODEL CONFIGURATION

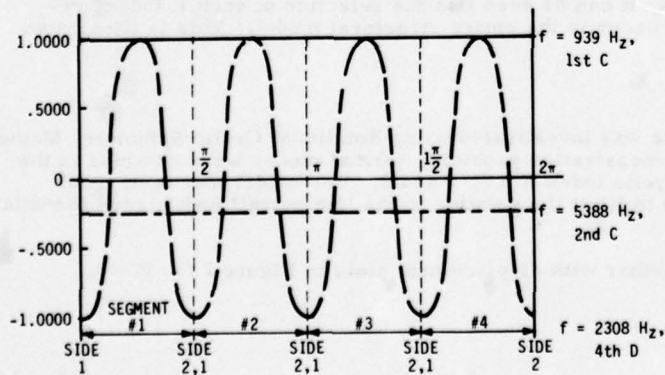
FOR K = 0

a) CALCULATED EIGENVALUES & EIGENVECTORS

GRID	f = 939	2308	5388
	\bar{u}^0	\bar{u}^0	\bar{u}^0
1	1.0000	-1.0000	-0.2770
5	1.0000	1.0000	-0.2770
9	1.0000	-1.0000	-0.2770
2	0.5700	-0.5667	0.2295
3	0.1841	-0.1858	0.2455



b) CIRCUMFERENTIAL PLOT OF VERTICAL DISPLACEMENT



c) RADIAL PLOT ALONG $\theta=0^\circ$

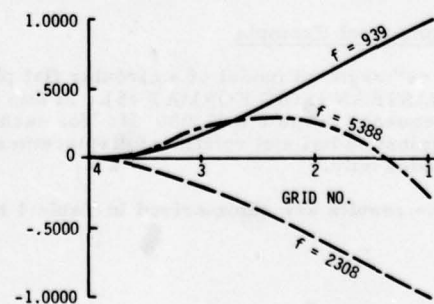


Figure 1. Deformation Plots of the Entire Structural Model (K = 0)

DISCUSSION

S.Gupta, Canada

In the case of 3-D single vane analysis, what boundary conditions were used at the vane-disk junction?

Author's Reply

In the stress/dynamic analyses of the 3-D single vane, the boundary condition considered includes the radial and axial enforced displacements calculated from the previous 2-D disc model, the remaining d.o.f. along the vane-disc junction are all constrained.

A.F.Storage, US

Did you use a different sequence number (K) for centrifugal stiffening effects?

Author's Reply

In the vane-disc segment models for the cyclic symmetry analysis, the differential stiffening effect was not included in the calculation. However, the DMAP alter sequence was under preparation for NASTRAM runs, the initial result was checked out by a simple circular disc model using plate elements. The centrifugal load is applied to the entire structure as a static case prior to the dynamic analysis, therefore different cyclic index (K) is not needed at that stage.

ANALYSE DES VIBRATIONS DE MOTEUR

Michel LALANNE	Professeur
Philippe TROMPETTE	Maître-Assistant
Rémy HENRY	Maître-Assistant
Guy FERRARIS	Ingénieur de Recherche

I.N.S.A. - Laboratoire de Mécanique des Structures
20, avenue Albert Einstein
69621 Villeurbanne - France

RESUME

Le contrôle des vibrations d'une structure s'effectue généralement au stade du projet par la détermination théorique des fréquences et modes. Les éléments principaux d'un moteur d'avion peuvent pratiquement être classés en 3 catégories : compresseur - chambre de combustion - turbine.

Ces éléments sont fixés ou en rotation et sont alors soumis à l'effet de Coriolis et à un raidissement supplémentaire introduit par la force centrifuge.

On présente ici une revue succincte du calcul des aubes minces et épaisses, des systèmes axisymétriques en rotation, et des ensembles disque-aubes.

Une fois le prototype du moteur réalisé il peut subsister des fréquences gênantes et au lieu d'effectuer des modifications de la structure destinées à déplacer ces fréquences on peut chercher à utiliser des matériaux amortissants entraînant une réduction suffisante de l'amplitude de résonance. Le calcul de ces types de structures amorties est esquissé.

La méthode numérique employée est celle des éléments finis. Les divers types de calcul : recherche des fréquences et modes, prédiction de l'amortissement introduit par l'adjonction du matériau sont illustrés par des applications à des éléments de moteur.

INTRODUCTION

L'aéronautique qui est à l'origine de bien des progrès de la technologie exige actuellement la mise au point de moteurs performants et sûrs. Les constructeurs sont donc intéressés par toute prévision susceptible de leur permettre un gain de poids, de performance et de durée de vie sans perte de sécurité.

Un moteur comprend schématiquement trois parties :

- a) la partie compresseur avec soufflante et étages basse et haute pression,
- b) la chambre de combustion généralement annulaire,
- c) la partie turbine avec étages haute et basse pression.

La soufflante et les étages de compresseur sont entraînés par des étages de turbine et reliés entre eux par des arbres ou tambours. Les parties mobiles tournent à des vitesses de rotation élevées de l'ordre de 10000 à 20000 tr/mn et plus pour le corps haute pression.

Les possibilités d'excitation par des forces ou des déplacements imposés à la structure sont nombreuses et une bonne appréciation de la durée de vie du moteur passe obligatoirement par une étude structurale fine. L'ingénieur doit donc essayer de prévoir le comportement dynamique des structures de manière à pouvoir les dimensionner convenablement ou à les modifier si une fois construites elles présentent des caractéristiques dynamiques gênantes.

Le problème majeur est d'éviter les vibrations sources de rupture par fatigue. Pour les parties tournantes vient s'ajouter le problème de dimensionnement aux contraintes centrifuges dues à la rotation.

Les possibilités d'analyse prévisionnelle du comportement statique et dynamique des structures mécaniques ont connu ces dernières années un développement considérable étroitement associé au développement des méthodes numériques. En effet, si sur le plan de l'écriture des équations peu ou rien n'a changé, par contre, sur le plan de leur traitement, l'analyse numérique et le développement des ordinateurs ont permis des progrès considérables. En particulier, en mécanique des structures, on utilise avec succès les possibilités offertes par la méthode des éléments finis. Elle permet par exemple de connaître avec précision les fréquences et modes d'un système complexe. Son rôle prévisionnel étant établi, la question est de savoir quelles démarches effectuer lorsque l'on rencontre dans les conditions de fonctionnement des fréquences susceptibles d'occasionner de graves dommages. Jusqu'à une période récente, les possibilités technologiques pouvaient se classer en deux catégories : ou modifier les valeurs des fréquences de résonance de la structure par adjonction ou enlèvement de matériau ou placer des étouffeurs de vibration. Ces deux solutions ont chacune leurs inconvénients : la première conduit très souvent à une augmentation de masse, dommageable sur le plan du rendement, la seconde entraîne le déplacement d'une ou plusieurs fréquences.

Depuis peu des recherches s'orientent vers l'utilisation de matériaux permettant d'introduire un amortissement important dans la structure des facteurs de surtension pour une large gamme de fréquences. Les problèmes posés par l'usage de ces matériaux sont encore nombreux, essentiellement liés à leurs caractéristiques mécaniques très variables en fonction de la température et de la fréquence, à leur résistance encore mal connue au vieillissement, à la fatigue et aux agents chimiques extérieurs.

L'objet de cette publication est de montrer quelques applications pratiques significatives des possibilités actuelles du calcul prévisionnel par éléments finis sur les moteurs d'avions.

On va présenter les paragraphes suivants :

- Mise en équations,
- Aubes de compresseurs,
- Liaison entre les étages compresseurs et turbines,
- Aubes de turbine,

- Ensembles disque-aubes,
- Amortissement sans effet de rotation.

MISE EN EQUATIONS

a) Structures en rotation

On présente ici très brièvement la manière dont sont établies les équations différentielles du comportement d'une structure en rotation.

D'une manière générale on calcule l'énergie cinétique T et l'énergie potentielle U de déformation. Les calculs sont effectués dans un repère lié au solide en rotation et les termes du second ordre sont introduits dans les relations déplacements-déformations, ce qui permet de faire intervenir les effets de rotation. La méthode des éléments finis est utilisée comme méthode numérique et les déplacements nodaux δ sont alors des coordonnées généralisées. On applique ensuite les équations de Lagrange [1] :

$$\frac{d}{dt} \left(\frac{\partial T}{\partial \dot{\delta}} \right) - \frac{\partial T}{\partial \delta} + \frac{\partial U}{\partial \delta} = 0 \quad (1)$$

Par définition :

$$T = \frac{1}{2} \int_{\tau} \rho \cdot v^t \cdot v \cdot d\tau \quad (2)$$

avec :

ρ , masse volumique
 v , vitesse

La structure est discrétisée et les termes de l'Eq(1) deviennent :

$$\frac{d}{dt} \left(\frac{\partial T}{\partial \dot{\delta}} \right) - \frac{\partial T}{\partial \delta} = M \dot{\delta} \dot{\delta} + C \dot{\delta} \dot{\delta} - \Omega^2 M_G \delta - F(\Omega^2) \quad (3)$$

avec :

M , matrice de masse
 C , matrice de Coriolis
 $-\Omega^2 M_G$, matrice de raideur supplémentaire
 $F(\Omega^2)$, force centrifuge

L'énergie potentielle s'écrit :

$$U = \frac{1}{2} \int_{\tau} \epsilon^t \cdot \sigma \cdot d\tau \quad (4)$$

avec :

ϵ , vecteur des déformations
 σ , vecteur des contraintes

Les contraintes et déformations sont reliées par :

$$\sigma = D \cdot \epsilon \quad (5)$$

D , matrice symétrique fonction des caractéristiques des matériaux.

D'où :

$$U = \frac{1}{2} \int_{\tau} \epsilon^t \cdot D \cdot \epsilon \cdot d\tau \quad (6)$$

On introduit les termes non linéaires dans ϵ :

$$\epsilon = \epsilon_l + \epsilon_{nl} \quad (7)$$

d'où il vient pour U :

$$U = \frac{1}{2} \int_{\tau} \epsilon_l^t \cdot D \cdot \epsilon_l \cdot d\tau + \int_{\tau} \epsilon_{nl}^t \cdot D \cdot \epsilon_l \cdot d\tau + \frac{1}{2} \int_{\tau} \epsilon_{nl}^t \cdot D \cdot \epsilon_{nl} \cdot d\tau \quad (8)$$

En faisant intervenir les contraintes initiales $\sigma_0 = D \cdot \epsilon_l$ et en négligeant la 3^e intégrale qui est d'ordre supérieur, l'Eq(8) se réduit à :

$$U = \frac{1}{2} \int_{\tau} \epsilon_l^t \cdot D \cdot \epsilon_l \cdot d\tau + \int_{\tau} \epsilon_{nl}^t \cdot \sigma_0 \cdot d\tau \quad (9)$$

On en tire :

$$\frac{\partial U}{\partial \delta} = K \delta + K_G(\sigma_0) \cdot \delta \quad (10)$$

avec :

K , matrice de raideur
 $K_G(\sigma_0)$, matrice de raideur des contraintes initiales σ_0

A partir des Eqs(1), (3), (11), on obtient le système différentiel qui traduit le comportement de la structure en rotation :

$$M \dot{\delta} \dot{\delta} + C \dot{\delta} \dot{\delta} + (K + K_G(\sigma_0) - \Omega^2 M_G) \delta = F(\Omega^2) \quad (11)$$

On suppose l'effet de Coriolis négligeable et on pose :

$$\delta = \delta_0 + \delta_1 \quad (12)$$

où δ_0 est solution de :

$$(K + K_G(\sigma_0) - \Omega^2 M_G) \delta_0 = F(\Omega^2) \quad (13)$$

Le système matriciel (13) est résolu par un processus itératif type Newton-Raphson.

Ensuite δ_1 satisfait à :

$$M\delta''_1 + (K + K_G(\sigma_0) - \Omega^2 M_G)\delta_1 = 0 \quad (14)$$

On recherche alors δ_1 sous la forme :

$$\delta_1 = \delta_{10} e^{j\omega t} \quad (15)$$

qui reporté dans l'Eq(14) fournit l'équation aux valeurs propres :

$$\omega^2 M \delta_{10} = (K + K_G(\sigma_0) - \Omega^2 M_G) \delta_{10} \quad (16)$$

dont les couples solution ω_i , δ_{10i} sont recherchés par itérations simultanées.

Dans le cas de structures axisymétriques [2], [3] les fonctions de déplacement ont prises sous la forme de développements en série de fonctions trigonométriques sinus, cosinus de l'angle polaire. Ces fonctions étant orthogonales dans l'intervalle $0-2\pi$, on aboutit à un ensemble de systèmes différentiels découplés établis pour chaque valeur de l'ordre n de la série trigonométrique. En particulier pour $n = 0$ le mouvement est symétrique et on a :

$$M_0 \delta''_0 + (K_0 + K_{G0}(\sigma_0) - \Omega^2 M_{G0}) \delta_0 = F(\Omega^2) \quad (17)$$

qui en procédant comme pour le système (13) permet de déterminer δ_0 et σ_0 ainsi que les fréquences et modes symétriques.

On aboutit ensuite pour $n \neq 0$ à :

$$M_n \delta''_n + (K_n + K_{Gn}(\sigma_0) - \Omega^2 M_{Gn}) \delta_n = 0 \quad (18)$$

Le traitement du système (18) est identique à celui défini par (13).

Dans le cas des ensembles disque-aubes [4], on observe si les aubes sont assez nombreuses un comportement analogue à celui des structures axisymétriques. On démontre qu'il faut ajouter aux énergies potentielle et cinétique du disque celles d'une aube multipliée par $N/2$, [2] avec N , nombre d'aubes.

b) Structures amorties

Dans la seconde partie de cet exposé on aborde le problème du contrôle des vibrations par l'utilisation de matériaux amortissants [5] et l'application à l'aéronautique [6]. On rappelle ici le principe d'obtention des équations.

Si la structure, en notation complexe, est soumise à un ensemble de forces :

$$F = F_0 e^{j\Omega t} \quad (19)$$

où :

Ω , est la pulsation de l'excitation.

Sa réponse est du type :

$$\delta = \delta_0 e^{j\Omega t} \quad (20)$$

On aboutit au système d'équations :

$$(-\Omega^2 M + j\eta_a K_a + K)\delta_0 = F_0 \quad (21)$$

avec :

M, K , matrices de masse et de raideur classiques
 K_a , matrice de raideur de la partie amortissante
 η_a , facteur d'amortissement structural.

En utilisant les p premiers modes du système non amorti ϕ_1, \dots, ϕ_p et en effectuant le changement de variables :

$$\delta_0 = (\phi_1, \dots, \phi_p) q_p = \phi \cdot q_0 \quad (22)$$

il vient :

$$(-\Omega^2 \phi^T M \phi + j\eta_a \phi^T K_a \phi + \phi^T K \phi) q_0 = \phi^T F \quad (23)$$

q_0 est un vecteur complexe et se détermine en résolvant l'Eq(23) pour les valeurs souhaitées de Ω . Les déplacements nodaux sont alors réduits de l'Eq(22).

Si au lieu de la réponse on souhaite connaître l'amortissement modal global de la structure pour le mode i : η_{gi} il se déduit aisément de la relation :

$$\eta_{gi} \cdot \phi_i^T K \phi_i = \eta_a \cdot \phi_i^T K_a \cdot \phi_i \quad (24)$$

AUBES DE COMPRESSEURS

Les aubes de compresseurs sont minces, vrillées et l'effet de rotation n'est pas négligeable tout au moins pour les plus basses fréquences.

Le comportement dynamique de ces aubes est défini par les Eqs(14), qui donnent la valeur des contraintes et déplacements initiaux et par les Eqs(16) qui permettent le calcul des fréquences et des modes. Les aubes sont modélisées par des éléments triangulaires plans à 3 noeuds et 6 degrés de liberté par noeud construits à partir de déformées définies en coordonnées d'aire [7].

On n'utilise pas d'éléments finis à double courbure car la surface moyenne de la coque représentant l'aube est mal connue, et les rayons de courbure qui correspondent à des dérivées secondes de l'équation de la surface sont alors eux-mêmes entachés d'une trop grande marge d'incertitude.

La figure 1 présente les résultats expérimentaux et calculés des modes 2, 3, 4, 5.

La figure 2 correspond à la variation des fréquences en fonction des vitesses de rotation.

Enfin, le tableau présente les valeurs des 10 premières fréquences à l'arrêt déduites du calcul et de l'expérience.

Fréquences Hz	1	2	3	4	5	6	7	8	9	10
Eléments finis	105	355	660	839	1361	1531	1603	2189	2377	2488
Expérimental	110	345	610	824	1382	1472	1670	2220	2642	2730

LIAISON ENTRE LES ETAGES COMPRESSEUR ET TURBINE

Ces liaisons sont axisymétriques et généralement minces. Leur comportement est déduit des Eq(17) fournissant les contraintes et déplacements initiaux et des Eq(18) qui permettent la détermination des fréquences et modes pour les différents ordres des développements des fonctions trigonométriques. Les parties minces sont modélisées par des éléments de tronc de cône droits à deux noeuds et quatre degrés de liberté par noeuds, $u, v, w, \frac{\partial w}{\partial s} = \psi$ et on a fait appel à la théorie des coques de Novozhilov pour l'expression des déformations.

Les parties épaisses sont modélisées par des éléments de tore triangulaire à 3 noeuds et 3 degrés de liberté par noeuds.

Ces 2 types d'éléments sont représentés sur la figure (3).

Deux applications sont présentées, la première est un capotage de moteur et l'effet de rotation n'intervient pas. Les fréquences et modes sont déduits du système différentiel (18) où $K_{Gn} = 0, \Omega^2 M_{Gn} = 0$, le maillage est effectué par des éléments minces et l'accord entre les résultats expérimentaux et calculés est satisfaisant (figure 4).

Le deuxième exemple est une structure composée d'un ensemble cône cylindre dont l'épaisseur est variable et qui contient des renforcements. Des éléments minces et épais sont utilisés, l'une des extrémités est considérée comme encastree, l'autre est schématisée par des ressorts et des masses.

On présente successivement :

- . les modes pour $n = 7$ (figure 5)
- . les fréquences de type cylindre puis de type cône (figure 6)

et on peut remarquer que :

- l'accord entre les expériences effectuées à l'arrêt et les calculs est satisfaisant,
- pour $n > 3$ les modes sont généralement de type cône ou cylindre et ceci est d'autant plus net que pour n déterminé, il s'agit de la plus basse fréquence,
- les fréquences augmentent avec la vitesse de rotation.

AUBES DE TURBINE

Les aubes de turbine sont épaisses et l'effet de rotation généralement négligeable. Comme dans le cas des aubes de compresseur le comportement dynamique de ces aubes est défini par les Eqs(14). On utilise comme élément fini un élément isoparamétrique à 24 noeuds et 3 degrés de liberté par noeuds [8], figure 7.

La figure 8 représente une aube de turbine fixée à un tambour par une attache dite en "pied de sapin". Cette structure est composée de 3 parties :

- (A) le corps de l'aube proprement dit,
- (B) la plateforme reliant le corps de l'aube au pied,
- (C) le pied.

L'aube est pratiquement encastree au niveau de (D) et il n'y a pas de continuité géométrique entre (1) et (B) et entre (B) et (C). La modélisation de la plateforme et du pied, c'est-à-dire de la partie entre (D) et (B) apparait très difficile. Elle est réalisée par un ensemble de raideurs et de masses dont les valeurs sont déduites des formules simples de la résistance des matériaux.

L'aube proprement dite a été modélisée par 9 éléments finis. Les résultats obtenus sont les suivants :

Fréquences	Expérience	Eléments Finis
Hz	$N = 0 \text{ tr/mn}$	$N = 0 \text{ tr/mn} ; N = 16000 \text{ tr/mn}$
F_1	1368	1370 1456
F_2	3133	3354 3401
F_3	4661	4755 4809

En fonctionnement la température est de l'ordre de 700°C d'où le module d'Young du matériau diminue et par voie de conséquence la raideur K . Le résultat final compte tenu des effets de rotation (K_G et $\Omega^2 M_G$) et de température est à 16000 tr/mn .

$$F_1 = 1334$$

$$F_2 = 3084$$

$$F_3 = 4355$$

Il apparait donc que l'influence de la température est plus grande que celle de l'effet de rotation.

Les modes sont difficiles à représenter et ne sont qu'esquissés dans la figure 9. Le premier est plutôt un mode de flexion, le deuxième de flexion torsion et le troisième se situe dans le plan de l'aube.

ENSEMBLE DISQUE-AUBES

Il arrive fréquemment que les aubes ne puissent être considérées isolement et qu'il faille tenir compte du couplage disque-aubes. Le calcul de ces types de structures n'est actuellement possible que si leur comportement est du type axisymétrique. Dans la mesure où il ne l'est plus, par exemple si le nombre d'aubes est faible, on ne peut procéder comme précédemment [9].

Dans le cas où les ensembles disque-aubes sont minces les aubes sont modélisées par des poutres où l'on tient compte des mouvements de flexion de torsion et longitudinal. Les disques sont représentés par des éléments axisymétriques.

Dans le cas où les ensembles disque-aubes sont épais, les aubes sont modélisées par des éléments super-paramétriques et le disque est représenté par des éléments épais.

Trois séries de résultats expérimentaux et théoriques sont présentées.

La première série de résultats correspond à un ensemble disque-aubes mince d'épaisseur constante. Pour n suffisamment grand les aubes apparaissent comme encastrées sur le disque. En effet, l'énergie potentielle de déformation des aubes est indépendante de n alors que celle du disque devient pour n assez grand proportionnelle à n^4 . On représente sur la figure 10 les résultats théoriques et expérimentaux pour le système au repos.

Sur la figure 11 on montre l'influence calculée de l'effet de rotation.

Le deuxième exemple est un ensemble disque (épais) aubes (16 plaques). L'accord entre les résultats théoriques et expérimentaux (points confondus) figure 12 est très satisfaisant.

Enfin, on présente le calcul d'un étage de moteur. Le disque est d'épaisseur variable et les aubes ont la forme usuelle d'aubes de turbine, fortement vrillées elles ne sont à la liaison avec le disque que légèrement inclinées par rapport à la verticale. L'accord entre les résultats théoriques et expérimentaux est convenable, les divergences peuvent vraisemblablement s'expliquer par l'impossibilité d'écrire une forme de continuité entre le disque et les aubes, (figure 13).

AMORTISSEMENT SANS EFFET DE ROTATION [6], [10]

On présente maintenant les possibilités d'amortissement d'un étage de stator, (figure 14).

La structure est constituée d'aubes partiellement recouverte de matériaux amortissants. Une aube a été modélisée par des éléments isoparamétriques et les liaisons aux extrémités sont représentées par des ressorts.

L'étude est faite à température ambiante avec un matériau ayant des caractéristiques proches du matériau à utiliser en haute température. Il s'agit du LD 400 et on présente les amortissements nodaux des deux premiers modes (figure 15). L'accord entre les résultats théoriques et expérimentaux est satisfaisant.

CONCLUSION

On vient de présenter divers aspects de l'aide que le calcul par éléments finis apporte dans la mise au point des moteurs d'avion. S'il est évident qu'un code de calcul ne doit jamais se substituer complètement à l'expérimentation, la pratique et le savoir faire, il n'en demeure pas moins que la prévision permet d'éviter des erreurs de conception, de déterminer à priori les parties des structures qui travaillent dans les conditions les plus sévères et de détecter la présence des fréquences de résonance.

Quant aux possibilités offertes par l'amortissement, elles sont seulement brièvement évoquées. En effet, les développements possibles de cette technique sont encore très liés à des impératifs technologiques.

REMERCIEMENTS

Les travaux ont été possibles grâce à des aides des organismes suivants : D.R.M.E., D.G.R.S.T., E.D.F., S.N.E.C.M.A., RATEAU.

REFERENCES

- [1] M. Lalanne, R. Henry, P. Trompette, Rotating blade analysis by the finite element method. I.U.T.A.M. Symposium on Dynamics of Rotors. Springer Verlag, 1974.
- [2] G.J. Wilson, J. Kirkhope, Analysis of coupled blade disc vibration in axial flow turbine and fans. 41th Shock and Vibration Bulletin.
- [3] P. Trompette, M. Lalanne, Frequencies and mode shapes in geometrically axisymmetric rotating structures. Applications to jet engine. 46th Shock and Vibration Bulletin.
- [4] P. Trompette, Etude dynamique des structures, effet de rotation, amortissement. Thèse d'Etat, 1976.
- [5] M. Paulard, P. Trompette, M. Lalanne, Response of thick structures damped by viscoelastic material with applications to layered beams and plates. 45th Shock and Vibration Bulletin.
- [6] M. Paulard, P. Trompette, M. Lalanne, D. Jones, M. Parin, Prediction of modal damping of jet engine stator vane. A.S.M.E. Paper 76 GT 60.
- [7] R. Henry, M. Lalanne, Vibration analysis of rotating compressor blades. Journal of Engineering for Industry, August 1974.

- [8] P. Trompette, M. Lalanne, Vibration analysis of rotating turbine blade. A.S.M.E. Paper 74, WADE 23.
- [9] R. Henry, Calcul des fréquences et modes des structures répétitives circulaires. En préparation.
- [10] D.I.G. Jones, C.M. Cannon, M.L. Parin, Controlling the dynamic response of jet engine components. 45th Shock and Vibration Bulletin.

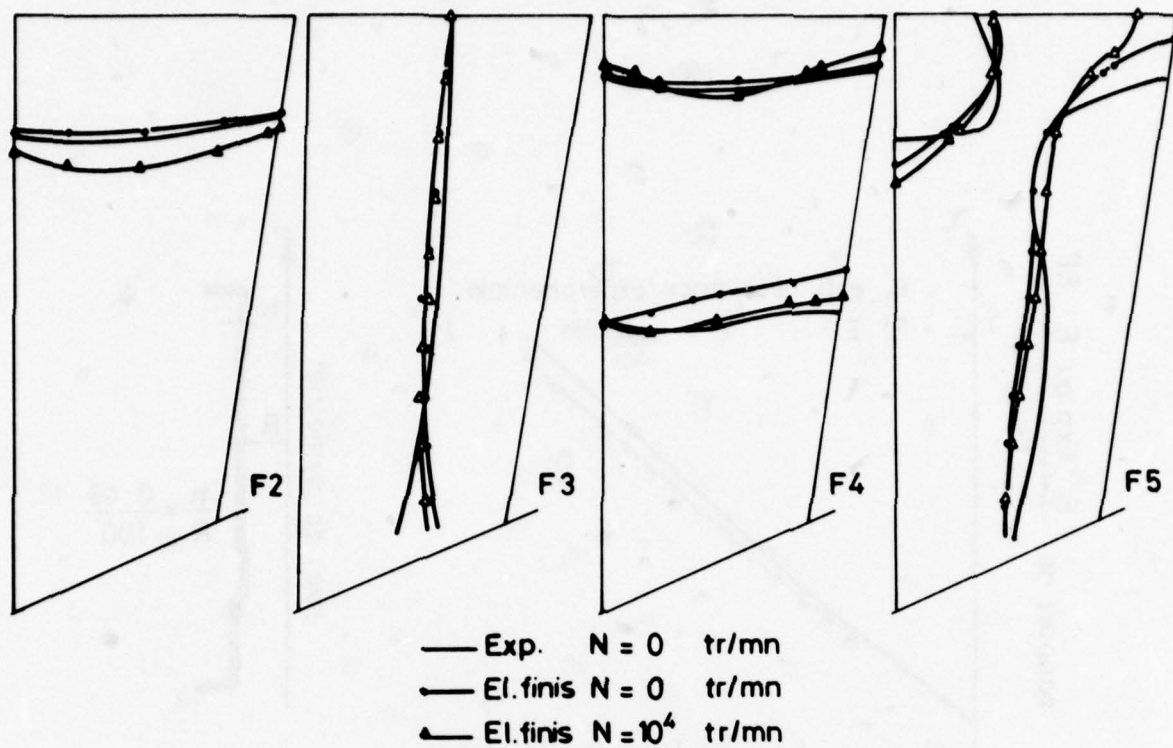


Fig. 1 : Modes 2,3,4,5 de l'aube de compresseurs

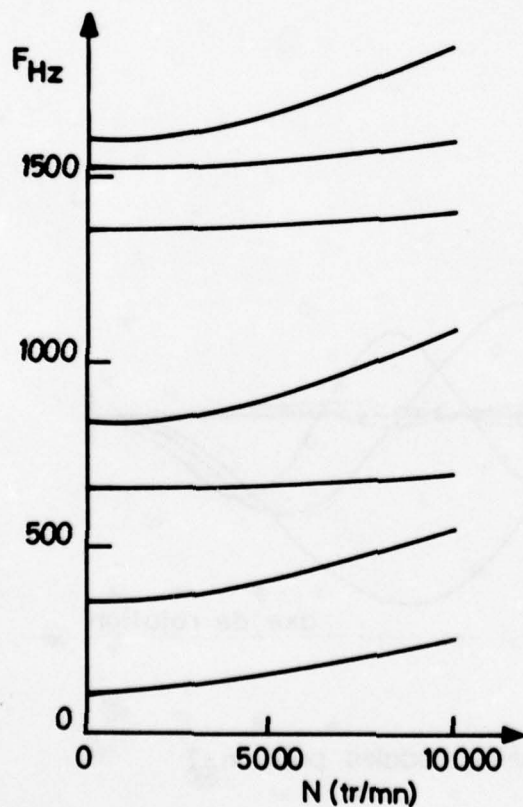


Fig. 2 : Variation de la fréquence en fonction de N

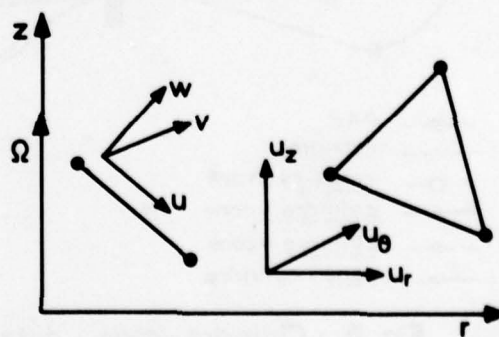


Fig. 3 : Élément pour structures axisymétriques

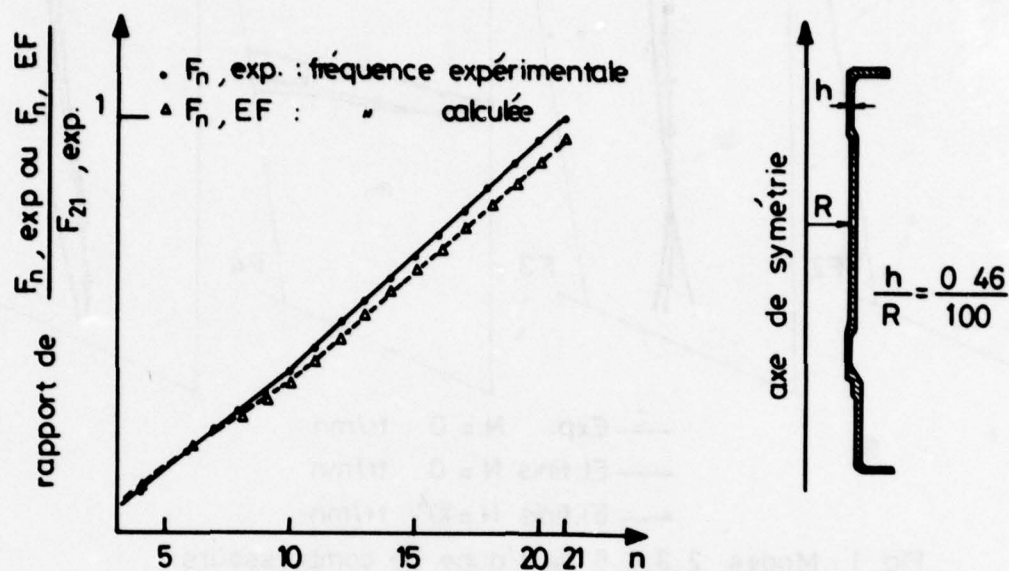
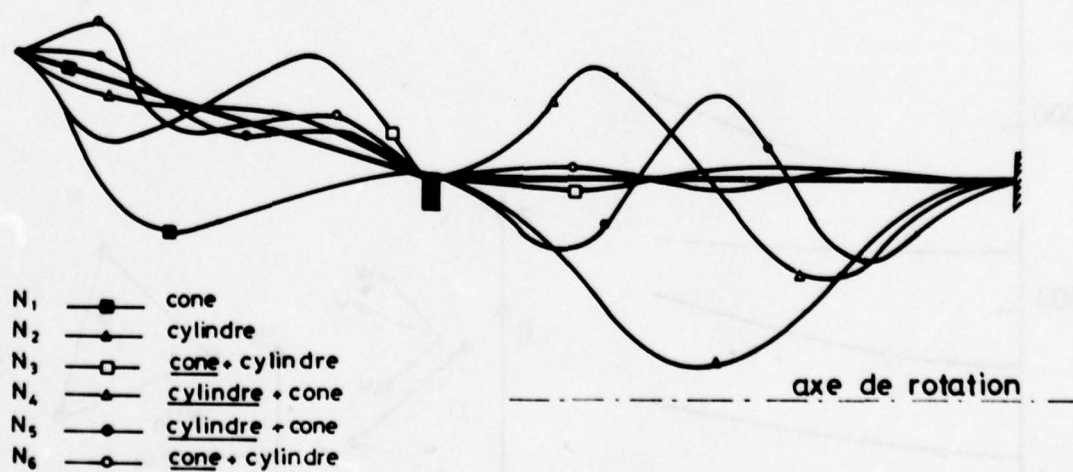


Fig. 4 : Fréquences de capotage

Fig. 5 : Cylindre-cone : déformées modales pour $n=7$

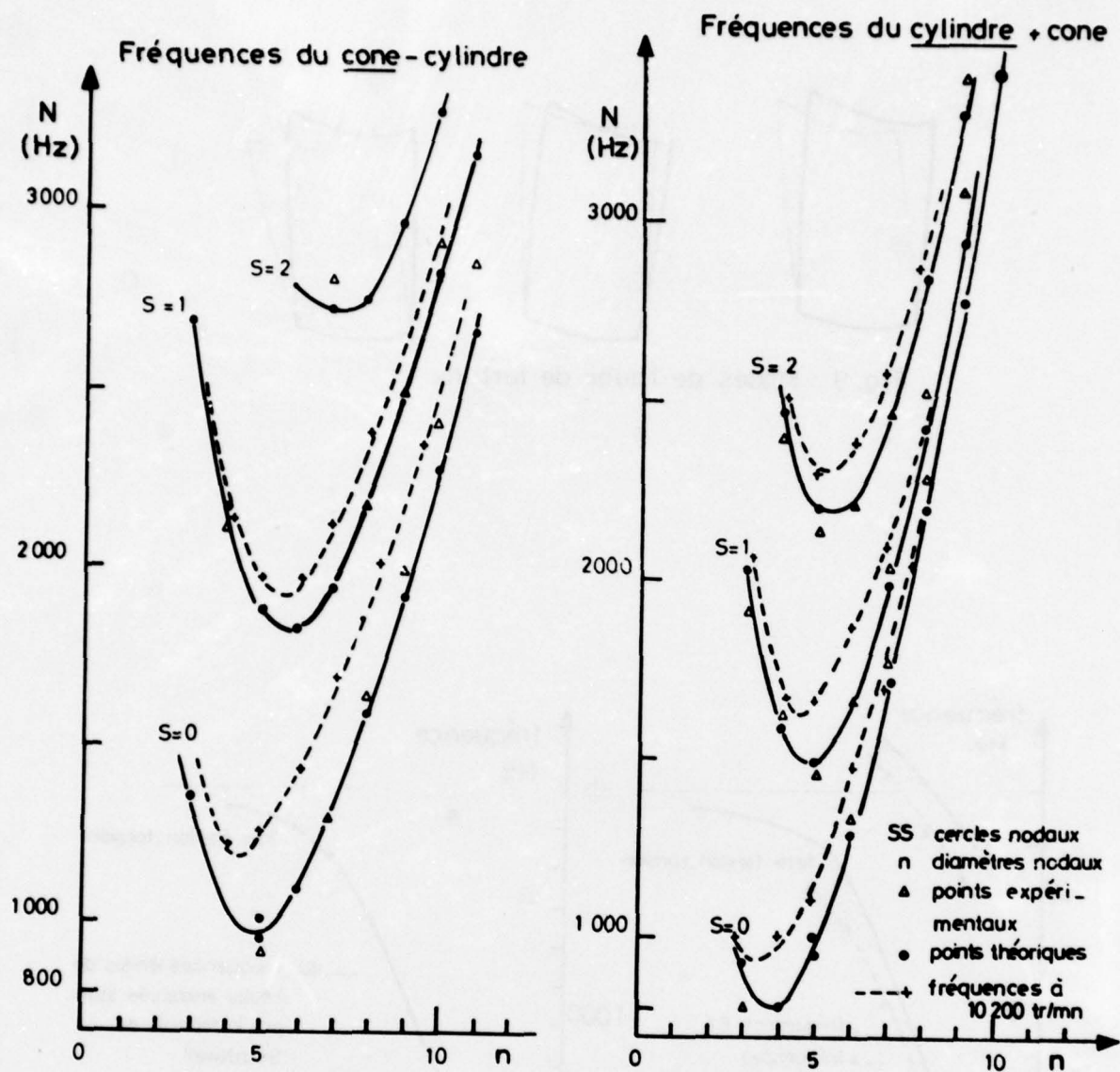


Fig. 6 : Fréquences de l'ensemble cylindre - cone

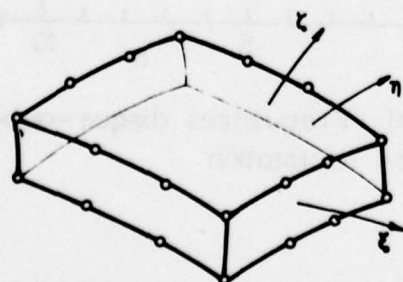


Fig. 7 : Élément isoparamétrique

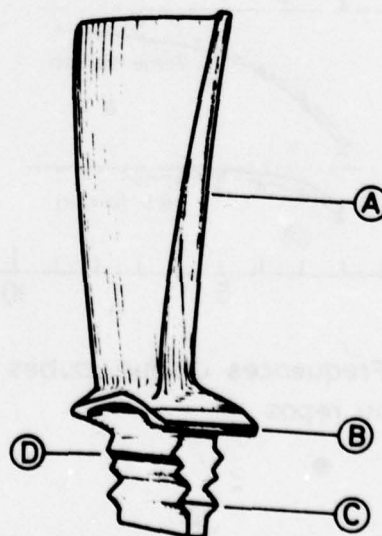


Fig. 8 : Aube de turbine

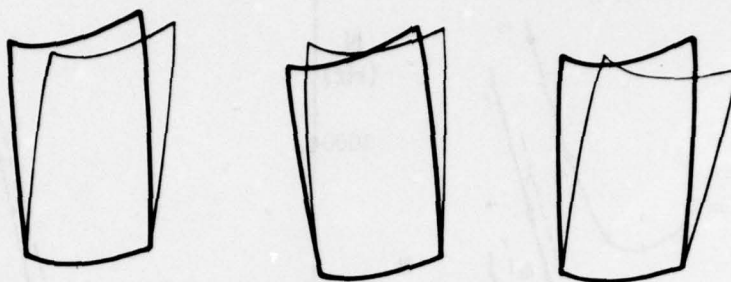


Fig. 9 : Modes de l'aube de turbine

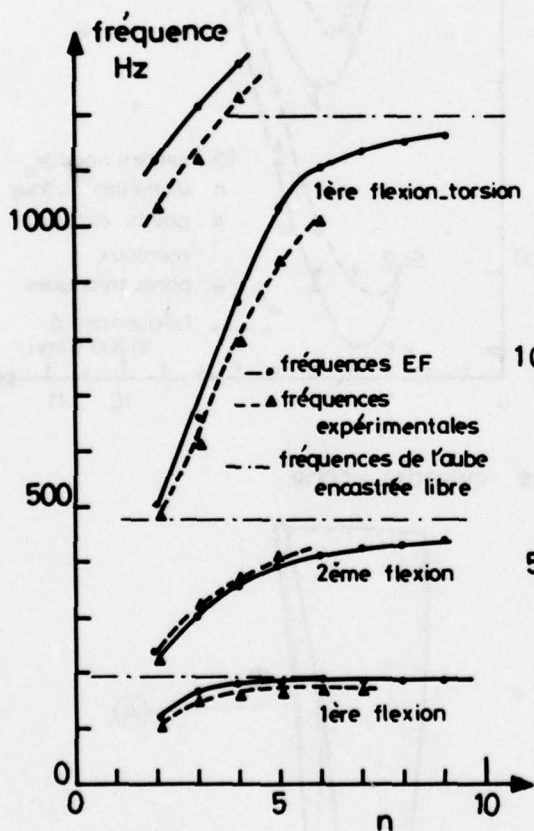


Fig. 10 : Fréquences disque-aubes minces au repos

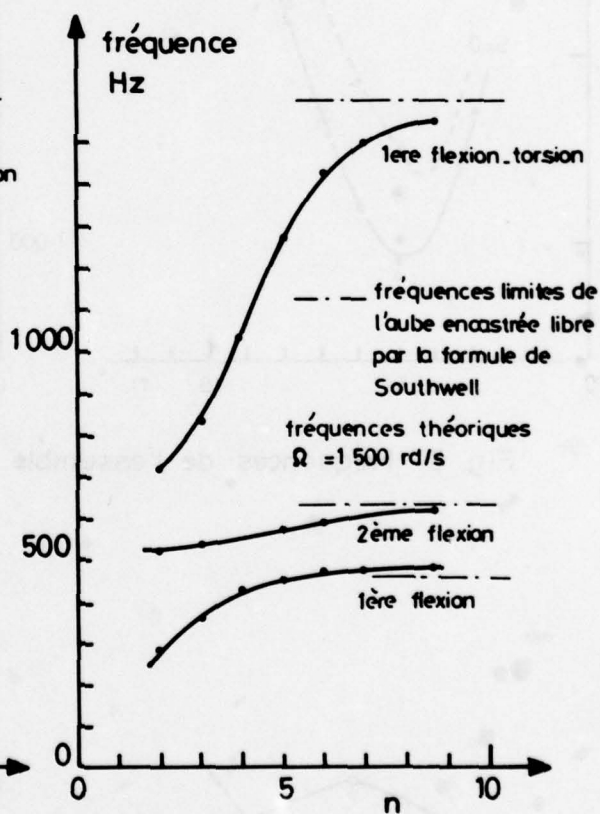


Fig. 11 : Fréquences disque-aubes minces en rotation

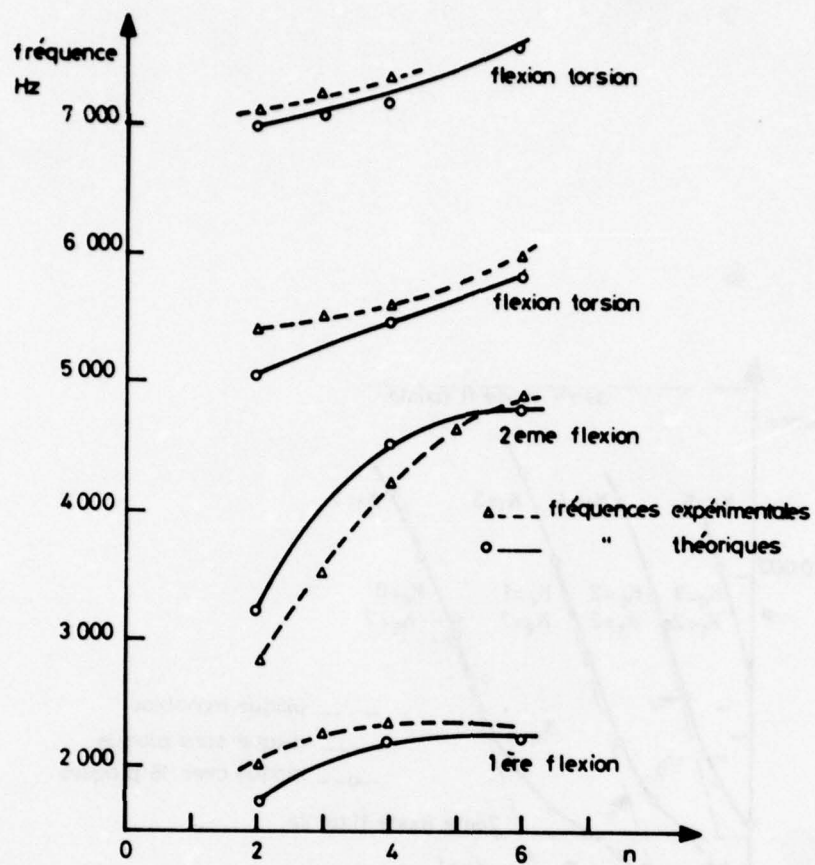


Fig.13 : Fréquences de l'étage du moteur

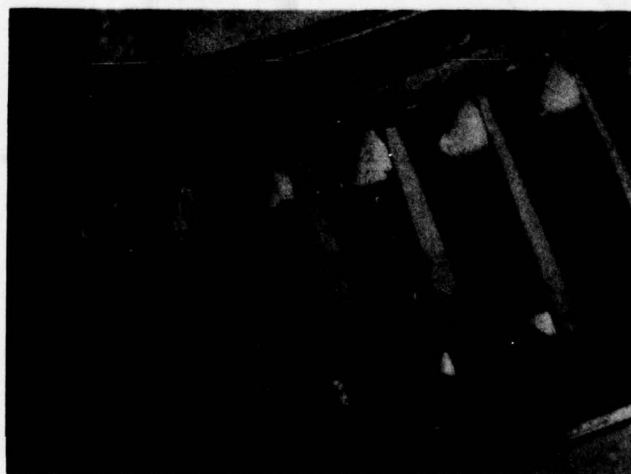


Fig.14 : Elément d'étage de stator

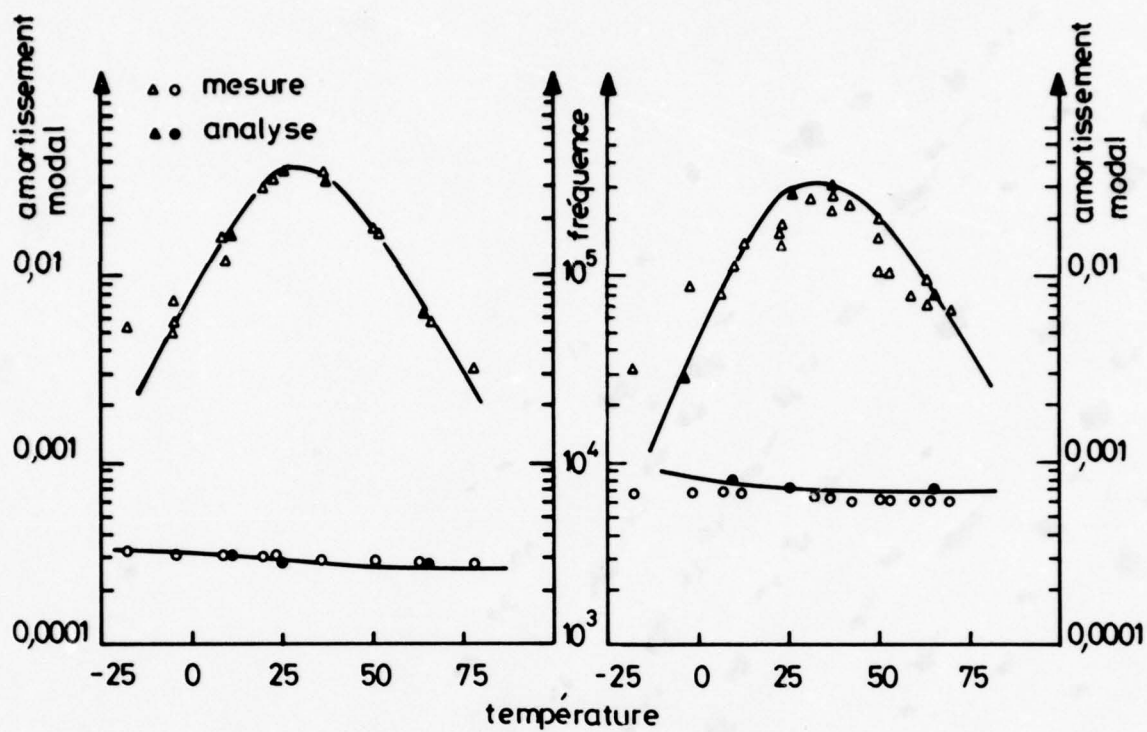


Fig. 15 : Amortissements modaux

Aircraft Engine Design Using Experimental Stress Analysis Techniques

by
Bernard L. Koff, Chief Engineer
Aircraft Engine Group
General Electric Company
Cincinnati, Ohio 45215

Summary

The past 25 years have seen significant advances in *theoretical* analyses through the use of computers and advancing techniques. Despite this, *experimental* analyses are used more extensively in aircraft engine design today than ever before, primarily because of the demands for extended component life.

This paper is a perspective of prominent experimental techniques used in current aircraft engine stress analyses. It addresses the verification of temperature, stress, steady state and dynamic deformation, pressure, and fatigue strength by employing: advancements in instrumentation, including high-energy X-rays and high durability strain gages; computers and software to reduce vast amounts of data; increased photoelastic capabilities; and advancements for reproducing loading and environmental conditions in laboratory component tests.

These experimental techniques and disciplines have continued to advance in both capability and importance, and the state of the art in structural engineering would be significantly reduced without them.

Introduction

During the late 50's, some experts suggested that by 1980 our theoretical analysis capabilities would become so advanced, through high technology and the use of computers, that the field of Experimental Stress Analysis (ESA) would be relegated to a minor role for aircraft engine design. Our understanding and capability in theoretical stress and heat-transfer analyses have, in fact, progressed several orders of magnitude beyond the most optimistic expectations. Rotating disk analyses that took an engineer three days to perform in 1950 could be completed in half an hour by 1960. Heat-transfer analysis techniques using computers were developed to make the critical-temperature predictions necessary to obtain realistic stress distributions for component design. Using computer techniques, complicated rotor shell and disk structures that took three to six months to approximate in 1960 could be analyzed, in a refined

manner, in one-sixth the time by 1970. Now blades can be analytically modeled to determine airfoil stresses and vibratory modes with an accuracy previously considered unattainable. Complex and highly redundant structures with many degrees of freedom are now routinely analyzed for critical frequencies and mode shapes, including identification of the most responsive modes.

In spite of these impressive advances in theoretical methods, experimental techniques to determine both steady-state and transient stresses and vibrations in gas turbine components are used more extensively today than twenty years ago. A major reason for this is the need to accurately determine component life. This has proven to be the most difficult of all analytical predictions because it involves an understanding both of inelastic material behavior and of the repeated strain range to which an engine part is subjected over a period of several years. In many cases, the operating conditions and resulting strain can only be learned in operational service, often too late to prevent costly mechanical failures. For accurate life predictions, comprehensive understanding is required of both the material behavior and the state of stress under the total range of operation as defined by the aircraft mission. The previously accepted ± 10 to 20 percent accuracy standard for stress analysis is no longer adequate since, as illustrated in Figure 1, small inaccuracies in calculated stresses can result in large life variations. However, by combining theoretical and experimental methods in a "hybrid analytical" model, a ± 5 percent accuracy for stress determination can be attained in critical parts, thereby reducing the variability in life calculations.

A key objective of ESA techniques is the accurate and timely determination and verification of stress and thermal gradients and temperatures in complex-geometry parts that function in high operational steady-state and alternating stress fields. The

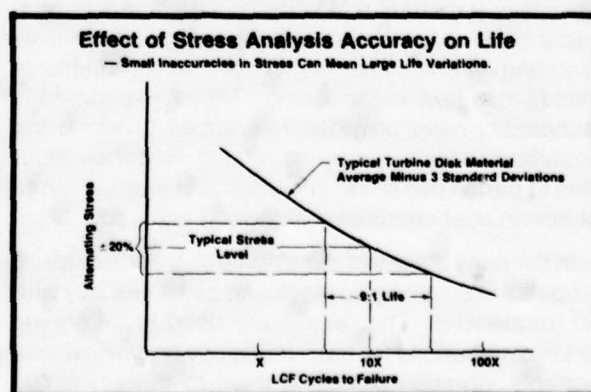


Figure 1

importance of establishing an accurate experimental model to either verify or supplement the theoretical analysis cannot be over-emphasized. Although seldom acknowledged, costly design mistakes have been associated with so-called "short cut" experimental testing. Over-simplified, experimental models that omit essential portions of the engine operational mission can result in misleading information and design mistakes. When such costly mistakes are discovered, a reevaluation of the experimental test usually reveals that one or more important operational factors were left out. To avoid these costly occurrences, a critical review of the experimental modeling and testing is necessary to assure that all mission simplifications are either unavoidable due to technology limitations, or approximated by using other techniques. The development of ESA methods that closely duplicate engine operation is destined to play an ever-increasing role in engine design and development.

A number of ESA techniques have been the primary tools used to measure the strains, temperatures, pressures, and accelerations which are critical to engine design and development, and improvements through evolution and the addition of newer ones have expanded the inventory. To apply ESA techniques effectively, an understanding of the uses, limitations, and interrelationships is essential. This paper addresses to the more prominent experimental techniques, their limitations, and how they are used in the design of aircraft engines today. With a few exceptions, the order of discussion broadly reflects a chronological sequence commonly followed in the design and development process.

Determining the Natural Frequency and Mode Shapes of Blading

It is accepted that a thorough understanding of dynamic responses in turbomachinery blades is essential to successful engine development. Experimental procedures and methods have performed an extremely important role in the advancement of analytical techniques by providing steady-state and alternating stress/strain response measurements in these important components. These experimental techniques have provided references to which the analytical models can be correlated, and then modified to permit use of the analyses over a broad range of operational conditions with good accuracy.

In the early stages of development, blades or blade models are driven by an electromagnet to excite natural frequencies. The results are used to determine strain distributions for each mode of vibration, while a portable vibration pickup is used to determine the nodal patterns for the respective modes. Figure 2

shows a comparison of analytical and experimental models for several modes to illustrate the accuracy of the analysis. The comparison in Figure 2 serves as an important check for assurance that the analytical model is properly constructed, thus enabling its use for a broad range of engine operating conditions. For example, the choice of the proper mesh size for the finite elements is critical to the accuracy of the analyses, especially for high frequency modes.

In many cases, it is desirable to obtain the actual mode shape over the entire blade. The use of holography, involving a type of photography where precise images are formed from light waves, has proven to be an accurate method for the overall understanding of mode shapes in airfoil structures. This technique utilizes a laser point source of coherent (in-phase)



Figure 2

light waves that produce transparent images of the blade surface in the form of complex interference fringes. When the holographic image of the blade is superimposed on the actual blade surface and the blade is vibrated, the differences between the images produce interference fringes at nodes and antinodes. When the exciting frequency of the blade matches the natural frequency, the interference fringes become sharply defined and can be recorded on a photographic plate. Figure 3 shows a comparison of a



Figure 3

three-dimensional (3-D), finite-element analysis and a holographic test for the first and fifth frequencies of a compressor blade. For the first flexural mode, the agreement between the analytical model and holographic measurement is within 1 percent. For the fifth mode, which is approximately ten times the frequency of the lowest fundamental, the calculated value is about 10 percent higher than the holographic result. This difference is mainly attributed to the modeling accuracy of the finite-element system and, as expected, indicates sensitivity of plate thickness in the higher modes. The fringes in the lower modes show remarkable agreement between the theoretical and the experimental techniques. Thus, the need for verification of mode shapes by alternate methods is shown to be essential to accurate stress determinations. Holography is not utilized as extensively as strain gages to measure stress because stress is a function of the second derivative of deflection and is not readily determined by holographic methods without an extremely accurate definition and interpretation of the holographic fringes. As a result, holography will play a secondary role until a practical capability to measure stress gradients is developed.

Once the blade nodal patterns and frequencies are determined under static conditions, the increase in frequency caused by the rotor centrifugal stiffening effect must be determined and a Campbell diagram constructed. This diagram, shown in Figure 4, is both experimental and theoretical. The blade centrifugal and thermal effects due to rotation are determined from an analytical model which must be refined and modified to have the frequencies at zero speed agree with experimental data. The crossings of the blade natural frequencies with the engine "per rev" excitations are potential high stress resonances. These regions, circled in Figure 4, are heavily influenced by design configuration selections such as the number, shape, and proximity of upstream and downstream struts and vanes. The Campbell diagram is important in turbomachinery design to aid the selection of airfoil

configurations that avoid high-stress resonances within the engine operating range. It also serves as a checklist and roadmap for instrumented-engine testing. For example, the vibratory modes revealed by the Campbell diagram establish the strain gage locations on the airfoil that are used to monitor and record stress levels during engine test. These pretest preparations are essential for prompt evaluation of dynamic responses during test.

Blade Structural Design and Analysis

In addition to the damaging resonances discussed above, the blading in a turbomachine is vulnerable to failure for a variety of other reasons. One common failure mode is associated with impact damage and subsequent fatigue failure resulting from forced vibration.

The airfoil, primarily through aerodynamic considerations, is relatively free of stress concentrations; however, discontinuity locations such as shrouds, airfoil-root/platform transitions, shanks, and dovetails create some high stress regions. The blade structure below the platform is of particular interest because discontinuities in the tensile load path from the airfoil, through the platform and shank, to the dovetail can introduce high stress concentrations which are commonly referred to as "end effects." A common practice, used to minimize engine damage resulting from blade failures, is designing the disk dovetail post to be stronger than the blade dovetail which, in turn, is designed to be stronger than the airfoil. This practice will reduce the total mass of fragments in the event of a failure. To achieve this objective, the effects of stress concentrations at successive junctions between the airfoil-root, platform, shank, and blade dovetail, as well as concentrations in the disk post, must be understood. Figure 5 presents end effects stress concentrations both for the suction and for the pressure surfaces at the airfoil-root of a radially loaded fan blade as a function of the blade chord. This stress distribution was determined by numerous strain gages in a bench test where a radial load was applied at the blade tip to simulate the centrifugal load induced by rotation. Application of this radial load must be carefully done to eliminate undesired bending moments that can influence the stress distribution at the blade root. Similarly, a twisting moment, to simulate torsion, and two orthogonal bending moments are separately applied to evaluate the stresses for all load combinations experienced during engine operation.

This experimental analysis is used as a master to evaluate and verify the accuracy of a finite-element computer model as shown in Figure 5. The model

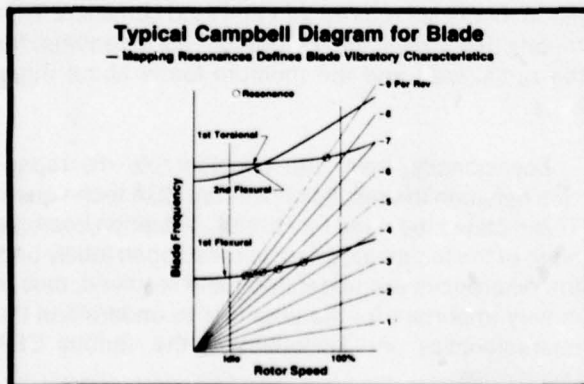


Figure 4

offers convenience in predicting the effects of design changes and combined loading. Note that the maximum stresses in the airfoil-root section are substantially higher than the average but are strategically placed away from the leading-edge region which is susceptible to foreign object damage.

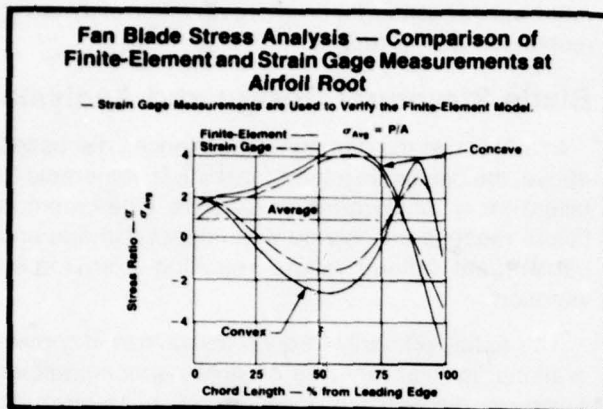


Figure 5

Advances in 3-D, photoelastic modeling and analysis have also proved valuable to understanding the stress gradients in the airfoil and the root end effects which include the lower shank and dovetail structure. The platform, shank, and dovetail regions have always been particularly difficult to analyze, especially for blades with high twist gradients and where pockets and cavities are machined in the shank to reduce the rim centrifugal load. The 3-D, photoelastic, stress-freezing method is practical for such analysis because of the diphasic material behavior occurring in many polymeric solids. The molecules in these materials are held together by primary and secondary bonds, and when such a material is subjected to loads at room temperature both sets of molecular bonds carry the applied load. However, when the temperature is increased to the critical level, the secondary bond is relieved, leaving the primary bond to carry the entire load. At this point, relatively large deformations occur but are still within the elastic range. If polarized light is passed through the solid, double refraction takes place with the relative retardation of the two light components (or fringe order) being linearly related to the stress. When the temperature is again lowered to room temperature with the loads still applied, the secondary molecular bonds reform; the deformation and the photoelastic fringe effect are locked-in just as they existed at the critical temperature. Because "thawing" and "freezing" occur on a molecular scale, thin slices may be cut from the "frozen stress" model for analysis without disturbing the deformation or the double-refraction properties.

The 3-D technique is used effectively by making a photoelastic blade model of epoxy resin and radially loading it to simulate centrifugal effects in the load path junctions of the airfoil-root, platform, shank, and dovetail. The load is applied in a stress-freezing oven by suspending the blade from a dovetail-slotted block of epoxy resin and hanging a weight from its tip using transits for precise load alignment. Figure 6 shows the stress distribution of the sectioned blade as a

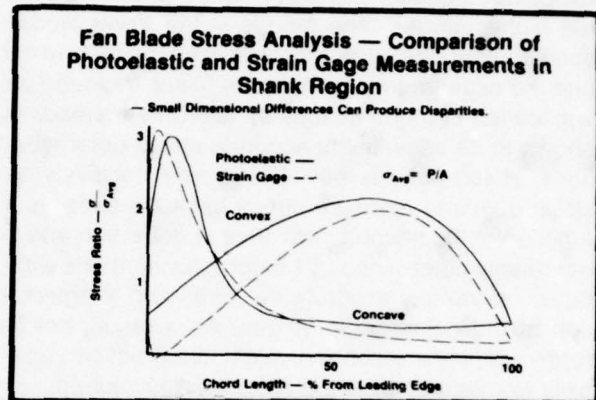


Figure 6

function of chord for the shank region below the platform. The variation between photoelastic and strain gage results was at least partially accounted for by small dimensional differences between the photoelastic model and the strain gaged part.

In contrast, stress analysis using a blade or blade model instrumented with strain gages has the capability of being bench tested repeatedly with different unit loads or even combinations of loads. However, the 3-D, photoelastic method offers the advantage of providing significantly more detail including, for example, the true peak stress in dovetail fillet regions where strain gage application is impractical. The disadvantage of the photoelastic method is that a new blade model is required for each load condition. This means that a minimum of four models is required for the radial load and the moment loads about three axes.

Occasionally, there are considerable discrepancies between the results of different ESA techniques. This dictates the need for careful evaluation because none of the techniques can be relied upon totally until the differences are understood and resolved; thus, it is very important for the engineer to understand the characteristics and limitations of the various ESA techniques.

Evaluating Blade Fatigue Strength By Bench Testing

The actual fatigue strength of engine components is best evaluated by bench testing where the parts are subjected to vibratory loads to induce failure. For example, an electromagnetic exciter is used to drive instrumented blades to failure in lower order vibratory modes. Higher mode failures are usually evaluated in a siren facility that has the capability of exciting higher frequencies with pulsating pressure waves. This testing of blades is performed to evaluate the design, material, and manufacturing processes under partially simulated conditions. For example, heating coils are used to provide thermal effects when hot fatigue testing is required. The evaluation includes a comparison of the blade fatigue strength with the basic material properties for assurance that the parent-metal fatigue strength is achieved in the finished part. The component blade strength occasionally falls below the predicted strength of the parent metal due to unpredicted stress gradients, materials properties under specification limits, and manufacturing process effects. The fatigue testing must be done at temperature conditions simulating engine operation. Once this testing is accomplished, a fatigue-limit diagram can then be completed for the blade as shown in Figure 7. Development of this diagram is, therefore, dependent on both experimental and theoretical results. This diagram is used in the design phase to show the alternative combinations of maximum

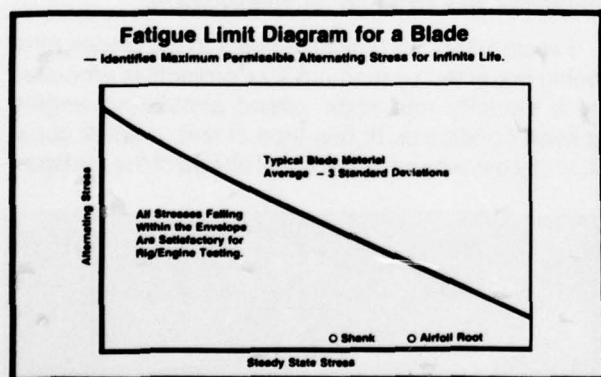


Figure 7

steady-state and alternating stresses that can be used for a particular material. The fatigue-limit curve identifies the maximum permissible alternating stress for infinite fatigue life (10^7 cycles). The HCF strength envelope is also used to establish the safe operating stress or "scope" limits for blading during component and engine testing in the development phase. Scope limits are prepared for each of the potential resonant conditions on the Campbell diagram. When the blade-vibration signals from the strain gages are displayed on an oscilloscope during testing, these

preestablished limits are used as a measure of the stress margin to crack initiation.

Experience has taught us to be prepared for short-duration, high-amplitude stress responses during resonances, operating transients, stalls, inlet distortions, off-schedule variable stator operation, or aeromechanical instability; any of these can cause low cycle fatigue (LCF) damage. To establish the LCF capability of the blade, a stress versus cycles-to-failure (S-N) diagram, similar to Figure 1, is constructed using fatigue data generated from material-characteristics testing. The S-N plot is essential in evaluating the life of blades subjected to high-amplitude fatigue and in evaluating the manufactured blade strength relative to test-bar data for the parent material. The LCF and HCF strengths of the blade should fall within a small scatter band with failures originating in the same general area and matching within 10 to 20 percent of the test bar data. When this occurs the capability of the material has been properly integrated with the design and manufacturing process.

Dynamic Testing in Rotating Facility

Determining component fatigue strength requires dynamic testing with centrifugal loading. This is achieved through the use of the "whirligig" shown in Figure 8 which is a rotating rig capable of running at engine speed. Vibratory stresses can be induced by arranging a series of high pressure air jets to impinge on the blading. For example, an eight-per-rev mode can be simulated by using eight nozzles to

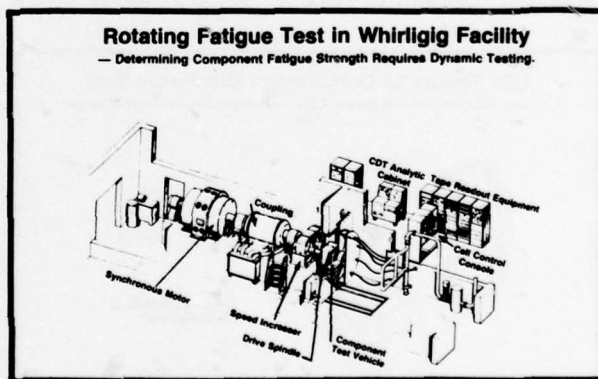


Figure 8

provide the stimulus or driving excitation. This facility has wide versatility and can be used to evaluate the strength and response of several configuration options in a back-to-back comparison. For instance, a low pressure turbine rotor was recently tested with two types of blade-shank designs and several internal platform damper configurations. The test showed that it was possible to reduce the measured vibratory

stress by a ratio of 3:1 when a certain combination of blade-shank thickness, damper weight, and contact angle was chosen.

The advantages of instrumented, dynamic testing in the whirligig are:

- The actual blade and blade-disk frequencies, including the rotational effects over the complete speed range, can be determined for a more accurate Campbell diagram (Figure 4).
- Analytical stress and frequency models, including the centrifugal effects, can be updated.
- Relative vibratory response of the blading can be evaluated as a function of the number and pressure level of the exciting air jet nozzles, and alternate design configurations can be evaluated for vibratory response. This is particularly important in developing effective blade-damping devices for turbine blades that operate at high temperatures and, therefore, have relatively low fatigue strength to resist both random and resonant vibratory modes.

For a case in point, Figure 9 shows a compressor discharge seal that failed in 2,500 fleet service cycles after operating successfully for 9,000 cycles in factory engine tests. Since determining and verifying failure modes are fundamental to successful design fixes, a transient thermal whirligig test was specifically designed to simulate fleet service operation. This was initiated after it had been established that accelerated factory endurance testing did not allow a sufficient cool-down cycle or thermal strain range

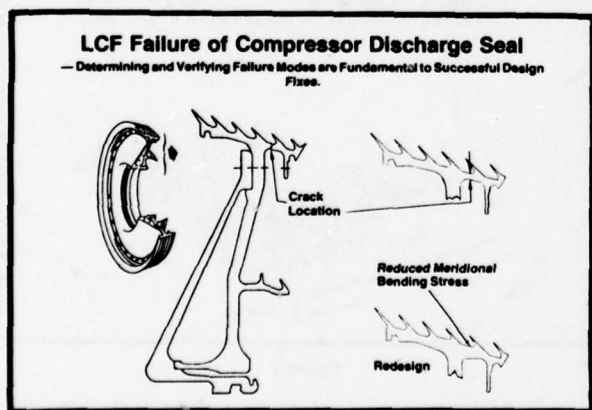


Figure 9

excursion as experienced in fleet service operation. When the part was both speed and thermal cycled to simulate fleet service operations, cracks were observed in the same location as those found in fleet service. A redesigned part with reduced meridional-bending stress was tested using the

same simulation technique, and 5:1 improvement in cyclic life was achieved. The improved part was promptly released for fleet service where a substantial life improvement was realized. Thus, transient heating and cooling in a rotating cyclic rig provided a more complete evaluation of the transient thermal stresses in a complex, rotating component.

Experimental Stress Analysis of Bird Strikes

The determination of bird strike capability, which is almost completely dependent on ESA techniques, utilizes the whirligig facility as an important evaluation tool. In combination with a compressed-gas gun that propels simulated birds into the rotor, the facility is used to approximate the stresses and deflections caused by bird strikes under engine-operating conditions. This technique is particularly useful in evaluating and understanding high-speed-impact situations where large, plastic deformations take place on blading, and analytical modeling using current theoretical techniques is not an accurate simulation. Experimental stress and deformation analyses of this type, often in conjunction with high speed photography, are used to determine the impact resistance of fan blades. A silicone rubber "bird" in the form of a cylinder is used for more consistent test results. Its use also avoids the substantial cleanup time required when actual bird carcasses are propelled into rotating blades. The silicone rubber projectiles are calibrated to match the particular size birds under investigation.

Figure 10 shows typical damage to fan blades after being impacted by medium-size projectiles propelled at a velocity and rotor speed simulating engine takeoff conditions. In this type of test, a crack occasionally developed in the airfoil ahead of the midspan



Figure 10

shroud as a result of the impact. This also duplicated several blade cracks found in fleet service after actual bird strikes. An analysis of the data indicated that an

impact at the blade leading edge, forward of the midspan shroud, could produce cracking under certain conditions of engine speed and aircraft velocity. The cause of this cracking was attributed to the abrupt change in stiffness at the airfoil-to-shroud transition which acted as a stress concentration. A modification to the shroud was made by removing material to provide a more gradual transition of section modulus from the airfoil to the shroud as shown in the platform view in Figure 11. Numerous blades reworked to this improved configuration were bird-impact tested in the whirligig under the same conditions, and none exhibited cracks. As a result of this experimental analysis, the modified blade was released to fleet service as a product improvement, thus verifying the importance of ESA techniques to the design refinement process.

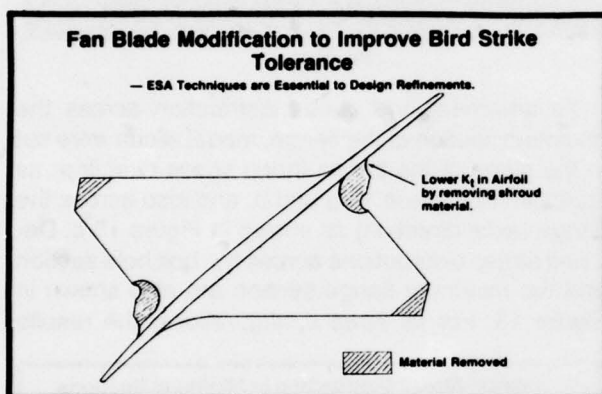


Figure 11

Engine Level Component Fatigue Testing

The analytical stress model for a complete, rotating component can be validated economically in a cyclic spin pit. Rotor assemblies, suspended from a reversible steam turbine drive, with rapid deceleration capability are run in an armored pit which is partially evacuated to reduce turbine drive power requirements and turbulent heating. A large number of start/stop cycles can be completed in a relatively short time to verify the calculated cyclic life. Detailed periodic inspection of stress concentration regions such as bolt holes, dovetails, circumferential loading slots, and flanges can be conducted during the test to identify possible wear, fretting, or crack-initiation sites. Cyclic rig testing, therefore, affords the advantage of determining component life without direct knowledge of the detailed state of stress. Occasionally this type of testing reveals unexpected areas of distress that were missed during prior analyses or component tests; thus, prompting reanalysis and perhaps additional testing to determine the root cause. The cyclic testing of engine components is

destined for increased popularity since effects of wear, fretting, bolt preload, and other stress concentration areas would be automatically included.

Static Structural Testing

Large engine structures can be statically loaded to determine operating-clearance deformations as well as the strain range required to predict cyclic life. An engine mounted on an aircraft pylon can be loaded to simulate the deflections that occur during operation. When the structure is instrumented with deflection transducers, deformation on large surface areas can be mapped and recorded. At the same time, strain gages placed in known and potential stress-concentration regions can be used to record peak stresses. All the stress and deflection input from the instrumentation is fed into the computer for quick and economical processing to analyze and evaluate the design configuration.

Engine System Vibration

Service experience has demonstrated that a smooth-running engine operates longer, with fewer problems, and at lower direct operating costs. Thus, precise balancing is an integral part of the engine assembly. Increased vibration level in a production or field engine, therefore, usually indicates a broken part or a missing piece from a blade. The use of accelerometers mounted on bearings and frames to measure vibration for on-line condition monitoring (mass imbalance, bearing failure, and stall detection) and long-term trending is becoming widespread. The vibration signatures are also used for fault isolation by matching them with the signatures from engines with known faults.

When high system vibration occurs during the early development phase, it often signifies the presence of a basic design problem such as shifting parts, resonance, and/or unstable internal aerodynamics. Accelerometers mounted in the bearings, frames, and casings are widely used to correlate the engine vibratory response with an analytical model. The analytical model is updated on the basis of this correlation, and design changes are recommended where necessary.

Recent advances in accelerometer technology have made it possible to obtain vibration signatures even at high-temperature locations. Also, the dynamic range has been extended to measure low-frequency/low-to-high amplitude as well as high-frequency/low-to-high amplitude responses. This extended thermal and frequency range in accelerometer measurements for application in ESA methods is particularly helpful in determining overall engine health and suitability for production release.

Photoelastic Analyses Using Rotating Models

An exciting application of photoelasticity which offers new inroads in stress-gradient determination for complex geometries, has been developed. Analysis of complete, polymer models of rotating assemblies including disks, blades, retainers and bolts is now possible. Rotational stresses are frozen into bladed disk assemblies in a specially designed vacuum oven. When mounted in such a facility, the model is slowly rotated by a variable-speed motor as the oven temperature is gradually increased. Temperature gradients in the model are minimized by carefully adjusting the rate of heating. When the critical temperature is reached, the oven is evacuated (for tests where air loads must be eliminated), and the rotor is brought up to the required speed to produce the deformation resulting from a preselected stress level. After the model has stabilized at the critical temperature, the oven temperature is slowly reduced with continuous monitoring and control of the temperature to limit temperature gradients. When the temperature has dropped low enough for the stress-freezing to be complete, the vacuum is slowly released, and rotation is stopped.

After the oven reaches room temperature, the model is removed and analysis begins. Thin slices are cut along planes where stress measurements are desired. These slices are placed in a polariscope to determine fringe orders and stress directions. Depending on the size and shape of the slices, either a diffused-light polariscope, a magnifying slice-analysis polariscope, or a polarizing microscope can be used. Because rotating models usually have a repetitive geometric pattern, several sets of slices can be cut with different orientations, using identical model areas, to completely define the state of stress, and/or duplicate slices can be cut in identical areas for confirmation of results. Stresses are calculated for the slices by conventional photoelastic techniques with the aid of a "fringe constant" determined from a bending or tensile calibration bar. These model stresses are then converted to engine-hardware stress values using standard scaling techniques.

Stress distributions around holes and scallops are critical to the life analysis of engine parts. For example the 3-D, photoelastic method utilizing rotating models was used to determine the stress gradients in the compressor rotor flange shown in Figure 12 a. To evaluate three different geometric configurations with one test, the original scallops and hole radii, Figure 12 b, were modified at two locations by generating both shallow and deep compound radii in the scallops and bolt holes as shown in Figures 12 c and 12 d respectively. After stress freezing, the fringe patterns

were recorded by photographing each configuration in polarized light. Subsequent analysis showed that, while the shallow compound radius was the better configuration for both the scallop and the bolt hole, only a small stress reduction was achieved because of a simultaneous increase in the local hoop stress.



Figure 12

To determine the stress distribution across the minimum section of the flange, model slices were cut in the plane of the flange (hoop stress direction) as indicated in Figures 13 a and b, and also across the flange (axial direction) as shown in Figure 13 c. Detailed stress distributions across the bolt hole section and the minimum flange section are also shown in Figure 13. For all three configurations, the results

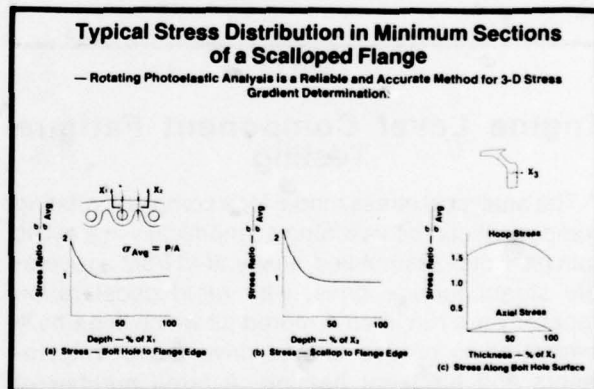


Figure 13

showed a hoop-stress gradient across the bolt hole axial surface as well as an axial-stress component; both gradients peak near the middle. The discovery of both hoop and axial stress gradients across the bolt hole thickness demonstrates the importance of this 3-D technique relative to life prediction where accurate stress analysis is essential. This photoelastic stress analysis has proven to be a reliable and accurate method for such detailed 3-D stress gradient determinations.

Aside from the fact that no method has as yet been developed to produce thermal stresses in photoelas-

tic models, there are always differences between the photoelastic model test and the actual engine part. The major ones fall into three categories:

- **Material Properties** — The most notable is Poisson's ratio which is 0.5 in a stress-frozen model as compared to 0.3 for virtually all engine parts.
- **Boundary Conditions** — The model must be "terminated" somewhere and mounted in a load fixture which is usually different than the actual engine component attachment.
- **Strain Level** — To obtain relatively high fringe orders and, thereby, greater optical accuracy, stresses are usually frozen into 3-D models at strain levels relatively higher than those of the prototype part. This can produce some differences in parts where stresses are not precisely linear with load (e.g., where beam-column effects, airfoil untwist, or contact pressure exist).

Although the differences between model and prototype are often small enough to be ignored, the design engineer should be aware of them. Where exceptional accuracy is important, it has become conventional practice to conduct separate theoretical analyses of the engine part and the photoelastic test model, using the best available methods and accounting for all known differences. The ratios of calculated part stresses to scaled calculated model stresses are then applied as correction factors to the photoelastic results.

Measurements By Indirect Instrumentation Techniques

Instrumentation to measure critical parameters is extremely important to the advancement of ESA techniques. Some measurements are either difficult or impractical to obtain with standard techniques using contact-type instrumentation such as thermocouples or strain gages. Therefore, the designer is often forced to use indirect measurement techniques.

One such technique involves using an optical pyrometer to record the relative temperatures of turbine blades. In this case, a cooled pyrometer is positioned to observe maximum blade-surface area. When calibrated against a reference thermocouple imbedded in the blade, usually in a cooler region, the optical pyrometer can record the relative temperatures of all the blades. This indirect method of optically recording blade temperature has been particularly useful in very high temperature areas where the application of imbedded thermocouples is not feasible. Also, the pyrometer is often the only means of locating the region of maximum blade-surface tem-

perature when it is not known in advance. The design and evaluation of turbine blade cooling systems has been one of the more notable, successful applications of optical pyrometry.

Another indirect measurement system is the high energy X-ray facility which is used to record the internal operating clearances or relative positions of parts during engine operation. Such a facility has the capability of taking X-rays of an operating engine at four frames per minute. The high intensity of the X-rays, using 8 million electron volts, requires a remote, shielded test site. A major contribution of high energy X-ray techniques is the identification of unusual operating clearances between internal engine components. Once identified, additional direct instrumentation can be used to determine or verify the cause in any problem area.

Blade Vibration Measurements Using Optical Light Probes

A relatively new, experimental technique involving optics has been developed for measuring vibratory tip-amplitude in blading during engine operation. Both synchronous (resonant response) and nonsynchronous (random, separated-flow response) blade amplitudes have been measured using this approach. Figure 14 shows a schematic of how blade amplitude and stress can be measured with either single or multiple light probes. Each light probe consists of a bifurcated fiberoptics scanner where light is transmitted to the blade tip through one branch. As the rotor blade passes under the probe, light is reflected from the blade tip into the other branch of the

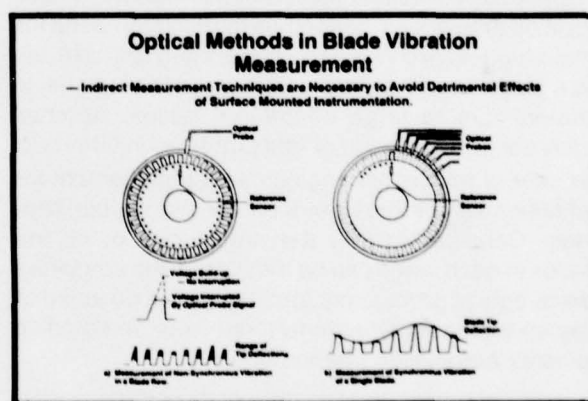


Figure 14

probe to trigger a signal. This method offers an indirect measurement technique that avoids the detrimental effects of surface-mounted instrumentation.

A single light is used to measure nonsynchronous vibrations such as those encountered in random separated-flow type responses. This optical method measures vibratory response by balancing a mag-

netic reference signal from the rotor against a fixed-light beam signal reflected from the rotating blades. Variation of the difference in timing between the magnetic signal and the light probe signal for each blade is a measure of blade tip deflection. When blades are not vibrating, the magnetic and the light probe signals both result in a constant pattern. However, when blades are vibrating randomly, there are variations in the timing difference between the magnetic reference and the light probe signals. This timing difference, which is proportional to blade vibration, is the output of the system.

The synchronous vibration (resonance), also shown in Figure 14, is recorded by locating multiple, fixed light probes over the rotor blade tips with an equal number of magnetic signal stimuli on the rotor. The multiple-light-probe method has the capability of measuring both synchronous and nonsynchronous frequencies at the cost of additional complexity. The light beam signals generated by a single blade in the row are balanced against the magnetic reference signals from the rotor. The reference signal from the rotor has a constantly spaced pattern as the equally spaced target magnets pass a single pickup. If the blade passing the light probes is not vibrating, the light beam and the magnetic reference signals will have a constant relationship. However, if the blade is vibrating in resonance, the multiple light-beam signals from the single blade will not have a constant relationship with the magnetic reference signals from the rotor, and this difference is a measure of the tip deflection of the vibrating blade.

Application of optical light probes to measure blade vibration amplitudes indirectly is particularly useful for small, high-speed engines where the gage size affects blade response and where gage life is a major problem due to large centrifugal forces. Another highly useful application of light probe techniques is in the core of multispool engines as a replacement for radiotelemetry or for large-diameter, high-speed slip-rings. Considering that the amplitudes of all the blades in each stage can be measured, the combined use of optical probes and strain gages is destined to play an increasingly important role in understanding complex aeroelastic phenomena.

Strain Gage Technology

The use of strain gages and thermocouples to measure stress and temperature of engine components in an operational environment has been the backbone of ESA. It follows, therefore, that innovations to improve the capability of leads and strain gages to survive testing (test survivability) will result in more data at lower cost. Figure 15 shows remarkable progress in test survivability for strain gage sys-

tems. For the past 15 years, ceramic strain gages have provided the major improvements. The centrifugal force acting on gage components is pro-

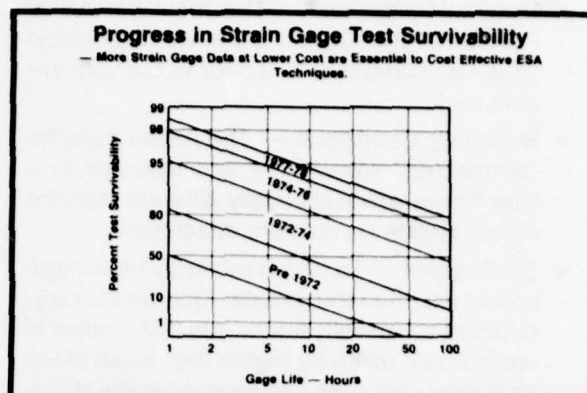


Figure 15

portional to mass, radius and velocity squared. As a result, a small engine can subject the leads and gages to more than four times the force experienced in a large engine. Lightweight gages and leads are critical to achieving data when used at ultrahigh rotational speeds. A comparison of a ceramic and a new, thin-film gage is shown in Figure 16. The thin-film



Figure 16

gage extends the capability of surface-mounted instrumentation to all engines. This gage, similar to a printed circuit, is only 0.3 mils (0.0076 mm) thick; hence, aerodynamic disturbances on the blade surface are essentially eliminated. This is particularly important for small-engine applications where the ceramic gages, which are 20 mils (0.51 mm) thick, often cause increased blockage in the blade-to-blade passage and also change the blade vibratory characteristics. Thin-film gages offer higher quality, lower cost, improved test survivability, and a 60% improvement in the strain level that can be measured. Normally, ceramic strain gages fail at approximately half the amplitude necessary to produce an airfoil failure; whereas tests with thin-film gages have permitted measurement of strain levels up to failure amplitudes.

The Application of the Fast Fourier Transform (FFT)

Another important aspect of ESA is the frequent interpretation of large amounts of data. The introduction of the Fast Fourier Transform (FFT) analyzer has opened new fields of data reduction and analysis of dynamic, time-varying vibration information. The FFT analyzer digitizes the analog signal from strain gages or accelerometers and transforms the information into the frequency domain (similar to the classical Fourier transform). The advantage of the FFT is that it utilizes the storage capacity and speed of the modern computer, using recently developed algorithms, to perform the transform very quickly (for example, the transform of a 1024-point data sample can be conducted in less than 100 milliseconds). The analysis of time-varying or speed-dependent data taken during transients is thus possible. The FFT analyzer can display the response magnitude and phase as a function of frequency and/or time.

The FFT system is capable of handling massive amounts of test data in a relatively short time and at low cost. This has relieved engineers from tedious calculations allowing more time to interpret the data and analyze results. For example, generating a Campbell diagram (as shown in Figure 4) from engine strain gage data requires approximately 20 hours of engineering and 4 hours of data-reduction time. In contrast, the FFT system generates the Campbell diagram automatically from test data with no engineering time and only 20 minutes of data reduction. Furthermore, the FFT system displays the amplitudes as well as the modal frequencies. This offers significant additional reductions in tape-playback and analysis time.

The versatility of the FFT system has been extended to reduce instrumented component-test and engine-test data from accelerometers, strain gages, thermocouples, pressure transducers (kulites), optical pyrometers, and optical probes. As a result, FFT

systems have played key roles in ESA varying from establishing the direction of traveling wave patterns in engine casings to defining pressure contours at the tips of rotating blades.

Lessons Learned and Future Prospects

Progress in development of the various experimental and analytical techniques is a continuing evolution of methods to overcome shortcomings.

An important perspective relative to using ESA is the desirability of using several methods, whenever possible, to measure the same parameter. Often, experimental results will be used to aid in constructing an accurate analytical model to evaluate stress and determine life. When only one experimental method is used, it is not uncommon to obtain misleading data without recognizing it. As a result, extreme care must be taken to check and recheck the measurement and data-reduction systems when only a single method is used.

Techniques to directly measure high temperature stresses and plastic deformations are among the most important and needed breakthroughs yet to come. Until we have adequate capability to make direct stress measurements in complex hot parts, Experimental Life Analysis (ELA) will continue to increase in popularity. Although ELA is not recognized as a science in textbooks, evaluating the part life directly offers a means of bypassing the need for stress determination and analysis. As a result, a "quiet revolution" is taking place with the increasing and widespread use of ELA in the aircraft engine industry. This is not surprising when one considers the cost of engine part failures where the "hot parts" replacement alone can account for 50 percent of the maintenance cost. Overall, ESA and ELA techniques will continue to improve through technological evolution and remain an essential and increasing part of aircraft engine design and development.

DISCUSSION

J.J.Blech, Italy

Could you comment on the possible applicability of optical measurement techniques to a hot component.

Author's Reply

I am afraid I cannot give this comment. We have only tested this so far in low temperature parts, basically the forward stages of a compressor. We have programmes under way, but mainly it is low temperature application at this time.

CONTRIBUTION DE LA PHOTOELASTICIMETRIE
A L'ETUDE DES PIECES DE TURBOMACHINES

par

J.L. GUILLO

Ingénieur - Expert

SNECMA Division Métallurgie-Résistance
 BP 81 - 91003 EVRY CEDEX

FRANCE

RESUME

Dans l'étude des pièces mécaniques, le domaine privilégié de la photoélasticimétrie est la recherche et la mesure des concentrations de contrainte locale.

Pour les applications industrielles, on utilise exclusivement la méthode du "Figeage des Contraintes" pour l'analyse des états tridimensionnels de contrainte.

Les moyens mis en oeuvre pour la préparation et la conduite des opérations de figeage sont décrits et les équipements présentés.

Les exemples d'application sont empruntés à l'étude des éléments vitaux d'un turboréacteur, au stade de la conception et du développement ; ils rendent compte de la diversité des pièces analysées et des modes de sollicitation appliquée.

Outre la connaissance des contraintes locales maximales dans les pièces, deux axes de recherche ont fait l'objet d'une attention particulière :

- l'étude des gradients de contrainte en profondeur, qui peut rendre compte de l'influence du facteur échelle dans la transposition aux pièces "moteur", des résultats d'essais de fatigue sur petites éprouvettes,
- la détermination du facteur d'intensité de contrainte K_I qui régit la propagation des criques sous sollicitations cycliques.

1. INTRODUCTION

Depuis quelques années, la photoélasticimétrie connaît un regain d'intérêt qui se manifeste par une somme importante de communications faites par d'éminents spécialistes dans différents congrès comme le VI^e Congrès International d'Analyse des Contraintes qui s'est tenu à Munich, R.F.A., en septembre 1978.

La plupart des travaux présentés concernent les bases scientifiques de la photoélasticimétrie, les différentes représentations des formes de lumière et les moyens modernes d'analyse optique à partir d'équipements sophistiqués dans lesquels prédominent des considérations de sensibilité, d'automatisme et de traitement numérique des données ; le phénomène à appréhender est la biréfringence, quelle qu'en soit l'origine, et l'analyse des contraintes n'apparaît qu'à titre d'application plus ou moins lointaine, illustrée de quelques cas "école" dont la solution est préalablement connue. Aussi, chacun peut se demander si la photoélasticimétrie est encore réservée à quelques chercheurs privilégiés ou si, désormais, elle est à la portée de l'ingénieur pour résoudre expérimentalement les problèmes de contrainte rencontrés dans l'industrie.

Dans l'exposé qui suit, on s'abstient de rappeler les lois de la photoélasticimétrie, supposées bien connues, pour ne s'attacher qu'à leur application en laboratoire industriel où les préoccupations des mécaniciens s'avèrent très différentes de celles des opticiens. A travers un échantillonnage d'applications concernant le dimensionnement optimal de pièces d'un turbo-réacteur aéronautique, pour lequel les impératifs de légèreté et de sécurité sont excessivement sévères, on montre que la photoélasticimétrie est devenue aujourd'hui une méthode d'analyse expérimentale des contraintes très fine et très fiable, et qu'elle apporte désormais aux bureaux de calculs une aide très précieuse, si non indispensable.

2. POSITION DU PROBLEME

Le potentiel de vie des réacteurs et plus particulièrement celui des pièces tournantes qui les composent, est directement lié aux phénomènes de fatigue oligocyclique (L.C.F.) tant sur le plan de l'amorçage des criques, que sur celui de leur propagation. Plus précisément les bureaux de calculs doivent pouvoir prédire avec la plus grande exactitude possible, le nombre de cycles de démarrage ou de vol type que devra subir la machine en toute sécurité.

Dans les limites de contrainte moyenne bien établies, le dimensionnement général des pièces ne pose aucun problème particulier avec les moyens de calcul actuellement disponibles. Cependant, les discontinuités géométriques fréquemment rencontrées dans les assemblages et les liaisons de pièces, présentent très souvent des zones de forte concentration de contrainte où l'intensité de la contrainte maximale, souvent très ponctuelle, conditionne toute la tenue de la pièce : alors que la connaissance de cette pointe de contrainte, et plus généralement du champ de contrainte environnant, reste encore très délicate par l'analyse mathématique, elle constitue le domaine privilégié de l'analyse photoélastique qui s'avère ainsi à la fois le complément et la validation des méthodes de calcul.

3. METHODES ET PROCEDES

3.1. Aspect général

Dans son application de base la photoélasticimétrie est limitée à l'analyse des deux contraintes principales s'exerçant dans un plan. Si de nombreux travaux peuvent encore se satisfaire de cette limitation, les problèmes complexes rencontrés dans les industries mécaniques requièrent l'emploi de procédés d'analyse tridimensionnelle. Plusieurs de ces procédés sont connus depuis fort longtemps :

- la méthode du "Figeage des Contraintes" a été proposée par G. OPPEL en 1936,
- celle de la "Tranche Incluse" par H. FAVRE en 1929,
- le revêtement photoélastique par A. MESNAGER en 1930,
- la méthode de la "Lumière Diffusée" par R. WELLER et H.P. JESSOP en 1941.

Cependant, leur application s'est diversement développée et alors que certaines méthodes restent encore l'apanage des laboratoires de recherche, d'autres se sont répandues dans la pratique, à la faveur de l'apparition, dans les années 50, des résines époxydes type Araldite, dont les qualités photoélastiques et les aptitudes au moulage ont contribué pour une large part au succès actuel de la photoélasticimétrie tridimensionnelle, notamment dans l'emploi de la méthode du "Figeage des Contraintes".

Bien qu'ayant participé aux développements de la méthode de FAVRE et de celle de MESNAGER, le laboratoire de la SNECMA n'utilise pratiquement plus que la méthode du "Figeage des Contraintes".

3.2. Rappel sommaire du principe du "Figeage des Contraintes"

Le figeage des contraintes s'effectue dans une maquette en matière plastique transparente que l'on soumet à son système de charge au cours d'un cycle thermique.

L'opération consiste à porter la maquette dans une étuve programmée, à une température légèrement supérieure à la température de transition du matériau, de l'ordre de 125°C ; au point de transition, les liaisons entre les chaînes macromoléculaires qui constituent le matériau sont modifiées et le module d'Young chute très rapidement dans un rapport de 200 à 1 environ, le matériau restant parfaitement élastique au-delà comme en-deçà du point de transition. La maquette ayant atteint uniformément cette température, on lui applique le système de charge statique simulant la sollicitation en service ; les contraintes et déformations appliquées, et les biréfringences concomitantes, sont reliées entre elles par les lois de la photoélasticité puisque le matériau reste parfaitement élastique. On ramène alors la température à l'ambiante, très lentement et linéairement pour ne créer aucun gradient thermique dans la masse de la maquette, en maintenant la charge rigoureusement constante.

Au cours du refroidissement, le matériau retrouve son module d'YOUNG élevé, et si l'on supprime la charge après retour à l'ambiante, on ne libère qu'une infime partie de la déformée apparue en température, dans le rapport des modules, ce qui permet d'avancer :

- que les déformations et biréfringences apparues lors de la mise en charge subsistent intégralement et indéfiniment dans la maquette après décharge à la température ambiante,
- qu'elles sont l'expression de l'état tridimensionnel des contraintes élastiques engendrées lors de la mise en charge.

L'analyse complète et détaillée des biréfringences permet en principe la mesure des trois contraintes principales en chaque point de la maquette. Pratiquement, on réduit considérablement le volume des analyses en se limitant à quelques plans principaux renfermant les contraintes les plus significatives. A cet effet, on découpe mécaniquement dans la maquette des feuillets plans de faible épaisseur, qui, moyennant certaines précautions, conservent intégralement les biréfringences propres à l'état de contrainte biaxial s'exerçant dans chacun de ces plans. L'analyse optique de chaque feuillet considéré comme maquette plane permet alors de remonter des biréfringences aux contraintes, suivant les lois de la photoélasticimétrie plane.

Sur le plan pratique, la méthode du figeage présente des avantages très nets par rapport aux autres méthodes citées ci-dessus, mais elle a l'inconvénient de détruire les maquettes, au moins partiellement, comme le montreront certaines illustrations.

4. MOYENS

L'application de la méthode pose au praticien trois problèmes :

- la reproduction en résine photoélastique de la pièce à étudier,
- la mise en charge représentative de la sollicitation en service,
- l'analyse optique précise de la biréfringence.

4.1. Pendant de nombreuses années, les maquettes ont été usinées à partir de bloc de résine, par les procédés d'usinage classique, (cliché 1). Sur le plan photoélastique, les résultats ont généralement été satisfaisants, moyennant des précautions particulières pour tenir compte de la fragilité du matériau et des effets parasites engendrés par échauffement lors de l'usinage. Par contre, sur le plan pratique, le coût et les délais d'exécution ont lourdement grevé les études photoélastiques et limité l'intérêt des bureaux d'études.

Un large développement de la photoélasticimétrie à la SNECMA a été impulsé par la mise au point d'une technique de moulage reproduisant fidèlement la pièce à étudier à l'échelle 1. Le procédé consiste à obtenir une empreinte en matériau approprié, par surmoulage direct de la pièce moteur, puis à couler dans ce moule la résine époxyde convenant à l'analyse photoélastique (voir cliché 2).

Les maquettes ainsi obtenues présentent une fidélité géométrique et une qualité optique très satisfaisantes ; elles sont généralement utilisées "brut de moulage", mais elles peuvent toujours subir une retouche ou un complément d'usinage.

4.2. Pour la mise en charge, il faut d'abord préciser que le figeage des contraintes ne peut se faire que sous sollicitation statique, la charge devant être maintenue rigoureusement constante pendant toute la durée du refroidissement qui varie de huit à quinze heures suivant la masse de la maquette.

Pour toute sollicitation en traction, flexion ou torsion, un système de poids et renvois divers convient généralement, les seules précautions à prendre concernent les dilatations thermiques différentielles entre les éléments métalliques du montage et la maquette en résine.

Pour les pièces tournantes, on reproduit aisément la sollicitation massique centrifuge (état de contrainte essentiellement statique), par la mise en rotation des maquettes avec maintien à vitesse constante pendant toute la durée du cycle de figeage. Par contre, il serait très difficile d'introduire certains types de sollicitation, tels les effets aérodynamiques ou magnétiques, et impossible d'appliquer un système de contrainte d'origine thermique ou vibratoire.

Le banc de figeage spécialement adapté aux pièces tournantes, a fait l'objet d'aménagements successifs et constitue aujourd'hui l'équipement principal du laboratoire. Devant l'impossibilité d'appliquer simultanément des efforts mécaniques et aérodynamiques dans un rapport de similitude constant, le figeage des contraintes dans les roues de compresseur ou turbine est effectué sous vide.

4.3. L'analyse optique qui constitue le centre des préoccupations pour les chercheurs, ne pose aucun problème en laboratoire industriel.

Le prélèvement des feuillets plans dans les plans principaux de contrainte (cliché 3) est effectué soit à la tronçonneuse à meule diamantée, soit plus simplement à la scie à métaux ; dans ce dernier cas, un léger polissage des faces est nécessaire.

Pour l'analyse des biréfringences, on dispose actuellement d'un éventail très large de photoélasticimètres de types divers, utilisant différentes méthodes de compensation. Dans les applications les plus courantes, la SNECMA utilise des équipements très simples :

- des polariscopes à grand champ, pour les observations d'ensemble (cliché 4),
- un microscope polarisant équipé d'un compensateur de Babinet pour l'analyse précise et locale des biréfringences (cliché 5),
- un projecteur de profil à grossissement X 50, équipé de filtres polarisants (cliché 6).

Cependant, pour des applications particulières plus approfondies, le laboratoire dispose d'un photoélasticimètre bidimensionnel automatique ROBERT.

Il convient de retenir que la quasi totalité des applications ici présentées ont été traitées sur les équipements les plus simples.

5. EXEMPLES D'APPLICATION

Ils ont été choisis parmi les pièces tournantes de turboréacteurs. Suivant le stade de développement du moteur concerné, les démarches photoélastiques sont différentes au niveau de la fabrication des maquettes :

- a) lors de l'étape "Avant Projet", les techniques de surmoulage ne peuvent être appliquées, les pièces prototypes n'étant pas encore réalisées ; dans ce cas, les maquettes, bi ou tridimensionnelles, doivent être usinées par les procédés classiques, le plus souvent sous forme de simulacre ou de géométrie simplifiée, à des échelles appropriées (clichés 7 et 8),
- b) dans la phase de réalisation, les prototypes sont progressivement disponibles ; ils peuvent alors être reproduits par surmoulage, à l'échelle 1. Les diverses variantes aboutissant à l'optimisation géométrique de la pièce sont généralement obtenues par retouches de la géométrie de base, soit par ablation, soit par apport de matière avec reprise d'usinage.

5.1. Soufflante de compresseur

5.1.1. Attache des aubes sur un disque de soufflante

a) Une étude préliminaire a été effectuée en photoélasticimétrie bidimensionnelle sur des maquettes en Polyméthacrylate de Méthyle (Plexiglass) (cliché 8). L'analyse a permis d'une part, d'optimiser le profil de l'alvéole (cliché 9) par le choix des raccordements circulaires ou progressifs, et d'autre part, de chiffrer l'influence des raccords d'usinage sur les intensités de contrainte. Les raccords ne pouvant être évités, on a pu fixer leur importance pour maintenir les surcontraintes au-dessous d'un certain taux, et les localiser de telle sorte que la surcontrainte n'affecte pas la contrainte locale maximale.

b) Une deuxième étude a porté sur l'influence de l'angle de brochage des alvéoles. Une expérience antérieure, acquise sur un disque de compresseur à jante mince (cliché 10), avait fait apparaître un accroissement voisin de 100% de la contrainte maximale, imputable à l'angle de brochage de 20°.

Il était important de juger de ces mêmes surcontraintes dans la jante épaisse du disque de soufflante. A cet effet, on a usiné un simulacre de disque (cliché 7), avec des alvéoles calées à différents angles, groupées en plusieurs secteurs. A ce stade du projet, les aubes n'existant pas, elles ont été simulées par des masses équivalentes.

Le cliché 11 met en évidence la surcontrainte due à l'angle de brochage, matérialisée par la différence des biréfringences dans les deux congés ; elle est nettement inférieure à celle que l'on rencontre dans les disques à jante mince, mais loin d'être négligeable.

Il est apparu que l'angle 0° constituait la solution optimale pour le disque, mais le problème se trouve alors déplacé dans le pied d'aube : la solution optimale de l'attache des aubes sur un disque passe par un compromis sur l'angle de brochage des alvéoles et par l'aménagement, entre le pied et le profil de l'aube, d'une zone de transition suffisamment haute, désignée "Echasse".

c) Enfin, la roue complète (cliché 12) a été analysée dans trois versions présentant chacune un angle de brochage des alvéoles différents (5° , 10° et 15°). Les trois types d'aubes correspondants sont présentés sur le cliché 13.

Le cliché 14 illustre les biréfringences figées dans la pale d'une aube, et le cliché 15, celles qui ont été analysées dans les feuillets plans prélevés dans un pied d'aube et dans le disque.

Par rapport à l'analyse de la roue simulacre, la distribution des contraintes et leur intensité maximale se sont avérées très différentes, particulièrement dans le pied d'aube.

5.1.2. Etude du talon supérieur de l'aube de soufflante

Avant même que l'attache de l'aube ait été arrêtée, un modèle métallique avait été réalisé avec un pied d'emprunt, pour les études aérodynamiques. Ce modèle a été utilisé pour l'exécution d'une maquette destinée à l'étude des contraintes dans le talon (cliché 16) ; l'intensité et la localisation exacte des contraintes maximales ont pu être déterminées, et à partir des premiers résultats, des modifications géométriques ont été introduites pour obtenir une solution optimale.

5.2. Tambour de compresseur

Il réunit dans une pièce "monobloc" les trois disques de compresseur et la bride d'assemblage au disque de soufflante (cliché 17).

Les maquettes du tambour, ainsi que celles des anneaux de labyrinthe et de butée, ont pu être obtenues entièrement terminées par les procédés habituels de surmoulage des prototypes métalliques et de coulée de la résine photoélastique. Par contre, la roue de soufflante qui ne pouvait être testée en vraie grandeur, vu ses dimensions, a été remplacée par une roue simulacre spécialement dimensionnée pour avoir les mêmes déformées radiales au niveau des trous d'assemblage.

Cette étude a permis de chiffrer les contraintes dans les attaches d'aube sur les disques, dans les différentes brides et dans les anneaux de labyrinthe et de butée.

5.3. Accouplement des arbres Turbine/Compresseur

Deux problèmes se posent au niveau de l'assemblage des deux arbres reliant les étages de turbine au compresseur :

- le premier concerne les cannelures ; leur optimisation porte sur trois points :
 - . le type de congé à la base des dents,
 - . le raccordement des extrémités aux parties lisses de l'arbre,
 - . la loi d'évolution des sections parallèles dans les deux parties mâle et femelle.
- le deuxième est relatif à la présence des trous du déshuileur ; les surcontraintes dans les trous doivent être atténuées par un renforcement local qui lui-même doit être raccordé progressivement pour éviter d'autres surcontraintes.

Il n'a pas été nécessaire dans ce cas de reproduire toute la longueur des deux arbres. La réalisation des maquettes a été effectuée à partir du surmoulage de pièces simulacres en alliage léger reproduisant uniquement, mais fidèlement, la géométrie des deux extrémités à assembler (cliché 18).

Les contraintes ont été figées sous une sollicitation en torsion.

Le cliché 19 illustre la distribution des contraintes sur le contour des trous et les surcontraintes locales observées en fin de portée des cannelures.

Les analyses successives, effectuées sur plusieurs définitions ont permis :

- de dégager la meilleure évolution des épaisseurs dans les deux éléments, mâle et femelle, pour la transmission du couple,
- d'optimiser les raccordements des extrémités de la partie cannelée aux parties lisses,
- d'adopter un profil "Anse de Panier" pour les fonds de cannelures,
- de définir l'importance du renforcement d'épaisseur au droit des trous du déshuileur.

5.4. Rotor de turbine

Différentes démarches ont été entreprises sur les pièces les plus importantes du rotor.

Les roues de turbine soumises à leur propre sollicitation massique centrifuge ont été analysées dans deux configurations :

- chaque roue "tournant isolément",

- "roues assemblées", avec anneaux de labyrinthe, et, dans un cas, avec cône d'entraînement.

Le tourillon arrière, peu concerné par la sollicitation centrifuge, a été analysé dans deux cas de charge, torsion et traction axiale.

5.4.1. Roues "tournant isolément"

La maquette de l'une des roues de turbine analysées figure sur le cliché 20 ; le disque et les aubes ont été obtenus "brut de moulage".

L'analyse optique a permis de chiffrer les contraintes sur le pourtour des alvéoles et les contraintes de flexion dans la coupe radiale (cliché 21). On remarquera la bonne répartition des contraintes, sans concentration localisée, dans ce fond d'alvéole de type "Anse de Panier".

Dans l'une des roues, le pied d'aube accuse une contrainte maximale nettement plus élevée que celle de la dent du disque (cliché 22), alors que les efforts appliqués et les sections au col sont pratiquement les mêmes. Il devient évident, que l'inégalité des contraintes doit être mise au compte de la différence géométrique entre le bulbe de l'aube et celui de la dent. L'amélioration a consisté à rapprocher la géométrie du pied de celle de la dent, en respectant la hiérarchie conduisant à une rupture du pied d'aube avant celle de l'attache du disque.

5.4.2. Roues assemblées

Dans le passé, l'assemblage des roues de turbine a souvent été assuré par des boulons ou tirants traversant la toile des disques. Cette solution pénalise les disques d'une très forte concentration de contrainte autour des trous de fixation.

Dans les nouvelles machines, les assemblages boulonnés sont extérieurs au corps du disque (cliché 23), les brides de fixation venant se raccorder à la jante ou parfois sur la toile du disque. La présence des trous de fixation entraîne toujours des concentrations de contrainte dans les brides, mais il est possible de les atténuer par un festonnage judicieux. Dans le cas présent, d'autres exigences imposées par des passages d'air de refroidissement ont compliqué le choix des festons et entraîné une étude très poussée au niveau de chacun des assemblages.

Après avoir analysé chaque élément tournant isolément, on a procédé à l'analyse des mêmes brides, anneaux de labyrinthe et cône d'entraînement, assemblés par deux, trois ou quatre (cliché 24).

Les géométries de bride dans un même assemblage pouvant être très différentes (cliché 25), et leurs épaisseurs souvent inégales, on a mis en évidence leurs influences réciproques qui se sont traduites par des valeurs de contrainte nettement différentes dans le cas de brides "tournant isolément", par rapport au cas de brides assemblées.

Le but d'une telle étude se résume à l'optimisation géométrique des festons (forme, rayon, flèche) telle que les contraintes maximales soient égales dans les trous et les festons.

5.4.3. Liaison Disques/Arbre de turbine

Elle est assurée par un jeu de deux cônes : le cône d'entraînement et le tourillon arrière (cliché 26).

a) Le premier est plus particulièrement concerné par la sollicitation massique centrifuge.

Dans une première étape, les contraintes ont été analysées après figeage en rotation dans la configuration "tournant isolément". Le cliché 27 illustre la répartition des contraintes autour des trous dans une première version.

Par la suite, l'optimisation du festonnage sur la périphérie a fait l'objet d'une recherche très poussée dans les deux configurations "tournant isolément" et "assemblé", en association avec celle des roues et anneaux de labyrinthes, voir § 5.4.2.

b) Le tourillon arrière, moins sensible à la sollicitation centrifuge, est concerné par les deux sollicitations s'exerçant sur l'arbre : le couple de torsion et l'effort axial.

L'analyse des contraintes a été faite séparément dans les deux cas de charge ; le cliché 28 illustre la répartition des contraintes autour des trous dans les deux cas.

A partir des relevés polaires des contraintes sur le contour de chaque trou, la superposition des deux états de contrainte se fait aisément par le calcul. On remarquera en comparant les clichés 28a et 28b, que les contraintes maximales se localisent différemment dans les deux cas : dans la combinaison des deux sollicitations, les valeurs maximales ne s'additionnent pas.

6. NOUVEAUX DOMAINES D'APPLICATION

Dans un cadre plus général, aux frontières de la recherche appliquée, deux thèmes de travail ont fait l'objet de quelques investigations dont les résultats sont assez encourageants. Ils se situent au-delà de la connaissance des contraintes dans les pièces et apportent des informations concernant le comportement en fatigue.

6.1. Le premier concerne la transposition des résultats de fatigue obtenus sur petites éprouvettes entaillées, aux pièces réelles de grandes dimensions. Dans le cas de forte concentration de contrainte, l'un des facteurs les plus déterminants est le facteur échelle, dont l'importance est connue depuis longtemps, mais encore mal dominée. Il peut être pris en compte dans la notion de gradient des trois contraintes mais plus particulièrement du gradient des contraintes en profondeur. En effet, on sait que deux éprouvettes de fatigue semblables mais dans un rapport d'échelle de 1 à 2, auront en fatigue un comportement différent, malgré un même taux de contrainte locale maximale et le même facteur de concentration K_t . Le fait que les gradients de contrainte en profondeur diffèrent dans le rapport inverse des échelles, peut expliquer la différence de comportement.

La connaissance des gradients de contrainte dans les pièces moteur et les éprouvettes de fatigue entaillées à partir des mesures photoélastiques, pourrait conduire, en attendant l'établissement de lois plus générales, à effectuer les essais de fatigue en utilisant des éprouvettes respectant à la fois :

- la même contrainte locale maximale,
- la même contrainte moyenne aux limites,
- le même gradient de contrainte en profondeur.

Comme la donnée photoélastique relative à l'intensité des contraintes ne traduit que la différence des contraintes principales, une opération supplémentaire, bien connue des spécialistes sous le nom de "Séparation des contraintes" est indispensable pour obtenir dans toute la pièce la carte complète des contraintes principales à partir de laquelle seront déduits les gradients des trois contraintes en profondeur, et tout spécialement le gradient de celle qui est maximale en surface.

A cet effet, deux voies sont actuellement proposées :

- l'intégration des équations d'équilibre à partir d'un bord libre, à l'aide des mesures ponctuelles et précises fournies par un photoélasticimètre automatique, du type ROBERT,
- la recherche d'une seconde donnée, telle que la somme des contraintes principales que peut fournir l'holographie.

L'expérience montre que la première voie convient mieux aux laboratoires industriels ; elle est pratiquée à la SNECMA qui est maintenant en mesure de chiffrer les gradients de contrainte en profondeur dans les pièces moteur.

6.2. Le second thème de recherche appliquée intéresse l'étude de la propagation des criques dans le mécanisme de la rupture.

Plusieurs approches ont été proposées pour exprimer la vitesse de propagation des criques en fatigue, mais l'une des plus couramment utilisées actuellement est la connaissance des facteurs d'intensité de contrainte K définissant le champ de contrainte à l'extrémité de la fissure. La détermination des facteurs K_I , K_{II} , K_{III} , correspondant aux modes de sollicitation I, II et III, a fait l'objet de nombreux travaux théoriques, mais les travaux expérimentaux sont encore très limités.

Dans les années 50, G. IRWIN et D. POST ont proposé de mesurer le facteur K en photoélasticimétrie. A leur suite, différents auteurs, SMITH et KOBAYASHI entre autres, ont proposé des méthodes dérivées de celles d'IRWIN, et ont fait état de résultats satisfaisants. Il restait à savoir si ces méthodes avaient atteint un développement suffisant pour être mises en pratique en laboratoire industriel.

Dans un premier temps, on a appliqué les méthodes précitées à la mesure du coefficient K_I dans quelques cas simples dont les solutions sont bien connues :

- l'éprouvette ASTM type CT (clichés 29 et 30)
- l'éprouvette ASTM type KT (cliché 31)
- la plaque plane à crique centrale traversante (cliché 32).

Comme souvent, la hiérarchie des difficultés n'est pas la même en laboratoire industriel et en laboratoire de recherche.

L'analyse de la biréfringence à l'extrémité de la crique ne nécessite aucun équipement sophistiqué : après avoir tenté d'utiliser le photoélasticimètre ROBERT, on est revenu à l'exploitation de photographies prises sur le projecteur de profil à grossissement X 50, (voir cliché 30) ; les résultats sont supérieurs à ceux du ROBERT et très satisfaisants.

Par contre, les difficultés s'accroissent dans l'exécution des maquettes, en particulier pour la réalisation des criques qui requiert des précautions extrêmes. Certains auteurs s'accommodent d'entailles à fond circulaire de faible rayon, $0,25 < r < 0,5$ mm, et parfois même rectangulaire, $0,25 < e < 0,5$ mm (voir cliché 33).

Or on sait qu'à l'extrémité de la crique, le champ de contrainte défini par K est très limité, dans un rayon de l'ordre de 0,05 à 1 mm ; on conçoit dans ce cas que l'entaille même très aiguë n'est pas représentative de la crique, et c'est pourquoi le laboratoire de la SNECMA opère toujours sur des criques exécutées par pénétration d'une lame effilée dans la maquette portée à l'état caoutchoutique par une montée en température.

Il est entendu que toutes ces mesures ne concernent que le domaine élastique, comme d'ailleurs les coefficients K qui caractérisent le champ de contrainte dans l'hypothèse d'un comportement élastique du matériau. Même dans ces limites, il reste beaucoup à faire pour fixer les conditions expérimentales et

l'influence de divers paramètres, en particulier du coefficient de POISSON ν dont la valeur se rapproche de 0,5 à la température du figeage des contraintes. Enfin, il reste à déterminer dans quelles conditions pourraient être abordées les mesures des coefficients K_{II} et K_{III} . Un programme de travail est en cours et des résultats sur K_{II} sont actuellement attendus sur la plaque plane à entaille centrale oblique et traversante.

7. POSITION PAR RAPPORT AU CALCUL NUMERIQUE

Chacun sait que les méthodes modernes de calcul ont fait ces dernières années des progrès considérables et certains peuvent être amenés à penser qu'elles éclipsent les méthodes analogiques à plus ou moins brève échéance.

La grande majorité des problèmes sera, assurément et fort heureusement traitée par les méthodes numériques, mais une part privilégiée sera toujours réservée à la photoélasticimétrie, en considération d'une part, de sa spécificité et d'autre part, du supplément de confiance dont bénéficient auprès des concepteurs, les résultats de toute expérimentation.

Mais plus qu'une confrontation avec les méthodes numériques, c'est une association de la méthode photoélastique avec les calculs qu'il faut rechercher et développer, car les calculs se trouvent enrichis par cette coopération.

En effet, si l'on peut considérer les résultats photoélastiques comme de simples compléments aux calculs dans certains cas prédestinés comme la recherche des concentrations de contrainte dans une pièce complexe ou dans un assemblage de pièces soumis à une sollicitation particulière, on doit plus justement les considérer comme base d'appui dans les études avancées.

Dans cette optique, le schéma des études les plus complexes peut s'articuler de la façon suivante :

- l'analyse photoélastique donne la carte complète des contraintes relevées dans une maquette en résine aux caractéristiques élastiques données, soumise à une sollicitation bien déterminée,
- guidée par les résultats photoélastiques, la méthode numérique affine le découpage en éléments finis dans les zones les plus critiques, et, éventuellement modifie ses conditions aux limites pour se rapprocher des valeurs données par la photoélasticimétrie,
- le programme de calcul, validé par la photoélasticimétrie, peut alors être appliqué dans différentes hypothèses élastiques, dans différentes configurations géométriques et dans toutes les conditions de sollicitation en service, vibratoire, aérodynamique et thermique, que l'analyse photoélastique ne peut prendre en compte.

Un dernier aspect peut être évoqué, le coût de l'opération. Quelle que soit la méthode choisie, il croît très rapidement avec la complexité de la pièce ou de l'ensemble à étudier :

- la réalisation des maquettes, malgré les avantages considérables des techniques de moulage, représente la part la plus importante du prix de revient des études photoélastiques ; c'est la raison pour laquelle elles resteront toujours onéreuses et réservées à l'étude des pièces engageant l'intégrité des matériels,
- de son côté, le calcul tridimensionnel par éléments finis fait rapidement appel à des moyens considérables dès que les pièces se compliquent.

Aussi, si la balance sur le plan économique penche fréquemment en faveur du calcul pour les pièces courantes, l'interrogation reste toujours posée dans le cas des pièces complexes :

- doit-on se contenter des résultats de calcul, d'un prix raisonnable, mais dont la fiabilité reste à confirmer ?
- où faut-il accepter une dépense supérieure pour acquérir une première confirmation expérimentale ?

Malheureusement, ou peut-être heureusement pour la photoélasticimétrie, la réponse n'est acquise qu'à posteriori : le calcul était souvent suffisant, mais il a fallu recourir à la photoélasticimétrie pour le démontrer.

8. CONCLUSION

La photoélasticimétrie n'est plus l'apanage d'un cercle de chercheurs ou d'universitaires en quête de sujet de thèse. Elle est entrée depuis plusieurs années dans la pratique industrielle où sa spécificité convient tout particulièrement à l'analyse des concentrations de contraintes très localisées, fréquemment rencontrées dans les pièces mécaniques.

Dans son application courante, elle ne nécessite pas d'équipements très compliqués mais une solide expérience des utilisateurs.

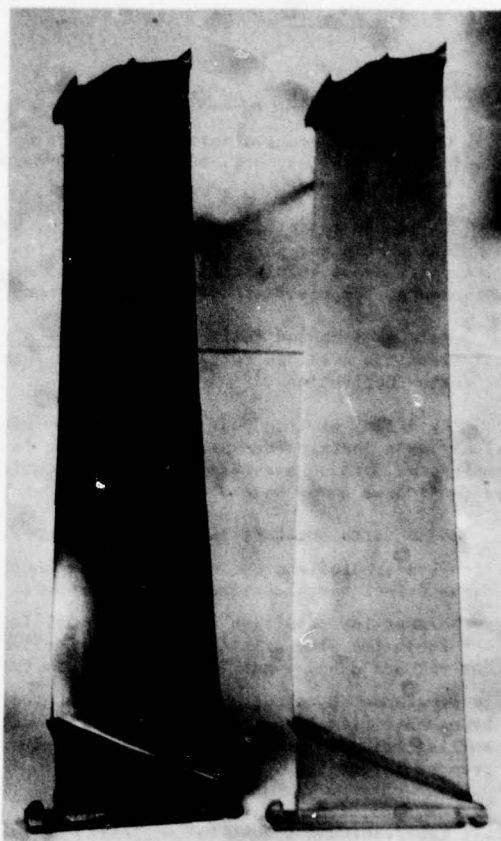
La diversité des études présentées montre tout le parti que peut en tirer un bureau d'études de conception de moteurs d'avions.

Pièce en alliage
de titane

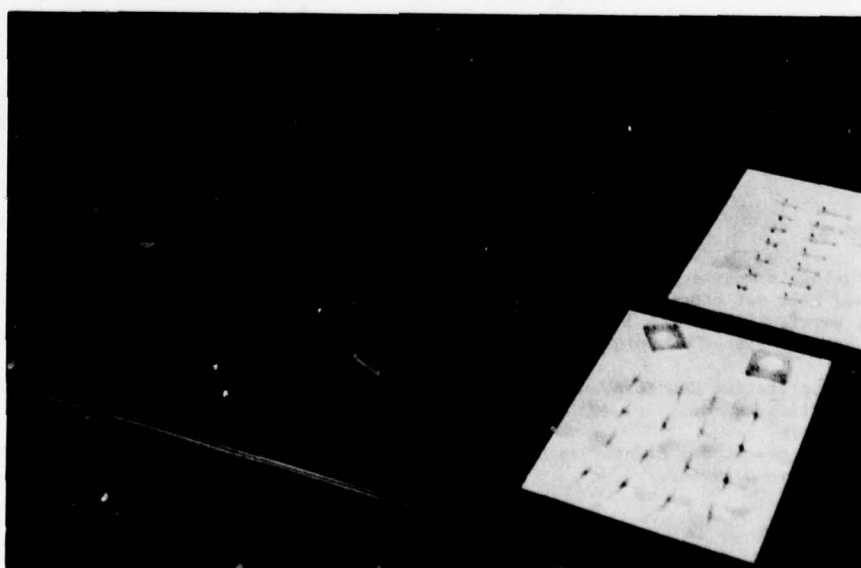
Maquette en résine
époxyde (Araldite)
obtenue par moulage



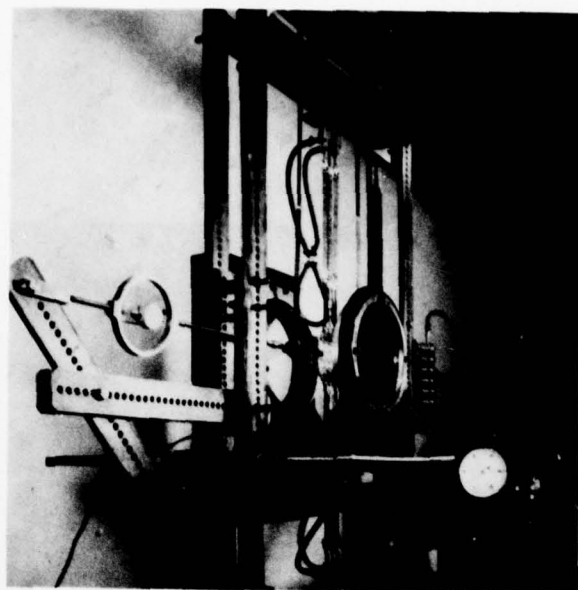
Cliché 1 - Disque de soufflante. Maquette entièrement
usinée, alvéoles brochés



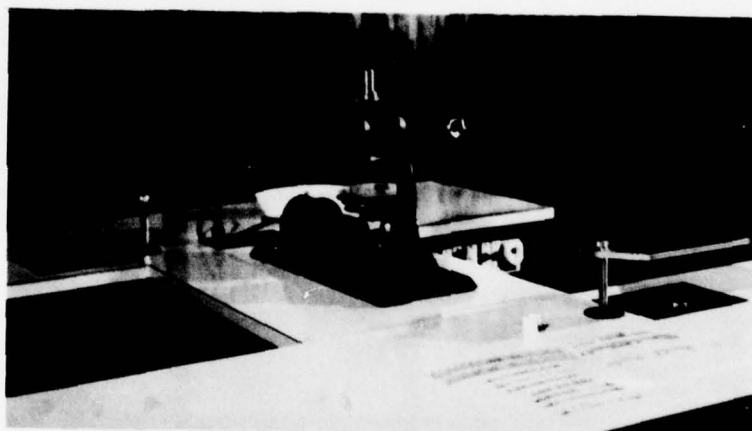
Cliché 2 - Aube de soufflante



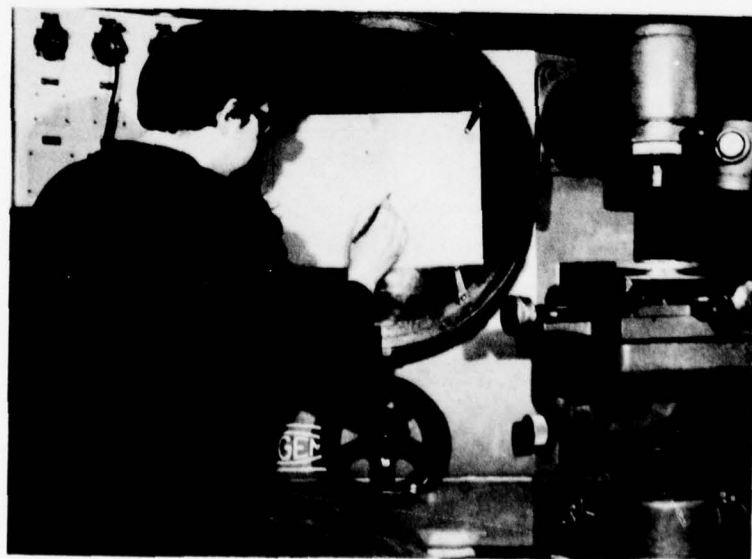
Cliché 3 - Feuilletés plans découpés dans les maquettes



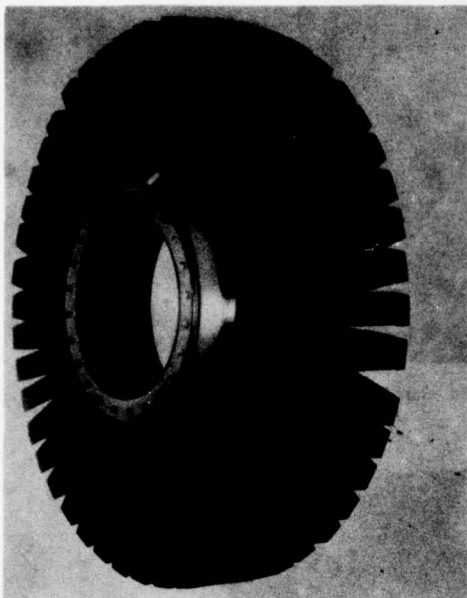
Cliché 4 - Polariscope à grand champ



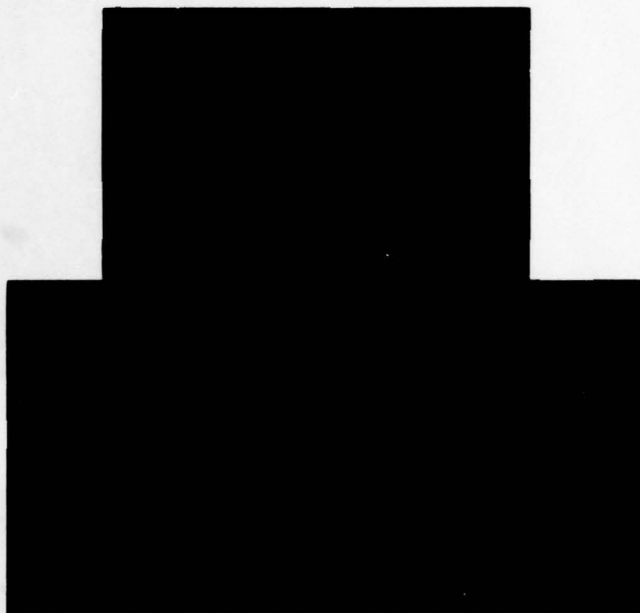
Cliché 5 - Microscope polarisant avec compensateur de BABINET



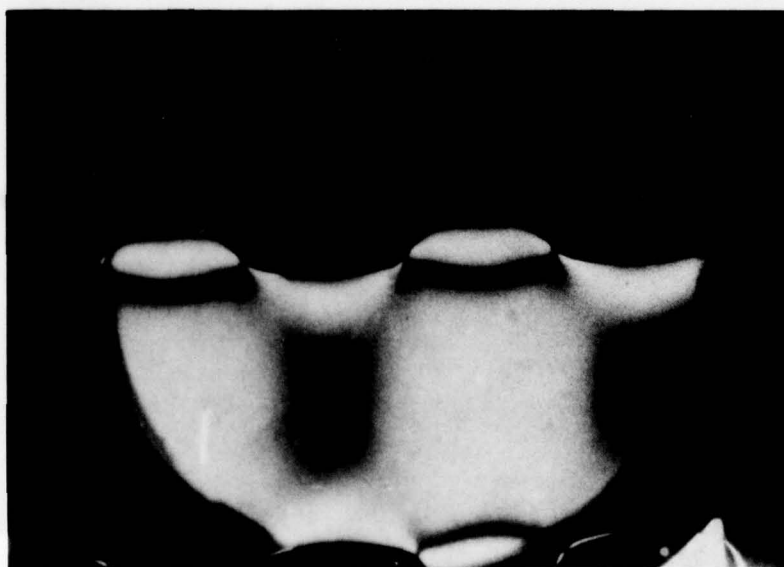
Cliché 6 - Projecteur de profil équipé en photoélasticimètre



Cliché 7 - Simulacre de roue de soufflante



Cliché 8 - Maquettes planes en Polymétacrylate de Méthyle (Plexiglass)



Cliché 9 - Isochromatiques observées en charge directe



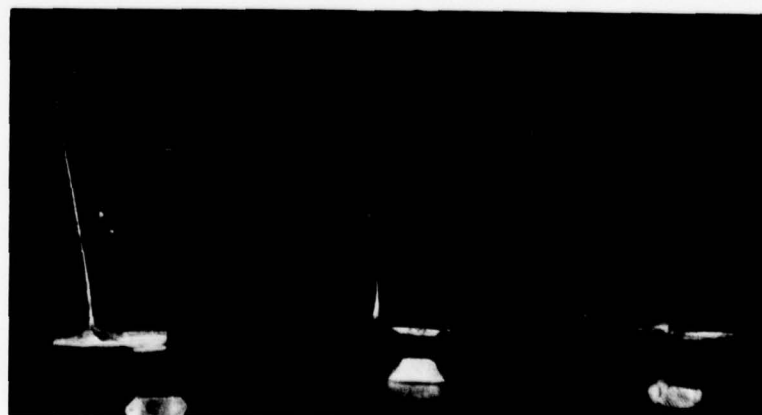
Cliché 10 - Influence de l'angle de brochage des alvéoles dans un disque à jante mince



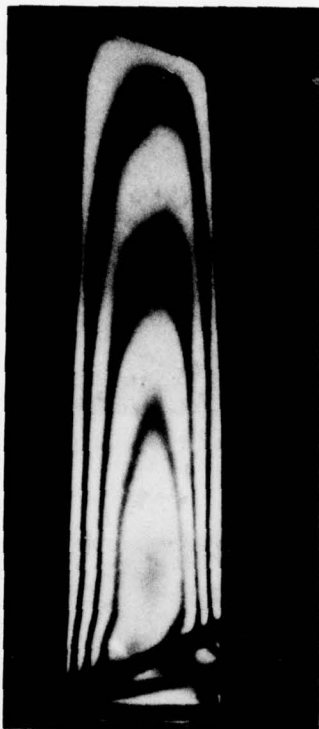
Cliché 11 - Isochromatiques observées dans des feuillets prélevés sur la maquette figée du cliché 7



Cliché 12 - Maquettes de roue de soufflante à l'échelle 1/2



Cliché 13 - Maquettes d'aubes à calage 5°, 10° et 15°



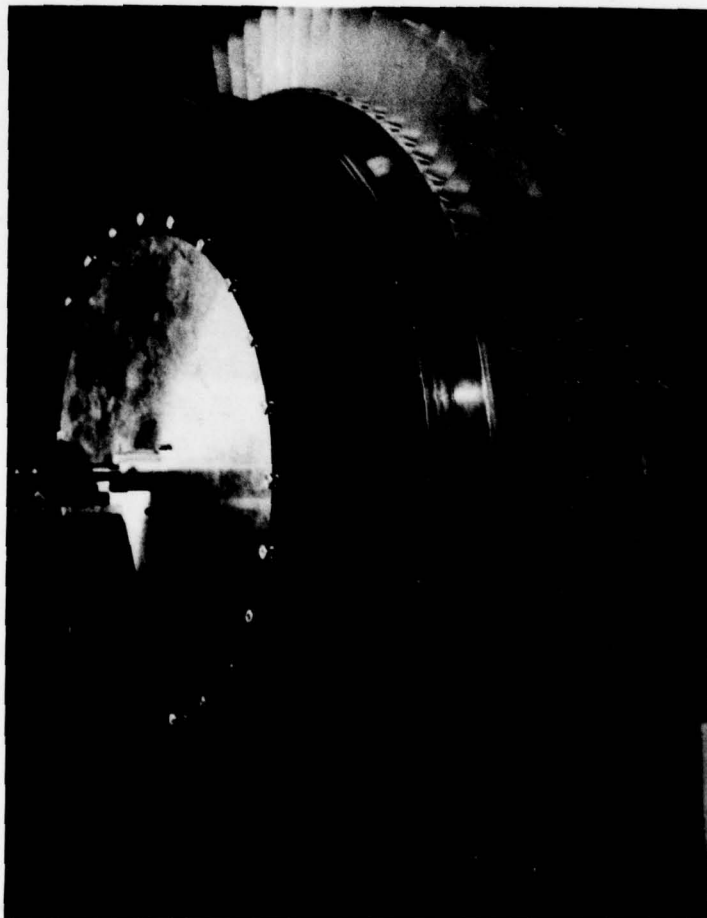
Cliché 14 - Isochromatiques observées dans la pale de l'aube de soufflante



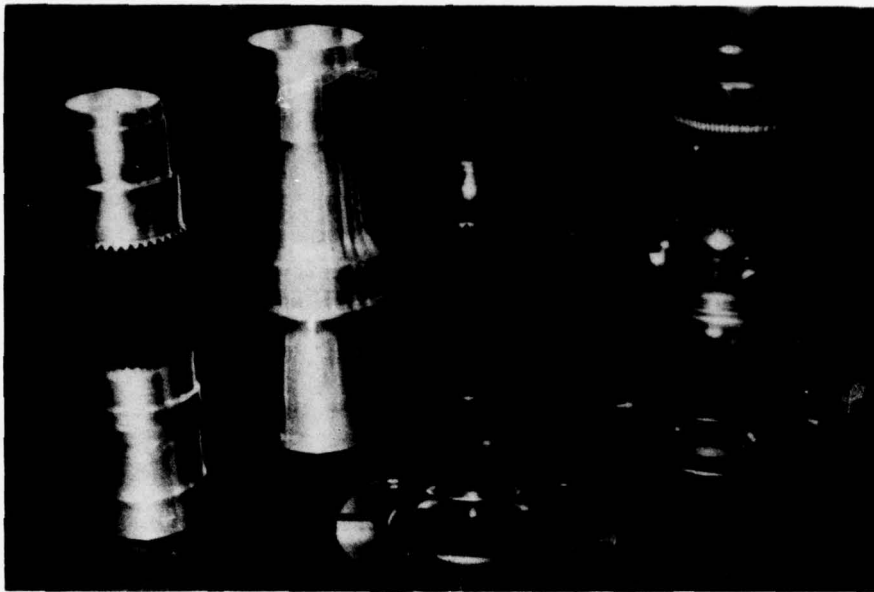
Cliché 15 - Isochromatiques observées dans l'attache de l'aube de soufflante du cliché 12



Cliché 16 - Maquette d'aube de soufflante

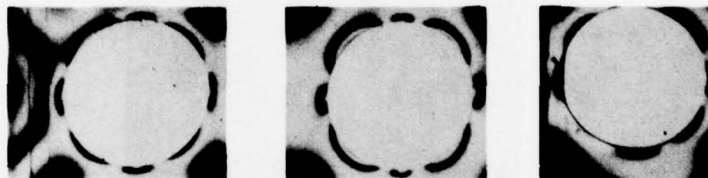


Cliché 17 - Maquettes de tambour de compresseur

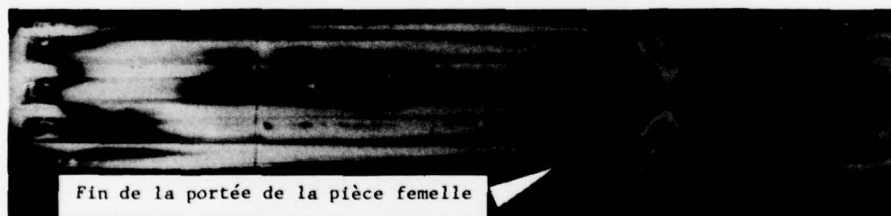


Pièces simulacres en alliage léger

Maquettes en Araldite

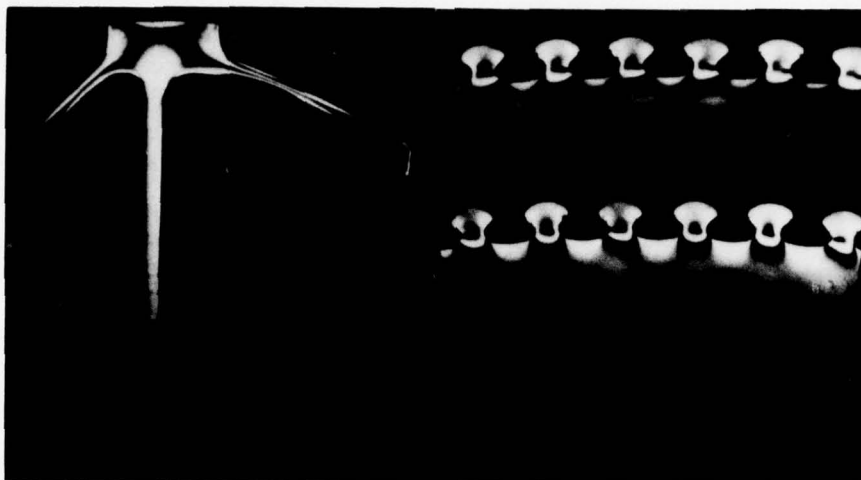
Cliché 19 - Accouplement d'arbres

Trous percés dans l'arbre - Examens dans l'épaisseur

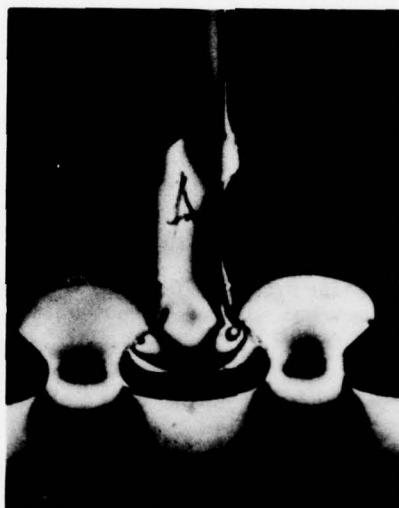


Fin de la portée de la pièce femelle

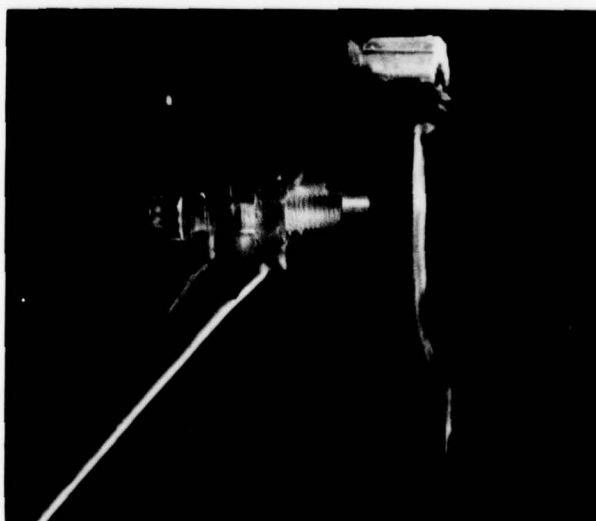
Cliché 19 - Isochromatiques observées après figeage en torsionCliché 20 - Maquette de roue de turbine



Cliché 21 - Isochromatiques observées dans les feuillets après figeage en rotation



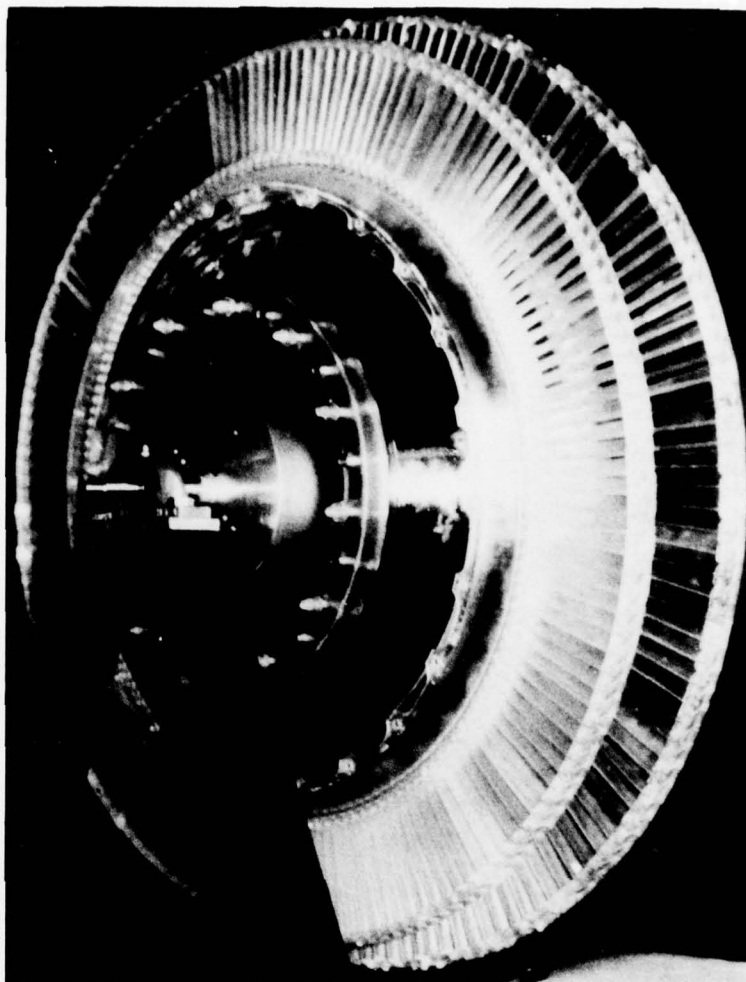
Cliché 22 - Isochromatiques observées dans l'attache de l'aube



Cliché 23 - Eléments de maquettes d'assemblage de disque (conception sans perçage des toiles)

Cliché 24

Maquettes de roues de
turbine assemblées



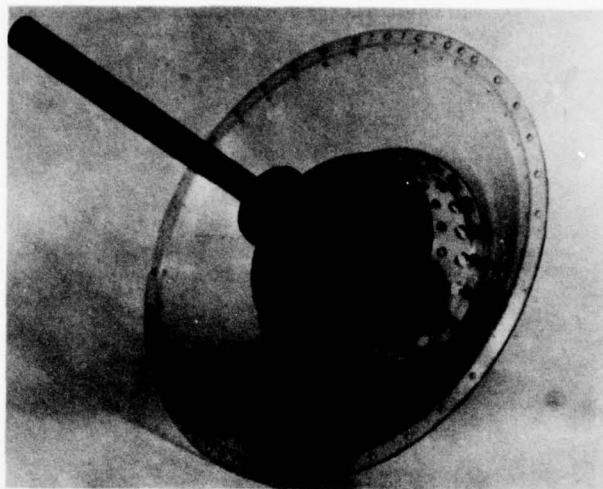
Cliché 25

Isochromatiques observées
dans divers types de
brides



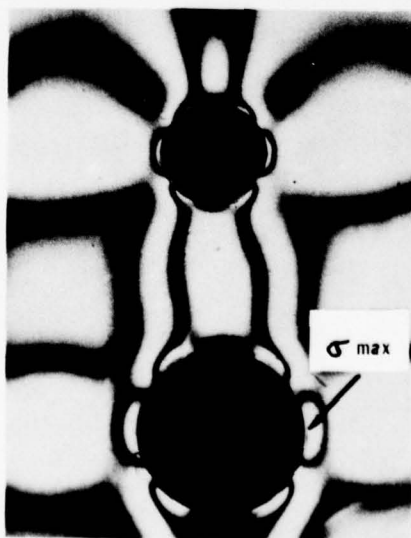
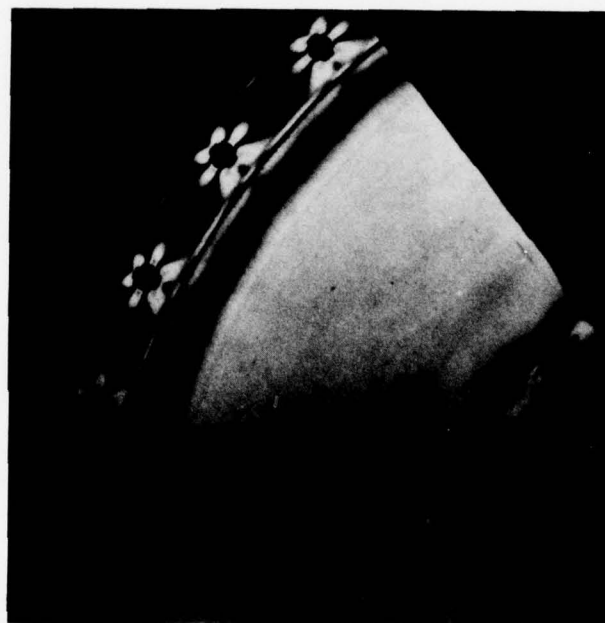
Cliché 26

Maquettes de tourillon
de turbine

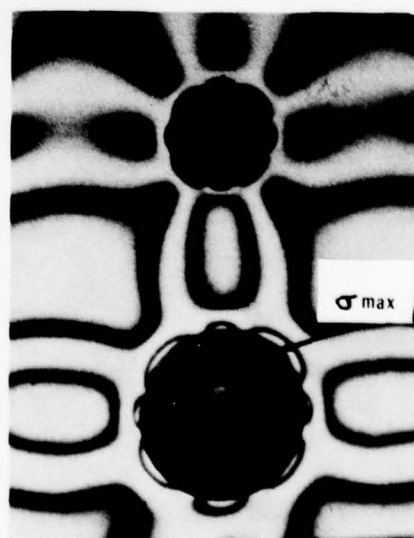


Cliché 27

Isochromatiques observées
dans le cône d'entraînement

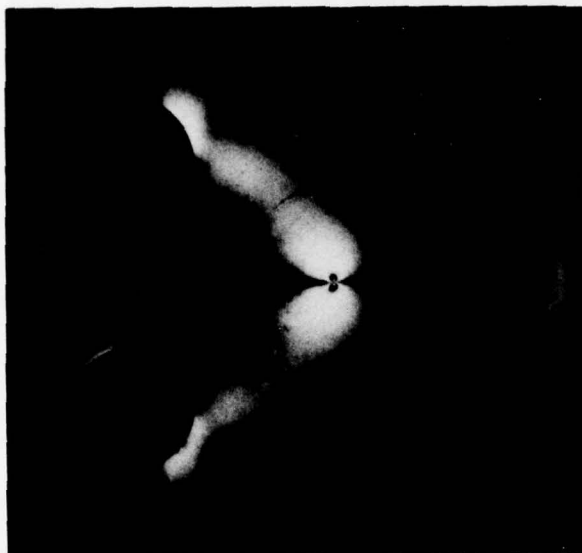


28a - En traction

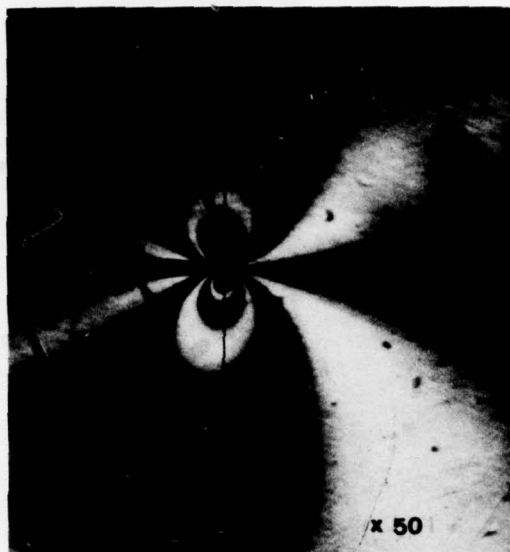


28b - En torsion

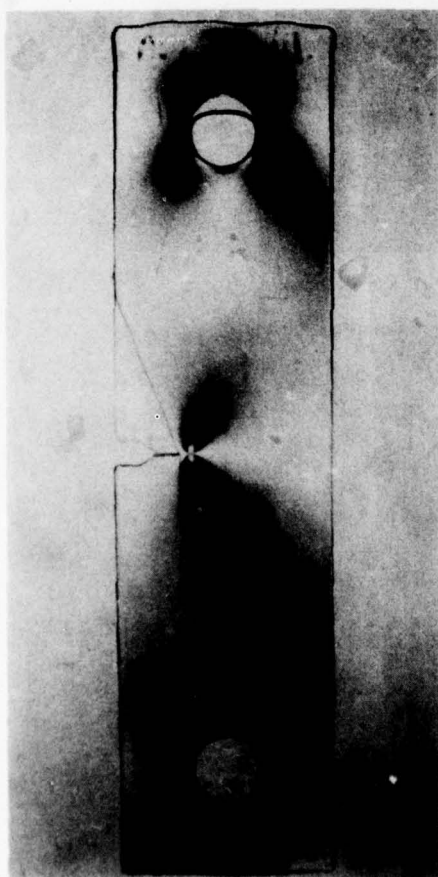
Cliché 28 - Isochromatiques observées dans le tourillon arrière



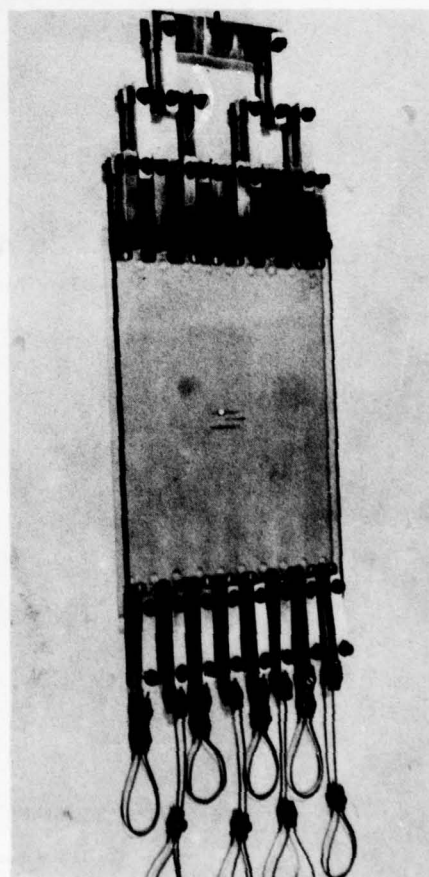
Cliché 29 - Isochromatiques observées dans une éprouvette CT - ASTM



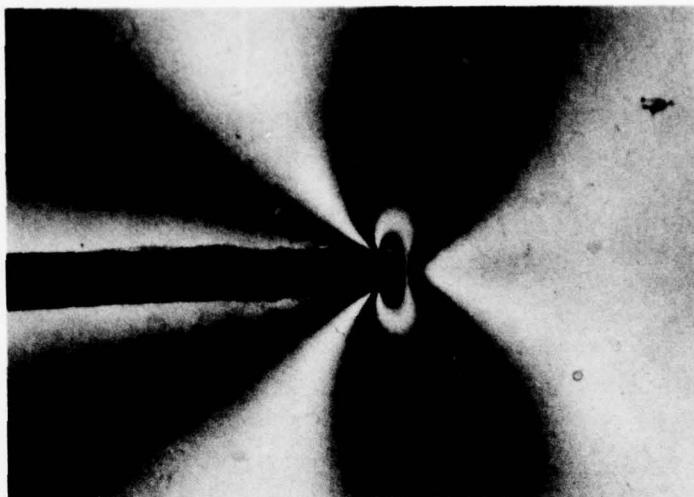
Cliché 30 - Détail des isochromatiques à fond de crique dans l'éprouvette du cliché 29



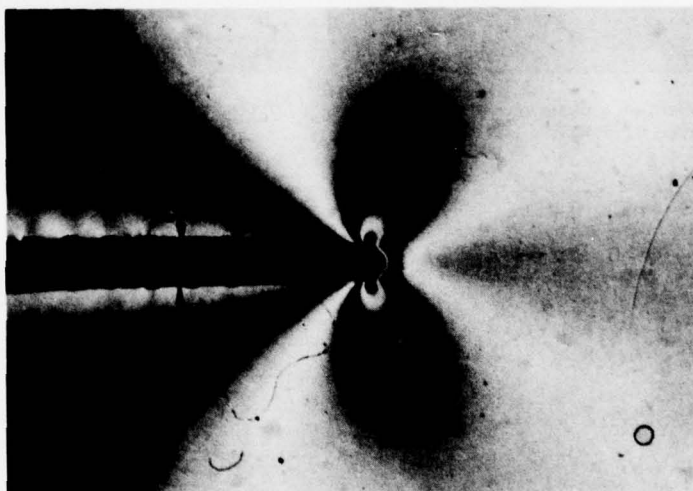
Cliché 31 - Isochromatiques observées dans l'éprouvette ASTM à entaille latérale



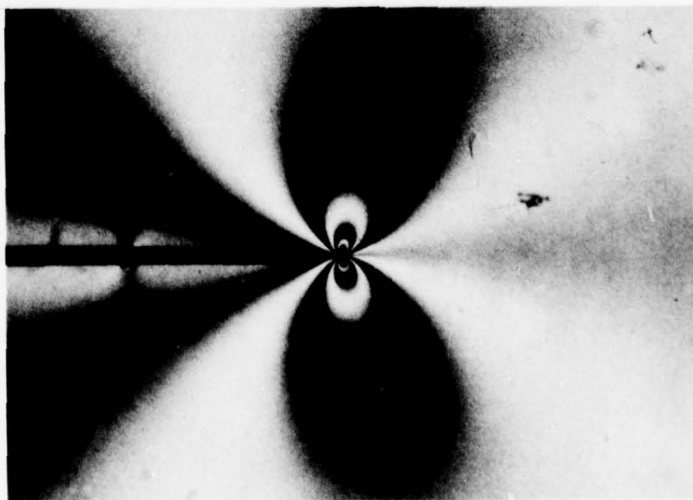
Cliché 32 - Maquette de la plaque à crique centrale traversante



33a - Fond circulaire, $r = 0,25$ mm



33b - Fond rectangulaire, $e = 0,5$ mm



33c - Fond avec crique

DISCUSSION

P.S.Kuo, US

Would you discuss the third dimensional and thermal effects on the accuracy of the photoelastic analysis.

Reponse d'Auteur

- (1) Influence de la troisième contrainte sur la précision des mesures.

Dans une maquette tri-dimensionnelle figée (exactement comme dans une maquette sous charge en temps réel), les lois de la photoélasticité relient l'ellipsoïde des contraintes d'axes X , Y et Z à celui des indices suivant ces mêmes axes, mais il n'est pas possible de mesurer chacun de ces indices en tout point de la maquette et de remonter aux trois contraintes.

Pour accéder aux contraintes, on doit isoler dans la maquette un plan principal de contrainte dans lequel l'ellipse des contraintes T_x et T_y peut être reliée à celle des indices n_x et n_y . La biréfringence observée dans ce plan ne dépend plus que de n_x et n_y (donc de T_x et T_y); le troisième indice n_z lié à la contrainte T_z n'intervient pas dans la biréfringence et n'a aucun effet sur la précision de la mesure.

- (2) Influence des effets thermiques

Le cycle thermique de figeage est très lent; la durée de refroidissement après application des charges s'étend entre 8 et 20 heures, suivant la masse de la maquette. Le refroidissement est piloté par deux thermocouples situés l'un au coeur, l'autre en surface d'une masse de matériau semblable à celle de la maquette et soumise près d'elle au cycle de figeage: le refroidissement imposé est tel qu'il n'y ait jamais plus de 1°C d'écart entre la température à coeur et celle de la surface. Dans ces conditions, la température peut être considérée comme homogène dans toute la masse de la maquette et les effets thermiques sur la précision des mesures sont absolument négligeables.

A CONTRIBUTION ON THERMAL FATIGUE IN COOLED TURBINE BLADING

W. Peschel, R. Schreieck
Motoren- und Turbinen-Union München GmbH
8000 München 50, Dachauer Str. 665

SUMMARY

Thermal fatigue is an important criterion for predicting the life of cooled turbine blading. Its causes are thermal stresses which arise from local inhibition of thermal expansion and which are not amenable to direct measurement. Their calculation requires knowledge of the temperature distribution in space and time.

In the case of turbine blading, temperature distribution in the mean section of the blade can readily be dealt with as a problem of heat conduction in a plane. For stress calculation, it is here assumed that the cross section remains plane. Stresses in the sectional plane and normal stresses in the direction of blade span result, the latter being the dominant ones.

For thermal fatigue test conditions, stress and strain profiles in the blade are calculated using measured and calculated temperature distributions. Non-elastic material behaviour (creep) is taken into account. In the thermal fatigue tests, the pattern of damage vary with superimposed external stresses; this behaviour is explained in the light of the calculated stress-strain cycles.

SYMBOLS

x, y	co-ordinates in the directions of the principle axes of inertia of the mean blade section
z	co-ordinate in the direction of the blade span
t	time
T	absolute temperature
σ	normal stress
ϵ	strain
F	spanwise tension force
A	blade cross section area
E	modulus of elasticity
ν	Poisson's ratio
α	coefficient of thermal expansion
u, v	bending deformation in directions x, y
w	displacement in direction z
φ	angle of twist
δ	pre-twist per unit length of blade
C_T	torsional stiffness
I_{xx}, I_{yy}	moments of inertia of blade cross section

1. MECHANICS OF DAMAGE TO TURBINE BLADES

In the interest of efficiency advanced gas turbine engines must be designed for high mechanical and thermal blade loading. It is necessary to predict the service life of turbine blades to arrive at a safe design. This requires familiarity with the various mechanics of damage limiting the life of a turbine blade:

- damage by foreign object impact; foreign objects are blown into the blade cascade by the gas stream
- vibration fatigue failure as a result of high-frequency excitement caused by the shafting or the gas stream and coming into resonance with the natural vibrations of the blade
- fatigue cracks as a result of cyclic changes in the mechanical and thermal loading; maximum thermal stresses occur because of steep temperature gradients especially in the transient load conditions
- creep rupture as a result of high steady state stress and temperature over sustained full-load operation
- corrosion of the blade surface by chemical attack of the combustion gases at high temperatures.

In the engine, these mechanics concur and may affect one another. In order to analyse and predict the complex damage to a blade in the engine, it is necessary to isolate these mechanisms as far as possible. The aim of this investigation is to analyse the

thermal fatigue and static creep damage under the influence of corrosive media in the environment.

2. THERMAL FATIGUE TESTS ON COOLED TURBINE BLADES

Fig. 1 shows one stage of a turbine in the engine and illustrates the blades in a stream of hot gas, the radial flow of cooling air through the blades, and the centrifugal tension acting on the turbine blade.

Fig. 2 shows the changes in speed, hot gas temperature and blade temperature for a typical load cycle on the turbine blade (idling - full load - idling). Turbine speed and mean blade temperature change almost synchronously. The rapid change in gas temperature in the transient phases, however, causes steeper temperature gradients in the blade than in the steady-state full-load condition.

For closer investigation of thermal fatigue, a test procedure was developed by MTU in which a turbine blade is tested under closely simulated operating conditions. Analysis of thermal fatigue is first carried out from the evidence provided by these tests because the external conditions are here considerably easier to control than in the engine. The test set-up consists of a combustion chamber, a cold air duct, a segment of a disc fitted with turbine blades, a device for applying a tensile load to the test blade, and an arrangement for cooling the blade with compressed air.

Data on thermal fatigue tests:

	Heating phase	Cooling phase
Gas temperature	$T_G = 1600 \text{ K}$	298 K
Mach No. of external gas flow	$Ma = 0.298$	0.180
Reynolds No. (referred to blade chord l)	$Re = 22132$	94124
Tensile load (steady-state values)	$G_z = 170 - 300 \text{ N/mm}^2$	$\epsilon - 2 \text{ N/mm}^2$

The airflow for blade cooling (5 % of the gas flow at $p_c = 2.15 \text{ bar}$, $T_c = 298 \text{ K}$ on entry) remained constant throughout the test. The external flow of hot gas or cold compressed air was cyclically altered by displacing the combustion chamber sideways with the tensile load being applied synchronously via a pneumatic actuator.

Fig. 3 shows a diagram of the arrangement of the test blade in the hot gas duct, with thermocouples for measuring blade temperature. A radiation pyrometer was also fitted to monitor the temperature at the trailing edge. Whilst only the first test blade was fitted with thermocouples for monitoring the temperature cycle, the pyrometer measurement was carried out on all blades for verification.

The test procedure has already been analysed in Ref. /1/. The test cycle consists of a heating phase and a cooling phase, each 30 seconds long, and a hold time of 5 minutes in the hot condition. Fig. 4 shows the changes in gas temperature, mean blade temperature and tensile load during the cycle. As a result of displacing the combustion chamber sideways, the gas temperature changes rather abruptly. In contrast, the blade temperature changes more slowly than it does in the engine cycle because the heat transfer coefficients are considerably lower than in the engine because the gas pressure is lower. In the cycle the tensile load is applied in approximate synchronism with the blade temperature. The steady-state tensile load was varied between the centrifugal load in the engine and a maximum of 60 % overload, referred to the mean blade section. The cycles were run in constant succession until cracking or rupture occurred, damage being determined by visual inspection as well as by interim dye checking. The results here shown were obtained using turbine blades from Inconel 100 without anti-corrosion coating.

3. CALCULATION PROCEDURE FOR TEMPERATURE AND STRESS ANALYSIS

The stressing of the turbine blade results from the external tensile load and the thermal stresses which are caused by local inhibition of thermal expansion. Knowledge of the transient temperature distribution in the blade is, therefore, the pre-requisite to calculating its stress and deformation conditions.

Planar heat conduction is assumed in the mean blade section for calculating the temperature using the finite element method (Ref. /2/). Fig. 6 shows the discretisation of the blade section using isoparametric finite elements. In addition to the convective heat transfer, as depicted in Fig. 5, heat radiation at the blade surface (in the trailing edge zone) is also taken into account. The determination of actual heat transfer coefficients is described in Ref. /3/.

For calculating steady-state and transient temperature distributions, the variation of the thermal conductivity, as well as the specific heat of the blade material with temperature was taken into consideration.

In order to calculate the stresses in the blade section, the deformation of the whole blade must be known, considering that thermal expansion is restricted can reflect in all directions. A 3-dimensional calculation of stress and deformation, however, requires the knowledge of the 3-D temperature distribution; the amount of calculating and measuring required would be unbearable, especially for determining the transient conditions.

Assuming that the blade section expands spanwise at a constant rate,

$$\epsilon_z = \frac{dw}{dz} = \frac{1}{EA} \left(F + (A) \int \epsilon \alpha T dA \right) \quad (1)$$

the distortions in the sectional plane can be calculated as a plane strain condition from the temperature distribution using the finite elements network as in Fig. 6. The variation of the modulus of elasticity and the coefficient of expansion with temperature is approximated by means of square polynomials. The spanwise stress amounts to

$$\sigma_z = E (\epsilon_z - \alpha \cdot T) + \nu(\sigma_x + \sigma_y) \quad (2)$$

Fig. 7 shows the steady-state temperature distribution and the distribution of the equivalent stresses in the blade section from this calculation. The equivalent stress is almost identical to the amount of spanwise stress σ_z , and its distribution is similar to the temperature distribution over the section. However, Equ. (1) does not describe the actual deformation behaviour, particularly for small tensile loads in the transient phases. The airfoil can bend from the heat as a result of the temperature gradients. Assuming that the blade sections remain plane, the following equations apply to thermal bending (see Fig. 8):

$$\begin{aligned} u'' &= \frac{d^2 u}{dz^2} = - \frac{1}{EI_{xx}} \cdot \int (A) E \alpha T x \, dA \\ v'' &= \frac{d^2 v}{dz^2} = - \frac{1}{EI_{yy}} \cdot \int (A) E \alpha T y \, dA \end{aligned} \quad (3)$$

In the case of pretwisted blades, yet another thermal twisting occurs:

$$\varphi' = \frac{d\varphi}{dz} = \frac{\delta}{C_T} \cdot \int (A) E \alpha T (r^2 - i^2) \, dA \quad (4)$$

$$\text{where } r^2 - i^2 = x^2 + y^2 - \frac{I_{xx} + I_{yy}}{A}$$

The prevailing shear stresses τ_{xz}, τ_{yz} are ignored here afterwards.

With regard to the boundary conditions, the thermal deformation of the blade can be calculated, from the profile of the integral values in Equ. (1), (3) and (4) along the blade span. Fig. 8 shows the thermal deformation of the blade in the steady-state conditions, but with no tensile load.

With external loading, the equilibrium and deformation problem can be solved using the theory of beams, with the thermal deformation entering into in the equation as a stress-free initial distortion. This calculation is made for each time step during the transient phases.

The spanwise strain in the mean blade section is, as a result of this calculation, expressed as follows:

$$\epsilon_z = w' - x \cdot u'' - y \cdot v'' + \delta r^2 \cdot \varphi' \quad (5)$$

Instead of using constant expansion (1), the total stress condition in the section is calculated as for a plane strain condition, but with spanwise strain varying with the location (5); cf. Ref. /4/.

The calculations on the blade here investigated gave negligibly small stresses σ_x, σ_y in the sectional plane; for this reason, the continued calculations could be confined to the single-axis stress condition

$$\sigma_z = E (\epsilon_z - \alpha \cdot T) \quad (6)$$

4. TEMPERATURE AND STRESS PROFILES IN THE THERMAL FATIGUE CYCLE

The steady-state temperature profile in the mean section of the turbine blade was calculated for the load cycle as described and was compared with the thermocouple readings. The computed steady-state temperature distribution (Fig. 7) after heating showed close agreement with the measurements, and in the transient phases the differences of computed from measured values were about 5 %, referred to the total temperature change. Fig. 10 shows the computed temperature profiles at the leading edge and on the pressure side during heating and cooling.

Due to the higher heat transfer coefficient at the leading edge, the temperature during heating and cooling here varies considerably faster than in the mid-portion of the cross section. Fig. 9 shows the temperature and stress distributions after 2 secs in the heating period. The high temperature gradient at the leading edge here causes severe compressive stresses. The stress calculation so far assumed a strictly elastic behaviour of the material. The stress distribution, unlike in the steady-state condition per Fig. 7, does not run in parallel with the temperature distribution, because a portion of the temperature gradient creates a thermal bending deformation.

Owing to the elevated temperatures the continued calculation must consider now also non-elastic behaviour of the material. Using evidence provided by short-time creep tests, a creep law was obtained of the McVetty type:

$$\dot{\epsilon}_c = \frac{d\epsilon_c}{dt} = \left(\frac{\sigma}{M}\right)^m \cdot e^{-t/\tau} + \left(\frac{\sigma}{N}\right)^n \quad (7)$$

The variation with temperature is considered by M and N.

For the creep strain rate $\dot{\epsilon}_z$ of the blade section, a deformation formula analogous to Equ. (5) applies, i.e., the rate of deformation is obtained from integration of the local creep rates (7) over the section, cf. Ref. /5/. Assuming a constant external load, the local stress variation will be:

$$\dot{\sigma}_z = \frac{d\sigma_z}{dt} = E (\dot{\epsilon}_z - \dot{\epsilon}_c) \quad (8)$$

Owing to the variation in temperature and external load the equilibrium and deformation condition along blade span is computed again for every time step, considering deformation by creep in the heating phase and during the hold time period.

Fig. 10 shows the variation of stresses at the leading edge and on the pressure side during the first cycle. As it will become apparent, considerable variations in stress occur also during the hold time because a portion of the inhibited thermal expansion is transformed into creep. This leads to correspondingly high residual stresses in the section after re-cooling.

The blade is cooled in a stream of pressurized cold air. At the leading edge the blade cools faster than in mid-portion; the tensile stress occurring is of almost the same magnitude as the compressive stress during the heating period. Fig. 11 shows the temperature and stress distributions after 2 secs in the cooling period. Apart from the stress distribution, it is also the stress relief previously achieved in the hold time which affects the stress distribution in the cooling phase. The residual stresses prevailing after cooling constitute the initial stresses for the next cycle, and these will reduce the stress peaks in the subsequent heating phases.

5. FAILURE ANALYSIS FROM THERMAL FATIGUE TESTS

Fig. 12 shows typical instances of damage noted in the thermal fatigue tests. Under low tensile load, fatigue cracks occurred at the leading edge after about 8000 cycles. These cracks gradually widened by oxidation at the flanks of the crack, and after a length of 2 mm had been reached, crack propagation slowed to a modest rate.

When the tensile load was increased, however, the formation of incipient creep cracks was noted. These cracks develop in the well-cooled mid-portion of the blade; the presence of creep pores was witnessed also at the edges of the cooling holes. The propagation rate of creep cracks was so fast that in most instances only creep rupture of the blade was noted.

Distinction can obviously be made between two separate mechanisms of damage. While the fatigue cracks in the leading edge area are caused by high thermal alternating stresses, a creep fracture will occur in areas under high tensile stress during the hold time.

Fig. 13 shows the computed stress-strain cycles at the leading edge for steady-state tensile loads of various magnitudes. The presence of loops is noted, although the material behaviour had been anticipated to be strictly elastic during the rapid load variations in the early transient phases. These loops are traversed during heating and cooling in opposite directions; they are attributed to the variation of the modulus of elasticity with temperature.

Under moderate tensile load, stress relief at nearly constant strain takes place during the hold time. This gives rise to residual stresses after cooling, while the strain reduces to nearly zero. Under raised tensile load, however, an amount of static creep strain is accumulated during the hold time. Owing to the primary creep behaviour the creep strain in the first cycle is somewhat higher than in the succeeding cycles.

Fig. 14 shows the stress and strain cycle (at low tensile load) versus temperature together with static strength values of the IN 100 material. The static yield point is not exceeded. The material reaches its minimum ductility at about $T = 1000$ K. Calculation of the number of stress cycles to first crack had so far failed to give satisfactory results and calls for further investigation. Prediction of the creep life, however, can be made satisfactorily. Comparison of stress with the creep life, in lieu of accumulation of the creep strains in every cycle, leads to an acceptable life prediction. The stress resulting from the external load is a determinant of the static creep strain. Fig. 15 shows a comparison with results of creep rupture tests on flat specimens in a combustion gas atmosphere, from Ref. /6/. The values gained from the specimens largely fit, for the respective temperature, in a scatter band the width of twice the life. The effect of hot gas corrosion, compared with test results taken in air, caused the times to rupture of the specimens to be cut in half. For the times to rupture of the blades, only the heating and hold time periods of each cycle (5.5 mins) were added together. The variation of the times to rupture with the external load on the blades gives a scatter band which, with the mean blade temperature, fits well in the time-to-rupture scatter band of the flat specimens.

6. CONCLUSIONS

Simulated thermal fatigue tests conducted on a test rig on turbine blades provided substantial evidence of the causative mechanics of damage. The noted patterns of damage were of two types indicative of creep failure or fatigue damage. Their calculation requires different approaches. While the creep failure can be predicted from the external load and the mean temperature at steady-state conditions, the determination of fatigue damage calls for the calculation of local stress-strain profiles during transient phases.

Owing to the gas temperature profile at the combustion chamber exit and owing to the blade cooling arrangement, the temperatures often reach a maximum at mid span, where the thermal design calculations are made. For stress computation, the deformation behaviour of the blade is first calculated using the beam theory; and generalising the plane strain condition, the stresses in the section are then calculated. The dominating effect of the spanwise stress σ_z as here noted must not necessarily apply in all cases.

Computation of the number of cycles to first crack from the maximum amplitude of strain are still not satisfying. For the lack of material data, the calculations still ignore the cyclic plastic behaviour of the material. It is assumed, however, at least for uncoated blades, the results from which are here shown, that apart from the strictly cyclic damage, there will also be damage as a function of time, by intercrystalline corrosion at the surface, to trigger the development of thermal fatigue cracks.

7. REFERENCES

- /1/ MTU München Fortschrittliche Kühlungstechnologien
ZTL-Bericht 4.02-7, 1976
- /2/ Pitttr, J. Calculation of Transient Temperature Fields with Finite Elements
Köhler, W. in Space and Time Dimensions
Int. J. Num. Meth. Eng. 8, 1974
- /3/ Köhler, H. Hot Cascade Test Results of Cooled Turbine Blades and Their
Hennecke, D.K. Application to Actual Engine Conditions
Pfaff, K. AGARD Conf. on High Temperature Problems in Gas Turbine Engines,
Eggebrecht, R. Ankara 1977, Conf. Proc. No. 229
- /4/ Kvitka, A.L. Calculating Blades of Gas Turbine Engines by the Finite Element
Voroshko, P.P. Method
Zaslotskaya, L.A. Problemy Prochnosti 6, 1976
- /5/ Beglinger, V. Zur Bestimmung der Lebensdauer von gekühlten Gasturbinen-
Suter, P. schaufeln
Turboforum 1, 1972
- /6/ Betz, W. Festigkeitsverhalten unter Heißgaskorrosion
Track, W. Abschlußbericht EUROCOPI-COST 50, D1/3, 1977
Schweitzer, K.
- /7/ Spera, D.A. Thermal Fatigue Testing of Simulated Turbine Blades
Calfo, F.D. NASA TM-X 67820, 1971
Bizon, P.T.
- /8/ Pisarenko, G.S. One Method of Thermal Fatigue Testing of Turbine Blades
Petrenko, A.I. Problemy Prochnosti 6, 1976
- /9/ Maya, T. A Study of Thermal Fatigue Life Prediction of Air-Cooled
Katsumata, I. Turbine Blades
Itoh, M. ASME-Paper 78-GT-63, London 1978

Acknowledgements

The present study was undertaken with funds from the German Ministry of Defence, for which we wish to express our appreciation. Special gratitude is due to Mr. W. Hoffmüller for conducting the thermal fatigue tests and to Mr. H. Sacher for calculating the transient temperature distributions.

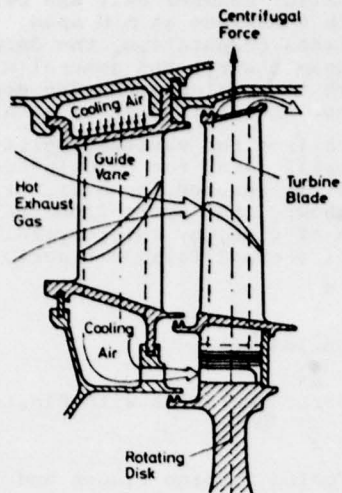


Fig. 1: Gas Turbine Stage with Applied Scheme of Loading

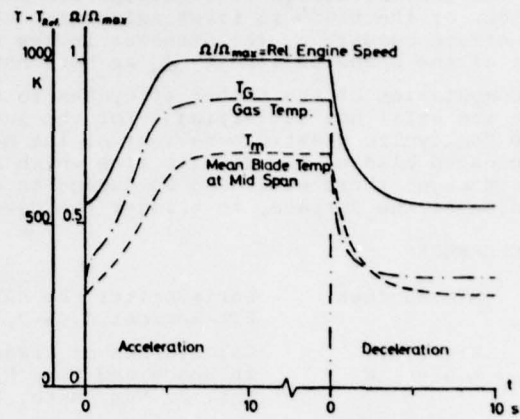


Fig. 2: Duty Cycle of the Turbine Blade

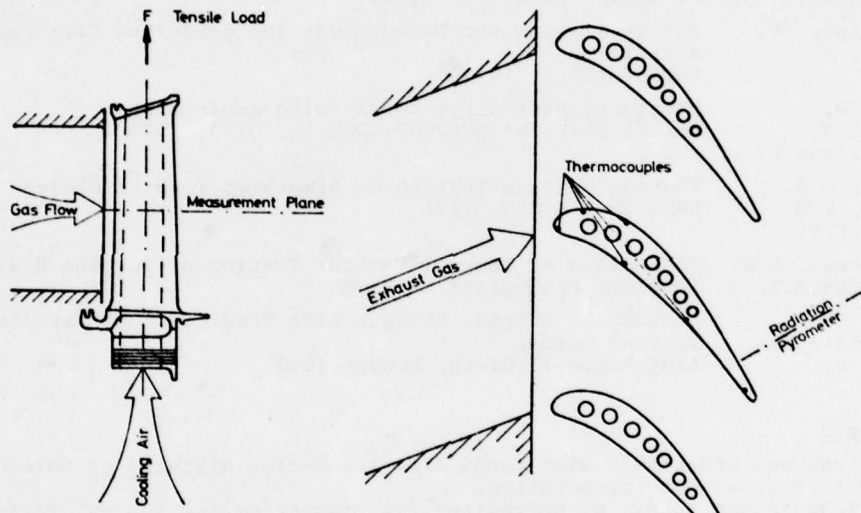


Fig. 3: Thermal Fatigue Test Scheme with Test Blade Instrumentation

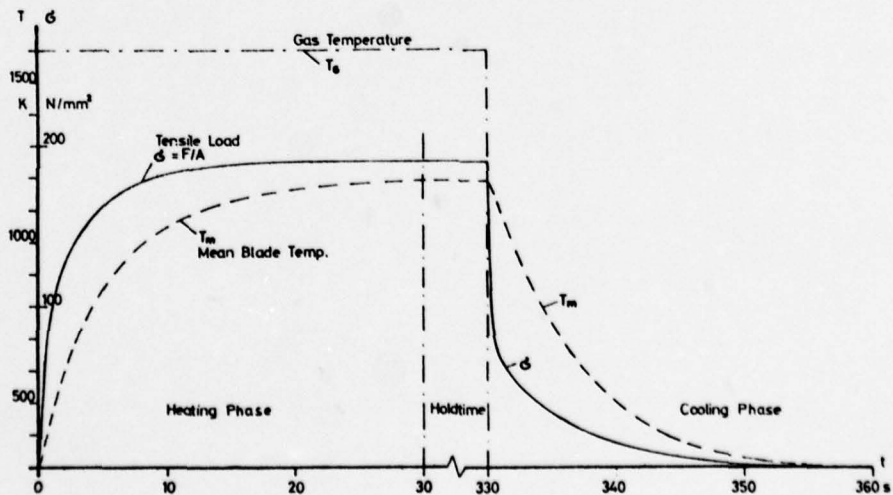


Fig. 4: Loading Cycle in the Thermal Fatigue Test

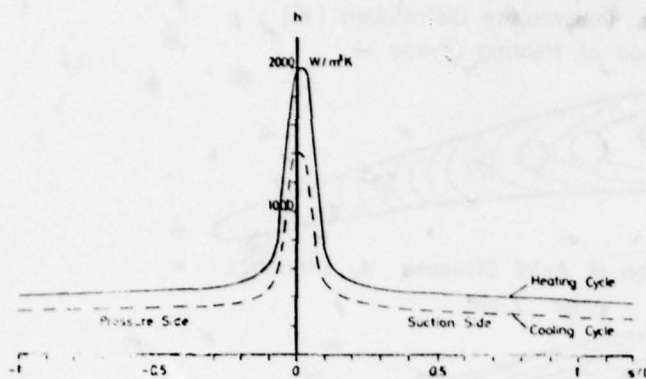


Fig. 5: Convective Heat Transfer Coefficient at Blade Surface in the Thermal Fatigue Test

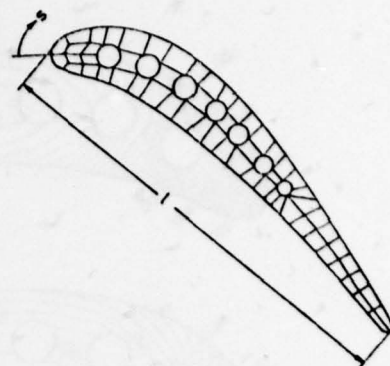


Fig. 6: Finite Element Discretisation of the Mid Span Cross Section

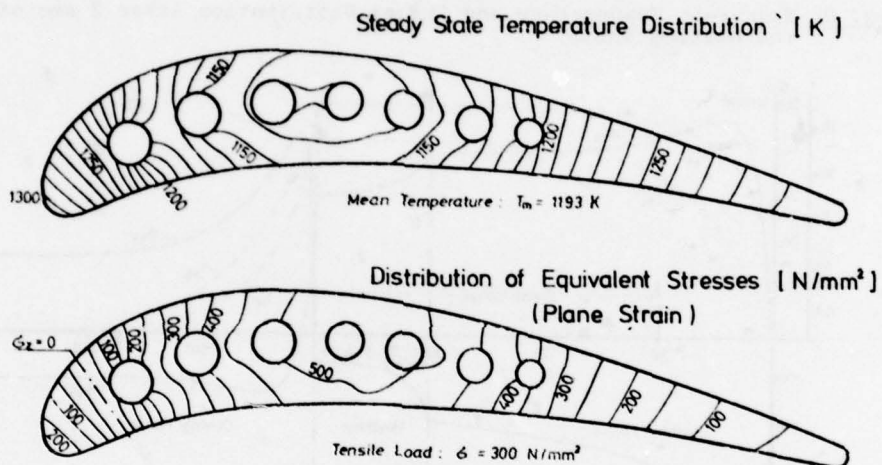


Fig. 7: Steady State Temperature and Stress Distribution at the Mid Span Cross Section

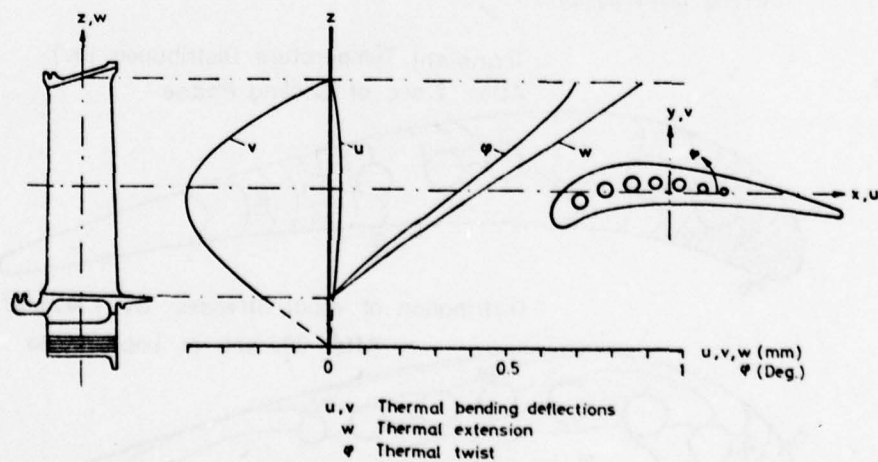


Fig. 8: Coordinate System and Free Thermal Deformation of the Airfoil at Steady State

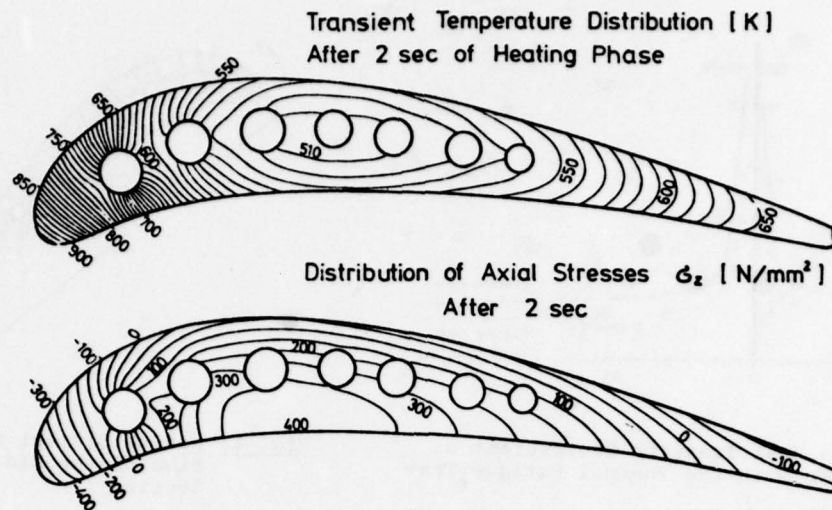


Fig. 9: Transient Temperature and Stress Distribution after 2 sec of the Heating Phase

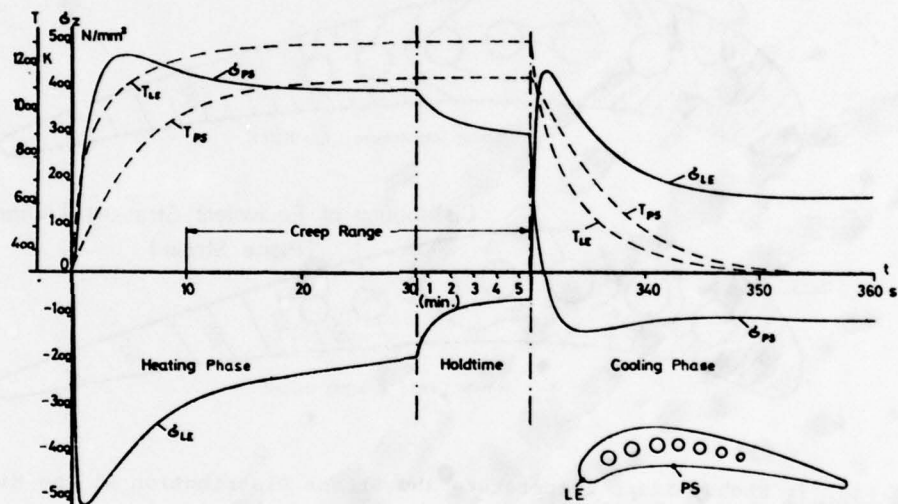


Fig. 10: Variation of Temperatures and Axial Stresses at Two Surface Points During Loading Cycle

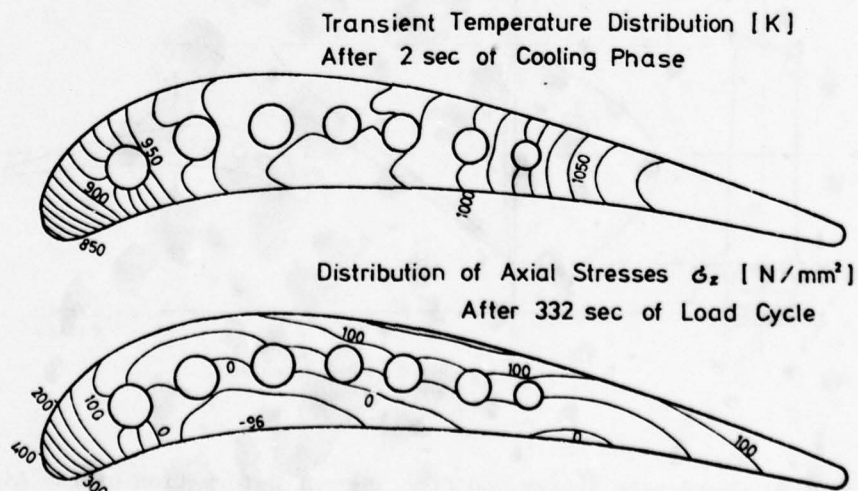


Fig. 11: Transient Temperature and Stress Distribution after 2 sec of the Cooling Phase

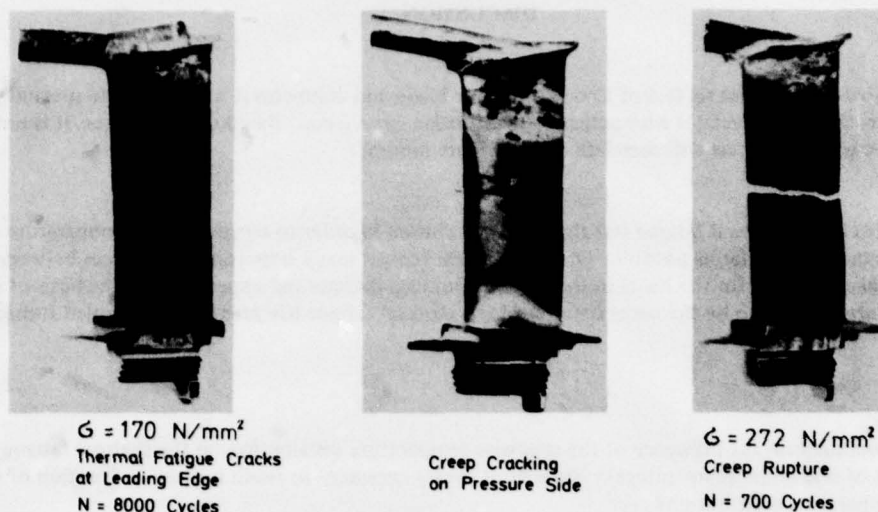


Fig. 12: Failure Modes Observed in the Course of Thermal Fatigue Testing

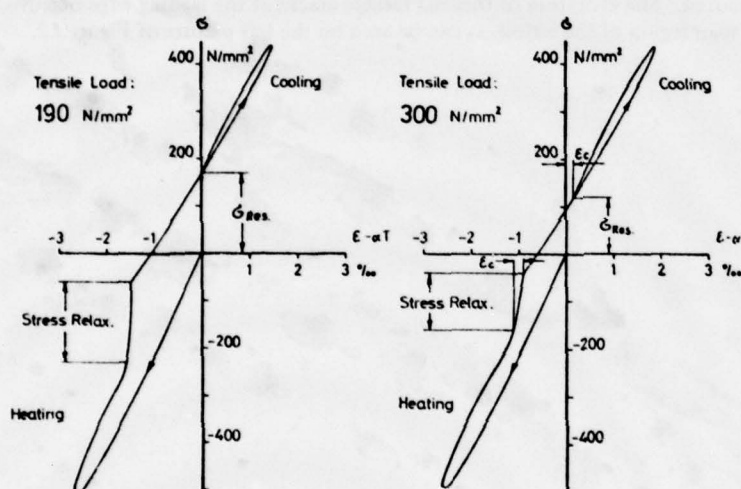


Fig. 13: Stress-Strain Cycles at Leading Edge for Two Magnitudes of Tensile Loading

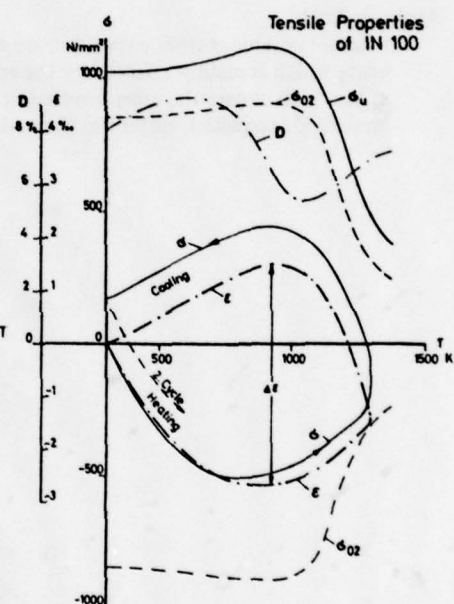


Fig. 14: Stress and Strain Cycle vs. Temperature in Comparison with Static Strength Properties

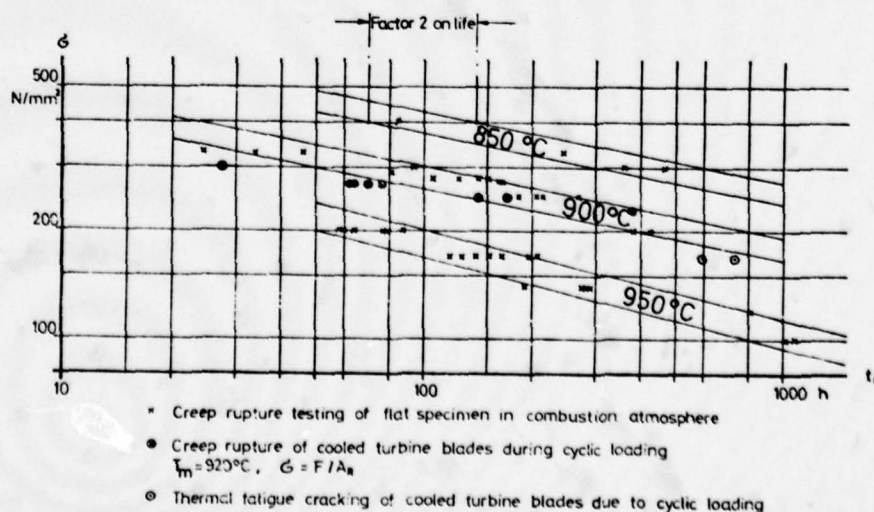


Fig. 15: Creep Rupture of IN 100 Test Specimen and Simulated Turbine Blades

DISCUSSION

B.L.Koff, US

The paper shows a hot static rig test of a cooled turbine blade and compares it with flat plate specimen. It does not show how this test correlates with actual cooled turbine experience. Based on experience, it is not likely that this type of experimental test will correlate engine failure modes.

Author's Reply

The test cycles in the thermal fatigue test rig have been chosen in order to correlate with temperature cycles in engine endurance tests as far as possible. Of course, there remain many important differences between test cycle and the actual conditions for the blade in the engine. But calculations and experience on the basis of our thermal fatigue tests are thought to be the necessary steps for a thermal fatigue life prediction of cooled turbine blades in the future.

J.Colpin, Belgium

Could you comment on the influence of the spanwise temperature distribution on the thermal fatigue evolution (or the point of maximum temperature). Number of cycles necessary to reach rupture in function of different spanwise temperature distribution?

Author's Reply

I cannot comment from experience on this, because we have not varied the spanwise temperature distribution in the blade which is mainly affected by the spanwise gas temperature profile. This profile has its maximum approximately at mid span, where the creep rupture occurred. The evolution of thermal fatigue cracks at the leading edge occurred on several spanwise locations in the mid span region of the airfoil, as can be seen on the left picture of Figure 12.

PREVISION DE LA DUREE DE VIE DES MOTEURS

par

D. GRANDOULIER

S.N.E.C.M.A.

Centre d'Essais de VILLAROCHE
77550 MOISSY CRAMAYELRESUME

Dans les turboréacteurs aéronautiques le compromis entre légèreté et endurance impose une prévision précise de la durée de vie des pièces. Les pièces dont la rupture mettrait en cause l'intégrité du moteur doivent être dimensionnées pour répondre à deux critères :

- éviter l'apparition d'une crique au cours de la durée de vie prévue de la pièce.
- s'assurer qu'un défaut non décelable au cours d'une révision générale n'évolue pas jusqu'à atteindre une taille critique avant la révision suivante.

Le but de cet exposé est de présenter, sur l'exemple d'un disque de turbine, une méthode de prévision de durée de vie en fatigue oligocyclique et de montrer l'importance de la connaissance des lois de comportement du matériau.

1. INTRODUCTION

Dans les turboréacteurs aéronautiques, les objectifs de masse et d'encombrement imposent aux constructeurs l'utilisation de matériaux performants, l'optimisation des formes pour limiter les contraintes locales, et la réduction des coefficients d'ignorance.

Cette réduction des coefficients d'ignorance suppose une analyse approfondie des sollicitations locales et une bonne connaissance du comportement du matériau.

Ces efforts sont particulièrement payants dans les rotors, car l'augmentation de la vitesse de rotation permet de réduire le nombre d'étages de compresseur et de turbine, donc à la fois la masse et le prix.

Aujourd'hui la maîtrise des systèmes de refroidissement et l'amélioration des performances des matériaux permettent de résoudre les problèmes de tenue en fluage et la principale limitation à l'augmentation du niveau de sollicitation est la fatigue oligocyclique.

Pour atteindre l'objectif de légèreté du moteur, il faudra donc admettre de faire travailler les matériaux au delà de la limite élastique et de limiter la durée d'utilisation de certaines pièces. Pour un disque par exemple, dont l'éclatement mettrait en cause l'intégrité du moteur, il est nécessaire de déterminer d'une part le nombre de cycles de fonctionnement à ne pas dépasser pour éviter l'apparition d'une fissure et d'autre part la périodicité des contrôles qui assurent qu'un défaut existant ne peut atteindre une taille critique. La détermination de ces limites est effectuée en plusieurs phases :

- Etablissement des spécifications qui précisent les objectifs et les conditions d'utilisation.
- Définition des pièces et acceptation des plans après vérification des objectifs par calcul et essais sur éprouvettes.
- Après réalisation de pièces et mise au point de la gamme de fabrication : essais partiels sur pièce réelle (ou éprouvettes prélevées dans une pièce réelle), ce qui permet d'ajuster la prévision de potentiel. Cette nouvelle estimation du potentiel peut aboutir à lancer des modifications si nécessaire.
- Démonstration d'une durée de vie initiale autorisée .
- Extension de cette durée de vie caractérisée par essais complémentaires sur des pièces ayant vieilli en utilisation

Nous nous limiterons ici à l'exposé des méthodes de prévision par calcul et essais sur éprouvettes appliquées à un disque.

Nous allons examiner successivement :

- les conditions de fonctionnement sur moteur et le calcul des sollicitations.
- les essais de caractérisation des matériaux et la transposition des résultats obtenus sur éprouvette à la pièce réelle.
- les précautions prises pour assurer une bonne fiabilité à la méthode de prévision.

2. CONDITIONS DE FONCTIONNEMENT SUR MOTEUR ET CALCUL DES SOLLICITATIONS

2.1. Conditions de fonctionnement moteur

Bien que les pilotes adaptent leur plan de vol aux parcours à effectuer et aux conditions météorologiques particulières, on peut schématiser le fonctionnement d'un appareil donné par un (ou plusieurs) vol type.

La planche 1 montre le vol type d'un moteur pour avion civil. On peut noter une accélération rapide jusqu'au régime maximum qui est maintenu pendant le décollage.

La montée puis la croisière sont effectuées à des régimes légèrement inférieurs.

A l'atterrissage le moteur est de nouveau soumis à une variation de régime importante lors de l'inversion de poussée.

La définition de cette mission permet, pour des conditions atmosphériques données, de calculer l'évolution des paramètres de fonctionnement du moteur.

2.2. Calcul des sollicitations

La photo de la planche 2 montre un disque de turbine, cette pièce est destinée à supporter l'effort centrifuge des aubes et à transmettre le couple développé par la turbine. De plus elle est soumise aux forces centrifuges internes et à des gradients thermiques. Les points critiques en fatigue oligocyclique sont essentiellement :

- l'alésage qui est soumis à une contrainte circonférentielle importante de traction.
- les alvéoles, usinés dans la jante, sont destinés à recevoir les pieds d'aubes.
La jante travaille à un niveau de contrainte moyenne beaucoup plus faible, mais la géométrie provoque des concentrations de contraintes.
- Dans d'autres technologies les trous de passage de tirants et les bossages qui les bordent peuvent également être critiques.

L'étude aérothermique du disque et de son environnement permet de déterminer à tout instant le champ de température de la pièce.

La planche 3 montre l'allure de l'évolution des températures de la jante et de l'alésage. On peut constater que l'alésage plus massif a un temps de réponse plus long, ce qui entraîne des gradients thermiques importants lors des accélérations et des décélérations.

Le calcul global de résistance fournit alors l'évolution de la contrainte et de la déformation moyenne dans chaque coupe du disque au cours de la mission type.

Les variations de contrainte tangentielle à l'alésage et dans la jante au cours des phases d'accélération et de décélération sont figurées sur la planche 3. Dans les zones présentant des concentrations de contrainte, le facteur de concentration peut être déterminé par diverses méthodes :

- éléments finis en bidimensionnel ou tridimensionnel.
- équations intégrales en bidimensionnel ou en tridimensionnel.
- photoélasticimétrie.

Le résultat d'un calcul d'alvéole de compresseur par éléments finis est présenté planche 4. Deux zones à fort gradient de contrainte sont mises en évidence :

la limite de portée et le fond d'alvéole.

Pour l'étude par photoélasticimétrie, une maquette de la pièce en résine époxyde est mise sous contrainte puis figée. Des lamelles sont ensuite prélevées dans les zones critiques et analysées par transparence en lumière polarisée. La biréfringence du matériau crée des franges d'interférence. Chaque isochromatique correspond à un écart constant entre les deux contraintes principales. On peut déterminer la contrainte sur le bord libre de la lamelle par comptage des franges.

L'application des facteurs de concentration aux contraintes moyennes par tranche, calculées en transitoire, permet de déterminer, en chaque point critique, la contrainte locale en supposant que le matériau reste élastique.

3. ESSAIS DE CARACTERISATION DES MATERIAUX ET APPLICATION A UNE PIECE COMPLEXE

Le but de ces essais est d'établir les relations entre l'état de sollicitation de la matière, le nombre de cycles qui provoque l'apparition d'une crique et la vitesse de progression d'une crique existante. Ces relations doivent être établies pour plusieurs températures et pour un certain nombre de formes de cycle (sollicitation alternée ou variant entre 0 et une valeur positive, avec ou sans temps de maintien sous charge maximum ou minimum).

La caractérisation d'un matériau en fatigue est donc longue et coûteuse. Il est nécessaire avant de l'entreprendre de bien sélectionner le matériau et de définir les essais sur éprouvette qui permettent de représenter le plus fidèlement possible le comportement des pièces qui seront réalisées.

avec ce matériau.

Choix du matériau à étudier.

La décision d'entreprendre l'étude complète d'un matériau pour disque dépend des points suivants :

- Les essais préliminaire de fatigue doivent démontrer que ce matériau apporte une amélioration à l'initiation ou à la vitesse de progression d'une crique en fatigue lente.
- La limite élastique, la rupture et la tenue en fluage doivent être suffisantes pour ne pas limiter le gain attendu en fatigue.
- Le matériau doit d'autre part satisfaire un certain nombre de critères, qui ne sont pas directement utilisés au stade dimensionnement qui garantissent son bon comportement :
résilience, sensibilité à l'entaille, sensibilité à la corrosion, stabilité structurale, allongement à rupture.

De plus, le prix, la facilité d'usinage, la soudabilité ou la forgeabilité peuvent orienter le choix vers un alliage.

3.1. Analyse de l'initiation d'une crique

3.1.1. Choix du type d'éprouvettes et du mode de sollicitations.

Comme nous l'avons vu précédemment les points critiques d'un disque sont, pour la plupart, des points soumis à de fortes concentrations de contraintes (facteur compris entre 1,5 et 3). Une démarche logique consiste donc à utiliser des éprouvettes entaillées, simulant la concentration de contrainte de la pièce à étudier, soumises à un effort cyclé.

L'éprouvette représente la zone critique de la pièce et l'interprétation des essais est simple. Cependant, si elle garde tout son intérêt au niveau de la comparaison, cette méthode peut conduire au niveau du dimensionnement à une prévision trop optimiste. En effet sur une éprouvette de taille réduite et à forte concentration de contrainte, plusieurs phénomènes peuvent perturber le comportement en fatigue :

- Le gradient de contrainte est beaucoup plus élevé que sur pièce réelle.
- La taille de la zone critique est très faible, ce qui réduit la probabilité de rencontrer un défaut.
- L'usinage du petit rayon destiné à réaliser la surcontrainte peut provoquer un écrouissage important de la zone critique, ce qui améliore sa tenue en fatigue.

Pour éviter ces inconvénients les essais sur éprouvette lisse ont été développés. Ce type d'éprouvette présente une zone utile beaucoup plus importante car la section complète est sollicitée.

Le mode d'usinage est plus facile à maîtriser. Cette éprouvette soumise à une charge cyclée est bien représentative des zones à faible gradient de contrainte comme par exemple l'alésage d'un disque. Dans les zones où le gradient de contrainte est plus élevé, l'éprouvette simule le comportement de l'élément de matière le plus sollicité de la zone plastique. Il est alors nécessaire de déterminer par calcul le comportement élasto-plastique de la zone critique pour utiliser les résultats d'essais sur éprouvettes lisses. Cependant, principalement du fait de la modification des caractéristiques du matériau au cours des cycles, il n'est pas possible d'imposer à l'éprouvette à la fois une loi de contrainte et une loi de déformation. Sur pièce réelle les zones plastiques sont très localisées. L'ensemble de la pièce travaille dans le domaine élastique et impose son déplacement à la zone plastique. Le paramètre le plus réaliste pour établir la comparaison avec l'éprouvette est donc la déformation.

3.1.2. Transposition des résultats obtenus sur éprouvette à une pièce réelle.

L'utilisation de résultats de fatigue obtenus sur éprouvettes lisses demande la détermination du cycle de déformation des points critiques. La théorie de NEUBER permet de déterminer simplement la contrainte et la déformation après plastification dans les zones à fort gradient de contrainte.

Sur la planche 5, nous pouvons voir l'application de cette méthode à une plaque percée d'un trou. Au point A situé à distance du trou, la contrainte varie entre 0 et σ_A . A la première mise en charge la contrainte réelle au point B est déterminée par l'intersection de la courbe d'écrouissage du matériau et l'hyperbole de NEUBER passant par le point (σ_B, ϵ_B) déterminé par le calcul élastique.

Pour déterminer le cycle stabilisé du matériau il est nécessaire d'utiliser une courbe d'écrouissage cyclique. Au déchargement, la variation de déformation élastique imposée au point B, est l'opposée de la précédente. Dans le cas où cette variation est suffisante pour que le point minimum dépasse la limite élastique de compression, ce point peut être obtenu par une construction analogue en compression, après avoir décalé l'origine du diagramme.

A partir des valeurs de déformation ainsi définies, il est alors possible de déterminer, par comparaison aux résultats d'essais sur éprouvettes, le nombre de cycles entraînant l'initiation d'une crique de fatigue sous un chargement simple.

Au cours d'un vol type, les contraintes en un point du disque n'évoluent pas suivant un cycle simple. Le vol type présenté sur la planche 1 fait apparaître, par exemple, un cycle secondaire dû à la remise des gaz au moment de l'inversion de poussée. Il faut donc décomposer le vol type en plusieurs cycles simples et évaluer le nombre de cycles susceptibles de provoquer une crique pour chaque cycle élémentaire. Le nombre de cycles de vol est déterminé par cumul linéaire des endommagements (loi de MINER). On peut aussi pour un même vol type étudier des conditions extérieures différentes, qui se traduisent par des cycles de contrainte différents. Nous appliquerons la même règle de cumul des endommagements.

Dans un disque la plupart des points critiques sont soumis à une contrainte "uniaxiale" ils sont toujours sur une face externe, et en général à l'intersection avec un trou ou un alvéole. Cependant au milieu de l'alésage d'un disque épais, on peut trouver la combinaison d'une contrainte circonférentielle élevée et d'une contrainte axiale de compression. De même dans le rayon de raccordement d'un bossage avec la toile du disque, la matière est soumise à un champ de contrainte bidimensionnelle. Les essais sous contrainte biaxiale étant complexes et coûteux, il est nécessaire d'utiliser les résultats d'essais monodimensionnels en déterminant une contrainte équivalente (VON MISES, JOSHI). Les essais sur éprouvettes sont effectués à différents niveaux de température, mais dans la majorité des cas, la température est maintenue constante.

Sur un disque de turbine, au cours de chaque essai, les variations de température peuvent être importantes. On se contente en général de prendre en compte la température maximale, ce qui constitue une sécurité. On pourrait imaginer un essai sur éprouvette avec cyclage simultané de la température et de la contrainte ou de la déformation. Cette caractérisation très lourde aurait l'inconvénient de n'être valable que pour une forme de sollicitation particulière.

3.2. Détermination de la vitesse de progression d'une crique :

Il est nécessaire de garantir qu'un défaut de fabrication ou une crique initiée en fonctionnement seront détectés avant d'atteindre une taille critique. La périodicité des contrôles est déterminée par le nombre de vols qui provoquerait la croissance d'un défaut, du seuil de détection jusqu'à la taille admissible.

Le matériau est caractérisé sur éprouvettes A.S.T.M. sollicitées en mode 1, c'est à dire que la flexion de l'éprouvette provoque l'ouverture de la crique. L'exploitation de ces essais permet de tracer des courbes reliant la vitesse d'évolution de la crique à l'amplitude de variation du facteur d'intensité de contrainte. Ce facteur dépend de la contrainte, de la taille du défaut et de la géométrie de la pièce. Les deux paramètres importants sont les valeurs K_0 en dessous de laquelle la crique ne progresse pas et K_C qui est le seuil de propagation brutale.

Le calcul du facteur d'intensité de contrainte peut être effectué par éléments finis ou par équations intégrales. Des études sont actuellement en cours pour mettre au point une méthode expérimentale utilisant la photoélasticité.

La planche 6 donne l'exemple d'une détermination par éléments finis. L'exemple étudié est celui d'une crique dans une dent de disque. La crique A est schématisée par une ligne de noeuds doubles qui sont progressivement séparés. Le facteur d'intensité de contrainte est calculé à partir de la variation du travail des efforts extérieurs due à un accroissement de la crique.

$$K = \sqrt{\frac{1}{2} E \frac{\delta W}{\delta S}}$$

avec E = module d'YOUNG

δW = travail des efforts extérieurs

δS = augmentation de la section de la crique

Ce calcul fournit donc une relation entre la longueur de la crique et le facteur d'intensité de contrainte K . Pour une longueur de crique et une géométrie données, le facteur K est proportionnel à la contrainte.

Son amplitude de variation (ΔK) détermine la vitesse de progression de la crique. Par intégration on obtient l'évolution de la longueur de la crique en fonction du nombre de cycles.

Ce résultat est transcrit sur la planche 7 qui donne le nombre de cycles autorisés en fonction de la longueur de la crique.

Le problème se complique de la même façon que pour l'initiation lorsque les cycles sont complexes et surtout lorsque la température varie au cours du cycle : on additionne les vitesses de progression correspondant à chaque cycle élémentaire et on prend en compte la température maximale.

L'application présentée ci-dessus porte sur une crique traversante. Dans les parties massives du disque telles jante et alésage, le front de progression d'une crique a une forme elliptique. En principe la même méthode de calcul peut être appliquée, mais il faut déterminer l'énergie liée à la progression de la crique par un calcul tridimensionnel. A chaque pas de temps la répartition des vitesses de progression le long du front de crique est calculée en minimisant l'énergie nécessaire par unité de surface supplémentaire criquée. Ce calcul

est très lourd et, au niveau dimensionnement, les seules approches possibles sont : le calcul en crique traversante ou l'application de formules empiriques lorsque la géométrie et le champ de contrainte ne sont pas trop complexes.

4. PRECAUTIONS PRISES POUR GARANTIR LA FIABILITE DE LA PREVISION

Pour garantir une bonne fiabilité à la prévision il est nécessaire d'agir à la fois sur la méthode de prévision et sur la constance des caractéristiques des pièces moteur. Une procédure statistique de conduite et de dépouillement des essais sur éprouvettes a été mise en place, elle a pour but :

- d'une part de fournir les caractéristiques minimales du matériau.
- d'autre part d'affecter à chaque courbe une catégorie qui donne à l'utilisateur le degré de confiance.

Des règles précises fixent la catégorie de courbe à utiliser en fonction de l'avancement de l'étude du moteur. La géométrie de la pièce est définie par le plan. La hiérarchisation des cotes permet de mettre en évidence les cotes critiques de la pièce. Le non respect de ces cotes entraîne le rebut de la pièce .

De nombreux facteurs interviennent sur les caractéristiques finales de la pièce : matière de base du lingot, condition de forgeage, de traitements thermiques, d'usinage, de traitements de surface ou de finition.

Il est prévu, au départ, des dissections détaillées des pièces principales puis, sur pièces usinées, des essais de fatigue en fosse de survitesse.

Ensuite, en production, on exécute des contrôles sur les matériaux de base, des essais sur éprouvettes attenantes et des dissections par sondages en nombre limité.

La stabilité de la qualité est essentiellement assurée par le figeage du processus de fabrication.

En particulier pour les pièces importantes des matériels civils, les autorités de certification exigent la rédaction de "méthodes de fabrication déposées" qui ne peuvent être modifiées sans accord.

Pour les pièces critiques, tout l'historique de fabrication est répertorié et le constructeur est capable de remonter jusqu'au lot de matière d'origine et la position de la pièce dans la barre.

5. CONCLUSIONS

Les constructeurs ont beaucoup progressé dans la connaissance des caractéristiques des matériaux. Bien qu'il soit encore difficile de déterminer de façon précise la durée de vie des pièces à partir des essais en laboratoire, les progrès réalisés ont permis une amélioration dans la prévision du comportement de celles-ci. Néanmoins, les essais partiels sur pièces réelles, avec simulation des conditions de fonctionnement moteur, les essais moteur au banc sol et altitude, puis les heures de fonctionnement en utilisation resteront nécessaires pour connaître de façon exacte les durées de vie réelles des pièces et garantir la sécurité.

L'amélioration de la prévision par calcul se traduit par un allègement des modifications nécessaires en développement, donc un gain en coût et en délai.

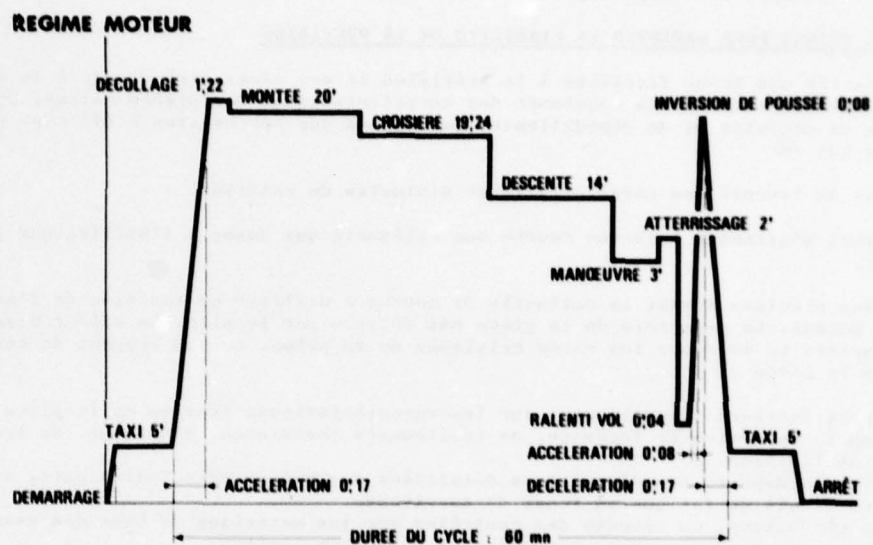


FIG. 1A

MISSION COMMERCIALE TYPE

Planche 1

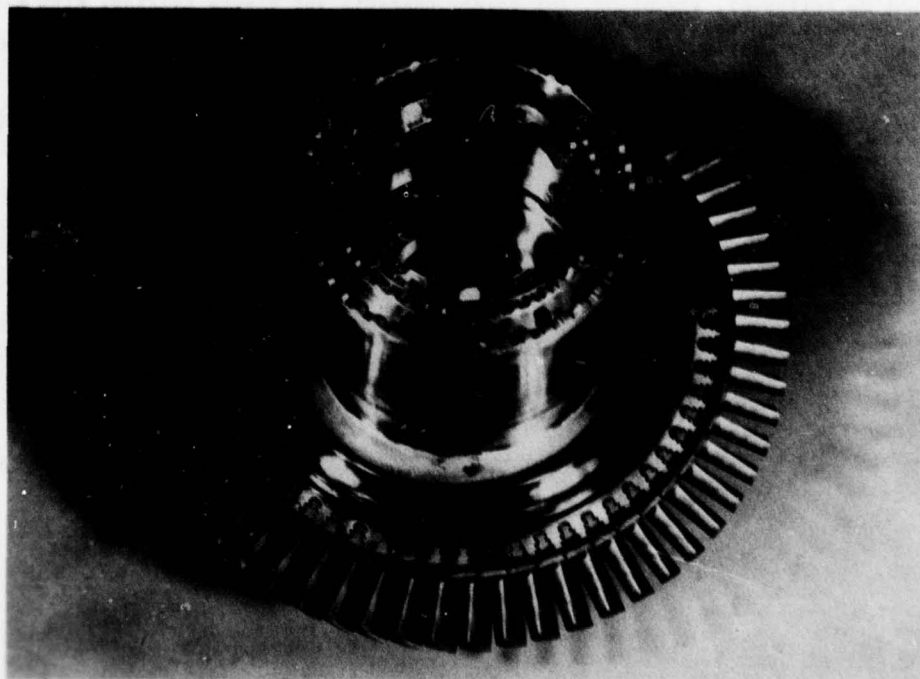


Planche 2 - DISQUE DE TURBINE

EVOLUTION DES CONTRAINTES ET TEMPERATURES DANS UN DISQUE

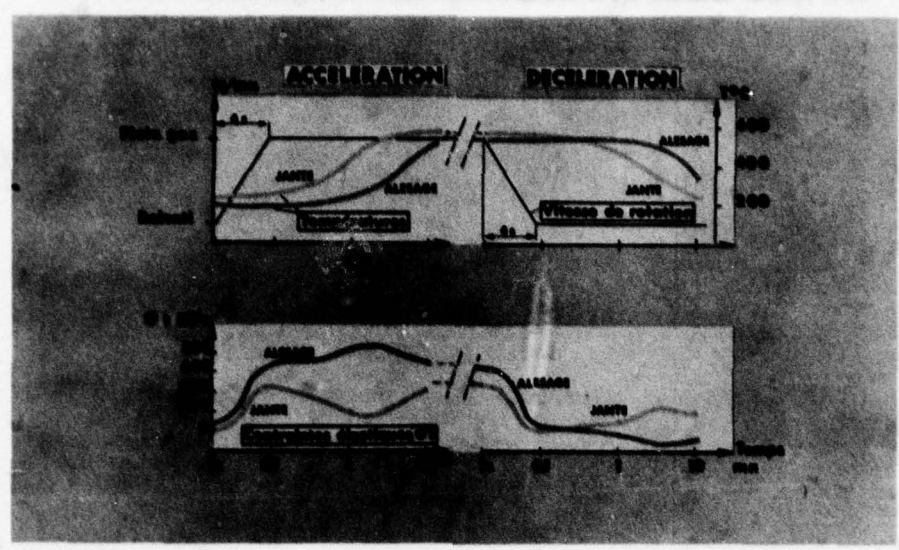


Planche 3

CHAMP DE CONTRAINTES EQUIVALENTES DANS UNE ATTACHE

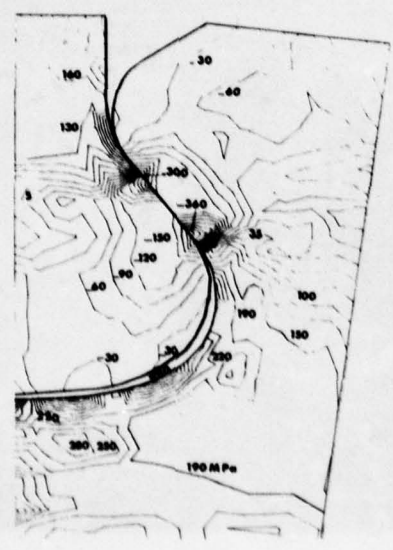


Planche 4

FATIGUE OLIGOCYCLIQUE. Cycles allongement contrainte

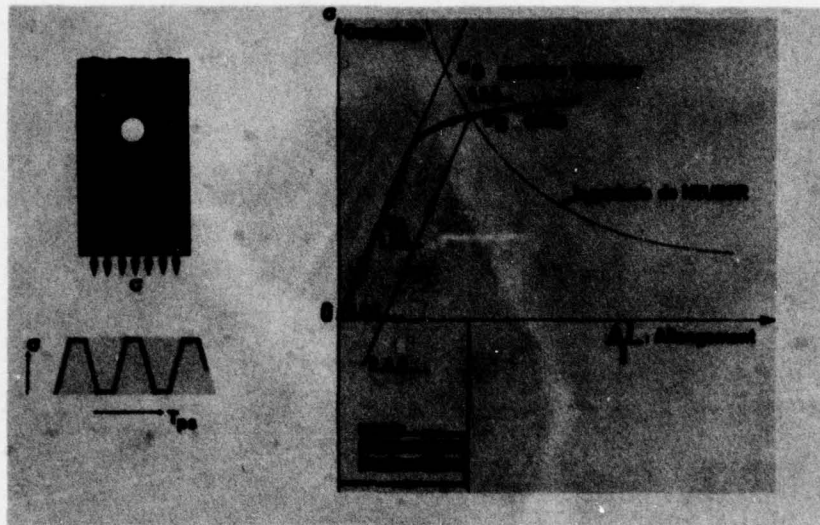


Planche 5

AMPLITUDE DE VARIATION DU FACTEUR D'INTENSITE DE CONTRAINTE

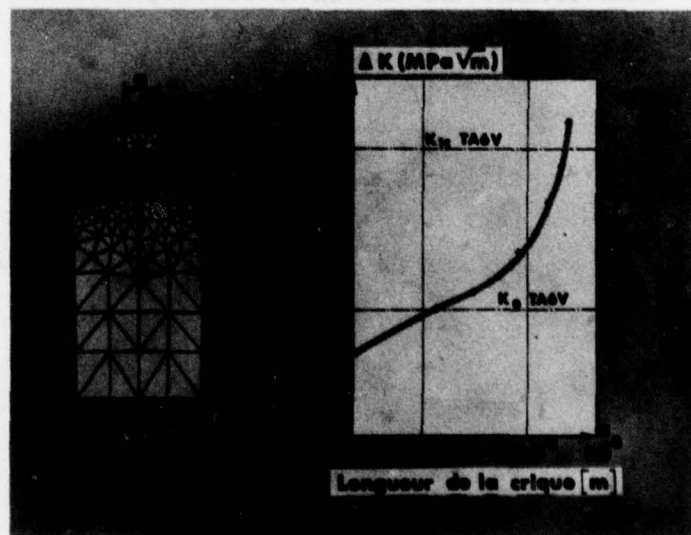


Planche 6

DUREE DE VIE RESIDUELLE

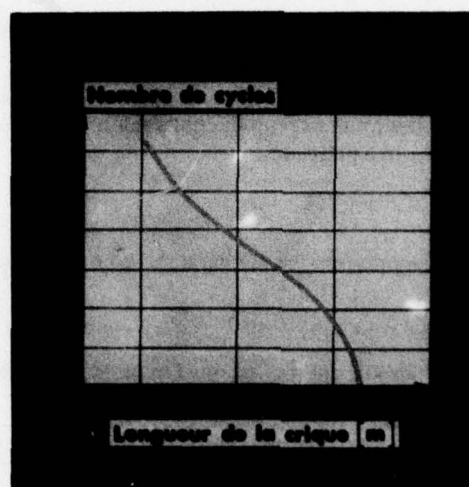


Planche 7

DISCUSSION

M.Holmes, UK

How do you take into account the difference between stress gradient and the volume of material surrounding a notch when relating the fatigue behaviour of a specimen to an aero engine component.

Reponse d'Auteur

Au niveau du dimensionnement d'une pièce, il est difficile de déterminer précisément l'influence de gradients de contrainte et l'influence de l'état d'écrouissage en surface de la matière.

C'est pourquoi, nous proposons d'utiliser une caractérisation en fatigue sur éprouvettes lisses à l'état rectifié. Ces éprouvettes ont l'avantage de fournir des résultats reproductibles (alors que l'usinage d'éprouvettes entaillées est difficilement contrôlable) et de donner une prévision.

B.L.Koff, US

The modified Neuber analysis has been proven to be inaccurate based on test results — have you verified the analysis based on this theory?

Reponse d'Auteur

Les calculs élastoplastiques en fond d'alvéole ont montré que l'hypothèse de Neuber permet de rendre compte, de façon simple, du phénomène de plastification avec une bonne approximation.

B.L.Koff, US

You show crack progression calculations for disks but you do not show how these calculations correlate with test data on bars or disk specimens.

Reponse d'Auteur

Le calcul de progression de crique que j'ai exposé est un calcul bidimensionnel qui suppose que la crique est traversante. Dans ces conditions, nous avons vérifié que la méthode de calcul de K donne les mêmes résultats que les formules classiques. La comparaison d'un calcul tridimensionnel avec des résultats d'essais sur disque n'a pas encore été effectuée.

"STRESS INTERPRETATION IN THE FINITE ELEMENT METHOD"

P. Beckers
First Assistant

University of Liège
Laboratoire d'Aéronautique
75, Rue du Val-Benoît
4000 Liège, Belgium

SUMMARY

The interpretation of the stresses obtained by a finite element model is not always a simple operation, especially, when crude meshes are used in three dimensional structures.

The paper compares first the classical methods based on the computation of local stresses at various points like the vertices of the elements or the Gaussian points. An alternative interpretation of the stresses can be based on the definition of energy conjugate stresses that have the nature of weighted average of the stresses. A third possibility is offered which is rather new. It is based on the definition of connecting forces that have a direct and simple interpretation in terms of surface tractions. The corresponding finite elements have been named "delinquent" elements as they are in fact displacement elements which use some of the connection modes of stress equilibrium elements.

It is shown on examples that none of the three interpretation techniques is in itself completely satisfactory in every situations, but that the combined use of them allows a much better caption of the state of stress.

1. INTRODUCTION

In the finite element method, the full continuity of stress tensor components is never necessary to ensure convergence of the solution. Both in displacement and equilibrium models, the stresses are discontinuous between adjacent elements.

Consequently the stress interpretation is much more difficult than the displacement interpretation. The first part of this paper deals with simple examples which show the type of difficulty that can be encountered in some particular situations. In the second part the new procedure of stress computation based on the energy conjugate stresses is presented. In the third part the convergence properties of energy conjugate stresses and forces are analysed and illustrated in a practical example. Finally it is shown that, using delinquent models, a good choice of the interface connectors can also help to the stress interpretation.

2. SOME EXAMPLES OF DIFFICULTIES OF STRESS INTERPRETATION

2.1. Displacement models

In a finite element displacement model, the local stresses σ are obtained directly from the strains ϵ by the relation

$$\sigma = H \epsilon \quad (1)$$

where H is the symmetric matrix of elastic coefficients and where strains are simply derived from the displacement field u . With classical finite element models practical experience shows that it is sometimes difficult to get a satisfactory interpretation of this type of stress output. The examples chosen to show the behaviour of the local stresses are very simple but representative of some practical problem of structural analysis in which membrane elements are working in spar or beam configuration. The first example consists in a cantilever beam, build in at one extremity and uniformly transversally loaded at the other one (fig.1). The structure is idealized by one single element. First we use the well known isoparametric eight nodes quadrilateral element of serendipity type [1]. Whilst the results for deflections and axial stresses are excellent, the shear stresses show a parabolic "variation" which provides an extremely poor representation of the actual stresses. Table 1 give the values of the shear stress at the integration points of the 3x3 Gauss rule, needed to obtain the exact integration of the stiffness matrix of the model.

Numbering of integration points	1	2	3
1	1.44	.51	1.44
2	1.38	.45	1.38
3	1.44	.51	1.44

TABLE 1. Shear stress at integration points of 3x3 Gauss rule

The 9 local values are sufficient to compute the shear load evolution along the beam. This leads to the representation of figure 1, which evidently has very little physical meaning. It can be shown that the difference between the maximum and minimum values of the shear load, taken over the length of the element is given by

$$T_{\max} - T_{\min} = 2 G t \left(U_m - \frac{U_1 + U_2}{2} \right) \quad (2)$$

where U_m is the horizontal displacement of the superior midedge, U_1 , U_2 the displacements of the corresponding vertices, G , the shear modulus and t the thickness of the beam. It is interesting to note that the exact value of the shear stress is obtained at the 2x2 Gauss points [2], and that the average of the shear

load over the element remains as expected, equal to the applied load. Similar results can be found in [1] and [3]. In this last reference, the same behaviour is observed in a box beam analysis for rectangular elements and for quadrilaterals formed by 4 triangles (fig. 2). The amplitude of shear loads oscillations decreases when the number of elements grows but, even for the finer mesh sizes, remains troublesome (fig. 4).

The preceding examples suggest that with these elements the stresses or similar quantities should never be calculated at nodes by averaging local values obtained at the vertices of the adjacent elements, but fortunately this type of discrepancy which can occur with many finite element displacement models is not so large in all the cases.

2.2. Equilibrium models

The difficulties encountered in the interpretation of the stress output using displacement models are not too surprising because the discretization of these models is made on the displacement field. Theoretically the equilibrium models should give much better stress results because they are based on the discretization of the stress field. In these models the internal equilibrium equations and the boundary conditions related to surface tractions are satisfied a priori. Unfortunately the continuity of stresses between elements is ensured only for the surface tractions modes and in practical applications, there can exist important discontinuity between the stress tensor components. The same problem of the cantilever beam is analysed with the quadrilateral equilibrium element [4]. The stress field is assumed to vary linearly in each triangle constituting the element. The results are given on figure 4.a for the stress components σ_x , σ_y , τ_{xy} . It can be observed that the boundary conditions are perfectly satisfied. Any computation for the shear load from the local values gives also the correct result. At the nodes, the stress components suffer important discontinuities and a nodal stress average will give the very bad results of figure 4.b.

When the mesh is refined the discontinuities decrease but as for displacement models a crude averaging procedure at the nodes of the structure can give very bad results and loss the main advantage of the equilibrium models which should be able to give exact surface traction modes at the boundaries.

3. THE NEW APPROACH OF THE ENERGY CONJUGATE STRESSES

3.1. Displacement models

These models are derived by application of the minimum total energy principle

$$\delta(U + P) = \delta\left(\frac{1}{2} \int_{vol} \epsilon' H \epsilon \, dvol - \int_{St} \bar{t}' u \, dS\right) = 0 \quad (3)$$

where U is the strain energy

P is the potential energy (in which the body forces are not considered here)

ϵ is the column vector of the strain components

H is a symmetric matrix of elastic coefficients

t is the column vector of surface tractions on St

u is the displacement vector

St is the part of the boundary where surface tractions are prescribed.

The prime denotes transposition and the bar prescribed values.

The displacement field in the finite element is discretized in the form

$$u = W(x) q \quad (4)$$

where W is the matrix of assumed shape functions. The column vector of the strain tensor components is then expressed in terms of generalized displacements by

$$\epsilon = \partial W q = B q \quad (5)$$

and the strain energy becomes

$$U = \frac{1}{2} \int_{vol} q' B' H B q \, dvol = \frac{1}{2} q' K q \quad (6)$$

where K is the stiffness matrix of the element.

Introducing the new parameters of the deformation modes, a , the strains can be defined as follows

$$\epsilon = M(x) a \quad (7)$$

As the principle may be applied only if the displacement field satisfies a priori the compatibility conditions $\epsilon_{ij} = D_j u_i$ or in matrix form $\epsilon = \partial u$, in the volume, the expression (7) must be identical to (5) and the parameters a are related to the generalized displacement q by

$$a = C' q \quad (8)$$

So the strain energy can be written as

$$U = \frac{1}{2} \int_{vol} a' M' H M a \, dvol = \frac{1}{2} a' I a. \quad (9)$$

This expression differs from (6) only by the choice of the parameters and the fact that the parameters a do not include the rigid body modes of the model. When using the minimum total energy principle, the stresses are only defined by

$$\sigma = \frac{\partial U}{\partial \epsilon} \quad (10)$$

With the discretization adopted, the stress field is described by a set of parameters b

$$b = \frac{\partial U}{\partial a} = I a = \int_{vol} M' \sigma \, dvol \quad (11)$$

which are weighted averages of the stresses and yield therefore only a "weak" knowledge of the stress state in the element. The matrix b contains the so-called energy conjugate stresses.

It is important to remark here that the local values of the stresses defined by (1) don't satisfy the equilibrium equations. As shown in the following the minimum total energy principle ensures only equilibrium in the mean sense for the weighted averages b , to which the local stresses are only related by the integrated relations (11).

In the absence of body forces, the virtual work (V.W.) consists only in the work done by the prescribed surface tractions:

$$V.W. = \int_{St} u' \bar{t} \, dS = \int_{St} q' W' \bar{t} \, dS = q' g. \quad (12)$$

It allows to define the generalized forces

$$g = \int_{St} W' \bar{t} \, dS \quad (13)$$

conjugate to the displacement modes q .

Alternatively the V.W. furnishes also the relation between energy conjugate stresses and generalized forces by (8) and (11)

$$g' q = b' a = b' C' q, \quad (14)$$

so that

$$g = C b. \quad (15)$$

Expressed in terms of weighted averages it gives by (13) and (11), the equilibrium relations between stresses and surface traction modes:

$$\int_{St} W' \bar{t} \, dS = C \int_{vol} M' \sigma \, dvol \quad (16)$$

This can be expressed in terms of the generalized displacements in the following way. By (6) and (12), the principle (3) becomes

$$\delta(U + P) = \delta\left(\frac{1}{2} q' K q - q' g\right) \quad (17)$$

and after variation of the parameters q , we obtain the well known relations

$$g = K q \quad (18)$$

equivalent to the equilibrium equations (16).

3.2. Equilibrium models

Stress diffusing equilibrium models are derived by application of the minimum complementary energy principle

$$\delta(\psi + Q) = \delta\left(\frac{1}{2} \int_{vol} \sigma' H^{-1} \sigma \, dvol - \int_{Su} \tau' \bar{u} \, dS\right) = 0 \quad (19)$$

where ψ and Q denote respectively the complementary stress energy and the potential energy. The application of this principle implies the satisfaction of the equilibrium equations:

$$D_j \sigma_{ij} + X_i = 0 \quad \text{in the volume} \quad (20)$$

$$\tau_i = \ell_j \sigma_{ji} = \bar{t}_i \quad \text{on } Su \quad (21)$$

(ℓ_j are the direction cosines of the outward normal)

In the following, the case without body forces only will be considered for simplicity.

Each stress component is represented by a linear combination of assumed modes $N_i(x)$, the intensity of the modes being noted b_i

$$\sigma = N(x) b \quad (22)$$

These modes must be chosen in such a way that the equilibrium equations in the volume are satisfied. The complementary strain energy ψ can be written

$$\psi = \frac{1}{2} \int_{vol} b' N' H^{-1} N b \, dvol = \frac{1}{2} b' J b \quad (23)$$

where J is the flexibility matrix. The generalized strains a can be defined by

$$a = \frac{\partial \psi}{\partial b} = J b = \int_{vol} N' \epsilon \, dvol \quad (24)$$

They are weighted averages of strains and this corresponds only to a weak knowledge of the strain field.

Let us turn now to the equilibrium requirements along the boundary. They concern only the interfaces as we have ruled out the body forces. Using relation describing the stress field, the surface tractions can be expressed by

$$t = L \sigma = L N(x_b) b \quad (25)$$

where L is a matrix of the direction cosines l_i and N is calculated on the boundary S_u . The surface traction modes described by t have to be uniquely determined by a set of generalized forces denoted g . These can be local values or derivatives or integrals of the surface traction or any combinations of these quantities provided that along each edge they define the surface tractions univocally. So it is possible to express the surface traction modes in terms of the generalized forces and shape functions $V(x)$:

$$t = V(x) g. \quad (26)$$

This expression is defined only on the boundary of the element.

But the generalized forces can also be calculated in terms of the stress field parameters

$$g = C b \quad (27)$$

where C is called the static matrix of the element. This relation cannot be inverted since the generalized forces are a priori not independent as they satisfy the global equilibrium equations. Note that the stress tensor has no unique value at the vertex. Therefore in pure equilibrium models, there are no variables associated with a vertex and the forces g are essentially interface variables.

The virtual work can be written alternatively

$$V.W. = \int_{S_u} \bar{u}' t dS = \int_{S_u} \bar{u}' L N b dS = a' b \quad (28)$$

$$V.W. = \int_{S_u} \bar{u}' V(x) g dS = q' g = q' C b \quad (29)$$

where q are the generalized (average) displacements conjugate to g . From (29)

$$q = \int_{S_u} V' \bar{u} dS \quad (30)$$

Comparison of the two expressions yields

$$a = C' q \quad (31)$$

where the transpose static matrix relates the generalized strains to the generalized interface displacements. From (24), (30) and (31), we obtain also the compatibility conditions in terms of weighted averages,

$$\int_{vol} N' \epsilon dvol = C' \int_{S_u} V' (x) \bar{u} dS. \quad (32)$$

This can also be expressed in terms of the parameters b of the discretized stress field. By (23) and (29) the principle (19) becomes

$$\left(\frac{1}{2} b' J b - b' C' q \right) \min \quad (33)$$

and after variation of parameters b , it yields

$$J b = C' q \quad (34)$$

equivalent to the compatibility conditions (32).

Finally as the matrix J is never singular the relation (27) gives

$$g = C b = C J^{-1} C' q = K q \quad (35)$$

which is the familiar form of the stiffness matrix for an equilibrium element.

3.3. Practical signification of the energy conjugate stresses

For the displacement models, the relation (11) furnishes the expression of the energy conjugate stresses, but now the question is: how to utilize these special stresses? If we examine the expression (7), we see that the weighting functions of the stress averages are nothing else than the shape functions of certain deformation modes for which definition is arbitrary provided they satisfy to the compatibility conditions (8). For all the elements which pass the patch test [5], a sufficient condition for convergence, the constant deformation modes, are included in the parameters a of relation (7). Their shape function will be equal to 1 and consequently, amongst the weighted average stresses of (11), we will find the simple averages in the element of the stresses or of linear combinations of them. In the simplest models as linear membrane triangles the averages of the stresses themselves are the unique averages we have at our disposal. For more sophisticated models other averages can be used but their interpretation is generally not so easy.

Keeping only the simple averages in mind, we can yet get some advantages of the use of the energy conjugate stresses. The comparison with equilibrium models will be very easy if in the expression (22) of the definition of the discretized stress field of equilibrium models we choose also parameters b which have the meaning of average value in the element. This is also always possible because the equilibrium model must contain the constant stress modes.

If we apply this procedure for all the models, we obtain a general stress output very easy to use and which interpretation is independant of the finite element model.

Looking at the preceeding example of the cantilever beam we know that for the single rectangular element the solution is exact for stress averages. Comparing now the results for an element composed of 4 triangles we observe a good agreement between the solutions obtained for equilibrium and displacement elements (fig. 5) if we take into account the fact that the energy differs from about 10% due to the crude mesh. For the same problem, table (2) gives other comparison of the quality of the stress output for a 4x4 regular mesh using quadrilateral equilibrium and displacement elements. Here the two solutions for shear stresses

are very close while the energies differ from about 1%.

$\frac{y}{h} \backslash \frac{x}{L}$	$\frac{1}{8}$	$\frac{3}{8}$	$\frac{5}{8}$	$\frac{7}{8}$	
$\frac{7}{8}$.77	.63	.62	.63	equilibrium
	.81	.63	.62	.63	displacement
$\frac{5}{8}$	1.23	1.37	1.38	1.37	equilibrium
	1.19	1.37	1.38	1.37	displacement

TABLE 2 : Comparison of the shear stress averages in the cantilever beam for displacement and equilibrium elements.

Before to analyse with more detail the properties of the complete set of energy conjugate stresses, we can make some observations on the simple stress averages.

First their definition is very general and allows to use the same procedure for all the types of elements. Secondly, their computation will be very cheap because they form a subproduct of the computation of the stiffness matrix. Thirdly they satisfy always the equilibrium equations in the mean sense of relation (16).

However some difficulties remain unsolved; first we cannot get any information at the boundary of the element and secondly, as the interpretation of higher order conjugate stresses is more difficult, only the simple averages are of direct use. The corresponding information given per element is quite limited although it must be noted that in a great number of practical problems it gives a sufficient picture of the stresses.

4. PROPERTIES OF THE ENERGY CONJUGATE STRESSES

4.1. Convergence properties

The problem of convergence in finite element method requires some mathematical means and is generally presented in the context of functional analysis [6]. Here we will limit us to give only intuitive physical argument which show that some quantities have special convergence properties. To analyse the convergence properties of the energy conjugate stresses the following argument can be used. Let us assume that, for an element, the approximate solution coincides with the exact solution at the points where generalized displacement are defined as shown in figure 6 for a quadrilateral quadratic element. In this element the only approximation will come from the shape functions $W(x)$ of the generalized displacements defined in (4). The equilibrium equation are satisfied uniquely in the mean sense of equations (15) and (16). These relations show that the convergence properties will be the same for the generalized forces g and the energy conjugate stresses b .

If we write now the virtual work principle

$$V.W. = \int_{St} \bar{t}' u \, dS = \int_{St} \bar{t}' W(x) \, dS \quad q_{\text{exact}} = \bar{g}' q_{\text{exact}} \quad (36)$$

we see that the convergence in energy is related only to the convergence of the generalized forces g , and by relation (15) to the convergence of the parameters b . Consequently we can expect that the g and b quantities will always converge very well.

4.2. Numerical example of the convergence.

It was shown in § 3.3. that if we limit us to the simplest energy conjugate stresses, i.e. the averages in the elements, it is possible to define exactly the same quantities when discretizing an equilibrium model. To analyse the convergence properties of parameters b , it is then possible to compare them in a dual analysis using exactly the same mesh for displacement and equilibrium models. So full advantage will be taken of the utilization of energy conjugate stresses. For instance for both analyses exactly the same stress output will be obtained.

The example chosen comes from industrial study. It consists in a rocket motor case, for which axisymmetrical idealization can be used. The complete structure, shown on fig. 7, has three different material properties. In the first part, denoted composite material, we have anisotropic material. The second part, denoted rubber joint, ensures the bounding between the vessel and the polar boss. The third part is made of aluminium alloy. For the linear analysis, the displacement model used is the isoparametric quadrilateral eight nodes element [1], and the equilibrium model used is a linear stress field quadrilateral element [7]. We know that the displacement and the equilibrium analyses give respectively a lower and an upper bound to the exact solution [8]. With the discretization chosen the gap between potential energy is only of 0.48%.

The principal stresses are given in figure 8 for the polar boss. The differences observed between the two analyses are always of the order of 0.5% and it is impossible to distinguish them in a graphic output as in fig. 8.

The hoop stresses also are in very good agreement, but it is more difficult to visualize them element by element. The unique manner to visualize scalar quantities is to compute iso-curves (fig. 9). So it is necessary to introduce interpolation formula which can alterate the initial results. However these interpolation formula can be very general because all types of elements give the same type of output.

In conclusion the dual analysis provides now a good procedure not only to compare energy or displacement results but also stress results. It is obvious that the dual analysis cannot be used for each analysis but it allows to qualify a mesh or a modelization for a particular class of problems.

4.3. Relation between energy conjugate stresses and other particular stresses.

In the very simple example of a quadratic bar, the integration of the stiffness matrix can be achieved exactly by using a 2 Gauss Point integration rule. This element possesses also two energy conjugate stresses. The associated weighting functions are a linear and a constant functions:

$$\begin{aligned} b_1 &= \int \sigma \, dx \\ b_2 &= \int x \sigma \, dx. \end{aligned} \quad (37)$$

If we write these integrals in the form of numerical integration the expression becomes

$$\begin{aligned} b_1 &= \sigma_1 G_1 + \sigma_2 G_2 \\ b_2 &= \sigma_1 x_1 G_1 + \sigma_2 x_2 G_2 \end{aligned} \quad (38)$$

where G_1 and G_2 are the weights associate to the Gauss points. In this particular case there exists an univocal relation between the parameters b and the special values of the stresses at the Gauss points. Thus these values form simply a change of base for the definitions of the parameters b and it is not surprising that these particular local values converge very well [9].

If we examine the case of the isoparametric eight nodes quadrilateral element of serendipity type [1] where sub integration is used, we can make the same type of observation. This element possesses 16 degrees of freedom and therefore 13 independent strain parameters. It is observed that when 2x2 Gauss rule is used for integration a kinematical mode is appearing which means that the integration losses 1 term in the rigidity. From relation (11) this can be interpreted in the sense that only 12 energy conjugate stresses are integrated in an approximate way. So for this element, relations of type (38) can also be written which relate the 12 energy conjugate stresses to the 12 local stresses at the integration points, but now the integrals are replaced by approximate quadrature formula.

Thus for this element, the 12 particular local stress output form a particular system of energy conjugate stresses and this fact confirms their property of super convergence. [2], [9].

Unfortunately this interpretation of energy conjugate stresses is not completely achieved for other elements and in all the cases but it seems that it will constitute a very interesting subject for further investigation.

5. INTERPRETATION OF THE GENERALIZED FORCES

The generalized forces constitute also a special stress output. They are related to the stresses by relations (15) and (16) and can be directly computed from the displacements by relations (18). It is important to note that they are a natural direct output of the computation. A difference with the stresses b is that they are not independent: they verify the global equilibrium equations of the element. It is well known that the generalized forces are very usefull to check the global equilibrium of the structure or to find the loads which are transmitted from a substructure to an other. However at the element level their interpretation is more difficult due to the presence of the corner loads for which it is impossible to separate as seen in expression (13) the effects of the surface tractions modes of the edges adjacents to the corner.

For elements of higher degree (2 or more), interface loads are present which come only from interface surface traction contribution. With a mixed formulation, it is possible to change the connector which is the displacement associated to this load into a equilibrium connector which will provide an easier interpretation of the surface tractions [5]. The procedure will consist in building a particular hybrid model [10].

For this purpose the principle (3) is modified by relaxing the compatibility condition on the interface S_u . The new principle is written

$$\left(\frac{1}{2} \int_{vol} \epsilon' H \epsilon \, dvol - \int_{St} \bar{\epsilon}' u \, dS - \int_{Su} t' (u - \bar{u}) \, dS \right)_{min} \quad (39)$$

The Lagrange multipliers t are easily identified as the surface tractions. Now the discretized fields are u in the volume and on the boundary St and the surface traction t on the boundary Su . The displacement are discretized as in (4) and the surface tractions as in (26). The principle becomes

$$\left(\frac{1}{2} \int_{vol} q' B' H B q \, dvol - \int_{St} \bar{\epsilon}' W q \, dS - \int_{Su} g' V' (W q - \bar{u}) \, dS \right)_{min} \quad (40)$$

In this principle the generalized displacements associated to the surface tractions modes introduced on Su are defined by the weighted averages:

$$\bar{q} = \int_{Su} V' \bar{u} \, dS \quad (41)$$

For example if the surface traction mode introduced on the interface is constant the conjugate displacement will be simply the average of displacement on the interface.

When a constant surface traction mode is introduced in an interface of quadratic displacement model it will only change the definition of the connectors. The local displacement becomes an average displacement and the weighted average of the surface traction becomes the intensity of the constant surface traction mode.

In membrane theory, when an equilibrium surface traction mode of degree n is defined on an interface the continuity properties of the displacement model will not be changed if the displacement field is of degree $n+2$.

The advantage of this procedure is that it allows to obtain directly in the interface the surface traction modes as in the equilibrium models. On the separation surface of two substructures constituted by many interfaces of displacement models for which the interface displacement connectors have been transformed in force connectors, there are two possibilities of connection :

- first, to connect the nodal displacements and the interface forces. In this case the solution is exactly the same as for the displacement models with only a change in the interpretation of the interface forces and displacements. The picture of surface traction modes will be given partially by the interface connectors and partially by the forces conjugated to the nodal displacements.

- secondly, to connect only the interface forces. In this case the separation surface between the two substructures will behave exactly as in equilibrium models. The picture of surface traction modes will then be obtained directly.

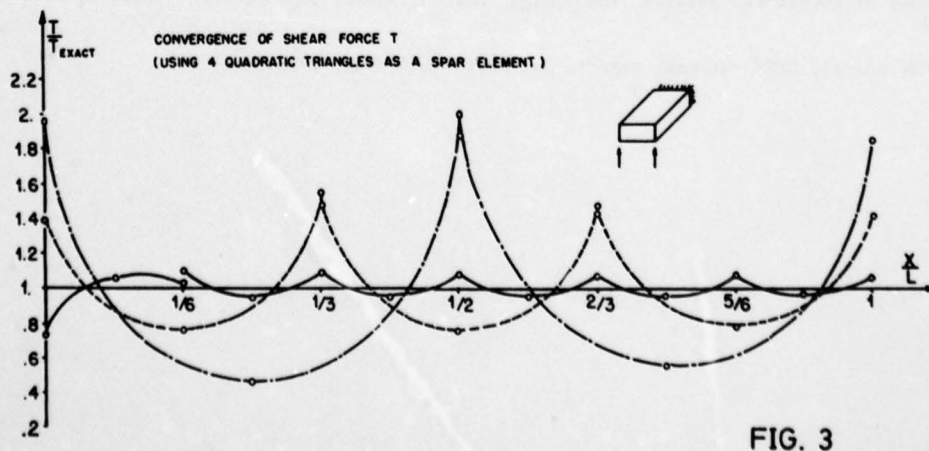
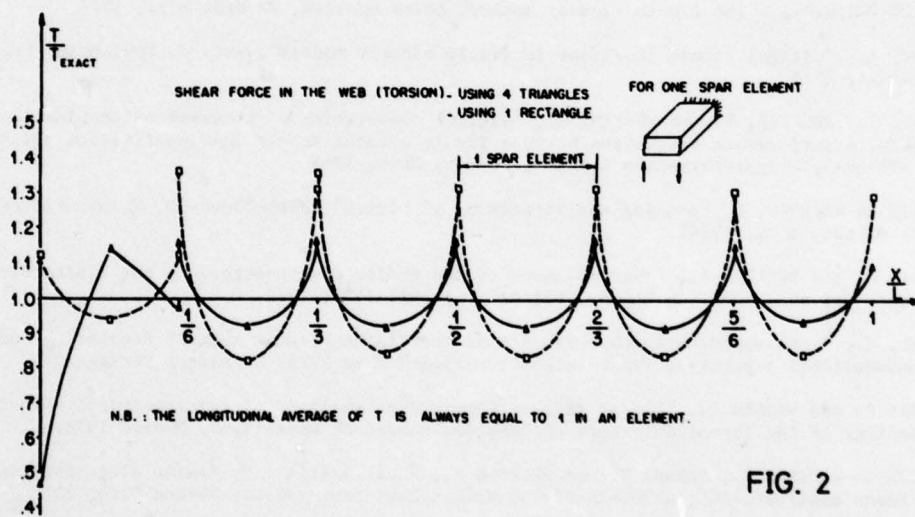
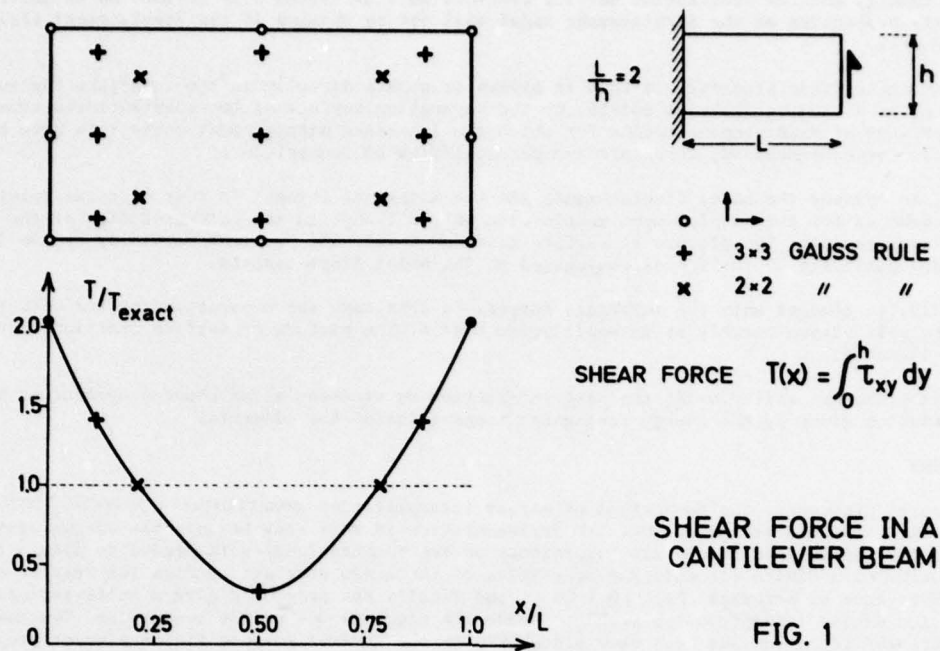
This last procedure will provide the best information on stresses along choosen boundaries and complete so the information given by the energy conjugate stresses inside the elements.

6. CONCLUSIONS

As a general procedure, the new method of stress interpretation constitutes a powerfull and very general tool to obtain a standard stress output. Its implementation is very easy because the energy conjugate stresses and the generalized forces are subproducts of the computational work needed to obtain the stiffness matrix of a finite element. The properties of these new stresses confirm the results of other works on convergence of stresses [2] [6] [9], and finally the procedure give a quite satisfactory response to the stress interpretation problem inside the elements and on the boundaries. The energy conjugate stresses technique has been used since 1970 in the general purpose finite element program SAMCEF developed at the university of Liège [11].

7. REFERENCES

- [1] ZIENKIEWICZ, O.C., "The finite element method", third edition, Mc Graw Hill, 1977
- [2] BARLOW, J., "Optimal stress locations in finite element models", Int. J. Num. Meth. Eng., 10, 243-51, 1976
- [3] SANDER, G., BECKERS, P., and NGUYEN, H., "Digital computation of stresses and deflections in a box beam. A performance comparison between finite element models and idealization patterns" AFFDL-TR-69-4, Wright-Patterson A.F.B., Dayton, Ohio, 1969
- [4] FRAEIJIS de VEUBEKE, B., "Bending and stretching of plates" AFFDL-TR-66-80, Wright-Patterson A.F.B. Dayton, Ohio, 1966.
- [5] SANDER, G. and BECKERS P., "The influence of the choice of connectors in the finite element method Int. Jnl. for num. meth. in Engng., Vol 11, pp 1491-1505, 1977
- [6] ZLAMAL, M., "Some superconvergence results in the finite element method" Proceedings of conference on "mathematical aspects of finite element methods" Rome 1975, Springer-Verlag 1977.
- [7] BECKERS P. and NYSSSEN C., "Linear and non linear dual analysis of axisymmetrical structures" Proceedings of the second conference on "Applied numerical modelling", Madrid 1978.
- [8] FRAEIJIS de VEUBEKE B., SANDER G. and BECKERS P., "Dual analysis by finite elements. Linear and non linear applications", AFFDL-TR-72-93, Wright Patterson A.F.B., Dayton Ohio, 1972
- [9] STRANG, G. and FIX G. "An analysis of the finite element method", Prentice Hall, 1973
- [10] PIAN T., "Formulations of finite element methods for solid continua" in "Recent advances in matrix methods of structural analysis and design" ed. Gallagher, Yamada, Oden, Univ. of Alabama Press. 1971.
- [11] SAMCEF manual, LTAS internal report, University of Liège, 1976.



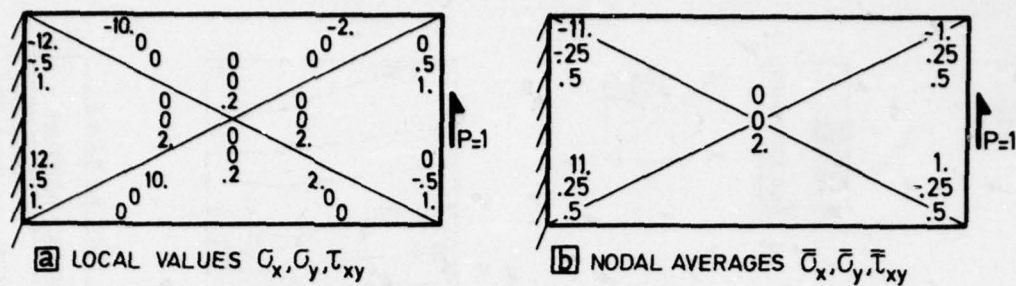


FIG. 4 EQUILIBRIUM MODEL LINEAR STRESS FIELD

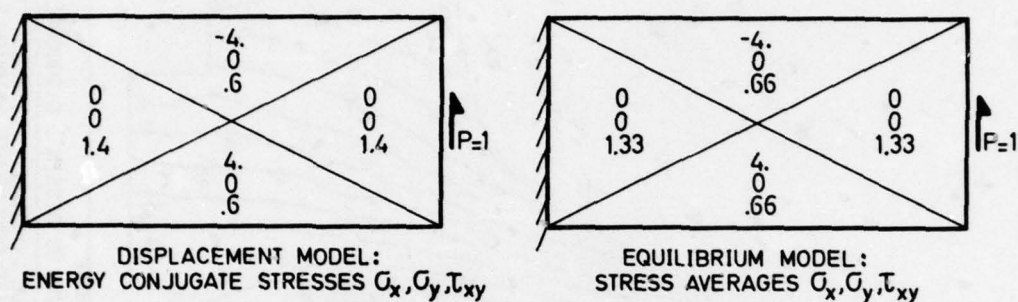
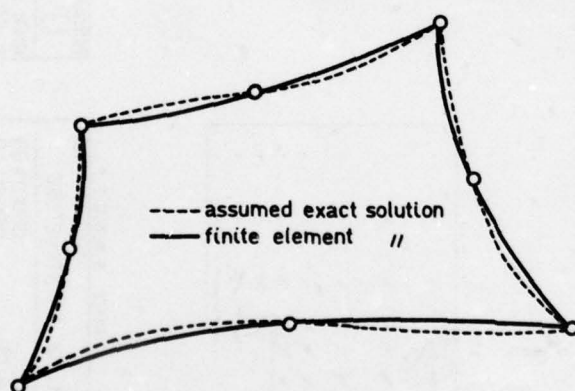
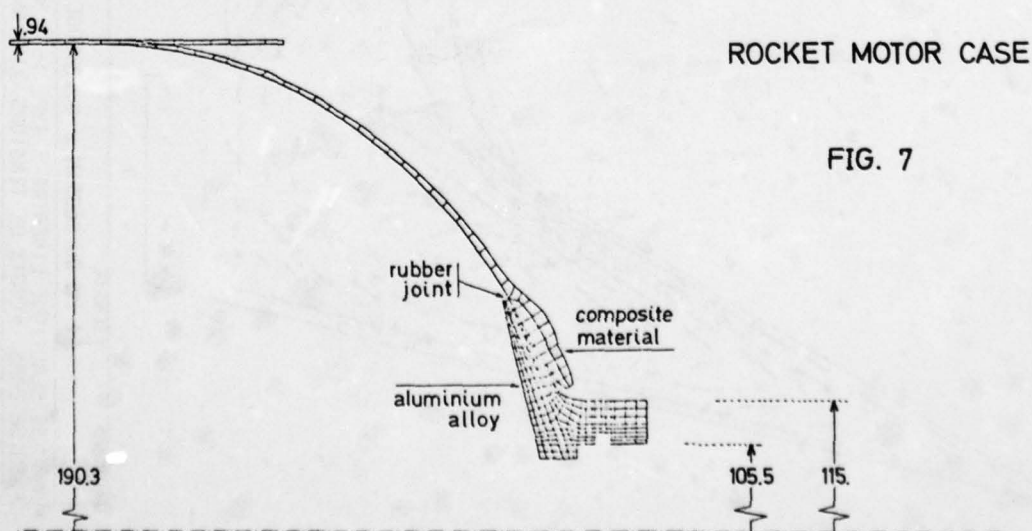


FIG. 5 COMPARISON OF ENERGY CONJUGATE STRESSES IN THE CANTILEVER BEAM



APPROXIMATE AND EXACT DEFORMATION MODES

FIG. 6



ROCKET MOTOR CASE

FIG. 7

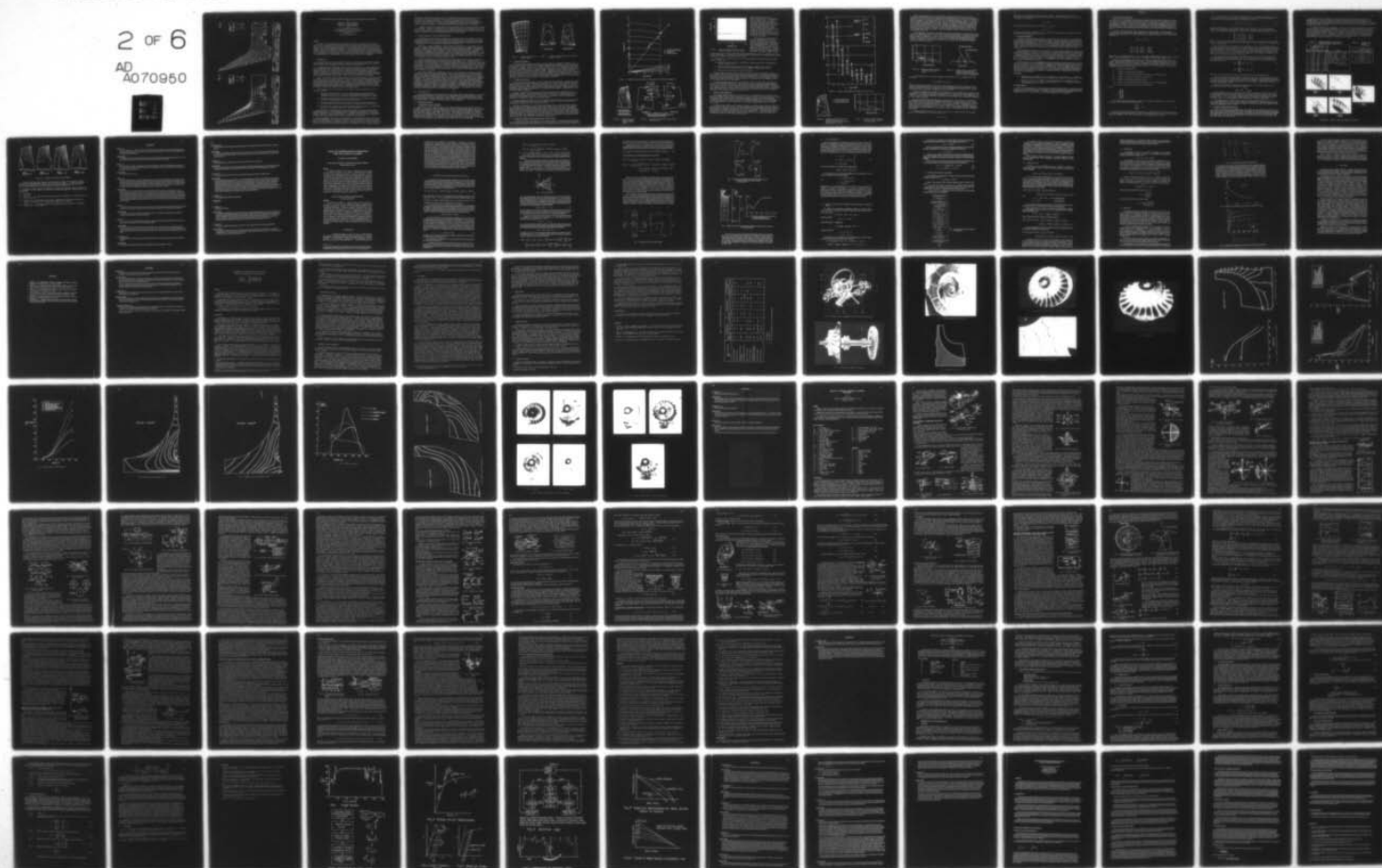
AD-A070 950 ADVISORY GROUP FOR AEROSPACE RESEARCH AND DEVELOPMENT--ETC F/G 21/5
STRESSES, VIBRATIONS, STRUCTURAL INTEGRATION AND ENGINE INTEGRI--ETC(U)
APR 79

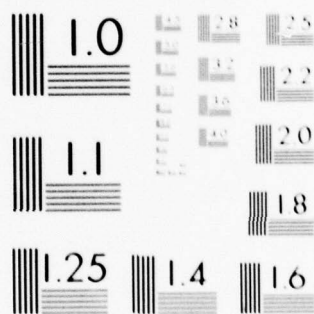
ADVISORY GROUP FOR AEROSPACE RESEARCH AND DEVELOPMENT--ETC F/G 21/5
STRESSES, VIBRATIONS, STRUCTURAL INTEGRATION AND ENGINE INTEGRI--ETC(U)
APR 79

AGARD-CP-248

NL

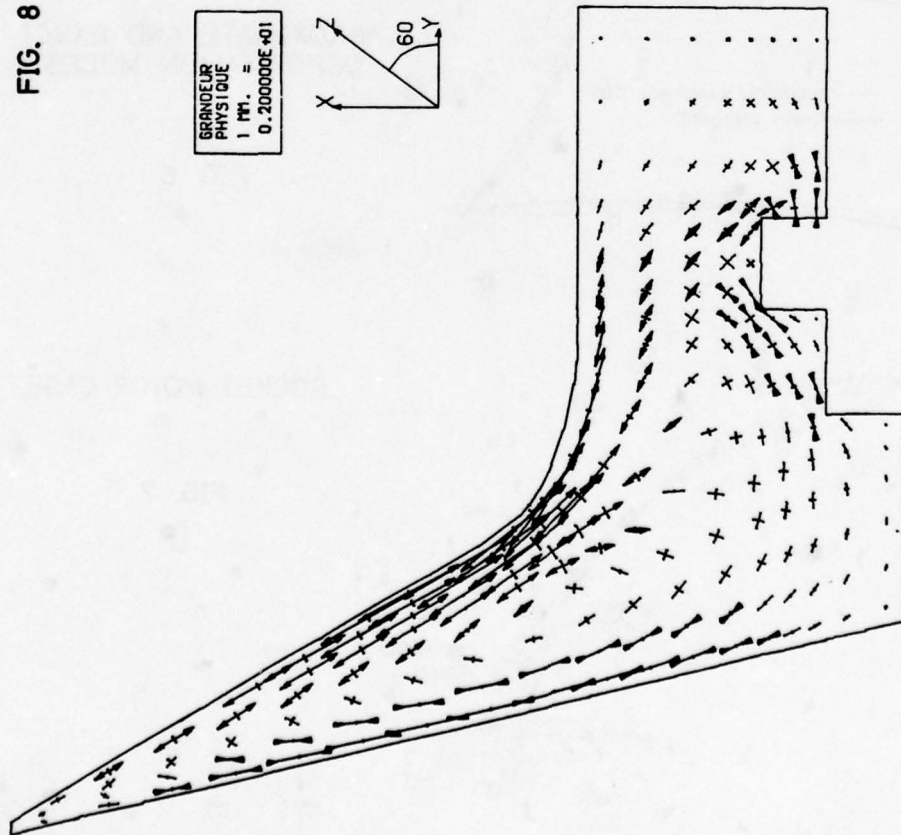
AD
A070950





MICROCOPY RESOLUTION TEST CHART
NATIONAL BUREAU OF STANDARDS-1963-A

FIG. 8



GRANDEUR
PHYSIQUE
1 MM. =
0.200000E+01

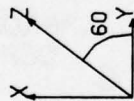
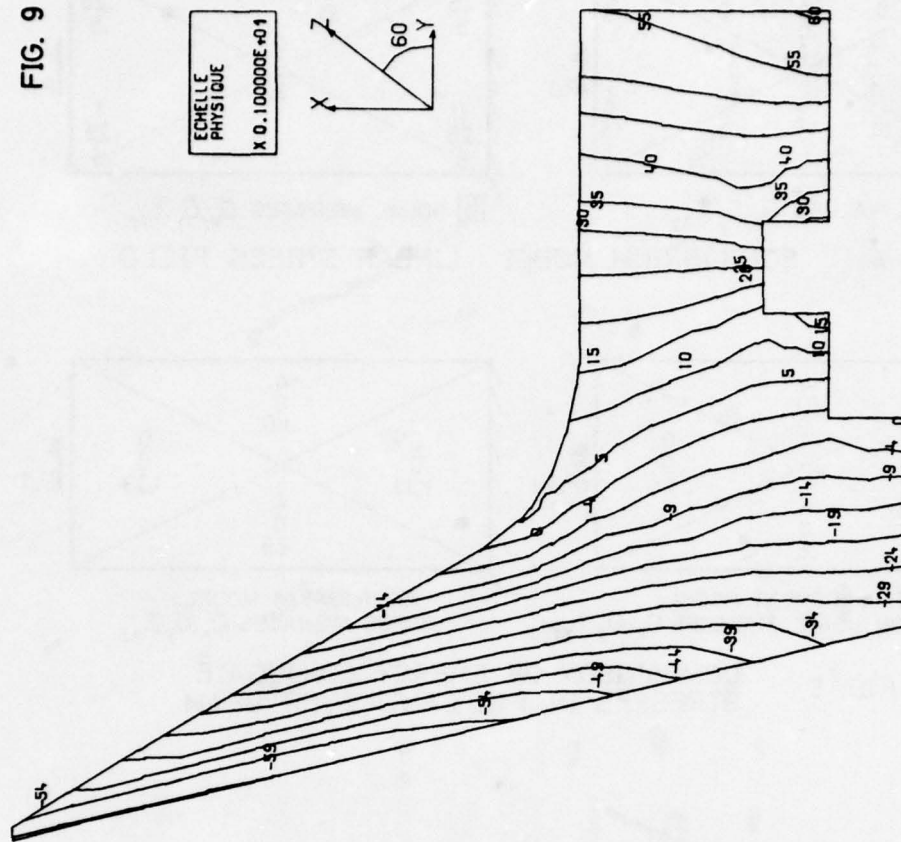
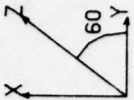


FIG. 9



ECHELLE
PHYSIQUE
X 0.100000E+01



TRACE S.A.M.C.E.F.

numéro	ECHELLE
0	1 MM DU DESSIN = 0.200000E+01 MM DE LA STRUCTURE
ANALYSE ELASTIQUE LINEAIRE TYPE 15 ND=2	
P=63.35 BARS	CROIX DE TENSIONS DU PLAN MERIDIEN
00001400	00001410
00001280	00001290
L.T.B.S. - UNIVERSITE DE LIÈGE	

TRACE S.A.M.C.E.F.

numéro	ECHELLE
0	1 MM DU DESSIN = 0.200000E+01 MM DE LA STRUCTURE
ANALYSE ELASTIQUE LINEAIRE TYPE 15 ND=2	
P=63.35 BARS	ISO-CONTRAINTES AZIMUTALES SIGMA THETA
00001280	00001290
L.T.B.S. - UNIVERSITE DE LIÈGE	

THREE-DIMENSIONAL FINITE-ELEMENT TECHNIQUES FOR GAS TURBINE BLADE LIFE PREDICTION

by

M.R. Peterson - Engineering Specialist,
 R.G. Alderson - Sr. Engineering Specialist,
 R.J. Stockton - Engineering Specialist,
 and

D.J. Tree - Supervisor Preliminary Design

AIRESEARCH MANUFACTURING CO. OF ARIZONA

A Division of the Garrett Corporation

P.O. Box 5217

Phoenix, Arizona, USA 85010

SUMMARY

The use of three-dimensional finite-element analyses in conjunction with test-derived data to predict the vibratory fatigue life of turbine blades is described. Vibratory strain measurements are interpreted and extended using predicted strain distributions from the finite-element analysis. The statistical nature of test data is considered. Also, some techniques employed in three-dimensional finite-element analyses to enhance their use for stress and vibration analysis are described. These techniques include a method for reduction of the size of the eigenvalue problem for vibration analysis by a transformation to generalized coordinates derived from static solutions. An example of the application of these methods to a turbine-blade analysis is presented.

1.0 INTRODUCTION

The blades and vanes of a typical gas turbine in service are subjected to cyclic loading arising from flow perturbations. Where excitation frequencies are consistent with a blade or vane resonance, a potential for failure exists.

In determining the suitability of a particular component for a given service life, engine experience during development and flight testing and results from instrumented engine tests are used. Bench testing of components, material property tests, and computer simulation of stress and vibration states provide additional information. Growing confidence in the capability of state-of-the-art stress and vibration computer simulations, particularly when used in conjunction with available test and field experience, suggests that more usable data exists than is currently being employed.

There is a need to rely on both analytical and test-derived data for the prediction of fatigue lives. This arises because of the difficulty in obtaining sufficiently detailed strain data from engine tests of a blade in its operating environment and is further complicated by blade-to-blade nonconformity. Also, strictly analytical techniques for the prediction of the forced vibratory response of the blade are limited by the complexities of simulating the range of excitation forces which may act on the blade. This paper discusses some aspects of both analytical vibration prediction and the use of engine test data for vibratory fatigue life prediction.

Life prediction for blades subject to high-cycle fatigue requires data from a number of sources:

- (a) Data from stress analyses is used to identify non-alternating strain components in the blade. Three-dimensional simulations capable of evaluating the effects of local details, attachments, and shrouds are needed.
- (b) Vibratory-strain prediction data is required to identify gauge locations and other requirements for bench and engine tests.
- (c) Vibratory-strain measurements obtained in engine tests are required to provide insight into the complex interaction between blade and environment.
- (d) Materials data suitable for the configuration under test must be accumulated and put into a format usable with other acquired data.

Any assessment of blade durability must rely heavily on results obtained from engine-strain tests. The methodology currently employed places emphasis on maximum strains recorded and on the interpretation of resonance implications. An alternative, in which the range of amplitude observed is considered in conjunction with vibration-analysis results, provides a wider base for durability predictions.

The life prediction method is illustrated for a turbine blade, using data from an engine-test sequence. For the most significant resonant condition observed, a survey of all data was made and a consistent set of values was obtained for nine gauges and six points in time at which the resonance occurred. The gauges were on different blades in differing locations, and analytical results were employed to provide a common footing.

Utilizing a strain-state simulation for the observed resonance, predicted strains were obtained not only for each gauge location, but also for all nodal points of the original finite-element analysis. For each point considered, 54 strain values were obtained which identified the range of strain experienced during the test sequence for this particular resonance. The strain distribution was compared with a distribution of material fatigue strengths to investigate the probability of failure of the blade.

A number of statistical distributions could be considered in evaluating these strains, e.g., Weibull, normal, log normal, etc. For simplicity, a normal distribution is assumed in this paper. Similarly, the nature of the material strength could be identified with a number of statistical distributions; again a normal distribution was assumed. These simplifying assumptions do not degrade the generality of the method.

2.0 THREE-DIMENSIONAL FINITE-ELEMENT APPROACH

The approach to vibratory-life prediction discussed herein uses a family of three-dimensional finite-element programs developed at AiResearch for the analysis of turbine-engine components (Ref. 1). These programs have been verified by engine component tests. A brief overview of some features of the finite-element methods is presented to provide a background for the life-prediction discussion in Section 3.0.

The family of three-dimensional finite-element programs used in this study includes codes for: model generation (MESH3), steady-state stress solution (ISO3DQ), vibration solution (ISOVIB), and result presentation and output processing (PROUT3). Program MESH3 automatically generates nodes, elements, loads, boundary conditions, and other model parameters for geometric configurations typical of certain turbine engine components. The steady-state stress-analysis program ISO3DQ and the vibration program ISOVIB have a common finite-element basis; both employ three-dimensional isoparametric elements, which are formulated as solid-and thin-shell versions to allow the representation of thin airfoils and attachments with the same element configuration.

Since the prediction of surface stresses is important for life analyses, the stress and vibration programs employ the method of Oden and Brauchli (Ref. 2) for computing "consistent stress distributions" using conjugate approximations. Although surface stresses are desired, the optimum points for evaluating stresses are within the element, rather than at the nodes or on the boundary. The stresses computed by the conventional method are discontinuous at the element boundaries. The conjugate stress technique yields a continuous distribution of stresses throughout the model. In the authors' experience, it also yields more accurate stress values than those obtained from the conventional computation or from nodal averaging of stresses.

The stress analysis of a component, such as a rotor blade, may require the modeling of details such as attachments and shrouds. This ordinarily leads to a finite-element model with a great many degrees-of-freedom. Also, the relative ease of model generation using program MESH3 has encouraged the use of large finite-element models. For vibration analysis, these large models would lead to long and costly solution times on the computer. Therefore, the vibration-analysis program, ISOVIB, makes use of a transformation method to reduce the number of degrees-of-freedom in the model. This method uses displacement patterns of the finite-element model, which may consist of substructures, as generalized coordinates. Since the modes of interest can usually be represented adequately with fewer generalized coordinates than nodal degrees-of-freedom, a transformation to generalized coordinates reduces the number of degrees-of-freedom in the vibration problem. The solution method employed in ISOVIB is described in more detail in the Appendix, which also contains a brief discussion of experimental verification.

3.0 LIFE PREDICTION

The life-prediction methods discussed in this paper combine experimentally- and analytically-obtained information. Vibratory strain measurements from engine testing provide data from discrete points on operating turbine blades. Analysis extends this data over the entire blade to quantify the total stress or strain environment. Statistical methods are then employed to furnish high-cycle-fatigue life estimates.

3.1 Information Sources

3.1.1 Steady-State Stress Analysis

Steady-state stress analyses were used to define centrifugal and thermal stresses in the blade. In practice, this is probably as reliable as experimental determination, since accurate steady-state strain-gauge measurements in the thermal environment of the engine are difficult to obtain. For this study, steady-state stress predictions are obtained from the finite-element model shown in Figure 1. This model was intended to be used for both static and vibratory stresses, thus a fine grid was used both at the root and at the tip where peak steady-state or vibratory strains were expected. Figure 2 depicts some results of this analysis. The distribution of effective stress on both sides of the blade is shown for the steady-state conditions under which life is to be predicted.

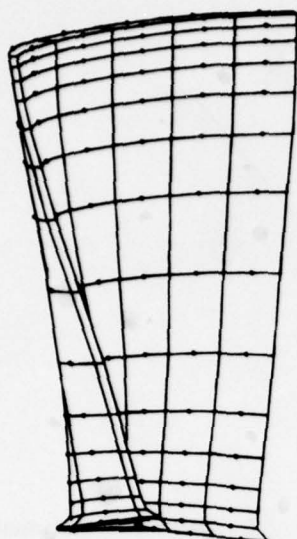


Figure 1. Turbine Blade Finite-Element Model.

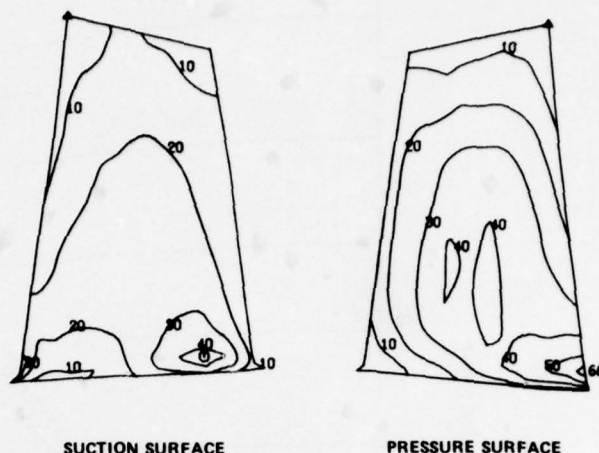


Figure 2. Turbine Blade Steady-State Effective Stress, kN/cm².

3.1.2 Vibration Analysis

The finite-element model of Figure 1 was also used for vibration analysis of the blade, utilizing the transformation methods discussed in the Appendix to reduce the number of degrees-of-freedom. Figure 3 is a Campbell diagram showing the predicted frequencies of vibration, together with the 35th order excitation line. In the engine tests an excitation was observed at 35E due to stator passage, accounting for the dominant blade vibrations observed slightly above 100-percent speed. Vibration analysis identified these dominant vibrations as being the seventh natural frequency occurring near 25 KHZ, for which the normalized mode shape is shown in Figure 4. Excitation of the first mode near 100-percent speed (5E) and of the sixth mode at approximately 90-percent speed (35E) was also observed. However, since the measured amplitudes of these modes were low, only the dominant seventh mode response is considered in the following discussion.

3.1.3 Vibration Test Data

Strain gauges were employed to monitor blade vibration frequency and amplitude during engine operation, with data transmitted continuously to magnetic-tape recording equipment through a slip-ring system. Practical limitations (e.g., cost, test duration, and slip-ring capacity) require selective placement of relatively few strain gauges, to obtain a maximum of information with respect to anticipated vibration modes. These techniques for obtaining turbine blade vibration data in an operating environment are widely used in the gas turbine-engine industry.

Figure 5 identifies the strain-gauge locations employed for the engine test of a turbine-blade system. These locations were selected to provide information from as many vibratory modes as possible during the test cycle. Selection of gauge locations is necessarily a compromise, since it is not known with certainty prior to testing which modes will be excited or produce the highest strains.

During the engine testing, nine strain gauges produced usable data. For each gauge, the dominant resonance was observed at six different points in time, corresponding to various engine conditions near 100-percent speed.

The major contributor to the vibration environment was a resonance around 25 KHZ. As indicated in the spectral analyzer photograph shown in Figure 6, the blade response during resonance was reasonably pure, with little contribution from other frequencies. Strain gauges located on the turbine disk measured no vibratory strain in this particular mode, and it was concluded that coupling through the disk could be neglected. This permitted the use of an analysis model that did not include disk details. The analytically predicted frequency of vibration for the mode (Figure 3) correlated well with the measured engine frequency. The holography testing provided good correlation with analytical predictions for the lower modes, as discussed in the Appendix.

3.1.4 Combining Analytical and Experimental Vibration Data

The relative-strain distribution in the vibration mode of interest may be determined from a free-vibration analysis by applying the displacements of the normalized-mode shape to the structural model. The strain levels in an operating blade may then be estimated by

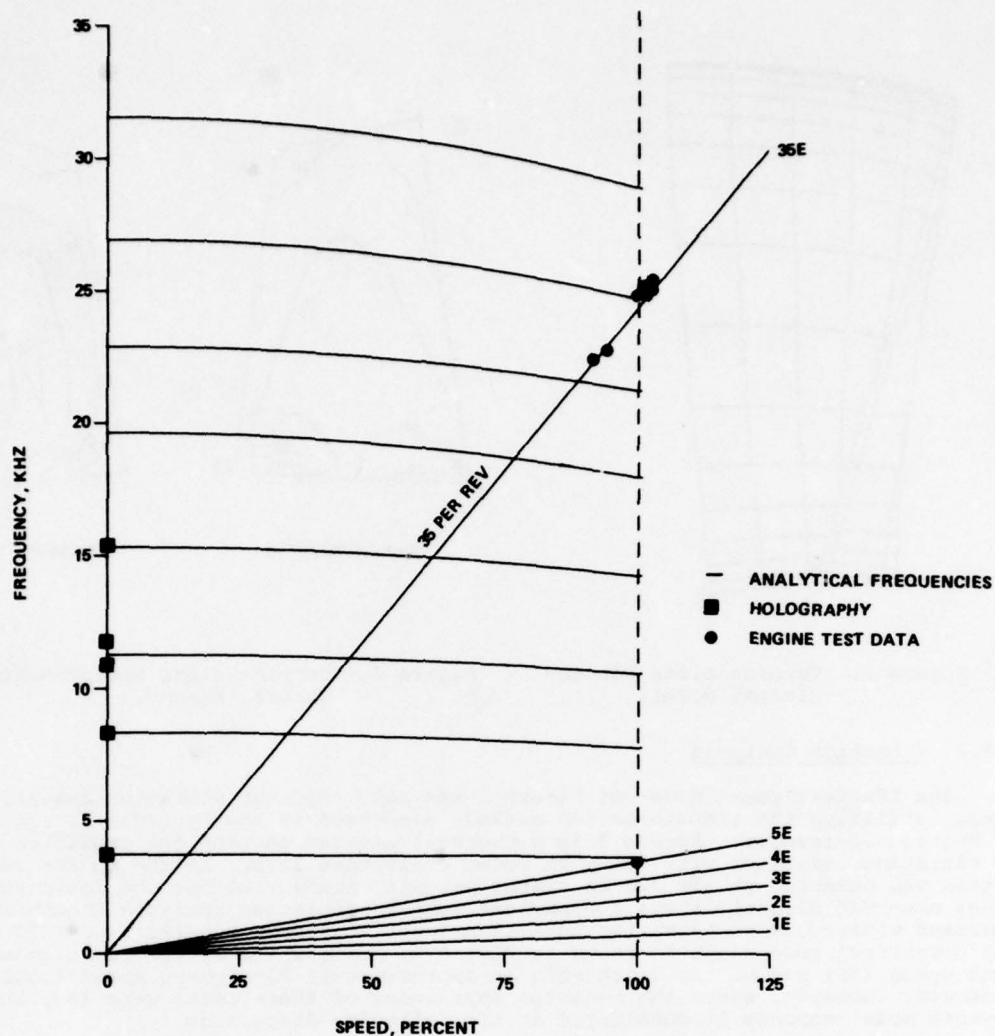


Figure 3. Campbell Diagram Comparing Measured and Predicted Frequencies.

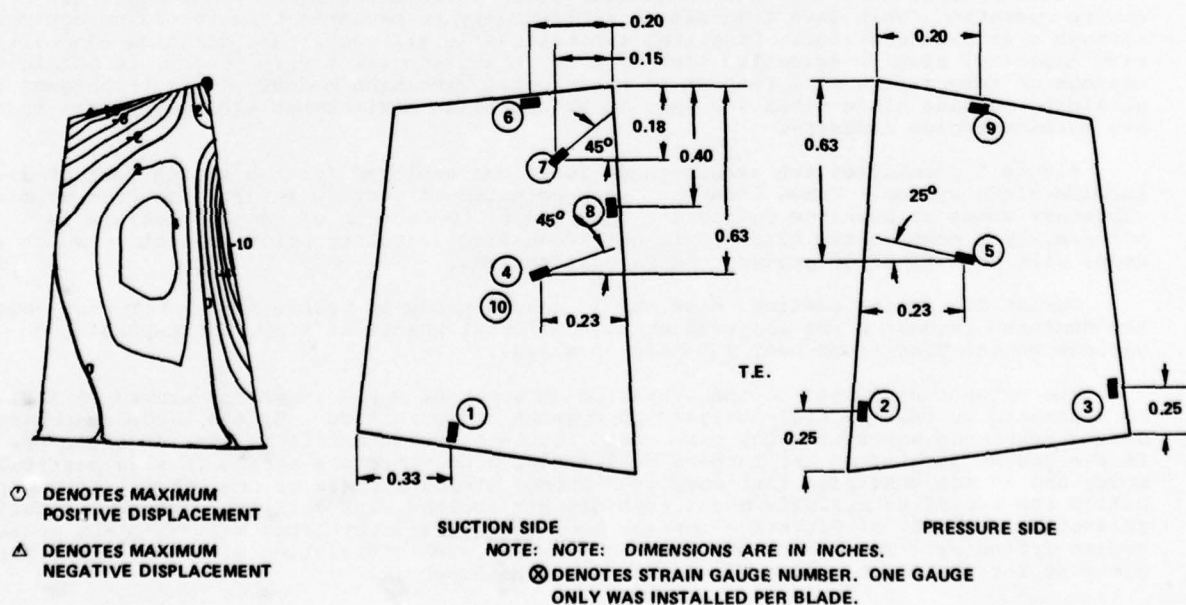


Figure 4. Normalized Mode Shape of Mode 7 for the Turbine Blade.

Figure 5. Typical Turbine Blade Strain Gauge Installation.

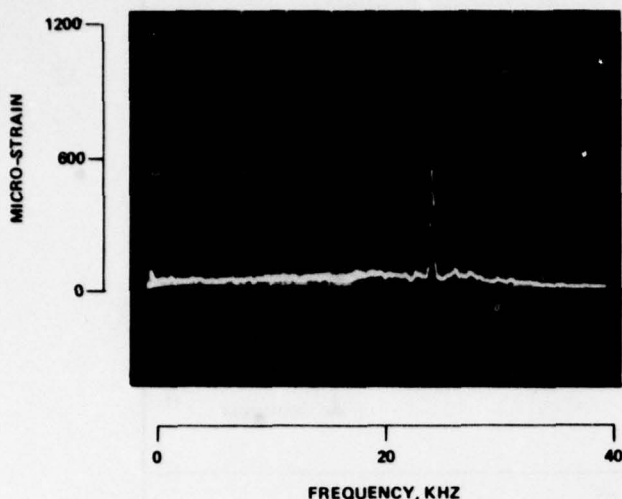


Figure 6. Spectral Analyzer Photo of Strain Versus Frequency for Strain Gauge 5.

using the engine-test data to assign a magnitude to the analytical strain distributions. In order to do this, strain values (from the predicted normalized distribution) consistent with the strain-gauge measurements were computed. This procedure involved the use of the finite-element output processing program to evaluate the strain field in the region of the gauge, to transform the strain field to correspond with the gauge orientation, and to average the strain over the region covered by the gauge.

The analytical strain distribution was then scaled to obtain a strain field over the whole blade surface consistent with a particular strain-gauge measurement. Having six strain measurements and a predicted strain distribution for each of nine gauges, it was possible to calculate a set of 54 scaling factors. Ideally, the 54 scale factors would have been identical, providing a simple factor

by which one could multiply normalized-strain predictions to obtain an estimate of actual-strain conditions. In reality, the factors reflect variations in conditions affecting the strength of resonance, and thus are not equal.

The variation in scaling factors for the nine gauges and six time points reflects several things, viz:

- (a) Blade-to-blade variations in dimensions, material properties, temperatures, loading, damping, etc.
- (b) Variations in engine conditions and excitation levels in the operating range, including acceleration rates, pressures, temperatures, etc.
- (c) Gauge position and wiring routing influences.

Assuming that the scale factors, like the strains, could be considered normally distributed, values of the mean and variance were calculated. Scaling of the normalized-mode vibratory strains by these values furnished predicted mean- and standard-deviation data which could be compared with the values obtained from strain measurements. Figure 7 compares the range of vibratory strains measured at resonance with the predicted mean and standard deviation for each gauge.

The maximum expected strain can be obtained by using a scale factor exceeding the mean by three standard deviations. This factor was used to scale the normalized-mode strain field, and the resultant principal strain on the turbine-blade pressure surface is plotted in Figure 8. The largest zero-to-peak value on the blade surface is predicted to be almost 1500 micro-strain, over four times the highest test-data point. This strain level was predicted for a location at which no gauge was applied and thus represented information not available directly from the test.

3.2 Fatigue Life Estimation

The Goodman-diagram approach is often used for the determination of fatigue lives. A modified Goodman diagram, such as that shown in Figure 9, may be constructed using various relations between the mean and alternating stresses. With no loss of generality in illustrating the overall method, the diagram used here assumes a straight line between the ultimate strength and the endurance limit for fully-reversed stress. In this example, the Goodman diagram is used to estimate the allowable alternating stress for a given cyclic life.

The data points shown on the diagram of Figure 9 have been plotted using alternating strain data from the engine test. The mean components were determined from the steady-state analysis. Figure 9 shows that the stresses at the strain-gauge locations are within the boundary representing an endurance limit for the material. The data points shown represent all the data available directly from the engine test. This data alone may not be sufficient for life prediction because of the difficulty in ascertaining that the minimum-life region in the blade is represented.

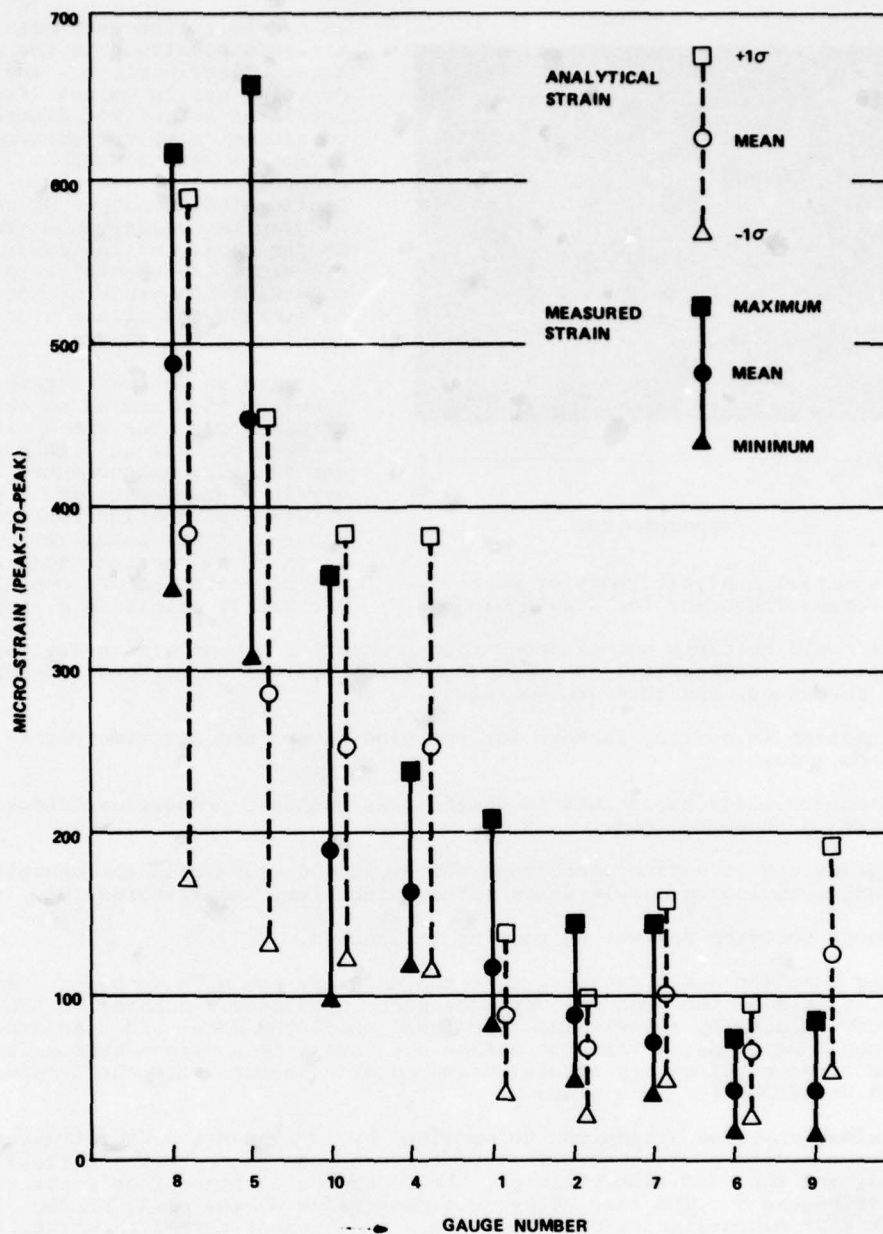


Figure 7. Ranges of Measured and Analytical Strain Data.

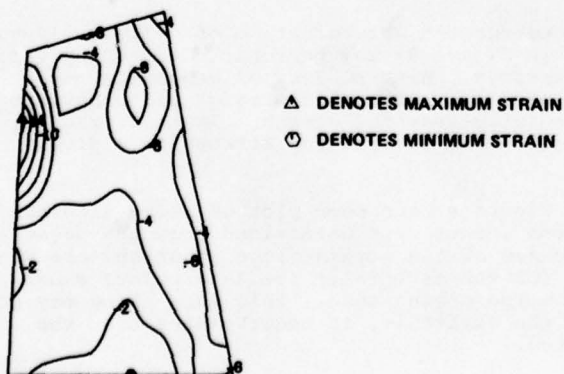


Figure 8. Vibratory Strain (Plus Three Standard Deviations) on Turbine Blade Pressure Surface. (Micro-Strain $\times 10^{-2}$).

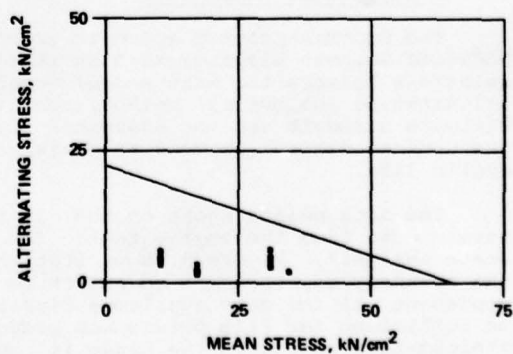


Figure 9. Modified Goodman Diagram for Peak Strains Measured in Engine Test.

Strain information over the entire blade is available through the use of the analytical strain distributions scaled using measured strains. Thus, the stress state at any point on the blade may be represented on the Goodman diagram. Figure 10 presents a Goodman diagram with stresses determined from the scaled analytical solution. The points shown correspond to the stresses at the nodes of the finite-element model. Using the finite-element output-processing program, values of alternating stresses were obtained as the differences between the Von Mises effective stresses at the nodes computed from the combined vibratory and mean stresses and the mean stresses alone. The diagram of Figure 10 shows that the stresses at two points are outside the desired fatigue limit. These points are located in a region of high mean stress near the airfoil root. Thus, the expanded strain data indicates an area of potential failure not evident from the strain-gauge data alone.

The comparison of allowable stresses and predicted stresses to determine the acceptability of the design must take into account the statistical nature of the applied stress and the material properties. If the local probability-of-failure is defined as the probability that the vibratory stress at any location exceeds the allowable alternating stress, the maximum such value for a blade will be indicative of the probability-of-failure of the blade. Typical distributions of the stress and the material allowable stress are shown in Figure 11.

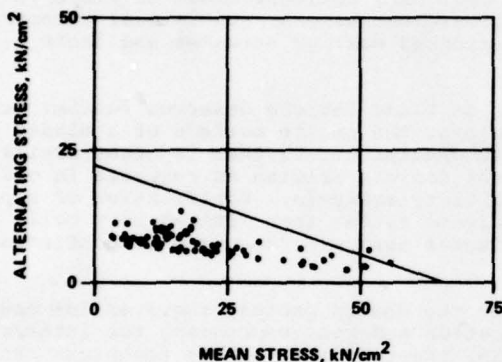


Figure 10. Modified Goodman Diagram Including Analytical Data.

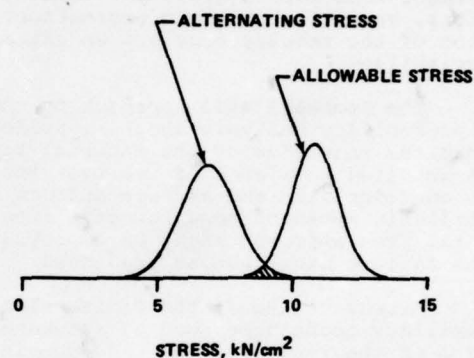


Figure 11. Typical Plot of Alternating Stress Distribution and Allowable Stress Distribution (Area of Overlap Exaggerated).

The probability that the stress exceeds the allowable value at resonance is then given by:

$$P_f = \int_0^{\infty} F_1(\sigma) P_2(\sigma) d\sigma$$

Where F_1 is the density function for the alternating blade stress at any point, and P_2 is the cumulative-probability function for the allowable stress, which depends on the number of cycles to failure. A computation of the probability-of-failure in 10^7 cycles at resonance for the airfoil yielded a value of 5×10^{-5} .

Since this probability is based on the assumption that the blade is at resonance, this value cannot be directly associated with failures in an engine unless the probability that a blade will be excited in the engine operating range is considered. This probability is a function of the resonant-frequency distribution of the blades and the frequency bandwidth of the resonant response.

For the turbine blade considered here, an analysis of the overlap of a band about the maximum excitation frequency (obtained from the response bandwidth) with the normal distribution of the resonant frequencies of the blades, indicated a potential for 2.1 percent of the blades encountering resonance in the operating range. The probability of a blade failure in 10^7 cycles depends on the probability-of-failure at resonance and the probability of resonance occurring in a blade. Since these probabilities are independent, their product is the probability of failure of a blade. This result is 1.05×10^{-6} for this blade.

The probability-of-failure of a turbine wheel due to a blade failure may be determined. The reliability of each blade, R_b , is:

$$R_b = 1 - P_{fb}$$

Where P_{fb} is the probability-of-failure for a blade. Then, assuming that the reliabilities for each blade are equal and independent, the overall reliability, P_w , of the n blades on the wheel is:

$$R_w = R_b^n.$$

The probability-of-failure of the wheel, P_f , is thus:

$$P_f = 1 - R_w.$$

For the turbine wheel considered here, $n = 36$, and the probability of a blade failure on the wheel is thus computed as 3.8×10^{-5} .

3.3 Concluding Remarks

The use of finite-element analyses in conjunction with test data for the prediction of turbine-blade fatigue lives has been described. The use of stress distributions from finite-element analyses provide a means for extending engine-test data to give a complete description of blade stresses. This may indicate potential failure points that are not evident from strain-gauge data alone. Since the test data reflects blade-to-blade variations, variation in blade excitation, and test-measurement errors, statistical interpretation of the results provides an estimate of the expected maximum stresses and their variability.

The probabilistic approach to the prediction of blade fatigue deserves further study. A probability analysis should consider conditions over the entire surface of a blade, and requires knowledge of the material fatigue data in greater detail than is often available.

A detailed knowledge of the test specimens and the failure origins is required in order to consider size and surface effects in the probability analysis. Verification of a probabilistic approach requires data from field experience rather than limited test cell data. The approach might be employed for a meaningful test program aimed at confirming the failure distribution predicted.

Extensive use of the finite-element method in the design process requires the use of auxiliary techniques such as automated mesh generation and post-processing for interpretation of the results. For life-prediction analysis, the conjugate-stress technique has proved valuable for computing improved surface stresses. Accurate computation of surface stresses, an inherent problem in current finite-element codes, requires awareness on the part of the user of assumptions employed, as well as continued theoretical development. For vibration analyses, the transformation method described in the appendix has proved efficient for large models.

REFERENCES

1. Alderson, R. G., Peterson, M. R., Stockton, R. J., and Tree, D. J., "Turbine Engine Components Stress Simulation Program-Final Report", AFAPL-TR-77-72, 1977.
2. Oden, J. T., and H. J. Brauchli, "On the Calculation of Consistent Stress Distributions in Finite Element Approximations," Int. J. for Numerical Methods in Engineering, Vol. 3, 1971.

ACKNOWLEDGEMENTS

Much of the development of the computer programs described herein was performed under Contract to the USAF Aero Propulsion Laboratory (Turbine Engine Stress Simulation Program, Contract Number F33615-74-C-2012). The authors would also like to acknowledge the contributions of Dr. J. W. Harvey to the initial development of the programs.

A.1 Vibration Solution Method

The cost of a vibration analysis using a detailed finite-element model may be prohibitive when a large number of degrees-of-freedom is involved. It is possible to reduce the number of degrees-of-freedom by considering only those displacements which significantly affect vibration in the modes of interest. Transformation methods exist for the implementation of this concept. The method employed here uses displacement patterns of the finite-element model as generalized coordinates. The finite-element mass and stiffness matrices are then transformed to these generalized coordinates, which reduces their size.

Consider a finite-element model composed of n substructures. The equilibrium equations for each substructure alone may be partitioned according to its internal nodes, and the nodes connecting it to other substructures, termed link nodes. For the j th substructure,

$$[K]_j \{r\}_j = \{R\}_j \quad (1)$$

or

$$\begin{bmatrix} K_{11} & K_{12} \\ K_{21} & K_{22} \end{bmatrix}_j \begin{Bmatrix} r_1 \\ r_2 \end{Bmatrix}_j = \begin{Bmatrix} R_1 \\ R_2 \end{Bmatrix}_j \quad (2)$$

where $[K]_j$ is the stiffness matrix, $\{r\}_j$ is the nodal displacement vector, $\{R\}_j$ is the load vector, and the subscripts 1 and 2 refer to internal and link nodes respectively.

Generalized coordinates are defined in the form of displacement modes of the finite-element model under selected load conditions. The generalized coordinates are of two types: internal generalized coordinates, generated with loads on internal nodes of each substructure with the link nodes fixed; and interface generalized coordinates, the displacements of the link nodes of the overall model due to loads applied to the link nodes. The following definitions are made:

- n = number of substructures
- M = number of generalized coordinates
- M_j = number of internal generalized coordinates in j th substructure
- M_b = number of interface generalized coordinates
- $\{\rho\}$ = vector of all generalized coordinates
- $\{\rho_j\}$ = vector of internal generalized coordinates for j th substructure
- $\{\rho_b\}$ = vector of interface generalized coordinates.

Then,

$$\{\rho\} = \begin{Bmatrix} \rho_1 \\ \vdots \\ \rho_j \\ \vdots \\ \rho_n \\ \vdots \\ \rho_b \end{Bmatrix}$$

The generalized coordinates are related to the nodal coordinates for the j th substructure by the coordinate transformation:

$$\begin{Bmatrix} r_1 \\ r_2 \end{Bmatrix}_j = [B_j] \{\rho\} \quad (3)$$

Since the internal generalized coordinates for each substructure are uncoupled from the internal generalized coordinates of the other substructures, the matrix $[B_j]$ contains many zero elements. This fact is exploited in the computation procedure.

The columns of matrix $[B_j]$ are displacement vectors generated by solving for selected static load conditions. The columns corresponding to $\{p_j\}$, the internal generalized coordinates for the j th substructure, are obtained by solving:

$$[K_{11}]_j \{r_1\}_j = \{R_1\}_j \quad (4)$$

for M_j load cases $\{R_1\}_j$. The columns of $[B_j]$ corresponding to $\{p_b\}$, the interface generalized coordinates, are the displacements due to selected loads on the interface nodes of the assembled substructures. Thus, these are obtained by solving for $\{r\}$ from:

$$\begin{bmatrix} K_{11} & K_{12} \\ K_{21} & K_{22} \end{bmatrix} \begin{Bmatrix} r_1 \\ r_2 \end{Bmatrix} = \begin{Bmatrix} 0 \\ R_2 \end{Bmatrix} \quad (5)$$

where Eq. (5) represents the equilibrium equation for the entire model (with the substructures combined) partitioned into internal and interface nodes, indicated by the subscripts 1 and 2, respectively.

Some freedom exists in determining the loads applied to the finite-element model to generate the generalized coordinates. Load distributions that yield displacement patterns that approximate the natural modes of the structure may be the most desirable, and provision has been made in the program for the input of load distributions, if desired. However, in practice it has proven satisfactory to use unit loads applied to points on the surface of the model, and to include loads corresponding to a rigid-body acceleration in each of the three global coordinate directions.

Once the generalized coordinate transformation matrix $[B_j]$ has been generated for each substructure, the finite-element mass and stiffness matrices for each substructure are transformed to generalized coordinates and superimposed to form the reduced system matrices $[\bar{M}]$ and $[\bar{K}]$.

$$[\bar{K}] = \sum_{j=1}^n [B_j]^T [K_j] [B_j] \quad (6)$$

$$[\bar{M}] = \sum_{j=1}^n [B_j]^T [M_j] [B_j] \quad (7)$$

where $[K_j]$ and $[M_j]$ are the stiffness and mass matrices for each substructure.

This linear coordinate transformation preserves the kinetic and potential energy of the system and leaves the eigenvalues of the system unchanged. The transformation reduces the size of the mass and stiffness matrices since the number of generalized coordinates in the transformed model is usually much smaller than the number of degrees-of-freedom in the original finite-element model.

The natural frequencies and vibration mode shapes of the complete structure are determined by solution of the eigenvalue problem:

$$[\bar{K}] - \omega^2 [\bar{M}] \{p\} = \{0\} \quad (8)$$

The eigenvalues of Eq. (8) determine the natural frequencies of the system and the eigenvectors are the natural modes in terms of the generalized coordinates. The eigenvalue problem is solved in program ISOVIB by using matrix iteration, based on the method of Turner (Ref. A-1). An alternate scheme employed to determine the frequencies in a specified range is a Sturm-sequence method with inverse iteration (Ref. A-2).

The eigenvectors are transformed to the finite-element coordinates by Eq. (3) to obtain the mode shapes in terms of displacements at the nodes of the finite-element model. These displacements are used to compute normalized stresses for each mode, employing the conjugate-stress solution of ISO3DQ.

A.2 Vibration Analysis Verification

Verification studies have demonstrated that ISOVIB provides accurate predictions of modal data. Reliable mode-shape definition is required for the life-prediction techniques under discussion. The verification studies have shown good agreement between experimental and predicted results for gas turbine-engine components as well as for relatively simple configurations. Two examples, discussed below, are typical of correlation studies that have been carried out for ISOVIB.

MacBain (Ref. A-3), reporting on the vibration of twisted cantilever plates, presented the mode shapes and natural frequencies obtained from holography testing and NASTRAN analysis. Table A-1 summarizes MacBain's frequency data for an aluminum plate, and compares it with the results of an ISOVIB analysis of the same configuration. Agreement between ISOVIB and the holography results is within 4 percent for eight modes, and within 6 percent for modes 5 and 6.

Of greater importance to the present application is the agreement between experimental and test data for actual engine hardware. The first five vibration modes of an IN-100 turbine blade were identified by holography testing and compared with ISOVIB predictions. Table A-2 summarizes these results. The holograms are shown in Figure A-1, and the predicted mode shapes appear in Figure A-2. Frequency and mode-shape correlation is quite good for modes 1, 2, and 4. Frequency agreement is within 3 percent, and experimental-mode shapes have been reproduced analytically. The predicted Mode 3 lies between the measured Modes 3A and 3B, which may not be distinct modes.

TABLE A-1. NATURAL FREQUENCIES FOR TWISTED CANTILEVER PLATE (ZERO RPM).

Mode	Frequency (Hz)			Notes
	From Ref. 1			
	Test	Nastran		
1	59	60	60	Angle of twist = 30 deg.
2	332	340	336	Plate length = 7 inches
3	479	504	494	Plate width = 3 inches
4	1006	998	1010	Plate thickness = 0.090 in.
5	1337	1427	1413	Poisson's ratio = 0.3
6	1743	1543	1844	Mass density = 2.587 X
7	2000	2020	2078	10^{-4} lb-sec ² /in. ⁴
8	2149	2248	2210	
9	2372	2275	2376	
10	2929	2912	2906	

TABLE A-2. TURBINE BLADE NATURAL FREQUENCIES.

Mode	Frequency (Hz)	
	Test	ISOVIB
1	3,635	3,727
2	8,405	8,338
3A	10,885	11,276
3B	11,668	
4	15,415	15,342



MODE 1
3635 HZ



MODE 2
8405 HZ



MODE 3A
10885 HZ



MODE 3B
11668 HZ



MODE 4
15415 HZ

Figure A-1. Turbine Blade Holography Test Results.

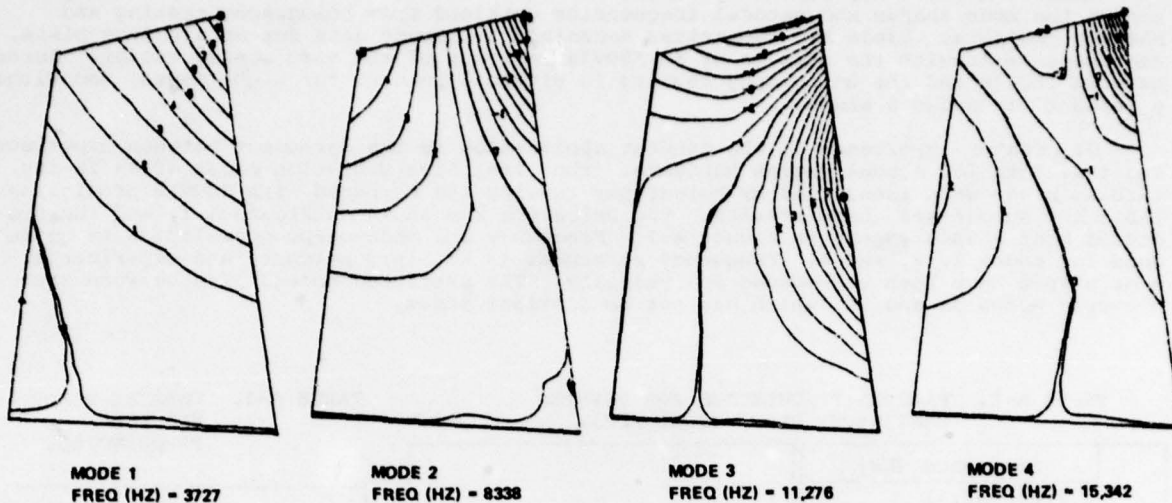


Figure A-2. Turbine Blade Normal Mode Shapes.

These two examples were obtained using relatively simple finite-element models, having a degree of complexity similar to that shown in Figure 1. It can be concluded that ISOVIB, together with the model used in the present study, provides sufficient accuracy for determination of mode shapes and natural frequencies.

In general, simple models will suffice to analyze the vibratory characteristics of solid blades. For more complex configurations, correspondingly more detailed models may be required.

A.3 References

- A-1. Rehfield, L. W., "Higher Vibration Modes by Matrix Iteration," J. Aircraft, Vol. 9, No. 7, July 1972.
- A-2. Gupta, K. K., "Eigenproblem Solution by a Combined Sturm Sequence and Inverse Iteration Technique," Int. J. Num. Meth. Engng, Vol. 7, 1973.
- A-3. MacBain, J. C., "Vibratory Behavior of Twisted Cantilever Plates," J. Aircraft, Vol. 12, No. 6, April 1975.

DISCUSSION

P.S.Kuo, US

I have two questions. 1. Could you explain a little further to us concerning your Campbell diagrams which show the frequency versus rpm's. The frequency is dropping, especially at high modes. Is this due to temperature effect or negative differential stiffness?

Author's Reply

The frequencies show a decrease with increasing rpm because the temperature was increased with rpm and the effect of temperature on frequency is greater than the centrifugal stiffening effect in this blade.

P.S.Kuo, US

Do you feel that in the first few modes where maybe stiffening effect is offset by temperature effect, causes it to come out fairly flat. However, in higher modes where this temperature effect is more predominant, that is why you get negative decreasing frequency.

Author's Reply

Yes, that seems to be the case.

P.S.Kuo, US

My second question, however, relates to earlier presentations where many foreign firms (French and German) have very sophisticated evaluations in photoelastics as well as other methods to predict fatigue life. Especially near the boundary where they use very careful evaluation of fringes and boundary stress concentrations. In turbine analysis you were considering fixed boundary conditions and used it for fatigue predictions. How do you feel this method compares to these more sophisticated techniques? Would you comment for us please?

Author's Reply

Here, the finite element method is used as a basis for the analysis. Of course, it has the capability for accurate detailed analysis of the stresses at blade roots but this region was not emphasized in this analysis. A comparison of finite element and photoelastic methods would require the consideration of cost, accuracy and many other factors that could not be adequately covered now. In comparison with other numerical methods, the finite element method has the advantage of generality, but the generation of finite element models has been costly in the past. The use of computer generated models has alleviated this and lead to more use of the finite element method, especially in preliminary design.

P.S.Kuo, US

If, I understand correctly, the approach you are taking now is more for initial design evaluation instead of a precisely sophisticated life prediction in which you need a very careful understanding of boundary stress concentration.

Author's Reply

This analysis was not used for final life prediction of the blade. The analysis presented should be viewed as an example of a technique that we have been studying.

P.S.Kuo, US

By the way, were you considering multiple constraint conditions simulating elastic boundary between the disk and blade or just using absolutely no need of boundary simulation?

Author's Reply

This analysis assumed a rigid, fixed boundary with the disk. This is often adequate for a blade integral with the wheel, as is the case here. However, for a more detailed analysis, it often is necessary to represent the effect of the blade attachment or disk. This may be done in several ways, one of which was used in the analysis presented in your paper.

R.L.McKnight, US

Did you go back, after the fact and explain the difference between your analytical predictions and the strain gage results.

Author's Reply

The sources of any differences could not be determined from the data available at the time.

R.D.McKenzie, UK

Your first slide showed the finite element mesh employed. Why was this mesh refined at the blade tip as well as at the root?

Author's Reply

For the steady state analysis, refinement of the mesh at the tip is not necessary. However, the model was used for both steady state and vibration analysis. Since tip bending was expected in some vibration modes, a refined mesh was used at the tip.

A.F.Storace, US

The transformation you talked about, was that a Guyan reduction sort of approach?

Author's Reply

No, it is not Guyan reduction. We generate generalized coordinates by applying loads to the model and computing the displacement patterns. The mass and stiffness matrices are transformed to these generalized coordinates.

A.F.Storace, US

It sounds a little bit like the Guyan reduction formulation which has problems with higher modes.

Author's Reply

By way of definition, Guyan reduction is a coordinate transformation of the mass and stiffness matrices using the static substructuring transformation. It is exact for static problems, in which it amounts to just an elimination of equations from the system, but it is approximate for dynamic problems. The procedure used here is different in that the generalized coordinates are not those of the Guyan reduction. The technique used here is more like a Rayleigh-Ritz analysis, where the Ritz functions are vectors of nodal displacements describing the deformed shape of the structure. The accuracy of prediction of the higher modes depends on the generalized coordinates and the higher modes may be less accurate than the lower modes. This is a limitation of most numerical methods. It has not been a practical limitation, since the higher modes are usually of less interest.

C.C.Chamis, US

Are you generating the influence coefficients?

Author's Reply

Yes.

C.C.Chamis, US

That takes a lot of time.

Author's Reply

They are generated simultaneously from static solutions. The transformation allows the model to be reduced to a size allowing an eigenvalue or dynamics solution within computer core storage. The generation of the generalized coordinates requires out-of-core matrix techniques similar to those used in a static solution. This computer time must be compared to that required for an out-of-core dynamic solution using the unreduced equations. The technique used here is usually more efficient than a dynamic solution on the unreduced model.

C.C.Chamis, US

You make an approximate assessment of where you want to apply unit loads for calculating deflections.

Author's Reply

Yes, although for many types of models the selection of loads is automated. For blade models, the selection emphasizes the use of loads normal to the blade surface to represent the transverse motion of the blade rather than the less important in-plane and breathing motions.

CALCUL DE CONCENTRATIONS DE CONTRAINTES DANS LES ALVÉOLES DE DISQUES*

par Madeleine CHAUDONNERET

*Office National d'Etudes et de Recherches Aéronautiques (ONERA)
92320 Châtillon (France)*

Résumé

La présence d'entailles dans une structure chargée, telles que les alvéoles dans les disques de turbines, est la cause de concentration de contraintes conduisant à des déformations élastiques et plastiques importantes ; de plus, les conditions de fonctionnement de la turbine comprennent des températures assez élevées pour provoquer des déformations viscoplastiques. En élasticité, on propose une comparaison avec la méthode des éléments finis appliquée à une section de la turbine. Une extension de cette méthode est entreprise pour résoudre les problèmes viscoplastiques par un procédé de linéarisation pas à pas dans le temps, le comportement du matériau étant représenté par des lois de comportement viscoplastique. Cette méthode est utilisée en particulier pour l'étude du comportement viscoplastique d'une plaque entaillée soumise à des essais de traction, et les résultats obtenus de cette manière sont comparés à ceux fournis par les essais ; cette comparaison montre un bon accord.

CALCULATION OF STRESS CONCENTRATIONS IN DISC ALVEOLES

Summary

The presence of notches in a loaded structure, such as alveoles in a turbine disc, is the cause of stress concentrations leading to important elastic and plastic deformations ; moreover, the turbine operating conditions involve temperatures high enough to provoke viscoplastic deformations. Such stress concentrations, and their evolution in time, are accounted for by the integral equation method. In elasticity, a comparison is proposed with the finite element method concerning a section of the turbine disc. An extension is undertaken of this method to solve viscoplasticity problems by a process of time-step linearization, the behaviour of the material being represented by viscoplastic constitutive laws. This method is used in particular to study the viscoplastic behaviour of a notched plate subjected to tensile tests, and the results obtained this way are compared with those provided by the tests, a comparison that shows a very good agreement.

1. - INTRODUCTION

La présence d'entailles, de coins, de zones de moindre résistance dans la plupart des structures réelles est la cause de concentrations de contrainte conduisant à des déformations élastiques et plastiques importantes et peuvent aller jusqu'à provoquer une rupture prématurée. Un calcul d'élasticité permet

*Ce mémoire a été présenté à la session 1978 de l'ATMA (Association Technique Maritime et Aéronautique) et est reproduit avec son aimable autorisation. Il sera publié dans le bulletin de cette Association avec la discussion à laquelle il a donné lieu au cours de la présentation.

la détermination d'un coefficient de concentration de contrainte dont la valeur ne dépend que de la géométrie de la structure envisagée, et en particulier de la forme de l'entaille. Dans la réalité l'importance de ces concentrations de contrainte est telle que, la plupart du temps, une zone de plasticité apparaît au voisinage de l'entaille ; le coefficient de concentration de contrainte dépend alors de l'intensité du chargement imposé mais demeure constant dans le temps. Par contre, lorsque le matériau obéit à un comportement viscoplastique, comme c'est en général le cas à haute température, ce coefficient varie au cours du temps. C'est ce qui se passe par exemple pour les disques des turbines à gaz des moteurs d'avions : en effet les performances de ces turbines sont conditionnées par les températures à leur entrée, et actuellement leurs conditions de fonctionnement conduisent à des températures suffisamment élevées pour provoquer des phénomènes de déformations viscoplastiques. De plus les technologies d'attache des aubes sur les disques de turbines confèrent à ceux-ci une structure alvéolée, provoquant ainsi une concentration de contrainte localisée en fond d'entaille, région où la viscoplasticité est donc particulièrement importante. Une méthode de calcul pour déterminer l'évolution de ce coefficient de concentration de contrainte apparaît donc nécessaire, et nous avons retenu la méthode des équations intégrales pour traiter ce problème.

2. - METHODE DES EQUATIONS INTEGRALES EN ELASTICITE

Cette méthode des équations intégrales est utilisée pour la résolution de problèmes d'élasticité linéaire depuis une dizaine d'années maintenant (aux U.S.A. à partir de 1967 avec Rizzo¹ et Cruse², en France avec Lachat depuis 1973)³. Rappelons que cette méthode est basée sur la relation suivante entre les valeurs des tensions t (vecteurs contrainte associés à la normale extérieure) et des déplacements u sur la frontière S du solide V considéré (obtenue par intégration de l'équation de Navier) :

$$c(x) \cdot u(x) = \int_V E(x, \xi) \cdot f(\xi) dv_\xi + \int_S E(x, \xi) \cdot t(\xi) ds_\xi - \int_S T(x, \xi) \cdot u(\xi) ds_\xi. \quad (1)$$

Les coefficients $E = (E_{ij})$ et $T = (T_{ij})$ dépendent des caractéristiques géométriques et élastiques du solide, $c = (c_{ij})$ de la géométrie du solide au voisinage du point x considéré ($c_{ij}(x) = \delta_{ij}$ pour un point intérieur, $c_{ij}(x) = \frac{1}{2} \delta_{ij}$ pour un point de S s'il y a continuité de la normale en ce point, f désigne les forces de volume).

La résolution numérique du problème se fait par discrétisation de cette équation intégrale (1) : ainsi dans le cadre de l'étude bidimensionnelle que nous avons effectuée, la frontière S a été approximée par une suite de segments de droites sur chacun desquels une variation linéaire des variables t et u a été imposée, ce qui permet alors d'écrire la relation (1) en chaque nœud de la discrétisation et conduit au système suivant :

$$[\alpha] \{u\} + [\beta] \{t\} = [\gamma] \{f\}$$

Les matrices $[\alpha]$, $[\beta]$ et $[\gamma]$ sont fonctions des coefficients E et T . Le second membre dépend de plus des forces de volumes (donnée du problème) et peut donc être calculé sans difficulté par intégration sur le volume V . Les vecteurs $\{t\}$ et $\{u\}$ sont respectivement constitués des composantes des vecteurs contrainte et déplacement aux nœuds de la discrétisation. Si le problème est bien posé, en chacun de ces nœuds, et pour chaque composante, l'une de ces valeurs t_i ou u_i est imposée par les conditions aux limites et le terme correspondant est passé au second membre, si bien que nous obtenons un système de $2n$ équations à $2n$ inconnues (n étant le nombre de points de discrétisation de S) :

$$[A] \{x\} = \{B\} \quad (2)$$

le vecteur $\{x\}$ est constitué des inconnues du problème, lesquelles sont donc déterminées après inversion de la matrice $[A]$.

Dans la pratique, l'établissement de ce système présente deux types de difficultés que nous voudrions aborder ici :

— la première est due à l'expression des coefficients E et T , expression donnée ci-dessous pour le cas bidimensionnel et qui présente des singularités en $\log r$ ou $1/r$ (r représentant la distance du point x pour lequel est écrite l'équation (1) au point courant d'intégration ξ)

$$E_{ij}(x, \xi) = \frac{-1}{4\pi(a + \mu)} [(a + 2\mu) \delta_{ij} \log r - a \partial_i r \partial_j r]$$

$$T_{ij}(x, \xi) = \frac{-1}{4\pi(a + \mu)r} \left[\frac{\partial r}{\partial n} (2\mu \delta_{ij} + 4a \partial_i r \partial_j r) + 2\mu (n_i \partial_j r - n_j \partial_i r) \right]$$

($a = \lambda + \mu$ en déformations planes, $a = \mu(3\lambda + 2\mu)/(\lambda + 2\mu)$ en contraintes planes.

Pour rendre compte de façon satisfaisante de ces singularités, les intégrations relatives à ces coefficients ont été effectuées analytiquement sur chaque segment de la discrétisation.

— d'autre part la formulation par équations intégrales utilise pour variable la tension t , et il peut exister des nœuds où celle-ci ne peut-être définie de façon unique (ce qui se produit par exemple dans le cas d'une discontinuité du vecteur normal (problème du coin)). Nous proposons de résoudre ce problème en considérant un tel point comme un point double : $O = (x, x')$ (fig. 1) ; x est supposé appartenir au segment S , x' au segment S' et le vecteur contrainte, resp. t et t' en chacun de ces points, peut alors être défini de façon unique. L'introduction d'un point double se traduit par l'introduction

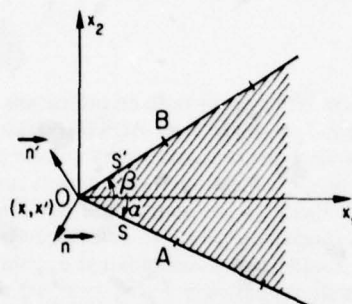


Fig. 1. — Notion de point double.

d'inconnues supplémentaires (deux en bidimensionnel), tandis que le nombre d'équations intégrales qui peuvent être écrites demeure inchangé (x et x' étant confondus, l'équation intégrale écrite en x est identique à celle écrite en x'). Il faut donc, pour obtenir un système d'équations non singulier, introduire d'autres relations entre vecteurs contrainte et déplacement (deux pour chaque point double). Le plus simple est d'écrire la continuité du vecteur déplacement au point considéré.

$$u_i(x) = u_i(x'), \quad i = 1, 2. \quad (3)$$

De telles équations ne sont évidemment valables que dans la mesure où u_i est une inconnue du problème en l'un au moins des points x et x' . S'il n'en est pas ainsi, il faut chercher d'autres équations (une ou deux suivant le type de conditions aux limites)⁴.

Un premier type d'équations peut être obtenu en écrivant la symétrie du tenseur des contraintes. En effet les vecteurs contraintes t et t' sont reliés au tenseur des contraintes σ par les relations ($\sigma(x) = \sigma(x')$).

$$t = \sigma n \quad t' = \sigma n'$$

Ces équations peuvent être considérées comme constituant un système dont les inconnues sont les quatre composantes du tenseur des contraintes. Le système peut-être résolu et la symétrie du tenseur des contraintes se traduit par la relation suivante :

$$n'_1 t_1 - n_1 t'_1 = n_2 t'_2 - n'_2 t_2$$

L'établissement de la seconde équation nécessaire est basée sur la continuité du tenseur des déformations ($\epsilon(x) = \epsilon(x')$). Utilisant le fait que la trace du tenseur des déformations est un invariant, nous pouvons en effet écrire :

$$\begin{aligned} t_1 \sin \alpha + t'_1 \sin \alpha - t_2 \cos \beta - t'_2 \cos \beta = & -\frac{2\mu}{h_A} \cos \alpha u_1(A) + 2\mu \left(\frac{\cos \alpha}{h_A} - \frac{\cos \beta}{h_B} \right) u_1(0) \\ & + \frac{2\mu}{h_B} \cos \beta u_1(B) - \frac{2\mu}{h_A} \sin \alpha u_2(A) + 2\mu \left(\frac{\sin \alpha}{h_A} - \frac{\sin \beta}{h_B} \right) u_2(0) + \frac{2\mu}{h_B} \sin \beta u_2(B) \end{aligned} \quad (5)$$

Ces équations (3), (4) et (5), permettent de résoudre, par la méthode des équations intégrales, tout type de problème, quelles que soient les conditions aux limites imposées.

Signalons enfin qu'une fois la "résolution sur le contour" effectuée, le tenseur des contraintes peut être calculé en tout point du solide. En effet les lois de l'élasticité et l'équation intégrale (1) permettent d'écrire la nouvelle équation intégrale ci-dessous :

$$\sigma(x) = \int_V D(x, \xi) \cdot f(\xi) dv_\xi + \int_S D(x, \xi) \cdot t(\xi) ds_\xi - \int_S S(x, \xi) \cdot u(\xi) ds_\xi \quad (6)$$

dans laquelle D et S sont définis en bidimensionnel comme suit

$$D_{ijh}(x, \xi) = \frac{1}{4\pi(a + \mu)r} [-2\mu\delta_{ij}\partial_h r + 2\mu\delta_{ih}\partial_j r + 2\mu\delta_{jh}\partial_i r + 4a\partial_i r\partial_j r\partial_h r]$$

$$S_{ijh}(x, \xi) = \frac{-\mu}{\pi(a + \mu)r^2} \left\{ \frac{\partial r}{\partial n} [8a\partial_i r\partial_j r\partial_h r + 2\mu\delta_{ij}\partial_h r + (\mu - a)(\delta_{jh}\partial_i r + \delta_{ih}\partial_j r)] \right. \\ \left. + n_i[(\mu - a)\partial_j r\partial_h r - \mu\delta_{jh}] + n_j[(\mu - a)\partial_i r\partial_h r - \mu\delta_{ih}] \right. \\ \left. - n_h[2\mu\partial_i r\partial_j r + (a - 2\mu)\delta_{ij}] \right\}$$

Différents calculs ont été effectués et nous en présentons ci-après deux exemples. Le premier concerne une plaque en alliage léger AU4G soumise à des sollicitations biaxiales. Le schéma de la plaque ainsi que la discrétisation utilisée pour le calcul (par raison de symétrie seul un quart de plaque a été étudié) sont donnés sur la figure 2. Dans ce cas la position du point le plus sollicité en contrainte ainsi que l'importance de celle-ci varient suivant le rapport des forces imposées. Les courbes de la figure 3 permettent de suivre l'évolution le long de l'entaille de la composante $\sigma_{\theta\theta}$ du tenseur des contraintes pour trois valeurs différentes du rapport $k = F_2/F_1 = \sigma_2^*/\sigma_1^*$, et de comparer les résultats du calcul avec ceux donnés par une étude expérimentale effectuée à l'ONERA sur une machine d'essais de tractions biaxiale.

Avec le deuxième exemple nous proposons une confrontation des deux méthodes de calcul : méthode des équations intégrales et méthode des éléments finis. Elle est relative à une portion de disque de turbine de moteur d'avion dont les efforts appliqués sont ceux exercés par l'aube de turbine (contrainte normale le long de EF) et des efforts de liaison (contrainte radiale sur AC). Le maillage utilisé pour les équations intégrales correspond aux nœuds du contour du maillage par éléments finis (figure 4). Les résultats présentés sur la figure 5 indiquent une excellente corrélation entre les deux méthodes.

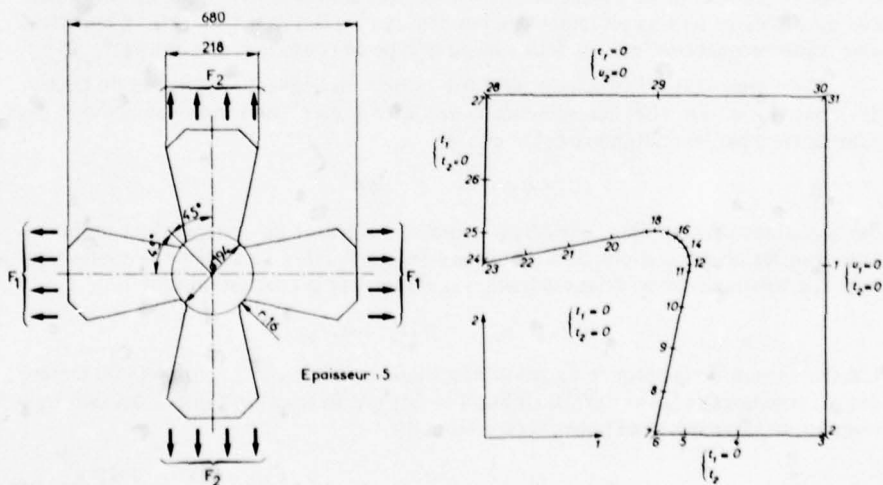


Fig. 2. — Schéma et discrétisation de la plaque entaillée.

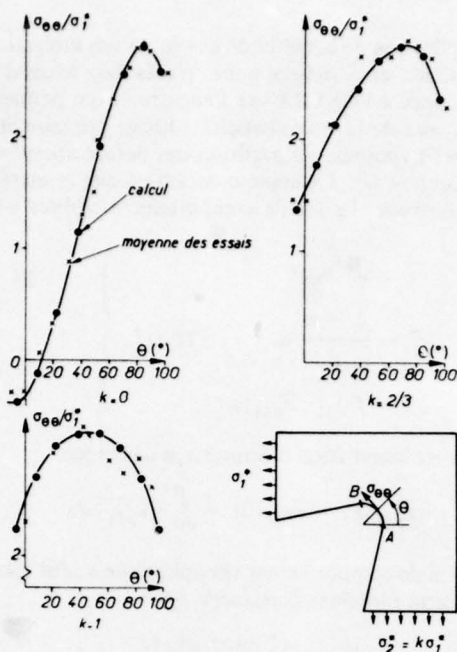


Fig. 3. — Evolution de la contrainte normale principale $\sigma_{\theta\theta}$ le long de l'arc AB
 — calcul par la méthode des équations intégrales
 x moyenne des essais

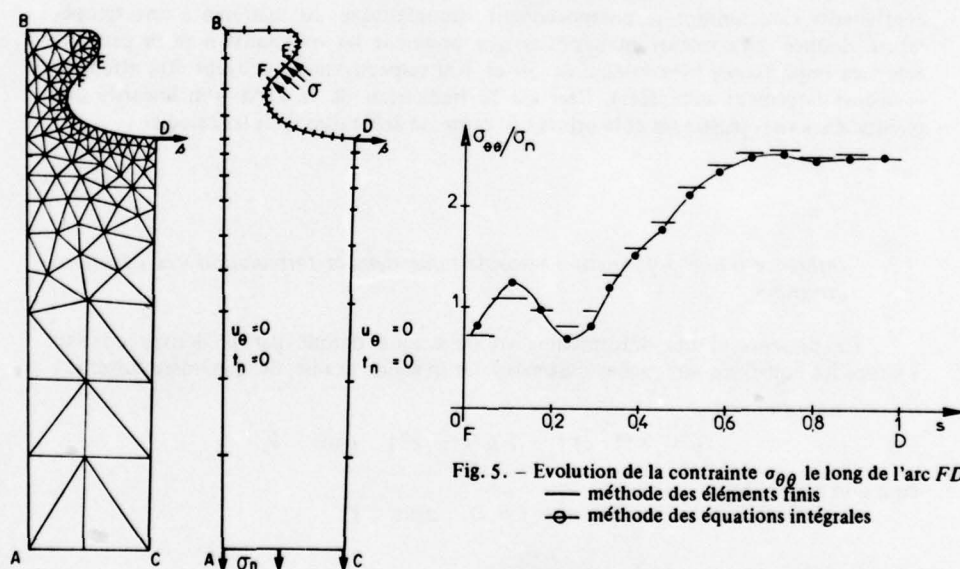


Fig. 4. — Maillage de la portion de disque utilisé pour la méthode des éléments finis et la méthode des équations intégrales

Pour tous les cas que nous avons étudiés, les résultats obtenus sont très satisfaisants ; les cas de concentration de contrainte sont, en particulier, très bien résolus ; la discrétisation linéaire par segments, utilisée pour les vecteurs contrainte, permet de rendre compte des fortes évolutions de ces quantités avec une meilleure précision que par la méthode des éléments finis pour une même finesse de maillage. De plus, à cause du faible nombre d'inconnues, la résolution d'un problème s'effectue en un temps de calcul très court.

3.1. – Loi de comportement⁵

Pour étudier l'application de la méthode des équations intégrales à la résolution de problèmes de viscoplasticité, nous nous sommes placés dans le cas d'une loi de comportement qui a été développée à l'ONERA par Lemaitre et qui permet de rendre compte des phénomènes principaux de la viscoplasticité : fluage primaire et secondaire relaxation, écrouissage. Outre l'hypothèse de partition des déformations, elle suppose que la déformation viscoplastique se fait à volume constant et que le matériau obéit à l'hypothèse de l'écrouissage isotrope. La loi de comportement utilisée sera alors du type :

$$\left. \begin{aligned} \dot{\epsilon} &= \dot{\epsilon}^e + \dot{\epsilon}^p \\ \dot{\epsilon}^e &= \frac{1+\nu}{E} \dot{\sigma} - \frac{\nu}{E} (\text{Tr } \sigma) \mathbf{1} \\ \dot{\epsilon}^p &= f(s_{11}, \tilde{e}_{p11}) s \end{aligned} \right\} \quad (7)$$

\tilde{e}_{p11} étant un paramètre de cumulation d'écrouissage défini par

$$\tilde{e}_{p11}(t) = \tilde{e}_{p11}(0) + \int_0^t |\dot{e}_{p11}| d\tau$$

Pour le calcul, la loi de comportement viscoplastique a été particularisée sous la forme d'un produit de deux fonctions puissances

$$\dot{\epsilon}^p = C^n \tilde{e}_{p11}^{-n/m} s_{11}^{n-1} / s$$

avec

$$C = \frac{1}{K} \left(\sqrt{\frac{3}{2}} \right)^{1+1/n+1/m}$$

(généralisation de la loi unidimensionnelle $\sigma = K \epsilon^{1/m} \dot{\epsilon}^{1/n}$) n est le coefficient de viscosité ; m , le coefficient d'écrouissage et K , le coefficient de résistance. Ces trois coefficients caractérisent le comportement viscoplastique du matériau à une température donnée. Les valeurs numériques que prennent les exposants n et m peuvent être très importantes (des valeurs de 50 et 100 respectivement peuvent être atteintes et même largement dépassées). Ceci est la traduction de la forte non linéarité des phénomènes viscoplastiques et la principale cause de difficultés dans les calculs.

3.2. – Influence d'une déformation viscoplastique dans la formulation des équations intégrales

La présence d'une déformation viscoplastique définie par sa dérivée conduit à écrire les équations auxquelles doit satisfaire le solide étudié, de la manière suivante : loi de comportement

$$\sigma = \lambda (\text{Tr } \dot{\epsilon}) \mathbf{1} + 2\mu (\dot{\epsilon} - \dot{\epsilon}^p) \quad \text{dans } V$$

équation d'équilibre

$$\text{div } \dot{\sigma} + \dot{f} = 0 \quad \text{dans } V$$

relation déformations – déplacements

$$\dot{\epsilon} = \frac{1}{2} [\text{grad } \dot{u} + (\text{grad } \dot{u})^t] \quad \text{dans } V$$

conditions aux limites

$$\begin{aligned} \dot{\sigma} n &= \dot{F} \quad \text{sur } S_\sigma \\ \dot{u} &= \dot{u}^d \quad \text{sur } S_u \end{aligned}$$

De la même façon qu'en élasticité on montre facilement que ce système d'équations est équivalent aux deux équations écrites ci-dessous :

$$(\lambda + \mu) \text{grad} (\text{div } \dot{u}) + \mu \Delta \dot{u} + (\dot{f} - 2\mu \text{div } \dot{\epsilon}^p) = 0 \quad \text{dans } V$$

$$\lambda (\text{div } \dot{u}) n + \mu [\text{grad } \dot{u} + (\text{grad } \dot{u})^t] n = \dot{F} + 2\mu \dot{\epsilon}^p \cdot n \quad \text{sur } S$$

La première de ces équations est en fait la dérivée de l'équation de Navier dans laquelle ont été introduites des forces de volume supplémentaires définies par

$$\dot{f}^P = -2\mu \operatorname{div} \dot{\epsilon}^P \quad (8)$$

Quant à la deuxième elle exprime les conditions aux limites en force du problème élastique correspondant aux forces de surface supplémentaires définies par

$$\dot{F}^P = 2\mu \dot{\epsilon}^P \cdot n$$

Ainsi, en ce qui concerne la résolution sur le contour, le calcul pourra être considéré à chaque instant, comme un calcul d'élasticité, la présence de phénomènes viscoplastiques se traduisant par l'introduction de forces de volume et de surface supplémentaires.

Notons que dans le cas particulier du bidimensionnel (hypothèse de déformations ou de contraintes planes), ces forces supplémentaires seront déterminées par :

$$\dot{f}^P = -(a - \mu) \operatorname{grad} (\operatorname{Tr} \dot{\epsilon}^P) - 2\mu \operatorname{div} \dot{\epsilon}^P \quad (9)$$

$$\dot{F}^P = (a - \mu) (\operatorname{Tr} \dot{\epsilon}^P) \cdot n + 2\mu \dot{\epsilon}^P \cdot n \quad (9b)$$

3.3. - Schéma général du calcul de viscoplasticité

Nous considérons à chaque instant t la dérivée par rapport au temps du système d'équations intégrales (2) soit :

$$[A] \{\dot{X}(t)\} = \{\dot{B}(t)\}$$

D'après ce qui précède $\{\dot{B}(t)\}$ peut-être considéré comme la somme de deux termes :

- l'un relatif aux données du problème sur la frontière (vecteurs contrainte et déplacement) qui pourra s'écrire sous la forme $[B_0] \{\dot{D}(t)\}$, $\dot{D}(t)$ étant la dérivée par rapport au temps de ces quantités données à l'instant considéré ;

- l'autre $\{\dot{C}(t)\}$ dû à la présence des forces de volume et de surface supplémentaires introduites par la viscoplasticité.

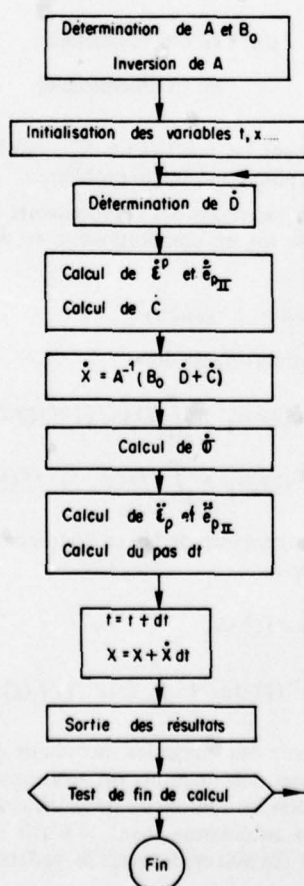


Fig. 6. - Schéma général du calcul de viscoplasticité au premier ordre.

La connaissance à l'instant t , et en tout point du domaine V , des tenseurs des contraintes σ et des déformations viscoplastiques ϵ^P permet de déterminer la vitesse de déformation viscoplastique en tout point et d'en déduire par intégration les valeurs des quantités $C(t)$ apparaissant au second membre du système (2). Le calcul de la variation du tenseur des contraintes peut ensuite être effectué en tout point de V comme indiqué ci-après, puis celui des dérivées secondes du paramètre de cumulation d'écroutissage et des composantes du tenseur des déformations viscoplastiques, ce qui permet de déterminer, comme nous le verrons plus loin, l'importance du pas dt à effectuer.

Enfin le passage de l'instant t à l'instant $t + dt$ se fait en utilisant des développements en série de Taylor. D'où l'organigramme de la figure 6 établi pour un calcul au premier ordre.

3.4. - Calcul de \dot{C} et de $\dot{\sigma}$

L'introduction, due à la viscoplasticité, de forces de volume et de surface supplémentaires conduit à ajouter au second membre des équations du système (2) la somme d'intégrales

$$\int_V E(x, \xi) \cdot \dot{f}^P(\xi) dv_\xi + \int_S E(x, \xi) \cdot \dot{F}^P(\xi) ds_\xi$$

\dot{f}^P et \dot{F}^P ont été définis précédemment par les relations (9) et (9b) ou (8) et (8b). \dot{f}^P est fonction des dérivées spatiales des composantes du tenseur des vitesses de déformations viscoplastiques dont la valeur n'est connue que point par point. Numériquement de telles dérivées ne peuvent être calculées de façon satisfaisante. Nous avons donc cherché à transformer cette intégrale de volume. Ceci est possible en utilisant le théorème de Green-Ostrogradsky qui nous conduit à écrire l'équation intégrale en déplacement sous la forme suivante.

$$\begin{aligned} cu(x) = & \int_S E(x, \xi) \cdot \dot{i}(\xi) ds_\xi - \int_S T(x, \xi) \cdot \dot{u}(\xi) ds_\xi \\ & - \int_V \text{grad}_\xi E(x, \xi) \cdot \dot{\sigma}^P(\xi) dv_\xi + \int_V E(x, \xi) \cdot \dot{f}(\xi) dv_\xi \quad (10) \end{aligned}$$

avec

$$\dot{\sigma}^P = (a - \mu) (\text{Tr } \dot{\epsilon}^P) \mathbf{1} + 2\mu \dot{\epsilon}^P \quad \text{en bidimensionnel,}$$

$$\dot{\sigma}^P = 2\mu \dot{\epsilon}^P \quad \text{en tridimensionnel.}$$

Les dérivées spatiales affectent maintenant les coefficients E_{ij} dont l'expression analytique est connue ; une telle dérivation ne pose donc aucun problème.

Enfin l'expression de $\dot{\sigma}$, en fonction des variations des déplacements et déformations viscoplastiques, s'obtient à partir de la loi de comportement et des relations déformations-déplacements

$$\dot{\sigma} = (a - \mu) \text{div } \dot{u} + \mu [\text{grad } \dot{u} + (\text{grad } \dot{u})^T] - \dot{\sigma}^P$$

l'équation intégrale relative au tenseur des contraintes sera donc

$$\begin{aligned} \dot{\sigma}(x) = & \int_S D(x, \xi) \cdot \dot{i}(\xi) ds_\xi - \int_S S(x, \xi) \cdot \dot{u}(\xi) ds_\xi + \int_V D(x, \xi) \cdot \dot{f}(\xi) dv_\xi \\ & + \int_V D(x, \xi) \cdot \dot{F}^P(\xi) ds_\xi + \int_V D(x, \xi) \cdot \dot{f}^P(\xi) dv_\xi - \dot{\sigma}^P \end{aligned}$$

Comme précédemment l'utilisation du théorème de Green Ostrogradsky permet de transformer l'intégrale de volume et d'écrire :

$$\begin{aligned} \dot{\sigma}(x) = & \int_S D(x, \xi) \cdot \dot{i}(\xi) ds_\xi - \int_S S(x, \xi) \cdot \dot{u}(\xi) ds_\xi \\ & + \int_V \text{grad}_\xi D(x, \xi) \cdot \dot{\sigma}^P(\xi) dv_\xi + \int_V D(x, \xi) \cdot \dot{f}(\xi) dv_\xi \quad (11) \end{aligned}$$

Les relations (10) et (11) font intervenir des intégrales de volume dépendantes de $\dot{\sigma}^P$ c'est-à-dire de la variation du tenseur des déformations viscoplastiques. Le calcul de telles intégrales nécessite une discrétisation de l'intérieur de la structure étudiée. Actuellement cette discrétisation est réalisée automatiquement, à partir de la discrétisation du contour, à l'aide de rectangles à l'intérieur desquels la variation de la dé-

formation viscoplastique $\dot{\epsilon}^p$ est supposée constante. Précisons que ces intégrales de volume n'affectent que des quantités dont la valeur a déjà été déterminée, les inconnues du problème demeurant sur la frontière du solide uniquement.

3.5. — Calcul du pas

La connaissance, à l'instant t , des inconnues du problème et de leur dérivée permet de déterminer leur valeur à l'instant $t + dt$ en utilisant un développement en série de Taylor limité au premier ordre

$$X(t + dt) = X(t) + \dot{X}(t) dt$$

Pour déterminer la valeur du pas dt nous utilisons une méthode de choix optimal, afin de garantir une bonne approximation de la loi utilisée, tout en choisissant une valeur de dt qui assure un compromis acceptable entre la précision souhaitée et un temps de calcul raisonnable. Ce choix est effectué sur la déformation viscoplastique cumulée $\tilde{\epsilon}_{p11}$ qui gouverne la forte non linéarité du problème. En utilisant pour ce coefficient un développement en série de Taylor au second ordre

$$\tilde{\epsilon}_{p11}(t + dt) = \tilde{\epsilon}_{p11}(t) + \dot{\tilde{\epsilon}}_{p11}(t) dt + \frac{\ddot{\tilde{\epsilon}}_{p11}(t)}{2} dt^2$$

Le pas dt est choisi pour rendre le terme $\ddot{\tilde{\epsilon}}_{p11} (dt^2/2)$ suffisamment faible devant $\dot{\tilde{\epsilon}}_{p11} dt$; dans ce cas le terme du troisième ordre et les suivants sont supposés négligeables. La convergence n'est assurée que de façon heuristique, la non influence des termes d'ordre supérieur pouvant ne pas toujours être vérifiée. Nous posons donc :

$$\left| \ddot{\tilde{\epsilon}}_{p11}(t) \frac{dt^2}{2} \right| \leq \eta \left| \dot{\tilde{\epsilon}}_{p11}(t) dt \right|$$

η étant le paramètre de précision choisi à l'avance, d'où

$$dt \leq 2 \eta \left| \frac{\dot{\tilde{\epsilon}}_{p11}(t)}{\ddot{\tilde{\epsilon}}_{p11}(t)} \right|$$

pour tout point du solide, ce qui conduit à choisir

$$dt = 2 \eta \min_{x \in V} \left| \frac{\dot{\tilde{\epsilon}}_{p11}(t)(x)}{\ddot{\tilde{\epsilon}}_{p11}(t)(x)} \right|$$

3.6. — Application

Un programme de calcul correspondant à la méthode que nous venons de décrire a été établi en bidimensionnel (hypothèse des contraintes planes ou des déformations planes). Il a, en particulier, été utilisé pour déterminer l'évolution des contraintes et déformations produites en tout point d'une plaque entaillée, dont le schéma est représenté sur la figure 7, et sollicitée dans le domaine viscoplastique. La présence dans cette plaque d'une entaille provoque une concentration de contrainte importante (en élasticité le rapport de la contrainte maximale, localisée en fond d'entaille, à la contrainte imposée "à l'infini" est ici de 2,5), ce qui provoque, dans cette région, des phénomènes viscoplastiques particulièrement importants.

Le matériau employé est l'alliage léger AU 2 GN, recuit pendant 24 h à 200 °C, matériau utilisé ici à la température de 180 °C. (A cette température le module de Young a pour valeur $E = 67000 \text{ MN/m}^2$ et le coefficient de Poisson $\nu = 0,3$). Des essais préliminaires de fluage et d'écrouissage relaxation sur éprouvettes unidimensionnelles ont permis de déterminer les coefficients caractéristiques du matériau, à la température considérée, pour la loi de Lemaitre, soit : $n = 20$, $m = 40$, $K = 520$ (unités : $\text{MN/m}^2, \text{s}$).

Des essais de traction sur plaques entaillées ont été effectués parallèlement. Au cours de ces essais, des mesures par jauges extensométriques à chaud ont permis de suivre l'évolution de la déformation en différents points de la plaque.

Nous présentons ici une confrontation des résultats obtenus par les essais d'une part, par le calcul limité au premier ordre d'autre part (calcul effectué avec l'hypothèse

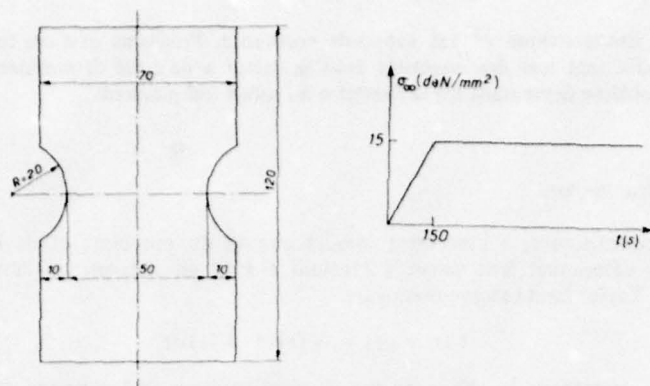


Fig. 7. - Schéma de la plaque entaillée et chargement imposé.

des contraintes planes), dans le cas d'un chargement en traction, imposé comme indiqué sur la figure 7 (écrouissage puis fluage). Sur la figure 8 est représentée la répartition, à un instant donné, de la déformation le long de l'axe Ox_1 de la plaque ; sur la figure 6, l'évolution au cours du temps de la déformation en différents points de cet axe. Nous pouvons remarquer la très bonne concordance entre les deux types de résultats, même lorsque les déformations sont importantes (elles atteignent 1 % au point de plus sollicité) et fortement non linéaires. Ces résultats nous permettent ainsi de confirmer à la fois la validité de la loi de comportement utilisée et celle de la méthode de calcul.

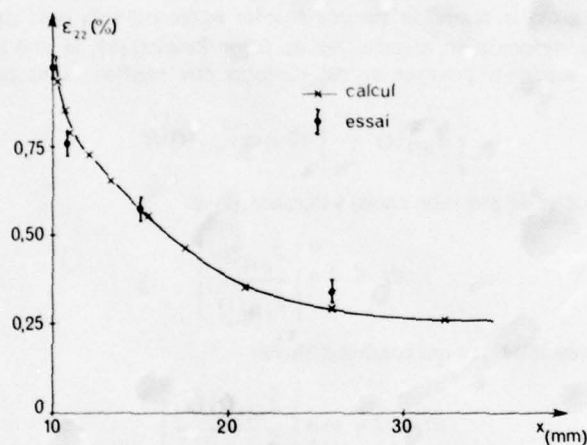
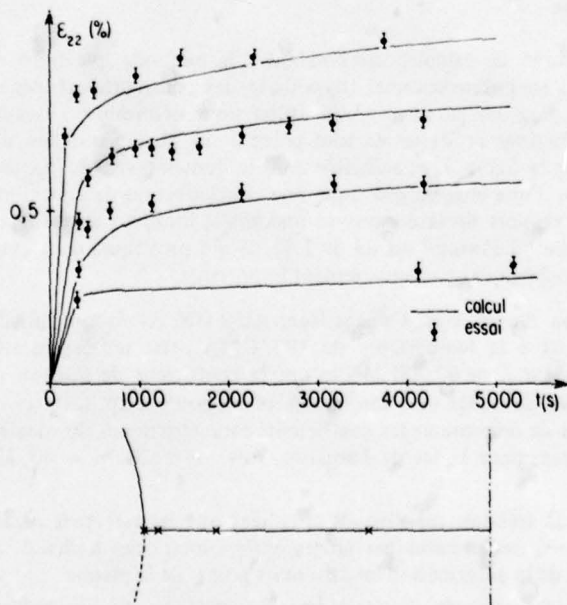
Fig. 8. - Répartition de la déformation ϵ_{22} le long de l'axe de symétrie ($t = 3800$ s).

Fig. 9. - Emplacement des jauges le long de l'axe de symétrie. Evolution de la déformation.

En ce qui concerne le calcul par la méthode des équations intégrales, il a été effectué pour un temps de maintien en fluage de 3 h, et a demandé, sur ordinateur IRIS 80, un temps de calcul de 60 mn ; 114 pas dans le temps ont été nécessaires pour traduire les 150 s d'écrouissage et 42 pas pour le fluage. Il est à noter, qu'arrivé à ce stade du fluage, les phénomènes viscoplastiques se stabilisent, et qu'en conséquence les pas deviennent importants (avantage de la méthode de choix du pas optimal décrite précédemment) ; la poursuite du calcul à ce niveau s'effectue alors rapidement. Un calcul au second ordre permettra de réduire ce temps de calcul, la même précision pouvant être obtenue par une intégration pas à pas beaucoup plus lâche.

Enfin il nous faut mentionner le faible nombre d'inconnues nécessaires à la résolution du problème : le contour de la plaque a été discrétisé à l'aide de 27 segments, conduisant ainsi à une matrice A , matrice du système à résoudre, de dimensions 54×54 ; le stockage de son inverse en mémoire centrale ne pose donc aucun problème.

4. - CONCLUSION

Les premiers résultats de calcul, portant sur un exemple, d'intérêt pratique (relatif au problème des fonds d'alvéoles de disques de turbine), et faisant intervenir à la fois une concentration de contrainte et des phénomènes de redistribution, ont été remarquablement recoupés par les résultats expérimentaux.

Par comparaison avec une méthode d'éléments finis, nous avons déjà noté la sensible amélioration apportée au calcul des contraintes. D'autre part, si une discrétisation de l'intérieur de la structure est certes nécessaire pour le calcul en viscoplasticité, elle ne requiert pas une grande précision puisque, dans notre cas, les intégrales de volume n'interviennent qu'au second membre du système à résoudre ; elles ne dépendent que de quantités déterminées à l'instant considéré du calcul et non pas des inconnues du problème. De plus, il reste que la résolution du problème ne s'effectue que sur le contour ; la matrice du système obtenu est par conséquent de dimensions très inférieures à la matrice de raideur correspondante calculée par la méthode des éléments finis. Puisque l'introduction de déformations viscoplastiques n'a, sur cette matrice, aucune influence, elle peut être inversée une seule fois au début de calcul, ses faibles dimensions ne posant, en général, pas de difficulté pour conserver son inverse en mémoire centrale, la résolution proprement dite se ramène donc à un nombre relativement faible d'opérations élémentaires.

Plusieurs améliorations de la méthode peuvent être envisagées. En particulier nous avons déjà remarqué qu'une méthode au second ordre serait avantageuse en ce qui concerne le temps de calcul ; le nombre d'opérations à effectuer pour chaque pas serait presque doublé, mais la représentation des différentes variables par série de Taylor très améliorée, et par conséquent le nombre de pas d'intégration pourra être très nettement diminué (dans un facteur supérieur à 2), sans diminuer pour autant la précision des résultats, ce qui finalement se traduira par une baisse sensible du temps de calcul. Pour ce qui concerne la discrétisation de l'intérieur de la structure étudiée, une discrétisation par triangles plutôt que par rectangles rendrait mieux compte de sa géométrie ; une variation linéaire de la déformation viscoplastique à l'intérieur de chacun de ces triangles est également à étudier. Par contre, compte tenu des autres approximations, la discrétisation de la frontière par des segments avec variation linéaire des inconnues semble suffisante.

L'extension de la méthode au cas tridimensionnel est également envisageable. Des difficultés sont prévisibles notamment au niveau des calculs d'intégrales mais les avantages relatifs à la diminution du nombre des inconnues par rapport à la méthode des éléments finis devraient être encore plus sensibles.

Signalons pour terminer que la méthode que nous venons de décrire peut encore être utilisée pour toute autre loi de comportement de type viscoplastique, y compris pour une loi faisant intervenir des paramètres d'écrouissage obéissant à des équations d'évolution supplémentaires : en utilisant une loi de ce type, développée à l'ONERA par Chaboche, nous avons pu traduire le comportement cyclique de structures⁶.

RÉFÉRENCES

1. RIZZO F. J., *An Integral Equation Approach to Boundary Value Problems of Classical Elastostatics*. Quart. Appl. Math., vol. 25, 1967, p. 89-95.
2. CRUSE T. A., *An Improved Boundary Integral Equation Method for Three Dimensional Elastic-Stress Analysis*. Comp. and Struct., vol. 4, 1974, p. 741-754.
3. LACHAT J. C., *Further Development of Boundary Integral Technique for Elastostatic*. Thèse, University of Southampton, février 1975.
4. CHAUDONNERET M., *Méthode des équations intégrales en viscoplasticité, application au calcul de concentrations de contrainte*. Thèse, Publication ONERA, n° 1978-1.
5. LEMAITRE J., *Sur la détermination des lois de comportement des matériaux élastoviscoplasticques*. Thèse, Publication ONERA, n° 135, 1971.
6. CHABOCHE J. L., *Viscoplastic constitutive equations for the description of cyclic and anisotropic behavior of metals*. Bulletin Acad. polonaise des Sciences. 6, Sciences Techniques, vol. 25, n° 1 (1977), p. 33-42.

DISCUSSION

R.B.Wilson, US

I wonder if you could comment on the question of computer time usage for doing the viscoplastic analysis as compared to an elastic analysis for the same geometry.

Reponse d'Auteur

Les calculs en élasticité sont très, très brefs, les calculs que j'ai présentés nécessitent moins d'une demi-minute de calcul sur ordinateur IRIS 80. Evidemment en viscoplasticité ce temps est très supérieur, pour le dernier calcul nous avons mis à peu près une heure sur IRIS 80, toujours.

Il est à noter aussi qu'arrivé au stade du calcul que nous avons en fin de fluage, les phénomènes se stabilisent et que, par conséquent, les pas que nous effectuons sont très importants. Le calcul se poursuit rapidement. C'est l'intérêt du choix du pas optimal que nous avons mentionné.

F.Sagendorph, US

When you find the viscoplastic zone do you get all the stresses and everything else inside that zone, and is it done automatically in your programme?

Reponse d'Auteur

Oui, pour calculer les forces de volume supplémentaires introduites par la viscoplasticité, je suis obligé de connaître le tenseur de contrainte en ces points, donc je peux calculer le tenseur de contrainte en tous points de la structure. Je les calcule par ce programme.

Comment by E.E.Covert, US

I think the idea of calculating the plastic stresses in an evolutionary way allows for the opportunity in the future to account for cyclic usage and strain accumulation and life prediction.

It is very easy for us to say, why don't you do that next. But it is probably very difficult. For the designer it would all the way be useful.

SOME THEORETICAL AND EXPERIMENTAL INVESTIGATIONS OF
STRESSES AND VIBRATIONS IN A RADIAL FLOW ROTOR

by

A. Grasso - FIAT AVIAZIONE S.p.A.
J.J. Blech - Centro Ricerche FIAT
G. Martinelli - Centro Ricerche FIAT
Italy

ABSTRACT

The problem of an integrally bladed radial compressor under the influence of a centrifugal force field has been attacked by several authors with various simplifying assumptions. As a consequence of development and refinement of Finite Element Method, a three-dimensional analysis is at present possible but it is very complicated and too difficult to handle.

In this paper two calculation methods based also on FEM are proposed. The first adopts a mixed three-dimensional and two-dimensional analysis, using plate elements for blades and axisymmetrical ring for the disk coupled by substructuring technique. The second implements axisymmetric anisotropic ring elements for the blades and the isotropic ring elements for the disk.

A dynamic analysis of the blade with F.E.M. is also presented.

As an example the various methods are applied to the centrifugal compressor design of the FIAT 6803 engine and compared with results of experimental investigation.

INTRODUCTION

In the design of a viable small gas turbine engine for helicopters and surface transport, special attention must be given to the attainment of low fuel consumption, high performance and low cost. An automotive turbine engine which is destined to compete with the presently existing piston engines must, therefore, at least reach those engines' achievements in the aforementioned items.

Among the gas turbine engine mechanical components, the compressor consumes most of the energy which is supplied to the engine by the fuel. Thus, it is of utmost importance to have its flow passages aerodynamically designed to the maximum attainable efficiency. Structural constraints upon the morphology of the impeller flow passages should not, therefore, interfere with its efficient operation. In addition, the requirements of high performance and low cost impose the further restrictions that the impeller be fabricated from light low cost materials, and that its configuration should yield a low moment of inertia, so that the engine is capable of a quick response to the operator's commands.

In an attempt to meet those targets, many engines which have been developed within the past two decades employ an aluminium alloy centrifugal compressor with thin and curved blades, which rotates at high speeds. Such an impeller will supply the required mass flow and pressure ratio with the least amount of spent energy. It will respond quickly, and its material and fabrication cost are acceptably low.

The FIAT 6803 gas turbine engine which has been described in (1)* is intended for truck or bus installation. A schematic of the general arrangement of the engine is shown in Fig. 1. The engine centrifugal compressor can be seen in the front of the engine. The complete gassifier rotor assembly with its bearings is shown in Fig. 2, and the impeller with its diffuser as mounted in the test rig are shown in Fig. 3. The impeller is cast of aluminium C355-T61 alloy. This alloy contains silicon and copper as the major alloying elements. It is recommended for light weight, high strength castings. Twenty two blades with radial exit are precision-cast in the impeller. Its rotational velocity is 33,000 r.p.m. (tip speed = 450 m/sec). The diffuser has 13 channels. A cross sectional view of the impeller is shown in Fig. 4.

The structural implications of the constructional constraints which have been mentioned before are as follows :

- Stress levels must be kept down. Although the maximum centrifugal stresses occur in the hub region, special attention must be paid to the impeller exit zone where the temperature may rise to levels for which the material strength is rather reduced and where the disk flexibility (and, thus, vibrational susceptibility) is the highest.

* Numbers in brackets indicate references which are listed at the end of the article

- Vibratory response of the blades in the inducer section, and of the disk at the air outlet section must be contained within acceptable levels.

In the course of the development of the FIAT 6803 engine, a few impeller failures have occurred. Those can be categorized in two types: blade failures in the inducer zone, and disk rupture near its outer diameter.

Blade failures in the inducer zone are shown in Figs. 5 and 6. Those failures have been attributed to vibratory alternating stresses causing fatigue in the material. After taking actions to avoid those failures, the problem has been eliminated and no such failures have re-occurred.

Only one disk failure has occurred, and it is shown in Fig. 7. The failure mechanism has been attributed to either centrifugal stresses acting on a "hot" (and therefore, weak) zone, or to alternating vibratory stresses causing material fatigue. A combination of the two could, of course, also be a cause of the failure.

This paper describes some of the experimental and analytical work which has been carried out in the course of elimination of the compressor failures.

1. TEMPERATURE DISTRIBUTION

The compressed air total absolute temperature reaches a value which is above 200°C. This fact, combined with the presence of hot engine components adjacent to the impeller back face chamber, rendered it necessary to establish the temperature distribution within the impeller. The knowledge of the temperature distribution was not important for the determination of the thermal stresses, for these are negligible, but rather for the establishment of the material strength distribution within the impeller.

The necessity of determining the impeller temperatures is amplified when its material strength deterioration at elevated temperatures is examined. In Fig. 8, the ultimate and yield strength of aluminium 355 alloy are plotted vs temperature. It can be seen that while the material does not exhibit any appreciable drop in its strength at the R.T. to 100°C temperature range, those values drop by some 10% approximately when a temperature of 150°C has been reached and then drop sharply to less than 50% of their R.T. values at a temperature level of 200°C. The drop in strength continues further as the temperature rises.

The impeller temperature distribution in the 100% speed steady state conditions was calculated by means of the NASTRAN finite element computer program. For the sake of practicality a simpler axisymmetric rather than the more complicated 3D model was chosen. Thus the impeller rotor was subdivided into an assemblage of toroidal rings having triangular meridional cross sections. The degree of success in the calculation of the temperature distribution depends heavily on the degree of reality with which boundary conditions are described. In the present case two types of boundary conditions were assumed: the surface of the impeller which is in contact with the shaft was given a prescribed temperature, whereas the remaining boundary surface was given convective boundary conditions. In order to account for the blades, a combined film coefficient was calculated in which the blades are assumed to act as a series of fins. The influence of adjacent engine components was disregarded.

The temperature distribution which resulted from this modelling is illustrated in fig. 9, where isothermal contours are traced over the impeller meridional cross section. The maximum temperature which was calculated within the impeller is 140°C. No experimental verification of this value has been carried out as yet.

The thermal stresses within the impeller were calculated and indeed, as mentioned before, showed to be negligible. Therefore, we dispose with their presentation here.

2. CENTRIFUGAL STRESS DISTRIBUTION

The stress distribution within a radial turbomachine, due to its rotation, is fully three dimensional with the eventual simplifications that blades may be modelled as shells and that the disk stresses exhibit periodicity.

The authors find, however, that the use of available computer software for a full 3D structural stress analysis of impellers is premature. The accuracy of results is subject to doubt and their resolution is weak. The difficulty lying mainly in limited computer capacity and still inadequate modelling techniques for the structure. Also, it required large investments and a great amount of time in obtaining results. To cite one example, Chan and Henrywood (2), using the finite element technique, reported 12 man working days to set up the problem and five hours of computer running time, for analyzing an impeller. Even their geometric model is simplified by assuming the blades to be flat and to lie in radial planes, and the disk geometry to be axisymmetric. This assumption permitted them to employ simple circumferential as well as blades elemental geometry. Only one element spanning to whole segment circumferentially has been used by them for modelling purposes in the disk. A compensation for the small numbers of elements was gained by assigning 90 degrees of freedom to each disk element.

The structural calculations which were performed in the course of the development of the 6803 engine impeller ranged from the development and implementations of fast on-line computer programs to a detailed finite element analysis by the substructures method.

Thus experience was gained as to the degree of manoeuvrability and accuracy of the various approximations.

3. DISK STRESSES

The disk meridional and tangential stresses along its back face are plotted in Figs 10 and 11 * von-Mises stresses were also calculated but are not presented here. We discuss below the various approaches which were employed to get the results which are presented in those figures.

In the first stages of the investigations a finite difference one-dimensional approach which is described in (3) as applicable to radial turbomachinery was programmed for the computer. This analysis although being 1D, takes formally into account the complex contour of the disk meridional cross section, the blades stiffening and additional loading effect and eventual circumferential bolt holes including the bolts themselves. To enable the handling of such a compound situation with a relatively simple tool, many simplifying assumptions were made. Those assumptions give rise to doubts concerning the accuracy of the results, let alone the applicability of the proposed approximation to the present situation. Much engineering intuition and modelling experience is needed when embarking on this approach. The impeller disk is considered throughout as a shallow thin shell (approximate shallow conical shell equations are used). This is hardly the case in many impellers. The bladed sections are handled as T beam sections and their loading as well as geometry is then spread all over the disk front face circumference. The advantage in using this method lies in the possibility of speedy on-line calculations. Thus, within a minimal amount of time, results are obtained, and the effect of a great many design changes can be quickly assessed. One of the curves in each Fig. 10 and 11 presents the results of this analysis (see Case 1).

The second stage of the computation involved a finite element axisymmetric model. The details of the numerical finite element presentation can be found in (4). This model is more time consuming than the previous one in both problem set up and computer running time. However, those increases may be considered minute and perhaps unimportant. The crux of the problem lies in the knowledge of a correct and efficient way of presenting the effect of the blades upon the disk. One may consider this effect as being a three folded one. First, the blades impose a radially outward traction, upon the disk, which will increase its stresses. Second, this traction, which acts over the front face, imposes a bending moment on the disk. Fortunately, in the present case, this bending moment counteracts the disk inherent moment due to its rotation which causes its forward bending. Thus, this effect of the blade load acts to reduce the disk stresses. Finally, the blades offer an additional stiffness to the disk, which further reduces the disk stresses.

In using the axisymmetric finite element computer program a study was carried out of the various effects listed above, as well as the total blades action upon the disk. At first, the disk was run by itself, without blades. Forward bending of the disk showed up. Back face stresses are shown in Figs. 10 and 11 (see case 2). Back face axial displacement is plotted vs the radius in Fig. 12, from which the disk forward bending is clearly seen (case 2) and, as expected, is the highest of all other cases considered. In a second run the blades load upon the disk was imposed. This load was computed by assuming the blades to be an assemblage of independent radial rays, calculating the centrifugal force which each of those strips exerts upon its root, and finally apportioning it to the disk front face in a ring-wise manner at the appropriate nodal points. The result was an obvious reduction in the forward bending of the impeller disk as illustrated in Fig. 12, case 3. The disk stresses were somewhat augmented (see case 3 in Figs. 10, 11).

In a further attempt to better account for the blades load distribution over the impeller front surface as well as for their stiffness, and still using an all axisymmetric model, the entire impeller meridional view (blades and disk) as shown in Fig. 4. was assumed to be one body of revolution. The blades, however, were assumed to be made of transversally orthotropic materials. The blades centrifugal load was simulated by assigning to the blade elements a reduced mass density. The density reduction factor ranged from a low value of .04 for elements near the disk tip to a maximum value of .21 at the hub zone. Similar to the density reduction the blade elements meridional-plane modulus of elasticity was reduced in accordance with their location. The elastic modulus which is associated with the tangential direction was set to be practically equal to zero, thus incapacitating the blade material to build up any circumferential stresses. Poisson's ratio in the meridional plane was assumed to be equal to that of the bulk material and the one associated with the circumferential direction was eliminated. Results of this model are given in Figs. 10, 11 and 12 (case 4). Figs 10, 11 and 12 include also results for the case when the "blade materials" were assumed to have no mass density at all and thus the stiffening effect of the blades upon the disk could be studied by itself (case 5).

* The impeller nomenclature which is used throughout this article is identical to the one which was used in (2)

At the end, an investigation was performed to determine the amount of stress which results from the disk bending. The disk back face was prevented from moving axially and the disk stresses were calculated. The resulting back face stresses are shown in Figs. 10 and 11 (case 6). They are smaller than any of the previously calculated stresses.

The final stage of the analysis utilized the NASTRAN system and implemented the method of substructures. In this method axisymmetry in the disk structural response was still assumed and the blades shell structure was modelled by an assemblage of interconnected plate facets. The interaction between disk and blades is such that compatibility is maintained between blades displacements at their roots and disk front face displacements. Moreover, the principle of virtual work as applied to the entire structure containing disk and blades is satisfied. The authors find this method as the most advanced, short of a fully 3D method, which can be still satisfactorily used for impellers. The disk back face stresses and axial displacements are plotted in Figs. 10, 11, 12 (case 7). Blade stresses are reported in the next paragraph. Radial and tangential stress contour maps as calculated by this method are illustrated in Figs. 13 and 14.

4. BLADE STRESSES

A simple preliminary calculation of the blade stresses can be performed by slicing the blade into independent radial rays and then analyzing each ray by itself. The blade root stresses calculated this way are shown in Fig. 15. This assumption basically neglects the axial stresses in the disk.

The axisymmetric finite element computer program where blades were also modelled as an axisymmetric structure can also be utilized to determine the blade stresses. The maximum principal stress is plotted in Fig. 15.

A third calculation of the blade stresses was performed by the NASTRAN program, assuming these blades clamped onto a rigid disk front face and idealizing them as interconnected plane facets. The results of this calculation are presented in Fig. 16 in the form of a contour map. In fig. 15 the blade stresses at the disk front face junction are given. In this assumption the disk forward bending action which will tend to increase the blade bending stresses at their roots is neglected.

Finally, the blade stresses resulting from the calculation by the method of substructures, the details of which were discussed in the preceeding paragraph, are illustrated in fig. 17. Again, their major stresses at the disk junction are shown in Fig. 15.

5. VIBRATORY BEHAVIOUR

A detailed experimental and theoretical investigation has been devoted to the blades vibratory response at the inducer section. This being the case since the failures illustrated in Figs. 5 and 6 were attributed to vibratory stresses causing fatigue in the blade material.

The experimental studies involved holographic and acoustic measuring of the impeller natural frequencies and mode shapes. The theoretical investigations included the calculation of the blades natural frequencies and mode shapes. The NASTRAN system was used for these calculations. For the sake of simplicity the blades were assumed to be clamped at their roots, thus modelling of the impeller disk was dispensed with. The experimental and theoretical results are given in table 1. Correlations between the various methods seem to be satisfactory. In the acoustic measuring technique, each individual blade's fundamental natural frequency has been recorded, and thus a comparison between seemingly similar blades could be made. The lowest frequency measured was 1705 Hz, the highest 1885 Hz. Damping of the vibrations was also measured. Fig. 18 illustrates the impeller mode shapes as obtained by holography.

To remedy the blade failures it has been proposed to make them stiffer by thickening their root zone. In table 1, experimental and calculated values for reinforced blades are given.

A second proposal was to cut out a portion of the blade at the inlet. Various cut-outs have been analyzed, and finally one has been proposed and performed. With this cut-out the blade has been stiffened and its natural frequencies raised (see Table 1). Up to date, no blade failure has been experienced with this modification. Deeper cut-outs could be performed if further blade failures are to occur in the future.

6. DISCUSSION OF RESULTS

Whereas the blade failure problem is considered as contained at present, the mechanism of the disk failure remains to be determined. Failure cause could be attributed to either of the two following items or to both :

1. Centrifugal stresses acting on a "hot" (and therefore, weak) zone
2. Material fatigue due to vibration

An experimental verification is necessary in order to determine the severity of each of the previously mentioned items.

It does not seem to be necessary to determine the disks centrifugal stresses experimentally. The theoretical values which have been obtained suffice in their accuracy. However, some doubts are present concerning the temperature distribution in the disk which depends on the correct statement of the boundary conditions. And since the material strength becomes sensitive to the temperature at levels near to which the gas total temperature is, it seems to be worthwhile to perform a temperature measurement on the disks back face in order to verify the assumed boundary conditions.

In a similar manner - the measured holographic impeller natural frequencies and modes (Fig. 18b) could interact, according to a vibrogram, with the 13 diffuser channels. However no monitoring of the disk vibrations had been made. Also, it is hard to identify a fatigue failure in this material, by examining the fractured zone. Thus, a measurement of the disk vibrations is necessary before establishing the severity of disk resonances.

As far as stress calculations are concerned, the 1D approach, in which simplifying assumptions were amassed, underpredicted the disk maximum stresses by some 20% (Fig. 11), and rendered it stiffer (Fig. 12). In addition, this investigation demonstrated that an axisymmetric model of the impeller disk with the assumption that blades are also represented by an axisymmetric isotropic material, gave sufficiently accurate results for both the disk stresses and the blade maximum stresses. The impeller "umbrella" vibrational natural frequencies were also calculated by this method and showed satisfactory correlation with measurements, the error being within 5% (Table 1).

It is also worthwhile to mention that this impeller possesses a moderate amount of convexity, and thus the portion of disk bending stresses as compared to the tensile stresses is not large. In turbomachines having concave back face profiles, the effect of bending will become more pronounced.

Calculating the blades stresses as if they are clamped to a rigid disk, gave a distorted and grossly underestimated stress distribution at the blades roots. The disk interaction with the blades strongly influenced the maximum stresses which were obtained in the blades.

ACKNOWLEDGEMENTS

The authors wish to express their thanks to the FIAT Research Centre for availing the information published here and to FIAT Aviazione for their encouragement to publish this article.

REFERENCES

1. Cerrato R., Cipolla G., Margary R. and Pignone G. : "The FIAT Gas Turbine Engine - Design and Development" ERDA - Fourth International Symposium on Automotive Propulsion Systems, Washington DC, April 1977, Vol. I.
2. Chan, A.S.L. and Henrywood, R.K. : "The Analysis of Radial Flow Impellers by the Matrix Finite Element Method". Royal Aeronautical Society Journal, 75, pages 850+860.
3. Löffler, K.: "Die Berechnung von rotierenden Scheiben und Schalen", Springer-Verlag, 1961.
4. Wilson, E.L.: "Structural Analysis of Axisymmetric Solids", AIAA Journal, 3, 1965, pages 2269-2274.

TABLE 1 - IMPELLER NATURAL FREQUENCIES (HZ)

NATURE OF VIBRATORY MODE	ORIGINAL BLADE			REINFORCED BLADE			ORIGINAL BLADE WITH CUT-OUT	
	LASER HOLOGRAPHY	ACOUSTIC	CALCULATED	LASER HOLOGRAPHY	ACOUSTIC	CALCULATED	LASER HOLOGRAPHY	CALCULATED
1st Blade Flexural	1753	1780	1866	1982	1950	2015	2400	2500
Blades at outlet	**	**	3436	**	**	-	**	-
Coupled disk with lobes and blades	4868	4862	*	5375	5800	5824	**	*
Disk umbrella and blades	-	-	-	5138	**	5400***	**	*
Blade 1st torsional	5690	5624	5590	-	-	8955	6802	7150
Blade 2nd flexural	8294	8574	8750	8603	9550	10590	-	9700
Disk umbrella coupled with blade 3rd flexural	9941	9450	*	-	-	*	-	*
Blade 3rd flexural	11277	11050,12450	10290	**	**	**	-	12600
Blade 4th flexural	17890	17300	**	**	**	**	-	**

* Not Modelled

** Not Searched

*** Utilizing an axisymmetric model with spread blades

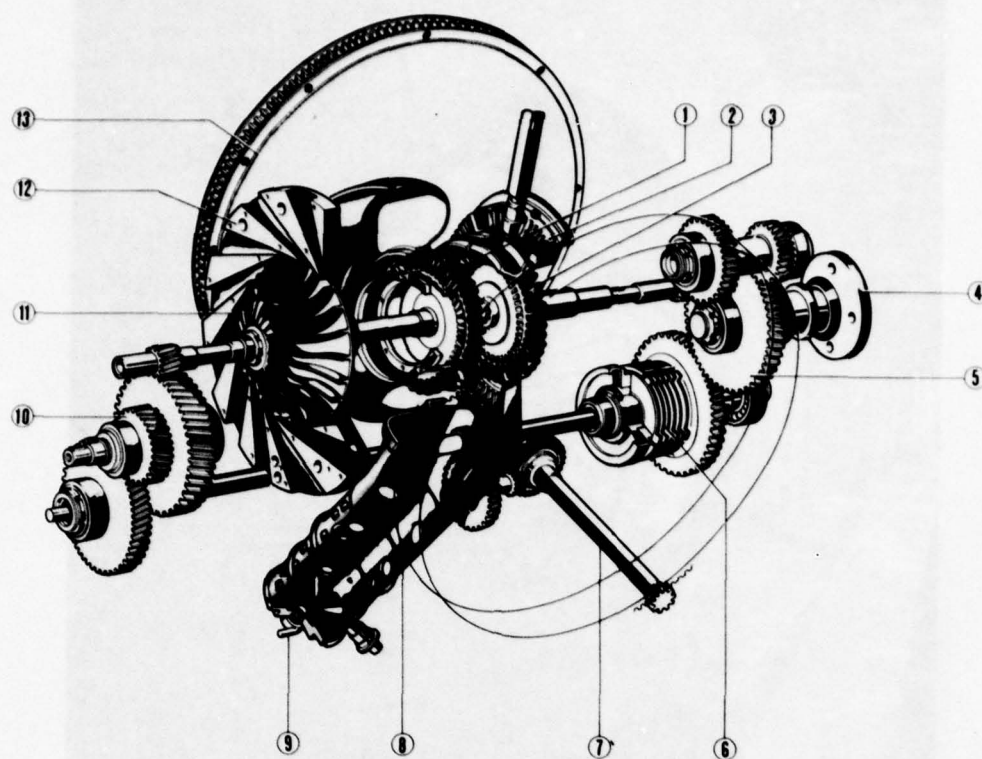


FIG. 1 - Schematic General Arrangement of the FIAT 6803 Gas Turbine Engine

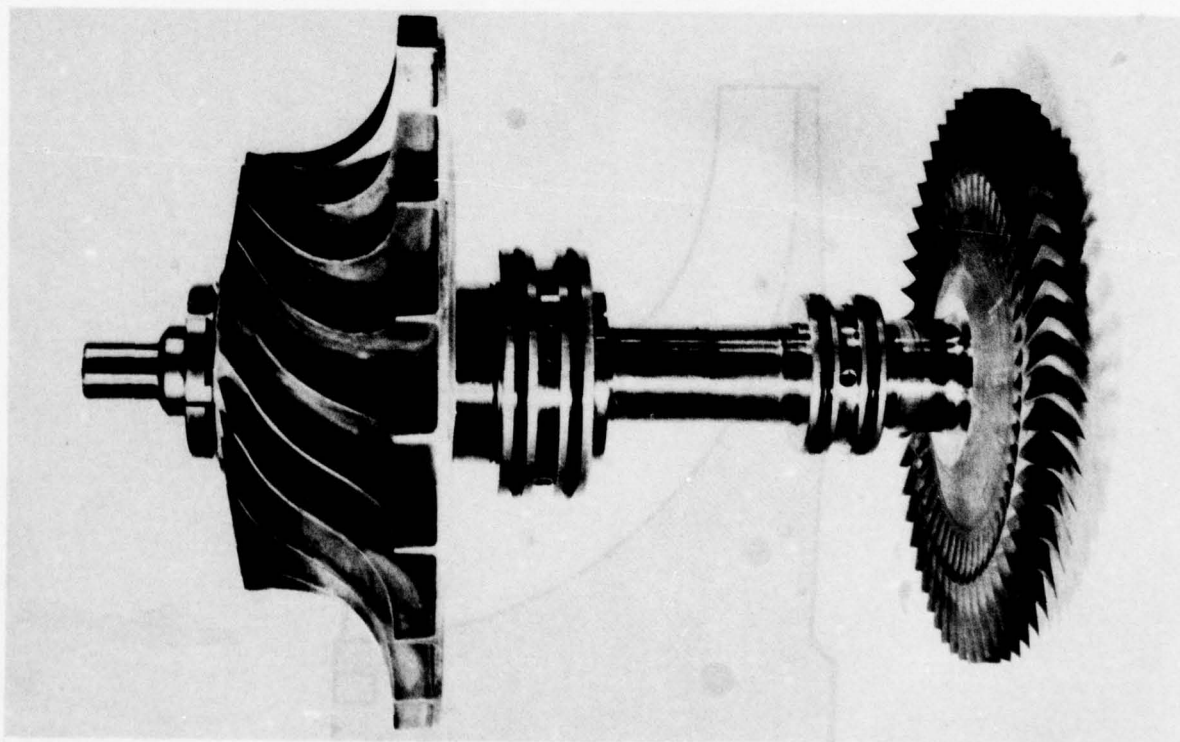


FIG. 2 - Gassifier Rotor Assembly with Bearings

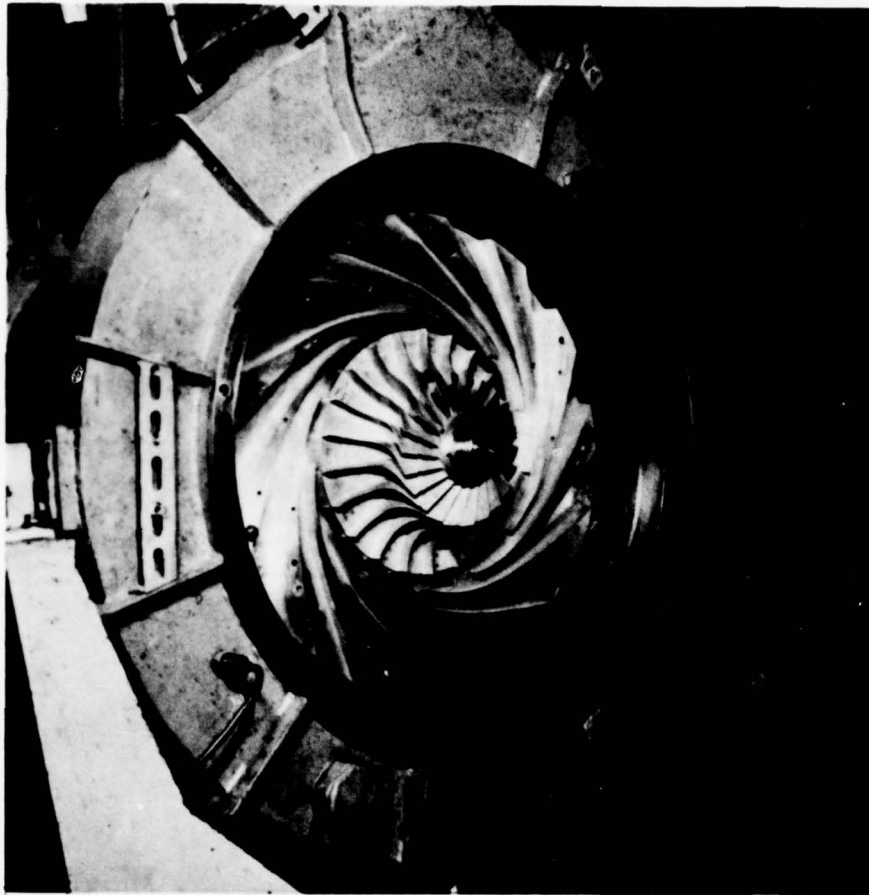


FIG. 3 - Centrifugal Compressor in Test Rig

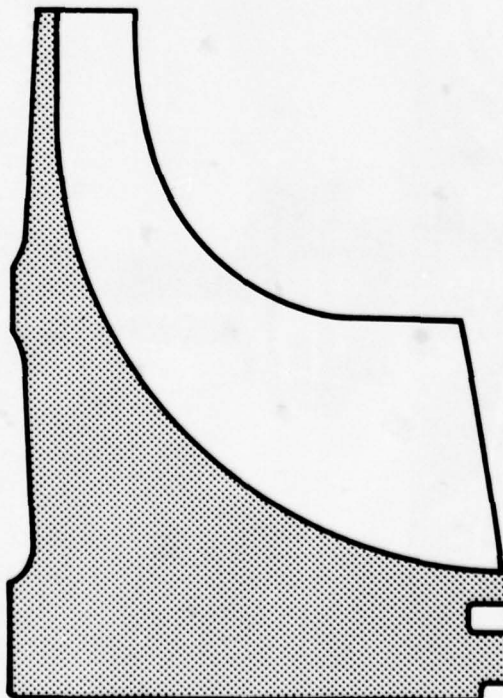


FIG. 4 - Impeller cross section



FIG. 5 - A compressor with Blade Failure in the Inducer Section

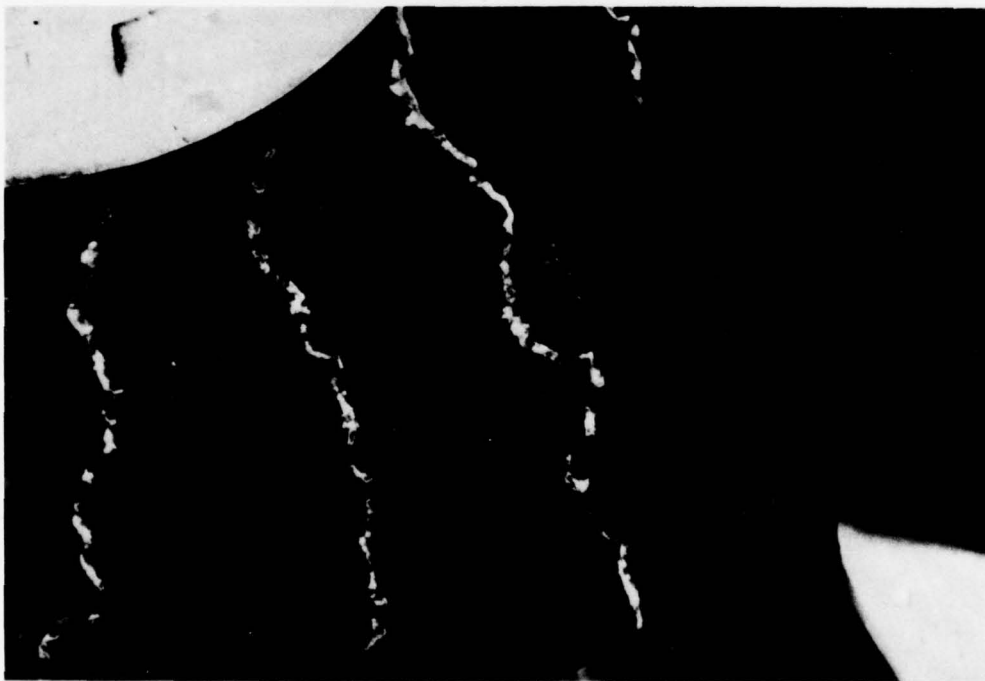


FIG. 6 - View of Filed Blades

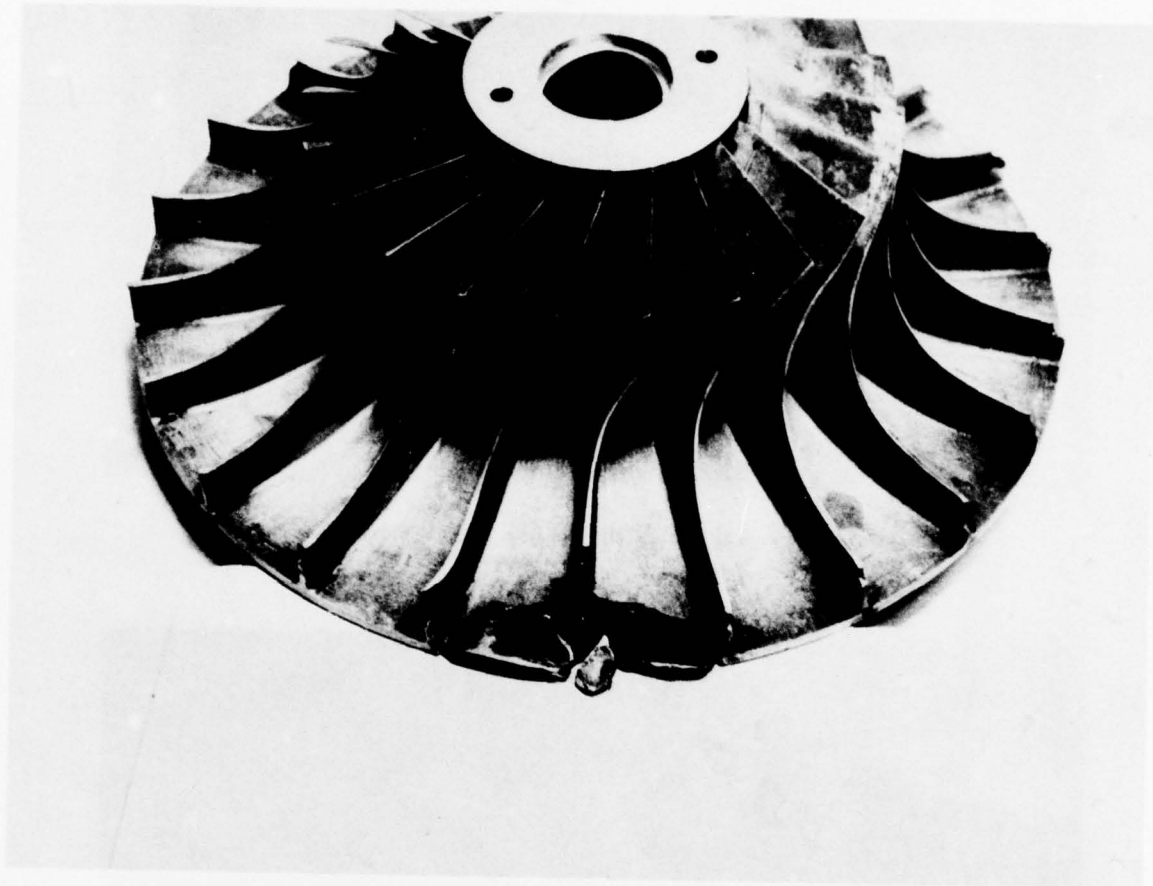


FIG. 7 - Disk Failure

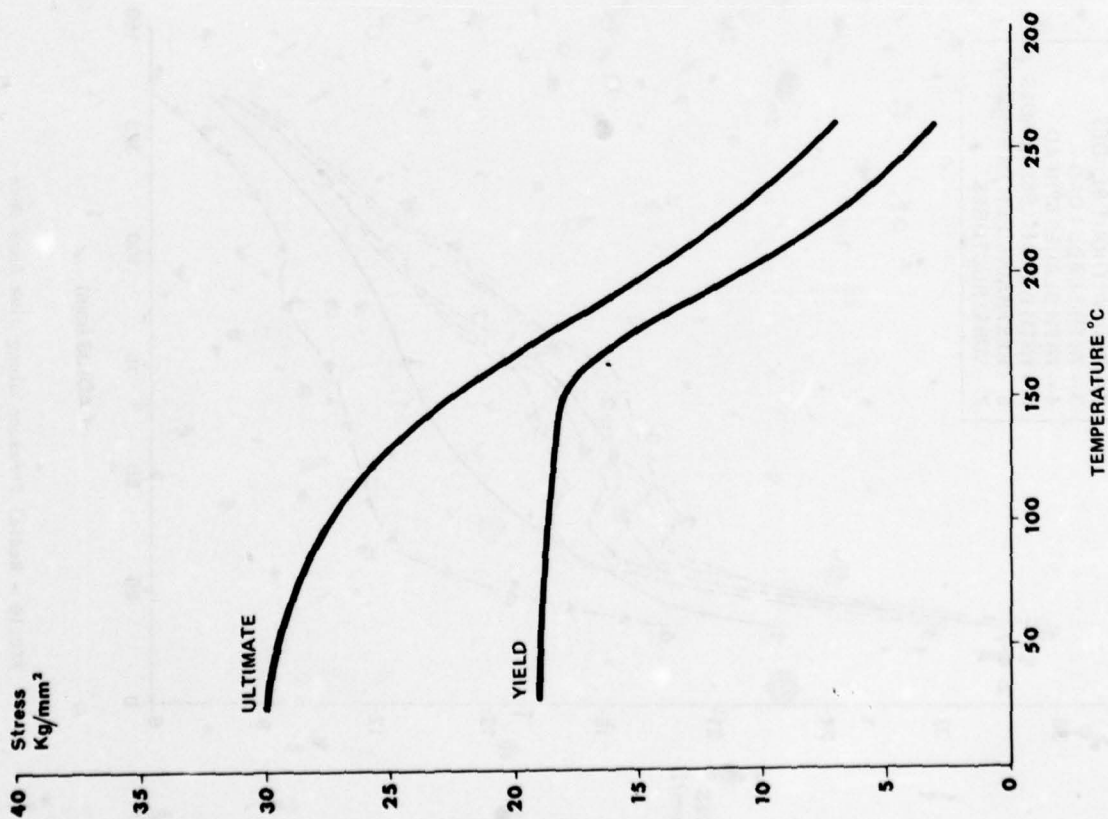


FIG. 8 - Strength of Aluminum 355 Alloy vs. Temperature

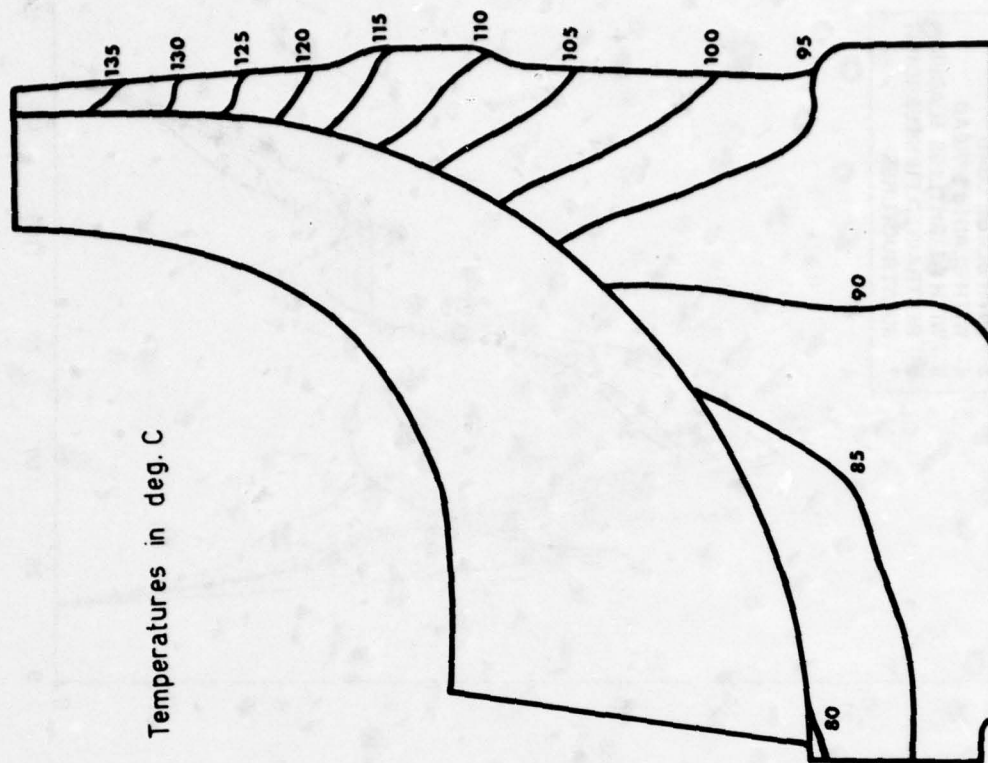


FIG. 9 - Temperature Distribution within the Impeller

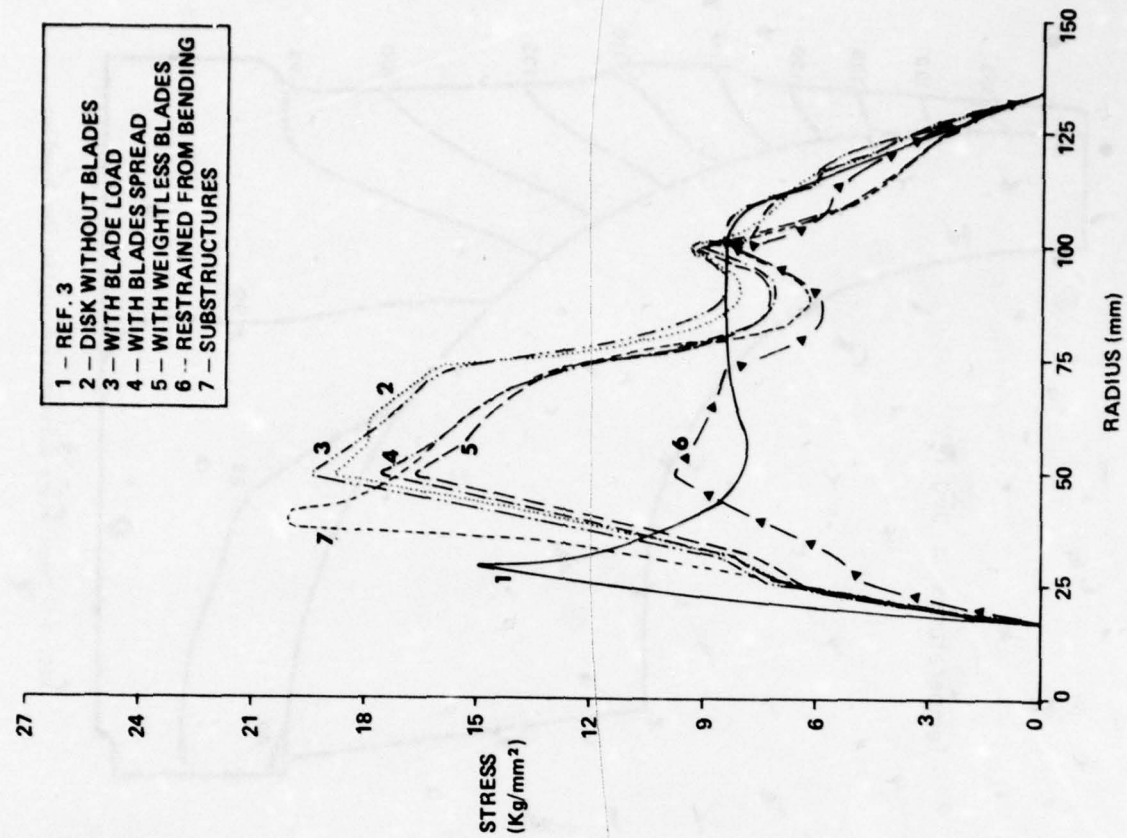


FIG.11 - Tangential stresses along Disk Back Face

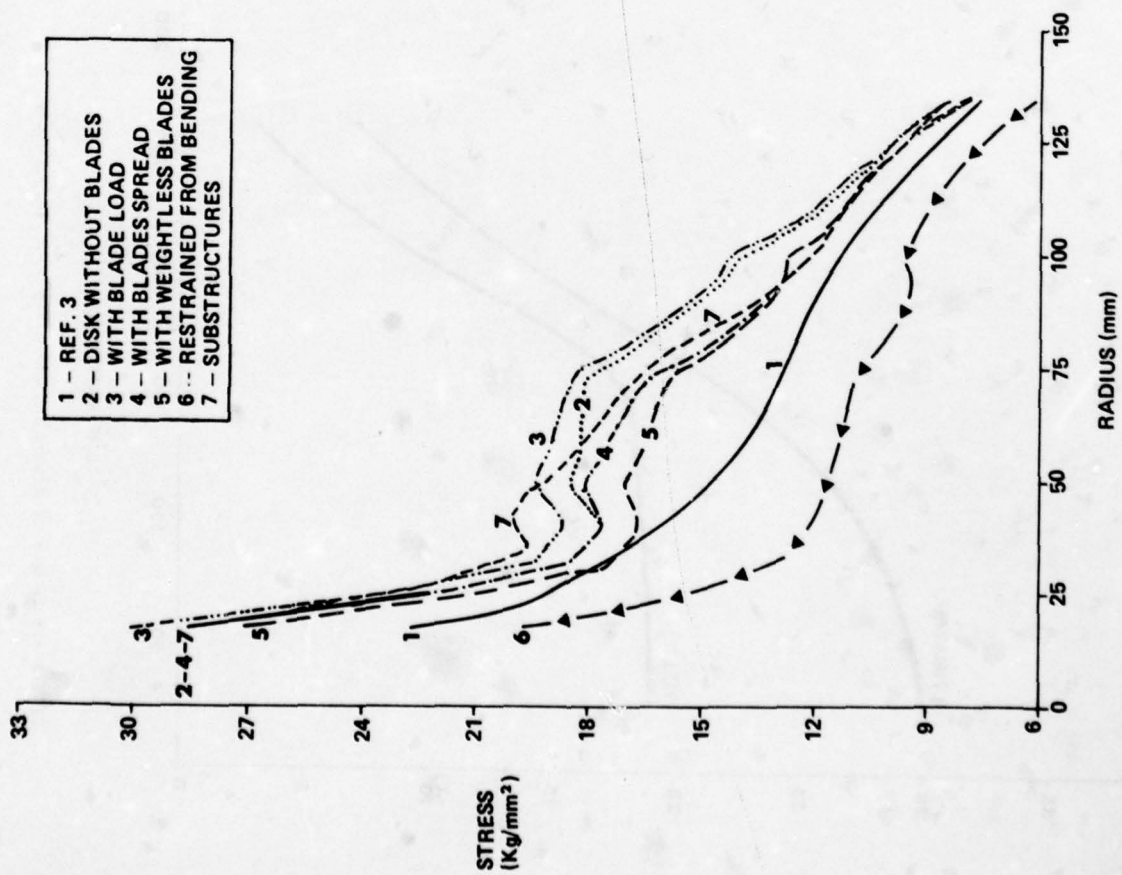


FIG.10 - Radial Stresses along Disk Back Face

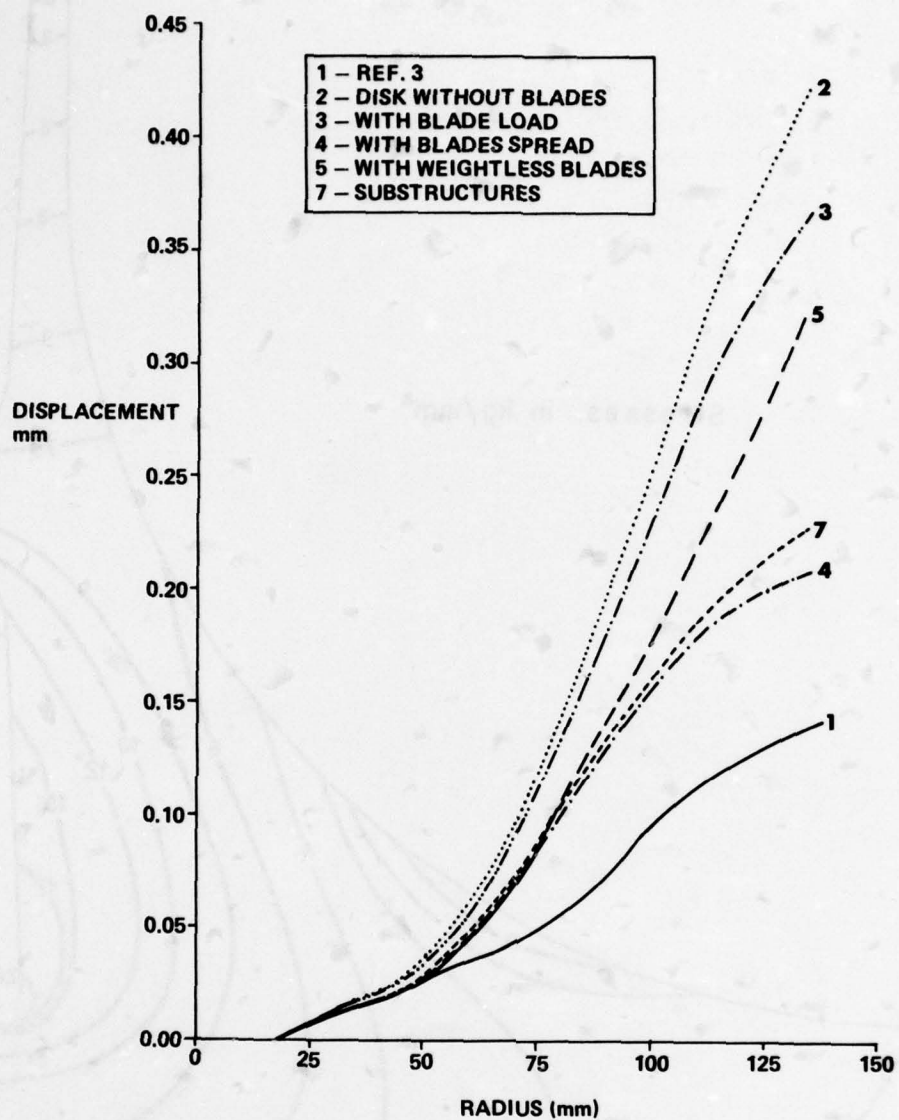


FIG.12 - Impeller Back-Face Axial Displacement

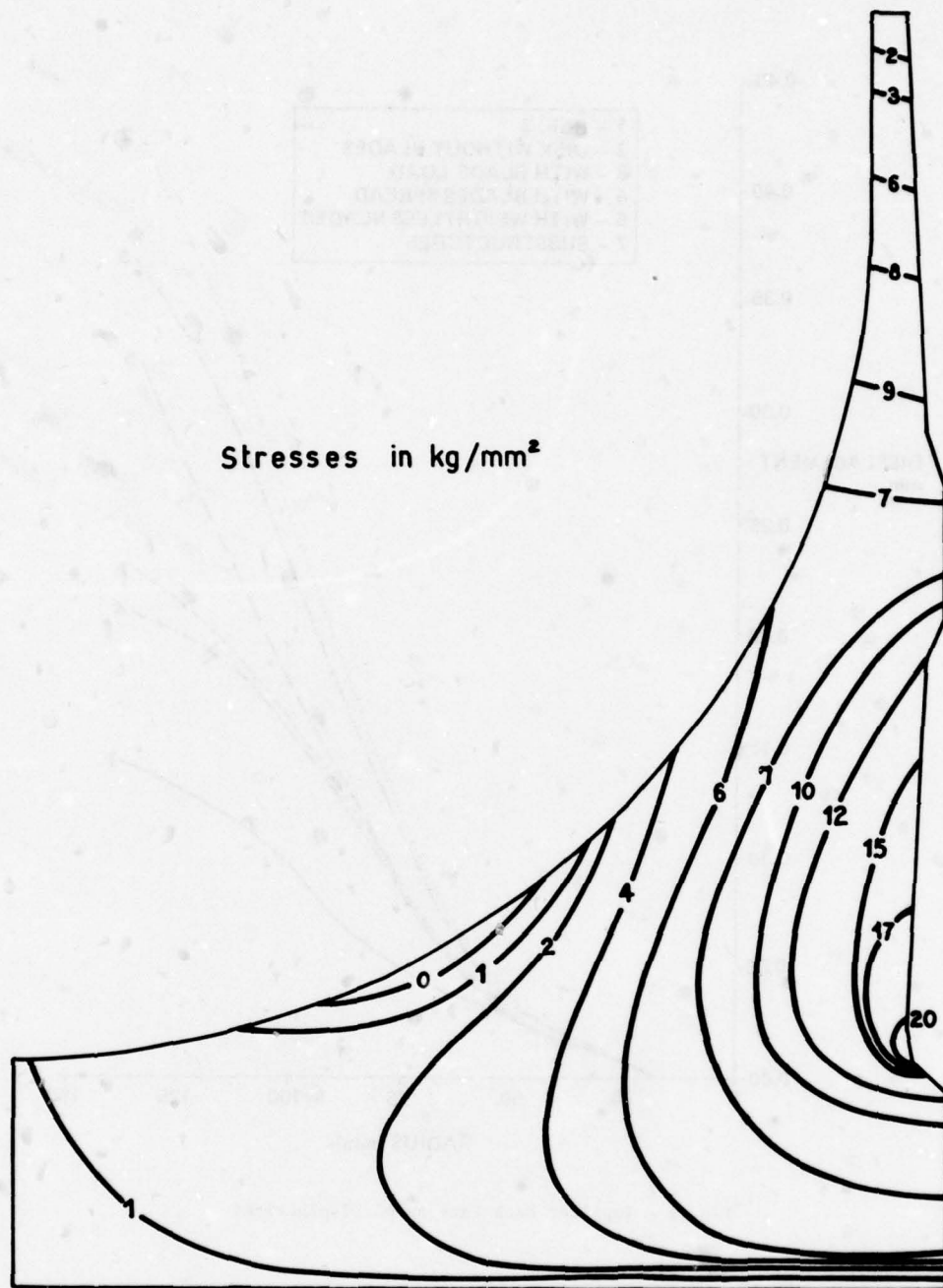


FIG.13 - Radial Stress Contour Map of Disk

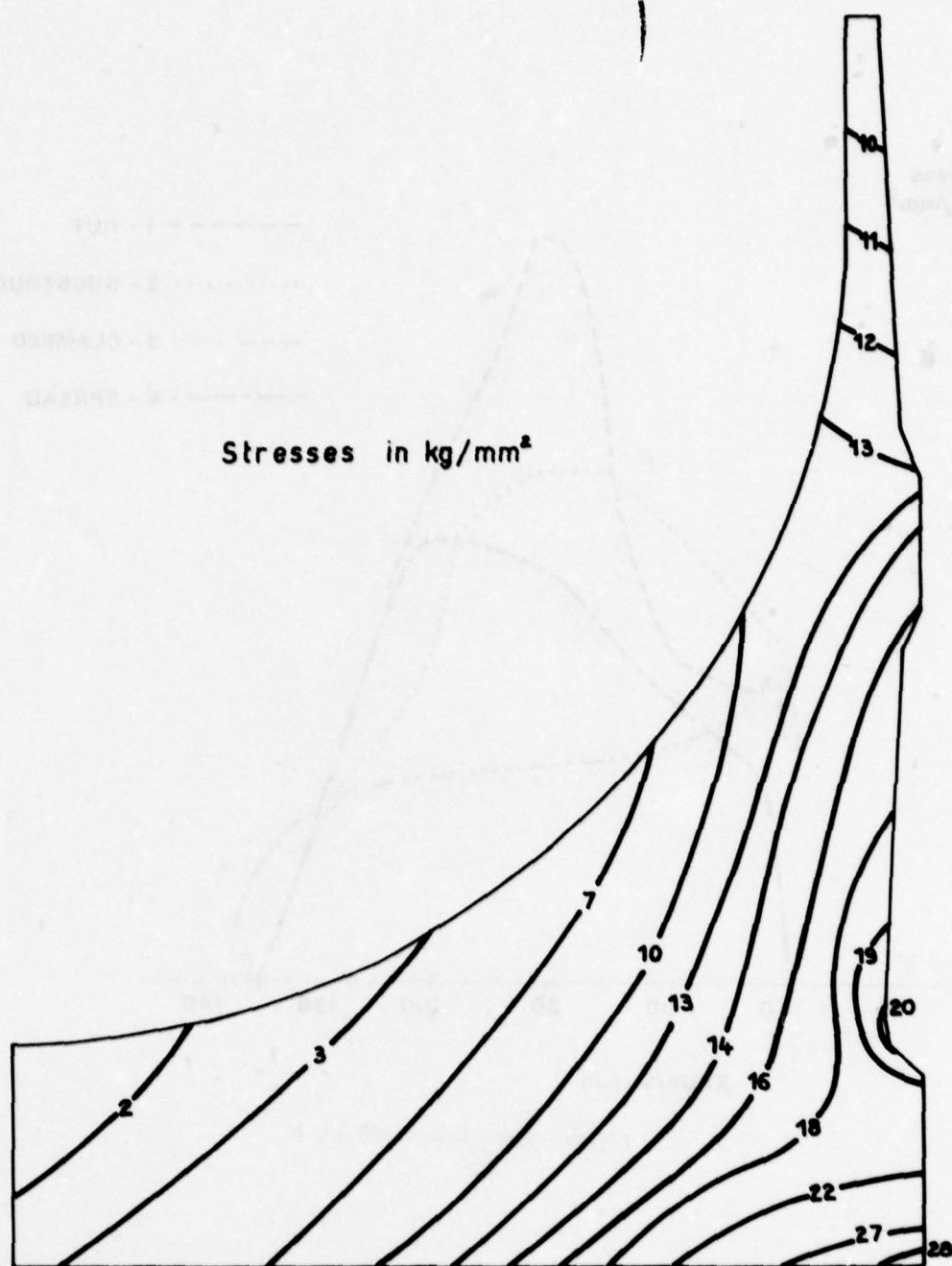


FIG.14 - Tangential Stress Contour Map of Disk

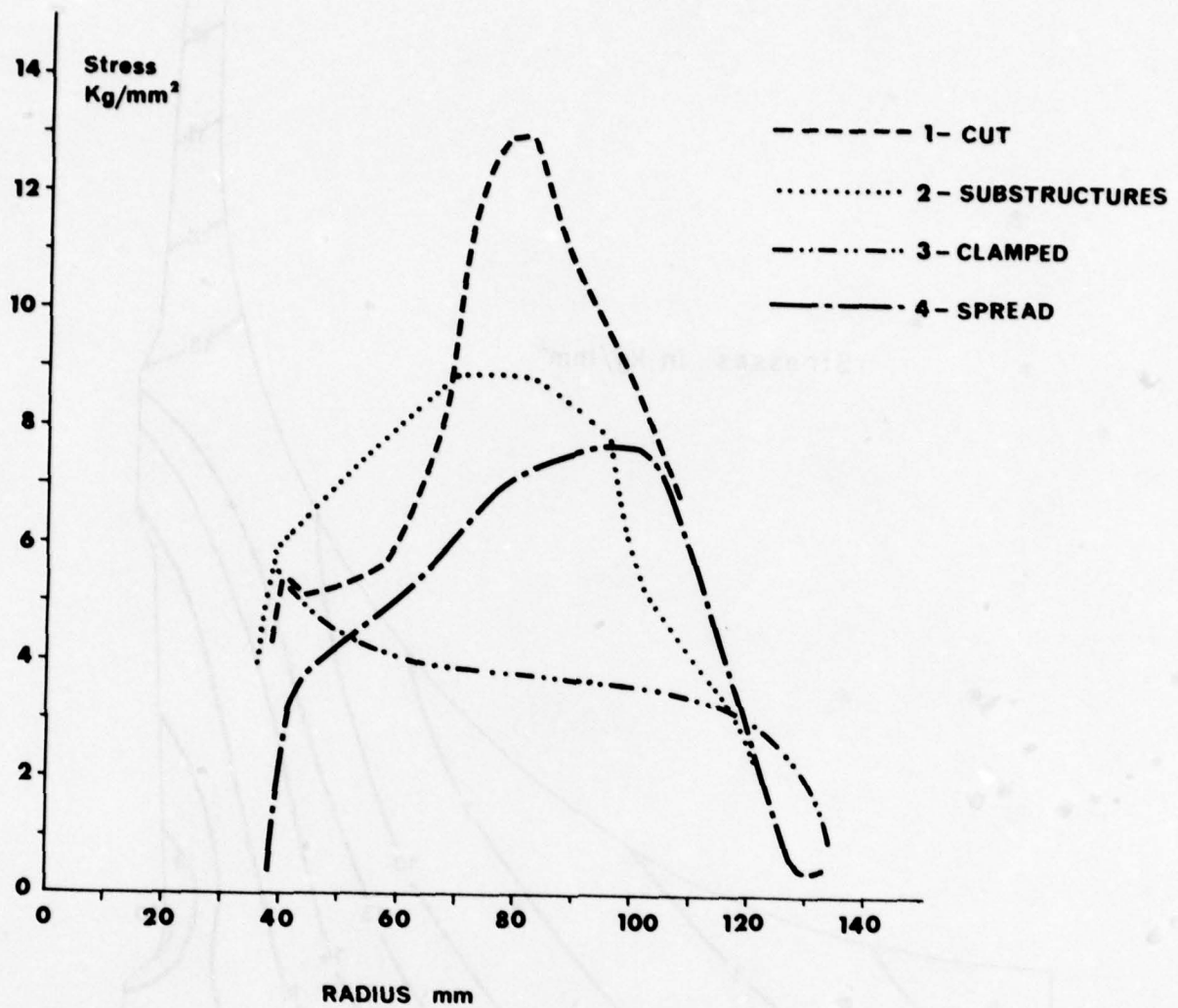


FIG.15 - Blade Root Stresses

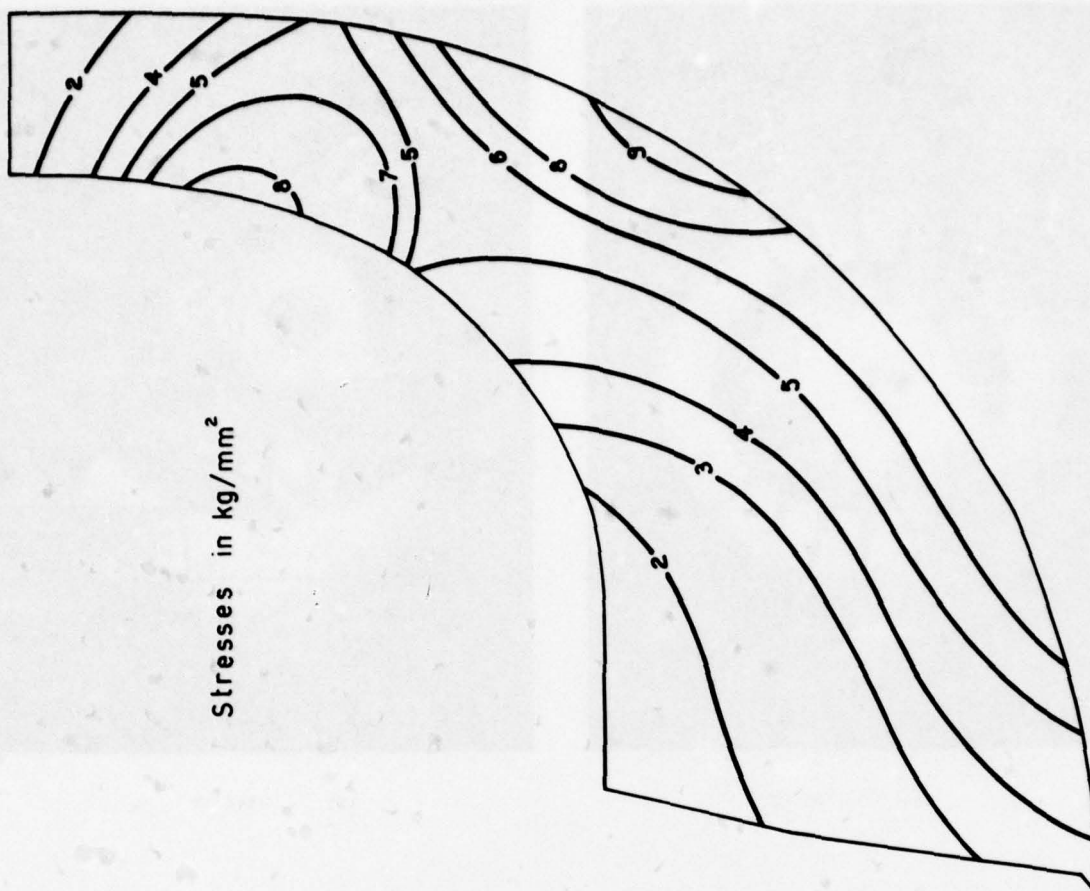


FIG. 16 - Blade Stresses when Rigidly Fixed

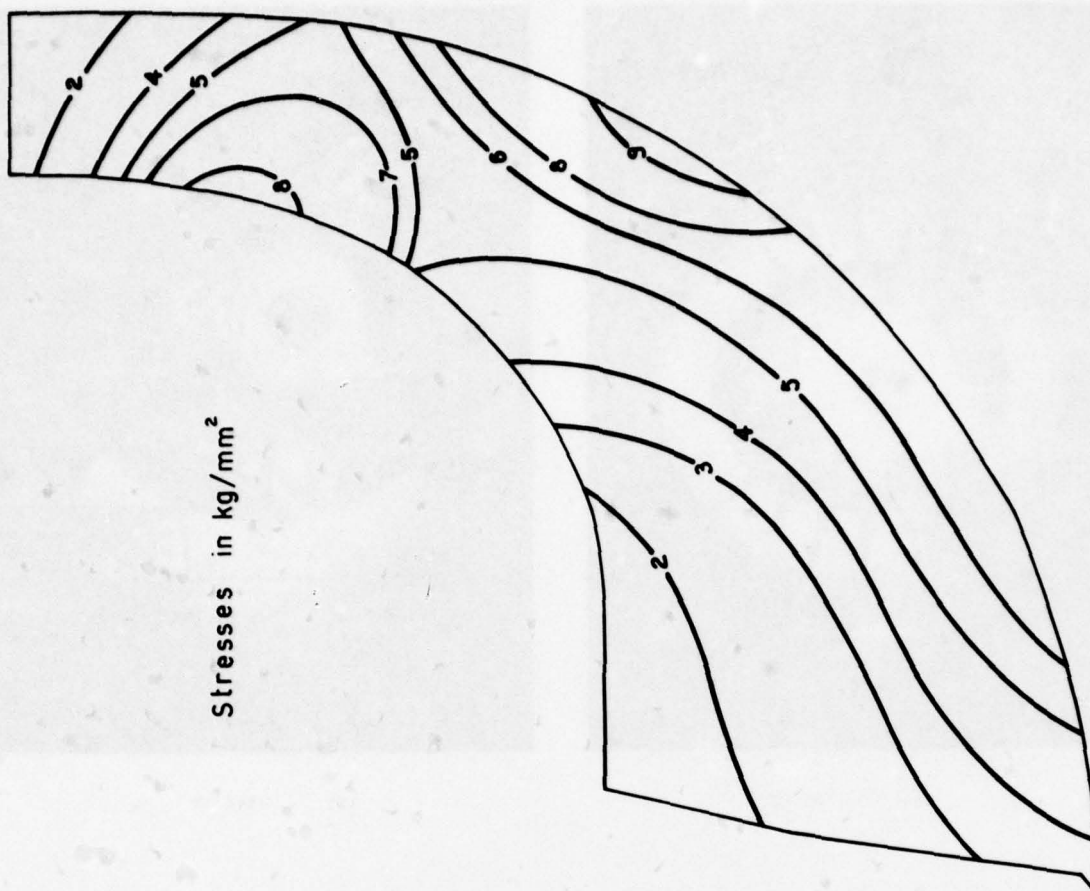
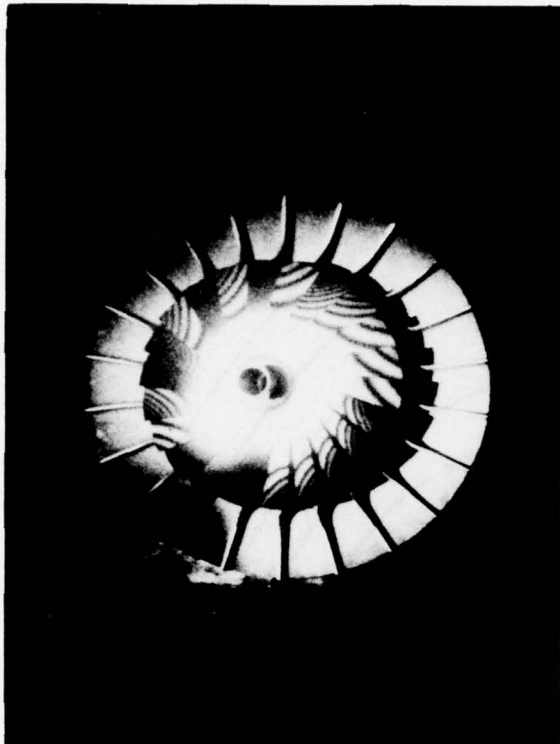
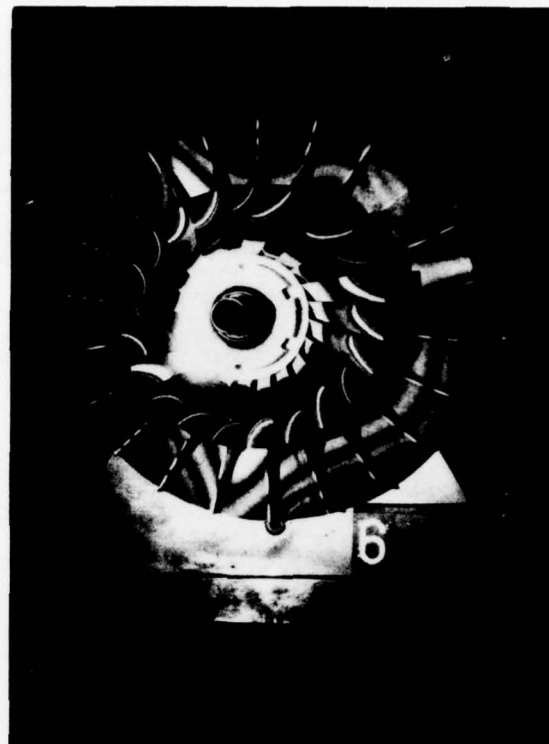


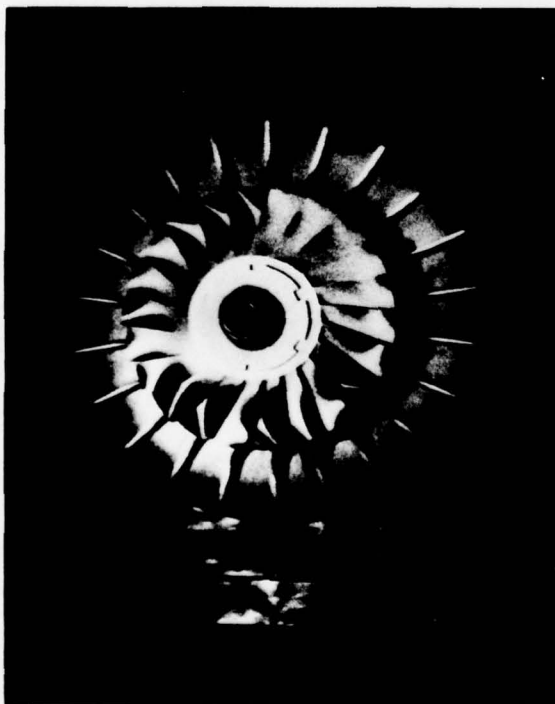
FIG. 17 - Blade Stresses. Method of Substructures



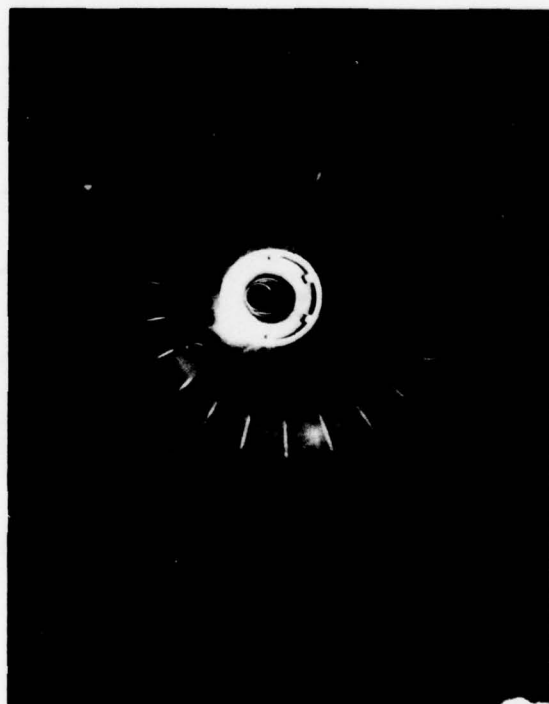
18a - 1753 HZ



18b - 4868 HZ

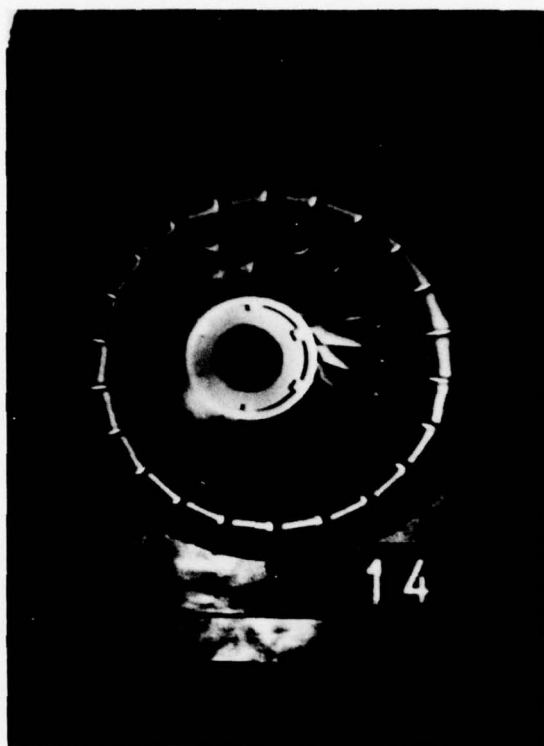


18c - 5690 HZ

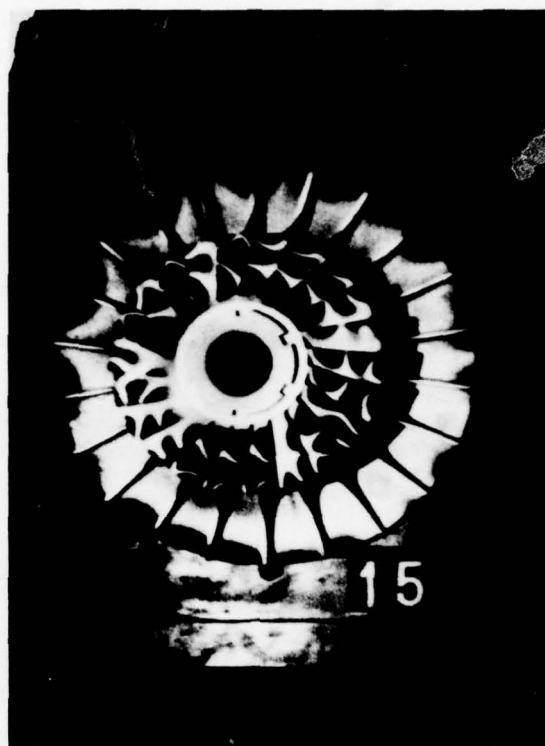


18d - 8294 HZ

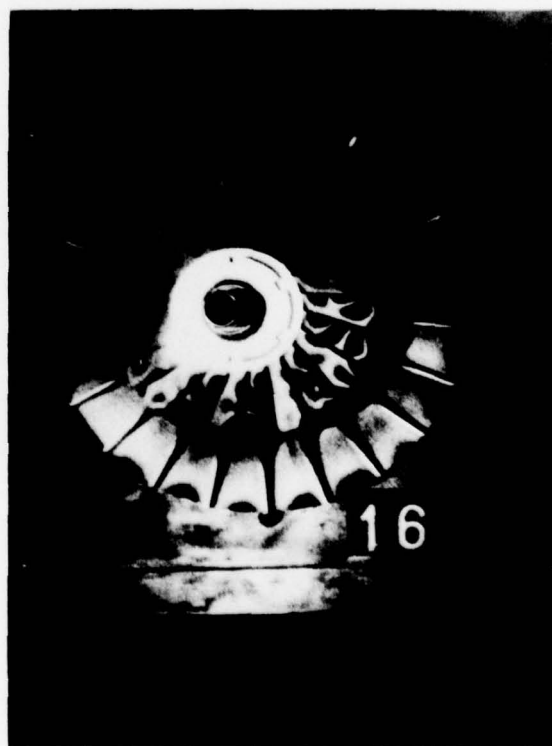
FIG.18 - Impeller Vibratory Modes as Obtained by Holography



18e - 9941 HZ



18f - 11277 HZ



18g - 17890 HZ

FIG.18 - Impeller Vibratory Modes as Obtained by Holography

DISCUSSION**A.F.Storace, US**

What substructuring method did you use?

Author's Reply

Substructuring was done by having the disk structure represented by axisymmetric ring elements whereas the 22 blades shell structures were represented by one ensemble of triangular plane facets. No attempt was made to find circumferential variations in stresses.

R.D.McKenzie, UK

How were blade frequencies calculated?

Author's Reply

The shell structure of the blades was represented by an ensemble of triangular plane facets. The boundary condition at the blade disk interface was assumed as a rigid fixity. The NASTRAN program was then used to obtain the results which are presented here.

E.E.Covert, US

How did you calculate heat transfer boundary conditions for thermal calculations?

Author's Reply

Blades were modelled as fins extending out of the disk-blade interface. An effective heat transfer film coefficient was then calculated combining the heat input of the compressed air into the disk front face and into the blades surfaces.

The disk back face film coefficient distribution was calculated in accordance with an air flow assumed there.

PREDICTION OF AEROELASTIC INSTABILITIES IN ROTORCRAFT ENGINE DESIGN

by

Dino Dini
Istituto di Macchine, Università di Pisa
56100 Pisa, ITALY

SUMMARY

Design of modern rotorcraft engines requires that aeroelastic considerations be included for prediction of instabilities due to engines-rotors-airframe interference.

Computational approaches are presented which have generality in the selection of stress analysis methods and are applicable to rotorcrafts involving a large number of operation variables.

An instability criterion for the prediction of fatigue effects of alternating stresses on engine structural integrity is identified and applied to the corresponding airframe behavior during high speed forward flight and severe rotorcraft maneuvers.

LIST OF SYMBOLS

P	= rotor power	C_L	= lift coefficient = $2L/\rho V^2 cb$
Q	= rotor drag torque	L	= rotor lift coefficient = $200 L/\rho (\Omega R)^2 S_0$
M, H	= bending moment, torsional moment	C_m	= pitching moment = $2M/\rho V^2 cb$
TM	= blade torsional moment	θ	= pitch angle, torsion angle
T, L, D	= thrust, lift, drag	ψ	= azimuthal angle
G	= centrifugal tension	α_v	= tilt angle
S	= shear force	ω	= natural frequency
F	= blade loading	u, v, w	= displacements
L	= twisting moment	j, k	= unit vectors
C	= torsional moment of inertia per unit length span	e	= offset
EJ	= bending stiffness		
$E_s J$	= torsional rigidity		
V	= velocity		
v	= flow induced velocity		
Ω	= rotor angular velocity		
μ	= tip speed ratio		
m	= mass per unit length		
$\lambda_n \Omega$	= associated frequency		
L_A	= aerodynamic moment		
Δp	= pressure jump through the rotor disk		
ρ	= density		
A, S	= rotor disk area		
W	= weight		
c, n	= blade chord, blade number		
C	= lift or drag coefficient		
b	= blade span		
R, r	= blade radius		
x	= r/R		
σ	= solidity ratio = $nc/\pi R$		
β	= flapping angle		

SUBSCRIPTS

av	= available, average
h	= hovering, horizontal
i	= induced
r	= radius, ring
p	= profile, precone
d	= descent
f	= forward
t	= tip
c	= climb
2	= ultimate wake
D	= drag
t	= thrust
l	= lift
m	= moment
ψ	= azimuth
e	= elastic

INTRODUCTION

The author experience on helicopter damages occurred in accidents caused by particular factors, and attributed to flight-crew error or materiel failure and malfunctioning, has enhanced the conviction that the rapid trim change determined by the pilot is often interfering on engine in such way to give inadequate fuel feeding during the corresponding transient maneuver. In fact, the rotor blade aeroelasticity, as result of cyclically variable airloads, makes hard the engine control actuation.

The helicopter is practically a flying engine, an all engine aircraft, figure 1, in which the operating drag torque is largely variable during high speed forward flight, sudden upgust and unstable behavior. The fundamental limitation on maneuverability is the rotor's maximum equilibrium thrust capability, as instantaneously delivered by gas turbine engines running at much higher rpm.

Fatigue limits imposed on helicopter engines are more severe than in other automotive applications, because of the vibration level induced in the engine core, also in normal flight conditions.

In forward flight, the behavior of hingeless rotor is better than articulated rotor, but the wrong way to fly, as a conventional rotorcraft does, is to be overcome by a rotating flexible disk with pitch angle changing during each revolution. Abrupt maneuvers have to be avoided by the pilot of present conventional helicopters.

Engine control is crucial in transient operating conditions. For determining its influence on fatigue and lifetime of the rotating parts, we start, in this paper, with a short review of single rotor helicopter operation in uniform flight, to consider afterwards flight instabilities and cyclically changing required power due to airloads and aeroelasticity.

Because of the rotor-fuselage integration, aeroelastic instabilities and fatigue limits in rotorcraft engines might be predicted for a more reliable control system design.

FLIGHT OPERATION OF CONVENTIONAL SINGLE ROTOR HELICOPTERS

In order to obtain a rotor inclination for forward flight, the blades must climb from point A to point B and then dive from point B to point A, figures 2 and 3, due to pitch changes which result in angle of attack variations.

Such pitch control during a complete cycle (revolution) has been called the cyclic pitch stick; and the change of blade pitch is known as feathering. With respect to the rotor head, the blades must flap downward in diving from B to A and flap upward in moving from A to B.

Two types of control are necessary for the operation of the main rotor during forward flight:

- collective pitch stick, to govern the amount of lift generated by pitching contemporarily all the blades;
- cyclic pitch stick, to control the amount of forward thrust by changing the pitch of each blade individually during one cycle.

For the commonly used control by cyclically changing blade pitch, the hub may remain fixed to the shaft, and the blade pitch will be varying cyclically by special means, figure 4. This means consists of blades

attached to the hub, which are free to flap and free to change their pitch angles. The blades are held in pitch through a linkage connecting them to the swash-plate.

A fixed plate, surrounding the main rotor shaft, can be raised, lowered or tilted, by action of the control rods. A rotating plate, attached to the fixed plate through bearings, can be identically moved, figure 5.

Figure 6 illustrates the method by which both collective and cyclic pitch are induced into the rotor blades, Ref. 1. Three control rods

blades, Ref. 1. Three control rods from the control sticks via the mixing unit

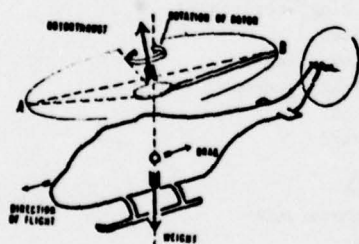


Fig. 2. Forward flight

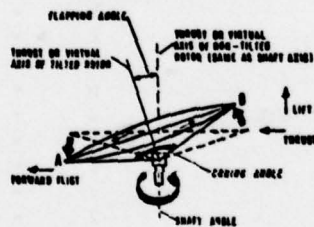


Fig. 3. Blade flapping

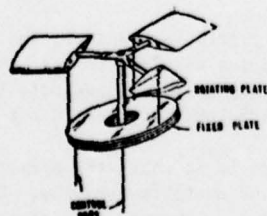


Fig. 4. Control by cyclic pitch-swashplate assembly

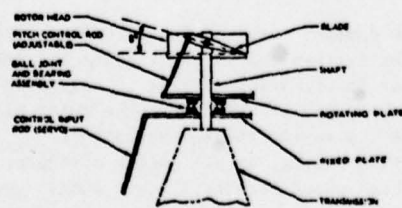


Fig. 5. Blade setting

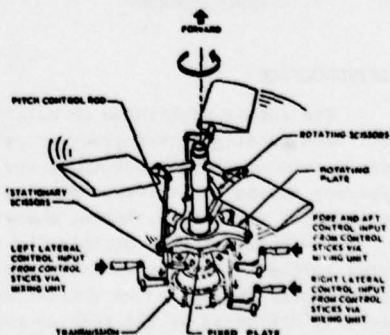


Fig. 6. Collective and cyclic pitch

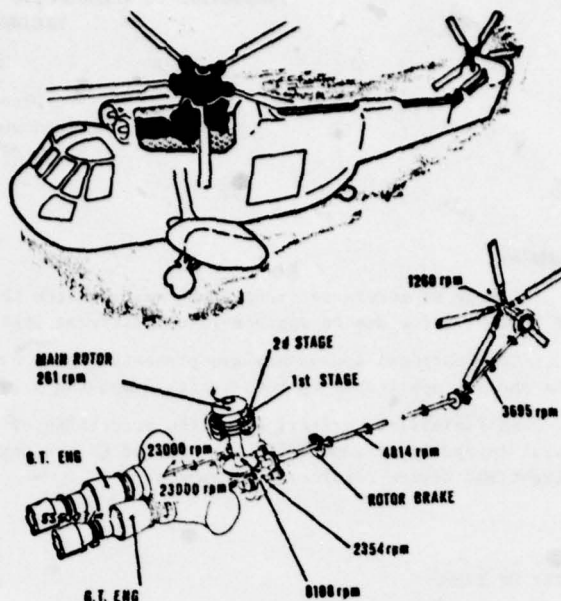


Fig. 1. The helicopter, practically an "all engine" aircraft

The fixed plate has four attachment points. Three of the points are connections for the input rods, while the fourth is reserved for the stationary scissory permitting the plate to translate and tilt but not to rotate. In figure 5 and 6, the fixed plate is low and level; the collective stick and the cyclic stick are there respectively full low and neutral.

By means of the mixing unit, cyclic and collective control may be used in any combination desired.

The blades at the lowest flapping point (A in figure 3) are not at their lowest pitch; as well as the blades at the highest flapping point (B) are not at their highest pitch. This is because of the precession property of the gyroscope, according to which an applied force is determining its consequential displacement 90 degrees in the direction of rotation from the point where the force is applied. For example, in the rotating disk of figure 8, an upward force applied to the right side of the disk would cause it to tilt upward 90 degrees of rotation from the point where the force would be applied. Thus, to achieve a forward rotor tilt, the force (pitch change) causing the blades to flap downward over the nose must be applied to the rotor on the right side of the helicopter; while the force causing the blades to flap upward over the tail must be applied on the left side of the helicopter. The blades will flap to the highest and lowest position, 90 degrees of rotation from where the pitch changes are applied. The cyclic pitch causing blade flap must be placed on the blades, 90 degrees of rotation before the lowest and highest flap are desired. For instance, when the pilot pushes the cyclic stick forward, the action will tilt the plate assembly in downward direction so as to place the lowest cyclic pitch on the blade over the right side of the helicopter.

Referring to figures 7 and 9, the plate input rods (servos) are located at 45 degrees angle to the longitudinal and lateral axes of the aircraft, for actuating up and down the lever tips which determine the blade feathering (pitch change). The relative power steering for the servos may utilize pressures as high as 1,500 - 3,000 psi.

Through the swash-plate method of rotor control, figure 4, it is easy to see how the addition of collective pitch causes greater thrust, figure 3. This is because all blades receive a pitch increase simultaneously. In the flight control rigging of a helicopter, the blades must be set at a predetermined angle, with collective pitch stick in its full low position, the plate level, and the cyclic pitch stick in neutral; so that the plate has no tilt, figures 5 and 6. The pitch control rods are then adjusted to place the rotor blade angle at, say, approximately 8 degrees above plane parallel with the rotor plate assembly. The required angle is chosen because it will produce normal autorotation rpm, considering blade twist.

For forward flight as an example, figure 9, utilizing the rigging figures of a current Sikorsky helicopter, Ref. 1, the corresponding movement of the cyclic stick has placed the pitch of the reference blade over the right side minus $5\frac{1}{2}$ degrees below a plane parallel to the rotor plate assembly. Moving the cyclic stick forward makes the blade on the right side reduce pitch to minus $5\frac{1}{2}$ degrees: a pitch change of $13\frac{1}{2}$ degree below the neutral reference of plus 8 degrees. It stands to justify that the blade on the left side would have a reading of plus $21\frac{1}{2}$ degrees; $13\frac{1}{2}$ degrees above the neutral reference of plus 8 degrees. The addition of collective pitch influences only the amount of thrust being produced by the rotor.

Pitch change is the only action controlled directly by the pilot. The other two actions, permitting the blades to flap, and to lead and lag in the plane of rotation, occur as natural function of pitch change and forces incurred during rotor operation, figures 10 and 11.

The original development of helicopters owes much to the introduction of hinges, about which the blades of an articulated rotor are free to move, eliminating the roll moment in forward flight and relieving the large bending stresses: an important step in the evolution of helicopters. Several problems are posed by the presence of hinges, figure 10, and dampers which are also fitted to restrain the leading and lagging motion, figure 12.

In recent years, improvements in blade design and construction have enabled rotors to be developed which dispense with the flapping and lagging hinges. These hingeless rotors, figures 13 and 14, have blades which are connected to the shaft in cantilever fashion, but which have flexible elements near the root, allowing considerable flapping and lagging freedom, as the flap hinge and the drag (lead-lag) hinge in the fully articulated rotors.

Now, a blade which is free to flap experiences large Coriolis moments in the plane of rotation, and a further hinge, called

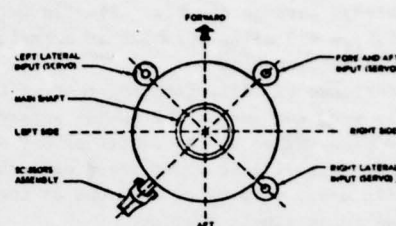


Fig. 7. Rotor control input positions

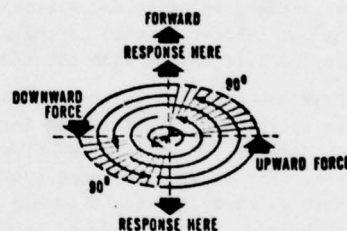


Fig. 8. Rotor gyroscopic precession

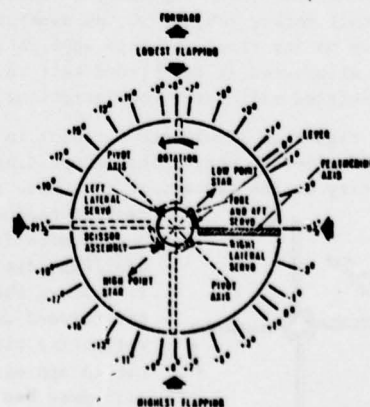


Fig. 9. Pitch change for forward flight in respect to a neutral reference of + 8°

the drag (or lead-lag) hinge, is therefore provided to relieve these moments. These rotor hinges are real in the articulated rotor (figure 10) and elastically equivalent in the hingeless rotor (figure 14). Essentially, the drag hinge is required in order that the blade may seek a position of equilibrium aft of the radial line, figure 11, in powered flight and autorotation, because of centrifugal and aerodynamic drag moments.

Offset distances, for both the hinges, real or elastically equivalent, are necessary for avoiding movements of the fuselage during the flight. Moments acting through the offset distances, will tend to line up the plane of the rotor head with the plane of rotation.

A single rotor helicopter must have some means of compensating for main rotor torque: this is the tail rotor, with its thrust applied in the direction against the force created by main rotor torque, figure 2.

The required airspeed to remain airborne in hovering flight, through lift by air flowing, is produced by rotating the blades through the air. The tip velocity may reach values as high as 450 miles per hour at normal rpm and 525 miles per hour in autorotation.

The increase of lift, from the root to the tip of the blade, varies with the radius (or speed) squared. Because also induced drag varies as the square of the speed, large amounts of induced drag will be experienced near the tips of the blades. Profile drag, varying as the cube of the speed, makes drag losses increasingly serious.

Such profile drag losses and that portion of the total induced drag losses caused by non-uniformity of inflow may be reduced by twisting the blade, so that higher pitch angles exist at the root of the blade than at the tip. Blade twist increases both the induced velocity (accelerated air) and the blade loading near the inboard section of the blade. In an ideally twisted blade the lift varies with the radius.

The blade twist pertaining to hovering flight extends its benefits to forward flight in the form of better rotor efficiency. Because the rotor blade tips operate at lower angles of attack, this area is unloaded sufficiently to postpone the occurrence of blade tip stall. Losses due to compressibility are also reduced because reduced lift coefficients cause the critical Mach number of the blade to increase. The relative wind, created by forward flight, effects not only the rotor blades but the entire helicopter. For instance, forward flight at 100 miles per hour is creating an airspeed differential of 200 miles per hour between the tip of the blade on the right (advancing) side of the helicopter and the tip of the blade on the left (retreating) side. Because lift (and thrust) varies as the square of the velocity, the variation or dissymmetry of lift between the two sides of the rotor disk becomes a serious problem. Dissymmetry of lift is caused by the fact that in forward flight the aircraft relative wind is additive to the rotational relative wind on the advancing blade, and subtractive on the retreating blade. Leaving the nose of the aircraft, the blade experiences a progressively decreasing amount of airspeed which reaches its lowest value over the left side of the aircraft and then increases to normal rotational velocity airspeed over the tail of the aircraft.

The blades may be cyclically feathered, decreasing the pitch on the advancing side and increasing the pitch on the retreating side, in order to equalize the lift on both sides of the rotor disk.

The tail rotor, subject to the same problem but with no ability to cyclically feather its blades, must rely solely on its flapping hinge application for equalizing the thrust dissymmetry. Thrust dissymmetry is generally eliminated in two-bladed tail rotors by utilization of a semi-rigid see-saw rotor hub, figure 15. In four-bladed tail rotor configurations the same results are obtained by the utilization of a delta hinge.

Figure 16 illustrates a rotor in forward flight at 100 miles an hour. Blade tip rotational velocity is 500 miles an hour. The interesting factor here is that while the main rotor shaft has no rotational velocity at its center, it does have airspeed. It is moving through the air at 100 miles an hour with the rest of the helicopter. The main rotor shaft has 100 miles an hour airspeed and, in the area from M to N, the air is actually blowing over the retreating blade from trailing edge to the leading edge.

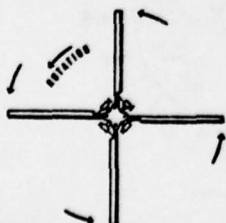


Fig. 12. Rotor dampers

It follows that, with a substantially constant rotor rpm, the greater the helicopter forward speed, the greater the advancing blade airspeed and the lesser the retreating blade airspeed. At 200 miles an hour, the helicopter's advancing blade tip is approaching 700 miles an hour airspeed, while the retreating blade's tip airspeed has been reduced to only 300 miles an hour. The critical Mach number of the advancing blade now becomes a problem, and the stalling out of the retreating blade tip poses an additional problem. While critical Mach values and drag divergence are not to be overlooked, blade tip stall is probably the more important

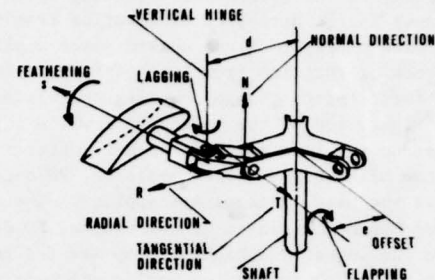


Fig. 10. Blade motion in articulated rotors

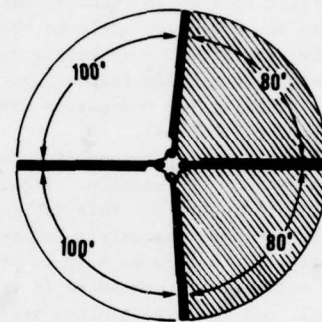


Fig. 11. Lead-lag motion in ground resonance

obstacle in the way of performance progress.

As a helicopter approaches higher and higher velocities, it encounters the basic factors causing stall. The retreating blade is losing airspeed. Its angle of attack at the tip is increasing. The loading at the tip is increasing; the blade stall is excessively loaded. Whenever the helicopter is flying at a forward high speed, where the retreating blade tips experience the beginning of stall, a vibration is felt in the cyclic stick and in the airframe itself. The vibration takes the frequency of the number of blades in the rotor system as applied to one rotation of the rotor.

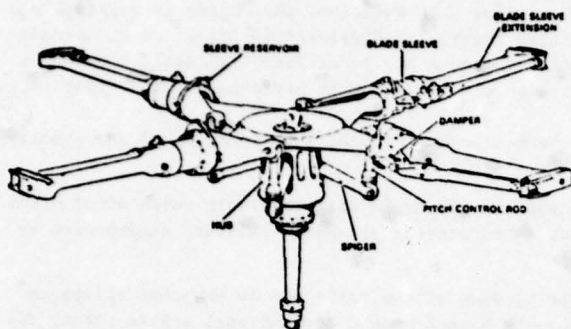


Fig. 13. Rotorhead of Westland W.G. 13 Lynx hingeless rotorcraft

With a four blade rotor, the vibration is a four per revolution. In figure 17, the airfoil is stalling at an angle of approximately 14 degrees, as shown by the shaded area. The tip of the retreating blade has the highest angle of attack and that from the reverse flow area outboard the angle of attack increases very rapidly. The advancing blade, on the other hand, possesses uniform low angle of attack.

In maneuvering flight, where sharp turns and abrupt pull-ups may be required, severe blade stall can be encountered because of rotor rpm decay or high load factors. Recovery in these cases is much more difficult, if the rotor is quite high loaded. Reduction of collective pitch and/or increasing rotor speed will help.

A chart or computer is utilized for the prediction of blade stall. The pilot is however expected to know and avoid the general conditions conducive to the stall condition. The important thing to remember is that blade tip stall is not solely associated with high aircraft velocities. It can occur, under certain conditions, at surprisingly low forward speed.

There are numerous unsteady aerodynamic events that may occur in a single revolution of a helicopter rotor system operating at moderate to high forward speeds. The severity of the dynamic airloads associated with the unsteady aerodynamic depends upon the specific operating condition. Some of the more severe operating conditions are: maximum forward speed in level flight, maneuvering flight, rapid descents, and flared landings in ground effect.

The practical limitations of rotor operation are much more analogous to turbine engine/inlet matching aerodynamics, where the fundamental problem is one of dealing with extreme, time varying, three-dimensional distortions of the rotor in flow distribution.

The impulsive airload, which can occur contemporaneously over large segments of the advancing side of the rotor disk, results in intense oscillatory structural loadings. The transient Mach number effects on the advancing blade include transient lift, drag, and pitching moments associated with the rapid

movement of the shock wave over the upper surface of the blade. The interaction of the shock wave and boundary layer can also induce transient shock stall.

Consideration of C_l versus C_m loop characteristics may be useful in analyzing dynamic stall.

Helicopter maneuvering flight is severely limited by unsteady aerodynamics, because of rapid increase in magnitude of the rotor oscillatory control loads and overall airframe vibration levels.

The important factors in the maneuvering flight unsteady airloads are wake geometry, tip-vortex flow, blade-

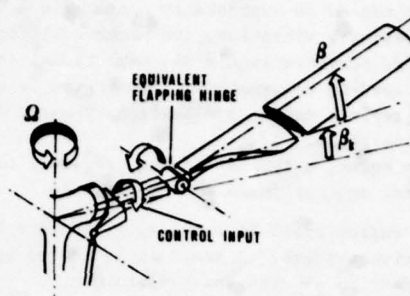


Fig. 14. Flapping equivalent system

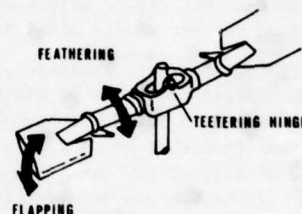


Fig. 15. Teetering rotor

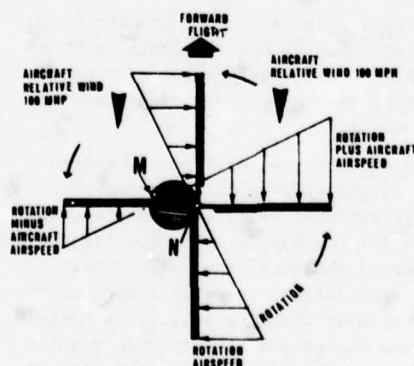


Fig. 16. Rotor in forward flight

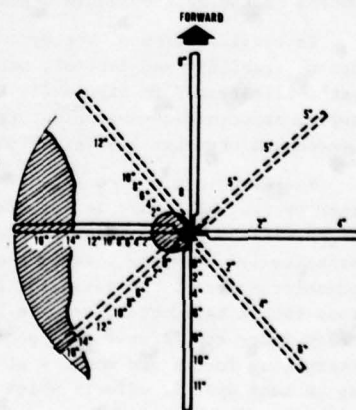


Fig. 17. Stall at an angle of 14°

vortex interaction, and dynamic stall.

A variable-geometry rotor could be a means to gain some control over the way tip vortices.

It is quite complex to simulate analytically flight maneuver loads on helicopter propulsion systems, considered as a whole from the rotor to the engine. High-performance gas turbine engines are sensitive to not only self-induced cyclically changing loads but also to extremely induced loads which result from helicopter maneuvers. These external loads cannot be adequately simulated for prediction of the complex force interactions; and experimental data, obtained from flight tests, are not sufficiently definitive.

The engine is expected to operate in a very hostile environment, being exposed to extremes of temperature, pressure, vibration, and mechanical forces within the engine. In addition, the engine is exposed to a variety of accelerations in all directions, thus imposing large inertial and gyroscopic forces on an already complex loading environment. The engine is expected to function under all conditions with small clearances between rapidly moving and stationary parts and to exhibit little degradation in performance after long periods of operation.

As it is known, a typical flight procedure consists of a check of output torque as a function of gas generator speed, against installed performance.

An engine stall is especially bad in a helicopter because of the rapid load reversals which occur in the rotor drive systems. A stall is indicated by a sudden drop in compressor discharge pressure accompanied by an increase in exhaust gas temperature.

Forward speed is limited by blade stall on the retreating side of the rotor and by compressibility on the advancing side of the rotor. In order to keep roll moments balanced on a conventional single rotor, the lift potential that can be developed on the advancing side of the rotor disc is limited by that which can be developed on the retreating side, figure 18.

According to the calculation, Ref. 2, of the forces acting on a rigid three blade rotor, figure 19 presents the azimuthal evolution of the blade local loads. The results obtained are satisfactory in respect to the ones measured in the S1 Modane wind tunnel, for the case of moderate advance ratio μ and of local incidences lower than that of profile stall. The calculation (for moderately loaded 3-blade rotor in figure 19, but valid also for heavy loaded rotor) accounts for compressible, three-dimensional and unsteady aerodynamics. The calculation has been adapted, with encouraging results, to the case of flexible blades.

From the rotor aeroelastic computer simulation of Ref.s. 3 and 4, figure 20, compares the measured and predicted time history of blade airloads.

The azimuthal evolution of the rotor torque is consequence of the n-blade airloads integration.

HELICOPTER SYSTEM INTEGRATION AND INTERRELATED FLEXIBILITIES, VIBRATIONS AND BLADE FLUTTER

The introduction of automatic flight control systems to helicopters has certainly enhanced their utilization, especially in the area of all-weather flight. Because of the high degree of systems integration, a complete system understanding requires a knowledge of the aerodynamic loops.

The propulsion system is also the support system, and the structural and aerodynamic complexities are compounded because of the integration. The propulsion-support system is also the means by which the control of the helicopter is accomplished.

In consideration of the dynamics of the helicopter and its influence on stability and control, one can look at the complex structural system illustrated in figure 21, Ref. 5, and consider the even more complex aerodynamic environment from whence come the many degrees of freedom and structural modes which exist.

The aerodynamic flow situation of a helicopter rotor is determined by its rotation. In forward flight, figure 2, the speed of flight will be superimposed to the rotational velocity, resulting in periodically changing velocities for the blades with opposite characteristics at the advancing and at the retreating side. That means that a helicopter, even in steady flight, is submitted to unsteady rotor conditions. The periodically changing velocities cause alternating forces and moments at the blades and at rotor hub, resulting in many dynamic effects which are determining the special characteristics of a helicopter.

When considering a helicopter under the aspects of dynamics, it consists of a complex system of an elastic fuselage and the rotating rotor. They represent an oscillating system which can be subject to self-excited oscillations under certain circumstances. They can occur either on ground or in the air and are called the classical ground and air resonance.

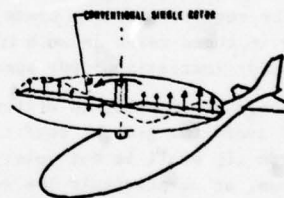


Fig. 18. Lift potential on the advancing and retreating blades

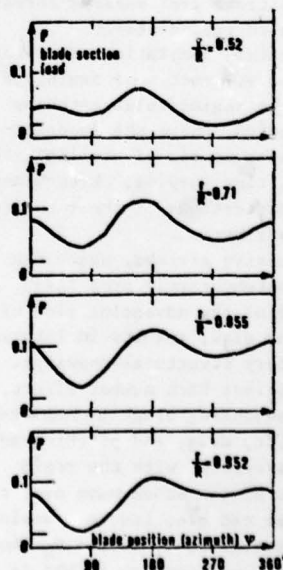


Fig. 19. Blade local loads

Up to the present time the frequency difference between rotor blade motions and fuselage oscillations has been sufficiently great to allow them to be considered separately. Recent studies have indicated that, because of the increased coupling between blades and fuselage as a result of increased hinge stiffness, this is no longer the case.

A simple explanation of the resonance occurring between fuselage motion and the in-plane motion of the rotor blades can be given by considering the motion of rotor center of gravity about hub for a stationary rotor but with the blades oscillating in the manner shown in figure 22, Ref. 6. For the four blades configuration and mode of vibration shown, it can be seen that the center of gravity rotates about the hub with a frequency Ω_i , this being the frequency of the fundamental in-plane blade motion. With the rotor rotating at a speed Ω , this wandering of the center of gravity results in a true rotation about the hub at a frequency $\Omega - \Omega_i$. Nominally, the frequency Ω_i is about 0.5Ω for the hingeless rotating blade and hence the critical resonance frequency is $\Omega - \Omega_i = 0.5 \Omega$.

The rotary wing itself basically does not have stability and control characteristics comparable to those of fixed wing vehicles. Particularly in forward flight the cycles imposed upon the rotor system can often enter regions of non-linearity, where their formulation for design purposes is extremely complicated. Problems arise from advancing and retreating blades, from interference of the rotor wake and blade passage, and from the various dynamic modes induced within the structure itself. Rotor blade stall is associated with the rapidly changing angle of attack which characterizes a helicopter rotor blade as it traverses the rotor disc, figure 52. Not only does the non-steady penetration of stall, particularly on the retreating side of the disc at high advance ratios, alter the lift characteristics of the airfoil; it also alters the lift and pitch moments for a given pitch control and shaft tilt. Negative aerodynamic damping results in excessive torsional loads feeding into the propulsion and control systems.

There are many different rotor blade hinge arrangements. Actually, the hingeless rotor, figure 13, is not really hingeless, since only flapping and lead-lag hinges have been removed, but not the feathering hinges. Truly hingeless rotors are presently being developed. At hingeless rotors the function of the hinges is replaced by a flap wise and chordwise (inplane) flexibility, thus reducing the structural moments by bending the blades.

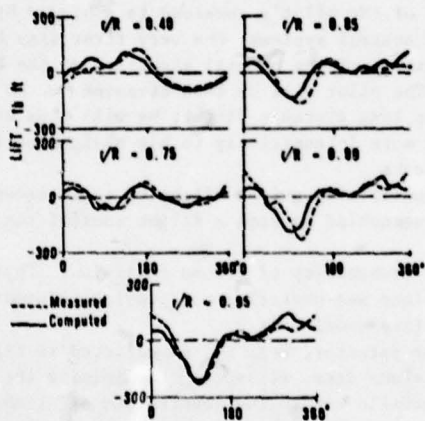


Fig. 20. Measured and computed time history of blade airloads

The effect of blade bending flexibility on articulated rotorcraft flight dynamics, figure 14, is significant but non substantial, and an analysis that assumes the blades are rigid in bending is often adequate. However, this is not true for hingeless rotors, figure 13.

The design philosophy is now to improve control dynamics by use of inner-loop feedback systems designed to improve helicopter handling characteristics, without changing the basic pitch or roll rate command type of control response. A distinction must be made between the integrated feedback system designed to be operative at all times and the auxiliary feedback systems that operate with only the basic controls. Articulated, figure 10, and teetering, figure 15, rotorcraft presently have auxiliary feedback system, so that flights can be made with or without the stability augmentation system (SAS). For hingeless rotorcraft with high speed capabilities, the increased gust sensitivity and increased angle-of-attack instability become increasingly more difficult to counteract without a feedback control system, Ref. 7.

Figure 23 is a simplified block diagram, for one axis, of the latest form of the Lockheed AMCS integrated mechanical feedback system, Ref.s. 8 and 9 and figure 24 and 25. The pilot input moment M_p combines with the feedback moment from cyclic flapping $k_r \beta_i$ to produce the input moment, to the floating gyro-swash-plate, $M = M_p - k_r \beta_i$, where k_r is the rotor feedback gain. The gyro acts as a first-order system with a lag τ . Its space-referenced attitude is given by $\theta = kM/(s + 1/\tau)$. The small term $1/\tau$ originates from the asymptot

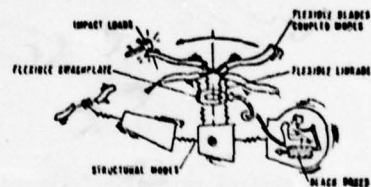


Fig. 21. Dynamics complexity of the structural system

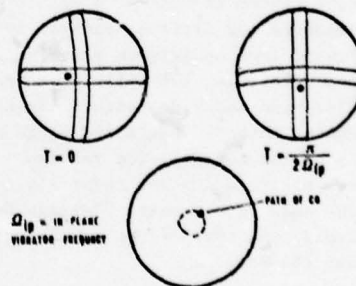


Fig. 22. Rotation of the center of gravity due to blade bending

ic alignment mechanism between gyro-swash-plate and fuselage, which can consist of either damping of the rotating gimbal axes or weak non-rotating centering springs. The difference between the gyro-swash-plate attitude is proportional to the cyclic pitch input $\theta_i = k_f(\theta - \theta_f)$, where $k_f = 0.7$, as indicated by the fuselage feedback loop. The cyclic pitch input θ_i is modulated by actuator and rotor dynamics to obtain the cyclic flapping $\beta_i = A\theta_i$. Cyclic flapping β_i is fed back as a gyro-swash-plate moment M and also produces the fuselage attitude change θ_f . θ_f is subtracted from the gyro attitude θ_i , so that the fuselage follows the attitude of the gyro which, in turn, is positioned by the pilot with the help of an attitude rate command $\dot{\theta}$.

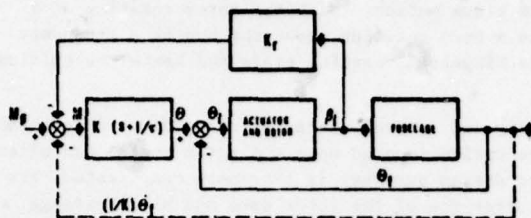


Fig. 23. Block diagram for the Lockheed AMCS

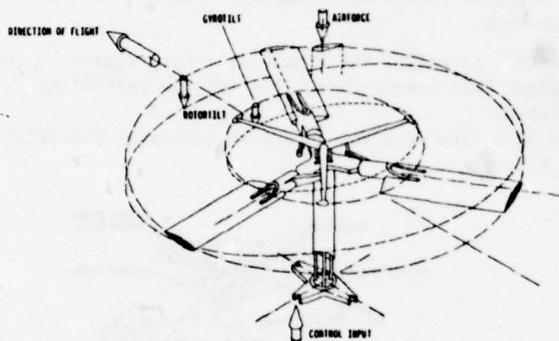


Fig. 25. Control gyro of the Lockheed rigid rotor

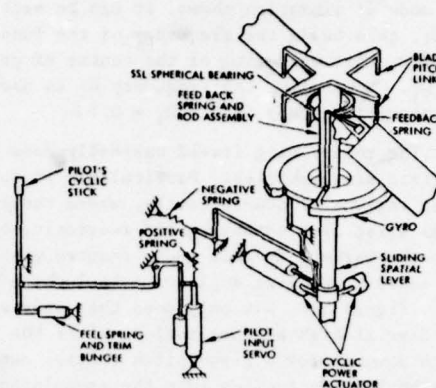


Fig. 24. Lockheed AMCS gyro-control system

The development of an optimal system concept for helicopters with all-weather capability belongs to the special problems on which the latest efforts have been concentrated. As a first and most important step, the relief of the pilot's workload is achieved by simple flight control systems, the very first step being, the elimination of the natural stability of the helicopter. The pilot will be less stressed on an all-weather long distance flight; he will thus be able to attend more intensively to his navigational and guidance tasks.

An automatically guided flight by radio reception will be enabled by such a flight control concept in-

volving attitude control, heading control and height control.

The closer the helicopter flies to the ground, the higher the probability of ground collision. Thus the need arises to provide a system that can sense terrain variations and obstacles and provide information to a control system to control aircraft maneuvers under all visibility conditions.

A composite low altitude control system with an external radar detector, Ref. 10, is depicted in figure 26. A forward looking azimuth scanning sensor provides elevation plane data, attempting to minimize the average clearance between the helicopter trajectory and the terrain profile within the constraints of climb, dive, acceleration and ride comfort limits. Data are furnished by electronic scanning, utilizing the phase interferometer method. Angle and range data are provided by synchronization and correlation of phase angle incidence of the terrain echo returns. The computer processes these data in combination with doppler derived helicopter velocity and radar altitude information, air data measurements and aircraft attitude and heading. In the case of automatic "Terrain Following", reference command signals are derived for the automatic flight controls, and the helicopter ultimately responds to cyclic and collective functions; the airframe response closes the loop.

Along with the consideration of dynamics, stability and control, we must consider the subjects of airloads, aeroelasticity, and mechanical instabilities. A structural instability excited by an oscillating air load could result in a unsteady, and possibly divergent dynamic situation. Coupling of structural modes in response to aerodynamic excitation is characteristic of the air resonance phenomenon. Whereas the problems of mechanical instability are from the structures and materials realm, one cannot ignore the direct coupling with aerodynamics which generate the driving force.

Unsteady airloads result from many phenomena as blade stalling, stall flutter, tip vortex/blade interaction, and other which generate both periodic and non-periodic loads. The error is extremely high in predicting both steady-state loads and transient loads. This is the direct result of the inability to properly represent the aerodynamic and dynamic conditions in mathematical model formulation. Mechanisms, as vibration absorbers, may be utilized for alleviating oscillating airloads, but a more effective mechanism is to reduce the driving force at its source.

The problem of fatigue has been recognized as an important aspect in the design of helicopters. Methods of predicting the fatigue and crack growth lives of structural components have, in turn, led to the need for more accurate loading spectra. The purpose of developing a realistic loading spectrum is to define a stress-time history that is representative of those stresses encountered by a component during actual usage. The informations that must be obtained in the development of helicopter fatigue fracture load spectra are:

The phenomenon is known as ground resonance because the vibration occurs when the aircraft is on the ground supported by its relatively soft tires and oleo struts, a support conducive to a low frequency movement. Ground resonance has always been one of the main dynamic problems of rotorcraft. The instability, created by the interaction of a helicopter's rocking on its tires and the oscillation of the blades about the drag hinges can cause destruction of the aircraft.

This type of dynamic instability occurs when a body vibration mode with horizontal rotor hub motion has a natural frequency equal to the rotor rotation frequency minus the blade lead-lag natural frequency, unless the body mode and the lead-lag blade mode are both sufficiently damped. Without aerodynamic forces on the blades, ground resonance cannot occur if the blade lead-lag natural frequency is higher than the rotor rotational frequency. Articulated blades cannot satisfy this condition and require friction or hydraulic dampers for the blade lead-lag motion in addition to adequate damping of those body modes for which frequency coalescence is possible. The most critical mode is usually the roll mode on the ground where the stiffness of the main landing gear determines the natural frequency of the body.

During ground resonance, the blades are definitely out of pattern. If one blade leads while an adjacent blade lags, the resultant out-of-balance condition of the rotor causes the shaft axis to follow the heavy or more centrifugally loaded section of the rotor. The common feature of ground and air resonances is the displacement of the centre of gravity of the rotor when the blades move out of phase with one another in the plane of rotation. Because both the rocking and the movement of the blades in and out of pattern excite each other to greater magnitudes, ground resonance forms an excellent example of negative stability or negative damping. Figure 11 illustrates how blades out of pattern can bias the centrifugal balance of the rotor system. The shaded portion of the rotor is the heavy side. Following the heavy side of the rotor, the shaft will describe a circle or eccentric which will cause the aircraft to rock, figure 22.

Ground resonance is the only major self-excited vibration applicable to helicopters utilizing articulated rotor systems. Analytical model for ground resonance, which neglects blade aerodynamic forces, is approximately valid for articulated rotors operating on the ground.

For semi-hingeless or hingeless rotors, the blade lead-lag natural frequency can be raised above the normal rotor rotational frequency. In this case, ground resonance (neglecting blade aerodynamic forces) cannot occur. Neither the blade lead-lag motions nor the landing gear require dampers to prevent the instability on the ground. Such blades are considered stiff inplane. Semi-hingeless or hingeless rotors designed with the blade lead-lag natural frequency below the normal rotor rotational frequency are called soft inplane. Such blades have a crossover rotor speed at which the blade lead-lag natural frequency equals the rotor rotational frequency. Below this crossover rotor speed, ground resonance cannot occur. Above this crossover frequency, the same precautions must be taken as for articulated blades. If the rotor rotational frequency minus the blade lead-lag natural frequency equals the frequency of a body mode having horizontal rotor motions, then both the blade lead-lag motion and the body motion must be sufficiently damped. For hingeless rotors on the ground and for any type of rotor in flight, aerodynamic effects become important and must be included in a stability analysis.

Air resonance is a much more recent phenomenon and has appeared with the introduction of the hingeless rotor. In this case it is found that the large hub moments which occur when the rotor tilts give rise to an airframe oscillation, even when the helicopter is airborne, which, although heavily damped and not really significant as a stability mode, may have a frequency close to that of the lagging motion of the blades. In coupled motion, the total blade damping is redistributed among the modes, and a weakly damped mode, such as the lag mode, becomes unstable. The ideal solution of the problem is to control the aeroelastic properties of the blade in such way that some of the high damping of the flapping motion is diverted into the lagging mode, and makes the whole system inherently stable.

Although the fuselage is a very complicated structure with distributed mass and stiffness, it can be regarded as a "free-free" beam acted upon by periodic forces at particular points. Considering the fact that a helicopter fuselage is fairly slender longitudinally, the most important forces are the vertical and lateral forces of the main rotor and the tail-rotor forces along the tail-rotor axis. To calculate this response, it is necessary to know the frequencies and mode shapes of the fuselage regarded as an assembly of elements, figure 28, having certain masses and stiffnesses. The first four mode shapes of the free fuselage are as sketched in figure 29, Ref. 11. The first two modes, (a) and (b), are rigid body modes whose natural frequencies are zero since no elastic deformation are involved.

The characteristics of a rotor with rigidly attached blades is determined by its aeroelastic behaviour. A rotor blade is of course very flexible, and the frequencies of the blade motion may coincide with the frequencies of forced motion of the natural frequencies of other parts of the helicopter. For engineering investigations, a simplified treatment is commonly used, assuming that the elastic cantilevered blade can be represented by a hinged, spring restrained, rigid blade. Practical rotor blades are quite flexible, in the sense that their first beamwise bending frequency is not very much greater than the once per revolution flapping frequency of an articulated rotor. For simple studies, it can be assumed that the blades have flexibility only in the flapwise direction and are infinitely stiff in the chordwise and torsional directions. The main features of such a flapping equivalent system are shown in figure 14; practically, it is a flapwise articulated rotor (figure 10) with a large hinge offset, Ref. 12. The flapping frequencies of hingeless rotor systems are about in the region of 1.1 to 1.2 of the rotor frequency; the equivalent hinge offsets are 12 to 22% of radius. In plane flexibility of rigidly attached blades can be treated in a similar way as flapping. The lagging motion, itself, behaves similar as in the case of articulation.

A system as described in figure 14, Ref. 13, with degrees in flapping, in chordwise and torsional direction, with additional control system flexibility, may be considered for fundamental studies. The elastic blade may be represented by a feathering hinge, a flapping hinge, and a lead-lag hinge, all elastically restrained. The analysis with the Bolkow BO-105 hingeless rotor helicopter, Ref. 13, assumes an additional outboard torsional hinge, also elastically restrained. The system is shown in figure 30. The rotor support is considered elastically attached to the body. Such MBB program, called "Blama" accepts up to 36 degrees of freedom: 8 for the body, 5 for the mast (excluding yaw), and 4 per blade (for up to 6 blades). The model includes precone, prelead, pitch-lead, pitch-flap, and flap-lead couplings.

Ref. 14 also considered empennage degrees of freedom.

Various hingeless rotor systems, with only 20% of the parts of an articulated rotor, are illustrated in figure 31.

Figure 32, Ref. 15, illustrates the different loading situation of a hingeless rotor and an articulated rotor with a small flapping hinge offset.

Figure 33, Ref. 16, shows the loading situation of a hingeless rotor in comparison to an articulated rotor.

Unsteady, or transient, aerodynamic phenomena contribute to rotor dynamic airloads. The stalled, impulsive, yawed and interference, flows are shown in figure 34, Ref. 17.

Stalled flow includes airfoil dynamic stall and tip-vortex induced dynamic stall: the first one associated with stall flutter due to airfoil modification.

Impulsive flow phenomena include blade-vortex interaction and transient Mach number effects.

Interference flow includes tail-rotor/main-rotor wake interaction, pylon-hub-engine exhaust interaction with the main and tail rotor, and wing body interference.

REQUIRED POWER IN HOVERING, FORWARD FLIGHT, AND MANEUVERS

The complex combination of external and internal operating forces and maneuver forces presents a big obstacle to determining the distortions occurring in the engine during helicopter flight. Because of rotor movement, case bending and ovalization, rotor shaft and blade bending, blade extensions, and thermal stresses, it is difficult to predict the relative movement of engine components under all flight maneuvers.

Abnormal vibrations in an engine installation may be caused by malfunctioning engine-mounted airframe accessories, engine mounts and other external connections, as well as by impulsive flow phenomena caused by blade-vortex interaction on the advancing side of the rotor disk. External airloads may be so highly unsteady to produce engine instabilities going from those accompanying the distinctive "blade slap" acoustic signature of some helicopter rotors to those determining engine fatigue, failures and stop.

The need for accuracy in calculations of engine-rotor performance can be emphasized by noting that a 1% change in the lifting capability of a rotor, at a given rotor input, may mean a 10% change in payload for the helicopter. From the other hand, accuracy in performance calculations is required because the engine could be not able to support instabilities due to unsteady airloads on the helicopter rotor.

Actual performance predictions within defined flight regimes and maneuvers may be carried out on the basis of induced velocity, thrust and power, related to rotorcraft operation.

The power required to support or propel the helicopter is divided between the overcoming of profile drag, parasite drag and induced drag, and the producing of climb and acceleration. Profile drag is the frictional resistance caused by the rotor blades as they pass through the viscous air. Induced drag is the drag incurred in the production of lift. Parasite drag is that which is incurred by any portion of the helicopter (fuselage, cowlings, landing gear, struts, etc.) which does not contribute directly to lift or thrust.

In order to keep the helicopter airborne, the rotor must produce thrust, by giving momentum to a mass of air. In so doing, power must be spent to produce acceleration of the air.

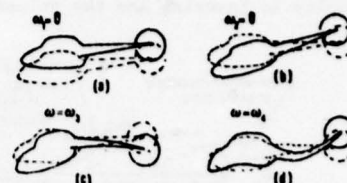


Fig. 29. Fuselage deformation modes

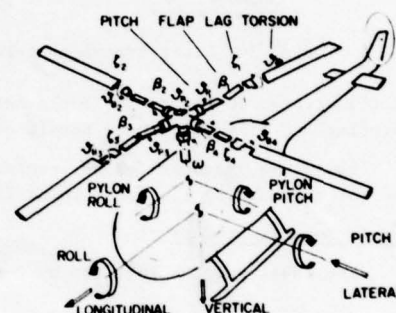


Fig. 30. System for MBB "Blama" program

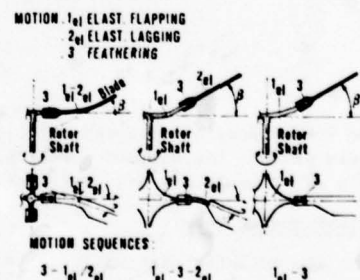


Fig. 31. Hingeless rotor systems

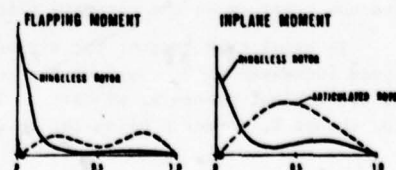


Fig. 32. Moments for the hingeless and articulated rotor

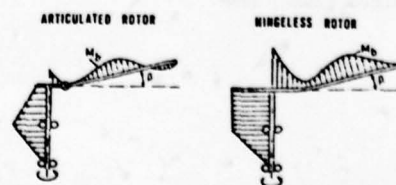


Fig. 33. Loading in rotors

For the normal hovering helicopter, 65% of the total available power might be for the overcoming of rotor induced drag and approximately 35% for rotor profile drag. In addition, the engine must supply power to turn the tail rotor and overcome friction in the transmissions and drive system, and rotor losses. In level flight, the sum of the values of each of the curves, figure 35, at any given airspeed would give the total power required. Profile drag power increases only slightly as normal forward speed is increased. At very high forward speeds, and as blade stall is entered, it mounts rapidly. Parasite power required, varying as the cube of the airspeed, increases very rapidly at higher speeds. At zero airspeed, the induced power requirement is quite high because the downwash velocity is near maximum value. An approximation of a resultant power required curve is offered in figure 36, considering the high induced velocity in hovering and the values of fuselage or parasite drag at the higher speeds.

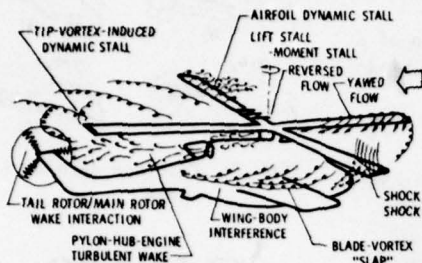


Fig. 34. Rotor transient aerodynamics

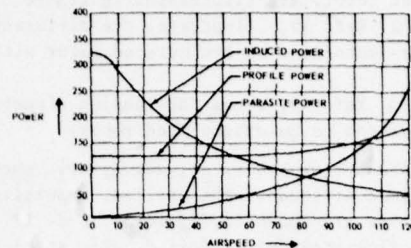


Fig. 35. Engine power distribution

As illustrated in figure 36, for a helicopter with adequate power, there is ample power available to permit hovering and climbing and to permit overlanding of the helicopter as airspeed is built up.

Power requirements for helicopters may be derived from the evolution of a physicomathematical model of the rotor according to the basic rotor theories.

Simple momentum theory -

The ideal power P required by a simple thrust generator is

$$P = T V + \frac{1}{2} v_i \cdot T \quad (1)$$

where T , V and v_i , denote thrust, flight velocity, and fully developed induced velocity. For the case of static thrust generation, "hovering", ideal induced power and thrust per horsepower are

$$P = \frac{1}{2} T v_i = \text{ft pds/sec} \quad (2)$$

$$T/P = 1,100/v_i = \text{pds/hp} \quad (3)$$

The lowest possible induced velocity in the fully developed slip-stream, in the static thrust generation, would produce the maximum thrust per horsepower.

This model would not be sufficient in dealing with practical problems of rotary wing aircraft.

Actuator-disc theory -

The actuator-disc analysis is better suited to simulate an open airscrew. An actual helicopter rotor is substituted with a disc perpendicular to the generated thrust and capable of imparting axial momentum to the fluid and sustaining pressure differential between its upper and lower surface. The thrust is uniformly distributed over the rotor disc across which there is a sudden jump of pressure Δp , as an assumption that the rotor has an infinite number of blades. No rotation or "swirl" is imparted to the flow, Ref. 18, and the pressure in the ultimate slipstream is the same as the pressure of the surrounding undisturbed air.

In axial translation: the air velocity far upstream of the rotor is the climb velocity V_c ; the airspeed increases to $V_c + v_{ic}$ at the rotor itself. Assuming that the pressure in the final wake is the same as the ambient pressure, we have an induced velocity v_{ic} half the value v_2 in the ultimate wake, and a rotor thrust T , (A and ρ being the rotor disc area and the air mass density)

$$T = \Delta p \cdot A = \rho A (V_c + v_{ic}) v_2 = 2 \rho A (V_c + v_{ic}) v_{ic} \quad (4)$$

In particular, in hovering flight (h), figure 37, $V_c = 0$, and thrust, induced velocity, and ideal induced power, are

$$T = 2 \rho A v_{ih}^2 \quad (5)$$

$$v_{ih} = \sqrt{T/2 \rho A} \quad (6)$$

$$P_{ih} = T v_{ih} = T^{3/2}/\sqrt{2 \rho A} = W^{3/2}/\sqrt{2 \rho A} \quad (7)$$

With a disc loading $T/A = 250 \text{ N/m}^2$ and a helicopter weight $W = 45,000 \text{ N}$

$$v_{if} = 10.2 \text{ m/sec} ; \quad 45,000 \cdot 10.2/1,000 = 453 \text{ kW}$$

and this would represent about 60 per cent of the total power in hovering flight, the rest being used to overcome the blade drag and tail-rotor and transmission losses. In practice the hovering power may be 10-15 per cent larger than the "ideal" value just calculated, Ref. 11.

The ideal hovering power, eqn. 7, expressed in horsepower (with T and v_{ih} in pds and ft/sec) becomes

$$P_{ih} = T \cdot v_{ih}/550 = \text{hp} \quad (8)$$

$$P_{ih}/T = \text{power loading} = v_{ih}/550 = \sqrt{W/2\rho A}/550$$

Solving eqn. 4 for v_{ic} , we have in vertical ascent

$$v_{ic} = -V_c/2 + \sqrt{V_c^2/4 + T/2\rho A} = -V_c/2 + \sqrt{V_c^2/4 + v_{ih}^2} \quad (9)$$

$$P_{ic} = T(V_c + v_{ic})/550 = W(V_c/2 + \sqrt{V_c^2/4 + v_{ih}^2})/550$$

In the same way, it is in vertical descent

$$T = 2\rho A(v_{id} - V_d)v_{id} \quad (10)$$

$$v_{id} = V_d/2 + \sqrt{V_d^2/4 + v_{ih}^2} \quad (11')$$

$$P_{id} = T(v_{id} - V_d)/550 = W(-V_d/2 + \sqrt{V_d^2/4 + v_{ih}^2})/550 \quad (11'')$$

The actuator disc theory is quite applicable to the cases of vertical ascent and hovering, but inadequate for performance predictions in vertical descent.

Assuming, as a better alternative, a pressure in the ultimate wake corresponding to the ambient pressure plus $\rho v_w^2/2$, we get, Ref. 11, an induced velocity in hovering about 6 per cent lower, for a given disc loading, than in the case of eqn. 6. Considering the small difference, it is reasonable to assume that the wake pressure and the ambient pressure are equal.

The vortex-ring state, figure 38, occurs when the rate of descent is of the same order as the induced velocity in hovering flight.

At higher rates of descent the recirculation ceases, the air slows down on passing through the rotor and the condition is known as the windmill-brake state, figure 39.

Of particular interest it is the state of "ideal autorotation", figure 40, in which there is zero mean flow through the rotor, so that $V_d = v_{id}$. This occurs when

$V_d/v_{ih} = 1.8$. This condition is equivalent to the motion of a circular plate broadside on to the stream which destroys the momentum of the air approaching it. The relative drag coefficient C_D may be carried out equating the thrust of the rotor to the drag of such disc

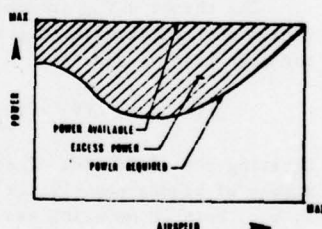


Fig. 36. Excess power

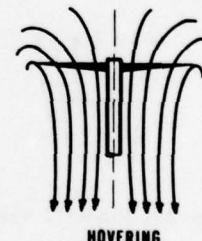


Fig. 37. Hovering flight

$$T = 2\rho A v_{ih}^2 = \rho V_d^2 A C_D/2 \quad (12)$$

from where $C_D = 1.23$, which is close to the drag coefficient of a circular plate.

The neglect of the swirl velocity is justified, because the flow upstream of the rotor is irrotational, and the swirl velocity behind the rotor, due to the bound circulation about the blades and the spiral vortex lines forming the slipstream, behaves a jump pressure Δp only about 0.5 per cent larger than the one before considered.

In the non-axial translation (forward flight), the ideal power required P_{if} , figure 41, for a flight speed V_f , is

$$P_{if} = T \cos \alpha_v \cdot V_f \sin \gamma + T \sin \alpha_v \cdot V_f \cos \gamma + T v_{if} \quad (13)$$

where the three distinct terms correspond to the powers to perform, respectively, the work against gravity in climb, the horizontal component of the total drag, and the induced power associated with the process of thrust generation. The thrust balancing the gross weight W times k_{vf} coefficient, accounting for the vertical drag in forward flight, is $T \cos \alpha_v = k_{vf} \cdot W$. For those cases when $T \cos \alpha_v = W$ and $T \sin \alpha_v/W$ quite small,

it may be assumed $T = W$ and

$$P_{if} = W(V_f \cdot \sin \gamma + D_{hf} \cdot V_f \cos \gamma / W + v_{if}) \quad (14)$$

with $D_{hf} = T \sin \alpha_v =$ horizontal drag.

In horizontal flight, as particular case, the first term is not considered.

In forward flight, figure 41, the flow velocity u in the direction of thrust and the vertical rate of climb are

$$u = 550 P_{av} / T \cos \alpha_v \quad (15)$$

$$V_c = 550 (P_{av} - P) / T \cos \alpha_v \quad (16)$$

where P_{av} and P are the ideal power available at the rotor and the power required in horizontal flight.

Blade element theory -

A more representative picture of all the blades belonging to a single rotor is permitted in a physico-mathematical model depicting the aerodynamic phenomena occurring at each blade element.

Considering, Ref. 19, the blade of a rotor composed of narrow elements dr wide, having a chord c_r and a defined airfoil section, we have on each element, figure 42, lift dL_r , profile drag dD_r , thrust dT_r , torque dQ_r and power dP_r required for axial translation and hovering

$$dL_r = \rho (\Omega r)^2 \cdot C_{lr} \cdot c_r \cdot dr / 2 \quad (17)$$

$$dD_r = \rho (\Omega r)^2 \cdot C_{dr} \cdot c_r \cdot dr / 2 \quad (18)$$

$$dT_r = dL_r \cos \phi_r - dD_r \sin \phi_r \quad (19)$$

$$dQ_r = (dL_r \sin \phi_r + dD_r \cos \phi_r) r \quad (20)$$

$$dP_r = dT_r (V_c + v_{ir}) + dD_r \cdot \Omega r \quad (21)$$

The section lift coefficient C_{lr} is equal $a_r \cdot \alpha_r$, where α_r is the slope of the lift curve for the airfoil of the blade element, with

$$\alpha_r = \theta_r - (\phi_{r1} + \phi_{r2}) = \theta_r - \tan^{-1} |(V_c + v_{ir}) / \Omega r|$$

The thrust dT_{rr} produced by an elementary ring of width dr and radius r in axial translation, figure 43, can be expressed according to the actuator disc theory, eqn. 4

$$dT_{rr} = 2 \rho A (V_c + v_{ir}) v_{ir} = 4 \pi r \cdot \Omega \cdot dr \cdot \rho (V_c + v_{ir}) v_{ir} \quad (22)$$

Equating the rigid side of eqn. 22 to the elementary thrust experienced by n number of blades eqn. 19 for b blades, we can solve for the induced velocity v_{ir} , both in hovering and vertical ascent (descent), as function of the tip speed $V_t = \Omega R$ and the rotor solidity $\sigma = n c R / \pi R^2$.

Knowledge of induced velocity distribution, along the blade, and hence of vertical lift coefficients, permits calculation of the rotor thrust and power in hovering and axial translation using the blade element approach. Substituting Rx for r and the non-dimensional v_{ir}/V_t for v_{ir} , we have from eqn. 22 the total drag in climb and hovering

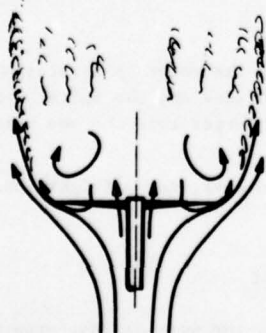


Fig. 40. Ideal autorotation flow

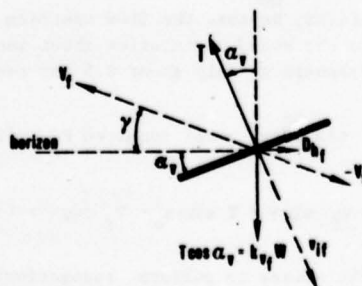


Fig. 41. Forward flight

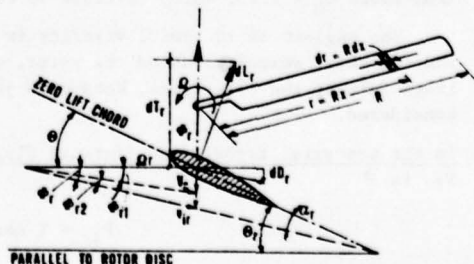


Fig. 42. Forward flight according the blade element theory

$$T_c = 4 \pi R^2 V_t^2 \rho \int_{x_i}^{x_e} (V_c/V_t + v_{ir}/V_t) v_{ir}/V_t |x| \cdot dx \quad (23)$$

$$T_h = 4 \pi R^2 V_t^2 \rho \int_{x_i}^{x_e} (v_{ir}/V_t)^2 \cdot x \cdot dx \quad (24)$$

where x_i is the inboard station of the blade and $x_e < 1$ takes into account the tip losses reducing the blade radius at the effective value $R_e = x_e R$. A computerized integration of eqns. 23 and 24 can be made through the analytical relation between v_{ir} and x .

The non-dimensional thrust coefficients, based on the disc area πR^2 , or referred to the blade area $b c R$, are, respectively, for instance in hovering

$$C_t = T_h / \pi R^2 \rho \quad ; \quad c_t = C_t / \sigma \quad (25)$$

For small angle ϕ_r assumption ($d T_h = d L_h$), the thrust of a blade element in hovering is

$$d T_h = \rho V_t^2 x^2 b c R \cdot dx \cdot C_l / 2 \quad (26)$$

and the total thrust and profile power, assuming C_l and C_d (profile drag coefficient) constant along the blade span, and integrating within $x = 0$ to $x = 1$

$$T_h = \rho V_t^2 \sigma \pi R^2 \cdot C_l / 6 \quad (27)$$

$$P_h = \rho V_t^3 \sigma \pi R^2 \cdot C_d / 8 \quad (28)$$

In axial translation as well as in hovering the induced power becomes

$$P_{ih} = 4 \pi R^2 V_t^3 \rho \int_{x_i}^{x_e} (v_{ir}/V_t)^3 x \cdot dx \quad (29)$$

A correct prediction of forces acting on the blade in forward flight, by the blade element theory, is obviously not possible.

In two-dimensional approximation, excluding all of the aspects of unsteady aerodynamics, corrections for oblique flow at various azimuth angles, effects of blade centrifugal field on the boundary layer, etc., the prediction may be simplified to the case of a steady-state flight.

The aircraft is moving at constant speed V_f along the inclined path where V_c is the vertical component and V is the horizontal component, figure 44. The speed component parallel to the airscrew disc is

$(V \cos \alpha_v - V_c \sin \alpha_v)$ and $(V - V_c \alpha_v)$ in the case when the tilt angle α_v is small, as it is usually in all helicopter flight regimes.

In the case of horizontal flight, the parallel component may be considered as identical with the speed of flight V_f . Measuring azimuth angle

from the blade downwind position, figure 45, the blade element perpendicular component is $V_b = V_f \cdot \sin \psi$. Consequently, for the blade element in figure 45, the total resultant velocity experienced in the plane of the disc will be $(V_t \cdot x + V_f \sin \psi)$.

With a blade without twist, the blade element in figure 45, at an azimuth angle ψ , has an angle of attack $\alpha_{r\psi}$ corresponding, figure 42, at the pitch angle $\theta_{r\psi}$ minus the total inflow angle $\phi_{r\psi}$.

Within the limits of the small angle assumptions, and lift coefficients expressed as after eqn. 21, total thrust $T \approx L$, profile drag torque Q_p , total drag torque Q , rotor profile drag power P_p and rotor total power P , result

$$T = \frac{1}{4} \sigma R^2 \rho \int_{x_i}^{x_e} \int_0^{2\pi} |(V_t \cdot x + V_f \cdot \sin \psi)^2 a_{r\psi} (\theta_{r\psi} - \phi_{r\psi})| dx \cdot d\psi \quad (30)$$

$$Q_p = \frac{1}{4} \sigma R^3 \rho \int_{x_i}^{x_e} \int_0^{2\pi} (V_t \cdot x + V_f \cdot \sin \psi)^2 \cdot C_{dr\psi} \cdot dx \cdot d\psi \quad (31)$$

$$Q = \frac{R}{2\pi} \int_{x_i}^{x_e} \int_0^{2\pi} \phi_{r\psi} \cdot x \cdot d L_{r\psi} \cdot d\psi + Q_p \quad (32)$$

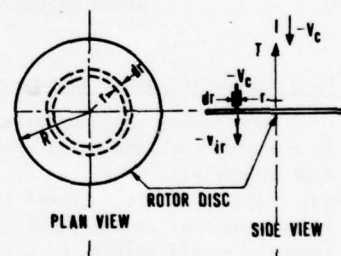


Fig. 43. Thrust by an elementary ring according the actuator disc theory

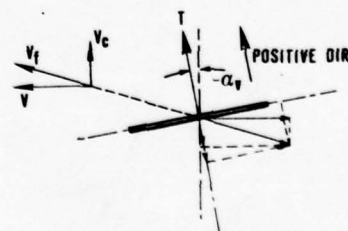


Fig. 44. Speeds in forward flight

$$P_p = Q_p \cdot \Omega \quad (33)$$

$$P = Q \cdot \Omega \quad (34)$$

The picture of the aerodynamic events obtained with the blade element theory, although much more detailed than that provided by the momentum theory, is still somewhat idealized.

Vortex theory -

The phisicomathematical models based on either the momentum or combined momentum and blade element theories cannot help to handle design problems and aerodynamic phenomena as tip losses, impulsive loading, etc. Various techniques of flow visualization reveal the presence of vortices in the wake in all regimes of flight, especially springing from the blade tips.

The vortex wake models developed by Ref. 20 for hovering flight are, figure 46; (a) the "simple" model in which each blade (represented by a lifting line) is assumed to shed a single vortex filament from the tip; (b) the simple model to which has been added an inboard vortex sheet shed from each blade at radii less than that where the maximum bound circulation occurs; and (c) a model in which each blade (again represented by a lifting line) sheds an inboard vortex sheet and an outboard vortex sheet which rolls up rapidly to form a tip vortex. Thrust and power coefficients are carried out for practical applications. More difficult task should be the development of a model for forward flight.

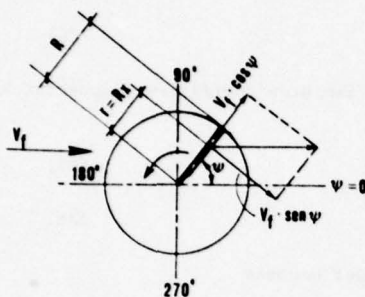


Fig. 45. Resultant velocity in the plane of the disc

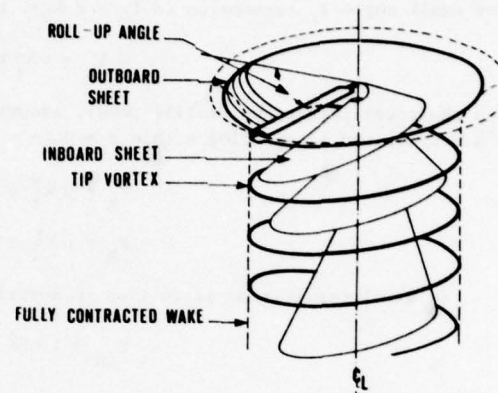


Fig. 46. Models of the vortex wake

Load factor and power in maneuvers -

Considering maneuverability, the load factor capability is most important. The limits are engine power in a steady turn and rotor stall in a deceleration turn. For future helicopters, g - levels over 2.0 up to high speeds will be required.

Peak engine power is required in maneuverability to make rapid changes in flight path and attitude under the precise control of the pilot, as, for instance, in hovering maneuvers (turns, jump take-offs and quick descents), accelerations and decelerations, and target acquisition. Load factor varies over a wide range through the maneuver. A typical turn maneuver is described on figure 47. In order to accomplish turn maneuvers, an analytic autopilot is required to present the pilot flight-path control in executing the maneuver with load factor as high as 2.0. After a load factor build up time, it follows a maneuvers execution time of 3 seconds during which the load factor equals or exceeds the specified level. For instance, the terrain-avoidance maneuver requires pull-up to achieve 1.75 g's at 150 knots within 1.0 second, sustain 1.75 g's for 3.0 seconds, push-over to achieve 0.0 g for 1.0 second. The BO-105 hingeless rotor helicopter, for instance, Ref. 12, offers the potential, as other modern helicopters, for acrobatic loop, figure 48.

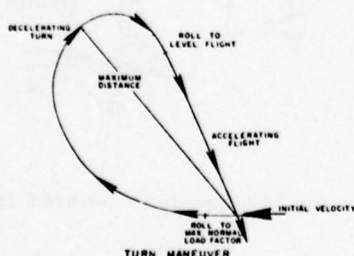


Fig. 47. Typical turn maneuver

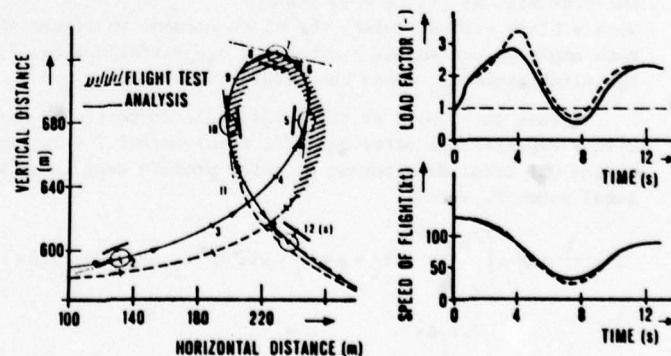


Fig. 48. Potential for acrobatic loop

In military helicopters, rapid and extreme maneuvers will be necessary, with: maximum load factors up to 2.5, roll angles up to 80 degrees, rolling speeds up to 50 degrees per second, pitch angles up to 40 degrees, and pitching speeds up to 40 degrees per second. The rapid rate of changes of these parameters up to their extremes will, of course, result in high loads and high consequential engine power.

From the point of view of the overall airframe vibration levels, there are severe limitations imposed upon helicopter maneuvering flight by unsteady aerodynamics. The source of the problem is usually a buildup in

the unsteady airloads induced by distorted wake flow, blade vortex interactions, and dynamic stall. Time histories of several aircraft state and control variables are shown in figure 49, Ref. 21, for a rapid deceleration from forward speed to the hover, whilst maintaining about constant height. This is a typical helicopter maneuver, figure 50, in which the fuselage attitudes attained are high, leading to reduced visibility of the ground, coinciding with maximum activity in terms of pitch rate and acceleration. Inspection of the collective pitch time history shows a very considerable variation, especially when the aircraft attitude is approaching its maximum, even though the rotor thrust level has changed very little throughout the maneuver. The same applies, though to a lesser extent, to the cyclic pitch change and the longitudinal flapping or disc tilt.

If a constant low height is to be maintained, then control must be very precise as any error could quickly place the aircraft in a dangerous situation.

ROTOR SHAFT TORQUE PERIODIC OSCILLATIONS IN FORWARD FLIGHT AND MANEUVERS DUE TO AEROELASTIC COUPLING ROTOR BLADES

The introduction of gas turbine power in helicopters and the evolution of rotor blade design have effectively removed the power limitation from helicopter performance. One of the more serious problems now limiting forward speed and gross weight is the occurrence of unacceptably large blade torsional oscillations due to the periodic stalling and unstalling of each blade on the retreating side of the rotor, Ref. 22. Even though the solution of the problem is significant in regard of performance gains, it impacts also on either the thrust producing capability or power requirements of the rotor system. If the oscillations are harmonic at high angle of attack, the relative damping may become negative and the blade may develop a self-excited limit-cycle oscillation, the so called "stall flutter". While the flutter of hingeless blades is due to the coupling between blade flapwise and lagwise motion, leading to instability at large blade pitch settings, the instability associated with stall flutter is due to the adverse time phasing of the aerodynamic torsional moment resulting from the loss of blade bound vorticity during torsional motion at high angles of attack.

Significant transient loading of engine structure itself will be associated with rotor blade torsional and flap-lag oscillations. Moreover g forces from helicopter turns, pull-ups, hard landings, etc., act on the lifting and thrusting rotor and cause displacement of the rotating parts of the engine, as consequence of accelerations as high as 10 g in some maneuvers. Large gyroscopic moments are created when a spinning body such as the turbo-engine rotates about some axis other than its spin axis. The size of these moments is a function of the body spin speed, mass and distribution of mass of the spinning parts about their spin axes (as transmission systems with roller gear reduction unit), and the helicopter pitch/yaw rate. The resultant forces cause damaging cyclic bending of the rotating disks, blades and shaft. Gyroscopic moments of military helicopters may be of the order of 200,000 ft-lb. It should be noted that gyroscopic forces are generated not only by helicopter maneuvers but can also be induced on engines. With the per cent occurrence of the standard maneuvers load spectrum the calculated lifetimes may be more than 5,000 hours for the rotor shaft, 11,000 hours for the rotor hub and 22,000 hours for the blades, and much less for the gas turbine engine.

Vibration in helicopters may lead to excessive levels of fatigue, discomfort and performance decrement. It is common practice to design, as far as it is possible, the fuselage such that the natural frequencies of the major normal modes are well separated from the rotor forcing frequency. The analysis may be applied to the problem of determining which part of the fuselage structure of a particular helicopter is most effective in reducing the rotor induced vibrational response in the region of the pilot's seat. In fact, in the design stage of a helicopter fuselage, the vibration levels are kept to a minimum, particularly in the crew and passenger area. This may be achieved by introducing vibration absorbers and also modification of the fuselage structure (damping elements mounted on the rotor head or in the fuselage), or by designing the gearbox and engine mountings so that the transmission of oscillatory forces is suppressed. The loading of the rotor shaft and the gearbox with its suspension is different in the two cases of articulated or hingeless rotor, in transferring high moments from the rotor blades to the hub and the fuselage, mainly by inclination of thrust vector (thus producing a moment around the center of gravity of the helicopter) in the first case, and, in second case, by combination of thrust vector inclination with a strong hub moment (thus combining these two moments).

Influence of blade flexibility and stall flutter on rotor shaft torque in forward flight -

Local blade loading and required instantaneous rotor torque are variable during the motion. For instance, figure 51 shows that the rotor blade of a particular helicopter in forward flight at tip speed ratio

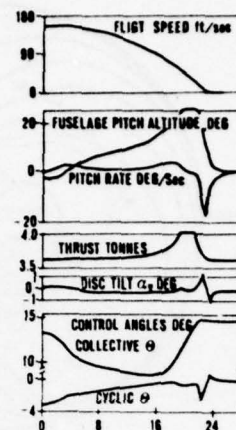


Fig. 49. A deceleration manoeuvre time history

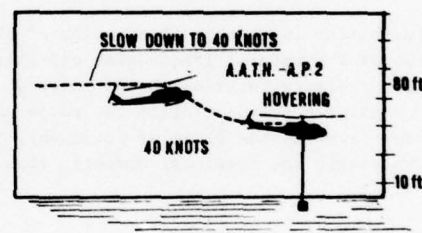


Fig. 50. Automatic approach

$\mu = (V \cos \alpha_{vf}) / \Omega R = 0.33$ has to operate at incidences which vary periodically each revolution. On the advancing side, the incidences are small while on the retreating side they are large and, for the greater part, correspond to angles well above the static stall angle of a typical blade section. As a given blade advances, the tip vortex from the preceding blade may pass closely underneath it, as indicated in figure 52 for $\mu = 0.2$, and the point of intersection moves inward along the blade as ψ increases. The flow disuniformity and the consequent variable shaft torque are enhanced by blade flexibility.

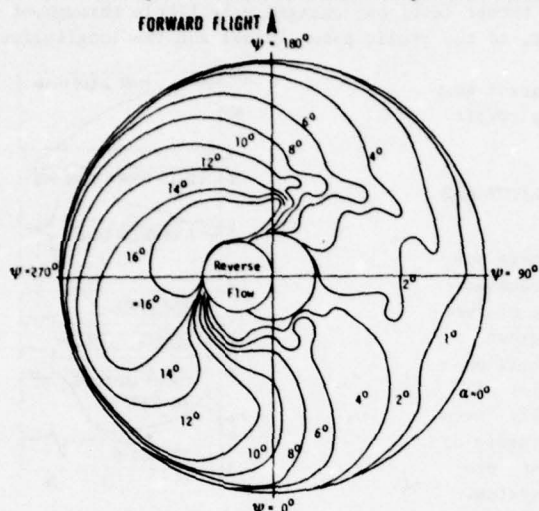


Fig. 51. Angle-of-attack distribution with non-uniform downwash. $V = 140$ knots

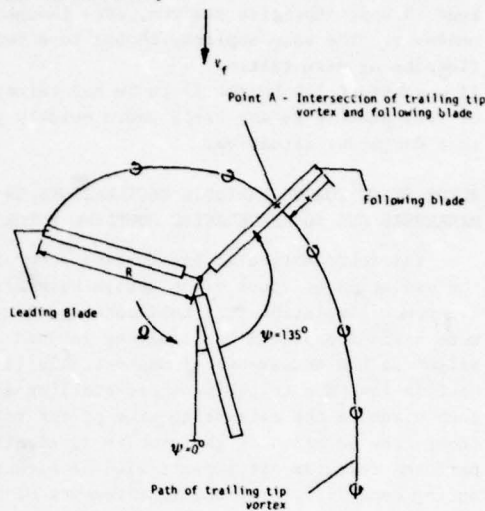


Fig. 52. Intersection of following blade with tip vortex trailing from a leading blade for $\mu = 0.2$

Flexibility introduces frequencies of the blade motion which may coincide with the frequencies of forced motion of the natural frequencies of other parts of the helicopter. The following equations, valid in the case of simple rotation and no forward flight, establish the flapwise bending as deflection of the blade in a plane perpendicular to the rotor hub plane, figure 53, the deformations of the blade in the lagging plane (i.e. in the plane of rotation), figure 54, and the blade torsional deflections under the action of aerodynamic and torsional moments, figure 55.

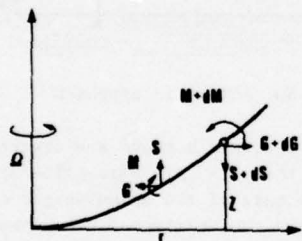


Fig. 53. Flapwise bending

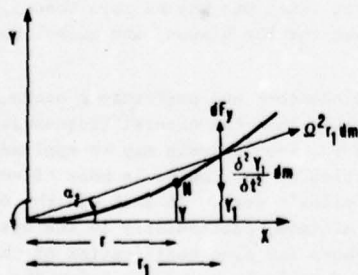


Fig. 54. Lagwise forces acting on blade

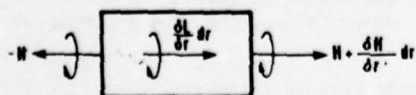


Fig. 55. Torsional moments acting on element

$$\frac{\partial^2}{\partial r^2} (EJ \frac{\partial^2 Z}{\partial r^2}) - \frac{\partial}{\partial r} (G \frac{\partial Z}{\partial r}) + m \frac{\partial^2 Z}{\partial t^2} = \frac{\partial F_z}{\partial r} \quad (35)$$

$$\frac{\partial^2}{\partial r^2} (EJ \frac{\partial^2 Y}{\partial r^2}) - \frac{\partial}{\partial r} (G \frac{\partial Y}{\partial r}) + m (\frac{\partial^2 Y}{\partial t^2} - \Omega^2 Y) = \frac{\partial F_y}{\partial r} \quad (36)$$

$$\frac{\partial}{\partial r} (E_s J \frac{\partial \theta}{\partial r}) - C \ddot{\theta} - C \Omega^2 \theta = \frac{\partial L}{\partial r} \quad (37)$$

Eqn. 35 is the result of the equilibrium of the blade element in the directions of shear forces $S(r)$, centrifugal tension G , and in the angular deflection under the bending moment $M = EJ \frac{\partial^2 Z}{\partial r^2}$.

Eqn. 36 defines the moment of inertial and aerodynamic forces acting on a given element of the blade about another point N of the blade itself.

Eqn. 37 is the result of the equilibrium of a blade element under the torques H acting on the sides and the elementary moment dL tending to twist the blade in the nose up and down sense.

In free flapping motion, with blade loading F_z zero as the case of the blade in "vacuo", eqn. 35 may be written with the right-hand side $\partial F_z / \partial r = 0$ and splitted, with the substitution of the solution in the form $Z = S(r) \cdot \phi(T)$, and referring to $x = r/R$ and $\psi = \Omega r$, as it follows,

$$\frac{d^2}{dx^2} (EJ \frac{d^2 S}{dx^2} - R^2 \frac{d}{dx} (G \frac{dS}{dx}) - m \lambda^2 \Omega^2 R^4 S) = 0 \quad (38)$$

$$\frac{d^2 \phi}{d\psi^2} + \lambda^2 \phi = 0 \quad (39)$$

being $\omega = \lambda \Omega$ the associated frequency.

The solution $Z = S(r) \cdot \phi(t)$ will be valid in the free flapping motion provided $S(x)$ and $\phi(\psi)$ satisfy eqns. 38 and 39 and the appropriate boundary conditions at the flapping hinge and the blade tip, for articulated hinged blade, and at $x = 0$ and $x = 1$ (blade tip), for hingeless blade.

The solution $S_n(x)$ for $\omega_n = \lambda_n \Omega$ of eqn. 38, depending upon the appropriate boundary conditions, represents the blade shapes, or the so called normal modes on account of an orthogonal property. Eqn. 39 defines the simple harmonic motion, for each λ_n value determining the frequency $\omega_n = \lambda_n \Omega$ of the corresponding n th mode shape in horthogonal coordinates $S_n(x)$ and x , or $Z_n(x)$ and w because $\partial S / \partial r = m \partial^2 Z / \partial t^2$. The solution of the general equation 35 of flapping motion depends upon the known blade loading F_z , variable with the azimuth coordinate ϕ_n , and refers to the simple case of axial flight. The difficulty of resonance for those modes with a natural frequency ω_n , equal or close to the rotor frequency, can be avoided by appropriate aerodynamic damping.

In free lagging motion, with blade loading F_y equal zero, eqn. 36 may be with $\partial F_y / \partial r = 0$ and splitted, with the substitution of the solution in the form $Y = R \cdot T(x) \cdot X(t)$, as it follows

$$\frac{d^2}{dx^2} (EJ \frac{d^2 T}{dx^2}) - R^2 \frac{d}{dx} (G \frac{dT}{dx}) - m (\nu^2 + 1) \Omega^2 R^2 T = 0 \quad (40)$$

$$\frac{d^2 X}{d\psi^2} + \nu^2 X = 0 \quad (41)$$

being $\omega = \nu \Omega$ the associated frequency.

The solution $Y = RT(x) \cdot X(t)$ will be valid in the free lagging motion, provided $T(x)$ and $X(\psi)$ satisfy eqns. 40 and 41 and the appropriate boundary conditions, the same as those of flapping motion. The lagging mode-shape equation 40 is identically in form to the flapping equation, except that the frequency ratio ν , defined by the simple harmonic motion, eqn. 41, appears as $(\nu^2 + 1)$ in the mode equation, because the centrifugal force field in the lagging plane is radial instead of parallel as in the flapping plane. For the n th the frequency ratio is $\nu_n = \omega_n / \Omega$.

For articulated blade with drag-hinge offset at $x = 0.05$, the first mode shape has a frequency ratio $\nu_1 = 0.274$, while, for hingeless blade, $\nu_1 = 0.55 - 0.7$ depending upon the stiffness near the root.

The solution of the equation 36 of lagging motion, for the response of the blade, depends upon the blade loading F_y .

The first mode frequency of lagging motion due to blade flexibility is 0.4-0.7 times the first mode frequency of flapping motion. But an intermodal coupling of the two frequencies is due to the fact that a blade which is free to flap experiences large Coriolis moments in the plane rotation (lagging plane).

In free torsional motion, with aerodynamic moment $L_A = 0$, eqn. 37 may be written with $\partial L_A / \partial r = 0$ and splitted, with the substitution of the solution in the form $\theta = Q(x) \cdot \zeta(t)$, as it follows

$$\frac{d}{dr} (E_S J \frac{dQ}{dr}) - C (\omega_\theta^2 - \Omega^2) Q = 0 \quad (42)$$

$$\frac{d^2 \zeta}{dt^2} + \omega_\theta^2 \zeta = 0 \quad (43)$$

being ω_θ the associated natural frequency. Considering the high degree of flexibility, we have, Ref. 11, in the first mode of motion, with a typical value of a supposed constant torsional stiffness and a root deflection half that at the tip at $\Omega = 0$, the non-rotating torsional frequency

$$\omega_\theta = 10.5 \text{ Hz}$$

which is about two and half times the typical rotor frequency. Thus, at normal rotor speed (4 Hz), the torsional frequency of the rotor blade is about 3.35 Ω , and may be so high as 6 Ω or even more.

Here above we have considered the flapping and lagging and torsional mode shapes and frequencies as independent of one another. But in reality, when the blade has built-in twist, there is elastic coupling between the flapping and lagging motion, as referred in Refs. 25 and 26.

Taking into account the blade deflections due to the forward flight, we have only small variations of the frequencies of the mode shapes.

The first flapping frequency ratio λ_1 of hingeless rotors usually lies within the range 1.08 to 1.17, whereas $\lambda_2 = 3.167$ and $\lambda_3 = 5.57$, in comparison to $\lambda_1 = 1$, $\lambda_2 = 2.58$ and $\lambda_3 = 4.60$ in the free flapping motion of the articulated rotor. Higher harmonic blade loads resulting from the flow conditions of forward flight produce alternating forces and rotor moments at the blade root and the hub of hingeless rotors. But, for a dynamically well tuned hingeless rotor these higher harmonic moments are relatively low compared to the first harmonic moments needed from trim or flight maneuvers.

With the development of helicopters capable of higher flight speeds, the problem of blade stall flutter has become one of major importance. Classical flutter involves coupling between two or more natural modes of vibration. In stall flutter, the flutter frequency tends to become equal to the natural torsional frequency. This implies that in this case the torsional (or pitching) motion predominates.

Large high-frequency oscillations in torsional moment, lift and aerodynamic moment, on the retreating side were detected in flight-test data taken from a rotor blade during a maneuver, as shown in the plot of figure

56, Ref. 27. This response was the result of dynamic stall induced by previously formed tip vortices which, under that particular maneuver flight conditions, pass under the blade at the azimuth positions indicated in figure 56.

The blade was analyzed next for an advance ratio $\mu = 0.1$. The rotational speed at which classical flutter occurs was determined. Then, stall-related instabilities were investigated. Blade motions for $\Omega = 4.8$ are shown in figure 57. The torsional displacement time history, while not strictly periodic, is nonetheless brought about by successive stall and unstall. The azimuth positions at which those events occur are marked by S and U, respectively, on the ψ - scale.

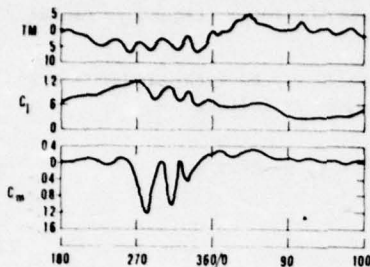


Fig. 56. Measured time history of section loading and moment coefficient and blade torsional response

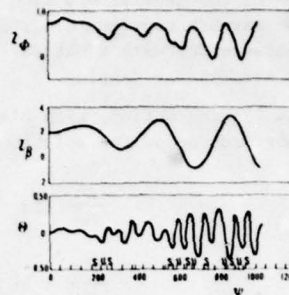


Fig. 57. Displacement time histories for stall flutter - $\Omega = 4.8$, $\theta_0 = 13$ degrees, $\mu = 0.1$

The effect of forward speed on stall-related instabilities was investigated by systematically varying the collective pitch angle and advance ratio, with $\Omega = 3.89$, Ref. 28. The results obtained are summarized in figure 58 as a plot of \bar{C}_L vs μ . As thrust is increased at a given μ , the rotor is seen to first encounter a region of excessive response, and then, for $\mu=0.2$ or less, a region where stall flutter occurs. As a result, stall flutter is confined to a region somewhat as indicated by the shaded area in figure 58. The suppression of stall flutter at high advance ratio is apparently caused by an effect similar to the one encountered at low rotor speed, whereby the flapping motion prevented as limit cycle from occurring. This can be seen from the blade motions obtained for $\mu = 0.3$ and $\bar{C}_L = 0.78$, figure 59.

In steady flight, the total drag torque Q and the rotor total power P , for example in the form of eqns. 32 and 34, however complicated, would be periodic with a frequency equal to the rotational frequency of the rotor. It is convenient to take as period the interval 2π , since this is the angle swept out by a blade in a complete revolution of the rotor. It is known that a periodic function can be represented by a Fourier series, figure 60

$$f(\psi) = a_0 - a_1 \cos \psi - a_2 \cos 2\psi - \dots - b_1 \sin \psi - b_2 \sin 2\psi \dots \quad (44)$$

to conform to the usual helicopter rotation.

For using torque and power expressions like eqns. 32 and 34, it is necessary to calculate their total values on the helicopter by adding the contribution of the individual blades.

In steady motion, these blade contributions are periodic, and a typical term for a given blade would be $a_n \cdot \cos n\psi$. If there are b equally spaced blades, the contribution of the neighbouring blades will be $a_n \cdot \cos n(\psi + 2\pi/b)$, and the total effect on such term of all blades is therefore

$$a_n \cdot \cos n\psi + a_n \cdot \cos n(\psi + 2\pi/b) + \dots + a_n \cdot \cos n[\psi + 2\pi(b-1)/b] \quad (45)$$

The frequency becomes proportional to the rotational frequency of the rotor. Lift and drag coefficients $C_{L\psi}$ and $C_{D\psi}$ to be used in expressions like eqns. 32 and 34 for total rotor torque and power have to be deduced experimentally, like the ones on figure 56. In this way, unsteady motion, as in maneuvers, flexibility and eventual stall flutter, may be taken into account.

During the last few years a number of complex analyses dealing with the cyclically variable total rotor

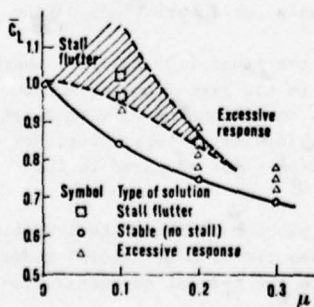


Fig. 58. Stall stability boundaries for $\Omega = 3.89$

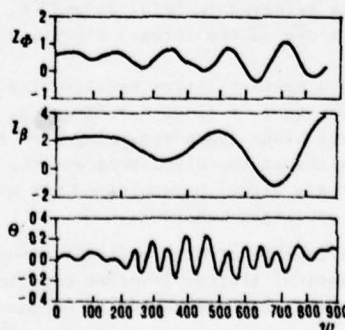


Fig. 59. Displacement time histories at high advance ratio - $\Omega = 3.89$, $\bar{C}_L = 0.78$, $\mu = 0.3$

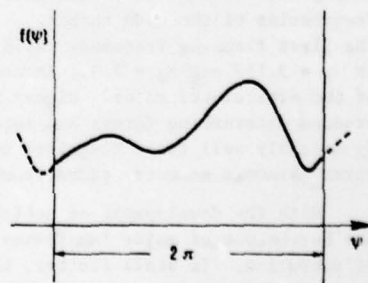


Fig. 60. Periodic function of the rotor torque

torque and power have been developed by the helicopter industry and have been implemented by sophisticated computer programs. Results from these programs have been compared in flight test and wind tunnel test data.

In a rotor simulation of this type, it is however difficult to compute the power local lift and drag coefficients as associated to inertia and aerodynamic effects due to blade feathering and bending moments. This may be accomplished by a very accurate analytic construction of the undeformed blade and a superposition of the blade elastic bending on this shape.

Influence of the blade aeroelastic stability and response on rotor shaft torque in forward flight -

The aeroelastic problem in forward flight is further complicated by the appearance of periodic coefficients in the equations of motion, and in the expressions of the azimuthal distribution of total rotor torque. The computation of the unsteady aerodynamic loads on a rotor blade is a formidable task in computational fluid mechanics.

It is only the recent work presented in Refs. 29 and 30 that gives a consistent treatment of this problem. And, from the other hand, the coupled flap-lag-torsional aeroelastic problem is simply a component, Ref. 31, of the coupled rotor-fuselage aeroelastic problem in forward flight.

The rotary wing aeroelastic problem described is often restricted basically to single-blade aeroelastic problem. In reality, interblade mechanical coupling between the rotor/fuselage and the control system can have a significant effect on aeroelastic stability and response of this complex aeroelastic system. A number of these problems pertaining to hingeless rotor flight dynamics have been reviewed in great details in Refs. 23, 30, 32 and 33.

The three partial differential non linear second order equations of equilibrium for the coupled flap-lag-torsional problem, relatively to a hingeless blade in hover, can be taken from Ref. 31 and correspond to the geometry of the problem shown in figure 61 and 62. Such equations, here omitted for brevity, take into account: stiffness EJ for flapwise and inplane bending, respectively; terms associated with elastic coupling; x , y and z displacements of a point on the elastic axis of the blade; elastic torsional deformation; distributed external loading torques in the x , y and z directions, respectively; resultant total loadings per unit length in the x , y , and z directions, respectively; centrifugal tension in the blade; torsional stiffness GJ . The solution of such equations indicates in general stable configurations for coupled flap-lag-torsional analyses, relative to hingeless blades in hover. Various blade configurations can be destabilized by pre-cone, droop, offsets, and negative built-in twist, which tends to reduce the stabilizing structural coupling effects.

The forward flight condition introduces considerable complications to rotary-wing aeroelastic stability and response problems.

From the aerodynamic point of view, it leads to a much more complicated representation of the unsteady aerodynamic forces. Moreover, it results in a region of reversed flow, which is also accompanied by locally stalled flow in the retreating blade region. The corresponding rotor total drag torque Q and the rotor total power P are function of the speed ratio μ and the azimuthal angle ψ during the revolution (cycle). A combination of unsteady aerodynamics (as referred to changing torque Q in the rotor cycle) and structural dynamics is represented by the rotary-wing aeroelastic response. This area has been recently reviewed in Refs. 34, 35 and 36.

PREDICTION OF AEROELASTIC AND VIBRATIONAL INSTABILITIES IN THE COMPLETE COUPLED ROTOR-FUSELAGE-CONTROL SYSTEM

The realistic rotary-wing aeroelastic problem is obviously the interblade mechanical coupling, or the coupling between rotor and the fuselage, or the coupling between the rotor/fuselage and the control system.

Prediction methods for estimating total aircraft dynamic stability and response characteristics have been developed by starting with a minimum number of degrees of freedom to describe the system.

However, the capability to simulate the total vehicle response and rotor loads due to a given pilot action is not now at the level to permit theoretical design of damage prevention devices.

Airloads in forward flight or in maneuvers are considered as result of an empirically modified uniform inflow which is dependent from the rotor ratio and shaft movement and from the unsteady blade aerodynamics due to an angle of attack cyclically variable, flight Mach number and blade shape.

For example, a single four-bladed, gyro-controlled hingeless rotor helicopter, may simulated as a model divided into three main parts: the rotor, the body, and the control system, related to one another.

The analysis becomes the simulation of a complete helicopter which involves a detailed dynamic description of the rotor and control system, as well as the conventional six degrees of freedom body dynamic description which operates both in a prescribed flight condition and in transient loads imposed by pilot inputs. In the first case, the aircraft is constrained to uniform flight, while the controls are engaged to obtain a force and moment equilibrium of the vehicle at that static condition, operating directly on main collective and cyclic pitch, tail rotor and aircraft attitude. In the second case, rotor, controls and airframe, are free to respond dynamically to external inputs.

The rotorcraft may be simulated dynamically in thirty coupled degrees of freedom: six for the body, four for

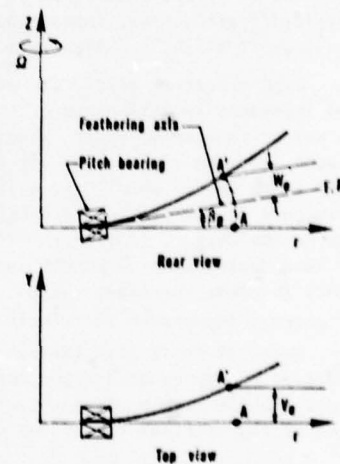


Fig. 61. Deformed elastic axis for a typical cantilevered performed rotor blade

the hub (pitch, roll, height displacement for deformation, and rotational speed), four for the combination of the control gyro/swash-plate. Motion of each of the four main rotor blades are simulated by two flapwise and one inplane modes and a pitch horn bending degree of freedom which couples blade feathering to the control gyro. In addition to these thirty degrees of freedom, it may be considered a first torsion mode for each blade. Since the frequency of this mode is usually over 4Ω , quite higher in comparison to the other dynamic mode of interest, a dynamic representation of this mode increases the computation complexity. This mode is included as a massless elastic response to blade torsion moments with a first order lag.

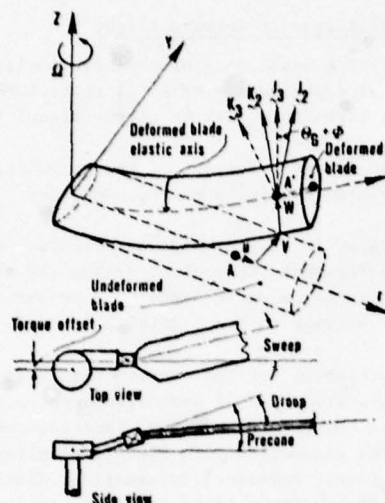


Fig. 62. General blade configuration and deformation

structure can be properly designed to minimize the transfer of high periodic forces and moments, into the basic rotorcraft structures, imposed particularly during the so-called transition flight regime between hovering and forward flight and high-speed flight.

High vibration levels are established by aerodynamic loading, and aeroelasticity of the rotor blades, and resonance amplification of the structure. As before mentioned, speed changes and periodic variation in the angle of attack encountered by the rotor blades generate alternating air forces once per revolution and at multiples of this frequency. Generally, only those forces which have a frequency that is multiple of the number of blades are transmitted to the structure in the vertical direction. If the frequency of the transmitted force, usually small in comparison to the weight, is near the structural resonance frequency, then large amplification may occur. Instead of considering each component separately, a coupled system and the effect of the interaction of the components (blades, fuselage, engine, etc.) is analyzed, in order to find out which structural components are of primary importance in calculating resonances.

Refs. 39 to 42 give the possibility to apply the Lagrange energy equations and the matrix methods to the determination of the undamped, natural coupled frequencies of the vertical vibrations of a tandem helicopter.

Programs of helicopter flight simulation have been under development for the past decade, Ref. 43. The analysis describes a wide variety of helicopter configurations single rotor, compound, tandem, or side-by-side, and covers a broad range of flight conditions, as hover, transition, cruise, or high speed. The programs are oriented in terms of preparing the input data and interpreting the results for performance, stability and control, and fully-coupled time-variant aeroelastic analysis during steady or maneuver flight.

In this way, vibration control has been achieved through rotor systems so designed to eliminate vibratory bending moments, detuning blades natural frequencies and the harmonics of rotational speeds, incorporation of isolating devices or dynamic absorbers.

Increased periodic forces are occurring when the rotor thrust is increased, during transition from hovering to forward flight, and at higher tip-speed ratios. The harmonics above the fourth are generally below 20 percent of the principal harmonic force. In turn, the magnitude of the harmonic forces other than the n th one for n -blade rotor is generally below 50 percent of the principal n -th harmonic.

The analysis of blade torque moments indicates the magnitude of the harmonic components to be about 4 ± 5 percent, respectively, of the steady components of the moments.

But, still now, rotorcraft are operated at reduced speeds, as much as 20% below the forward velocity that they might otherwise achieve, because of vibratory environments.

However, the understanding the sources of vibration is more and more required for reaching forward speed as high as 200 knots.

The model with thirty degrees of freedom may be written in matrix form, and can handle hover, forward flight, and maneuver flight conditions.

Ref. 38 is referring about a single two-dimensional model of the fuselage comprising 25 elements and 60 degrees of freedom (two translational and one rotational at each node), figure 63. Both vertical and horizontal responses at the pilot's seat have been computed. The excitation on the structure is an oscillatory couple of frequency 21.7 Hz applied at the top of element 1 as shown in the figure. Through the continuous variation of the stiffness of some elements during the sinusoidal excitation force, there is the possibility to absorb the vibration. The calculation makes possible to know before-hand which are the most sensitive areas of the fuselage structure to limit vibration response in the crew and passenger area.

Efficient design practice for rotorcraft, which includes appropriate vibration analysis, requires: an estimation of rotor loads on the fuselage structure based on fully aeroelastic analysis; an adequate knowledge of the structural characteristics to determine coupled natural frequencies and mode shapes; an evaluation of in-flight vibration and fuselage response.

This work takes a very high long and expensive work at the IBM 370/168-type computer time. In such a way, the hub supporting struc-

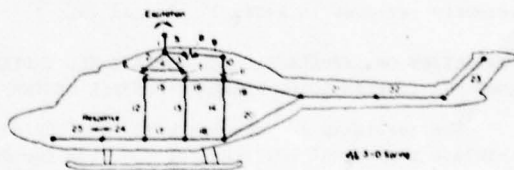


Fig. 63. Structural model

Basic inputs for helicopter performance prediction are aircraft data, airfoil characteristics, engine data under various altitude and power-setting conditions, and mission flight segments (ascent, maneuver, descent and steady state). Important characteristics for the airfoil are the variation of section lift and drag data with Mach and Reynolds numbers. Basic data of the assumed propulsion system are power rating vs temperature and pressure altitude, and SFC and fuel flow vs partial power.

The performance prediction procedure starts with calculations for hovering outside of ground effect, considering main and tail-rotor induced and profile power, as in the computer program of Ref. 44, and vertical downwash drag because of the rotor flow velocity distribution on the airframe.

A more complex performance prediction procedure follows for forward flight, incorporating vortex theory in determining airframe drag, power required in horizontal flight at higher speeds, maximum rate of climb at various altitudes, and, finally, aerodynamic and aeroelastic limits (stall, stall flutter, excessive pitch link loads, etc.) to maximum flight velocity.

PREDICTION OF AEROELASTIC INSTABILITIES AND FATIGUE LIMITS IN ROTORCRAFT ENGINES

It is a bad way to fly as a helicopter does. Even though the flight accident statistics refer about pilot error or autorotation landing as recurring cause of crash, the propulsion system is more often responsible to fail because of its original deficiency in satisfying instantly excessive loading factors imposed on the cyclically variable rotor torque during the pilot transitional inputs from a flight segment to another. The computerized fuel control is effectively inadequate to establish continuous equilibrium between shaft drag torque and delivered engine torque, in that resulting excessive rpm inertial dissipation.

Moreover, limitations are imposed upon the operation of helicopters as a result of the high aeroelastic vibration levels encountered in flight, and transmitted to the driving engines. The associated high periodic loads on the engine rotating parts, particularly during the so-called transition flight regime between hovering and forward flight and during high-speed flight, are contributing substantially to materiel fatigue and consequential high rate of replacement and maintenance of component parts. Extreme flight conditions are right and left turns, rolling pull-outs, longitudinal reversal, cyclic and collective pull-ups, slope landings and starts.

Output shaft rpm cannot vary generally more than 10 percent, and gas turbine engine operation may become critical at the minimum rpm values, with a consequential loss of rotor thrust.

Surge still exists in engines that have been abused. Repeated surging and the attendant transient torsional loads from the engine can cause damage to the airframe components.

The interstage bleed system automatically relieves the compressor of a small amount of air, during the period of the engine acceleration cycle, at slight loss of power. The entire sequence operation should be controlled by the fuel control which should sense gas producer rotating speed, fuel flow and pilot demand, therefore ensuring proper opening and closing of the interstage air-bleed.

To provide the desired surge margin, the angle of attack of the inlet air to the first stages of the compressor rotor must be within the stall-free operating range of the transonic airfoil (first stages of the compressor). Since this stall-free operating range varies with compressor speed, it becomes necessary to vary the angle of attack as a function of compressor speed, through angular variation of the first stages inlet vanes. A servo valve is located within the fuel control to actuate synchronically the fuel feeding. The fuel flow system sequence is unable to follow abrupt or high frequency changes of required engine torque.

The fuel control is a hydro-mechanical device, with fuel regulator and power turbine governor. The acceleration and deceleration fuel flow control may be in excess of the engine's ability to immediately produce the desired power. To get a good performance, the amount of fuel added to the air in the combustor must be exact at all times, in acceleration, deceleration and steady state engine operation. As a result, the engine should be brought through transitory condition as rapidly as possible, keeping the rotorcraft out of dangerous mixtures. Boost pumps, check, metering, dump, pressurizing and shutoff valves, and pressure regulator, of the automatic fuel flow system, are a very complex matter, susceptible of possible malfunctioning or failure during rapidly changing operation. The emergency fuel system must be operated with some care to avoid engine damage. Gas producer governor and power turbine governor are sensing any deviation in steady state of the corresponding compressor-turbine rotor and free turbine rotor. The transient air-bleed control on the compressor rotor of the gas producer turbines is not able to operate correctly during power turbine rotor acceleration. Unsteady airloads on the helicopter main rotor might be so high to stop at all the combustion process.

As shown on figures 9 and 51, the lifting capability in forward flight of a rotor blade is changing with azimuthal angle. Using a multi-blade rotor, the corresponding thrust disuniformity is highly attenuated. The oscillating aerodynamic forces of the individual blades are superimposed in the rotor hub section. With increase of blade number, more rotor harmonic loads on the fuselage are considerably reduced. The oscillating vertical forces during, say, a 140 knots horizontal flight, for rotors with different numbers of blades, are shown in figure 64. The basic blade passage frequency is much lower on the two-blade rotor, which is an unfavorable effect on the aircraft vibrations. The substantial vibratory improvements with a higher number of blades is that the blade passage frequencies normally get outside of the body resonance frequency regions, so that the exciting forces cannot come through into the airframe.

As for the vertical force in the rotor hub section, the engine driving torque is variable with the azimuthal angle in forward flight. Thus, the torque may be expressed by a Fourier series, eqns. 44 and 45. An instability criterion for the prediction of the corresponding flow distortions and aeromechanical responses, and the fatigue effects of alternating stresses on the engine "life" may be found.

High speed forward flight -

In this condition, figures 2, 3 and 16, the multi-blade rotor drag torque is variable during each revolution because of:

- cyclic pitch control (by blade feathering) of the amount of forward thrust for each blade, following the methods of figures 4, 6 and 9, in a different way according the flapping and lagging motion of the articulated rotor, figures 10, 11 and 12, or the hingeless rotor, figures 13 and 14, with blade stall vibration and unsteady aerodynamic effects at very high flight speed;
- coupled flap-lag-torsional multi-blade aeroelastic effects, figure 20, stall flutter and air resonance;
- coupled rotor/fuselage, figures 21 and 34, aeroelastic feedback effect on the rotor.

Adimensional amplitude $\Delta Q/Q$ and frequency Ω/Ω_{av} rotor torque cyclic variations may be, near the maximum flight speed, respectively, of the order of 0.1 and 0.05, as compared with the measured values of $\Delta C_1/C_{1av}$, $\Delta C_T/C_{Tav}$, $\Delta \theta/\theta_{av}$, $\Delta Z_8/Z_{8av}$, $\Delta Z_9/Z_{9av}$, figures 16, 18, 19, 20, 45, 51, 56, 57, 59 and 64. The cyclically variable rotor drag torque Q is reduced in amplitude and disuniformity to the shaft of the free (power) turbines. For a single-engine/single-rotor helicopter, the speed reduction ratio between the engine and main rotor is now about 80:1 and will increase in the foreseeable future. In the same speed ratio the rotor torque disuniformity and frequency is diminished on the engine shaft. The gas turbine engines that have been designed primarily for helicopter use, such as the General Electric T-58, the Lycoming T-53, figure 65, and Allison T-63, were required to have an integral gearbox, to reduce the output speeds and the main rotor speeds to approximately 6,000 and 300 rpm. In the power distribution system, the power turbines are running at high supercritical speed and the relative vibration amplitudes are safely controlled by one properly designed and located spring-mounted damper. In the UH-1 helicopter, powered by a Lycoming T-53-L-11, with a takeoff rating of 1,100 horsepower at 21,000 rpm, this speed is reduced to 6,050 rpm through a nose-mounted gearbox, figure 66.

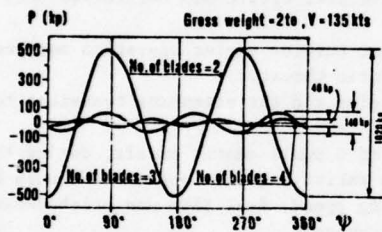


Fig. 64. Oscillating vertical forces on rotors with two, three and four blades

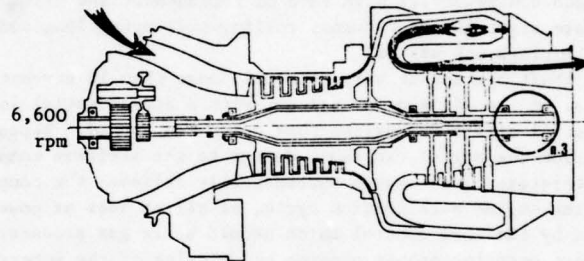


Fig. 65. Two-spool gas turbine

When the rotor drag torque Q is reduced about 80 times to the free (power) turbines, there is in general sufficient damping, through the engine gear box (between power shaft and drive shaft) and the planetary gear unit (between drive shaft and rotor shaft), with passive heat production, to absorb the most part of the rotor drag torque disuniformity during the low speed forward flight at limited vibrational and aeroelastic effects. But, when the forward speed is so high to start blade stall vibration and large amplitude aeroelastic effects, the engine is quite largely influenced and cannot compensate the required power fluctuations through the automatic fuel control action. We may expect in this case considerable power turbines vibration and engine flow distortion.

With Q_e and ω_e corresponding to the power turbines shaft torque and its angular speed, the power balance at each azimuthal angle value may be expressed

$$Q_e \cdot \omega_e (1 - \eta_1) = Q \cdot \Omega \quad (46)$$

where η_1 is the mechanical efficiency due to power dissipation through the reduction gears. The engine torque from eqn. 46

$$Q_e = Q(1 - \eta_1) \Omega / \omega_e = (Q_{av} + \Delta Q) (1 - \eta_1) \Omega / \omega_e \quad (47)$$

is cyclically variable, depending upon the rotor torque, expressed on the basis of eqns. 43 and 44, and the changing mechanical behavior (η_1). It is $\omega/\Omega = 80$ times smaller than Q . And, since both gas turbine and helicopter rotors operate at a tip speed based on Mach number, this rotational speed ratio will increase with advanced technology engines, where the turbine inlet temperatures will probably still increase appreciably.

At constant forward flight speed, the control fuel setting is such to deliver, with a fuel flow $G = \text{pds/sec}$ at net heat value $K = \text{Btu/pd}$, a fuel power $G \cdot K \cdot 237.5/550 = \text{hp}$, corresponding to the following mechanical balance

$$G \cdot K \cdot 237.5 = (Q_{av} \cdot \Omega_{av} + Q_c \cdot \omega_{ec}) / \eta_t \eta_m = \text{pds} \cdot \text{ft/sec} \quad (48)$$

where Q_c , ω_{ec} , η_t and η_m , are the torque and rotational speed of the compressor turbines, and the thermal and mechanical efficiencies.

Now, the cyclically variable power turbines rotational acceleration $d\omega_e/dt$ is depending upon the inability of the fuel control systems to vary instantaneously the delivered power, eqn. 48, and it may be expressed as

$$\frac{d\omega_e}{dt} = \Delta Q \cdot \Omega / \omega_e (J_e + J_1 + J_2 + J_3 + J_r) \quad (49)$$

where J_e is the power turbine rotor system moment of inertia, and J_1, J_2, J_3, J_r are the moment of inertia reduced (through the square rotation speed ratios) to the power turbine shaft, respectively of, figure 66, engine box gear, drive shaft, planetary unit gear, and helicopter main rotor. (In the complete system of figure 1, it has to be taken into account the tail rotor torque disuniformity and the reduced moment of inertia of the relative driving system).

The rotational acceleration is cyclically variable according the expression of ΔQ and Ω . Practically, such acceleration is also influencing the gas producer rotor speed, introducing flow distortions and aeromechanical effects in all the engine.

From the thermodynamical point of view, high speed forward flight in helicopters, induces mismatching in the rotating components and then operation in low performance parts of their map, and compressor and turbines lack of efficiency. It is even possible that the faulty component puts itself in the situation where it is finally poorly used. Margins to limit such risks have to be introduced by the designer; they can not be substituted by ignorance factors according advanced prediction techniques.

The thermal differences and consequential mechanical deformations reduce blade tip and seals clearances and involve adjacent component interactions (as temperature and pressure profiles, wakes, turbulence are generated upstream and downstream), in this kind of modern high loaded turbomachinery. Rematching actions are contributing to diminish the materiel fatigue limits.

The aeromechanical response in a rotor blading operating in a circumferential distortion is the periodic forcing. The relative inflow condition consists of a superposition of terms with harmonic time variation. The frequency would be $60 nN$ Hertz, where n is an integer and N is the rotational speed in rpm. In practice the Fourier harmonic periodicity comprehends $n = 1$ and, in some degree, all other n . In addition to the possibility of increased levels of turbulence, the degradation of flow in the axial blading may lead to the onset of self-excited blade vibration (stall flutter) or self-excited fluid oscillation (stall propagation). The propagating stall may be treated, from an aeromechanical point of view, as any other periodic gust. The frequency, however, is not an integer multiple of the rotational speed, but usually between 40 and 60 percent of the rotor speed. Stall flutter may occur during compressor surge, and the relative period in which the flow is reversed is two or three orders of magnitude greater than the period of natural blade vibrations.

From the mechanical point of view, periodic and inertia blade loadings may have serious consequences with respect to the discs and shafts to which these blades are attached. Flutter may be expected to exert oscillatory blade root reactions. The beam-like vibrations of the shaft have as their genesis the excitation by a rotating stall pattern. The higher harmonics of the excitation over the discs may provoke relevant flexural modes of forced vibration.

As the compressor blades are often secured and held in place by spring-loaded locking plates and pins, the fatigue limits are shortened by stall flutter and stall propagation.

A mathematical model for prediction of the aeromechanical response of helicopter engines to rotor angular vibration and consequential time-dependent flow pressure and temperature distortion is beyond the scope of the present work. It is however possible to combine flow parameters and alternating stresses to get for them numerical solutions for the engine vibration problem in high speed forward flight.

The problem of fatigue limits is an important aspect in the design of helicopter engines, due to the development of loads spectra heavier than in fixed wing aircraft engines. Newer and more accurate methods of predicting the fatigue and crack growth lives of rotorcraft engine structural and rotating components are needed.

The typical fatigue problem of helicopter engines is high-temperature and cycle-fatigue. At elevated temperatures the need for reliable procedures for lifetime prediction of gas turbine engines is of increasing concern, considering deformation during cyclic loading and environmental effects. If one assumes that damage in creep is effectively the same as damage in fatigue, then a linear interaction relationship can be established.

Frequency modifies the behavior at high temperatures. An increase in frequency reduces the inelastic strain per cycle by excluding time dependent deformation processes, or it reduces the time available for environmental attack in each cycle.

Environmental effects on the fatigue of aircraft engines have been neglected in the past. Damage behavior was analyzed by fatigue and fracture mechanics without paying much attention to the environment. But, from the time of the broad utilization of helicopters in level flight, over the sea and in extreme cold-weather operations, some laboratories started to investigate corrosion fatigue, now to be overimposed to the high temperature and frequency fatigue investigation. In gaseous environments such as air, water vapour has been shown to be the species damaging to the fatigue life of aluminium and its alloys, and steel. The effect of the more aggressive environment of Na Cl solution was demonstrated. Systematic studies of fatigue life of

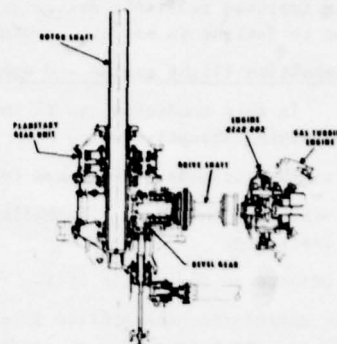


Fig. 66. UH-1 transmission system

titanium alloys have been carried out in corrosive environments. The effect of stressing variables and frequency changes on fatigue crack growth, for aluminium and titanium alloys, have been established. The significance of water vapor is reflected in recent results of fatigue tests in air of varying humidity. Corrosion fatigue and stress corrosion cracking have been studied in connection with fatigue crack propagation and frequency effects.

Reliability of critical engine components is adversely affected by operational flight fatigue in a sub-zero temperature environment. Flight speed and engine torque operational red-lines are easily exceeded because of the greater horse power capabilities of the engines in the denser atmosphere.

Analytical prediction tools that accurately account for the basic fatigue mechanism can, through the resulting improved realistic design criteria, be efficient in avoiding structural failure of engine components due to fatigue in helicopter high speed forward flight.

Transition flight regime and extreme flight maneuvers -

In this condition, as in the deceleration maneuver time history on figure 45, the rotor drag torque is varying abruptly during each revolution, because of:

- sudden airloads overimposed to the cyclic pitch control of the rotor thrust;
- vibration and blade flexibility effects, overimposed to stall flutter and flap-lag-torsional blade aeroelasticity;
- effects on the engine of the strongly aeroelastic system corresponding to the rotor-fuselage integration.

The aeroelastic instability is such to determine considerable power turbine rotational acceleration, eqn. 49, as consequence of very large and abrupt rotor torque ΔQ variation. The fuel control system might be unable to maintain the needed rotational speed of the engine.

More in general, the engine rotating parts are subjected to aeroelastic deformations, and the flow is undergoing considerable distortion and unsteadiness.

The prediction of engine fatigue life because of maneuvers in service is still based upon static methods or cumulative damage theories, with inaccurate results. To fulfill the high requirements of rapid maneuverability with damage tolerance, it is necessary to have available adequate sizing of the engine components.

The fatigue load on the engine under service conditions generally has a more or less arbitrary or random character. However, it may well be assumed that the accumulation of fatigue damage under such an arbitrary fatigue load is a process which occurs in the material in a classical fatigue test, where the load is varying sinusoidally with a constant mean load and a constant load amplitude.

The calculated life will depend on the type of available data, on corrections made to these data by accounting for deviating aspects. If a new design has a high similarity with a previous design, it is clear that most valuable information should come from the service record of the older design.

As conclusion, it is easy to monitor with standardized methodology the vibrational levels of the engine rotating parts and the interactions with stators and envelopes, during the transitional operation of helicopters, but it is difficult to predict theoretically and evaluate practically how much the fatigue life of an helicopter engine might be less than the one of the corresponding static wing aircraft engine. The overall situation is not as bad it might seem. Helicopter technology is rapidly progressing, and the discontinuity of the lifting rotor is substantially absorbed by the very high engine rpm, and the service-life of all engine components are increasing. With the advent of hingeless rotors, the epoch of the older helicopter undergoing fatigue problems, with low service-lives for the engine components, has gone. However, helicopter engines are still requiring frequent inspections of damages occurred in service, Ref. 46, and 1,000 operating hours of the more dynamically loaded components are to be taken as a satisfactory lifetime target for reliability in flight.

From the other hand, fixed wing aircraft turbine engine life has grown to an average engine overhaul limit of 1,000 hours; and life commitments on advanced engines are approaching 2,000 hours on components in hot gas stream.

The structural analysis of the engine design cycle is the first phase of life prediction, regarding stress, strain and energy, deflection, etc., provided precise values of boundary conditions are available and used for input. Boundary conditions include all pressures, temperatures and forces, on a critical component, and are determined with instrumentation. The rotating components to be considered as critical are disks, blades and shafts, with high levels of kinetic energy. Data recorded would include rpm excursion for take-off, landing, transition regimes, and air-maneuvers, to pick up in subcycles the most severe magnitude and frequency movements.

The second phase of life prediction is the determination of critical material properties as combination of endurance stress, ultimate stress, and fracture toughness, in its duty cycle throttle settings. Manufacturing processes will be considered in the choice of the material properties as they usually have a pronounced effect on the fatigue characteristics of engine utilized materials.

The third phase of life prediction is the comparison between the previous results, through empirically established and component correlated "life curves". In helicopter engines the majority of loads are repeating, fluctuating and rapid applied, centered as damage accumulation from fatigue. Precise understanding of which failure are probable to be dominant for a given component is of paramount importance in the life analysis of all the engine's mechanical-structural systems. Low cycle thermal fa-

tigue would be a major problem with dilution cooled combustors as well as thermal distortion, buckling, oxidation, and burning, in order to design and estimate the life of a combustor accurately. In its mechanical-structural system, a turbo-engine is presenting critical points where are occurring maneuver loads, aeroelastic effects, creep for burst resonance, stress rupture creep yield, distortions, containments, thermal fatigue and erosion. For that, in the determination of the service life of an helicopter engine component, one must be aware that many failure modes are so dependent upon the engine usage, and that a new life analysis must be accomplished for each new flight vehicle application. A high degree of repeability and the implementation of practical methods for monitoring performance based on overall condition of the engine and associated systems are needed.

To avoid reliability degradation in helicopter engines because of random fatigue effects due to sudden transitional maneuvers in flight, it is necessary to organize reliability problem identification and correction action programs, Ref. 48. However, to minimize maintenance problems of the user in the field, and thus obtain maximum utilization of the engine, a full developmental test cycle in all mission load spectra should be completed. In this way, the helicopter engine will appear from now on less responsible of crashes in the flight accident statistics.

REFERENCES

- [1] J.R. Montgomery: "Sikorsky Helicopter Flight Theory for Pilots and Mechanics", Sikorsky Aircraft, Division of United Aircraft Corporation, June 1964.
- [2] J.J. Philippe and C. Armand: "ONERA Aerodynamic Research Work on Helicopters", AGARD Conference No. 233 Rotorcraft Design, Moffett Field, California, May 1977.
- [3] R.A. Piziali: "A Method for Predicting the Aerodynamic Loads and Dynamic Response of Rotor Blades", USAAVLABS TR-65-74, January 1966.
- [4] R.A. Piziali: "Rotor Aeroelastic Simulation - A Review", AGARD Conference Proceedings No. 122 Specialist Meeting on Helicopter Rotor Loads Prediction Methods, Milan, March 1973.
- [5] P.F. Yaggy: "The Role of Aerodynamics and Dynamics in Military and Civilian Applications of Rotary Wing Aircraft", AGARD Lectures Series No. 63 on Helicopter Aerodynamics and Dynamics, Von Karman Institute, Brussels, April 1973.
- [6] H.B. Johnson: "The Effect of Semi-rigid Rotors on Helicopter Autostabiliser Design", AGARD Conference Proceedings No. 86, Konstanz (Germany), June 1971.
- [7] K.H. Hohenemser: "Hingeless Rotorcraft Flight Dynamics", AGARDograph No. 197, Ames Directorate U.S. Army Air Mobility R & D Laboratory, Moffett Field, Calif. 94035, USA, September 1974.
- [8] A.J. Potthast and J.T. Blaha: "Handling Qualities Comparison of Two Hingeless Rotor Control System Designs", 29th Annual National Forum, American Helicopter Society, May 1973.
- [9] R.C. Heimbold and D.C. Griffith: "Synthesis of an Electromechanical Control System for a Compound Hingeless Rotor Helicopter", J. Am. Hel. Soc., Vol. 17, No. 2, April 1972.
- [10] J.P. Murphy, H.L. Walker and L. A. Kaufman: "An Integrated Low Altitude Flight Control System for Helicopters", AGARD Conference Proceedings No. 86, Konstanz (Germany), June 1971.
- [11] A.R.S. Branwell: "Helicopter Dynamics", Edward Arnold, London, 1976.
- [12] G. Reichert: "Basic Dynamics of Rotors Control and Stability of Rotary Wing Aircraft Aerodynamics and Dynamics of Advanced Rotary - Wing Configurations", AGARD Lecture Series No. 63, April 1973.
- [13] H.B. Huber: "Effect of Torsion - Flap - Lag Coupling on Hingeless Rotor Stability", 29th Annual National Forum, American Helicopter Society, Washington D.C., May 1973.
- [14] R.T. Lytwyn, W.L. Miao and W. Woitsch: "Airborne and Ground Resonance of Hingeless Rotors", J. Am. Hel. Soc., Vol. 16, No. 2, April 1971.
- [15] G. Reichert: "Loads Prediction Methods for Hingeless Rotor Helicopters", AGARD Conference Proceedings No. 122, Milano, March 1973.
- [16] G. Reichert: "The Impact of Helicopter Mission Spectra on Fatigue", AGARD Conference Proceedings No. 206, Ottawa, April 1976.
- [17] J.F. Ward and W. H. Joung Jr.: "A Summary of Current Research in Rotor Unsteady Aerodynamics with Emphasis on Work at Langley Research Center", AGARD Conference Proceedings No. 111, Marseilles, September 1972.
- [18] W.F. Durand: "Aerodynamic Theory, Vol. IV, Section L, Dover Publications, New York 1963.
- [19] W.Z. Stepniewski: "Basic Aerodynamics and Performance of the Helicopter", AGARD Lecture Series No. 63, Von Karman Institute (Brussels), April 1973.
- [20] D.C. Gilmore and I.S. Gartshore: "The Development of an Efficient Hovering Propeller/Rotor Performance Prediction Method", AGARD Conference Proceedings No. 111, Marseilles, September 1972.
- [21] I.A. Simons: "Advanced Control Systems for Helicopters", Vertica, Journal of Rotorcraft and Powered Lift Aircraft, January 1976.

- [22] N.D. Ham and M.I. Young: "Torsional Oscillation of Helicopter Blades Due to Stall", J. Aircraft, Vol. 3, No. 3, May-June 1966.
- [23] N.D. Ham: "Helicopter Blade Flutter", AGARD Report No. 607, January 1973.
- [24] W.P. Jones, W.J. McCroskey and J.J. Costes: "Unsteady Aerodynamics of Helicopters Rotors", AGARD Report No. 595, presented at the 34th AGARD Structures and Materials Panel Meeting, Lingby (Denmark), April 1972.
- [25] J.C. Houbolt and G.W. Brooks: "Differential Equations of Motion for Combined Flapwise Bending, Chord wise Bending and Torsion of Twisted Non-uniform Rotor Blades", NACA Rep. 1346, 1958.
- [26] A.J. Sobey: "Dynamical Analysis of the Shaft-fixed Blade", R. Aircr. Establ. Tecn. Rep. 73175, 1974.
- [27] P. Crimi: "Dynamic Stall", AGARDograph No. 172, November 1972.
- [28] J.F. Ward: "Helicopter Rotor Differential Pressures and Structural Response Measured in Transient and Steady - State Maneuvers", J. Am. Helicopter Soc., Vol. 16, No. 1, January 1971.
- [29] P. Friedmann and J. Shamie: "Aeroelastic Stability of Trimmed Helicopter Blades in Forward Flight", First European Rotorcraft and Powered Lift Aircraft Forum, University of Southampton, England, 1975; published in Vertica, Vol. I No. 3 1977.
- [30] J. Shamie and P. Friedmann: "Aeroelastic Stability of Complete Rotors with Application to a Teetering Rotor in Forward Flight", AHS Preprint No. 1031, presented at the 32nd Annual National V/STOL Forum of the American Helicopter Society, Washington, D.C., 1976.
- [31] P. Friedmann: "Influence of Modelling and Blade Parameters on the Aeroelastic Stability of a Cantilevered Rotor", AIAA Journal, February 1977.
- [32] W.L. Miao and H. Huber: "Rotor Aeroelastic Stability Coupled with Helicopter Body Motion", Rotorcraft Dynamics, NASA SP-352, 1974.
- [33] W.L. Miao, W.T. Edwards and D.E. Brandt: "Investigation of Aeroelastic Stability Phenomena of a Helicopter by In Flight Shake Tests", NASA Symposium on Flutter Testing Techniques, Flight Research Center Edwards, 1975.
- [34] R. Dat: "Aeroelasticity of Rotary Wing Aircraft", AGARD Lecture Series No. 63, Brussels, April 1973.
- [35] R. Dat: "Unsteady Aerodynamics of Wing and Blades", IUTAM Symposium on Flow - Induced Structural Vibrations, Springer Verlag, Heidelberg, 1974.
- [36] R.A. Ormiston: "Comparison of Several Methods for Predicting Loads on a Hypothetical Helicopter Rotor", Journal of the American Helicopter Society, Vol. 19, No. 4, 1974.
- [37] R.M. Carlson and A.W. Kerr: "Integrated Rotor/Body Loads Prediction", AGARD Conference Proceedings No. 122 on Specialist Meeting on Helicopter Rotor Loads Prediction Methods, Milan, March 1973.
- [38] G.T. Done and A.D. Hughes: "Reducing Vibration by Structural Modification", Vertica, January 1976.
- [39] G.W. Brooks: "Analytical Determination of the Natural Coupled Frequencies of Tandem Helicopters", Journal of Am. Helicopter Soc., Vol. 1, July 1956.
- [40] J.E. Yeates Jr, G.W. Brooks and J.C. Houbolt: "Flight and Analytical Methods for Determining the Coupled Vibration Response of Tandem Helicopters", NASA Report 1327, 1957.
- [41] J.L. Synge and B.A. Griffiths: "Principles of Mechanics", McGraw Hill, 1959.
- [42] L.A. Pipes and A. Louis: "Matrix Methods for Engineers", Prentice Hall, 1963.
- [43] R.L. Bennet: "Rotor System Design and Evaluation Using a General Purpose Helicopter Flight Simulation Program", AGARD Conference Proceedings No. 122, Milan, March 1973.
- [44] J.P. Magee, M.D. Maisel and F.J. Davenport: "The Design and Performance Prediction of Propeller/Rotor for VTOL Applications", Proceedings of the 25th Annual ARS Forum, No. 325, May 1969.
- [45] D. Dini: "Simple Solutions of the Helicopter Propulsion System Made Possible Using Closed Cycle for the Working Fluid", AGARD PEP 31st Meeting on Helicopter Propulsion Systems, Ottawa, June 1968.
- [46] D. Dini and L. Giorgieri: "Testing Simulation of Damages Occurred in Service", AGARD Conference No. 215 on Power Plant Reliability, The Hague, April 1977.
- [47] R.J. Hill: "A Procedure for Predicting the Life of Turbine Engine Components", AGARD Conf. No. 215, The Hague, April 1977.
- [48] G. Facca and L. Giorgieri: "Military Engine Deterioration in Service Connected with Life Cycle Costs", AGARD Conference No. 215, The Hague, April 1977..

ACKNOWLEDGMENTS

The author wishes to gratefully acknowledge the contribution made by Mrs Gigliola Cei and Mr Andrea La pucci in typewriting and drawing the present paper.

DISCUSSION

S.S.Gupta, Canada

What would you recommend as a design load (g loading) factor for use in engine mounting design? What are typical loadings actually seen by civil and military helicopters? How does your analysis compare with measurements?

Author's Reply

Since I have not been in charge of the turbo engine design I am reluctant to recommend a specific design load factor you are asking in your first question. Nevertheless I think that normal aeronautical turboengines are exposed to accelerations as high as 10 g in maneuvers. I believe that 10 g would be the normal design load factor for both civil and military helicopters. But considering some abrupt maneuvers pilots may be forced to use acceleration could reach values of about 15 g. My analysis is a consequence of malfunctionings discovered after helicopter crashes. In those occasions, I carried out bench tests of the fuel control system and I saw the phase delay in fuel feeding during abrupt power variations.

APPLICATION OF ENGINE USAGE ANALYSIS TO COMPONENT LIFE UTILISATION

M. Holmes
National Gas Turbine Establishment
Pyestock, Farnborough, Hants GU13 OLS
England

© Controller, HMSO London 1978

SUMMARY

The maximum life potential of aero engine components can only be realised in service if it is established how they are being used by monitoring engine parameters during operation in service aircraft. The analytical methods used for determining low cycle fatigue usage are an important aspect of the work and form the subject of this paper. The influence of data availability and computing capability on the procedures to use are highlighted by comparing the software appropriate to an airborne unit monitoring engine rev/min with that for a ground-based computing facility analysing recorded flight data.

LIST OF SYMBOLS

D	fatigue damage
E	elastic modulus
K	constant
L	life in stress cycles
m	slope of fatigue curve
N	rotational speed
S	stress
T	temperature
ΔT	temperature change
ϵ	strain

SUFFICES

c	constant
e	elastic
E	refers to zero based stress cycle
hi	high
L	limiting value of mean stress
lo	low
n	relates to Neuber expression
p	plastic
ref	reference
u	ultimate tensile strength
y	yield strength
1,2,3, etc	relate to various constants

1. INTRODUCTION

A detailed knowledge of how aero engines are operated in service is an essential part of studies aimed at extending component lives and thus reducing life cycle costs. The development of airborne data recording equipment, based on the compact cassette system, has furthered this objective in the UK by enabling engine performance parameters on selected aircraft to be recorded in flight for analysis on ground based computing facilities. The background to this work is described in Reference 1, which also outlines the variety of uses to which the information is being directed.

One of the most important objectives so far has concerned the establishment of component life usage in military aero engines. Low cycle fatigue usage on critical rotating parts, such as discs and shafts, and consumption of creep and thermal fatigue on hot-end components have attracted most attention. These are high cost items and developments in aero engine technology are leading to higher component stresses and operating temperatures without any relaxation in life and reliability requirements, so justifying the importance attached to the work.

In addition to work associated with continuous data recording equipment, airborne monitoring equipment is also being developed which will determine component life usage in flight and indicate the life consumed on a counter display for reading during the post-flight inspection. This low cost equipment known as a low cycle fatigue counter (LCFC) will have no permanent data storage facility but is nevertheless attractive for wider application than the comprehensive but more expensive recording equipment.

In parallel with the hardware development, attention is also focussed on identifying the most accurate methods of calculating component life usage from engine performance data and it is this aspect of the work with which this paper is concerned. Only methods of estimating low cycle fatigue usage are dealt with, being the area in which the analytical procedures are most highly developed. The influence of the available engine performance parameters, the data processing capability and data storage facilities on the choice of analytical procedures are highlighted. Two approaches to LCF usage calculation are suggested as illustrative examples, one for a ground-based general purpose data recording facility, the other for the low cycle fatigue counter.

2. DETERMINATION OF LOW CYCLE FATIGUE USAGE2.1 Background

Aero engine rotating components are subjected to cyclic loads arising from throttle movement or aircraft manoeuvres, a typical variation in engine rev/min during flight being shown in Figure 1. On highly stressed components this leads to accumulation of fatigue damage at stress raising features eg the bore of a rotating disc, which may lead to cracks and eventual failure. Components whose failure might be catastrophic to the aircraft structure are therefore generally limited to a permitted safe life. Any extension of safe life gained from analysis of operational usage is thus a significant factor in reducing life cycle costs.

Component safe lives can be predicted at the design stage by considering the load variation anticipated in service together with fatigue data appropriate to the material and component in question. In addition, samples of components are usually cyclically rig tested over constant amplitude load cycles

to confirm the design prediction. Thus the safe life is determined in terms of a permitted number of load cycles, a cycle generally being defined from zero to maximum stress to zero, often referred to as a major cycle. Safety factors are included in the estimation of safe life to allow for scatter in material fatigue properties, taking into account the limited number of components which can be cyclically tested.

This life has then to be expressed in terms of a number of safe flying hours from a knowledge of how an engine is actually being used in service, to enable an operator to determine when to remove an engine for component replacement. The complex loading history has thus to be analysed to determine the fatigue damage accumulated on the component under investigation in terms of the number of major cycles.

If flight data recordings from a few selected aircraft are being analysed on ground processing equipment, sufficient flights need to be recorded to give a representative fatigue usage for the aircraft type over the range of missions it may be required to fly. Alternatively, if an airborne monitoring unit such as the LCFC is fitted to all engines in a fleet it will monitor fatigue usage on individual engines and no allowance need be made for the scatter in usage between different engines in the fleet. In principle, however, both systems may use the same procedures in calculating fatigue usage from engine performance parameters and this can be conveniently considered as involving five separate steps as illustrated in Figure 2.

Many methods have been proposed for dealing with each of these steps but the complete procedure for application to aero engine component lifeing must take into account the constraints of weight and volume that military aircraft impose on airborne recording and monitoring equipment. The selection of which methods to use will depend upon the engine performance data that can be measured, the fatigue data which exists for the component being monitored and the computing capability of the equipment. In some of the following sections, therefore, the available options are discussed.

2.2 Load history in terms of stress or strain

Stress or strain on a rotating component is dependent upon one or more of the following effects:-

- centrifugal loads
- temperature gradients
- pressure difference across opposite faces
- clamping loads on bolted assemblies
- torque loading
- gyroscopic loads
- residual stress arising from the manufacturing process

Whilst account may be taken of these loads at the design stage for worst case operating conditions in the flight envelope by using sophisticated stressing methods, it is clearly impracticable to perform this on engine performance data gathered in flight, which experience on military aircraft shows may contain up to 100 changes in condition per flight. Some simplifying assumptions have thus to be made in the interests of keeping the computing task within acceptable limits. Before this is discussed further, however, it is worthwhile considering the merits of whether to calculate fatigue damage in terms of the stress or the strain history.

The most important consideration here is the basis on which the materials fatigue data have been derived ie from constant stress or constant strain amplitude cycling. Whilst the merits of strain controlled cycling have been generally recognised as being more representative of the cycle experienced on rotating components in aero engines, the difficulty in the control of such tests and the expensive laboratory machines and control equipment involved have until recently not favoured their use. Consequently, the wealth of fatigue data applicable to aero engine components is found to be for constant amplitude stress cycling. In addition, data on the effect of mean stress or strain on fatigue life (explained in Section 2.4) is almost entirely related to the stress cycling situation. Stress is therefore the obvious choice on which to base fatigue damage calculations at the present time.

For rotating components the dominant influence on stress is centrifugal load. Torque and gyroscopic loads have very little effect on disc stresses and pressure differences also generally contribute an insignificant amount. Clamping loads and residual stresses are usually constant after the initial shakedown cycles and vary little with operating conditions. Their contribution may be accounted for by the addition (or subtraction) of a fixed value to the centrifugal and temperature gradient effects. An equation of the following type has been shown to give a good description of disc stresses:

$$S = S_c + K_1 N^2 + K_2 \Delta T + K_3 \Delta T \cdot T + K_4 \Delta T^2 \quad \dots(1)$$

where S_c = constant stress
 N = rev/min
 ΔT = temperature change across the lifing feature
 T = temperature at life limiting feature
 K_1 to K_4 are constants

Leathart and Greig (Ref 2) have shown by the use of such an equation that, provided full stress analyses are performed at four different sets of N , ΔT and T , the constants K_1 to K_4 can be easily derived and that the equation is applicable to the range of N , ΔT and T experienced in service.

Two equations similar to Eq. (1) may be needed to describe hoop and radial stresses respectively for components such as discs which are subjected to a bi-axial stress field. From these an equivalent stress, such as the Von Mises stress, can be calculated for relating the stress history with the fatigue data. Thus from a measurement of engine rev/min and ambient temperature, given details of an engine's performance characteristics and the relationship between gas temperature and metal temperature, T and ΔT on a specific component can be calculated and the stress history determined. This calculation may be quite lengthy, particularly if corrections have to be included to allow for the lag between gas temperature

change and the subsequent metal temperature change. It can therefore only be justified when component stresses are known to be seriously affected by temperature gradients,

A simplifying assumption is to consider only the variation of stress with centrifugal loads by using the following relationship:

$$S = K N^2 \quad \dots(2)$$

K is a constant and can be obtained from a stress analysis at a reference condition, generally the maximum stress seen in normal operational service, ie

$$K = \frac{S_{ref}}{N_{ref}^2} \quad \dots(3)$$

$$\text{whence } S = \frac{S_{ref}}{N_{ref}^2} \cdot N^2 \quad \dots(4)$$

The calculation of S_{ref} can of course include temperature and other effects so that this simple relationship can take account of these effects on the assumption that they too are proportional to (rev/min).

Stresses calculated using either Eq. (1) or Eq. (4) should be appropriate to the lifing feature on the component being monitored, ie at the stress concentrating notch or change in component shape. It is not unusual in aero engine discs for these to exceed the yield point of the material and be plastically redistributed into the surrounding material. Whilst plasticity can be readily taken into account using finite element methods, the computing task is considerable and it is impracticable to adopt this approach for large numbers of operating conditions. Simplifying assumptions, which involve the definition of stress, may therefore have to be adopted.

2.2.1 Nominal stress

With this approach, only the nominal stress in the bulk of material away from the stress concentration is determined. Provided that the materials fatigue data have been obtained from testing components with an identical stress concentration feature and in the same material to the one being monitored, then the relationship between nominal and true stress will be the same in each case, so permitting the fatigue behaviour to be correlated on a nominal stress basis.

2.2.2 Peak elastic stress

The concept of the peak elastic stress assumes that the concentrated stress continues to be directly related to strain above the material yield point, as illustrated in Figure 3, and may exceed the material ultimate tensile strength (UTS). The materials fatigue data must be based on the same stress definition, and whilst data from testing identical components to the one being monitored is always preferred, when this is not available the peak elastic stress approach does enable data from other specimens and components to be used.

A problem may arise, however, when taking account of the mean stress in a cycle (explained in Section 2.4) when either the UTS or yield strength is used to define the limiting value of mean stress, as a peak elastic stress above the nominal UTS is not admissible. One way of overcoming this anomaly is to express the UTS in peak elastic terms, that is by multiplying the nominal UTS by the stress concentration factor. Although this gives a neat arithmetical solution there is little experimental evidence to support its general application and the use of peak elastic stress must therefore be used with caution.

2.2.3 True stress

A further approach is to estimate the true stress from the peak elastic stress by using the Neuber relationship:

$$S_p \epsilon_p = S_e \epsilon_e \quad \dots(5)$$

Norris (Ref 3) has shown that if the plastic region of the stress/strain curve is described by the equation:

$$S_p = K \epsilon_p^n \quad \dots(6)$$

$$\text{then } S_p = \left(\frac{S_e^2}{E} \cdot \frac{1}{K^n} \right)^{\frac{n}{n+1}} \quad \dots(7)$$

where S_p = elastic-plastic or true stress
 ϵ_p = elastic-plastic or true strain
 S_e = peak elastic stress
 E = elastic modulus
 K and n are constants

It is not necessary, however, to calculate true stress using Eq. (7) for all stresses above the yield point as consideration of the manner in which aero engine rotating components are load cycled in service will show. The first major stress cycle on a highly stressed component may take it above the yield point as shown by the line a b in Figure 4. Removal of external loads will cause the stress to fall along the cyclic-elastic line b c such that a residual compressive stress will be present at the concentration for zero external load, sustained by the large amount of unyielded elastic material surrounding the

smaller yielded portion. Further load cycles will move up and down line c b always assuming that the peak stress on subsequent cycles never exceeds the initial one. If it is further assumed that any point d on line c b is related to point f on the initial elastic line by the constant increment K_n ;

$$\text{where } K_n = (S_e - S_p) \text{ at max load conditions} \quad \dots(8)$$

$$\text{ie } K_n = S_e - \left(\frac{S_e^2}{E} \cdot \frac{1}{K_n^n} \right)^{\frac{1}{n+1}} \quad \dots(9)$$

$$\text{then in general } S_{\text{true}} = S_{\text{elastic}} - K_n \quad \dots(10)$$

In practice, line c b may be affected by cyclic creep and gradually drift across to a position more like g h, but very little data are available on either the magnitude or the rate at which this may occur on engine components. Adherence to line c b, however, will always give the highest estimate of true stress and hence the most conservative damage calculation. On very highly stressed components, compressive yield may occur when the component is unloaded and subsequent load cycles may follow a hysteresis loop as shown in Figure 5. Where this occurs an approximate mean cyclic-elastic straight line can be used as a simplification to aid the computation, but very little data exists for this situation making it particularly important in this case to use materials data generated from testing components as representative as possible of the one being monitored.

2.3 Cycle and identification

The complex stress history has now to be reduced to a series of stress cycles which can be related to the fatigue properties of a material. Watson and Dabell (Ref 4) review a number of cycle identification techniques and show that the so-called "rain flow" method identifies both large and small cycles whilst not breaking up the larger ones into a number of smaller ones which contribute less fatigue damage. A logic diagram, shown in Figure 6, gives the rain flow analysis. It is one which can analyse a whole flight in a sequential manner, requiring only the minimum of data storage and thereby permitting it to be readily programmed into relatively simple data analysis equipment. An example of rain flow logic applied to a stress profile is given in Figure 7 from which it can be seen that the method takes no account of the rate at which stress is applied or removed, nor does it allow for the effect of remaining at a constant stress level between a sequence of cycles. It is also assumed that the interruption of a large stress cycle to complete a number of smaller stress cycles does not affect the damage associated with the large cycle. Reference 4 gives examples which show that the method is generally conservative in use compared with other techniques, however, and is therefore the preferred one for aero engine application. It nevertheless seems worthwhile pursuing further investigations of these effects to identify possible improvements to cycle identification methods.

2.4 Effect of mean stress

The fatigue behaviour of a material is invariably described in terms of the life in zero - high - zero constant amplitude cycles. Before these data can be used therefore, the stress cycles so far identified, most of which have a non-zero minimum, have to be converted into the equivalent zero based cycle which contributes the same amount of fatigue damage ie to allow for the so called mean stress effect (Ref 5).

Gerber proposed a parabolic relationship between stress range and mean stress, shown in diagrammatic form in Figure 8, where a line of constant life and hence constant fatigue damage per cycle has a limiting mean stress equal to the ultimate strength of the material. Later modifications of this relationship by Goodman and Soderberg introduced a linear relationship which, in the case of Soderberg has a limiting mean stress established by the yield stress, also shown in Figure 8. Any point on a constant damage line, with maximum and minimum stress values of S_{hi} and S_{lo} respectively, is related to the zero based cycle ($S_{lo} = 0$) where the stress amplitude is twice the mean stress by the equation:

$$S_E = S_L \left(\frac{S_{hi} - S_{lo}}{S_L - S_{lo}} \right) \quad \dots(11)$$

where S_E = amplitude of zero based cycle

S_L = limiting value of mean stress at zero amplitude

Salt (Ref 6), on the other hand, obtained a family of constant damage lines from smooth specimen data, shown in Figure 9, which follow the Goodman line at low mean stress but fall off towards the Soderberg line at higher mean stress and these are probably more typical of the mean stress effect than the simple Goodman straight line. Such data are seldom available, however, and in their absence the Goodman line is generally preferred to the Gerber parabola for high integrity components as it gives the more conservative estimate of fatigue damage, with the Soderberg relationship also finding application when an even more conservative approach is required. This is an area where considerably more research is required, particularly for materials in which the ultimate strength is considerably greater than the yield strength. The effect of mean stress on stress cycles which include both elastic and elastic-plastic effects also needs further investigation as has already been indicated in Section 2.2.

2.5 Fatigue damage per cycle

Fatigue life associated with each stress cycle can be obtained from the materials fatigue curve. As has already been emphasized it is important to ensure that the definition of stress on the fatigue curve is consistent with that already used in the earlier calculations. Data should preferably be obtained by testing specimens or components with stress concentration features representative of the component in question. The minimum property fatigue line should be used to allow for the inherent scatter

in fatigue properties, usually taken to be the line situated 3 standard deviations below the mean.

Fatigue properties are generally dependent upon material temperature and this effect may be allowed for by using normalised stress values ie stress divided by ultimate strength, both being temperature dependent to approximately the same extent. Experimental data gathered by Evans and Tilly (Ref 7) suggests that this form of presentation is valid when no creep-fatigue interaction is present, which is generally the situation found on gas turbine discs. The same technique may also be used when allowing for the mean stress effect (Section 2.4) by expressing mean and alternating stresses in normalised terms. There is less experimental justification for such an approach in this case, which therefore seems to be an area worthy of further investigation.

Fatigue data can be stored either in equation form or as tabulated data in data processing equipment. For the airborne application, however, a further simplification may be made to reduce the computational task. It is found that fatigue data plotted on logarithmic axes generally approximate to a straight line which can therefore be described by the simple relationship:

$$L = K S^{\frac{1}{m}} \quad \dots(12)$$

L = life in cycles corresponding to stress S

m = slope of fatigue line

K is a constant which may be found at a reference stress condition

$$\text{ie } K = \frac{L_{\text{ref}}}{S_{\text{ref}}^{\frac{1}{m}}} \quad \dots(13)$$

$$\text{hence } \therefore L = L_{\text{ref}} \left(\frac{S}{S_{\text{ref}}} \right)^{\frac{1}{m}} \quad \dots(14)$$

2.6 Fatigue damage summation

Finally, the fatigue damage associated with each separate cycle has to be summated. O'Neill (Ref 8) has comprehensively reviewed 17 cumulative damage theories, some based on metallurgical theories of material failure but mostly related to experimental results to which empirical equations have been fitted. He concludes that none of the equations shows a clear superiority for general application over the linear rule proposed by Miner, of which most of the empirical equations are modifications. The linear rule states that:

$$\sum_{i=1}^j \frac{n_i}{L_i} = D \quad \dots(15)$$

n = number of cycles corresponding to life L

i to j are the range of cycle stress amplitudes

According to Miner, $D = 1$ when some failure criterion is reached

Miner's criterion of failure was the just visible crack condition, which fortunately is consistent with that currently used on aero engine discs. The linear law is consistently criticised by workers in the fatigue field as it has been shown that the limiting value of D is dependent upon the loading sequence. Experimental results have been obtained which show that the linear rule can under estimate fatigue damage in some cases by factors of 2 or 3 (Ref 9). The value of D should therefore be set at a value less than 1 and preferably determined from fatigue tests on representative components or specimens under simulated operational load cycles. The use of minimum property fatigue data offers some protection against the conservative answer given by the linear rule when $D = 1$. It is arguable whether this is sufficient protection, however, and the subject of fatigue damage summation is clearly one which would benefit from further investigation.

3. APPLICATION OF LCF USAGE PROCEDURES

As an illustration of how the procedures for calculating LCF usage may be influenced by the computing capability of the analysis equipment, two applications at extreme ends of the range with which the author has been involved are described.

3.1 Ground data processing station

The ground data processing station comprises a small general purpose digital computer, with 32,000 words of quick access data storage and a magnetic disc back up store, linked to a tape cassette reader. Engine performance parameters are recorded on a number of engine types, ranging from a single parameter, rev/min, on one engine type to several parameters including throttle position, rev/min, temperatures and pressures on other engines. Provision is made for calculating LCF usage on any one of the highly stressed components on each monitored engine.

Clearly the requirement here is for flexible operation which is most easily achieved by maintaining the five steps in the calculation procedures as separate routines in the computer software. Each routine can contain all the options described in Section 2 as subroutines, so that the user can select the sequence appropriate to a particular application.

The following is typical of the sequence which might be chosen for the final stage compressor disc on a two shaft engine known to be sensitive to temperature when the monitored engine parameters include rev/min from both shafts and intake temperature.

- Step 1 Calculate stresses from

$$S = S_c + K_1 N^2 + K_2 \Delta T + K_3 \Delta T \cdot T + K_4 \Delta T^2 \quad \dots(1)$$

where ΔT and T are estimated from steady state engine performance relationships

- Step 2 Identify S_{hi} and $S_{\ell o}$ using rainflow logic

- Step 3 Calculate the stress amplitude and mean stress from S_{hi} and $S_{\ell o}$ and determine S_E from tabulated data describing the mean stress effect

- Step 4 Determine L corresponding to S_E from tabulated fatigue data

- Step 5 Summate fatigue damage using linear relationship

$$D = \sum_{i=1}^j \frac{1}{L_i} \quad \dots(15)$$

3.2 Low cycle fatigue counter

The LCFC is an item of avionic equipment which is specified to have minimum first cost, low volume and weight, and high reliability. To meet these objectives only the minimum of electronic hardware can be employed. The counter monitors only engine rev/min and displays accumulated fatigue damage on a limited number of channels for reading on the post-flight inspection. A 16 bit microprocessor is used with program stored in read-only memory, having a very limited random access memory for intermediate calculations and no facility for permanent data storage. The equipment, although used for different engine types, must have the maximum degree of commonality so as to reduce manufacturing costs.

The flexibility of a ground-based data processing station is obviously not applicable here and the synthesis of the five separate steps into a single expression of damage in terms of monitored engine rev/min appears attractive. This can be achieved as follows by using the simplest option at each step.

- Step 1 Assume $S \propto N^2$

- Step 2 Use rainflow logic to identify S_{hi} and $S_{\ell o}$ (which will correspond to N_{hi} and $N_{\ell o}$) and from Eqs. (4) and (10)

$$S_{hi} = \left(\frac{S_{ref,e}}{N_{ref}^2} \cdot N_{hi}^2 \right) - K_n \quad \dots(16)$$

$$S_{\ell o} = \left(\frac{S_{ref,e}}{N_{ref}^2} \cdot N_{\ell o}^2 \right) - K_n \quad \dots(17)$$

- Step 3 Assume a linear relationship between stress range and mean stress

$$S_E = S_L \left(\frac{S_{hi} - S_{\ell o}}{S_L - S_{\ell o}} \right) \quad \dots(11)$$

- Step 4 Express fatigue data according to Eq. (14) using true stress definition

$$L = L_{ref} \left(\frac{S_E}{S_{ref,e} - K_n} \right)^{\frac{1}{m}} \quad \dots(18)$$

- Step 5 Summate fatigue damage using linear relationship

$$D = \sum_{i=1}^j \frac{1}{L_i} \quad \dots(15)$$

Combining Eqs. (16), (17), (11), (18) and (15) into a single expression gives

$$D = \frac{1}{L_{ref}} \left[\frac{\left(\frac{N_{hi}}{N_{ref}} \right)^2 - \left(\frac{N_{lo}}{N_{ref}} \right)^2}{\frac{(S_L + K_n)(S_{ref,e} - K_n)}{(S_L S_{ref,e})} - \frac{(S_{ref,e} - K_n) \left(\frac{N_{lo}}{N_{ref}} \right)^2}{S_L}} \right]^{-\frac{1}{m}} \quad \dots (19)$$

Eq. (16) contains only the variables N_{hi} and N_{lo} determined by rainflow logic from N , with the constants K_n , S_{ref} , N_{ref} , S_L being appropriate to the component being monitored. Only these constants therefore need to be changed when the equipment is being used for a variety of engine types, being held in a read only memory integrated circuit component. If nominal or peak elastic stress is used throughout instead of true stress Eq. (1) is the same except that $K_n = 0$.

4. DISCUSSION

Estimation of LCF usage on operational aero engine components has been shown to require a number of simplifying assumptions. Some of these are the result of the limited understanding of the behaviour of material at highly stressed regions on components subjected to random loading. Areas particularly requiring further experimental work concern the influence of mean stress on fatigue behaviour and the summation of fatigue damage from the complex load cycle.

The use of strain rather than stress in life calculations also deserves further examination as this is the basis upon which laboratory fatigue data on a variety of specimen types and components is likely to be correlated, particularly with regard to the material behaviour in the plastic strain region. Strain is also a parameter which allows creep and material cyclic plasticity to be more readily taken into account. These are effects to which future disc materials in advanced aero engines may be increasingly susceptible.

The fact that a single preferred procedure for calculating LCF usage cannot be recommended is symptomatic of the constraints with which the aerospace engineer is often faced. The weight and space limitations on instrumented military aircraft for objectives which are not essential to mission performance inevitably demand a compromise on the number of parameters that can be recorded and on the complexity of the airborne equipment. A solution being considered in the UK is to fit comprehensive data recording equipment to a few selected aircraft of one type, with the simpler low cost monitoring equipment being more universally applied. Any discrepancies between different procedures used in the two equipments can be identified by ground analysis of flight data recordings and a factor used to correct the output of the simpler unit if required. Preliminary work by the author has shown that this factor depends upon the materials fatigue data, the peak stress in the monitored component and its sensitivity to temperature and most importantly the operational load cycles. Over a number of typical flights the average correction factor to be applied to the LCFC output can be readily established.

Although this paper has dealt primarily with LCF usage on military aero engines the concepts are also applicable to civil engines, particularly for business jets or small aircraft fleets whose operators may not have the sophisticated monitoring systems used by the large airlines. The LCFC in particular could find a ready market in this area.

5. CONCLUSIONS

1. Monitoring of LCF usage in operational military aircraft is an essential aid to maximising the life of highly stressed rotating components to the benefit of life cycle costs.

2. Procedures used for estimating LCF usage depend upon the materials data available and the computing capability of the equipment used to reduce engine performance parameters into estimated fatigue damage. Simplifying assumptions can be used to reduce the whole procedure to a single equation for application in a low cycle fatigue counter.

3. The need for further experimental investigation of materials fatigue behaviour, particularly under random loading at stress levels above the yield point, is indicated.

REFERENCES

1. Hurry, M. F., and Holmes, M., Military engine usage monitoring developments in the UK, ASME Paper 78-GT-65, April 1978.
2. Leathart, A. B., and Greig, A. W. M., A risk analysis of low cycle fatigue lives of engine components NGTE Memorandum M77018 to be published.
3. Norris, G. M., Stress redistribution by the Neuber rule compared with two dimensional finite element stress analysis, Unpublished work at NGTE 1974.
4. Watson, P., and Dabell, B. J., Cycle counting and fatigue damage, Journal of the Society of environmental engineers, September 1976.
5. Duggan, T. V., and Byrne, J., Fatigue as a design criteria, Macmillan Press 1977.
6. Salt, T. L., A designers approach to the fatigue failure mechanism, Paper at reliability and maintainability symposium. Annual proceedings, Philadelphia 23-25 January 1973, Published by IEEE 1973.
7. Evans, W. J., and Tilly, G. P., Low cycle fatigue behaviour of gas turbine alloys. Proceedings of the I Mech E 1974 Vol 188 27/74.
8. O'Neill, M. J., A review of some cumulative damage theories, Australian research laboratories report ARL/SM 326, June 1970.
9. Osgood, C. E., Fatigue design, John Wiley Press 1970.

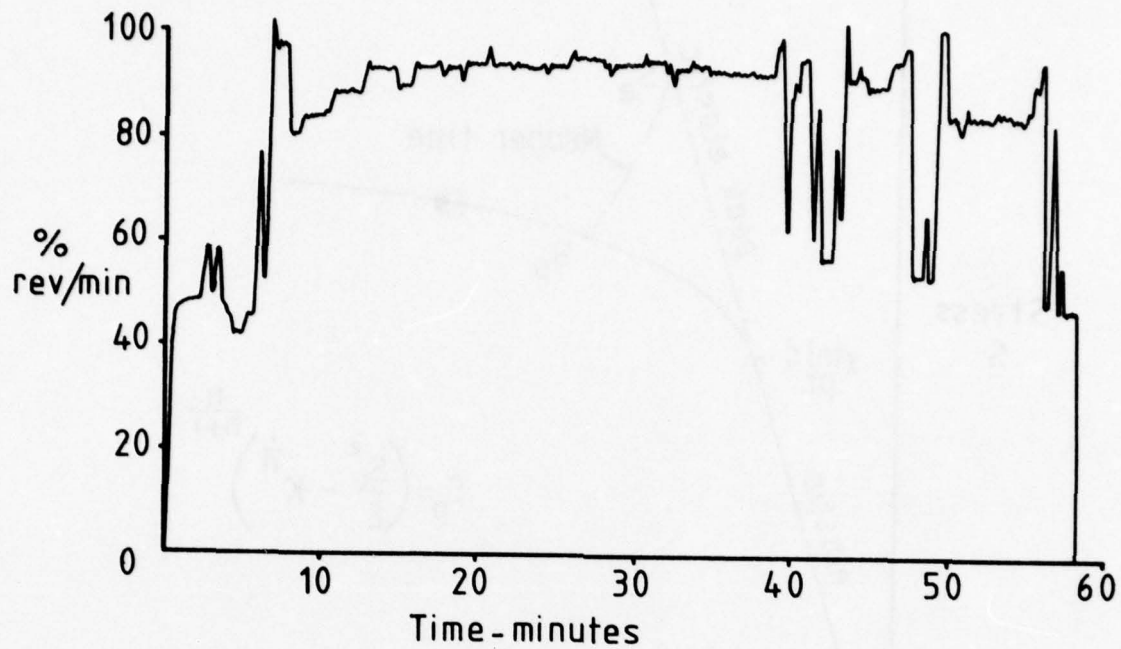


Fig 1 Flight Profile

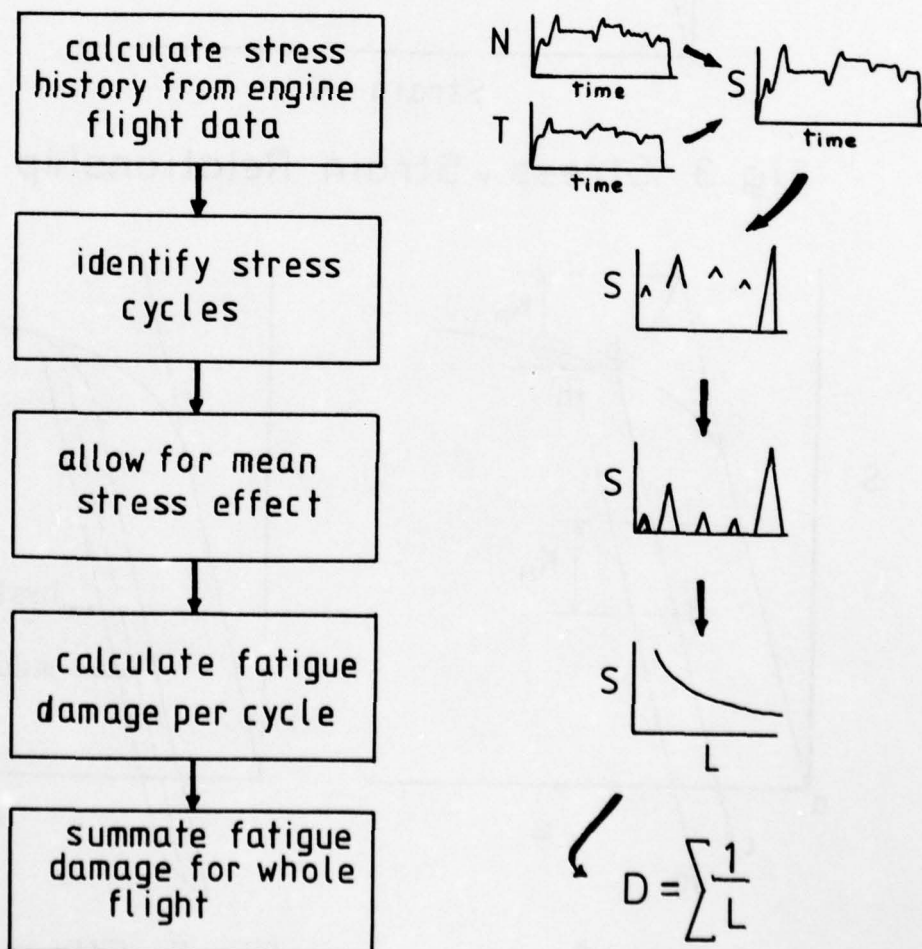


Fig 2 Calculation of LCF Usage

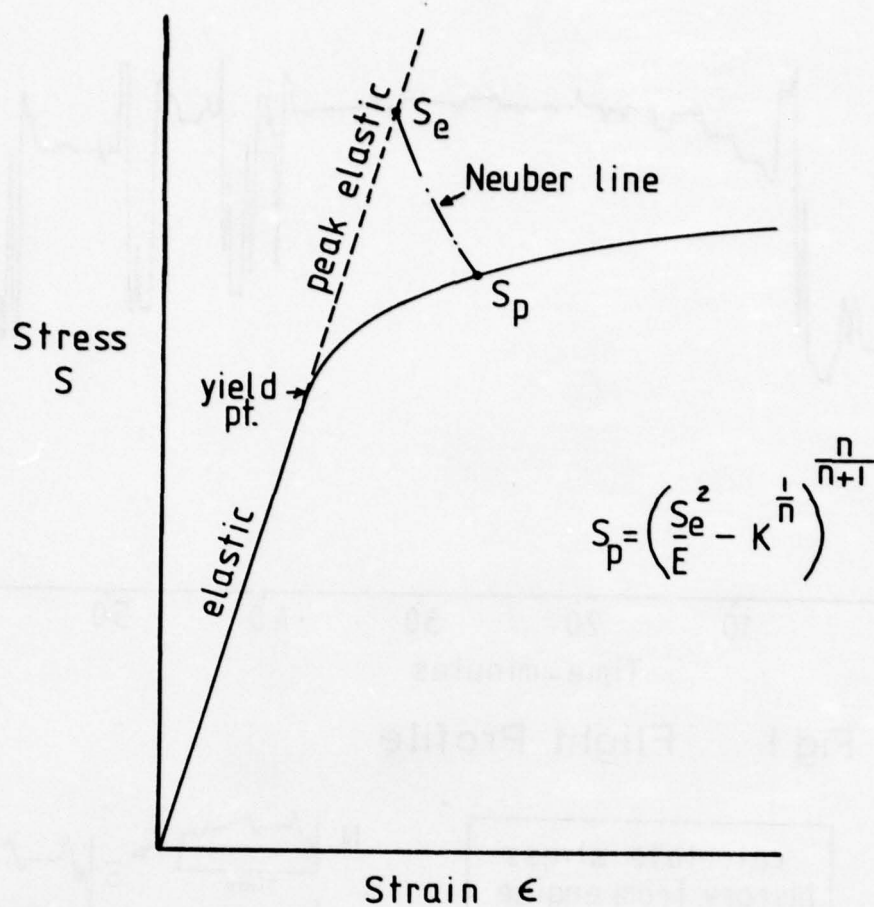


Fig 3 Stress v Strain Relationship

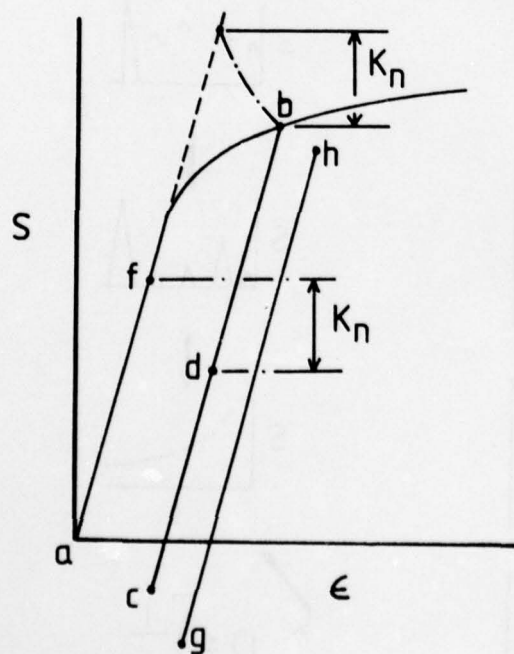


Fig 4 Cyclic Stress v Strain

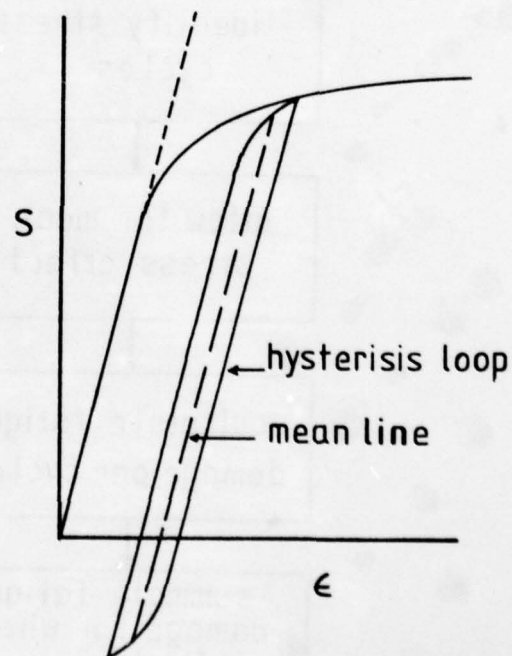
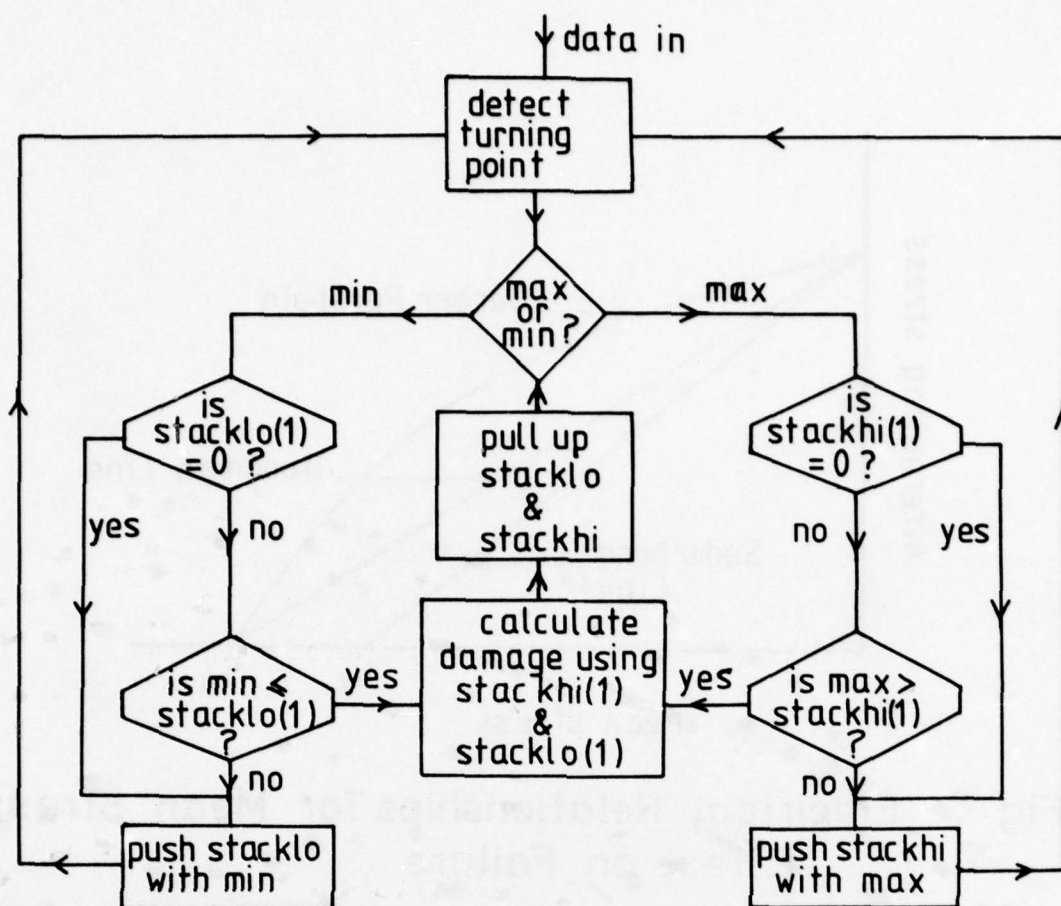


Fig 5 Effect of Compressive Plasticity



stackhi is a stack of maximum values. stacklo is a stack of minimum values. Both stacks have latest value at location(1), pushing a stack moves the values in each location down one place, pulling a stack moves them all up one place.

Fig 6 Rainflow Logic

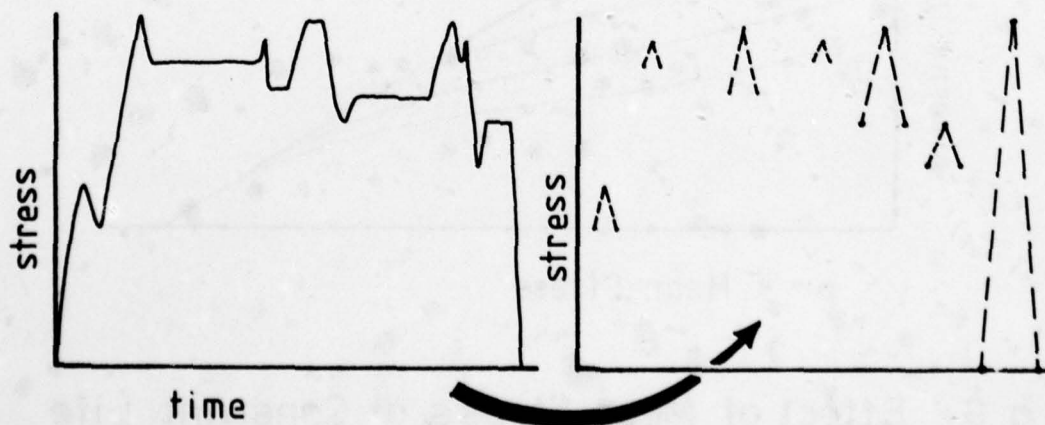


Fig 7 Application of Rainflow Logic

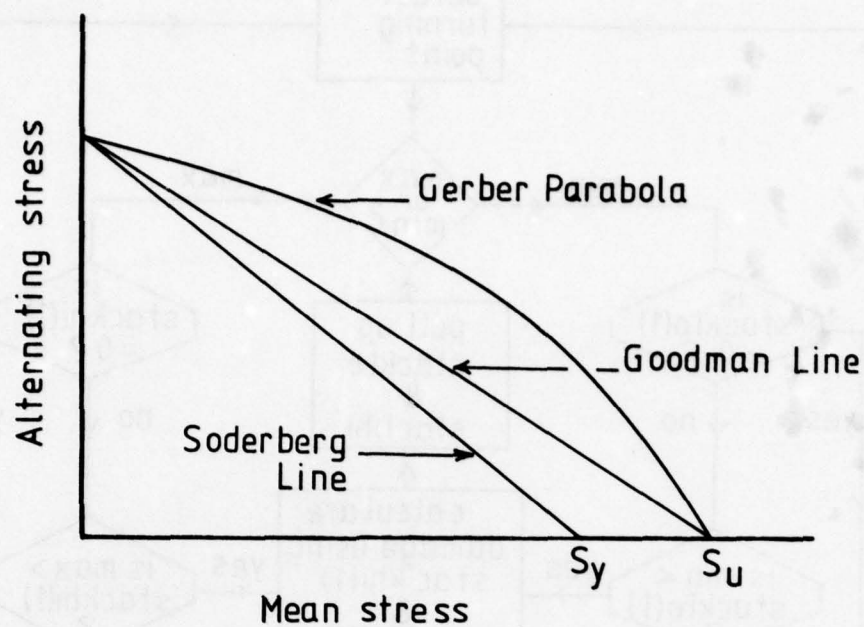


Fig 8 Empirical Relationships for Mean Stress Effect on Failure

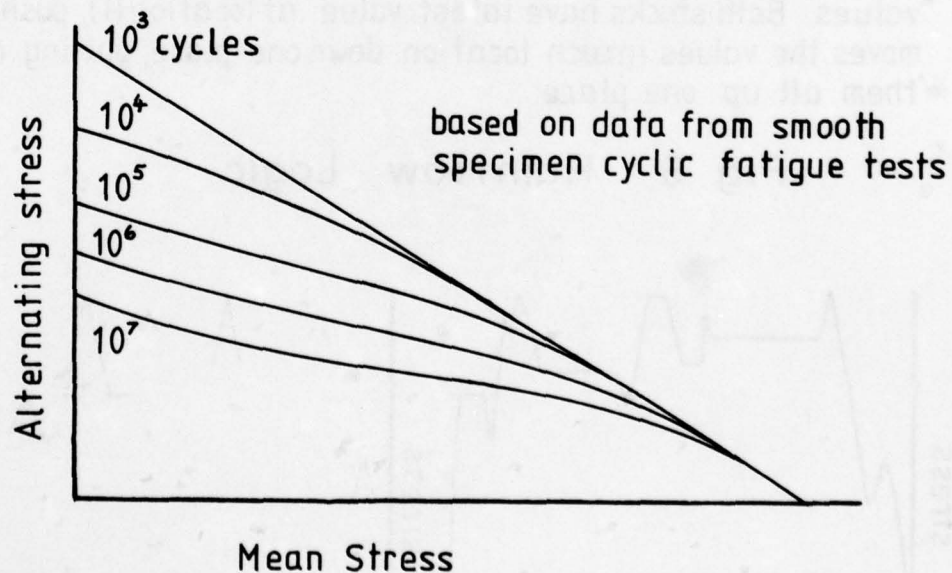


Fig 9 Effect of Mean Stress at Constant Life

DISCUSSION

R.L.McKnight, US

Do you have a strategy in your package for handling variable temperature effects and multiaxial stress/strain?

Author's Reply

Temperature effects certainly can be accommodated on the ground data processing facility and in Equation (1) of my paper I show total stress proportional to residual stress in the component, a term proportional to RPM squared; and three additional terms which are a function of the temperature gradient across the stress concentration and the temperature at that point. These temperatures may be deduced from the performance parameters on the monitored engine, which implies that not only RPM must be recorded but also intake temperature and pressure and possibly fuel flow or throttle position. The effects of temperature are taken into account in the airborne unit by incorporating them in the reference stress condition of Equation (3).

R.L.McKnight, US

What about the fatigue data that you correlated against? Do you end up using maximum temperature fatigue data curve?

Author's Reply

In taking into account the variation of fatigue properties with temperature, I suggest that the stress be non-dimensionalized as stress divided by ultimate strength of the material, assuming that both the fatigue properties and the ultimate strength vary in the same proportion with temperature. This is only an approximation to the real situation.

A.J.Atkinson, US

It strikes me that an engine is a very complicated structure and it would seem to be much more practical to record the operating parameters and be able to do the calculations on the ground for any one of a number of parts whose life you may be concerned about as opposed to doing a simplified calculation in the air and having only a few recorded damage cycles. Would you like to comment on this?

Author's Reply

Any aero engine component, as you know, will contain up to 20 or more disks and shafts, and in each of those components there may be up to two or three life-limiting features. So, typically, in any aero engine there can be 60 features that ought to be monitored. To monitor life usage in a large fleet of engines thus becomes a significant logistics task and many people would prefer to reduce the flight data to just a few numbers which can be read by ground crew on the post-flight inspection, as proposed for the LCF counter. Now, inevitably, this means a loss in accuracy compared to the full comprehensive analysis on the ground, but I believe these inaccuracies can be identified and, provided one or two aircraft types in a fleet have the full recording capability and a limited full analysis takes place alongside the airborne recording equipment, then correction factors can be determined and applied to the low cycle fatigue counter. So it's a question of balancing cost, complexity and logistics and in my opinion this goes against a full comprehensive analyses on all engines of any particular fleet.

A.J.Atkinson, US

Are there any experimental data which verify the relationships presented with actual engine component life or crack initiation/propagation/failure?

Author's Reply

I have discussed the five steps involved in the estimation of fatigue usage from measured engine performance parameters. The published literature in the fatigue field contains much experimental data to substantiate individual steps in the procedure, mainly based on specimen testing in fatigue rigs. There is less experimental evidence, however, to substantiate the application of the whole procedure to aero engine component fatigue usage in operational service. This evidence is extremely difficult to collect as the safe-life philosophy adopted for limiting the lives of rotating components means that they are removed before cracks develop. There is no way of knowing how much life potential remains in such components removed from service.

A.J.Atkinson, US

Can life be predicted so much more accurately that the cost savings derived in the ability to use parts longer outweigh the associated data acquisition and analysis costs?

Author's Reply

The cost benefits of engine usage monitoring are most apparent in military aircraft where it has been established that a wide scatter in fatigue usage exists for aircraft flying a range of missions. The LCF counter is particularly

applicable in this situation. Life-cycle cost studies in the UK indicate that the procurement cost of the LCF counter can be recovered within one year's operation on one front line aircraft investigated.

E.E.Covert, US

- (1) Which is best: air load calculation for a few points or record all data?
- (2) Are data fed back to designer?
- (3) Is fracture mechanics applicable?

Author's Reply

An option which should satisfy most requirements is to adopt dedicated airborne monitoring systems without data storage facilities for all aircraft in a fleet, together with comprehensive monitoring equipment on a few aircraft in that fleet. The latter can provide the data base from which the output of the former can be interpreted. The data bank is also valuable in support of the many other objectives of usage monitoring outlined in Reference 1.

The engine designer needs to play an integral part in the whole monitoring programme, thus ensuring the feed back of data into product improvement programmes for current and future aero engines.

The fracture mechanics approach to life prediction is becoming increasingly important and needs to be taken into account as engine usage analysis develops. There are no fundamental obstacles to achieving this objective; and I see no published work which suggests that there is a better and more consistently accurate method than the linear law proposed by Miner.

A.Alexander, US

As a point of information, there is a paper by Bagdorf and Kross in which they have looked at a statistical approach to the amount of fracture microcracks in a material versus the nominal strains in three dimensions and they do have a semi-empirical approach, but it's slightly more accurate than the Miner approach.

Author's Reply

I am always sceptical about plans for better accuracy because in aero engines we have to cope with a wide range of materials and loading situations. Have they demonstrated that it is better for steel, nickel alloys, titanium, powder materials, for high and low temperatures, for complex loading, or stress concentration with a whole range of K_T ? I have my doubts that any method will be universally applicable, but certainly papers such as the one you mentioned ought to be read so that the general data bank can be improved on this subject.

C.C.Chamis, US

Since we seem to be on the subject of philosophy, it seems to me that what you describe would be a data acquisition of flight input variables for analysis.

I think that linear degradation rule and fatigue test data from uniaxial data are a first approximate step for life prediction of engine parts subjected to complex loads which result in triaxial stress fields. Now, to take a uniaxial test specimen to generate smooth fatigue data and try to make any good assessment of how material behaves under spectra fatigue, which the data here indicated, we can smooth out the zero stress base which in itself is not very realistic. It would seem to me that this definitely requires additional discussion. Further yet we have triaxial stress state and those data available to show that the material does not behave the same on the triaxial stress state as it does on the uniaxial small fatigue specimen.

Here I am trying to make the following point: It would seem to me that if you have equipment and data acquisition system as you propose here, and if you can go one step beyond what you have suggested, suppose you could put a strain gauge somewhere on what is estimated to be a high stress point and you record as a function of time during flight exactly what the stress or strain is at that point. Now pass that information on to someone else who can try to interpret how this information can be used and integrate it back into the design. We have indicated here that the linear fatigue rule called by Miner's or whatever else may be applicable is conservative design. I will go one step further: we want to know how much life we have remaining on our part. We cannot discard material as often as we did in the past or as thoughtlessly. So it seems to me that all these points somehow should be considered. If you found out that, in your case, in the absence of anything better, the linear fatigue rule is well and good, put it in that context. On the other hand, to say that a uniaxial fatigue specimen will solve all the problems on a complex triaxial state as it may exist in the root of a notch, would seem to me highly speculative.

The two engine performance parameters monitored in service, though a good start, are not sufficient to determine even approximately material or component structural response at some local point.

Author's Reply

It is obviously desirable to be able to monitor the stress on a component directly rather than estimate it from a performance parameter. A strain gauge would give such an output but the reliability of such devices for in-service

engines is at the moment inadequate. As I see it, measurement technology has not yet produced any other way of obtaining stresses on components in operational aero engines other than estimating them from performance parameters. However, there is a lot to be said in defense of performance parameters because RPM is the dominant operational parameter that affects stress, and you can measure RPM very easily and accurately. Temperature gradients are also important and may be estimated from RPM and other performance parameters.

C.C.Chamis, US

I agree in taking the RPM as being the dominant point. But the thing here that causes fatigue, low-cycle fatigue, which also is superimposed on high-cycle fatigue in the actual part which comes to be vibrations, is a function of the two variables you are measuring. Here the other direct method would offer an advantage.

Author's Reply

Yes, I agree that the high-cycle fatigue superimposed on the low-cycle fatigue behavior is very important and this is something we must take a very close look at. However, a transducer and signal conditioning equipment suitable for looking at steady variations in stresses is probably not suitable for looking at vibratory stresses. No operator likes to carry around more transducers, analysis, and recording equipment than is absolutely necessary for the mission. Particularly, in a fighting vehicle the mission is most likely to be successfully completed on an aircraft with the minimum of non-essential equipment. We must be careful therefore lest we start putting too much monitoring equipment on operational aero engines.

Now I'd just like to take up your other point about the use of uniaxial specimen data in support of LCF usage monitoring. I hope that I didn't suggest that uniaxial data must be used, as uniaxial data is only used when there is no other data available. I support the use of specimens which most closely resemble the component in question being monitored. Only when that data isn't available and the best that is available has to be used, would I fall back on uniaxial smooth specimen data.

BOUNDARY-INTEGRAL EQUATION ANALYSIS OF AN ADVANCED TURBINE DISK RIM SLOT

R. B. Wilson, R. G. Potter, J. K. Wong
Engineering Department
Commercial Products Division
Pratt & Whitney Aircraft Group
East Hartford, CT. 06108
U. S. A.

SUMMARY

Rapid advances have been made in recent years in elastic three dimensional structural modeling. The finite element method has proved an effective means for tracking load transfer through complex structures. The more recently developed boundary-integral equation (BIE) method is particularly effective for the resolution of high stress gradients and is therefore particularly suitable for the analysis of parts containing stress risers. Incorporation of the three dimensional BIE method as a design tool requires its calibration for geometries representative of those of engineering interest. This paper describes the stress analysis of a turbine disk rim slot using the BIE method and presents comparisons of the numerical results with data from a model test program.

INTRODUCTION

A necessary part of the design and analysis cycle in the manufacture of gas turbine engines is the ability to evaluate the stress state in an engine component, both for general design purposes and to provide input for the life prediction process. The increased geometrical, material and loading complexity of advanced engine designs requires the use of three dimensional numerical stress analysis in order to avoid the long lead times and high costs associated with complete reliance on component or model testing as well as the oversimplifications sometimes required for the use of two dimensional analysis.

The finite element method provides an excellent and readily accessible method for the study of general load transfer through complex structures. It is not, however, particularly well suited for the resolution of high stress gradients. In the design of turbine engines it is often high gradient regions near structural details such as notches and fillets which prove to be life limiting. It is therefore necessary to develop and calibrate three dimensional stress analysis methods suitable for use in these regions.

In recent years the boundary-integral equation (BIE) method has been shown to be especially well suited for problems requiring the resolution of high stress gradients (References 1, 2). The numerical implementation of the method now allows relatively straightforward modeling of complex structural details and permits solution of meaningful problems with a reasonable investment of both engineering and computer time.

This paper discusses the mathematical basis and numerical implementation of the BIE method, compares it with the finite element method for a relatively simple problem and then describes a combined analytical and experimental program to calibrate the BIE method for a complex geometry of interest in gas turbine engine applications.

THE BOUNDARY-INTEGRAL EQUATION METHOD

Derivation of the Boundary-Integral Equation

The BIE method is based on classical analytical results in elasticity and potential theory. It depends on the reciprocal work theorem and on the existence of an infinite body point load solution to the equilibrium equations. The development is described briefly below for the three dimensional case. A much more detailed development in both two and three dimensions may be found in Reference 3, which also contains an extensive bibliography.

Let V be an elastic body (possibly multiply connected) with surface S . If t_j, u_i and t'_j, u'_i represent two sets of surface tractions and displacements for which the body is in equilibrium then, by Betti's reciprocal work theorem,

$$\int_S t'_j u_i dS = \int_S t_j u'_i dS \quad (1)$$

For any infinite homogeneous elastic body there is a point load solution $U_{ij}(p, q)$ to the equilibrium equations (References 4 and 5). $U_{ij}(p, q)$ is the displacement in the x_i direction at the field point q due to a unit load in the x_j direction at the source point p . Closed form expressions for this point load solution exist for isotropic materials (the Kelvin solution) and for transversely isotropic materials (Reference 6). It has also been recently shown that efficient numerical calculation of the U_{ij} can be carried out for general anisotropic materials (Reference 7). Differentiation of U_{ij} and use of Hooke's law allow the calculation of a corresponding point load function for stresses. By identifying the primed quantities in Eq. 1 with the point load solution, applying Eq. 1 to the region V with a small sphere centered at the point p deleted and taking appropriate limits the Somigliana identity for the interior displacements is obtained,

$$u_j(p) = \int_S t_i(Q) U_{ji}(p, Q) dS - \int_S u_i(Q) T_{ji}(p, Q) dS \quad (2)$$

where Q denotes a point on S and T_{ji} is derived from the point load solution.

A further limit operation, in which the interior source point p is allowed to approach a boundary point, P , leads to the boundary-integral equation

$$u_j(P)/2 = \int_S t_i(Q) U_{ji}(P, Q) dS - \int_S u_i(Q) T_{ji}(P, Q) dS \quad (3)$$

relating the boundary displacements and tractions without explicit reference to the interior of the body. The BIE (Eq. 3) cannot be solved in closed form except for a few very simple geometries and would have little practical significance without modern computing capabilities.

Numerical Solution of the Boundary-Integral Equation

The numerical solution of Eq. 3 involves two types of approximation. First, the surface of the real part is modeled as an assembly of surface patches of some specified form. Second, some relatively simple functional variation of displacement and traction is assumed on each surface patch. These two assumptions allow the integrals occurring in Eq. 3 to be evaluated, leading to a system of linear algebraic equations in the unknown boundary data.

Two different approaches have been used for the solution of the three dimensional problem.

1. The surface, S , is modeled using plane triangular elements and boundary data are assumed to vary linearly over each element. This allows the exact calculation of the integrals in Eq. 3 but requires a large number of elements to model complex geometries. This approach is discussed in Reference 1.
2. Both the geometry and boundary data variation over a surface patch are modeled using shape functions, such as the quadratic isoparametric shape functions shown in Figure 1. Complex geometry and boundary data variations can be modeled using fewer elements but the integrations must be carried out numerically (References 8, 9, and 10).

In either case Eq. 3 is evaluated with the source point P placed successively at each of the nodal locations defining the boundary data variation. Each evaluation leads to linear algebraic equations which generally involve, because of the surface integrals, all of the unknown boundary data. The resulting linear system is full, rather than having the banded structure associated with the finite element method. After the boundary solution has been found, a numerical implementation of Eq. 2 allows calculation of displacement and, by appropriate differentiation, stress, at interior points.

Two different three dimensional BIE codes were used in the work discussed in this paper. The BINTEQ code (Reference 1) utilizes plane triangular elements with exact integration. The more recently available BASQUE code, Reference 8, models geometry using quadratic isoparametric shape functions and provides a choice of linear, quadratic or cubic boundary data approximation. The BASQUE program was originally developed at the Centre Technique des Industries Mecaniques, Senlis, France.

Comparison with 3D Finite Element Analysis

This section discusses the BIE analysis of a low cycle fatigue specimen. The presence of curved surfaces, a stress concentration and three dimensional effects make the problem representative of those encountered in design analysis, while the relatively simple geometry allows direct comparison of accuracy and efficiency with the finite element method.

A cross section of the specimen is shown in Figure 2. The specimen is pin loaded at A and B. The solid line shows the simplified shape used for both the BASQUE and NASTRAN analyses. A very refined BASQUE analysis was first run to provide three dimensional baseline results. Less refined BASQUE maps were then used, in order to determine the minimum cost analysis yielding satisfactory results.

The map used for the BIE analysis is shown in Figure 3. The same idealization was used on the free surface and in the specimen midplane. One element was used through the thickness except in the immediate neighborhood of the notch. This map consisted of 28 elements and 84 nodes, requiring a run time of 65 cpu sec. The peak hoop stresses (tensile and compressive) and the peak transverse stress were accurate to better than 2 percent compared to the baseline results. The results of this analysis are shown in more detail in Figures 4, 5 and 6.

A NASTRAN analysis of the specimen was then carried out using the breakup shown in Figure 7. Two elements were used through the thickness for the entire map, since NASTRAN does not currently have a 15-node isoparametric element for mesh transition. The NASTRAN map was designed to match the BASQUE surface map as nearly as possible while avoiding extreme element shapes. The NASTRAN map had 16 HEX20 elements and 141 nodes; the analysis required 48 cpu sec. The results, while in good qualitative agreement with the baseline results, were significantly less accurate than the BASQUE results. The maximum hoop stress in the notch was 11 percent low, the maximum compressive stress 17 percent high, and the peak transverse stress 10 percent low. The results of the NASTRAN analysis are also shown in Figures 4, 5 and 6.

A second NASTRAN analysis was done using the same map in the cross section, but with four elements through the thickness. This analysis (32 elements, 245 nodes) required 85 cpu sec. The peak stress results did not improve over those cited above, although response through the specimen thickness was somewhat smoother. It is clear that to achieve the same level of accuracy as the BASQUE analysis would require refinement of the NASTRAN map in the specimen cross section. Based on the present NASTRAN analyses and on plane strain finite element analyses of the specimen, the minimum NASTRAN mesh required would have at least three elements through the thickness and at least a 4-by-6 mesh in the cross section. The analysis would require approximately 225 cpu sec. (72 elements, 477 nodes), almost 3.5 times as long as the BASQUE analysis.

BIE ANALYSIS OF A TURBINE DISK RIM SLOT

Turbine disk rim slots, which retain the blades in a gas turbine engine rotor assembly, produce strain concentrations in the disk rim under the inertia loadings of the disk and the attached blades. To supply cooling air to the turbine blades, cooling holes are machined into the disk rim, and exit in the disk rim slots. Determination of the stress field at the intersection of the disk rim slot with the cooling hole is essential to predict turbine disk low cycle fatigue life and to optimize cooling hole and rim slot geometries.

Testing, either of models or actual components, is expensive and can involve very long lead times. In addition, it yields information whose validity is restricted to the particular geometry tested. It is thus necessary to use numerical stress analysis methods. While appropriately chosen two dimensional analyses are suitable in many situations, the rim slot/cooling hole intersection problem is representative of a class of problems in which three dimensional effects are important. As discussed above, three dimensional finite element techniques are not especially suitable for resolving stress concentrations. In addition, the modeling of a disk rim geometry (Figure 8) for finite element analysis is itself a complex process.

The BIE method is an attractive alternative to the finite element method, but before it can be used as a part of the design analysis process it must be calibrated for a problem representative of those solved in the actual design process. In order to suitably calibrate the BIE method a combined test and analytical program was carried out. The program involved the comparison of strain gage data from a scale model of a disk rim with analytical results obtained using the BINTEQ BIE code. The results demonstrate the applicability and efficiency of the BIE method for this class of problems. The following sections discuss the test program, the BIE analysis, and the correlation of results. The final section discusses the application of the more recently available BASQUE code to this problem.

Disk Rim Model Test Program

Figure 8 shows a schematic of the type of disk rim geometry used in this program. The cooling holes run radially from the disk bore to the rim. Since detailed strain gaging of actual hardware was not practical, it was decided to construct a 6X (six times actual size) model. Construction of an actual disk at this scale was not possible, so a rectilinear model containing five rim slots was used. Figure 9 shows the test model both in cross section and parallel to the rim slots. The cooling hole geometry is also shown. The straight sides of the cooling hole are a feature of the disk design which originally motivated the model test program.

A major concern at the rim slot/cooling hole intersection is the effect of blending, or smoothing, the intersection of the cooling hole and rim slot. The test and numerical study were carried out for two different intersection geometries, Figure 10. In one case (referred to as the first geometry) the intersection was unblended, in the other case (second geometry) the intersection with the rim slot was smoothed, as shown in Figure 10.

Since in the rectilinear case a blade pull does not give rise to a transverse stress in the model, independent loads were applied in the radial and tangential directions using hydraulic cylinders. This was intended to allow modeling of the actual disk load state using superposition. The model is shown installed in the test rig in Figure 11. Strain gage data was taken primarily from the center rim slot. Both sides of the center rim slot and cooling hole were instrumented and the results averaged because of the symmetry in loading and geometry.

BIE Analysis of Disk Rim

A three dimensional stress analysis was carried out for the center rim slot. Because of the geometrical symmetry, only one-quarter of the center rim slot was actually modeled. At the time the program was begun the BASQUE BIE code was not yet available. The BINTEQ program has problem size restrictions which made it impossible to model the entire geometry using the BIE method alone. As a result, a two-stage numerical analysis was adopted. First, a relatively crude finite element model of the quarter section was built and solved, using eight node isoparametric elements. The finite element model used is shown in Figure 12. In order to resolve the detailed behavior in the rim slot and cooling hole a BINTEQ map of the rim slot region was constructed. The BINTEQ maps for both the first and second geometries are shown in Figure 13. The displacements from the finite element analysis were applied as boundary conditions to the top and bottom surface of the BIE models.

The finite element analysis required about 1.5 hours of computer (IBM 370/168) time. The BINTEQ analyses for both geometries used 436 plane triangular elements and each took about 1 hour of cpu time.

Correlation of Results

The analytical and test results were compared in terms of strain concentration factors, defined as

$$K_t = \frac{\text{local strain}}{\text{nominal strain}}$$

where the nominal strain for each load case is

$$\text{nominal strain} = \frac{\text{force}}{(\text{area}) \times (\text{Young's modulus})}$$

Considerable care was taken to calculate consistent nominal strains for the test and BIE results.

Figures 14 through 17 shows the correlation, at several locations, between test and BIE results for both geometries and both load states. Results are presented for two lines of strain gages in the rim slot and two in the cooling hole near the rim slot/cooling hole intersection. The BIE and test results agree quite well both in magnitude and in variation of strain over the surface. The largest differences between the test and analytical results occur in situations in which rather rapid variations occur over relatively large elements, for example on the flat surface of the cooling hole or in the portion of the rim slot away from the intersection with the cooling hole. The analytical results in these areas can be improved by mesh refinement or rearrangement, or by the use of a BIE program such as BASQUE which incorporates a higher order modeling capability. Some preliminary results obtained using the BASQUE code are discussed below.

Effectiveness of Higher Order BIE Modeling

When the BASQUE code became available it was used to repeat the analysis of the second (blended) cooling hole geometry. The map used for this study is shown in Figure 18, along with the corresponding BINTEQ map. The use of isoparametric shape functions for geometry modeling allows the representation of the structure with less than one-quarter of the number of elements required for the BINTEQ analysis. Further the computer time required (using quadratic boundary data variation) was eleven minutes compared to almost sixty minutes for the BINTEQ analysis.

An example of the improvement in accuracy offered by the higher order code is shown in Figure 19, which compares BASQUE, BINTEQ and test results for plane 4A (in the cooling hole) under tangential load. The peak strain predicted by the BINTEQ analysis is 8 percent low relative to the test data. The peak strain predicted by the BASQUE analysis, using a much cruder map, is only 1 percent low.

CONCLUSIONS

The BIE method has been shown to be capable of predicting rapidly varying stress and strain fields in complex geometries, using either plane triangular or higher order elements. Ease of geometrical modeling and higher order boundary data variation combine to make shape function based codes, such as BASQUE, most efficient for the majority of design analysis use.

In order to allow full use of the BIE method in engineering analysis, development of certain additional capabilities is required to model the blade attachment/disk lug interaction. The ability to incorporate thermal stresses due to a nonsteady temperature field is also required in many gas turbine engine applications.

ACKNOWLEDGMENTS

The BASQUE computer code was originally developed by Drs. J. C. Lachat and J. O. Watson at the Centre Technique des Industries Mechaniques, Senlis, France. The BINTEQ code was developed by Dr. T. A. Cruse at Carnegie-Mellon University.

The authors wish to thank Mr. D. W. Snow who did the baseline three dimensional analysis of the fatigue specimen.

REFERENCES

- 1) Cruse, T. A., "An Improved Boundary-Integral Equation Method for Three Dimensional Elastic Stress Analysis", *Comp. & Struct.*, 4, (1974) 741-754.
- 2) T. A. Cruse and R. B. Wilson, "Advanced Applications of Boundary-Integral Equation Methods", *Nuclear Engineering and Design*, 46, (1978) 223-234.
- 3) T. A. Cruse, "Mathematical Foundations of the Boundary-Integral Equation Method in Solid Mechanics", AFOSR-TR-1002, Accession No. ADA 043114 (1977).
- 4) F. John, *Plane Waves and Spherical Means Applied to Partial Differential Equations*, Interscience, 1955.
- 5) J. L. Synge, *The Hypercircle in Mathematical Physics*, Cambridge Univ. Press, 1957.
- 6) Y. C. Pan and T. W. Chou, "Point Force Solution for an Infinite Transversely Isotropic Solid", *JAM*, 43, *Trans. ASME*, 98, Series E, 608-612 (1976).
- 7) R. B. Wilson and T. A. Cruse, "Efficient Implementation of Anisotropic Three Dimensional Boundary-Integral Equation Stress Analysis", *Int. J. Num. Meth. Engrg.*, in press.
- 8) J. C. Lachat and J. O. Watson, "Effective Numerical Treatment of Boundary-Integral Equations", *Int. J. Num. Meth. Engrg.*, 991-1005 (1976).
- 9) F. J. Rizzo and D. J. Shippy, AFOSR-TR-76-0841, Accession No. ADA 027718 (1976).
- 10) F. J. Rizzo and D. J. Shippy, AFOSR-TR-77-0950, Accession No. ADA 043118 (1977).

AD-A070 950

ADVISORY GROUP FOR AEROSPACE RESEARCH AND DEVELOPMENT--ETC F/G 21/5
STRESSES, VIBRATIONS, STRUCTURAL INTEGRATION AND ENGINE INTEGRI--ETC(U)
APR 79

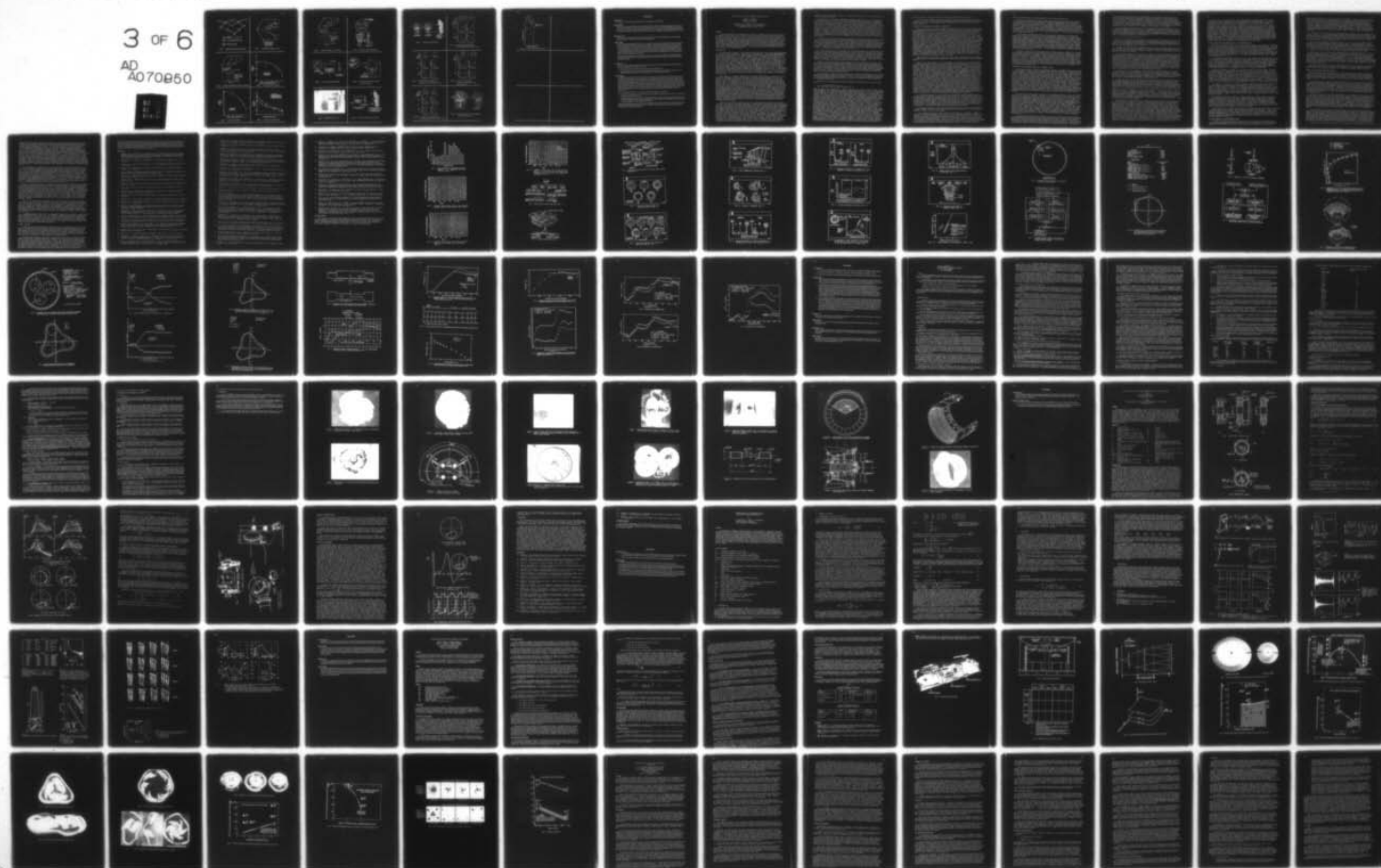
UNCLASSIFIED

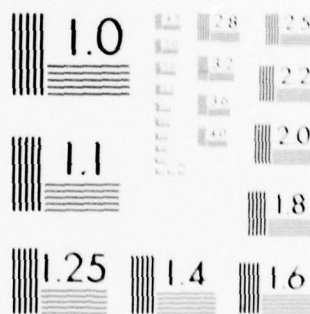
AGARD-CP-248

NL

3 OF 6

AD
A070B50





MICROCOPY RESOLUTION TEST CHART
NATIONAL BUREAU OF STANDARDS-1963-A

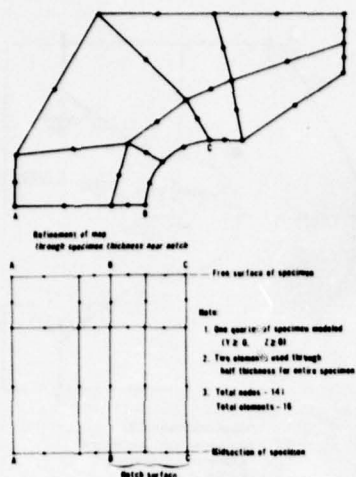


Figure 7 Finite Element Map For LCF Specimen

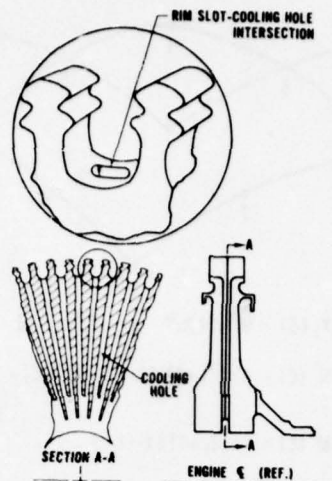


Figure 8 Rim Slot-Cooling Hole Intersection

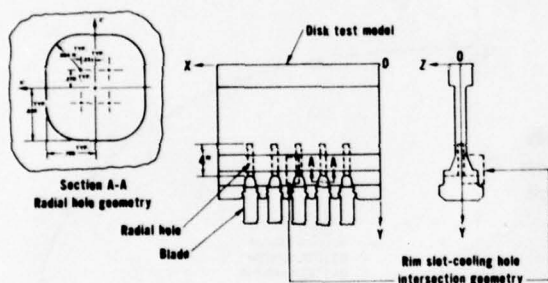


Figure 9 Disk Test Model With Radial Holes

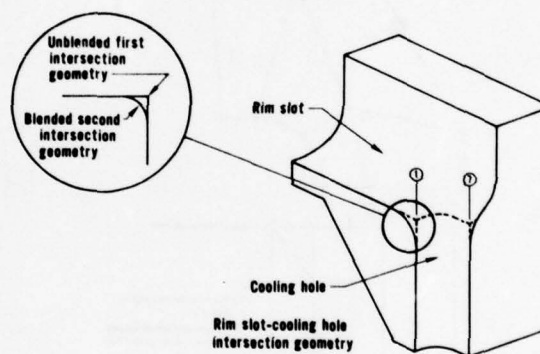


Figure 10 First and Second Rim Slot-Cooling Hole Intersection Geometries

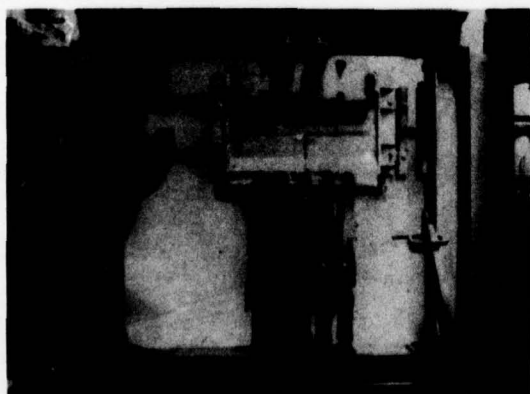


Figure 11 Disk Rim Model in Test Rig

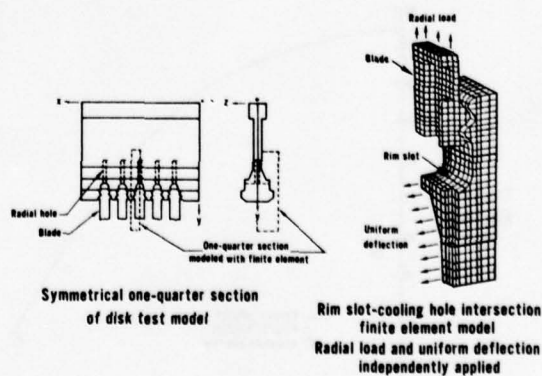


Figure 12 Three-Dimensional Finite Element Model

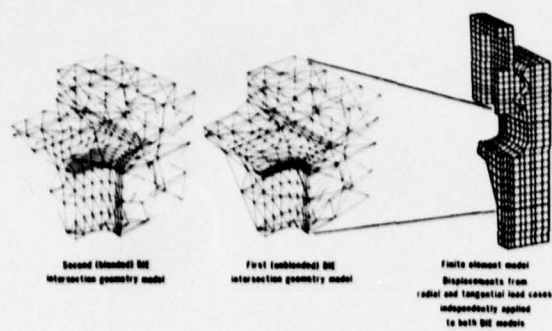


Figure 13 Three-Dimensional BIE Models

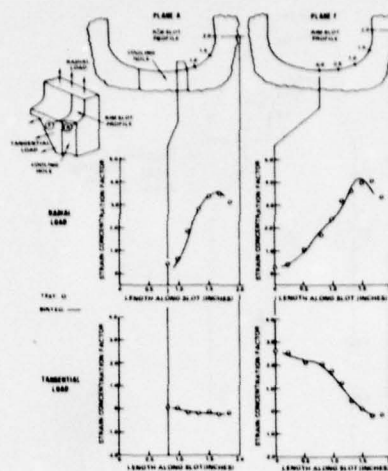


Figure 14 Correlation of Test and BIE Results
First Intersection Geometry, Planes A and F

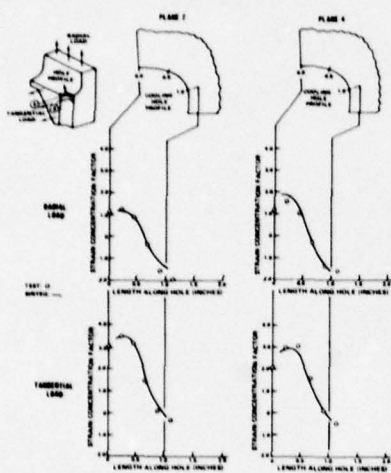


Figure 15 Correlation of Test and BIE Results
First Intersection Geometry, Planes 2 and 4

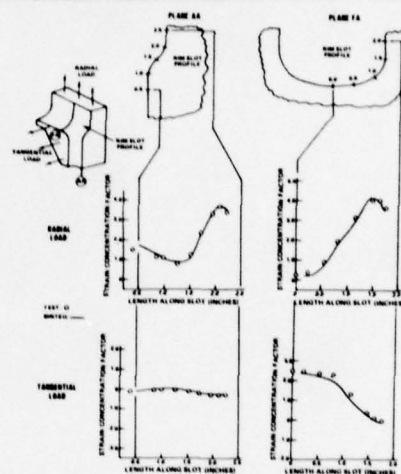


Figure 16 Correlation of Test and BIE
Results Second Intersection Geometry,
Planes AA and FA

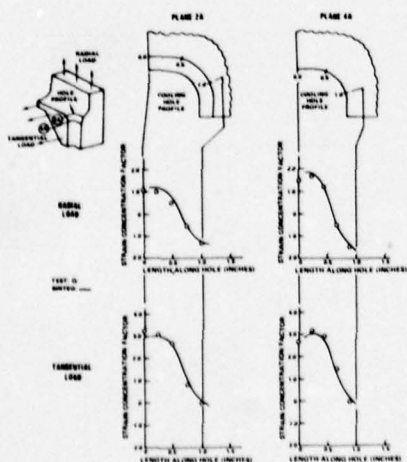


Figure 17 Correlation of Test and BIE Results
Second Intersection Geometry, Planes 2A and 4A

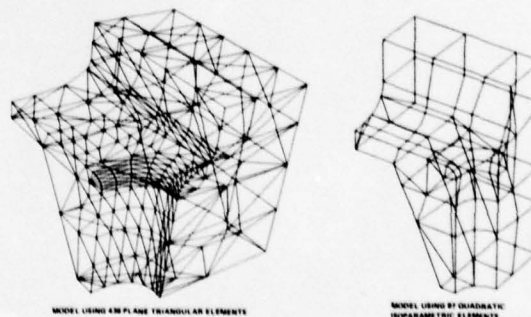


Figure 18 BIE Maps for Analysis of Turbine Disk Rim
Slot-Cooling Hole Intersection

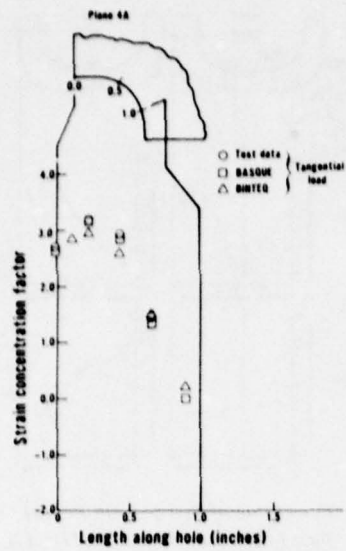


Figure 19 Effect of Higher Order BIE Modeling

DISCUSSION

J.J.Blech, Italy

Could you comment whether integrating across the singularities poses problems?

Author's Reply

This has in the past posed problems, and was the subject of some rather extensive study during the early development of the BIE method. I think it fair to say that this problem has now been resolved through careful attention to the numerical integration schemes used and through indirect or exact evaluation of the most highly singular terms. This question is discussed in some detail in some of the references to the papers; in particular numbers 1, 3, 8 and 9.

R.D.McKenzie, UK

The presence of cooling air will give rise to significant thermal stresses in the neighbourhood of the air passage. Would the speaker comment on the problem of evaluating these?

Author's Reply

There is no presently available BIE code which can handle the time dependent thermal loads which are required in the mission analysis of hot engine components. A method for dealing with this problem was developed during a recently completed Air Force contract with Pratt & Whitney, and is discussed in the final contract report (by T.A.Cruse and myself). A main objective of the present work was the demonstration of the BIE method's ability to accurately and efficiently calculate concentrated stresses and strains in complex geometries subject to rather complex mechanical loads. Such a demonstration was essential before undertaking the effort of modifying a BIE code to accept time dependent thermal loads.

Further, while thermal effects are clearly present in the disk rim area, the major loading is usually mechanical. It is hoped that the thermal effects can perhaps be taken into account without resorting to a full three dimensional thermoelastic analysis.

C.C.Chamis, US

Were the boundary values for displacements and forces used in the boundary-integral solution those determined from the 3-D finite element analysis? If so, then

- (1) the running time savings cited are not realistic and fair comparisons; and
- (2) the good agreement between boundary-integral predicted strains and measured strains is mostly due to the global solution for the displacement field obtained via the 3-D finite element analysis.

Author's Reply

The displacements (but not stresses) on the top and bottom surfaces of the BIE model were taken from the results of the finite element analysis. If these displacements were significantly in error then no analysis method could, except by accident, obtain accurate local results in the rim slot and cooling hole. Given the good accuracy achieved for these boundary displacements, the quality of the local results in the cooling hole and rim slot depends on the ability of the analysis method to resolve rapidly varying stresses and strains in a complex geometry. A considerable body of evidence indicates the superiority of the BIE method in this regard. In particular, the printed version of this paper discusses the calculation of concentrated stresses in a low cycle fatigue specimen using both the higher order BIE code and NASTRAN. The BIE results are significantly better than the NASTRAN results for the same computing cost.

As far as computing time (or cost) is concerned, the main conclusions to be drawn are:

- (1) The BIE code using higher order variation of geometry, displacements and tractions is much more cost-effective than the older linear variation code.
- (2) The total computer time used for the combined finite element and BIE analysis is significantly less than would have been required if a finite element model detailed enough to resolve the concentrated stresses had been used. This is particularly clear for the higher order BIE code.

Finally, I should note that we have since carried out (entirely with the higher order BIE code) an analysis of a one-half section of a blade attachment and disk rim. This larger and geometrically more complex problem required a total of about 25 minutes of computing.

ENGINE ROTOR BURST CONTAINMENT/CONTROL STUDIES

Ermett A. Witmer
 Thomas R. Stagliano
 José J.A. Rodal

Department of Aeronautics and Astronautics
 Massachusetts Institute of Technology
 Cambridge, Mass. 02139, USA

SUMMARY

Studies of records of uncontained rotor bursts in commercial aviation both in the U.S. and abroad indicate that the rate per million engine hours has continued to hover near 1 for more than the past decade. Of these, serious damage resulted at a rate of about 0.13 per 10^6 engine hours; while this rate is very small, efforts to reduce the hazard of non-containment continue. Three principal means are commonly pursued to this end: (1) proper airframe/engine/system layout and redundant design to minimize the consequences of non-containment, (2) inspections to detect and to reduce the incidence of rotor failures as well as the adoption of design details which will tend to produce small-fragment failures first rather than heavy energetic fragments, and (3) the use of containment or deflector structure to control dangerous fragments. The present paper mainly reviews some of the recent work in the latter category.

INTRODUCTION

In recent years, surveys of the number and type of engine rotor burst non-containments in the U.S. and U.K. commercial aviation have been reported -- covering generally the period 1962 through 1976 [1-5]. Some excerpted results from those studies are shown here for convenient reference. For example, Mangano et al. [1] report the incidence of uncontained rotor burst as shown in Fig. 1 for U.S. commercial aviation during 1962-1976; although the number per year varies, these incidents persist at a rate of more than 15 per year. Similarly, Gunstone [2] reports the combined "world wide and U.S." commercial aviation engine total non-containments per million engine hours for the period 1964-1975 as shown in Fig. 2; here it is seen that the non-containment rate has persisted at about one per million engine hours. Of greatest concern, perhaps, from the safety standpoint are the heavy energetic fragments which result from engine disk bursts. Figure 3a shows a "worldwide" history of engine disk fragment non-containments [2], while Fig. 3b identifies how these are distributed between turbine-disk and compressor-disk fragments -- per million engine hours; these high-energy incidents of non-containment are seen to occur at a rate of about 0.4 per million engine hours. References 1 through 4 also indicate the frequency of occurrence as a function of the phase of flight, the reported categories of the causes of failures, etc.

More recently, a similar comprehensive survey and study has been reported [5] by the SAE Ad Hoc Committee on Engine Containment. Included are a chronology of the type of failures, the causes of failures, the resulting aircraft damage (assessed in four categories ranging from damage only to the nacelle of the affected engine to severe aircraft damage), etc. It is pointed out [5] that the world airline accident summary prepared by the U.K. CAA on all commercial turbine powered aircraft powered by Detroit Diesel Allison, General Electric, Pratt & Whitney, and Rolls Royce for the period January 1, 1962 through December 31, 1975 shows that: (a) of the 1258 accidents from all causes, only 33 (or 2.62%) were caused by engine non-containment, (b) 4 (1.06%) of 381 hull losses can be attributed to engine-fragment non-containment, and (c) only 39 (0.33%) of 11,690 fatalities from all causes are because of engine non-containment. These statistics can be interpreted as indicating that engine rotor fragment non-containment is responsible for an extremely small percentage of the total number of accidents, hull losses, and fatalities. This has been brought about by the vigilant, diligent, and persistent efforts of the engine designers and manufacturers, the aircraft designers, and the day-to-day alertness of the airline operators and maintenance personnel as well as the leadership and cooperation of the FAA, the UK CAA, and similar agencies -- each has played a highly significant role. While all of these groups exert constantly their best efforts to minimize and/or prevent engine rotor bursts and any ensuing damage, it is clear that engine rotor failure and fragment-generation will continue to occur. Efforts to reduce non-containment and the consequences of such non-containment should continue unabated.

Forney [6] has described concisely the FAA's philosophy and approach to the matter of engine rotor integrity and non-containment. Gunstone [2] has also discussed the UK CAA's views on engine rotor fragment non-containment. These two viewpoints, not unexpectedly, are remarkably similar, with some differences in detail. In general, all feasible measures to reduce the incidence and the severity of engine rotor bursts are advocated -- so that any fragments which do occur are as light as possible. However, there is clear recognition that engine rotor bursts will continue to occur; accordingly, there is strong emphasis on measures to reduce the consequences of non-containment. Sought [2,6] is "an adequate level of aircraft invulnerability". Each agency indicates requirements and guidelines for achieving this goal. Briefly, the aircraft shall be designed to be acceptably invulnerable to engine rotor fragment debris by the appropriate locating of critical parts, structures, controls, etc., by duplicating or otherwise providing redundant systems, by the use of local armoring, deflector shields, etc. There is also recognition [1-6] that complete containment of engine rotor burst fragments may result in greater damage and danger than permitting the judicious penetration and escape by initially-produced fragments in a

"harmless direction" wherever feasible. In this context the use of local shields and deflectors becomes attractive.

McCormick [7] of the Boeing Commercial Airplane Company, Wallin [3] of the British Aircraft Corporation, and Wignot [8] of the Lockheed California Company have described their current design practices to cope with the engine rotor burst problem. Representative is the description by McCormick [7]: "Current design practices to minimize this hazard (of non-containment of engine fragments) include configuring the aircraft to reduce the risk of: (1) loss of additional thrust, (2) fuel fed fires, (3) loss of critical systems, and (4) loss of structural integrity. These objectives are accomplished by: (1) controlling the relative location and spacing of engines and critical systems, (2) use of redundant systems, (3) use of dual load path structure, and (4) use of fire protection systems. In addition, where configuration peculiarity indicates, consideration is given to special shielding of critical components. The application of these concepts is of course very dependent upon the basic airplane configuration. Also, any measure to reduce the hazard of non-containment engine fragments must be evaluated in terms of overall aircraft safety."

Wallin [3] has offered his personal description of design considerations and concepts used in analyzing and coping with the engine rotor failure hazard for the Concorde. Several self-explanatory figures from Wallin's paper serve here as excellent illustrations of representative approaches. Figure 4 depicts Wallin's engine rotor failure hazard tree; Fig. 5 shows the use of the local armor shield concept; and Fig. 6 indicates precautions to minimize engine rotor failure damage with respect to aircraft systems and fire precautions. Further very informative illustrations of engine rotor fragment design considerations, precautions, and practice are given in Ref. 3.

Hill [9], Duttweiler [10], and Doherty [11] have described design considerations and details, materials and manufacturing processes, and the use of non-destructive evaluation techniques to achieve increased engine rotor life and reliability. Kaufman [12] reviews a number of design innovations and guidelines leading to engine rotors of improved reliability as well as having the deliberately designed-in feature of "insuring" that engine rotor bursts if and when they occur will be such as to produce small rather than large energetic fragments. A detectable relatively-mild engine rotor burst rather than a highly energetic and potentially much more dangerous rotor burst is sought.

Morelli [13] has described the highly important role of the aircraft operator, his systematic maintenance and inspection procedures, his innovative role in devising effective in-the-field inspection techniques, as well as the close collaboration between the user and the engine manufacturer in alerting each other to potential failure problems and to prevent such problems. Clearly, these activities have been highly important in keeping the number of dangerous engine rotor burst failures to such a remarkably low percentage figure. However, Morelli has emphasized the need for improved in-the-field diagnostic capabilities for detecting imminent failures.

As noted earlier, despite the best efforts of the engine manufacturer and the airline operator-maintenance-inspection personnel, engine rotor bursts with fragments of significant mass and kinetic energy will continue to occur. Thus, one must continue the practice of vigilant airframe-engine-system design to minimize the hazard of either contained or non-contained rotor bursts.

McCarthy [4] has presented an excellent summary of typical types of rotor failures from:

- (a) low cycle fatigue (Fig. 7)
- (b) high cycle plus low cycle fatigue (Fig. 8)

These figures are self-explanatory. Figure 8 depicts some causes of disk failures arising from overheating [4]. Some multiple blade release cases are shown in Fig. 9, while various "typical shapes" of bladed disk fragments are depicted in Fig. 10. Data on the number and size distribution of burst rotor disk segments for both compressors and turbines are of concern; such data are shown in Fig. 11 where the maximum dimension of the largest fragment is given as a percentage of the bladed disk diameter. For compressor rotor disks, large fragments occur rather frequently; about 40 percent of those largest fragments were uncontained (cross-hatched region). For turbine rotor disks, smaller fragments occur more frequently; the percentage distribution of uncontained failures is shown also in Fig. 11. Fragment weight as a percentage of bladed disk weight is shown by McCarthy [4] in Fig. 12 for compressor and turbine rotor bursts. To illustrate the range of typical fragment velocities at release, maximum disk rim speeds are shown [4] in Fig. 13 for a number of engine compressor and turbine rotors; this value is chosen since it is representative of the center-of-gravity velocity of a fragment consisting of a rim piece plus several attached blades. Note that these velocities lie between about 400 and 1300 ft/sec. Thus, as McCarthy has pointed out, fragments in this velocity range can be stopped or deflected by conventional armor such as steel or titanium plate rather than special materials which are needed for much higher impact velocities. Next, the percentage of rotor fragment kinetic energy in (a) translation and (b) rotation are shown in Fig. 14 as a function of the included angle θ of the fragment sector. The angular spread from the rotor disk plane of rotor burst debris escaping the casing is shown in Fig. 15 as a function of fragment weight; for very heavy fragments, the angular spread is typically about ± 5 deg. but can extend to about ± 30 deg. for the lightest fragments. Finally, Fig. 16 shows schematically potentially the direction and energy of debris emerging from the casing; this is of some interest from the point of view of selecting the layout and relative locations of

aircraft controls, and other systems to minimize the hazard from such debris.

With this brief overview of engine rotor burst problems and phenomena, let us continue this survey by reviewing some of the experimental and theoretical work that has been carried out to study the containment and/or deflection of both engine rotor and other simpler fragments.

EXPERIMENTS ON FRAGMENT CONTAINMENT OR DEFLECTION

During about the past decade the Naval Air Propulsion Test Center under NASA sponsorship has conducted many engine rotor fragment containment/deflection tests in their spin chamber facility [1, 14, 15]. Most of these tests were devoted to studying containment ring responses to rotor burst fragments from T58 turbine rotors or J65 turbine rotors. In some cases the rotor was modified so that it would burst at a selected rpm into 2, 3, 4, or 6 equal-size pie-shaped rotor-disk fragments with attached blades. In other cases only one blade of a fully-bladed rotor would be caused to come off to impact the containment-ring "casing" (and the oncoming still-attached blades of the spinning rotor). Single-layer single-material rings as well as multilayer, multimaterial rings were used. In some tests the rotor burst and the subsequent fragment impact and interaction were photographed through a viewing port by a high-speed Dynafax camera; these photographs have provided valuable insight into the principal phenomena accompanying impact and interaction of very complex fragments with containment rings. In other tests the containment ring was sandwiched between "heavy guide plates" which insured that the attacking fragments would not inadvertently escape from the plane of the containment ring and thus give a misleading impression of the ability of a given ring to contain fully the basic fragment attack; in these tests the thickness of a containment ring of given axial length was varied in order to determine the minimum thickness required to contain fully a given type (and kinetic energy) of engine-rotor-fragment attack. These valuable experiments, conducted at the NAPTC, are discussed more fully in Refs. 1, 14, and 15, as well as in a paper to be presented at this meeting by Mangano and his co-workers.

Hagg and Sankey [16] report the results of spin-chamber experiments by Westinghouse to contain smooth cylindrical disk segments by means of cylindrical 1020 steel containment shells.

Gerstle [17] reports that in 1972 the Boeing Co. initiated an experimental program to evaluate lightweight shields for engine fragment burst containment. In their impact mechanics laboratory, powder-driven guns were used to launch simulated engine rotor fragments to impact against titanium, Kevlar, or metal-Kevlar panels. These panels were impacted by steel cubes and rods at various incidence angles with respect to the surface of the panel. Containment threshold data were obtained. Some of these data as reported by Bristow et al. [18] are shown in Fig. 17; shown here is the uninstalled weight per unit area of various materials required to contain a fragment (or fragments) of given translational kinetic energy. These experimental threshold containment data pertain to (1) the Boeing impact tests on titanium and Kevlar panels, (2) the NASA/NAPTC spin chamber tests for T58 turbine rotor tri-hub bursts against several types of containment rings [1, 14, 15], and (3) the Westinghouse data [16] on 1020 steel cylindrical shells subjected to smooth-rotor-disk fragment attack. Although this plot is on a log-log scale and the impacting fragments have various geometries, all of the data except that for the Kevlar panels fall roughly on a single line. The Kevlar data suggest the possibility that this or similar material may be useful in providing containment structure and/or shields of significantly lighter weight than conventional metal structure such as aluminum, steel, titanium, etc. can provide. To realize this benefit, however, the Kevlar material must be in a portion of the structural configuration such that the Kevlar is permitted to stretch readily in order to absorb the kinetic energy of the fragment so as to arrest the motion and to contain the fragment, or to reduce the kinetic energy of the fragment to an acceptably small value before Kevlar rupture and fragment escape occurs. Hence, proper layout, configuration, and installation/attachment matters must be addressed carefully to achieve a practical and effective Kevlar-based containment-structure design.

If the Kevlar material is to be used in locations where elevated temperature and temperature cycling occurs, one must investigate and allow for these effects. Some data on these effects on Kevlar performance are given in Ref. 18. More recent studies of the use of Kevlar by itself and in combination with various other materials to produce containment structures are reported, for example, by Bristow et al. [19] and Weaver [20], and by discussers of those papers. Two of the items of concern raised are (1) the effect of fluids such as oil in lubricating the Kevlar and perhaps reducing its containment effectiveness and (2) the possible danger from fires because of fluid soak-up (or "wicking") by the Kevlar. These effects and their alleviation are being studied.

Incidentally, the use of Kevlar-based protective clothing to protect law enforcement personnel, combat soldiers, pilots, etc. from bullets and shrapnel has received much attention; see Refs. 21 and 22, for example.

It was noted earlier that certain multilayer multimaterial containment rings were studied in the NAPTC experiments [15]. Holms [23] has discussed recently a number of concepts for achieving fragment containment with the "least weight penalty" by using multilayer multimaterial rings or panels with the proper sequence of types of materials and properly-chosen layer thicknesses. Currently, some of these concepts are being explored in a systematic experimental program being conducted at the Naval Air Propulsion Test Center by the cooperative efforts of NAPTC and NASA-Lewis personnel. Also, recently Gardner [24] has discussed some concepts for and some experience in the use of ceramic composite

materials and structures to provide protection from turbine disk bursts.

Although Kevlar-based and ceramic-composite materials/structures possess attractive attributes, most of the current containment shields and containment rings consist of simple metallic single-layer construction. A complete understanding of and the ability to predict accurately the responses of these simpler structures to impact attack by either complex or simple fragments has not been demonstrated. For certain types of (1) fragments and (2) fragment impact conditions, experimental data have been accumulated so that conservative design to cope with limited types of fragments and fragment attack conditions can be accomplished. For structure/material and fragment-type-and-impact conditions differing significantly from that data base, one seeks the availability of rational and validated theoretical prediction methods.

In the process of developing theoretical methods for predicting the responses of simple single-layer metal structures to low speed impact attack such as is typical for engine rotor fragments, the need for and lack of detailed measurements of impact-induced structural response data for well-defined conditions of both the fragment and the containment structure became apparent. Also, it has been appreciated for a long time (and the NAPTC photographic studies have confirmed in considerable detail) that rotor blades and/or bladed-disk fragments undergo rather severe changes in shape as they impact and interact with a containment or deflector structure; this rapidly changing geometry greatly complicates the interpretation of transient structural response measurements (strains, deflections, and motion) of fragment-impacted structures when one attempts to compare such measurements with theoretical predictions. The accompanying geometric and material behavior are often highly nonlinear.

In order to obtain impact-induced structural response data wherein both the fragment and the impacted structure are well-defined (that is, the attacking fragment has a known and "unchanging geometry" throughout the impact-interaction attack), experiments have been carried out to measure the responses of simple beams and panels of ductile metals such as aluminum to impact by a steel sphere. Such measurements are reported, for example, in Refs. 25, 26, and 27. These data are very useful for evaluating the reliability and accuracy with which one can predict theoretically the transient responses of fragment-impacted structures under clear well-defined conditions. Thus, if one can verify that reliable predictions can be accomplished for these well-defined conditions, one can proceed from a sound base to take into account more complicated conditions involving, for example, complex deformable fragments, etc.

PREDICTIONS OF STRUCTURAL RESPONSE TO FRAGMENT IMPACT

Various approaches for predicting structural response to fragment impact can be found in the literature. These include (a) approximate analytical methods, (b) combined analytical-experimental (or semi-empirical methods), and (c) numerical methods. Approximate analytical methods apply usually to only very simple types of impact configurations and problems, and involve often highly simplifying assumptions (see, for example, Refs. 16, 25, and 28). Semi-empirical methods are developed for special separate categories of (a) types of structural configurations/materials and (b) types of fragments; a body of experimental data is generated for each such category -- and provides the "final basis" upon which predictions are made for design or other purposes. In the present review, these first two categories of prediction methods will not be discussed further because of time and space constraints. Instead, a brief review of some work carried out to date in numerical methods for predicting impact-induced structural response will be made. Further, since interest centers principally upon containing, deflecting, or otherwise controlling low-speed impacting fragments by the use of light-weight shield or containment structures, these structures will be required to undergo large deflections and will almost invariably experience a considerable degree of inelastic behavior. Thus, a highly nonlinear transient structural response problem involving geometric and material nonlinearities must be analyzed and solved.

It should be noted that typical engine rotor fragment velocities of about 400 to 1300 ft/sec must be taken into account. However, it is the component of that velocity perpendicular to the impacted structure which governs mainly the "intensity" of the impact interaction; that perpendicular component in turn ranges roughly from 200 to 700 ft/sec. In principle one could employ finite-difference and/or finite-element computer codes which model both the attacking fragment and the impacted target structure as 3-D solids in order to predict the impact-induced through-the-thickness stress waves and associated elastic-plastic flow and deformation. Such computer codes include, for example, HEMP[29], HELP[30], STRIDE[31], EPIC[32], and PISCES[33]. However, these codes apply to only certain simple fragment geometries such as cylindrical rods or spheres. In some codes the target is treated as a single layer, single material body but in others as of multilayer, multi-material construction. Elastic-plastic deformation and flow as well as sliding interfaces between fragment and target or between the layers of layered targets are taken into account in some of these programs. Thus, a fairly comprehensive accounting of the principal phenomena are accommodated but the computer storage requirements and computing expense are substantial.

In view of these considerations and the fact that engine rotor burst containment/control experiments show usually that structural response types of damage rather than intense through-the-thickness stress-wave-induced damage (such as spall fracture) are commonly observed in single-layer and multilayer containment structures leads one to seek a simpler, less expensive means of predicting theoretically the primary behavior: the transient structural response rather than the so-called material or stress-wave response. Accordingly,

the containment/control structure is represented as a "structure" (rather than a 3-D solid), and two categories of structural response are studied: (a) 2-D structural response wherein the principal deformation or deflection of the structure (beams, rings) lies in one plane -- with two components of deflection and (b) 3-D structural response (of panels, plates, and shells) wherein the displacements have three significant components. With respect to the attacking fragment, one of several simplified models can be employed to represent its behavior during the impact-interaction. It is this simpler "engineering modeling" and analysis which will be reviewed in the remainder of this paper.

There are many finite-difference and finite-element structural dynamic analyses and computer programs which have been or could be adapted for this type of analysis. Time and space limitations, however, preclude a review and categorization of these analyses -- our apologies to the many authors whose pertinent developments and papers must be omitted. Hence, only several illustrative examples will be discussed here, and these examples are those with which the authors are most familiar.

2-D Impact-Induced Structural Response

Consider an initially-circular single-layer containment ring whose axial length is comparable to the corresponding dimension of a single rotor blade as depicted in Fig. 18. In this case one expects the containment ring to undergo essentially 2-D deformation response. Such an experiment was carried out at the Naval Air Propulsion Test Center [34] and the pertinent data are listed in Table 1.

Let the ring structure be represented spatially by finite elements such as the curved ring elements [35, 36] employed in the JET 3 program of Ref. 37. Large deflections as well as elastic-plastic, strain hardening, and strain rate mechanical behavior of the ring material are taken into account.

In one scheme explored for estimating the interaction effects between the attacking fragment and the containment ring, the blade fragment is idealized as being straight and non-deformable; the local impact behavior between the fragment and the ring, however, is regarded as being (a) perfectly elastic, (b) perfectly inelastic, or (c) intermediate between these conditions by employing a coefficient of restitution e of $e=1$, $e=0$, or $0 < e < 1$ for cases (a), (b), or (c), respectively. Impulse-momentum and energy conservation relations are employed to estimate for a single impact the momentum imparted to an "impact-affected region" of the ring centered about the impact point -- as depicted in Fig. 18; the fragment suffers a corresponding decrement of velocity or momentum. For convenience, this approach is termed herein the collision-imparted velocity method CIVM. The effects of friction between the fragment and the structure can also be taken into account by employing a selected value for the coefficient of sliding friction μ .

Shown in Fig. 19 is an information flow schematic for the prediction of ring and fragment motions in the CIVM approach. Here the finite element equations of motion for the ring and the rigid-body equations of motion for the fragment are solved in small increments in time Δt by using a selected timewise finite difference operator; for example, the timewise central difference operator is employed in the calculations reported in Ref. 35 and in the CIVM-JET 4B computer program of Ref. 38.

Illustrated in Fig. 20 are predictions of ring configuration and fragment location at 810 microseconds after initial impact for the NAPTC Test 91 conditions shown in Table 1. In the impact quadrant the ring was modeled by 10 equal-length cubic-cubic elements; 6 equal-length elements were used in each of the other 3 quadrants. For these calculations, coefficients of restitution of $e=0$ and $e=1$ were used. The 2024-T4 aluminum ring material was regarded as elastic, perfectly-plastic with a strain-rate (EL-PP-SR) dependent yield stress $\sigma_y = \sigma_0 [1 + \frac{\dot{\epsilon}}{D}]^{1/p}$ where σ_0 is the static yield stress, $\dot{\epsilon}$ is the strain rate, and D and p are material constants. For these calculations, $D = 6500 \text{ sec}^{-1}$ and $p = 4$ were assumed [39]. Also, frictionless impact and interaction ($\mu = 0$) between the ring and the blade was assumed for the cases illustrated here. Fairly good agreement between the predicted and observed deformed ring configuration is noted, but the predicted vs. observed fragment motion is not good. This latter disagreement stems mainly from ignoring (a) friction and (b) the changing mass moment of inertia of the actual deforming blade. Later calculations included these effects.

A second means for accounting for the impact-interaction between the impacting fragment and the ring is termed, for convenient reference, the collision force method CFM. In this approach the fragment is treated as being deformable rather than rigid, and idealized types of deformation-sequence configurations are selected -- as depicted, for example, in Fig. 21. Explored in Ref. 40 were the following two idealizations -- the steel blade was assumed (a) to remain straight but to shorten in an elastic, perfectly-plastic (EL-PP) fashion or (b) to curl in a simple plausible assumed-mode fashion; these are termed, respectively, the elastic, perfectly-plastic shortening-blade model (EL-PP-SB) and the EL-PP-CB model where CB refers to curling blade. These modes of behavior combined with a step-by-step collision/inspection set of rules permitted following the process. At any given instant, applicable values of the governing deformed-blade configuration parameters were identified. These in turn were related via energy methods to the component of the force applied by the blade perpendicular to the surface of the attacked containment ring -- and equal-and-oppositely to the fragment itself. Similarly, equal and opposite tangential forces (from friction) were postulated to be μ times the normal-to-the-surface component. A self-explanatory flow chart for the CFM process is given in Fig. 22.

Shown in Fig. 23 for NAPTC Test 91 are CFM deformed ring predictions at 626 micro-seconds after initial impact for the EL-PP-SB model and the EL-PP-CB model for the case in which the friction coefficient μ is assumed to be 0.15 and the perfectly-plastic yield stress of the steel-alloy blade is assumed to be $\sigma_{of} = 160,000$ psi. Fairly good agreement between experiment and these EL-PP-CB model predictions is observed. Reference 40 shows the ring response to be rather insensitive to plausible values of the friction coefficient, but the motion of the blade itself is much more sensitive to μ . In the CFM scheme one must keep track of the time-varying geometry of both the deforming blade and the deforming containment ring in order to determine when and where the successive collisions occur. Hence, it is evident that if one were to use this method to analyze structural response to impact by, for example, a disk-rim fragment (or several fragments) with perhaps from 3 to 10 blades attached on each (each blade of which will undergo sequential different deformations), one would be faced with a substantial book-keeping task to define the space occupancy of the complex deforming fragment; the advisability of seeking a less complex scheme is clear. Accordingly, subsequent attention has been given to the use of greatly idealized rigid fragments in conjunction with the CIVM scheme.

Tri-Hub Rotor Burst Attack Against a 2-D Containment Ring

One type of postulated engine rotor fragment attack which has received much discussion is that in which the rotor bursts into 3 equal segments (termed a tri-hub burst). One fragment of this type is shown schematically in Fig. 24. The NAPTC has conducted many tests involving tri-hub burst attack against various single-layer and multilayer containment rings. Recently NAPTC Test 201 involving tri-hub attack of a T58 turbine rotor at 19,859 rpm against a cast 4130 steel containment ring of 7.50-in inner radius, 0.625-in thickness, and 1.50-in axial length was conducted [41]. High-speed photographs showed the severe deformation incurred by many of the blades during the impact/interaction process; this is depicted schematically in Fig. 24.

For convenience and geometric simplicity, each such fragment has been idealized for use in the CIVM-JET 4B computer code [38] as a rigid circular body of the same mass and mass moment of inertia as the pre-impact fragment, with the same CG location, translational velocity, and rotational velocity as the actual fragment at postulated release. As indicated in Fig. 24, one might elect to represent the actual fragment by an idealized fragment of "properly selected radius r_f ". An examination of this rotor indicates that reasonable minimum and maximum values for r_f would be about 2.56 and 4.20 inches, respectively; the use of these as well as an "intermediate" value of 3.36 inches was explored.

Figure 25 indicates the geometric, test, and modeling data for this case. The ring has been modeled by 48 equal-length ring elements. The point of initial impact of each of the three fragments is indicated in Fig. 25; element numbers and node identification are also given. The uniaxial static stress-strain properties of 4130 cast steel were approximated by piecewise linear segments with the stress-strain pairs: $(\sigma, \epsilon) = 80,950$ psi, .00279; 105,300 psi, .0225; and 121,00 psi, .200 via the mechanical sublayer model; strain rate effects [39] were approximated by using $D = 40.4$ sec⁻¹ and $p = 5$. Shown in Fig. 26 is the predicted ring configuration at 1000 microseconds after initial impact. The predicted inner surface and outer surface strains at the mid-element location of elements 1 and 4 are given in Fig. 27; for this calculation, frictionless impact $\mu=0$ and $r_f = 2.555$ in were employed.

The effects of friction for otherwise identical modeling are indicated roughly by the Fig. 28 comparison of deformed ring configurations at 1200 microseconds after initial impact for $\mu=0$ and $\mu=0.3$. Similarly, the effects of idealized fragment radius r_f are seen in Fig. 29 where deformed ring profiles at 1200 microseconds after initial impact are shown for $r_f = 2.555$ in and $r_f = 3.360$ in. It is evident that if one chooses an unduly large idealized fragment radius r_f , this "rigid fragment" will constrain the ring to restrict its bending strain contribution so that unrealistically small total strains will be produced at the "convex lobes" -- compared with that which the actual "effectively-smaller-radius" fragment will produce.

The use of an idealized fragment of constant radius will clearly make it impossible to obtain complete time history agreement between predicted and measured inner-surface and/or outer-surface strains on the ring. However, the hope is that a properly-chosen effective r_f will lead to reasonable predictions vs. experiment of maximum strains produced as a function of circumferential location. Further calculations and measurements are needed to assess the reliability with which this can be done. However, at the cost of greater complexity and computational expense, one can devise and use a fragment model which more closely simulates the behavior of the actual fragment.

Note, finally, that a comparison between the predicted and observed permanently-deformed ring configuration is not shown. This is the case because the calculation at $\Delta t=1$ micro-second has been carried out only to 2400 microseconds after initial impact. Whereas peak response occurred near 1200 microseconds, the ring is still springing back considerably at the 2400 microsecond time. A longer calculation would be necessary in order to permit making a reasonable estimate of the permanent-deformation configuration in order to compare with the measured configuration.

2-D Beam Response to Steel-Sphere Impact

In order to obtain appropriate and detailed 2-D transient structural response data under well-defined impact conditions so that a definitive evaluation could be made of the adequacy of the approximate collision-interaction analysis employed in the CIVM scheme,

some simple experiments have been conducted at the MIT-ASRL. Beams of 6061-T651 aluminum with nominal 8-in span, 1.5-in width, and 0.10-in thickness and with both ends ideally clamped (see Fig. 30) have each been subjected to midspan perpendicular impact by a solid steel sphere of one-inch diameter [26]. Impact velocities ranged from those sufficient to produce small permanent deflection to those needed for threshold rupture of the beam. Spanwise-oriented strain gages were applied to both the upper and the lower (impacted) surface of the beam at various spanwise locations. In each test, transient strain measurements were attempted for 8 of the gages; after each test, permanent strain readings were obtained for all surviving gages. Also, permanent deflection measurements were made.

An inspection of each specimen indicates that except near the point of impact itself (i.e., where $|x| > 0.8$ -in) and near the clamped ends, the beam underwent essentially 2-D deflection behavior; pronounced 3-D behavior occurs near the point of initial impact. Hence, the 2-D structural response code (CIVM-JET 4B) may be expected to provide valid comparisons for $0.8 < |x| < 3.7$ in. Accordingly, such calculations and comparisons are in progress, and some preliminary results are shown next.

For the test and specimen identified as CB-18 in Ref. 26, the entire beam has been modeled with 43 equal-length cubic-cubic finite elements. The beam material has been modeled as having either elastic, strain-hardening (EL-SH) or EL-SH-SR behavior where the uniaxial static stress-strain curve has been approximated by the σ, ϵ pairs: $\sigma, \epsilon = 41,000$ psi, .0041; 45,000 psi, .0012; and 53,000 psi, .1000. For the EL-SH-SR conditions, $D = 6500 \text{ sec}^{-1}$ and $p = 4$ have been assumed. For CB-18 initial steel-sphere impact occurred at a velocity of 2794 in/sec; a state of large permanent deflection was produced.

Shown in Fig. 31 are predicted and measured strains at spanwise station $x = 1.50$ in from the midspan impact point. At this 2-D structural response location, there is fairly reasonable agreement between predicted and measured strains. Figure 32 shows the predicted transient vertical displacement response at $x = 1.0$ in for both the EL-SH and the EL-SH-SR case. From these and longer-duration plots, the estimated respective permanent deflection is 0.63 and 0.58 in; the measured value is 0.60 in. While the comparisons shown here indicate encouraging agreement, more extensive calculations and comparisons are needed before a firm assessment can be made of the adequacy of the procedure embodied in the CIVM-JET 4B computer code [38].

Note that the CIVM-JET 4B computer code deals with the impact-induced 2-D responses of single-layer structures from idealized rigid fragments. A similar computer code CIVM-JET 5B [42] can be applied to multilayer hard-bonded 2-D Bernoulli-Euler structures.

Simple 3-D Structural Response Studies

Of concern here are situations in which the fragment-impacted structure undergoes pronounced 3-D rather than 2-D deformation. Appropriate methods of structural response analysis and corresponding well-defined experimental transient structural response data which will serve to permit making a clear evaluation of the adequacy and/or accuracy of proposed prediction schemes are needed. Some contributions to this process are described here.

Although structural response analyses for fragment impact against initially-curved as well as initially-flat target structures are of interest, it is useful to minimize the complexities while checking the adequacy of the basic building blocks in the analysis process. Hence, attention has centered on impulse and impact experiments and theoretical analysis of initially-flat structures. Experiments involving steel-sphere impact against (1) narrow-plate (or beam) specimens [26] as well as (2) square uniform-thickness panels with four clamped edges and (3) panels of type (2) but with integrally-machined stiffeners of rectangular cross-section [27] have been conducted; all of these panels consisted of 6061-T651 aluminum.

Similarly, Gerstle [42] reports measurements of the responses of initially-flat rectangular panels of Kevlar 49 with thin steel facing sheets, which were subjected to impact by a 1-in non-rotating steel cube with an incidence angle of 60 degrees with respect to the plane of the shield. Gerstle has employed essentially a CIVM-type impact-interaction scheme in conjunction with the PETROS 3 spatial finite-difference analysis and code of Ref. 44 to form a converted code called EBCAP [45]. Comparisons of EBCAP predictions with the Boeing measurements are discussed in Ref. 42. Incidentally, there are a number of other spatial finite-difference codes similar to PETROS 3 which have extended capabilities, and which could be adapted similarly to fragment-impact-induced structural response predictions. Such codes include, for example, REPSIL [45], PETROS 3.5 [47], and PETROS 4 [48].

Finite-element analyses have also been developed to predict the large-deflection elastic-plastic transient responses of plates and shells to prescribed transient or impulse loads. An example of this type of analysis is reported in Ref. 49. This finite-element analysis has been adapted to produce the computer programs PLATE and CIVM-PLATE for predicting the structural responses of initially-flat panels to, respectively, prescribed impulse loading or rigid-fragment impact [50]. Studies are currently in progress to assess the accuracy and reliability of the code predictions when applied to analyzing (1) the responses of the Ref. 27 explosively-impulsed aluminum panels and (2) the responses of the Ref. 26 aluminum beams and the Ref. 27 aluminum panels subjected to steel-sphere impact.

Chosen here for convenient illustration are preliminary CIVM-PLATE predictions of the

response of steel-sphere-impacted narrow-plate (or beam) specimen CB-18 of Ref. 26; the initial impact velocity of the one-inch diameter steel sphere which impacted along the normal to the surface was 2794 in/sec. For computational thrift, only one quarter of the specimen was modeled (see Fig. 30) -- by a 2 by 11 mesh of flat plate elements having 6 degrees of freedom per node, with symmetry conditions imposed along $x = 0$ and $y = 0$; this finite element mesh is shown in Fig. 33. Initial impact was assumed to occur at $(x,y) = (0,0)$ whereas it actually occurred at about 0.06 in from this location. Figure 34 demonstrates that this 3-D structural response model exhibits 3-D deflection predictions -- vertical displacements predicted along $y = 0$ (the centerline), $y = 0.375$ in, and $y = 0.75$ in as a function of spanwise location x are shown at 900 microseconds after initial impact. The anticipated larger displacement is seen to occur along $y = 0$, with decreasing displacements (at given x -locations) at positions more remote from the center of impact. Figure 35 shows the predicted vertical transient deflection of the center of the plate $(x,y) = (0,0)$ and the observed permanent deflection at this location; reasonable agreement is evident. Finally, it is of perhaps even of more interest to examine the predicted and measured longitudinal strains at various spanwise stations on the upper surface of narrow-plate (or beam) specimen CB-18; these comparisons are discussed in the next paragraph.

First, however, it should be noted that an examination of the actual test specimen shows that pronounced 3-D deformations occur near the point of initial impact (i.e., for $0 \leq |x| \leq 0.8$ in) and perhaps also near each clamped end; elsewhere, however, the specimen seems to have exhibited 2-D response behavior. Shown in parts a,b,c, and d, respectively, of Fig. 36 are the CIVM-PLATE predictions and the measurement of extensional upper-surface strain along $y = 0$ at stations $x = 0, 0.6, 1.2$, and 3.7 in. Shown also are the CIVM-JET 4B 2-D beam response predictions, and the measured permanent strains. Here one expects to and does find reasonable agreement between both of these predictions and transient strain measurements at "2-D station" $x = 1.2$ in, but these two predictions are expected to show greater differences between them at stations $x = 0, 0.6$, and $x = 3.70$ in. At $x = 0$, these predictions do exhibit very distinct differences between them; unfortunately, no measured transient strain data are available at $x = 0$.

Next, it should be noted that the computer codes CIVM-JET 4B and CIVM-PLATE as implemented apply to large deflections, but the strains must be small. Recently, this small-strain restriction has been alleviated [51] in a modified version of the CIVM-JET 4B 2-D structural response code; the resulting transient upper-surface longitudinal Lagrangian strain-tensor predictions are also shown in Figs. 36a, 36b, 36c, and 36d. It is seen that the proper accounting for large strain behavior results in significantly different transient strain predictions at stations $x = 0$ and 3.70 in from the former "small strain predictions" but lesser differences are seen at stations $x = 0.6$ and $x = 1.2$ in. Note that station 3.70 -in is very close to the clamped end ($x = 4.00$ in) where very large strains occur there, and the consequences are felt at station 3.70 in as well. Also, it appears that the "large strain prediction" should result in better agreement with the measured permanent strains.

Finally, the importance of including large strain behavior in analyses and computer codes for predicting the large-deflection, large-strain responses of ductile metal structures has long been recognized. Proper large strain static formulations for such problems are reported, for example, by Osias [52], Needleman [53], and McMeeking and Rice [54]. They show comparisons between predictions and experiments involving the static load-deflection behavior of a narrow strip or notched thin panels subjected to tensile loads. Considerable thickness changes and necking occur, and predictions compare favorably with experiments; although clearly large strains must have occurred, no direct strain comparisons are shown.

A transient, dynamic, plane strain or axisymmetric large-strain computer program called HONDO has been developed by Key [54]. An extension of HONDO to analyze the large-strain dynamic responses of 3-D solids has led to the WULFF code reported by Biffle and Gubbels [56]. Only recently, however, have both transient response predictions (by HONDO) and measurements been reported for truly large strains [57] -- many earlier examples by other authors involved peak strain levels typically less than about 4-6 per cent. Further such theoretical-experimental comparisons are needed.

SUMMARY COMMENTS

A brief review has been given of collected data on the occurrence and types of commercial aircraft engine-rotor fragments, especially the uncontained fragments. The guidance of the FAA and the UK-CAA together with the efforts of the engine designers, aircraft designers, and airline operators/maintenance personnel has resulted in a remarkably good safety record with regard to the engine-rotor fragment containment/control problem. However, engine rotor failures persist at a nearly constant rate, and continued vigilant effort is required to cope properly with this problem.

Some experimental studies carried out to investigate the impact-interaction of both complex engine rotor fragments and simple fragments with various types of single-layer and multilayer containment structures were reviewed. The resulting data have been used (a) to develop empirical design rules and (b) to evaluate proposed theoretical methods for predicting the impact-induced responses of containment structures. Examples of typical numerical methods for predicting the large-deflection, elastic-plastic transient structural responses of simple 2-D and 3-D containment shields (rings, panels, etc.) were illustrated. For ductile shield materials, the proper accounting for large strains is an important ingredient since threshold containment conditions involve large strains;

pertinent well-defined experimental transient response data and theoretical-experimental correlation studies are needed to permit evaluating the reliabilities of theoretical prediction methods to analyze impact-induced containment threshold conditions. Extensions of these engineering type theoretical prediction capabilities would be useful to analyze the impact-induced transient structural responses of proposed lightweight multi-layer, multimaterial containment shield designs.

REFERENCES

1. Mangano, G.J., Salvino, J.T., and DeLucia, R.A., "Rotor Burst Protection Program: Experimentation to Provide Guidelines for the Design of Turbine Rotor Burst Fragment Containment Rings", NASA CP-2017, An Assessment of Technology for Turbojet Engine Rotor Failures, 1977, pp 107-149.
2. Gunstone, G.L., "Engine Non-Containment -- The UK CAA View", NASA CP-2017, 1977, pp 11-32.
3. Wallin, J.C., "Engine Non-Containment -- UK Risk Assessment Methods", NASA CP-2017, 1977, pp 45-63.
4. McCarthy, D., "Types of Rotor Failure and Characteristics of Fragments", NASA CP-2017, 1977, pp 65-92.
5. Anon., "Report on Aircraft Engine Containment" Society of Automotive Engineers, Inc., Aerospace Information Report AIR 1537, October 1977.
6. Forney, A.K., "Federal Aviation Administration's Approach to Engine Rotor Integrity", NASA CP-2017, 1977, pp 1-9.
7. McCormick, R.B., "Rotor Burst Protection Criteria and Implications", NASA CP-2017, 1977, pp 37-43.
8. Wignot, J.E., "Designing the L-1011 to Minimize Rotor Failure Effects", NASA CP-2017, 1977, pp 97-100.
9. Hill, J.T., "Design of Rotors for Improved Structural Life", NASA CP-2017, 1977, pp 331-346.
10. Duttweiler, R.E., "Materials and Manufacturing Processes for Increased Life/Reliability", NASA CP-2017, 1977, pp 347-368.
11. Doherty, J.E., "NDE -- A Key to Engine Rotor Life Prediction", NASA CP-2017, 1977, pp 369-382.
12. Kaufman, A., "Turbine Disks for Improved Reliability", NASA CP-2017, 1977, pp 389-411.
13. Morelli, J.J., "Some Airline Experience in Preventing Engine Rotor Failures", NASA CP-2017, 1977, pp 413-418.
14. Martino, A.A. and Mangano, G.J., "Rotor Burst Protection Program. Phase V - Final Report on Problem Assignment NASA DPR-105", NAPTC-AED-1901, U.S. Navy, May 1969 (Available as NASA CR-106801).
15. Mangano, G.J., "Rotor Burst Protection Program. Phases VI & VII -- Exploratory Experimentation to Provide Data for the Design of Rotor Burst Fragment Containment Rings", NAPTC-AED-1968, U.S. Navy, March 1972 (Available as NASA CR-120962).
16. Hagg, A.C. and Sankey, G.O., "The Containment of Disk Burst Fragments by Cylindrical Shells", Journal of Engineering for Power, Transactions ASME, April 1974, pp 114-123.
17. Gerstle, J.H., "Analysis of Rotor Fragment Impact on Ballistic Fabric Engine Burst Containment Shields", Journal of Aircraft, Vol. 12, No. 4, April 1975, pp 388-393.
18. Bristow, R.J., Davidson, C.D., and Gerstle, J.H., "Advances in Engine Burst Containment" in AGARD Report No. 648 on Advances in Engine Burst Containment and Finite Element Applications to Battle Damaged Structure, September 1976, pp 1 - 6.
19. Bristow, R.J. and Davidson, C.D., "Development of Fiber Shields for Engine Containment", NASA CP-2017, 1977, pp 217-234.
20. Weaver, A.T., "Lightweight Engine Containment", NASA CP-2017, 1977, pp 235-245.
21. Roylance, D., Wilde, A., and Tocci, G., "Ballistic Impact of Textile Structures", Proceeding of the Army Symposium on Solid Mechanics, 1972: The Role of Mechanics in Design -- Ballistic Problems, AMMRC MS 73-2, September 1973, pp 232-240.
22. Anon., "Protective Armor Development Program -- Vol. I: Executive Summary, Vol. II: Technical Discussion, Vol. III: Appendices", Aerospace Corporation, Aerospace Report No. AIR-75(7906)-1, Vol. I, Vol. II, Vol. III, December 1974.

23. Holms, A.G., "Concepts for the Development of Light-Weight Composite Structures for Rotor Burst Containment", NASA CP-2017, 1977, pp 295-330.
24. Gardner, P.B., "Ceramic Composite Protection for Turbine Disc Bursts", NASA CP-2017, 1977, pp 277-295.
25. Goatham, J.I., and Stewart, R.N., "Missile Firing Tests at Stationary Targets in Support of Blade Containment Design", Journal of Engineering for Power, Transactions of the ASME, Paper No. 75-GT-47, March 1975.
26. Witmer, E.A., Merlis, F., and Spilker, R.L., "Experimental Transient and Permanent Deformation Studies of Steel-Sphere-Impacted or Impulsively-Loaded Aluminum Beams with Clamped Ends", NASA CR-134922 (MIT ASRL TR 154-11), October 1975.
27. Witmer, E.A., Merlis, F., Rodal, J.J.A., and Stagliano, T.R., "Experimental Transient and Permanent Deformation Studies of Steel-Sphere-Impacted or Explosively-Impulsed Aluminum Panels", NASA CR-135315 (MIT ASRL TR 154-12), May 1977.
28. Goldsmith, W., Impact -- The Theory and Physical Behaviour of Colliding Solids, Edward Arnold (Publishers) Ltd., 1960.
29. Wilkins, M.L., "Calculation of Elastic-Plastic Flow". Lawrence Radiation Laboratory, Livermore, UCRL-7322, Rev. 1, Jan. 1969.
30. Hageman, L.J. and Walsh, J.M., "HELP: A Multimaterial Eulerian Program for Compressible Fluid and Elastic-Plastic Flows in Two Space Dimensions and Time". (Vol. I - Formulation; Vol. II - Fortran Listing of HELP), BRL CR No. 39, Systems, Science, and Software, La Jolla, Calif., May 1971.
31. Kreyenhagen, K.N., Read, H.E., Rosenblatt, M., and Moore, W.C., "Hardening Technology Studies -- III, STRIDE Code Solutions and Extension to Multimaterial Systems". SAMSO-TR-69-16, Dec. 1968.
32. Johnson, G.R., "High Velocity Impact Calculations in Three Dimensions", Journal of Applied Mechanics, Transactions of the ASME, March 1977, pp 95-100.
33. Hofman, R., "PISCES 2DL, Manual 2, Input Manual". Physics International, April 1972.
34. Private Communication from A. Martino, U.S. Naval Air Propulsion Test Center, Phila, Pa., 1970.
35. Wu, R.W.-H. and Witmer, E.A., "Finite-Element Analysis of Large Transient Elastic-Plastic Deformations of Simple Structures, with Application to the Engine Rotor Fragment Containment/Deflection Problem", ASRL TR 154-4, Aeroelastic and Structures Research Laboratory, Massachusetts Institute of Technology, January 1972. (Available as NASA CR-120886.)
36. Rodal, J.J.A. and Witmer, E.A., "Finite Element Nonlinear Transient Response Analysis of Simple 2-D Structures Subjected to Impulse or Impact Loads", Massachusetts Institute of Technology, MIT ASRL TR 182-1 (also MIT-EL 76-004) June 1976.
37. Wu, R.W.-H. and Witmer, E.A., "Computer Program - JET 3 -- to Calculate the Large Elastic-Plastic Dynamically-Induced Deformations of Free and Restrained, Partial and/or Complete Structural Rings", ASRL TR 154-7, Aeroelastic and Structures Research Laboratory, Massachusetts Institute of Technology, August 1972. (Available as NASA CR-120993.)
38. Stagliano, T.R., Spilker, R.L. and Witmer, E.A., "User's Guide to Computer Program CIVM-JET 4B to Calculate Large Nonlinear Transient Deformations of Single-Layer Partial and/or Complete Structural Rings to Engine Rotor Fragment Impact", MIT ASRL TR 154-9, March 1976. (Available as NASA CR-134907.)
39. Ting, T.C.T., "The Plastic Deformation of a Cantilever Beam with Strain Rate Sensitivity under Impulsive Loading", Brown University TR 70, Contract Nonr-562(10), July 1961.
40. Zirin, R.M. and Witmer, E.A., "Examination of the Collision Force Method for Analyzing the Responses of Simple Containment/Deflection Structures to Impact by One Engine Rotor Blade Fragment", ASRL TR 154-6, Aeroelastic and Structures Research Laboratory, Massachusetts Institute of Technology, May 1972. (Available as NASA CR-120952.)
41. Private communications from G.J. Mangano, R. DeLucia, and J. Salvino, U.S. Naval Air Propulsion Test Center, Trenton, New Jersey 1975-1976.
42. Wu, R.W.-H., Stagliano, T.R., Witmer, E.A. and Spilker, R.L., "User's Guide to Computer Programs JET 5A and CIVM-JET 5B to Calculate the Large Elastic-Plastic Dynamically-Induced Deformations of Multilayer Partial and/or Complete Structural Rings", MIT ASRL TR 154-10, February 1977.
43. Gerstle, J.H., "Analysis Method for Kevlar Shield Response to Rotor Fragments", NASA CP-2017, 1977, pp 261-275.

44. Atluri, S., Witmer, E.A., Leech, J.W., and Morino, L., "PETROS 3: A Finite Difference Method and Program for the Calculation of Large Dynamically-Induced Deformations of Multilayer Variable Thickness Shells", MIT ASRL TR 152-2, November 1971.
45. Gerstle, J.H., "EBCAP: A Computer Program to Analyze Rotor Fragment Impact on Plate/Shell Containment Shields", Boeing Document D6-44273, March 1977.
46. Santiago, J.M., Wisniewski, H.L. and Huffington, N.J. Jr., "A User's Manual for the REPSIL Code", BRL Report No. 1744, October 1974 (AD A003176).
47. Pirotin, S.D., Berg, B.A. and Witmer, E.A., "PETROS 3.5: New Developments and Program Manual for the Finite-Difference Calculation of Large Elastic-Plastic Transient Deformations of Multilayer Variable-Thickness Shells", BRL CR 211 (MIT ASRL TR 152-4) February 1975.
48. Pirotin, S.D., Berg, B.A., and Witmer, E.A., "PETROS 4: New Developments and Program Manual for the Finite-Difference Calculations of Large Elastic-Plastic, and/or Viscoelastic Transient Deformations of Multilayer Variable-Thickness (1) Thin Hard-Bonded, (2) Moderately-Thick Hard-Bonded, or (3) Thin Soft-Bonded Shells", BRL CR 316 (MIT ASRL TR 152-6), September 1976.
49. Wu, Richard W-H. and Witmer, E.A., "Finite Element Predictions of Transient Elastic-Plastic Large Deflections of Stiffened and/or Unstiffened Rings and Cylindrical Shells", AMMRC CTR 74-31 (MIT ASRL TR 171-4), April 1974.
50. Spilker, R.L., Witmer, E.A. and French, S.E., "Finite Element Nonlinear Transient Response Analysis of Panels Subjected to Impulse or Impact Loads", MIT ASRL TR 154-14 (in preparation).
51. Stagliano, T.R., Witmer, E.A., and Rodal, J.J.A., "Some Considerations in the Analysis and Design of an Aircraft Engine Rotor Fragment Container/Deflector System", MIT ASRL TR 154-13 (in preparation).
52. Osias, J.R., Prepared Discussion-Workshop on Applied Thermoviscoplasticity, The Technological Institute, Northwestern University, Evanston, Illinois 60201. Coordinated by S. Nemat-Nasser, Sponsored by NSF, October 13 and 14, 1975, pp. 159-175.
53. Needleman, A., "A Numerical Study of Necking in Circular Cylindrical Bars", J. Mech. Phys. Solids, Vol. 20, 1972, pp 111-127.
54. McMeeking, R.A. and Rice, J.R., "Finite Element Formulations for Problems of Large Elastic Plastic Deformation", Int. J. Solids Structures, Vol. 11, 1975, pp 601-616.
55. Key, S.W., "A Finite Element Procedure for the Large Deformation Dynamic Response of Axisymmetric Solids", Computer Methods in Applied Mechanics and Engineering, 4, 1974, pp 195-218.
56. Biffle, J.H. and Gubbels, M.H., "WULFF -- A Set of Computer Programs for the Large Displacement Dynamic Response of Three-Dimensional Solids", Sandia Lab., Albuquerque, New Mexico 87115, SAND 76-0096, August 1976.
57. Longcope, D.B., and Key, S.W., "On the Verification of Large Deformation Inelastic Dynamic Calculations Through Experimental Comparisons and Analytic Solutions" Presented at International Joint Energy Conference, Houston, Texas, Sept. 1977 Published in: Pressure Vessels & Piping: Computer Program Evaluation and Qualification Edited by D.Dietrich, ASME, N.Y., N.Y.

ACKNOWLEDGMENTS

The authors' research has been supported largely by the Lewis Research Center of the National Aeronautics and Space Administration under Grant NGR 22-009-339, with technical advice from NASA-Lewis personnel Solomon Weiss and Arthur G. Holms. The authors also wish to acknowledge the advice and assistance of some former and present co-workers: Dr. John W. Leech, Dr. Richard Wu, Dr. Robert L. Spilker, and Fred Merlis.

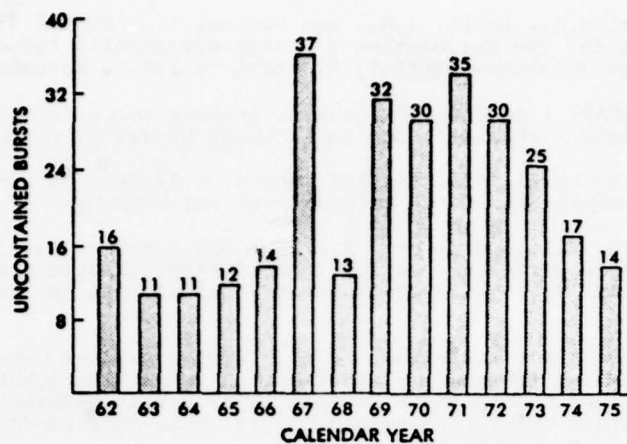


FIG. 1 THE INCIDENCE OF UNCONTAINED ROTOR BURSTS IN U.S. COMMERCIAL AVIATION 1962-1976 (REF. 1)

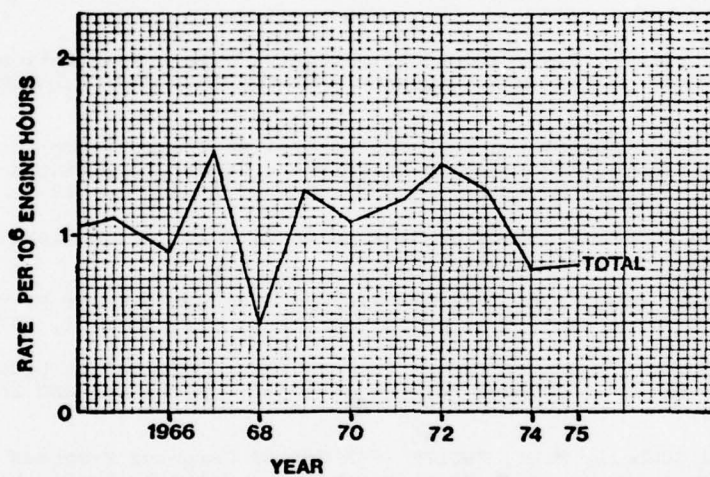


FIG. 2 COMBINED (WORLD-WIDE) AND US (USA REGISTER) ENGINES TOTAL NON-CONTAINMENT RATE (REF. 2)

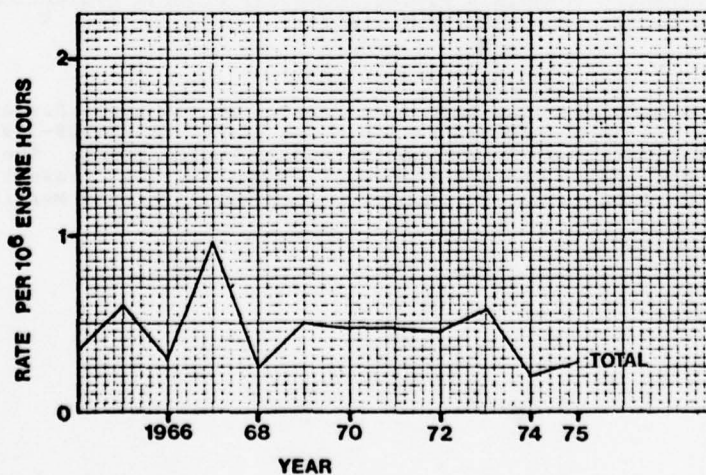


FIG. 3a COMBINED (WORLD-WIDE) AND US (USA REGISTER) ENGINES DISK FRAGMENT NON-CONTAINMENT (REF. 2)

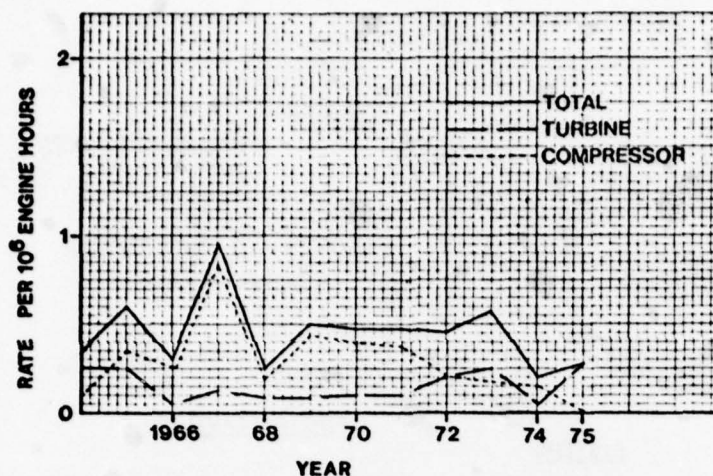


FIG. 3b COMBINED (WORLD-WIDE) AND US (USA REGISTER) ENGINES DISK FRAGMENT NON-CONTAINMENT RATE SHOWING RATES FOR TURBINES AND COMPRESSORS SEPARATELY (REG. 2)

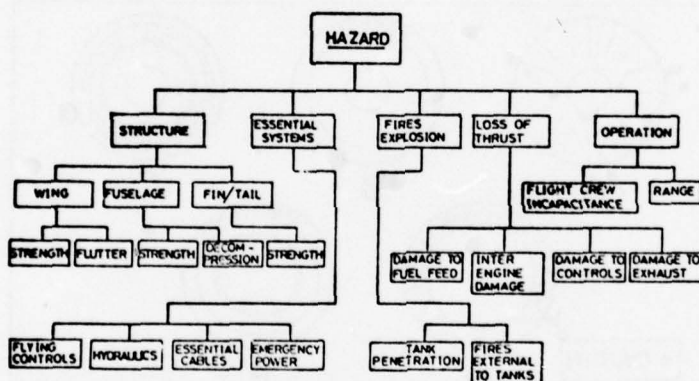


FIG. 4 ENGINE ROTOR FAILURE HAZARD TREE (REF. 3)

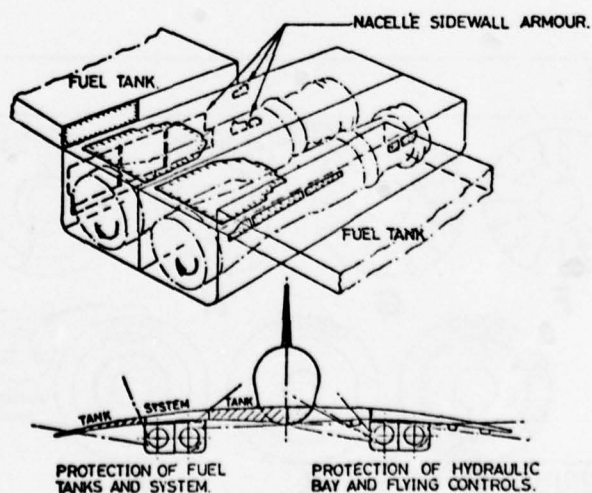


FIG. 5 CONCORDE ARMOUR PLATE (REF. 3)

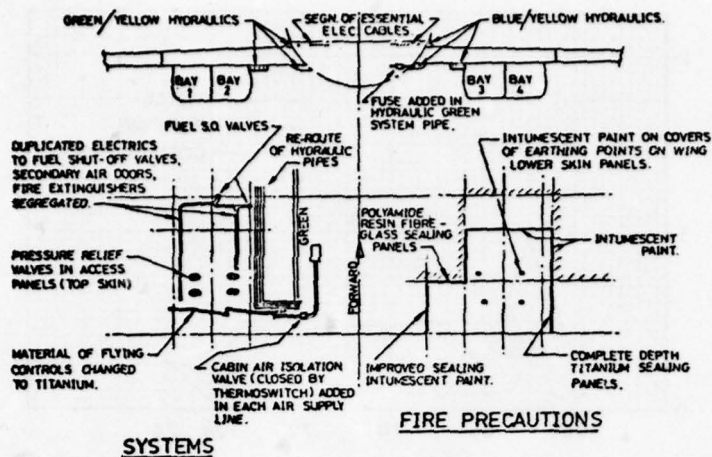


FIG. 6 CONCORDE DESIGN PRECAUTIONS TO MINIMIZE ROTOR FAILURE DAMAGE (REF. 3)

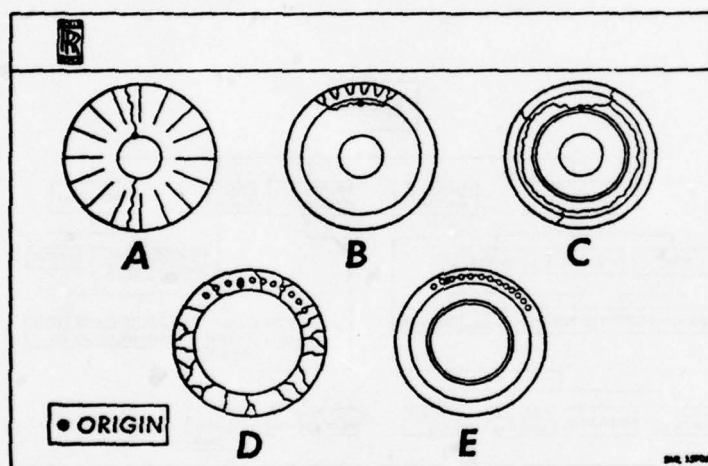


FIG. 7 TYPES OF ROTOR FAILURE FOR LOW CYCLE FATIGUE (REF. 4)

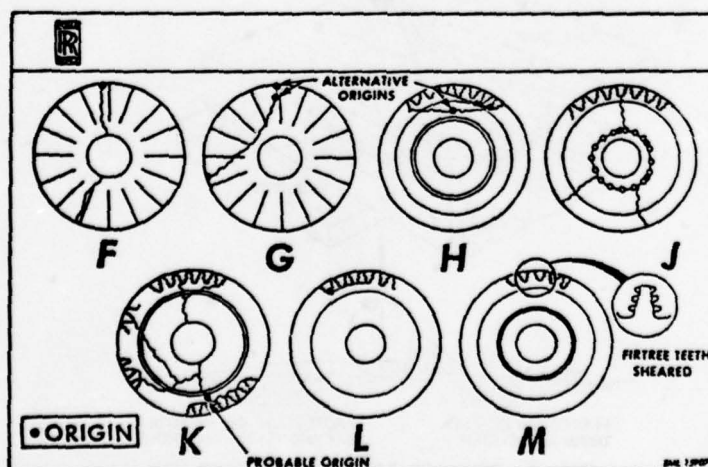


FIG. 8 ROTOR FAILURES IN HIGH CYCLE PLUS LOW CYCLE FATIGUE (REF. 4)

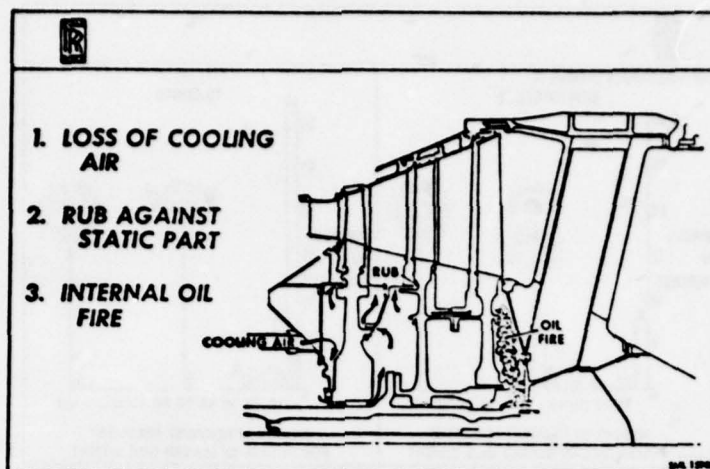


FIG. 9 DISK OVERHEATING PROBLEMS (REF. 4)

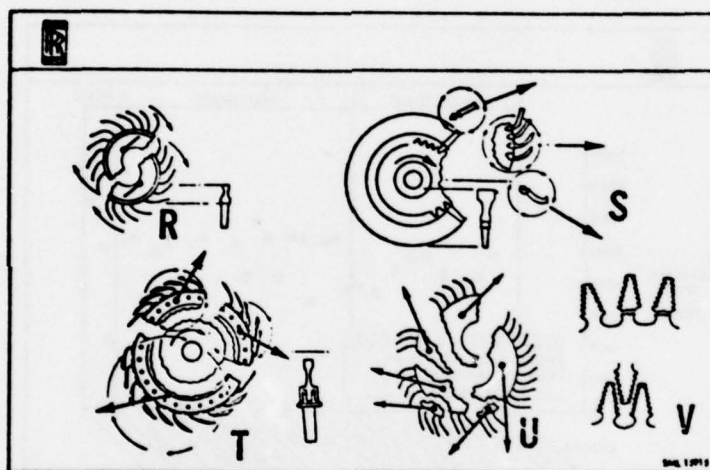


FIG. 10 SHAPES OF FRAGMENTS (REF. 4)

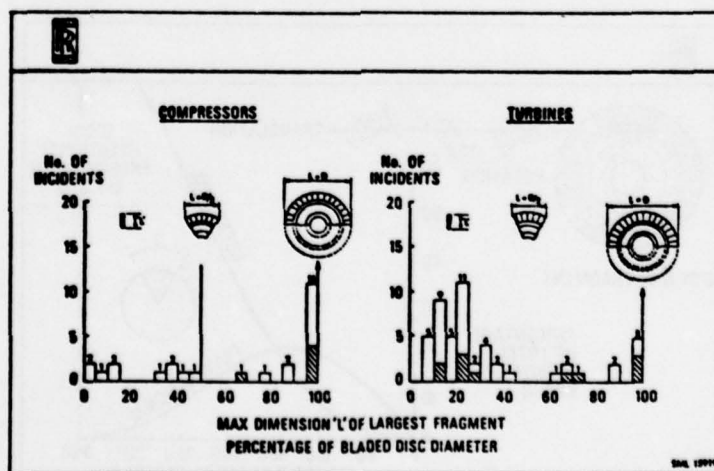


FIG. 11 MAXIMUM DIMENSION OF LARGEST FRAGMENT AS A PERCENTAGE OF BLADED DISC DIAMETER (REF. 4)

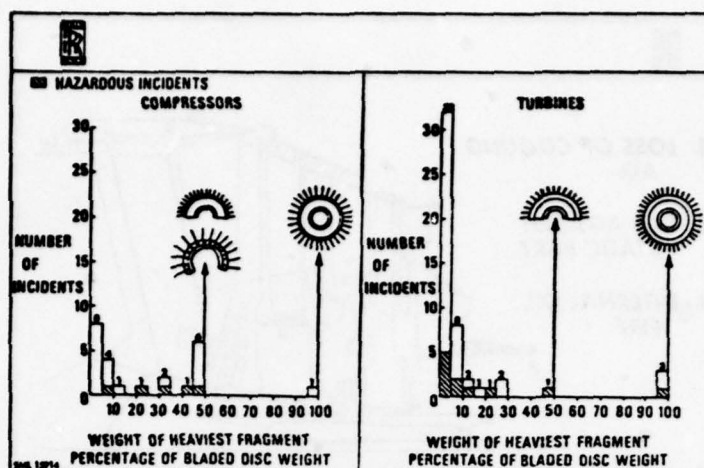


FIG. 12 INCIDENCE OF WEIGHT OF FRAGMENT AS A PERCENTAGE OF BLADED DISK WEIGHT (REF. 4)

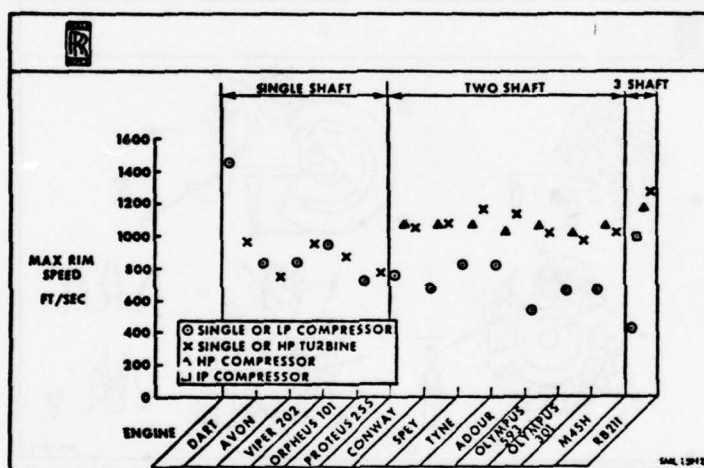


FIG. 13 TYPICAL FRAGMENT VELOCITIES (REF. 4)

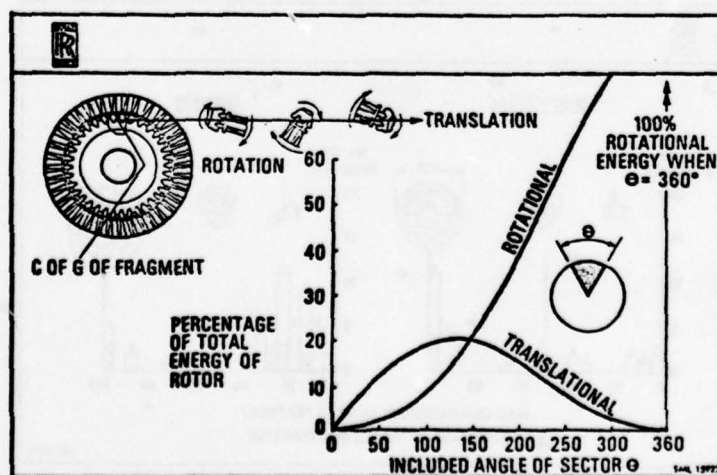


FIG. 14 PROPORTION OF TOTAL FRAGMENT KINETIC ENERGY IN TRANSLATION AND ROTATION AS A FUNCTION OF THE INCLUDED ANGLE θ OF SECTOR (REF. 4)

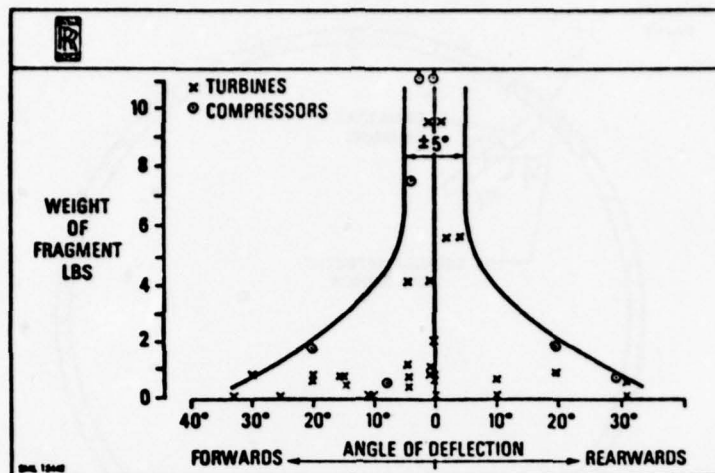


FIG. 15 DEBRIS SPREAD ANGLE VERSUS WEIGHT OF FRAGMENT (REF. 4)

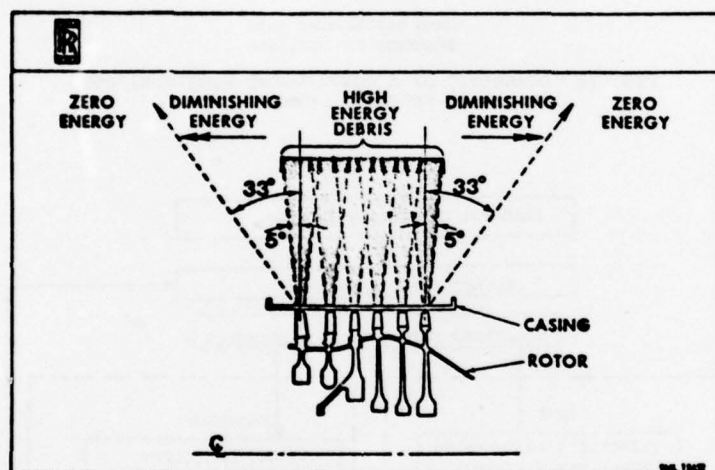


FIG. 16 DIRECTION AND ENERGY OF EMERGING DEBRIS (REF. 4)

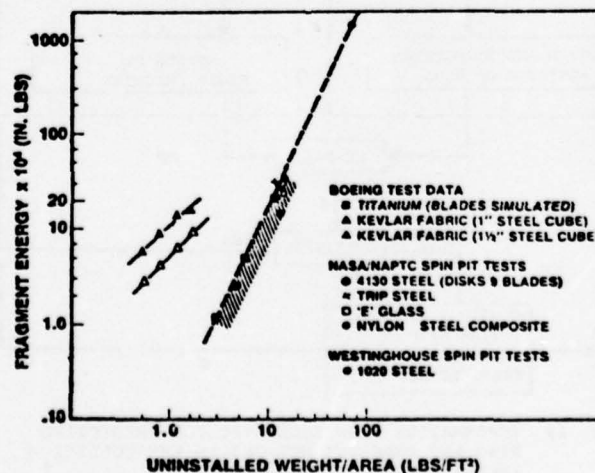
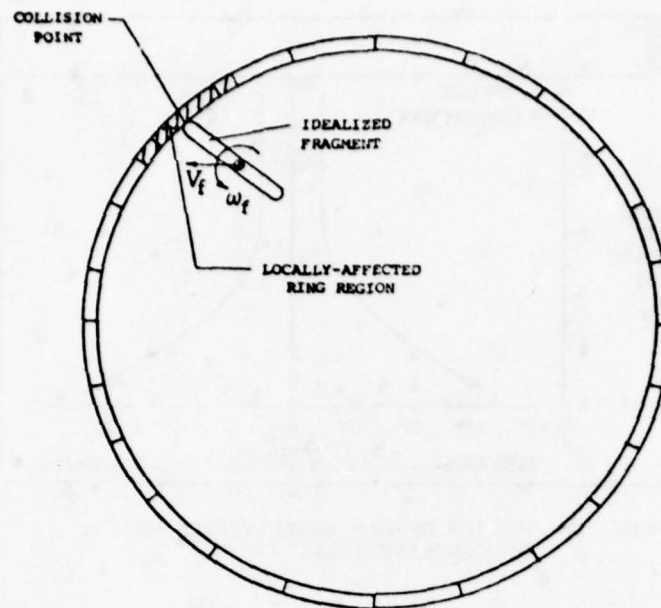


FIG. 17 CONTAINMENT PERFORMANCE (REF. 18)



RING DISCRETIZED INTO
SEGMENTS FOR ANALYSIS

FIG. 18 SCHEMATIC OF A CONTAINMENT RING SUBJECTED TO SINGLE-FRAGMENT IMPACT

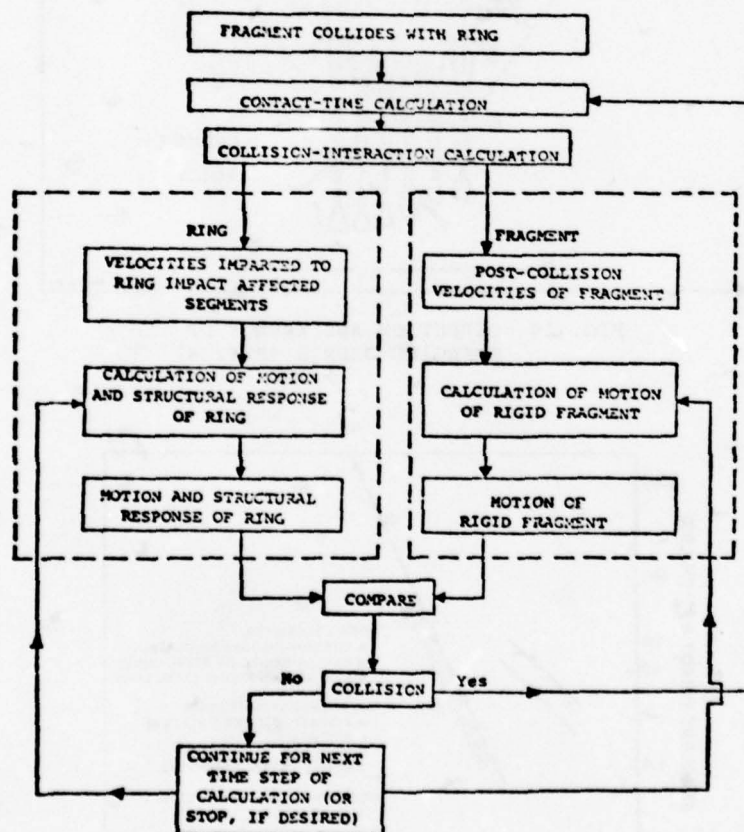


FIG. 19 INFORMATION FLOW SCHEMATIC FOR PREDICTING RING AND FRAGMENT MOTIONS IN THE COLLISION-IMPARTED VELOCITY METHOD

TABLE 1
DATA CHARACTERIZING NAPTC RING TEST 91

<u>Ring Data</u>		<u>Test 91</u>
Outside Diameter (in)		17.619
Radial Thickness (in)		0.152
Axial Length (in)		1.506
Material		2024-T4
Elastic Modulus E (psi)		10 ⁷
PP Yield Stress σ_0 (psi)		50,000
<u>Fragment Data</u>		
Type		T-58 Single Blade
Material		SEL-15
Outer Radius (in)		7.0
Fragment Centroid from Center of Rotation (in)		4.812
Fragment Tip Clearance from Ring (in)		1.658
Fragment Length (in)		3.5
Fragment Length from CG to Tip (in)		2.188
Fragment Weight (lbs)		0.084
Fragment Moment of Inertia about its CG (in lb sec ²)		2.163×10^{-4}
Failure Speed (RPM)		15,644.4
Fragment Tip Velocity (ips)		11,467.
Fragment Centroidal Velocity (ips)		7,884.
Fragment Initial Angular Velocity (rad/sec)		1,638.3
Fragment Translation KE (in lb)		6,756.
Fragment Rotational KE (in lb)		290.3

o --- EXPERIMENT
 x ---- CASE CR-11B (EL-PP-SR, $\epsilon = 0$)
 ▲ --- CASE CR-10B (EL-PP-SR, $\epsilon = 1$)
 — RING BEFORE INITIAL IMPACT

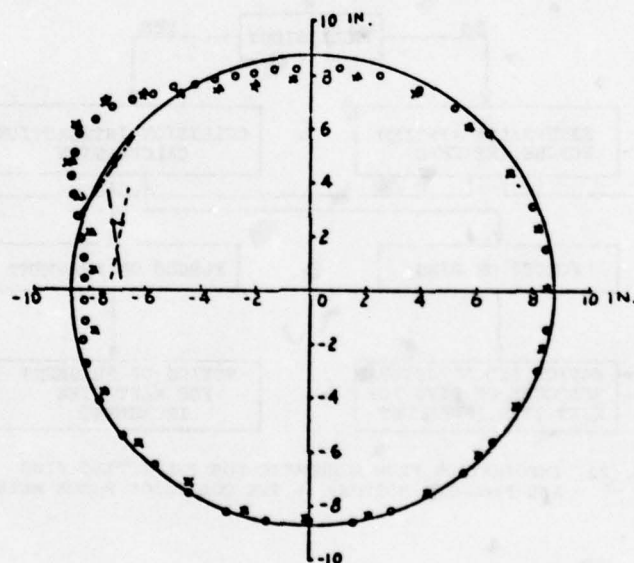


FIG. 20 COMPARISON OF CIVM PREDICTIONS WITH EXPERIMENT AT 810 MICROSECONDS AFTER INITIAL IMPACT FOR THE FREE CIRCULAR RING SUBJECTED TO SINGLE-BLADE IMPACT IN NAPTC TEST 91

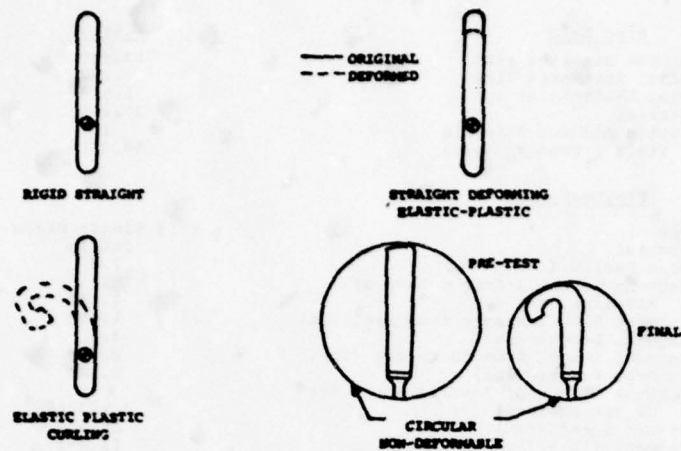


FIG. 21 SCHEMATICS OF ACTUAL AND IDEALIZED FRAGMENTS

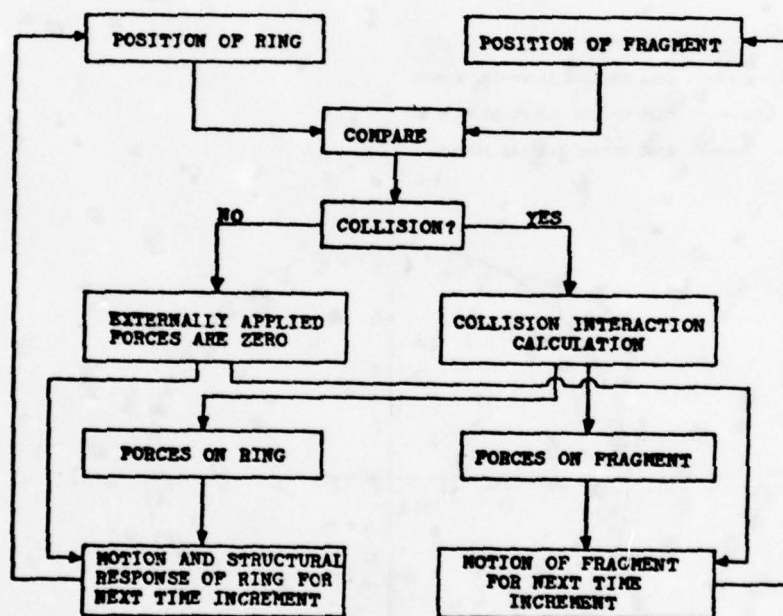


FIG. 22 INFORMATION FLOW SCHEMATIC FOR PREDICTING RING AND FRAGMENT MOTIONS IN THE COLLISION FORCE METHOD

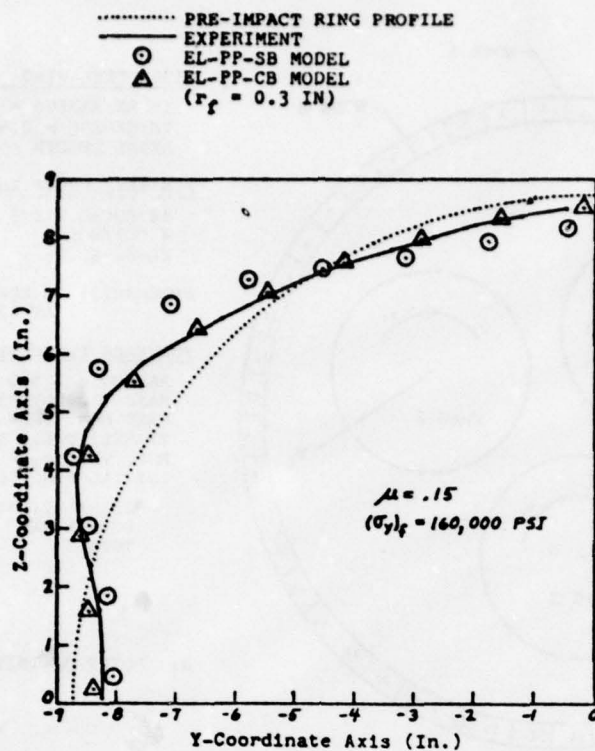


FIG. 23 COMPARISON OF CFM PREDICTIONS FOR EL-PP-SB AND EL-PP-CB BLADE MODELS FOR $\mu = .15$ BLADE/RING IMPACT VERSUS EXPERIMENTAL DEFORMED RING DATA FOR NAPTIC TEST 91 AT 626 MICROSECONDS AFTER INITIAL IMPACT

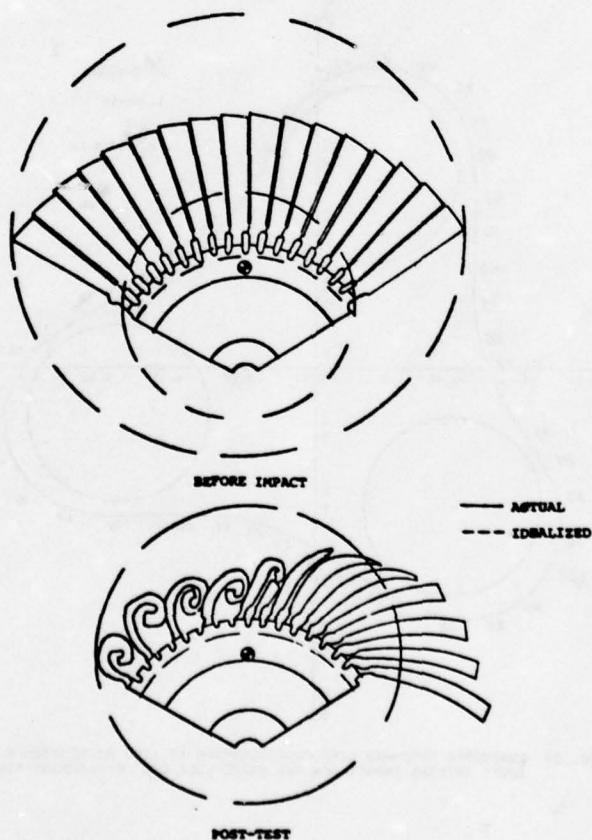
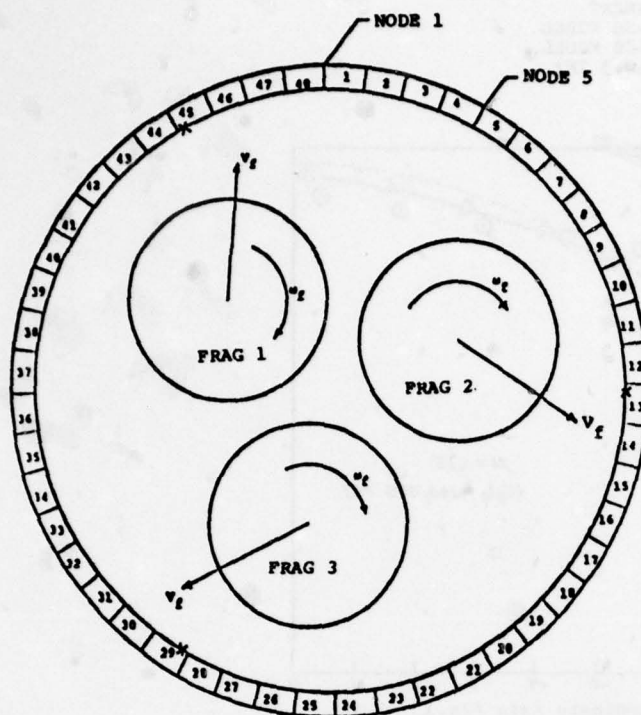


FIG. 24 SCHEMATICS OF PRE-TEST AND DEFORMED TRI-HUB DISK/BLADE FRAGMENTS, AND IDEALIZED MODELS

**4130 STEEL RING**

INNER RADIUS = 7.50 IN
 THICKNESS = 0.625 IN
 AXIAL LENGTH = 1.50 IN

FINITE-ELEMENT ANALYSIS

48 EQUAL ELEMS (FULL RING)
 4 DOF/NODE
 EL-SH-SR

FRAGMENTS: 3 EQUAL CIRCULAR
 AT 120-DEG. SPACING

FOR EACH FRAGMENT

RADIUS = 2.555 IN
 MASS = 0.009395 (LB-SEC²)/IN
 MASS MOM. INER. = 0.06899 IN-LB-SEC²
 TRANSL. VEL., v_f = 5816.7 IN/SEC
 ROT. VEL., ω_f = 2079.6 RAD/SEC
 INITIAL KINETIC ENERGY
 TRANSLATIONAL = 158,942 IN-LB
 ROTATIONAL = 149,177 IN-LB
 TOTAL = 308,119 IN-LB

X: POINT OF INITIAL IMPACT

FIG. 25 GEOMETRIC, TEST, AND MODELING DATA FOR THE 4130 STEEL CONTAINMENT RING SUBJECTED TO TRI-HUB T58 ROTOR BURST IN NAPTC TEST 201

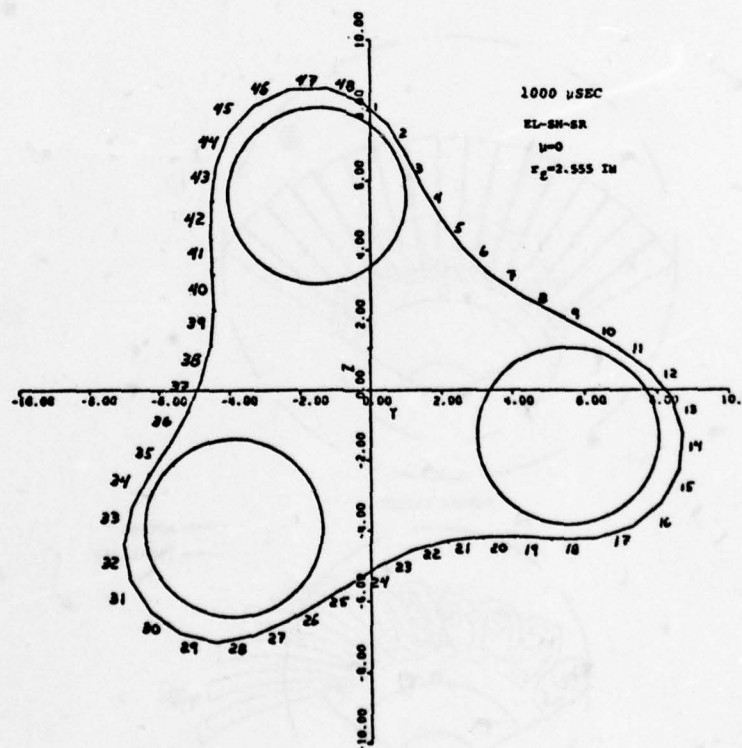


FIG. 26 PREDICTED DEFORMED RING CONFIGURATION AT 1000 MICROSECONDS AFTER INITIAL IMPACT FOR THE NAPTC TEST 201 CONTAINMENT RING

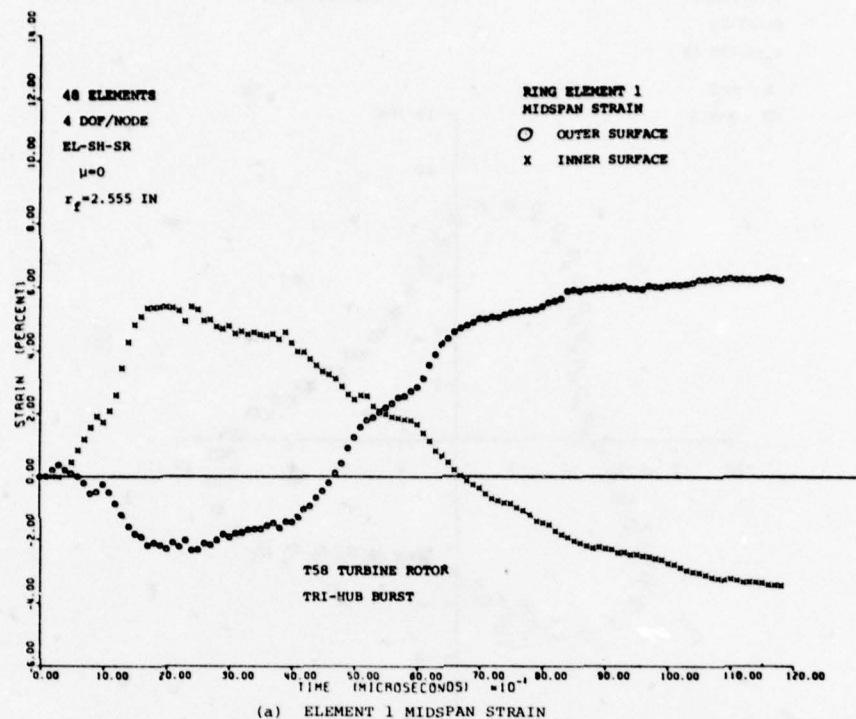


FIG. 27 PREDICTED TRANSIENT STRAIN ON THE NAPTC TEST 201 CONTAINMENT RING

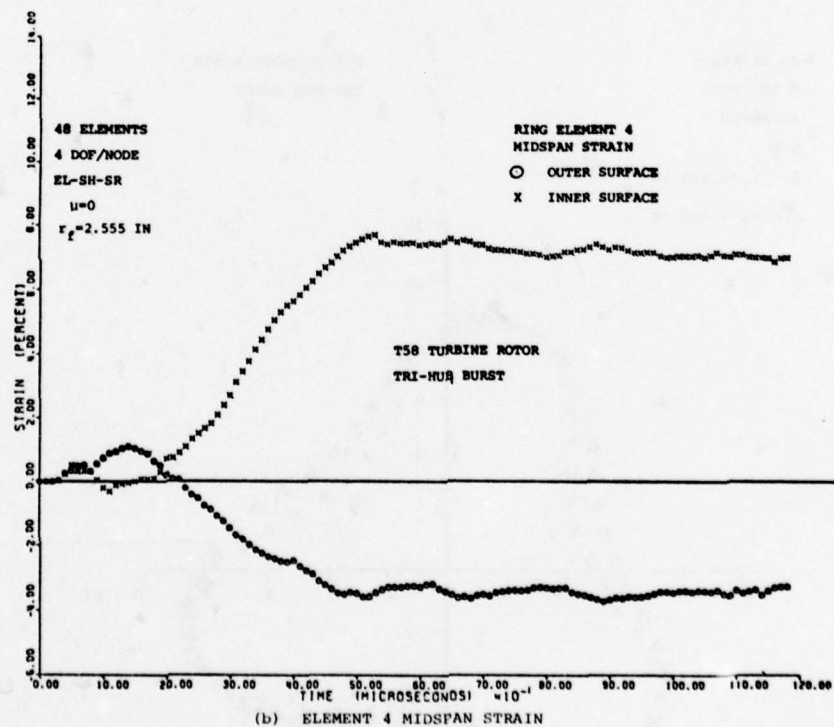


FIG. 27 CONCLUDED (NAPTC TEST 201 RING)

48 ELEMENTS
4 DOF/NODE
EL-SH-SR
 $r_f = 2.555$ IN
X $\mu = 0$
O $\mu = 0.3$

T58 TURBINE ROTOR
TRI-HUB BURST

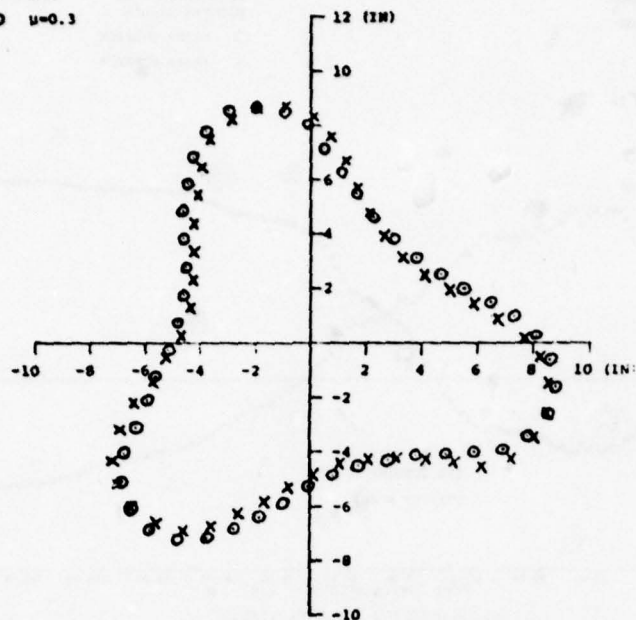


FIG. 28 COMPARISON OF PREDICTED DEFORMED RING CONFIGURATIONS AT 1200 MICROSECONDS AFTER INITIAL IMPACT FOR $\mu = 0$ AND $\mu = 0.3$ WITH $r_f = 2.555$ IN FOR THE NAPTC TEST 201 CONTAINMENT RING

48 ELEMENTS
4 DOF/NODE
EL-SH-SR
 $\mu = 0$
X $r_f = 2.555$ IN
 Δ $r_f = 3.360$ IN

T58 TURBINE ROTOR
TRI-HUB BURST

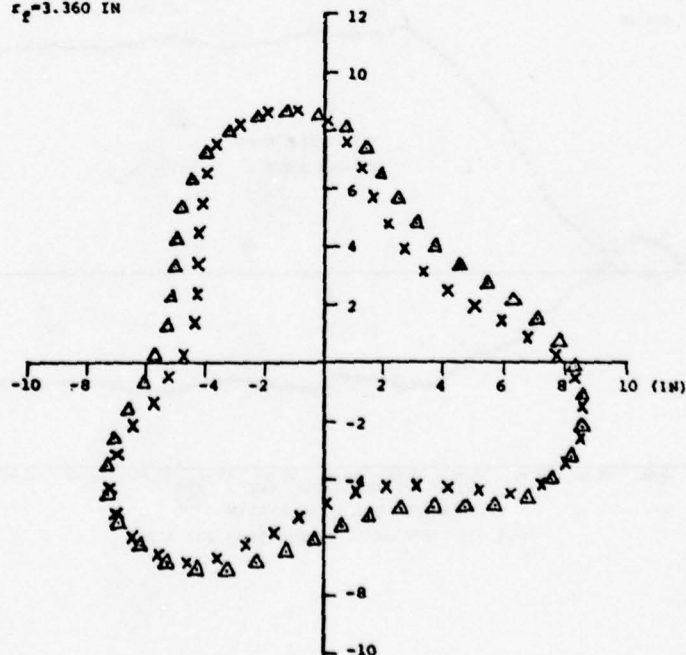


FIG. 29 COMPARISON OF PREDICTED DEFORMED RING CONFIGURATIONS AT 1200 MICROSECONDS AFTER INITIAL IMPACT FOR TWO DIFFERENT FRAGMENT-SIZE MODELINGS AND FRICTIONLESS IMPACT CONDITIONS FOR THE NAPTC TEST 201 CONTAINMENT RING

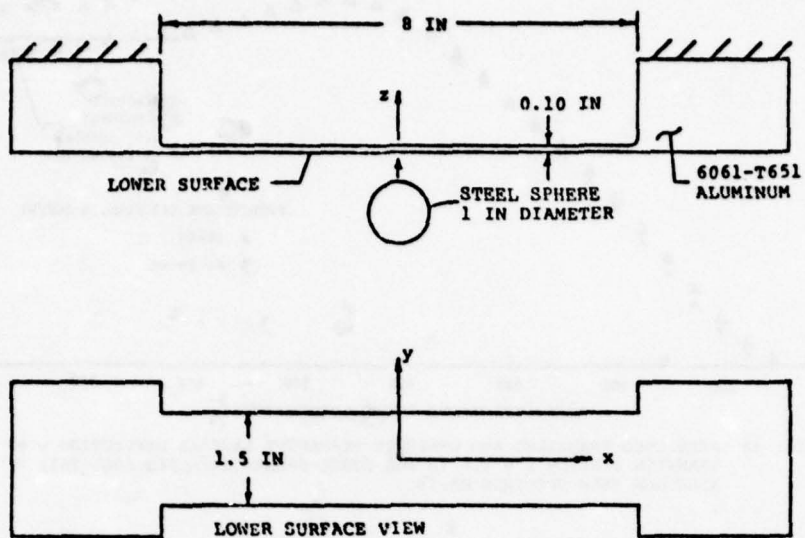


FIG. 30 SCHEMATIC OF 6061-T651 NARROW PLATE OR BEAM MODEL SUBJECTED TO IMPACT BY A ONE-INCH DIAMETER SOLID STEEL SPHERE

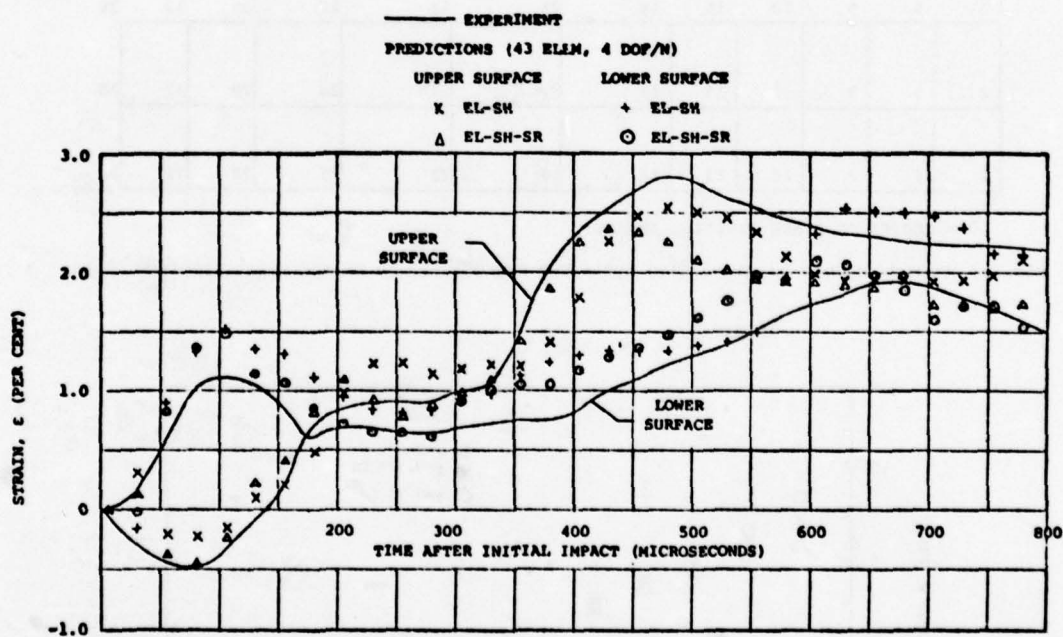


FIG. 31 TRANSIENT STRAIN AT SPANWISE STATION $x = 1.50$ IN OF STEEL-SPHERE-IMPACTED 6061-T651 ALUMINUM BEAM MODEL CB-18

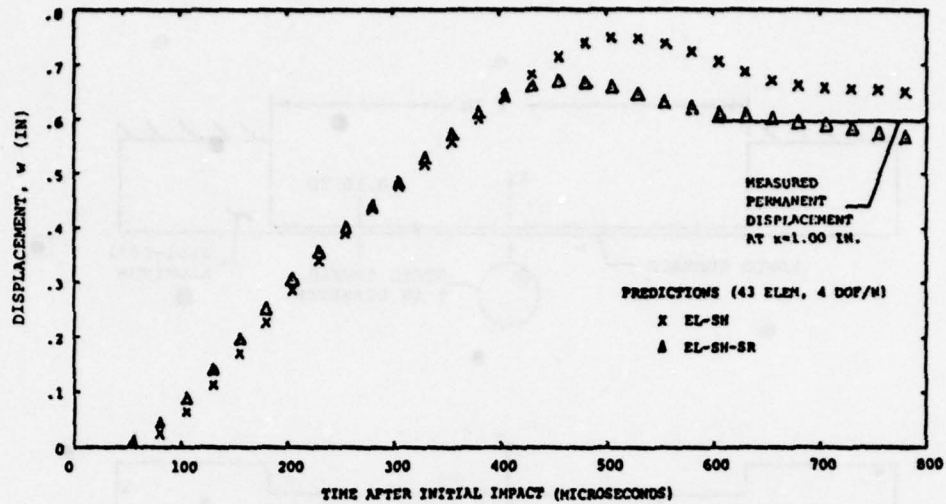


FIG. 32 PREDICTED TRANSIENT AND OBSERVED PERMANENT LATERAL DEFLECTION w AT SPANWISE STATION $x = 1.0$ IN FOR STEEL-SPHERE IMPACTED 6061-T651 ALUMINUM BEAM SPECIMEN CB-18

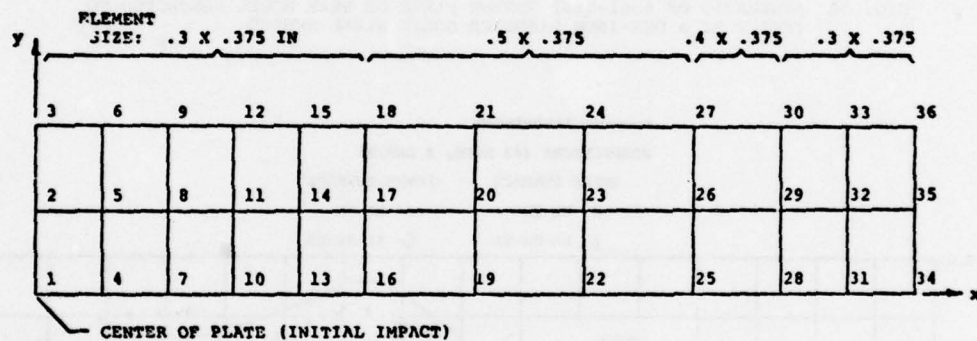


FIG. 33 FINITE ELEMENT ARRAY USED TO REPRESENT ONE QUARTER OF NARROW-PLATE SPECIMEN CB-18

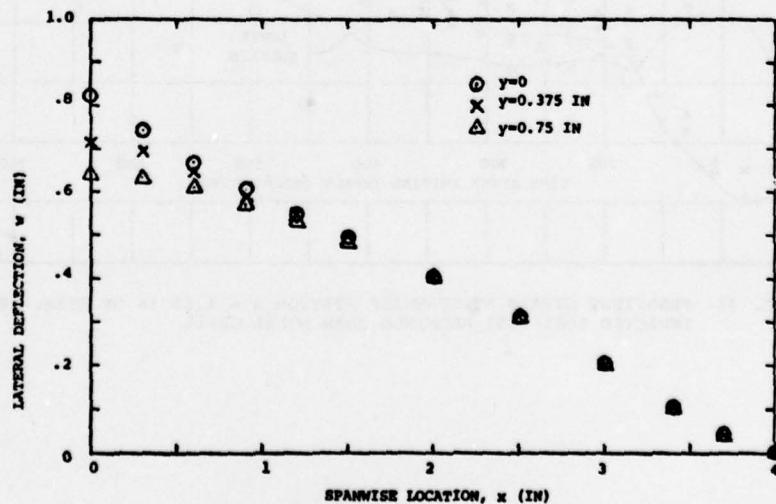


FIG. 34 PREDICTED LATERAL DEFLECTION DISTRIBUTION AT 900 MICROSECONDS AFTER INITIAL IMPACT FOR NARROW-PLATE SPECIMEN CB-18

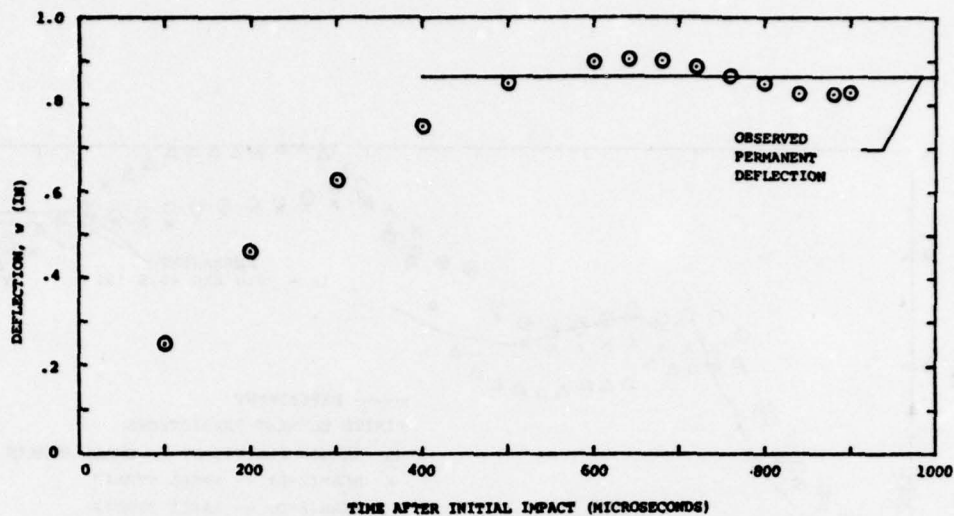


FIG. 35 PREDICTED TRANSIENT AND MEASURED PERMANENT DEFLECTION OF NARROW-PLATE SPECIMEN CB-18 AT PANEL CENTER $(x,y) = (0,0)$

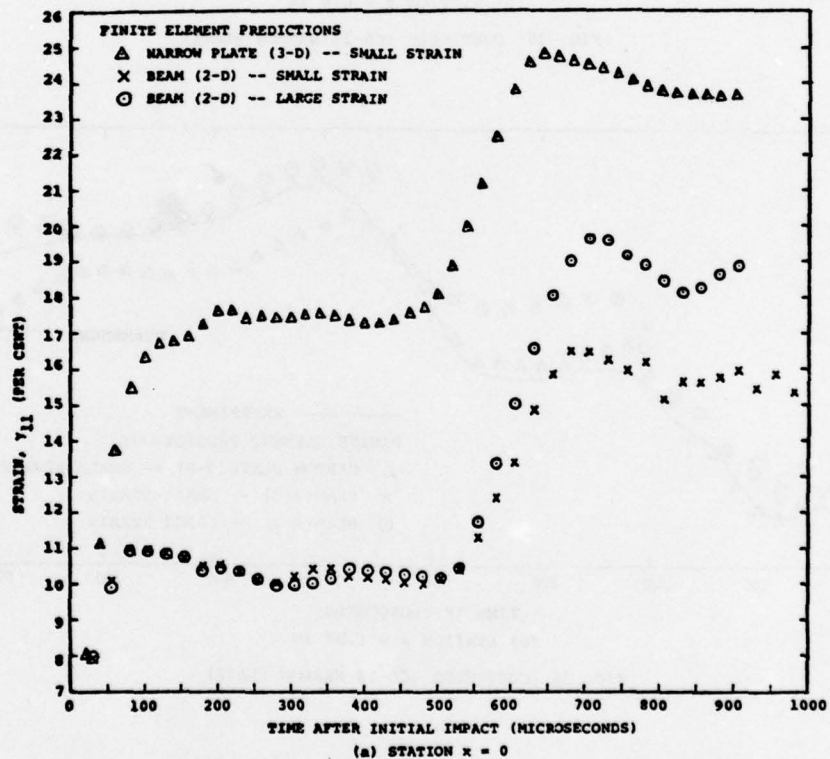


FIG. 36 COMPARISONS OF PREDICTIONS VERSUS MEASUREMENTS FOR UPPER-SURFACE LONGITUDINAL STRAIN AT VARIOUS SPANWISE STATIONS OF STEEL-SPHERE IMPACTED NARROW-PLATE SPECIMEN CB-18

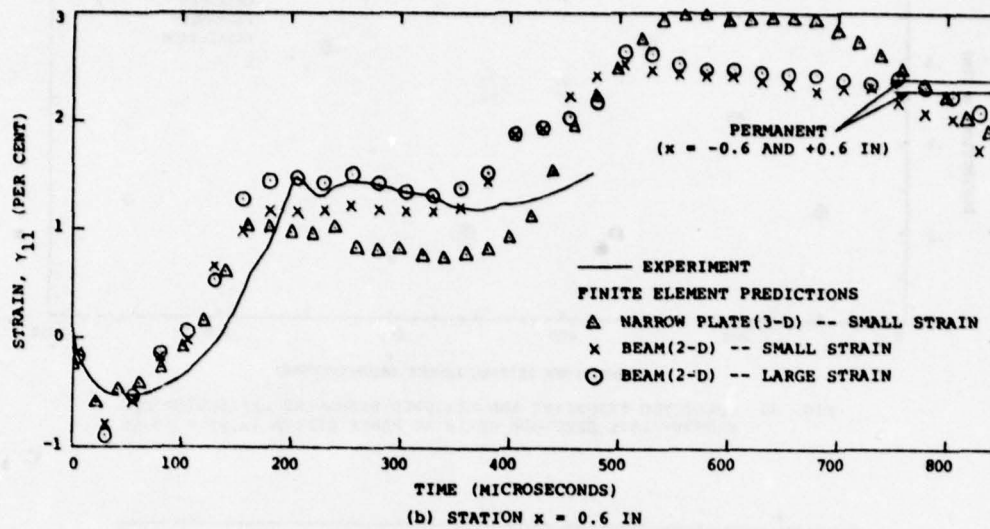


FIG. 36 CONTINUED (CB-18 NARROW PLATE)

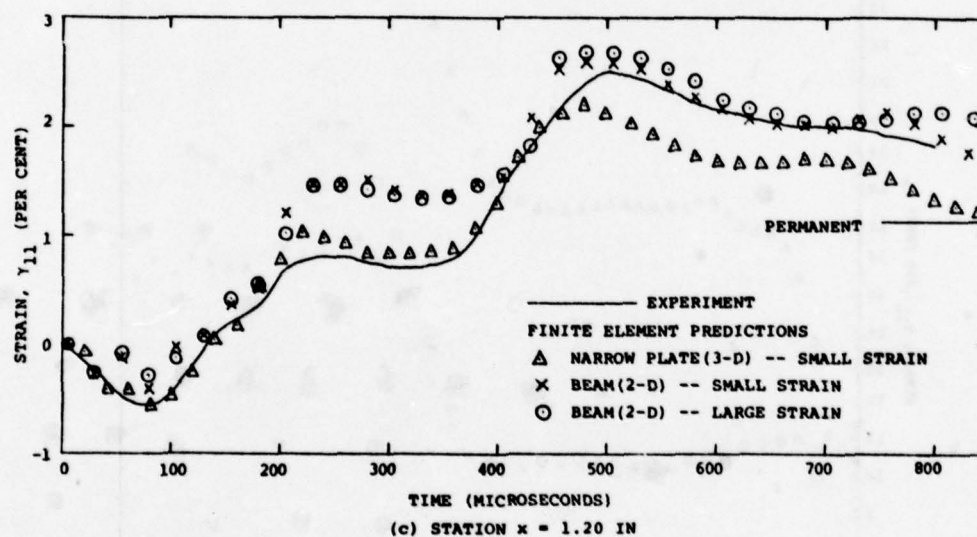


FIG. 36 CONTINUED (CB-18 NARROW PLATE)

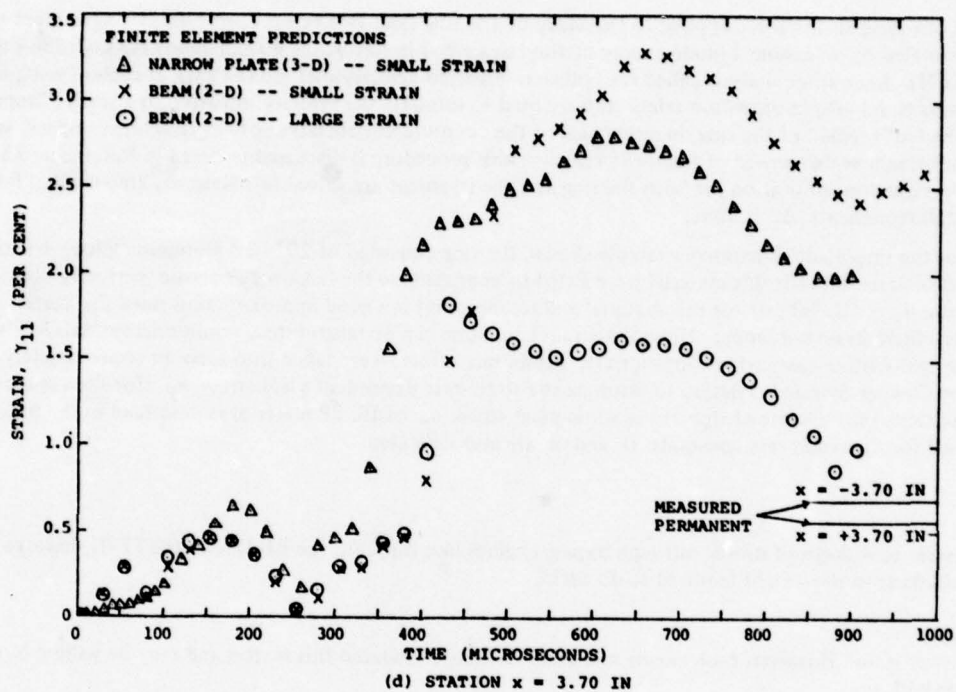


FIG. 36 CONCLUDED (CB-18 NARROW PLATE)

DISCUSSION

C.C. Chamis, US

- (1) What were the initial and boundary conditions on the containment ring for the single-blade impact analysis?
- (2) How was the impact force or exchange of momentum varying or established as a function of time?
- (3) How were the strain rate and strain hardening parameters of the ring selected? What were the values used?

Author's Reply

- (1) The containment ring was a free ring initially at rest and was permitted to undergo 2-d displacements in the plane of the ring. The single blade had known: dimensions, mass, pre-impact mass moment of inertia about its center of gravity, as well as a known pre-impact CG translational velocity and rotational velocity.
- (2) In one analysis the force applied to the blade by the ring (and vice versa) during blade/ring contact was estimated by an assumed-mode energy method described in Reference 40 and called the collision-force method (CFM). In another analysis called the collision-imparted velocity method (CIVM), at each of a sequence of impacts, impulse/momentum relations were used to estimate the velocity imparted to a small ("impact-affected") region of the ring on either side of the circumferential station of ring/fragment impact, as well as the attendant decrement of fragment velocity; this procedure is discussed in detail in References 35 and 38. The equations of motion for both the ring and the fragment are solved in a timewise step-by-step fashion in small increments Δt in time.
- (3) For the ring/blade illustrative example shown, the ring consisted of 2024-T4 aluminum alloy. Uniaxial static stress-strain data for this material were fitted to approximate the behavior as elastic, perfectly-plastic (EL-PP) with $\sigma_0 = 50,000$ psi; for this material and temper, that is a good approximation since this material exhibits very little strain hardening. However, strain hardening can be taken into account readily; this has been done for many other cases where appropriate. Strain rate effects were taken into account approximately by using the Cowper-Symonds relation to estimate the strain-rate-dependent yield stress σ_y (for time-independent plasticity) from a knowledge of the static yield stress σ_0 of EL-PP material as described in the paper; values used for the strain rate constants D and p are also indicated.

M. Aarnes, US

If you were to disk-proof one of our high bypass engines like the CF6, the RB211, or the JT9D, have you made any calculations as to the weight required to do such?

Author's Reply

The answer is no. However, each engine manufacturer has considered this matter and may be willing to share its estimate with you.

D.K. Hennecke, FRG

Figure 3b suggests that the number of compressor disk failures decreases while that of the turbines increases. Is that just an oddity of the statistics or a real tendency? If it is a tendency, is it the result of increasing turbine inlet temperature?

Author's Reply

The cited information is from Reference 2 and represents the results from a significant data base. Hence, the trend appears to be real, and may be associated with increasing turbine inlet temperatures. For more detailed information on this matter, I recommend References 2 and 4.

PETITES TURBOMACHINES :
EXPERIENCES SUR LA RUPTURE DES DISQUES
PAR J.M. FOUILLASSAR et
A.R. VON DER MUHLL

RESUME

Sur des Turbomachines de petites dimensions tout au moins, la construction de blindages capables de retenir intégralement tous les débris en cas de rupture de disques semble réalisable avec une pénalité de masse très acceptable.

L'expérience d'incidents survenus dans la pratique et surtout l'exploitation d'essais systématiques de ruptures de disques dans des conditions réelles de fonctionnement apporte des enseignements utiles :

- forme et dimensions des éléments les plus pénétrants ;
- formes et dispositions les plus efficaces à donner aux éléments servant de blindage ;
- matériaux les mieux adaptés à l'emploi comme blindage.

Pour des rotors dont la sécurité repose sur le fait que les aubages s'arrachent sans rupture du disque ou du tambour proprement dit en cas de défaillance par survitesse, les essais ont également confirmé la confiance qu'on pouvait avoir dans les éléments de blindage construits selon les mêmes principes d'évaluation.

1. EXPOSE DES MOTIFS

L'expérience acquise avec des turbomachines d'aviation de dimensions réduites et moyennes fait apparaître qu'il est sans doute plus facile, pour celles-ci que pour des machines plus grandes, de prévoir une construction capable de contenir intégralement les débris en cas de rupture de disque.

La pénalité en masse, liée à un tel blindage efficace est - tout au moins pour ces petites turbomachines - d'un ordre de grandeur raisonnable.

C'est pourquoi il a semblé utile de résumer les expériences acquises à ce sujet sur des moteurs construits par TURBOMECA.

Outre les enseignements pratiques recueillis avec des ruptures des disques proprement dits, nous donnerons aussi quelques exemples de blindages construits pour retenir des pales rapportées.

Certains des essais relatés concernent des pales de fan ou compresseurs d'entrée de turboréacteurs à double - flux. D'autres essais ont porté sur la retenue de pales de roues pour lesquelles la sécurité est basée sur le fait que les pales s'arrachent sans rupture du disque en cas de survitesse accidentelle. Le blindage doit, dans un tel cas, être conçu pour contenir tous les débris des pales.

Toutes ces expériences fournissent l'occasion d'esquisser brièvement les méthodes et les procédés mis au point pour assurer que les dégâts restent contenus dans le moteur et ne mettent pas en danger l'aéronef sur lequel il est monté.

2. HISTORIQUE

2.1 Généralités

L'expérience sur laquelle nous nous basons est en partie déjà ancienne, puisqu'il y a trente ans que TURBOMECA livre en série de petites turbomachines d'aviation.

La rupture d'un disque de rotor, par son caractère soudain et par la gravité des conséquences qu'elle peut entraîner, constituait un vrai cauchemar pour le constructeur.

A cette époque, rappelons-le, les méthodes de calcul des durées de vie des éléments essentiels des moteurs et les notions de fatigue oligocyclique ("low cycle fatigue") en étaient encore à leurs débuts. Il y a à peine dix ans que ces conceptions sont entrées, pour la première fois, dans les textes des Règlements de Navigabilité. Il n'est donc pas étonnant que des événements désastreux comme une rupture de disque aient été en ce temps-là couverts par la plus extrême discrétion. Des informations sur les circonstances, les effets et les causes de ruptures de disques ont longtemps été traitées de manière absolument confidentielle. Il était alors pratiquement impossible de savoir à quoi s'en tenir au point de vue technique.

A titre anecdotique, nous nous souvenons avoir entendu en 1970, le responsable technique d'un grand constructeur de turbines d'aviation affirmer qu'aucune rupture de disque non contenue n'avait été rencontrée sur des moteurs de sa marque. Ceci, au moment même où les Autorités de Navigabilité, qui avaient commencé à s'occuper sérieusement de ce problème, publiaient les premières statistiques sur les conséquences des éclatements de disques en vol. Or ces statistiques incluaient plusieurs avions équipés de moteurs de la marque en question....

Un constructeur de moteurs qui rencontre des incidents graves d'intégrité de disques n'a pas intérêt - pour des raisons commerciales évidentes et pour le bon renom de sa marque - à le crier sur les toits. Mais au niveau technique un tel événement apporte des enseignements dont il faut tirer parti, pour améliorer la fiabilité du matériel à l'avenir. L'esprit avec lequel ces problèmes sont désormais envisagés a heureusement évolué depuis le temps auquel nous nous sommes reportés. Peut-être tout simplement, parce que les constructeurs se sont aperçus que leurs concurrents rencontraient des problèmes de même nature ? En tous cas l'intérêt du progrès technique semble avoir, désormais, pris le pas sur le secret individuel.

2.2 Une expérience de rupture de compresseur centrifuge

C'est dans cet esprit que nous relatons maintenant une expérience vieille de plus de vingt ans. Lors d'un essai d'endurance au banc d'un turbomoteur d'hélicoptère du type ARTOUSTE II, un cas de rupture de rotor de compresseur centrifuge en alliage d'aluminium forgé a été rencontré (Juillet 1957).

Considéré d'abord comme un cas d'espèce et attribué aux conditions particulières de l'essai, ce type de rupture a été analysé plus à fond quelques années plus tard, lorsque des cas semblables sont survenus à nouveau, mais cette fois sur des moteurs en service de vol sur hélicoptère. Une modification de la construction de ce compresseur a évité, par la suite, la récurrence de ruptures de ce type. Quant aux rouets de compresseurs centrifuges conformes au dessin d'origine, leur emploi a été limité en durée de service et en nombre de cycles par une consigne de navigabilité, en attendant leur remplacement, lors d'une révision, par des rotors du nouveau modèle.

Ces événements avaient constitué pour TURBOMECA un premier contact avec la réalité assez dure des limites de vie des éléments essentiels et avec les mesures de sécurité à prendre sur du matériel en service en série, pour assurer la poursuite des vols. Mais ces incidents avaient fourni un enseignement utile : malgré l'importance des dégâts causés au moteur, par la rupture complète du rouet, en trois segments à 120°, les débris ont toujours été intégralement contenus par les carters. Le travail de déformation, fourni par les diffuseurs, les brides de liaisons et les carters situés dans le plan radial autour du rotor, suffisait pour contenir les débris. De sorte que la rupture du disque était certes un incident grave mais ne tournait pas à la catastrophe. (Figures 1 et 2).

2.3 Ruptures de disques de turbines monoblocs

D'autres expériences, plus traumatisantes ont été enregistrées vers 1970. Des ruptures de disques de turbines ont démontré que l'énergie des débris était supérieure au travail absorbé par les carters environnants. Des morceaux de disques, projetés à l'extérieur du moteur, pouvaient être (et l'ont été dans un cas particulier) à l'origine d'accidents graves pour les aéronefs équipés du modèle en question de turbopropulseur.

Ces incidents ont été ressentis de manière d'autant plus pénible par le constructeur, que celui-ci commençait à ce moment à se préoccuper sérieusement des problèmes de limite de vie en fatigue des roues de turbine. Des essais prolongés de moteurs complets en endurance cyclique semblaient avoir justifié des valeurs de vie cyclique bien supérieures au nombre de cycles accumulé par les disques défaillants.

Le doute a été jeté tout d'abord sur la représentativité des essais en cycles thermiques au banc d'essai. Mais la vraie raison des défaillances a été trouvée avec plus de vraisemblance dans le manque d'homogénéité de la structure des matières utilisées alors pour les roues de turbine. La dispersion des caractéristiques du matériau constituait un risque qui avait été sous-estimé. Dans les dix dernières années, la connaissance des caractéristiques des matériaux a utilisé à fait d'énormes progrès. En même temps, les méthodes de contrôle métallurgique se sont améliorées et affinées de telle manière que des gâlets de matière présentant des plages non homogènes ne sont plus admis en fabrication.

Les événements auxquels nous faisons allusion ont enseigné, tout d'abord, que le fragment de disque avec pales qui avait la plus grande force de pénétration, présentait un angle au centre d'environ 114°. On retrouve la notion de 1/3 de disque, considéré depuis toujours comme typique. Cela, malgré la présence dans le disque des 4 trous pour les tirants ou vis d'assemblage des divers étages de turbines, dans ce cas particulier (Figures 3 et 4)

À la suite des incidents enregistrés, au banc d'essai et en vol, TURBOMECA a entrepris une campagne d'essais sans précédent pour mettre au point un bouclier de blindage de turbine efficace. À partir du modèle de rupture de disque défini ci-dessus, des essais d'éclatement en vraie grandeur ont été effectués au banc sur des moteurs complets, dans les conditions réelles de vitesse de rotation et de température de la puissance maximale. Cette campagne représente sans doute le plus grand effort jamais consenti dans ce domaine par un constructeur de moteurs. Il faut en convenir, les faibles dimensions de l'ASTAZOU ont permis de pousser les essais à fond, ce qui n'aurait sans doute pas été possible avec des moteurs plus grands.

Notre campagne a conduit, pour maîtriser le problème à sacrifier, par destruction partielle ou totale, pas moins de 10 machines. Huit, dans une première phase, pour acquérir une définition appropriée du blindage de turbine. Deux autres essais - poussés également jusqu'à éclatement du disque de turbine - ont été faits ensuite pour confirmer la bonne tenue du blindage ainsi défini. (Figure 5).

Nous nous sommes un peu étendus sur cette campagne systématique d'essais, car elle a fourni les bases de nos connaissances pratiques. Dans ce domaine, en effet, la littérature était - surtout à l'époque considérée, extrêmement maigre.

De cette façon nous avons pu déterminer :

- Les formes à donner au blindage pour lui assurer la meilleure résistance radiale à l'éclatement et aussi pour empêcher les débris de s'échapper axialement
- Le choix de la meilleure matière à utiliser pour un blindage de turbine.

Nous reviendrons tout à l'heure, avec une analyse plus détaillée des résultats de cette série d'essais, sur le problème de la contenance des débris de disques de turbines monoblocs. Il était nécessaire de montrer, pour commencer, pourquoi ce problème était l'objet des préoccupations du constructeur et de citer les moyens mis en œuvre à l'époque pour fournir une solution appropriée.

2.4 Ruptures de pales de fan

Contenir l'éclatement de pales de soufflante sur des moteurs à grand rapport de dilution est un autre problème que TURBOMECA a eu l'occasion de traiter de manière pratique. Sur ce genre de rotors, les risques de rupture de pale sont de deux origines différentes :

- D'une part, la rupture spontanée des pales par suite de fatigue vibratoire à haute fréquence ou par fatigue digocyclique. Dans un tel cas, les cycles de fatigue lente ne sont pas - comme pour les disques et pales de turbines - des cycles thermiques, mais des cycles de contraintes dues à la variation de la vitesse de rotation.
- D'autre part la rupture des pales consécutive à l'impact de corps étrangers lourds et de grandes dimensions, tels que les oiseaux moyens ou les gros oiseaux.

De manière générale on peut penser que les techniques de calcul et d'essai devraient désormais permettre au constructeur de se prémunir contre les ruptures spontanées de pales par fatigue. Par contre - sauf peut-être sur de très gros moteurs - il semble bien qu'aucune structure de pale de fan premier étage

n'est en mesure de résister sans rupture à l'impact de l'oiseau lourd, tel que le prescrivent les règlements de navigabilité. Or, au point de vue de la contenance des débris, quelle que soit l'origine de la rupture de pale, le problème reste le même. Il est même un peu plus compliqué dans le cas des ruptures provoquées par l'impact des corps étrangers, car il faut contenir, en plus de la ou des pales cisailées par l'impact, la masse de l'oiseau lourd, si celui-ci n'a pas été, par chance, réduit en menus fragments ou en bouillie dès son arrivée dans le premier étage tournant. (Figure 6).

De nombreuses expériences instructives sur le blindage de pales de fans ont été acquises par TURBOMECA. Tout particulièrement avec les moteurs du type ASTAFAN, turboréacteurs à double flux à très grand taux de dilution tournant à vitesse constante. La caractéristique du fan avant, entraîné par le générateur de puissance par l'intermédiaire d'un réducteur de vitesse est d'être à pas variable. Les essais d'ingestion de corps étrangers sur cette nouvelle formule de fan ont été conduits avec une grande rigueur pour en démontrer la bonne tenue ; on peut dire sans exagérer que la méthode a parfaitement justifié les espérances, tant selon les critères de résistance aux impacts des corps étrangers que selon ceux de la contenance, des débris.

Des expériences du même ordre ont aussi été recueillies sur plusieurs autres types de turboréacteurs à double flux à double corps de formule classique, tels que l'ADOUR et le LARZAC dont la responsabilité de la partie compresseur incombe à TURBOMECA. En résumé, les méthodes mises au point pour l'évaluation des blindages ont permis de réaliser les enveloppes et carters de ces divers moteurs de manière à maîtriser les débris des ruptures de pales de fan.

2.5 Ruptures de pales rapportées de turbines libres

Dans certaines constructions de turbines à pales rapportées, la sécurité du disque en cas de survitesse incontrôlée, repose sur le fait que les pales s'arrachent alors de leur logement sans entraîner un éclatement du disque. ("... to be shed at overspeed"). Dans les moteurs produits par TURBOMECA, cette technique trouve son application pour les roues de turbines libres (ou de puissance) des turbomoteurs d'hélicoptères à double corps.

Dans ce type de moteur, le niveau de survitesse de la turbine libre, dans le cas éventuel de coupure instantanée de l'arbre de sortie est limité par l'intervention du circuit de régulation du moteur, parfois doublé encore par un dispositif de protection de survitesse, à une valeur qui n'entraîne aucun danger pour l'intégrité du rotor.

Toutefois, les règlements de navigabilité des moteurs et des hélicoptères, les exigences imposées pour la justification de l'intégrité des rotors en survitesse, ainsi que les considérations découlant de l'analyse des pannes des circuits, obligent finalement à tenir compte de "doubles pannes". Dans cette application particulière, on doit envisager l'occurrence simultanée de deux défaillances :

- rupture instantanée de l'arbre de transmission de puissance (en un point quelconque : accouplement flexible, arbre proprement dit, pignon de boîte de transmission, etc).
- non fonctionnement du circuit de régulation (ou du dispositif de protection de survitesse).

Cette hypothèse de défaillance simultanée de deux "circuits", dont on peut discuter la probabilité, conduit à des valeurs de survitesse très élevée pour la roue de turbine. En effet, au moment de l'incident, on peut supposer que le couple moteur de la pleine puissance s'exerce sur la turbine, dont le moment d'inertie de masse, qui s'oppose à l'accélération en rotation, est très faible.

Pour explorer ces conditions de survitesse de roues de turbines libres, des essais avaient été effectués en 1964 déjà sur un moteur du type TURMO III C3 (type de moteur de la classe 1500 ch équipant l'hélicoptère trimoteur SA 321 "SUPER-FRELON"), dont la turbine libre comporte deux étages. L'essai avait été réalisé en coupant réellement l'arbre de sortie de puissance à l'aide d'un outil de tour, dans les conditions de la puissance maximale, après avoir débranché tous les dispositifs de régulation et de limitation de vitesse de la turbine libre. La survitesse enregistrée, supérieure à 170% a conduit à l'arrachement de la majorité des pales du deuxième étage de turbine et à des dégâts considérables dans la section de la turbine libre. Les débris n'ont pas été intégralement contenus, mais il n'y a pas eu projection de fragments à haute énergie. Les disques de turbine sont restés intacts. (Figure 8).

Des essais analogues ont été réalisés plus récemment sur le moteur TURMO IV C, du modèle équipant l'hélicoptère bimoteur SA 330 "PUMA", où la turbine motrice est à un seul étage. Bien que la vitesse de la turbine libre ait été poussée, dans ce cas à 164,5% de la vitesse nominale, dans les conditions de température de turbine correspondante au fonctionnement normal, durant 5 mn, aucune rupture de disque, ni de pale, ne s'est produite. En conséquence, l'essai n'a pas apporté de démonstration sur le point particulier de la contenance des débris éventuels.

Toutefois il a prouvé de manière suffisamment évidente pour être acceptée par les Autorités de Navigabilité, qu'une désintégration de la roue de turbine libre par suite de survitesse était d'une probabilité extrêmement lointaine, même dans le cas d'une double défaillance des circuits. Une expérimentation jusqu'à rupture n'a donc pas été jugée nécessaire.

Enfin, sur un moteur d'hélicoptère à turbine libre de conception récente, l'ARRIEL, des essais justifiant la contenance des pales en cas d'arrachement par survitesse ont été effectués.

Ces essais ont démontré que les pales étaient effectivement "larguées" à une survitesse de 156% de la vitesse maximale de service, conformément aux calculs. Ils ont prouvé aussi que l'anneau de blindage, conçu pour retenir les pales dans ce cas, était réellement en mesure de le faire. (Figure 9)

3. ANALYSE DES ESSAIS DE RUPTURE DE DISQUES DE TURBINES MONOBLOCS

3.1 Modèle de rupture

La technologie usuelle des moteurs TURBOMECA "classiques" comporte un assemblage des divers étages de disques de turbine par denture "curvic coupling", l'ensemble étant serré par 4 boulons ou tirants axiaux. Cette construction conduit en cas de rupture de disque, à deux fragments principaux faisant à peu près 1/3 et 2/3 du disque, comme indiqué ci-dessus (au § 2.3).

Sans entrer dans le détail, on peut décrire le processus conduisant à la destruction d'un disque de la manière suivante :

Les contraintes thermiques et centrifuges finissent par provoquer des criques dans la jante du disque, entre les pales et à proximité de celles-ci. La répétition des cycles de contraintes cause une propagation des criques, dont la rapidité dépend de très nombreux facteurs dont nous citons quelques-uns :

- (1) - dessin du disque, de sa jante, des pales
- (2) - caractéristiques de la matière, (résistance à la fatigue en fonction des contraintes alternées et de la température, vitesse de propagation des entailles)
- (3) - sévérité du cycle en température : contraintes centrifuges et contraintes thermiques.
- (4) - répartition des températures des gaz à la sortie de la chambre de combustion. Jusqu'à une époque récente encore, certains de ces facteurs - en particulier la caractérisation de la matière au point de vue de la propagation des criques - étaient loin d'être parfaitement connus.

Des essais d'endurance en cycles thermiques et dynamiques avaient pour but de déterminer le nombre de cycles jusqu'à l'apparition des premières criques et de surveiller ensuite la vitesse de propagation de celles-ci. Il était ainsi possible d'établir une vie sûre prévue en cycles au-dessous de laquelle une désintégration du disque était de probabilité extrêmement lointaine. La vie cyclique de service autorisée était ensuite fixée à une valeur, bien inférieure à celle de la vie sûre prévue (divisée par un facteur de 2 à 4).

De plus, pour la sécurité, des disques présentant déjà des criques d'une longueur considérable avaient été soumis à des essais d'intégrité en survitesse conformes à l'épreuve des règlements de navigabilité.

C'est ainsi que des disques monobloc de turbines du turbopropulseur BASTAN sur lesquels la plus grande crique mesurait une longueur totale de 34 mm de pénétration ont subi sans rupture l'épreuve de survitesse à 115% de la vitesse maximale de service pendant 5 mn, à une température d'entrée des gaz au moins égale à celle du régime de décollage.

La même vérification avait été faite aussi sur des disques de moteurs du type ASTAZOU, de plus petite dimensions, présentant une crique maximale de 18 mm de longueur.

Tous les essais auxquels nous nous référons étaient effectués, il faut le noter, avec des machines complètes, au banc d'essai "FROUDE", dans des conditions réelles de vitesse, de température et de puissance.

Pour effectuer les essais de blindage, lors de la campagne systématique d'expérimentation décrite au § 2.3, ci-dessus, il a été procédé comme suit.

- A - Afin d'obtenir une possibilité de rupture, le disque de turbine était préalablement entaillé selon le croquis de la Figure 4. Les trois entailles, d'environ 1,2 mm de largeur (deux entailles radiales à 114° l'une de l'autre, la troisième entre deux trous de vis d'assemblage) étaient pratiquées par électro-érosion.
- B - Le disque était alors remonté dans la machine, et cette dernière était installée au banc, FROUDE, avec une protection extérieure adéquate de sécurité (épaisseur de sable entre deux tôles).
- C - Le moteur était alors soumis à des cycles de variation de puissance, entre la charge maximale (puissance de décollage) et le ralenti vol (charge nulle). La durée du cycle était de l'ordre de 3 mn. Le type de moteur en question est équipé d'un circuit de régulation à vitesse constante, l'essai se faisait donc, soit à la vitesse nominale maximale, soit à 103 ou 104% de celle-ci.
- D - Par suite de la propagation des criques dans le disque, à partir des entailles l'éclatement était obtenu assez rapidement (entre 1 cycle et quelques dizaines de cycles).

3.2 Matières pour le blindage

Cette campagne d'essais a mis en évidence que les matériaux possédant un grand allongement à la rupture se comportaient infiniment mieux que ceux possédant une haute résistance. (Voir Tableau ci-dessous)

Matériau	Résistance à la rupture R, en MPa	Limite élastique E, en MPa	Allongement à rupture A, en pour cents	Comportement
Maraging	1800	1600	10	Mauvais
Fluginox vieilli	1000	640	26	Médiocre
HS 25	1000	400	60	Bon
Fluginox	600	260	50	Bon
Z10CNT 18	600	300	50	Bon

Pour le classement des matériaux on aurait pu penser à utiliser les critères $E \times A$, ou $R \times A$ mais le meilleur critère de sélection est donné par le travail absorbé par traction sous choc d'une éprouvette cylindrique au mouton CHARPY.

(Figure 10)

Les matériaux que nous avons étudiés à ce point de vue sont donnés dans le tableau suivant.

Matière	Travail de traction au choc à froid
<u>Métaux légers</u>	
A S 7 G	-
A G 6	3
A S 6 M	8
A Z 5 G	15
A G 5	22,5
<u>Titane</u>	
TA 6 V	34
<u>Aciers</u>	
Maraging	45
Z12CNDV12	53
15CDV6	53
30NCD16	55
FLuginox	75
N.75	84
X 20 T2	90
Z 10 CNT 18	95
Ni 263	103
HS 25	160

Finalement, en raison de son prix de revient modéré et de sa bonne capacité, l'alliage Z10CNT18 semble le mieux adapté à un blindage dans la section des turbines. La qualité de ces divers matériaux de blindage sont rapportées soit au Z10CNT18, soit à l'AG5, avec lesquels les essais de base de contenance de débris ont réellement été effectués.

Il est d'ailleurs probables que des matériaux nouveaux, spécialement adaptés à ce genre de travail et encore supérieurs à l'HS25, pourront être mis au point.

3.3 Forme de blindage

Les essais ont démontré qu'il était important d'équilibrer axialement la matière de l'anneau de blindage, pour éviter que les fragments s'échappent vers l'avant ou vers l'arrière. Une fixation axiale robuste du blindage s'est avérée indispensable.

Il est aussi recommandé de disposer le blindage le plus près possible, radialement, du disque à retenir.

Les essais ont montré qu'entre l'énergie cinétique totale du fragment d'un tiers de disque et l'énergie d'allongement à rupture de la partie d'un anneau de blindage en contact avec le bord extérieur du fragment, il existe un rapport pratiquement constant, ce qui correspond au rendement de transformation de l'énergie cinétique. (Figure 11)

A titre d'exemple, un fragment de disque d'une énergie totale de 32 000 joules est parfaitement contenu par un anneau en Z10 CNT 18 d'une section radiale de 9 mm et de 28 mm de longueur axiale. (Énergie du disque entier : 100 000 joules)

Pour les types de moteurs (ASTAZOU XII, XIV, XVI) ayant servi de support à la campagne d'essais d'éclatements de turbines, le blindage adopté a reçu la forme représentée par les figures 12 et 13 extraites du manuel d'entretien. On voit que la surface intérieure du blindage a été rainurée. Ceci permet en quelque sorte un guidage des débris à l'intérieur de l'anneau, tout en augmentant à masse égale, la rigidité en flexion du blindage. On a ainsi obtenu que les fragments ne s'échappent pas dans le sens axial. D'autre part, l'ovalisation locale de l'anneau, à l'endroit de l'impact est un peu atténuée par la plus grande rigidité. On évite ainsi qu'en appuyant sur le carter de turbine, le blindage, forcément déformé par le choc vienne à percer cette enveloppe extérieure. (Fig.14).

On trouvera au § 6.2, ci-après une indication sur la masse de ce dispositif.

4. BLINDAGES POUR DES AUBES DE FAN

4.1 Nature du problème

Le problème de la construction d'un blindage capable de contenir les pales de compresseurs axiaux est rendu plus complexe par l'effet de poinçonnement, qui n'est pas facile à traiter de manière rigoureuse.

On se trouve en quelque sorte dans les mêmes conditions que les spécialistes des armes de poing, qui ont été conduits à définir un certain nombre de notions empiriques pour évaluer les effets des impacts des projectiles de revolvers et de pistolets. Ces notions sont rappelées ici parce qu'elles sont de nature à illustrer les effets de pales rompues sur les parties du moteur qui les entourent.

Les professionnels des armes (et même les lecteurs occasionnels de romans policiers) savent qu'un projectile de petit calibre lancé à grande vitesse peut parfaitement traverser un adversaire de part en part. Même si la blessure cause une lésion qui sera - à terme - mortelle, un tel impact peut laisser à l'ennemi le temps de poursuivre son attaque. Alors qu'une simple boule de pétanque ou un gros caillou, un galet, lancé à la main - c'est à dire avec une vitesse initiale faible - brisera net l'élan d'un agresseur même s'il n'est pas touché dans une partie vitale.

Pour caractériser ces effets, la balistique des petites armes fait donc usage des notions spécifiques suivantes, à partir des données fondamentales de calibre (d), de masse (M) et de vitesse initiale (V) du projectile :

- $E = \text{Energie cinétique du projectile} = \frac{1}{2} M.V^2$
(notion absolument classique)
- $StP = \text{Puissance d'arrêt ("Stopping Power")}$,
c'est l'énergie cinétique multipliée par la surface frontale du projectile :

$$StP = \frac{1}{2} M.V^2 \cdot \frac{\pi}{4} d^2$$

(La "puissance d'arrêt" est la caractéristique recherchée par les armes de gros calibre de la Police, par exemple, un "44 Magnum" a un StP de 10 à 20 fois supérieur à celui d'un "22 long rifle", dont, la vitesse initiale est cependant du même ordre.

- $Perf = \text{Perforation}$

C'est la quantité de mouvement du projectile divisée par sa surface frontale et affectée d'un "coefficient de pénétration (K) :

$$Perf = K \cdot \frac{M.V}{\pi d^2}$$

On peut constater que si l'effet de choc reste immuable, quelle que soit la nature de la cible, le coefficient de pénétration "K", sera extrêmement variable selon :

- la nature du projectile (matière : plomb, bronze, acier, plomb chemisé d'acier ou de laiton, etc) ;
- la forme du projectile (sphérique, cylindro-conique, creux, etc) ;
- la nature du milieu rencontré (brique, ciment, métal, planches, sacs de sable, chair, os, etc)

Lors de l'étude d'un blindage destiné à contenir les fragments de pales, on se trouve confronté à des problèmes de même diversité que l'évaluation de la perforation par un projectile d'arme légère.

L'effet de poinçonnement dans un blindage va, lui aussi dépendre de la quantité de mouvement des débris et de leur "calibre" c'est à dire de la manière dont ils attaquent le blindage : l'effet sera fort différent si l'extrémité de la pale se présente perpendiculaire au blindage, ou si la pale se couche et frappe sur une plus grande surface. Le "coefficient de pénétration, lui aussi, sera différent selon la matière des pales (alliage léger, matériel composite, titane ou acier). Bien entendu la matière du blindage et sa disposition sont aussi des facteurs déterminants pour savoir, si oui ou non, le blindage sera traversé par coup de poinçon. Pour l'effet d'impact d'objets lourds et diffus (par exemple des oiseaux moyens et gros ou un amas de débris provenant d'une série de pales - fixes ou mobiles - cisailées) l'analogie avec la notion de "puissance d'arrêt" peut également être utile.

4.2 Quelques expériences pratiques.

Nous l'avons dit plus haut (§ 2.4), il ne semble pas possible qu'une structure de pale de fan premier étage, sur un moteur de dimensions moyennes, soit capable de résister à l'impact de plein fouet d'un gros oiseau, sans être cisailée. Dans le cas du turboréacteur LARZAC (de la classe des 1400 kg de poussée) le calcul suivant avait été fait :

Masse de l'oiseau : 1,800 kg Vitesse d'impact : 210 m/s
calibre de l'oiseau: 127 mm (diamètre du canon à poulets)

La "puissance d'arrêt" de ce projectile, calculée selon les méthodes balistiques, se trouve être 2500 fois celle du "44 Magnum", la plus puissante arme de poing connue - Il n'est donc pas étonnant qu'un impact de ce genre conduise à des dégâts considérables.

Dans le cas du LARZAC, le tir d'oiseau lourd effectué au Centre d'Essai des Propulseurs à Saclay, dans les conditions ci-dessus, a, en effet cisailé net les 4 pales du fan qui ont directement reçu l'impact axial de l'oiseau. Trois autres pales se sont cassées immédiatement après, pour mettre la masse de l'oiseau en rotation. Il convient de noter que l'ensemble des débris (oiseau + pales cassées) est resté contenu radialement.

Le plus grand nombre d'essais de blindage de pales de fan a été effectué sur des moteurs du type ASTAFAN, comme mentionné déjà (§ 2.4). Comme ces pales sont montées à pas variable dans le moyeu de ce type de moteur, il était indispensable d'apporter la démonstration que cette construction n'est pas plus vulnérable qu'une construction avec des pales fixes. Les essais ont porté sur des pales en alliage léger et sur des pales en titane avec des diamètres de fan de 500 à 800 mm et des vitesses de 12000 à 7000 tr/mn. Les résultats ont constamment vérifié les évaluations et démontré que les débris étaient correctement contenus par le blindage.

Comme matière pour ces blindages le choix s'est porté sur l'alliage léger AG5 pour lequel le produit R.A est de 400 cmKg ou 40 joules au cm.

Finalement on peut mettre en évidence un rapport à peu près constant entre l'énergie libérée par une aube et l'énergie à rupture d'un élément d'anneau de longueur égale à la corde tangentielle de l'aube à retenir, sur une largeur égale à la longueur axiale du profil de tête. Par exemple une pale en titane animée d'une énergie de 6460 joules est retenue par un anneau de blindage en AG5 de 70 mm de longueur axiale et de 8 mm d'épaisseur, avec une sécurité de l'ordre de 2. (Par suite de la possibilité d'un pas nul il

faut prévoir le containment sur une faible largeur).

5. BLINDAGE POUR PALES RAPPORTEES DE TURBINES

5.1 Principe -

Le problème de la contenance des pales de turbines rapportées peut se résoudre selon les mêmes principes que ceux utilisés pour les disques monobloc, mais en se contentant d'épaisseurs d'anneaux plus réduites. Pour l'évaluation des dimensions, la même méthode que celle décrite pour contenir les pales de fan est applicable.

5.2 Observations

Nous avons insisté au § 2.5 plus spécialement sur le cas du blindage pour les pales conçues pour être arrachées du disque en cas de survitesse. C'est en effet le cas où l'énergie cinétique des pales est la plus élevée (2 à 2,5 fois l'énergie correspondant à la vitesse normale de service). Dans le cas des types de moteur à simple corps, c'est à dire où la turbine est directement liée à l'arbre portant les compresseurs, les cas de survitesse importante sont d'une probabilité encore beaucoup plus lointaine. Cela provient à la fois du type de construction et du type de circuit de régulation utilisé sur ces moteurs. Un blindage efficace peut donc être construit avec une masse moindre.

Le nombre des pales que l'on considère comme capables de s'arracher du disque (une pale isolée, deux pales avec un morceau du disque interpale, trois pales avec deux interpales ?) a souvent été l'objet de discussions.

La rupture d'une première pale, selon l'expérience, peut toujours conduire à une salade généralisée de plusieurs aubes de la rangée. Il faudra bien que le blindage soit capable de contenir l'ensemble de ces dégâts.

Comme la méthode d'évaluation utilisée s'applique quel que soit le nombre de pales rompues, la discussion sur le nombre de ruptures nous paraît revêtir un caractère académique, sous l'aspect du blindage.

Par contre, le balourd résultant sur le mobile n'est certes pas le même si une seule pale, ou si tout un secteur de pales se détachent du disque. Le problème est alors que les paliers et la structure des carters du moteur soient en mesure de résister aux efforts violents causés par le balourd. Comme dans tout problème de construction, il faut considérer l'ensemble. Il serait naïf d'avoir disposé un blindage capable de retenir tous les débris, peu gênant, léger et pourvu de toutes les qualités, si l'incident d'une rupture de pale devait conduire à une désintégration du moteur par ailleurs.

6. BLINDAGE PARTIEL OU INTEGRAL

6.1 Protection contre l'éclatement des rotors de divers types.

Dans ce qui précède nous avons exposé des problèmes relatifs au blindage capables de retenir, soit des éclatements complets de disques de turbine, soit des arrachements de pales de fan, soit des arrachements de pales rapportées de turbine. C'est en effet dans ces trois domaines que nous avons eu l'occasion d'acquiescer le plus grand nombre de données expérimentales, et effectué la majeure partie de nos essais systématiques.

Les principes d'évaluation de la capacité des blindages à contenir ces divers types de défaillance, que nous avons pu déduire de ces expériences, s'appliquent à tous les types de rotors. Nous les avons aussi vérifiés expérimentalement sur le blindage de rotors de compresseurs axiaux et de rouets centrifuges, ce qui a confirmé la validité des méthodes d'évaluation. Comme ces séries d'essais n'ont pas eu, à notre point de vue, la même importance historique que les quelques campagnes d'expérimentation décrites plus haut, il ne vaut peut-être pas la peine de s'y attarder, dans le cadre de la présente étude.

Toujours est-il que nous estimons désormais être en mesure de construire des moteurs de petites et de moyennes dimensions de manière à leur assurer un blindage intégral contre toute rupture de partie tournante, si cela s'avère souhaitable.

6.2 Bilan de masse

Il y a finalement un bilan à établir entre l'augmentation de masse que l'on veut consentir et la probabilité de défaillance des éléments tournants.

L'établissement d'un tel bilan peut conduire à des solutions différentes, suivant le type d'utilisation auquel se destine un moteur. Pour un turbomoteur d'hélicoptère, par exemple, pour lequel la légèreté est un facteur essentiel, il pourra être décidé de concevoir le blindage seulement de façon à contenir les pales arrachées, mais pas les ruptures complètes de disques, ces dernières étant considérées comme d'une probabilité extrêmement lointaine. Par ailleurs, les entrées d'air des hélicoptères sont généralement protégées par des grilles contre l'ingestion de corps étrangers lourds, ce qui diminue la probabilité de destruction des premiers étages de compresseurs par impacts extérieurs.

Pour fixer les idées nous donnons ci-après quelques indications de masse pour divers blindages sur différentes catégories de moteurs TURBOMECA :

- A - Pour un turbopropulseur ASTAZOU XIV ou XVI, (respectivement 850, 1020ch) le blindage intégral des turbines (Figures 12 et 13, § 3.3) conduit à une augmentation de masse de 8,5 Kg, soit moins de 4,3% de la masse du moteur équipé.
Pour les versions ultérieures de ces types de moteurs, où les turbines sont exécutées non plus en roues monobloc, mais avec des pales rapportées, le blindage conçu pour retenir seulement les pales pèse 3,5 Kg, soit moins de 1,8% de la masse du moteur.
- B - Le turbomoteur d'hélicoptère MAKILA (1800 ch) pèse, entièrement équipé, 238 Kg. Cette masse comprend déjà le blindage capable de retenir les pales de turbine. Si le moteur devait être équipé de blindages capables de retenir intégralement la rupture des disques et des pales (compresseurs axiaux, roue d'entrée et rouet centrifuges, turbines du générateur et turbine libre), l'augmenta-

tion de masse serait de 7,3 Kg, soit environ 3,1 % de la masse actuelle.

6. CONCLUSIONS

De ce qui précède, on peut voir que le problème de réaliser un blindage capable de retenir intégralement dans le moteur les débris de ruptures de disques et, à plus forte raison, de pales peut trouver une solution satisfaisante, au prix d'une pénalité de masse raisonnable.

Cette constatation est valable pour des moteurs à turbines de dimensions réduites et moyennes. C'est, en effet, sur cette catégorie de moteurs que l'expérience, qui est à la base de notre exposé, a été acquise et que des essais systématiques d'efficacité de blindages ont pu être effectués.

Les principes qui peuvent guider l'évaluation de la capacité d'un blindage à résister à la désintégration des disques ou des pales ont été sommairement indiqués. Nous n'avons intentionnellement pas donné de "recette de cuisine" trop précise, conscients de la diversité des cas qui peuvent se présenter et de l'impossibilité qui existe à tenir compte de tous les facteurs.

Si cet exposé a réussi à démystifier un sujet longtemps considéré comme confidentiel et à fournir aux constructeurs quelques données exploitables, le but que nous nous étions fixé sera atteint.



FIGURE 1 TURBOMOTEUR ARTOUSTE II, RUPTURE D'UN ROUET DE COMPRESSEUR
CENTRIFUGE EN ALLIAGE LEGER (1957)

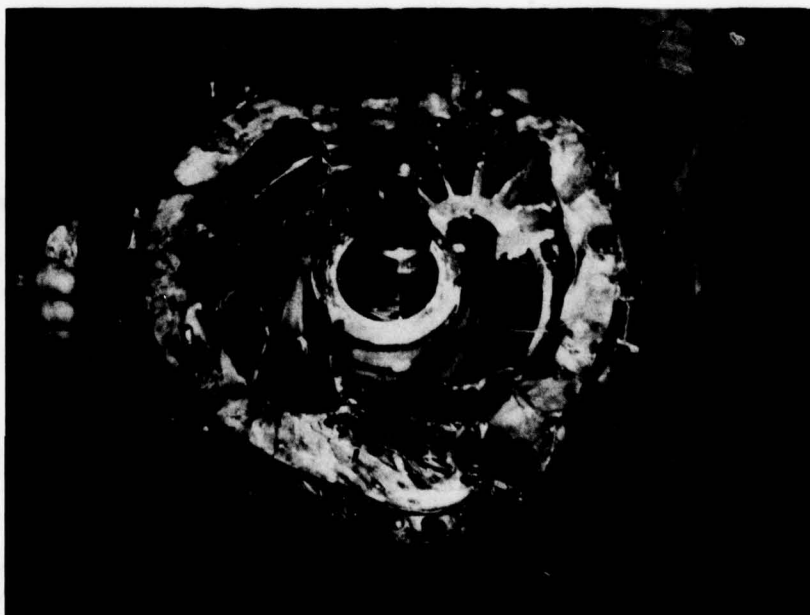


FIGURE 2 MEME INCIDENT : LES DEGATS SONT ENTIEREMENT CONTENUS DANS
LE MOTEUR



FIGURE 3 ECLATEMENT D'UN DISQUE DE TURBINE ASTAZOU (1969)
DEGATS NON CONTENUS DANS LE MOTEUR

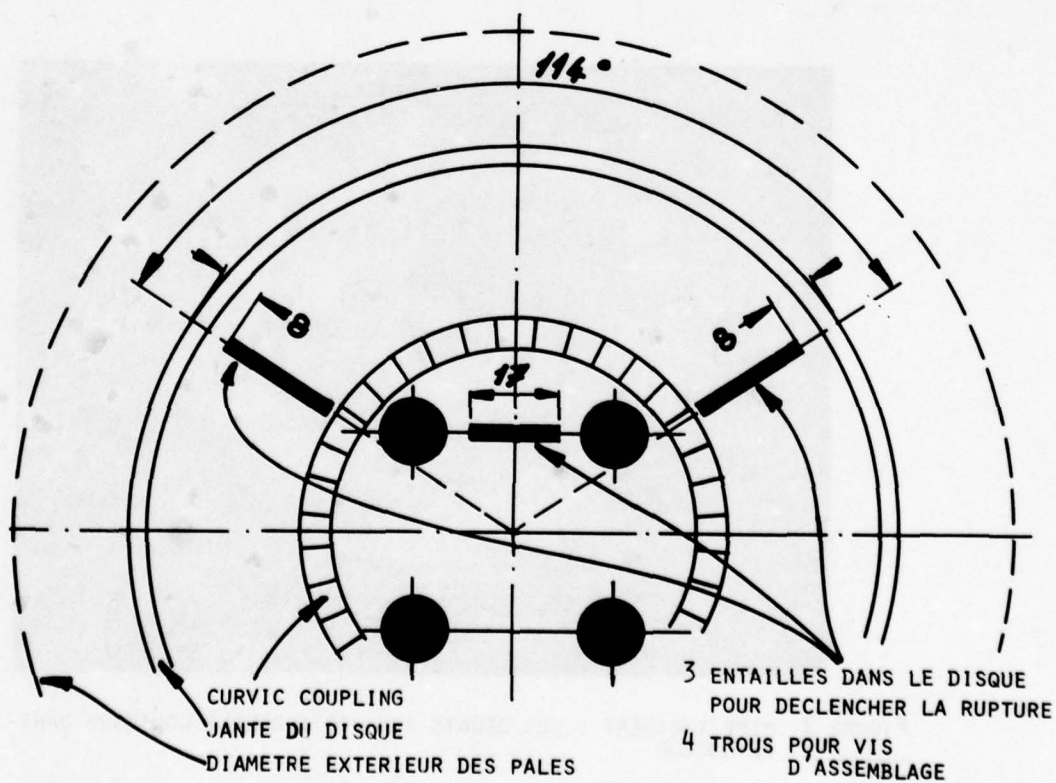


FIGURE 4 : MODELE DE DISQUE DE TURBINE
PREPARE POUR ESSAIS DE RUPTURE

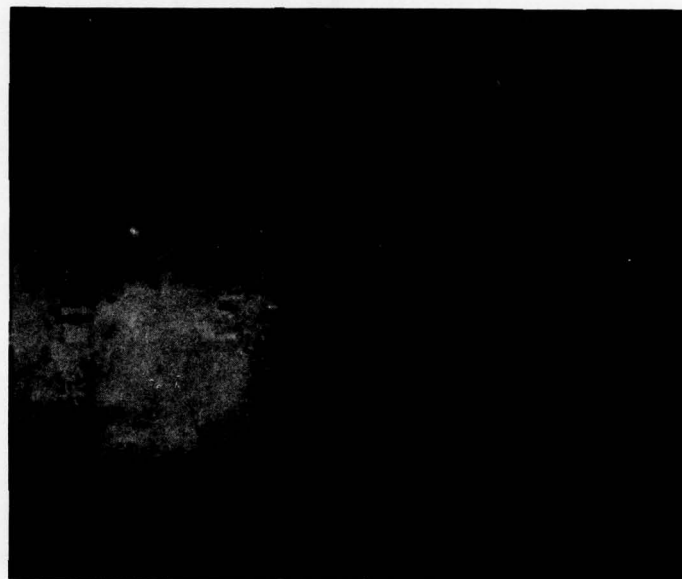


FIGURE 5 CARTER DE TURBINE APRÈS ESSAI D'ECLATEMENT DE DISQUE DE TURBINE AVEC BLINDAGE, L'ENVELOPPE EST BOSSELEE PAR ENDROITS, MAIS AUCUN DEBRIS NE L'A PERCEE. (DEGATS CONTENUS).

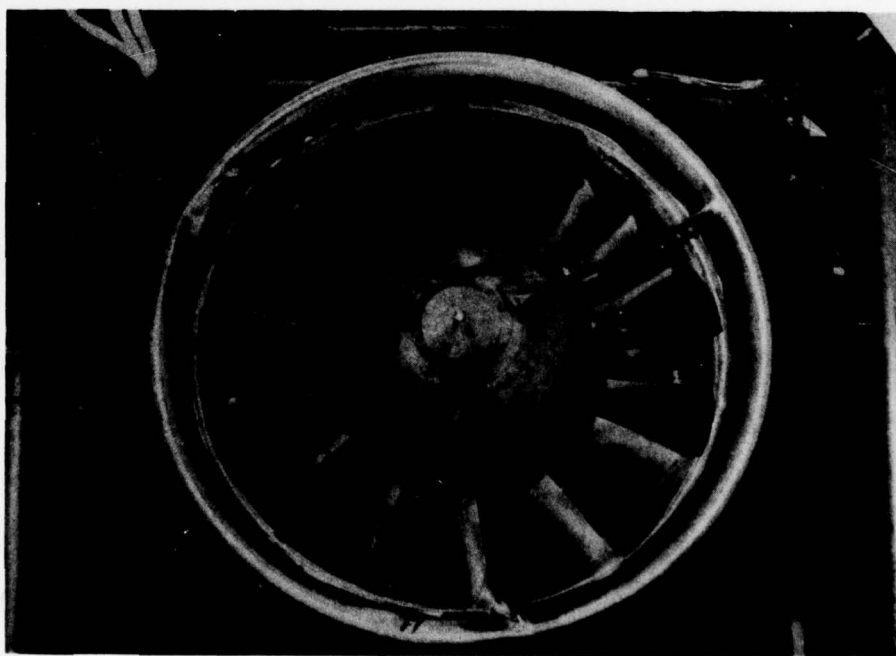


FIGURE 6 ASTAFAN IV, TURBOREACTEUR A DOUBLE FLUX.
RUPTURE DE LA PALE DE FAN N° 11 PAR ESSAI IMPACT D'OISEAU LOURD
(1,8 KG, 100 M/S)

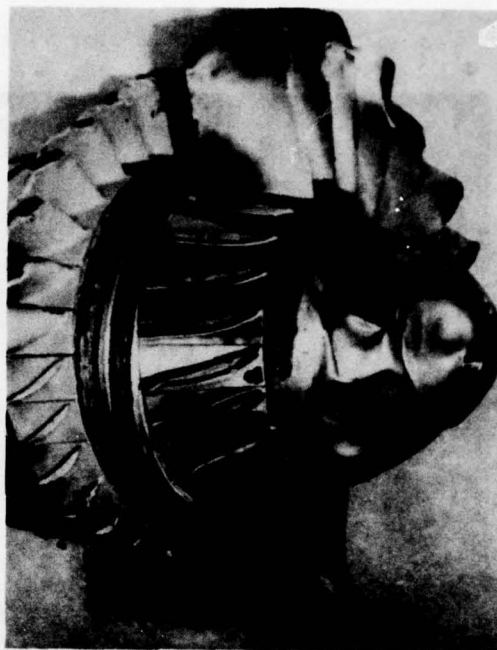


FIGURE 7 TURBOREACTEUR LARZAC, ESSAI D'INGESTION D'OISEAU LOURD (1,8 KG, 210 M/S). RUPTURE DE 7 PALES DU FAN 1ER ÉTAGE.



FIGURE 8 TURBOMOTEUR TURMO III C3 (1964), ESSAI DE SURVITESSE DE TURBINE LIBRE PAR COUPURE D'ARBRE DE SORTIE SANS PROTECTION. ARRACHEMENT DE PALES DE TURBINE 2E ÉTAGE À N = 170%.

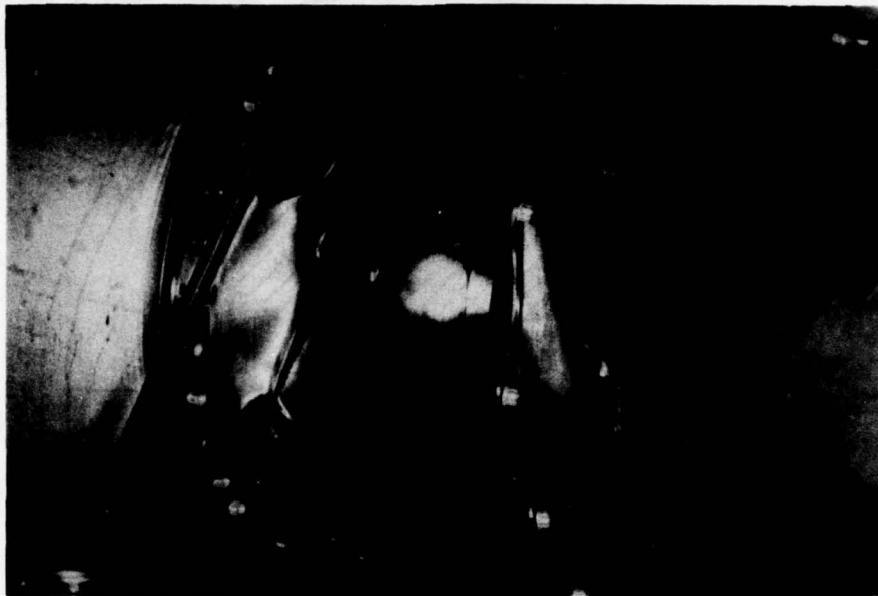


FIGURE 9 TURBOMOTEUR ARIEL (1978). ESSAI DE SURVITESSE DE TURBINE LIBRE AVEC ARRACHEMENT DES PALES A $N = 156\%$, CONTENUES PAR ANNEAU DE BLINDAGE,

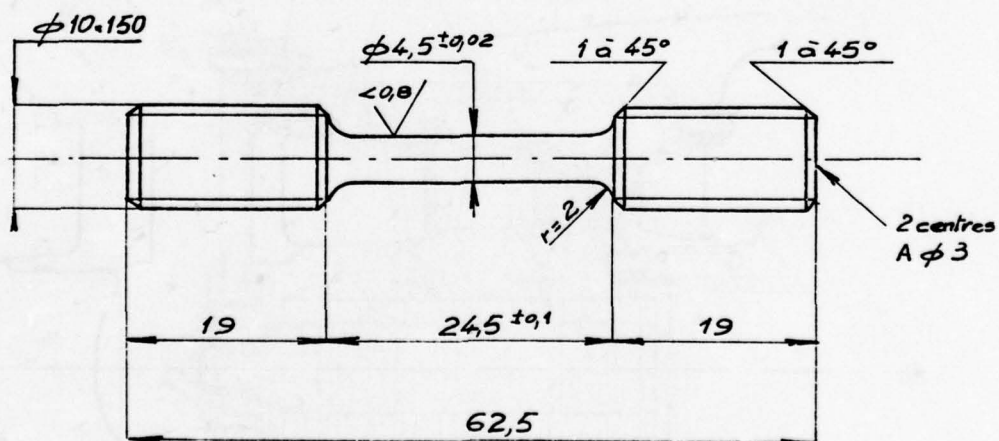


FIGURE 10 EPROUVETTE D'ESSAI DE TRACTION AU CHOC AU MOUTON CHARPY.

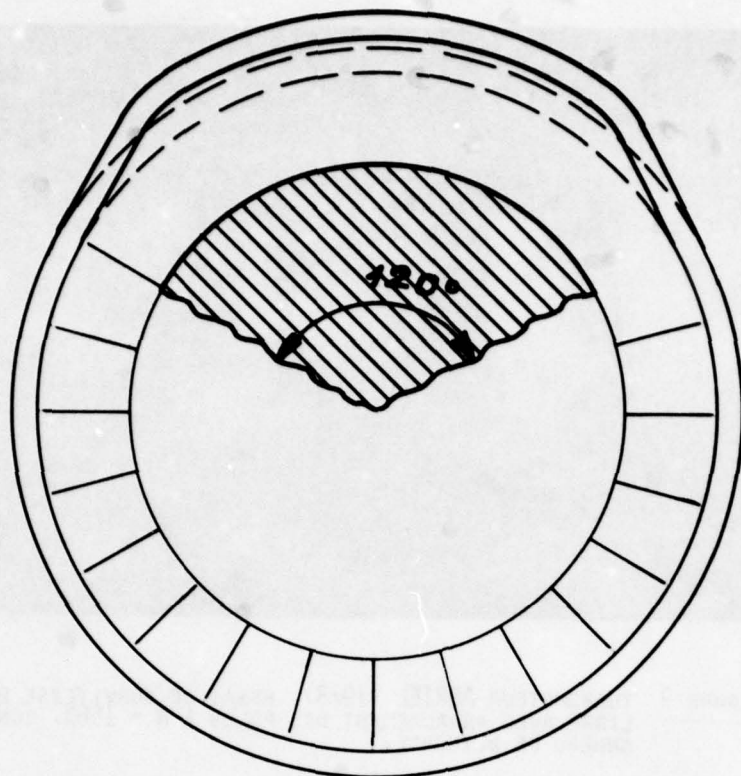


FIGURE 11 : ALLONGEMENT DE LA PARTIE D'UN ANNEAU DE BLINDAGE
APRES CONTACT AVEC UN FRAGMENT DE $\frac{1}{3}$ DE DISQUE

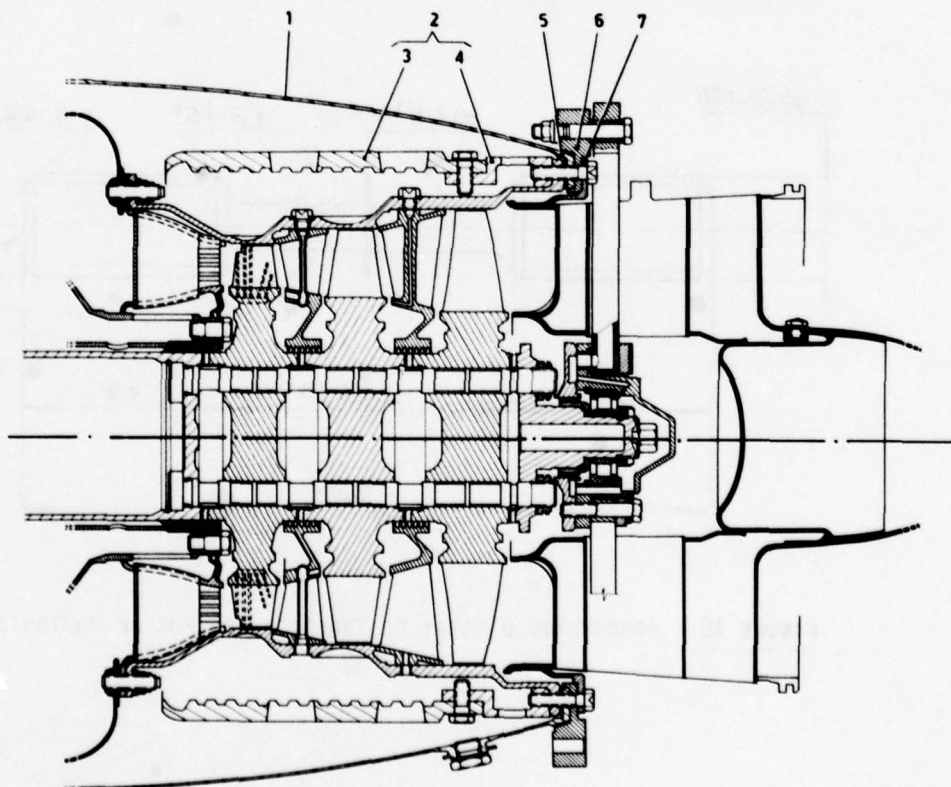


FIGURE 12 DISPOSITION DU BLINDAGE INTEGRAL DE TURBINES MONOBLOC
SUR ASTAZOU XVI.

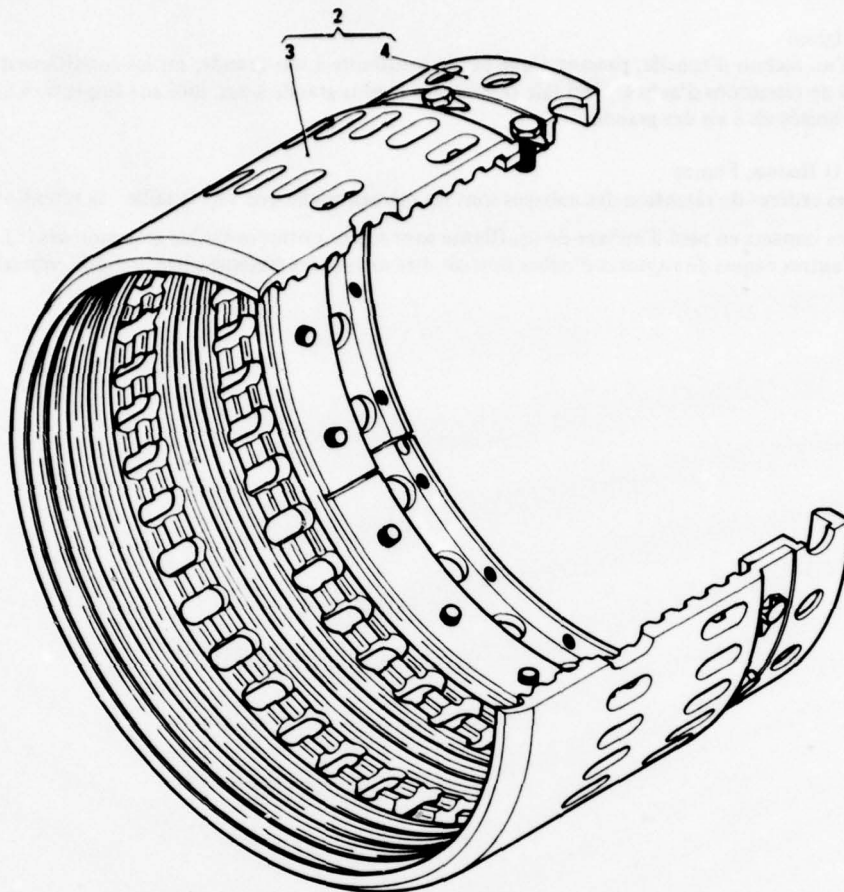


FIGURE 13 ANNEAU DE BLINDAGE INTEGRAL POUR TURBINES MONOBLOC ASTAZOU XVI

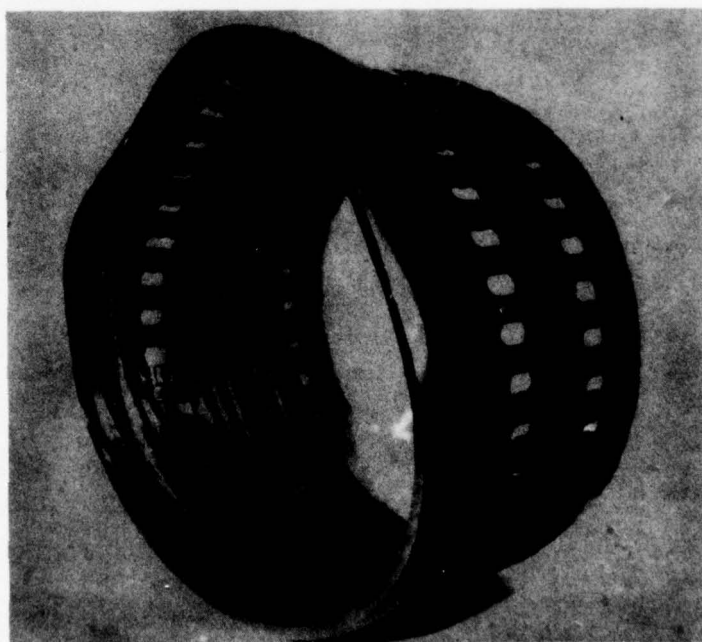


FIGURE 14 ANNEAU DE BLINDAGE APRES ESSAI D'ECLATEMENT DE TURBINE.
DEBRIS CONTENUS.

DISCUSSION

J.Colpin, Belgium

Effet d'un facteur d'échelle, passant d'une petite soufflante à une grande, sur les conditions d'application et les critères de rétentions d'aubes. Ceci fait référence à la plus grande sensibilité aux impacts extérieurs (ruptures) des petites unités vis à vis des grandes.

Reponse de D.Hedon, France

- (1) Les critères de rétention des aubages sont les mêmes quelle que soit la taille: la rétention *doit* être assurée.
- (2) Les impacts en pied d'aubage de soufflante sont moins critiques sur les gros moteurs (section plus forte), mais d'autres causes de ruptures d'aubes doivent être envisagées (fatigue oligocyclique, vibrations).

AN INVESTIGATION OF VIBRATION DAMPERS IN GAS-TURBINE ENGINES

by
R. Holmes
University of Sussex
Brighton BN1 9QT
U.K.

B. Humes
Royal Armament Research and Development Establishment
Sevenoaks, Kent
U.K.

SUMMARY

The function of a vibration damper in a gas-turbine engine is to reduce rotor vibration and transmitted force to the engine frame. In early designs the outer races of the rolling-element bearings supporting the rotor were rigidly built in to the engine frame. In many current designs the outer races are instead cantilevered from the frame on a ring of supports known as a squirrel cage. The resulting flexibility allows outer race movement. This movement takes place within a cylindrical oil container which allows a radial clearance of about 0.010 in, constituting a squeeze film. In some designs the squirrel cage support is dispensed with, and the squeeze film is relied upon to provide sufficient lift to avoid metal-to-metal contact between the outer race of the rolling element bearing and the oil container. The work described in this paper is concerned with both applications.

NOTATION

A	$\pi\eta R(1/c)^3/\sqrt{k_m}$	Q	$P/mc\omega^2$
b	Negative pressure factor in equations (8)	Q_1	$P_1/mc\omega^2$
c	Radial clearance of squeeze film	Q_2	$P_2/mc\omega^2$
C_J	Dynamic journal (or rotor) centre	Q_C	$P_C/mc\omega^2 = u/c$
e	Eccentricity of journal in bearing	R	Journal radius
F	Dynamic force transmitted to engine frame	T	Transmissibility
k	Stiffness of retainer spring per land	t	Time
\bar{k}	$k/m\omega^2$	u	Displacement of rotor centre of mass from geometric centre due to addition of unbalance mass or loss of mass
l	Squeeze-film land length	β	$\eta R l^3/mc\omega$
m	Rotor mass per land	ϵ	Dynamic eccentricity ratio (= e/c)
p	Local film pressure	η	Oil viscosity
P_{st}	$P/2Rl$	θ	Angular measure from line of centres in direction of rotation
P_1, P_2	Squeeze-film forces	ψ	Dynamic attitude angle
$P_{11}, P_{12}, P_{21}, P_{22}$	Component film forces in equations (8)	ω	Frequency of dynamic load
kcc	Restoring force per land due to retainer spring	ω_n	$\sqrt{k/m}$
P_C	Rotating force vector per land	(')	$d/d(\omega t)$

INTRODUCTION

In early designs of gas turbine engine the rolling element bearings which supported the rotor were mounted directly into the engine frame, Fig. 1a. However, the squeeze-film damper has now become a standard application in gas-turbine construction. In one variety of damper an oil film is relied upon to provide damping and is placed in parallel with a retainer spring support system which provides flexibility. This support system is designed to be sufficiently soft as to ensure that the lowest natural frequency of the rotor-bearing system is well below the speed range of the engine. In this way rotor vibration and transmitted forces can be each kept at a low level. The spring support system usually takes the form of a set of bars fixed at one end to the outer race of the rolling-element bearing in which the turbine rotor runs and at the other to the engine frame, Fig. 1b. The purpose of the damping element is to ensure that excessive rotor vibrations and transmitted forces are not encountered during run-up or at off-design speeds. Depending on the oil-supply pressure, which varies from one design to another, the squeeze-film annulus may run full or incomplete. For many applications of this type the support system is preloaded to ensure that at start-up the outer race of the rolling-element bearing is concentric in the squeeze-film annulus. During subsequent running any vibration is assumed to produce a concentric orbit. For such an application the squeeze-film bearing is not called upon to provide a load-carrying capacity and consequently if the oil-supply pressure is of reasonable magnitude, the squeeze-film annulus remains full.

In the second application the retainer-spring support system is dispensed with and the squeeze-film is called upon to provide support as well as damping, Fig. 1c. Rotation of the outer race of the rolling-element bearing is then usually prevented by an anti-rotation pin. When the rotor is at standstill the rolling-element bearing lies at the base of the

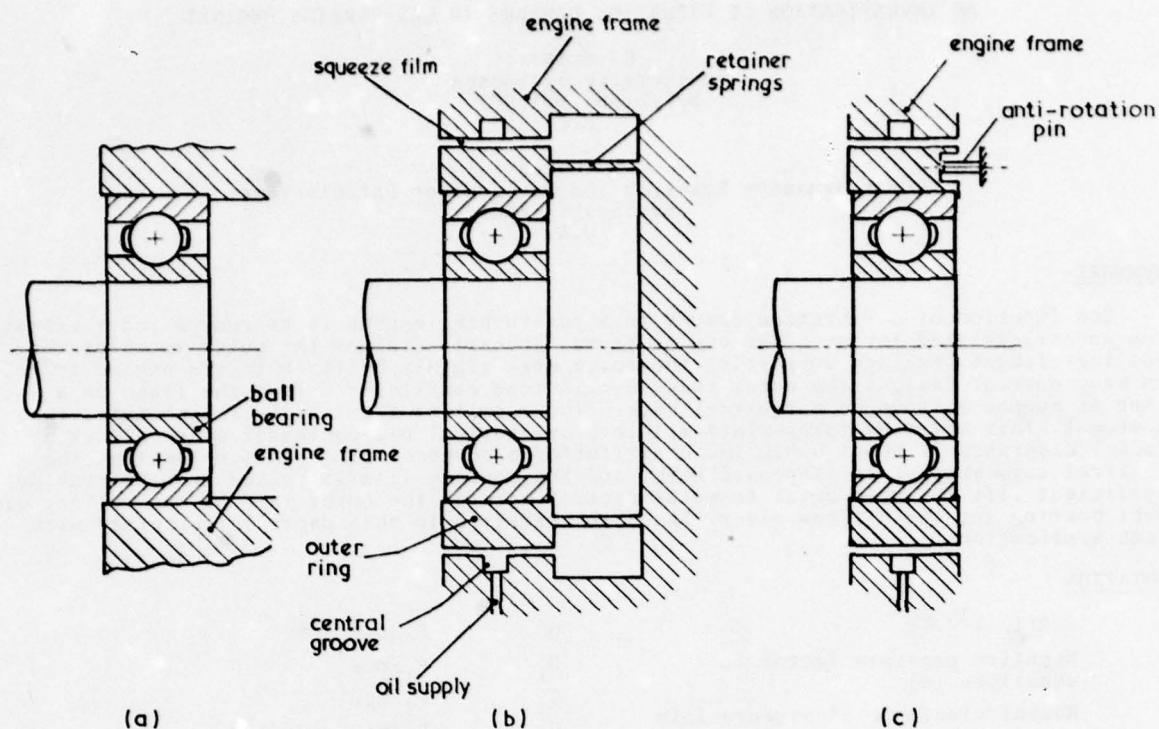


Fig 1. Types of ball-bearing support

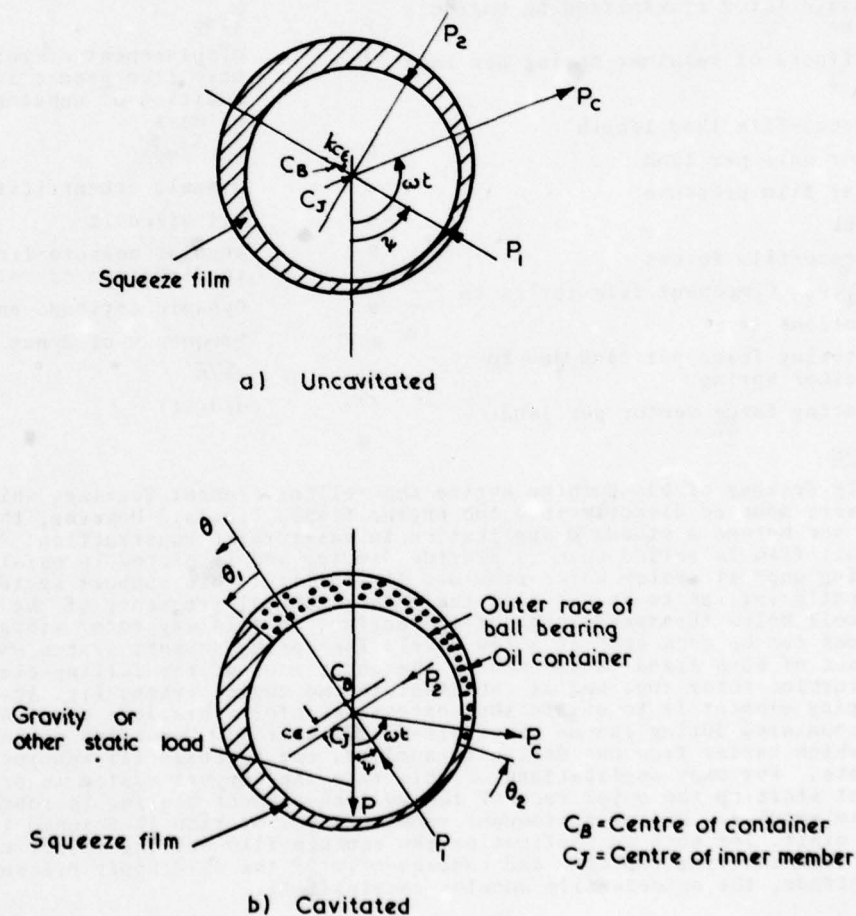


Fig 2. Squeeze-film bearing

oil container and is free to move radially without rotation. It is well known that a squeeze-film alone has no static-load capacity in the absence of a dynamic load. With both loads present lift must therefore depend on the rate of change of eccentricity and/or of attitude angle.

This paper investigates the feasibility and reliability of the squeeze-film both as a damper and as a load-carrying member. In both applications, the squeeze-film is almost invariably supplied from a central circumferential oil groove which effectively separates the bearing axially into two parts or lands. In what follows all governing parameters will be assumed to be appropriate to one land.

THEORETICAL TREATMENT

(i) Use as a damper with retainer spring support

Fig. 2a shows a ball bearing outer race within the oil container (the bearing), under the action of a restoring force $k\epsilon$ due to the stiffness of the squirrel cage retainer spring. Vibration arises from a centrifugal force $P_c = m\omega^2$ due to unbalance. The amplitude of orbital motion depends on $k\epsilon$, P_c , P_1 , and P_2 . The last two forces, P_1 and P_2 , are those arising hydrodynamically from the squeeze-film, which is assumed to be of 360° circumferential extent. Any gravity load is assumed to be neutralised by a preload in the retainer spring. The equations governing the concentric motion of the shaft centre are then

$$\begin{aligned} P_c \cos(\omega t - \psi) - P_1 - k\epsilon &= -m\epsilon\omega^2 \\ \text{and } P_c \sin(\omega t - \psi) - P_2 &= 0 \end{aligned} \quad \dots\dots(1)$$

where ϵ is the dynamic eccentricity ratio resulting from unbalance. In equations (1) the squeeze-film forces P_1 and P_2 have been shown from hydrodynamic considerations [1], to be given, for concentric motion, by

$$\begin{aligned} \text{and } P_1 &= 0 \\ P_2 &= \frac{\pi\eta R l^3}{c^2(1-\epsilon^2)^{3/2}} \cdot \epsilon\omega \end{aligned} \quad \dots\dots(2)$$

Equations (1) may be made non-dimensional by dividing by $m\omega^2$ to give

$$\begin{aligned} Q_c \cos(\omega t - \psi) &= -\epsilon(1 - \bar{k}) \\ \text{and } Q_c \sin(\omega t - \psi) &= \frac{\pi\eta R}{m\omega} \left(\frac{1}{c}\right)^3 \cdot \frac{\epsilon}{(1 - \epsilon^2)^{3/2}}, \end{aligned} \quad \dots\dots(3)$$

where $Q_c = P_c/m\omega^2 = m\omega^2/m\omega^2 = u/c$

and $\bar{k} = k/m\omega^2 = (\omega_n/\omega)^2$

Putting $\beta = \frac{\pi\eta R(1/c)^3}{m\omega}$, equations (3) may be rewritten to give

$$\begin{aligned} \frac{u}{c} \cos(\omega t - \psi) &= (\bar{k} - 1)\epsilon \\ \text{and } \frac{u}{c} \sin(\omega t - \psi) &= \pi\beta\epsilon/(1 - \epsilon^2)^{3/2}, \end{aligned}$$

whence, after some manipulation,

$$\left(\frac{u}{c}\right)^2 \cdot \frac{(1 - \epsilon^2)^3}{\epsilon^2} \cdot \left(\frac{\omega}{\omega_n}\right)^4 = A^2 \left(\frac{\omega}{\omega_n}\right)^2 + \left[1 - \left(\frac{\omega}{\omega_n}\right)^2\right]^2 (1 - \epsilon^2)^3, \quad \dots\dots(4)$$

where

$$A = \frac{\pi\eta R}{\sqrt{km}} \left(\frac{1}{c}\right)^3$$

and

$$\omega_n = \sqrt{k/m}.$$

Assuming a fairly typical value of $A = 0.2$, say, a family of response curves of $\frac{\epsilon}{(u/c)}$ versus ω/ω_n may be constructed for different values of u/c (Fig. 3a). From these curves an indication can be obtained as to the amount of vibration ϵ , suffered by the gas turbine rotor in the symmetric mode.

Of equal importance is the dynamic force F transmitted to the engine frame. This force is given by

$$F = [P_2^2 + (k\epsilon)^2]^{1/2} \quad \dots\dots(5)$$

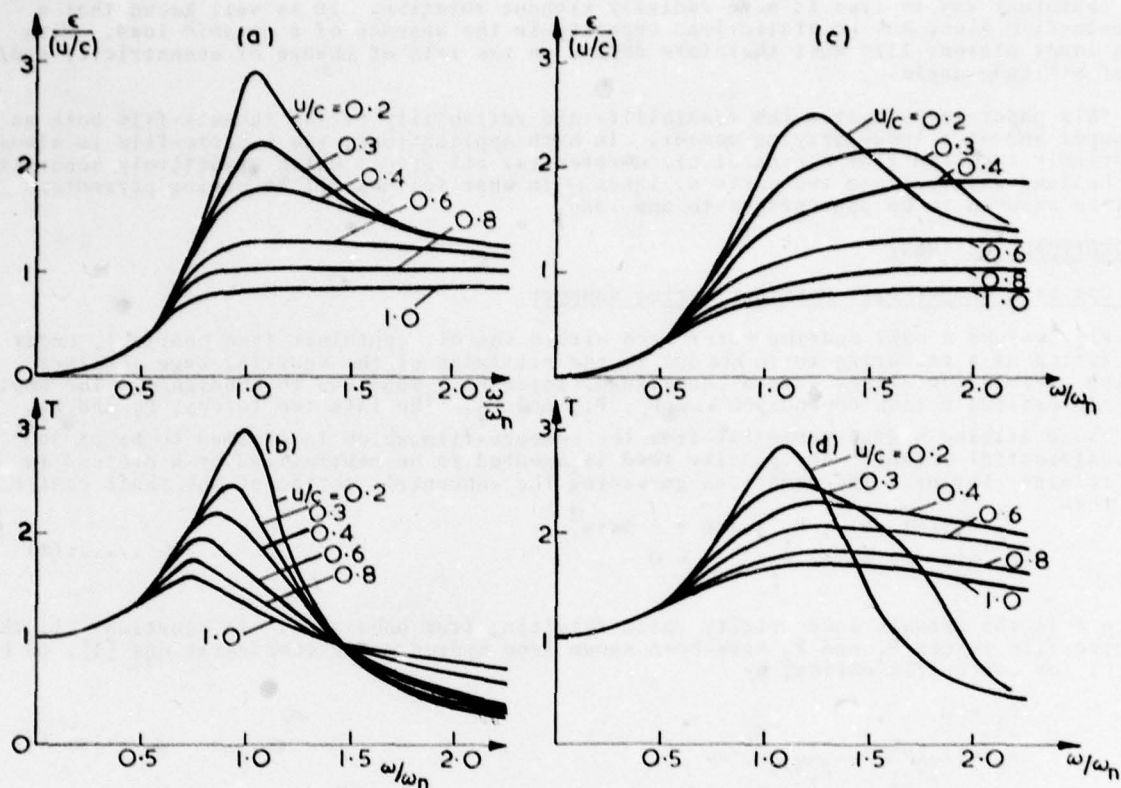
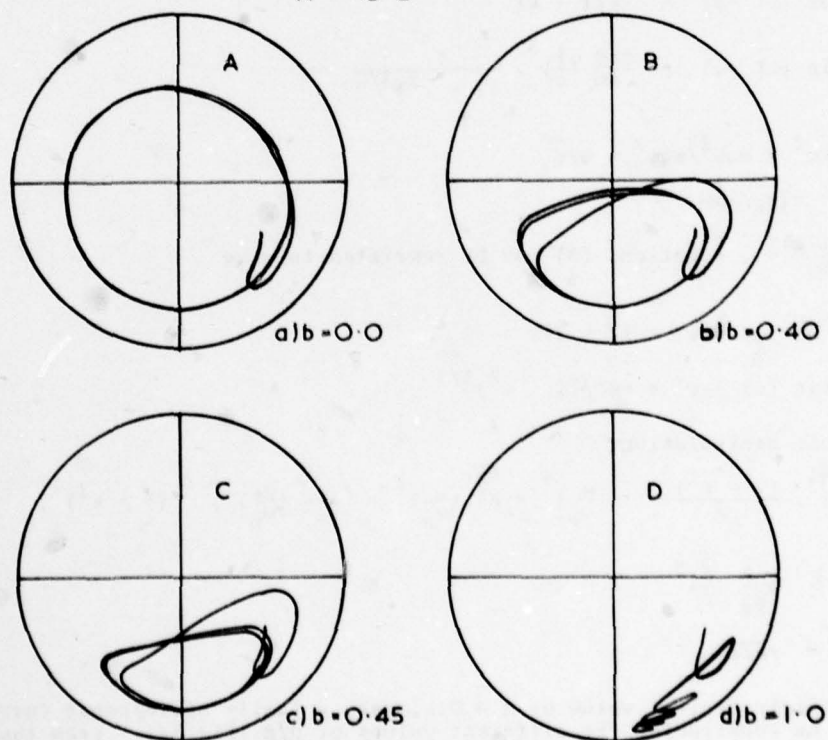


Fig 3: $\epsilon/(u/c)$ and Transmissibility v/ω_n

a and b Full film
c and d Half-cavitated film
A = 0.2



$Q = 0.90$, $Q_c = 2.26$, $\beta = 0.61$

Fig.4 Theoretical vibration orbits for four values of factor b

and is best expressed as a ratio (the transmissibility) of the unbalance force P_c . Thus transmissibility T is given by

$$T = F/P_c \quad \dots\dots(6)$$

Again, assuming a value of A of 0.2, a family of curves showing the dependence of T on ω/ω_n for different values of u/c is shown in Fig. 3b. An inspection of Figs. 3a and 3b shows that both $\epsilon/(u/c)$ and the transmissibility T depend upon u/c . This is expected since the system is essentially non-linear. Also only for ω/ω_n above $\sqrt{2}$ is T less than unity. This should thus be made to correspond to the normal operating range of the engine, when it can be readily seen from Figs. 3a and 3b that a low value of u/c is desirable on three counts - low vibration amplitude, low transmissibility and low transmitted force.

Now suppose that the supply pressure is insufficient to maintain a positive pressure in areas of the squeeze film where the boundary surfaces are instantaneously separating. For the sake of simplicity assume that as a result the squeeze film becomes half cavitated. It may then be shown, e.g. (2), (3), that P_2 is halved and that P_1 is no longer zero, being given by

$$P_1 = \frac{2\eta R l^3 \omega}{c^2} \cdot \frac{\epsilon^2}{(1 - \epsilon^2)^2}$$

The effect of such cavitation is shown in Figs. 3 c, d which reveal a deleterious influence on transmissibility when u/c is 0.4 or above. Extra caution is then required in balancing a turbine rotor if there is any likelihood of cavitation taking place in its squeeze-film bearings. Alternatively, the oil supply pressure should be made high enough to prevent cavitation.

(ii) Use of a squeeze-film as a load-carrying member without spring supports.

Owing to the absence of a retainer spring in this application the squeeze-film must now support the gravity load of the rotor as well as the dynamic load due to rotor unbalance. During periods of appreciable subatmospheric pressure, cavitation may well now occur in portions of the film even with a reasonable oil-supply pressure. The dynamical equations of motion are more complex than equations (1) since circular concentric whirl cannot be assumed. The equations are, with reference to Fig. 2b,

$$\begin{aligned} -P_1 + P \cos \psi + P_c \cos(\omega t - \psi) &= m c (\ddot{\epsilon} - \dot{\psi}^2 \epsilon) \\ \text{and} \quad -P_2 - P \sin \psi + P_c \sin(\omega t - \psi) &= m c (\epsilon \ddot{\psi} + 2 \dot{\epsilon} \dot{\psi}) \end{aligned} \quad \dots\dots(7)$$

The squeeze-film forces P_1 and P_2 are deduced by solving the so-called Reynolds equation which governs the pressure generation in a lubricant film, and they are based on the assumption that the squeeze-film cavitates over a portion of the clearance region, in which the oil-film pressure is less than a prescribed minimum. This portion is defined by oil-film limits θ_1 and θ_2 , Fig. 2b, whose values at a particular axial location depend on the oil supply pressure to the central circumferential groove and on the pressure at which the oil cavitates.

Now it may be shown that the hydrodynamically-generated pressure in a squeeze-film is negative over about 180° of the annulus but it has been experimentally observed by some workers (4), (5), (6), that under dynamic conditions an oil film can support pressures considerably less than atmospheric before cavitating. We thus write the squeeze-film forces

$$\begin{aligned} P_1 &= P_{11} + b(P_{12} - P_{11}) \\ \text{and} \quad P_2 &= P_{21} + b(P_{22} - P_{21}) \end{aligned} \quad \dots\dots(8)$$

where P_{11} and P_{21} are the forces derived for the 180° film of positive hydrodynamic pressure (7) and P_{22} are the oil-film forces derived for the full 360° film (1). ($P_{12} - P_{11}$) and ($P_{22} - P_{21}$) represent the forces emanating from the region of negative hydrodynamic pressure and account for the effects of supply pressure and oil-cavitation pressure. The coefficient b is set to prescribe the generation of squeeze-film forces due to resultant oil pressures in this region.

Equations (7) may be made non-dimensional by dividing throughout by $m c \omega^2$. Thus,

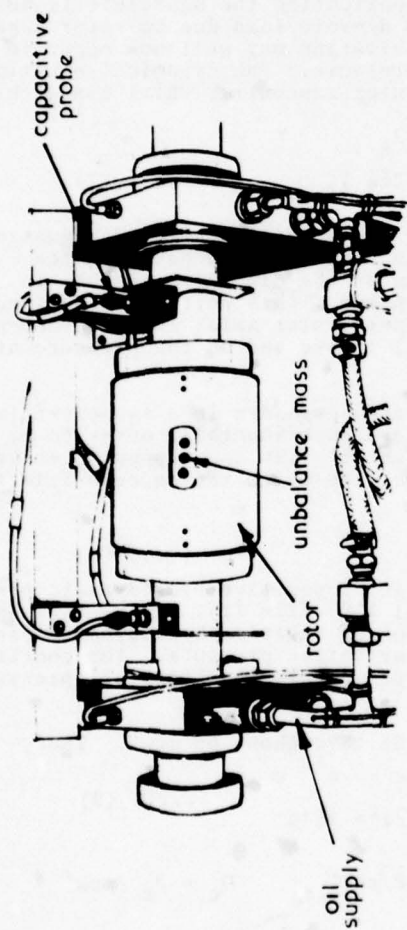
$$\begin{aligned} -Q_1 + Q \cos \psi + Q_c \cos(\omega t - \psi) &= \epsilon - \psi'^2 \epsilon \\ -Q_2 - Q \sin \psi + Q_c \sin(\omega t - \psi) &= \epsilon \psi'' + 2 \epsilon' \psi' \end{aligned} \quad \dots\dots(9)$$

where

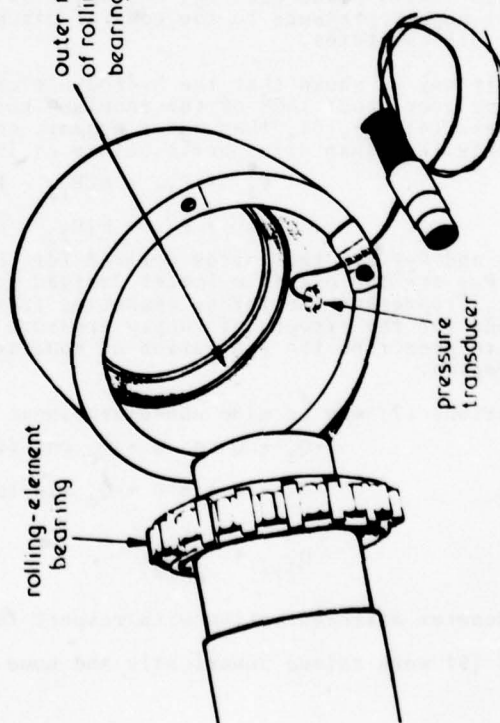
$$Q_{1,2} = \frac{P_{1,2}}{m c \omega^2}, \quad Q = P / m c \omega^2, \quad Q_c = P_c / m c \omega^2$$

and (') denotes differentiation with respect to non-dimensional time ωt .

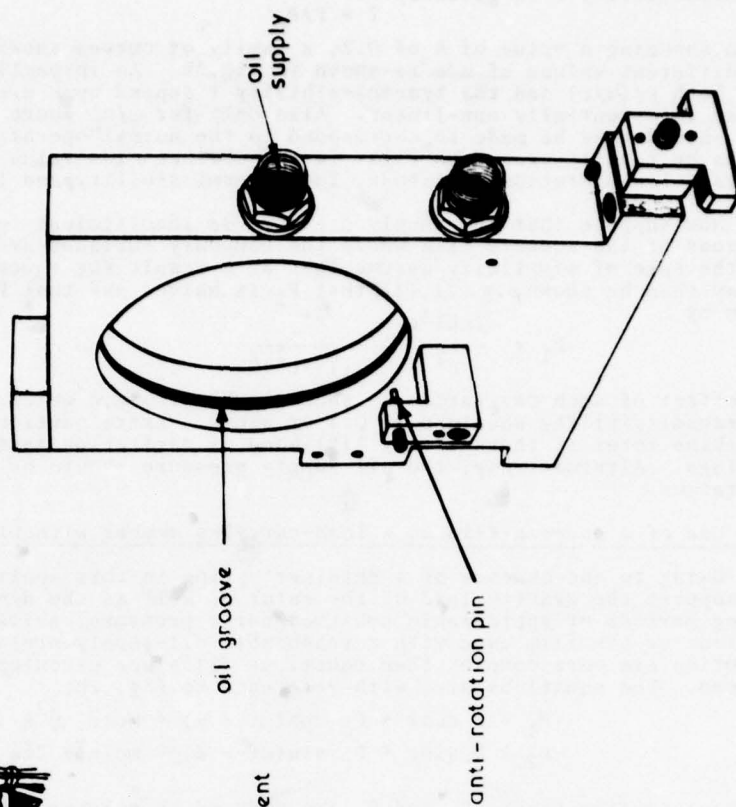
Equations (9) were solved numerically and some of the results will now be outlined.



a) GENERAL VIEW OF TEST RIG



b) SQUEEZE RING AND PRESSURE TRANSDUCER



c) SQUEEZE BEARING PEDESTAL

FIG. 5

RESULTS OF COMPUTATIONS

It is known from static considerations that if we put $Q_c = 0$, the squeeze-film bearing will exhibit no load-carrying capacity under the action of a non-dimensional static load Q . If, however, an unbalance load Q_c is added, it is instructive to investigate the journal centre locus to determine whether steady-state orbits are achieved. Fig.4 shows such orbits for four values of the negative pressure factor b . Each circle in Fig.4 is called the clearance circle and its radius represents the radial clearance between the journal (moving member) and the bearing (stationary member).

The presence of steady state orbits may be explained physically by the fact that the centrifugal load induces a value of ψ' , the effect of which is now sufficient to replace the more conventional journal rotation term. A hydrodynamic action is thus produced and creates a load-carrying capacity to counteract the static and dynamic load components Q and Q_c .

The feasibility of relying on squeeze-films to support such machine elements as gas-turbine rotors is thus shown to be consistent with a theoretical analysis which allows cavitation. If the annulus is full ($b = 1.0$) the rotor merely spirals to the base of the clearance circle and no lift is achieved.

DESIGN OF EXPERIMENT

An experimental rig was built, Fig.5a, to simulate as accurately as possible within certain space limitations a small gas turbine rotor supported on rolling element and squeeze-film bearings [8]. The inner elements of the assembled squeeze-film bearing were a case-hardened and ground steel ring which was attached to the outer race of a ball bearing, Fig.5b. The radial rolling clearance was reduced by interference fits of both the steel ring on the outer race of the bearing, and of the inner race on the rotor shaft. The resulting clearance was such that no radial motion of the outer race relative to the inner race was possible and a negligible amount of pitching of the ring and outer race took place. The material used for the pedestals was cast iron, which was chosen for ease of machining and for good rubbing properties should metal to metal contact occur between the pedestal and the squeeze ring. The pedestal consisted of two bearing lands which were separated by a central circumferential oil supply groove, Fig.5c. The dimensions of the groove were designed so as to make negligible any hydrodynamic pressures that may be generated in the groove due to squeezing action. The bearing diameter and land length were made 5 in. (127 mm) and 0.43 in. (10.9 mm) respectively, and a radial clearance of 0.0082 in. (0.21 mm) was used. After assembly of the rotor and fitting of the squeeze ring assemblies, the rotor was dynamically balanced. A known mass was then applied to give a specified degree of unbalance to excite the symmetric mode of vibration during running up to speeds restricted to about 4000 rev/min. Displacement measurements of the rotor centre were taken from capacitive probes in the horizontal and vertical planes, Fig.5a. The rotor was seen initially to rest at the base of the clearance space and at low speeds to roll or slide across the pedestal surface. Further increase in rotor speed resulted in visible lift, until a speed was reached when the amount of lift at the base of the clearance circle remained essentially constant, regardless of increases in speed between 2000 and 4000 rev/min. The size of the orbit however increased continuously with speed. Fig. 6 shows the orbit obtained for the values of the governing dimensionless groups used in Fig.4 and for a supply pressure of 2 lbf/in² (13.8 kN/m²), sufficient to provide an adequate oil supply. Comparison of Figs.4 and 6 shows that for a value of b of 0.45, reasonable agreement as to orbit size and disposition is obtained. This value of b gave further reasonable comparisons when other values were used for the governing non-dimensional groups.

Fig.7a shows the computed hydrodynamic pressure generated in the squeeze-film at a mid-land position at the base of the clearance circle as a function of non-dimensional time ωt and for $b = 0.45$. In this figure p_{st} denotes the pressure due to the applied static load component P , that is $p_{st} = \frac{P}{2Rl}$. For the experimental bearing in question the value of b was equal to about 10 lbf/in² (69 kN/m²). Fig.7a thus gives the predicted pressures in the most loaded part of the squeeze-film and shows a maximum negative value of about -540 kN/m², indicating the presence of tensile stress. Although large this negative value is not unlike negative pressures observed in journal bearings [4],[5] and squeeze bearings [6] by other workers.

A pressure transducer mounted in the squeeze-ring, (Fig.5b) indicated a similar pattern of pressure at the base of the clearance circle, Fig. 7b. The secondary pressure peak was due to the rotor centre moving round the tail T of the orbits indicated in Figs. 6 and 7a. A pronounced negative-pressure region can also be observed amounting to about -40 lbf/in² (-276 kN/m²). This confirms that not only can the oil in the squeeze-film support subatmospheric pressures but tension forces also must exist. The heights of the main pressure peaks are considerably less than predicted in Fig.7a. The implication of this is that the shaft is subjected to much smaller squeeze-film forces than the theoretical analysis would suggest, a feature also noted by White [3]. A modification of the theoretical model to allow for experimentally observed limitations to the maximum and minimum pressures resulted in a general lowering of the vibration orbit in the clearance circle. This agreed with experimental finding as a comparison of the orbits of Figs.6 and 7a will show. As to the reason for the observed low positive pressure peaks, the indications are that cavitation bubbles trapped in the squeeze-film are responsible, a reason suggested by White [3]. Unlike a normal turbine bearing in which the journal rotates, there is no effective inducement for such bubbles to remove themselves except by the presence of a sufficient

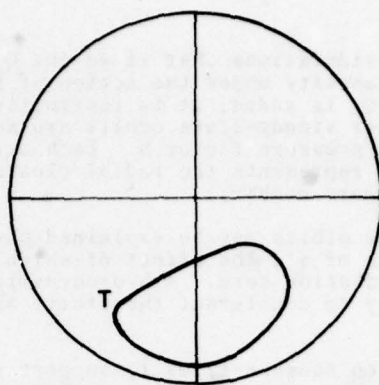


Fig. 6 Experimental vibration orbit
 $\beta = 0.61$, $Q = 0.90$, $Q_c = 2.26$

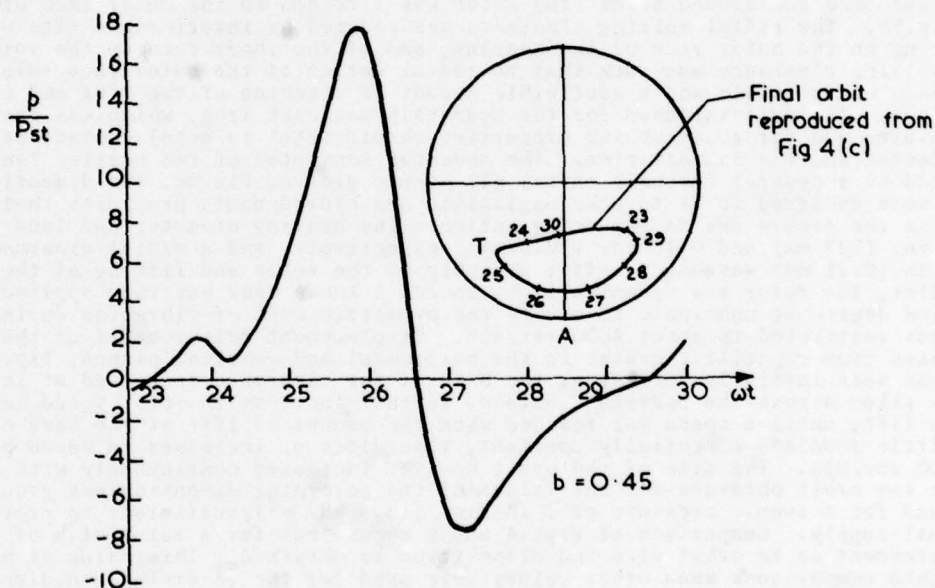


Fig. 7a Dynamic squeeze film pressure at Base A
 of clearance circle

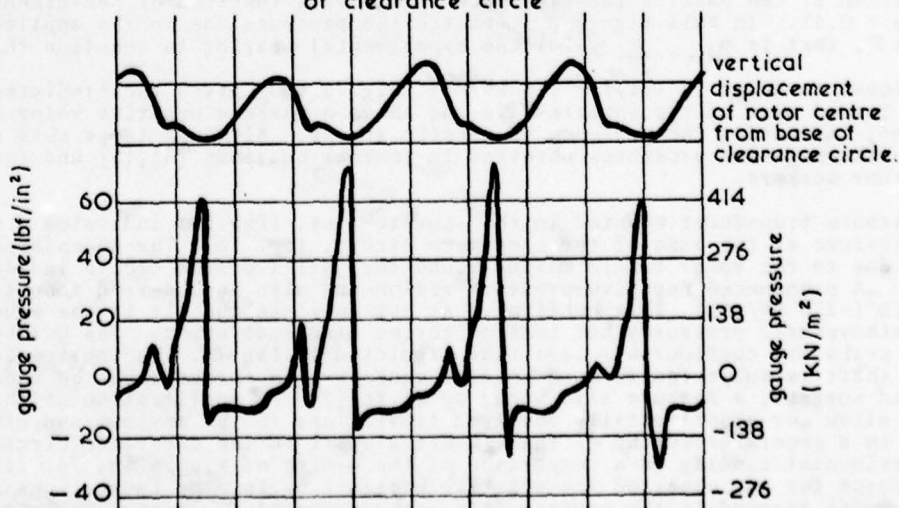


Fig. 7b Experimental pressure at base of clearance circle

supply pressure. On occasions when they did appear to vent fully, the experimental vibration orbit was seen to suddenly jump to a somewhat greater size, higher in the clearance circle.

CONCLUSIONS

For the application in which the squeeze-film is relied upon to provide damping only, and where the rotor load is carried by a retainer spring support system, equations have been presented from which an estimate can be made of vibration amplitude and of the force transmitted to the engine frame. Cavitation is shown to have a deleterious effect.

Where the squeeze-film is relied upon to provide a load-carrying capability as well as damping, cavitation must be allowed to be generated in the film. A comparison of predicted and experimental vibration orbits for given values of Q , Q_c and β showed that a theoretical model based on a squeeze-film allowing a limited negative gauge pressure gave reliable predictions of vibration orbits and a qualitative indication of dynamic pressure. The effect of the negative oil pressure is to draw the journal down towards the bottom point of the clearance circle. Observations that increase in supply pressure had a similar effect were consistent with this view as such an increase results in a reduced cavitation region. Fig.4d shows that in the limiting case of a 2π squeeze-film no orbit is established and the shaft centre merely spirals downward to reach the bottom point of the clearance circle at time equals infinity. The use of the negative pressure factor b has enabled a qualitative understanding to be reached of the feasibility of the squeeze-film bearing as a load-carrying member. The value of this factor probably depends upon the operating conditions, notably the static load. A considerable amount of research work, both theoretical [8], [9], [10] and experimental [11] - [17] is now taking place and it is recommended that particular attention be paid to the role of subatmospheric squeeze-film pressures in governing bearing performance. It is concluded that such a bearing is worth exploiting, due to its simplicity, in gas-turbine construction, provided that care is taken to ensure that the forces transmitted to the engine frame [7] are not excessive.

REFERENCES

- [1] HOLMES, R. 'The damping characteristics of vibration isolators used in gas turbines'. Jnl. Mech.Eng.Sci, Vol.19, No.6, 1977, pp.271-277.
- [2] COOPER, S. 'Preliminary investigation of oil-films for the control of vibration'. I.Mech.E. Lubrication and Wear Convention, 1963, paper 28, pp.305-315.
- [3] WHITE, D.C. 'Squeeze-film journal bearings'. Ph.D. Thesis, Cambridge, 1970.
- [4] DYER, D. and REASON, B.R. 'A study of tensile stresses in a journal-bearing oil film', Jnl. Mech.Eng.Sci. 18, 1, Feb.1976, pp.46-52.
- [5] PATRICK, J.K. 'Detection of tensile stresses in an oil film by means of a balanced pressure piston', Proc. Inst.Mech.Engrs., 1968, 182 (3G), 73-74.
- [6] FEDER, E., BANSAL, P.N. and BLANCO, A. 'Investigation of squeeze-film damper forces produced by circular central orbits', A.S.M.E. paper No. 77-GT-30.
- [7] HOLMES, R. 'The non-linear performance of squeeze-film bearings'. Jnl.Mech.Eng.Sci., Vol.14, No.1, 1972, pp.74-77.
- [8] HUMES, B. 'The non-linear performance of squeeze-film bearings.' D.Phil Thesis, University of Sussex, 1977.
- [9] GUNTER, E.J., BARRETT, L.E. and ALLAIRE, P.E. 'Design of non-linear squeeze-film dampers for aircraft engines', A.S.M.E. Jnl.Lub.Tech. Vol.99, No.1, Jan.1977, pp.57-64.
- [10] HIBNER, D.H., KIRK, R.G. and BUONO, D.F. 'Analytical and experimental investigation of the stability of intershaft squeeze film dampers', A.S.M.E. Jnl. Eng'g for Power, Vol.99, No.1, Jan.1977, pp.47-52.
- [11] GLIENICKE, J. and STANSI, U. 'External bearing damping - a means of preventing dangerous shaft vibrations in gas turbines and exhaust turbo-chargers', C.I.M.A.C. Conference, Barcelona, 1975, pp.287-311.
- [12] JONES, M.G. 'An experimental investigation of squeeze film hydrodynamics', National Gas Turbine Establishment Report No.R320, Jan.1973.
- [13] THOMSEN, K. and ANDERSON, H. 'Experimental investigation of a simple squeeze-film damper', A.S.M.E. Jnl. of Eng'g for Ind., May 74, p.427.
- [14] VANCE, J. and KIRTON, A. 'Experimental measurement of the dynamic response of a squeeze-film bearing damper', A.S.M.E. Jnl.En'g for Industry, Nov. 1975, p.1282.
- [15] TØNNESSEN, J. 'Experimental parametric study of a squeeze-film bearing'. A.S.M.E. Jnl. of Lubrication Technology, April 1976, pp.206-213.

- [16] BOTMAN, M. and SHARMA, R.K. 'Experiments on the transient response of oil-film dampers'. A.S.M.E. Paper No. 77-GT-31.
- [17] BOTMAN, M. 'Experiments on oil-film dampers for turbomachinery'. A.S.M.E. Paper No. 75-WA/GT-19.

ACKNOWLEDGEMENTS

The authors acknowledge the facilities placed at their disposal by the School of Engineering and Applied Sciences, and by the Computing Centre, University of Sussex, to carry out this work. Thanks are also due to the National Gas Turbine Establishment for financial support.

DISCUSSION

M. Botman, Canada

- Was the leakage of oil through the sides of the damper measured or taken into account in the analysis? Possibly this would explain the difference found in the experimental and theoretical peak pressures.
- What is the physical explanation of the double humps found in the experimental pressures?

Author's Reply

I would like to thank Mr Botman for his comments and I am very pleased to answer them, as follows:

The numerical method adopted in the computed solutions takes as its starting point the Reynolds lubrication equation which automatically allows for oil circulation, both axially and circumferentially. Oil flow was not measured experimentally since it could only have revealed an aggregate effect rather than time variations.

Regarding Mr Botman's second point, this is best answered with reference to Figure 7a, where it can be seen that for $\omega t = 24$ to 25 a dip occurs in the dynamic pressure and the journal centre progresses around the tail T of the orbit. In this way the journal centre suffers a slight deceleration and it is this that temporarily relieves the pressure before it starts once again to rise as ωt increases and the journal centre drops lower in the clearance circle.

MODAL ANALYSIS OF COMPRESSOR BLADES BY MEANS OF IMPULSE EXCITATION

by

U. Bolleter, J. Eberl, E. Buehlmann
Sulzer Brothers Limited
8401 Winterthur, Switzerland

SUMMARY

An experimental method of modal analysis is described which is based on impulse excitation. Due to low damping the application to free-standing turbomachinery blading requires special care in the digital processing of the data. The modal behaviour particularly with respect to bending and torsional coupling is demonstrated using a subsonic compressor blade as an example. Measured damping coefficients and inter-modal phase differences are discussed. Applications of the quantitative results of stress responses to point excitation are illustrated. Thus stresses due to various assumed loads allow one to judge the importance of higher modes, stress ratios for various modes can be an aid to failure analysis, and multiple strain measurements can yield an estimate of aerodynamic loads.

LIST OF SYMBOLS

f_r	Resonance frequency of r^{th} mode
$F_k(\omega)$	Fourier transform of force signal at location k
g_r	Damping coefficient for structural damping model
$g_{r1}; g_{r2}$	Extracted damping coefficients prior to averaging
$H_{ik}(\omega)$	Transfer function, response at gage location i due to impulse at location k
j	Imaginary unit
L	Blade length
N	Number of data points around a resonance frequency to be included for modal extraction, usually $N = 5$
r	Mode index
R	Radius of circle, see Fig. 7
t	Time
T	Time window
U_{kr}	Magnitude of modal parameter for force location k
α	Artificial damping coefficient
γ_{pr}	Modal stress ratio between reference gage location i and gage location p
$\epsilon_i(\omega)$	Fourier transform of strain signal at gage location i
ζ_r	Modal damping ratio for viscoelastic model
$\theta(\omega)$	Phase angle of transfer function
σ_p	Calculated stress at location p
ϕ	Angle, see Fig. 7
ϕ_{kr}	Phase of modal parameter for force location k
ψ_r	Modal vector with elements $U_{kr}e^{j\phi_{kr}}$
ω	Circular frequency
ω_r	Circular resonance frequency of r^{th} mode

1. INTRODUCTION

In recent times modal analysis by impact testing has become a widely used tool for the treatment of vibration problems. It allows one to investigate complex structures which are difficult to model analytically. For industrial application to turbomachinery blading the modal analysis must be simple and fast. In addition special problems in data acquisition and analysis techniques, due to the small size and low damping of blades, must be overcome.

This paper describes the various problems and possible solutions and illustrates the successful application to a particular blade.

2. METHOD OF TESTING

2.1. Measurement of transfer functions

The transfer functions between dynamic strain and force at desired locations on the blade are obtained by impulse excitation. As Fig. 1 shows the excitation pulse (force) and the response signal (strain) are filtered, digitized and transformed into the frequency domain. The transfer function is determined as:

$$H_{ik}(\omega) = \frac{\epsilon_i(\omega)}{F_k(\omega)} = \frac{\epsilon_i(\omega) F_k^*(\omega)}{|F_k(\omega)|^2} \quad (1)$$

Conceptually simple the method poses some special problems when applied to such light structures as turbomachinery blading. The impulse must be quite short to excite the entire desired range of frequencies, often up to 5 kHz. At the tip the blades are of relatively low mechanical impedance. Thus a sharp force pulse can only be obtained with a hammer of small mass. A piezoelectric load cell (e.g. Kistler, Type 9213) works well.

A small tip, made from Nylon, is attached with wax. Additional weights can be screwed to the back (Fig. 2). Due to the mass in front of the piezoelectric element the sensitivity must be obtained from a dynamic calibration. Either the acceleration of a softly suspended mass can be measured, when hit with the hammer or alternatively an other, small, stiff piezoelectric load cell placed on a stiff support can be hit directly for calibration purposes. Figure 3 shows the dynamic sensitivity of the hammer used for various added weights. Figure 4 shows typical excitation pulses and their spectra obtained from the blade of Fig. 10. The hammer with 2 grams of added mass yields acceptable results; although a loss of force towards the tip of the blade (point 52) at high frequencies is apparent. When adding 5 grams of mass to the hammer an unacceptable double pulse appears at the tip. Careful matching of the hammer mass and tip elasticity to the particular blade under test is essential. For a well defined excitation the blade can only be hit perpendicular to the blade surface, including blows straight on the leading and trailing edges. For twisted blades therefore a cylindrical coordinate system must be used.

To improve the signal-to-noise ratio a time window is used over the excitation pulse (Fig. 5). Further semi-conductor strain gages are used in a constant current circuit. The gage must be placed where it will be sensitive to all modes to be investigated. Normally the trailing edge near the root is chosen with the gage sensitive axis oriented along the blade height. Usually 5 blows are averaged for one transfer function.

To obtain sufficient resolution for the modal analysis the data block must be at least of size 2048 points in the time domain. Zoom transforms are not considered practical for blades as individual testing for each mode leads to excessive measuring and analysis time. A continuous check of signal-to-noise ratio and repeatable excitation is necessary. The coherence function is, therefore, displayed on a screen together with the transfer function. When accepted, all transfer functions are stored on disc together with the location and coordinate direction of excitation. A certain transfer function can be assigned to more than one location to allow one to display the motion of points in directions which are not excitable. For example the motion of point 42 in the chord-direction would be obtained from the transfer function measured at point 41 in the chord-direction (Fig. 10).

The two channel analysis as described has been implemented on a commercially available minicomputer based system (Time/Data TDA-1L) programmed with TSL (Time Series Language by Time/Data). Examples of transfer functions and corresponding coherence functions from the blade of Fig. 10 are shown in Fig. 6. The stress levels indicated were obtained from the strain simply by multiplication with the modulus of elasticity.

2.2. Modal analysis

For each resonance the frequency f_r , damping ratio ζ_r , magnitude U_r and phase ϕ_r is now extracted from the transfer functions. After evaluation of a number of other methods we found that an extraction method based on the work of Kennedy and Pancu [1] is well suited for blades; since their damping is usually low and their resonance frequencies are sufficiently spaced. The extraction method used follows in part Ref. [2].

Employing the structural damping model, the transfer function, written for a specific mode, r , is

$$\frac{\epsilon}{F}(\omega)_r = \frac{U_r \cdot e^{j\phi_r}}{1 - \left(\frac{\omega}{\omega_r}\right)^2 + j\zeta_r \omega \omega_r} + \bar{K} \quad (2)$$

Near $\omega = \omega_r$ the transfer function is dominated by the r^{th} mode, and the contribution of all other modes, \bar{K} , is assumed to be constant with frequency. It can then be shown, e.g. [2], that $\frac{\epsilon}{F}(\omega)$ describes a circle in the complex plane (Fig. 7). Its radius R and center coordinates x_0 , y_0 are obtained from a circle fitted to the N data points, employing a least square error condition, leading to the set of linear equations

$$\begin{bmatrix} \Sigma x & \Sigma y & N \\ \Sigma xy & \Sigma y^2 & \Sigma y \\ \Sigma x^2 & \Sigma xy & \Sigma x \end{bmatrix} \begin{Bmatrix} a \\ b \\ c \end{Bmatrix} = \begin{Bmatrix} -\Sigma(x^2 + y^2) \\ -\Sigma(x^2 y + y^3) \\ -\Sigma(x^3 + xy^2) \end{Bmatrix}$$

with

$$x_0 = -\frac{1}{2} a$$

$$y_0 = -\frac{1}{2} b$$

$$R = \sqrt{\frac{a^2}{4} + \frac{b^2}{4} - c}$$

x, y = coordinates of the N data points in the complex plane. Summation over N points.

The resonance frequency ω_r is obtained from the minimum of the function $\frac{d\omega^2}{d\phi}(\phi)$.

The differentiation is approximated by a finite difference

$$\frac{d\omega^2}{d\phi} \approx \frac{\omega_i^2 - \omega_{i-1}^2}{\phi_i - \phi_{i-1}} \text{ at } \phi = \frac{\phi_i + \phi_{i-1}}{2}$$

The minimum is found from fitting a polynome

$$y = A\phi^2 + B\phi + C$$

in the least square sense to the $N-1$ values of $\frac{d\omega^2}{d\phi}$. The angle ϕ_r corresponding to ω_r is then given by $\phi_r = -B/2A$.

The value for ω_r is found by linear interpolation of the function $\omega(\phi)$. From Eq. (2) and Fig. 7 it follows:

$$\phi_r - \theta = \arctan \frac{g_r}{1 - \left(\frac{\omega}{\omega_r}\right)^2} \quad (3)$$

The quantities ϕ_r (see Eq. 7) and ω_r are known, and values for θ and ω are available as data points. Thus g_r can in principle be obtained from any data point, except $\omega = \omega_r$. We calculate g_r at two frequencies equally spaced around ω_r (linear interpolation on one side is used) to yield g_{r1} and g_{r2} . The following quantities are printed out and further used:

$$\text{Frequency: } f_r = \frac{\omega_r}{2\pi} \quad (4)$$

$$\text{Damping ratio: } \zeta_r = \frac{1}{2} g_r \frac{\omega}{\omega_r} \approx \frac{1}{2} g_r \quad (\text{near res.}) \quad \text{with } g_r = \frac{1}{2} (g_{r1} + g_{r2}) \quad (5)$$

$$\text{Magnitude: } U_r = 2g_r R \quad (6)$$

$$\text{Phase: } \phi_r = \frac{1}{2} \pi + \phi_r \quad (\text{see Fig. 7}) \quad (7)$$

Three tests are made to ensure proper extraction of the modal parameters:

- check of circle fit: $0.8 < \frac{R_i}{R} < 1.2$ (see Fig. 7)
- check of phase: ϕ_r within range of ϕ for N data points
- check of damping: $|g_{r2} - g_{r1}| < 0.2 g_r$

Prior to modal extraction the impulse response as obtained from the transfer function (by inverse Fourier transform) is multiplied by an exponential time window, $\exp(-\alpha t)$. Thus an artificial but known damping is introduced for which the extracted modal parameters are corrected. For lightly damped modes the extraction does not work without this exponential window. Numerically the application of the time window directly to the response of the structure after each impact would be preferable, but this precludes the possibility of experimenting with various time constants for the modal extraction. Figure 8 shows an impulse response and a transfer function without and with an exponential window applied. Corresponding listings of the extracted modal parameters are shown in Table 1. Here - as for most analysis - 5 data points are used for the extraction ($N = 5$). Without window modes number 1, 3, 4, 6 and 8 could not be extracted (error condition 3 is indicated). The parameters of the remaining modes are only slightly affected by the time window with $\alpha = 2.5$, which allows extraction of all modes for this case.

The ability of the extraction method to separate fairly close resonances has been checked by analyzing computed transfer functions for a two degree of freedom system. Figure 9 shows such a transfer function where the two peaks are separated by 10 frequency lines only. The extracted values agree quite well with the true values.

To improve the accuracy of the modal parameters, after modal extraction is completed, the resonance frequencies and the damping ratios for each mode are averaged over all measuring locations of the entire structure. Furthermore, the magnitudes are corrected to correspond to the averaged damping ratios (Eq. 6). After the initial estimation of the

resonance frequencies to be analyzed and after selection of a proper exponential time window (usually $\alpha = 2$ to 4) the modal extraction for all transfer functions runs fully automatic. If one of the error conditions is encountered, e.g. due to insufficient signal-to-noise ratio for points near a nodal line, the automatic analysis continues, but the corresponding magnitude is set to zero. This poses no problem for the subsequent display of the mode shapes as the true magnitude would have been small anyway. After all modal parameters for the structure are extracted the magnitudes and phases are automatically formed into animated mode shape pictures and are displayed on the screen. For the display, part of a commercially available program (MESA by Time/Data) is used.

The measurements and the analysis of a blade with about 50 locations, each excited in two coordinate directions, takes about one day.

3. AN EXAMPLE

The blade of Fig. 10 was analyzed for 6 different blade lengths. Fig. 11 shows the resonance frequencies. As expected the resonance frequencies of the bending modes follow approximately a L^{-2} -law (slope -2 on log-log graph of Fig. 11), whereas the resonance frequencies of the torsional modes follow approximately a L^{-1} -law (slope -1). This leads to "crossover"-points which in reality can not exist; since no two modes can have the same resonance frequency when coupling is present. In the "crossover" region the frequencies approach each other to a degree which depends on the modal coupling. The mode shapes of the approaching modes combine to coupled motions. On Fig. 11 the second bending, first torsional and edgewise modes approach each other in the region of 90 to 130 mm blade length. In the same region the third bending mode changes over to the second torsional mode. This is shown in Fig. 12 and is clearly illustrated in the movie which is part of the presentation of this paper.

Some interesting observations can be made on the damping ratios and the range of phase angles of a certain mode (Fig. 13):

- The damping ratios vary over a range of more than 1 : 50 with the first bending and the first torsional modes showing the smallest, the edgewise and the coupled modes the highest damping.
- There exists a fairly good correlation between the range of phase angles for a certain mode and the damping, the range of phase angles increasing with the damping.
- Above a certain damping ratio - somewhere around $\frac{1}{2}$ to 1 % of critical damping - most mode shapes must be treated as complex modes, i.e. the assumption of real modes with all motions in phase or out-of-phase is insufficient.

Obviously the measured damping ratios and possibly some of the observations made should not be applied to blades under operating conditions without further considerations such as damping in the blade root, aerodynamic damping and increase in damping at higher stress levels for certain materials.

4. APPLICATIONS

With the modal parameters known for the desired number of modes, M , and assuming a viscoelastic model the stress can be expressed as

$$\sigma_p = \sum_{r=1}^M \frac{\gamma_{pr} \{\Psi_r\}^T \{F\}}{\left[1 - \left(\frac{\omega}{\omega_r}\right)^2 + j2\zeta_r \left(\frac{\omega}{\omega_r}\right)\right]} \quad (8)$$

The factor γ_{pr} describes the modal stress ratio between a gage location, p , considered on the blade and the location of the strain gage, i , used for the modal analysis. The modal vector $\{\Psi_r\}$ contains the complex modal parameters with magnitude U_{kr} and phase Φ_{kr} according to equation (2). Near resonance the contribution of all other modes becomes negligible and therefore summing up can be omitted.

In a first example the results of the modal analysis are used to determine the resonance stresses at a certain location on the blade as a function of modal number and blade length. The blade considered is shown in Fig. 10. Its qualitative vibrational behaviour is discussed in section 3. As reference point for the stress comparison the location of the strain gage used for the transfer analysis was chosen (trailing edge, concave side near the root). For each blade length investigated and its corresponding modes the product of modal vector and excitation vector is formed and related to the calculated value for the first bending mode (modal stress ratio). The results of this evaluation for three different cases of dynamic loading are presented in Fig. 14, namely

- a) Equally distributed dynamic in-phase load, orthogonal to blade chord.
- b) Equal dynamic in-phase load along blade tip, orthogonal to blade chord.
- c) Equal dynamic in-phase load along leading edge, orthogonal to blade chord.

As to be expected the change in mode shapes with different blade lengths is manifested quantitatively as a variation of modal stress ratios. The results basically give expression to the fact that - disregarding a possible mode shape dependence of the overall damping in an engine - stresses at higher modes may be significant when excited at resonance.

The modal analysis also finds applications to investigations associated with fatigue failures of turbomachinery blading. When searching for the excitation source it is essential to find out the vibration mode under which the failure originated. For that purpose the modal analysis yields the stress ratio between the failure location and another characteristic position on the blade, usually the point of maximum stress under fundamental vibration. The following example shows values of the stress ratios between the failure location at the trailing edge and the point of maximum stress for the first bending mode for a compressor blade.

Vibration mode	1	2	3	4	5
Resonance frequency [Hz]	660	2300	3300	4100	6500
Stress ratio	0.5	2.8	0.3	2.0	8

These figures lead to the conclusion that mode 1 and mode 3 vibrations are unlikely to cause a fatigue failure at the trailing edge. This holds true as long as both locations are of equivalent strength, that is different stress concentrations or metallurgical properties do not exist.

The estimate of unsteady aerodynamic loads is a further example for the application of modal analysis. If a number of strain gages are placed on a blade in such a manner that each one is particularly sensitive to a certain mode then it is possible in principle to determine the intensity of each considered mode. Furthermore, some information about the unsteady aerodynamic load on the blade can be gained; since each mode has a corresponding spatial sensitivity to the applied dynamic load. Obviously the load distribution can at best be determined as an average pressure in as many regions as there are modes to "sense" the pressure. Alternatively the strength of the same number of assumed orthogonal pressure distributions can be determined. Experiments and numerical simulations for such a procedure have shown that it only works, with acceptable uncertainties, in a narrow frequency band between some neighbouring resonance frequencies, i.e. where no single mode dominates the response.

5. CONCLUSIONS

Although modal analysis by impact testing has become a widely used tool for the treatment of vibration problems, its application to light structures such as the blades of turbomachines raises a few special difficulties. For example, careful matching of the hammer mass and tip elasticity to the particular blade under test, and the introduction of artificial damping for the modal extraction is shown to be essential. Because of the excessive measuring and analysis time involved zoom transforms are not considered practical for industrial application to blades. Thus it is necessary to use a large data block and a modal extraction method working successfully on relatively widely spaced frequency lines. Also the modal extraction as well as the synthesis of the animated mode shape pictures should run fully automatically.

The modal analysis of a compressor blade showed complicated mode shapes for blade lengths for which two or more resonance frequencies are close together. Damping of the various modes was found to vary strongly. Most modes with damping ratios above $\sqrt{2}$ to 1 % of critical damping showed complex modal behaviour, i.e. the assumption of real modes with all motions either in phase or out-of-phase is insufficient.

6. REFERENCES

- [1] Kennedy C.C., Pancu C.D.P.,
Use of Vectors in Vibration Measurement and Analysis.
Journal of the Aeronautical Sciences, Vol. 14, No. 11, Nov. 1947
- [2] Klosterman A.L.,
On the Experimental Determination and Use of Modal Representations of Dynamic Characteristics
Ph. D. Dissertation, Univ. of Cincinnati, 1971.

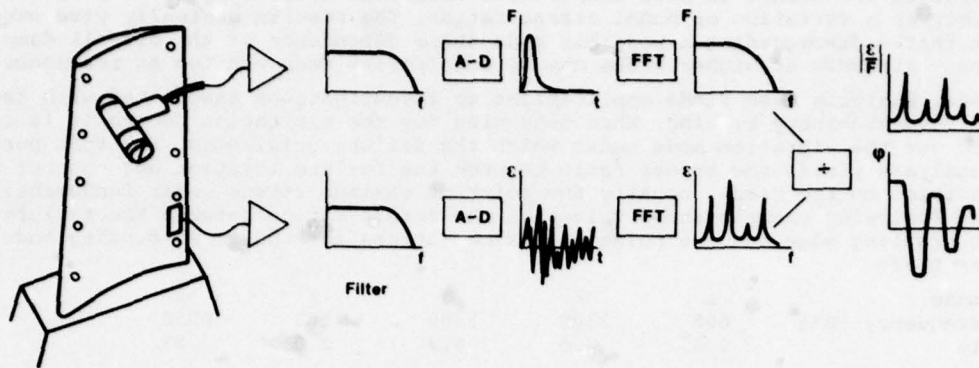


Fig. 1
Block diagram for the determination of transfer functions by impulse excitation.

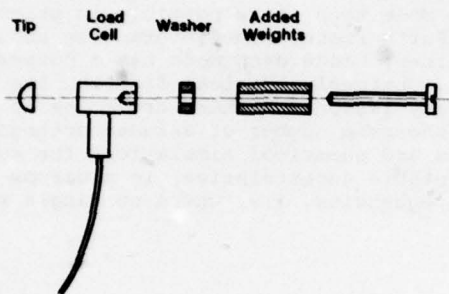


Fig. 2
Hammer with load cell Kistler Type 9213.

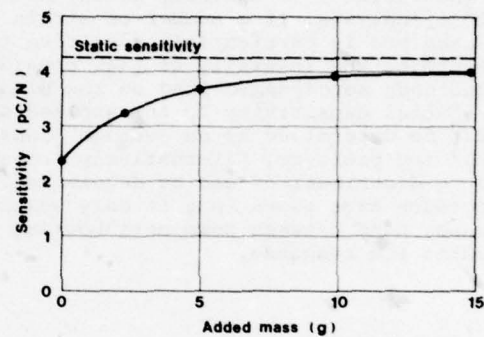


Fig. 3
Dynamic sensitivity of the hammer as a function of the added mass.

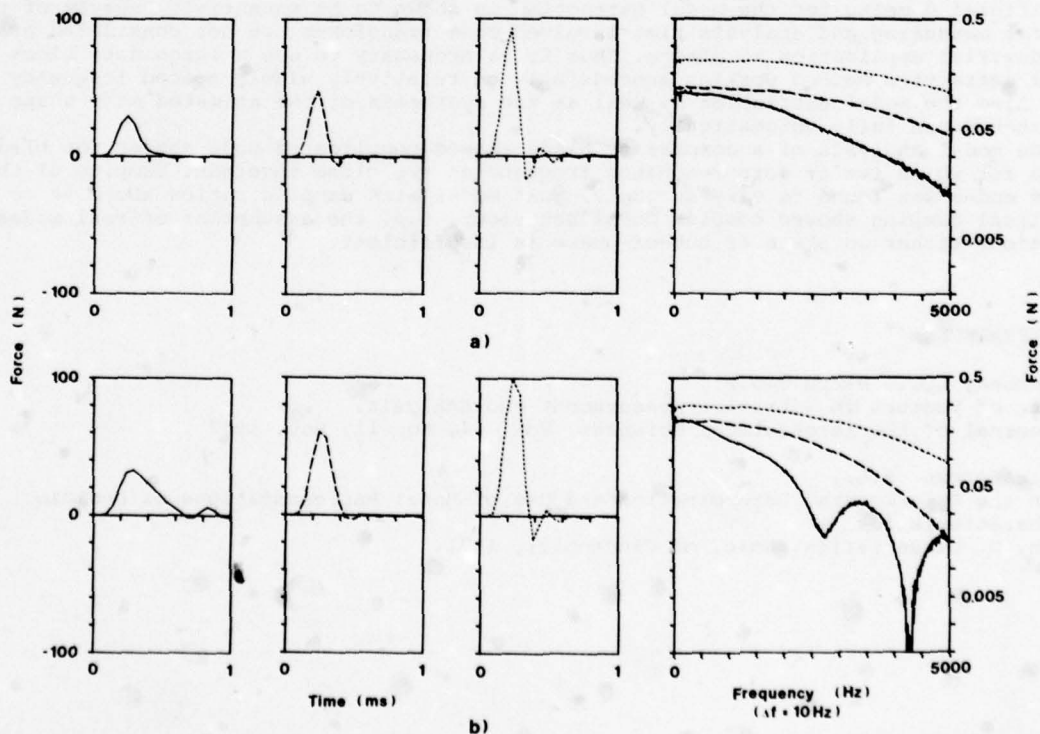


Fig. 4
Force pulses and their frequency spectra,
a) 2 grams of added mass | — Excitation location no. 52 (tip, see Fig. 10)
b) 5 grams of added mass | ---- Excitation location no. 40
| Excitation location no. 12 (root)

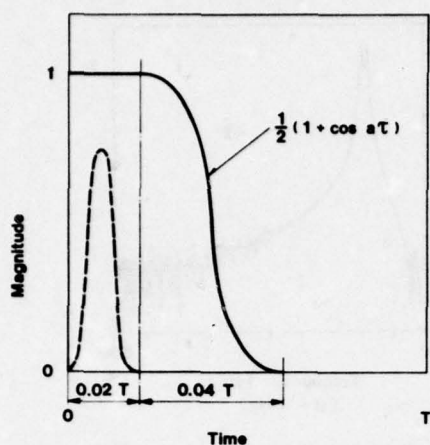
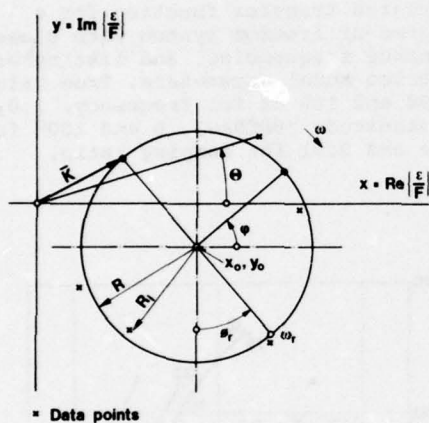


Fig. 5
Time window (—) over excitation pulse (---).



□ Data points

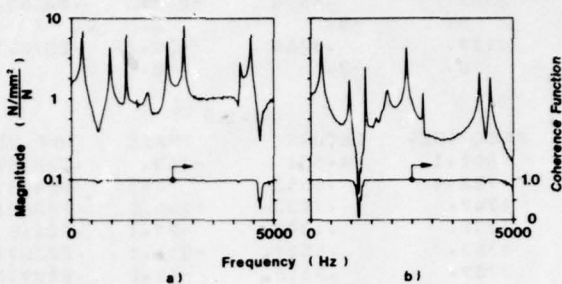


Fig. 6
Measured transfer functions and coherence functions,
a) excitation location no. 52 (see Fig. 10)
b) excitation location no. 38

Fig. 7
Section of a transfer function around a resonance plotted in the complex plane with a circle fitted for modal extraction.

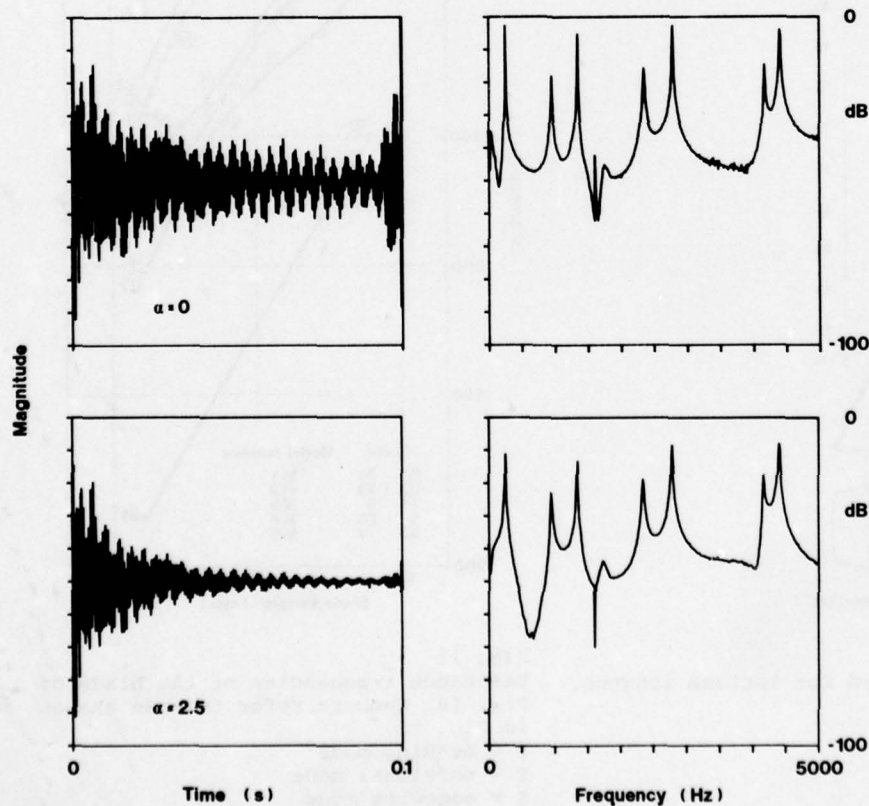


Fig. 8
Impulse response and transfer function at point 52 (Fig. 10), without time window ($\alpha=0$), and with time window ($\alpha=2.5$)

#	FREQ (HZ)	BETRAG	PHASE	DMP VERH
1	0.	-3.	0.	0.
2	952.9	.6176	-10.8	.004248
3	0.	-3.	0.	0.
4	0.	-3.	0.	0.
5	2353.	.6574	-210.4	.003634
6	0.	-3.	0.	0.
7	4177.	.3184	-39.0	.001597
8	0.	-3.	0.	0.

#	FREQ (HZ)	BETRAG	PHASE	DMP VERH
1	261.1	4.671	-163.	.0007591
2	952.4	.6563	-3.5	.004457
3	1347.	.7933	-182.5	.000351
4	1730.	.1307	-27.1	.02416
5	2353.	.6527	-211.1	.003579
6	2787.	.9515	-19.2	.000936
7	4177.	.3286	-40.9	.001628
8	4415.	.8308	120.7	.0009751

Table 1
From transfer functions of Fig. 8 extracted modal parameters. Magnitudes (BETRAG) not in N/mm^2 , phases uncorrected for measurement system phase differences.

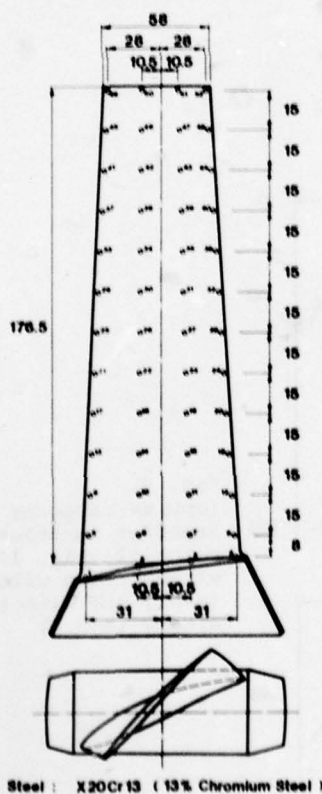


Fig. 10
Compressor blade analyzed for various lengths.

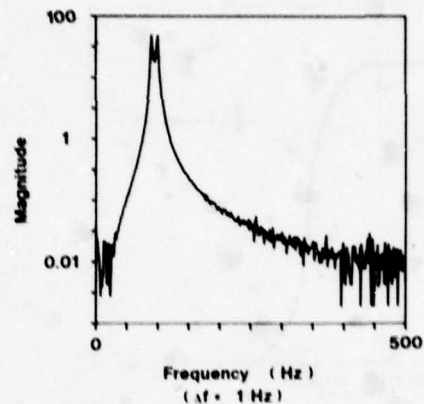
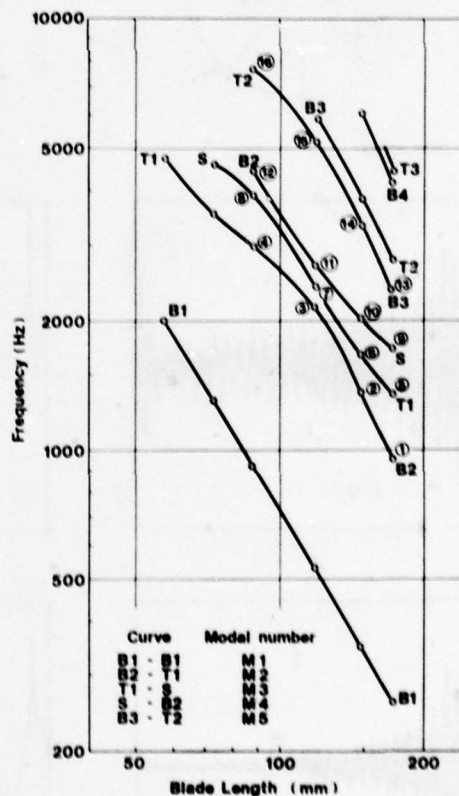


Fig. 9
Calculated transfer function for a 2-degree of freedom system with close resonance frequencies, and listing of extracted modal parameters. True values are 90 and 100 Hz for frequency, 1.0 for magnitude (BETRAG), 0 and 180° for phase and 0.01 for damping ratio.



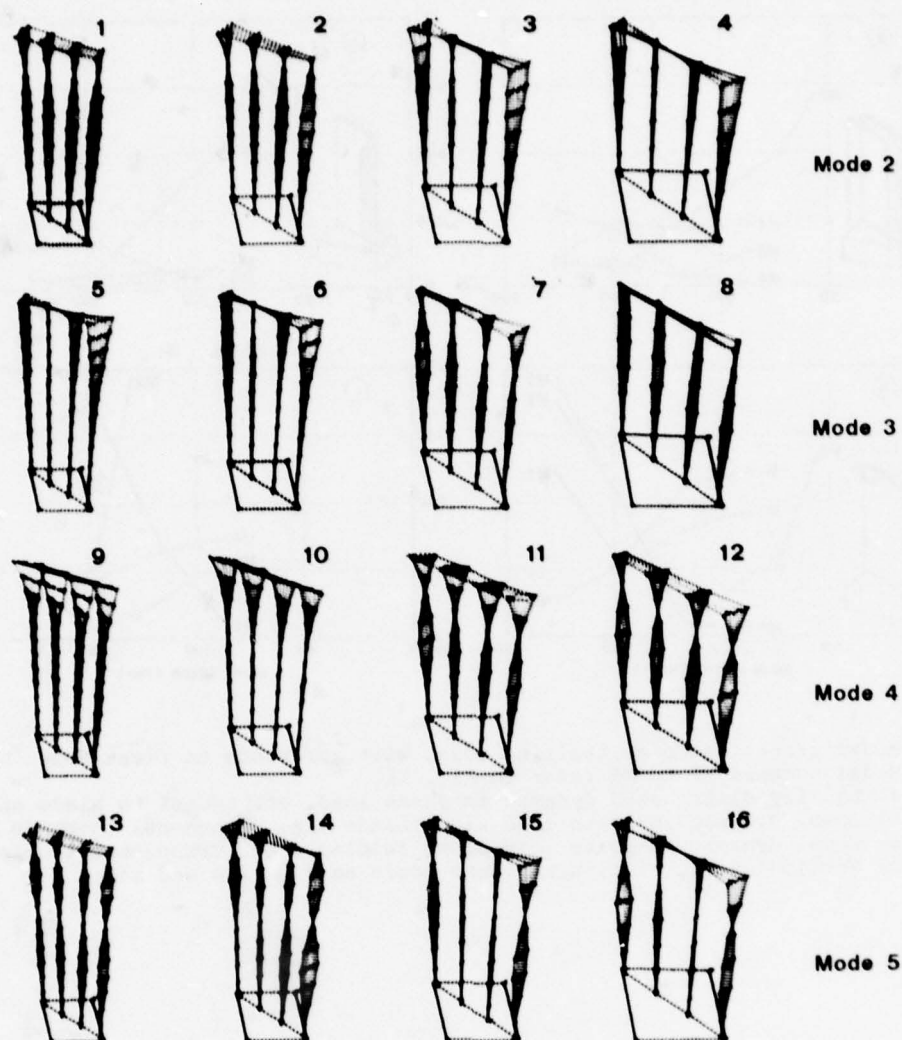


Fig. 12 Mode shapes. Numbers refer to Fig. 11.

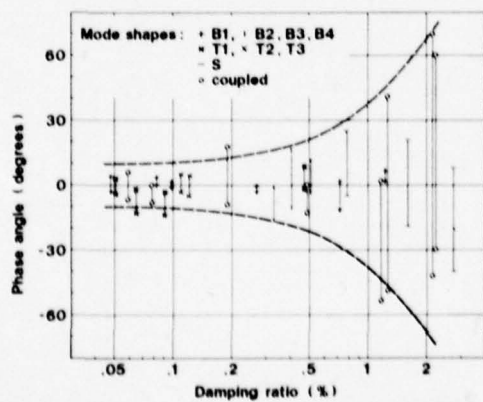


Fig. 13
Range of phase angles of individual modes
as a function of the damping ratio.
B = bending mode
T = torsional mode
S = edgewise mode

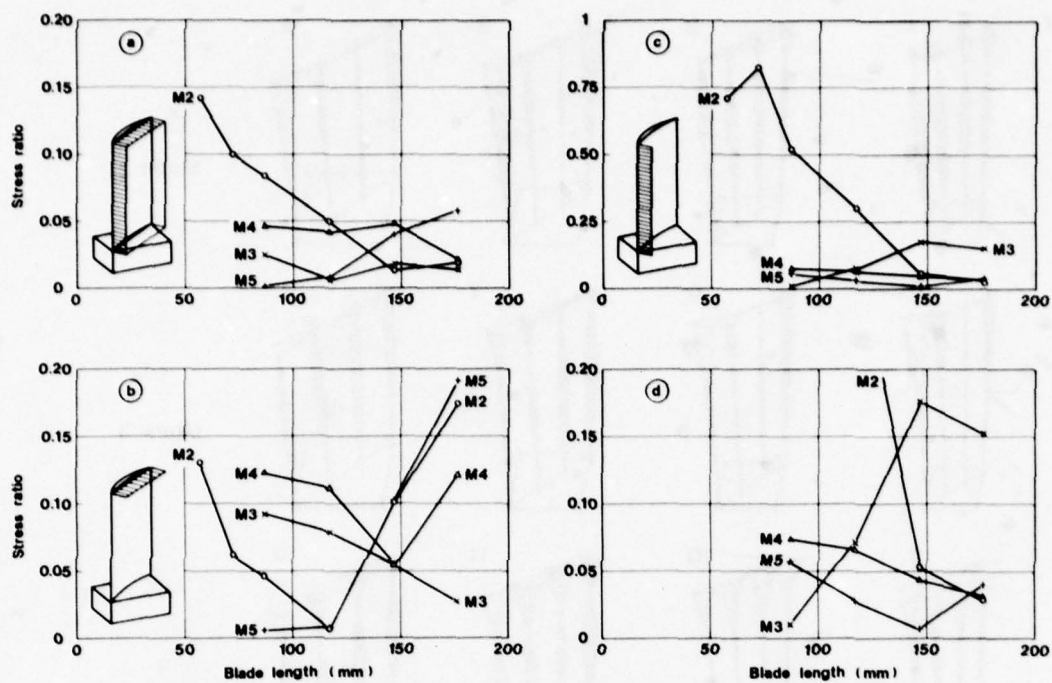


Fig. 14

Modal stress ratio at trailing edge, with reference to first mode.
Modal numbers M2 to M5 refer to Fig. 11.

- a) Equally distributed dynamic in-phase load, orthogonal to blade chord
- b) Equal dynamic in-phase load along blade tip, orthogonal to blade chord
- c) Equal dynamic in-phase load along leading edge, orthogonal to blade chord
- d) Section of Fig. 14c, using same scale as Fig. 14a and 14b.

DISCUSSION

E.K.Armstrong, UK

I should like to enquire further about the method excitation to obtain the response in the direction of the blade chords. Were any special precautions taken and how was the data obtained for the point along the blade chord?

Author's Reply

No extra precautions were taken for the excitation in the chord direction other than special care and some experience on the part of the operator. It is important to maintain a good coherence function. For twisted blades a cylindrical coordinate system is used in order to keep the excitation in the chord direction over the entire blade height. Excitation is done only at the stiffer edge, the remaining points along the chord being assigned the same transfer function.

R.Holmes, UK

I would like to congratulate the authors on an excellent paper and to ask the following question. Does the nature of a compressor blade preclude the use of contact methods of excitation such as PRBS testing, which should theoretically give a fuller frequency spectrum in the excitation?

Author's Reply

For the small lightweight blades which were tested mechanical attachments would seriously distort the mode shape especially the higher ones. It is recognized that excitation methods other than impulses can lead to more accurate transfer functions and should indeed be used if possible. Excitation methods which require mechanical attachments however are usually more time-consuming and thus the simple excitation with hammers may be justified for modal surveys even for large structures.

ROTOR BURST PROTECTION: DESIGN GUIDELINES FOR CONTAINMENT

James T. Salvino - Aerospace Engineer
 Gaetan J. Mangano - Aerospace Engineer
 Robert A. DeLucia - Mechanical Engineer
 Naval Air Propulsion Center
 Research & Technology Division
 Trenton, New Jersey 08628

ABSTRACT

Presented are the results of tests that were conducted to develop guidelines for the weight optimum design of turbine rotor burst fragment containment rings. The ring materials used for each of the several ring configurations were Kevlar 29 cloth, centrifugally cast 4130 steel and coiled 304 stainless steel.

A comparative assessment of the containment capability for each material is provided in terms of a specific energy variable that was developed for this purpose. Also included in this assessment is the effect of the number of equal pie sector shaped fragments on the ring containment capability.

SUMMARY

Presented are the results of systematic experimentation conducted to provide design guidelines for turbine rotor fragment containment rings. The experiments consisted of a series of rotor burst containment tests in which rotors of two different diameters were modified to ensure burst at their respective design speed into various numbers (2, 3 and 6) of pie-sector fragments. These fragments, for the base design evaluation, impacted rings made from 4130 cast steel that concentrically encircle the rotors at a radial clearance of 0.5 inches. The ring axial lengths were varied in three steps of 0.5, 1 and 2 times the axial length of the rotors and their radial thickness was varied until fragment containment was achieved. Explanation of the data illustrates how the experimental results could be used by designers to determine the size and weight ring required to contain the fragments of a particular rotor. In addition, a comparison is made between the containment capability of cast 4130 steel rings and rings made from Kevlar 29 cloth and coiled 304 stainless steel.

SYMBOLS

SCFE	specific contained fragment energy
R_i	containment ring inner radius, in; m
KE _R	kinetic energy of rotor at burst, in-lb; J
ρ	ring material density, lb/in ³ ; kg/m ³
L _{RG}	containment ring axial length, in; m
L _{RT}	rotor rim axial length, in; m
W_R	containment ring weight, lb; kg
t	ring radial thickness
t^1	ring radial thickness required for containment, in; m
ALR	containment ring to rotor axial length ratio
NF	number of fragments
ID _R	inside diameter of containment ring, in; m

INTRODUCTION

The Rotor Burst Protection Program (RBPP) is sponsored by the National Aeronautics and Space Administration (NASA) and conducted by the Naval Air Propulsion Center (NAPC) in conjunction with the Massachusetts Institute of Technology (MIT). The objective of the program is to develop guidelines for the design of lightweight devices that can be used on aircraft to protect passengers and the aircraft structure from the fragments of failed gas turbine engine rotating components.

SPIN FACILITY DESCRIPTION

The experimental testing to support this program is being conducted in the NAPC Rotor Spin Facility shown in figure 1. The facility has two spin chambers; the smaller of which can accommodate rotors up to 40 inches (1.02m) in diameter and has a working height of 32 inches (0.813m). The larger chamber, which was used for the effort described in this paper, is comprised of a heavy walled (1 inch thick) vacuum vessel that is protected by a 5-inch thick laminated steel inner liner. The working space, within the inner liner, is 10 feet (3.05m) in diameter with a height of 6 feet (1.83m). It was designed to accommodate rotors of the largest aircraft engines and has access ports for optical and electrical instrumentation. In a typical test situation the rotor/blade to be intentionally failed is suspended vertically from an air turbine drive motor which mounts on the chamber lid as shown in figure 2. A family of air turbine drive motors are available to produce rotor speeds up to 150,000 rpm (15,700 rad/s). To minimize the power required to accelerate the rotors to failure, the test chamber is evacuated during test to produce a vacuum of approximately 10mm Hg.

The high-speed photo system, which documents the failure mechanics, is comprised of a continuous framing camera and photo lighting unit. The camera is capable of producing 225 sequential pictures at a framing rate of 35,000 frames per second. The lighting unit has an output of 12 million beam candlepower. These are just a few of the unique features of the facility.

PROGRAM DESCRIPTION

A test program was established to develop empirical guidelines for the design of minimum weight turbine rotor fragment containment rings made from various materials. This paper reports on the testing conducted to develop the empirical relationships and design guidelines using cast 4130 steel as a baseline and presents the comparative containment capability of coiled 304 stainless steel and Kevlar 29 cloth.

Empirical design guidelines were developed by experimentally establishing the relationship between a variable that provides a measure of a ring's capability to contain fragments and several other variables that provide the configurational characteristics of the rotor fragments and containment ring. Prior exploratory testing identified those variables which had a significant influence on the containment process and identified a variable that could be used as a measure of containment ring capability.

The variable that provided this measure of containment ring capability was termed the Specific Contained Fragment Energy (SCFE) and was derived, by dividing the rotor's kinetic energy at burst by the ring weight which will contain this energy ($SCFE = KE_R \div W_R$).

The four ring and rotor characteristics chosen for test because of their suspected influence on the containment process and the range of each of these variables are listed below:

- a. The ring inner diameter (ID_R). Two diameters, one approximately twice as large as the other (31.64 inches (0.804m) and 15 inches (0.381m)) were used for test with rotors having correspondingly larger and smaller tip to tip diameters (the CW J65 and GE T58 engine turbine rotors having tip to tip diameters of 30.64 inches (0.778 m) and 14 inches (0.356 m) respectively). The burst energies of these rotors at their nominal designed operating speed were 10^7 and 10^6 in-lbs (35100 J and 3510 J) for the larger and smaller rotor, respectively. For each size rotor the fragment energy was held constant, from test to test, by holding speed constant and only varying the number of fragments generated.
- b. The ring axial length (LRG). Three lengths were used that corresponded to 0.5, 1 and 2 times the rim axial lengths of the large and small rotors which were nominally 1.25 and 1 inch (0.032 m and 0.0254 m), respectively.
- c. The number of rotor fragments generated at burst (NF). The rotors were modified to fail at their respective design operating speeds of 8,500 rpm (890 rad/s) for the J65 rotor and 20,000 rpm (2094 rad/s) for the T58 rotor and to produce 6, 3 or 2 pie-sector fragments.
- d. The ring radial thickness (t). The ring thickness was varied until fragment containment was achieved for the different combinations of ring inner diameter; ring axial length; and number of rotor fragments.

The resultant test matrix is shown in figure 3; and the procedure for ring thickness variation to achieve containment is shown schematically in figure 4.

Other variables which would, in some way, influence the magnitude and orientation of the forces that create the deformations and displacements of the ring and rotor fragments, and therefore affect the containment process are as follows:

- a. The mechanical properties of the rotor and ring materials.
- b. The fragment velocities.
- c. The fragment masses and mass distributions.
- d. The rotor-to-ring radial tip clearance.
- e. The rotor tip-to-hub diameter or radius ratio.

Although these factors would significantly influence the containment process, with the exception of the ring material used for containment, the variability of these factors, as a function of rotor size, is constrained within relatively narrow limits by the dictates of the "real world" acceptability of the rotor aerothermal and structural design. For all practical purposes then, for a given rotor size, these factors would be essentially invariable and the results generated by the experiments conducted would be generally applicable to all turbines as a function of rotor size. This would be so because the experimental scheme presented incorporates, either purposely through the variables of test or inherently because actual rotors are used, all of the factors that could (with the exception of ring material properties) significantly influence the rotor fragment containment process.

Although the mechanical properties of the materials used to make a containment ring can vary widely and are considered to be important factors in containment ring design, the ring material used for the development of empirical design guidelines was the same from one test to another. Cast 4130 steel was chosen because it was readily available in the centrifugally cast form which simplified fabrication of the rings into various radial thicknesses and axial lengths. Using this material as a baseline allowed the establishment of the effects of other variables on the containment process exclusive of material influences and once these effects were firmly established an assessment of the influence of various ring materials were explored.

DESIGN GUIDELINES SYNTHESIS

The functional relationship between the dependent (SCFE) and independent variables (ALR, NF, ID) of test are presented conceptually in figure 5. Once these relationships are established through test, they provide the information needed to design an optimum weight ring for a turbine rotor fragment containment application. Given these relationships, the procedure would be as follows:

a. Three basic things would have to be known about the rotor to proceed with the design analysis:

- (1) The kinetic energy (KE_R) of the rotor at burst.
- (2) The rotor tip diameter (ID_R).
- (3) The rotor rim axial length (L_{RT}).

These are characteristics that are usually known or can be easily calculated by a designer.

b. The relationships between the SCFE, the number of fragments, and rotor diameter, for constant ratios of ring to rotor rim axial length, provide the information needed to design the lightest weight ring required to contain a particular type failure. For a given analysis, this value of SCFE would be obtained from the curves in figure 5 (or equations derived from regression analyses of the data points developed through test) for the size rotor being considered; the number of rotor fragments that result in producing the most adverse containment condition with respect to the weight of ring (the lowest SCFE value in the SCFE-NF plane); and the optimum ring to rotor rim axial length ratio ($L_{RG}/L_{RT} = ALR$), which is represented by the highest contour line. The SCFE value that is obtained by this exercise is divided into the total anticipated energy of the rotor to yield the optimum (lowest) weight steel ring that will be required to contain the fragments. This procedure is expressed in equation (1).

$$W_t = \frac{KE_R}{SCFE} \quad (1)$$

The weight so derived is then used in the following equation (2) which expresses the thickness of ring required for containment as a function of all other known dimensional variables.

$$t^1 = \left[R_i^2 + \frac{W_t}{\rho \pi L_{RG}} \right]^{1/2} - R_i \quad (2)$$

The value of weight derived in equation (1) can be substituted in equation (2) to yield perhaps a more useful form:

$$t^1 = \left[R_i^2 + \frac{KE_R}{\rho \pi L_{RG} SCFE} \right]^{1/2} - R_i \quad (2a)$$

where:

Ring inner radius (R_i) for practical considerations, equals the rotor tip radius because rotor-to-casing operational clearances and considerations of minimum ring weight both dictate that the ring and rotor radius be almost equal.

The ring axial length (L_{RG}) is calculated by the multiplication of the optimum axial length ratio (ALR , value of the highest contour in figure 5) and the rotor rim axial length L_{RT} .

c. This data synthesis and design analysis would provide the lightest weight ring configuration (ID , radial thickness, and axial length) that would be needed to contain the fragments generated by a turbine rotor burst of known size and energy. The analysis is generally applicable to axial flow turbines used in aircraft gas turbine engines.

TEST PROCEDURES

The test set-up and procedures were basically the same for each test conducted: Rings being evaluated for their containment capability, as measured by the SCFE, were supported between rigid steel plates and positioned so that they concentrically encircled rotors that were vertically suspended (plane of rotation horizontal) in the spin chamber from the output shaft of the air turbine motor used to spin the rotors to their burst speed. The steel plates were used to prevent the fragment from escaping over the sides of containment rings, simulating real engine operational conditions where the rotating components are bounded by stator vanes. This set-up is shown in figure 2. The radial tip clearance between the rotor and ring was maintained at 0.50 inch (1.27 cm). The two different size rotors described previously were modified, as shown in figure 6, to ensure failure in 2, 3 and 6 pie-sector shaped fragments at their nominal operating design speeds.

During test, the spin chamber was evacuated to a vacuum pressure of 10mm Hg to minimize the drive power required to accelerate the rotors to burst speed.

METHODS OF ANALYSIS

Because of the nature of the test program conducted, the analysis of results was relatively straight forward; it depended on two things:

- a. Whether or not the ring being subjected to test contained the rotor fragments generated. (Contained means that the fragments did not pass through or escape from the confines of the containment ring).
- b. and if it did contain, what was the associated ring SCFE (by definition no SCFE could be derived for a ring that did not contain the fragments).

The rotor burst energy from test-to-test, was held constant as a function of rotor size. However, variations in burst energy for a given rotor size did occur during test because of small unpredictable variations in rotor burst speed. These variations stemmed from such factors as: material property scatter; dimensional tolerance differences; flaws or cracks (scrap turbine rotors from high time military engines were used); and other such inherent and induced rotor-to-rotor anomalies. To account for these "experimental" variations in analyzing the burst test results, a policy was adopted whereby results which had a speed variation greater than $\pm 2.5\%$ of the design burst speed were not used for the assessment of a ring's SCFE.

The other element beside speed that established the rotor energy at burst was the mass moment of inertia of the two turbine rotors used for test. The values of inertia for each rotor were determined experimentally using the torsional pendulum method (reference 3).

RESULTS AND DISCUSSION

The results of test are presented in plotted form in figures 7, 8, 9, 15, and 16. These plots are actually plane sections of the conceptual three dimensional (variable) plot shown in figure 5, but in these instances using the test data developed. The intent here is to show the functional relationship between the SCFE and the significant test variables: ring inner diameter (ID_R); number of fragments (NF); and ring axial length (ALR).

a. SCFE - NF Relationship for Small Rotors; Figure 7. It can be seen from these curves that for small rotor containment the SCFE is for all practical purposes independent of the number of pie-sector shaped fragments generated at burst. This indicates that rings of the same weight would be required for containment regardless of the number of fragments generated at rotor burst in the range of from 2 to 6 fragments and having a total (translational and rotational) energy content of approximately 10^6 in-lbs (3510J). A corollary of this would be that a worst fragment number condition for small rotor containment with respect to ring weight does not exist.

b. SCFE - ALR Relationship for Small Rotors; Figure 8. The relationship shown in this figure indicates that an optimum value for ring axial length exists. For the size rotor tested, an optimum lightweight ring for containment is derived when the axial length of the ring is made equal to that of the rotor; that is where $ALR = 1$.

c. SCFE - ID Relationship for 2, 3, and 6 Fragment Bursts at $ALR = 1$; Figure 9. These relationships are incompletely documented except for the 6-fragment data because the radial thickness required for large rotor containment of the 2 and 3-fragment bursts exceeded that which was available from inventory (4130 cast steel circular rings with an ID of 31.64 inches (0.804 m) having a maximum radial thickness of 4.1875 inches (.106 m) and weighting 169 lbs.). However, the relationship shown in figure 9 does indicate that the amount of fragment energy that a pound of ring material can contain decreases with the rotor size (energy content); that is, for the same ring to rotor axial length ratio, ring material, and number of fragments generated at burst, the containment capability of the larger ring, as measured by the SCFE (on a contained energy per unit weight basis) is lower than for a small ring. This indicates that the practice of extrapolating small rotor containment ring results to large rotor containment ring applications would be invalid.

d. SCFE - NF Relationship for Large Rotor Containment at $ALR = 1$; Figure 15. The relationship in this figure, though not definitive because containment was not achieved for the 2 and 3 fragment burst, indicates that the SCFE is dependent on the number of fragments (NF) generated at burst. This differs from the small rotor results, which indicated that the SCFE and NF were almost independent. The trend of this relationship indicates that the capability of a ring to contain increases as the number of fragments generated increases or, conversely, as the number of fragments generated at burst decreases the containment situation with respect to ring weight becomes more adverse, i.e., more weight is required.

e. SCFE - ALR Relationship for Large Rotor Containment of 2-Fragment Bursts; Figure 16. Only limited tests were conducted to explore this relationship because trends indicated that the weights of ring required for containment were becoming very high. Figure 16 tends to show that an optimum axial length might exist in the neighborhood of $ALR = 1$. This is consistent with the results of the small rotor results, which because of the abundance of test data, was more conclusive in indicating an optimum $ALR = 1$.

COMPARISON BETWEEN CONTAINMENT RING DEFORMATION

To provide some feel for the ring and fragment distortions that normally accompany the containment process, the post-test conditions of rings and rotors from several selected tests (both contained and uncontained) are shown photographically in figures 10 through 14.

In addition, figure 17 shows high-speed photographic results that depict the mechanics of large and small rotor containment in which a 3-fragment rotor burst is involved. It can be seen from these visual data that the gross deformations and displacements experienced by the steel rings in a general sense are basically the same and therefore independent of size. On the basis of this data, it was concluded that a valid functional relationship between SCFE and rotor diameter/ring ID might be experimentally derived and be generally applicable.

MATERIAL COMPARISON TEST RESULTS

Exploratory tests (3 fragment burst) were conducted to assess the containment capability of coiled 304 stainless steel and Kevlar 29 cloth rings for large rotors as compared to centrifugally cast 4130 steel rings previously discussed. The comparison is made using a 330 lb (150 kg) 4130 cast steel ring (could not contain 2 or 3 fragments) as the base line weight knowing that a heavier 4130 steel ring is required to contain three fragments. It was decided to limit 4130 to this weight since it would not only be considerably expensive to purchase larger material for test but impractical, since 330 lbs is already

considered too heavy for aircraft use. Since a successful containment using 4130 cast steel was achieved on a 6 fragment burst, it was used in figure 18 to show the overall trend that exists between the SCFE-ID, for this material. In order to further define this trend additional 6 fragment data is required for all materials tested.

COILED STAINLESS STEEL RINGS

The coiled rings consisted of one continuous spiral of 304 stainless steel strip .048 inch (0.001 m) thick wrapped like a clock spring. Three fragment burst tests were conducted to evaluate the coiled 304 stainless steel ring which had axial lengths of 2.5 inches (0.063 m) and 3.75 inches (0.095 m). No containments were achieved using the coiled rings having a 2.5 inch (0.095 m) axial length. A ring weighing 165 lbs (75 kg) and having an axial length of 3.75 inches (0.095 m) was required to contain a large rotor 3-fragment burst. This 165 lb ring represents a weight reduction over a 4130 cast steel ring of at least 50% and is equivalent to the weight of 4130 steel required to contain a 6-fragment burst.

KEVLAR RINGS

The Kevlar rings for the large rotors, had axial lengths of 9 inches (0.23 m) and 12 inches (0.31 m). The rings were made extra wide to prevent the fragments from escaping over the sides since cloth rings lack structural rigidity in the axial direction. A Kevlar ring which had an axial length of 9 inches (0.23 m) and weighted 57 lbs (26 kg) was the optimum configuration tested that contained a 3-fragment burst. Tests were also conducted with small rotors using Kevlar 29 cloth rings having an axial length of 6 inches (0.15 m). A ring weighting 6.7 lbs; 3.0 kg (a weight reduction of 1.9 lbs; 0.863 kg compared to the base-line weight for small 4130 steel rings) was required to contain the 3-fragment burst of a T58 rotor. Axial length optimization of Kevlar rings and the remains affects of number of fragments to be examined.

The results presented graphically in figure 18 and tabulated in Table 1, show that; the containment weight can be reduced using Kevlar 29, by 83% (330 lbs to 57 lbs; 150 kg to 26 kg) and 22% (8.6 lbs to 6.7 lbs; 4.0 kg to 3.0 kg) for large and small rotors respectively.

FUTURE PLANS

The systematic containment experimentation will be continued using multi-layered composite rings. The program is designed to evaluate the containment capability of the composite rings and determine which of the layers or combination of layers has the most significant effect on the containment process.

TABLE I

Material Comparison Results For
3-Fragment Containment of J65 Rotors

Ring Material	SCFE	Ring Wt. (W_R) Lbs. (kg)	% Wt. Reduction
Cast 4130 Steel	29,259	330 (150) uncontained	Base Line
Coiled Stainless Steel	51,847	165 (75)	≥ 50
Kevlar 29	150,461	57 (26)	≥ 83

Material Comparison Results For
3-Fragment Containment of T58 Rotors

Ring Material	SCFE	Ring Wt (W_R) Lbs (kg)	% Wt. Reduction
Cast 4130 Steel	88,444	8.6 (4.0)	Base Line
Kevlar 29	173,717	6.7 (3.0)	22

REFERENCES

1. REPORT - Mangano, G. J., "Rotor Burst Protection Program - Phases VI and VII; Exploratory Experimentation to Provide Data For The Design of Rotor Burst Fragment Containment Rings", Naval Air Propulsion Test Center, NAPTC-AED-1968 of March 1972.
2. REPORT - Martino, A. A. and Mangano, G. J., "Turbine Disk Burst Protection Study", Final Phase II-III Report on Problem Assignment NASA DPR #R105, Naval Air Propulsion Test Center, NAPTC-AEL-1848 of February 1967.
3. TEXT - Freberg, C. R. and Kemler, E. N., "Elements of Mechanical Vibration", John Wiley & Sonce, Inc., New York, 1949 (Page 23).

4. REPORT - Mangano, G. J., Salvino, J. T., and DeLucia, R. A., "Experimentation To Provide Guidelines For The Design Of Turbine Rotor Burst Fragment Containment Rings", Final Report on Problem Assignment NASA DPR C-41581-B Mod. 6, Naval Air Propulsion Test Center, NAPTC-PE-98 of March 1977.

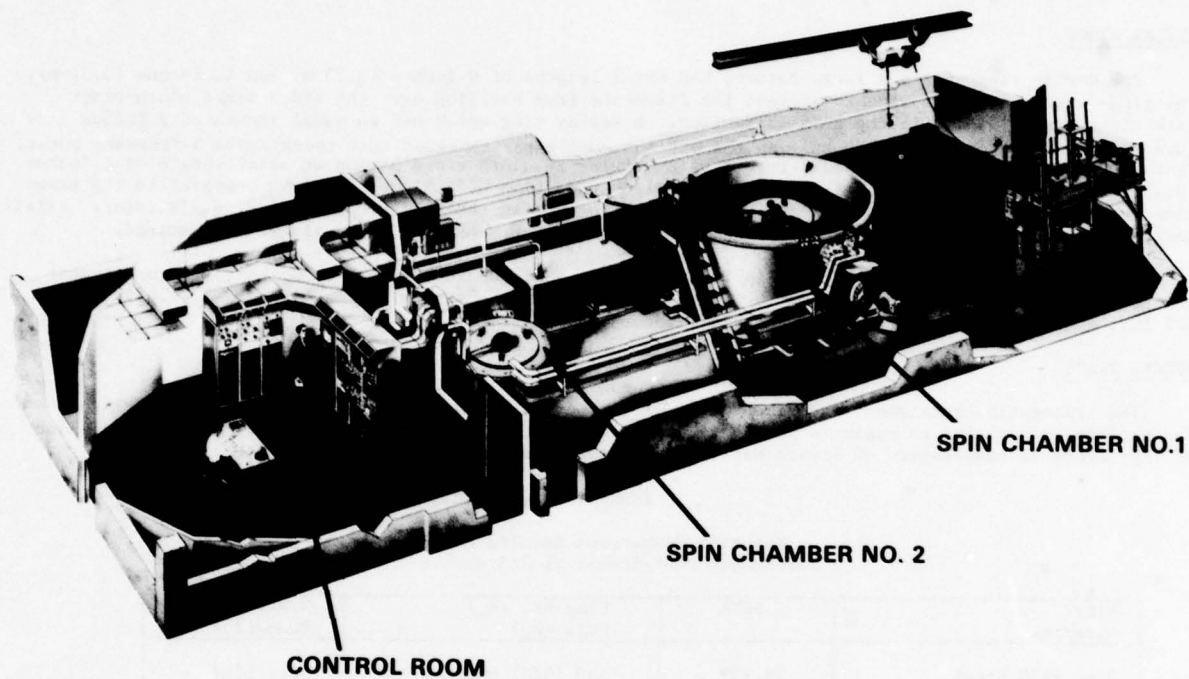


Fig.1 Containment evaluation facility

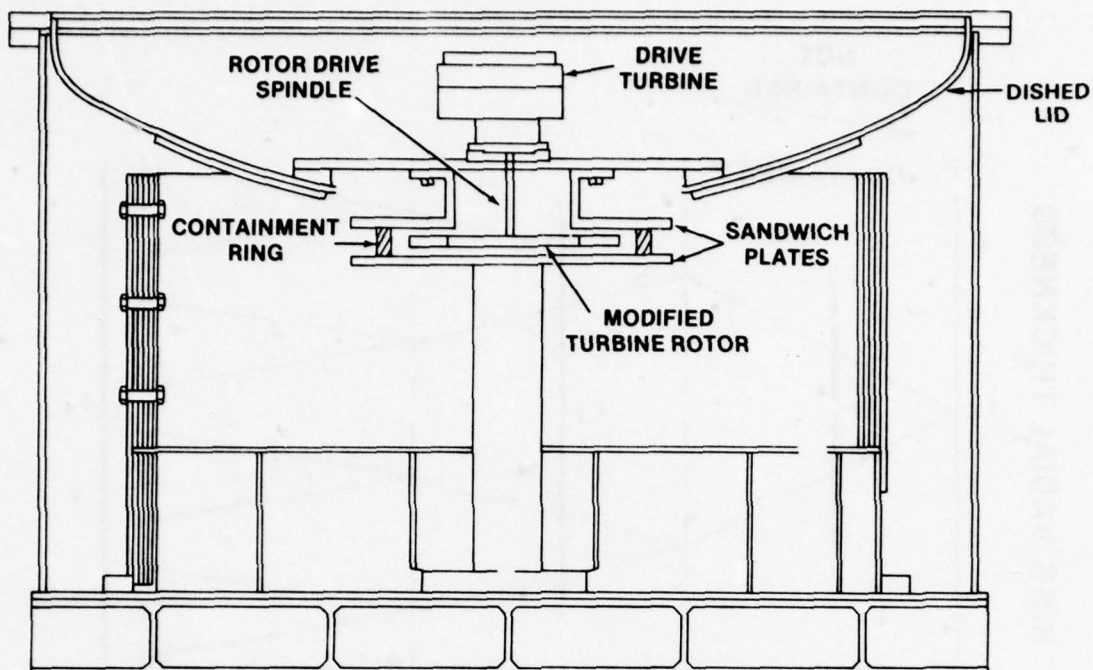


Fig.2 Typical containment test set-up

		ID 15			ID 32		
		NF 2	NF 3	NF 6	NF 2	NF 3	NF 6
ALR 1/2	t ₁						
	t ₂						
	t ₃						
	t ₄						
ALR 1	t ₁						
	t ₂						
	t ₃						
	t ₄						
ALR 2	t ₁						
	t ₂						
	t ₃						
	t ₄						

WHERE: ALR = RING TO ROTOR RIM AXIAL LENGTH RATIO (NUMBER DENOTES RATIO)

ID = RING INNER DIAMETER (SUBSCRIPT DENOTES NOMINAL DIAMETER IN INCHES)

t = RING RADIAL THICKNESS (SUBSCRIPT REFERS TO NO. OF TRIALS TO ESTABLISH CONTAINMENT THICKNESS)

NF = NO. PIE SECTOR SHAPED ROTOR FRAGMENTS (SUBSCRIPT DENOTES NO. FRAGMENTS)

Fig.3 Small/large rotor containment test matrix

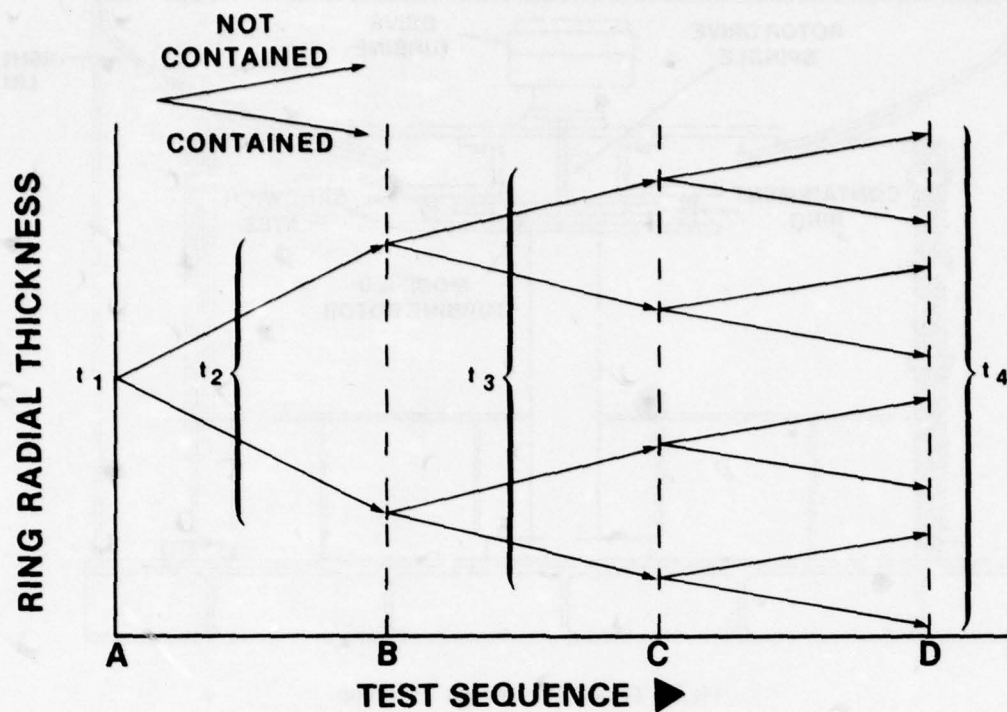


Fig. 4 Ring thickness variation scheme

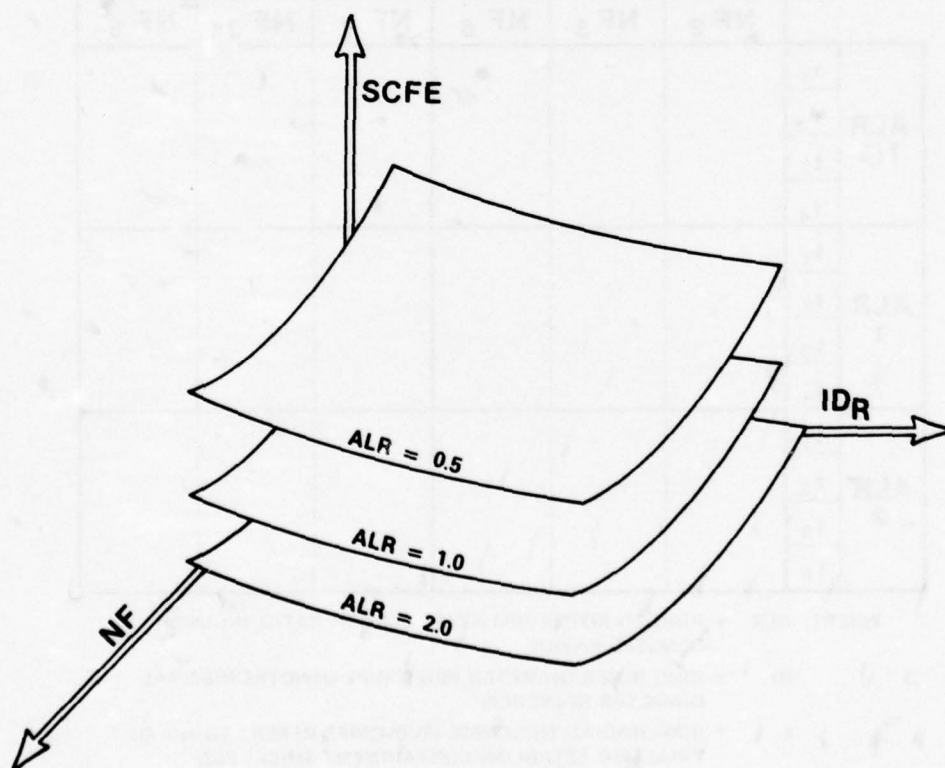
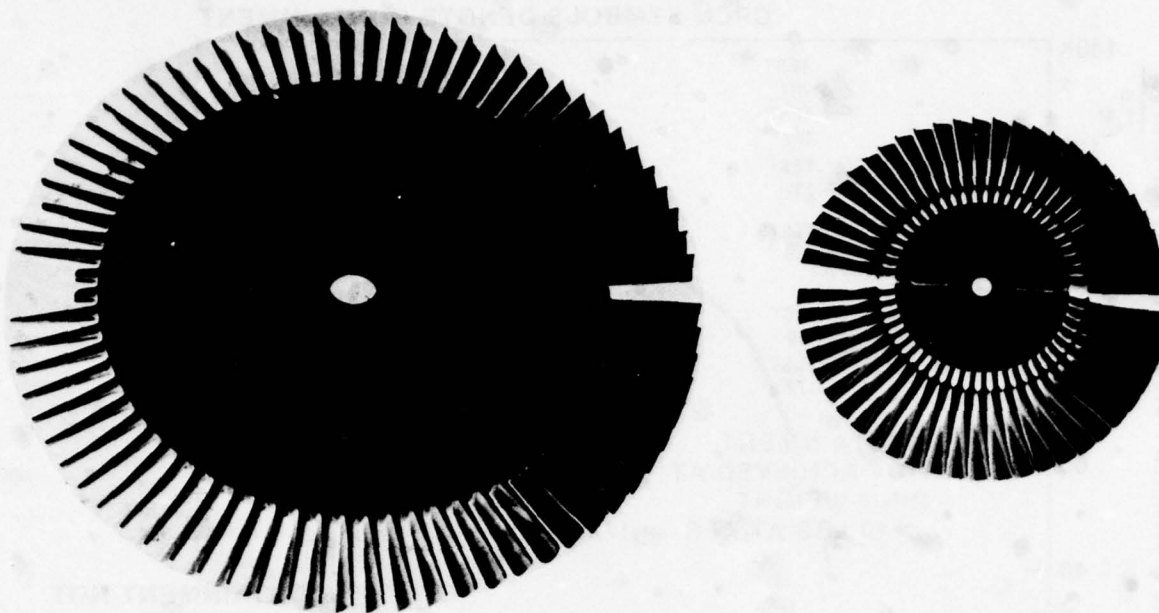


Fig. 5 Conceptual relationships between containment program test variables



J-65 2ND STAGE TURBINE

T-58 POWER TURBINE

Fig.6 Typical rotor modifications for containment tests; 2-fragment burst (NF = 2)

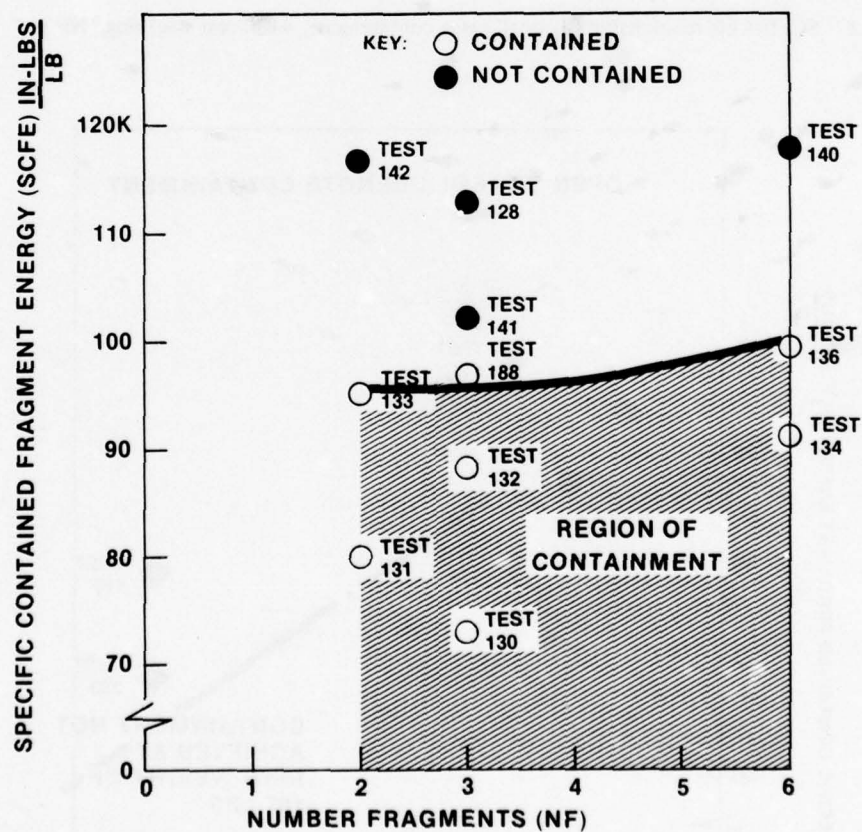


Fig.7 SCFE-NF relationship for small rotor containment; 4130 cast steel ring, ALR = 1

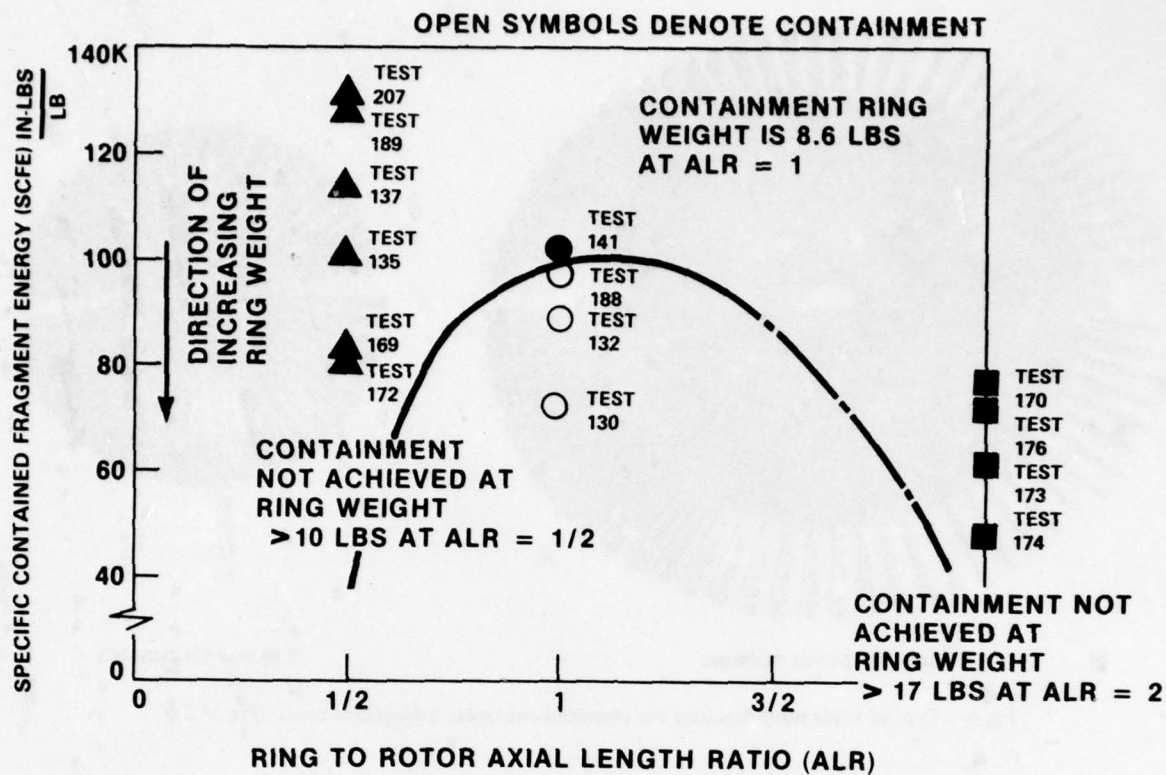


Fig.8 SCFE-ALR relationship for small rotor containment; 4130 cast steel ring, NF = 3

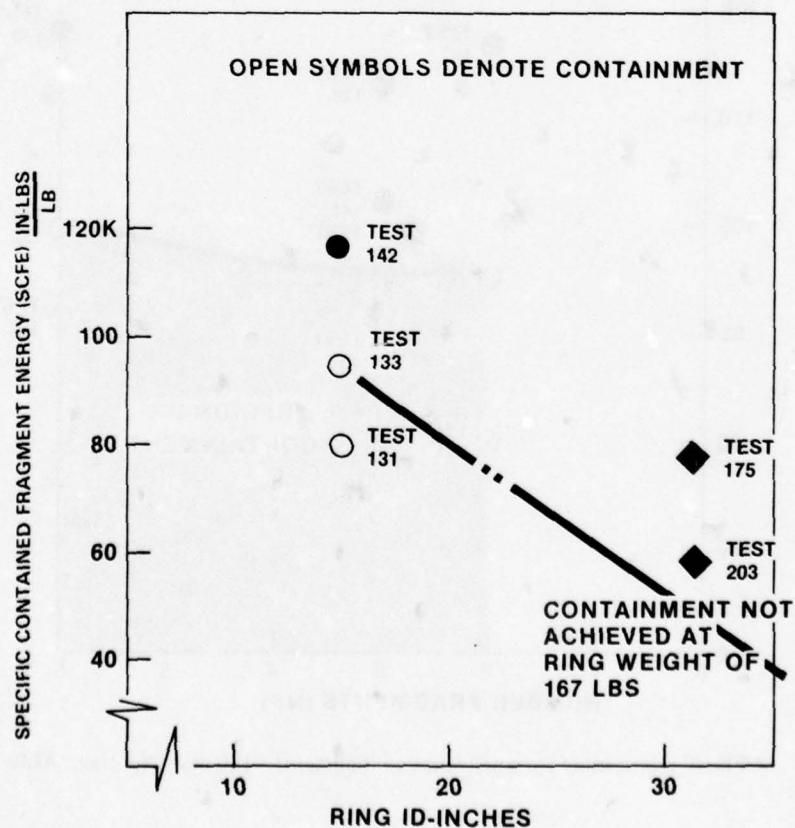


Fig.9 SCFE-ID_R relationship; 4130 cast steel ring where ALR = 1 and NF = 2



Fig. 10 Small rotor 3 fragment containment post test results



Fig. 11 Small rotor 2 fragment containment post test results

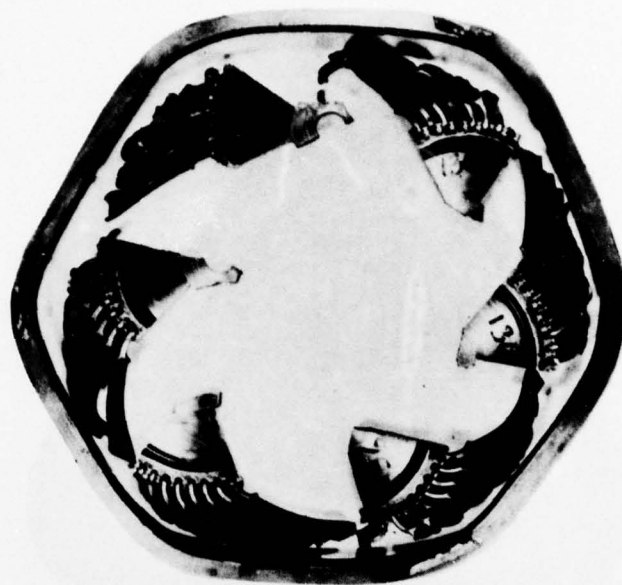


Fig.12 Small rotor 6 fragment containment post test results



Fig.13 Small rotor 2, 3 and 6-fragment containment post test results



Fig.14 Large rotor 2, 3 and 6 fragment containment post test results

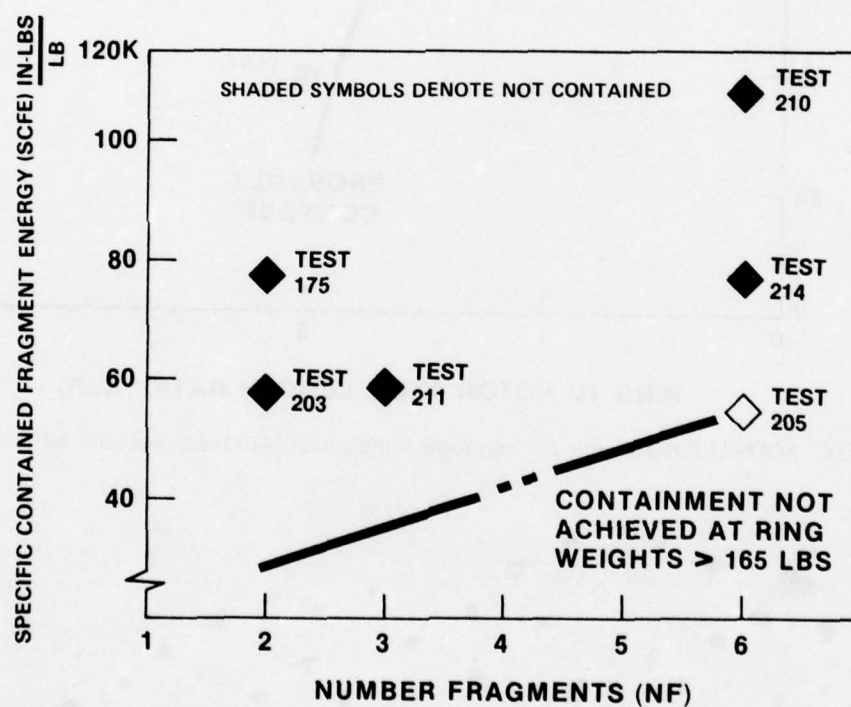


Fig.15 SCFE-NF relationship for large rotor containment; 4130 cast steel ring, ALR = 1

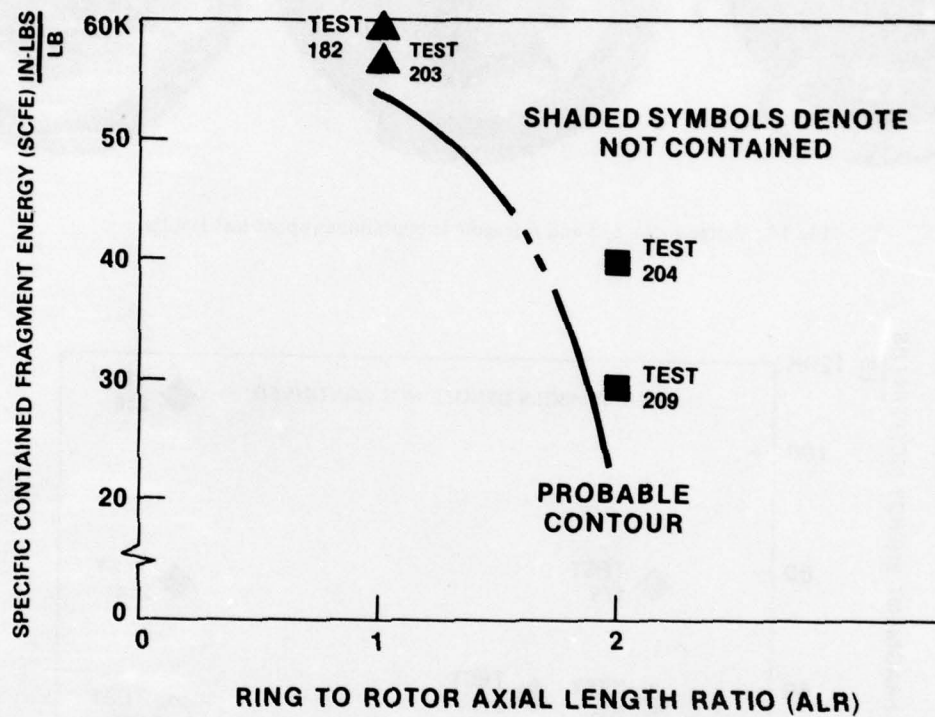
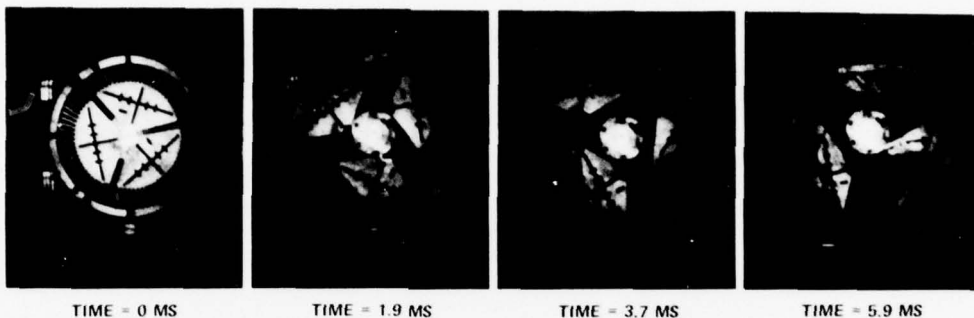


Fig. 16 SCFE-ALR relationship for large rotor containment; 4130 cast steel ring, NF = 2

LARGE ROTOR CONTAINMENT TEST (145)

ROTOR DIA:
30.6 IN.
BURST SPEED:
6311 RPM
FRAMING RATE:
15320 PPS



SMALL ROTOR CONTAINMENT TEST (67)

ROTOR DIA:
14.0 IN.
BURST SPEED:
18829 RPM
FRAMING RATE:
14821 PPS

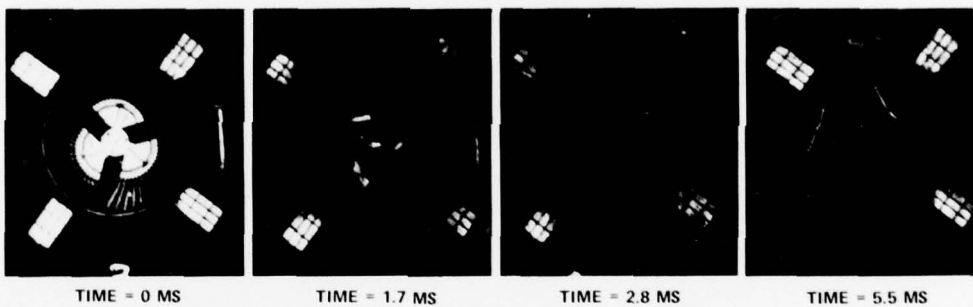
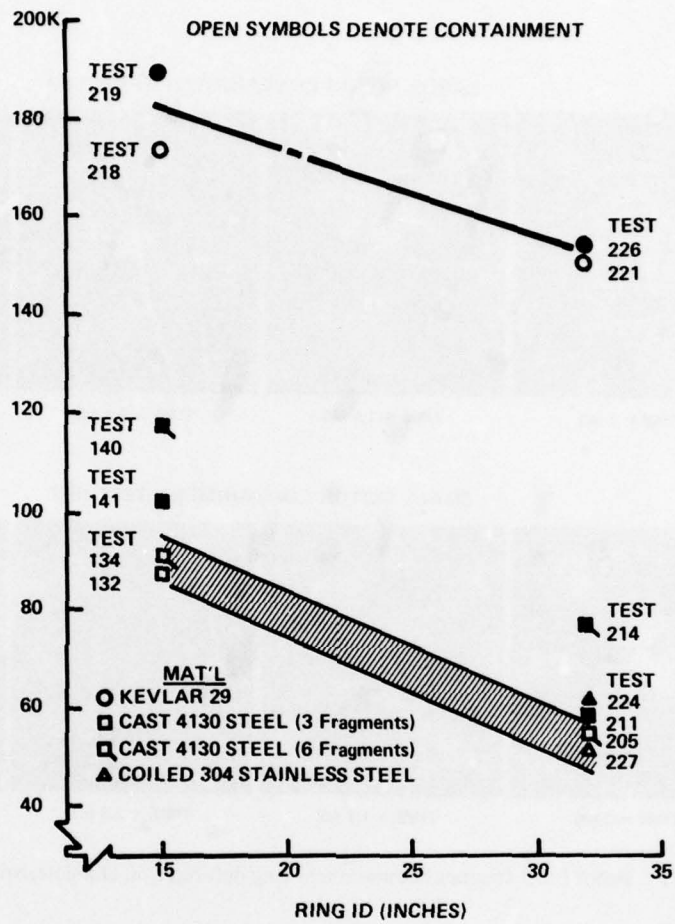


Fig.17 Rotor burst fragment containment ring deformation characteristics

Fig.18 SCFE-ID_R relationship

Engine/Aircraft Structural Integration
An Overview
by

T. E. Dunning, Stress Research Chief
M. N. Aarnes, Propulsion Specialist
G. L. Bailey, Structures Specialist
The Boeing Company
P.O. Box 3999
Seattle, Washington 98124

SUMMARY

In commercial aviation today, fuel accounts for roughly 80% of the propulsion system-related expenses and about 40% of the total airplane operational cost. According to industry statistics, the airlines consumed over 10 billion gallons of fuel last year and most likely will exceed 15 billion by the mid-eighties. By the end of this decade 75% of this fuel will be used by current high bypass ratio engines.

These high bypass ratio engines run most of their lives with specific fuel consumption (SFC) deterioration exceeding 3%. Boeing, experiencing this problem on the 747/JT9D, launched a Propulsion System and Airframe Structural Integration Program (PANSIP) to study the effects of airplane flight loads on rotor clearances which directly impact SFC and engine life. This early work indicated that a savings of at least 1% in SFC could be realized by a well planned engine-airframe structural integration.

Structural integration as discussed in this paper is a systematic approach to the structural installation of an engine in an airplane. It is a formally planned program by the two manufacturers. It requires agreeing on structural modeling techniques, building a computerized data base, jointly performing the overlapping analyses, and planning the propulsion system testing. Most of the tools for a successful integration program are available today and have been used to varying degrees. However, as yet there has been no complete, scheduled PANSIP effort for a major airplane program.

This paper will point out some of the previous engine installation problems and will discuss current efforts concerning deficiencies of today's installations and the role of PANSIP in future installations.

BACKGROUND

Airplane manufacturers must carefully study the engine options and start working with the engine manufacturer long before the launching of any airplane program. Historically, these studies and the interface coordination were limited to basic engine/airframe performance matching. Recently we have come to realize that the lack of concentrated effort on structural integration has resulted in two distinct problems: structural deficiencies which show up dramatically just before or soon after introduction into service and higher than anticipated operating costs due to increased fuel burn and premature maintenance.

A few examples of engine structural problems will be discussed involving the 747/JT9D, DC10/CF6, SST/GE4 and the L1011/RB211. Although each of these involves commercial airplanes with high bypass engines, similar examples could be found in military arena also.

The 747/JT9D program initially suffered airplane delivery schedule slide due to engine installation problems discovered late in the development phase as discussed in Reference 1. Substantial engine case ovalization occurred which caused excessive rotor clearances and high specific fuel consumption. The problem was solved by modifying the engine mount configuration with the help of a sophisticated finite element analysis of the engine and backup testing. At that time this analysis was an advancement in the state of the art of engine/airframe integration which had previously relied heavily on the build and test approach.

The DC-10/CF6 program met their initial delivery schedules, however, the operational flight environment produced engine structural surprises not found on the engine test stand (References 2 and 3). These problems were promptly solved by General Electric by increasing seal clearances and changing booster liner material. A better understanding of the aircraft's operational load environment and resulting engine internal deflections could have led to better clearance control in the engine development phase and precluded the need for the extra effort expended by General Electric.

The SST/GE4 posed a unique propulsion system in that the engine was only one-third of the total 40 foot nacelle length. Its first bending frequency when calculated late in the program, turned out to have a coincidental frequency with the cantilevered wing support beam. This was a real concern since engine case deflections due to vibrations and flight loads were still to be determined. If this program had continued it would have had an engine/propulsion system/airframe structural integration problem of the most challenging magnitude.

The L1011/RB211 experienced problems soon after introduction into service when cracking occurred in the titanium fan disks (Reference 4). This caused a serious disruption of airline operations and only through international engine community support did a successful disk emerge (Reference 5). Engine airframe structural analysis early in the program might have significantly reduced the magnitude of the problem.

To get a better perspective of operating cost, Figure 1 shows a breakdown of airplane cost in general. Even though the engines seem small in comparison to the airframe, they account for roughly 50% of the operational cost of a wide-body aircraft. Further, it can be noted that fuel is about 40% of the airplane's operational cost and roughly 80% of the propulsion system-related expense. According to industry statistics as depicted in Figure 2, the airlines consumed over 10 billion gallons of fuel last year and most likely will exceed 15 billion by the mid-80s (Reference 6). By the end of this decade 75% of this fuel will be used by current high bypass engines.

Since fuel constitutes such a large part of the airplanes' operational cost, it is well worthwhile to look at fuel prices over the years. This trend delineated in Figure 3 shows that since 1972, domestic jet fuel cost has increased by 235%.

The engine companies being fully aware of the fuel cost trend impact on the operator's profit have made improvements in engine design in general as shown in Figure 4. The possibility exists that the fuel consumption can be halved from the early turbojets by the end of the century by focusing on engine clearance control and engine usage.

Engine airframe structural integration is directly tied to engine fuel consumption as shown in Figure 5. This figure shows typical performance deterioration trends of turbofan engines. Already after 200 to 300 flight cycles a loss of better than 2% in SFC can be expected. This will gradually increase probably by another percent or two until the first high pressure turbine is refurbished which will gain back some of the SFC loss. Module or engine refurbishment philosophy depends on engine and operator.

Research done in this area so far shows that the fuel consumption deterioration is caused to a large extent by the airloads and thermal transients which yield increased clearances in addition to erosion/corrosion of and dirt on airfoils. Hence, engine-airframe structural integration plays a vital part in SFC retention.

Engine maintenance costs are affected by the fact that the engine operates in a deteriorated mode most of the time causing increases in the engine operating temperature. The engine structure must respond to higher working temperatures and higher thermal stress cycles. The net result is more rub and further component life reduction.

Other items of prime importance to any airplane operator is the ease of propulsion system inspection, maintenance, and repairability. For instance, a case in point is shown by Figures 6 and 7. These graphs show actual premature engine removals of the JT9D/747 and CF6/DC10 in United Airline service (Reference 7). These graphs depict basically the success or failure of the propulsion system, not only in terms of maintenance cost, but also in dispatch reliability. It is rather evident that experience and forecast do not match regardless of engine and it seems like rather extensive and expensive engine and/or installation modifications would be needed, before the original promises can be met.

CLEARANCE CONTROL

The common denominator in the problems discussed is clearance control. When the loss of clearance control results in severe rubbing, engine structural damage may occur; when loss of control results in increased tip clearance, SFC deteriorates and maintenance increases. This important design parameter clearance control, will now be considered in more detail.

Figures 8, 9, and 10 shows the relationship between SFC and operating clearances (Reference 8). SFC is inversely related to efficiency as shown in Figure 8. As a rule of thumb for wide-body aircraft today, a 1% decrease in high pressure turbine efficiency amounts to a 1% increase in SFC. Efficiency is inversely related to clearance as shown in Figure 9. The figures also point out that not all engines have the same clearance sensitivity. For instance, the F101 and CFM56 engines require extra care in mounting and operation and to avoid high efficiency losses. Airframe operating clearances for the JT9D and CF6 high pressure turbines are shown in Figure 10. The figure also illustrates one of the reasons why lower aspect ratio blades are desirable.

Since rotor clearance control is such a major source of airplane fuel economy, there is a need to minimize and retain the average clearance throughout the engine.

A balanced clearance design must provide tight average clearance at all operating conditions. And to accomplish such a design, many conflicting considerations must be taken into account during the trade study and followup testing. The availability of exact mission and engine usage as well as concept of installation from the airplane manufacturers at this point in time is of paramount importance.

For instance, it is important to note that as the net output of the thermodynamic cycle is decreased, such as at low power conditions and flight idle, the influence of component performance on cycle efficiency increases. Since operating speeds and temperatures also decrease at part power, turbine clearances may open, reducing component efficiency. It is imperative to consider clearances at part power for those engines where part-power operation is significant.

Another consideration is the rate with which parts heat up or cool down. Specifically, a very heavy turbine rotor or a high radius-ratio compressor disk may not heat to steady state in less than five minutes after throttle advanced to maximum from idle, while casing and shroud supports may reach operating temperatures in the first minute, whereas, combustor and air-cooled turbine airfoils will achieve maximum temperature in less than 10 seconds. This means that at a constant measured turbine discharge temperature, the maximum thrust will build up slowly to the design value and build up rapidly and then drop until steady-state clearances are attained. At constant required thrust, a higher than desirable turbine inlet temperature will result while steady state clearances are achieved. Both conditions are undesirable and can be minimized by good clearance-control designs.

It is of vital importance that the airplane manufacturer recognizes the economic value of the effects of clearance control on performance, durability and SFC so that they can help in achieving a balanced "tight" operating clearance design. In the early stages of design, the engine designer must consider both static and transient growth of rotor versus the stationary parts of the engine in regard to airplane thrust demand. He must consider methods of manufacture, assembly, rotor bearing support locations, rotor dynamics, casing out-of-roundness, etc. All of these are "in house" variables. However, when the engine is installed on the airplane, a host of new variables enter the area of clearance control: enclosure, airplane induced engine maneuver loads, attached structures such as inlets, nozzle and plugs, location of accessory, bleed, etc.

It is a well-known fact that engine casings do bend due to thrust, inlet, and maneuver loads. The nature of the bending deflection curve and localized shell/frame deflections depend on the location of the thrust and other mount points with respect to the engine centerline. High bypass engines are especially subjected to casing deflections due to engine thrust. The thrust mounts are often located far off the centerline because it is convenient in the engine/airplane installation. This causes large shear and bending moments which then deflect the engine static structure. The effect of engine static structure deflection is less on an engine whose rotors are straddle-mounted on frames, rather than overhung rotors and/or rotors riding on "soft" oil damped bearings. Engine case bending is also harmful to rotor dynamic in that it can cause additional rotor eccentricities and bearing misalignment thus causing bowed rotors and rub problems, be it seals or blades.

For the engine companies to perform the above analysis, the airplane manufacturer must carefully study the installation options and mission requirement. He must delineate thrust, altitude, Mach number, total air temperature, and airplane induced engine loads as a function of elapsed flight time in order to determine the true airplane/engine usage criteria. This is depicted in Figure 11. He must further work with the customer and the engine company to determine the anticipated detailed engine usage as shown in Figure 12, from which the engine test cycle can be defined as delineated in Figure 13. Thus, the thermal efficiency and component durability improvement programs can be defined and maintenance cost and SEC estimated. This engine airplane performance and structural integration is sketched out in Figure 13 in terms of development of engine operational cost analysis.

SOURCES OF PROBLEMS

Considering the complexity of the clearance control analysis and the effect of extremely small dimensional changes on performance, it becomes easier to understand how the past installation problems came about.

Problems can result from human error or oversight in engineering, manufacturing and management. These are usually minimized by the use of a checking system where every significant dimension and decision undergoes multiple scrutiny.

Another contributing factor could have been the reluctance of the engine manufacturers share technology with each other. Because of the historically fierce and healthy competition that had grown between these companies, not only was direct communication very much limited but also communication with third parties was restricted to protect trade secrets. While this attitude was laudable in general, it probably slowed the infusion of the more advanced analysis techniques and especially those requiring joint effort with the airframe companies.

While more joint effort and less human error may have alleviated some problems, the new high-bypass engines represented a huge step forward in engine technology and, as such, introduced other problems that probably could not have been anticipated. A whole phase had been omitted in what should have been the proper development of these large power plants. This omission was caused by the birth of the space age.

Starting in 1958, the United States became involved in a competition with Russia to develop space hardware. In most Government agencies which allocated research and development funds the emphasis was on spacecraft, rocket engines, cryogenic tankage, miniaturized electronics and the like. The funds for research in aviation and aircraft engines naturally dried up. Along with a dearth of funds came a scarcity of personnel as the glamour of space exploration lured engineers and scientists from the mundane aircraft industry. All this occurred at a time in history when development work would normally be underway on new power plants of the late 60s. And so the high bypass engines came into being ahead of their state-of-the-art in terms of structures, materials, cooling, clearance control techniques, etc.

ELEMENT OF A PANSIP

By taking into account the things which have contributed to problems in the past and by taking advantage of advancements in analysis techniques, data sharing, and engine testing, it should be possible to formulate a workable propulsion system and airframe structural integration program (PANSIP). A program which will assure the clearance control throughout the airplane operating regime for the life of the engine.

Propulsion System and Airframe Structural Integration Program (PANSIP) in its simplest connotation, is an audit system for ensuring that the components of the propulsion system and related airframe function as a structural unit. In its broadest connotation it is a systematic and scientific work plan for optimizing engine/airframe structural integration from preliminary system sizing, through design development flight test and beyond.

Much of the past difficulty with engine structures, i.e., clearance control and durability can be neutralized by improvements in the process of development, analysis, testing and engine/airframe integration. Consideration must be given to three major factors: (1) a controlled and detailed flow of activity concerned with the structural integrity of the propulsion system, starting with the baseline airplane requirements of propulsion systems and airframe sizing, and carrying through engine/airframe design and development; (2) early recognition of needed technology, testing and data required from other sources (such as airplane induced loads and engine usage), that would be recognized and become part of the detailed flow of activity; and (3) a means of monitoring the system that would allow tightened controls and quick recognition of high risk areas for fast correction.

A PANSIP program must consist of four major elements: the plan, the integrated data base, finite element analysis, and a comprehensive test program.

The Plan

A plan is the necessary first step. It requires recognition on the part of management of each company that the other has something to contribute and something to gain from an early coordinated joint effort. To allow the plan to evolve as has happened in the past is to have no plan. An early selling job must be done to expose all decision makers to the LCC savings that will result from funding a comprehensive PANSIP program.

The plan must span the time from airplane requirements through design and analysis and include the development and certification testing. Even after completion of flight test it will leave behind a tool and a data bank ready to respond to the inevitable question regarding mission changes, airplane growth, and service problems.

The purpose of the plan is to formalize commitments by both companies to generate and update input for the integrated data base and to conduct interrelated analyses. The plan must make provisions for the iterative design process that produces optimum results and feedback from testing to the data bank.

A conceptual layout of a PANSIP is shown in Figure 14. In studying this layout, it should be kept in mind that the final objective is to assure structural integrity and low LCC by thoroughly understanding the loads, stresses and engine clearances which are labeled Engine Airframe Structural Analysis OUTPUT. This is the output from a number of airframe and engine computer programs covering static and dynamic structural analyses and engine performance analysis.

The Integrated Data Base

The integrated data base (IDB) is the second major element of the PANSIP program. It is a computerized compilation of all the data generated by both companies to be used as input for the various engine and airframe analyses. The data is stored in a facility that has a direct computer link with each company.

In the simplest of terms, the IDB would use the computer to store and retrieve the required data. New advancements in what is called the third and fourth generation of the computer, have made this type of data retention another prime function of the computer system. The computer has two other attributes needed for IDB: its capability to do large numbers of operations instantaneously, a feature that facilitates quick access to specific data; and its capacity for accepting highly logical instructions that allows the necessary complexity in the data storage. Putting these all together, using the computers as a repository for great volumes of data in the form of an Integrated Data Base, is today a practical and workable idea.

To meet the requirements of PANSIP and also make the intercompany and interdisciplinary communication possible, the organizations and structuring of the IDB has to be carefully considered. Since the engine/airframe integration is a computerized activity itself, satisfying special storage requirements would become an internal computer activity of the two companies, where the complexities would be handled through known computer techniques. The needs of communication between disciplines and companies would require a simple and straight-forward interaction with the IDB. It is this need that will define the organization of IDB. Because of this, the IDB organization would be selected to correspond to

the logical makeup of the two products--engine and airframe--and the integration of both. As in any computer activity, logical format must be developed to allow the development of computer software and codes that will interact with the framework. One possible organization of IDB is shown in Figure 15.

The Detail Levels (DL) within the proposed IDB can be treated and discussed as two separate entities, namely the Engine Data Base (EDB) and the Airframe Data Base (ADB). However, linked together they form the IDB in PANSIP. For this discussion, DL1 would entail EDB and ADB. The second level, DL2, would contain the key information pertaining to the engine and airplane, followed by DL3, which is the model level. From thereon, as DL descends the details of the model increase to the extent that it goes beyond the scope of this paper.

The IDB organization chart will also be stored in the computer so it can be displayed on the terminal as convenient menu, for depicting the tools used and their chain of command for interaction. It should be noted that the names and amount of data and detail levels need not be known at the inception of the airplane program, as long as it is recognized that the versatility in the shape of the organization and the logic in amount and type of data is maintained.

This would then allow the basic developments of IDB to be applicable to any engine and/or airframe program and would be able to encompass all phases of PANSIP.

Finite Element Analysis

The finite elements analysis is the current state-of-the-art tool for calculating structural deflections and internal loads. This analysis method has been used extensively by the airframe engineers for over 20 years. It has been upgraded and verified by testing until we now have justified confidence in its capabilities. In general its accuracy is limited only by the fineness of the grid making up the model.

Each airframe company has one or more finite element system in use by its engineers. Although all systems are based on the same principles and do essentially the same job, they each have their own unique input/output formats. This can be a problem when setting up a format for the IDB. Ideally, it should be possible to use IDB output as direct input to the finite element analyses. Options are: both companies use a common Government program such as NASTRAN; both companies use a program belonging to either (this is possible with the computer data link); or each use its own program by modifying input to suit.

Figure 16 shows the joint effort required to conduct the finite element analysis. The finite element models will evolve through the design process. They begin with coarse models to estimate structural stiffness for flutter and dynamic studies. Finer models grow with the need for internal loads and deflections for seal design, etc. The models are continuously updated until they represent the released drawings. The models are used separately by each company to advance the design of its structure and combined by each to calculate interaction forces and deflections.

The most refined models will be used to calculate engine internal clearances. These clearances will indicate which operational conditions contribute most to SFC deterioration and maintenance problems. The models may be used to investigate possible changes in airplane flight profiles and thrust management that would minimize these problems. If airplane usage changes are not practical, structural changes may be studied using the model to find effective redesigns.

Engine/Airframe Testing

The fourth major element of PANSIP is testing. Current engine testing consists of two phases:

1. Steady state ground testing
2. Flight testing

The objective is to experimentally evaluate the engine/propulsion system's thermodynamic performance and structural durability and to certify the flight (air) worthiness of the propulsion system.

Much of the engine testing today is devoted to cyclic endurance ground testing as shown in Figures 17 and 18. These abbreviated missions have been developed because it is impractical to include the long steady-state legs of commercial airplanes or bomber usage such as climb, cruise loiter and descent. The objective is to have a test engine accumulate more thermal cycles than any other engine in the fleet. The fleet leader should identify mechanical failure modes and thermal deficiencies such as performance degradation before they occur in operation and with sufficient lead time to permit timely corrective action.

By using the fleet leader engine concept, numerous design limitations are revealed. However, not all parts are subjected to the maximum thermal strain range produced by actual flight conditions because the long-term creep effects and thermal reversals caused by sustained cooling-heating cycles are not completely simulated. The larger engine parts such as disks take considerable time to heat and cool contrary to the lighter parts such as airfoils and sheet metal parts, i.e., combustor, frames, etc. As a result, the

larger mass parts tend to stabilize at some intermediate temperature during the specific endurance cycle, thus, avoiding the total thermal impact of the actual flight cycle. Because of these limitations, accelerated thermal cycling alone in its present form cannot screen out all the structural deficiencies. Thus, the obtained information must be used with discretion in life and mission severity analysis.

To improve or better define the airplanes mission impact on the engine, the airframe company must provide a more detailed usage criteria in terms of the four basic engine variables, altitude, Mach number, thrust requirements and excursion rates. These variables can be synthesized statistically based on past airplane usage experience as shown earlier in Figure 12.

The development of engine operational cost analysis, as shown in Figure 3, are most valuable for mission trade studies and for optimizing the engine cyclic endurance test. This will enable the engine/airplane manufacturers to independently or jointly study the impact of the airplane mission--not only the engine--but also on the propulsion system as such. It also points out the need for incorporating into any test the throttle transients due either to pilot usage or automatic flight control.

Since engine flight testing comes late in the program development, both thermal and structural deficiencies revealed at this point in time, are not only costly to correct, but may be of such nature that they carried into the customer's airplane usage. This is unfortunate, since it causes loss of revenue to the operator and dissatisfaction with the product.

To improve this situation, it would be desirable to acquire a ground flight test facility that would simulate a multitude of flight conditions as well as the exact engine usage excursion rates. This facility should not only be capable of testing the engine per se, but also the total propulsion system including strut and part of its attachment structure, or in case of a buried engine, the associated airframe structure. The capability to ground test operating turbine engines under flight maneuver conditions would be an extremely valuable asset to current and future engine development and manufacturing programs. There is currently no ground based test facility which can simulate acceleration and angular rate maneuvers on an operating engine.

Today, engines are initially flight tested on a tried and proven multi-engine airplane. Even though there are no imminent dangers to the airplane, the general flight testing is cautious in approach and data at the extreme maneuver conditions might not be obtained. Even if the willingness exists to exert the engine to the extreme corner of the flight envelope, the flight bed most likely would not be able to attain them.

Today's trend towards higher bypass ratio, lighter weight and more fuel efficient engines, has led to an ever-increasing thrust-to-weight ratio. This means that the demand to maintain the minute clearances between stationary and rotating engine parts, permits only controlled transient relative movements for performance and SFC retention.

Therefore, early engine data from realistic tests are of vital importance, since for the most part, stresses, strain, and temperatures are time dependent, and the structural engine and airplane dynamics is very difficult to determine analytically. Thus, viable test data is needed not only to determine component durability, but also in providing basic data for upgrading and instilling confidence in the complex analytical tool in the process of being developed.

Presently, rotor clearance design and control are limited largely by the unavailability of accurate clearance measurement instrumentation. Without such instrumentation, data is not available to substantiate prediction correlations relating to centrifugal and thermal growth phenomena in seals, turbine disks, airfoils shrouds, and various static structure. This limitation results in the development of, for instance blade-shroud growth system by trial and error and, without complete knowledge of engine usage and flight loads, the engine is more than likely to yield undesirable field clearance. SFC and component durability will suffer, which in turn, decreases performance and increases LCC. Besides the engine premature removal rate will be higher than anticipated as the process of trial and error of clearance control is carried out by the fleet operators.

It should also be noted that nowhere in the United States is there an engine test rig that can perform simulated flight tests on full scale propulsion system hardware, a must, of course, in future study of clearance control and validation of engine/airplane integration analysis.

Hence, determining a realistic test data base by simulating actual throttle excursion and flight maneuver forces are more important to current and future propulsion systems than those in the past.

RECENT APPLICATIONS OF PARTIAL PANSIP

Two examples will be presented of engine installations where some of the elements of the formalized PANSIP can be recognized: first, the 747-JT9D effort which was initiated to research engine case ovalization and evolved into a Government-funded operational cost study; second, the YC-14/CF6 design effort involving a unique and surprisingly successful installation.

747/JT9D

When it was determined prior to flight test that unacceptable case deflection was occurring due to the method of thrust attachment, Boeing and P&WA initiated a joint finite element analysis effort for the pursuit of a viable solution to the thrust attachment problem. The correlation between analysis and test is shown in Figure 19 for the mechanically loaded, cold engine structure. The result substantiated the value of refined analysis techniques in the field of engine installation studies.

This classic analysis was most valuable in the commencement of the 747/JT9D joint PANSIP effort (1974-1976) when the assembly of the first JT9D NASTRAN modeling was performed. The intent of this research program was to assess the feasibility of using such models to identify potential propulsion system integration problems early in the design process rather than during development when hardware modifications have adverse effect on program cost and schedule. The JT9D/747 installation had the advantage that it is mature enough to provide experimental data and current enough to be representative of the next generation engines. And equally important, was the fact that there existed a finite element idealization of earlier vintage as previously stated. This reduced modeling time and cost.

The first study was directed to perform a detailed flexible-body simulation of the propulsion system, even though up to this period of time, it was not generally used in structural simulation of the airframe. In case of airplanes with wing mounted engines, the flutter model typically utilizes a simple beam idealization of the propulsion system. The engine manufacturer is concerned with airplane forces and frequencies, forces and frequencies that will cause flexing of the engines superstructure. They are also interested in the stiffness of engine associated structure, such as the inlet, nozzle, plug, thrust reverser, strut, etc. as they affect clearance control, fuel usage and durability.

The P&WA/Boeing 747 propulsion system analysis required careful attention to interface definition and data exchange. The task was simplified since NASTRAN and the CDC 6600 computer were used by both companies and data tapes could be exchanged directly.

The NASTRAN propulsion system model and subassemblies were developed as shown in Figure 20. The emphasis of this study was the dynamic behavior of the propulsion system and the strut. The nacelle/strut combination was assumed to be symmetric about the vertical plane through the engine centerline. Symmetric and antisymmetric behavior could then be calculated with a half model. Secondary structural components such as cowls, thrust reversers, accessories, etc., were included as discrete or distributed masses to bring the mass properties of the model to within 5% of the actual hardware. Gyroscopic stiffening terms of the rotor mass points were set to correspond to engine steady-state cruise operating conditions. The dynamic model is shown in Figure 21.

Since the main objective of this joint effort was accomplished and amply described (Reference 9), it will suffice for the purpose of this paper to point out a few results and reiterate some of the conclusions drawn, since they gave the impetus to continue the joint effort for further modeling refinement and deflection studies. Figure 22 shows the relative positions of some of the modes evaluated. Depicted in Figure 23 is the inlet fan case rocking mode and that would be important in the consideration of fan clearance control; Figure 24 shows the tail wagging mode which is of interest especially if it corresponds to a rotor frequency.

The cooperative 747 propulsion system vibration analysis effort was extended in 1976 to include structural deflection analysis. The previously developed NASTRAN model was upgraded and used for studying the causes of non-recoverable short-term performance deterioration, which seems to be more pronounced on the new high bypass engines than the older low bypass engines.

The results of the propulsion system deflection analysis with respect to thrust and maneuver loads, shows the deformation of propulsion system structural members and the relative motion between static and rotating parts. If the motion exceeds available clearances, rub and wear will follow, hence, permanent loss of efficiency. These deformations or rubs will vary both axially and circumferentially throughout any engine as shown in Figure 25 (Reference 10). The deformation patterns are general in nature and display the progress General Electric/Boeing and Pratt & Whitney/Boeing have made in developing comprehensive analytical models of the CF6 and JT9D engines.

These models can be used to examine the effect of flight loads on short-term performance degradation as proposed by NASA (References 11 and 12).

It should be noted that these deflection contour maps such as shown in Figure 25 have been generated for various steady state loads and temperatures. They are of prime importance in analysis of short-term engine performance deterioration and engine/airframe integration studies. They will give a quick relative display of the "goodness" of various propulsion system load sharing design and integration schemes with respect to the effect of flight loads, thermal transients, on the static deflection of the engine structure.

It was concluded that:

- o Further study is needed to determine propulsion-system modeling requirements. Finite element technology originated in the airframe industry where extensive emergence studies and correlation with airplane tests were carried out.

Similar studies are needed in propulsion system type structure to establish requirements on model grid size versus accuracy and the best representation of complex features such as flanges, bearing frames, and variable guide vane holes in the compressor case for a particular level of analysis, i.e., preliminary design development or final system design verification.

- o Propulsion system major components such as the inlet cowl, engine cases, and tailcone, which are directly attached, develop strong dynamic structural interactions that can be accurately described by integrated structural models. The NASTRAN computer program was found to be adequate and excellent for predicting large scale interdependence of propulsion system structural components, but could not compete with specialized inhouse programs for defining less global behavior such as engine rotor-frame vibration (critical speeds).
- o Application of general purpose models for the prediction of deflection-related behavior, such as short-term engine performance deterioration caused by seal wear from flight loads, promises to have a significant impact on the design process during the evolution of future aircraft.
- o To determine the effects of casing shell deformation, the three dimensional finite element model overcame shortcomings of the planar (beam and spring) model simulation. The three-dimensional approach offers the advantage of using changes in radial clearances between the rotating and static components to evaluate and modify the load paths and the rigidity of the engine structures. This information can then be used to provide additional understanding of the engine system during high unbalance events initiated by the ingestion of birds, ice, tire treads, or similar large foreign objects.

Even though Pratt and Whitney has concluded from the previous exercise that flight induced seal rub causes most of the short-term (250 flight or less) deterioration in engine performance, there exists today only a basic understanding as to the amount of SFC deterioration that can be attributed to flight loads or thermal transients within the engine. It is obvious that the engine itself becomes a very redundant structure under thermal loading. Creep ratcheting or plain yielding will occur due to thermal transients. Since creep is highly nonlinear in its initial stages, the effect on creep ratcheting on severely strained redundant structure could be considerably magnified by flight loads over the first few hundred flight cycles. This continued settling of the static and rotating structure, certainly would be a most pronounced during the initial phases of engine operation (see Figure 5). The following asymmetric portion of the SFC curve seem to be a result of natural rotor alignment as a result of its own eccentric, growth operational realignment of the static structure, and the propulsion systems exposure to the majority of the flight conditions with the first 200 to 300 flight cycles.

Thus, the engines structure will continue to settle after each refurbishment along the same pattern as when new, due to diametrical variations in hardware already introduced, rotor and static eccentricities due to axial stackup, flange looseness, varying looseness of blades and vanes, etc., and the fact that after each refurbishment, the engine will again see the probability spectrum of flight loads be it air or thermal. Therefore, P&WA/Boeing's continued joint analytical and testing effort under NASA's sponsorship will be of the greatest value.

YC-14/CF6

The YC-14 program used some of the major elements of the PANSIP approach previously discussed. A data bank was set up to allow General Electric and Boeing remote access to engine and airframe structural data and incidentally, performance data. A finite element analysis of components and the combined engine-structure model was performed. Some rig and flight testing was performed.

The YC-14 engine installation shown on Figure 26 is truly unique (Reference 13). The airframe is designed to take advantage of the Coanda effect, wing upper surface blowing, to provide high lift for short field operation. This necessitated locating the engine above and forward of the wing box. The engine is contained in the propulsion pod which is cantilevered off the front spar. A D-shaped exhaust nozzle is used to mix the primary and fan air flow and spread it over the trailing edge flaps. The prototype program required that the existing engines be installed with a minimum modification.

The distribution of thrust in the propulsion pod caused a potentially serious deflection problem. Figure 27 illustrates the difference between a standard CF6 installation and the YC-14 type. On a standard installation, the bare engine static thrust is combined with a forward acting inlet blow off load and an aft acting nozzle load to produce a net engine mount thrust load. On the YC-14 installation the exhaust nozzle is attached to the structure rather than the engine. As a result, the net engine mount thrust load without the aft acting nozzle load would be substantially higher (Reference 14).

The increase in axial load at the thrust mount produced two adverse conditions: an increase in deformation locally at the thrust mount; an increase in "backbone" bending due to higher induced vertical load at the rear mount as shown in Figure 28.

AD-A070 950

ADVISORY GROUP FOR AEROSPACE RESEARCH AND DEVELOPMENT--ETC F/6 21/5
STRESSES, VIBRATIONS, STRUCTURAL INTEGRATION AND ENGINE INTEGRI--ETC(U)
APR 79

UNCLASSIFIED

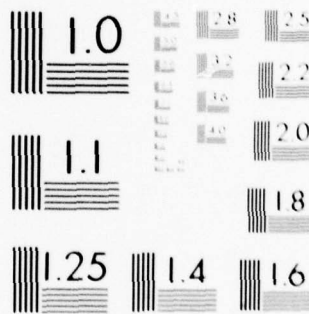
AGARD-CP-248

NL

4 OF 6

AD
A070950





MICROCOPY RESOLUTION TEST CHART
NATIONAL BUREAU OF STANDARDS 1963-A

Since major modification of the engine was out of the question, it was necessary to create another load path for the thrust. Four air actuators were installed typing the aft face of the fan case to the forward face of the structure as seen in Figure 29. The actuators were manifolded to the 10th stage bleed pressure. The load was not affected by relative engine-structure deflection and therefore was not redundant.

To help assure that this modification would be safe and effective, a finite element analysis of the CF6 engine was jointly undertaken by General Electric and Boeing. With General Electric providing drawings and consultation, Boeing constructed a finite element model using the NASTRAN analysis system. Analysis showed that with the air actuators, engine deflections and internal clearances would be less than on a conventional installation as shown in Figure 28. Engine ground run-up test and airplane flight tests verified the design. This joint effort set the stage for the more extensive cooperative effort that followed which included a direct computer link between companies and a full scale deflection verification test.

In order to eliminate the air actuators and reduce engine/structure relative deflections, alternate engine mount concepts were studied. The most appealing concept included linkages attached to each side of the fan case for transmitting vertical and side loads (see Figure 30). The side load path was redundant, that is, the side loads and fan case deflection were dependent upon structure deflection. To insure that structural deflection during severe airplane maneuvers would not cause engine clearance problems a comprehensive analysis and test program was initiated.

The CF6 engine finite element model which had been constructed for the YC-14 analysis was sent to General Electric for familiarization and upgrading. To expedite the process General Electric and Boeing research staffs set up a direct computer link. The computer link enabled General Electric to use Boeing computers and software for NASTRAN modeling, analysis and data display. Boeing, at the same time was able to expand the model by adding the inlet, primary nozzle and plug which are bolted to the engine as shown in Figure 31. An up-to-date model was continually available to both companies.

The structural analysis showed that the redundant installation would be acceptable from the standpoint of strength and deflections. General Electric used a full-scale fan case deflection test to verify the analysis results.

The significant advancement in cooperative effort was the direct computer link between the two companies. Having immediate access to a model that was kept current by both companies resulted in substantial saving of time and eliminated the expense of false starts. As the speed and convenience of the computer link became apparent, the procedure was also used for sharing General Electric's engine data base needed for performance analysis.

STRUCTURAL INTEGRATION IMPROVEMENTS

Most of the tools to implement a proper PANSIP are available. A basic plan has always been negotiated between the companies, it needs expansion to include the inter-company analysis and testing efforts. The Integrated Data Bank uses existing computer facilities. Finite element Analysis is now a standard tool in all large engineering groups. One area needing improvement has been mentioned, namely, additional test facilities.

Another area needing improvement is in propulsion system flight loads where data available is marginal.

Load-variation on aircraft structures is caused by a variety of external fluctuating forces. Resulting load-time histories are classified on the basis of loads origin.

Random Process

- o Atmospheric turbulence
- o Runway roughness
- o Acoustic vibrations

Event Sequences

- o Maneuver loads
- o Ground-air-ground cycles (take-off and landing)
- o Pressurization cycles

Sequences of individual events such as gust loads can only be described approximately by a statistical distribution of exceedances. Typically, these distributions give neither information about temporal sequence of individual peak values nor individual rates or frequencies of the recorded variable. Exceedance curves shown in Figure 32 thus represent the envelope of maximum and minimum in a relative frequency of occurrence sense only. Thus, the detail load histories needed by the engine designers cannot be extracted from these curves.

Load-time histories resembling random vibrations may be described by means of the theory of random processes. The application of power spectral analysis to randomly varying loads as shown in Figure 33, especially gust loads and to some extent ground loads, is being explored to an ever-increasing degree.

However, the largest aircraft cyclic loads data bases of a probabilistic nature are altitude/velocity/acceleration (VGH) recordings that are not particularly suitable for sequence accounting. These are shown in Figure 34. Analysis of such recordings, comprising accelerations due to gust, maneuvers, take-off, landing impact, and taxi, have provided information on the magnitude and relative frequency of occurrences for each successive generation of airplanes. Airplane center-of-gravity accelerations require many assumptions and much analysis for conversion into probable loads histories for different aircraft components such as the engines. Furthermore, typical total recordings of loads are only a fraction of one airframe's lifetime even though it is of great significance to engine clearance control and performance retention. Airplane loads have been, and still are, aimed at extrapolation on a probabilistic basis, to deal with the fleet life of the airframe and not engine SFC retention and durability.

Thus, it has to be concluded that the airplane's effect on engine flight loads is today rather nebulous, but is one of the most important areas of future research in terms of fuel burn.

Future airplane developments must include a systematic propulsion system load research program. This research should (1) review historical engine deterioration trends and attempt to correlate these with engine design and airplane usage, and (2) lay out a full scale engine and/or propulsion system load program, and size it in terms of required analysis, testing cost and schedule. This is of prime importance since it will give a clear overview of what has been done, what are the technology needs and what can be achieved in the near future.

Figure 16 shows that such a program should contain, in addition to the historical aspect, two main branches:

- 1) Airplane aerodynamics
- 2) Propulsion system performance.

These branches when integrated define the various propulsion system internally and externally generated loads and their effect on the associated propulsion system hardware. These have been previously discussed in Reference 10.

Basically these airplane induced engine loads are derived from the:

- o Nacelle
- o Thrust
- o Aerodynamic
- o Accelerations (g's)
- o Gyroscopic

PANSIP AND FUTURE AIRCRAFT

The discussion so far has pointed out the need for improved structural integration of engines and airframes, better loads definition, upgrading of testing techniques, computerized communications between engine and airframe teams, development of an Integrated Data Base and what has been done so far in the field of engine/airplane structural integration using large structural finite element programs, such as NASTRAN.

As the engine/airframe system becomes a more integral entity in terms of load sharing, controls, stealthiness, fuel systems, vulnerability requirements, etc., the need for computerized intercompany communication and engine/airframe performance and structural programs become more critical.

To bring this point of view out more clearly, one needs only to examine such airplane concepts as V/STOL (Reference 15). Looking at Figure 35, it is quite evident that this airplane has many unique and different types of engine-airframe interfaces. For instance, the two engines are mounted behind the variable pitch lift/cruise fans which rotate to provide thrust vectoring for V/STOL operation and the variable pitch lift fan in the nose, and are driven by the redundant transmission system. Further, during high speed flight, the nose fan is disengaged and the airplane is conventional in appearance and operation; whereas during V/STOL operation, flight control is accomplished by varying thrust in both magnitude and direction of all fans as shown in Figure 35. Roll and pitch control moments are generated by increasing and decreasing the thrust from side to side for roll and fore and aft pitch. The roll and pitch thrust variation result from changes in blade pitch angle with appropriate power transfer among the fans. Yaw control is accomplished by tilting the thrust vectors in a spanwise direction.

From the prior discussion it is quite evident that propulsion runs all around this aircraft to the extent that in terms of current engine/airframe structural integration procedures, it would result in an engine-airframe company impasse in regard to determining whom is doing what to whom. An airplane program such as V/STOL, with its multitude of interwoven propulsion-airframe interfaces and related safety problems, seem quite comprehensive to undertake without upgrading the concept and program for propulsion-airframe integration and testing.

However, in developing the program for future engine-airplane integration it is well worth remembering that any new system now as in the past, is a conglomerate of compromises aimed at balancing performance, cost and delivery schedule to satisfy some stated operational requirement. These compromises must be made without benefit of complete knowledge and are therefore prone to error and dispute, because the various components and sub-systems have inherently different degrees of risk and anticipated times of development. For instance, propulsion and airframe do not have the same gestation periods in general. Each system must be planned and built with a clear recognition of individual characteristics of the program's integration needs. Generalizations and extrapolations are dangerous, as the last 25 years of airplane system development have shown, and across-the-board rules can be counter productive. Any time the industry strives for a new system, commercial or military, whose capability requirements are substantially beyond the current state-of-the-art, the uncertainties of risk are extremely great. Therefore, ways and means must be found and initiated to reduce the risk. It is believed that a well planned propulsion system and airframe structural integration program would be one of the most important aspects of any new airplane development plan.

Another important aspect of integration programs is the definition of engine usage within the flight mission, because the engine designer must know at the earliest possible time that basic requirements of:

- o Thrust
- o Engine usage
- o Weight
- o Cost and Schedules

An examination of these shows that performance is usually known shortly after the first engine goes to test. If the performance falls short of expectations, major improvement programs are launched immediately to both understand and correct deficiencies. The weight of the engine is known even before the drawings go to manufacturing. The initial cost is reasonably understood as well as the timing, but cost and delivery date are closely dependent variables. In contrast, however, mechanical reliability, durability and maintainability, which are linked directly to engine usage, are all related and have in the past been an unknown for most of the development time, thus, production tooling becomes committed, before mechanical programs occur. When these initially dormant problems occur, they have detrimental effects on performance and maintenance cost as shown earlier in Figures 5, 6, and 7.

It is believed that the impact of these "built-in problems" can be reduced by gaining a better definition of airplane's effect on engine flight loads, and engine flight usage in regard to basic mission severity.

REFERENCES

1. Aviation Week, November 17, 1969, Page 34.
2. National Transportation Safety Board Safety Recommendations A-72-82, 83.
3. National Transportation Safety Board Safety Aircraft Accident Report, AAR-76019.
4. Interavia, August 1973.
5. Flight International 25, January 1973.
6. Aviation, February/March 1978, Page 43.
7. J. K. Goodwine, Powerplants for Wide-Body Aircraft--What We Bought and What We Got, AIAA Paper, 1975.
8. Available on request.
9. J. L. White, E. S. Todd, Normal Modes Vibration Analysis of the JT9D/747 Propulsion System, AIAA/SAE Paper 76-732, July 1976.
10. M. N. Aarnes, J. L. White, Propulsion System and Airframe Structural Integration Analysis, AIAA Paper 75-1310, September 1975.
11. Available on request.
12. AIAA July/August 1978, Page 47.
13. Lucas J. Kimes, YC-14 Engine Installation Features, AIAA Paper No. 74-972, August 1974.
14. R. K. Tuten, F. R. Housley, P. J. Hess, Installation Effects on the CF6-50 in the YC-14 Aircraft, SAE Paper.
15. J. M. Zabinsky, P. Gottlieb, G. W. Jakubowski, Mechanically Coupled Lift Fan Propulsion and control for Multi-Mission V/STOL Aircraft, SAE Paper No. 751100, November, 1975.

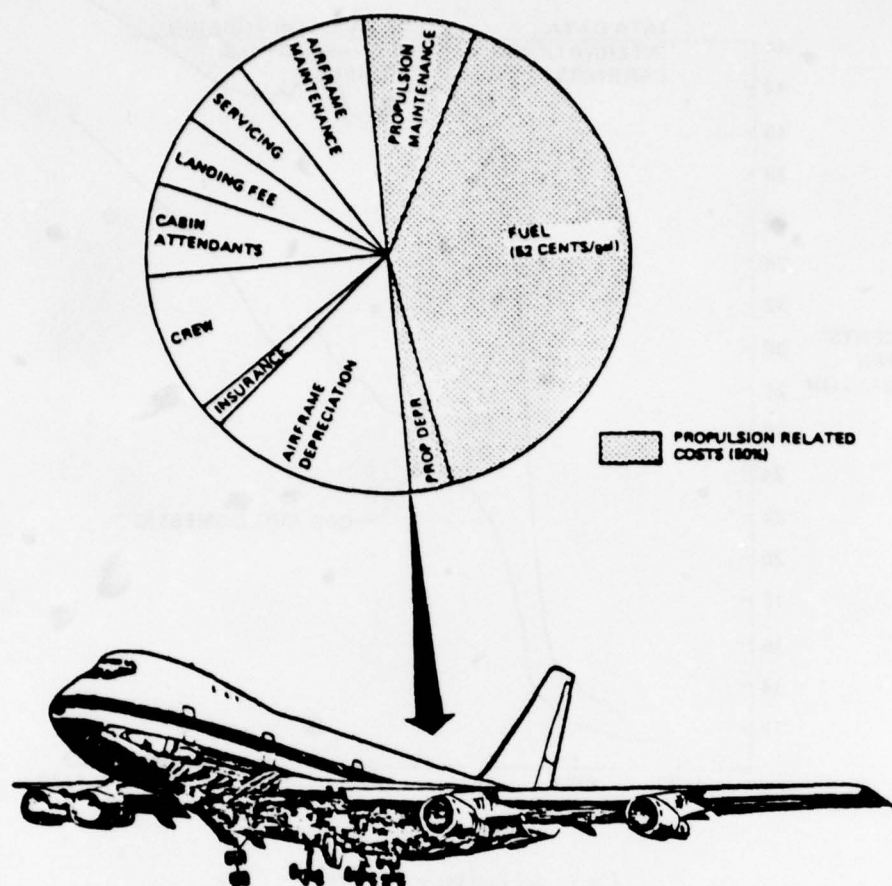


Fig.1 Typical wide-body commercial transport operating cost breakdown

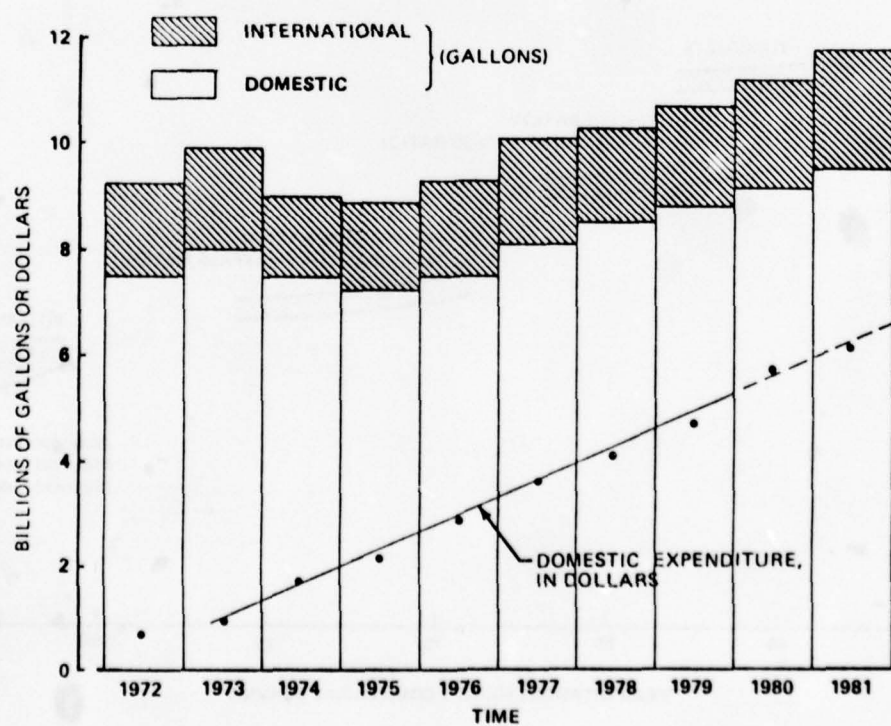


Fig.2 Commercial aviation fuel consumption, domestic and international

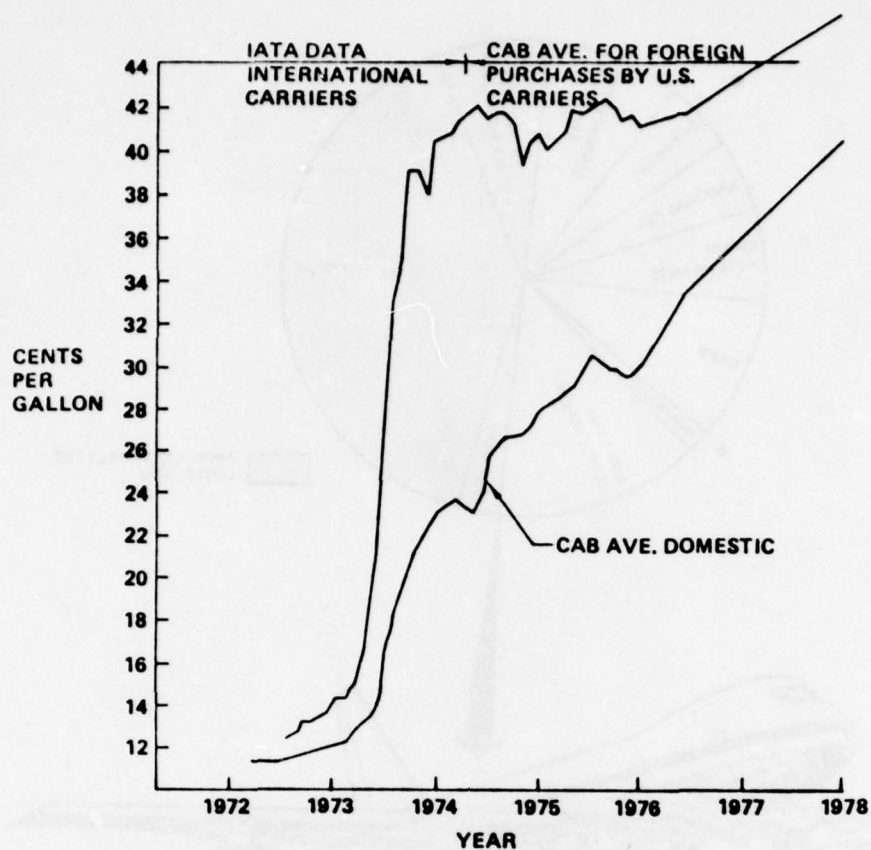


Fig.3 Jet fuel price comparison

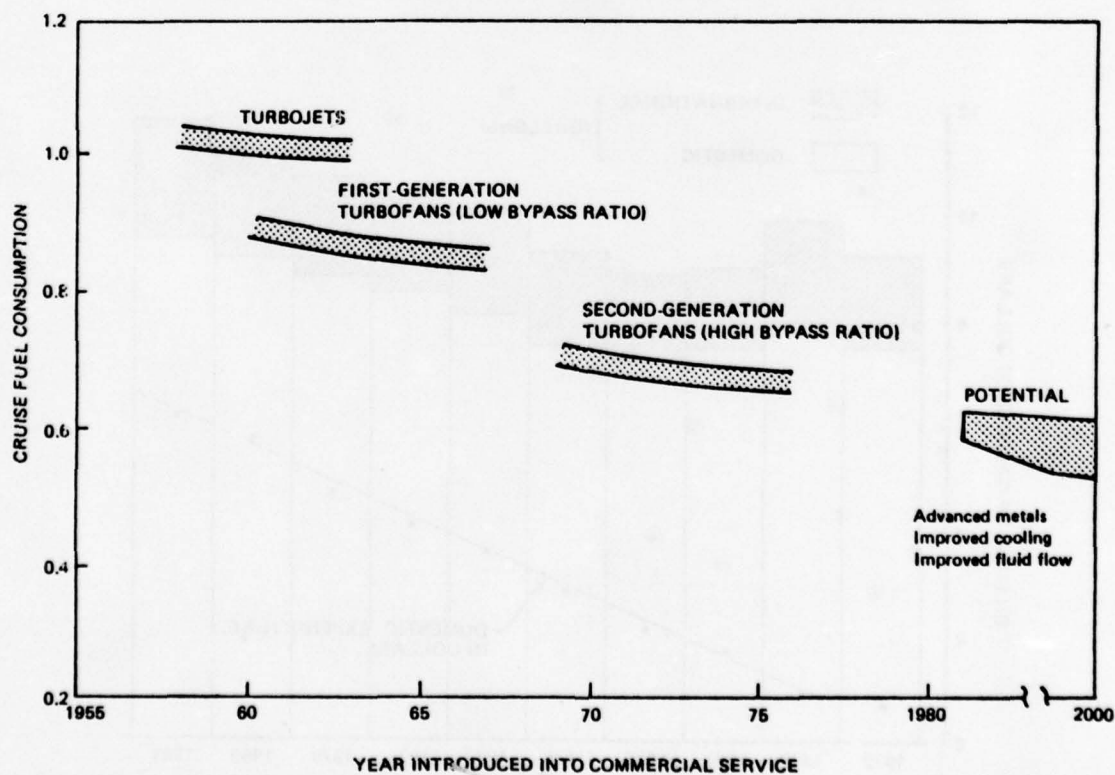


Fig.4 Fuel consumption improvement

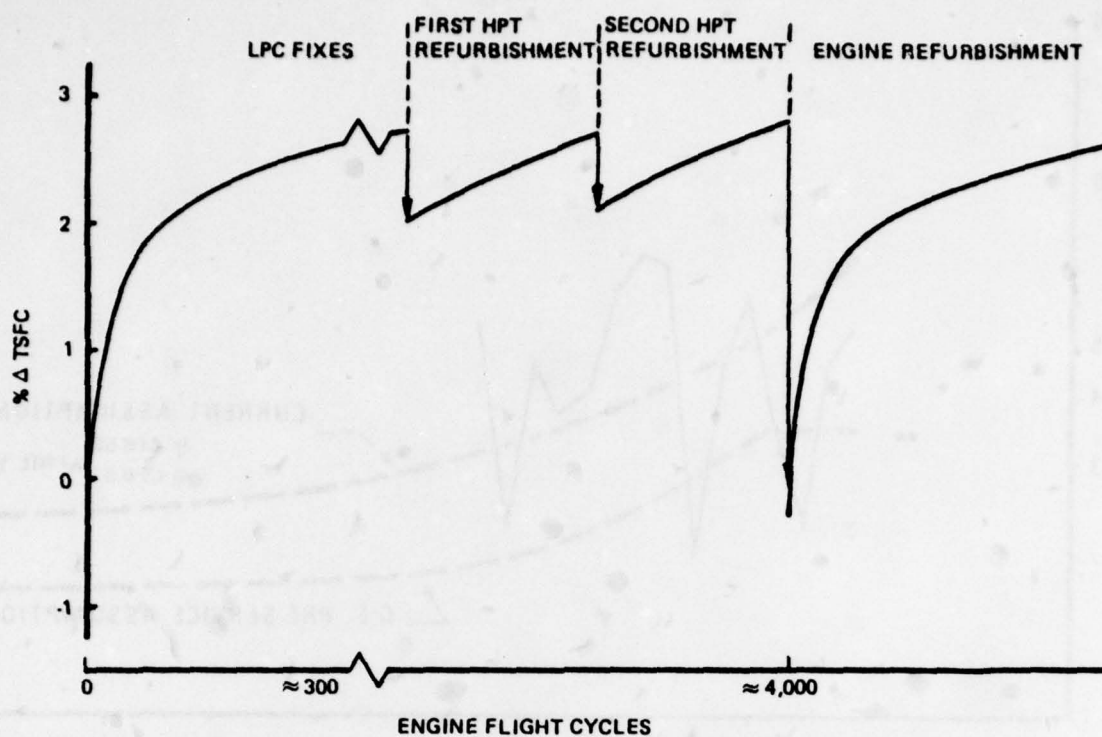


Fig.5 Fuel consumption deterioration trends

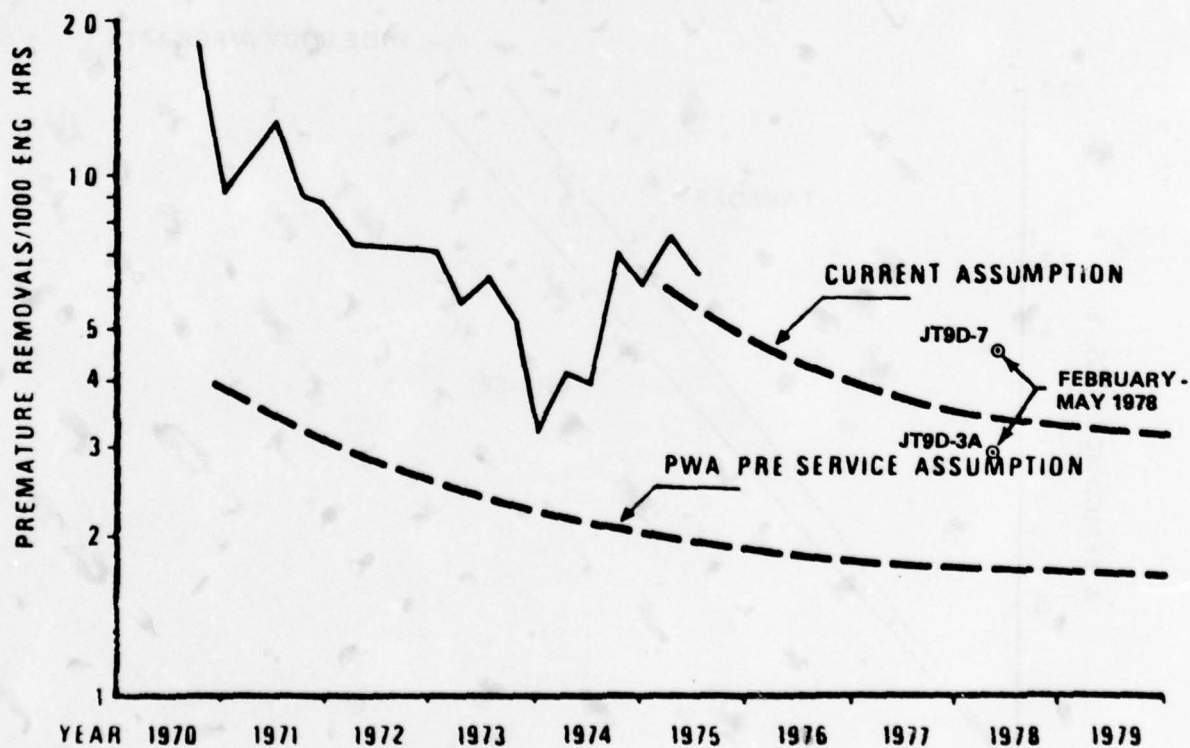


Fig.6 JT9D-3A premature removals

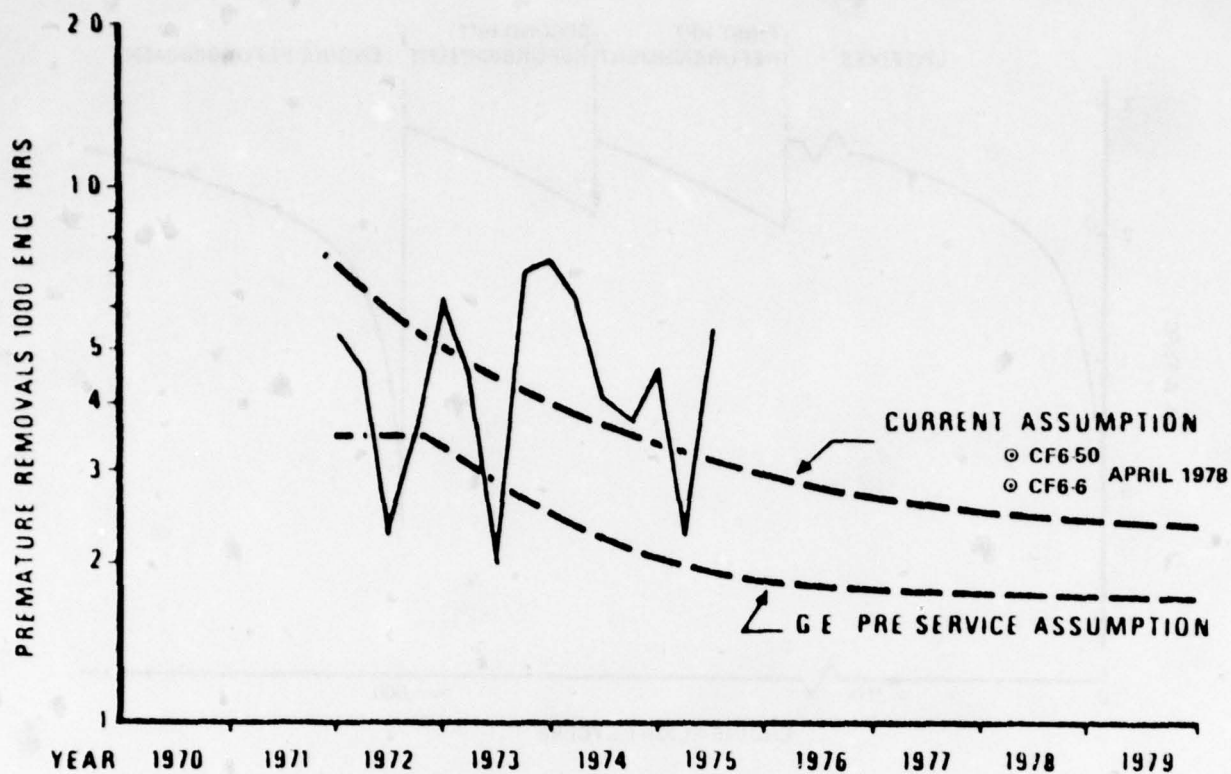


Fig.7 CF6-6 premature removals

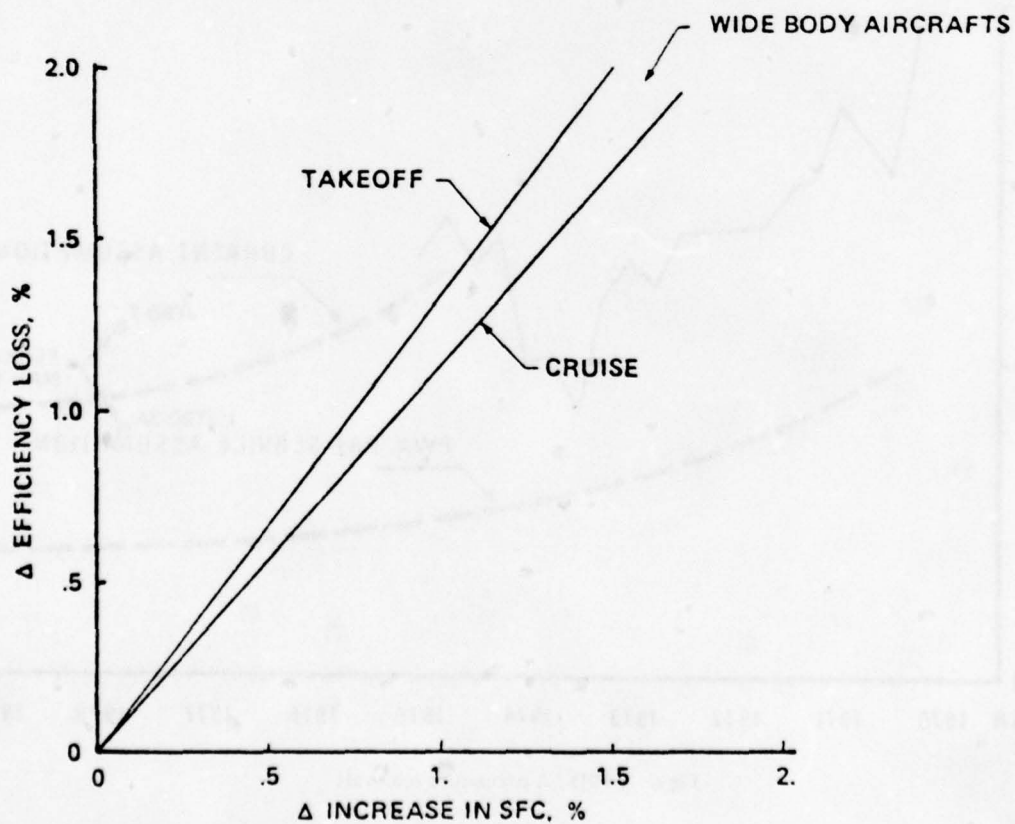


Fig.8 General increase in SFC with loss in high pressure turbine efficiency (high bypass engine)

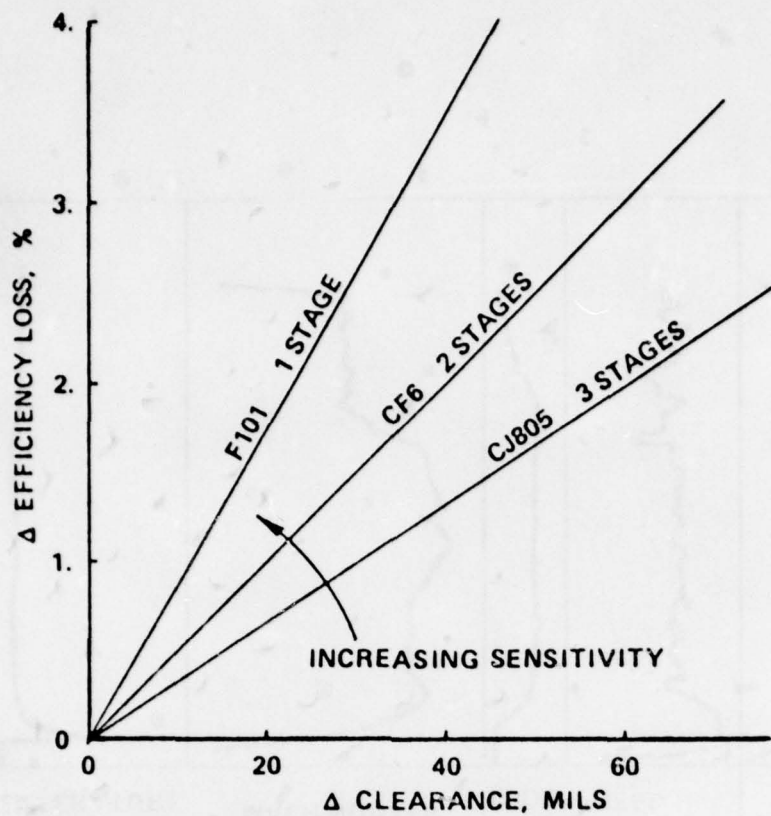


Fig.9 High pressure turbine efficiency loss with tip clearances

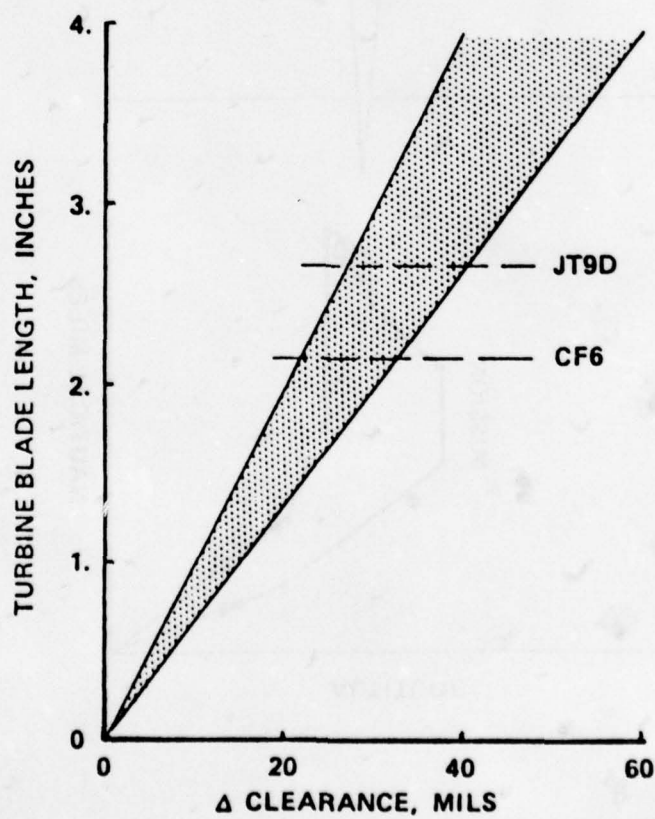


Fig.10 Typical airfoil clearances

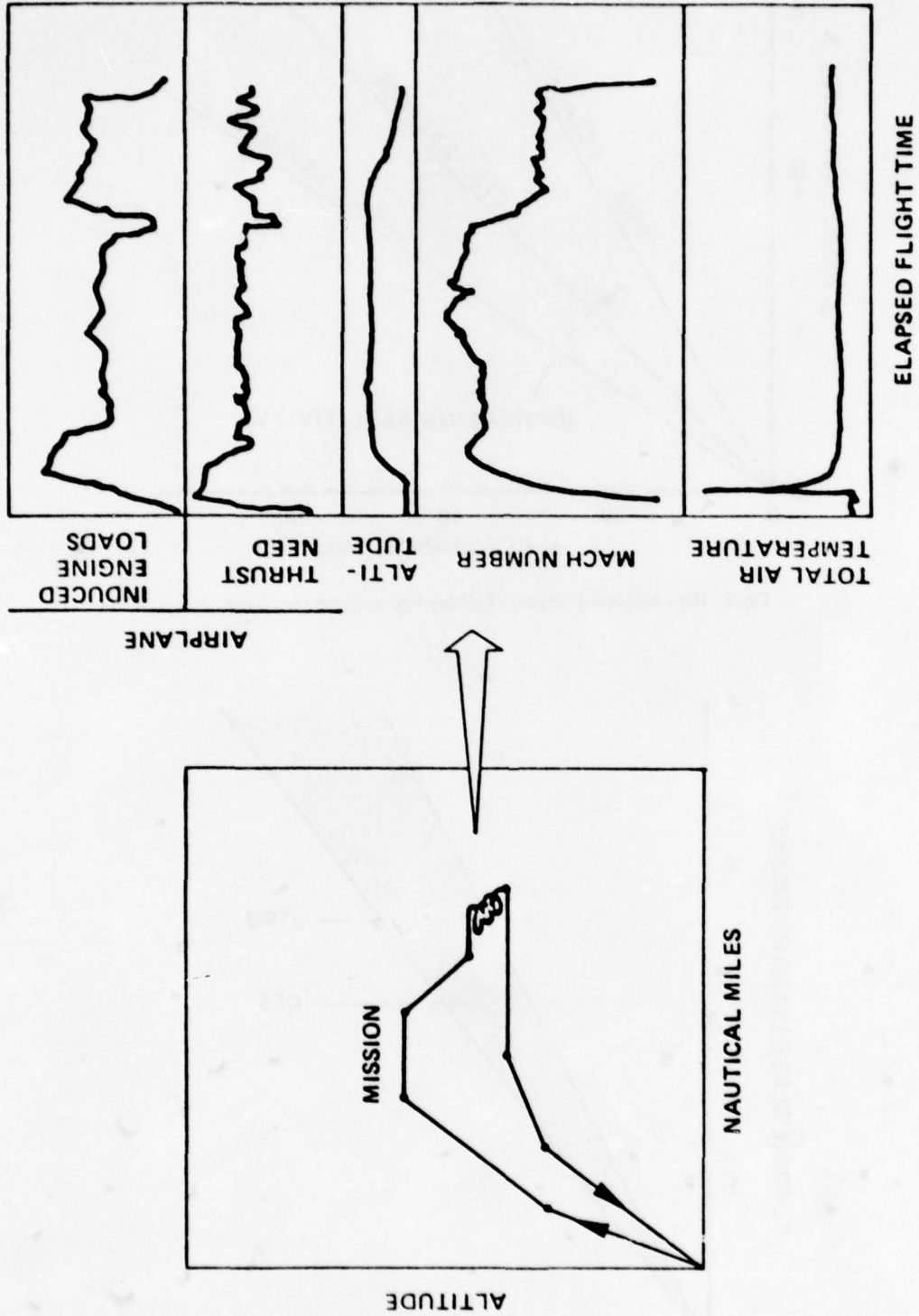
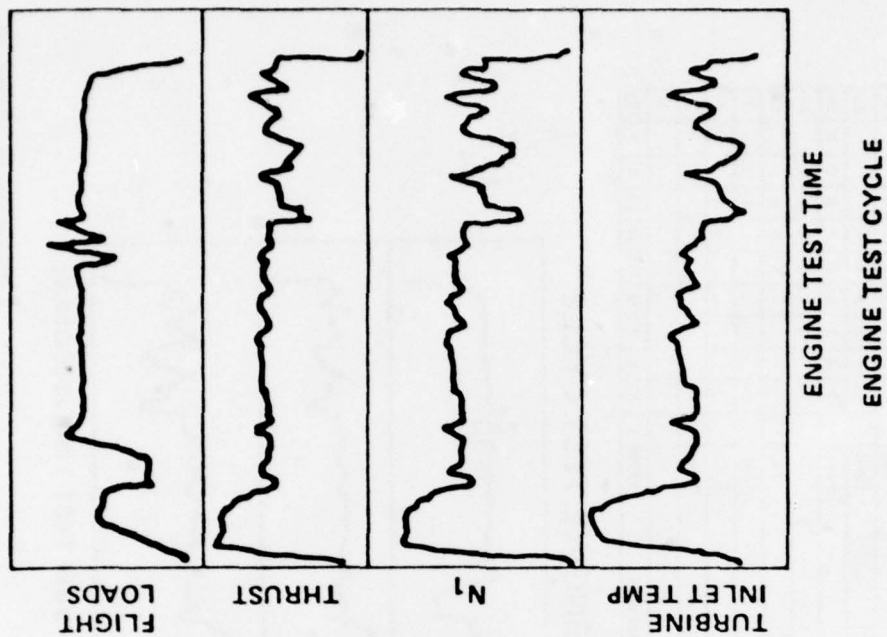


Fig.11 Airplane usage



	N1 final excursion range (%)	Number of excursions																Σ
		50 to 55	55 to 60	60 to 65	65 to 70	70 to 75	75 to 80	80 to 85	85 to 90	90 to 95	95 to 100							
N1 initial excursion range (%)	95 to 100		50					2	1								3	
	90 to 95		100				1	1	2	1							6	
	85 to 90		260				2	1	6	7	7						23	
	80 to 85		440	1	2	3	3	5	7	7	5	2	3				38	
	75 to 80		310				2	1	2	8	6	2					21	
	70 to 75		240						1	5	9						15	
	65 to 70		100						1	4	1	1					7	
	60 to 65		50								4	1					6	
	55 to 60		30									1					2	
	50 to 55		20										1				1	
Total segment time (seconds)		1,620	1	2	5	7	15	21	38	23	6	3	121					

PERCENT N1 HISTOGRAM AND EXCURSION MATRIX

Fig.12 Engine usage

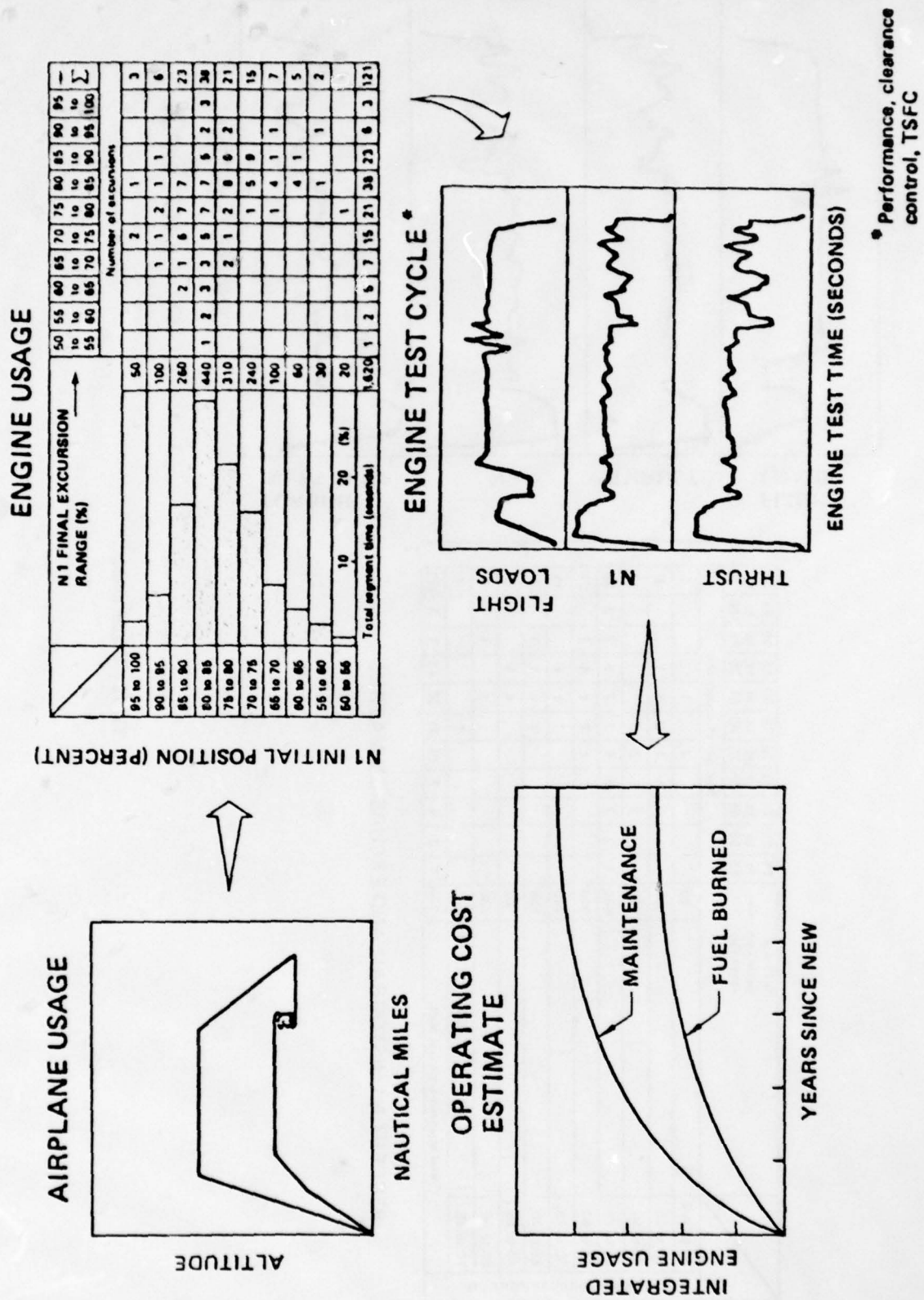


Fig.13 Development of engine operational cost analysis

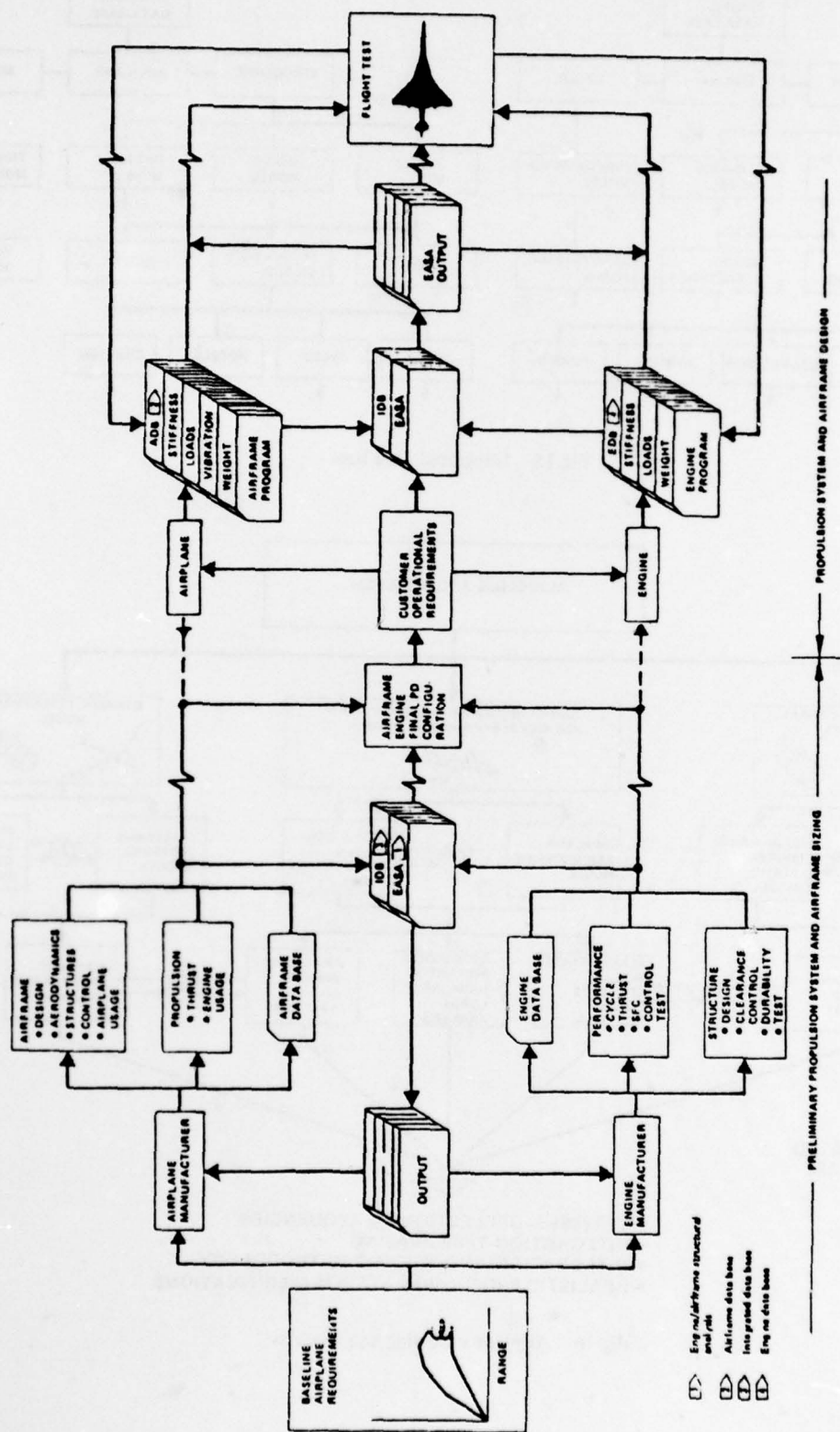


Fig. 14 Propulsion system and airframe structural integration program (PANSIP)

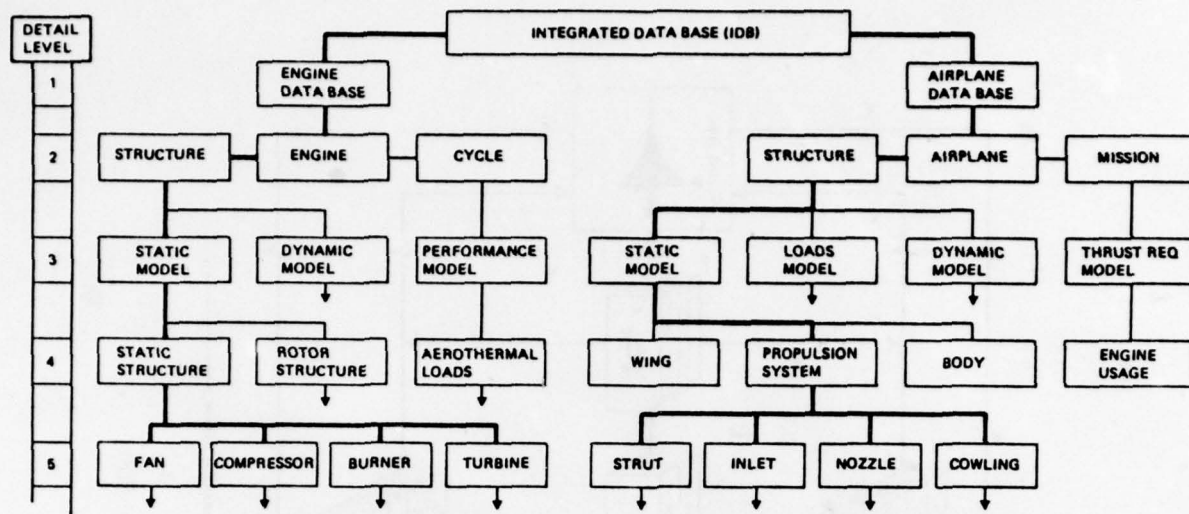


Fig. 15 Integrated data base

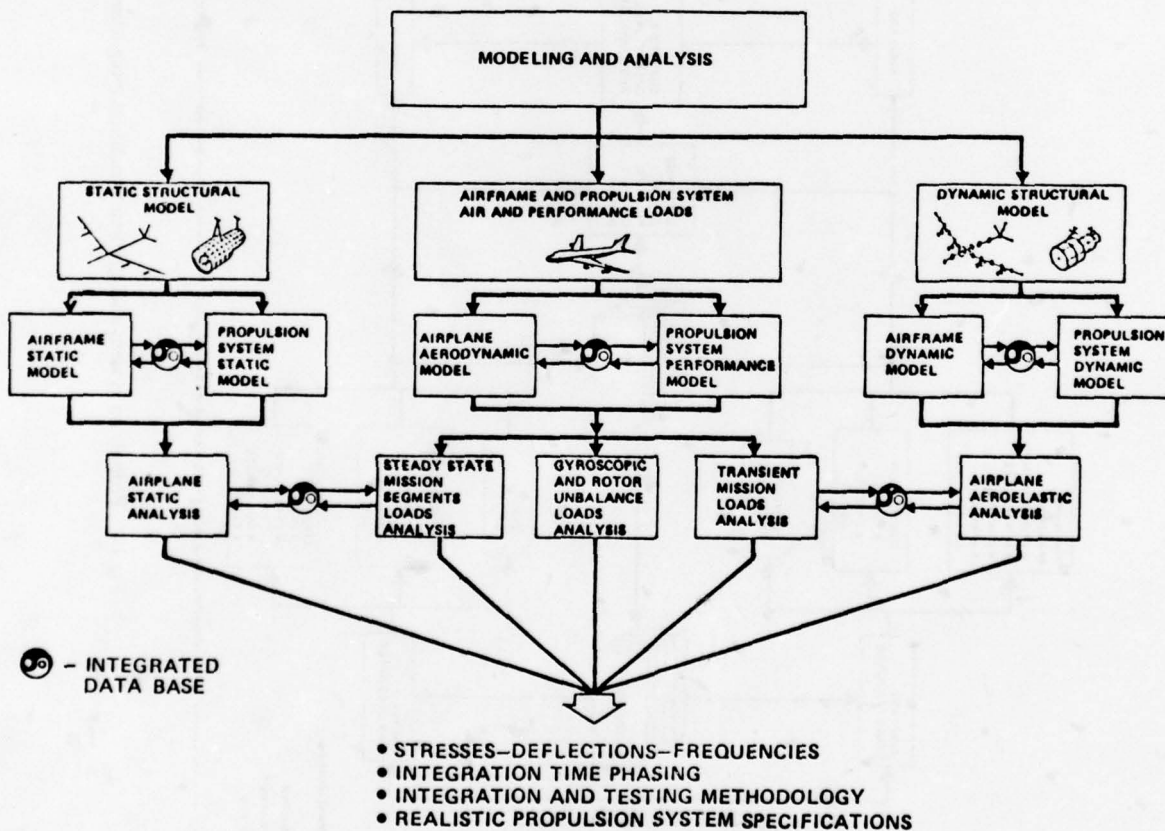


Fig. 16 Airplane modeling and analysis

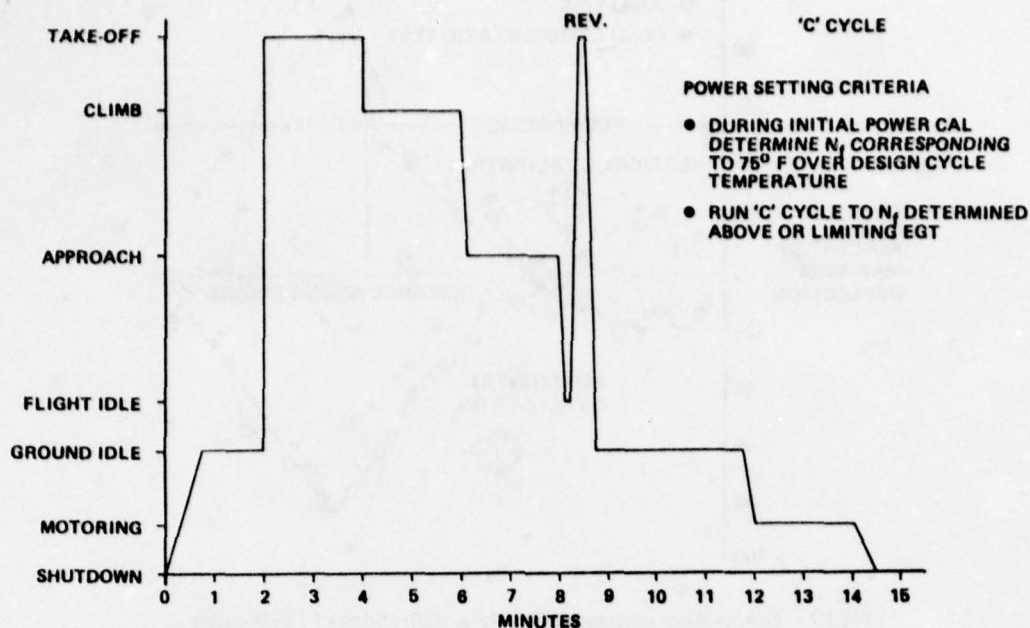


Fig. 17 CF6 simulated service cycle

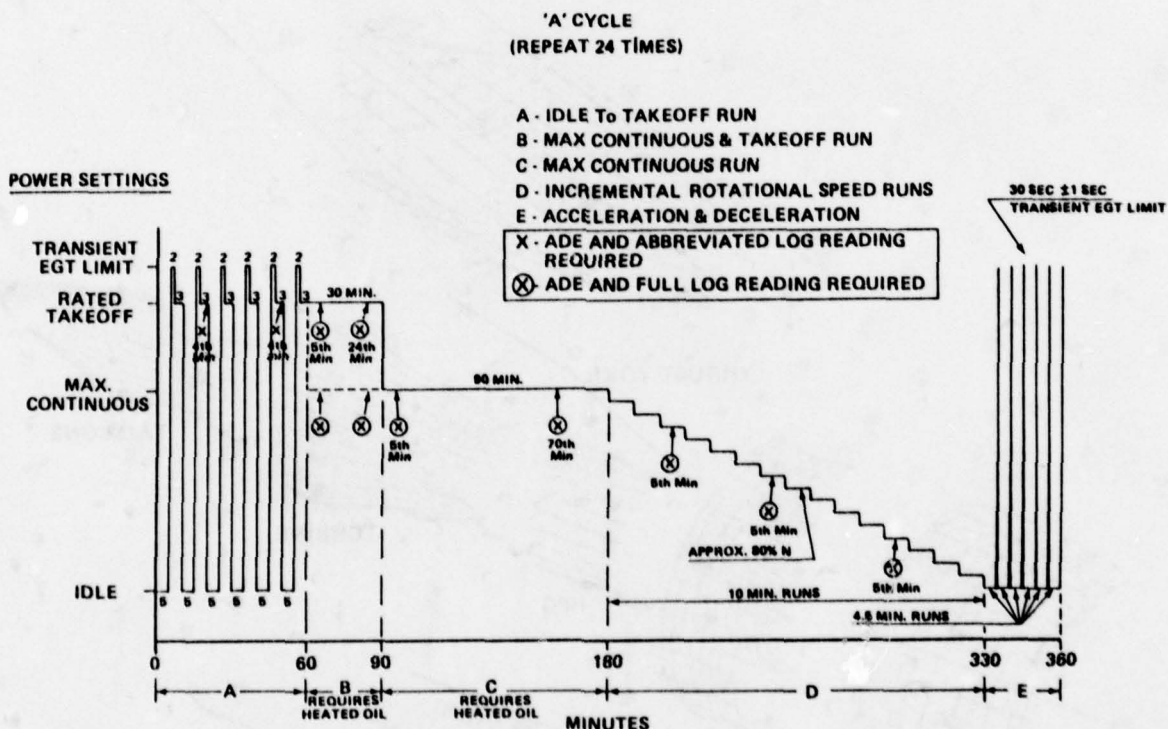


Fig. 18 CF-6-6 FAA 144 hour endurance certification cycle

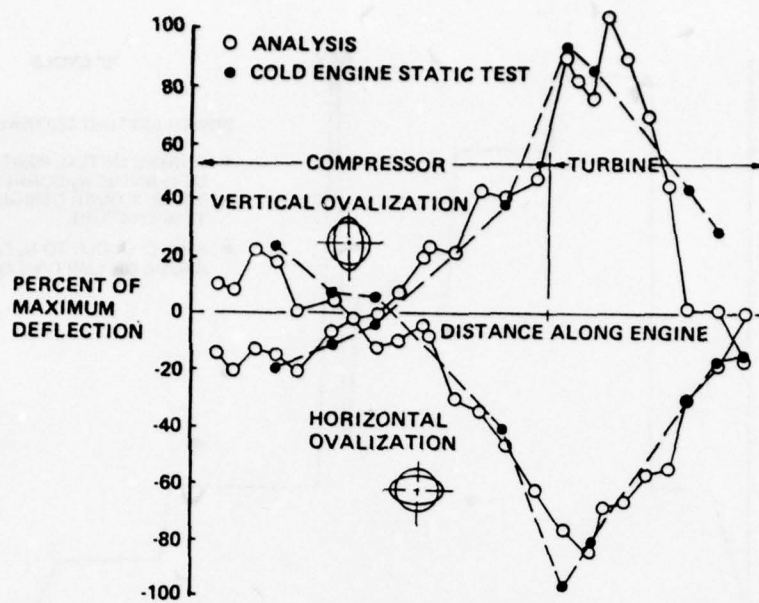


Fig.19 Test/analysis correlation for static deflections of JT9D casing

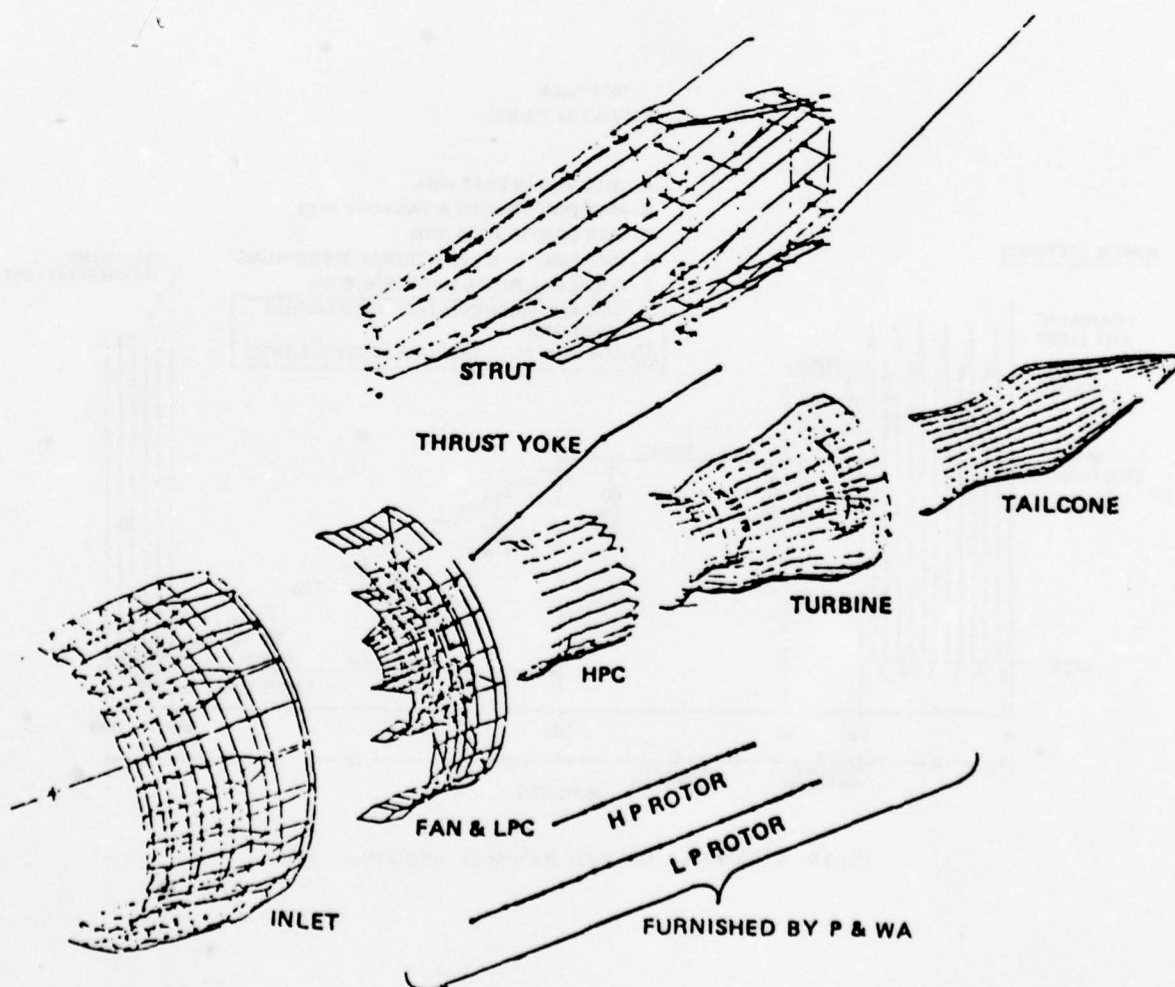
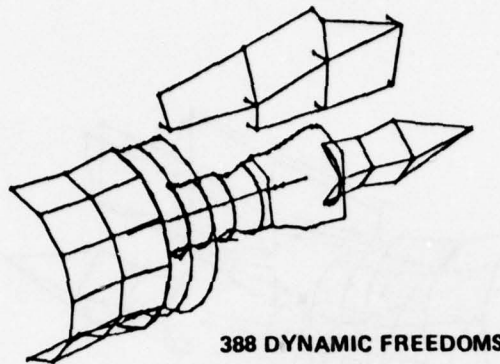


Fig.20 JT9D-7/747 propulsion system substructures



388 DYNAMIC FREEDOMS

Fig.21 Integrated propulsion system dynamic model

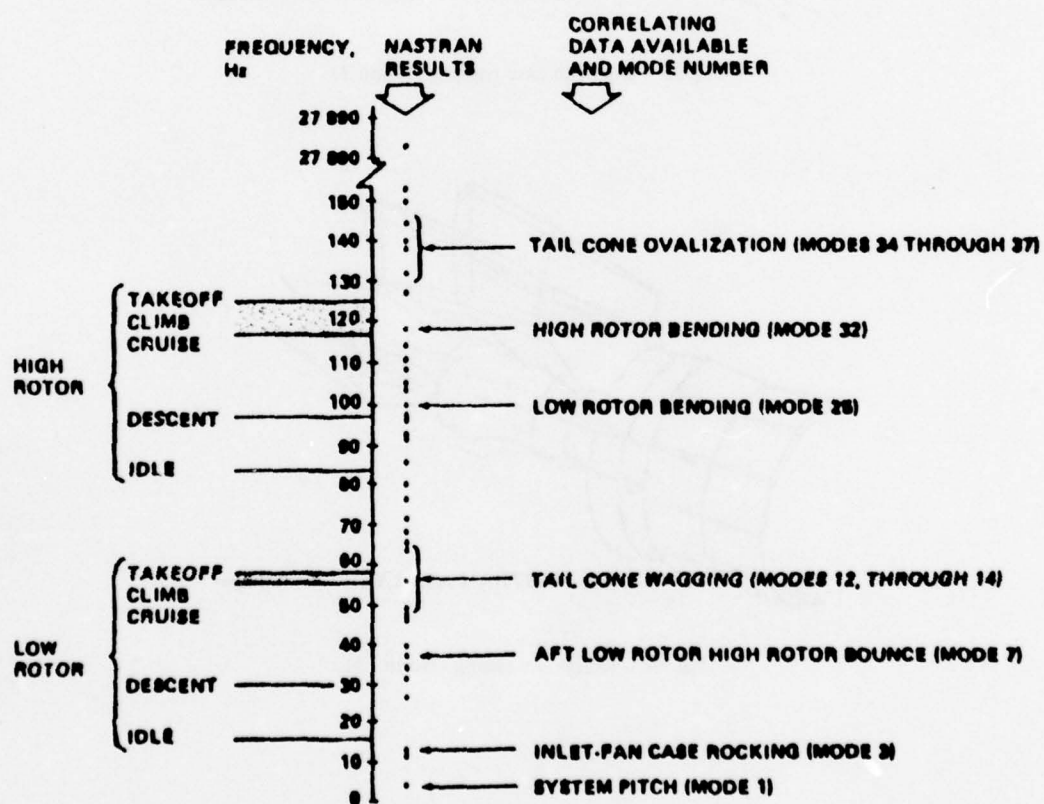


Fig.22 Relative positions of modes evaluated

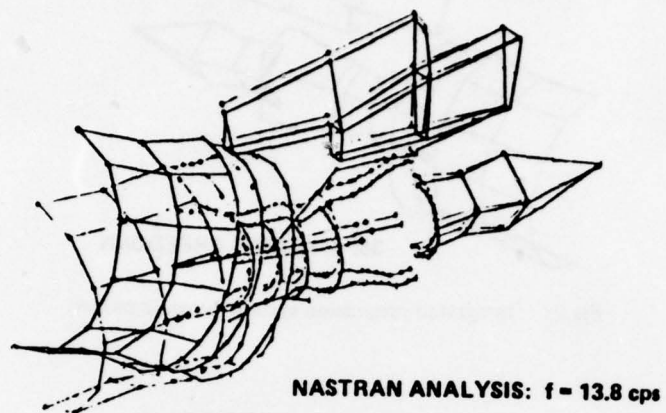


Fig.23 Inlet-fan case rocking (Mode 3)

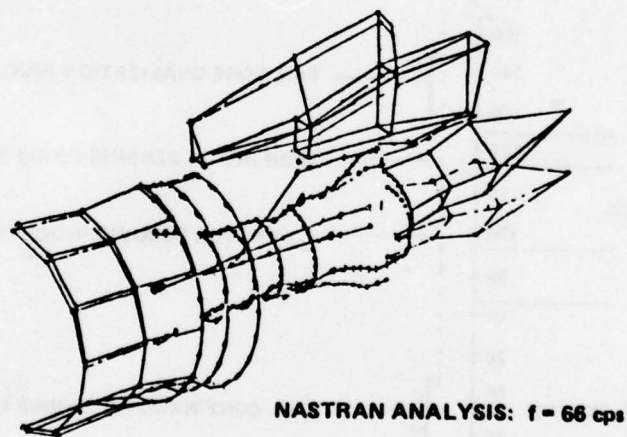


Fig.24 Tailcone wagging (Mode 13)

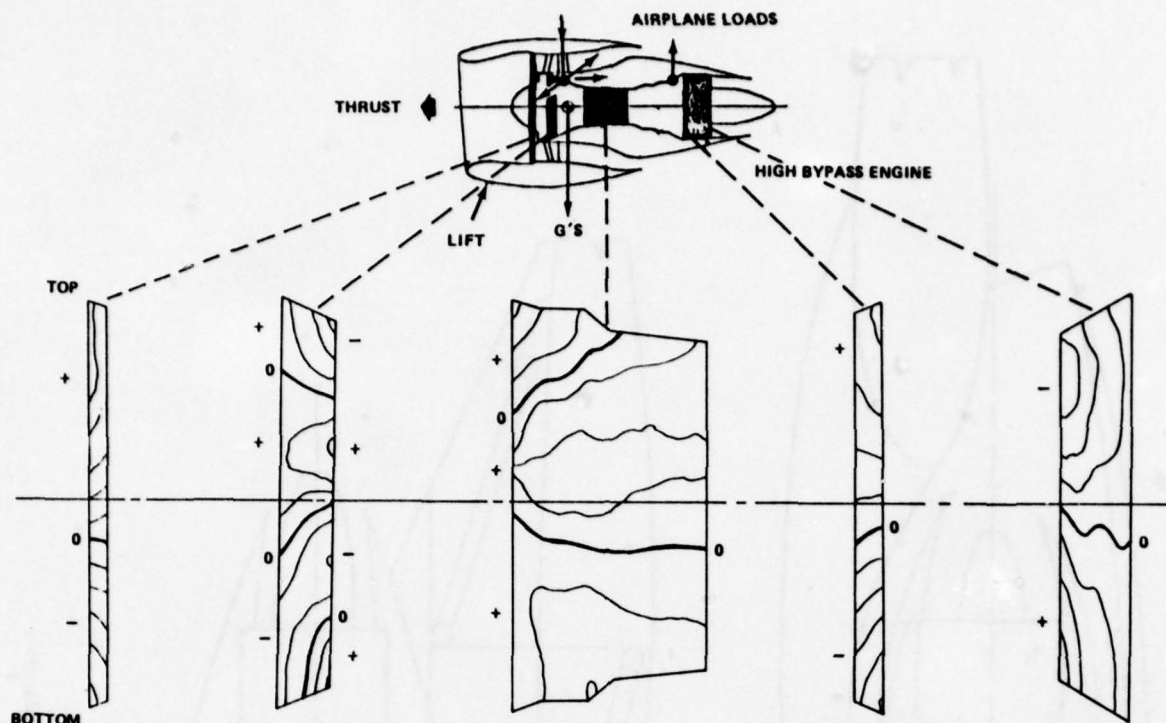


Fig.25 Typical flight load induced clearance changes

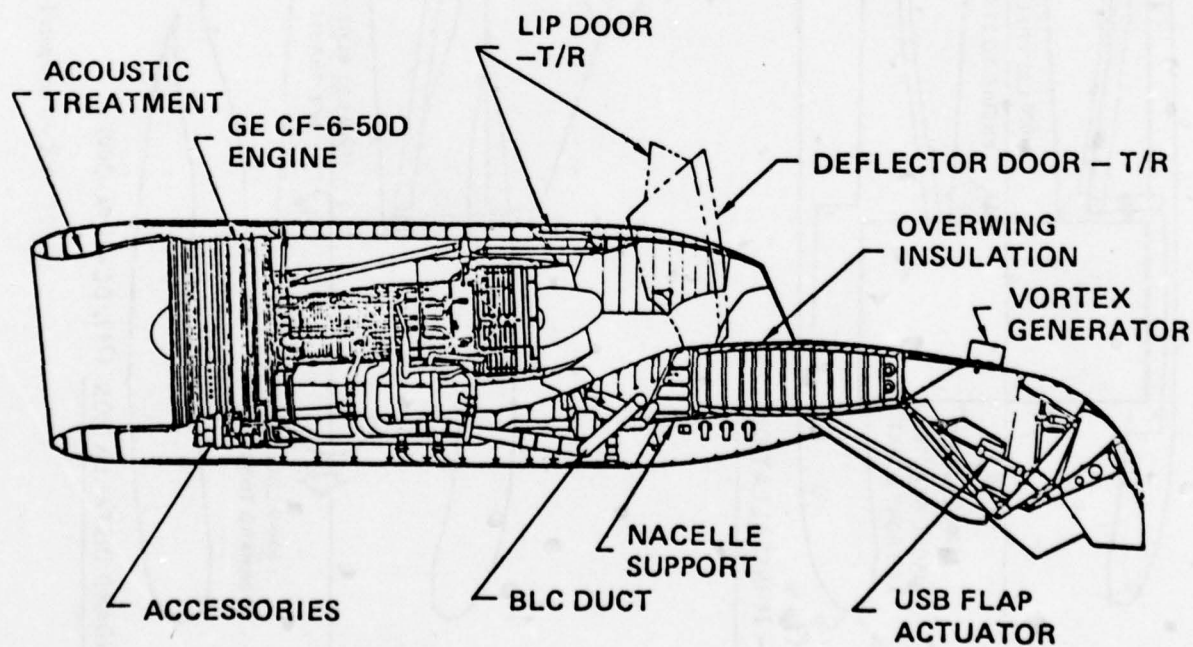
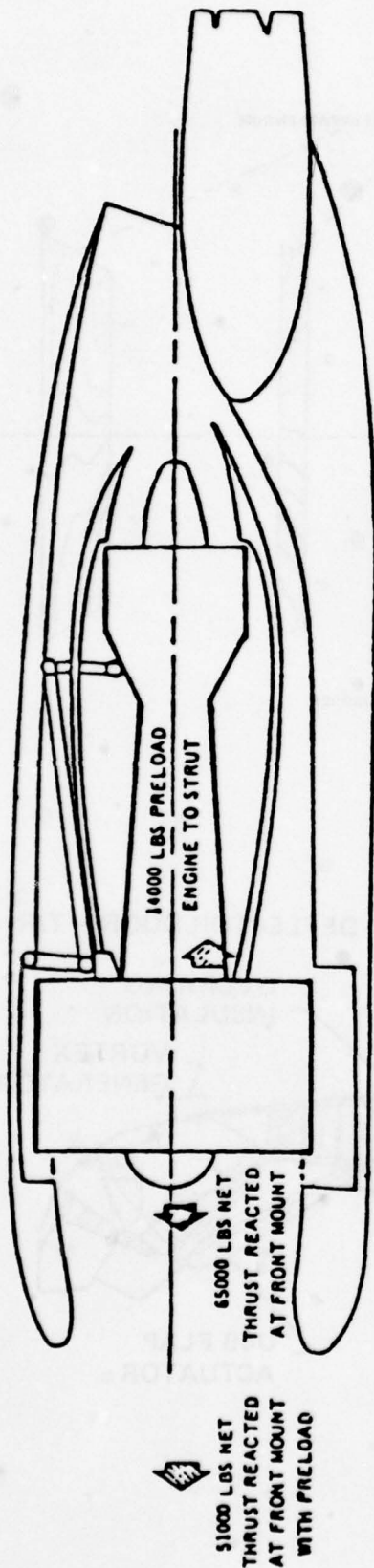
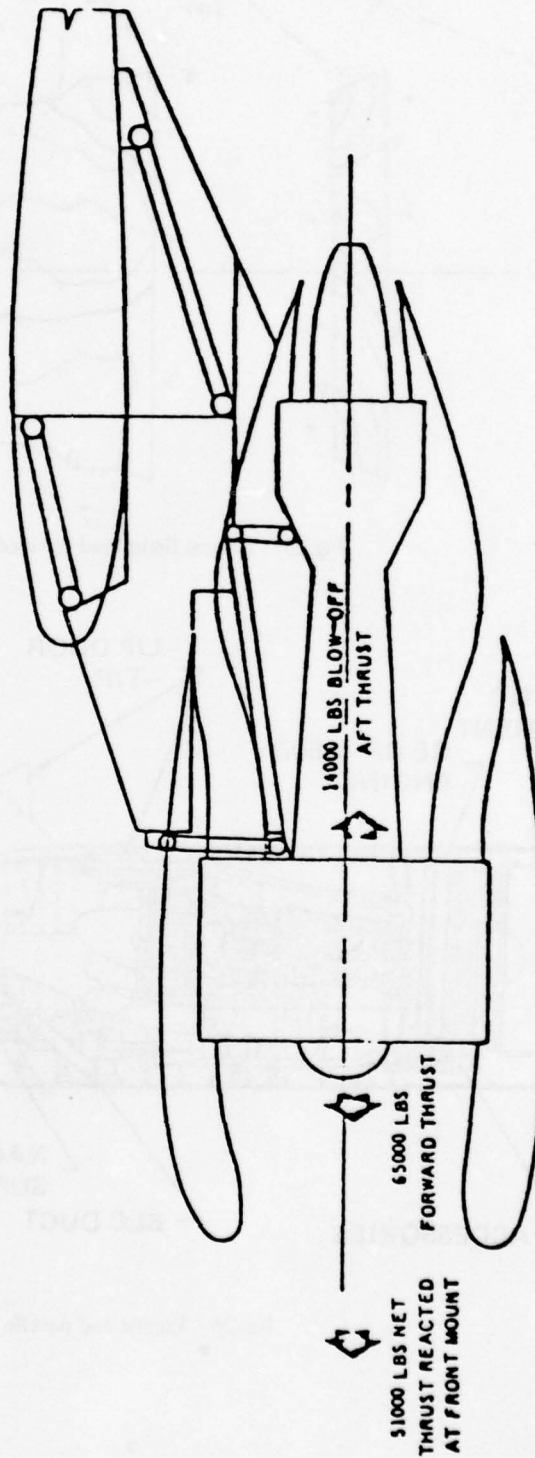


Fig.26 Engine and nacelle cross section



CF6 YC-14 INSTALLATION



CF6 STANDARD INSTALLATION (747, DC-10, A-300)

Fig. 27 Y/C-14 compared to standard installation

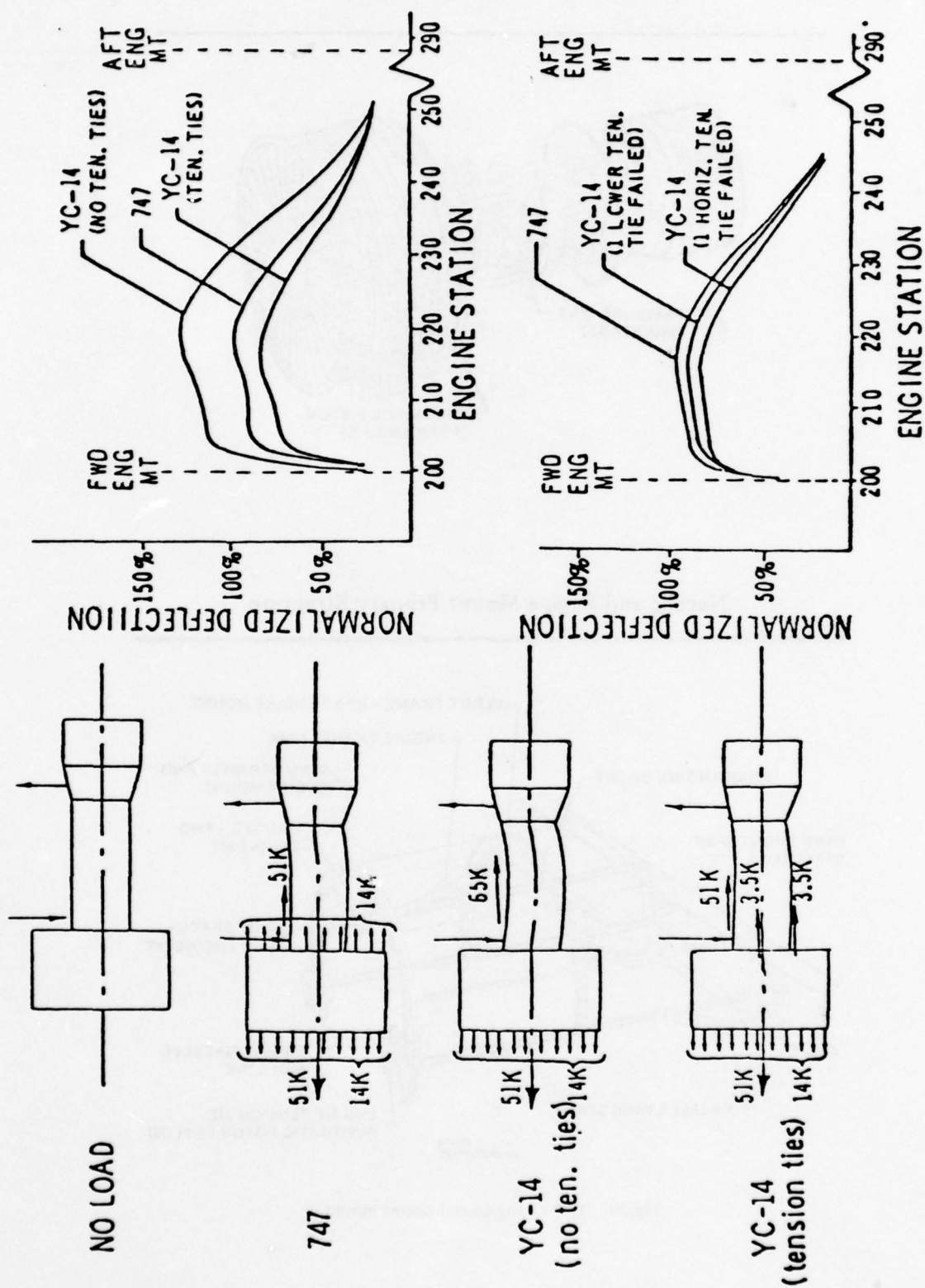
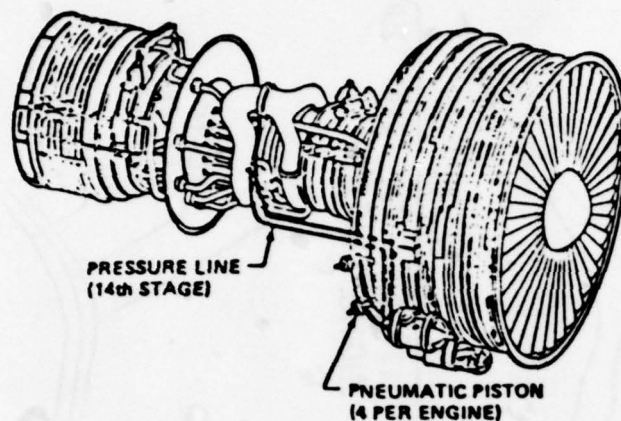


Fig. 28 Y/C-14 static analysis

CF6-50 with Engine Tension Ties



Nacelle and Engine Mount Primary Structure

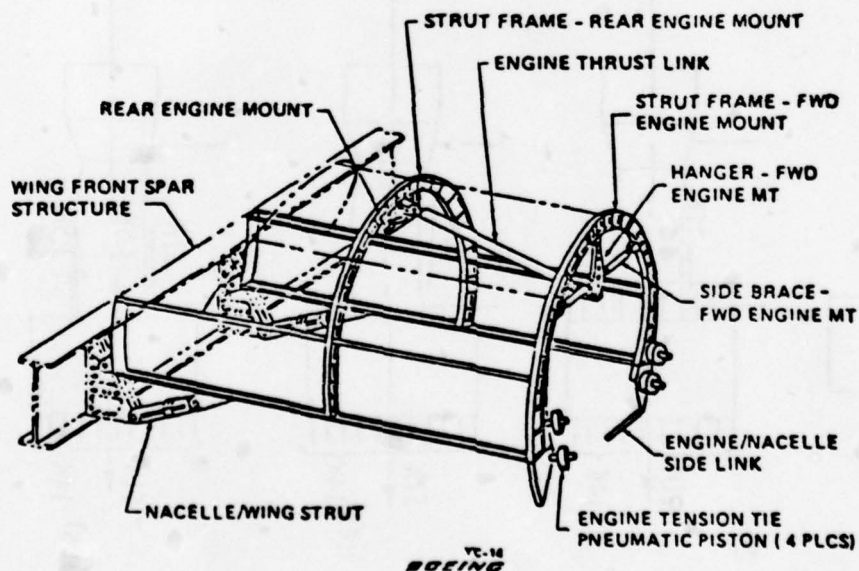
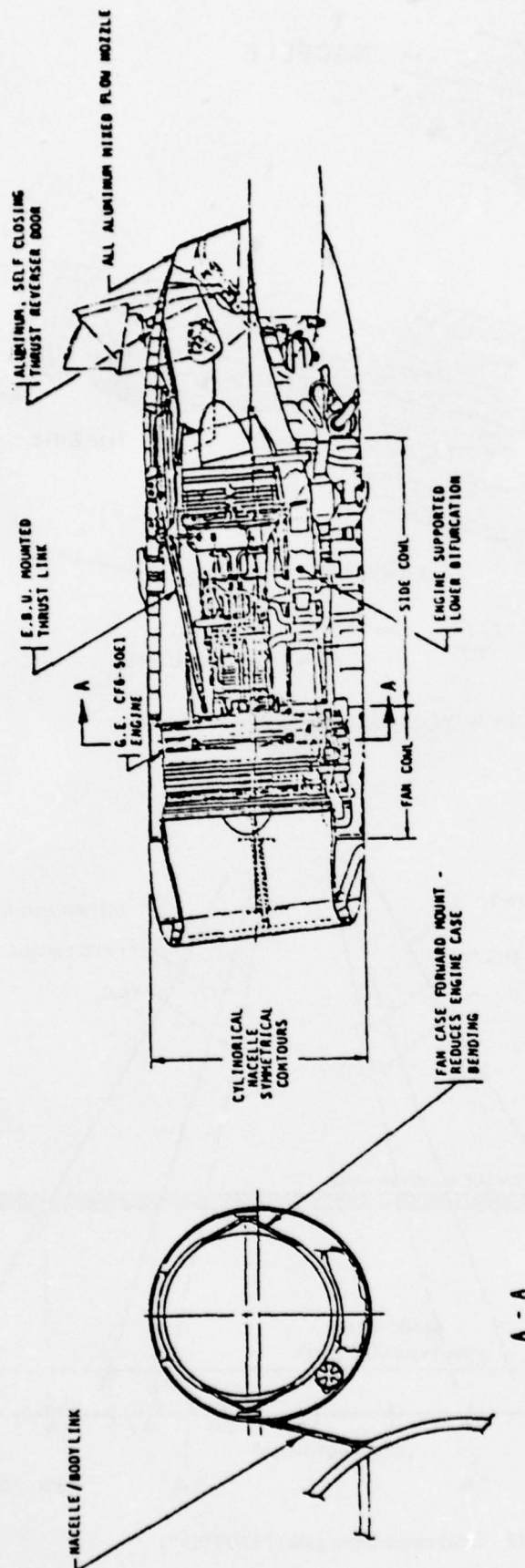


Fig.29 Y/C-14 engine and engine mount



ENGINE INSTALLATION

Fig.30 Engine installation

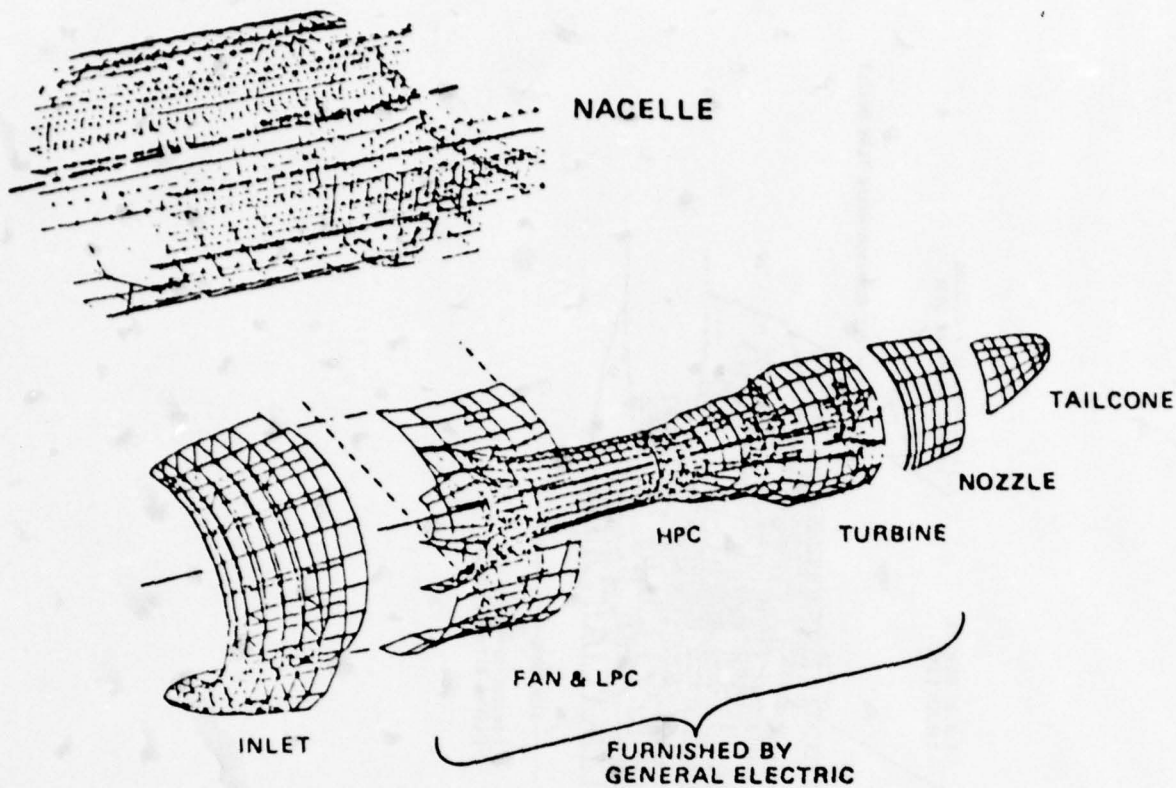


Fig.31 CF6-50/YC-14 propulsion system substructures

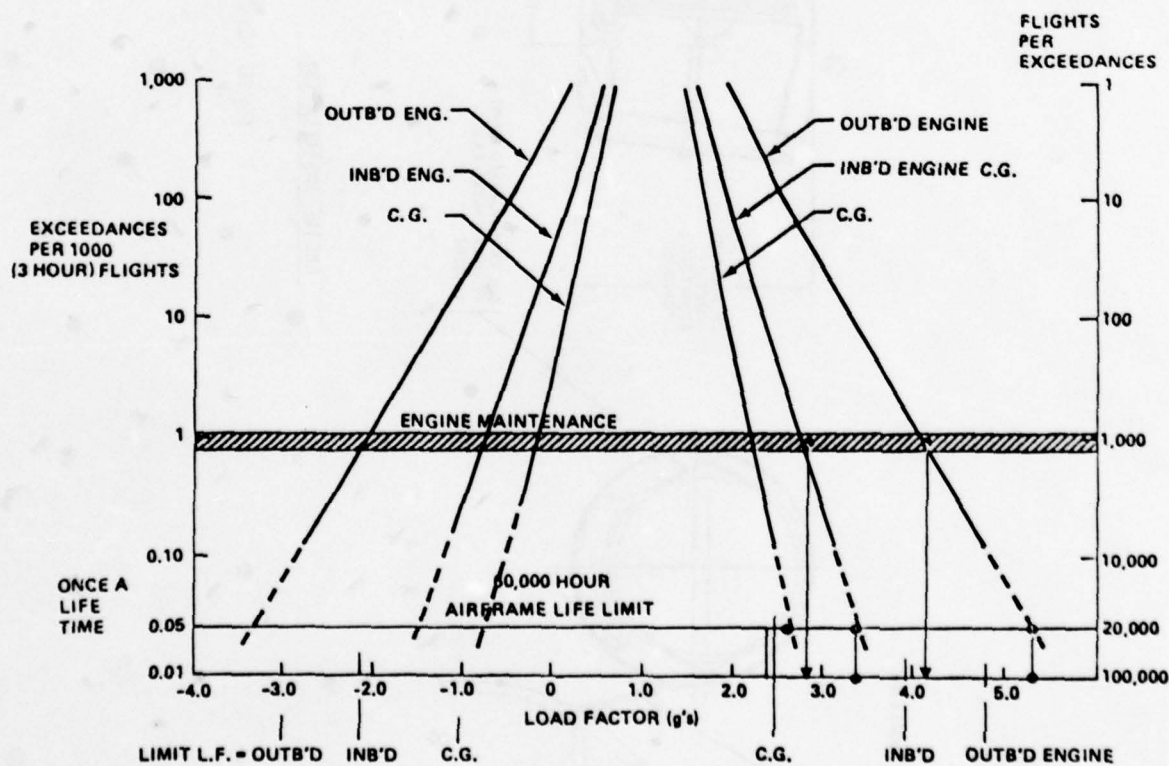


Fig.32 Load exceedance data (747/JT9D-7)

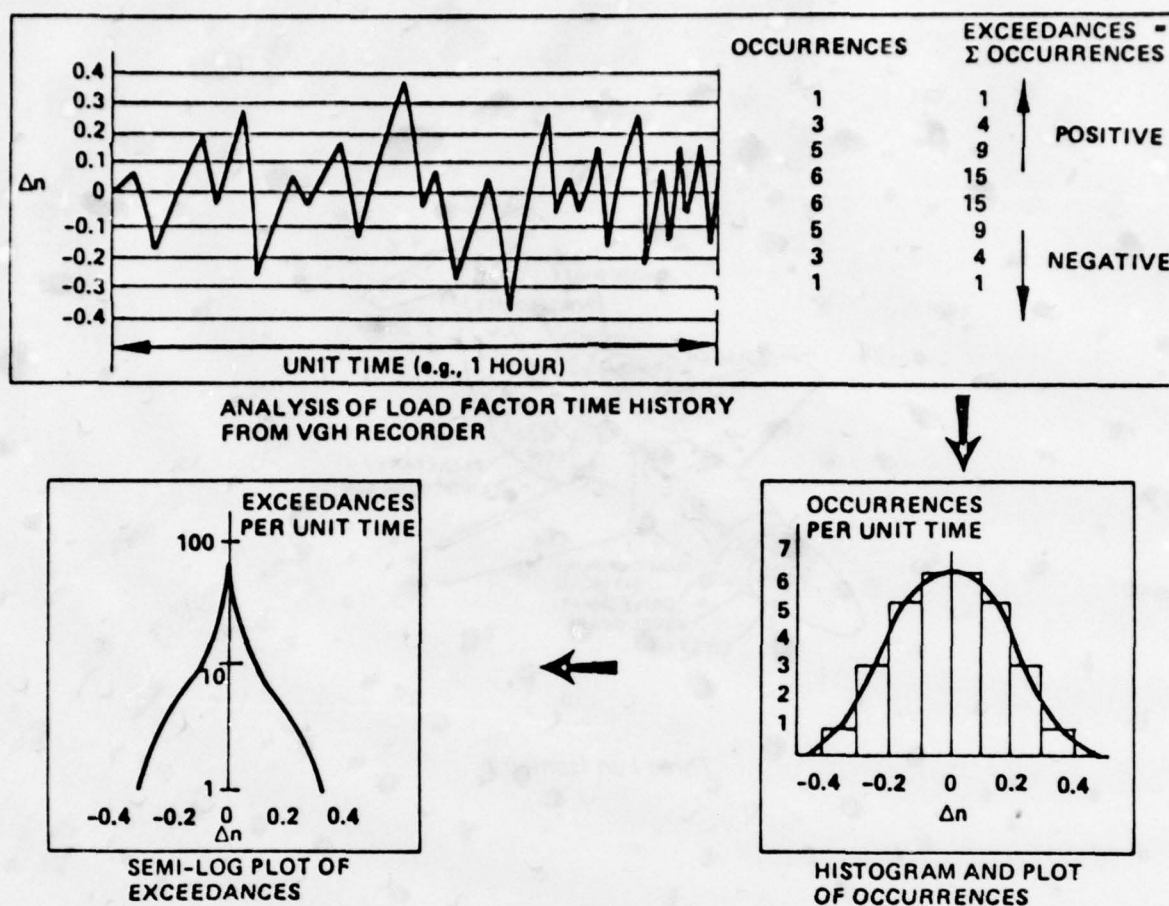


Fig.33 Load exceedance data derivation

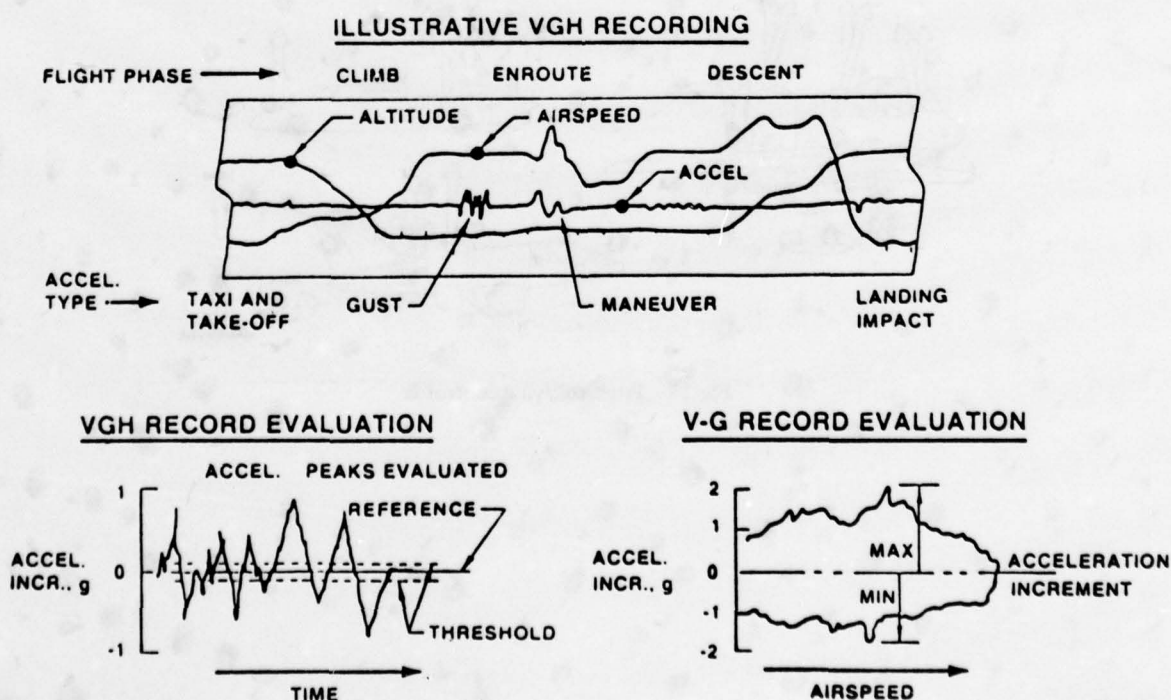
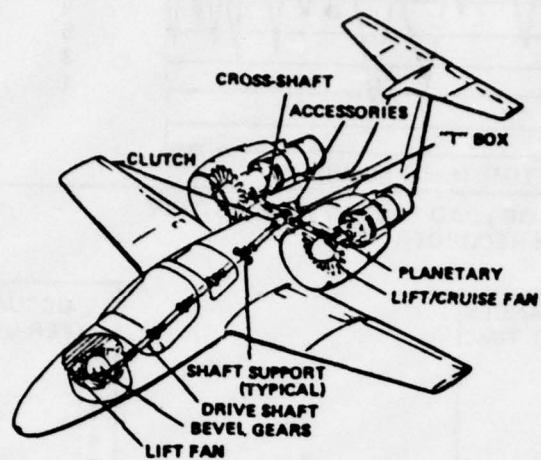


Fig.34 Center-of-gravity acceleration traces from VG and VGH recorders



Three Fan Isometric

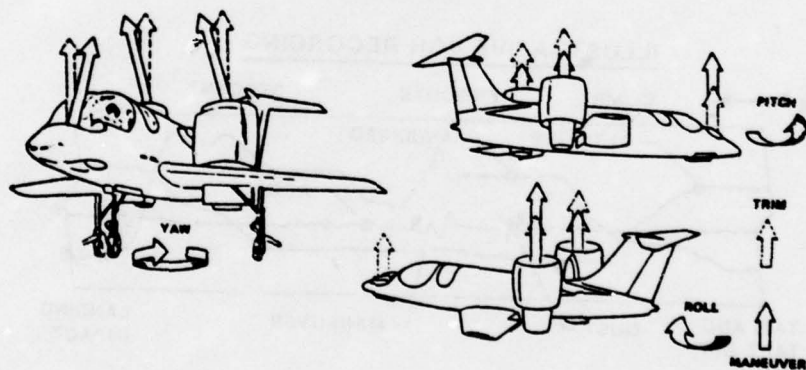


Fig.35 Pitch/roll/yaw control

DISCUSSION

J.G.Mitchell, US

In what areas do you see the greatest need for experimental data to complement the sophisticated analytical programs?

Author's Reply

Improved interface loads between the airframe and the engine and

- engine attachment loads, not envelopes, but actual conditions.
- engine accelerations for actual airplane flight conditions.
- engine operational data such as throttle setting, RPM, temperatures, etc.
- engine inlet and pod airloads for all flight conditions.
- analysis verification of extreme conditions such as blade loss.

DYNAMIC PRESSURE LOADS IN THE AIR INDUCTION SYSTEM OF THE TORNADO FIGHTER AIRCRAFT

by

K. W. Lotter and N. C. Bissinger

Messerschmitt-Bölkow-Blohm GmbH
Military Airplane Division
D 8000 München 80
Postfach 801160
Germany

SUMMARY

During compressor stall the peak pressure in the inlet duct can exceed the steady state inlet total pressure by a wide margin. The heavy pulses created by an engine stall/duct hammer shock have repeatedly caused structural problems during flight testing of high speed airplanes. For the Tornado fighter airplane the auxiliary air intake doors had to be reinforced due to failures during heavy surges. The pressure loads during hammer shock dictate the structural design of the air inlet and duct. Hammer shock pulse strength has been found to be primarily dependent on overall compressor pressure ratio. Structural design of the Tornado air induction system has originally been based on TF30 engine surge pressure data, available at that time. Extensive dynamic pressure measurements were made at a rake immediately ahead of the engine as well as in the inlet duct and the forward inlet including the fixed and movable ramps during full scale inlet/engine compatibility tests carried out at supersonic conditions in Cell 4 of the NGTE/Pyestock, England. Engine stalls were created intentionally by off-design inlet ramp positions and by modulating engine bleed air and/or engine power extraction. The surge overpressures ahead of the compressor used for duct design were essentially confirmed by these tests. The hammer shock pressures measured along the inlet duct and on the movable ramps allowed reliable load assessments for the series aircraft intake structure to be made.

LIST OF SYMBOLS

A	Duct area	Subscripts:	
F	Force	o	Free stream condition
H _p	Pressure altitude	1	Compressor entry
L	Intake duct length	2	Compressor exit
M	Mach number	dyn.	dynamic (overpressure above steady state level)
P	Pressure	loc.	local
t	Time	min.	identifies peak surge underpressure
u	Shock propagation velocity	max.	identifies peak surge pressure or max. value
V	Calibrated flight speed	B. V.	Bleed void
x	Downstream distance from cowl lip	R	Lower ramp side
α	Intake incidence relative to local flow condition	E. F.	Engine face
β	Auxiliary air intake door bracket angle	S	Steady state static
θ	Auxiliary air intake door opening angle	T	Total
		—	averaged
		ref.	Reference

1. INTRODUCTION

Structural damage in the engine air intake has repeatedly been recognized during flight testing of new supersonic airplanes (ref. 1, 2). The reason for this are the heavy pressure pulses created by engine stall, generally designated as *hammershock*. The peak pressure ahead of the engine following an engine stall can exceed the inlet total pressure by a wide margin and, therefore, represents the critical load for the intake structure. Accurate knowledge about this pressure during design is essential for determining the inlet structural requirements.

Due to the complex phenomenon pure theoretical prediction of surge pressures is difficult and the designer is forced to rely largely on available experimental data. Various correlations have been published for different engines (ref. 2 to 7) but there is still a lack of generality, because the peak pressure is not only dependent on the engine considered but also on the stall triggering method. Further variables influencing the stall pulse strength are engine inlet Mach number, fan bypass ratio and cycle pressure ratio. Most correlations to date have shown the peak stall pressure to be a function of overall compressor pressure ratio.

If an existing engine is being installed in a newly developed airframe the *hammershock* strength in front of the engine is known from tests in similar installations. The designer is then faced with the problem to predict the peak pressure amplification and/or attenuation along the intake considered. In cases where engine- and airframe development coincides the only way is to apply data available from an engine with comparable layout.

This paper is concerned with the description of the engine face-, duct- and forward intake peak pressures applied for structural design of the European fighter airplane Tornado (*fig. 1*) and the experimental data obtained during the development phase from full scale intake/engine compatibility tests. The Tornado has jointly been developed by Germany, United Kingdom and Italy. It is powered by two Rolls Royce RB199-34R engines, especially designed to fulfill the versatile requirements for that new all-weather multi-role fighter aircraft. No information on *hammershock* pressures produced by these engines was available during aircraft prototype design in 1969 because engine and airframe development were initiated at the same time.

The critical design loads for the intake duct, therefore, were based on published *hammershock* data produced by the TF30 engine which has a similar bypass ratio. Available pressure data measured earlier in the intake of the Concorde airplane were used to predict the loads on the movable intake ramps and in the boundary layer bleed void. The applied peak pressures were later essentially confirmed during full scale tests with an intake/engine combination by intentionally produced engine surges.

2. TORNADO PROPULSION SYSTEM

The Tornado is powered by two RB199-34R, three-spool turbofan engines with afterburners, buried side by side in the aft end of the fuselage. The overall arrangement is shown in *fig. 2*. A variable-geometry two dimensional intake is provided for each engine and each intake is controlled by an electrohydraulic control system to ensure high operational efficiency. The air intakes are disposed on each side of the forward fuselage. They are of the all external compression type with the compression wedges oriented horizontally, forming the upper surface of the intake. The first ramp is fixed, the second ramp is variable. The subsonic ramp is mechanically linked to the second ramp and both are operated by a single actuator.

The intake boundary layer is bled through the wide slot formed between the trailing edge of the second ramp and the leading edge of the subsonic ramp.

Each intake is equipped with two blow-in type auxiliary air intakes (*fig. 3*). The twin doors of each auxiliary air intake are slaved through a bracket and are spring pre-loaded. Hydraulic dampers mounted on the duct side of each of the inner doors will prevent structural damage during engine surge.

3. INTAKE DESIGN LOADS

During design of the Tornado the *hammershock* pressures which the RB199-34R would produce were unknown since engine development was started at the same time. For the intake duct design, therefore, the data available at that time from the TF-30 engine (obtained in NASA Cell 1 A. T. F.) were applied. This was thought justified since the TF-30 engine cycle is comparable to that of the RB199.

Due to the limited knowledge about the *hammershock* phenomenon the upper boundary of the available TF-30 data was used as the basis for design (*fig. 4*).

The Tornado forward intake geometry is very similar to that of the Concorde. Use could, therefore, be made of the experience gained from surge pressure attenuation over the Concorde forward intake. The thus derived longitudinal distribution of the peak surge pressure for the engine intake, applied for prototype design, is also shown in fig. 4.

Early surge pressures gathered from the RB199-34R flying test bed (Vulcan) were essentially within the assumed pressure limit.

Further confirmation, however, was necessary with the intake operating at supersonic conditions in order to confirm and define the design-limiting loads for the series aircraft. The relevant tests will be described in detail in section 5.

4. AUXILIARY AIR INTAKE DOOR FAILURES

During early prototype flying auxiliary air intake door failures happened due to excessive hammer shock loads. These high loads were created by heavy surges following bird ingestion and reheat overfueelling. The damage occurred to the brackets which link the inner and outer doors together (see fig. 3). When the doors are partly or fully open, i.e. during high engine rating at low flight speed and on the ground respectively, the hammer shock pressure can penetrate into the space between the doors and create high tension forces in the brackets. The magnitude of the hammer shock pressure between the doors was underestimated during prototype design due to lack of data. Fig. 5 shows details of the broken bracket.

For a constant differential pressure acting on the outer door, the bracket tension force increases rapidly as the auxiliary intake door approaches the fully open position (see fig. 6). This is because of the fact that the angle β between the bracket and the door reduces to small angles as the door angle increases.

In order to obtain more precise knowledge about the true door loads the brackets were instrumented with strain gauges during the following flight test period. The bracket force measured during a hammer shock is presented in fig. 7. The trace directly reflects the pressure fluctuation in the intake duct during a hammer shock which can be seen from typical hammer shock pressure signatures, as shown later in fig. 12. The trace for the door angle in fig. 7 shows that the damper allows the door only to close by a small amount and thus prevents banging the door against the frame.

For redefining the auxiliary intake door loads a correlation was made between the measured peak bracket forces and the relevant engine face peak surge pressures. By applying the relationship between bracket force and door angle (fig. 7) an equivalent door differential pressure was calculated for the front and the rear doors. This differential pressure is depicted in fig. 8 versus door angle for flight at sea level which yields the most critical pressures. These pressures were used for the redesign of the auxiliary intake doors. The modified design incorporated reinforced inner and outer doors, alteration of the door hinge, stronger bracket and bracket joints and finally repositioning of the brackets to increase the angle β in the fully open door position.

5. INTAKE/ENGINE COMPATIBILITY TEST

Tests were made at supersonic speeds in Cell 4 at NGTE, Pyestock, England with a full scale intake/engine combination as the main contribution to the intake/engine compatibility program. The prime object of these tests was to investigate the intake and engine operation under supersonic flight conditions with the intake controlled both by the automatic Air Intake Control System and manually to test the effect of ramp excursions on engine behaviour. The manual control enabled extreme subcritical and supercritical intake conditions so that the intake could be operated into buzz and at flow conditions with high dynamic distortion, respectively. The engine was run in dry and reheat condition and a slave loading system was employed to represent the electrical and hydraulic power off-take requirements from the HP spool.

Since engine surges could be produced intentionally during these tests provision was made to measure the dynamic pressure over the intake and in the duct during hammer shock cycles to gather data under realistic conditions for assessment of the dynamic loads to be applied for the series aircraft design.

5.1 Test Set-Up

The supersonic powerplant test cell at NGTE, Cell 4, is shown in fig. 9. The 5 ft x 5 ft supersonic free jet is produced by a nozzle having two flexible walls moving between fixed side plates. The intake is mounted in the central part of the nozzle and is subjected to conditions experienced in free flight. The engine exhaust is ducted to the main gas coolers through a water-cooled diffuser. The range of incidences was varied from $\alpha = -2^\circ$ to $+9^\circ$ during these tests.

5.2 Instrumentation

To measure the intake dynamic flow distortion, a rake incorporating 40 steady state pitot tubes and 40 Kulite pressure transducers was fitted in front of the engine (fig. 10). Additionally, 11 high response static pressure transducers and 2 total pressure transducers for the measurement of the pressure time history during intake hammershock were installed at different intake locations. 2 static pressure transducers were located at opposite sides of the duct wall in the rake plane to measure the hammershock pressure level ahead of the engine, 4 were distributed over the forward intake and 5 were mounted in the bleed void above the movable ramps. Engine surges were detected using the NGTE surge monitor which displayed the HP compressor delivery pressure gradient dP/dt on an oscilloscope. Other intake and engine data for the benefit of intake and engine control systems and detailed engine investigations are not described in this paper.

5.3 Data Acquisition

All dynamic pressure signals were recorded on an AR1600 and some on an FR1300 magnetic tape recorder. The AR1600 signals are frequency modulated on centre-frequencies of 40 kHz, 70 kHz, 124 kHz, 256 kHz and 384 kHz. The AR1600 tape speed during recording was 60 inches per second. The smallest frequency range of a signal, therefore, was about 1 kHz. The FR1300 signals are frequency modulated at 27 kHz. The recording tape speed was 15 inches per second. The signal frequency range is 5 kHz. For identification purposes a time code and the intercommunication of the test operators were also recorded on the tapes. Fig. 11 shows the data recording system and the arrangement for data replay and analysis.

For analysis of the surge pressures the signals on the AR1600 tape were played onto a FR1300 tape. The AR1600 tape was run with a tape speed of 60 inches per second. The exit filters were set to cut-off frequencies above 1 kHz. The FR1300 tape speed was 15 inches per second during the recording and $1\frac{7}{8}$ inches per second during the replay of the data. The pressure traces were reproduced on an eight-channel pen writer using a paper speed of 5 and 100 mm/sec respectively. The high paper transmission speed was used for detailed evaluation of the surge pressures. For a more exact investigation of the pressure rise-time during a surge, selected pressure signals were again replayed from the AR1600 and the FR1300 tape onto a Honeywell Visicorder 1858 CRT using 1882 LGD amplifiers with a cut-off frequency of 12.5 kHz and a sampling rate of 50 samples/sec. The frequency range of these traces was 5 kHz.

5.4 Surge Initiation

During the main compatibility tests which included investigations like effect of compressor bleed, power-off take from the HP spool at dry and reheat condition, ramp angle and pitch transients etc., the engine was run successfully without major problems.

A number of surges was, therefore, produced intentionally to investigate procedures to recover the engine after a surge and also, to produce intake hammershocks for the recording of dynamic intake pressures. The procedure adopted was to set up a steady test condition, take a scan of all data and then change one variable which finally produced a surge. The changes incorporated

- closing of the engine bleed
- increasing of slave load to extreme conditions
- increasing of intake ramp angle (reduce intake throat)
- driving the intake into buzz

5.5 Measured Hammershock Pressures

In fig. 12 the surge pressure time histories of a typical surge at $M_0 = 2.0$, $\alpha = 2^\circ$ in Cell 4 are shown for different locations in the intake. The surge shown was triggered by increasing the slave load. The time delay between the pressure rise at the two rake plane stations (Stn. 52 and 53) indicates that the shock is not like an ideal wave normal to the duct centre line. The peak pressure at both locations, however, reaches nearly the same level. The time for a whole hammershock cycle is about 60 milliseconds and the upstream movement of the pressure wave can be recognized by the time delay between the pressure rise at the individual traces. It is also reflected in the figure that the surge overpressure (the increment above the steady state pressure) at the rake plane ahead of the engine (traces 52, 53) is exceeded at several stations in the forward intake, that is in the intake throat region (traces 47 and 41) and in the extreme corners of the bleed void (traces 44 and 45).

The peak surge pressures of a number of intentionally produced surges are presented in fig. 13 for the different locations in the intake versus the peak surge pressure at the engine face (rake plane). The test conditions comprise free stream Mach numbers from $M_0 = 1.6$ to 2.0 and incidences from $\alpha = -2^\circ$ to $+5^\circ$. The pressure rise above the pre-surge steady state pressure due to a hammershock is plotted in fig. 14 for different locations in the intake. The high pressure rise in the intake throat and the extreme bleed void corners for nearly all surges can be seen from that picture. A plot of these pressures versus fuselage station is shown in fig. 15, the local overpressures being referred to the

overpressure at the engine face. The relative large scatter band of the data follows from the fact that the shape of a hammer shock wave varies from surge to surge resulting in different pressure distributions along the intake. The general trend, however, is that the surge pressure rise increases as the duct area (fig. 16) reduces. A rapid pressure decrease can be seen upstream of the cowl lip.

This trend has also been observed in the intake of the F-111 fighter and was subsequently applied to the YF-16 fighter intake design (ref. 8).

The peak surge pressures measured in Cell 4 in front of the engine compressor are plotted versus overall compressor pressure ratio in fig. 17 and compared with the prototype design pressure which was based on TF-30 maximum surge pressures. It can be seen that all test data are below or just on the prototype design line. For this reason it was decided to retain the prototype design pressures for the series aircraft.

6. LOAD ASSESSMENT

6.1 Intake Diffuser

The surge pressure loads for the intake diffuser are determined by applying the peak surge pressure correlation of fig. 17 together with the relevant data for the freestream total pressure, the intake pressure recovery and the compressor pressure ratio. Cold, standard and hot atmospheres are to be considered to identify the most critical pressure loads for the intake structure. The result of such a calculation for a cold day atmosphere is shown in fig. 18 which presents the peak surge pressure as a function of flight Mach number and altitude. It was shown that the highest pressures are associated with the cold day atmosphere because of the resulting higher corrected airflow and compressor pressure ratio. It should be mentioned here that during stress calculations structure temperatures for the different climatic conditions must be considered in conjunction with the pressures because the duct strength is heavily affected by temperature at extreme operating conditions like high flight Mach number at low altitude.

Consideration must also be given during intake diffuser design to the magnification of the normal operation duct underpressure due to hammer shock. At zero and low flight speeds the steady state duct pressure reduces below ambient pressure as the engine mass flow is increased. The negative cycle of the hammer shock wave (see fig. 19) further reduces this underpressure and therefore defines another critical load case for the intake structure. For the low speed flight conditions the most representative and comprehensive data were available from surges in the Vulcan flying test bed (F. T. B.).

Fig. 19 shows the maximum measured underpressures obtained during flights with the F. T. B. in front of the engine as a function of overall compressor pressure ratio (ref. 9). The broken curve represents the mean of all measured data. For duct strength, however, the solid curve was proposed in order to cover the most critical surge cases. The two data points on the left hand side below the solid curve are not critical with respect to maximum underpressure because they were recorded at low compressor pressure ratios which do not occur in flight regimes yielding to extreme underpressures. The duct differential pressures deduced from the solid curve are shown in fig. 20 for "combat" engine power setting at different flight Mach numbers and altitudes. The determining underpressure can be seen to occur at sea level take-off conditions.

6.2 Movable Intake Ramps

6.2.1 Third Ramp

The longitudinal shape of the travelling wave which can be determined by comparison of the time histories from transducers at different longitudinal locations is shown in fig. 21 on the lower side of the third ramp. The most critical load on this ramp occurs at the moment when the hammer shock wave front reaches the ramp leading edge. For the wave shape shown in fig. 17, the peak hammer shock pressure is felt nearly over the whole ramp length while the upper ramp side is still subjected to the steady state bleed void pressure. Approximation of the wave shape by a constant pressure distribution of the peak pressure level overestimates the ramp load by only 3 %. The third ramp differential pressure, therefore, was predicted by applying the peak hammer shock pressure over the whole length of the lower ramp side and the pre-surge steady state bleed void pressure over the upper side. For typical supersonic ramp positions the Cell 4 test data showed that the absolute hammer shock pressures in the region of the third ramp were of nearly the same level as in the engine face rake plane (see fig. 13). For this reason, the engine face pressures presented in fig. 14 were applied as the peak pressures to the lower side of the third ramp.

The resulting ramp differential pressures for constant calibrated flight speeds are also depicted in fig. 21 for Mil. Spec. cold day climatic conditions which yielded to maximum pressures.

6.2.2 Second Ramp

The *hammershock*, produced by an engine surge, moves upstream from the engine through the intake duct and "hits" the second ramp at the trailing edge. There, it is "split" into one part which moves on top of the second ramp into the bleed void and into another part which moves along the intake side of the second ramp and finally is expelled out of the intake. The maximum difference between the pressures exerted by these two shocks onto the second ramp defines the design load of the second ramp and its actuation system.

Analysis of the surge pressure time histories of the dynamic pressure pick-ups (fig. 12) on the second ramp showed that the propagation velocity of the "bleed-side" shock is higher than that of the "intake-side" shock. The maximum pressure jump across the shock front increases along the ramp for the "bleed-side" shock. The maximum pressure jump across the "intake side" shock front decreases substantially during the shock's movement along the second ramp because it diffuses into the atmosphere.

The relative complex loading of the second ramp during a *hammershock* necessitates the definition of a simplified model for the calculation of the second ramp design load, see fig. 21. The shock velocities were assumed to be constant and were derived from the Cell 4 surge pressure time history traces. Furthermore, the shocks moving along the second ramp were considered to have a square wave pressure distribution with a known magnitude. The measured maximum pressures along the "intake side" of the ramp were averaged, whereas on the "bleed-side" of the ramp the maximum shock pressure was assumed to act over the whole ramp length. Thus, the magnitudes of the shocks were defined as percentages of the engine face surge pressures. With these assumptions the moment around the second ramp hinge point due to the surge overpressures was derived analytically as a function of time. The calculation of the magnitude of the maximum moment was straightforward. For design purposes this maximum moment was converted into an equivalent constant ramp load.

These maximum equivalent second ramp loads as a function of Mach number are given in fig. 21 for the maximum flight speed V_{max} .

7. CONCLUSIONS

Data from early TF30 engine surges were used to establish the Tornado intake *hammershock* pressures. The correlation of engine face peak *hammershock* pressure in terms of overall static compressor ratio from the TF30 engine was applied to the RB199 engine. Extensive data from full scale Tornado intake/engine compatibility tests with intentionally produced surges confirmed the earlier assumptions. These tests also provided data for the peak pressure levels along the intake duct and in the forward intake structure, especially on the movable ramps so that reliable pressure load calculations for the series aircraft could be performed.

The *hammershock* pressure loads for the inlet duct, the movable ramps and auxiliary intake doors are dominant design factors. The magnitude of these pressures significantly affects the intake structure weight. Aircraft and engine designers, therefore, should jointly investigate design techniques which reduce the strength of compressor stall and allow attenuation of the *hammershock* pressures in the intake. The relevant propulsion system performance degradation would probably be more than compensated by structure weight reductions resulting in overall mission performance improvements.

8. REFERENCES

- 1 L. M. Randall and W. H. Hand
Integration of Inlet and Engine - An Airplane Man's Point of View
SAE Paper No. 680287, Air Transportation Meeting New York, April/May 1968
- 2 F. L. Marshall
Prediction of Inlet Duct Overpressures Resulting from Engine Surge
Journal of Aircraft, Vol. 10, No. 5, May 1973, pp. 274 - 278
- 3 D. R. Bellman and D. L. Hughes
The Flight Investigation of Pressure Phenomena in the Air Intake of an F111A Airplane
AIAA Paper 69-488, Colorado Springs, Colo., 1969
- 4 D. A. Choby, P. L. Burstadt and J. E. Calogeras
Unstart and Stall Interactions between a Turbojet Engine and an Axisymmetric Inlet with 60-Percent Internal-Area Contraction
TMX 2192, 1971, NASA
- 5 D. P. Morris and D. D. Williams
Free-Jet Testing of a Supersonic Engine/Intake Combination
Aeronautical Journal, Vol. 74, March 1970, pp. 212-218

- | | | |
|---|--|--|
| 6 | G. A. Mitchell and
D. F. Johnson | Experimental Investigation of the Interaction of a Nacelle-Mounted Supersonic Propulsion System with a Wing Boundary Layer
TMX 2184, March 1971, NASA |
| 7 | A. P. Kurkov, R. H. Soeder
and J. E. Moss | Investigation of the Stall Hammershock at the Engine Inlet
Journal of Aircraft, Vol. 12, No. 4, pp. 198-204 |
| 8 | P. J. Evans and P. P. Truax | YF-16 Air Induction System Design Loads Associated with Engine Surge
Journal of Aircraft, Vol. 12, No. 4, April 1975, pp. 205-209 |
| 9 | G. A. York and
R. G. Hercock | RB199-018/5 Vulcan F. T. B. Intake Static Pressures during Surge, Flight Results
RR-Note GN17587 |

ACKNOWLEDGEMENT

The authors of this paper wish to acknowledge the valuable help which came from discussions with Mr. C. P. Stocks, British Aerospace, Warton Division, U.K.

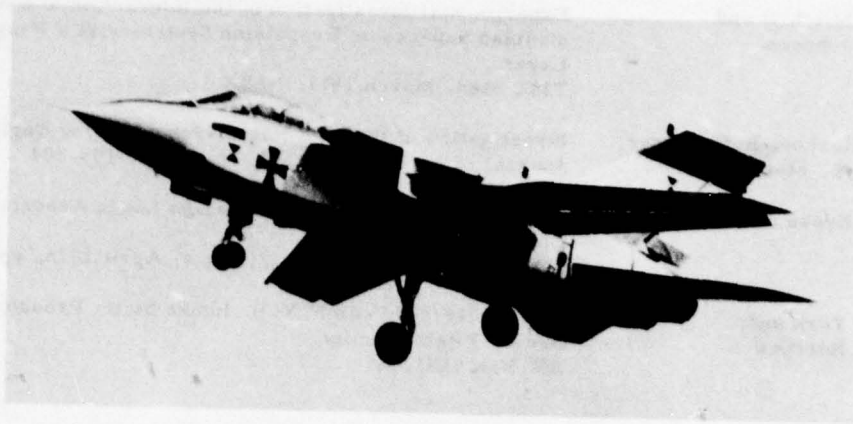


Fig.1 Tornado multi-role fighter

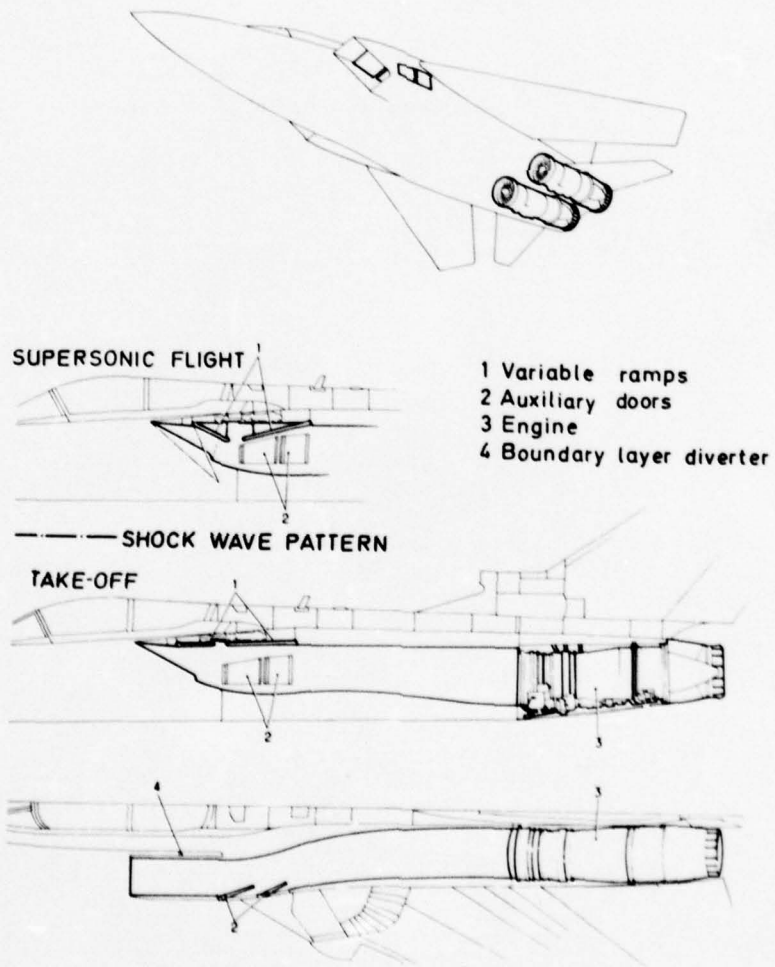


Fig.2 Tornado propulsion system

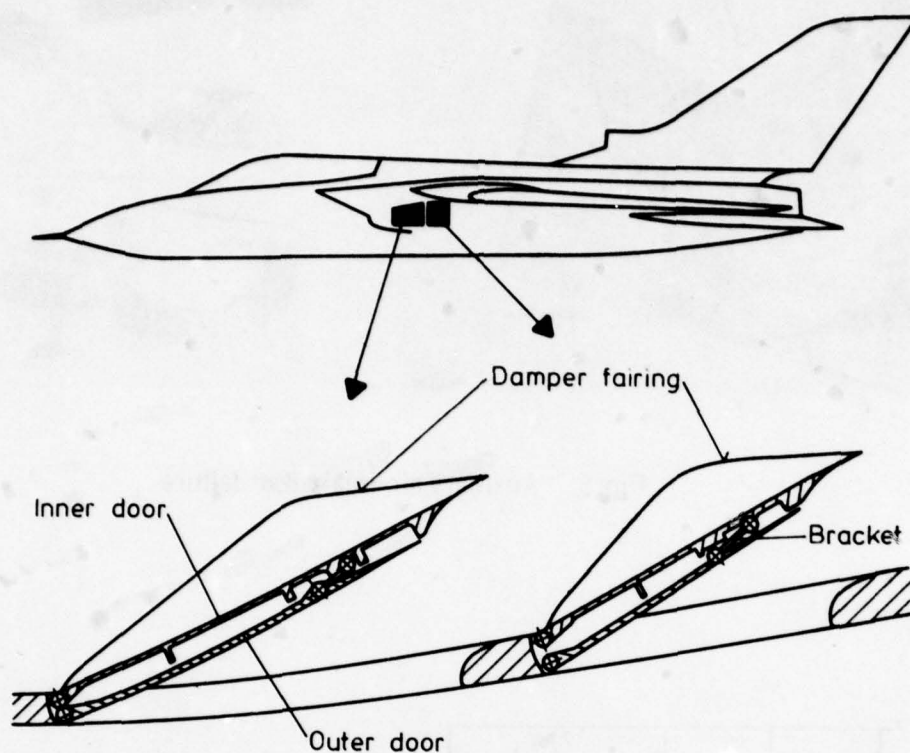
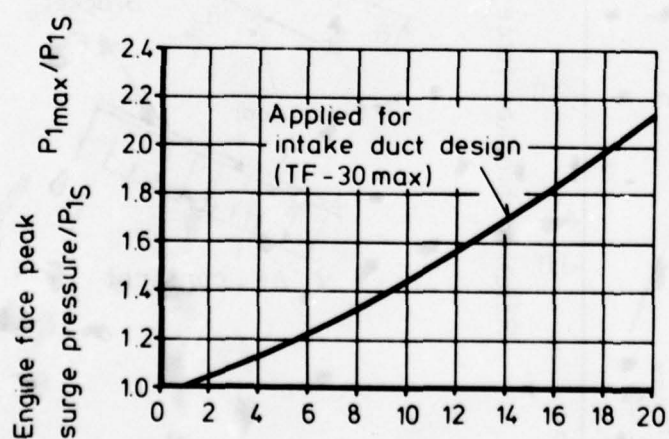
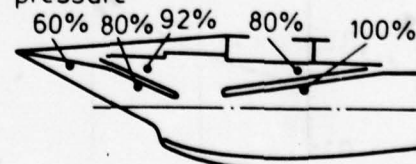


Fig.3 Auxiliary air intake doors (schematic)



Peak surge pressure distribution;
percentage of engine face surge
pressure



Compressor overall static pressure ratio; P_{2S}/P_{1S}

Fig. 4 Prototype intake design loads

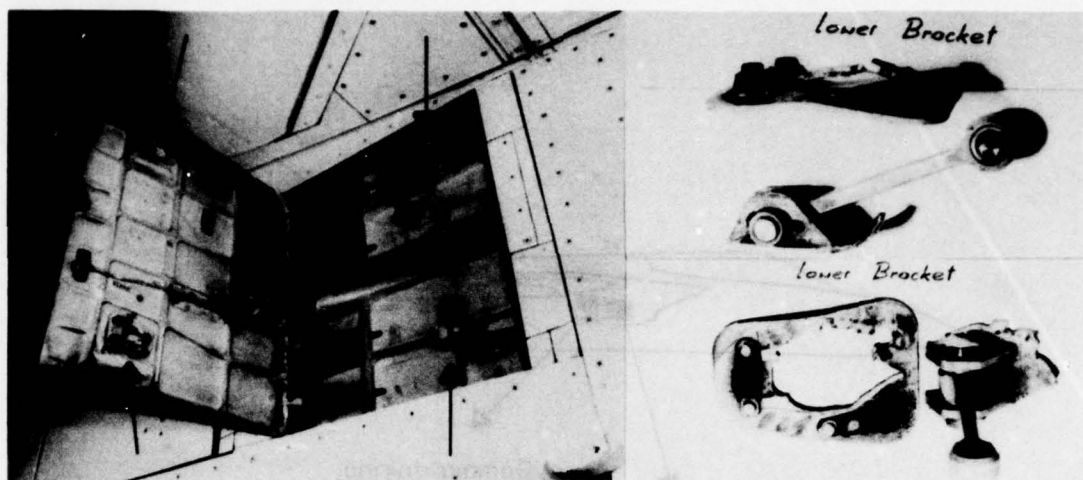


Fig. 5 Auxiliary air-intake door failure

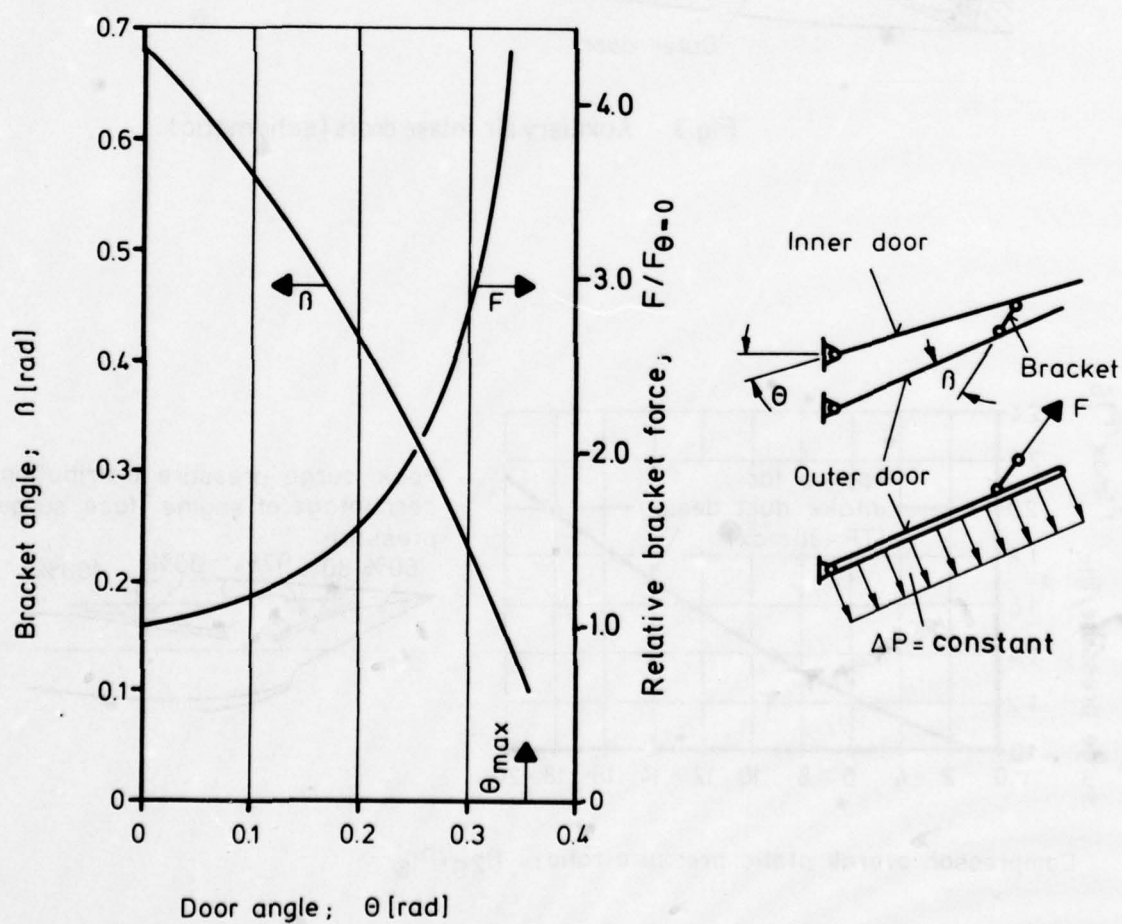


Fig. 6 Bracket force variation versus auxiliary intake door position

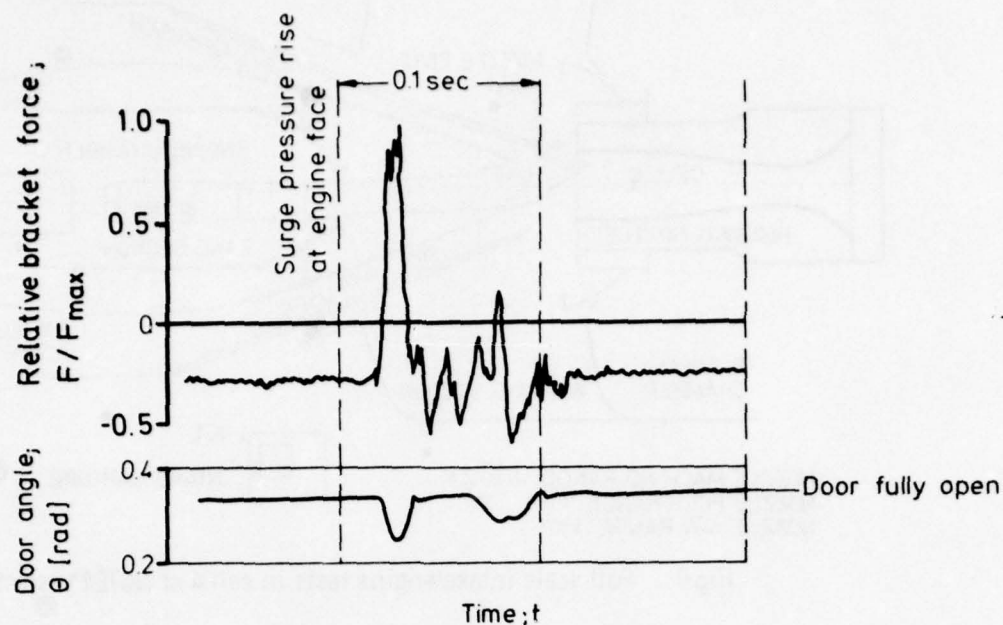


Fig.7 Bracket force and door angle variation during hammershock

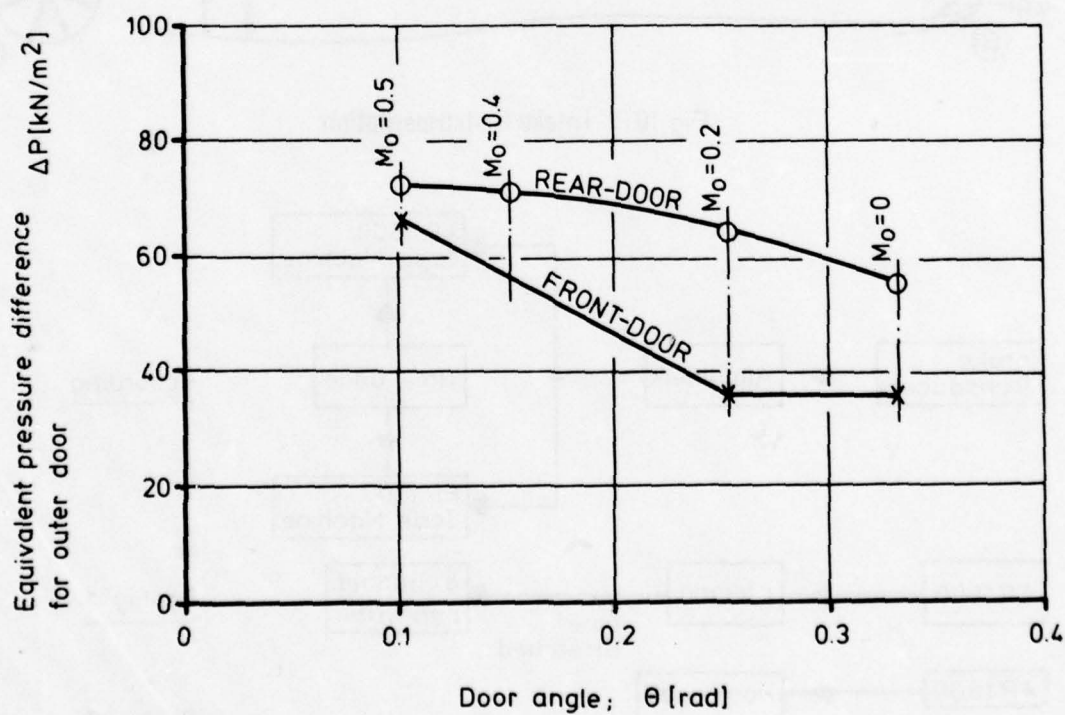


Fig.8 Design differential pressure for outer auxiliary air intake doors



$$M_0 = 2.0$$

$$\alpha = 2^\circ$$

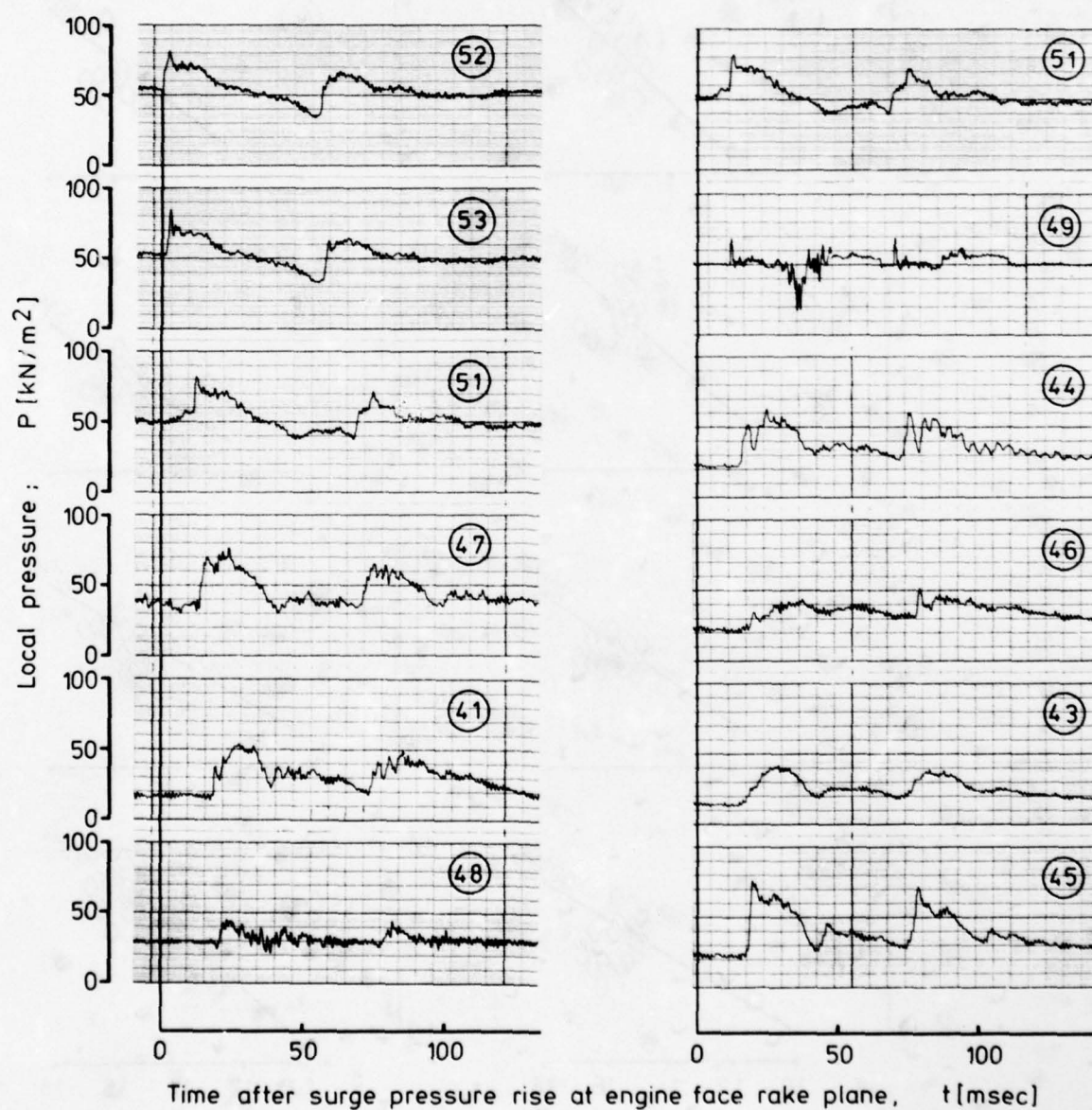


Fig. 12 Surge pressure histories in intake and duct

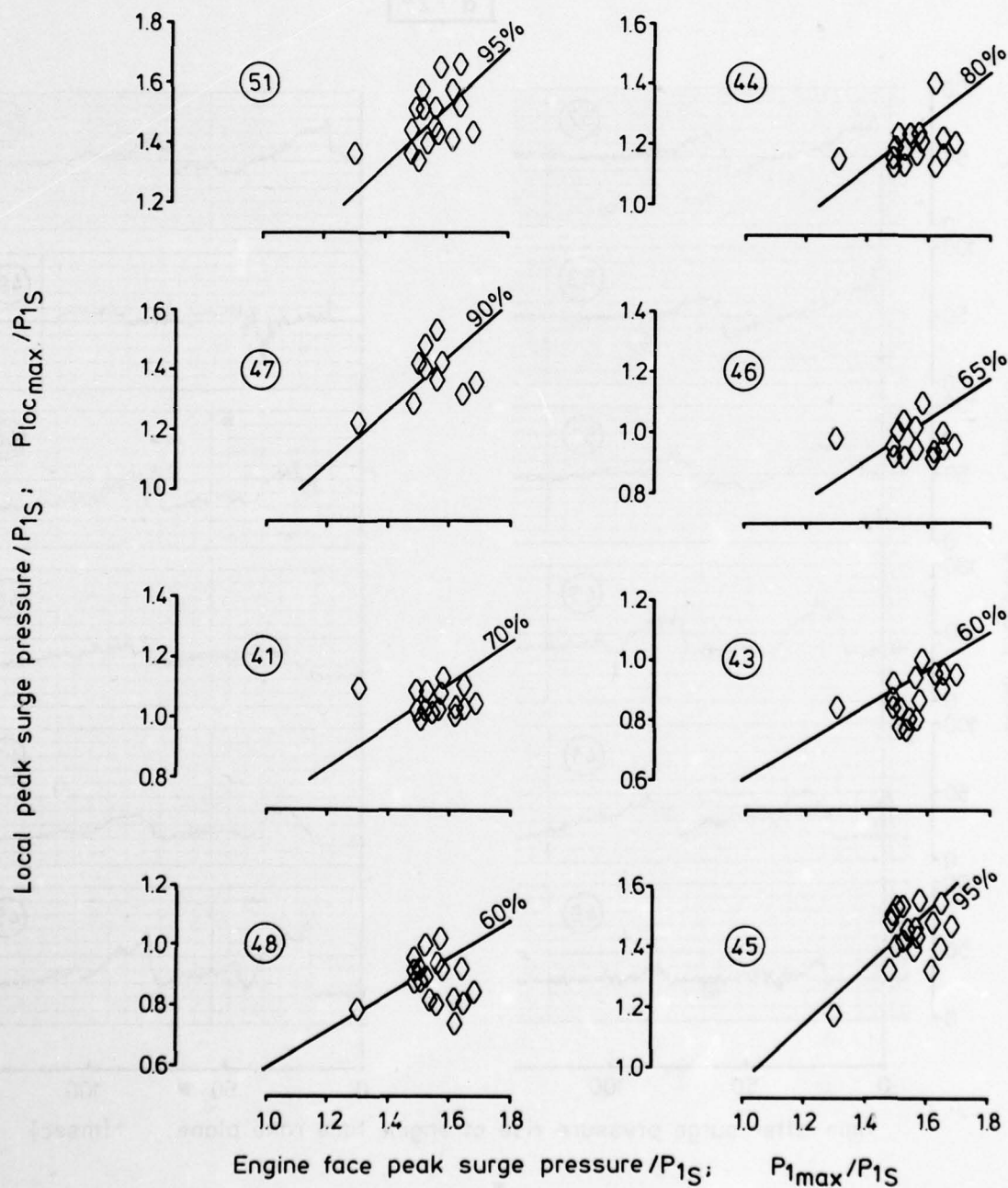
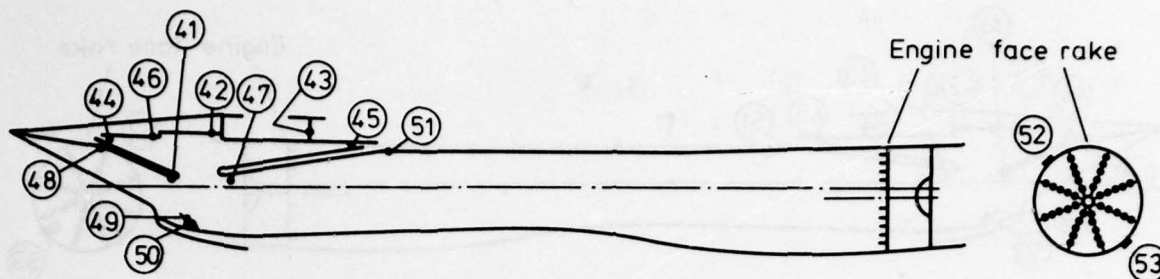


Fig.13 Peak surge pressure distribution

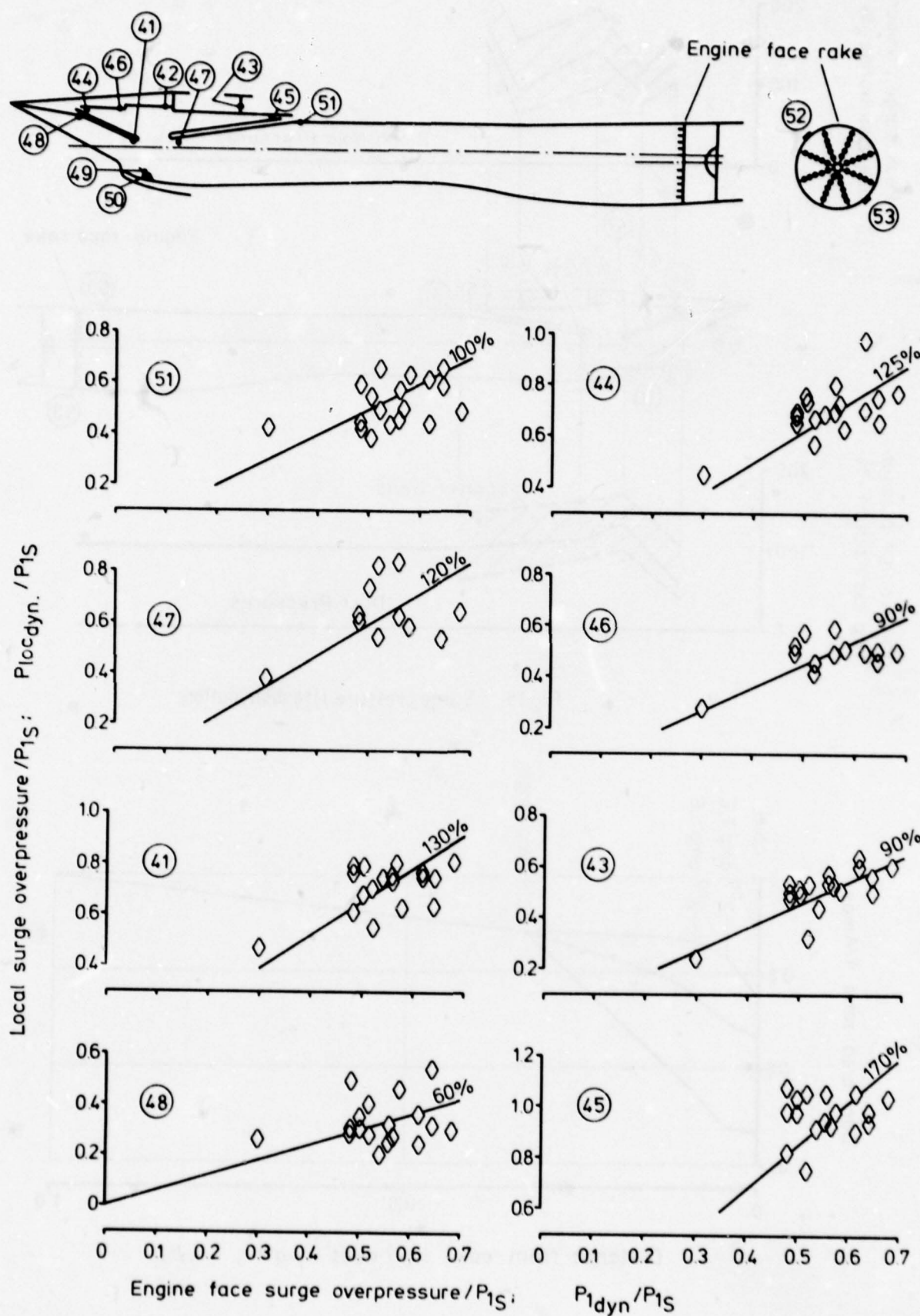


Fig.14 Surge pressure rise distribution

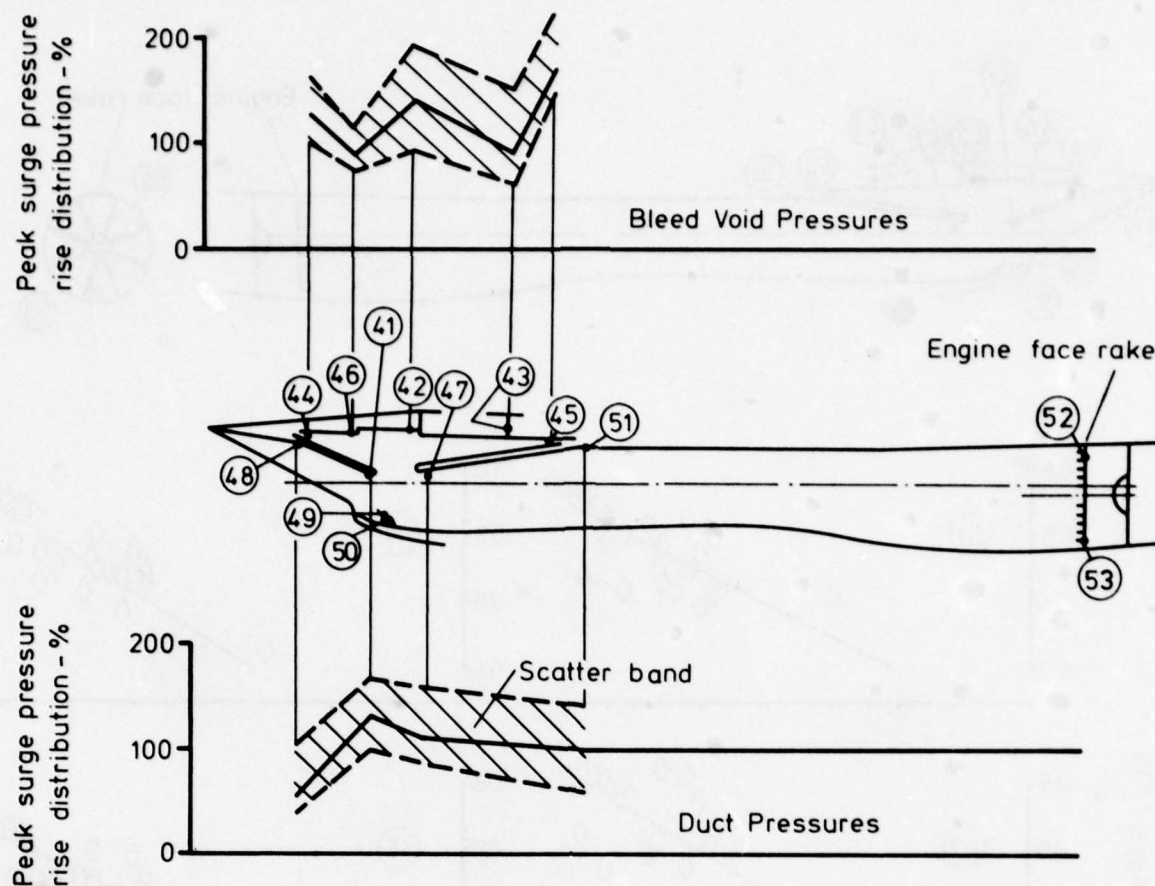


Fig.15 Surge pressure rise distribution

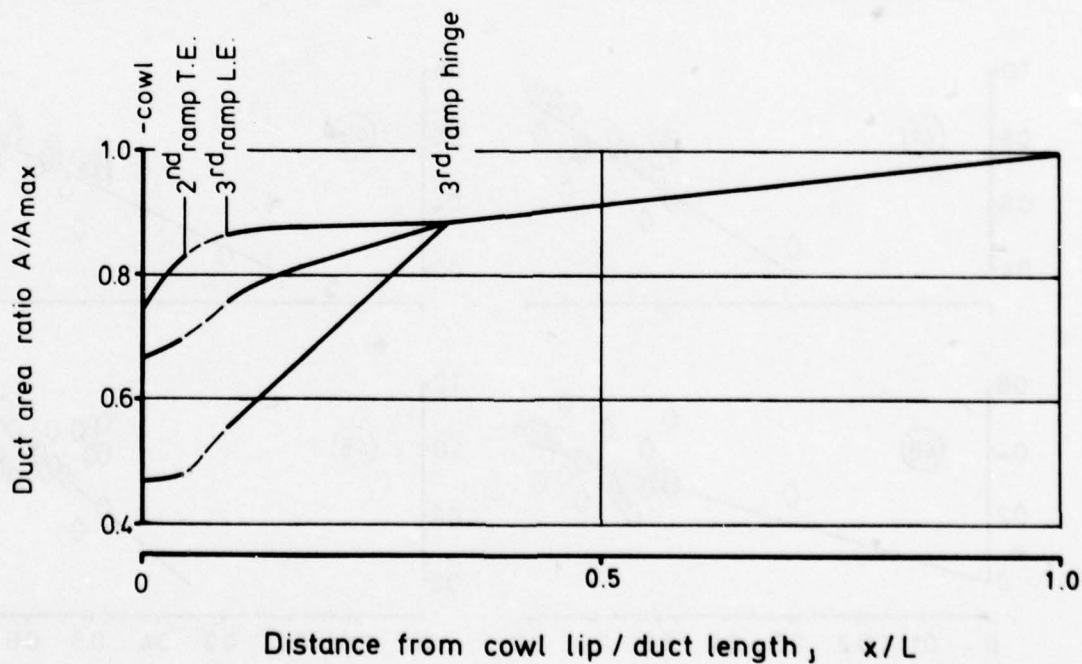


Fig.16 Duct area distribution

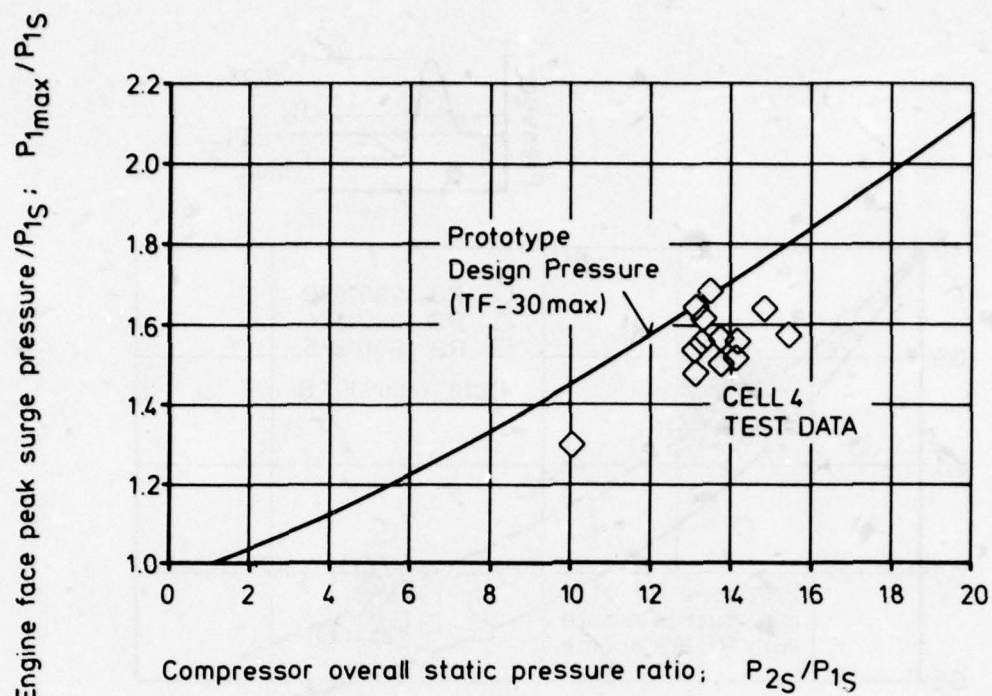


Fig.17 Comparison of measured engine face surge pressures with prototype design pressures

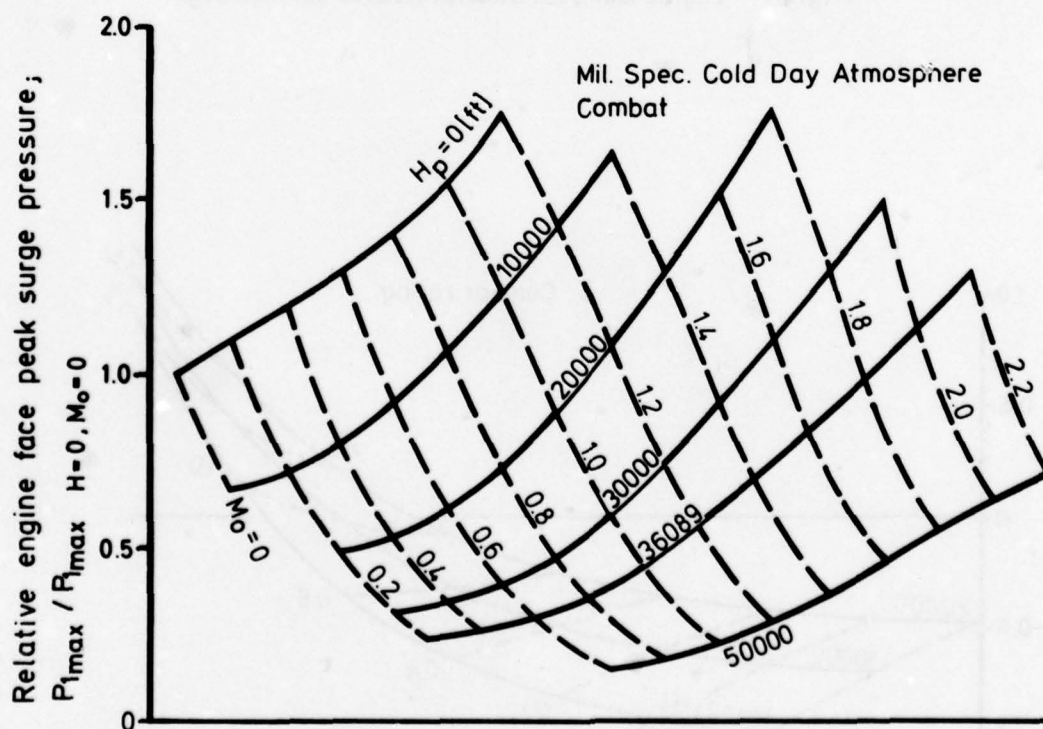


Fig.18 Peak surge pressures in front of engine for series aircraft design

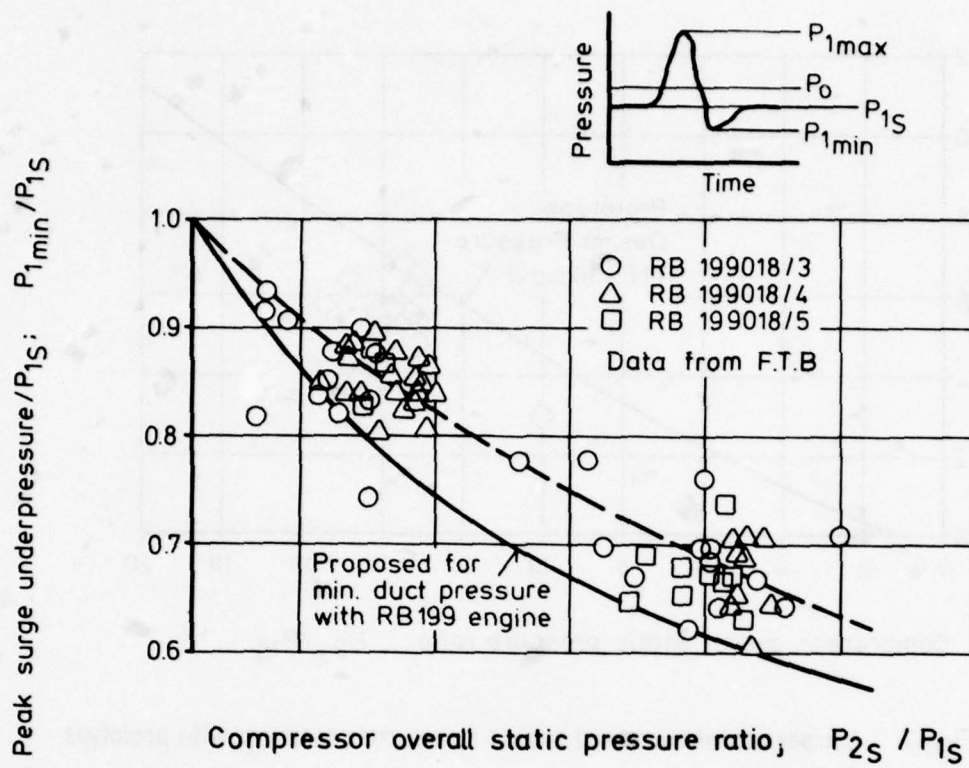


Fig. 19 Engine face peak underpressures during surge

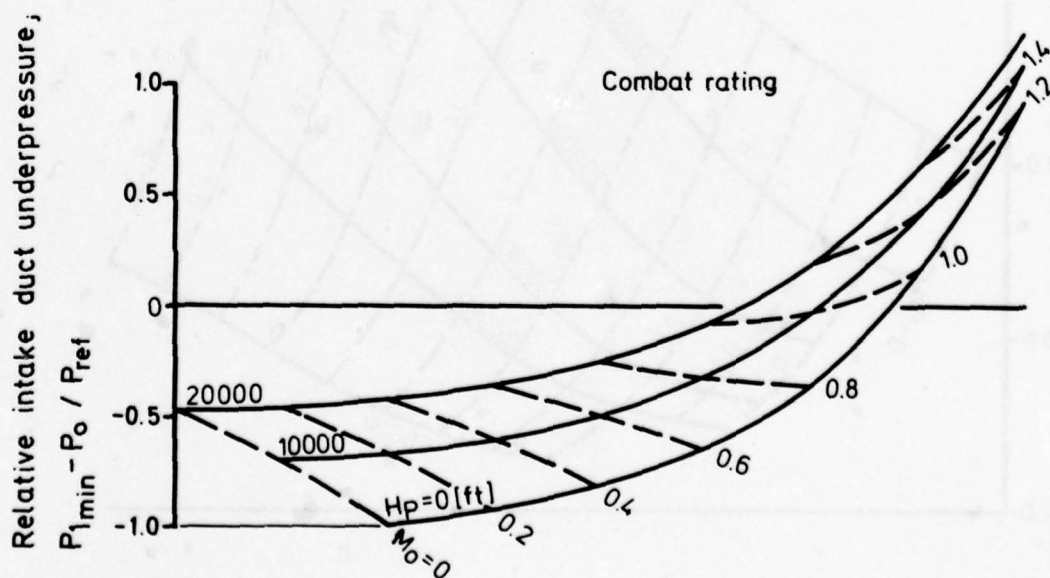


Fig. 20 Intake duct peak underpressures

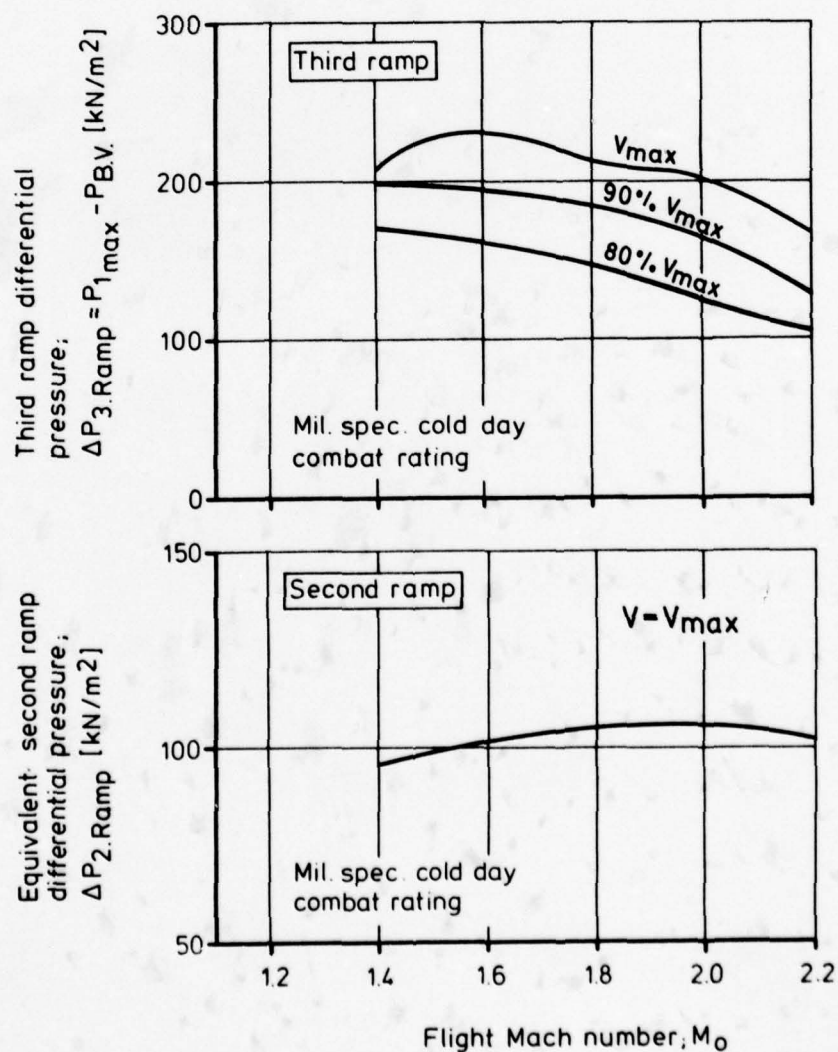
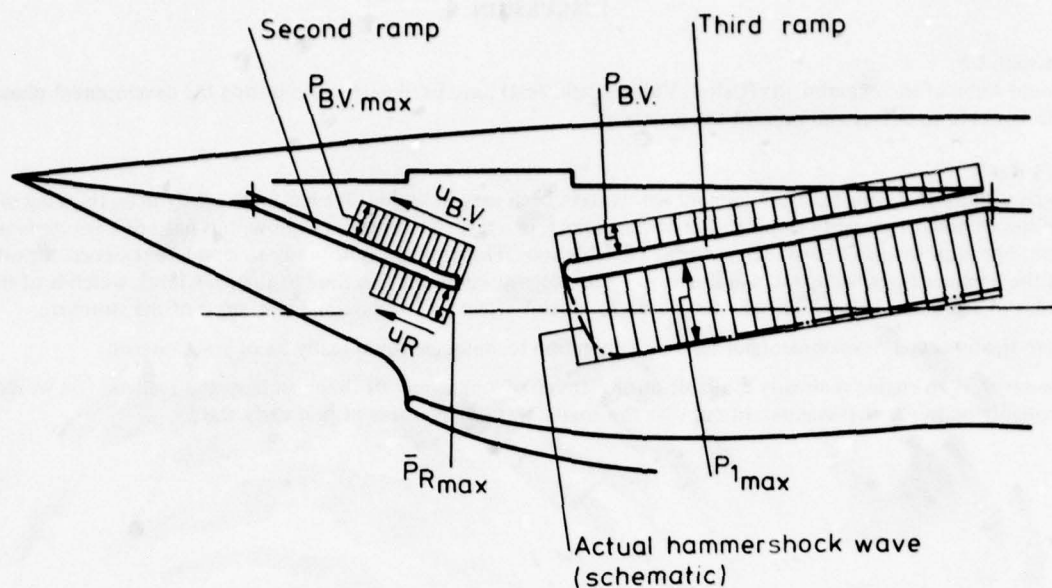


Fig. 21 Design load assessment for third and second intake ramp

DISCUSSION

J.G.Mitchell, US

Could some of the experiments (Cell-4, Vulcan flight test) have been performed during the development phase of the Tornado to detect and prevent the problem?

Author's Reply

Such tests early during the development would have been very desirable. We have repeatedly been thinking of possibilities of how to properly simulate the hammershock in a test rig. As far as I know, this has not been performed elsewhere and we don't have such a device available too. The problem is not only to simulate the correct peak level of the hammershock wave but also the wave shape, i.e. especially the rise time to the peak level, which is of the order of 1 msec or below. The rise time has a dominant effect on the dynamic behaviour of the structure.

Investigations and developments of relevant simulation techniques would really be of great interest.

However, if an engine is already available during design of a new aircraft the most easy and realistic test would probably be to use that engine. In our case the engine was not available at that early stage.

HANDLING PROBLEMS THROUGH COMPRESSOR DETERIORATION

by

Ir. J.P.K. Vlegghert
 Performance and Evaluation Dept
 National Aero Space Laboratory NLR
 Anthony Fokkerweg 2
 1059 CM AMSTERDAM
 The Netherlands

SUMMARY

RNLAF has experienced performance loss and an increased rate of in-flight compressor stalls due to compressor deterioration of some of their 15 year old engines. Investigation on the Maintenance Depot test bed showed that significant loss of air mass flow occurred near the surge line under conditions which were not covered by the normal post-overhaul acceptance tests. Also it was found that impending stall was always preceded by increasing pressure fluctuations, although the level of these pressure fluctuations varied with different engines. A method was developed to routine-check for this phenomenon.

The surge margin of the affected engines was recovered by replacing the rear compressor casing. Further investigation is being conducted by the engine manufacturer to narrow down the reason for the engine's behaviour.

1. INTRODUCTION

With increasing age beyond the teething-trouble period one naturally expects some deterioration in performance. On jet engines in first instance this takes the shape of an increase in Specific Fuel Consumption (SFC), usually combined with an increase of Turbine Entry Temperature (TET) for the same thrust, or conversely, when TET is limiting, a reduction of maximum thrust. Neither of these aspects usually bothers the military operator much, as the increased fuel consumption only results in a slight reduction of flying time and he generally has plenty thrust, for safety any way. This is in marked contrast with a civil operator who has to fly from A to B and who will see his fuel budget go up and may see his (performance-limited) payload go down, while component replacement to keep performance will make his maintenance budget go up.

There is another aspect however which should bother the military operator, and that is loss of stall margin in the compressor. This leads to an increased occurrence of in-flight compressor stalls, which may be further compounded by a decreased ability to recover from a stall. With single-engined aircraft - especially when on a low-level mission - this may result in loss of the aircraft. Usually the post-overhaul testing of the engine consumes only part of the stall margin necessary for trouble-free military operation, therefore a critical loss of stall margin may pass unnoticed.

This type of problem has occurred in the Royal Netherlands Air Force (RNLAF) with some of their older engines.

2. POST-OVERHAUL CHECK

The post-overhaul test is the most extensive check the engine is submitted to; it generally consists of a functional check for proper assembly (leaks) and adjustment, a handling- and a performance check. The engine has to meet certain minimum values for maximum thrust, both with and without After Burner (AB), and maximum values for SFC (at lower thrust) and - for taxiing considerations - idle thrust. The handling tests entail all normal throttle movements, AB transients and - numerically - time from start-up to steady idle and slam accel time to maximum thrust. These tests, apart from checking the accel schedule of the Main Fuel Control (MFC) also ensure a certain minimum stall margin which is required for engine acceleration, as during this time the compressor will be loaded above the normal Operating Line.

All these tests are normally executed on a static test bed which is usually equipped with a bellmouth intake for the engine, to ensure standard base line conditions. A newly overhauled - or extensively repaired - engine is furthermore given a Functional Check Flight (FCF) in which the slam accel time is measured at altitude and the aircraft transonic acceleration time is determined to check thrust minus drag. As a further handling check the aircraft acceleration is continued to high Mach numbers; the high Compressor Inlet Temperature (CIT) in combination with inherent intake pressure distortion forms the ultimate check on engine stall margin.

3. ENGINE CHARACTERISTICS

The engine in question is a medium compression ratio single shaft straight jet with variable final nozzle, which for its off-design running relies on Variable Stator Vanes (VSV). These are positioned by a hydraulic servo system as a function of RPM ($=N$) and CIT, but not N/\sqrt{CIT} . At high CIT - when engine rotational speed is normally constant - VSV are scheduled slightly more open than for the equivalent N/\sqrt{CIT} under test bed conditions, which means that the standard test bed performance is not fully representative for high-Mach conditions.

As the VSV are normally scheduled towards the closed position when RPM is decreasing the possibility exists to determine some kind of a (low corrected speed) stall margin by

locking VSV in the fully open position and decreasing RPM till inevitably stall occurs, which should not happen above a certain value. The so-called decel stall margin for this engine is measured in RPM, dependent of course on fully open VSV position and CIT. Originally the engine was pulled into stall to determine this value, but as stall is an explosive happening which does any engine a lot of no-good this practice was discontinued, and the decel stall procedure is stopped a certain safe distance from the average-new-engine stall point. This, while minimizing possible high cycle fatigue damage to blades and vanes, however has the disadvantage of allowing a certain reduction of stall margin to pass unnoticed. Generally, when an engine fails the decel stall test, it also fails the FCF and vice versa, therefore the two are compatible.

4. OPERATIONAL EXPERIENCE

The first indication of discrepancy was a deficiency of high-Mach acceleration in some aircraft/engine combinations, noted by clocking high-altitude runs. Flight testing with two instrumented aircraft and three engines revealed that the phenomenon moved with the engine, thus exonerating aircraft drag. The engine controlling parameters i.e. RPM, EGT, VSV and ABFF were nearly on schedule and therefore responsible for only a small part of the discrepancy. Half the discrepancy was caused by the engine mass flow being lower than predicted at low corrected RPM and high VSV setting, as is shown in fig. 1). This was measured on test bed with the VSV locked in the fully open position; the standard test bed performance falling within the tolerance band and therefore not giving rise to any suspicion. The problem was corrected by a change in the RPM controlling law.

Years later an increase in compressor stall incidents began to give some concern. An overhaul depot test program was initiated with two engines which both had experienced in-flight stall. As a decrease in massflow at constant RPM entails a higher angle of attack of blades and vanes, and therefore a reduced stall margin, mass flow was measured as well as decel stall RPM, and both were found defective. It was found that compressor stall margin could be restored by renewing the rear compressor casing + vanes.

5. TEST RESULTS

5.1 Stall Margin

For comparison purposes, compressor mass flow was measured at 90 % corrected RPM, both with VSV at normal schedule and in the fully open position and the comparison value Q90;17 was then interpolated linearly for the normal open position of 17°. Further tests showed this value to be sensitive to different compressor replacements and to correlate closely with decel stall RPM, (see fig. 2) even though that value is considerably lower than 90 % RPM.

Extensively instrumented tests revealed that initial stall occurred between stage 6 and 9 (see fig. 3) and that prior to stall an increasing pressure fluctuation was measured at the point instrumented for differential pressure variations, which was stage 6 in this case (Fig. 4). Further measurements on another engine with simpler instrumentation showed that the pressure fluctuations start rising abruptly at some RPM above decel stall, which seems to be equivalent with buffet onset, and then rise linearly with decreasing RPM (Fig. 5). In this case differential pressure was measured at stage 9 (DP9) for the simple reason that this is accessible on any engine - also in flight if desired - by mounting a modified bleed air manifold tapping (Fig. 6).

Various replacements were tried in the compressor, by far the most effective being replacement of the rear compressor casing + vanes; this improved Q90;17 by 5 % on three engines, effectively restoring the stall margin and doing away with any DP9 fluctuation above decel stall check RPM. On the strength of these results a fleet test was initiated in which Q90;17 and DP9 were measured in the field on every engine to select those which required this replacement.

5.2 Stall Recovery

On decel stall, RPM will drop within 2 seconds to below idle; stall recovery can usually be effected by releasing VSV from their fully open position and retarding the Power Lever (PL) to idle. However figure 7 shows that DP9 after an initial drop starts rising again while accelerating back to idle and only vanishes after idle RPM is reached and the MPC reverts to steady-state fuel flow. Figure 8 shows that a hang-up will occur if during this period PL is moved to demand more thrust as the pilot will be sorely tempted to do.

The Flight Manual - recommended procedure for stall recovery is stopcock - relight. Figure 9 shows that this instantly clears the stall and that recovery is quicker than when PL is only moved to idle. However another engine showed DP9 recurrence - and considerably longer recovery time - after stopcock-relight (Fig.10) which presumably indicates deficient sub-idle stall margin in this engine. This engine also showed DP9 excursions during normal start-up to idle and during slam acceleration, which the other engine did not. There is apparently a difference though between acceleration to idle after normal start-up and after stall recovery with PL in idle as the "good" engine only showed a DP9 in the latter case while max EGT was about 50°C higher. According to the engine manufacturer the hot-metal-to-air heat transfer in the latter case is responsible for a somewhat higher combustion efficiency during acceleration to idle as well as possibly for some stage mis-match which might transiently reduce the stall margin. Factory tests are underway to determine sub-idle stall margin for such an engine.

5.3 Field Results

Air mass flow is measured on the air base test bed using static shoes in the bellmouth after suitable calibration, and a limit was set equivalent to the decel stall limit. Mass flow is calculated (while the engine is still running) on a programmable pocket computer, which also gives the effective turbine flow Area Factor $AF = Q \sqrt{EGT/CPR}$ as a check. On the basis of this result the decision is made whether to run a decel stall check or not. To prevent high-cycle fatigue damage during execution of this decel stall test also DP9 is measured, and an arbitrary limit was set of 2 psi peak-to-peak, indicating on a simple a-c voltmeter from a piezo-resistive pressure transducer in the bleed air manifold tapping. On the basis of these tests engines were selected for replacement of the rear casing.

The relation of mass flow at 90 % corrected RPM vs Vane Position Indication (VPI) varied considerably between engines near the fully open position. On some engines, mass flow instead of increasing steadily with VPI as the factory predicts, show a maximum beyond which mass flow decreases again (Fig. 11). Likewise the factory has found through executing bleed inflow stall tests on an engine which experienced an in-flight stall that the constant speed lines (with fixed VPI) above the normal operating line have a much reduced slope of CPR vs mass flow relative to the new engine. These effects indicate a lower stall margin while the engine performance near the normal operating line is hardly affected.

On the engines that were pulled into stall a wide variation of DP9 (from 1,5 to 6 psi ptp) was apparent, this is probably due to the fact that different engines stall first in different places, and a stall in stage 9 produces the highest values of DP9. No engine of the type used by the RNLAF has stalled without exhibiting a P9 considerably in excess of "background noise" (generally 0,5-1 psi).

In figure 12 the maximum DP9 at the decel stall limit is shown versus Q90;17 it is apparent that in general DP9 is higher as this mass flow is lower. On replacement of the rear casing mass flow improves and DP9 vanishes indicating a sound engine again.

6. POSSIBLE REASONS FOR DETERIORATION

The most likely reason for the compressor deterioration is corrosion caused by repeated low level flight through polluted air. Both industrial pollution and sea air have taken their toll, among other aspects in limiting through corrosion the slight movement of the vanes in the T-slots of the casing, which is necessary for vibration damping. Repeated replacement of these vanes throughout the life of the engines has resulted in T-slot wear which is responsible for vane twist and increased tip clearance. Overhaul limits are generally based on remaining strength and not on performance or stall margin, which therefore predictably will cause trouble sooner or later.

Other corrosion aspects are roughness of the flow surfaces and some profile variation, probably mainly at the leading edges. An entirely different aspect is the flight envelope of fighter aircraft, which allows a high g-loading through which some permanent ovalisation of the casing could result. It is not known to what extent each of these aspects contributes to the loss of stall margin in some engines, but it is clear that the sum-total can be too much.

The typical flattening of constant-speed lines at high VPI and at CPR above the normal operating line indicates a flow loss due to high blade loading, probably caused by secondary flow losses near blade- and vane tips which through boundary layer displacement reduce the effective flow area of the compressor mainly at the back end.

7. CONCLUSIONS

1. Compressor deterioration which only has a slight effect on the operating line may have a much larger influence on stall margin and handling.
2. Especially stall recovery may take considerably longer than accelerating through the same RPM range from normal start-up.
3. For the subject engine type good correlation exists between the low corrected speed stall margin and the mass flow measured with vanes open.
4. The subject engine type also exhibits easily measurable pressure fluctuations prior to stall.
5. Using a combination of mass flow- and pressure fluctuation measurement engines were selected for component replacements to restore stall margin.
6. Similar measurements are employed to monitor stall margin on all engines.

ACKNOWLEDGEMENTS

The author wishes to express his appreciation to the personnel of the Maintenance Depot Woensdrecht and to the Airforce Bases of Volkel and Leeuwarden for their marvellous co-operation throughout this investigation. Also he would like to thank the RNLAF for permission to publish this paper.

This investigation could not have proceeded without the vigorous support of the NLR Instrumentation Department, for which thanks are due to Mr. Jan van Doorn. Especial mention deserve Mr. Frans Ketting who developed the DP9 instrumentation through several cycles of increasing usefulness and Mr. Willem van Dorp who always managed to adapt his electronics to forever varying requests for parameter registration.

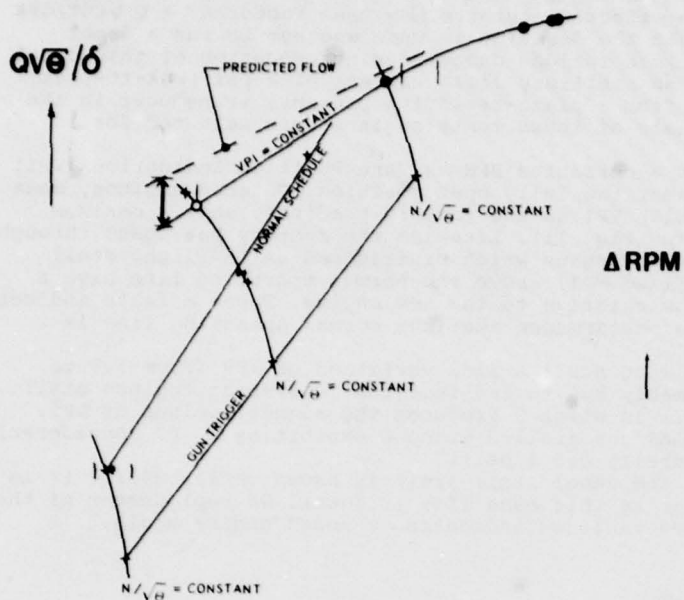


Fig. 1 Carpet plot of Airflow vs Corrected RPM and Vane Position

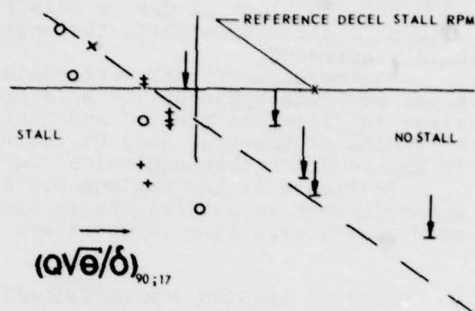
 ΔRPM 

Fig. 2 Decel Stall Margin vs Reference Airflow

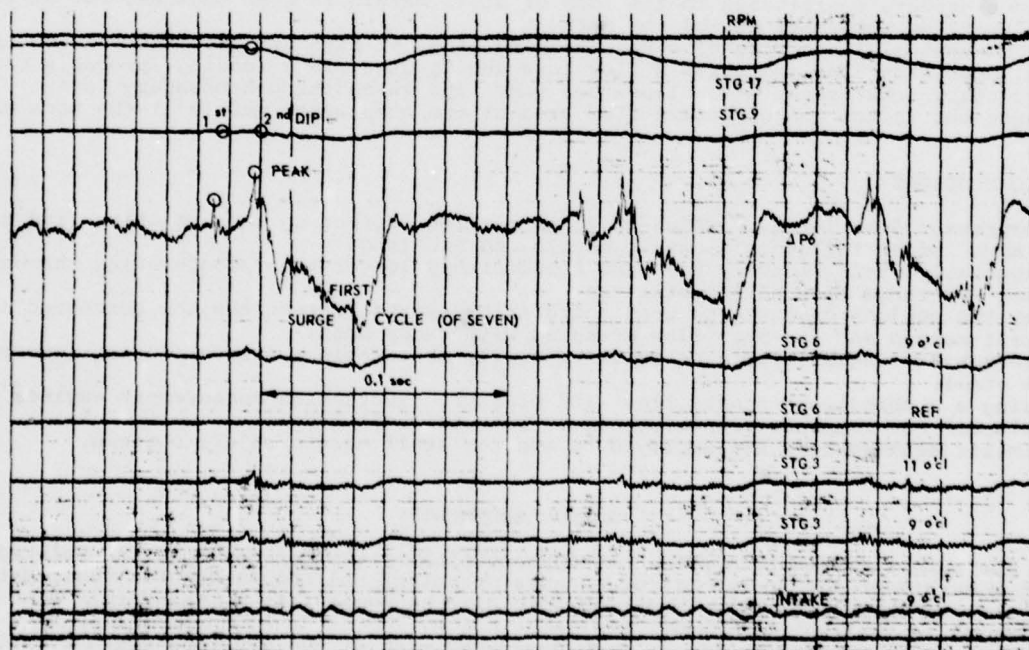


Fig. 3 Detail of Decel Stall (Pressure Variations)

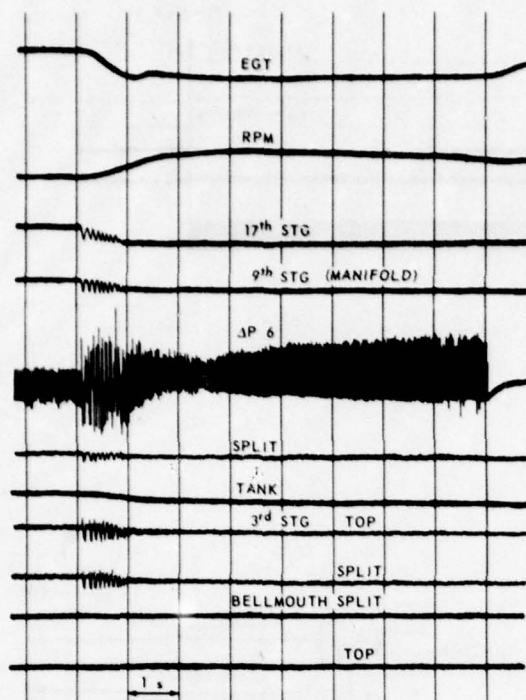


Fig. 4 Parameter Variation during Decel Stall

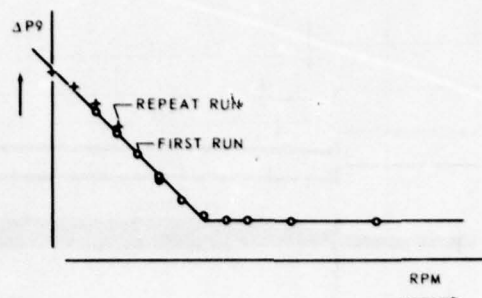
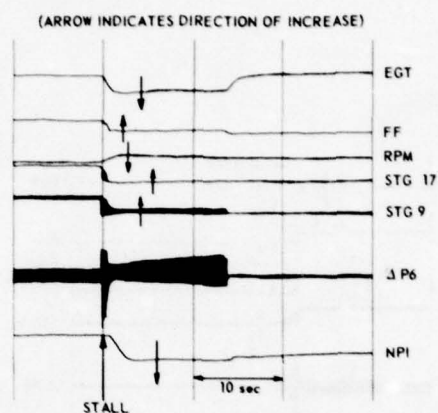
Fig. 5 Variation of pressure fluctuations (ΔP_9) vs RPM during Decel Stall Check

Fig. 7 Stall and Recovery from Idle

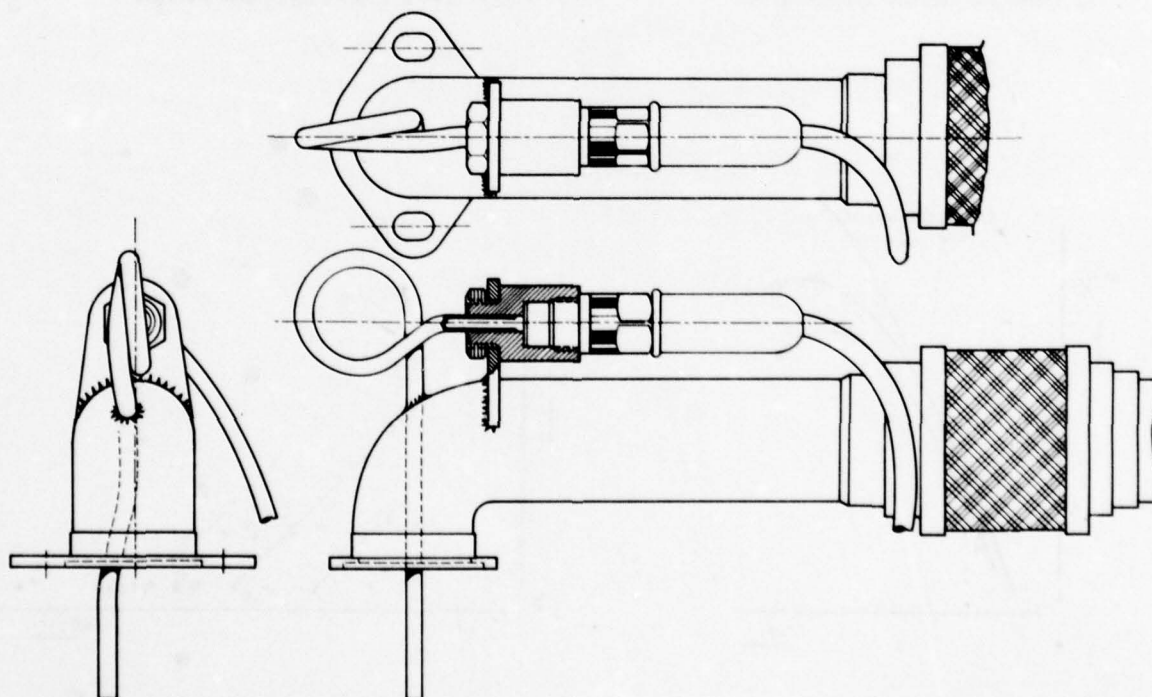


Fig. 6 Bleed Air Manifold Tapping

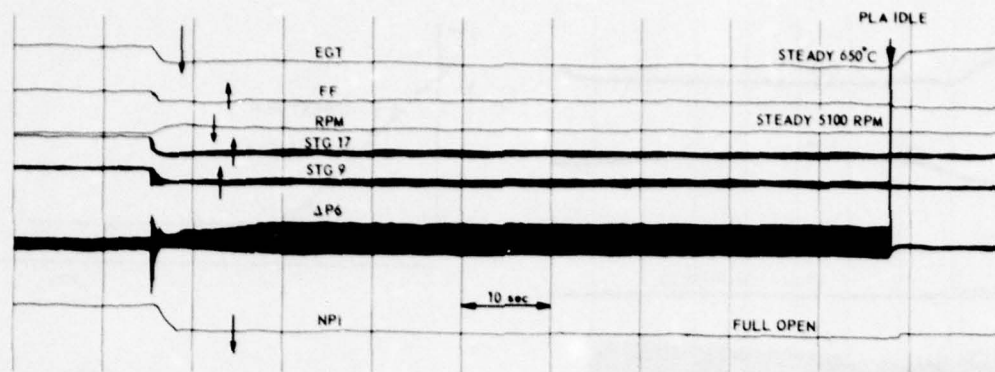


Fig. 8 Stall and Hang-up (PL demand before recovery)

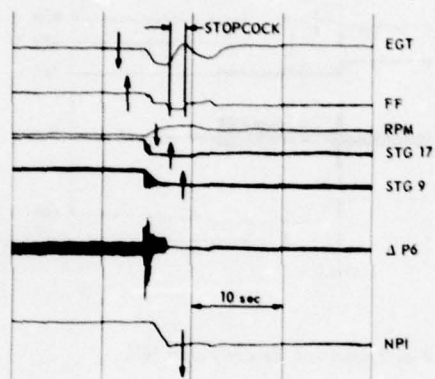


Fig. 9 Stall and Recovery Stopcock-Relight

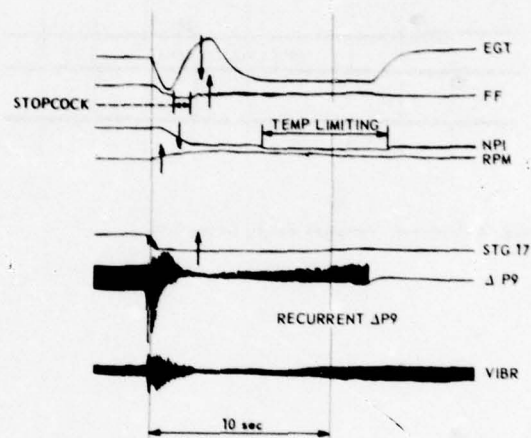
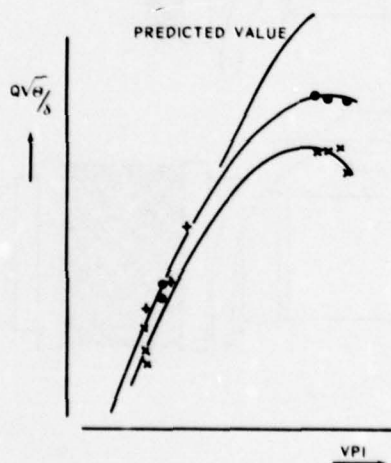
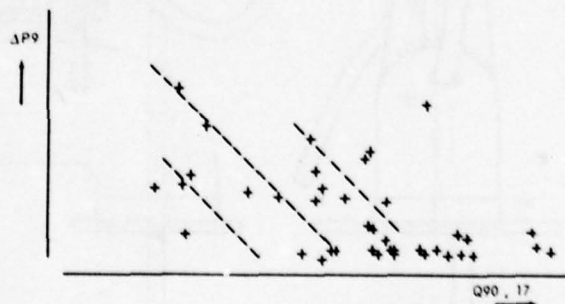
Fig. 10 ΔP_9 Recurrence during Stall Recovery

Fig. 11 Airflow vs Vane Position for constant Corrected RPM

Fig. 12 Max ΔP_9 during Stall Check vs Reference Airflow for a number of engines

DISCUSSION**J.G. Mitchell, US**

Was there a consistency of flight conditions which induced stall?

Did stall occur during transient, i.e. throttle change or Mach number or altitude change?

Author's Reply

The condition most likely to induce compressor stall is high supersonic Mach number in level accelerating flight; it is usually preceded by some snaking of the aircraft. Otherwise stalls have occurred during air combat manoeuvring and also in steady low level cruise; but under the last condition we suspect tip vortex ingestion from the leading aircraft in the formation. With the refurbished compressor no more cases have occurred.

SMALL TURBINE ENGINE INTEGRATION IN AIRCRAFT INSTALLATIONS

by

M. ROTMAN
R.K. BLINCO

PRATT & WHITNEY AIRCRAFT OF CANADA LTD.
BOX 10, LONGUEUIL, QUEBEC, CANADA J4K 4X9

Summary

Various design and development problems related to the integration of small turbine engines in aircraft installations are reviewed. Important considerations in turbo-prop installations are vibration transmissibility, propeller-whirl flutter, engine structure strength and stiffness, mount failure modes, and nacelle clearances. Additional requirements are adequate compartment ventilation and engine oil cooling with minimum aerodynamic loss. The installations of the PT6 series of turbo-prop engines are discussed in particular.

Introduction

The PT6 series of turbine engines has been in production at Pratt & Whitney Aircraft of Canada Ltd. since the early sixties. A large number of models have evolved from the initial design and they are used in a great variety of applications. Some of these are stationary, marine or surface transportation applications. However, the widest application of the PT6 engine is in airborne installations, as main propulsion units in helicopters and general aviation aircraft. In the Spring of 1978 the total number of PT6 engines produced exceeded 13,000 and the total running time of all units exceeded 31 million hrs.

Leading the family of PT6 turbo-prop applications the PT6 models A-20 and A-27 are used in such light aircraft as, for example, Beech A-90 and Embraer EMB-110. The more powerful PT6A-41 is used in commuter aircraft, such as Beech A-200. The PT6A-50 is the powerplant in the De Havilland Aircraft of Canada Ltd. STOL aircraft DHC-7. There are a number of other PT6 turbo-prop applications, some in aircraft of new design and some in modified existing designs. A recent surge in interest in the PT6 has occurred in the application to agricultural aircraft. A cross-section of the PT6A-41 is shown in Figure 1.

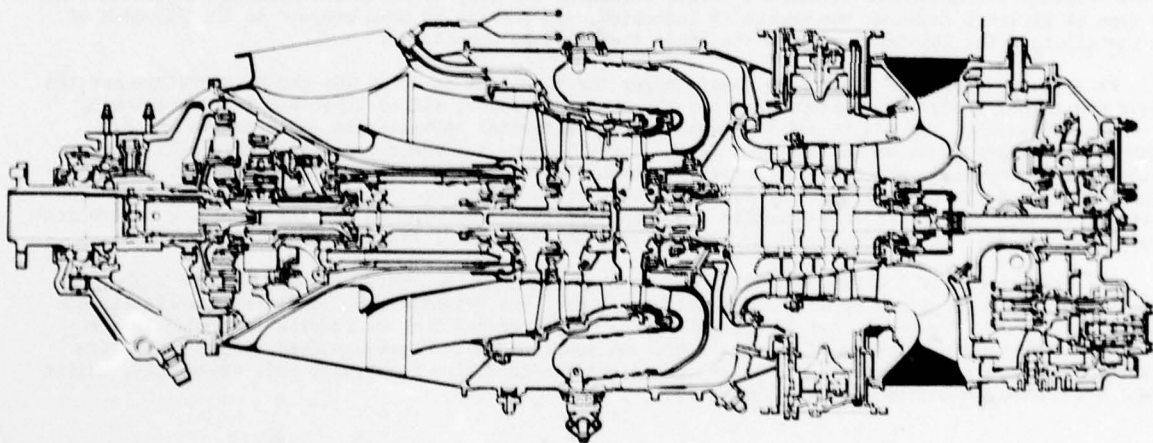


Fig. 1 - Cross-Section of PT6A-41

Many of these applications require, in the A/C design phase, installation support from P&WC to ensure optimum integration of the powerplant in the aircraft and adherence to the related airworthiness requirements. It is the purpose of this paper to review the more significant aspects of installations, structural and otherwise, that must be considered in the design phase. The choice of propeller and the required power for a particular application to produce the desired performance has already been resolved at this stage and, therefore, falls outside the scope of this paper.

A typical installation of a PT6 turbo-prop engine in a nacelle is shown in Figure 2. For such an installation some of the requirements concern the following:

- strength and stiffness
- vibration isolation
- propeller whirl flutter
- installation induced engine vibration
- accessories
- compartment ventilation
- engine integrity

Each of these items will be discussed separately.

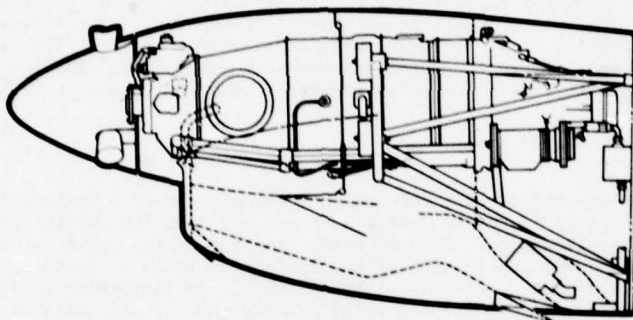


Fig. 2 - Typical PT6 Installation

Strength & Stiffness

The Type Certificate for an engine in a particular aircraft installation is awarded after the successful completion of a program of rigorous testing and detailed theoretical analyses, as prescribed in the relevant Airworthiness Standards. These Standards are very specific for aircraft engines and for the type of aircraft in which the engine is installed. In particular with respect to the strength of the installation the Standards provide the loads that must be considered.

From the viewpoint of the engine manufacturer the important loads on the engine structure are the torque and thrust loads on the propeller, and the manoeuvre loads, all of which are to be reacted by the engine structure, the mounts and the supports. In a typical installation where the mounts are located in a single plane behind the c.g. of the installation, the manoeuvre loads, primarily those acting on the propeller, may cause high bending moment and shear loads in the engine casing. The gyroscopic moments on the propeller due to yaw and pitch accelerations must be taken into account. Accessories, such as electrical generators and pumps, which are mounted on the engine casing are subject to manoeuvre loads. Their attachment or support must be checked for strength.

The development of the PT6 series of engines over the years has been directed towards higher powerlevels, lower propeller speeds, and reduced weights. The weight of the complete installation has steadily increased (Figure 3), but the weight of the propeller and the accessories increased faster than that of the engine itself. Increased power and lower propeller speeds demand larger propellers (Figure 4) and increased torques. Installation weight per installed horsepower and, especially, engine weight per installed horsepower have decreased.

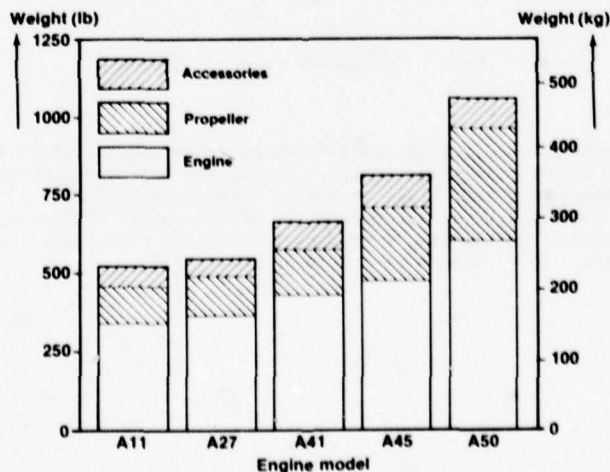


Fig. 3 - Weights of Some Installations

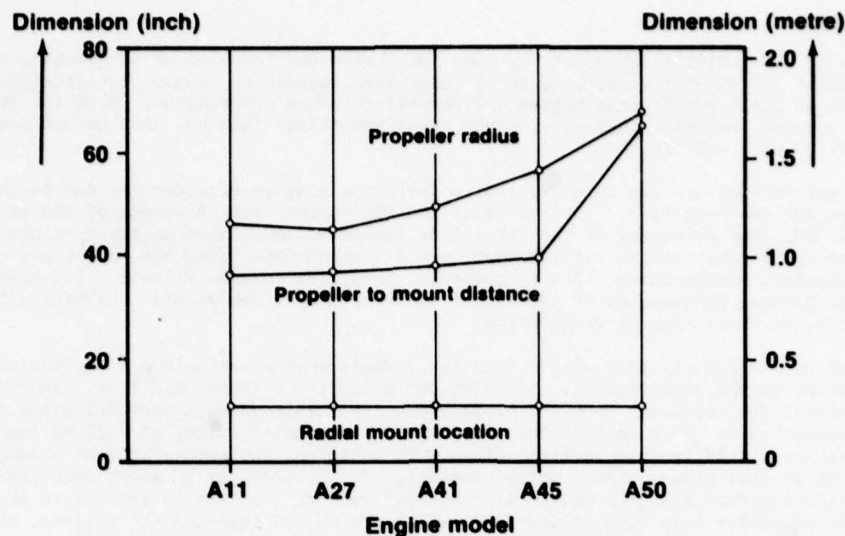


Fig. 4 - Significant Dimensions

The implication of this trend for the engine designer is that the structural strength of engine casings, mount attachments, and accessory supports has become more critical and must be the subject of detailed analyses in each individual installation. The implication for the aircraft manufacturer is that the choice of propeller, mounts, and accessories may have an important effect on some details of the engine design.

The choice of the mounts and the design of the nacelle and engine support structure are in general not the responsibility of the engine manufacturer. In most installations there is, however, a close interaction between the aircraft and engine designers, and the mount supplier. This ensures that all requirements are taken into account. As a result new designs benefit from all relevant past experience. In many instances Pratt & Whitney Aircraft of Canada has provided support in the design, the theoretical analysis, and in testing of installation components that are not part of the engine itself.

The mount stiffnesses are of concern primarily with regards to the isolation of the aircraft from the engine and propeller generated vibrations. The static deflections of the installation on soft mounts must be considered also in the non-structural connections between the aircraft and the installation, such as engine and propeller controls, electrical and hydraulic connections, and in the required clearances between the installation and the aircraft and nacelle structures. An indication of typical vertical deflections at the c.g. of the installation and the propeller under 1g loads is given in Fig. 5.

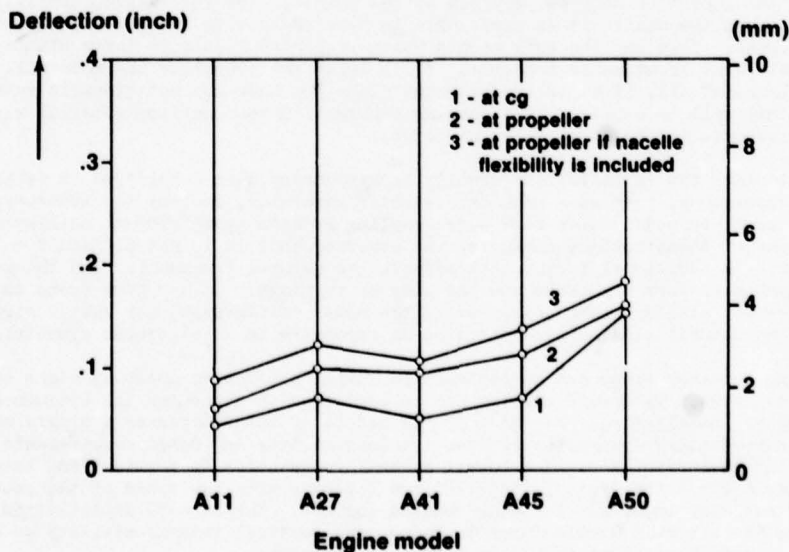


Fig. 5 - Static Deflections

Vibration Isolation

The design of the installation mounting, i.e. the choice and location of the mounts, and the design of the mounts and support structure, is of increasing importance in new installations to ensure optimum isolation of the aircraft from engine and propeller induced vibrations. With the trend to relatively more powerful engines and larger, lower speed propellers this has also become a requirement that is more difficult to satisfy.

The principal excitations for which vibration isolation must be provided are due to unbalances in the engine rotors and the propeller. The rotors of the PT6 engines run at speeds of the order of 30,000 to 40,000 RPM. The frequency of the vibrations caused by unbalances on these rotors is too high to be transmitted by flexible mounts without appreciable attenuation. They are therefore, of little concern to the aircraft manufacturer. The frequency of propeller induced vibration is, however, of the same order as the natural frequencies of the engine installation on its mounts. Careful attention must be paid, therefore, to these natural frequencies.

The typical engine installation with a relatively rigid engine casing has 6 degrees-of-freedom, representing motions in the direction of, and rotations around, the three main axes. In general, these motions and rotations are coupled. However, usually the installation has a vertical plane of symmetry through the propeller axis. This implies that the c.g. of the installation, as well as two of the three principal inertia axes, lies in this vertical plane. In addition, the mounts must be arranged symmetrically with respect to that plane. Under those conditions the 6 installation modes corresponding to the natural frequencies separate into two groups of 3 modes: symmetric modes with motions in the vertical plane through the propeller axis such as vertical motion, pitch and fore-and-aft motions, and axisymmetric modes with motions not limited to this plane such as lateral motion, yaw and roll around the propeller axis. In the special case where there is an additional horizontal plane of symmetry through the propeller axis, both with regard to the inertia and the mount stiffnesses, the fore-and aft and roll motions will occur in separate modes uncoupled to any other motion. These two modes cannot be excited by propeller unbalance and, furthermore, they usually occur at relatively high frequencies. Consequently, they do not contribute to the vibrations due to propeller unbalance which are transmitted through the mounts.

The two motions in the vertical plane, i.e. vertical motion and pitch, in the axisymmetric installation will in general occur in two modes coupled in a certain ratio, which is different for each mode. This coupling is due to the fact that in general the c.g. of the installation is not located in the plane of the mounts, or more precisely, due to the fact that the combined stiffnesses cannot be resolved into two linear stiffnesses acting at the c.g. Such a mode, consisting of vertical and pitching motion in a certain ratio, can be regarded as representing the motion of the installation around a fixed point on the propeller axis. The location of this nodal point on the axis determines the relative amounts of vertical and pitching motion. For example, if the nodal point coincides with the c.g. the mode consists of pure pitching motion, and if the nodal point is far forward or aft of the c.g. it is primarily vertical motion. A similar description can be given for the two modes with motions in the horizontal plane, i.e. lateral motion and yaw. It follows, therefore, that the four modes of interest in the axisymmetric case can be categorized by the plane in which their motion occurs and by the location of the nodal point on the propeller axis around which the installation appears to rotate.

The importance of each mode for the isolation of the aircraft from vibration due to propeller unbalance depends on 3 characteristics. These are the natural frequency of the mode relative to the propeller speed, the location of the nodal point on the propeller axis with respect to the propeller and mount planes, and the amount of damping provided by the mounts. For low transmissibility of propeller unbalance loads through the mounts it is preferable to have modes with low natural frequencies relative to the propeller speed. This implies soft mounts which will also result in large static deflections. As far as the nodal point location is concerned, if it is at the propeller the mode will not be excited by propeller unbalance at all, if it is in the mount plane the mode may not transmit vertical loads although it certainly will be excited. The damping inherent in the isolator material will generally affect the nodal response in the more important modes.

In practical cases the installations usually lack symmetry when considered in detail. Most often the inertias of accessories, such as a pump or a starter/generator, destroy the symmetry. The analyses result, in these cases, in modes which show some coupling between symmetric and anti-symmetric motions. However, usually one of these motions dominates the other so that it is not difficult to recognize the nature of the mode. An additional factor that affects the natural frequencies and the modes is the stiffness of the mount support structure and the wing or fuselage. It has been found that these structural stiffnesses, although large compared to the mount stiffnesses, may have a significant effect. In some cases the structural stiffnesses introduce an asymmetry in an otherwise symmetric installation.

The preceding considerations can be implemented during the design phase by means of straight forward computer analyses. Trade-off studies can be conducted to determine the optimum mount arrangement for a particular installation. For most of the models of the PT6 series a single mount plane with 4 mounts gives a satisfactory compromise between transmissibility and other requirements such as propeller-whirl flutter instability. The lowest natural frequencies in vertical and lateral directions are shown in Figure 6 for a few typical installations together with the speed of the propeller. The lateral modes are not very important for wing mounted engines. In the A-50 installation a special effort was made by the aircraft manufacturer to reduce the vertical transmissibility as much as possible. This resulted in a configuration of mounts in more than one plane.

The response of the installation to propeller unbalance is shown in Figure 7 for the deflection at the c.g. and in Figure 8 for the load transmitted through the mounts. The analysis was done for an unbalance of 10 oz.in. (720 gr.cm.) which is a reasonable unbalance for this size of propeller. A comparison of Figures 5 & 7 indicates that the dynamic deflections due to this propeller unbalance are significantly smaller than the static deflections. The transmissibility, which is the ratio of the transmitted load to the unbalance load is much smaller than one, indicating satisfactory vibration isolation.

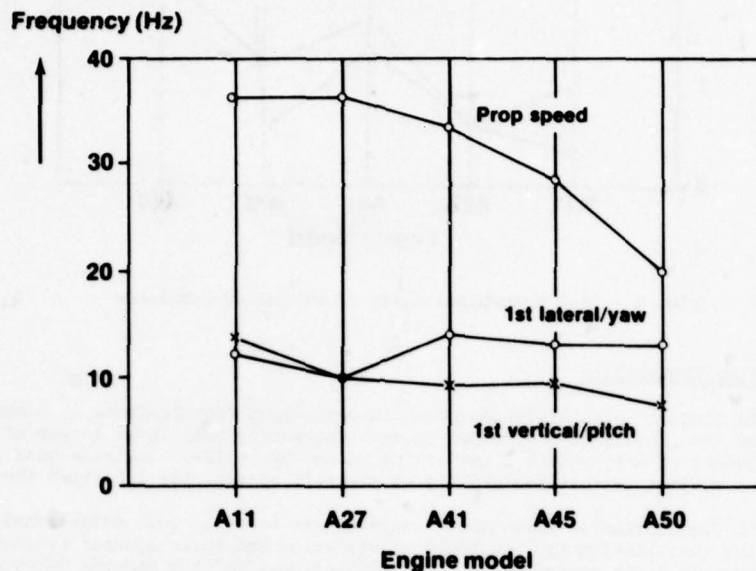


Fig. 6 - Significant Frequencies

Occasionally the suggestion is made that focusing of the mounts may be beneficial. This is accomplished by rotating the bolt axes of the individual mounts so that they are all directed towards the same point, the focus, on the propeller axis. Figure 9 shows the transmissibility as a function of location of the focus on the propeller axis. It is clear that focusing of the mounts in this case is not beneficial with respect to transmissibility.

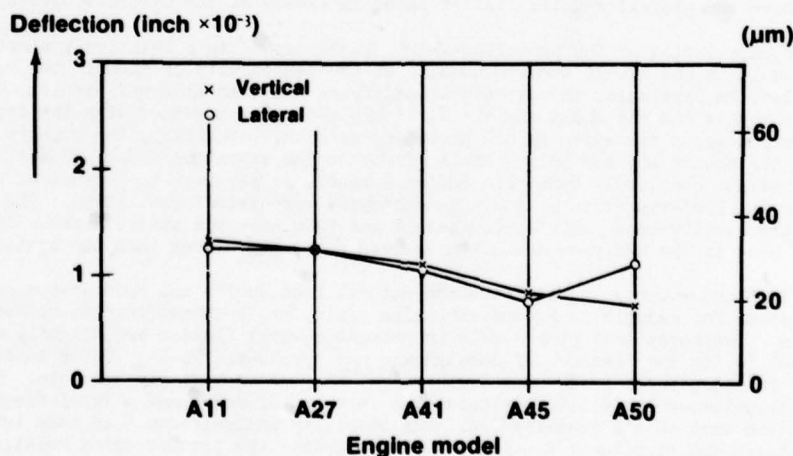


Fig. 7 - Dynamic Deflections at C.G. Due to 10 oz.in. (720 gr.cm.) Unbalance at Propeller

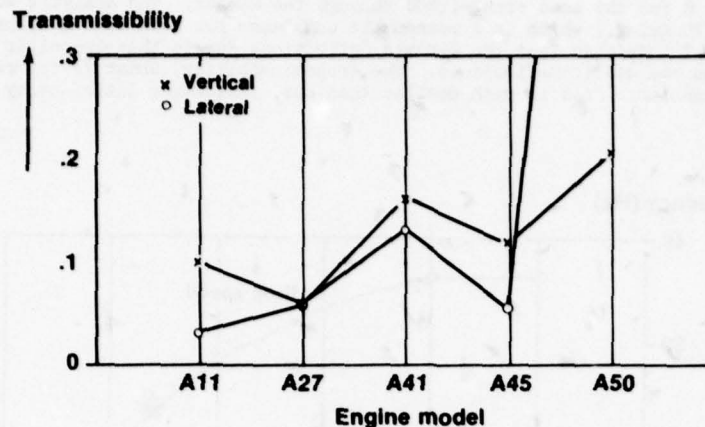


Fig. 8 - Load Transmissibility of Propeller Unbalance

Propeller-Whirl Flutter Instability

Propeller-whirl flutter instability can occur in turbo-prop installations at a certain aircraft speed. At this speed the installation vibrates in ever increasing amplitudes in one of its vibration modes under the influence of aerodynamic loads acting on the propeller. Analyses must show that new installations are not subject to this instability at aircraft speeds upto 1.2 times the dive speed.

The theoretical formulation on which these analyses are based is well established. Important characteristics of the installation are the modes of vibration and their natural frequencies, the aerodynamic and gyroscopic loads generated by propeller motions, and the damping inherent in the system. In new designs the determination of the optimum mount configuration and mount support structure always requires, apart from the usual strength analyses, the calculation of unbalance load transmissibility and the propeller-whirl flutter speed.

In PT6 installations the trend to higher power, larger propellers, lower propeller speeds, and softer mounts has increased the sensitivity to propeller-whirl flutter instability. In most cases the standard mount arrangement with a single mount plane is adequate. In special cases it has been found that mounts located in several engine planes will provide both improved transmissibility and propeller-whirl flutter speed.

An additional requirement is that an installation with a single probable failure of any one mount must still have the propeller-whirl flutter speed in excess of the aircraft dive speed.

Although the calculation of the propeller-whirl flutter speed is a relatively simple problem the accuracy of the result is not always assured because of the sensitivity of the flutter speed to some of the design variables, in particular the structural stiffness and damping coefficients. The structural stiffnesses of the mounts and the mount support structure determine together with the structural inertias the vibration modes discussed in the preceding section. Generally, the support structure is much stiffer than the mounts and has only a small effect on the vibration modes. Sometimes the support structure is not completely symmetric and as a result it may have the important effect of coupling symmetric and anti-symmetric modes in an otherwise symmetric installation. The stiffnesses of rubber isolators are usually known only approximately and then only for static cases. The dynamic stiffnesses to be used in the analyses are often assumed to be 30% higher than the static ones.

Because of this uncertainty in stiffness the natural frequencies and mode shapes of the actual installation, as found for example in ground vibration tests, may be significantly different from the calculated results. The modes that play a role in propeller-whirl flutter are slightly different from the vibration modes due to the presence of aerodynamic and gyroscopic loads. These loads are, however, not dominant over the structural loads and, furthermore, they are relatively accurate. For this reason a good basis for propeller-whirl flutter calculations is a set of modes and natural frequencies measured in a ground vibration test on the installation. The stability analysis can then take into account the additional aerodynamic and structural damping terms and predict the flutter speed relatively accurately. Of course, this approach is only possible after a certain mount design has been implemented. It is therefore, useful only for certification purposes of more or less standard installations.

The structural damping provided by the mounts and the support structure is generally unknown. In rubber mounts it decreases with increasing frequency. The various vibration modes are also affected differently by the mount damping depending on the direction of deformation of the mounts. Since the flutter speed is usually very sensitive to the modal damping, which includes the aerodynamic damping, the lower limit of the flutter speed for zero damping is often used for certification purposes. However, in installations where the propeller-whirl flutter speed for zero damping is unacceptable it is of course necessary to calculate this speed for the most accurate value of mount damping that is obtainable. In some modes the onset speed of instability for small values of damping turns out to be very sensitive to the amount of modal damping. These modes can be disregarded because they will be suppressed by realistic amounts of damping. In the flutter analysis of the failed mount cases the main difficulty is the definition of the single probable failure of any one mount. After a mount failure some stiffnesses

will be reduced to zero but not the stiffnesses in the mount directions that take up main thrust or torque loads. An additional complication in the failed mount cases may be the loss of symmetry after mount failure and the resulting coupling of modes.

Other factors that may have to be considered in the flutter analyses are the effect of reduced air density at high altitude, and the effect of high temperatures near the engine on the mount characteristics. Also, it cannot always be assumed that the engine behaves as a rigid body. In an installation with a single mount plane and a heavy propeller the effect of casing flexibility on the natural frequencies may have to be considered.

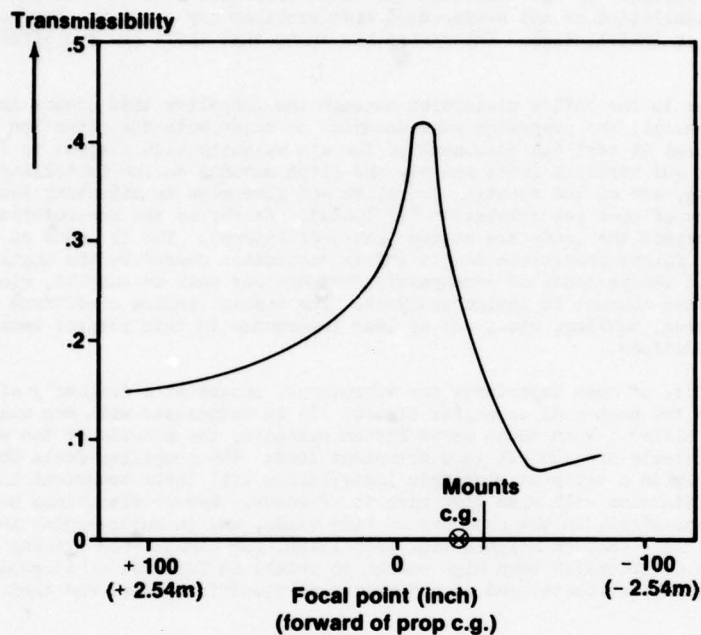


Fig. 9 - Effect of Focusing of Mounts on Transmissibility of Propeller Unbalance

Figure 10 shows propeller-whirl flutter speeds as calculated for a number of typical PT6 installations. Considerable variation in the results is apparent depending on mount and support stiffnesses and the other effects discussed earlier. The effect of mount focusing on the propeller-whirl flutter speed is presented in Figure 11 for the same installation as in Figure 9. Here again focusing has a strong effect, but is not necessarily beneficial.

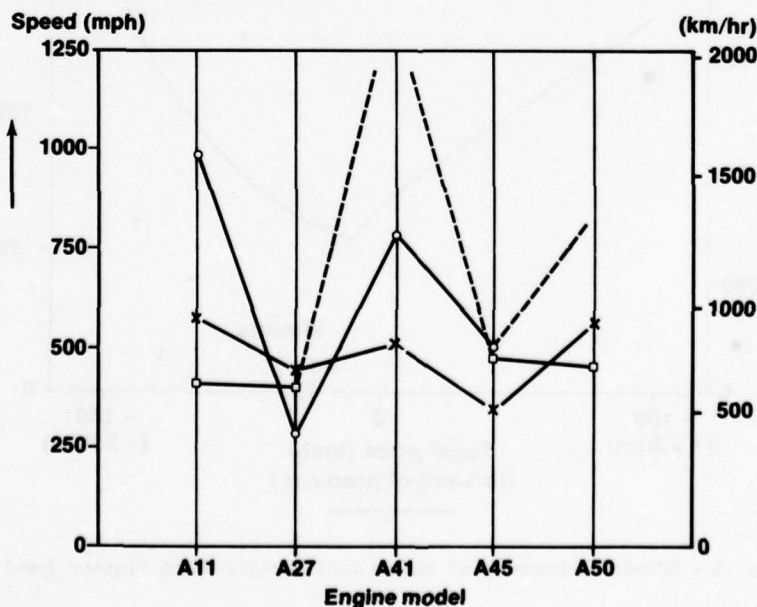


Fig. 10 - Propeller-Whirl Flutter Speeds

Installation Induced Engine Vibration

The development testing of new engines occurs primarily in test cells. In long term endurance runs engine components are subjected to various operating environments. If necessary these components are modified until they satisfy the life requirements. This development testing takes care of those engine components which do not normally benefit from extensive theoretical analyses during the design phase, such as many non-rotating parts and accessories. Since high-g loading cases e.g. landing loads and manoeuvre loads, are not simulated in test cell endurance runs additional static tests may be necessary to show that these requirements are satisfied.

Engine vibrations caused by internally generated excitations such as rotor unbalance, gear meshing, or rotor blade unsteady aerodynamics, are well simulated in test cell running. However, engine vibrations due to unsteady aerodynamic effects related to the propeller blades are generally not present at realistic levels. If the importance of these propeller related aerodynamic effects in a particular engine installation is not appreciated some problems may occur and may have to be corrected early in the life of an installation. Experience has shown that there are two effects that must be considered.

The first is due to the inflow distortion through the propeller that occurs in actual aircraft installations. In general, the propeller axis does not coincide with the direction of flight. Hence, there is a small lateral or vertical component of the air velocity with respect to the propeller which gives rise to lateral and vertical loads and yaw and pitch moments on the installation. These loads, which are non-rotating, act on the rotating propeller and give rise to vibratory loads on the propeller shaft with a frequency of once per revolution (1P loads). As far as the non-rotating components of the installation are concerned the loads are static (non-oscillatory). The 1P loads on the rotating parts which occur in normal flight conditions due to inflow distortion caused by the angular location of the propeller axis and the presence of aerodynamic obstructions such as nacelle, wing, or fuselage, are routinely taken into account in design analyses. The special inflow conditions that may occur during ground manoeuvres, taxiing, etc., are of less importance in this respect because of the limited duration of these conditions.

The second effect, of more importance for vibrations, occurs at a frequency of n times per revolution where n is the number of propeller blades. It is associated with the wakes shed by the individual propeller blades. When these wakes hit an obstacle, the nacelle or the wing, both the propeller and the obstacle are subject to a transient load: the propeller feels the presence of the obstacle and v.v. Only in a truly axisymmetric installation will these transient loads not occur. In general, inflow distortion will also give rise to nP loads. Severe vibrations have been encountered in aircraft ground manoeuvres, in the presence of side winds, and in multi-engine installations in conditions of unequal flow through neighbouring propellers, for example for braking and making turns. These vibrations have occasionally been high enough to result in failures of accessories mounted on the engine casing, of exhaust ducts, and of hydraulic and electrical lines and their connections at the casing.

Inflow distortion is in general an important consideration in the design of the first few stages of compressors. However, in the PT6 series of engines, which have a circumferential inlet at the rear of the installation inflow distortion is not a factor in the structural design of the compressor.

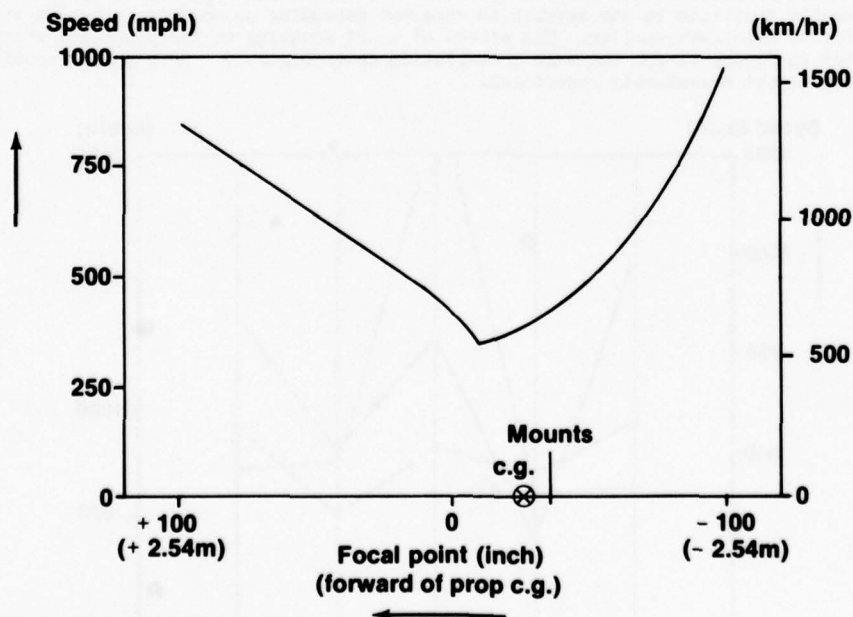


Fig. 11 - Effect of Focusing of Mounts on Propeller-Whirl Flutter Speed

Accessories

Accessories and their effect on the general engine installation strength have been discussed earlier. It is useful to consider several other accessory requirements in the installation and the contribution made by these towards overall power plant integrity.

Accessories can be grouped as aircraft supporting, engine supporting and engine indicating. Each group has a part to play in the successful integration of engine to airframe.

If we look at the three groupings in detail the following list can be made:

<u>Aircraft Supporting:</u>	hydraulic pump alternator drive air conditioning pump drive air conditioning air supply vacuum pump drive
<u>Engine Supporting:</u>	starter oil cooler control connections fuel boost pump
<u>Engine Indicating:</u>	oil temperature and pressure fuel temperature and flow compressor speed propeller speed engine power (torque)

Aircraft Supporting Accessories

Accessories in this category are mounted on the engine which supplies a power drive to the accessory.

All connections at the engine interface are stressed to withstand loads for typical accessories under the critical manoeuvre conditions of MIL-L-5007. This is a general approach necessary where an engine type may be installed in several different airframes all designed to different manoeuvre loading criteria.

It is also necessary to consider the maximum power available at each pad to drive aircraft equipment and the effect that power-off-takes have on engine performance. During the engine development program, all limitations are investigated on structures rig tests and the engine is operated at maximum off-take loads to substantiate the effect on performance of power-off-take separately and combined.

Engine Supporting Accessories

Engine supporting accessories are essential to the engine for operation within the stipulated installation limitations. The Installation Manual defines minimum starter torque characteristics for successful starts. Control cable connection requirements with actuation loads are also defined.

One of the most important engine supporting accessories is the engine oil cooler. This item is not attached to the engine in PT6 installations. Housed within the power plant envelope, it uses air as the media to reject heat. It is in the interest of aircraft performance that air flow to the heat exchanger is kept to a minimum. It is equally important to engine durability that the oil is cooled sufficiently to ensure normal engine operation well within the oil temperature limits. The two critical design cases for the size of the oil cooler are aircraft static and hot day single engine climb conditions.

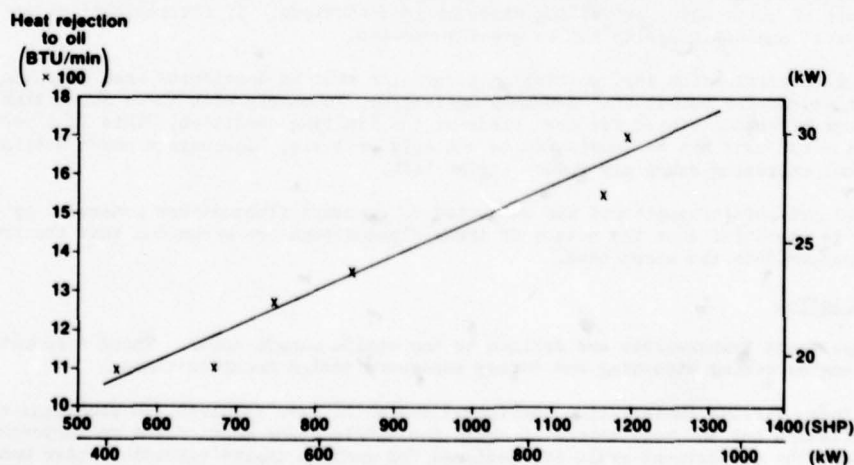


Fig. 12 - Growth Engines Need Bigger Oil Coolers

On the PT6, heat rejected to the oil has been seen to maintain a reasonably consistent rate of increase with engine growth in terms of mechanical power (Fig. 12). Variations about the mean line are attributed to gearbox rotational speeds and to a lesser extent to thermal rating of the engine. The thermal rating affects this trend in only a minor way due to the oil wetted surface being small in the hottest part of the engine, the #2 bearing, and the inclusion of a thermal blanket which separates the #3 and #4 bearing housing and the reduction gearbox from the exhaust gas temperature.

In the cross-section of the PT6 (Fig. 1) the main roller and ball bearing cavities can be identified. These as well as the reduction gearbox with plain bearings throughout the transmission system are the main targets for the lubrication system. The #2 bearing conditions must be such that coking will not be induced due to hot oil. In the reduction gearbox good load carrying and low foaming properties must be maintained. The #1 bearing, while not in an extremely hot zone, must transmit compressor thrust. Its life is quite critical and can be related to oil temperature (Fig. 13). The oil temperature considered here is the average oil temperature in the bearing cavity. Of the total oil flow in the engine, it is estimated that 90% is acting as a coolant.

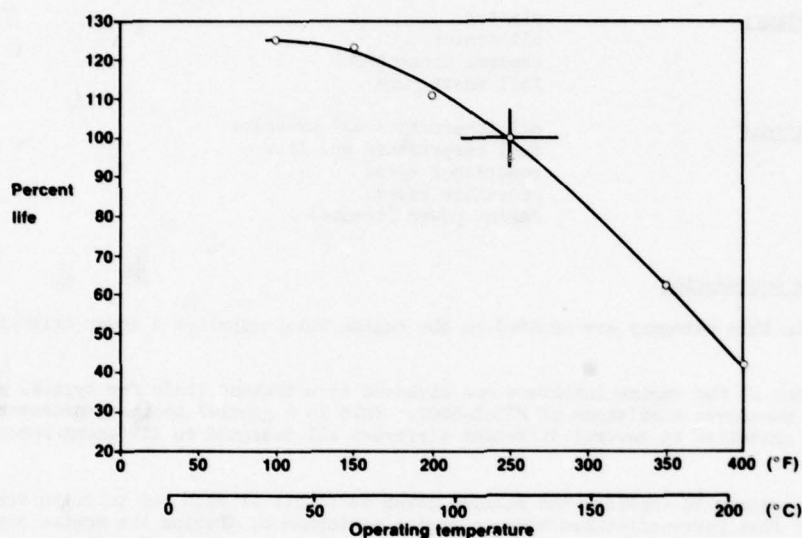


Fig. 13 - Bearing Life Reduces with Increase of Oil Temperature

Relative to total oil system volume the engine oil flow rate is high. This means that oil tank settling time is very low thus endorsing the need for oil with good resistance to foaming. As with viscosity, coking, gumming and good film strength, foaming resistance is enhanced by ensuring normal operation at low oil temperatures. For further reference see SAE paper 680211. The PT6 Gas Turbine, Lubricants and Fuels, by A.W. Stewart and J.P. Harding.

Engine Indicating Accessories

Engine indicators, while not usually having sufficient mass to load engine connections do have an extremely important roll to play in maintaining the efficiency and integrity of the engine. Transmitters connected directly to engine casings or via various forms of isolators are subject to engine vibrations and must transmit reliable information to the pilot. It is on this information that the pilot bases his use of power under prevailing atmospheric conditions. If the indications are not reliable then overall engine integrity can be greatly reduced.

During engine certification instrumentation accuracies must be considered when computing maximum demonstration conditions for normal and emergency operation. To comply with these quite tight limits the instruments are often calibrated for zero error at the limiting condition. This is a perfectly acceptable practice but must not be considered as the only criteria. Inaccurate power setting instruments in the normal operating range may reduce engine life.

Oil and fuel pressure transmitters are subjected to pressure fluctuations generated by the engine fluid pumps. It is essential that the nature of these fluctuations are known and that the transmitters are designed to accommodate the worst case.

Compartment Ventilation

Engine compartment temperatures are defined by the engine manufacturer. These temperatures are used during the engine casing stressing and during accessory design considerations.

There are today various installation configurations which have required, on occasion, a special approach to ventilation but the most common is again the single plane mount found on turbo-propeller applications. Here the compartment seals are designed for maximum engine excursion under manoeuvre conditions. It has not been found necessary to seal the forward section of the engine, where relative movement between engine and cowl is at its highest because the gaps around propeller spinner and exhaust ducting have invariably proven to provide adequate ventilation flow when supplemented by an exit grill.

The required ventilation flow for a given installation can be estimated and suitable supplementary porting can be provided if thought necessary.

A typical curve generated to allow for a reasonable estimate of the required ventilation flow rate (Fig. 14) must consider the compartment volume, cowling material and surface finish, maximum nacelle skin temperature and the design temperature differences throughout the system.

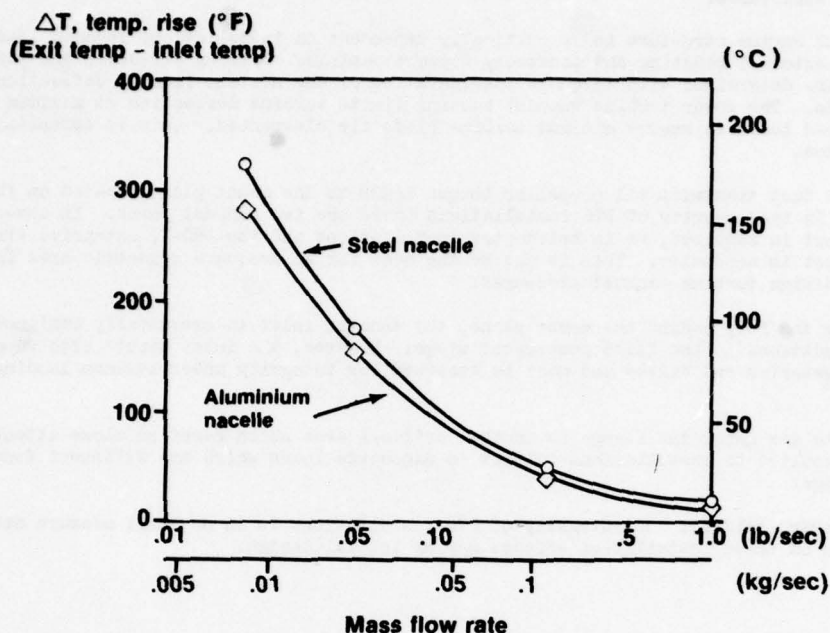


Fig. 14 - Required Cooling Air Mass Flow

Where fire extinguishant is necessary this data can be used to determine the quantity necessary to comply with certification needs. When electrical equipment is installed requiring ventilation air this equipment must discharge its air such that a fire in the equipment will not spread through the installation. This almost always necessitates the incorporation of special fireproof exhaust ducting and in many cases inlet ducting.

Compartment temperatures after engine shutdown must also be determined as control cables and accessories subjected to extreme compartment conditions during engine soak-back may be life affected. Results of typical soak-back characteristics are shown in Figure 15. Here it can be seen that the engine vibration isolators are subjected to air temperature above that seen under normal operating conditions. Items in the exhaust duct area are also subjected to more severe conditions in this non-operating mode.

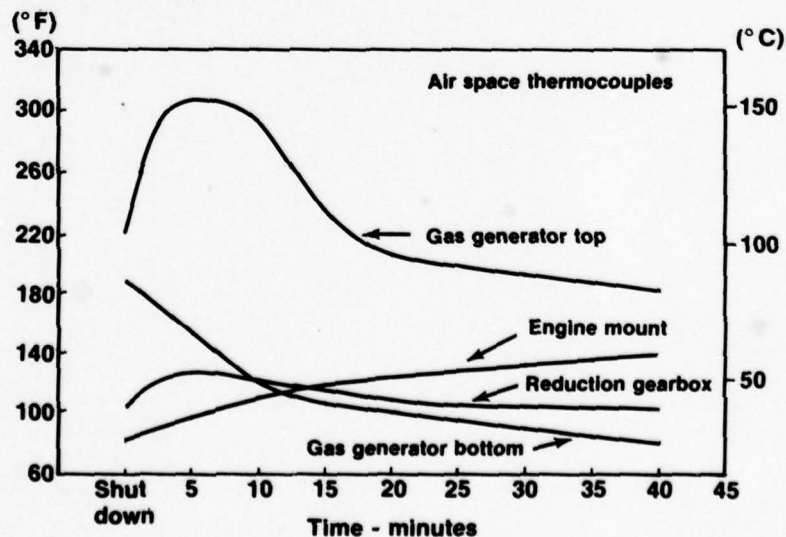


Fig. 15 - Soak-Back Temperatures of Interest

Engine Integrity

The preceding considerations individually contribute to installation integration and as a whole determine the integrity of the power plant. Previously mentioned was the fact that the propeller/power plant/airframe combination is very often chosen after the propeller and power plant components have been individually designed and developed. It is essential that initial design requirements for the engine cover all installation effects sufficiently without adversely implying excessively heavy and expensive engine structures.

The internal engine structure is as critically dependent on installations induced loads as are the more obvious external mounting and accessory support casings. Bearing air seals and turbine tip seal clearances are determined with adequate consideration of the maximum induced deflections due to installation loads. The power turbine support housing limits turbine deflection at maximum propeller and gearbox induced loads to ensure minimum turbine blade tip clearances. This is essential for turbine performance.

The exhaust duct transmits all propeller torque loads to the mount plane located on the gas generator case. In the majority of PT6 installations there are two exhaust ports. In cases where a single exhaust port is required, as in helicopter installations and the DHC-7, extensive strengthening of the exhaust duct is necessary. This is due to the need for an adequate geometric area for the exhaust gases to ensure design turbine exhaust pressures.

Rearward on the PT6, behind the mount plane, the annular inlet is essentially designed for optimum inlet conditions to the first compressor stage. However, the inlet struts also support the oil tank and all accessories and drives and must be stressed for integrity under maximum landing load conditions.

The inlet to gas generator flange is another critical area which receives close attention when PT6 engines are applied to installations subject to manoeuvre loads which are different from those of the original design.

The high regard held for the integrity of PT6 installations is in no small measure attributable to the care taken on these installation effects during initial design.

DISCUSSION

J.G.Mitchell, US

Why wasn't flutter induced in wind tunnel tests of the propeller/engine? Was Reynolds number simulated?

Author's Reply

All flutter results presented are theoretical results. Propeller-whirl flutter tests have not been found necessary. Presumably they could be done in special wind tunnels but not in test cells where most engine tests are done.

DETERMINATION DES EFFORTS DYNAMIQUES DUS A UN BALOURD AUX ATTACHES D'UN MOTEUR MONTE EN PODE

B.SCHNEIDER
 AVIONS MARCEL DASSAULT-BREGUET AVIATION
 78, quai Carnot
 Saint-Cloud
 92214
 France

RESUME

La perte d'une aube du rotor produit des efforts de balourd qui se transmettent aux attaches du moteur sur le pôle.

Les réactions de ces attaches sont calculées, en fonction de la vitesse angulaire du rotor, au moyen de la matrice de flexibilité du pôle, des caractéristiques inertielles du moteur rigide ainsi que de la masse généralisée, de la fréquence de l'amortissement et de la déformée des modes souples du moteur dont on a pu disposer.

Ceci pose des problèmes vu la complexité de l'essai de vibrations d'un moteur ; on n'a pas pu utiliser des modes souples du moteur, dont la fréquence reste assez basse pour intervenir dans le couplage, parce que leur mesure n'a pas pu être faite complètement.

Il apparaît en outre que l'amortissement des modes est un paramètre fondamental, comme dans tout phénomène d'excitation, et qu'un soin tout particulier doit être apporté à sa détermination lors de l'essai au sol. De même, le calcul des forces généralisées nécessite la connaissance de la déformée du rotor de chaque mode souple utilisé ce qui impose la mise en place de capteurs spécialisés lors de l'essai de vibrations.

NOTATIONS

h	déplacement des attaches moteur suivant les axes
i	indice des coordonnées généralisées
j = $\sqrt{-1}$	
k	exposant de la loi de Wohler approchée
l	indice caractérisant un effort en une certaine attache du moteur sur le mât et suivant une certaine direction.
m	masse du balourd
q	coordonnées généralisées
r	distance du balourd à l'axe de rotation
s	indice relatif aux modes souples
t	temps
x, y, z	coordonnées du centre de gravité du balourd dans un système d'axes lié au centre de gravité du moteur.
A	indice caractérisant une grandeur rapportée aux attaches du moteur sur le mât.
B	indice caractérisant le balourd
C	matrice de flexibilité
F	effort aux attaches moteur $F = F' + j F''$
K	matrice de raideur
M	matrice des masses généralisées
Q	affixe complexe des coordonnées généralisées
T	matrice de transformation - Indice supérieur de transposition
W	travail - énergie
\Re	partie réelle
\mathcal{E}	énergie cinétique
α	amortissement structural
δ	déplacement suivant les bielles, aux attaches avant latérales, suivant les axes aux autres attaches.
δ_y, δ_z	déplacement suivant les directions y ou z du centre de gravité du balourd dans le ième degré de liberté normalisé.
ω	pulsation ou vitesse angulaire de rotation du moteur en rad/s
\vec{Q}	vecteur complexe des déplacements du balourd
$\{ \}$	matrice ligne
$\{ \}^T$	matrice colonne
$\{ \}^T$	matrice diagonale
T	indice supérieur : transposition.

1. INTRODUCTION

Les conditions de certification d'un avion de transport civil imposent (FAR 25) de démontrer :

- que la perte totale d'un moteur ne met pas en cause la sécurité,
- que la perte d'une aube d'un des étages du rotor n'entraîne pas des efforts de fatigue susceptibles d'amener la rupture d'une attache du moteur sur le mât pendant la durée d'un vol.

La première condition se démontre sans ambiguïté par des calculs de flutter et/ou des essais en soufflerie sur maquette dynamique.

La deuxième condition fait l'objet de notre présente étude. Nous désirons montrer que les calculs nécessaires mettent en jeu le comportement dynamique complexe des systèmes couplés mât/moteur. Cette complexité ne peut être dominée que par une connaissance dynamique aussi précise que possible tant de la structure cellule que de la structure du moteur, rendue nécessaire par l'évolution des avions de transports civils, dont les moteurs supportés par des mâts très souples sont rendus eux-mêmes plus souples par la recherche d'allègements.

Le calcul s'effectue dans une base modale qui comporte les degrés de liberté du moteur libre rigide et ses modes souples. Le mât est introduit par sa matrice de raideur calculée par éléments finis et condensée aux degrés de liberté du moteur. La masse du mât est négligée.

L'énergie cinétique est calculée à partir des données inertielles du moteur et des mesures de ses modes souples dans un essai de vibrations du moteur libre suspendu.

L'énergie potentielle se compose du terme calculé pour le mât à partir de la matrice de raideur et des valeurs mesurées pour le moteur libre.

Les fonctions de transfert s'obtiennent à partir du calcul de réponse du système des équations de Lagrange aux forces généralisées d'excitation du balourd.

Nous examinons les différents aspects de ce calcul, les parties qui en sont discutables, et suggérons l'amélioration des mesures et des données, qui pourrait rendre le résultat plus fiable particulièrement aux fréquences élevées.

2. DESCRIPTION

La présente étude concerne l'avion de transport civil Mercure 100 (fig.1) sur lequel les moteurs Pratt et Whitney JD8D15 sont placés en pôle sous la voilure.

La figure 2 montre la structure du mât qui est fixée de façon continue sous l'intrados des nervures de voilure. C'est pourquoi il sera supposé encasturé dans les calculs suivants.

Le moteur est fixé isostatiquement sur le mât, la figure 3 représente ces liaisons. On remarque, d'avant en AR :

- deux bielles articulées qui transmettent des efforts suivant leur direction
- un point central avant qui reçoit des efforts horizontaux, longitudinaux (X) et latéraux (Y)
- un point central arrière qui transmet des efforts verticaux (Z) et latéraux (Y).

3. METHODE GENERALE

Le déplacement d'un point du moteur est défini par la combinaison linéaire des 6 modes rigides et d'un certain nombre de modes souples du moteur libre. Les coefficients de participation de ces modes constituent les coordonnées généralisées q du problème dont la formulation sera faite au moyen des équations de Lagrange.

3.1 Energie cinétique

Les modes souples du moteur libre étant des modes propres, mesurés lors d'un essai au sol, sont orthogonaux entre eux et avec les modes rigides.

L'énergie cinétique s'écrit donc :

$$\text{Eq. (1)} \quad \mathcal{E} = \frac{1}{2} \dot{q}^T M \dot{q}$$

M étant une matrice diagonale dont les termes seront trois fois la masse du moteur (comprenant les accessoires et éléments suspendus sous le mât) les inerties de roulis, tangage et lacet, c'est-à-dire les masses généralisées des modes rigides et celles des modes souples. Ceci suppose que la masse du mât est répartie entre le moteur et ses attaches (sur la voilure, ou sur un bâti d'essai). Le mât se comporte alors comme un ressort pur sans énergie cinétique. La comparaison des modes propres calculés sur l'avion avec les modes mesurés lors de l'essai au sol de vibration a montré que cette répartition était justifiée, au moins aux basses fréquences. En effet les modes voilure se comportent alors comme des modes d'ensemble en ce qui concerne la liaison mât-moteur.

3.2 Energie élastique

Elle est la somme de 2 termes :

- l'énergie de déformation du moteur dans ses modes souple

$$\text{Eq. (2)} \quad \frac{1}{2} q_s^T M_s \omega_s^2 q_s$$

q_s étant les coordonnées généralisées relatives aux seuls modes souples, M_s les masses généralisées mesurées des modes souples, ω_s les pulsations mesurées de ces modes souples.

- et l'énergie de déformation du mât dans la base totale des modes retenus rigides et souples.

Nous disposons d'une matrice K_A de raideur du mât, calculée par éléments finis en 1141 degrés de liberté et condensée au niveau des déplacements suivant les directions X, Y, Z des attaches mât-moteur.

La figure 4 donne les valeurs numériques de la matrice de raideur du mât rapportée aux attaches moteur ainsi que les caractéristiques inertielles du moteur rigide.

En fait, les deux bielles articulées qui retiennent le moteur à l'avant suppriment deux degrés de liberté.

Il nous faut donc condenser la matrice de raideur K_A . Soit T une matrice carrée de transformation géométrique qui projette sur les directions Y et Z les déplacements suivant les perpendiculaires aux bielles et suivant les bielles ; cette matrice laisse donc les déplacements des points milieu avant et arrière inchangés. Cette matrice ne contient que les sin et cos de l'angle des bielles avec la direction OY, des 1 et des zéros. C'est une matrice orthogonale.

Nous distinguons dans T la sous matrice T_1 qui projette les déplacements perpendiculaires aux bielles

$$\text{Eq. (3)} \quad T = \begin{bmatrix} T_1 & T_2 \end{bmatrix}$$

La matrice de flexibilité

$$\text{Eq. (4)} \quad C_A = K_A^{-1}$$

est transformée en une matrice

$$\text{Eq. (4)} \quad T^T C_A T$$

qui relie les déplacements et les efforts, suivant les perpendiculaires aux bielles et suivant les bielles pour les attaches avant, et suivant les directions X Y Z pour les autres attaches.

Les efforts réels s'exerçant seulement suivant la direction des bielles par suite des articulations on peut supprimer les deux premières lignes et colonnes de cette matrice de flexibilité. Un calcul simple de sous matrices montre qu'il reste $T_2^T C_A T_2$; la matrice de rigidité correspondante s'écrit :

$$\text{Eq. (5)} \quad (T_2^T K_A^{-1} T_2)^{-1}$$

Il faut noter que T_2 n'est pas une matrice carrée.

Si l'on revient aux déplacements h et aux efforts s'exerçant suivant les directions X Y Z aussi bien aux attaches des bielles qu'aux autres, la nouvelle matrice de rigidité s'écrit :

$$\text{Eq. (6)} \quad T_2 (T_2^T K_A^{-1} T_2)^{-1} T_2^T$$

En effet, la matrice T_2 qui figure à gauche exprime simplement la projection sur les axes X Y Z des efforts s'exerçant suivant les bielles. La matrice T_2^T qui figure à droite exprime la projection sur les axes des déplacements δ_b dans la direction des bielles (et suivant les axes pour les autres attaches, on a alors une sous matrice unité).

$$\text{Eq. (7)} \quad \delta_b = T_2 h \quad T_2^T \delta_b = T_2^T T_2 h = h$$

car on remarque que $T_2^T T_2$ est une matrice unité bien que T_2 soit rectangle.

Mais les degrés de liberté q choisis pour mettre notre problème en équation sont les six déplacements q du moteur rigide dans un système d'axe X Y Z ayant son origine au centre de gravité du moteur auxquels s'ajoutent les modes souples.

$$\text{Eq. (8)} \quad h = T_3 q$$

La matrice T_3 comprend une première sous matrice exprimant les déplacements des attaches du réacteur suivant les axes dans un déplacement de corps rigide et une deuxième sous matrice donnant les déplacements de ces attaches suivant les axes dans les déformées des modes souples.

L'énergie de déformation du mât dans la base des coordonnées généralisées q s'écrit donc finalement :

$$\text{Eq. (9)} \quad q^T T_3^T T_2 (T_2^T K_A^{-1} T_2)^{-1} T_2^T T_3 q$$

3.3 Forces gyroscopiques

Elles n'ont pas été introduites. Dans une étude précédente nous avons calculé les modes propres en présence des forces gyroscopiques et nous avons pu constater que leur influence était négligeable. Par ailleurs les déplacements du moteur dans les modes de tangage et lacet, sous l'influence des forces de balourd restent faibles.

Il en sera donc de même des forces gyroscopiques.

3.4 Forces de dissipation

Dans le cas des modes souples nous avons introduit l'amortissement de structure α mesuré aux essais de vibrations au sol. Pour les modes rigides nous avons utilisé un amortissement forfaitaire de 10 % ce qui correspond à une moyenne des valeurs mesurées lors de l'essai au sol sur avion pour les modes de pendule, tangage, lacet. Les forces de dissipation sont supposées découplées.

3.5 Excitation

Le balourd est introduit comme une force extérieure. Ceci suppose l'hypothèse justifiée suivante : la perte d'une ailette est négligeable au niveau de la masse et des modes propres du moteur suspendu. Elle ne devient importante qu'au niveau des forces de balourd lorsque le moment statique de la masse manquante par rapport à l'axe de rotation est multiplié par le carré de la vitesse angulaire.

La force tournante est remplacée par deux forces harmoniques en quadrature, l'une horizontale, l'autre verticale.

$$\text{Eq. (10)} \quad F_y = m \omega^2 r \cos \omega t \quad F_z = m \omega^2 r \sin \omega t$$

m étant la masse de l'ailette manquante

r la distance de son centre de gravité à l'axe de rotation

ω la vitesse angulaire du rotor en rad/s

t le temps

δy et δz étant les déplacements du centre de gravité de l'ailette manquante dont les coordonnées sont dans un système d'axes liés au centre de gravité du moteur.

$$\text{Eq. (11)} \quad \begin{Bmatrix} \delta y \\ \delta z \end{Bmatrix} = \begin{bmatrix} 0 & 1 & 0 & -z_B & 0 & x_B & \delta y_i \dots \\ 0 & 0 & 1 & y_B & -x_B & 0 & \delta z_i \dots \end{bmatrix} \begin{Bmatrix} dq \end{Bmatrix}$$

δy_i et δz_i désignant les déplacements de ce centre de gravité dans le ième degré de liberté.

Le travail des forces extérieures, forces de balourd est :

$$\text{Eq. (12)} \quad dW_B = m \omega^2 r [\cos \omega t \quad \sin \omega t] \begin{Bmatrix} \delta y \\ \delta z \end{Bmatrix}$$

3.6 Equations de Lagrange

En posant :

$$\text{Eq. (13)} \quad K = T_3^T T_2 (T_2^T K_A^{-1} T_2)^{-1} T_2^T T_3 + \begin{bmatrix} m_{s_i} \omega_i^2 \end{bmatrix}$$

les équations de Lagrange s'écrivent :

$$\text{Eq. (14)} \quad M \ddot{q} + 2\alpha M \omega \dot{q} + K q = m \omega^2 r \left[\cos \omega t \begin{Bmatrix} 0 \\ 1 \\ 0 \\ 0 \\ 0 \\ 0 \\ x_B \\ \delta y_i \end{Bmatrix} + \sin \omega t \begin{Bmatrix} 0 \\ 0 \\ 1 \\ 0 \\ 0 \\ 0 \\ -x_B \\ \delta z_i \end{Bmatrix} \right]$$

Nous nous intéressons uniquement à la solution asymptotique qui est la plus défavorable. Nous pouvons donc poser :

$$\text{Eq. (15)} \quad q = \Phi(q) \quad q = \bar{q} e^{j\omega t} \quad \text{avec} \quad j = \sqrt{-1}$$

et \bar{q} signifiant partie réelle

Nous posons également :

$$\text{Eq. (16)} \quad \Phi = \begin{Bmatrix} 0 \\ 1 \\ 0 \\ 0 \\ 0 \\ 0 \\ x_B \\ \delta y_i \end{Bmatrix} - j \begin{Bmatrix} 0 \\ 0 \\ 1 \\ 0 \\ 0 \\ 0 \\ -x_B \\ \delta z_i \end{Bmatrix}$$

De sorte qu'en remontant aux affixes le système d'équations de Lagrange s'écrit :

$$\text{Eq. (17)} \quad M \ddot{Q} + 2M\alpha\omega \dot{Q} + KQ = m\omega^2 r \Phi e^{j\omega t}$$

soit après simplification par $e^{j\omega t}$

$$\text{Eq. (18)} \quad \bar{Q} = m\omega^2 r [-M\omega^2 + j2M\alpha\omega^2 + K]^{-1} \Phi$$

3.7 Efforts de balourd aux attaches mât-réacteur

Au moyen de la matrice T_3 du § 2.2 nous passons des coordonnées généralisées q , ou \bar{Q} , aux déplacements des attaches mât-réacteur.

$$\text{Eq. (19)} \quad h = T_3 \bar{Q}$$

auxquels correspondent les efforts F suivant les axes $X Y Z$ aux attaches mât-réacteur.

$$\text{Eq. (20)} \quad \{F\} = T_2 (T_2^T K_A^{-1} T_2)^{-1} T_2^T T_3 \bar{Q} = T_2 (T_2^T K_A^{-1} T_2)^{-1} T_2^T T_3 (Q' + jQ'') = \{F' + jF''\}$$

h et F sont complexes comme \bar{Q} ; ce qui représente la rotation du vecteur force balourd et le déphasage introduit par les forces d'amortissement.

Comme nous nous intéressons seulement aux valeurs maximales des efforts nous calculons le vecteur des modules soit :

$$\text{Eq. (21)} \quad \{|F_\ell|\} = \{\sqrt{F'_\ell{}^2 + F''_\ell{}^2}\}$$

l'indice ℓ représentant ici l'effort suivant une direction en un point de fixation mât-moteur.

La fréquence angulaire de rotation ω du moteur balaye l'intervalle compris entre 0 et le régime de décollage.

4. APPLICATION

4.1 Degrés de liberté

En plus des 6 modes rigides nous voulions introduire des modes souples du moteur. C'est pourquoi nous avons effectué l'essai de vibrations au sol d'un moteur suspendu élastiquement à très basse fréquence.

Il faut dire que le moteur était nu et ne comportait pas le grand nombre d'accessoires qui certainement auraient apporté un amortissement supplémentaire. De plus nous n'avions accès qu'à l'extérieur du moteur c'est-à-dire que si les déplacements des attaches du moteur (figurant dans T_3) sont aisément mesurables, par contre nous ne connaissons pas les déplacements δ_{y_i} et δ_{z_i} des aubes de rotor susceptibles de donner du balourd. A leur place nous utilisons les déplacements du carter moteur situé au droit de l'étage de rotor choisi. A fréquence relativement élevée il est certain que les modes de "respiration" du carter peuvent différer des flexions de l'arbre du rotor.

Les modes souples identifiés se situent aux fréquences suivantes :

35,7 Hz	Torsion carénage arrière
45,46 Hz	Flexion verticale 2 noeuds
50,71 Hz	Flexion horizontale 2 noeuds
55,8 Hz	Flexion verticale 3 noeuds
67,52 Hz	Flexion horizontale 3 noeuds
70,9 Hz	Modes à allure de 3 noeuds
73,35 Hz	Modes à allure de torsion
75,25 Hz	
75,66 Hz	
77 Hz	Mode à allure de torsion
83,4 Hz	Mode complexe
102,8 Hz	Mode complexe

Malheureusement sur ces 12 modes identifiés seuls 2, la flexion verticale 2 noeuds et le mode complexe à 102,8 Hz purent être suffisamment caractérisés pour être utilisables dans le calcul. C'est à dire que l'on put mesurer la masse généralisée, l'amortissement de structure et la déformée celle-ci restant cependant limitée aux formes extérieures.

La figure 5 présente les déformées de ces deux modes souples.

La figure 6 montre :

- à gauche les 6 fréquences propres du système avec moteur rigide et rappelle les 2 fréquences propres des modes souples du moteur introduits dans le calcul,
- à droite les huit fréquences propres de l'ensemble moteur-mât les degrés de liberté étant les 6 déplacements rigides et les 2 modes souples mesurés du moteur.

On constate que la perturbation due aux 2 modes souples conduit principalement :

- à une baisse de la fréquence du dernier mode rigide,
- à une augmentation importante de la fréquence du deuxième mode souple ; ceci vient du fait que l'attache arrière restreint la déformée du mode souple en l'un de ses points de plus grand déplacement. Il est probable que si les modes souples qui n'ont pu être suffisamment caractérisés avaient été disponibles pour le calcul, le résultat aurait été différent.

Il est de plus vraisemblable que l'absence d'introduction de masses sur le mât et sa schématisation comme un ressort pur n'est plus réaliste à ces fréquences. Un calcul approché a montré qu'un mode propre du mât se situait vers 75 Hz.

Malgré ces remarques nous avons laissé subsister, à titre indicatif, le deuxième mode souple mesuré dans le calcul et poursuivi l'étude de la réponse du système dynamique à l'excitation du balourd.

4.2 Efforts aux attaches du moteur

Nous avons dans un premier temps calculé l'évolution de l'effort aux attaches pour un balourd unitaire affectant chacun des étages du rotor.

Puis nous avons choisi de calculer les efforts en module relatifs à la perte d'une aube

- d'étage n° 1 de soufflante (fan)
 - de l'étage n° 7 du compresseur haute pression
 - de l'étage n° 1 de la turbine haute pression
 - de l'étage n° 4 de la turbine basse pression
- celle-ci correspondant au balourd maximum de chaque élément du rotor.

Le régime de décollage correspond à une excitation à 147 Hz pour les éléments basse pression et 205 Hz pour les éléments haute pression

A titre d'illustration nous donnons planche 7 l'évolution de la composante verticale de l'effort appliqué à une attache latérale avant pour la rupture d'une aube de turbine haute pression.

Les échelles verticales sont logarithmiques.

Dans un autre cas, effort en Z sur l'attache arrière lors de la perte d'une aube de turbine haute pression, la valeur aberrante de 115 000 daN avait été atteinte.

Compte tenu des réserves faites précédemment, et que nous rappelons plus loin, il n'a pas été tenu compte des efforts rencontrés à la fréquence du deuxième mode souple pour l'analyse de la tenue de la structure.

4.3 Résistance des attaches

Les efforts maximaux sont atteints, pour les attaches avant, aux résonances à 9 et 18 Hz ; ces fréquences ne sont que traversées lors de la mise en route et de l'arrêt des réacteurs ; elles se situent en dessous du régime moulinet en vol qui est de 34 Hz pour le rotor basse pression. Leur marge est considérable par rapport aux efforts statiques déterminants.

Le calcul de tenue en fatigue a été effectué pour l'attache arrière en prenant pour effort rencontré en vol la résultante des efforts maximaux en Y et en Z pour l'excitation due au balourd du 4e étage de la turbine basse pression ; soit environ 3600 daN à la fréquence de résonance de 33 Hz correspondant au 5e mode propre.

Nous supposons d'abord qu'une aube de turbine 4e étage casse en vol, que les vibrations soient telles que le pilote coupe le réacteur qui prend son régime de moulinet. Ce qui, soit dit en passant, n'a pas pour effet de les atténuer, au contraire.

Si l'on suppose une loi de durée de vie en fatigue de la forme

$$N = \left(\frac{F_{\text{rupture}}}{F} \right)^k$$

N étant la durée de vie en nombre de cycles

F l'effort appliqué en module soit 3600 daN

F_{rupture} la charge de rupture soit 9340 daN

on trouve pour une durée de vie d'une heure correspondant à la durée d'un vol une valeur de k de 12, valeur possible bien qu'un peu optimiste.

Remarquons que le pilote ne réduira pas jusqu'à obtenir une excitation à la résonance puisqu'au fur et à mesure qu'il diminuerait le régime, le niveau de vibrations augmenterait. Il s'en tiendra, par exemple, à un niveau égal au 1/10 de celui de la résonance, ce qui correspond à un régime supérieur de 4 Hz (ou 240 tr/mn) au moulinet vol ; à ce point la remontée d'amplitude lorsque la fréquence diminue est déjà notable.

En se limitant à une valeur de k égale à 4, valeur défavorable, et dans les conditions de réduction moteur précédentes, la durée de vie devient 450 000 cycles.

La fréquence étant maintenant de 37 Hz ceci correspond à environ 3 heures et demie. Nous pouvons encore prendre un facteur de dispersion de 3,5 et tabler sur une durée de vie d'une heure c'est-à-dire celle d'un vol.

5. REVUE CRITIQUE DES ELEMENTS INTERVENANT DANS CETTE ETUDE

Bien que l'avion soit conçu pour pouvoir poursuivre son vol même en cas de perte de l'un des moteurs, la perte d'une aube du rotor n'aura donc pas cette conséquence dramatique : le pilote pourra réduire le régime et attendre l'escala prévue pour faire déposer le moteur.

D'ailleurs, le but de cet exposé n'était pas de démontrer cet aspect "fail safe", mais plutôt de faire le point des éléments nécessaires à cette démonstration.

Nous allons maintenant les passer en revue de façon critique :

5.1 Caractéristiques inertielles du moteur rigide

Elles sont fournies par le motoriste mais doivent être complétées par les éléments fabriqués par l'avionneur et suspendus avec le moteur sous le mât : entrée d'air, capots, carénages, accessoires, etc...

La connaissance que l'on a des masses et position du centre de gravité est suffisante. Celle des moments d'inertie, de roulis en particulier, l'est déjà moins.

La mesure de ces moments d'inertie se heurte à des problèmes de précision et de mise en œuvre vue la taille des éléments.

5.2 Flexibilité du mât

La matrice provient d'un calcul d'élément finis.

L'expérience montre qu'elle est obtenue de manière satisfaisante. On pourrait concevoir de la mesurer. On pourrait aussi effectuer un essai de vibration du moteur monté sur le mât, le tout fixé sur bâti ; et limité aux six premiers degrés de liberté ; ce qui permettrait également la vérification, globale, des caractéristiques inertielles du moteur par comparaison des résultats d'essais et du calcul des modes propres.

Là encore la difficulté provient de la taille des éléments et elle se situe principalement au niveau du bâti.

Dans l'exemple que nous avons traité la validité des caractéristiques inertielles ainsi que celle de la matrice de flexibilité du mât a été vérifiée à un niveau encore plus intégré puisque cela s'est fait au moyen de l'essai de vibration au sol de l'avion complet comparé aux calculs sur plans. La correspondance s'est révélée très satisfaisante.

5.3 Amortissement structural

C'est le paramètre fondamental d'une étude comme celle-ci, car la pointe de résonance est à peu près inversement proportionnelle à l'amortissement.

Il ne peut être tiré de considérations théoriques et ne peut que provenir d'un essai de vibration au sol.

C'est un paramètre certainement non linéaire et qu'il faudrait déterminer pour une plage suffisante des forces d'excitation. Malheureusement les essais au sol sont généralement effectués avec des moteurs bons de vol.

Pour garantir leur aptitude ultérieure et les protéger du "brinelling", le motoriste limite fortement l'amplitude des vibrations que l'on pourrait introduire, ou demande que le moteur soit maintenu en rotation ce qui complique considérablement l'expérimentation, en particulier pour la détermination d'un paramètre aussi délicat que l'amortissement.

La valeur prise pour les modes rigides, 10 ‰, est sans doute valable quel que soit le moteur et l'avion.

En ce qui concerne les modes souples il faudrait pouvoir disposer d'un moteur réformé mais équipé cependant d'un nombre suffisant d'accessoires et de sous-structures telles que entrée d'air, capots lorsqu'ils sont attachés au moteur, etc... Ces éléments sont en effet susceptibles d'introduire de l'amortissement, principalement par les frottements s'exerçant aux liaisons.

5.4 Modes souples du moteur

Leur détermination correcte nécessite de pouvoir placer des capteurs à l'intérieur du moteur, sur l'arbre rotor en particulier, et sans doute aussi de pouvoir l'exciter à des amplitudes suffisantes. On retrouve les remarques précédentes.

La gamme de fréquences à couvrir entre le moulinet (ou même la fréquence zéro si l'on s'intéresse aux transitoires) et le régime de décollage est étendu. Il y aura beaucoup de modes à mesurer ce qui conduira à un essai assez long.

5.5 Calcul du moteur et du mât

Cette difficulté jointe au fait que les modes propres du mât seul interviennent à fréquence élevée, nous oriente vers une étude théorique globale du moteur souple et du mât au moyen d'une méthode d'éléments finis dont les résultats, c'est-à-dire les modes, devraient être contrôlés par un essai au sol de vibrations.

Ce travail dépasse les possibilités de l'avionneur et doit d'abord être commencé par le motoriste d'autant plus qu'un même type de moteur peut équiper des types d'avions différents.

Bien entendu il existe une frontière commune, aux points d'attache, et la compatibilité des schémas moteur, mât, carénages et accessoires doit être assurée. Ce qui implique, à partir d'un certain stade, la coopération du motoriste et de l'avionneur.

Il semble bien que ce soit dans cet esprit qu'ait été conduite l'étude des modes normaux de l'ensemble moteur JT9D avion 747, le terme d'intégration ayant même été utilisé dans certains des articles publiés à ce sujet (cf références 1 et 2).

Dans ce domaine beaucoup reste encore à faire.

6. CONCLUSIONS

A partir d'un cas concret rencontré lors de la certification d'un avion civil, nous avons exposé la méthode utilisée pour étudier l'influence de la perte d'une aube de rotor sur la tenue du mât.

Nous avons insisté sur les difficultés rencontrées par l'avionneur, qui proviennent d'une connaissance insuffisamment fine du comportement dynamique du moteur. Nous ne doutons pas que l'avenir voit se développer une coopération approfondie et fructueuse entre avionneur et motoriste, indispensable à la résolution de ce problème.

- Références :
- 1 - J.L. WHITE and E.S.TODD Normal modes vibration analysis of the JT9D/747 Propulsion System J.Aircraft Vol.15 Janv.1978, pp.28-32.
 - 2 - M.N.AARNES and J.L.WHITE Propulsion System and Airframe Structural Integration Program J.Aircraft Vol.12 April 1975, pp. 234-2342.

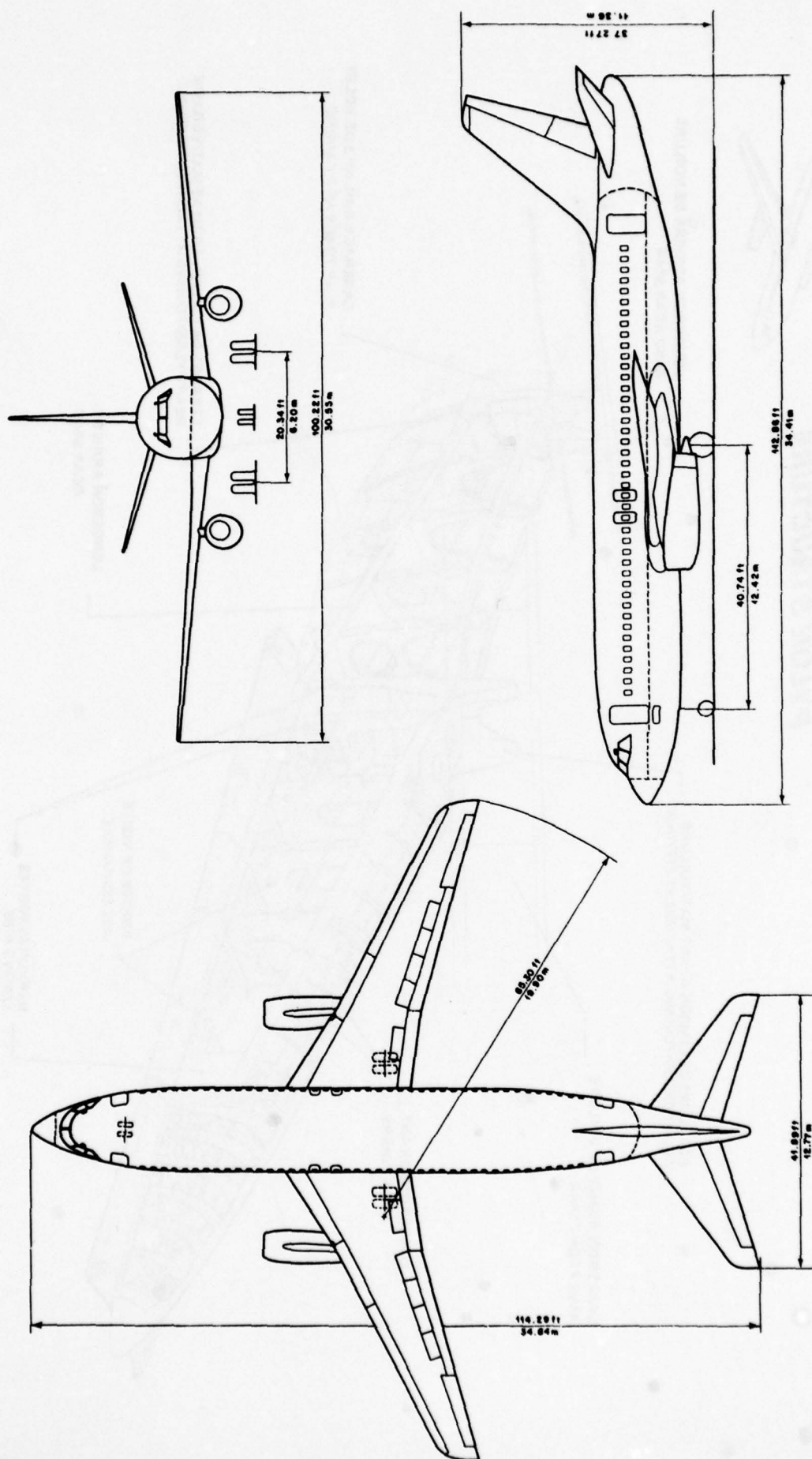


Figure 1 Avion Mercure 100



PYLON STRUCTURE

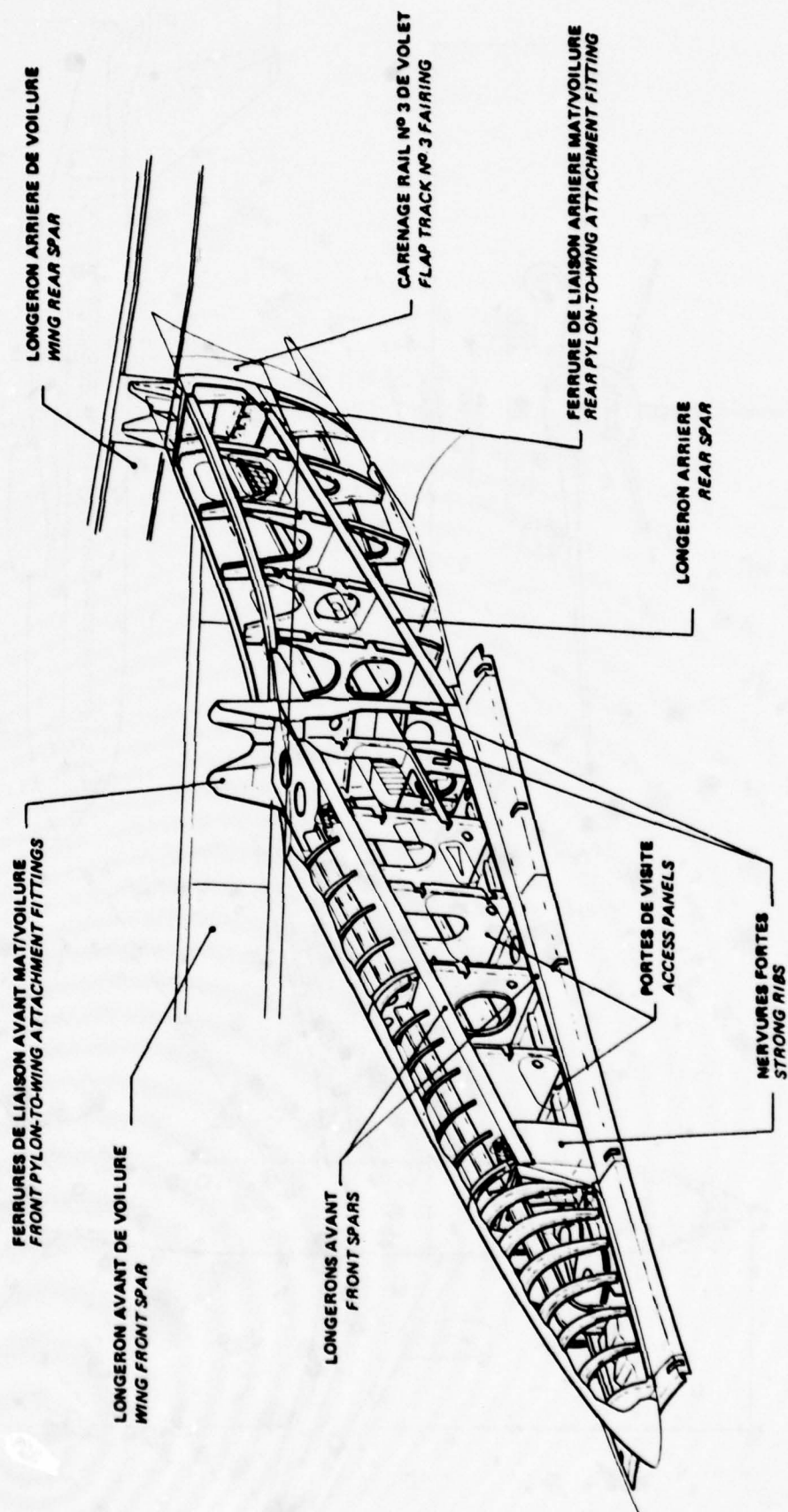


Figure 2 Structure du mât

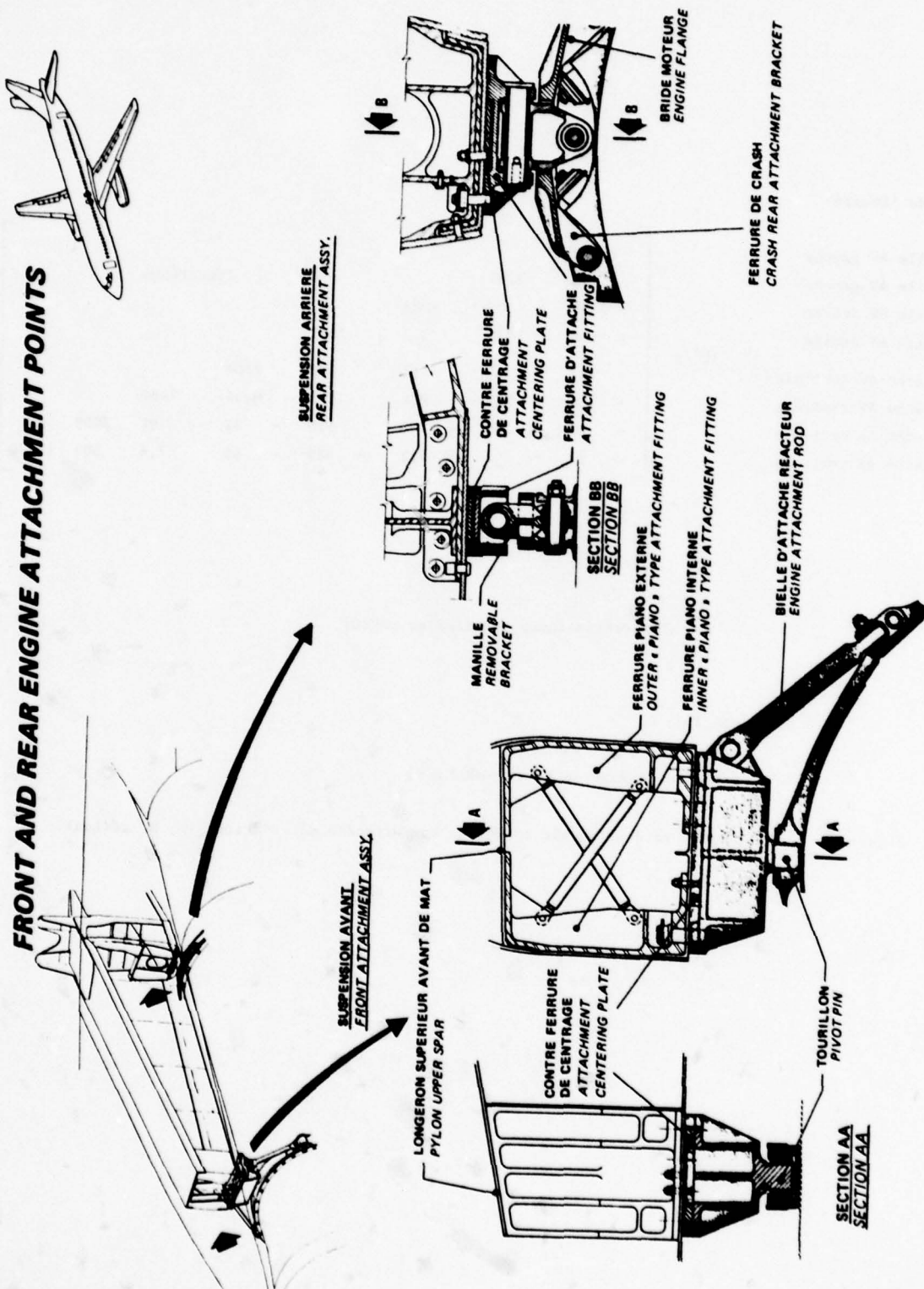


Figure 3 Suspensions avant et arrière du moteur

Degré de liberté

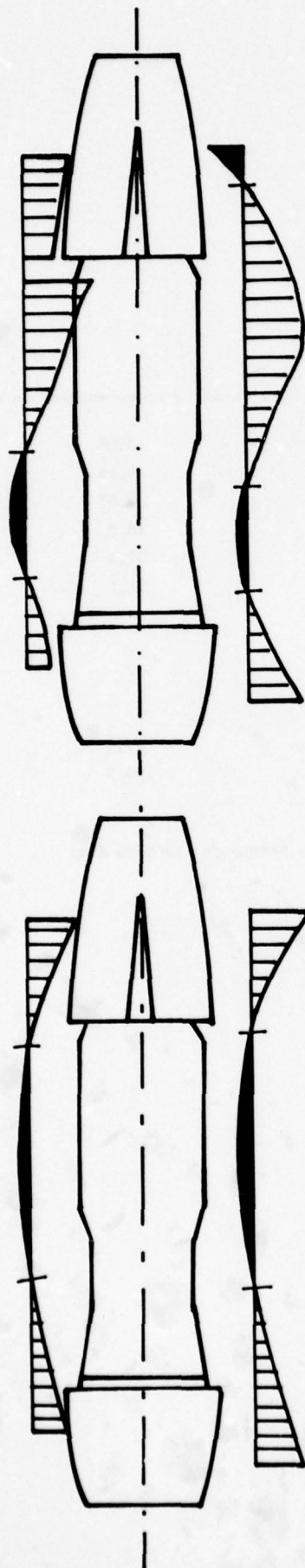
y bielle AV gauche	3903								
z bielle AV gauche	325	2284						Symétrique	
y bielle AV droite	- 2587	309	3903						
z bielle AV droite	- 306	- 1920	322	2292					
x attache AV centrale	27	339	- 18	358	2106				
y attache AV centrale	- 1224	- 752	- 1224	753	0,44	2468			
y attache AR centrale	- 23	- 449	- 27	570	- 32	- 91	2089		
z attache AR centrale	- 27	- 257	- 3,3	- 429	- 49	7,6	583	16170	

Caractéristiques inertielles moteur

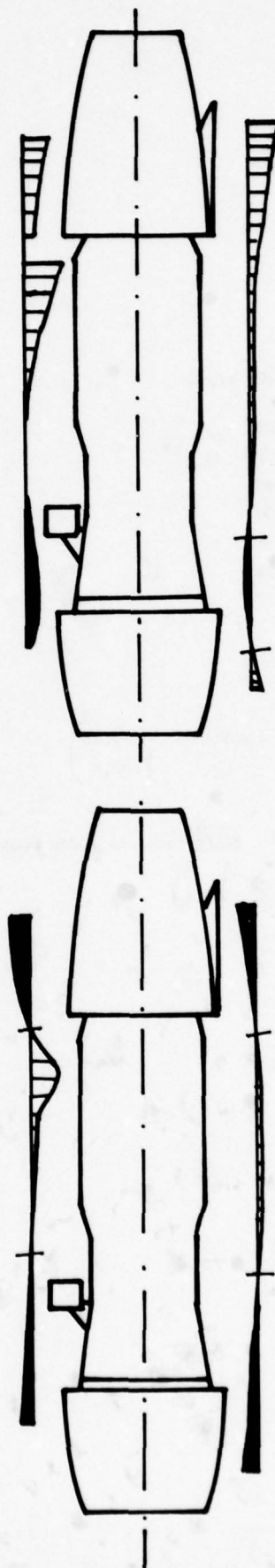
Masse 2405 kg

Inertie de roulis $290 \text{ m}^2 \text{ kg}$ Inertie de tangage ou lacet $3000 \text{ m}^2 \text{ kg}$

Figure 4 Matrice de raideur du mât rapportée aux attaches mât réacteur (m, N, radian)



Fréquence 45,46 Hz
 Amortissement 33 ‰
 Masse généralisée 330 m²kg



Fréquence 102,8 Hz
 Amortissement 18 ‰
 Masse généralisée 544 m²kg

Figure 5 Modes souples du moteur nu

Avec moteur rigide		En ajoutant 2 modes souples du moteur	
	3,09		3,09
	6,51		6,48
	8,93		8,97
	18,90		18,8
	32,96		32,3
	57,76		31,1
(Pour mémoire modes moteur souple			
Flexion verticale 2 noeuds	45,46		45,9
Mode complexe	102,8		190,5

Figure 6 Influence des modes souples sur les fréquences propres (Hz)

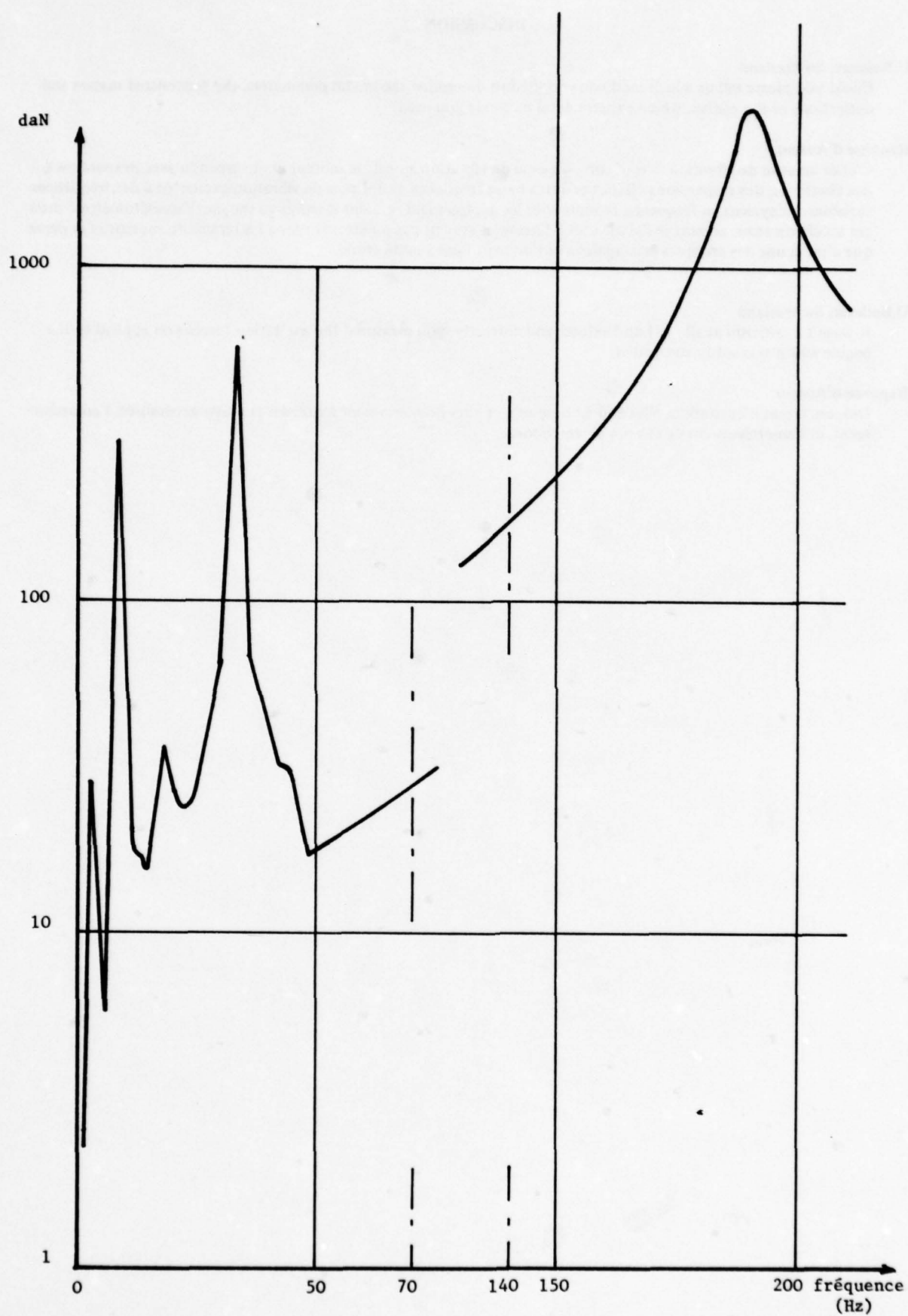


Figure 7 Composante verticale de l'effort appliqué à une attache latérale.
Rupture d'une aube de turbine haute pression.

DISCUSSION

U. Bolleter, Switzerland

Could you please tell us which methods you used to determine the modal parameters, the generalized masses and deflections of the engine, which experimental methods you used?

Reponse d'Auteur

C'était un essai de vibration, c'est-à-dire, un essai de vibration au sol; le moteur était suspendu avec des sandows, des élastiques, des suspensions élastiques à très basse fréquence et des pots de vibration excitaient à des fréquences variables, balayaient en fréquence ce moteur et les déplacements étaient mesurés au moyen d'accéléromètres; mais ces accéléromètres, comme je l'ai dit tout à l'heure, n'avaient pas pu être montés à l'intérieur du moteur et je pense que c'est là une des critiques principales que l'on peut faire à cette étude.

U. Bolleter, Switzerland

It wasn't a criticism at all. If I understood you correctly, you measured the excitation forces you applied to the engine which was softly suspended.

Reponse d'Auteur

Oui, ces forces d'excitation, elles étaient connues, et elles nous servaient à calculer la masse généralisée, l'amortissement, et l'amortissement de chacun de ces modes.

INTEGRATION OF AN AIRFRAME WITH A TURBOFAN AND AFTERBURNER SYSTEM

by

Michael S. Wooding
Principal Designer
Advanced Projects Department
British Aerospace
Aircraft Group
Warton Aerodrome
Preston
Lancashire PR4 1AX
England

and

Harry Hurdis
Head of Preliminary Installation Design
Advanced Projects Department
Rolls-Royce Limited
Aero Division
P.O. Box 31
Derby DE2 8BJ
England

SUMMARY

In the future as technological advances become more sophisticated improving significantly the performance of a conventionally installed military engine will become more difficult and optimum cost effectiveness less easy to achieve.

Examination of some less conventional configurations shows that, advantages may be obtained as a result of a degree of engine to airframe integration. This might involve the afterburner, nozzle and engine bypass duct.

This paper describes some alternative ways for achieving this and gives indications of weight, performance and cost trade-offs that might result for a single engine fixed wing combat aircraft.

1. INTRODUCTION

Significant improvements in military engine installed performance will become harder and more costly to obtain by conventional means and this will be more so in the future as advances in technology become more sophisticated and performance requirements more demanding.

With the ever increasing quest for improvement, efforts must be concentrated on reducing aircraft drag and mass.

In conventional installations, whether the engine and afterburner is installed within the fuselage or in a separate nacelle, clearances must be provided for a physical separation between the engine and aircraft structure to cater for in-flight structural deflections, the needs of the actual installation process and to provide a passage for a flow of ventilation or cooling air. In the case of a pure jet engine however, the magnitude of the engine surface temperatures are such as to preclude the possibility of omitting the ventilating passage between the hot surfaces and the aircraft structure. With a turbofan (bypass) engine the core is blanketed by the comparatively cold air flow from the Fan or LP compressor and so long as this is ducted effectively to the afterburner the airspace previously provided can be dispensed with and integration of the engine duct with the airframe becomes a possibility. Ventilating air is however required to disperse fuel vapour in the zone where the engine accessories are located.

This paper includes some of the preliminary work done jointly by British Aerospace and Rolls-Royce to determine the prospects for cost effective solutions along these lines.

The engine used for this work was a development of the well proven Rolls-Royce Military Spey two shaft, turbofan engine which has a bypass ratio of 0.7. In ISA sea level static conditions this engine gives approximately 24000 lb. of thrust with afterburner lit.

2. THE CONVENTIONAL INSTALLATION

Fig.1 shows a conventional installation arrangement for this combination from which comparisons can be drawn and it is evident that the clearance allowed between the tailplane mounting frame and the engine body to a large extent determines the general shape and cross-sectional area of the tail of

the fuselage. The 'blended' body shaped rear fuselage of this design is of conventional construction and employs sculptured frames to carry the engine, moving fin, and tailerons. The structure is lined internally to prevent the spread of fire, provide structural stability and to allow for the passage of cooling and ventilation air. Aft of the tailplane frame light fairings extend the fuselage shape to the engine nozzle. Removable load-carrying doors below the engine allows for its removal downwards and the lower portions of the fin and tailplane frames are therefore also detachable.

3. THE INTEGRATION

The initial integrated installation investigated is shown in Fig.2, referred to as the 'divided duct' version, and in common with all the other alternatives employs an afterburner pipe which is attached to and becomes part of the rear fuselage. The top half section of the bypass duct now forms the inner lining of the fuselage structure, the lower half being detachable for engine removal. The bare engine with bypass duct and afterburner pipe removed, shown cross-hatched in the figure, now consists of the LP and HP compressors, combustion chamber and turbine section. In addition it also carries the afterburner gutter assembly and fuel system. This latter feature having the advantage of precluding the necessity for breaking down fuel piping when the engine is withdrawn and is an important issue from an operating and maintenance point of view.

The afterburner pipe, see Fig.3, which is bolted directly to the titanium tailplane frame also carries the variable nozzle control and operating jacks, the working loads of which are transmitted by subsidiary structure to be reacted by the tailplane frame. The fuselage contour continuity is achieved over the afterburner pipe section by the use of light alloy removable fairing panels which also serve to give access to the nozzle jacks.

The titanium afterburner pipe carries a series of internal heatshield liners to provide it with thermal insulation by ensuring the presence of a protecting jacket of cool bypass air. The liners are similar in concept to those fitted to conventional afterburner pipes and operating experience with contemporary engines has shown that the lives of the liners are well in excess of those for the engine. Thus, neither the liners nor the afterburner pipe are likely to be the cause of costly maintenance action, but because of the method of attachment proposed the pipe can be replaced readily if necessary.

The engine external case temperatures considered are based on current experience and figure 4 shows the gradients that can be expected on a conventional installation in two extreme cases. It is seen that the afterburner pipe outer surface part of which, in the case of the integrated arrangement proposed, would also do duty as the fuselage structure inner skin, will operate at a temperature in the region of the tailplane frame of between 320°F (160°C) and 446°F (230°C). These levels are realised for the ISA sea level static combat rating, and at 36,000 ft. altitude Mach 2 (afterburner lit) conditions respectively. Operating temperatures of this order are well within the capabilities of the aircraft structural materials under consideration. However, provision could be made for a flow of cooling air to pass through the aircraft structure if this were found to be necessary.

The variable nozzle is carried in effect upon the aircraft structure, as also are the associated screw jacks and nozzle actuator motor. These can be designed to be powered either by pneumatics or hydraulics from the aircraft systems. Considerable operating experience has been accumulated in controlling civil aircraft engine thrust reversers from the aircraft systems and thus with the incorporation of the necessary safety precautions, it is believed that a satisfactory nozzle actuating and control system can be achieved.

The nozzle area sensing and control to the drive mechanism will be the only connection necessary between the engine and the aircraft rear fuselage section requiring disconnection when the engine removal is undertaken.

The first of several possibilities which have been considered for the integration of the bypass duct, already indicated in Fig.2, is shown in greater detail in Figure 5. In this design the top half cross-section of the duct is formed by the inner lining of the aircraft structure and becomes integrated with it, its lower longitudinal edges carrying a rigid seal pressure shoe. The lower half of the duct is detachable downwards and as shown in Fig.6 is secured in position by heavy-duty toggle type fasteners, seal carriers are mounted on its upper longitudinal edges and these rigidly interlock with the pressure shoe of the top portion locating it in position, they also contain a longitudinal seal which could consist of a shaped metal strip or perhaps a high temperature silicone rubber. Conventional circumferential metal piston ring type seals are fitted at either end to mate with the detachable half of the duct. Fuselage structural frames extend downward together with two longitudinal diaphragms to support the lower exterior aircraft skin and are shaped to give access to the fasteners for removal of the duct lower half and provide a landing for the engine removal door.

Although an integrated installation employing a bypass duct arrangement, such as that described, is not believed to impose a weight penalty, when compared to a conventional installation, clearly the large pressure differential acting across the duct, in this case about 50 lb/in.² (3.5 kg/cm²), makes the necessity for any longitudinal joints very undesirable and two alternative ways for avoiding this are suggested. Fig.7 shows an arrangement that merits further consideration and in which the rear section of the bypass duct can be slid forward, thus shortening the engine by a sufficiently large margin to allow for its withdrawal downwards. This is referred to later as the 'telescopic' duct arrangement.

For the particular engine under consideration the rear mounting attachment has been moved forward and this is possible with a relatively small internal re-arrangement. The rearward portion of the bypass

duct is separate from the engine and forms an interconnection, it is attached by a readily removable clamp joint to the aircraft structure. A circumferential piston ring joint completes the connection with the engine and would be designed to allow sufficient movement to cater for differential deflections etc. A fully articulating arrangement is not suggested because of the relatively short length/diameter ratio of the connecting duct but further work may show that this would be an acceptable alternative solution. Engine withdrawal is achieved by sliding the bridging bypass duct portion forward, thus shortening the engine sufficiently to allow for its removal without disturbing the fixed afterburner pipe. The reduction in fuselage cross-sectional area conferred by the integrated reheat pipe feature is only marginally eroded by this alternative arrangement, when compared with the 'divided' duct design previously described, and this is because of the relatively small clearances now necessary between bypass duct and aircraft structure. A reduction in engine mass will be realised through the transfer of the attachment of these engine components to the aircraft structure.

Fig.8 shows one further possible alternative and in this case the bypass duct aft of the rear engine mounting together with the afterburner pipe is formed as an integral part of the aircraft fuselage, the engine carrying only the afterburner gutters. To remove the engine it is first necessary to draw the rear fuselage section off backwards and the attraction or otherwise of this proposition will depend on the bulk and mass involved and on the mass of other large assemblies which may be attached.

The extent to which controls and systems would have to be disconnected would need consideration. It is possible that a minimum fuselage cross-sectional area distribution, and maximum mass reduction may be achieved by this arrangement, although it may only be attractive for particular aircraft configurations.

In all the integrated systems the basic engine weight has been reduced and although this is due to the fact that some of the conventionally accepted parts of the engine have been transferred to the aircraft the net effect is a saving in aircraft weight. The separation of the afterburner nozzle from the engine has resulted in a redistribution of the forces to be reacted by the engine mountings. Since the cross sectional area at the rear of the basic engine upon which the internal pressure can act has been increased the front suspension is subjected to increased thrust loads. Although in some circumstances an increase of some 40% in these loads can occur, only a moderate increase in the weight of the steel intermediate case, which houses this mounting, will be necessary. In addition to the foregoing the engine carcass can also be lightened because of the relocation of the afterburner and nozzle. This fact and the elimination of aerodynamic side loads from the latter have resulted in a reduction of bending moments within the basic engine and this has contributed to a weight saving.

The resultant engine weight reduction, taking the above points into consideration, is estimated to be in the order of 30 lb. (13.6 Kg).

The nozzle area sensor will be on the afterburner, whereas the control will be engine mounted. No complications are anticipated because the engine and afterburner are separate since nozzle pressure and position signals, probably transmitted electrically, will be the only ones requiring disconnection on engine removal.

4. PERFORMANCE IMPROVEMENT

The work that has been done so far has indicated performance improvements both as a result of drag reduction and weight saving. Both the 'divided' and 'telescopic' duct integration schemes considered here can return a similar reduction in rear fuselage cross sectional area as shown in Fig.9, and at the plane of the tailplane frame this amounts to a reduction of about 11%.

Drag reduction estimates have concentrated on the improvement in the cross sectional area distribution of the fuselage only and a single engine configuration, such as that described, is likely to show a smaller return than might be the case for a similar twin engine design. At subsonic speeds little improvement is likely since afterbody drag depends mainly on the degree of separated flow present and no change has been made to the nozzle design and base area which have a large contributory effect. For supersonic speeds above $M = 1.2$ the estimates show a reduction of the order of 7.5% of total clean aircraft drag. No account has been taken in the foregoing of the beneficial effect of rear fuselage shape improvement on the area distribution of the complete aircraft, for example, the inclusion of flying surfaces. It is possible that the net drag reduction may be greater than that estimated and by the same token the drag rise characteristics may also be improved. Performance comparison estimates for a typical aircraft have been based on a subsonic combat mission study. The high thrust to weight ratio and modest wing loading considered necessary to achieve the mission performance goals combine to provide a substantial thrust/drag margin, thus minimising performance benefits due to drag reduction. For subsonic speeds this design is unlikely to show increases in sustained turn rate, SEP (Specific Excess Power) and transonic acceleration of more than 1%, however, at supersonic speeds these parameters are likely to increase to approximately 8%. Further, if the aircraft were flown on a supersonic interception mission, as shown in Fig.10, the penetration distance would also be increased by about 8%. Clearly for the case where an aircraft is designed for a supersonic mission, the performance and size benefits could both become significant. Typical cases studied by British Aerospace indicate that a return of about double the foregoing values of sustained turn rate, SEP and transonic acceleration can be expected. Preliminary comparative estimates have shown that a saving in weight of approximately 77 lb. (35 Kg) can be expected from the 'telescopic' duct arrangement when compared to a conventional design. A somewhat smaller saving realised for the 'divided' duct arrangement is due to the need to add strengthening for the removable feature of the lower half of the bypass duct.

5. COSTS

Savings in costs can stem from the possibility that exists to reduce the size of the aircraft and for the mission shown in Fig.10 the empty weight could be reduced by about 264 lb. (120 Kg) i.e. about 1.4% of aircraft empty weight. For a fleet of 200 aircraft this could show an acquisition cost saving of about £13M, and assuming a 15 year life and 300 hour/year utilisation a further saving in fuel costs of approximately £21M can be added making a total saving of £34M. Further savings, less easy to quantify, may be possible and these come under such headings as spares and logistic support. For example, the transfer of engine parts to the aircraft has advantage in reducing engine maintenance costs and the engine when removed from the aircraft has its critical parts more readily accessible for inspection and repair. Spare engines are smaller and lighter and this reduces the cost of storage and transport. Since the parts transferred have a longer life than the engine, fewer spares may be required and total procurement cost reduced.

6. CONCLUSIONS

The work that has been described in this paper has covered the initial steps that might be taken along the road of engine/airframe integration for a turbofan engine and has shown that benefits in the form of performance improvement and cost savings exist and are to be had for a small increase in technical risk. It is hoped to deepen this work in the future to seek even fuller integration leading to further drag reduction and performance gains. It is hoped to consider other configurations, for example, twin engined designs, where the integration may prove more cost effective, and to explore the degree to which it may augment performance improvements resulting from the adoption of such features as improved propulsion nozzle configurations.

The Authors wish to thank their respective Companies for permission to present this paper, and to their colleagues for their help in preparing it. They are personal views of the Authors and do not necessarily reflect the approach of our respective companies.

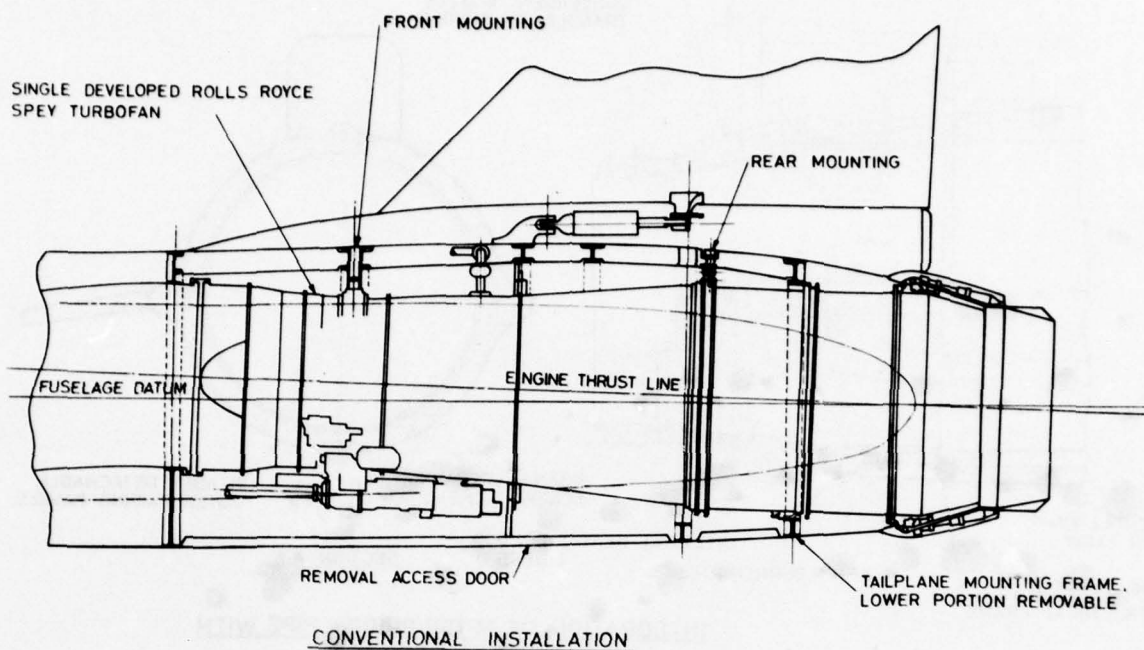


FIG 1

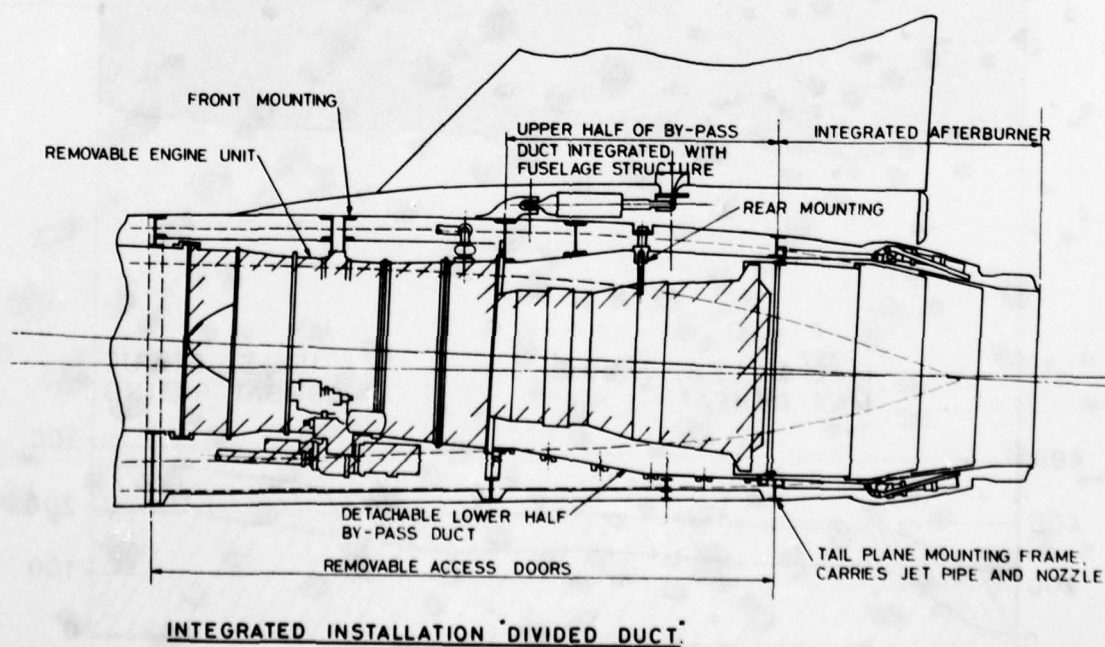


FIG 2

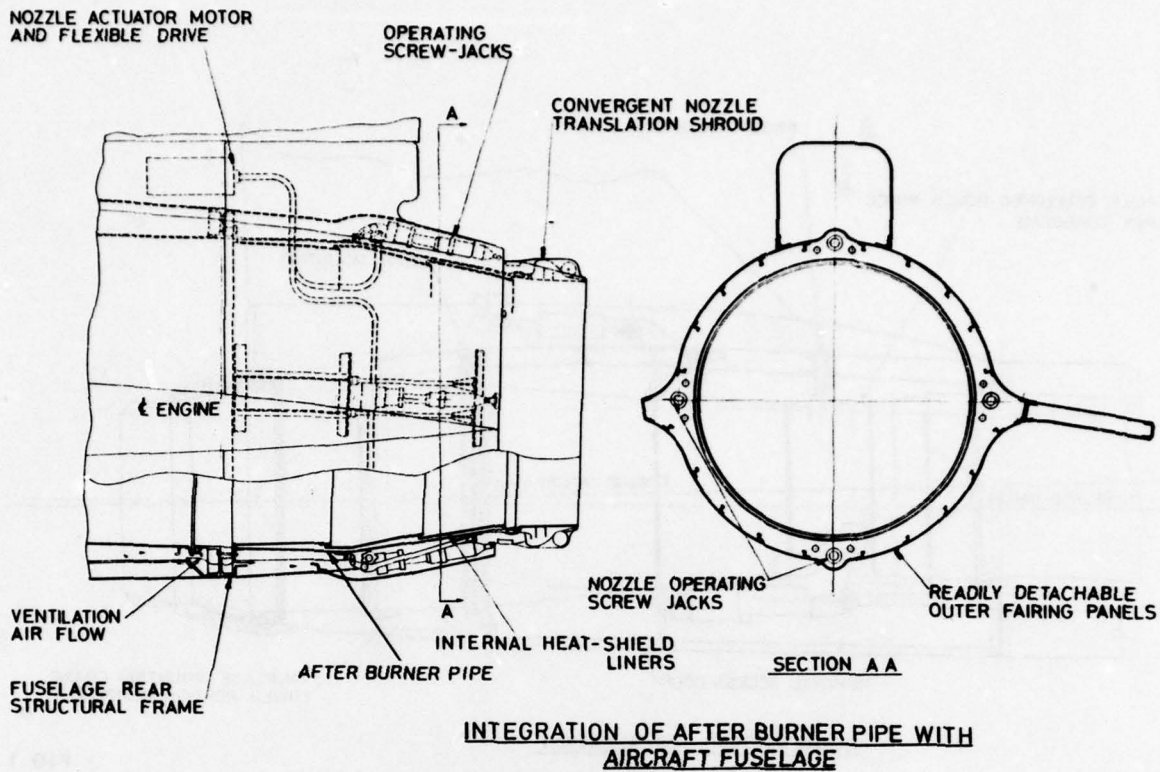


FIG. 3

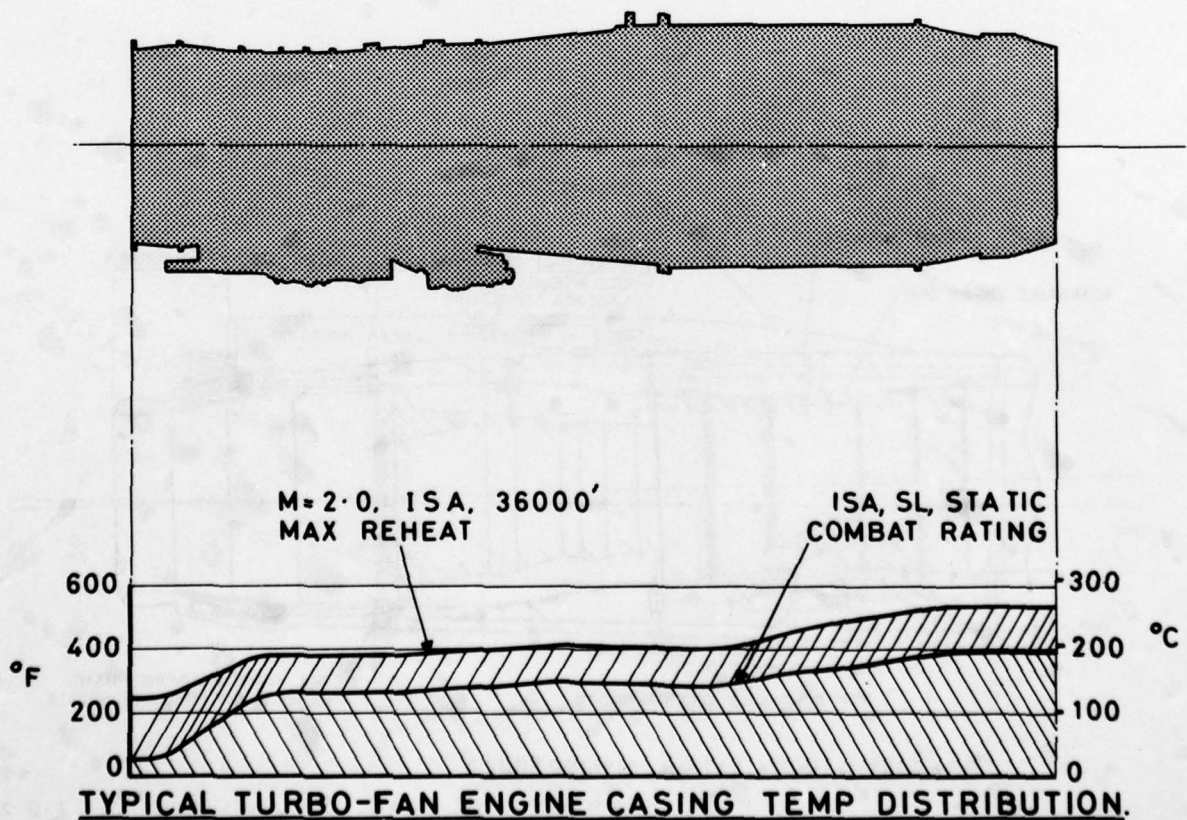


FIG 4

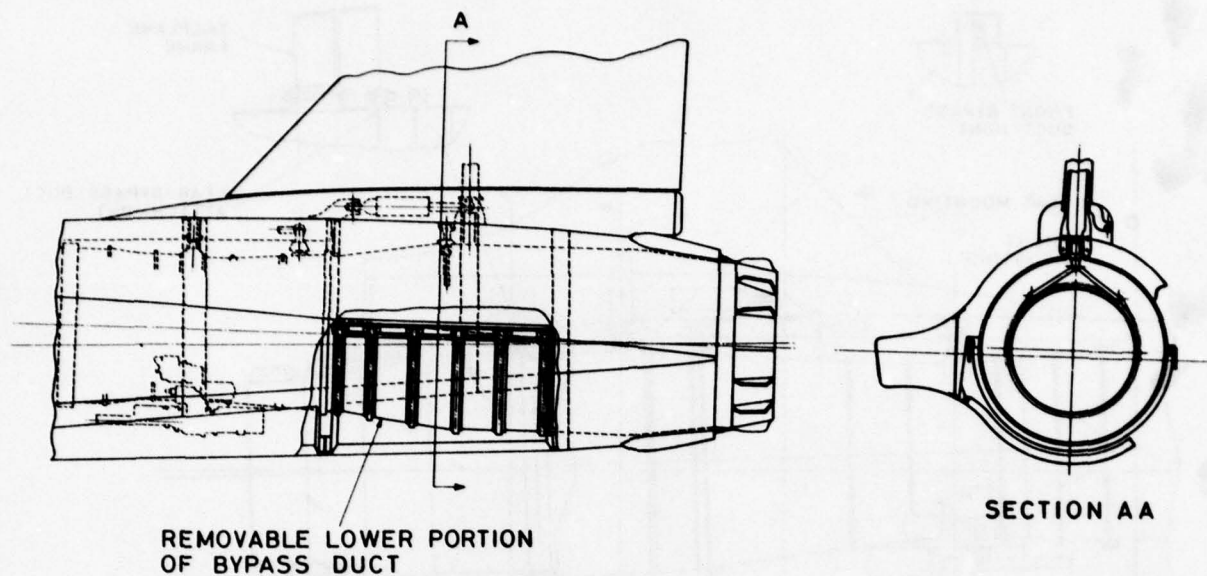


FIG 5

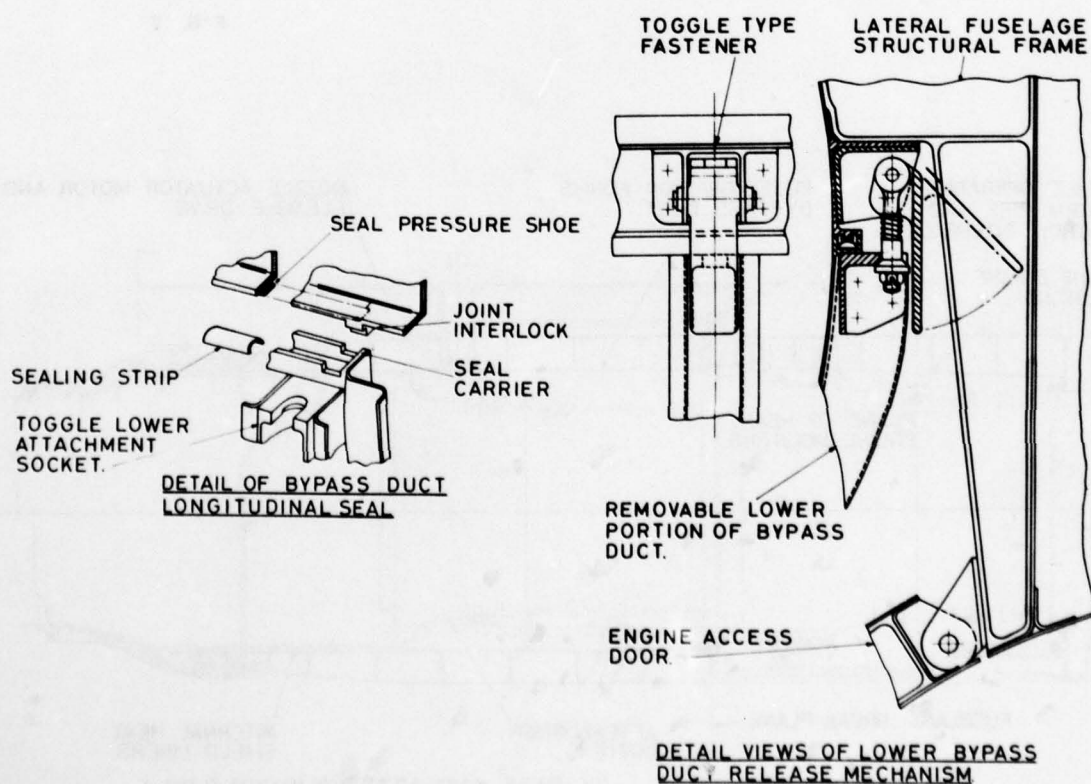
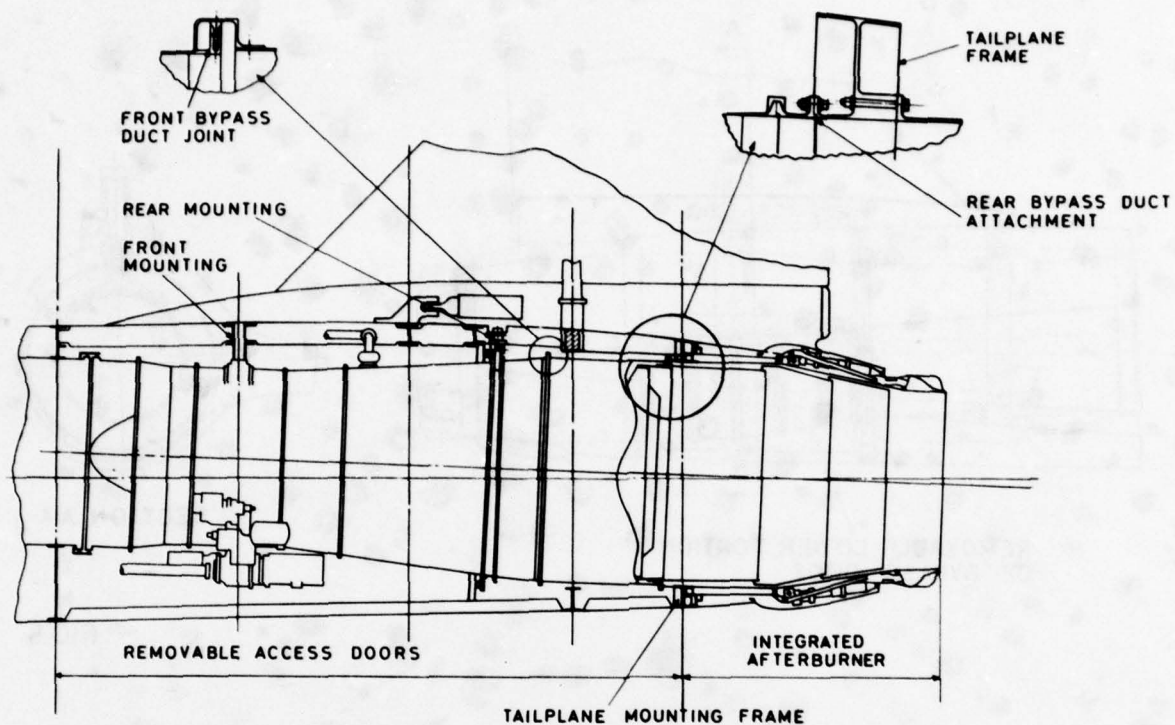


FIG 6



INTEGRATED INSTALLATION (TELESCOPIC DUCT)

FIG. 7

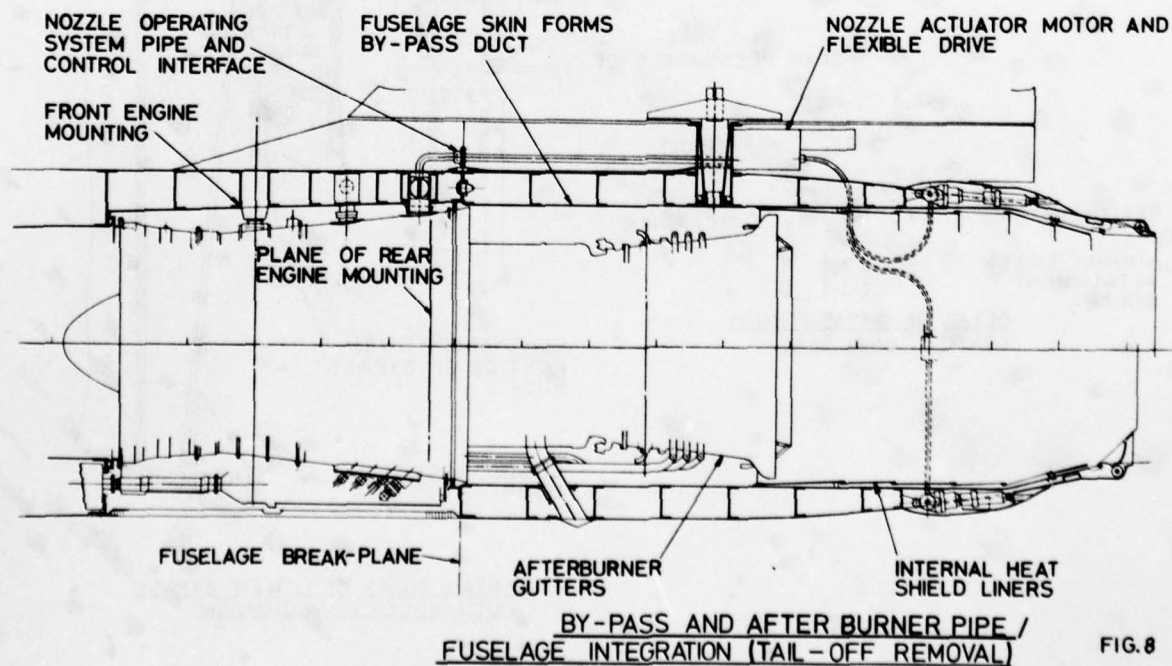
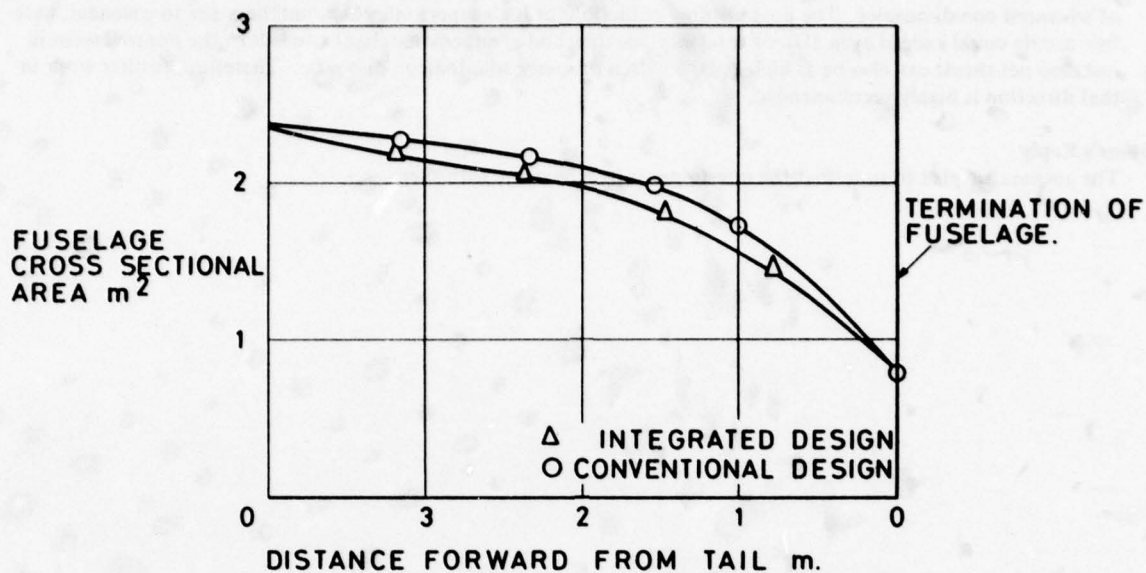
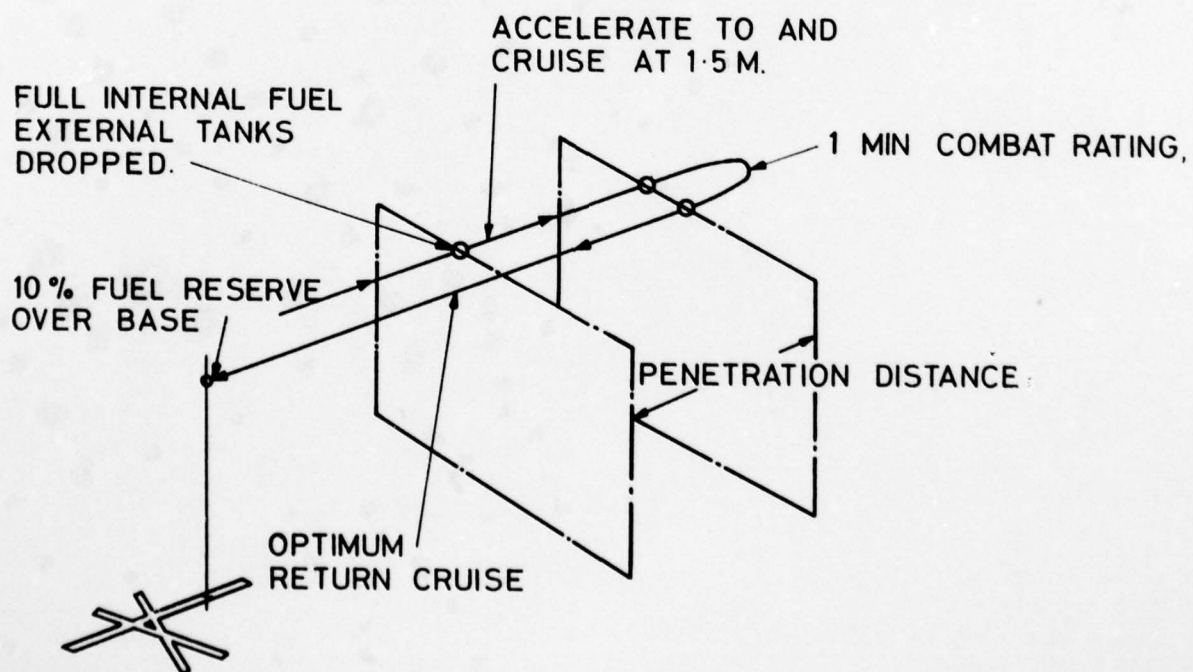


FIG. 8



CROSS SECTIONAL AREA DISTRIBUTION.

FIG. 9



SUPERSONIC INTERCEPTION
MISSION 20 K. FT ALTITUDE

FIG. 10

DISCUSSION

K.Lotter, FRG

I would like to emphasize what you said in your last sentence, i.e. that further studies should include investigations of advanced con-di-nozzles. The possible drag reductions at high supersonic Mach numbers due to a slender, base-free nozzle could exceed even 10% of total airplane drag and at supersonic flight conditions the improvement in installed net thrust can also be as high as 10% with a properly adapted con-di-nozzle. Therefore, further work in that direction is highly recommended.

Author's Reply

The authors are glad to note that the questioner is in agreement with them.

A NEW FACILITY FOR STRUCTURAL ENGINE TESTING

by

Captain Robert L. B. Swain and Dr. James G. Mitchell
 Arnold Engineering Development Center
 Arnold Air Force Station, Tennessee 37389

SUMMARY

Current and planned test facilities are designed to test an engine over a range of flight speeds and altitudes. However, no existing or approved facility can simulate the maneuver environment an engine actually experiences in flight. It has become apparent in recent years that maneuver-induced forces are contributing to major problems in engine durability and operational efficiency. Engine development trends toward closer tolerances, lighter cases, etc., will cause the problems to become even more severe in the future. The Facility Planning Division at Arnold Engineering Development Center, Tennessee, has studied the requirements for a facility capable of simulating aircraft maneuvers for the last five years and, with the assistance of experts from the engine community, has evolved a facility concept known as the Turbine Engine Loads Simulator (TELS). A description of the proposed facility and its potential benefits to the engine development process are presented.

LIST OF SYMBOLS

M = gross gyroscopic moment (ft-lb)
 I = moment of inertia of the rotor about its spin axis (lb-ft²)
 ω = spin velocity of the rotor (rad/sec)
 Ω = pitch-up angular velocity (rad/sec)
 g = acceleration due to gravity (ft/sec²)
 F = blade force perpendicular to the plane of the rotor disc (lb)
 m = mass of the blade (lb-sec²/ft)
 r = distance from the spin axis to the radius of gyration of the blade (ft)
 θ = angular displacement of the blade relative to the turn (Ω) axis.

INTRODUCTION

The outstanding performance of modern turbine engines has been achieved through an evolutionary process spanning three decades. Thrust-to-weight ratio is a significant indicator of jet engine performance, and Fig. 1 illustrates how it has improved during the past 30 years. Aerodynamic advances are noted in improved stage pressure ratios and flow path refinements. Material advances along with improved cooling system design have permitted engine operation at higher, more efficient temperatures. Structural and material advances have permitted considerable weight savings. The result of all these improvements is today's turbine engine containing approximately 40,000 individual parts which must function with incredible precision to realize the performance potential of the engine. Clearances between rotating and static components along the flow path must be maintained to within a few thousandths of an inch to prevent significant losses in thrust and efficiency while exposed to an operating environment which imposes severe thermal and mechanical stresses on the engine components. These stresses inevitably take their toll on engine performance and durability. As engine performance deteriorates in operational service, fuel flow must be increased to restore the lost thrust, resulting in increased temperatures, shorter engine life and occasional catastrophic failures.

BACKGROUND

Many of these thermo-structural problems appear as the engine gradually yields to the forces inherent in its operational environment. Some can be adequately analyzed and properly accounted for in design since they are predominantly unidirectional and affect only one or two components. For example, the centrifugal acceleration of high-speed compressor and turbine blades can exceed 30 thousand g's. However, the resulting forces are analytically dealt with fairly easily because they act in a single direction, causing only tensile stresses to arise in the blade, and they affect primarily the blade and the disc to which it is attached. Much more difficult to accommodate are those forces which change direction as the engine rotates or those which feed back into the remainder of the engine, thus affecting clearances and forces on other components. A great deal of time and money have been spent to date on studies of those environmental effects which can be duplicated or simulated in today's ground test facilities. With the advent of advanced computational techniques combined with a vast amount of accumulated empirical data, engine designers are developing methods of dealing with many of these difficult structural problems.

DEFINITION OF LOADS

There is one major source of complex structural forces which remains relatively unexplored; i.e., aircraft flight maneuvers. Conventional ground test facilities are unable to simulate aircraft maneuvers, while flight test suffers from lack of timeliness, high cost and extremely limited data acquisition due to space and weight restrictions. When an aircraft performs a flight maneuver, it exposes the engine to forces it never experiences in a static test cell. These forces are primarily composed of centripetal forces produced by the linear acceleration of a changing flight path and gyroscopic moments induced by the spinning rotor reacting as a gyroscope to the rotation of the

aircraft. Calculations show that forces arising from aircraft maneuvers are sufficient to cause major problems in an engine. Today's combat aircraft are maneuvered in excess of 10 g's on a regular basis. In a 10-g turn an engine may suddenly "weigh" 35 thousand pounds and produce contortions in the engine case and rotor which affect bearing loads and clearances throughout the engine. For years, engine designers have attempted to determine the complex effects of such maneuver-induced inertial loading by applying calculated forces to hard points on the engine case and measuring the resulting deflections. Since the loads were lumped, the rotor was sometimes absent and the other operating forces were missing, the static loads test was crude at best; but it was the only method of obtaining an experimental approximation of the engine's response to inertial loads. But as modern engines have become more efficient structurally, they have presented fewer "hard" points on which to apply the simulated loads. In fact, the F101 engine is the first modern turbine engine developed in this country without being subjected to a static load test. There was simply nowhere to realistically apply the loads.

To analytically determine the distribution of an inertial load among the five or six rotor shaft bearings, it is necessary to know or assume a value for the mass and stiffness distribution of the rotor and the case. To solve for the relative displacements and forces, the case and rotor are often treated as two concentric springs. To adequately account for the asymmetries of the mass and stiffness of the case and rotor, considerable computer capacity is required for even the simple case where the engine is not operating. The complexity of the problem greatly escalates when one now tries to account for the operational effects of the engine; e.g. a non-uniformly heated shaft and case, the aerodynamic pressure within the engine which tends to stiffen the case, and a spinning rotor which tends to straighten the rotor shaft.

If we additionally allow the engine to rotate about its pitch or yaw axis (which will occur in almost every high-g maneuver), powerful gyroscopic forces enter the picture which make the solution to our "simple" problem even more difficult. When some of our current engines are rotated at $3\frac{1}{2}$ radians per second, as specified in MIL-E-5007D, gyroscopic moments in excess of 200,000 ft-lb are generated by the rotor against the engine bearings. The gross magnitude of the moment is simple to calculate using the equation:

$$M = I \omega \Omega / g \quad (1)$$

However, the difficulty again arises not in calculating the magnitude of the force but in determining how and where the force will manifest itself within the engine. To compound the problem, gyroscopic effects are not intuitively obvious and thus one sometimes fails to anticipate their true nature and location. For instance, when accounting for the macroscopic gyro forces, one must not fail to consider also the microscopic forces (those forces peculiar to an individual component). It can be shown that the gyroscopic forces acting on a rotor blade within the engine is given by the Equation (2). See Figure 2.

$$F = m r \omega \Omega \cos \theta \quad (2)$$

Note that the term $\cos \theta$ causes the force to be cyclic; i.e., positive during half of the rotation and negative during the other half. Using values typical for a 30 thousand pound thrust high performance turbofan engine, the maximum gyroscopic bending force on a fan blade would be ± 740 lb, compared to a steady aerodynamic force of 475 lb. Thus, not only does the gyro force exceed the aero force by a sizable margin, but the aero force is quasi-steady while the gyro force is cyclic, tending to bend the blade back and forth each revolution. Every piece of rotating hardware is subjected to similar gyroscopic effects in addition to all the other inertial and operational forces active at that moment. Within this realistic force environment, the task of calculating the clearance between a certain compressor blade and its seal or determining individual component design loads becomes difficult indeed.

Approximate solutions to such problems can only be obtained by making numerous simplifying assumptions and/or enlarging the finite element grid to allow computers to handle the problem in a reasonable time and within the machine capacity. Even then, the accuracy of the resulting solution must be seriously questioned. Without empirical data to validate the required assumptions and simplifications, larger safety factors must be designed into a component to compensate for the lack of confidence in the analytical data. With engine designers attempting to squeeze even more thrust and efficiency from future engines, it is becoming increasingly obvious that a test facility is needed which can bridge the gap between conventional ground test facilities and flight test; a test facility capable of generating the empirical data base necessary for further innovative improvements to the engine structure.

TURBINE ENGINE LOADS SIMULATOR

Personnel at the Arnold Engineering Development Center began working with military and civil aviation experts in 1973 to study the maneuver loads problem and some possible simulation solutions. As a result of preliminary studies, a concept evolved which came to be known as the Turbine Engine Loads Simulator (TELS). Subsequent study has focused on further refinement of the basic concept and definition of sub-system requirements and capabilities. As currently planned, TELS will be configured basically as a very sturdy centrifuge with a 4 degree-of-freedom engine mount which will orient an operating engine in any attitude and at any position on the arm to simulate the desired maneuver (See Fig. 3).

TELS will be capable of simulating any combination of inertia loads to 15 g's and turn rates up to 3.5 radians/sec. Thus all the engine's internally generated and externally applied loads will be simulated simultaneously. This capability is sufficient to satisfy current test requirements as well as anticipated future test requirements for remotely piloted vehicles and other high performance aircraft.

TELS Instrumentation:

TELS will employ advanced diagnostic instrumentation to accurately measure the engine's response to simulated aircraft maneuvers. Part of this instrumentation consists of an X-ray unit, which will permit direct observation of internal engine components on a TV monitor while the test is in progress. The real-time capability permits precise alignment of the X-ray unit to compensate for relative movement between the engine and X-ray unit due to varying test conditions. It also supplies immediate data for decision-making; e.g., whether to proceed to more severe test conditions. Operating concurrently with the real-time system, the X-ray detector will obtain primary diagnostic data by direct exposure of high resolution radiographic film at a maximum rate of one frame per second. The X-ray source will be synchronized with the engine, emitting a five-microsecond pulse each revolution of the rotor. A typical radiograph will require approximately 200 pulses for proper exposure, with actual exposure time determined by the thickness of the metal which the beam must penetrate. The X-ray source and detector will be mounted in a frame which will rotate about the engine and provide for axial and radial translation, thereby permitting full radiographic coverage of a large section of the engine without the necessity of stopping TELS to reposition the X-ray unit. Much work has been done by Rolls Royce, Pratt & Whitney and General Electric in the field of turbine engine radiography. Fig. 4 shows some of the results of that work and Fig. 5 demonstrates the improvements obtainable using the computer enhancing techniques developed during the space program. A clearance measurement accuracy of five mils has been demonstrated by Pratt & Whitney using a system similar to that envisioned for TELS.

Unique Capability:

The greatest amount of useful data from the diagnostic instrumentation can be obtained when the engine is subjected to precisely known test conditions and the various maneuver effects are separated to determine the relative contribution of each effect to the overall engine response. Even flight testing cannot supply this type of information. TELS has this capability due to the unique design of the hinge-gimbal engine mount. To apply gyroscopic loads only, the engine is positioned directly over the pedestal. To obtain g loads with no gyroscopic loads, the engine is positioned at the desired arm radius and pitched to a vertical position by actuating the hinge on the engine mount. The engine rotor axis now parallels the rotation axis of TELS, and thus the gyroscopic rotation rate is zero. At any selected g-load condition, the simulated gyroscopic rotation rate can be adjusted to any value from zero to the TELS rotation rate simply by pitching the engine to the appropriate hinge angle between the vertical and horizontal positions. The combined gyroscopic and inertial loads can be applied to the engine in the desired direction by rotating the turret and rolling the engine within the mount. The four degree-of-freedom hinge-gimbal mount allows TELS to simulate the combined inertial and gyroscopic loading conditions of any maneuver within its broad test envelope.

Potential Uses:

TELS will be able to make a significant contribution at every stage of the engine development process with its simulation flexibility and diagnostic capability. During the early research stages, individual components and sub-assemblies can be tested to generate empirical data to verify a new design. For example, considerable effort is being directed toward development of composite (graphite-epoxy, etc.) fan blades for turbofan engines. Since the elastic modulus and other material properties differ markedly from the metals now being used, it would seem prudent to determine the reaction of the new composites to the steady and oscillatory maneuver forces they will eventually experience in flight. Early detection of any problems would surely result in cheaper fixes and could possibly prevent the costly program delay which usually results when a major deficiency is not detected until the engine is flight tested. As the development process continues, TELS can provide previously unavailable information regarding component interaction and structural integrity of major assemblies. For instance, a bearing and oil system rig could be tested to determine its flight performance long before it would normally experience such conditions. Finally, the prototype engine can be tested while operating to determine its response to maneuver forces at an early date and without risking the loss of an aircraft and pilot. When used in conjunction with Accelerated Mission Testing (AMT), TELS can reproduce a lifetime of maneuvers in just a few days. Maneuver loads are not currently simulated in AMT, and it has consequently been noted that some of the wear patterns and component longevity differ considerably from those observed in flight engines. For engines already in service, TELS can provide extremely valuable diagnostic data to detect the cause of existing problems and help effect their solution.

CONCLUSION

Current trends in turbine engine development point to future engines which will operate at higher thrust, temperature and pressure levels with corresponding improvements in aerodynamic, thermodynamic and structural efficiency. Such optimized engines will necessarily be light and flexible and thereby more subject to internal component movement in reaction to applied loads. At the same time, future combat aircraft and remotely

piloted vehicles will be highly maneuverable, capable of subjecting an engine to increased inertial and gyroscopic forces. To reconcile the apparently incompatible trends toward closer operating clearances, more flexible engines and more maneuverable aircraft, additional information must be obtained to allow a more complete understanding of how engines react to the total force environment they see in flight. Advanced computational techniques will certainly play a vital role in the theoretical analysis and development of future structural design concepts, and TELS will provide the empirical data to validate and improve mathematical models. TELS will also provide experimental verification of computer results and test innovative design concepts. TELS will be uniquely capable of providing the required data as well as enabling the engine designer to attack engine deterioration and life cycle performance problems.

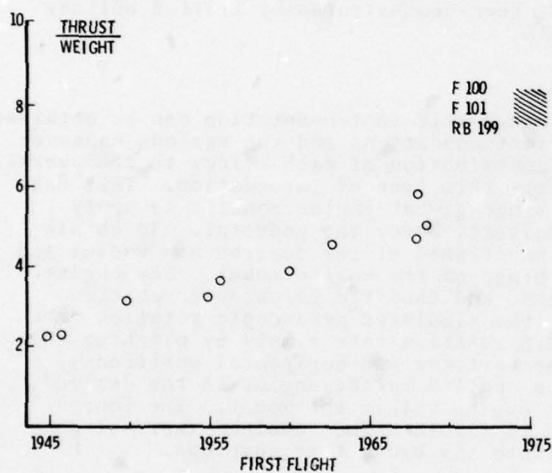
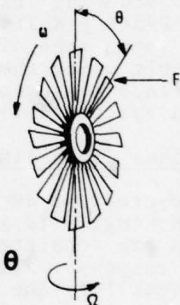


Fig. 1 - MILITARY JET ENGINE PROGRESS

ω = ROTATIONAL VELOCITY OF ROTOR
 Ω = YAW RATE OF ACFT.
 r = DISTANCE FROM SHAFT TO CENTER
 OF GYRATION
 M = MASS OF BLADE
 θ = ROTATIONAL ANGLE OF BLADE



$$F_B = M\omega\Omega r \sin\theta$$

EXAMPLE:

ASSUME $M = 5 \text{ #/g}$ $\Omega = 3.5 \text{ rad/sec}$ $\omega = 10,000 \text{ RPM}$ & $r = 1.3 \text{ FT.}$

$$\text{THEN } F_{B_{\max}} = (5) (1047) (3.5) (1.3) (\pm 1) = \pm 740 \text{ #}$$

TYPICAL CORRESPONDING AERODYNAMIC FORCE ON SAME BLADE $\approx 475 \text{ #}$

NOTE:

GYRO FORCES EXCEED AERODYNAMIC FORCES BY 55%

WHILE ALL OTHER BLADE FORCES ARE QUASI STEADY-STATE, GYRO FORCE ARE CYCLIC, PUSHING FORWARD-THEN REARWARD-THEN FORWARD AGAINST THE BLADE IN FULL MAGNITUDE ONCE EACH REVOLUTION.

Fig. 2 - LOADS ACTING ON INDIVIDUAL BLADES

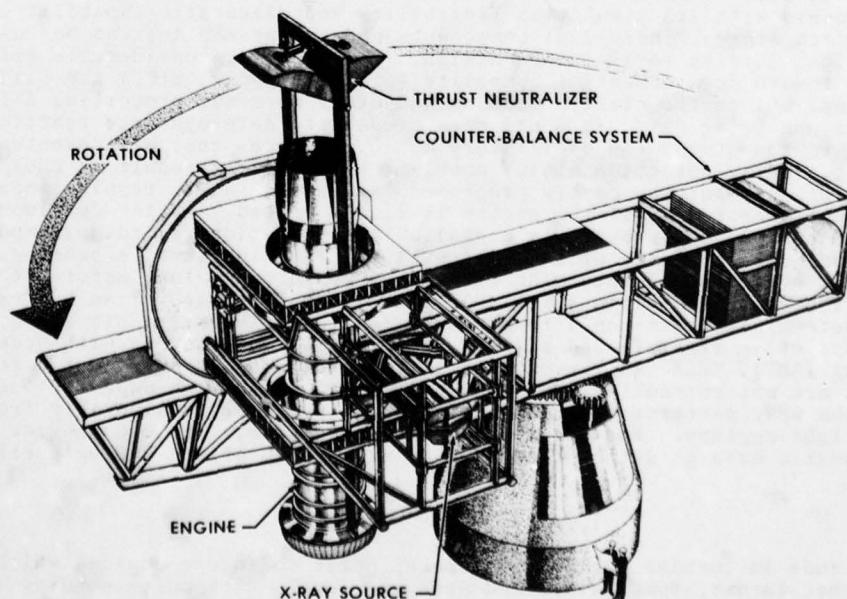


Fig. 3 - TURBINE ENGINE LOADS SIMULATOR

AD-A070 950

ADVISORY GROUP FOR AEROSPACE RESEARCH AND DEVELOPMENT--ETC F/6 21/5
STRESSES, VIBRATIONS, STRUCTURAL INTEGRATION AND ENGINE INTEGRI--ETC(U)
APR 79

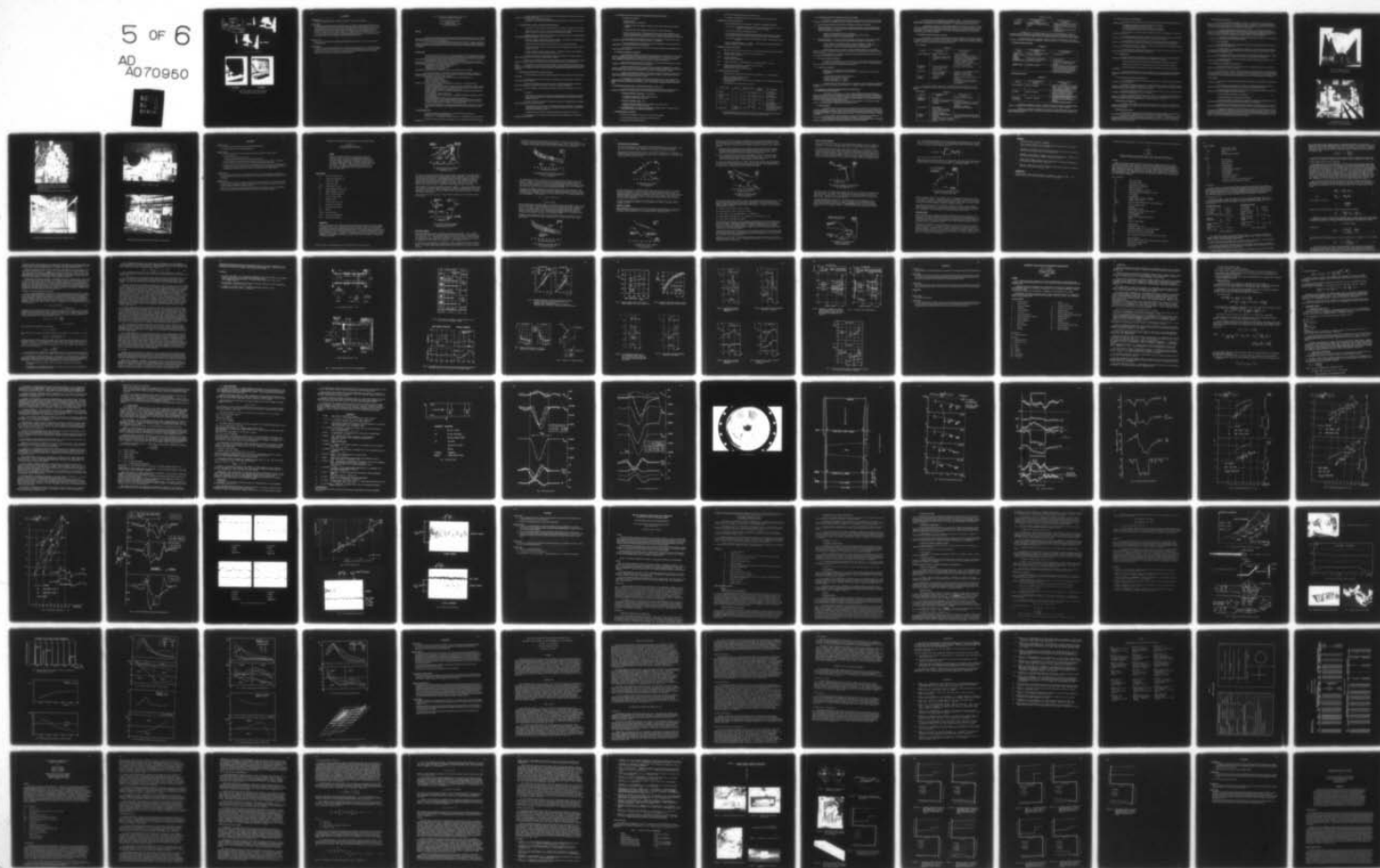
UNCLASSIFIED

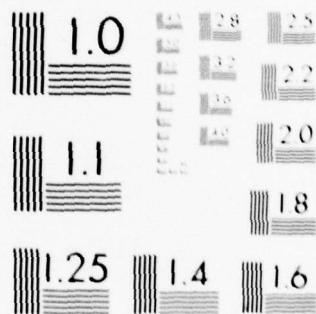
AGARD-CP-248

NL

5 OF 6

AD
A070950





MICROCOPY RESOLUTION TEST CHART
NATIONAL BUREAU OF STANDARDS-1963-A

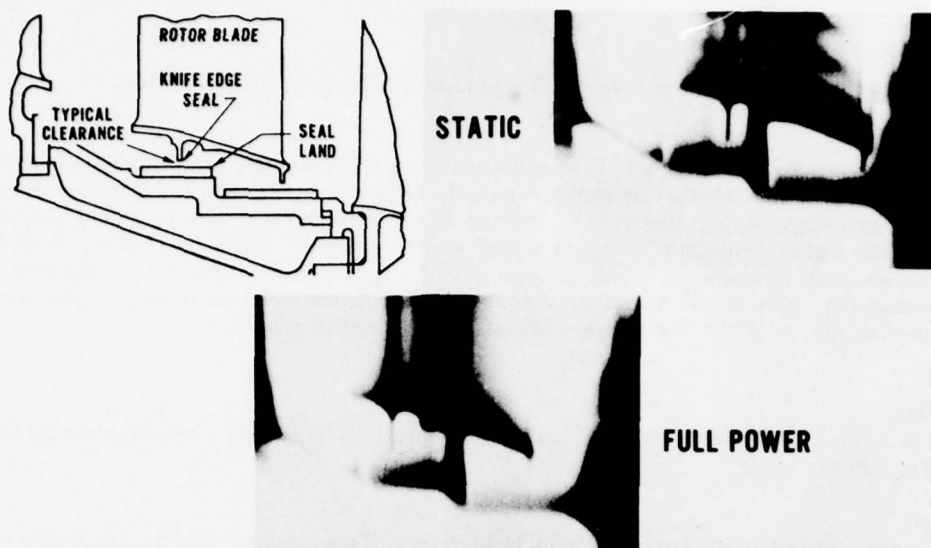


Fig. 4 - TURBINE ROTOR MOVEMENT

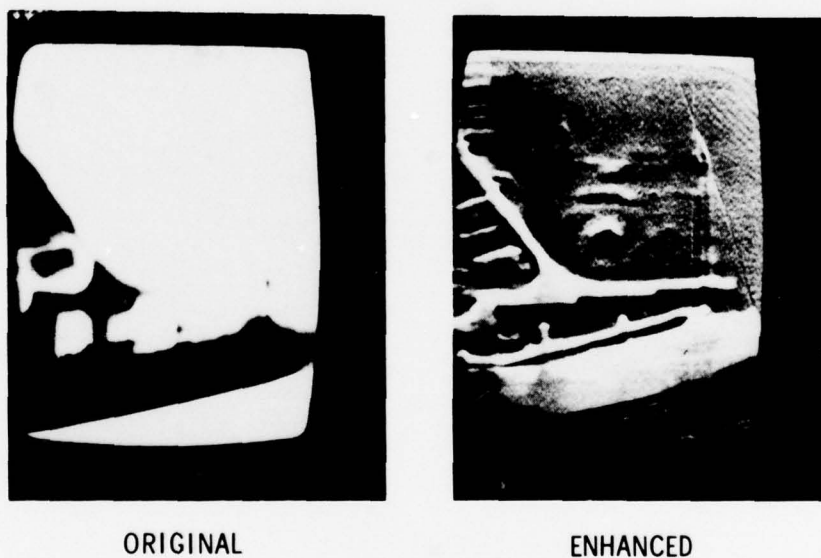


Fig. 5 - RADIOGRAPH SHOWING INTERNAL LABYRINTH SEAL ASSOCIATED WITH A MAIN BEARING OF A RUNNING AERO-TURBINE ENGINE

DISCUSSION

J.D.McDonel, US

Will there be capability for transient testing with your facility? (Transient structural loads).

Author's Reply

The engine mount will not be capable of slewing fast enough, nor will the centrifuge change rotation rate quickly enough to accurately simulate the varying turn rates and inertial loading of a transient maneuver. However, since a typical maneuver has a duration of several seconds, and the engine rotates 200–300 revolutions each second, it is highly probable that the "transient" maneuver appears to the engine to be a gradually changing steady load. Therefore, we should be able to get a fairly accurate view of a transient maneuver by performing steady state tests at various points along the maneuver trajectory. Additionally, calculations have shown that the maneuver onset rate contributes less than 5% of the overall maneuver loads for most aircraft maneuvers.

D.Hedon, France

The use of X-rays needs protective devices because the rays used are very strong. How can you cope with it in a rotating assembly?

Author's Reply

The location of the facility will greatly aid us in the protection of surrounding property. The facility will be located in a fairly remote part of our base, and we also have a lead shield behind the primary detector that will stop almost all the primary beam, and all we would have to worry about then would be scatter radiation and that has been adequately accommodated by a safety perimeter around the facility.

.../...

La réglementation actuelle assure la sécurité des vols par un ensemble de vérifications qui conduisent à envisager trois niveaux possibles selon :

- la probabilité et l'importance des ingestions ,
- la phase du vol pendant laquelle elles sont susceptibles d'intervenir et les liens avec la sécurité du vol.

1.1. Evènements pouvant entraîner la défaillance complète d'un moteur

Par principe , il s'agit d'évènements ne pouvant affecter qu'un moteur de l'avion au cours d'un même vol :

- ingestion d'oiseau lourd (4 livres) (oiseaux ne vivant pas en bandes) pendant la phase de montée ;
- autres corps étrangers lourds au régime maximum admissible par le moteur.

Ces évènements peuvent entraîner une perte de poussée complète du moteur mais ne doivent pas placer l'avion dans une situation catastrophique. Ceci exclut notamment :

- la projection latérale de débris pouvant perforer le fuselage , les réservoirs ou des éléments vitaux de l'avion. La rétention doit être assurée par les carter ,
- l'initiation de feux que les moyens de lutte installés sur l'avion ne pourraient maîtriser ,
- l'introduction d'efforts (couple ou vibrations) que la structure de supportage du moteur ne pourrait accepter sans rupture ,
- tout autre conséquence pouvant entraîner un danger : impossibilité d'arrêter le moteur défaillant , pollution massive du système de conditionnement d'air , etc.

Ces critères ne peuvent être vérifiés que par un essai en vraie grandeur sur un moteur complet. Cet essai est particulièrement onéreux à cause de la destruction de la machine.

D'autre part , les modifications que cet essai peut entraîner en cours de développement peuvent affecter des parties structurales majeures du moteur et donc avoir un impact important sur le coût du développement.

NOTA : La démonstration de rétention d'une aube de soufflante , dont les conséquences sont de nature voisine à certains cas d'ingestion , peut dans certains cas recouvrir (parce que plus sévère) le cas d'ingestion d'un oiseau lourd. Dans ce cas un seul essai sur moteur complet peut apporter la démonstration de satisfaction des deux points du règlement.

1.2. Evènements pouvant affecter tous les moteurs de l'avion

Le plus contraignant est l'ingestion simultanée d'oiseaux par tous les moteurs de l'avion dans la phase de décollage.

C'est de plus , l'un des cas les plus fréquents de collision entre avions et oiseaux , et il présente un risque majeur pour la navigabilité.

Ce risque est couvert dans les règlements par l'essai d'ingestion d'oiseaux moyens (ingestion de petits oiseaux lorsque ce cas est plus sévère) de 700 g , le moteur étant au régime de décollage.

A l'issue de l'ingestion , le fonctionnement des moteurs doit être tel qu'ils permettent le retour au sol de l'avion.

Ceci suppose :

- le retour rapide à des performances minimales acceptables dans la phase de décollage. Ces performances devront donc permettre de retrouver la poussée disponible sur l'avion après la défaillance complète d'un moteur ,

La poussée ou la puissance minimale seront donc par exemple de 75 % des performances de décollage pour un quadrimoteur ou de 50 % pour un bimoteur.

- La possibilité de manoeuvrer le moteur et de fonctionner à régime intermédiaire. Les transitoires rapides peuvent cependant être exclus , le pilote ayant pour consigne de conduire avec délicatesse les moteurs ayant subi de tels incidents.

- La capacité de fonctionner pendant un temps correspondant à la manoeuvre de retour au sol.

Les conséquences de ces exigences de fonctionnement sont très importantes pour la conception et le dimensionnement des moteurs.

1.3. Evénements pouvant demeurer ignorés de l'équipage ou d'occurrence plus fréquente

Entrent dans cette catégorie :

- l'ingestion de grêle ,
- l'ingestion de pluie avec deux aspects :
 - i) l'ingestion de pluie à forte puissance (décollage) pouvant affecter notamment les marges au pompage ,
 - ii) l'ingestion de pluie à faible puissance pouvant conduire à l'extinction des moteurs.
- l'ingestion de sable et gravier. Ce dernier point ne figure que dans certains règlements, car il concerne moins la navigabilité que la maintenabilité (l'érosion des aubages concerne en priorité les coûts d'exploitation ; la contamination des circuits est couverte par ailleurs dans les règlements).

Les conséquences fonctionnelles doivent être faibles et les dégradations éventuelles ne doivent pas entraîner de danger avant leur détection par l'utilisateur (inspection , maintenance).

Ce type d'incident établit une frontière entre les critères de navigabilité (que seuls considèrent les réglementations) et les contraintes d'économie de maintenance.

Les contraintes imposées dans ce domaine par les exploitants deviennent plus contraignantes que les exigences minimales de sécurité.

1.4. Evolution des règlements de navigabilité

Les règlements de navigabilité correspondant aux ingestions sont très récents sous leur forme actuelle. En effet , les règlements européens sont en vigueur depuis le début des années 70 et le règlement F A R depuis 1974. Les règlements applicables aux versions dérivées de moteurs déjà certifiés sont ceux qui correspondent au moteur origine (pour éviter une procédure de certification complète pour chaque version dérivée).

Aussi très peu de moteurs aujourd'hui en exploitation ont-ils satisfait rigoureusement les critères de navigabilité contenus dans les réglementations désormais applicables.

Certains organismes recommandent une augmentation de sévérité des règlements dans ce domaine. Avant une évolution dans ce sens des critères de navigabilité , il semble raisonnable d'attendre que les critères actuels aient été appliqués rigoureusement et que l'expérience en vol ait confirmé la nécessité de leur évolution.

L'application des règlements actuels sur ce plan pourrait cependant être imposée aux moteurs dérivés (sous forme de conditions spéciales) lorsque l'évolution est importante par rapport au moteur origine ou lorsque celui-ci n'a pas satisfait rigoureusement les critères actuels.

Une harmonisation des règlements actuels serait souhaitable à court terme. Elle simplifierait les échanges nombreux (certifications pour importations , certifications conjointes) entre les services officiels de navigabilité. Elle serait la démonstration d'une cohérence accrue , tous les moteurs respectant alors des critères identiques.

2. EVOLUTION DES MOYENS D'ESSAIS - PRESENTATION DU BANC TX DU C.E. Pr.

Le C.E. Pr s'est doté en 1973 d'une nouvelle installation spécialisée dans les essais d'ingestion. La conception et l'utilisation de cet équipement sont liés aux contraintes propres à ce type d'essais spéciaux :

- i) Utilisation discontinue de l'installation ; ce qui suppose :
 - la réduction au maximum des investissements immobilisés ,
 - un équipement simple et facile à entretenir.
- ii) Coût élevé du matériel en essai ; donc :
 - moyens de mesure et de diagnostic assurant le bénéfice maximum des essais ,
 - fiabilité des installations d'essai et de mesure.
- iii) Diversité des essais , ce qui nécessite des possibilités d'adaptation rapide. La définition retenue est un compromis entre ces exigences contradictoires.

2.1. Description générale et utilisation

Il s'agit d'une aire bétonnée (55 m x 25 m) avec trois zones principales :

- i) Une zone abritée pour le tir sur cibles fixes ou sur petits moteur ,
- ii) Une zone de tir sur moteurs en plein air

.../...

iii) Une cabine de contrôle commune aux deux zones d'essai.

Les servitudes sont distribuées à partir de la cabine de contrôle aux deux aires d'essai.

a) Utilisation de l'aire de tir sur cible fixe

Il s'agit essentiellement d'essais d'évaluation de composants et d'éléments d'hélicoptères :

- Tirs sur plaques : évaluation des capacités de rétention de matériaux pour carters, des caractéristiques de fragmentation de matériaux pour aubages.
- Tirs de morceaux de disques sur éléments de carters.
- Tirs sur aubages fixes. Bien que non totalement représentatifs (absence de champ centrifuge), ils permettent à coût réduit une première évaluation des aubages (étude de la fragmentation).
- Tirs sur grilles : principalement entrées d'air d'hélicoptères (grêlons, oiseaux moyens, oiseaux lourds).
- Tirs sur éléments d'hélicoptères : verrières, bord d'attaque de rotors et autres éléments sensibles, surtout pour la résistance à la grêle.

b) Utilisation de l'aire de tir sur moteurs

Cette zone d'essai a été mise en service en 1974. Y ont été notamment effectués les essais suivants :

- 1975 : - Oiseaux moyens (évaluation, deux tirs de deux oiseaux de 700 g).
- Barreaux de glace (évaluation).
- 1976 : - Grêlons (certification)
- Oiseaux moyens (certification)
- 1977 : - Grêlons (certification) : 25 grêlons \varnothing 25mm et 25 grêlons \varnothing 50mm en une volée.
- 1978 : - Oiseaux moyens (certification) : 7 oiseaux de 700 g en une rafale.
- Rétention d'une aube Fan (certification)
- Oiseau lourd (deux tirs d'un oiseau de 1800 g).

2.2. Caractéristiques des canons utilisés

Les canons sont tous réalisés selon le même principe, particulièrement économique et fiable.

- Tube acier standard sans usinage spécial.
- Culasse à raccordement rapide.
- Réservoir d'air comprimé avec obturateur souple déchiré pour le tir par l'éclatement d'un détonateur pyrotechnique.

Leurs principales caractéristiques sont les suivantes :

Type de canon	Longueur	Diamètre	Vitesse	Masse projectile	Mode de propulsion
Grêlons	7 m	25 mm	30 à 300 m/s	20 à 40 g	Air comprimé bourre polystyrène
Grêlons ou petits oiseaux	7 m	50 mm	30 à 300 m/s	60 à 120 g	Air comprimé bourre polystyrène
Barreau de glace	1,5 m	rainure	< 40 m/s	< 800 g	Air comprimé
Oiseau moyen	7 m	100 mm	15 à 200 m/s	700 g	Air comprimé bourre polystyrène avec système d'arrêt.
Oiseau lourd *	12 m (modulaire 6 x 2 m)	170 mm	30 à 400 m/s	2000 g	Air comprimé - conteneur acier et polystyrène avec dispositif d'arrêt.

* Les performances de ce canon permettent des vitesses de tir simulant la vitesse relative entre les objets ingérés et les aubages eux-mêmes, pour des projectiles jusqu'à 2000 g.

2.3. Caractéristiques générales de l'installation de mesure et de contrôle

Seuls sont fixes certains équipements spécifiques à la conduite des tirs. Les instruments de mesure et d'analyse sont modulaires et amovibles pour faciliter l'adaptabilité et diminuer le coût des matériels immobilisés.

- a) Mesures classiques Capacité de 250 mesures avec acquisition et traitement par ordinateur.
- b) Équipement d'ingestion - Commande des servitudes (éclairage haute intensité, systèmes photographiques, séquençement des canons) par un programmeur équipé d'un système d'interdiction de tir dans le cas de conditions défavorables, par exemple :
 - paramètres de fonctionnement du moteur hors objectif,
 - défaillance des systèmes de mesure, d'enregistrement ou de prises de vues,
 - interdiction commandée par le responsable d'essai.

- c) Mesures en transitoire. C'est un des éléments de diagnostic importants pour ce type d'essais. L'analyse des paramètres est fait à une cadence qui dépend des événements se produisant en cours d'essai :

- cadence (100 Hz) pour les phénomènes brutaux (transitoire d'ingestion, pompage, etc...),
- cadence moyenne (10 Hz) pour les transitoires normaux (accélérations, coupure, etc...),
- cadence lente (0,1 Hz) pour l'évolution des paramètres en endurance après tir.

L'acquisition des paramètres (jusqu'à 50) est faite sur bandes magnétiques avec code horaire commun. Ces mesures sont extraites en temps différé par un ordinateur à une cadence choisie en fonction des phénomènes à analyser.

Par cette technique, des paramètres calculés et des mesures individuelles peuvent être obtenus avec une cadence d'échantillonnage choisie à posteriori.

- d) Mesures de contraintes et vibrations

Ces mesures sont essentielles pour l'analyse de l'essai et de la mécanique des ruptures éventuelles.

La capacité de mesure est de 150 voies, par unités modulaires de 10 voies. La quantité de matériel installé est adaptée en fonction des besoins spécifiques de chaque essai.

- e) Équipement de visualisation

- i) Vidéo 5 voies avec enregistrement sur magnétoscopes.
- ii) Photographie. Un éclairage haute intensité (puissance 45 kW) permet la prise de vues rapides pendant les tirs :
 - 3 caméras très haute vitesse (5000 à 8000 images/s)
 - 5 caméras rapides (300 à 1000 images/s)
 - 2 caméras " temps réel " (64 images/s)
 - 2 appareils photographiques (5 images/s)

Ces équipements permettent de visionner les tirs et d'analyser l'ordre et le mécanisme des différentes dégradations, la nature et le développement des feux éventuels, la rupture d'accessoires ou d'éléments d'habillage, les fuites, etc....

3. ÉVOLUTION DE LA CONCEPTION DES MOTEURS POUR L'AMÉLIORATION DU COMPORTEMENT AUX INGESTIONS

L'amélioration du comportement d'un moteur aux ingestions peut être extrêmement difficile si sa conception initiale ne s'y prête pas. La satisfaction des critères (réglementaires et opérationnels) de résistance aux impacts de corps étrangers ne peut donc pas être une simple vérification effectuée sur un matériel conçu uniquement pour les performances. Elle doit être au contraire le résultat d'une approche globale à tous les stades de l'élaboration d'un projet, pouvant influencer des options fondamentales.

Nous voudrions ici dégager les lignes générales d'une telle approche, sur le plan de la conception d'abord, des principes de gestion du programme de développement ensuite.

3.1. Conception générale

La réduction du bruit émis par les réacteurs fait depuis plusieurs années partie des objectifs de base de l'architecture générale des moteurs. Considérées comme prioritaires, les options correspondant à la lutte contre le bruit ont été appliquées extensivement même si elles n'étaient pas souhaitées par les aérodynamiciens (espacement entre soufflante et redresseur, choix du nombre d'aubes par exemple) ou si elles influent sur le poids (revêtements acoustiques...).

Les moyens d'études et de recherches mis en oeuvre pour cette réduction sont considérables et il est exclu qu'une option soit examinée avec intérêt si elle apporte une pénalité sur le plan du bruit émis.

Une telle attitude n'a pas encore été adoptée pour la résistance aux ingestions et pourrait probablement conduire à des progrès considérables, influant de façon sensible sur les coûts d'exploitation. .../...

Sur les moteurs double flux à grand taux de dilution par exemple, la soufflante peut jouer pour le coeur du moteur le rôle de système d'auto-protection (centrifugation - division). Pour que ce rôle soit efficace, la position relative des éléments doit être adaptée en conséquence, et il s'agit d'options d'architecture de base.

L'exploration de principes de conception générale augmentant la résistance aux ingestions et limitant les coûts de réparation pourrait correspondre à une évolution de l'équilibre coût - performance - poids. Les exploitants seraient peut être les premiers à accepter des performances moins brillantes s'ils trouvaient des avantages correspondant sur les coûts de maintenance et sur la sécurité. Les méthodes d'analyse de la valeur pourraient trouver là un champ d'application privilégié.

3.2. Principaux éléments concernés par les ingestions

Nous tenons ici, l'exemple de moteurs double flux à taux de dilution élevé et n'avons pas l'ambition de proposer pour chacun des éléments concernés des solutions permettant de résoudre tous les problèmes d'intégrité. Cet examen a surtout pour but de souligner le nombre des parties critiques et l'importance d'une approche globale dans laquelle la résistance aux ingestions est une préoccupation permanente.

a) Veine secondaire

TABLEAU I

Éléments	Nature des défauts liés aux ingestions	Nature de l'action à la conception
Aubes de soufflante	Rupture - Comportement en flexion. Fragmentation (cisaillement). Propagation des défauts (vibrations).	Vitesse périphérique. Dessin des nageoires inter-aubes ou des talons (une possibilité de chevauchement évite une trop grande rigidité locale et permet l'absorption d'énergie. Matériau - épaisseur du profil. Absence de flutter - fréquences propres avec et sans chevauchement.
Abradable de soufflante.	Contact ou interaction avec le carter dans les cas de balourd maximal.	Épaisseur - Choix du matériau.
Cône de nez.	Givrage - Accumulation de glace ingérée ensuite. Rupture sous impact.	Dégivrage - Forme permettant la centrifugation précoce de la glace. Épaisseur - Choix du matériau.
Carter de soufflante.	Perforations Vibrations.	Matériau à grand allongement à rupture - Épaisseurs. Modes vibratoires ne devant pas être excités par les contacts des aubages sur les abrasables.

Pour la veine secondaire (tableau I) la zone critique pour l'ingestion d'oiseaux est la partie périphérique de la soufflante à cause de la faible épaisseur relative des profils et de l'importance des vitesses relatives.

b) Veine primaire

TABLEAU II

Éléments	Nature des défauts liés aux ingestions	Nature de l'action à la conception
Carters Compresseurs	Perforation.	Épaisseur au droit des aubages
Abradables	Feu Titane par contact titane/titane Combustion ou explosion des abrasables.	Cloison anti-feu Profondeurs compatibles avec le balourd maximal et les excursions longitudinales maximales. Matériau non combustible.
Aubes mobiles	Fragmentation Nota : La fragmentation est un facteur majeur de dégradations secondaires en aval. Contact avec redresseurs.	Épaisseur du profil - Matériau.
Marges au pompage.	Érosion des abrasables chute de rendement. Dégradation des marges au pompage. Marges au pompage lors d'ingestion de pluie.	Marge au pompage suffisante pour tolérer les érosions maximales et les dégradations de profils.

TABLEAU II (suite)

Eléments	Nature des défauts liés aux ingestions	Nature de l'action à la conception
Chambre de combustion	Perforation ou rupture de la tête. Extinction lors d'ingestion de pluie au ralenti.	Epaisseur et forme des parois (l'effet des ingestions diminue avec le taux de pression et le nombre d'étages de compression). Marges de fonctionnement au ralenti et en décélération.

La dégradation de la veine primaire (tableau II) est une des causes principales de la baisse de performances ou de l'impossibilité de fonctionnement après ingestion. De plus des défauts de faible ampleur peuvent entraîner des dégâts secondaires considérables affectant le fonctionnement ultérieur et grévant les coûts de réparation.

La veine primaire est donc un des points essentiels d'action pour l'amélioration de la résistance aux ingestions ; la prévention des ingestions (centrifugation , division des masses , etc. . .) est une des clefs de cette action .

c) Ensembles tournants et structures

TABLEAU III

Eléments	Nature des défauts liés aux ingestions	Nature de l'action à la conception
Liaisons d'ensembles tournants Arbres.	Vrillages - Cisaillement des liaisons lors de chocs en rotation.	Dimensionnement
Réducteur (éventuel)	Cisaillement des dents de pignons	Dimensionnement
Supports de paliers	Excentricité avec balourd	Ajustement de la souplesse de la structure interne. Choix des fréquences propres.
Supports moteur	Déformation - rupture	Dimensionnement pour balourd maximal. Etude du comportement dynamique dans la gamme des fréquences d'excitation. Dimensionnement au couple de décélération maximale (cas du blocage).

d) Habillage et équipements

TABLEAU IV

Eléments	Nature des défauts liés aux ingestions	Nature de l'action à la conception
Tous accessoires	Rupture de supportage	Résistance à des niveaux vibratoires très élevés , qualité du freinage des liaisons. Absence de mode vibratoire dans la gamme des fréquences d'excitation.
Tuyautages	Rupture en vibrations	Absence de modes vibratoires dans la gamme des fréquences d'excitation. Utilisation de tuyauteries souples. Dispositifs absorbant l'énergie vibratoire.
Boîte support d'accessoires.	Ruptures de supportage	Dimensionnement des supportages. Possibilité de déplacements relatifs des éléments. Dispositifs d'absorption d'énergie.

La défaillance d'accessoires (tableau IV) apparemment mineurs peut conduire à des pannes majeures (défaillance de régulation ou de lubrification par exemple) ou causer des fuites et des risques d'incendies.

Equipements , accessoires et tuyautages doivent donc dès leur définition initiale faire l'objet d'un souci du détail suffisant pour qu'une pièce mineure de supportage ou de cheminement malheureux ne vienne pas affecter les résultats obtenus par ailleurs.

.../...

3.3. Gestion du programme de développement

Si les essais de certification d'un moteur nouveau ont lieu lorsque le programme de développement est extrêmement avancé :

- la conception et l'architecture générales sont figées depuis longtemps ,
- la définition de détail du type de moteur est fixée ,
- le constructeur recherche une certification aussi rapide que possible ,
- toute modification peut remettre en cause les résultats d'autres essais.

Dans ces conditions , si le moteur essayé ne satisfait pas les critères réglementaires , les difficultés peuvent être considérables :

- les modifications touchant des pièces majeures du moteur sont évitées au maximum car elles risquent de causer au programme de développement des coûts et des délais supplémentaires excessifs.

- la satisfaction des critères de navigabilité est alors recherchée dans un contexte étroit influant au minimum sur le coût du programme et si possible ne remettant pas en cause d'autres étapes de la certification.

Cette approche rend quasiment impossibles les améliorations qui perturbent le déroulement du programme et elle limite par là même les possibilités de progrès.

Une approche globale et cohérente pendant toute la durée d'un programme est donc nécessaire à l'obtention de résultats quant à l'amélioration de la résistance aux ingestions.

3.3.1. Etudes d'amont

Bien que ne faisant pas partie du programme de développement lui-même , elles sont indispensables et conditionnent le résultat. Parmi celles qui nous semblent les plus importantes , nous citerons :

- l'étude des critères d'architecture générale permettant d'accroître la résistance aux ingestions ,
- l'étude des matériaux pouvant être envisagés dans le futur pour leur influence sur l'intégrité ,
- l'étude des conceptions ou des dispositifs susceptibles de protéger les moteurs ou leurs parties les plus sensibles.

Ces études d'amont devraient être poursuivies suffisamment loin (essai au banc partiel d'ingestion ou même essai sur démonstrateur) pour donner un ensemble de solutions directement exploitables dans tous les avant - projets.

3.3.2. Phase initiale du programme de développement

C'est la période pendant laquelle les actions pour l'amélioration de la résistance aux ingestions pourront être menées avec le plus d'efficacité.

Cette période est la partie du programme de développement pendant laquelle des modifications majeures (définition de pièces critiques , définition de structures) ne touchant pas à la conception générale du moteur peuvent être introduites sans influencer de façon notable sur la durée globale et le coût.

Le principe essentiel est l'obtention des assurances techniques concernant le futur respect des critères de résistance aux ingestions dès que possible au cours du programme.

En effet , le coût et l'augmentation de masse dus à l'introduction de modifications ~~sont~~ croissants au fur et à mesure de l'avancement du programme. Quasi-nuls sur la planche à dessin , ils deviennent considérables lorsque les étapes de certifications sont entamées et augmentent encore lorsque le matériel est en service.

a) Essais partiels sur aubages fixes

Ces essais ne sont pas entièrement représentatifs (absence de champ centrifuge). Cependant ils ont l'avantage d'être peu coûteux , très rapides à mettre en oeuvre et de permettre ainsi une première évaluation (surtout au plan de la fragmentation) .

b) Essais d'évaluation en fosse

Les tirs sur rotor complet ou partiel en fosse complètent les résultats précédents. Ils permettent d'évaluer une définition initiale ou des modifications avant même qu'elles aient pu être essayées sur moteur.

Intervenant très tôt dans le programme de développement , ces essais vont donner une partie des garanties techniques nécessaires au déroulement sans risques du programme de certification. Les modifications qui apparaîtront pourront être étudiées et évaluées avec un délai suffisant pour permettre de les optimiser et de limiter leur impact sur la masse et les performances.

.../...

c) Evaluation sur moteur complet

Les essais en fosse permettent d'étudier et d'évaluer les améliorations de composants (premiers étages de rotor) mais ne simulent pas tous les phénomènes possibles lors d'ingestions , ce que seuls des essais sur moteur complet peuvent faire. Là encore , les essais officiels vérifiant les critères de navigabilité interviennent très tard dans le programme et font courir un risque important à son déroulement.

Ce risque est considérablement réduit si des essais d'évaluation ont pu avoir lieu suffisamment à l'avance. Ces essais auront permis de vérifier la représentativité des essais en fosse , d'étudier le comportement des parties qui ne peuvent être évaluées au banc partiel , de mettre en évidence les éventuels problèmes d'intégration , les dommages secondaires et de voir le comportement des accessoires dans des conditions représentatives.

Ces acquisitions sont inestimables pour la sécurité qu'elles procurent ensuite lors de la fin du programme. Leur prix est celui d'un des premiers prototypes disponibles.

3.3.3. Essais de certification

Si les étapes précédentes ont été menées à bien , les essais de certification devraient avoir surtout un caractère de vérification ou de démonstration.

En réalité , détenir une certitude absolue sur le résultat de ce type d'essais est extrêmement difficile et des dispersions assez importantes (dues essentiellement aux dommages secondaires ou aux accessoires) peuvent être rencontrées entre deux essais voisins.

Aussi les essais d'ingestion pour la certification doivent être effectués aussitôt que possible. Le risque qu'ils comportent en sera atténué et les modifications intervenant à la fin du programme seront évitées.

Les économies réalisées alors doivent compenser largement l'effort nécessaire pendant la première partie du programme de développement.

3.4. Conclusions sur la conception et le développement

Une approche systématique des moyens de réduction de la sensibilité des réacteurs aux ingestions suppose une attitude adaptée de la part des constructeurs.

Cette attitude conduit à accorder une place privilégiée aux objectifs d'intégrité dans les études d'amont et dans la conduite des programmes. Cependant , cette attitude n'est pas seulement une source de coûts supplémentaires ; elle apporte une réduction importante des risques technologiques en cours de développement et peut constituer un argument commercial , les exploitants étant particulièrement sensibilisés par les coûts de maintenance et de réparation.

4. CONCLUSIONS

L'amélioration de la résistance des turbomachines aux ingestions est un des facteurs de l'augmentation de la sécurité des vols.

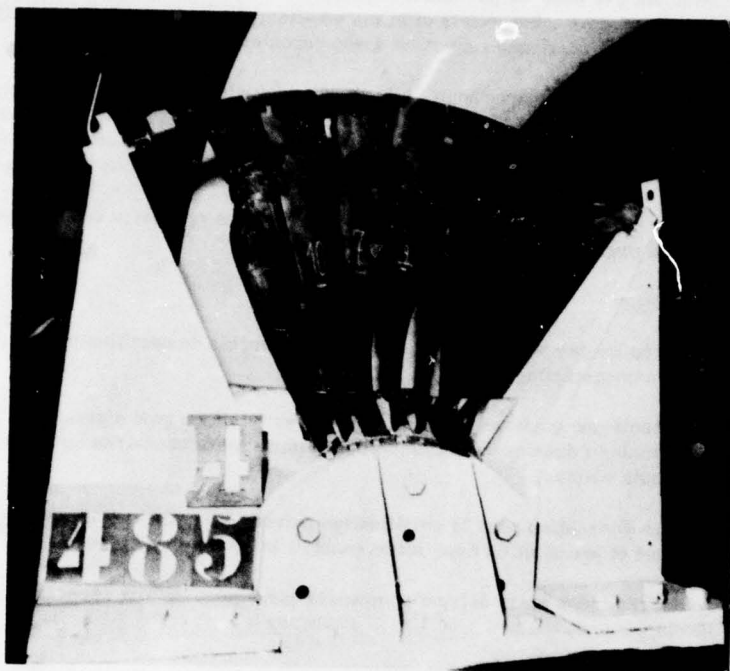
Les motoristes ont accru leurs efforts dans ce domaine et ils disposent des moyens d'évaluation et d'essais nécessaires. Les directions préférentielles de la poursuite de ces efforts nous semblent être :

- l'étude des conceptions d'architecture générale diminuant la sensibilité aux ingestions, notamment en prévenant l'entrée des corps étrangers dans le générateur de gaz ,
- le souci du détail pour l'habillage et les accessoires ,
- une gestion appropriée des programmes de développement.

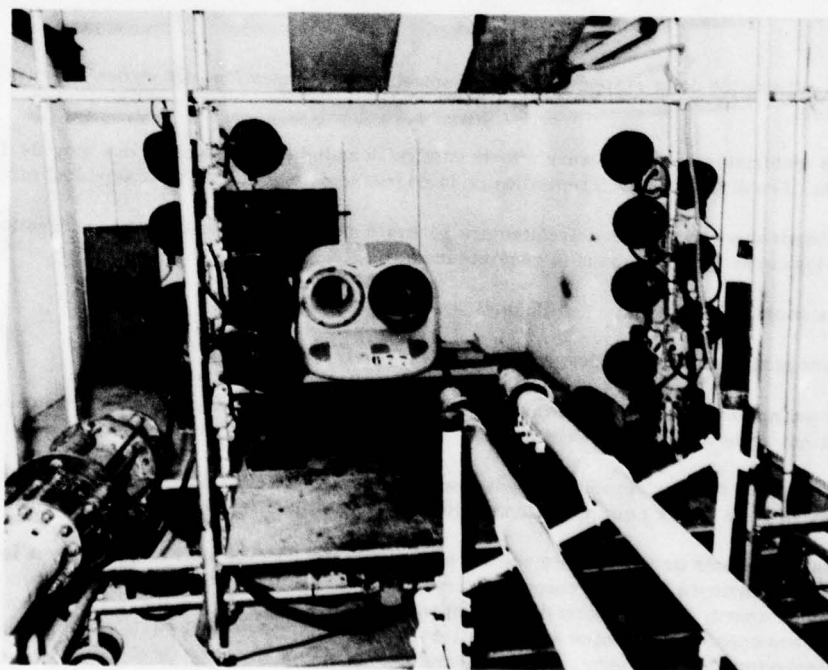
La poursuite de cet effort est imposée par les contraintes des règlements de navigabilité et par la pression des exploitants qui recherchent une réduction des coûts de réparation et de maintenance.

Une gestion de développement tenant compte de ces contraintes doit permettre de réduire le risque (en coûts de développement et en délais) que représentent les épreuves officielles et fournir un argument commercial utile.

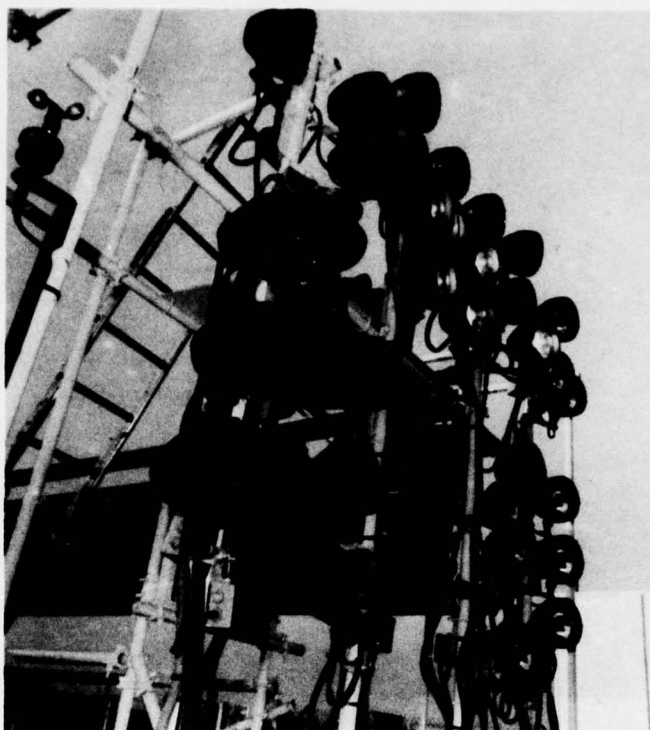
Les règlements de navigabilité actuels sont suffisamment exigeants et précis pour imposer une attitude de ce type chez les constructeurs. Ils sont encore trop récents pour que les moteurs en service commercial aujourd'hui les satisfassent complètement. Une évolution des règlements ne semble donc pas indispensable à court terme, et il sera possible de juger de son opportunité lorsque seront en service des moteurs ayant subi de façon rigoureuse les épreuves prévues. Une harmonisation des règlements serait cependant souhaitable.



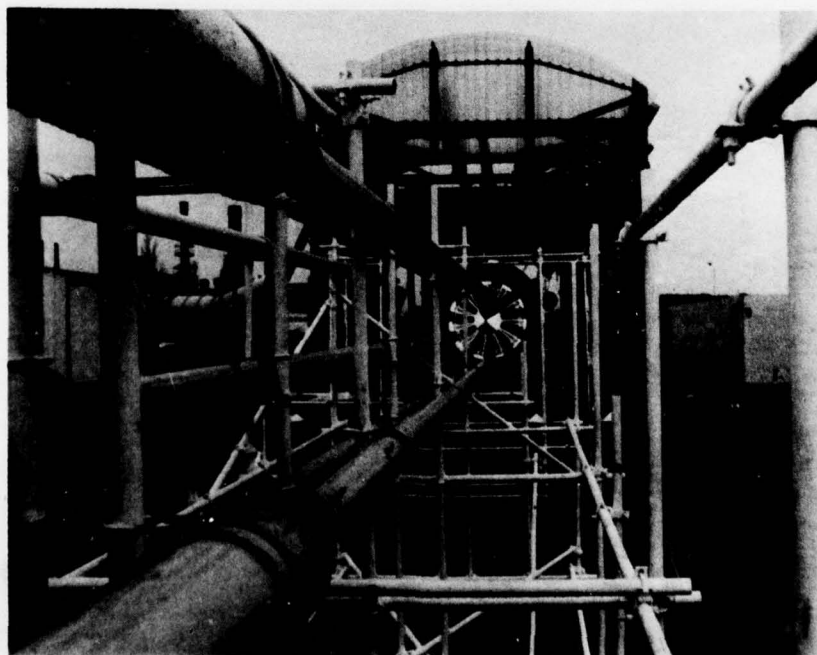
MONTAGE D'ESSAIS POUR TIR
SUR SECTEUR D'AUBAGE FIXE



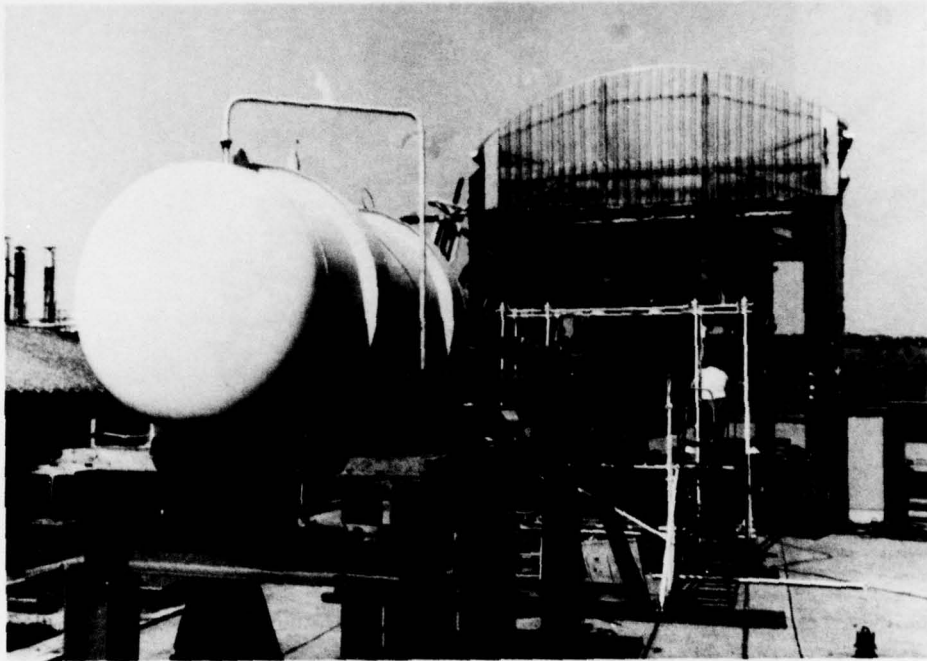
TIR D'OISEAUX MOYENS (700 g)
SUR ENTREE D'AIR D'HELICOPTERE



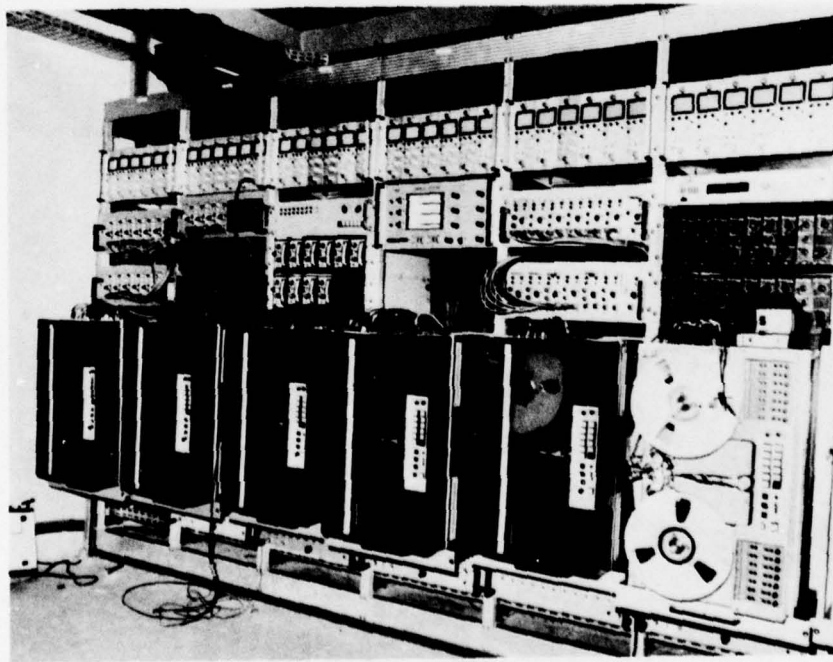
. BATTERIE DE 26 CANONS A GRELE POUR TIR DE 25
GRELONS DE DIAMETRE 25mm ET 25 GRELONS DE
DIAMETRE 50mm.
. ECLAIRAGE HAUTE INTENSITE ET CAMERAS RAPIDES



BATTERIE DE 7 CANONS POUR TIR EN RAFALE D'OISEAUX MOYENS



CANON A OISEAU LOURD



UNITES MODULAIRES DE MESURES DE VIBRATIONS ET CONTRAINTES

DISCUSSION

G.J. Brown, Canada

- (1) Could you describe the birds used in these tests, their specific density?
- (2) Could you describe the blade failure triggering method.

Reponse d'Auteur

- (1) Les oiseaux utilisés sont des poulets d'élevage conservés dans un congélateur et dégelés avant tir.

Ce choix a été dicté par:

- la recherche d'une standardisation des essais,
- la simplicité d'un approvisionnement de projectiles de masse calibrée.

Des essais comparatifs avec des oiseaux sauvages (goelands, corbeaux) effectués sur cible fixe et en fosse sur rotor ont montré que les caractéristiques de choc initial étaient identiques à masse égale.

- (2) Le largage d'aube est effectué par l'éclatement d'un détonateur placé dans la racine de l'aube (un meulage crée un affaiblissement initial de la racine). Le détonateur est alimenté par un condensateur par l'intermédiaire d'un transformateur permettant le passage entre la structure fixe du moteur et le rotor basse pression.

J. Colpin, Belgium

Est-ce que vous pourriez nous donner votre opinion sur l'influence des nageoires de soufflante sur la rupture des aubes notamment la position radiale, la localisation radiale de ces nageoires sur la susceptibilité à la rupture des aubes de soufflante?

Reponse d'Auteur

L'absence de nageoires permet une déformation importante des bords d'attaque d'aube. La présence des nageoires ou de talon d'aube au voisinage de ces nageoires ou des ces talons cause une rigidité plus importante qui ne permet pas des déformation importantes de laubage sans déchirure.

Donc, la présence de nageoires trop rigides augmente les problèmes de fragmentation, et donc il y a un équilibre à trouver dans les possibilités de formation des bords d'attaque de l'aube au voisinage des nageoires.

THE EFFECT OF INTAKE CONDITIONS ON SUPERSONIC FLUTTER IN TURBOFAN ENGINES

by

D.G. Halliwell

Head of Aeroelastic Research
Rolls-Royce Limited, Aero DivisionSUMMARY

The nature of supersonic flutter, to which high tip speed, front stage fans of modern aircraft turbofan engines are susceptible, is introduced briefly. The effect of varying engine intake conditions of altitude, flight speed and ambient temperature are examined and test data is compared with theory. Some important flight conditions for minimum flutter margins in typical civil and military applications are outlined. The effect of engine intake type is then covered with respect to the degree of pressure distortion presented to the fan. A tentative relationship is derived between this distortion and flutter onset speed.

LIST OF SYMBOLS

N_1	fan rotational speed, rpm
T	intake total temperature, $^{\circ}\text{K}$
θ	T relative to 288°K
M	flight mach number
$m\sqrt{T/P}$	intake massflow function
ρ_s	intake stagnation density, lb/ft^3
δ	damping logarithmic decrement
K'	1000 ft altitude above S.L.
H	fraction of blade height
D	diametral node no.
P	total pressure at fan face
A	annulus area at fan face
D_A	area distortion parameter
$T.O.$	take-off
$S.L.(S.)$	sea level (static)
$T.E.T.$	turbine entry temperature
$KIAS$	knots indicated airspeed

1. INTRODUCTION

The basic characteristics of supersonic unstalled flutter have been examined in a number of papers on the subject [e.g. 1, 2]¹. Front stage fans of modern turbofan engines with part-span shrouds or clappers are particularly susceptible to this type of instability, because of their high tip speed, high aspect ratio, relatively lightweight blading, and the enhanced degree of coupling between blade flap and torsion modes provided by the shroud ring. The performance characteristics of such a fan stage are shown in Fig.1. The supersonic flutter regime has a steep stress gradient, sensitive to speed and pressure ratio as illustrated. Its margin above the fan's design speed is of crucial importance, and both empirical correlations and unsteady work theoretical models are normally used to determine this margin.

¹
Footnote: Figures in square parentheses refer to references at the end of the paper.

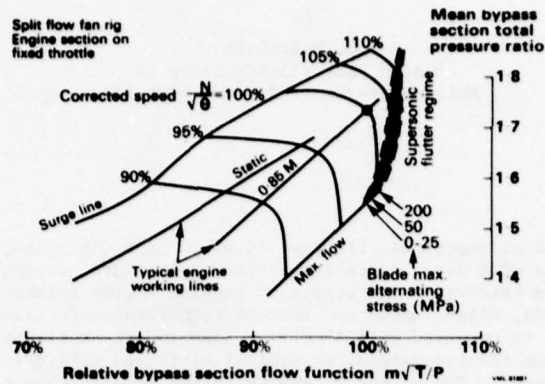


Fig.1 Model Fan Characteristics Showing Stress Boundaries of Unstalled Supersonic Flutter

The result of a typical theoretical analysis is shown in Fig.2, for an unstalled high speed condition on a shrouded fan assembly, using current unsteady aerodynamics theory [3]. The various nodal diameter vibration patterns of the assembly potentially can be excited in forward or backward rotating waves relative to the rotor. The Aerodynamic Damping logarithmic decrement of each mode is plotted against the vibration Wave Speed relative to the rotor. It is seen generally that the forward wave has the minimum damping and therefore is the least stable and that, in particular, flutter is most likely to occur in a 4 diameter mode rotating at about twice rotor speed. The backward wave, on the other hand, is stable and is near-stationary relative to the casing.

Such a prediction as the above is governed by many input parameters. Some can be optimised, within other constraints, during the design of the fan itself. Others, such as the intake conditions, are determined by both the type of engine installation and the aircraft operating envelope. This paper examines some of the factors in this second category using, where possible, test data to illustrate the related flutter behaviour.

Unless otherwise specified, the type of flutter referred to throughout is of the unstalled, supersonic variety.

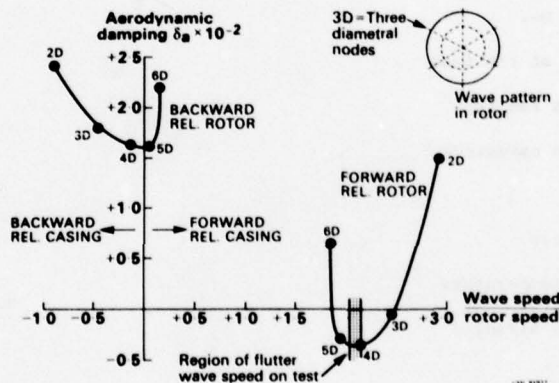


Fig.2 Variation of Aerodynamic Damping and Flutter Wave Speed with Mode Number (Second Family Modes)

2. EFFECT OF AIR DENSITY

Aerodynamic Damping ($\log. dec. \delta_a$) is directly proportional to air density. Thus, for flutter onset, when δ_a is negative for a particular mode, we would expect the effect of reducing density to be favourable; i.e. at high altitude one would have to run the fan faster to reach flutter than on a sea level test bed. In addition, the gradient of stress-increase with speed when flutter has been reached will be more gradual at the lower density. These points should hold whether density is changed either by forward speed or by altitude, or by some combination of both.

On the face of it, this means that it is important to check out a demonstrator engine or development fan rig at the highest intake density condition likely to be encountered by the service derivative engine. In fact, this depends upon the particular aircraft operation to be fulfilled as Section 4 will show.

A collection of test points are plotted in Fig.3 in terms of fan corrected speed ($N_1/\sqrt{\theta}$) at flutter onset against the intake stagnation air density (ρ_s). Flutter has been defined at a low stress level, about 30 MPa, on or near the blade maximum stress position. More than one fan type is included in the correlation which justifies the way in which it is used subsequently.

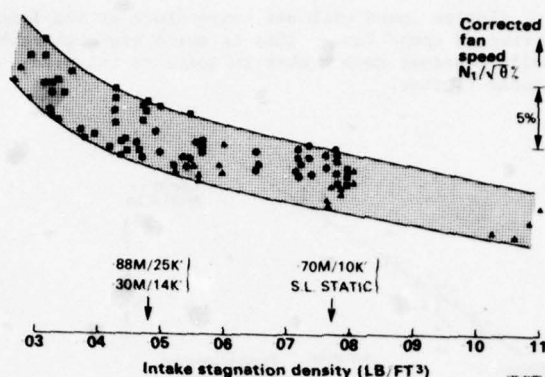


Fig.3 Effect of Intake Air Density on Supersonic Flutter Onset - Accumulated Test Data for ~30 MPa Stress

The expected effect of density is verified, but at the low density end the effect is more marked than at high density. This is partly due to the more favourable stress gradient referred to earlier. Density values for two different pairs of flight conditions are marked on Fig.3, each pair having a different combination of altitude and flight Mach Number for the same density. Points are included in the correlation for all these conditions showing that, within the data bandwidth, the density effect holds for both altitude and flight speed variation.

Returning to the theoretical prediction of Fig.2, the value of δ_a at flutter onset will be equal in magnitude to the logarithmic decrement of Mechanical Damping (δ_m) in the fan assembly. δ_m is a difficult quantity to determine, but its value will be reasonably independent of air density and also of fan speed within the restricted high speed range we shall consider. δ_a , however, depends upon both these parameters. Thus, we have,

$$\begin{aligned}\delta_a &= -\delta_m \text{ at flutter onset} \\ &\propto \rho_s \\ &= \text{function } (N_1/\sqrt{\theta})\end{aligned}$$

Knowing the theoretical relationship between δ_a and $N_1/\sqrt{\theta}$ at constant density [e.g. Figs.12 of 1,2] we can construct curves of constant damping on the corrected speed/density diagram, to compare with the test data of Fig.3. This has been done in Fig.4, for a suitable range of δ_m . The shape of these curves is broadly similar to that of the test data with the slope increasing towards low density. A mechanical damping of about .008 gives general agreement with the test data over a reasonable density range, and is close to values which have been measured for the appropriate modes in laboratory and spinning pit testing, e.g. from the work of [4].

Improvements in total damping measurement at varying air density and in the prediction accuracy of aerodynamic damping should permit a more thorough comparison to be made along the lines of Fig.4 in the future.

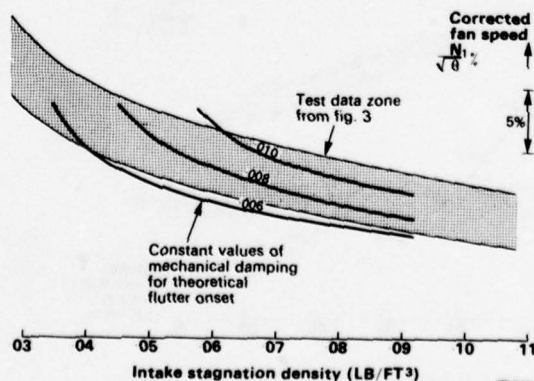


Fig.4 Comparison of Theoretical Prediction of Flutter Onset with Test Data for Varying Air Density

3. EFFECT OF INTAKE AIR TEMPERATURE

The curve of corrected flutter onset speed with density established in Fig.2 is not unique. It does not hold for large changes of air temperature at an otherwise constant operating condition. In fact, the spread of data in Fig.2 is partially due to ambient air temperature variation.

Fig.5 shows the variation of flutter speed with air temperature at sea level. The data obeys approximately a constant corrected speed law. This is quite reasonable when it is remembered that constant $N_1/\sqrt{\theta}$ gives virtually constant Mach Number relative to the blade, which is one of the major parameters governing supersonic flutter.

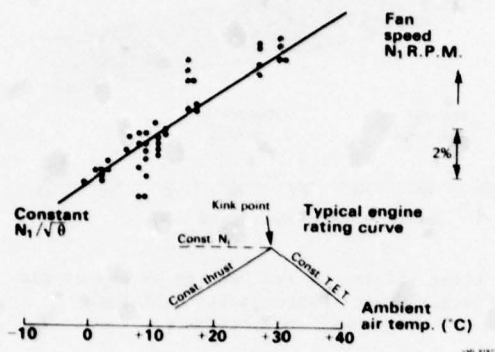


Fig.5 Typical Variation of Flutter Onset Speed with Ambient Air Temperature

The above relationship is very important when the engine thrust curve or rating curve is compared with the flutter boundary. Fig.5 shows a typical flat-rated engine thrust curve. Below the 'kink-point' temperature the thrust is constant, which approximates to constant $N_1/\sqrt{\theta}$ for the fan. Above the kink-point, the turbine entry temperature (T.E.T.) is constant, causing a marked reduction of $N_1/\sqrt{\theta}$ as ambient temperature increases. Thus, for this type of engine, it is sufficient to examine the kink-point condition, as this will establish the minimum flutter margin at any particular altitude and flight speed.

It should be noted that for an engine which does not have a 'flat-rated' thrust curve, it may be necessary to introduce an N_1 limiter or even an $N_1/\sqrt{\theta}$ limiter if there is a potential flutter problem on cold days.

4. OPERATION OF AIRCRAFT

Having established the variation of the fan's flutter boundary with density and that (with certain provisos) the ambient temperature effect can be satisfied by taking the kink-point condition, we can examine the off-design operation of a derivative engine in a typical aircraft.

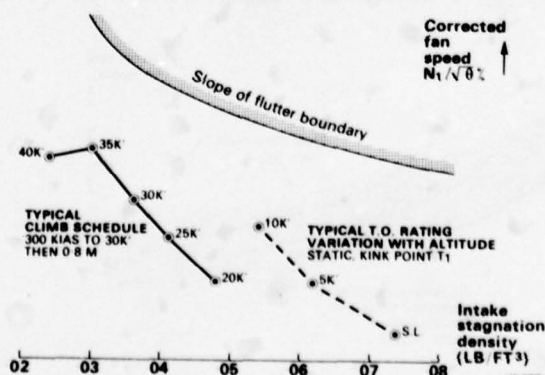


Fig.6 Comparison of Slope of Flutter Boundary with Typical Civil Aircraft Operation

Taking first a civil transport aircraft, some important operating points are compared with the flutter boundary in Fig.6. The highest fan corrected speed conditions to be considered are take-off at high altitude and constant air-speed climb up to the aircraft's cruise altitude. In both cases it is seen that the slope of the flutter boundary with change of density lies in a favourable direction.

- (a) As take-off altitude is increased, the air density reduces and the flutter speed recedes, although the margin between flutter and the engine rating does tend to reduce. Note that the points shown are alternative static take-off conditions, and that as forward speed is applied the rated $N_1/\sqrt{\theta}$ will reduce, thus improving the flutter margin.
- (b) In the second case on Fig.6 a continuous climb schedule is shown. As altitude is gained, the fan corrected speed increases until the stratosphere is reached. The slope of the flutter boundary also increases, such that there is a minimum flutter margin at or near to the top of climb just before a lower rating for cruise is selected.

It is part of the design process of a new engine to make sure that the above margins are adequate. To be taken into account are many factors, such as thrust growth of the engine and deterioration of the fan in service, in determining what initial margins are acceptable. If the margins are unnecessarily large, a penalty may be incurred via excess fan weight.

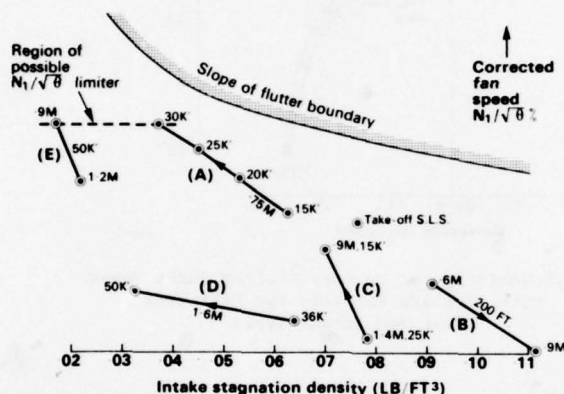


Fig.7 Comparison of Slope of Flutter Boundary with Various Military Aircraft Operations

Next we examine operation in a military aircraft. Here there are many more possibilities to consider than in the civil case, whether it be for a multi-role combat aircraft or for several aircraft designed for different specialised missions with a common engine. A selection of cases has been taken, as labelled in Fig.7, plus normal take-off, where each one is plotted on the corrected speed/density diagram. These are:

- (A) Subsonic climb at 0.75M to 30,000 ft. altitude.
- (B) Low level strike at 200 ft. between 0.6 and 0.9M.
- (C) Aerial combat in the range 0.9M/15,000 ft. to 1.4M/25,000 ft.
- (D) Second segment climb with reheat for interception in the stratosphere at 1.6M.
- (E) High altitude reconnaissance at 50,000 ft.

The most obvious point from Fig.7 is that high flight Mach Number cases are the least problem from the flutter viewpoint, because the high ram intake temperature suppresses the fan corrected speed. The low level strike at high subsonic speed (case B) might have been expected to be a problem because of the high intake stagnation density. However, the attendant high intake temperature ensures that here also the fan corrected speed is suppressed and the flutter margin is more favourable than, say, at the take-off condition.

The highest fan corrected speeds occur at the top of the subsonic climb and in the slow speed, high altitude reconnaissance role. The latter is not a real problem because of the very low air density, but it might be preferable to impose an $N_1/\sqrt{\theta}$ limiter for performance reasons in this case and for flutter reasons in the subsonic climb case.

Therefore we see that the worst military flight conditions for supersonic flutter are not really different from the civil case. This is convenient from the point of view of developing a fan design which may be adopted in both fields.

5. EFFECT OF INTAKE DISTORTION

So far we have considered operation with clean, uniform intake conditions, such as is provided by an airmeter in a test cell. However, we would expect the susceptibility of a fan to flutter to be influenced by the quality of the intake airflow as well as by its mean pressure and temperature.

It is fortunate that for once the laws of nature work in our favour. It is found that the most perfect case in terms of intake symmetry tends to give the lowest flutter onset speed. A measure of circumferential distortion, as found in real aircraft intakes, helps to suppress flutter. It is analogous to mechanical detuning - physical asymmetry in the rotor will split the orthogonal components of the normal vibration mode and make their excitation at a common frequency more difficult than for the perfectly tuned rotor [5]. In the case of flutter, where the airflow provides the vibration energy input, asymmetry in the fan airflow can provide detuning of an aerodynamic nature.

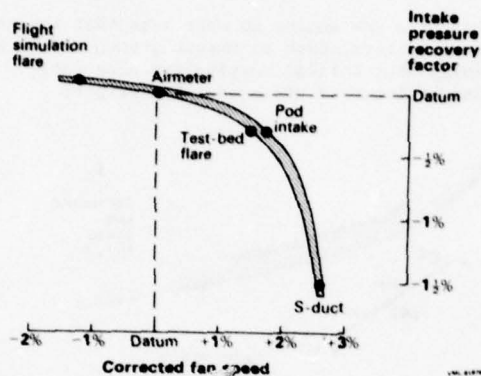


Fig.8 Variation of Average Flutter Onset Speed with Pressure Recovery for Different Test Bed Intake Types

The effect is illustrated in Fig.8, where averaged test data for a given fan behind different intake types is presented. The intake pressure recovery factor is used as a measure of the quality (in performance terms) of the intake. It is seen that the most efficient intakes are also the most flutter prone. The area of the 'knee' of the curve is of special interest because this gives the biggest flutter improvement for the least intake loss.

As a further demonstration of this effect, the onset of flutter can be correlated in terms of a circumferential distortion parameter. At a given blade height, H , the circumferential total pressure factor presented to the fan face, $(P_{\max} - P_{\min})/P_{\text{mean}}$, has been calculated for various intake types and plotted against H in Fig.9. The maximum value of $P_{\max} - P_{\min}$ occurs typically near the fan tip for a pod intake, whereas for a buried installation it occurs much lower down the blade.

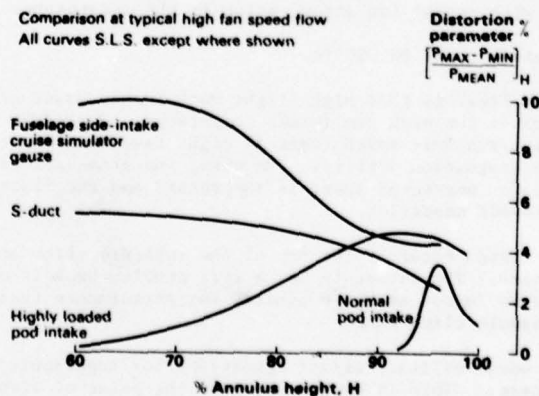


Fig.9 Comparison of Circumferential Distortion Parameter for Different Intake Types

It is next necessary to integrate the above pressure factor over an appropriate part of the blade span. Because the maximum excitation forces and amplitudes occur near the blade tip, the outer part of the span is the most relevant; in fact the outer 50% of annulus area has been used here. Thus we have an area distortion parameter defined as:

$$D_A (50-100) = \frac{2}{A} \int_{50\%}^{100\%} \left[\frac{P_{\max} - P_{\min}}{P_{\text{mean}}} \right] \cdot dA$$

where A is the fan inlet annulus area.

This parameter has been plotted in Fig.10, for various intake test points, against the elevation of flutter onset speed above that measured with an airmeter. An arrow attached to certain points means that flutter was not present with that intake at the maximum speed reached.

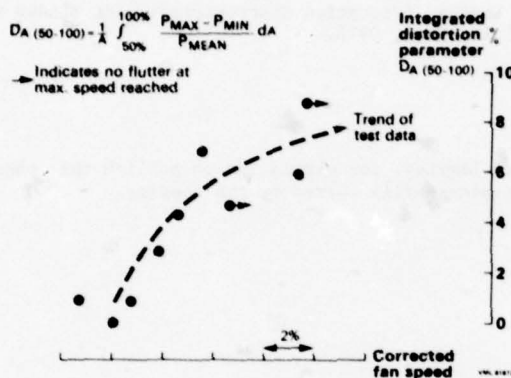


Fig.10 Correlation of Integrated Distortion Parameter with Average Flutter Onset Speed for Different Intake Types

The trend previously referred to is confirmed; that is, circumferential distortion can be beneficial to supersonic flutter. The implications of this are manifold. For example, there exists the possibility of deliberately designing an intake to improve flutter margins. This is unlikely to find favour with those responsible for engine performance, however, and it is possible that any tendency of a fan towards part-speed stall flutter could be exacerbated.

One positive outcome of this work is the general conclusion that customary rig and development engine testing with airmeters can be counted upon to give near to the lowest flutter speed. With aircraft-type intakes the flutter margins should certainly be no worse and could even be better. This is important as a lot of unnecessary test time and expenditure can be saved.

6. CONCLUDING REMARKS

We have seen that supersonic flutter for different flight conditions can be correlated in terms of intake stagnation density, although the correlation is not unique with respect to ambient air temperature. Sea level testing will give close to the minimum corrected flutter speed with normal test cell intakes, whereas for real aircraft intakes the flutter speed will tend to be higher. It is shown that flutter onset speed can be correlated with either the intake efficiency or the circumferential distortion presented to the fan.

The minimum flutter margins in service will depend upon the engine's rating curves and the flight envelope of the aircraft. It is found that the worst cases tend to be at take-off from high altitude airfields and at maximum climb or continuous ratings near the top of the aircraft's lowest speed climb schedule. Normally it will be adequate to examine the 'kink-point' temperature case. Whilst these general observations can be used for project work, it is necessary, however, to examine closely all the high corrected speed areas of any firm application, in relation to the flutter boundary of the particular fan design adopted.

REFERENCES

1. MIKOLAJCZAK, ARNOLDI, SNYDER and STARGARDTER,
Pratt & Whitney, 'Advances in Fan and Compressor Blade Flutter Analysis and Predictions',
Journal of Aircraft, Vol.12, No.4, April 1975.
2. HALLIWELL, D.G. Rolls-Royce Limited, 'Fan Supersonic Flutter: Prediction and Test Analysis',
Aeronautical Research Council R & M No.3789, November 1975.
3. NAGASHIMA T. and WHITEHEAD D.S. Cambridge University, 'Aerodynamic Forces and Moments for
Vibrating Supersonic Cascades of Blades', CUED/A-Turbo/TR 59, 1974.
4. HOCKLEY, FORD and FOORD, Rolls-Royce Limited, 'Measurement of Fan Vibration using Double
Pulse Holography', ASME No.78-GT-111, April 1978.
5. EWINS, D.J., Imperial College, London, 'Vibration Characteristics of Bladed Disc Assemblies',
Journal Mech. Eng. Science, Vol.15, No.3, 1973.

ACKNOWLEDGEMENT

The author wishes to thank Rolls-Royce Limited, for permission to publish this paper. Views expressed therein are his own and not necessarily shared by the Company.

UNSTEADY ROTOR BLADE LOADING IN AN AXIAL COMPRESSOR WITH STEADY-STATE INLET DISTORTIONS

by

M. LECHT

and

H.B. WEYER

Deutsche Forschungs- und Versuchsanstalt für Luft- und Raumfahrt E.V.,
 Institut für Antriebstechnik, Linder Höhe, 5 000 Köln 90, W.Germany

SUMMARY

This paper primarily deals with the unsteady flow phenomena within rotor blade channels of a subsonic and a transonic axial compressor stage subjected to different types of steady-state inlet distortions. Especially circumferential nonuniformities in total pressure as well as in preswirl flow have a serious impact on aerodynamically induced blade flutter and flow instabilities. A simple steady state measuring technique with conventional probes and pressure taps combined with an adequate data analysis was used to investigate the unsteady rotor flow with particular respect to the variation of the blade loading during rotor revolution. Some relevant results of this investigation are submitted and discussed.

LIST OF SYMBOLS

A_{ld}	ideal lift force
c_A	lift coefficient
c	circulation coefficient
c_n	normal force coefficient
C	absolute velocity
C_u	absolute tangential velocity
ΔC_u	change in absolute tangential velocity
D_i	hub diameter
D_a	tip diameter
F_n	normal force on airfoil elements
$F_{n_{red}}$	reduced normal force
$\Delta F_{n_{red}}$	peak-to-peak reduced normal force difference
h	airfoil element height
i	incidence
I	Distortion Intensity
l	chord length of rotor blade element
\dot{m}	compressor mass flow
P_t	total pressure
ΔP_{tot}	Maximum total pressure difference
R	Radius
$\frac{R-R_i}{R_a-R_i}$	relative blade height
t	cascade pitch
T	tangential blade force
U	tangential speed of a rotor blade element
w	velocity relative to a rotor blade
w_∞	mean vector of relative velocities
x^*	axial coordinate related to the axial blade width
α	angle of attack
β	angle between relative flow vector and axial direction
$\Delta\beta$	relative flow angle change
γ	blade stagger angle
ϵ	glide angle

LIST OF SYMBOLS

θ	screen sector angle
π_{tot}	total pressure ratio
ρ	density
ϕ	circumferential position

INDICES

a	tip location
ax	axial direction
i	hub location
max	maximum value
min	minimum value
u	circumferential direction
HP	high pressure
LP	low pressure
Δ	difference of values
-	average of values
1	in front of the rotor (measuring plane 1)
2	behind the rotor (measuring plane 2)

INTRODUCTION

In recent years the aircraft engine-inlet integration has attracted considerable attention in order to overcome those problems arising with inlet distortions. Non-uniform inlet flow conditions do not only affect the compressor stall margin but result in severe unsteady aerodynamic load of the rotor blades thus initiating or aggravating air-foil vibrations and flutter. In this paper therefore an attempt is made to quantify the unsteady blade forces as a function of steady-state inlet distortion parameters.

EXPERIMENTAL SET-UP

Two different axial compressor stages of the same overall dimensions however of quite different pressure ratio have been used for the experimental study. The main overall design parameters of both the stages - the subsonic and the transonic one - are listed below:

LP-compressor-stage

tip diameter	D_a	= 400 mm
hub diameter	D_i	= 200 mm
tip speed	u_a	= 146 m/s
flow coefficient	c_{ax}/u_a	= 0.53
	\dot{m}	= 8.7 kg/s
pressure coefficient	ψ_{is}	= 0.52
	π_{tot}	= 1.065
number of rotor blades	z	= 24
pitch-chord-ratio rotor	t/l	= 0.63-0.9
hub-tip ratio		0.5
	NACA-65 Profiles	

HP-compressor-stage

tip diameter	D_a	= 400 mm
hub diameter	D_i	= 200 mm
design tip speed	u_a	= 425 m/s
design pressure ratio	π_{tot}	= 1,5
design mass flow	\dot{m}	= 17.3 kg/s
number of rotor blades	z	= 28
pitch-chord ratio rotor	t/l	= 0.5 - 0.78
hub-tip ratio		0.5

DCA-, MCA-Profiles

All tests were carried out with outlet guide vanes to have complete compressor stages, however during the program main emphasis was given to the rotor flow studies, except overall stage performance measurements.

Fig.1 shows a cross-sectional view of both the Test rigs involved. The spoiler position as well as the various measuring planes are indicated too.

The spoiler support has been designed to be continuously rotated over 360 degree to allow for conventional probe and wall pressure tap readings up- and downstream of the rotor at any point relative to the spoiled area.

Screen induced circumferential total pressure distortions of various sector angles

and intensities for both stages as well as a sinusoidal absolute inlet flow angle distortion (positive and negative preswirl) have been applied to investigate the unsteady aerodynamic rotor blade load effects. Fig.2 gives a survey on the different distortion types as well as of the intensities applied. The total pressure distortion is characterized by its sector angle θ and by its intensity which is equivalent to the screen total pressure loss

$$\text{Intensity } I = \frac{\Delta p_{\text{tot}}}{\frac{\rho}{2} \bar{c}_{ax}^2}$$

Relating the total pressure loss to the dynamic head at compressor inlet has the advantage of the intensity to remain fairly constant along the compressor's speed lines.

UNSTEADY ROTOR RELATIVE INLET CONDITIONS

Any steady state but circumferentially nonuniform inlet flow is always associated with substantial relative flow - incidence and / or velocity-disturbances at the rotor entrance, obviously initiating heavy unsteady rotor flows. The effect of a square wave total pressure distortion and of a sinusoidal preswirl distortion on the relative inlet flow field of the HP transonic rotor is illustrated in Fig.3 presenting the corresponding circumferential distribution of relative flow angle and velocity. The total pressure distortion (left hand diagram) leads primarily to a flow angle disturbance while the preswirl distortion (right hand diagram) causes a severe velocity disturbance. (Here, it has to be noticed that the circumferential axis is equivalent to a time axis in the rotor frame.) The plots point out that - with the total pressure distortion-the rotor will operate at different throttle settings on one speed line, while - with the preswirl distortion - it will operate along a line of constant throttling (Ref.1).

For total pressure distortions associated with severe incidence disturbances an attempt was made to relate the maximum change of flow angle (during one revolution) to the distortion intensity. Assuming no reaction of the rotor on its inlet flow field the following relationship of any total pressure defect with the axial flow velocity exists:

$$\Delta p_{\text{tot}} = \rho \bar{c}_{ax} \Delta c_{ax} \quad (1)$$

with

$$\bar{c}_{ax} = \frac{c_{\text{max}} + c_{\text{min}}}{2}$$

The intensity is given by

$$I = \frac{2 \Delta p_{\text{tot}}}{\rho \bar{c}_{ax}^2} \quad (2)$$

based on the circumferentially averaged axial velocity component:

$$\bar{c}_{ax} = \frac{360 - \theta}{360} c_{\text{max}} + \frac{\theta}{360} c_{\text{min}}$$

Equations (1) and (2) describe the equivalent axial velocity defect as a function of the distortion intensity. Now, the corresponding relative flow angle variation can easily be found by derivating the following relation deduced from inlet velocity triangle

$$\beta = \arctan(u/c_{ax})$$

resulting in

$$|\Delta \beta| = \frac{(u/\bar{c}_{ax})^2}{1 + (u/\bar{c}_{ax})^2} \frac{\Delta c_{ax}}{u} \quad (3)$$

Considering only 180°-sectors ($\bar{c}_{ax} = \bar{c}_{ax}$) the combination of equations (1) to (3) leads to:

$$\Delta \beta = \frac{1}{2} \frac{u/\bar{c}_{ax}}{1 + (u/\bar{c}_{ax})^2} I \quad (4)$$

In reality however the upstream flow phenomena are more complex than described by the simple estimation given above. Normally the inlet axial flow velocity defect is attenuated by the reaction of the rotor which tends to accelerate the upstream flow in the distorted area, thus decreasing the relative flow angle difference $\Delta \beta$. Due to the

acceleration the static pressure in the distorted area drops down initiating cross flows on either side of the distorted region. This swirl flow always directed towards the distortion center tends to increase again the relative flow angle difference $\Delta\beta$.

Results calculated for the LP rotor from eq.(4) (hatched area), are compared to the experimental peak-to-peak data ($\Delta\beta_{\max}$) in Fig.4 for max. and min. mass flow rates. For the tip sections the effect of acceleration and of swirl flow on $\Delta\beta$ seems to be of the same magnitude, thus the experimental results happen to agree quite well with the estimated data. For the root sections the effect of swirl flow obviously prevails the acceleration effect probably due to radial flow components (s.Ref.2).

Concerning the distortion behaviour throughout the rotor - reported here as the ratio of exit to inlet distortion intensity - Fig.5 reveals that mainly attenuation takes place over the blade height with an increasing tendency towards blade tip. Amplification occurs only in the hub region at low mass flow rates near surge. The exit distortion intensity is identically defined as the inlet datum and based on the minimum flow quantity average over the same sector angle as in front of the rotor. The dynamic pressure to relate on is calculated from the rotor exit overall average total pressure, average total temperature, the flow area and the inlet mass flow.

ANALYSIS OF UNSTEADY ROTOR BLADE LOADING

Due to the above described relative flow field disturbances associated with steady-state inlet flow distortions it is obvious that equivalent oscillating fluid forces will act on each blade, entering and passing the distorted flow area. In the following an attempt is made to quantify these forces by analysing and correlating the experimental flow field data in front and aft of the LP and HP rotor. Fig.6 presents two blades of a compressor cascade with the relevant forces of interest (Ref.3). The tangential force component T on a blade section of the height h corresponds to the momentum change throughout this section:

$$T = \rho c_{ax} h t \Delta W_u \quad (5)$$

t = blade pitch

Together with the axial force resulting from the cascade static pressure rise and axial momentum change the tangential force T yields the airfoil lift A which always is perpendicular to the direction of the mean relative flow vector w_∞ . In order to simplify this data analysis the profile drag is assumed to be small so that the lift coefficient c_A equals approximately the circulation coefficient c_Γ

$$c_A \approx c_\Gamma = 2 \frac{l}{l} \frac{\Delta W_u}{w_\infty} \quad (6)$$

l = chord length

The normal force coefficient then follows:

$$c_n = c_A \cos \alpha \quad (7)$$

The normal force F_n acting on cascade element of the height h at the radius R is given by:

$$F_n(R) = c_n(R) \cdot \frac{\rho}{2} \cdot w_\infty^2(R) \cdot l \cdot h \quad (8)$$

Considering only blade or airfoil sections it is useful to reduce the normal force by the section area $l \cdot h$ and moreover by the factor $(\rho/2) u_a^2$, if there are rotors with different tip speed u_a to be compared. Thus the reduced blade normal force ($F_{n \text{ red}}$) finally is a function of normal force coefficient c_n , of local relative flow velocity w_∞ , and of rotor tip speed u_a :

$$F_{n \text{ red}} = c_n \left(\frac{w_\infty}{u_a} \right)^2 \quad (9)$$

As an example Fig.7 presents the reduced normal force on several blade sections (various heights) of the LP-rotor with cleans inlet flow as a function of flow coefficient.

The evaluation of blade normal forces in the presence of circumferential nonuniform flow on both sides of the rotor requires to correlate the flow field data upstream and downstream of the rotor. Due to flow complexity this is a very difficult process, however might be simplified for practical purposes by the following assumptions:

1. Meridional streamlines follow constant relative blade heights throughout the rotor,
2. Streamlines on circumferential planes of constant relative height correspond to the absolute flow velocity vectors.

The circumferential correlation of data may be established by an approximative function describing the change of absolute tangential velocity along the nondimensional rotor axial length x^* which is found from a laser anemometer study of the internal flow field of both the LP and HP compressor rotor (Fig.8):

$$\Delta C_u = \Delta C_{u\max} [1 - (x^* - 1)^2] \quad (10)$$

The circumferential streamline shift between the measuring planes of interest follows from eq.(10) assuming the axial velocity to be an average of the inlet and outlet value (s.Ref.1).

In the following the blade normal forces evaluated from the experimental flow field data as described above are presented in some detail for both the LP and HP rotor. Fig. 9a - f shows the circumferential variation of the reduced normal force of blade elements near hub and blade tip for the different distortion configurations shown in Fig.2.

With any square wave total pressure distortion at inlet (Fig.9a - e) the rotor blades are always subjected to heavy transient force fluctuations. All diagrams (9a - e) - their x-axis correspond to the direction of blade rotation - demonstrate that the rotor blades diving into the distorted region are momentarily discharged, then however they undergo a typical transient force variation the slope of which depends on the time spent within the region (compare 90° and 180° sector). Peak load is achieved when leaving the low pressure area. At high distortion levels and near surge operation (min. mass flow), the data (Fig.9d) reveal that a local flow separation occurs near hub which leads to a drop in blade loading as indicated by the dashed line at bottom. The analogue HP (transonic) rotor data evaluation shows a very similar tendency in normal force behaviour. The generally lower level of the reduced force is primarily due to the great difference in the tip speed of both rotors (factor of 2.5) yielding lower reduced forces for the HP rotor although the actual forces are obviously stronger. Comparing the total pressure with the preswirl type of distortion reveals that preswirl disturbance applied to the HP rotor creates even more intense blade force fluctuations than the already high level total pressure distortions.

In order to get a close view on the effect of distortion level and distortion area width on the oscillating blade normal forces the peak values (maxima as well as minima) of the circumferential force distributions (s.Fig.9a - f) are presented in Fig.10 and 11 as a function of distortion intensity with the sector angle θ as a parameter. Fig.10 represents the data achieved for the LP rotor at maximum mass flow rate. Fig.11 shows the results gained for the near surge operating point of both LP and HP rotor. Concerning the LP rotor, the bandwidth of the blade normal force rises substantially with increasing distortion level, however no important effect of the sector angle becomes evident from the plots. Near hub the bellmouth type of force distribution develops quite symmetrical with respect to the clean inlet force datum (steady-state force level: dash-pointed line), while at tip the minimum blade force remains nearly constant and only the maximum values contribute to the increasing force bandwidth with growing distortion intensity.

Fig.11 illustrating the fluctuating force situation for the near surge operating point also presents those results available from the HP rotor. These results fit quite well into the LP rotor data for the near tip blade sections, however, less agreement is achieved for the hub region which is probably due to hub separation occurring in this compressor already at clean inlet flow because of only smooth hub contraction associated with high blade loading.

Fig.12 demonstrates the mere peak-to-peak amplitude of the reduced normal force just to give a direct impression on the strength of the oscillating blade forces. The amplitude is plotted against the distortion intensity with the relative blade height and the sector angle as parameters. The dynamic force component increases considerably with the distortion level, particularly if the intensity exceeds a value of 1. Concerning the LP rotor mass flow rate and relative blade height seem to be of minor influence on the amplitude of the unsteady blade forces, whereas for the HP rotor the force amplitude near hub is half that one of the tip section, probably because of this compressor's tendency to hub separation. Generally the HP rotor shows a similar tendency as the LP rotor, however, due to the limited test data available no basic conclusions can be drawn at the moment; more extensive and detailed investigations on high pressure ratio transonic rotors are required to clarify these complex phenomena.

CONCLUSIONS

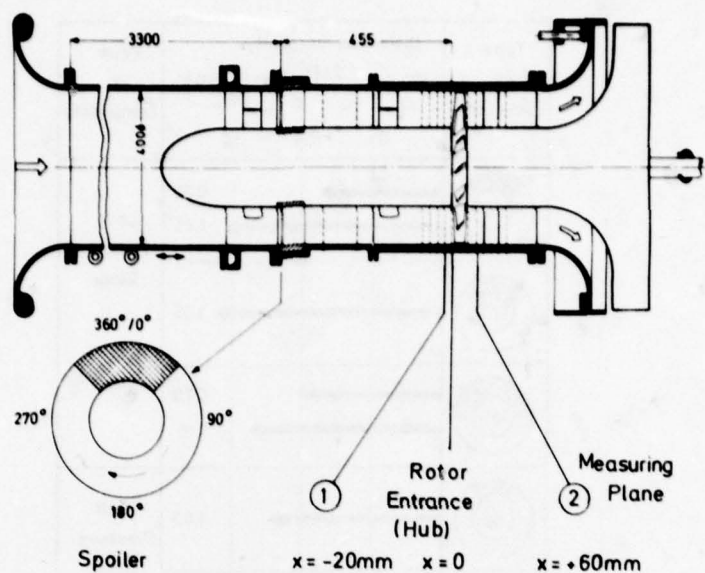
Steady-state flow distortions in compressor inlets always create disturbances in relative flow velocity and flow angle ahead of rotors which often lead to strong unsteady aerodynamic blade loadings and consequently to heavily transient and oscillating blade forces. Total pressure distortions are primarily associated with relative flow angle disturbances whereas preswirl distortions cause mainly relative flow velocity disturbances.

Experimental studies on a subsonic and a transonic rotor originally aimed at investigating the aerodynamic response of compressor stages on inlet distortions have been extended to analyze the unsteady rotor blade forces resulting from inlet flow inhomogeneities. The analysis is based on an appropriate definition of blade normal force referred to the rotor tip speed. The studies have revealed that the peak-to-peak force amplitude depends particularly on the distortion intensity. Distortion area and

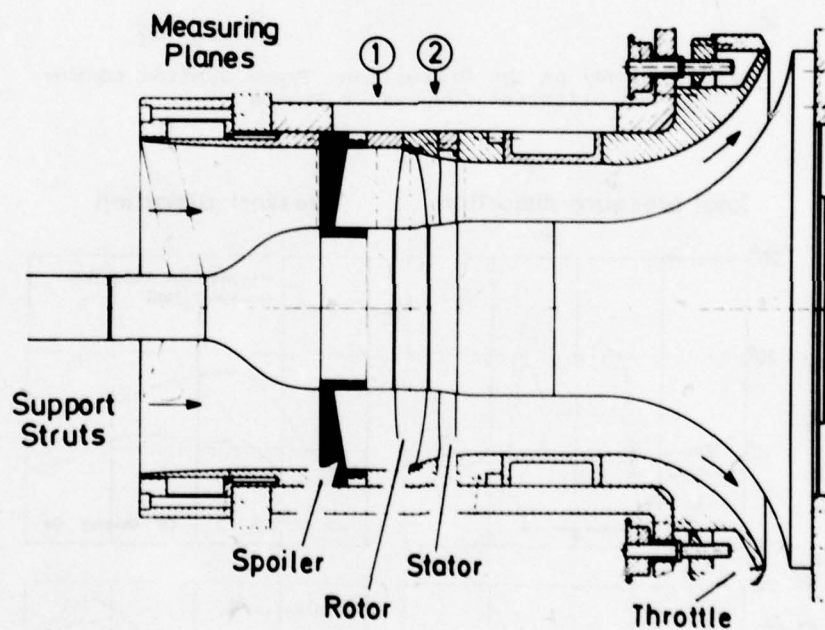
compressor operating conditions on the contrary seem to be of minor influence on the unsteady force magnitude; preswirl distortions tend to create more intense blade force fluctuations than even very strong total pressure distortions.

REFERENCES

1. M. Lecht, H.B. Weyer On the Unsteady Aerodynamic Rotor Blade Loading in a Transonic Axial Flow Compressor with Steady-State Inlet Distortion.
IUTAM Symposium on Aeroelasticity in Turbomachines, Paris 18./23. Oct. 1976,
R.F.M. Numéro spécial
2. G.M. Callahan Attenuation of Inlet Flow Distortion Upstream of Axial Compressors.
Dissertation, Lehigh University, 1968.
3. B. Eckert, E. Schnell Axial- und Radialkompressoren (Section D III),
Springer-Verlag, Berlin 1961, 2. Auflage.



a) Low Pressure Stage (LP)



b) High Pressure Stage (HP)

Fig.1 Cross Sectional View of the Test-Compressors




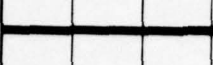

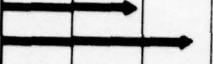





Type of Distortion	Distortion Intensity $I = \frac{2(P_{tmax} - P_{tmin})}{\rho C_a x^2}$			Type of Compressor
	0.4	0.8	1.2	
				Low Pressure Stage $U_a = 146 \frac{m}{s}$
				
				
				High Pressure Stage $U_a = 360 \frac{m}{s}$ (85% speed)
				
	Preswirl Distortion (Sinusoidal absolute flow angle) $\pm 25^\circ$			

Fig.2 Survey on the Distortion Types applied to the Two Different Compressor Stages

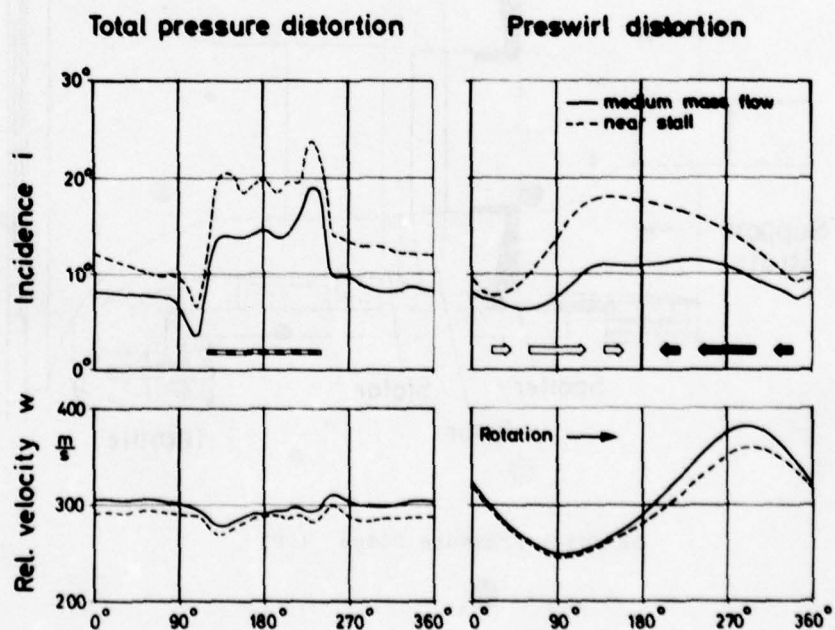


Fig.3 Circumferential Distribution of Incidence Angle and Relative Velocity in Front of the HP-Rotor (50 % Blade Height).

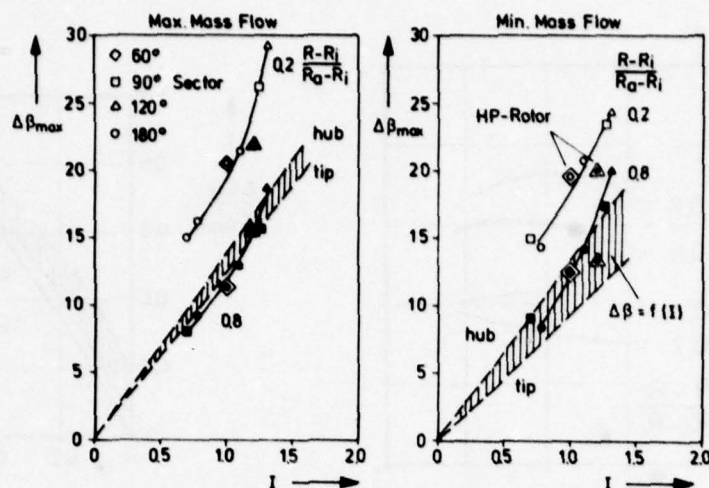


Fig.4 Maximum Variation of Relative Flow Angle in Front of the LP and HP-rotor as a Function of Total Pressure Distortion Intensity.
(Hatched Area: Estimation with Eq.(4) Valid for LP-Rotor only, 180° Sector. Doubled Symbols: HP Rotor)

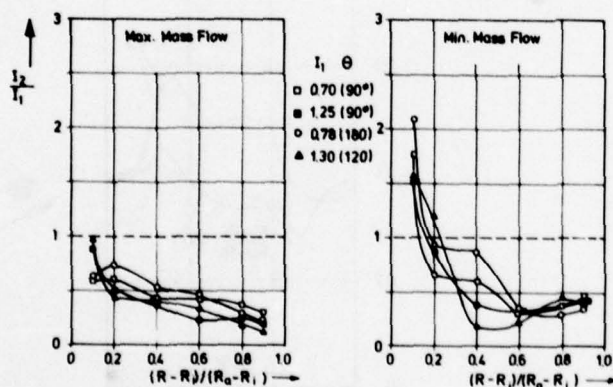


Fig.5 Radial Distribution of LP-Rotor Distortion Intensity Attenuation

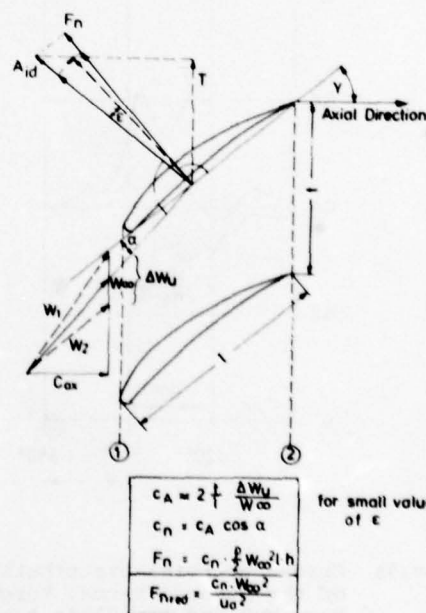


Fig.6 Forces on a Cascade Airfoil

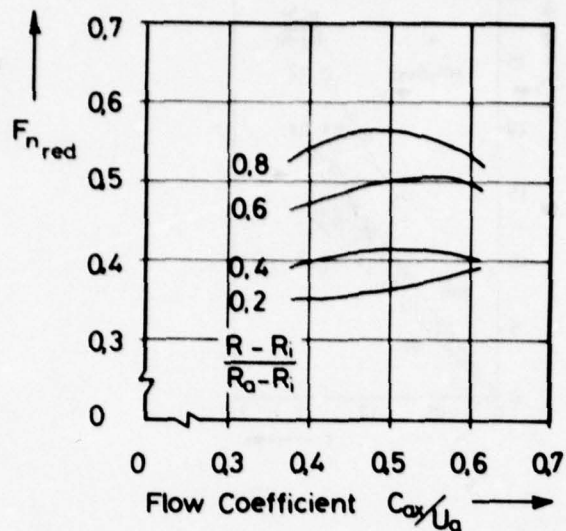


Fig. 7 Reduced Normal Force of LP-Rotor Blade Elements with Clean Inlet Flow

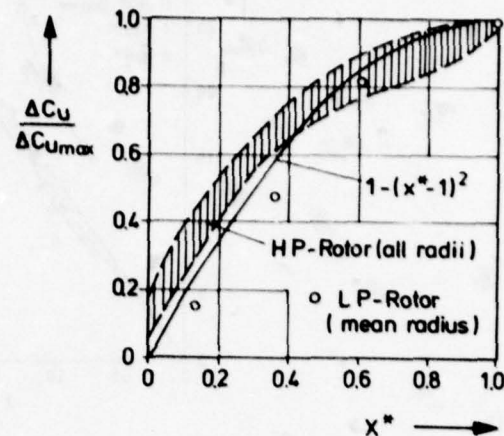


Fig. 8 Change of Absolute Tangential Flow Velocity along Rotor Axial Length

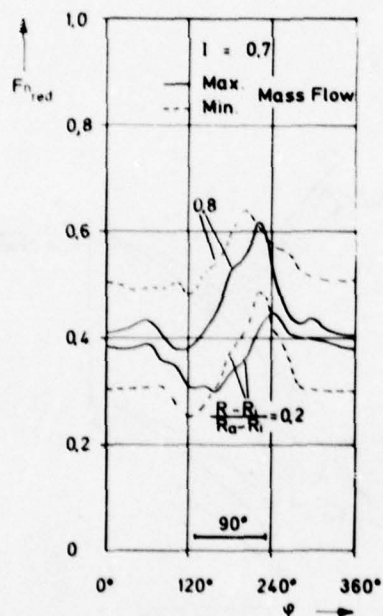


Fig. 9a Circumferential Distribution of the Reduced Normal Force in Near Hub and Tip Blade Sections for a Total Pressure Distortion (LP-Rotor)

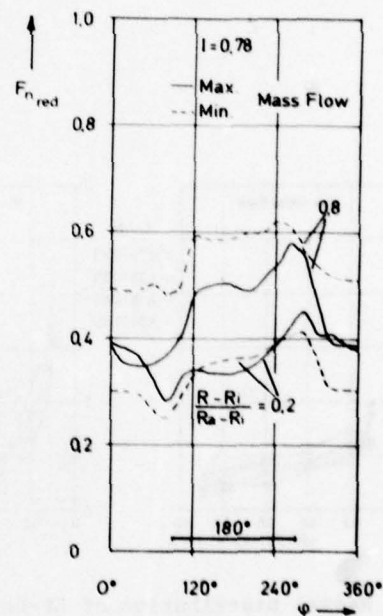


Fig. 9b Continued for Total Pressure Distortion (LP-Rotor)

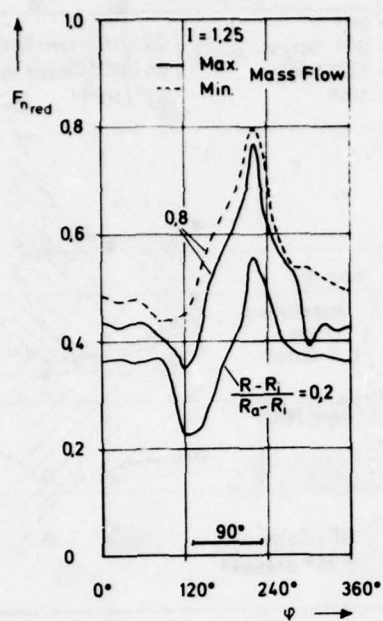


Fig. 9c Continued for Total Pressure Distortion (LP-Rotor)

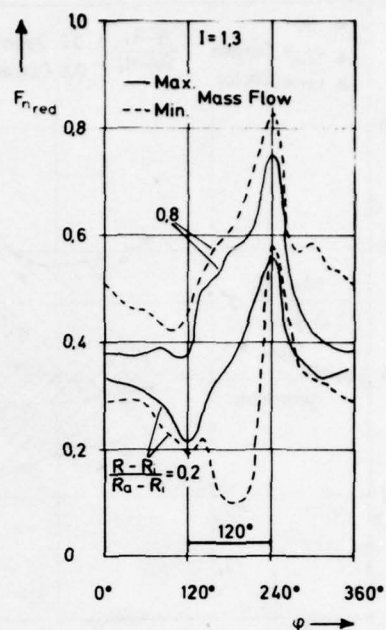


Fig. 9d Continued for Total Pressure Distortion (LP-Rotor)

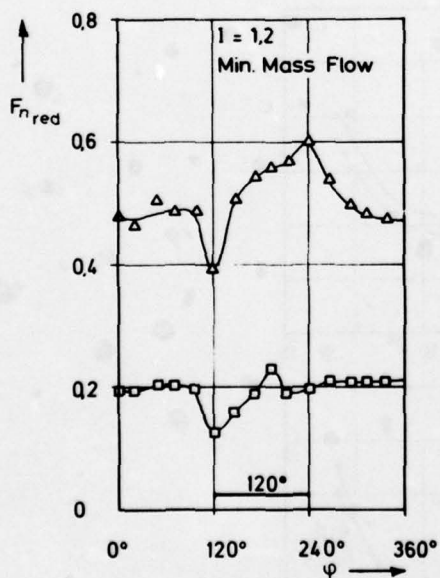


Fig. 9e Continued for Total Pressure Distortion (HP-Rotor)

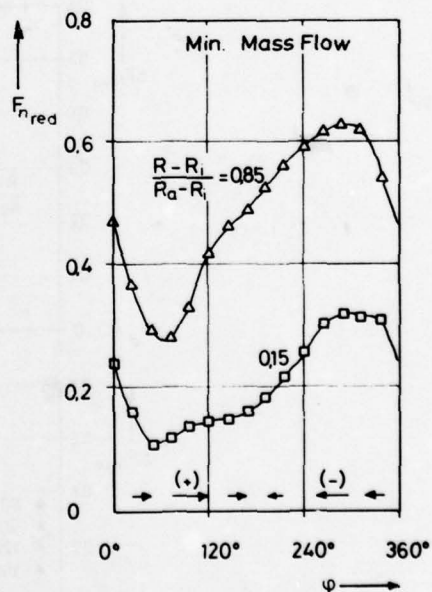


Fig. 9f Continued for + 25° Sinusoidal Preswirl Distortion (HP-Rotor)

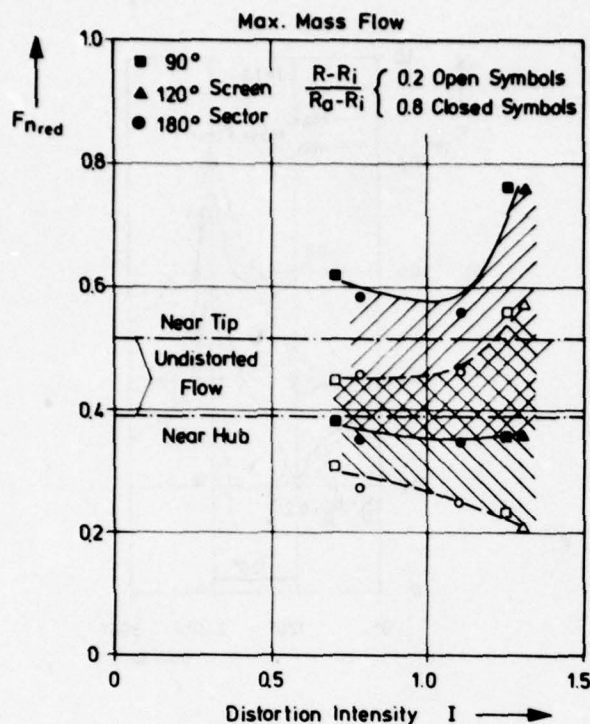


Fig. 10 Envelope of Minimum and Maximum Reduced Normal Forces Near Hub and Tip Blade Sections (LP-Rotor) as Function of Distortion Intensity.

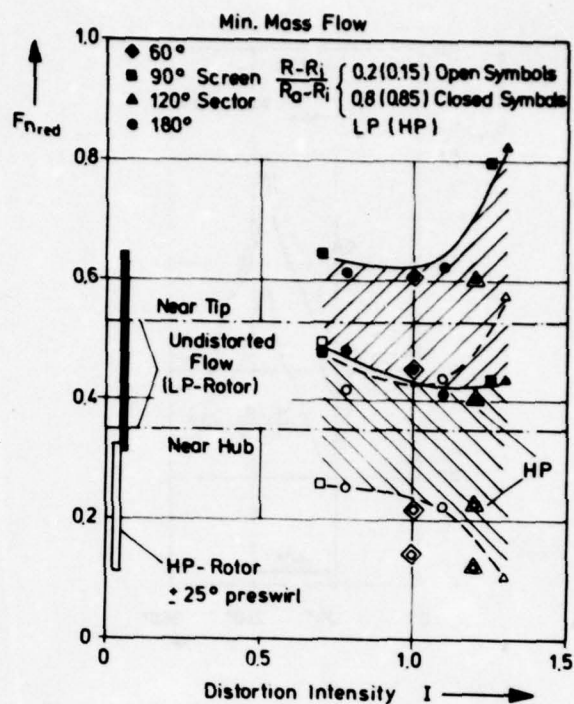


Fig. 11 Continued (LP- and HP-Rotor)

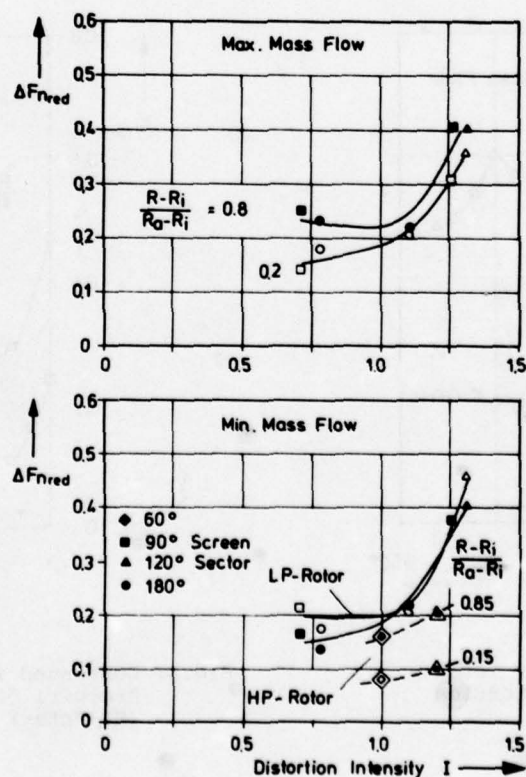


Fig. 12 Peak-to-Peak Amplitude of Reduced Normal Force as Function of Distortion Intensity

DISCUSSION

J.J.Adamczyk, US

Did you consider the potential field interaction that results from a total pressure interaction with an isolated stage?

Author's Reply

With respect to the theoretical estimation of the peak-to-peak relative flow angle change no interaction was taken into account. Whereas in the experimental values this interaction is included, because measured values in front of the rotor were used, which of course are influenced by the potential field of the stage.

J.Colpin, Belgium

Did you try to average your values to get the average value for the response of the compressor; and if you did, how did you evaluate those mean values? Did you introduce, for example, an average value of the axial inlet velocity?

Author's Reply

Yes.

J.Colpin, Belgium

That was just an area average?

Author's Reply

In order to quantify the inlet distortion intensity we used an average dynamic head resulting from mass flow, inlet area, total temperature and area averaged total pressure. But for a rough approximation at the expected relative flow angle change a circumferential average of axial inlet velocity is used within the definition.

DISTORTIONS, ROTATING STALL AND MECHANICAL SOLICITATIONS

Dr. J. COLPIN

Institut de Mécanique
 Université de Liège
 75, rue du Val-Benoît
 LIEGE
 BELGIUM

SUMMARY

A one stage axial flow compressor is studied aerodynamically and mechanically when operating with moldistributed inlet flow, i.e. inlet flow total pressure distortions and rotating stall.

A theoretical model is presented which calculates the distortion propagation through the compressor stage. That enables the computation of the unsteady aerodynamic loading of the rotor blades.

The theoretical results are successfull compared with the measured flow fields.

An experimental study defines the rotating stall characteristics of the compressor stage and relates the blades vibrations and stresses with the existence of a distortion and/or rotating stall cell.

LIST OF SYMBOLS

a	-	Sound velocity	t	-	time
C	-	blade chord	u	-	axial velocity
C_1	-	entropy constant	v	-	tangential velocity
f	-	frequency	β	-	relative flow angle
H	-	total enthalpy	δ	-	stagger angle
i	-	incidence	γ	-	specific heat ratio
k	-	reduced frequency	ΔP	-	total pressure loss coefficient
N	-	rotational speed (RVS/Min)	ω	-	angular velocity
P_0	-	total pressure	θ	-	camber angle
P	-	static pressure	ϕ	-	diameter
Q	-	mass flow	ψ	-	stream function
R	-	gas constant	ψ	-	total pressure coefficient
R	-	radius	ρ	-	specific mass
S	-	entropy	σ	-	stress (pascals)

Superscript

R. Relative motion

Subcripts

1.- upstream rotor

2.- downstream rotor

Ax - Axial

IN - Inner

Loc - Local

NOM - nominal

OUT - outer

Per - Peripheral

Ref - Reference

I. INTRODUCTION

Among the aerodynamical factors affecting the turbomachines surge lines, efficiencies and mechanical blade sollicitations, inlet flow distortions and rotating stall play a primary role.

These two different aerodynamical phenomena have different origins but both create non uniform unsteady internal flows which generate dynamic flow transfer functions through the blade rows and thus unsteady loadings on these blades.

The inlet flow distortions are externally imposed boundary conditions for the compressor. They can be of temperature, pressure or foreign gases. Their sources can be due to swallowed airframe wakes, high incidences or sideslip flight conditions, supersonic unsteady shock boundary-layer interactions, inlet structure, nozzle flow of fired missiles etc ...

The consequences of inlet flow distortions, in compressor, are surge margin reductions, nominal point performances decreases, higher blade stresses; in combustor and turbine, they are flame out risks and overheating problems.

The rotating stall phenomenon is a spontaneous aerodynamic response of a compressor to too high loadings on the bladings. The internal flow attempts a reorganization to reach the asked operating conditions, with the minimum possible losses. In fact, the choice of the flow between surge and rotating stall configuration will depend on the radial equilibrium of the flow (ref.1) and on the compressor geometry, primarily internal volumes (ref.2).

Rotating stall is mainly studied in part speed compressor regimes because of the major importance of the phenomenon under such conditions. However, what is generally called the surge line of a compressor, at higher operating speeds, is simply the continuation of the rotating stall region from low to high speeds (ref.3). This is important for the prediction of the "surge line" in theoretical models.

The consequences of the rotating stall are of two types :

- difficulty or impossibility to cross the rotating stall region during starts up, this being due to the hysteresis linked with the phenomenon (ref.1,3).
- too high blade stresses resulting from the aerodynamic sollicitations which are often close to fundamental resonant frequencies of the bladings. Let us remember that the rotating stall cells generally propagate circumferentially with a peripheral velocity close to half the one of the compressor rotor.

Classical solutions are : first stages blades strengthening (part span shrouds), variable geometry, bleed valves to derive a part of the compressor mass flow.

From the preceeding observations, one realizes the necessity to develop theoretical prediction tools applicable both for compressor aerodynamic performances predictions and unsteady aerodynamic loadings of the blades.

A great deal of work was devoted in the past to study the two described phenomena and we will just name here some of them, concerning the detailed flow investigations, theoretically and experimentally.

The non uniform flow field going through the compressor can be approximated using the linearized flow equations (ref.4,5,6,7). This does not enable the prediction of the flow evolutions with large perturbations or close to the surge line.

Non linear analysis were introduced to treat the steady state problem, i.e. distortion by ADAMCZYK and CARTA (incompressible) (ref.8) and MAZZAWY (compressible + correlations) (ref.9).

In the unsteady flow cases, i.e. rotating stall, TAKATA (incompressible) (ref.10) and ORNER (compressible) (ref.11) have presented two of the most important contributions.

All those theories concern the aerodynamic aspects, but potentially contain the possibility to be used in vibration analysis by inclusion of the blade mechanical characteristics. However, this was not yet done, at the author's knowledge.

On the experimental side, important contributions are due to LECHT and WEYER (ref.12), MOELKE (ref.7) and PEACOCK (ref.13).

Our own contribution to the problem deals with the study of the inlet flow distortion effects theoretically and experimentally. We have decided to restrict our analysis to total pressure distortions influences.

The theoretical model (ref.14) is developed to eliminate some restrictions previously introduced i.e. small perturbations and/or compressibility.

The experimental aspect treats

- the global aerodynamic compressor response
- the study of the internal flow field (in connexion with theoretical predictions)
- the rotating stall characteristics, with the interaction due to the presence of a steady state pressure distortion
- the blade mechanical stresses and vibration characteristics in presence (of) the aerodynamic phenomena described.

2. THEORETICAL MODEL

A one stage axial flow compressor is modeled as shown on figure 1. The hypothesis for the flow outside the blade rows are : non viscous, two-dimensional, stationary. The flow remains subsonic in the absolute frame of reference.

The steady state Euler equations are expressed in function of the main variable ψ (stream function), for the flow outside the blade rows. The detailed equations derivations are reported in reference 14.

One obtains finally

$$\begin{aligned} (a^2 - u^2) \frac{\partial^2 \psi}{\partial x^2} - 2uv \frac{\partial^2 \psi}{\partial x \partial y} + (a^2 - v^2) \frac{\partial^2 \psi}{\partial y^2} \\ = \rho^2 a^2 \frac{\partial H}{\partial \psi} - \rho^2 \frac{a^2}{\gamma R} (a^2 + (\gamma - 1)(u^2 + v^2)) \frac{\partial S}{\partial \psi} \end{aligned}$$

A second equation is necessary to describe the flow field, calculating the specific mass, i.e. the energy conservation equation.

$$\frac{\gamma}{\gamma - 1} C_1(\psi) \rho^{\gamma+1} - H \rho^2 + \frac{1}{2} \left[\left(\frac{\partial \psi}{\partial x} \right)^2 + \left(\frac{\partial \psi}{\partial y} \right)^2 \right] = 0$$

The subsonic solution coming from equation (2) is chosen (cfr. hypothesis).

The solution of this equation is determined using a finite difference technique applied to equation (1) on the domain presented on figure 1.

If the boundary conditions of that domain can be specified on the outer limits, the internal B.C. formed by the blade rows have also to be evaluated. Thus transfer functions at the blade rows were defined, i.e. relating the inlet and outlet flow fields at the rotor (ref.14) :

Continuity :

$$\rho_2 u_2 = \rho_1 u_1 - C_{Ax} \frac{\partial \rho_1}{\partial t}$$

$$\begin{aligned} \text{Energy : } H_2^R = \frac{1}{1 - \frac{C_{Ax}}{2\rho_1 u_1} \frac{\partial \rho_1}{\partial t}} \left[H_1^R \left(1 - \frac{C_{Ax}}{2\rho_1 u_1} \frac{\partial \rho_1}{\partial t} \right) - \frac{1}{\rho_1 u_1} \int_0^{C_{Ax}} \frac{\rho \mu}{\cos^2 \beta_{loc}} \frac{\partial \mu}{\partial t} dx \right. \\ \left. - \frac{C_{Ax}}{2\rho_1 u_1 R} \left(p_2 \frac{\partial S_2}{\partial t} + p_1 \frac{\partial S_1}{\partial t} \right) \right] \end{aligned}$$

To derive these equations, acoustic Strouhal number and relative mass flow fluctuations are considered to be small.

The variation of entropy through the rotating blade row results of two contributions.

- 1.- Entropy transport through the blade channels, depending on the inlet entropy non uniformities

$$\Delta S_A = S_{1,t_0 - C_{Ax}/u_1} - S_{1,t_0}$$

2.- Viscous generation

$$\Delta S_B = -R \ln \left\{ \left(1 - \bar{\omega} \left(1 - \frac{P_1}{P_{01}} \right) \right) \left(\frac{H_1^R}{H_2^R} \right)^{\frac{C_p}{R}} \right\} \frac{\Delta S_A}{R}$$

To modelize the exit stator, a semi-actuator disk approach is followed. The NACA correlations are used to evaluate the circumferential distribution of losses and deviation angles.

The exit boundary-condition expresses the annulation of the circumferential static pressure gradient at outlet.

This condition is formulated by the momentum equation, projected along the direction.

$$\frac{\partial^2 \psi}{\partial x^2} \left[u(\alpha^2 - u^2) \right] + \frac{\partial^2 \psi}{\partial x \partial y} \left[(u(\alpha^2 - 2u^2)) \right] - \frac{\partial^2 \psi}{\partial y^2} u v^2 = 0$$

A parametric study, based on the present model, shows the respective importances of different compressor parameters (ref.14). The beneficial effects of large blade chords (fig.2) and high blade stagger angles (fig.3) is demonstrated, among other aerodynamic influences, i.e. aerodynamic loading, distortion circumferential extent etc ...

A comparison is made between the theoretical model predictions and the experiments. This will be discussed after the description of the experimental procedures and results.

3. EXPERIMENTAL STUDY3.1. Experimental test set up

Tests were done on the high speed compressor test facility R4 of the Von Karman Institute. This facility is a closed loop with intermediate cooling in the settling chamber. The test fluid was air at a pressure closed to atmospheric pressure.

The compressor rotor has the following main characteristics :

$$\phi_{\text{outer}} = 0.4 \text{ m}$$

$$\phi_{\text{in}} \phi_{\text{out}} = 0.5$$

$$N_{\text{nom}} = 10.000 \text{ RPM}$$

$$\left(\frac{P_{02}}{P_{01}} \right)_{\text{nom}} = 1.2$$

$$Q_{\text{nom}} = 11 \text{ kg/sec}$$

$$N_{\text{blades}} = 25$$

The downstream stator is formed by 30 blades located 2 chords away from the rotor. It turns the flow back towards the axial direction.

A distortion support is mounted 3 rotor chords upstream of the rotor. The rotation of the support enables to record circumferential non uniformities of the flow field. A rectangular screen, mounted on the support, generates an inlet total pressure distortion (fig.4.)

A different instrumentation is used to record the aerodynamic performances (pneumatical probes and transducers with automatic data acquisition); the rotating stall characteristics (hot wires) and the blade vibrations. For this last task, a strain gauge bridge is mounted at the root section of a rotor blade, approximately at mid-chord. The electrical signal is transmitted from relative to absolute motion using rotary mercury contacts. The different probes locations in the test section are presented on figure 5.

3.2. Aerodynamic performances

The global influences of different distortion configurations are investigated, varying systematically the circumferential extent of the perturbation zone(s).

The loss in stall margin increases going from a 180° distortion configuration to a 120° situation (fig.6). This evolution agrees with the simple parallel compressor analysis assuming outlet total pressure constant,

$$SM = 1 - \frac{P_{01 \text{ MINI}}}{P_{01 \text{ MEAN}}}$$

where $P_{01 \text{ MINI}}$ = minimum total pressure a inlet

$$P_{01 \text{ MEAN}} = \frac{1}{2\pi} (\Theta P_{01 \text{ MINI}} + (2\pi - \Theta) P_{01 \text{ MAXI}})$$

Θ = distortion circumferential extent.

The situation is stabilized and moreover improved from D120 to D2 x 45 (two distortions sectors of 45° degrees each.). This is due to the existence of the unsteady flow behaviour in the distorted region, which delays the blade boundary layers separations. For decreasing unitary extents of distortions, the loss in stall margin is going down.

An improved parallel compressor model is proposed (ref.15) to take into account these unsteadiness influences. The global performances predictions reach a very good degree of agreement with experiments.

In order to have a deeper insight and understanding of the internal flow, detailed measurements are necessary. They were performed circumferentially and radially. A typical example of obtained map is shown on figure 7, for a rectangular distortion of 120°. One can immediately trace the circumferential variations of incidence angles leading to circumferentially varying blade loadings. The correlation of the traces of P01, P02 and T02 shows the increased loading in the distortion "wake" with a noticeable peak just at the exit of the distorted zone (exit is defined with reference to the rotor rotation).

A detailed analysis of such experimental results (ref.15) emphasizes the influences of the velocity triangles, from tip to hub, with a far better behaviour in the tip region where the stagger angles are much higher than in the hub region (fig.8). This agrees with the parametric study based on the theoretical model (ref.14).

Also, the distortion circumferential extent was recognized as a fundamental parameter, enabling us to link the global compressor performances with the detailed measurements by an insight on the unsteady blade operation.

Unfortunately, we were not able to establish any definite correlation between steady and unsteady losses coefficients and deviation angles, because of the circumferential flow redistributions between rotor leading and trailing edges and the measurement planes. This is still a critical point in order to be able to predict accurately the unsteady blade loadings due to distortions.

The detailed flow measurements can be interpreted in terms of blade loadings, using the local ψ , i characteristics curves (fig.9, 10, 11). The circumferential blade loading distributions evaluate following hysteresis loops which are to be compared with the ones characterizing isolated airfoils unsteady operations (ref.16, 17).

The surfaces covered by these hysteresis loops grow with reducing radius values. The maximum incidences fluctuations are met in the hub region.

Important overloadings are observed for mid and hub sections. This is the consequence of boundary layers remaining attached to the blades, even at incidences higher than the stalling ones, i.e. a dynamic stall delay phenomenon.

A reduction in the operating mean mass flow produces higher incidences fluctuations then pressure ratio modifications; this is due to the shape of our characteristics having low $\partial\psi/\partial\alpha$ slopes. No fundamental changes are observed when operating close to the surge line. However the maximum incidence value is submitted to a lower growth than the "out of the distortion" one.

The unsteady operation curves are systematically located below the unperturbed ones. The reason is the lower efficiencies encountered when operating with inlet distortions. Our coefficient ψ being a total pressure coefficient, and not a work coefficient, includes also this efficiency information.

For our specific compressor design (i.e. free vortex with axial inlet velocity) it is shown that the dynamic forces applied on the blades with a distorted inlet, are much smaller in the tip than in the hub region, thanks to smaller surface, hysteresis loop and smaller incidence fluctuations. The forces fluctuations in the hub section are approximately twice the one existing at the tip. This confirms the parametric study of reference 14, and emphasizes the improvements given by the use of high peripheral velocities on the two aspects of distortion attenuation and blade dynamic forces (low ψ and $\dot{\psi}$).

Having presented a theoretical approach to solve the distortion problem, it is necessary to compare it to the experimental results discussed above. However, it is important to notice that the prediction of a rectangular distortion is particularly difficult due to high flow gradients induced by the perturbation. The calculation procedure tends to smooth out the circumferential variations of $\partial\psi/\partial\alpha$ as the stream function ψ is our main variable. This point can explain some of the discrepancies between theory and experiments.

The figure 12 summarises the outlet total pressure field predictions, for different radius locations. The accuracy reached is satisfactory despite some discrepancies in the distortion edges regions due to :

1. Rectangular distortion (sec above)
2. Dynamic loss models used (ref.10) consequence of the lack of direct measurements resulting from the distance separating the rotating blade row and the measurement plane. Thus, the dynamic stall region existing in the exit zone of the distortion is badly predicted.

However, the proposed theoretical model seems to be a safe basis for further developments. A pseudo three dimensional extension is actually under way. It consists in the superposition and coupling of cylindrical planes of different radii. The radial velocity components are therefore neglected because the main flow fluctuations are considered to interest mainly the circumferential direction. Consequently, we will be able to predict the unsteady blade aerodynamic loadings over the radius.

3.3. Rotating stall

The rotating stall characteristics of our model is determined using nowadays classic hot wires probes. Two of them are located with a 180° phase angle to obtain the configurations of figure 13. Going into stall induces the generation of two cells, diametrically located, moving at 56 % of the rotor angular velocity. A further closing of the back pressure valve leads to surge. When reopening the throttle valve, a change from two to one cell is recognized, this last configuration keeping almost the same propagation velocity. The rotating stall cells disappear for a higher mass flow coefficient than the one existing at the onset of the phenomenon.

The two aspects, i.e. different mass flows and cell(s) configurations when going in or out of the stall, defines the hysteresis loop of that unsteady phenomenon. This is emphasized on figure 14 where the compressor pressure increase versus a mass flow function is plotted, at mid span.

The respective locations of change in cell configuration is indicated by 2c → 1c.

There is no stable operation point between the maximum and the minimum values of the pressure rise. This indicates the occurrence of a large stall configuration with generation of a double discontinuous characteristic. Moreover a radial observation of the flow shows a simultaneous onset of the rotating stall over the whole compressor radius.

Having recorded the pressure variations in function of the back pressure for different compressor rotational speed, it is important to notice the similarity of the hysteresis cycles. That shows that even at high speeds, up to conditions where compressibility begins to play an important role, the same rotating stall characteristics are conserved. This is important, as noticed earlier, for the compressor "surge" line prediction.

According to GREITZER (ref.2), a coefficient is introduced to separate the rotating stall and surge regions.

$$B = \frac{U}{2a} \sqrt{\frac{V_p}{A_c L_c}}$$

V_p = Plenum volume
 A_c = Comp. cross section
 L_c = Comp. length
 U = Periph. veloc.
 a = Sound velocity

For $B > 0.7$ a surge phenomenon

< 0.7 a rotating stall phenomenon.

In our case, at the rotational speed of 8000 RPM, we observe rotating stall with a $B \approx 0.52$.

Measurements at higher speeds were not performed, to avoid any blade failure. Up to that value we agree with the GREITZER's analysis.

When a distortion is located in front of the compressor, one could expect significant changes in the rotating stall characteristics. Indeed, the inlet velocity flow field is completely transformed and tends to modify the equilibrium of the flow stream. In fact, no significant change is observed neither about the propagation velocity nor about the onset of the cells over the whole radius. Moreover the cells propagating velocities stay constant even in the distortion wake. The number of cells is not fixed by the number of distorted zones; one rotating stall cell is observed with two lobes of distortions.

This tends to show that the rotating stall phenomenon responds to the integral or averaged characteristics of the compressor and not to local particular flow evolutions.

3.4. Blade vibrations

Our study being devoted to unsteady phenomena related to the rotating blade row, we are interested in the dynamic stresses applied to the blades. Their levels and the vibration characteristics have to be analysed with respect to the excitation solicitations, i.e. rotating stall and distortions.

A gauge bridge and an electric signal transmission through rotating slip rings give an image of the stresses occurring in the root section of a blade; a priori there is located the most solicited blade section both in traction and in bending.

When rotating stall takes place, the blade vibrates at its first resonant frequency in bending (fig.15).

$$f_{res} = 480 \text{ Hz}.$$

This frequency is quite high and results from the rigid design of the compressor blades. There is a damping of the oscillations taking place between the impulses soliciting the blade crossing a stall cell.

The stresses produced in the root section are for that case ($N = 5300$ trs/min) : centrifugal and steady bending :

$$\sigma_1 = 60.10^6 \text{ pascals}$$

unsteady fluctuations :

$$\sigma_2 = \pm 115.10^6 \text{ pascals}.$$

For higher rotational speeds, the traction stresses will increase quadratically with Ω

$$\sigma_t = 100.10^6 \text{ pascals at } 10.000 \text{ RPM}.$$

while the bending stresses will increase proportionally with Ω .

The unsteady term increases also proportionally with Ω . (tests done at \neq velocities lower than 5000 RPM).

Extrapolating our measurements to 10.000 RPM, we reach :

$$\sigma = (170 \pm 230).10^6 \text{ pascals}.$$

From those values, we see that the dynamic term is of the same order of magnitude than the steady state one and can push the stresses to a very high level with respect to the material (here steel with elastic limit at 900.10^6 pascals). Furtheron, the blade are solicited in the fatigue mode and not stationnarily.

A steady state inlet distortion induces also dynamic stresses to the rotating blades (fig.16). Each time one blade enters in the distorted region, it is submitted to a large change in incidence, then in loading (fig.9, 10, 11). Between the two presented cases there are two differences

- a. different rotational speed
- b. different distortion intensity (lower, for D 180)

We still recognize a blade vibration at 480 HZ with a characteristic impulse by revolution taking place at frequencies of 100 HZ (D 180) and 166 HZ (D 120). There is a neat damping between the peak solicitations.

The levels of dynamic stresses are important for the case of (D 120, RPM 10.000) than the one measured for the rotating stall configuration.

$$\sigma_{dist} = \pm 100.10^6 < \underset{\text{stall}}{\sigma_{rot}} = \pm 230.10^6$$

However, the distortion exists at high speeds, in normal operation, while rotating stall is met generally at lower speeds. Then, the distortion impact on blade vibrations is the most dangerous one, and it can reach too high levels.

Generally the first bending mode is lower than the figures we obtained (480 HZ) for the first compressor rows. In that case, the damping between the exciting flow pulses will be lower, this increasing the risk of higher dynamic stresses close to resonance. A premature mechanical failure of our measurement system did not enable us to progress furtheron in that study which is of the utmost interest.

4. CONCLUSIONS

The impacts of distortions and rotating stall are enlightened both on the aerodynamic and mechanical points of view.

The compressor global performances losses are related to different distortion configurations and analysed using detailed flow insights. A prediction model is presented and compares successfully with the experimental results.

The unsteady blade loading fluctuations show the magnitude of the aerodynamic forces acting on the blades, these fluctuations decreasing with the blade radius.

The rotating stall develops over the whole blade span and induces a discontinuous compressor characteristic curve. A permanent inlet flow distortion does not seem to modify the rotating stall characteristics.

The blade vibrations induced by distorted flows (i.e. inlet flow distortion or rotating stall) are of the same order of magnitude than the steady state stresses; this could influence badly the life duration of the first stage compressor blades.

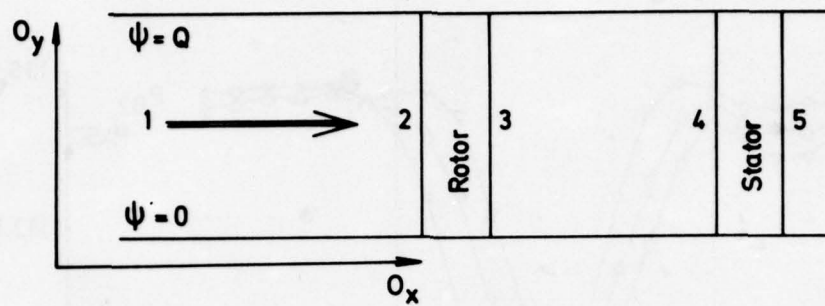
In the future, the proposed theoretical model will be extended to quasi tridimensional compressor configurations with the aim of predicting the internal flow field and the unsteady forces fields acting on the bladings. Furtheron, precise informations related to rotor aerodynamic characteristics in unsteady operations will have to be collected in order to improve the model predictions (i.e. losses and outlet flow angles).

REFERENCES

1. J.FABRI Gas turbine unstable flow regimes.
VKI LS 1978 - 2 (off design performances of gas turbines)
2. E.M.GREITZER Surge and rotating flow in axial flow compressors.
Jnl. of Eng. for Power, April 76 - TRANS. ASME -
3. J.COLPIN Influences de distorsions d'entrée sur les performances et le comportement aérodynamique d'un compresseur axial.
Thèse de doctorat - Univ. de Liège - 1977
4. G.M.CALLAHAN; A.H.STENNING Attenuation of inlet flow distortion upstream of axial flow compressors.
Jnl. of Aircraft, Vol.8, n°4, 1971.
5. F.EHRICH Circumferential inlet distortions in axial flow turbomachinery
J.A.S. Vol.24, n°6, 1957
6. Y.TANIDA Inlet distortion and blade vibrations in turbomachinery
Proc. 2nd Int. Symp. on Air Breathing engines (ICAS)
Sheffield - 1974
7. H.MOKELKE Predictionstechnique
AGARD LS 72 - 1974
8. J.J.ADAMCZYK Unsteady fluid dynamic response of an isolated rotor with distorted inflow
AIAA P.74 - 49, 1974
9. R.S.MAZZAWY Multiple segment parallel compressor model for circumferential flow distortion
AGARD CP 177 - 1975
10. H.TAKATA; S.NRGANO Non linear analysis of rotating stall
ASME P 72 GT3 - 1972
11. N.ORNOR Prediction du décrochage tournant dans les compresseurs axiaux
Thèse de doctorat, I.P.Mons/IVK - 1976
12. M.LECHT, H.WEYER Experimental investigation of a transonic axial flow compressor stage with steady state inlet flow distortion
Proc. 2nd Int. Symp. on Air Breathing Engines (ICAS)
Sheffield 1974
13. R.E.PEACOCK, J.OVERLI; Rotor dynamic stall observations in a compressor with circumferential pressure distortion
ARC 35.260 - Turbo 304.
14. J.COLPIN Propagation of inlet flow distortions through an axial compressor stage
ASME Paper 78-GT-34 - London 1978
15. J.COLPIN Inlet flow distortions in axial flow compressors
Israël Jnl. of Technology - Haifa 1977
16. F.O.CARTA Unsteady normal force on an airfoil in a periodically stalled inlet flow
J. of Aircraft, Vol.4, n°5, 1967
17. W.J.Mc CROSEY; J.J.PHILIPPE Unsteady viscous flow on oscillating airfoils
ONERA TP 1362, 1974.

ACKNOWLEDGMENTS

The VON KARMAN INSTITUTE and IRSIA are gratefully acknowledged for having supported this work.



BOUNDARY CONDITIONS

1	$\psi_1 = 0 \text{ à } \psi_1 = Q$
2,3	$P_3 = P_2 (\bar{u}, \omega, \beta, P_2 \dots)$ $Q_3 = Q_2 \text{ (MASS FLOW)}$
4,5	$P_5 = \text{Cste}$ $P_5 = P_5 (P_4, \bar{u}, \omega, \beta)$ $Q_5 = Q_4$

LATERAL	Périodicity
BOUND.	CONS. MASS FLOW

Fig.1 Calculation domain

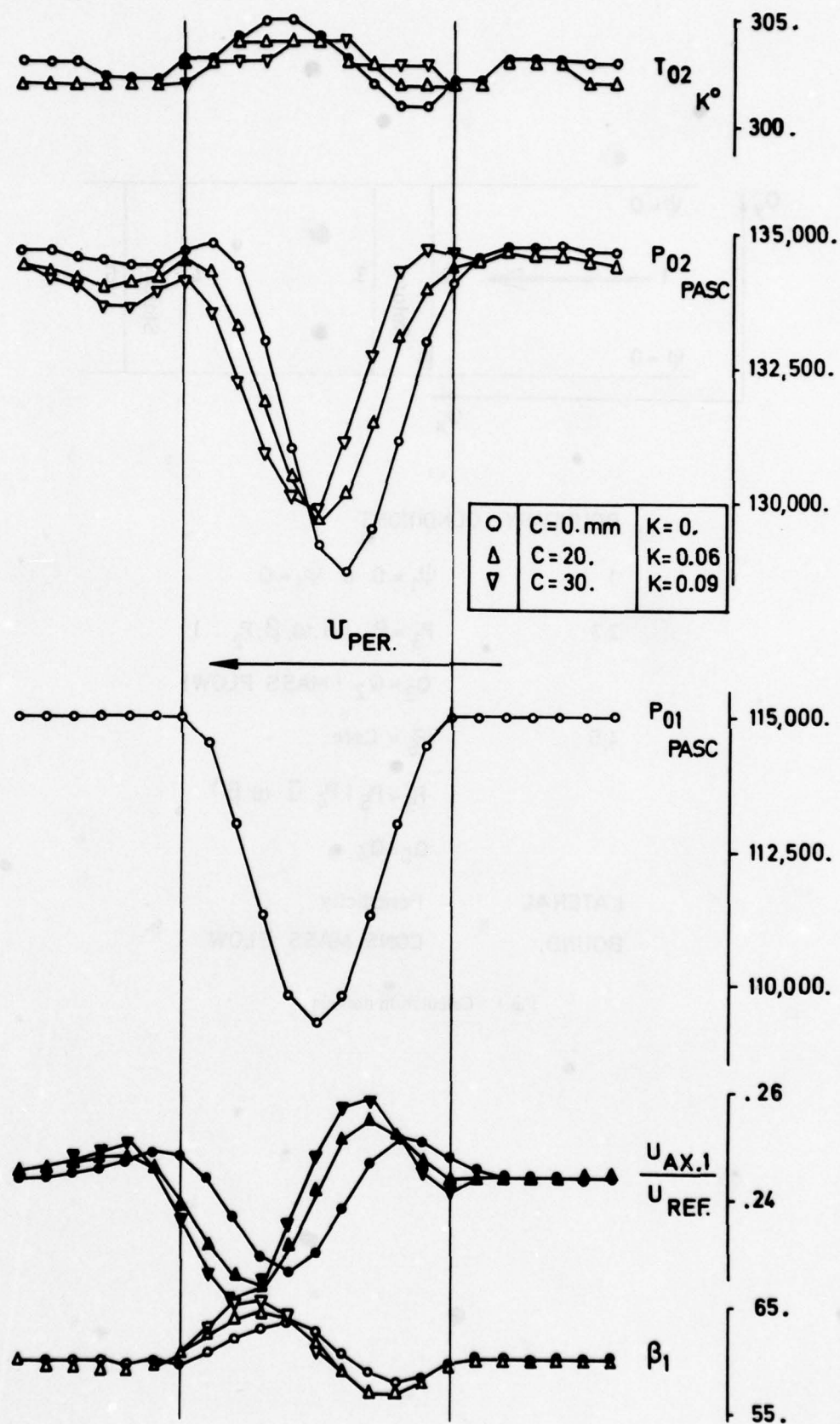


Fig.2 Rotor chord variations

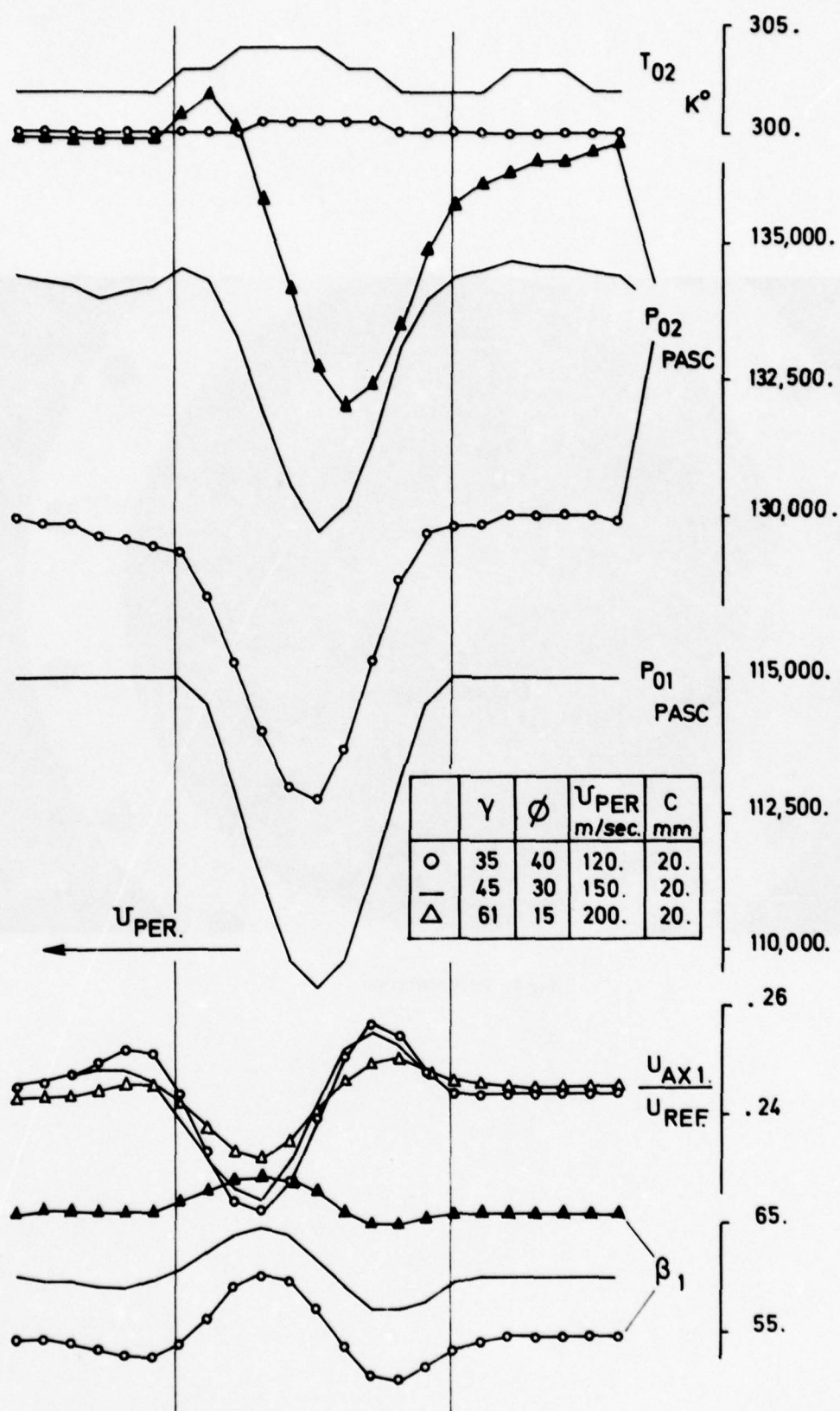


Fig.3 Rotor stagger angle variation

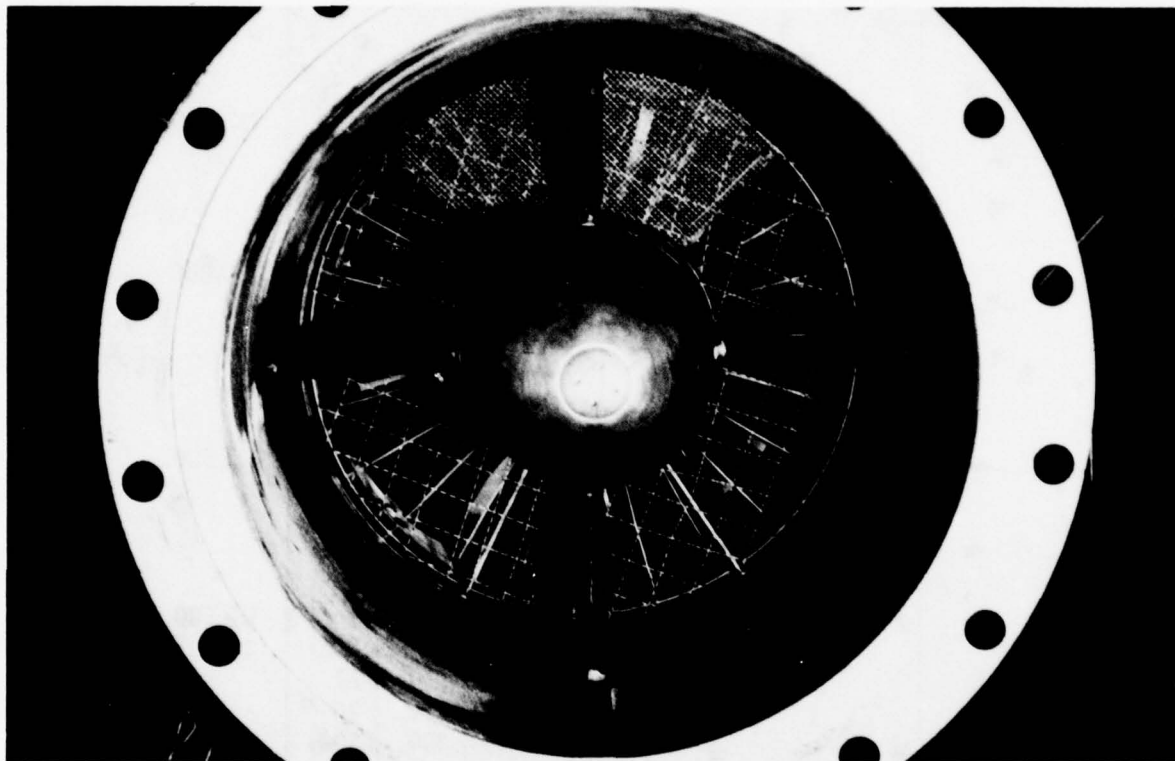


Fig.4 Inlet distortion

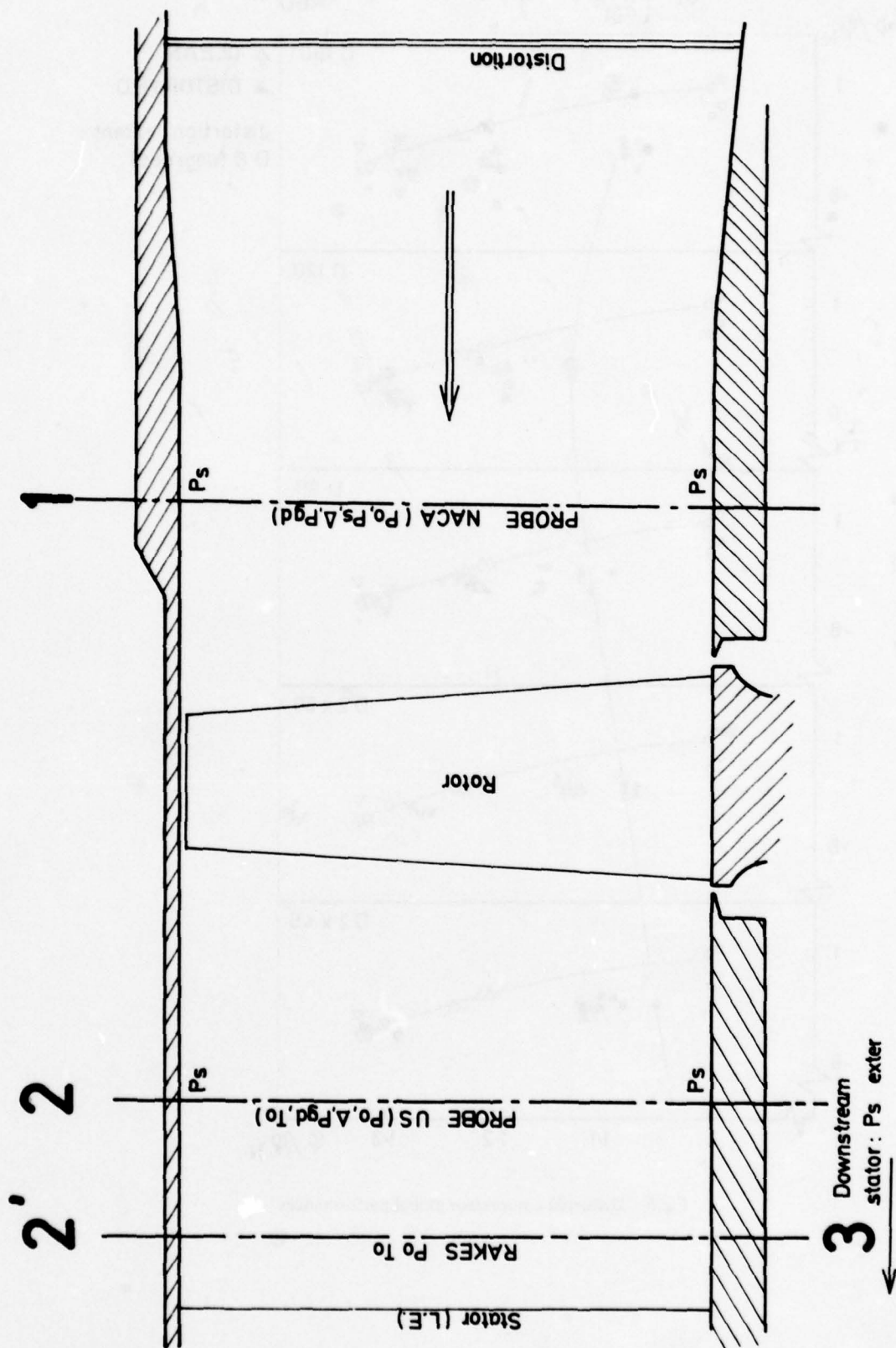


Fig.5 Instrumentation sections

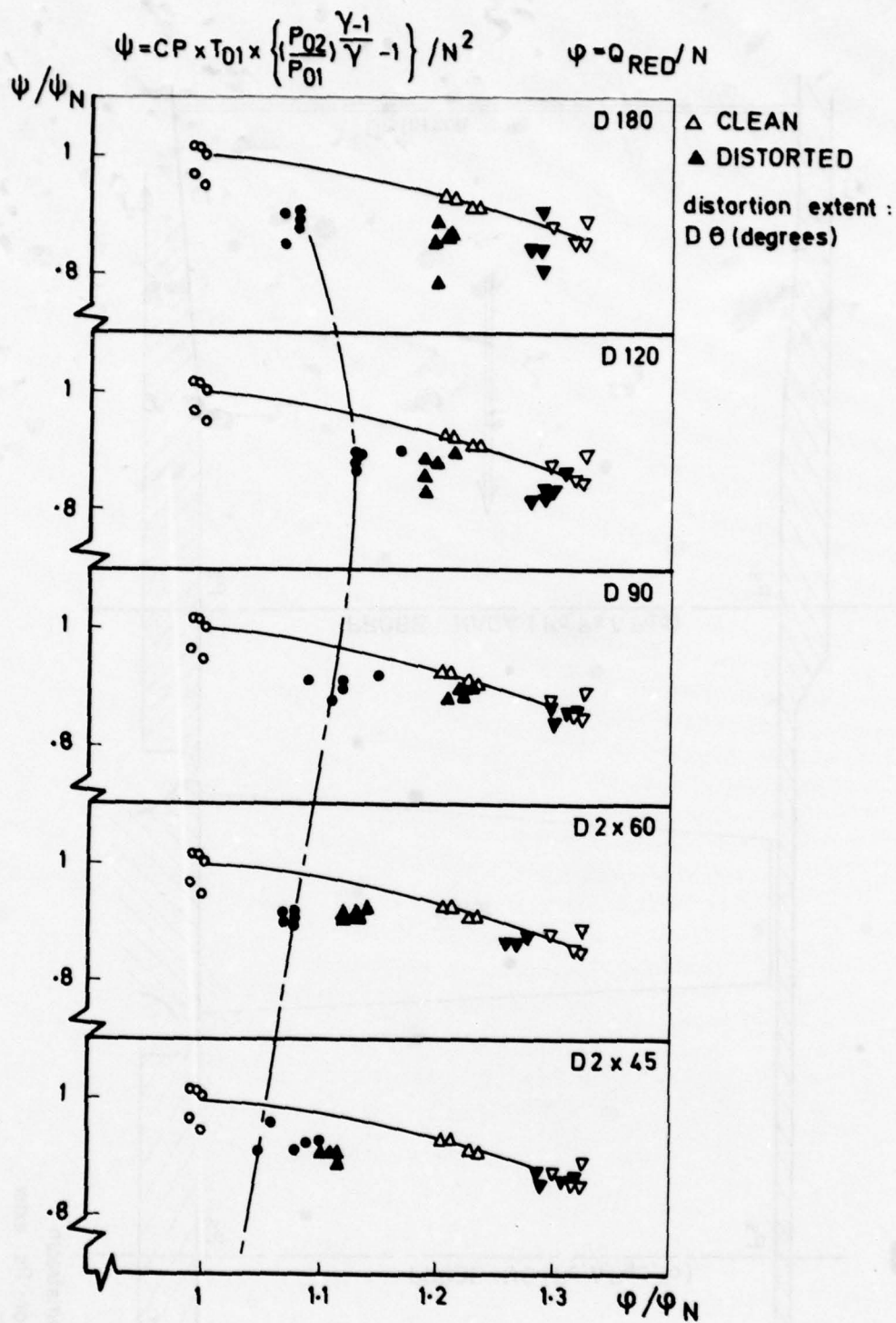


Fig.6 Distorted compressor global performances

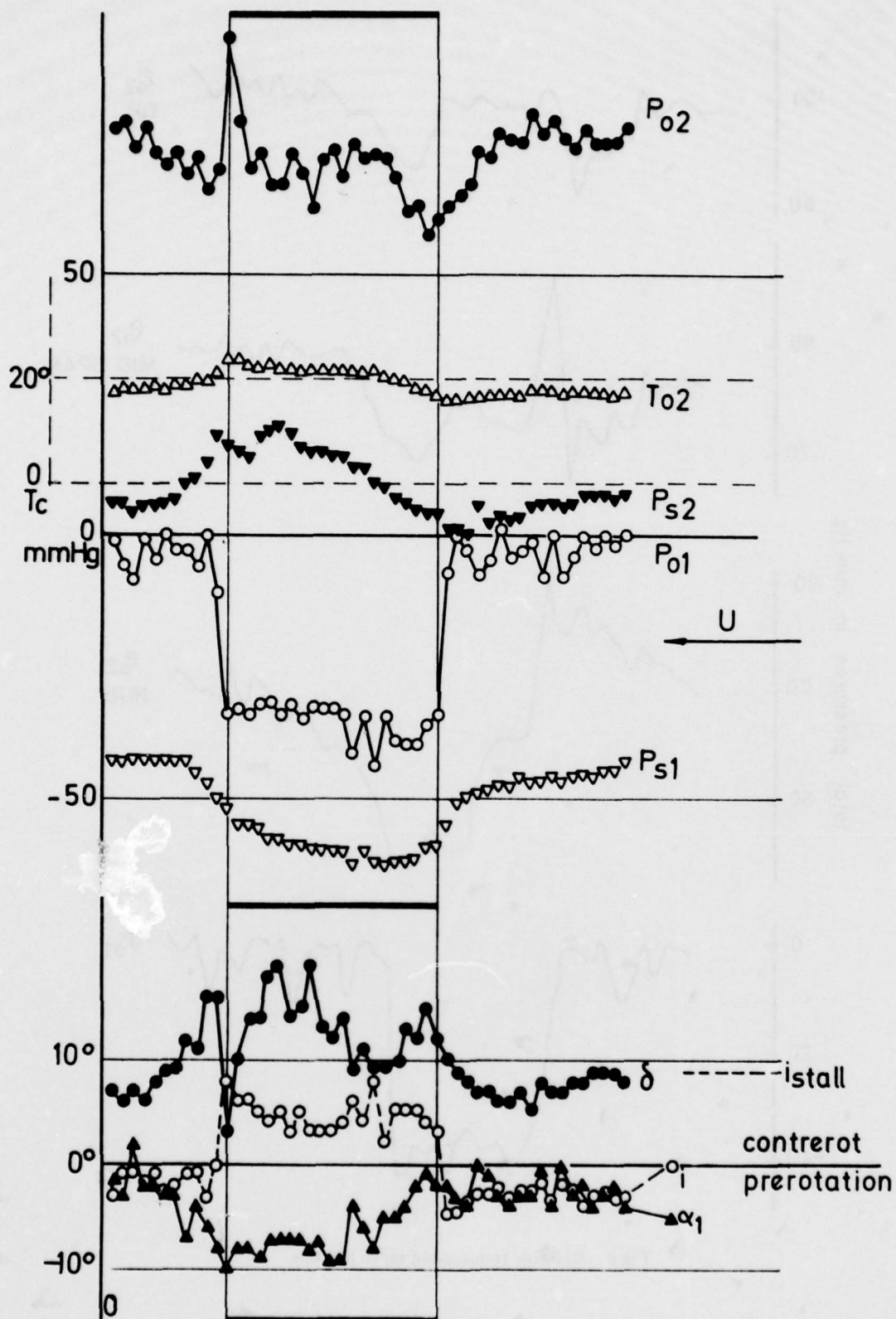


Fig.7 Distorted flow (D120)

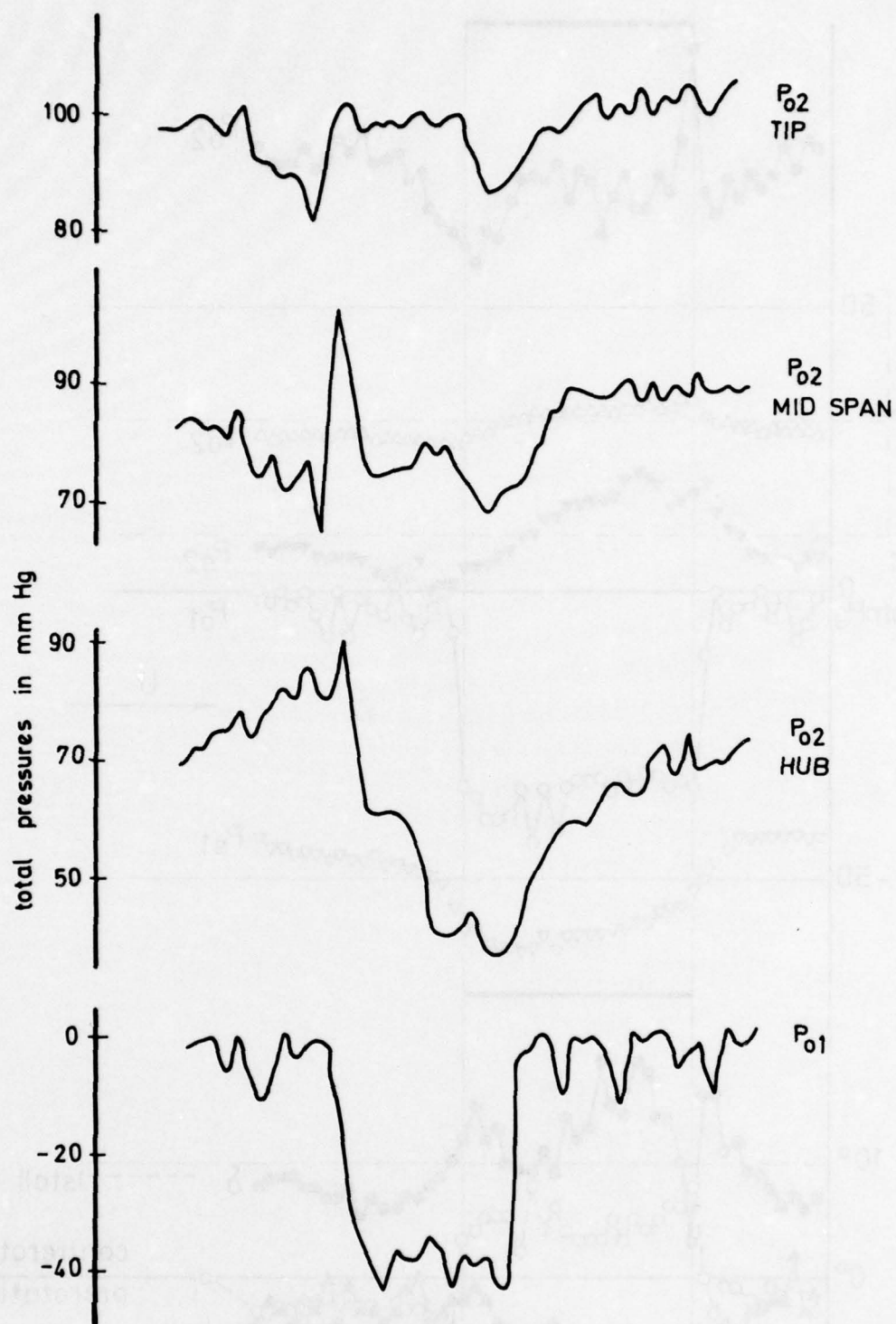


Fig.8 Dynamic transfer and radial location

$$\psi = C_p T_{01} \left[\left(\frac{P_{02}}{P_{01}} \right)^{\frac{R}{C_p}} - 1 \right] / U^2$$

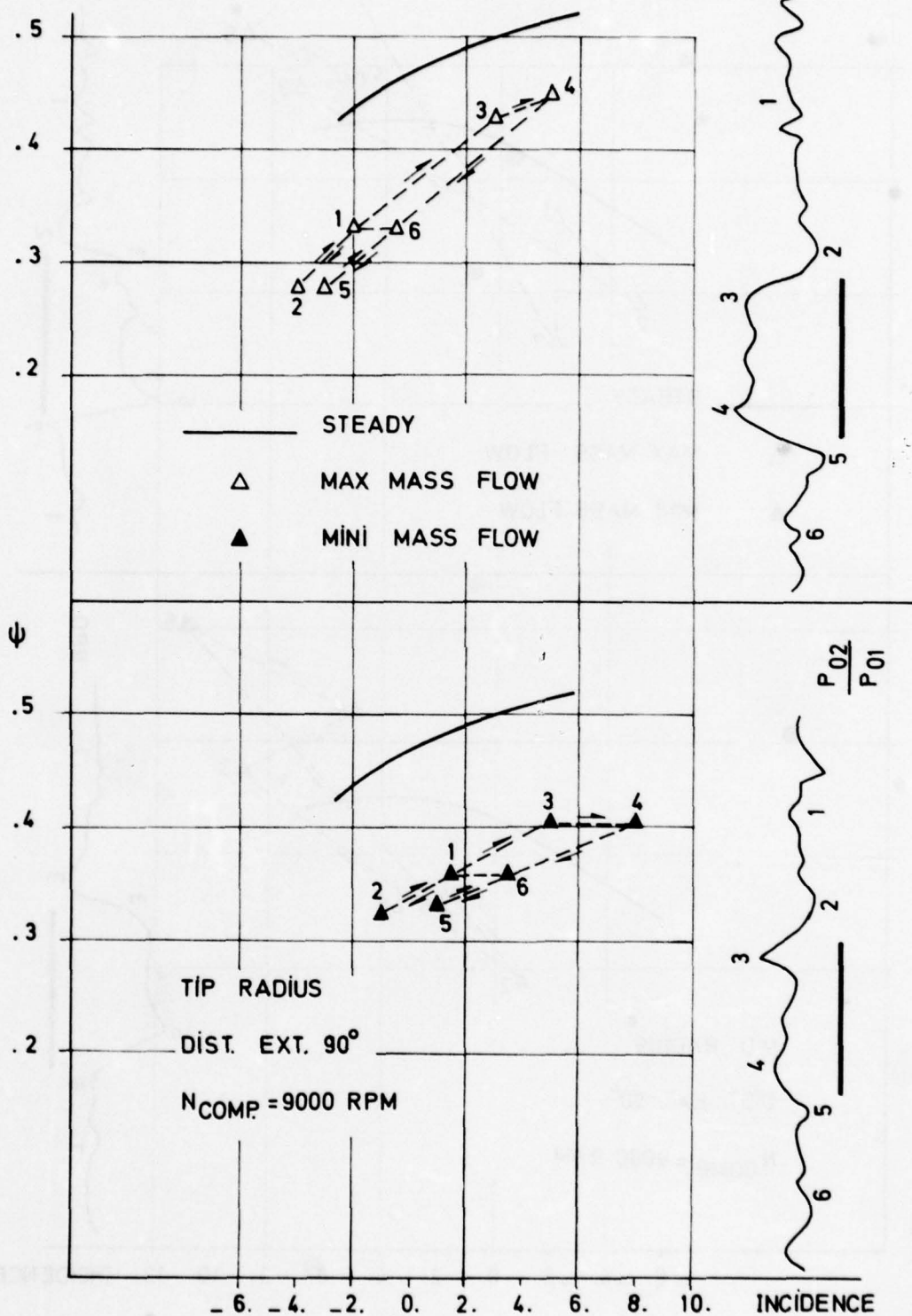
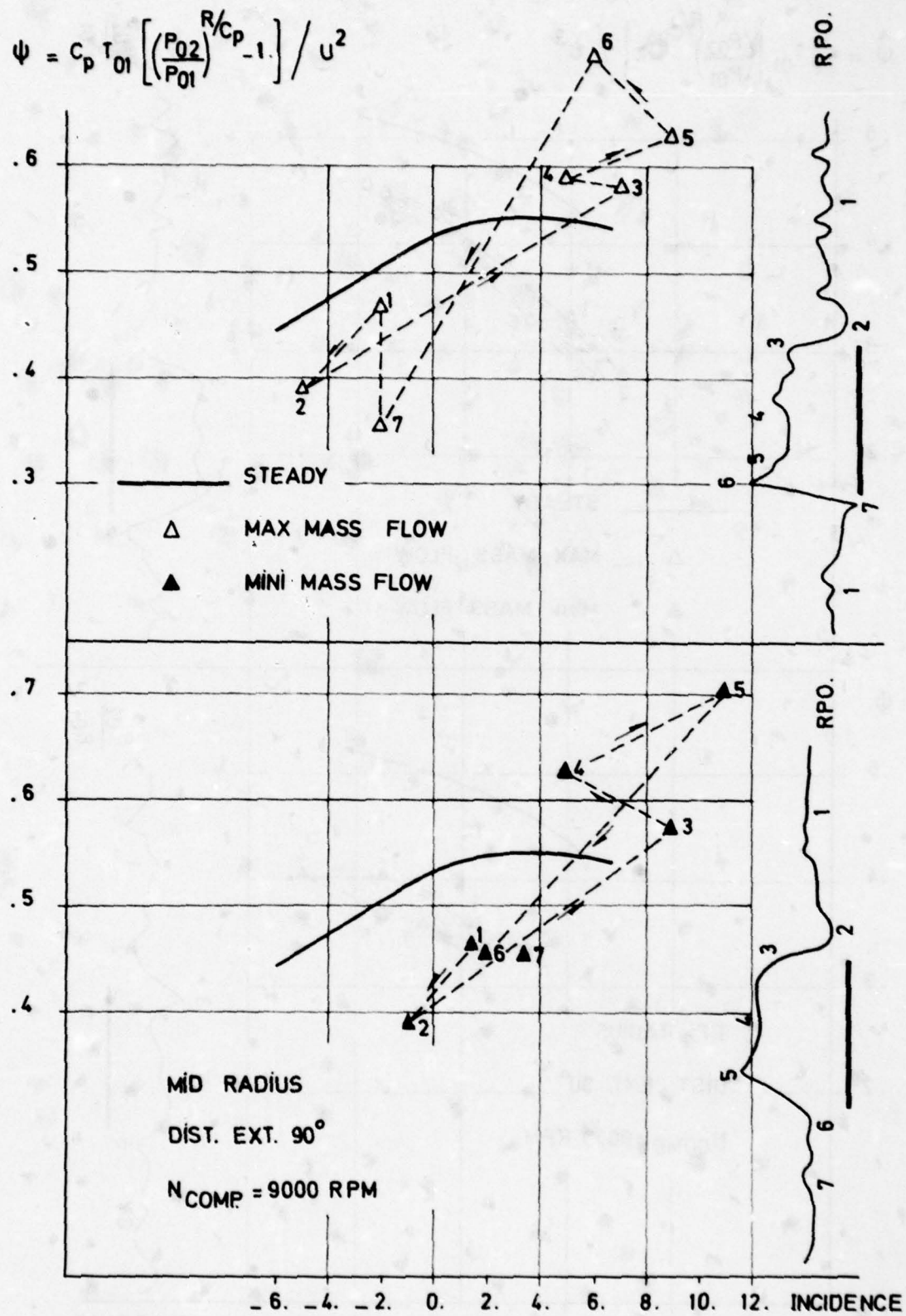
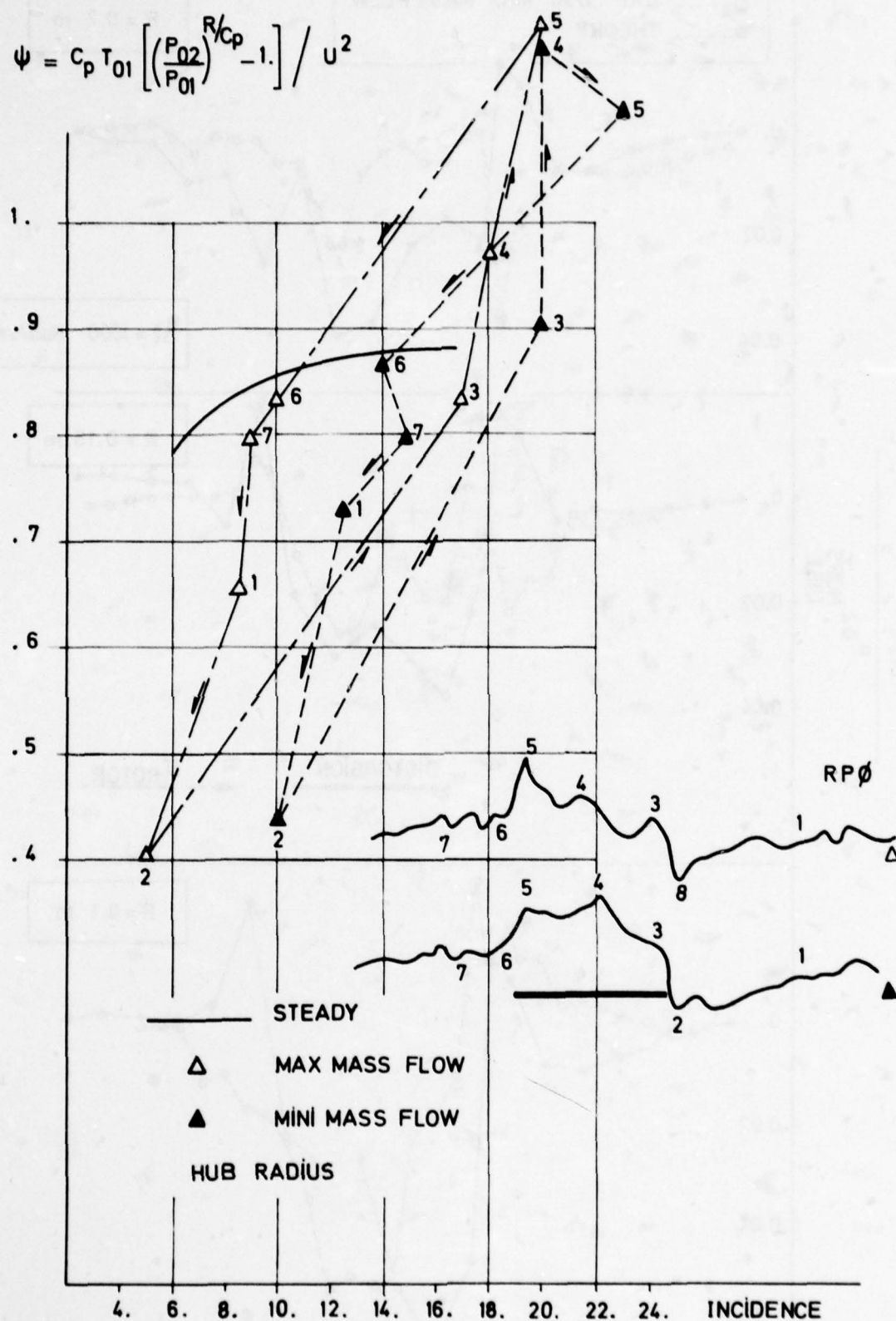


Fig.9 Unsteady blade characteristics $\psi = \psi_{(i)}$

Fig. 10 Unsteady blade characteristics $\psi = \psi(i)$

Fig.11 Unsteady blade characteristics $\psi = \psi(i)$

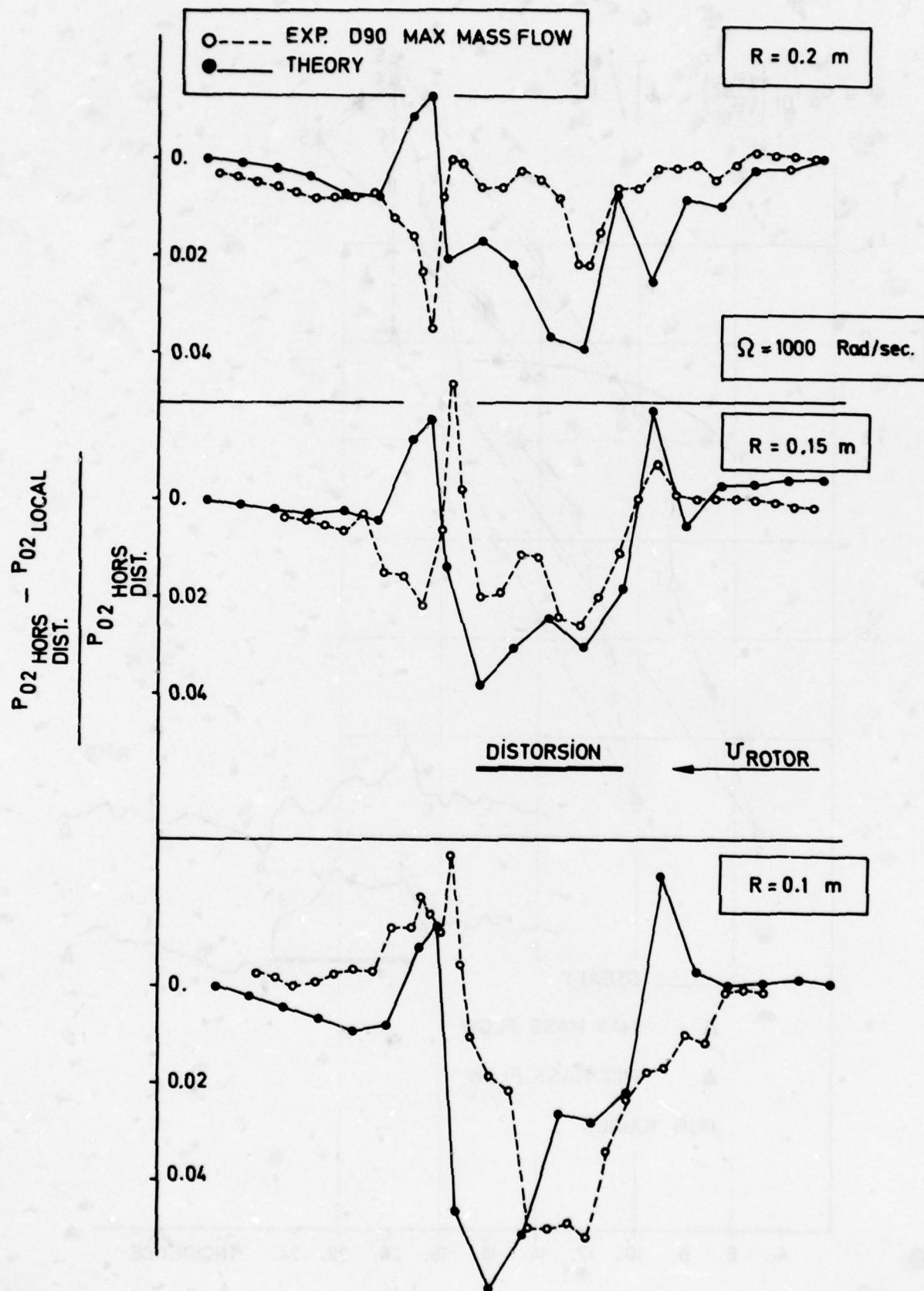
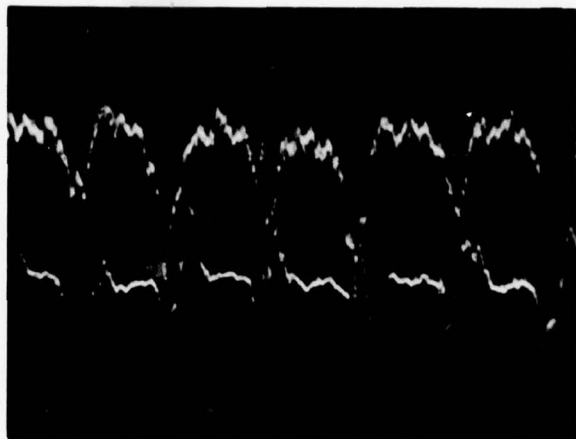
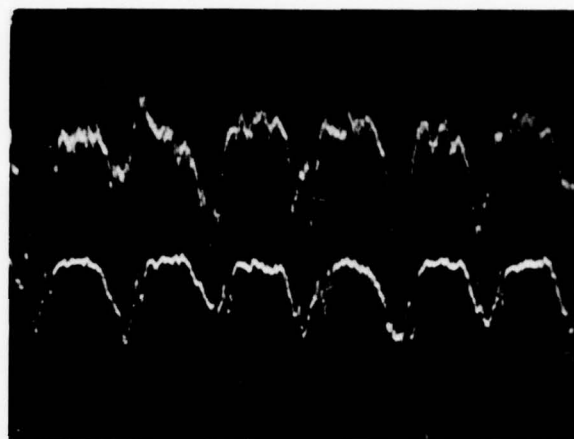


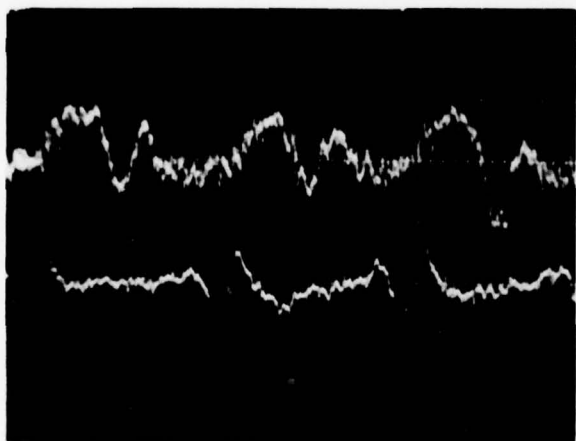
Fig.12 Compressor total pressure prediction downstream the rotor



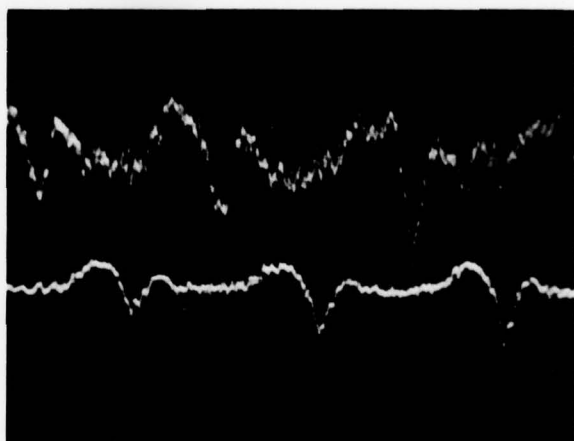
2 CELLULES
N 6300
 $V_C: 56\%$
VANNE 200



2 CELLULES
N 6750
 $V_C: 56\%$
VANNE 200



1 CELLULE
N 6400
 $V_C: 63\%$
VANNE 255



1 CELLULE
N 6750
 $V_C: 61\%$
VANNE 255

Fig.13 Rotating stall without distortion

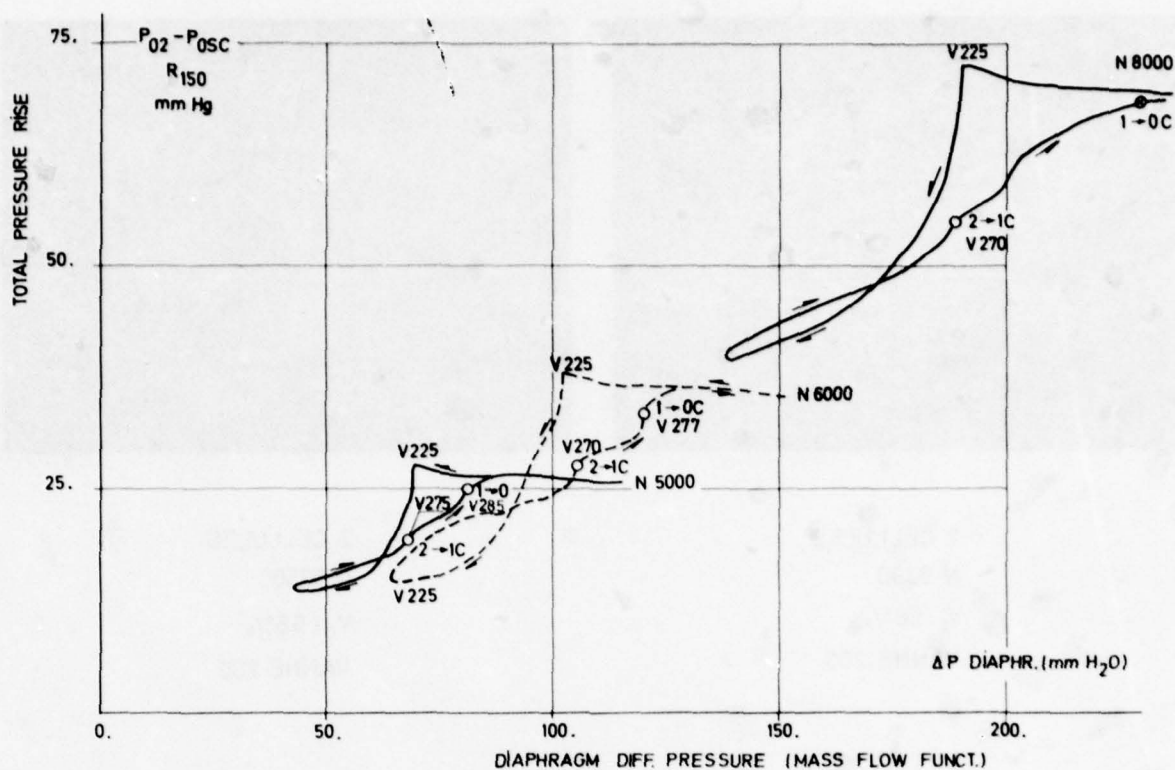


Fig. 14 Rotating stall hysteresis

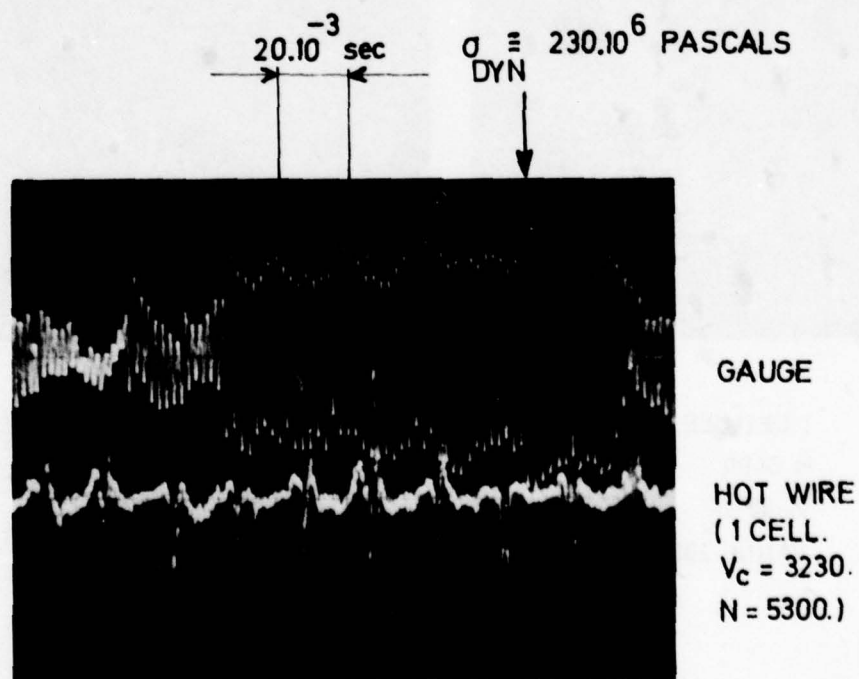


Fig. 15 Rotating stall and blade vibrations

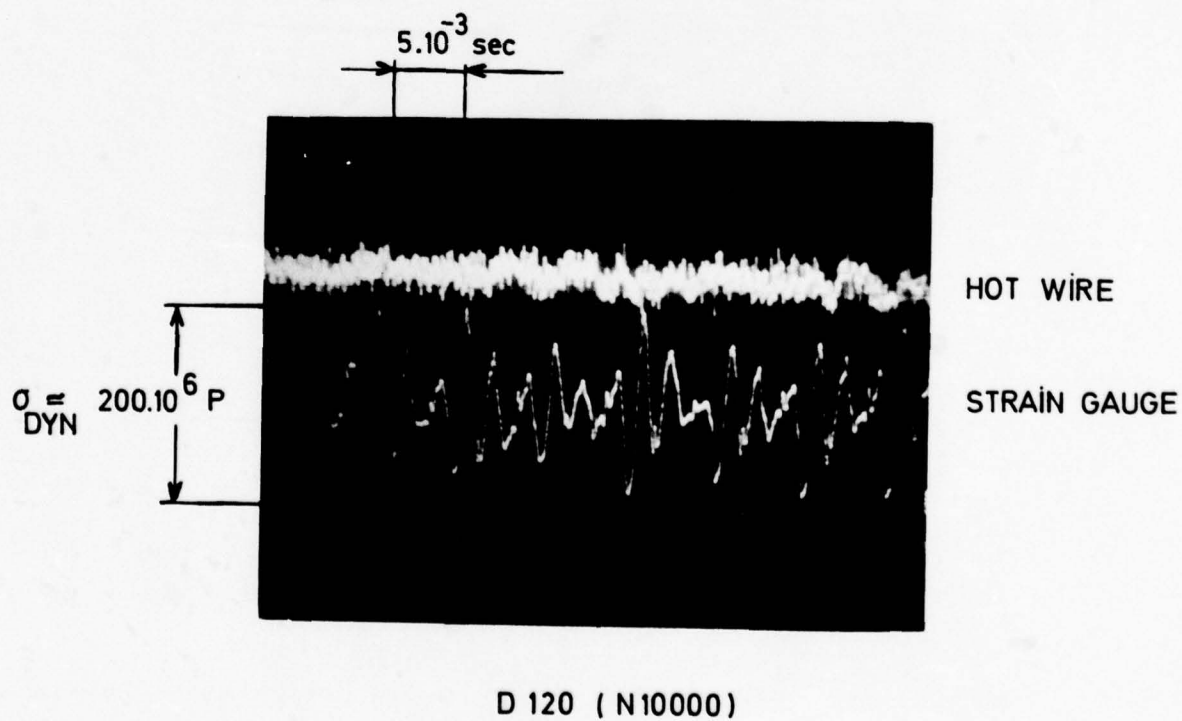
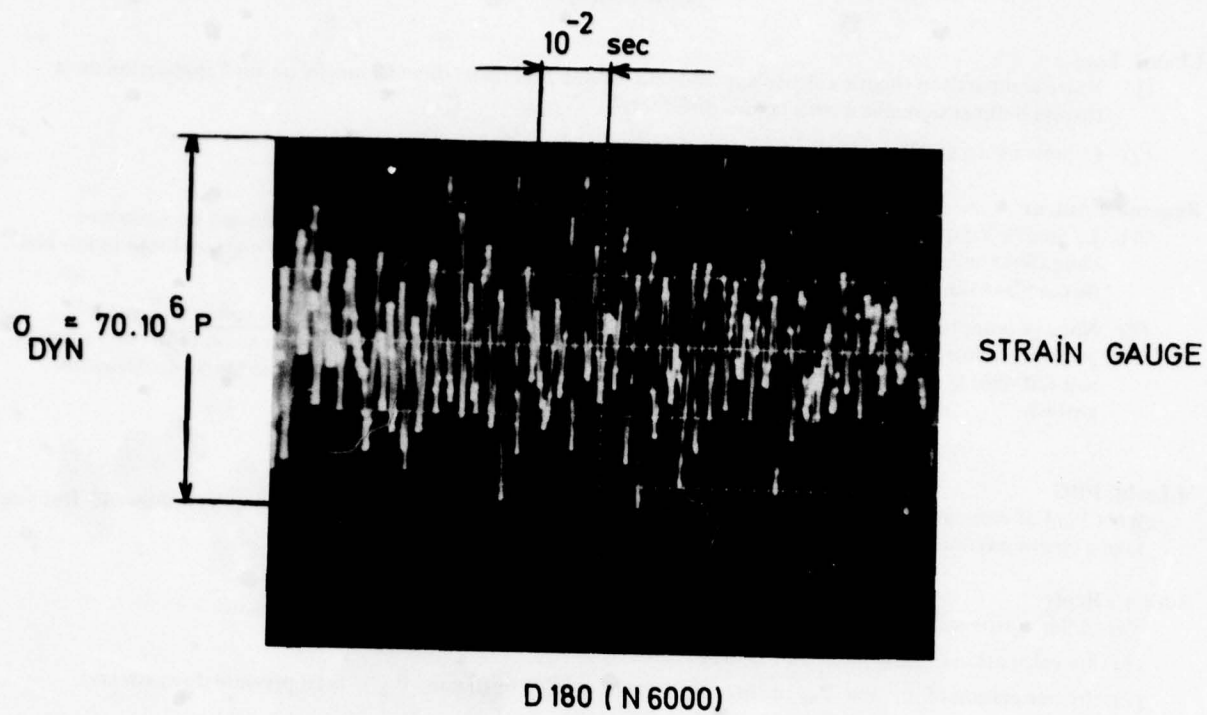


Fig. 16 Distortion and blade vibrations

DISCUSSION

J.Fabri, France

- (1) Votre comparaison théorie-calcul s'appuie-t-elle sur une théorie tri-dimensionnelle ou sur l'application de la théorie bidimensionnelle à trois rayons différents?
- (2) Comptez-vous établir ultérieurement une théorie tri-dimensionnelle?

Reponse d'Auteur

- (1) Le modèle est quasi-tridimensionnel. Les effets d'écoulements radiaux sont négligés devant les variations circumférentielles. Nous "superposons" donc 3 calculs 2-D à 3 rayons différents avec une condition limite aval de couplage sur la pression statique.
- (2) Nous ne comptons pas développer un modèle complètement tridimensionnel, ayant la conviction que le problème pourra déjà être traité très correctement en suivant notre approche, pourvu qu'un effort de recherche soit fait dans le domaine des fonctions de transfert, instationnaires des rangées d'aubes (angle de déviation, pertes).

M.Lecht, FRG

What kind of correlation did you use in getting the unsteady characteristics ψ over incidence you showed? Did you take a circumferential shift into account?

Author's Reply

Yes. I link upstream and downstream flows:

- (1) by calculation of flow mean part through rotor
- (2) by correlation of β_1 and P_{02} profiles (β_1 — relative angle upstream; P_{02} — total pressure downstream).

ÉTUDE DES INSTABILITÉS AÉROÉLASTIQUES DES COMPRESSEURS EN SOUFFLERIE DE GRILLE RECTILIGNE D'AUBES

par Edmond Szechenyi, Henri Loiseau et Brigitte Maquennehan*

*Office National d'Etudes et de Recherches Aéronautiques (ONERA)
92320 Châtillon (France)*

* SNECMA (Centre d'Etudes de Villaroche)

Résumé

La plupart des instabilités aéroélastiques rencontrées dans les turbomachines, en particulier sur le premier étage des compresseurs, se produisent dans des conditions d'écoulement que l'on ne sait pas calculer à l'aide de la théorie seule. La nature même de ces instabilités n'est pas toujours connue, et les essais en soufflerie de grille rectiligne d'aubes permettent, en premier lieu, de comprendre le mécanisme physique des phénomènes observés dans les compresseurs. Les résultats expérimentaux sont ensuite utilisés pour élaborer des modèles mathématiques qui servent à effectuer des calculs de prévision.

Une nouvelle soufflerie de grille rectiligne d'aubes a été mise en service à l'ONERA (Etablissement de Modane) en mars 1977. Elle permet de simuler les écoulements subsoniques et transsoniques jusqu'au voisinage de Mach 1, avec des incidences atteignant 12 degrés, et, en supersonique, à des nombres de Mach fixes grâce à des tuyères interchangeables.

Les premiers essais, dans cette installation, mettent en évidence plusieurs types de flottement. L'étude paramétrique, dont on donne les premiers résultats, montre l'influence de la fréquence réduite, de l'incidence, de la position de l'axe de tangage et du nombre de Mach. Quelques résultats obtenus en supersonique sont également donnés.

STUDY IN A STRAIGHT CASCADE WIND TUNNEL OF AEROELASTIC INSTABILITIES IN COMPRESSORS

Abstract

Most of the aeroelastic instabilities encountered in turbomachines, in particular in compressor first stages, occur in flow conditions that can not be calculated on purely theoretical bases. The very nature of these instabilities is not always known, and tests in a straight cascade wind tunnel should make it possible, first, to understand the physical mechanisms of phenomena observed in compressors. The experimental results would then be used to develop mathematical models to be used for prediction calculations.

A new straight cascade wind tunnel entered into service at the ONERA Modane Test Centre in March 1977. It permits the simulation of subsonic and transonic flows up to very close to Mach 1 with angles of attack reaching 12 degrees, and of supersonic flows at fixed Mach numbers thanks to interchangeable nozzles.

The first tests in this facility brought to light several kinds of flutter. The parametric study, of which the paper gives the first results, shows the influence of reduced frequency, incidence, pitch axis position and Mach number. A few results obtained in supersonic regime are also given.

Introduction.

L'étude expérimentale des phénomènes aérodynamiques dans les compresseurs eux-mêmes, ou sur des machines simplifiées simulant les grilles annulaires, se heurte à des difficultés pratiquement insurmontables. Les montages en grille rectiligne, bien que criticables à certains points de vue (1) sont moins difficiles à réaliser. Ils sont très utilisés en aérodynamique stationnaire. En installation, les couplages entre les aubes et les réflexions sur les parois sont très différents de ceux qui existent dans les grilles annulaires. Les effets tridimensionnels ne sont pas représentés. Cependant, si on construit des grilles comportant un assez grand nombre d'aubes, de manière à diminuer les effets de parois et à se rapprocher de la grille de longueur infinie, il est possible d'étudier très correctement les phénomènes localisés qui représentent une grande partie des instabilités rencontrées dans la pratique, flottement de décrochage par exemple, et que l'on ne sait pas étudier sur le plan théorique.

La soufflerie de grille rectiligne, mise en service à l'ONERA (Centre de Modane), en Mars 1977, simule d'aussi près que possible, les conditions dans les machines réelles étudiées : taux de compression (ou incidence), nombre de Mach et fréquence réduite. Au cours de cette communication, cette installation sera décrite, ainsi que les méthodes de mesure. Quelques résultats d'essais seront présentés montrant le caractère des instabilités aéroélastiques en écoulement sub et transsonique. L'application des résultats au compresseur sera évoquée. Tout d'abord la nature des problèmes de stabilité aéroélastique qui se manifestent dans les compresseurs sera rappelée.

Généralités.

Nature des vibrations dans les turbomachines.

Il y a deux catégories principales de vibration : celles qui sont dues à la nature oscillatoire des écoulements et celles qui résultent de couplages entre l'écoulement et le mouvement des aubes. Les premières sont du type "oscillations forcées"; les forces qui les provoquent sont entièrement indépendantes du mouvement des aubes et elles existent au sein même du fluide : excitations à des fréquences multiples de la vitesse de rotation, décollement tourment, pompage, etc... Les secondes, qui seules font l'objet de

la présente étude, sont dues à des forces, agissant sur les aubes, et qui sont provoquées par leur propre mouvement. Ces instabilités aérodynamiques se classent en trois types principaux (voir la figure 1) :

- le flottement de décrochage, (zone 1)
- les flottements supersoniques, (zone 2)
- les flottements de blocage. (zone 3)

Le premier type de flottement se produit en écoulement sub ou transsonique, quand on augmente le vannage, c'est-à-dire l'incidence, à l'approche de la ligne de pompage. Comme son nom l'indique, il est dû à des phénomènes de décollement de la couche limite sur l'extrados des aubes.

Le flottement supersonique se manifeste en régime élevé de rotation, pour des nombres de Mach nettement supersoniques (jusqu'à 1,6). Le débit reste sensiblement constant. L'incidence est faible et ne semble pas avoir beaucoup d'importance dans le mécanisme de cette instabilité.

Le flottement de blocage apparaît en régime dévanné. L'écoulement est sub ou transsonique. L'incidence est faible ou négative. Il existe surtout dans les redresseurs, alors que les deux premiers affectent les roues mobiles (premier étage).

Les deux derniers types sont caractérisés par la présence d'un choc intérieur au canal interaube. Les déplacements vibratoires des chocs et des aubes sont synchrones, avec un déphasage qui conditionne la stabilité. Ils sont prévus par la théorie (1). Mais les interactions entre la couche limite et les ondes de choc, qu'aucune théorie ne prend en compte, peuvent les accentuer ou les affaiblir.

Il semble actuellement que le flottement de décrochage soit le plus répandu dans les compresseurs. Ceci explique l'effort fait par l'ONERA pour traiter ce type de problème.

Notations.

L	: envergure d'une aube,
M	: nombre de Mach,
M_θ	: coefficient aérodynamique instationnaire du moment résultant sur une aube,
P_t	: pression génératrice de la soufflerie,
S	: surface portante d'une aube,
V	: vitesse de l'écoulement (m/sec)
c	: corde d'une aube,
m_θ	: coefficient aérodynamique instationnaire du moment résultant mesuré en grille rectiligne (bidimensionnel),
α	: angle de calage,
β	: angle de déviation,
θ	: amplitude de vibration angulaire,
ϕ	: angle de phase mesuré en soufflerie,
Φ	: angle de phase relative du moment résultant (par rapport au mouvement vibratoire d'une aube de compresseur)
$\psi(x)$: déformée d'une aube,
ω	: fréquence angulaire,
ω_R	: fréquence réduite ($\omega c/2V$).

Moyens et méthodes d'essais.

Méthodes.

- Mesure des pressions instationnaires :

Les efforts instationnaires sont mesurés au moyen de capteurs de pression. Ceux-ci (20 à 25) sont répartis régulièrement selon la corde, côté extrados et côté intrados. Les membranes sensibles de ces capteurs, montés à l'intérieur de la maquette, sont situées à quelques dixièmes de millimètre seulement des prises de pression, de façon à ne pas commettre d'erreurs sur le déphasage ou le module de la pression dans le domaine des fréquences considérées (inférieures à 700 Hz). Les capteurs utilisés sont du type Kulite. Ils sont, soit cylindriques, quand l'épaisseur de la maquette est assez grande, soit plats (épaisseur maximale : 0,5 mm). Les figures 2a et 2b montrent comment ces capteurs sont disposés dans l'un et l'autre cas. Les réponses accélérométriques ne sont pas négligeables : cette correction est faite pendant les mesures mêmes. Si l'aube se déforme en oscillant, un découplage du capteur est nécessaire afin qu'il ne soit pas sensible aux contraintes locales.

- Mesure des pressions stationnaires :

Toutes les tentatives pour mesurer les pressions stationnaires en même temps que les pressions instationnaires, c'est-à-dire avec les mêmes capteurs, ont montré que la précision n'était pas suffisante, sauf dans certains cas particuliers, en raison des dérives dues aux variations de température. Les systèmes de compensation thermique diminuent l'erreur mais pas assez pour avoir une bonne précision. Un système a été proposé récemment (2) mais n'a pas encore été essayé. Il est donc préférable d'utiliser une aube fabriquée spécialement pour les mesures de pression stationnaire, en utilisant la méthode classique du scanning-valve.

- Mesure des forces et moments instationnaires:

Les forces et moments agissant sur toute l'aube sont obtenues soit en intégrant les pressions, soit en mesurant les variations des fréquences et des amortissements.

L'intégrale des pressions se fait en temps réel. La valeur donnée par chaque capteur est affectée d'un coefficient de pondération individuel qui tient compte, d'une part, de la surface intéressée par le capteur et, d'autre part, de la distance à l'axe de référence, pour le calcul des moments.

L'aube est montée sur rappel élastique qui lui impose une fréquence de résonance et un amortissement que l'on mesure sans vent. Les variations avec vent sont proportionnelles aux forces et moments globaux.

Ces deux méthodes de mesure, entièrement indépendantes, donnent les mêmes résultats si l'écoulement est bidimensionnel. Lorsque l'incidence croît, les écoulements secondaires, qui prennent naissance au voisinage des parois, aux extrémités des aubes, ne doivent intéresser qu'une faible partie de l'envergure. Il y a lieu de s'en assurer, et le moyen le plus simple pour cela est de comparer les résultats donnés par les deux méthodes de mesure. Dans le cas où le désaccord est important, il faut agir sur les réglages de la soufflerie.

- Soufflerie : (figure 3)

a) Principales caractéristiques.

La soufflerie a été conçue pour l'étude des flottements subtrans et supersoniques. Elle est implantée au centre de Modane-Avrieux où sont situées les grandes souffleries de l'ONERA. Elle consiste en une grille rectiligne de 6 à 10 aubes (selon le pas relatif). Les deux aubes centrales peuvent être mises en vibration à des fréquences situées entre 50 et 600 Hz environ. Les mouvements d'oscillation s'effectuent soit en tangage autour d'un axe quelconque, soit en translation (pompage).

L'angle de calage possible (front de grille par rapport au plan moyen tangent au bord d'attaque des aubes) va de 15 à 60 degrés. L'angle du front de grille par rapport à la direction de la vitesse à l'infini amont peut aller de 10 à 75 degrés. L'incidence (plan moyen tangent au bord d'attaque des aubes par rapport à la direction de la vitesse à l'infini amont) est réglable de -5 à 15 degrés, par rotation d'ensemble de la grille. Le calage n'est donc pas modifié par cette variation de l'incidence.

La veine transsonique permet des nombres de Mach situés entre 0,4 et 1,0. La pression génératrice va de 1 à 2,5 bars. La première veine supersonique a été conçue pour Mach 1,45 et elle admet une pression génératrice de 4 bars.

La longueur de la grille est de 600 mm et sa largeur (envergure des aubes) est de 120 mm.

b) Fonctionnement.

La soufflerie est alimentée par de l'air sous pression contenue dans des sphères, elles-mêmes alimentées par un compresseur puissant. Cette soufflerie à rafales est pratiquement une soufflerie continue en sub et transsonique, car le compresseur maintient la pression dans les sphères à un niveau suffisant pendant des souffles de plus d'une heure.

La périodicité de l'écoulement dans les canaux de la grille est contrôlée au moyen de 30 prises de pression situées sur la paroi au voisinage de la grille (amont et aval). Cette périodicité est obtenue en réglant les volets à l'aval. Le temps de réglage est de l'ordre de 2 minutes. Des exemples de la périodicité sont donnés par la figure 4 qui permet de se faire une idée de la qualité du réglage à Mach et incidences élevées.

Les dispositifs de fixation, de suspension et d'excitation des aubes sont placés de façon à pouvoir visualiser et sonder par voie optique (strioscopie, ombroscopie, vélocimétrie laser) la totalité du canal interaube central. Les phénomènes instationnaires sont enregistrés par un système strioscopique ou ombroscopique à étincelles (exemple : figure 5).

- Grilles :

a) Montage des aubes :

Les mesures sont effectuées sur aube fixe (valeurs stationnaires) et sur aube vibrante excitée à l'une ou l'autre des fréquences de résonance imposées par les dispositifs de suspension. Ces dispositifs, identiques aux deux extrémités de l'aube, sont encastrés sur deux blocs reliés à la soufflerie par des ressorts de faible rigidité. Ces ressorts filtrent les vibrations propres de la soufflerie et permettent les dilatations de l'aube sans engendrer de précontraintes gênantes.

Ce découplage peut être supprimé si l'on effectue des mesures de pression, ou si l'on ne désire obtenir que la partie imaginaire des forces et moments globaux. En effet, pour que les pressions instationnaires soient valables, il suffit de connaître avec précision le mouvement de l'aube aux points de mesure. Ceci est possible à condition que les fréquences de résonance soient éloignées les unes des autres et, donc, que les modes propres soient peu sensibles à de légères variations des conditions d'encastrement. Ces modes propres sont, ainsi, connus dans le vent à partir des essais de vibration sans vent et la mesure de l'amplitude aux points d'excitation suffit pour connaître l'amplitude en n'importe quel autre point. D'autre part, les forces et moments globaux imaginaires, c'est-à-dire en phase avec la vitesse de vibration, sont calculés en faisant la différence entre l'amortissement avec vent et l'amortissement sans vent. Ce dernier est toujours très petit par rapport au premier. Il varie peu en fonction des conditions d'encastrement et la mesure reste précise.

b) Excitation des aubes :

Elle est faite à l'aide de 4 excitateurs, dont deux sont visibles sur la figure 6. Ces excitateurs sont couplés mécaniquement à des capteurs qui mesurent la vitesse de vibration au point exact d'application de la force sinusoïdale. Dans ces conditions, il est facile, par asservissement, de créer un amortissement artificiel de valeur suffisante pour contrer les amortissements aérodynamiques négatifs. On évite ainsi des instabilités destructrices, et l'on peut effectuer des mesures à l'intérieur des domaines de flottement.

- Acquisition et dépouillement :

Les signaux analogiques des pressions, de la portance et du moment instantanés (calculés en temps réel par sommation des pressions) sont enregistrés, après filtrage, sous forme numérique, au moyen d'un échantillonneur bloqueur et d'un multiplexeur. Ainsi, 64 voies peuvent être sondées simultanément à une cadence totale de 120 KHz environ.

Le dépouillement est fait, soit en temps quasi-réel, soit en temps différé, au moyen d'un ordinateur HP 2100 associé à un système de Fourier.

Les résultats sont obtenus sous forme de module et phase (par rapport au mouvement de vibration des aubes). Le cas échéant, tous les harmoniques peuvent être obtenus jusqu'à la fréquence maximale de calcul. Cette fréquence dépend de la fréquence d'échantillonnage employée à l'enregistrement.

- Définition du domaine d'écoulement à simuler :

Le domaine à étudier est déterminé d'après les résultats des essais qui sont effectués sur compresseur chez le constructeur.

Les mesures sont faites par deux méthodes différentes :

a) sondes optiques :

Elles donnent les fréquences et amplitudes de vibration de l'ensemble des aubes à la limite du domaine d'instabilité.

b) Jauges de contrainte :

Quelques aubes seulement peuvent être équipées. Mais cela permet de connaître les amortissements de tous les modes propres des aubes sur tout le chemin parcouru dans le diagramme pression-débit, par analyse de la réponse à la turbulence.

Exemples de résultats obtenus à l'occasion d'essais pour un compresseur MC 1.

- Essais sur le compresseur :

Une zone de flottement de décrochage assez étendue (zone 1 sur la figure 1) apparaît entre la ligne de fonctionnement nominale et la ligne de pompage. Les nombres de Mach, à la frontière de ce domaine d'instabilité, vont de 0,75 à 0,95, avec des incidences entre 6 et 15 degrés environ. Les Mach et incidences considérés sont ceux de la coupe de tête de l'aubage du premier étage, pour des raisons qui seront exposées plus loin.

La figure 7 montre un spectre de la réponse à la turbulence, à l'approche du flottement. L'analyse de ce spectre montre que l'amortissement diminue et l'on peut ainsi prévoir le flottement avant l'apparition des vibrations.

Dans ce spectre, il faut distinguer les raies qui sont dues à des réponses vibratoires à des fréquences multiples de la vitesse de rotation (les plus fines) des raies qui sont dues à des réponses vibratoires des aubes sur leurs fréquences propres, excitées par la turbulence (raies plus larges). Il faut, pour que l'analyse soit valable, que ces dernières soient nettement séparées des premières, c'est-à-dire que les vitesses de rotation soient choisies au cours même de l'essai.

- Essais en grille :

Les résultats présentés concernent un mouvement vibratoire de tangage autour de la mi-corde de l'aube, à des fréquences, nombres de Mach et incidences variables. Les mesures donnent le module du coefficient aérodynamique instantané de moment m_θ ($m_\theta = \frac{\text{Moment}}{1/2 \rho v^2 b \pi s c/2}$), et sa phase par rapport à la force de rappel mécanique (c'est-à-dire par rapport à l'accélération angulaire). Dans ce repère, si θ est compris entre 180 et 360 degrés, l'aube est instable (amortissement aérodynamique négatif.).

Les pressions sont mesurées séparément du côté de l'extrados et du côté de l'intrados. A l'intrados, les valeurs sont peu différentes de celles qui existent, à incidence nulle ou faible, c'est-à-dire des valeurs théoriques calculées en fluide parfait, quel que soit le braquage de l'aube. C'est donc du côté de l'extrados que la connaissance de la répartition des pressions est la plus importante et il ne sera question dans ce texte que des mesures à l'extrados.

Le coefficient de pression K_p ($K_p = \frac{\text{Pression}}{1/2 \rho v^2}$) est évalué de la même manière que le coefficient global du moment m_θ , en module ($|K_p|$) et en phase avec les mêmes références.

a) Influence de la fréquence : (figures 8 et 9)

À très basse fréquence, le module de m_θ est donné par l'intégrale de la différence des pressions stationnaires aux positions extrêmes que prend l'aube au cours de l'oscillation. Quand il y a décollement, les répartitions de pression sont très différentes de celles qui existent à incidence nulle ou faible, et le coefficient m_θ est très différent de celui calculé par la théorie linéaire, $m_{\theta l}$. On pourrait s'attendre, néanmoins, à ce que sa valeur se rapproche de $m_{\theta l}$ quand la fréquence augmente. Il n'en est rien,

au contraire : m_θ croît fortement avec la fréquence, comme le montre la figure 8. Cependant, la variation de la phase est telle que l'amortissement aérodynamique devient positif au-dessus d'une certaine valeur de la fréquence réduite, et ceci quel que soit le nombre de Mach ou l'incidence.

On voit, sur la figure 9, les répartitions de pression correspondant aux résultats globaux de la figure précédente. Au cours de l'intégration des pressions, pour avoir le moment par rapport à l'axe de tangage, les valeurs dans les quadrants 2 et 4 donnent des résultats négatifs, et celles des quadrants 1 et 3, des résultats positifs. On constate que l'instabilité, lorsqu'elle existe, est principalement due aux pressions vers le bord d'attaque. On remarque que le module des pressions, $|K_p|$, est très différent, selon la corde, des valeurs théoriques calculées sans décollement.

A noter aussi que la fréquence joue peu sur le niveau des pressions. L'influence importante sur le couple (m_θ) provient essentiellement des différences de phase.

b) Influence de l'incidence (figures 10 et 11) :

Le module de m_θ a une évolution rapide à partir d'une incidence de 2 degrés. Il passe par un maximum très marqué vers 5 degrés, puis il décroît jusqu'à 6 degrés. Ce domaine d'incidence correspond à l'apparition du décollement qui s'étend progressivement sur toute l'aube. Ensuite, quand l'écoulement est complètement décollé, le module de m_θ varie peu en fonction de l'incidence. La phase évolue beaucoup plus régulièrement dans tout le domaine d'incidence considéré.

Il est à noter que la présence d'un choc (à Mach 0,8 par exemple), a une action importante sur la valeur de l'incidence à laquelle apparaît le décollement. Mais quand celui-ci est installé, le comportement en fonction de l'incidence est le même qu'aux vitesses faibles. Ceci peut s'expliquer par le fait qu'avec un décollement important, il n'y a plus de choc à la surface de la maquette : l'action de la couche limite l'emporte sur celle du choc.

L'instabilité apparaît à des incidences de plus en plus élevées quand la fréquence réduite augmente.

La progression de la zone décollée se voit très bien quand on regarde l'évolution des répartitions de pression (figure 11). Entre le bord d'attaque et la mi-corde, le sens de propagation des pressions va du bord d'attaque vers le bord de fuite, en l'absence de décollement, et du bord de fuite vers le bord d'attaque en présence de décollement (voir la phase en fonction de l'incidence). En même temps, le maximum du module de K_p recule du bord d'attaque vers le bord de fuite.

c) Influence du nombre de Mach (figures 12 et 13) :

Le nombre de Mach, dans certaines limites, qui dépendent de l'incidence (inférieur à 0,85 dans le cas de la figure), a peu d'influence sur le module et même sur la phase. Au delà d'une certaine valeur, quand le choc est assez fort, il y a une modification rapide du type d'écoulement : le décollement en amont du choc disparaît. En même temps, l'amortissement devient positif.

La répartition des pressions garde la même allure au-dessous de ce nombre de Mach limite. On note seulement une légère translation des courbes aussi bien sur le module que sur la phase.

Application au compresseur :

Selon certaines hypothèses, la stabilité aéroélastique des aubes du compresseur réel peut être calculée directement à partir des résultats des mesures effectuées en soufflerie de grille rectiligne. Ces hypothèses sont les suivantes :

- Bidimensionnalité de l'écoulement par tranches, c'est-à-dire tranches indépendantes et écoulements secondaires tridimensionnels négligeables,
- Couplage aérodynamique entre les aubes faible par rapport aux phénomènes localisés.

Dans le cas du flottement de décrochage, ces conditions sont assez bien satisfaites.

Il faut, d'autre part, connaître :

- L'incidence et le nombre de Mach locaux en fonction de l'envergure dans le diagramme pression-débit : ces valeurs sont calculées.
- Le ou les modes propres de vibration : ils sont calculés (seul moyen de les connaître en fonction de la vitesse de rotation). Le calcul peut être vérifié, à vitesse nulle, expérimentalement sur une aube encastrée.

Considérons, par exemple, le cas d'une aube pour laquelle l'instabilité concerne le premier mode de torsion. La partie réelle du moment des forces instationnaires est donné par :

$$M'_\theta = \frac{1}{L} \int_0^L m_\theta(x) \cos \phi(x) \psi^2(x) dx$$

et la partie imaginaire par :

$$M''_\theta = \frac{1}{L} \int_0^L m_\theta(x) \sin \phi(x) \psi^2(x) dx$$

d'où

$$\phi = \tan^{-1} \frac{M''_\theta}{M'_\theta}$$

L'aube est instable si ϕ est compris entre 180 et 360 degrés ($M''_\theta < 0$)

$\psi(x)$ est la déformée du mode considéré projetée sur les normales au squelette de l'aube

$\Psi(x)$ et $\Phi(x)$ ne sont pas des fonctions analytiques de x (position en envergure). Un calcul par tranche est donc effectué. On a :

$$M'_{\theta} = \frac{1}{N} \sum_{n=1}^N m_{\theta n} \cos \Phi_n \Psi^2(x_n)$$

$$M''_{\theta} = \frac{1}{N} \sum_{n=1}^N m_{\theta n} \sin \Phi_n \Psi^2(x_n)$$

avec : N : nombre de tranches quand x va de 0 à L .

En toute rigueur, il faudrait essayer en soufflerie les profils correspondant aux différentes tranches. En fait, la déformée (figure 14) ne présente de grandes amplitudes qu'au voisinage de la coupe de tête, et l'énergie introduite par les forces aérodynamiques est concentrée à 90 % vers l'extrémité de l'aube. Il peut, néanmoins, exister des cas où l'essai de deux ou trois profils serait nécessaire.

Conclusion .

La soufflerie de grille rectiligne d'aubes de l'ONERA, mise en service en Mars 1977 est opérationnelle depuis le début de 1978 en sub et transsonique. Des essais en supersonique (tuyère à Mach 1,45) seront effectués prochainement. Les méthodes de mesure des forces aérodynamiques s'appuient essentiellement sur des capteurs de pression, conçus et fabriqués en 1978 et logeables dans un profil dont l'épaisseur est inférieure à 0,6 mm. Ils ont donné d'excellents résultats.

La connaissance des répartitions de pression en module et en phase et de leur évolution en fonction de l'incidence, de la fréquence et du nombre de Mach, est nécessaire à l'élaboration d'un modèle mathématique des forces instationnaires. On constate qu'en présence d'un écoulement décollé celles-ci sont très différentes des valeurs calculées sans décollement de couche limite. Le plus souvent, elles ne sont pas du même ordre de grandeur. Il serait donc vain d'espérer obtenir de bons résultats théoriques sans prendre en compte la couche limite qui joue un rôle primordial dans le mécanisme de ces instabilités. Les résultats obtenus expérimentalement peuvent être utilisés directement pour améliorer la forme des profils ou pour connaître les meilleures conditions de calage et de pas relatif, par exemple, ce qui est déjà très important pour les constructeurs. Mais il est souhaitable que cette étude ne reste pas purement empirique, et pour cela il est nécessaire qu'un effort théorique soit porté sur l'étude de la couche limite décollée.

Références.

1. SALAUN R. - Calculs des pressions aérodynamiques instationnaires subsoniques sur des ailettes de compresseur. La Recherche Aérospatiale n° 1973-1
2. WELSH B.L. et PYNE C.R. - A method to improve the temperature stability of semiconductor strain-gauge pressure transducers. RAE Tech. Report 77155 (Octobre 1977).
3. LOISEAU H., LEPOINT G. et MAQUENNEHAN B. - Recherches exploratoires sur l'aéroélasticité des aubes des turbomachines. AGARD cnf. Proc. 177 (1976) mémoire n° 8.
4. LECLERC J. - Théorie linéarisée de l'écoulement subsonique dans une grille droite bidimensionnelle. La Recherche Aérospatiale n° 1971 - 3.
5. LOISEAU H. et NICOLAS J.R. - Forces aérodynamiques instationnaires en grille rectiligne d'aubes subsonique. IUTAM. Paris. Octobre 1976.
6. LOISEAU H. et MAQUENNEHAN B. - Instabilités aéroélastiques dans les compresseurs et essais en soufflerie de grille rectiligne d'aubes. IUTAM. Paris. Octobre 1976.

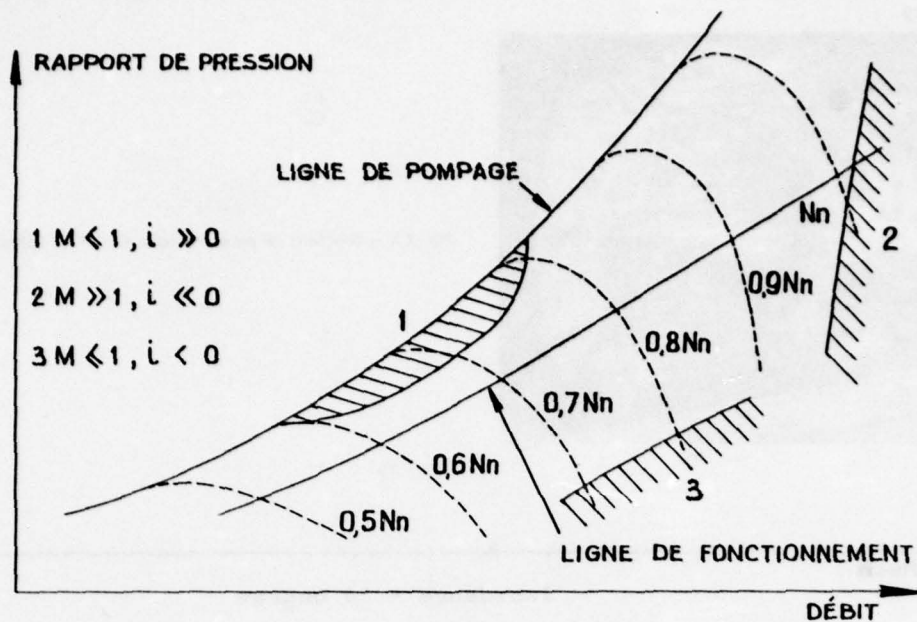


Fig. 1 - Principaux domaines de flottement rencontrés dans les compresseurs.

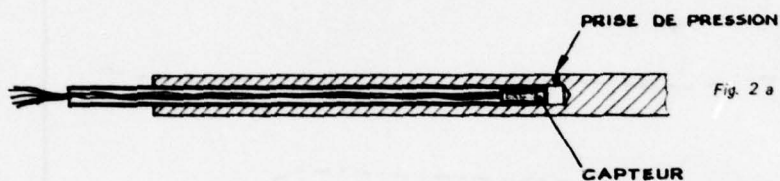


Fig. 2 a - Montage d'un capteur cylindrique.

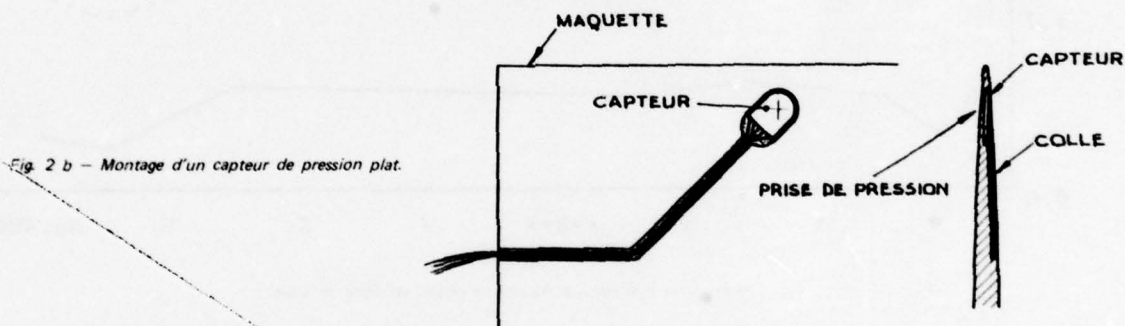


Fig. 2 b - Montage d'un capteur de pression plat.

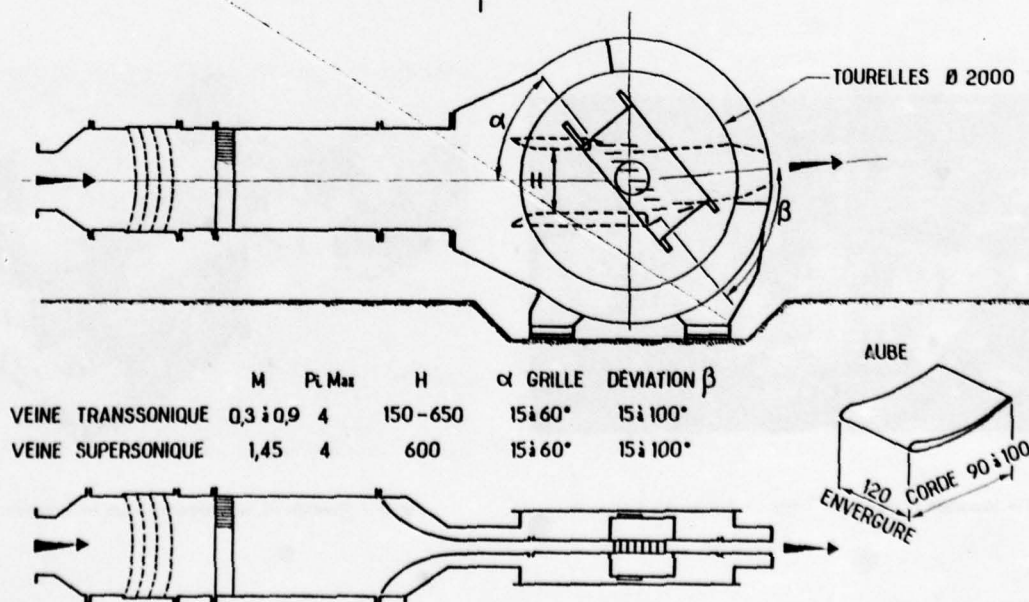


Fig. 3 A - Soufflerie de grille rectiligne d'aubes sub-trans et supersonique.

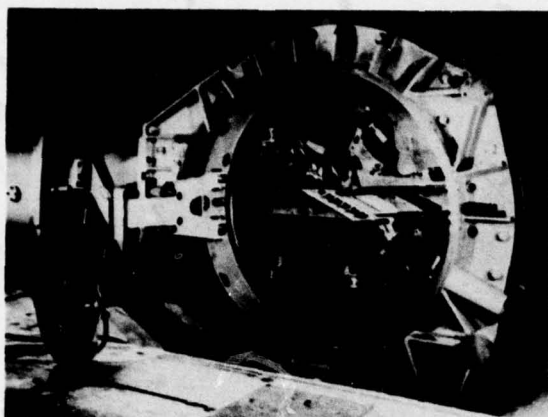


Fig. 3 b - Soufflerie de grille rectiligne d'aubes de l'ONERA.

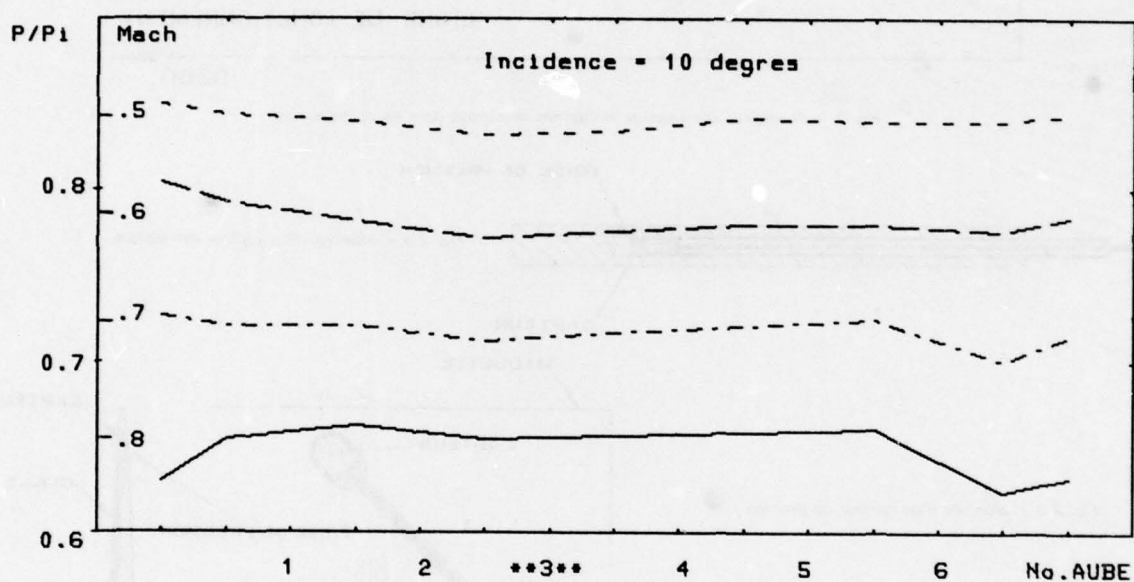


Fig. 4 - Pressions à la paroi à 90 mm en amont du front de grille.

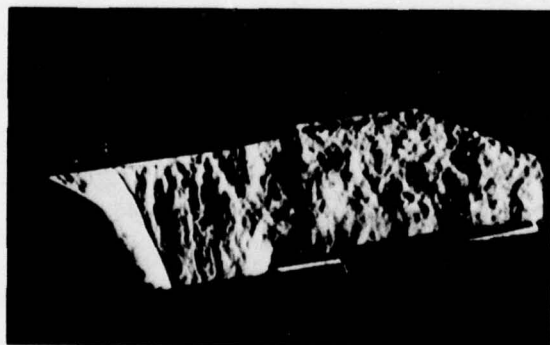


Fig. 5 - Visualisation d'un canal interaube. Strioscopie à étincelles.

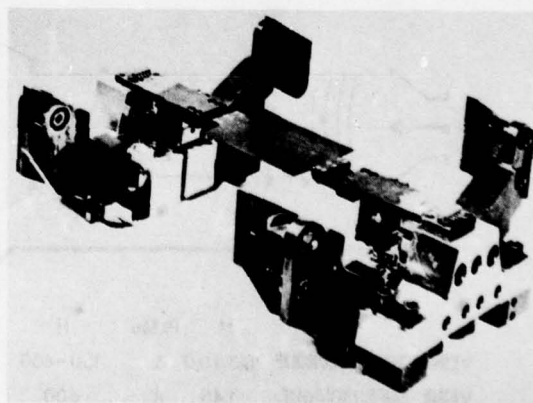


Fig. 6 - Montage du mécanisme de mise en vibration.

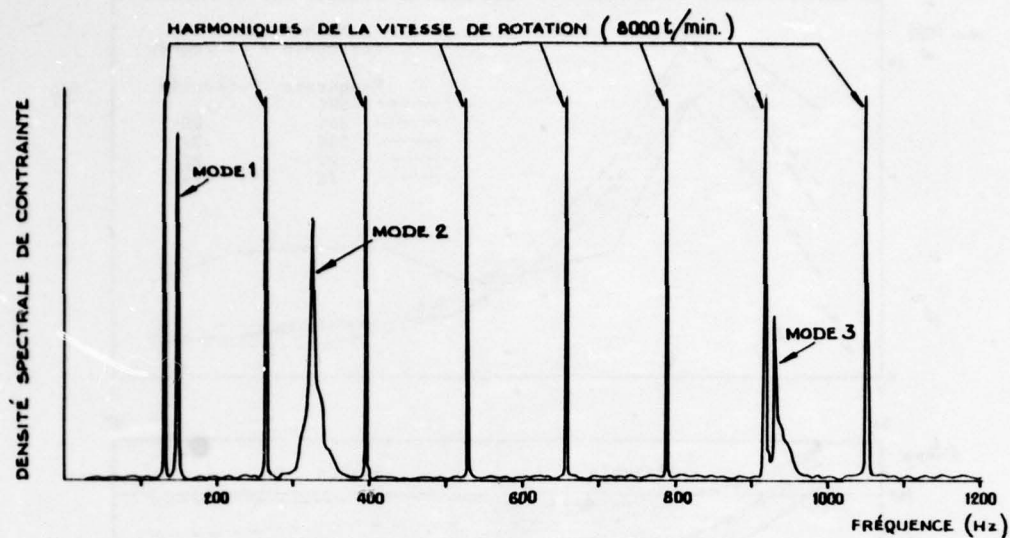


Fig. 7 — Spectre de puissance de contraintes mesurées sur une aube d'un compresseur tournant.
Excitation des modes par la turbulence.

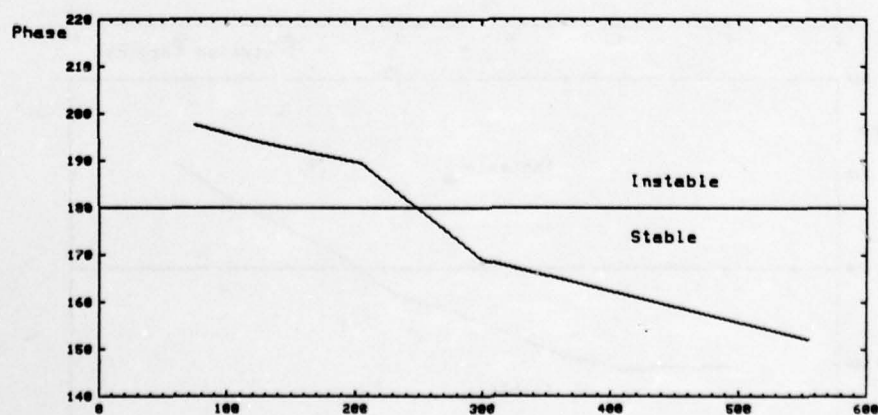
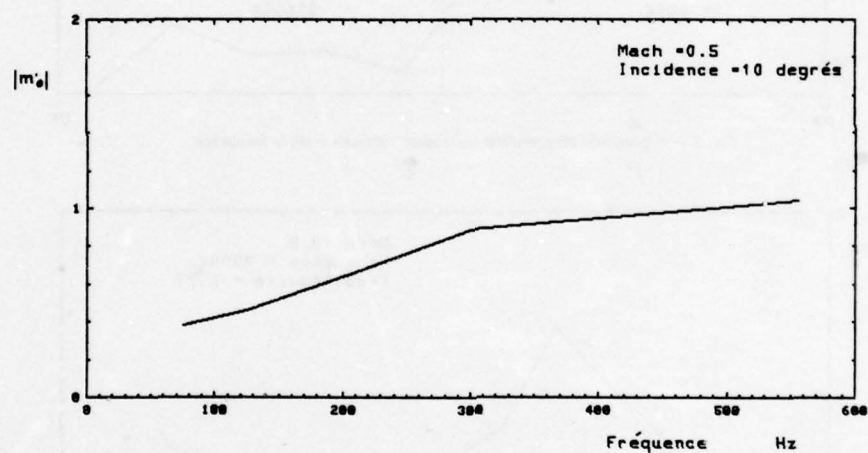


Fig. 8 — Module et phase du moment instationnaire. Influence de la fréquence.

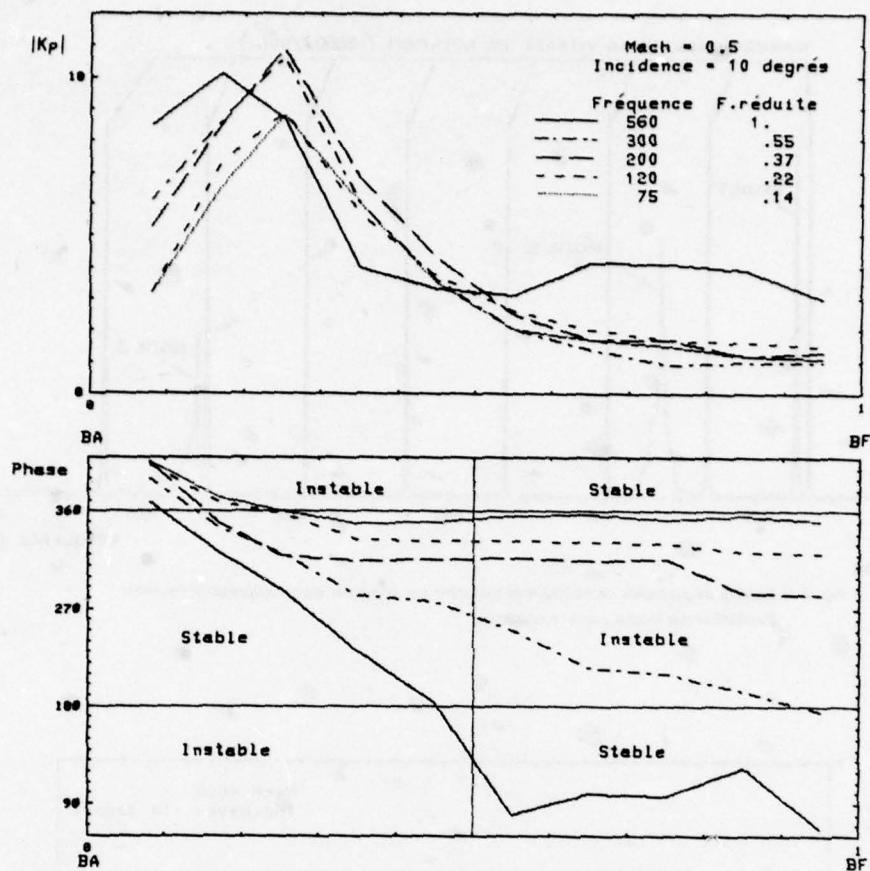


Fig. 9 - Répartition de pressions (extrados). Influence de la fréquence.

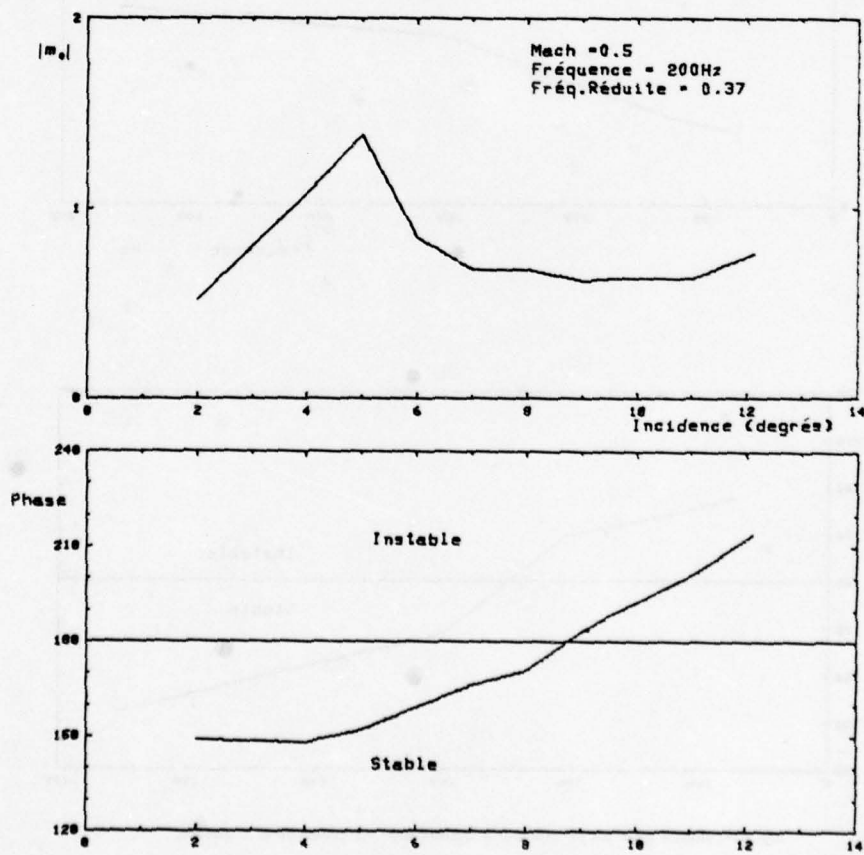


Fig. 10 - Module et phase du moment instationnaire. Influence de l'incidence.

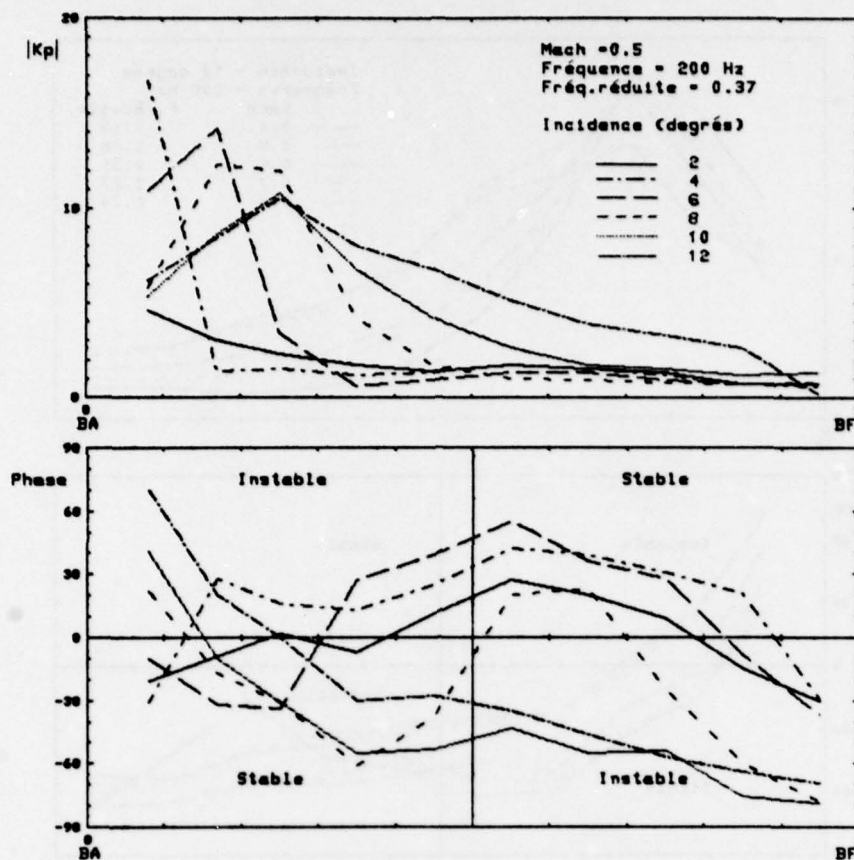


Fig. 11 - Répartition de pressions (extrados). Influence de l'incidence.

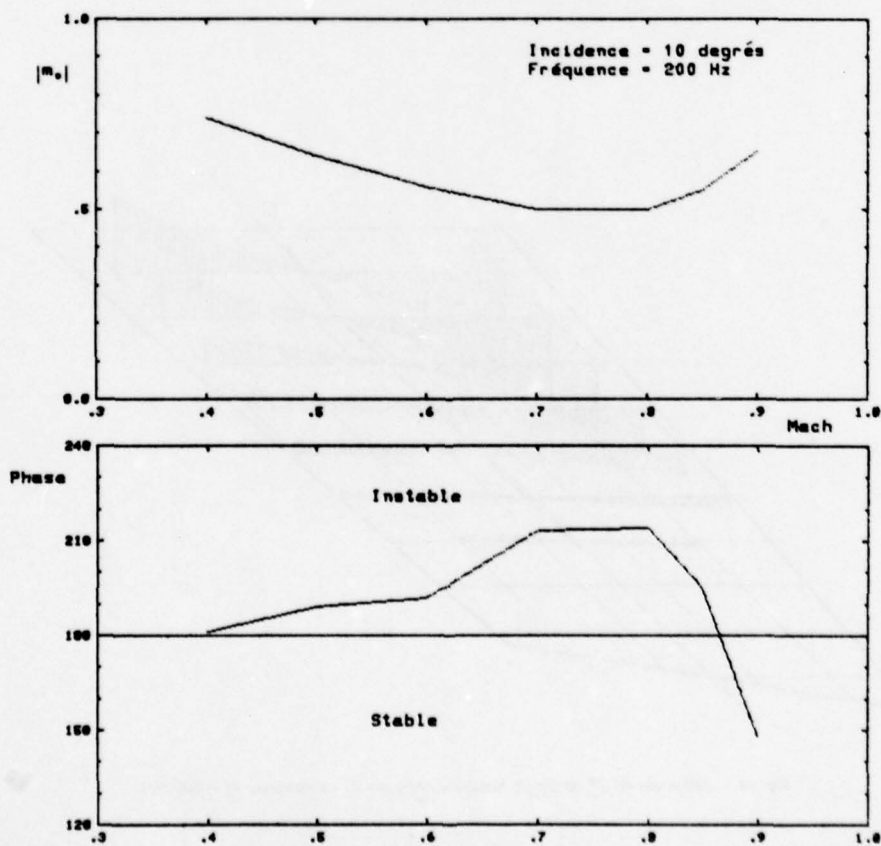


Fig. 12 - Module et phase du moment instationnaire. Influence du Mach.

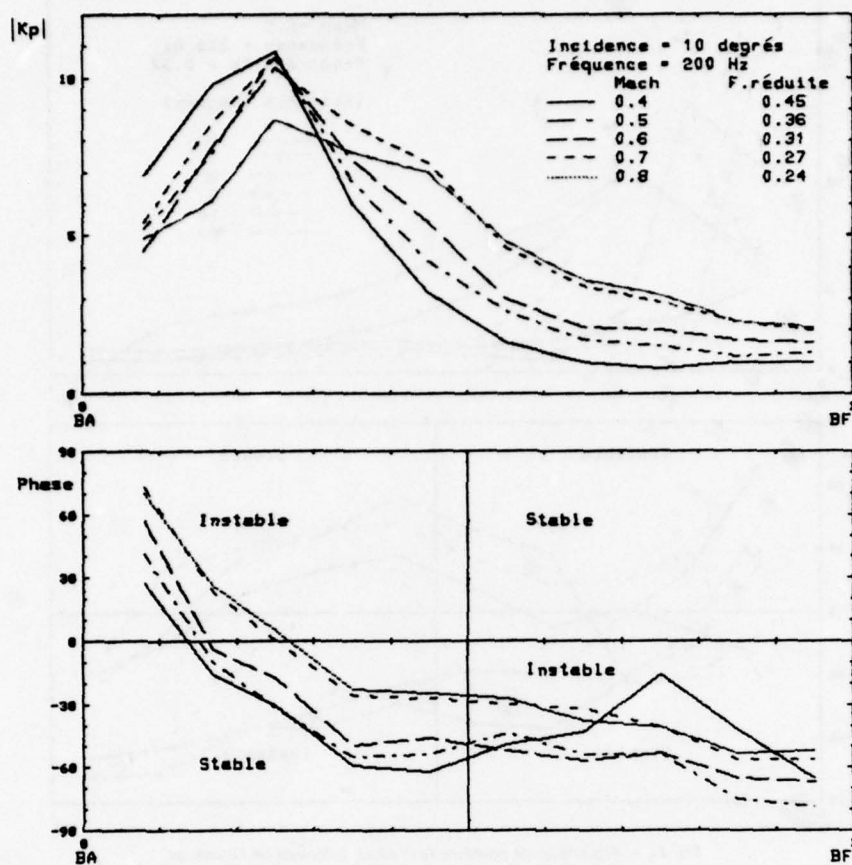


Fig. 13 — Répartition de pressions (extrados). Influence de la vitesse.

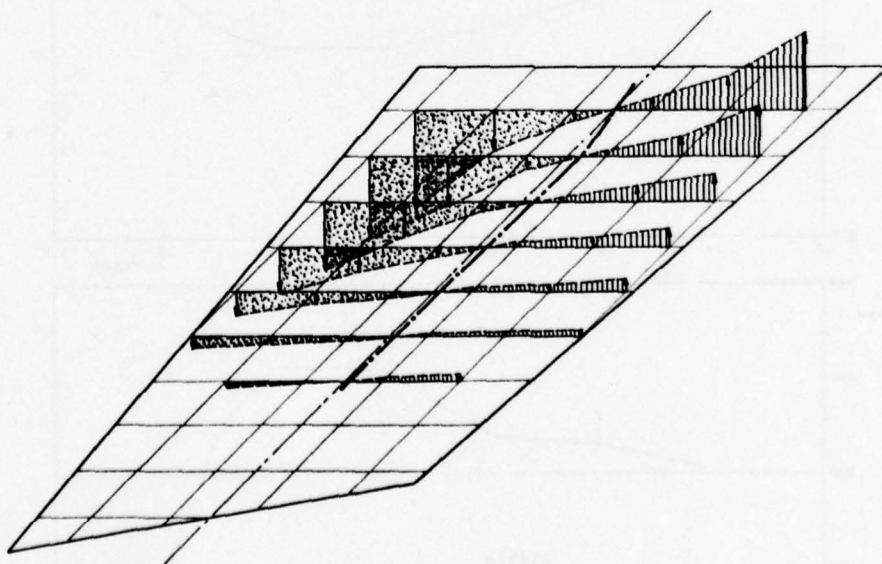


Fig. 14 — Déformée du 1^{er} mode de torsion d'une aube de compresseur ($f = 600$ Hz).

DISCUSSION

J.Colpin, Belgium

Le couplage du stall flutter et du décollement tournant au niveau des caractéristiques de l'écoulement dans cette zone. Est-ce que vous pourriez donner des commentaires, est-ce que vous découpez complètement les deux phénomènes, est-ce que vous pensez qu'il y a des interactions?

Reponse d'Auteur

Je ne pourrais pas répondre exactement à votre question. Je ne connais pas très bien les caractéristiques dans le compresseur même. Mais les essais qui ont été faits sur ce compresseur montrent bien un flottement de décrochage indépendant de tout autre phénomène et particulièrement du décollement tournant. Le décollement tournant est un phénomène assez cohérent tandis que ce phénomène là est complètement découplé. On arrive à trouver un flottement sur une seule aube, c'est-à-dire, on arrive à la limite du flottement sur une aube qui aurait peut-être un angle d'incidence un peu plus grand que les autres ou une imperfection quelconque. Les autres aubes ne commenceront à flotter que plus tard.

Il est possible évidemment qu'il existe par ailleurs un flottement bien établi dans toute la roue, qu'il y ait un couplage et peut-être un décollement tournant.

Mais le flottement de décrochage est indépendant de ces autres phénomènes.

Commentaire de J.Colpin, Belgium

Si je peux me permettre un petit commentaire, on a souvent observé du côté du décollement tournant, juste avant l'initiation de ces phénomènes, des vibrations à haute fréquence qui apparaissent juste avant l'initiation de décollement tournant. L'origine en est peut-être le stall-flutter de certaines des zones.

S.Fleeter and R.E.Riffel, US

Recognizing the many difficulties associated with obtaining valid unsteady aerodynamic data, the authors are to be congratulated for their valuable contribution. With regard to the mode shape resonance difficulties, was the high frequency mode shape measured, i.e. was the spanwise deformation of the airfoil leading edge determined at the high vibratory frequencies? What amplitudes of vibration were obtained with the drive system and was the mode shape 2-D, i.e. was the mode line truly spanwise? Also, would you please comment on your calibration procedures, in particular, the static, dynamic, and acceleration calibration procedure and the resulting corrections to the data. Was the cascade blade profiles scaled from an actual rotor section contour, i.e. same blade angles, thickness-chord ratios, etc. or were the sections modified for the lack of streamline convergence within the cascade.

Author's Reply

The blade mode shapes were determined by means of transient tests. The shapes of all the modes up to a frequency of 800 Hz were obtained. For the torsional mode in question in the paper, the spanwise nodal line is almost exactly straight (i.e. 2-D).

Calibration procedures are needed only for amplitude and unsteady pressure measurements. Standard calibrated accelerometers are used for amplitudes while the pressure transducers are calibrated by means of a moving piston type pressure reference instrument.

The linear cascades tested are directly scaled from the blade tips of actual rotors with the same profiles, blade angles and thickness to chord ratios.

REVIEW OF THE AGARD S&M PANEL EVALUATION PROGRAM OF THE
NASA-LEWIS "SRP" APPROACH TO HIGH-TEMPERATURE LCF LIFE PREDICTION.

by Marvin H. Hirschberg
NASA Lewis Research Center
Cleveland, OH 44135

SUMMARY

Twenty laboratories in six countries participated in this program, each testing its own materials of interest under its own laboratory conditions. In this way the results obtained provided validation of the Strainrange Partitioning (SRP) method for a wide range of materials and insured maximum usefulness to each of the participating laboratories. The first, very necessary step in the evaluation of any life prediction approach - assessing the ability of the method to predict life of simple laboratory specimens subjected to complex loading, was thereby taken. The culmination of this program was the Specialists Meeting that was held in Aalborg, Denmark in April of 1978. At that meeting the various investigators shared their findings, thus providing the basis for an in-depth evaluation of the SRP method. While the results were variable from laboratory to laboratory, most investigators agreed that the SRP method was a significant step toward life prediction in the presence of high temperature and cyclic stresses.

INTRODUCTION

Since advanced turbine engine materials for military applications are being used to a high fraction of their ultimate capabilities, there is a great need for more meaningful high temperature mechanical property tests on these materials as well as for improved analytical techniques for predicting their service life. One particularly vexing problem has been the difficulty in describing and predicting the behavior of materials subjected to the high temperatures and the loading conditions, such as creep-fatigue interactions, encountered in engine component service. The panel, has made an attempt to address this problem by supporting a cooperative program aimed at the evaluation of the Strainrange Partitioning (SRP) approach for the analysis and prediction of low-cycle high temperature fatigue life. This approach involves an entirely different way of dealing with creep-fatigue interaction than considered heretofore and is a product of the high temperature fatigue research conducted at the NASA Lewis Research Center.

WHAT IS SRP?

Since the early 1950's, a variety of materials characterization and life prediction techniques have been developed to fulfill the immediate needs of designers and builders of high-performance, energy-conversion equipment that must operate reliably for long periods of time at high temperatures. Although most of the approaches offered some unique advantage, they all had deficiencies of one sort or another. Also, since the early 1950's a large quantity of high temperature, low-cycle fatigue data has been generated on a host of alloys. In many instances these data were determined to answer a single specific question relative to a particular design requirement, and little regard was given to the generation of data that would have general applicability to future problems. As a consequence, the designer is faced with a choice of life prediction techniques and a vast quantity of diverse, sometimes contradictory, and often inappropriate low-cycle fatigue test data.

It was out of this environment that the SRP approach was formulated in 1971 (ref. 1). In the intervening years we have developed considerable insight into its capabilities and recognize the technological impact the approach offers in the design of components that must resist failure due to the interaction of high temperature creep and fatigue. The primary advantage of SRP rests on its high degree of generality. Relatively few test data are necessary to characterize a material in terms of SRP, and the results are applicable to complex strain cycles. Not only is the approach a general and fundamental one, but it also appears to offer better accuracy than other available methods in predicting life than has been possible heretofore (ref. 2).

REVIEW OF SRP CONCEPTS

The Lewis Research Center has long been involved in the development of theories and approaches for dealing with low-cycle fatigue behavior of materials. A most important transition from a stress approach to a strain approach occurred with the formulation of the Manson-Coffin law (ref. 3). We then went to the total strain approach with the inclusion of the elastic portion of the total strainrange (ref. 4). The Manson-Hirschberg method of universal slopes was then developed (ref. 5), which made it possible to estimate total strainrange versus life behavior from conventional short-time tensile properties. It was, of course, recognized that these approaches were all limited to temperatures below the creep limit. Our first attempts to account for creep effects were the 10 percent rule (ref. 6) and the creep-modified 10 percent rule (ref. 7). These techniques represented most of the available high temperature test data well, but they were not sufficiently conservative for cases involving long hold times or where large creep strains could be accumulated. An attempt to remedy this was made with the life fraction approach (ref. 8). Unfortunately, that method involves extensive analytical procedures and was unable to explain some of the experimental observations regarding the damaging effects of compressive stress. The next step was the formulation of the SRP method which holds promise for overcoming deficiencies in previous methods.

The basic premise for SRP is that in any hysteresis loop there are combinations of just two directions of straining and two types of inelastic strain. The two directions are, of course, tension (associated with a positive inelastic strain rate) and compression (associated with a negative inelastic strain rate); the two types of inelastic strain are time dependent (creep) and time independent (plastic). By combining the two directions with the two types of strain, we arrive at four possible kinds of strainranges that may be used as basic building blocks for any conceivable hysteresis loop. These define the manner in which a tensile component of strain is balanced by a compressive component to close a hysteresis loop. What was next proposed, was that the Manson-Coffin relationship (which represents the inelastic strainrange versus life behavior for materials below the creep limit) be expanded to four relationships for dealing with materials above the creep limit.

Once these relationships have been generated for a material, there remains the question of how to to apply them to a more complex loading problem in order to predict life. This is accomplished in two parts. First, the hysteresis loop for the cycle being analyzed must be partitioned into its inelastic components. Second, a damage rule, which we have developed and termed the interaction damage rule, is applied in order to predict the life associated with the combination of applied strainranges.

It is this total process of generating the individual failure life relationships, partitioning a hysteresis loop into its component strainranges, and combining the effects of these components to determine life, that we have called the SRP method. References 9-21 contain descriptions of all the various aspects of SRP as well as several examples of the ability of the method to correlate and predict the fatigue life of specimens subjected to complex loading conditions.

THE COOPERATIVE EVALUATION PROGRAM FOR SRP

Background

The AGARD Structures and Materials Panel has had a long and active interest in researching subjects that are of a critical nature and of common interest to the NATO community. In keeping with this tradition, the Panel, in the Spring of 1971 deemed it highly advisable to initiate specific activities in the area of low cycle high temperature fatigue (LCHTF).

At the Fall 1972 S&M Panel Meeting, Mr. Drapier, who was charged by AGARD with the coordination of the various activities on this subject, submitted a document entitled "Ad Hoc Group on Low Cycle High Temperature Fatigue - Status Report" (ref. 22), which reviewed the LCHTF work being carried out by the laboratories in the various NATO nations interested in this problem. In the fall of 1973, Mr. Drapier presented to the S&M Panel his in-depth report entitled "Survey of Activities in the Field of Low Cycle High Temperature Fatigue" (ref. 23).

Through the continuing efforts of Mr. Drapier, supported by this Panel, AGARD has published a volume containing the papers presented at the Specialists Meeting on Low Cycle High Temperature Fatigue (ref. 24) held in Washington D.C. in April of 1974. At this meeting, experts were invited to provide replies to a number of questions raised by the organizers; each subject was introduced by a paper, the purpose of which was to survey the problem areas associated with that subject and to orient and focus the subsequent discussion.

One of the conclusions of the above noted Specialists Meeting was the recognition of the need for more reliable life prediction methods that are applicable to LCHTF gas turbine components. It was in the Spring of 1975 that this author presented an invited pilot paper to the AGARD Working Group on High Temperature Materials, suggesting a cooperative program aimed at evaluating the ability of the SRP method to predict life in the creep-fatigue range. This program was approved by the S&M Panel and Messrs Hirschberg and Drapier were designated program coordinators. The laboratories surveyed (ref. 23) were then contacted by the coordinators and invited to participate in the program.

Program Objectives

Twenty laboratories in six countries participated in this program, each testing its own materials of interest under its own laboratory conditions so that the results obtained would provide validation for a wide range of materials and would insure maximum usefulness to each of the participating laboratories. In using a common set of definitions, data sheets, and format for data presentation, it was also possible to collect and tabulate the various sets of data and present them as a single body of high temperature creep-fatigue data. The objective here, was to produce a reference body of data easily usable by any other investigator. What we have taken here, was the first, very necessary step in the evaluation of a life prediction approach - the evaluation of the ability of this method to predict the life of specimens subjected to complex loading from specimen data obtained from simple tests. One could not hope to obtain reliable life predictions for engine components if it were not possible to reliably predict the lives of well controlled laboratory specimens. The culmination of this program was a Specialists Meeting held in April of 1978, that brought together the investigators with the objective of sharing their laboratory testing experiences to permit an in-depth evaluation of the SRP method, and provide maximum exposure to the findings and recommendations of a distinguished body of specialists.

Program Organization

The program was organized and conducted by the two coordinators appointed by AGARD. Mr. Drapier acted as the focal point for coordinating the activities among the European participants and this author had the equivalent responsibilities for the U.S. participants. In the initial phase of this activity, Mr. Drapier had the responsibility of surveying numerous laboratories in the NATO community to determine their interest in participating. Mr. Drapier was in an excellent position to make this survey since he had previously made another survey in this area (ref. 23). Once the interested laboratories had been determined, a NASA report (ref. 25) was sent to each describing in detail what SRP was, how SRP tests could be run, and suggesting numerous aspects of SRP that needed broader verification. This report was translated into both French and German and made available to those selected laboratories as well. Sufficient time was given for the review of this report and those laboratories which initially expressed interest were again surveyed to finally establish whether or not they wished to participate in the program. Once this was determined, the coordinators then constructed a timetable for the program, that included such items as interim program review meetings (described in Mini-Symposia section), dates for completion of the testing portion of the program as well as for the written final report, and the final Specialists Meeting. The coordinators were also responsible for arranging the Specialists Meeting and assembling the final AGARD Report containing the papers and discussions held at this meeting.

Program Participants

Table I lists the principal participants in this program along with their organizations. There were of course many other persons involved in the individual testing programs as well as those that contributed to the success of the Specialists Meeting. These names and organizations are far too numerous to list here. Most of these persons can, however, be identified in the AGARD publication of the proceedings of the meeting (ref. 26).

Program Data Generation and Collection

In order to be able to easily construct a set of tables describing all the data generated in the evaluation program, it was necessary to first agree upon common definitions and terms, as well as data sheets that all the participants could use. The data sheets were used for reporting all the fatigue data, as well as background information defining the materials used in the investigations. This information included chemical composition, material processing and heat treatment, and the conventional mechanical properties for each of the alloys tested. These data sheets were used to ensure that pertinent information was reported in a consistent manner. One of the sample data sheets is shown in Table II. Copies of all the data sheets were sent to the NASA Lewis Research Center where Mr. J.F. Saltsman transcribed the information to a computerized format for ease of storage, analysis, and retrieval.

Mini-Symposia

One of the prime reasons for the success of this activity was the interaction afforded the investigators from the mini-symposia. They provided the opportunity for critical in-depth interchanges of ideas, concerns, testing techniques, as well as the evaluation of test results that were a benefit to all the participants.

In order to assure maximum participation in these symposia, separate meetings were held in the U.S. and in Europe. During the course of the evaluation program, Mr. Drapier arranged three meetings for the European participating laboratories. They were held at the National Physical Laboratory in England, the Center for Metallurgical Research in Belgium, and the National Gas Turbine Establishment in England. This author arranged three similar meetings for the U.S. participating laboratories. Two such meetings were held at the NASA Lewis Research Center and one at the Air Force Materials Laboratory. This author was the only one who attended all six symposia and was thereby able to keep the laboratories on both sides of the Atlantic informed and up to date regarding all aspects of the SRP evaluation program. In addition to reports presented orally by this author at each symposia, meeting minutes were distributed to all the participating laboratories.

RESULTS OF THE SRP EVALUATION PROGRAM

The culmination of the SRP cooperative evaluation program was an AGARD sponsored Specialists Meeting where papers were presented, and where extensive discussions were held. These papers, including their individual evaluations and recommendations regarding the SRP method, as well as all the tabulated test data are given in reference 26. A brief review of these follows:

Specialists Meeting

The Specialists Meeting was held in Aalborg, Denmark on the 11th and 12th of April, 1978. Seventeen presentations were made in three separate sessions with a fourth session devoted entirely to discussion. Preprints for all of the presentations were available at the meeting and had been distributed to all the speakers prior to the meeting. Recorders were assigned to each of the sessions for the purpose of documenting the sense of the discussions that followed each session. The condensation of these discussions also appears in reference 26.

Data Tabulation

All of the data collected from the participating laboratories were tabulated in a common format and appear in the appendix of reference 26. In this form, it represents an extremely valuable body of creep-fatigue data covering a variety of engineering alloys. As much of the raw data as possible were included in the tabulations so that future analyses and interpretations can be made with a minimum of effort and a maximum of reliability. An example of the creep-fatigue test data for one alloy is shown in Table III.

Evaluation of the SRP Method

The general consensus of the investigators involved in this program was positive and in agreement that the SRP method was a significant step forward in high temperature low-cycle fatigue life prediction. There did emerge from this program several concerns and recommendations regarding SRP. These dealt primarily with the problems associated with the application of SRP to cases involving small inelastic strains (and therefore long lives). The difficulties associated with partitioning these narrow hysteresis loops and the present inability of SRP to handle mean stress effects were also noted. The specifics regarding these concerns and recommendations can be found in the individual papers of reference 26.

CONCLUSIONS

In as much as this cooperative evaluation program was the result of a request of the AGARD S&M Panel Sub-Committee on High Temperature Materials, it would be desirable to review their conclusions regarding this program. The following was extracted from the Summary Record of the 46th Panel Meeting:

"Informal discussions were held with the members of the Sub-Committee with the following conclusions:

The Strainrange Partitioning Cooperative Program was an outstanding success because

- a) It provided an additional 19 laboratories in 6 NATO nations with a new method for physical testing
- b) It provided a broad base of experience in using the new approaches and the methods for handling the data
- c) while the results were variable from laboratory to laboratory, most investigators agreed that the strainrange partitioning method was a significant step toward life prediction in the presence of high temperature and cyclic stresses. "

The above is in effect an integration of all the conclusions of the individual participants in this program. Each of the investigators have included their own conclusions in their written papers and these are available in reference 26.

REFERENCES

1. Manson, S. S.; Halford, G. R.; and Hirschberg, M. H. "Creep-Fatigue Analysis by Strainrange Partitioning". First Symp. on Design for Elevated Temperature Environment, Am. Soc. of Mech. Engrs., 1971, pp. 12-28.
2. Freche, J. C.; et al. "Materials and Life Prediction. Selected Technology for the Gas Industry". NASA SP 5103, 1975, pp. 281-327.
3. Manson, S. S. "Behavior of Materials Under Conditions of Thermal Stress". NACA TN 2933, 1953.
4. Smith, R. W.; Hirschberg, M. H.; and Manson, S. S. "Fatigue Behavior of Materials Under Strain Cycling in Low and Intermediate Life Range". NASA TN D-1574, 1963.
5. Manson, S. S. "Fatigue: A Complex Subject - Some Simple Approximations". Exp. Mech., vol. 5, no. 7, July 1965, pp. 193-226.
6. Manson, S. S. "Interfaces Between Fatigue, Creep, and Fracture". Intl. J. Fract. Mech., vol. 2, no. 1, 1966, pp. 327-363. Also Proc., 1st Intl. Conf. Fract. vol. 3, Yokobori, Kawasaki, and Swedlow, eds., Jap. Soc. Strength and Fract. Mats., 1966, pp. 1387-1431.
7. Halford, G. R.; and Manson, S. S. "Application of Method of Estimating High-Temperature Low-Cycle Fatigue Behavior of Materials". Am. Soc. of Metals Trans., vol. 61, no. 1, March 1968, pp. 94-102.
8. Manson, S. S.; Halford, G. R.; and Spera, D. A. "The Role of Creep in High-Temperature Low-Cycle Fatigue". Ch. 12 in Advances in Creep Design, Smith and Nicolson, eds., Appl. Sci. Publ., Ltd., London, 1971, pp. 229-249.
9. Manson, S. S. "The Challenge to Unify Treatment of High Temperature Fatigue - A Partisan Proposal Based on Strainrange Partitioning". Fatigue at Elevated Temperatures, STP-520, Am. Soc. for Testing and Mat., 1972, pp. 744-775.
10. Halford, G. R.; Hirschberg, M. H.; and Manson, S. S. "Temperature Effects on the Strainrange Partitioning Approach for Creep-Fatigue Analysis". STP 520, ASTM, 1973. pp. 658-669.
11. Manson, S. S.; Halford, G. R.; and Nachtigall, A. J.: Separation of the Strain Components for Use in Strainrange Partitioning". Symposium on Advances in Design for Elevated Temperature Environment, ASME, 1975, pp. 17-28.
12. Saltzman, J. F.; and Halford, G. R. "Application of Strainrange Partitioning to The Prediction of MPC Creep-Fatigue Data For 2 1/4Cr-1Mo Steel". NASA TM X-73474, 1976.

13. Manson, S. S.; and Halford, G. R. "Multiaxial Rules for Treatment of Creep-Fatigue Problems by Strainrange Partitioning". 1976 ASME-MPC Symposium on Creep-Fatigue Interaction. MPC-3, ASME, 1976, pp. 299-322.
14. Halford, G. R.; and Manson, S. S. "Life Prediction of Thermal-Mechanical Fatigue Using Strainrange Partitioning". Thermal Fatigue of Materials and Components, ASTM STP 612, Spera and Mowbray, Eds., Amer. Soc. for Testing and Mat., 1976, pp. 239-254.
15. Conway, J. B.; Stentz, R. H.; and Berling, J. T. "High-Temperature, Low-Cycle Fatigue of Copper-Base Alloys for Rocket Nozzles; Part II- Strainrange Partitioning and Low-Cycle Fatigue Results at 538 C". NASA CR-135073, 1976. (MAR-TEST Inc.)
16. Annis, C. G.; VanWanderham, M. C.; and Wallace, R. M. "Strainrange Partitioning Behavior of an Automotive Turbine Alloy". NASA CR-134974, 1976. (P&WA, Florida)
17. Saltsman, J. F.; and Halford, G. R. "Application of Strainrange Partitioning to the Prediction of Creep-Fatigue Lives of AISI Types 304 and 316 Stainless Steel". Trans., ASME, Vol. 99, Ser. J, No. 2, May 1977, pp. 264-271.
18. Manson, S. S.; and Zab, R. "A Framework For Estimation of Environment Effect in High Temperature Fatigue". Proceedings of the Conference on Environmental Degradation of Engineering Materials. Virginia Tech Printing Dept., V.P.I. & State Univ., Blacksburgh, VA, 1977. pp. 757-770.
19. Kortovich, C. S. "Strain Partitioning of Three Alloys in Ultrahigh Vacuum Using the Step-Stress Method". NASA CR-135187, 1977. (TRW, Inc.)
20. Halford, G. R.; Saltsman, J. F.; and Hirschberg, M. H. "Ductility Normalized-Strainrange Partitioning Life Relations for Creep-Fatigue Life Prediction". Proceedings of the Conf. on Environmental Degradation of Engineering Materials. Virginia Tech Printing Dept., V.P.I. & State Univ., Blacksburgh, VA, 1977, pp. 599-612.
21. Oldrieve, R. E. "Fractographic Evaluation of Creep Effects on Strain-Controlled Fatigue-Cracking of AISI 304LC and 316 Stainless Steel". NASA TM-78913, 1978.
22. Drapier, J. M. "Ad Hoc Group on Low-Cycle High Temperature Fatigue - Status Report". AGARD-R-604, 1973.
23. Drapier, J. M. "Survey of Activities in the Field of Low-Cycle High Temperature Fatigue: Critical Report". AGARD-R-618, 1974.
24. AGARD Conference Proceedings No. 155 "Specialists Meeting on Low Cycle High Temperature Fatigue". AGARD-CP-155, 1974.
25. Hirschberg, M. H.; and Halford, G. R. "Strainrange Partitioning- A Tool for Characterizing High-Temperature Low-Cycle Fatigue. NASA TM X-71691, 1975.
26. AGARD Conference Proceedings No. 243 "Characterization of Low Cycle High Temperature Fatigue by the Strainrange Partitioning Method. AGARD-CP-243, 1978.

TABLE I

CONTRIBUTORS TO THE SRP EVALUATION PROGRAM

Annis, C. P&WA - United Tech Corp Box 2691 W Palm Beach, FL 33402 U.S.A.	Brinkman, Dr. C. R. O R N L - Box X Metals & Ceramics Div Oak Ridge, TN 37830 U.S.A.	Chaboche, Dr. J. L. O N E R A 29 Ave de la Div Leclerc 92320 Chatillon France
Day, M. F. National Physical Lab Div Mat'l's Applications Teddington, Middlesex TW11 0LW, England	Drapier, J. M. FN Formetal Division de FN Herstal B-4400 Herstal Belgium	Ellison, Dr. E. G. Univ of Bristol Dept of Mech Engrng Queens Bldg, Univ Walk Bristol, BS8 1TR, England
Halford, Dr. G. R. NASA Lewis Research Ctr 21000 Brookpark Rd Cleveland, OH 44135 U.S.A.	Hancock, Prof. P. Cranfield Inst of Tech Dept of Materials Cranfield, Bedfordshire MK43 0AL, England	Hirschberg, M. H. NASA Lewis Research Ctr 21000 Brookpark Rd Cleveland, OH 44135 U.S.A.
Hyzak, Capt. J. AFML / LLN WPAFB, OH 45433 U.S.A.	Kortovich, Dr. C. S. TRW, Inc 23555 Euclid Ave Cleveland, OH 44117 U.S.A.	Manson, Prof. S. S. Case Western Reserve Univ Glennan Bldg 10900 Euclid Ave Cleveland, OH 44106 U.S.A.
Massarelli, Dr. L. LTM / CHR Via Induno 10 20092 Cinisello B. Milan, Italy	Howack, Dr.-Ing. H. D F V L R Linder Höhe 5000-Köln, 90 Fed. Rep. of Germany	Perruchet, C. C E A T Poste 436 Ave Andre Guillaumet, 23 31056 Toulouse France
Popp, H. G. General Electric Co. MPTL - AEG Evendale, OH 45215 U.S.A.	Quaranta, Dr. S. FIAT-Laboratori Centrali Strada Torino, 50 10043 Orbassano (Torino) Italy	Sprinthall, S. H. Rolls Royce, (1971) Ltd Derby Engine Div Box 31, Derby DE3 8BJ England
Stentz, R. H. Mar-Test, Inc 45 Novner Dr Cincinnati, OH 45215 U.S.A.	Weaver, M. J. Nat Gas Turbine Estab Pyestock, Farnborough Hants, GU14 0LS England	Zamrik, Prof. S. Penn State Univ Hammond Bldg University Park, PA 16802 U.S.A.

TABLE 11

SAMPLE DATA SHEET

STRAIN-RANGE PARTITIONING TEST SUMMARY RECORD									
1									
GENERAL INFORMATION:									
1. Name of laboratory		2. Responsible engineer		3. Date of test		4. Material designation		5. Material heat number	
6. Test type		7. Sketch of strain-time waveform		8. Temperature of test, °C		9. Specimen number		10. Temperature of test, °C	
RATE DATA: (Half-Life Values):									
11. Cyclic frequency, Hz		12. Tensile strain rate, %/sec.		13. Compressive strain rate, %/sec.		14. Tensile hold time, sec.		15. Compressive hold time, sec.	
16.		17.		18.		19.		20.	
STRESSES (Half-Life Values) in units of MPa:									
21. σ_t		22. σ_c		23. $\Delta\sigma$		24. $\Delta\sigma_t$		25. $\Delta\sigma_c$	
26. $\Delta\sigma_t$		27. $\Delta\sigma_c$		28. $\Delta\sigma$		29. $\Delta\sigma_t$		30. $\Delta\sigma_c$	
31. $\Delta\sigma_t$		32. $\Delta\sigma_c$		33. $\Delta\sigma$		34. $\Delta\sigma_t$		35. $\Delta\sigma_c$	
STRAINS (Half-Life Values) in units of %:									
36. $\Delta\epsilon_t$		37. $\Delta\epsilon_c$		38. $\Delta\epsilon$		39. $\Delta\epsilon_t$		40. $\Delta\epsilon_c$	
41. $\Delta\epsilon_t$		42. $\Delta\epsilon_c$		43. $\Delta\epsilon$		44. $\Delta\epsilon_t$		45. $\Delta\epsilon_c$	
FAILURE DATA									
36. N_0 , cycles to first indication of cracking (note method of detection)									
37. N_1 , cycles when ratio of max tensile to max comp. stress decreases 10% from half-life or stabilized value.									
38. N_2 , cycles when stress range decreases by 5% from half-life or stabilized value									
39. N_3 , cycles for complete fracture									
40. t_f , test time for complete fracture, hours									
41.									
42.									
43.									
44.									
45.									
46.									
47.									
48.									
49.									
50.									
51.									
52.									
53.									
54.									
55.									
56.									
57.									
58.									
59.									
60.									
61.									
62.									
63.									
64.									
65.									
66.									
67.									
68.									
69.									
70.									
71.									
72.									
73.									
74.									
75.									
76.									
77.									
78.									
79.									
80.									
81.									
82.									
83.									
84.									
85.									
86.									
87.									
88.									
89.									
90.									
91.									
92.									
93.									
94.									
95.									
96.									
97.									
98.									
99.									
100.									

Strain-Time Waveform

Stress-Time Waveform

Temperature-Time Waveform

Hysteresis Loop

Fracture Surface

TABLE III

LABORATORY: NPL
MATERIAL: IN738LC

CREEP-FATIGUE DATA

RATE DATA & STRESSES

SPEC NO	TEST TYPE	TEMP-C TEN/COMP	FREQ HZ	RATE DATA (HALF-LIFE VALUES)				STRESSES (HALF-LIFE VALUES) MPa			
				TEN	COMP	STRAIN-RATE %/SEC	HOLD TIME-SEC	TEN	COMP	MAX	RELAXATION TEN
SPEC NO	TEST TYPE	TEMP-C TEN/COMP	FREQ HZ	TEN	COMP	STRAIN-RATE %/SEC	HOLD TIME-SEC	STRESS RANGE		RELAXATION	
								MAX	MIN	MAX	MIN
SPEC NO	TEST TYPE	TEMP-C TEN/COMP	FREQ HZ	TEN	COMP	STRAIN-RATE %/SEC	HOLD TIME-SEC	TEN	COMP	CYCLIC STRAIN	
										MAX	MIN
SPEC NO	TEST TYPE	TEMP-C TEN/COMP	FREQ HZ	TEN	COMP	STRAIN-RATE %/SEC	HOLD TIME-SEC	TEN	COMP	HARDENING %	
										MAX	MIN
DCH28	HRSC	850/850	8.0E-01	1.3E 00	1.3E 00	0	0	343.0	542.0	885.0	0.0
DCH42	HRSC	850/850	2.5E-01	1.0E 00	1.0E 00	0	0	892.0	916.0	1808.0	0.0
DCH79	HRSC	850/850	5.0E-01	1.0E 00	1.0E 00	0	0	427.0	648.0	1075.0	0.0
DCH85	HRSC	850/850	3.8E-01	1.0E 00	1.0E 00	0	0	751.0	826.0	1577.0	0.0
DCH41	BCCR	850/850	7.8E-03	7.0E-01	7.0E-01	50.0	75.0	350.0	350.0	700.0	0.0
DCH43	BCCR	850/850	6.5E-03	1.0E 00	1.0E 00	75.0	100.0	400.0	400.0	800.0	0.0
DCH73	BCCR	850/850	1.0E-03	1.0E 00	1.0E 00	250.0	700.0	550.0	550.0	1100.0	0.0
DCH94	BCCR	850/850	9.6E-03	1.0E 00	1.0E 00	38.0	63.0	450.0	450.0	900.0	0.0
DCH39	CCCR	850/850	3.6E-03	1.0E 00	1.0E 00	0	275.0	930.0	500.0	1430.0	0.0
DCH40	CCCR	850/850	8.3E-02	1.0E 00	1.0E 00	0	10.0	690.0	400.0	1090.0	0.0
DCH45	CCCR	850/850	3.7E-02	7.0E-01	7.0E-01	0	25.0	455.0	300.0	755.0	0.0
DCH67	CCCR	850/850	6.8E-02	1.0E 00	1.0E 00	0	12.0	731.0	400.0	1131.0	0.0
DCH46	TCCR	850/850	7.5E-02	8.0E-01	8.0E-01	12.0	0	300.0	710.0	1010.0	0.0
DCH66	TCCR	850/850	2.1E-02	9.0E-01	9.0E-01	45.0	0	350.0	846.0	1196.0	0.0
DCH68	TCCR	850/850	9.8E-03	8.0E-01	8.0E-01	100.0	0	190.0	640.0	830.0	0.0
DCH93	TCCR	850/850	1.7E-03	1.0E 00	1.0E 00	600.0	0	450.0	958.0	1408.0	0.0

STRAINS & FAILURE DATA

SPEC NO	TOTAL EL	STRAIN RANGES (HALF-LIFE VALUES) %				CC	FAILURE DATA-CYCLES				TF-HRS
		IN	PP	PC	CP		NO	NI	N5	NF	
DCH28	0.700	0.668	0.032	0.000	0.000	0.000	--	--	--	6178	1.92
DCH42	2.000	1.160	0.845	0.000	0.000	0.000	--	--	--	19	0.01
DCH79	1.000	0.920	0.080	0.000	0.000	0.000	200	--	45	475	0.13
DCH85	1.300	1.040	0.257	0.000	0.000	0.000	--	--	--	160	0.12
DCH41	0.700	0.530	0.168	0.000	0.000	0.136	1500	--	--	2214	22.90
DCH43	1.000	0.590	0.410	0.000	0.000	0.290	90	--	--	147	14.50
DCH73	2.000	0.655	1.345	0.000	0.000	1.145	--	--	--	3	0.68
DCH94	1.300	0.726	0.574	0.000	0.000	0.343	40	--	--	74	7.70
DCH39	2.000	0.770	1.230	0.430	0.800	0.000	--	--	--	15	1.00
DCH40	1.000	0.730	0.270	0.170	0.100	0.000	115	--	105	228	1.56
DCH45	0.700	0.640	0.057	0.036	0.021	0.000	850	--	750	1259	16.00
DCH67	1.300	0.880	0.420	0.250	0.170	0.000	94	--	82	210	1.20
DCH46	1.000	0.800	0.197	0.113	0.000	0.084	700	--	550	1056	4.30
DCH66	1.300	0.890	0.410	0.000	0.000	0.000	65	--	70	92	2.80
DCH68	0.700	0.566	0.134	0.087	0.000	0.047	2000	--	1950	2099	48.20
DCH93	2.000	0.840	1.160	0.285	0.000	0.875	15	--	18	25	4.60

THE UNSTEADY AERODYNAMICS OF A CASCADE IN TRANSLATION

by

Sanford Fleeter*
Ronald E. Riffel
Thomas H. Lindsey
Mark D. Rothrock

Cascade and Flow Systems Research
Detroit Diesel Allison Division
GENERAL MOTORS CORPORATION
Indianapolis, Indiana 46206
USA

SUMMARY

The advent of high tip-speed, high work, blading in the fan stages of advanced gas turbine engines has led to the recognition of a new type of blading instability — unstalled supersonic flutter. As a result, a concerted effort to develop an appropriate predictive mathematical model has taken place. To determine the range of validity and to direct refinements to the basic flow model, fundamental supersonic oscillating cascade data are required. The experiment described herein is directed at significantly extending the range of existing supersonic cascade data to include translation mode oscillations. In particular, the fundamental time-variant translation mode aerodynamics are determined for the first time for a classical airfoil cascade in a supersonic inlet flow field over a range of interblade phase angles at a realistic reduced frequency value. These unique experimental data are then correlated with predictions obtained from an appropriate state-of-the-art harmonically oscillating flat plate cascade aerodynamic analysis.

LIST OF SYMBOLS

C	airfoil chord
C_p	unsteady pressure coefficient ($C_p = p/\frac{1}{2}\rho U^2 \frac{h}{C}$)
M	Mach number
R_c	cascade pressure ratio
R_{xr}	normalized auto-correlation function
R_{xyr}	normalized cross-correlation function
U	inlet velocity
f	frequency
h	translational amplitude
k	reduced frequency ($k = \omega C/U$)
p	measured unsteady pressure amplitude
p_s	inlet static pressure
γ	ratio of specific heats
θ	phase lag
ρ	inlet air density
ω	angular frequency

INTRODUCTION

The advent of high tip-speed, high-work, blading in the fan stages of modern gas turbine engines has led to the recognition of a new type of blading instability — supersonic unstalled flutter. In this region of instability, the incidence angle is small and the tip region of the blade row is operating in a supersonic relative flow field. The stresses encountered during this type of flutter can be catastrophically large, with all of the blade tip sections harmonically oscillating at their natural frequencies with a constant interblade phase angle. Both predominantly bending (translation) and torsional modes of vibration have been observed. As this supersonic unstalled flutter boundary crosses the compressor operating line at high tip speeds, it imposes a definite design constraint on the high speed operation of the engine and, hence, has been receiving a great deal of attention.

Unstalled supersonic flutter is fundamentally an inviscid phenomena caused by the phase lag of the flow field relative to the motion of the airfoils. As this type of flutter tends to become more severe as the pressure ratio is lowered, the

*Presently at Purdue University, West Lafayette, Indiana

generally used analytical model assumes an inviscid, essentially supersonic flow with a subsonic axial component through a differential radial height fan stage operating at a pressure ratio of one. This differential fan stage is then developed into a two-dimensional rectilinear cascade. The cascade airfoils are assumed to be thin (most often zero thickness flat plates) and executing small harmonic torsion or translation mode oscillations. These assumptions lead to mathematical simplifications which result in a linearized, two-dimensional, constant coefficient (for the case of flat plate cascades), partial differential equation for the perturbation velocity potential. Various solution techniques have been and are currently being applied to this mathematical model.

A semi-infinite cascade with a subsonic leading edge locus was considered by Verdon⁽¹⁾ and Caruthers⁽²⁾ using finite difference techniques and by Brix and Platzer⁽³⁾ with the method of characteristics. Nagashima and Whitehead⁽⁴⁾ presented a third approach involving dipole distributions while Yates⁽⁵⁾ developed another linearized characteristics approach. These solutions are all in good agreement with each other. As a semi-infinite cascade is involved in these analyses, it is assumed therein that the asymptotic values for the unsteady pressure distributions and aerodynamic forces and moments obtained by computing the flow past a sufficient number of blades are representative of the infinite cascade.

Using Laplace transform techniques Kurosaka⁽⁶⁾ obtained a solution for an infinite cascade valid for low reduced frequency values and has recently extended these results to higher reduced frequencies⁽⁷⁾. Sisto and Ni⁽⁸⁾ using the time-marching technique and Verdon and McCune⁽⁹⁾, Verdon⁽¹⁰⁾, and Goldstein⁽¹²⁾, have also considered the infinite cascade in supersonic flow with a subsonic axial component.

To determine the range of validity and direct refinements to the basic flow model, fundamental supersonic, harmonically oscillating aerodynamic cascade data are required. Such data have been obtained in the torsion mode for a single airfoil⁽¹³⁾, a classical airfoil cascade⁽¹⁴⁾, and an MCA (Multiple-Circular-Arc) airfoil cascade⁽¹⁵⁾.

The current effort reported herein is directed at significantly extending the range of the above described supersonic cascade data by developing the necessary new experimental techniques and then obtaining relevant translation mode cascade data. In particular, the fundamental time-variant translation mode aerodynamics are determined for the first time for a classical airfoil cascade in a supersonic inlet flow field. The reduced frequency value for this experiment is representative of that noted for bending flutter in rotors. All of the unsteady aerodynamic data are correlated with predictions obtained from a state-of-the-art harmonically oscillating flat plate cascade analysis.

EXPERIMENTAL FACILITY

The Detroit Diesel Allison rectilinear cascade facility, shown in Figure 1, was conceived and built as a research tool to evaluate the aerodynamic and aeroelastic characteristics of compressor and turbine blade sections. The facility is a continuous flow, non-return, pressure-vacuum type wind tunnel with the test section evacuated by means of two primary steam ejectors. Up to 10 lbm/sec of filtered, dried, and temperature-controlled air may be used.

The test section configuration used in this investigation is shown in Figure 2. As can be seen, the entrance flow to the test section is generated by fixed nozzle blocks yielding a Mach number of 1.30. The orientation of a wedge with respect to this nozzle exit flow specifies the test section Mach number, i.e., the shock or expansion wave generated by the wedge determines the cascade inlet conditions.

To aid in the establishment of the cascade inlet periodicity, bleed chambers are provided on the lower nozzle block, as indicated. Adjustment of the bleed rate through these chambers allows the inlet flow field to the rear (bottom) portion of the cascade to be affected. The inlet flow field to the front (upper) portion of the cascade is affected only by the wedge position, with the first passage controlled to some extent by the splitter position. The build-up of the boundary layer in this first passage can produce area ratios such that this passage cannot be started. Hence, suction is provided along the front portion of the splitter to remove the boundary layer and start this first passage.

Active cascade inlet sidewall boundary layer control is also provided to assure the two-dimensionality of the cascade flow field. This is accomplished with the suction strip seen in Figure 3. It contains five discrete regions yet still permits the schlieren system to be utilized to view the cascade wave system.

Disturbances generated at the lower endwall run downstream of the cascade in the supersonic flow regime and thus can have no influence on the cascade performance. The upper endwall of the tunnel, on the other hand, is crucial in that it can influence the whole flow field downstream of the cascade and prevent the formation of a periodic exit flow field. The shape of this upper endwall also uniquely determines the cascade pressure ratio under started supersonic exit operating conditions. The most crucial portion of the upper endwall is in the early stage of compression. Here the flow splitter provides the capability to both bleed and blow. The blowing

capability, in conjunction with adjustments of the exit plenum pressure and the angle of the tailboard attached to the splitter, permits the setting of the streamline shape in this region and thereby sets the throttle condition to the first two channels of the cascade. The remaining problem is to not allow the cascade shock expansion system which impinges upon this tailboard to reflect back into the cascade. This is accomplished by making this upper tailboard porous with a 50% open area as well as having it open to the exit plenum pressure. This effectively produces a streamline representation of an infinite cascade at the design pressure ratio, as established in the first passage and results in a periodic exit flow field.

AIRFOIL CASCADE AND INSTRUMENTATION

The two-dimensional cascade utilized in this investigation was comprised of five double-trunnion airfoils, characterized by a 3.00 in. (7.62 cm.) span, a 3.00 in. (7.62 cm.) chord, and a 0.087 in. (0.220 cm.) maximum thickness at the 50 percent chord location. The airfoil profile, indicated schematically in Figure 4, consists of a flat suction surface and a triangular pressure surface. The cascade physical parameters are listed in Table I.

The proper steady-state aerodynamic performance instrumentation necessary to quantitatively describe the cascade flow field was provided. Sidewall static pressure taps were used to establish the cascade inlet and exit pressure distributions. This information together with schlieren flow visualization was used to establish the steady-state periodicity of the cascade.

To achieve realistic reduced frequency values, maintain a two-dimensional airfoil mode shape, and also maximize the imparted airfoil oscillatory amplitude for a given input driving power, unique airfoils fabricated from graphite/epoxy composite material were necessary. The airfoils were fabricated from a combination of pre-impregnated Kevlar cloth and graphite mat injected with epoxy resin under pressure into a booking mold. Cloth fiber orientation was controlled to meet prescribed torsional and bending stress requirements while maintaining a low density and a high modulus of elasticity.

Hollow steel trunnions were attached to the airfoils at mid-chord. Cloth insertion and epoxy fill into the trunnions provided adequate strength at the critical airfoil-trunnion interface stress locations. Splines located on the trunnion were used to mount the airfoils into the translational drive system.

The fabrication of the airfoils from graphite/epoxy composite material necessitated the use of nonconventional instrumentation techniques. In particular, to maintain the desired overall composite material properties with no degradation of the airfoil surface contours, provisions for dynamic instrumentation were embedded in one airfoil during fabrication. This involved molding the dynamic pressure transducer lead wires into the airfoil as part of the lay-up and molding process. The ends of the lead wires were then exposed and the transducers attached. These flush-mounted Kulite LQ Series dynamic pressure transducers were staggered across the span of the airfoil on both the pressure and suction surfaces. Figure 5 shows a view of this unique dynamically instrumented airfoil. The chordwise distribution of these transducers is identical on the airfoil pressure and suction surfaces, with their locations presented in Table II, and also schematically depicted in Figure 4.

TRANSLATION MODE DRIVE SYSTEM

A schematic of the translation mode drive system is presented in Figure 6. Since translation is movement normal to the chord, no bearing or other rigid axial restraint is necessary. The airfoil is positioned with the two flexible mounts consisting of a "squirrel cage" support which attaches to the spline on the airfoil trunnion by indexing over six grooves and attaching through a replaceable spring bar to a rigid mount. The indexing tabs ensure torsional restraint with no blade angle slippage. The airfoil trunnion splines are positioned axially on these devices by a driver arm clamped and piloted to the trunnion with an attached spacer tube which nests over the indexing tabs of the squirrel cage.

Translational excitation forces to each blade are supplied through the drive arm from the computer controlled electromagnets. Driving mechanisms are located on each airfoil trunnion so that proper excitation of the two-dimensional translation motion of the airfoil can be accomplished. Modification of the spring bars and/or mass control of the driver arm can be used for minor frequency adjustments of individual blades.

The double-trunnion airfoils and spring bar assemblies are mounted in plexiglas windows, thereby permitting schlieren flow visualization, and this complete assembly then installed in the test section, as seen in Figure 7. The computer controlled electromagnets excite the translation mode drive system at the airfoil-drive system natural frequency, thereby imparting the desired translation mode oscillation to the airfoil cascade at precisely controlled interblade phase angle values (16,17). Strain gages mounted on the spring bar assemblies exhibit excellent sensitivity to the translational airfoil oscillations, and allow the measured strain gage signals to be converted to translational amplitudes.

DATA ACQUISITION AND ANALYSIS

With the tunnel in operation and the steady-state cascade periodicity properly established, as determined by the sidewall static pressure taps and the schlieren flow visualization, the computer controlled translation mode drive system is made operational. This results in controlled harmonic oscillations of the airfoil cascade at a prescribed frequency and interblade phase angle value. The resulting time-variant spring bar mounted strain gage and airfoil surface pressure transducer signals are digitized at rates to 100,000 points per second by a 16-channel analog-digital converter and multiplexer system, and stored on a magnetic disk. These digitized data are analyzed on-line to determine the fundamental aerodynamic characteristics of the unsteady phenomena. The parameters of interest include the amplitude of the airfoil motion and the pressure disturbance, the frequency, the interblade phase angle, and the phase difference between the unsteady pressures and the airfoil motion as characterized by the strain gage signal on the dynamically instrumented airfoil, i.e., the aerodynamic phase lag data is referenced to the motion of the dynamically instrumented center airfoil in the cascade.

The amplitude of the airfoil motion and the pressure disturbance are determined by fitting a second order least square function to the data, differentiating it, and evaluating the maximum. The pressure disturbance amplitude is then non-dimensionalized into an unsteady pressure coefficient, C_p , as defined in Equation 1:

$$C_p = \frac{p}{\frac{1}{2} \rho U^2 \frac{h}{C}} = \frac{p}{\frac{1}{2} \gamma M^2 p_s \frac{h}{C}} \quad (1)$$

where p is the measured unsteady pressure amplitude, ρ is the fluid density, U is the inlet velocity, γ is the ratio of specific heats, p_s is the inlet static pressure, and h/C is the ratio of the translational amplitude to the airfoil chord.

The frequency of the time-dependent data is determined through the autocorrelation function. This function describes the dependence on the values of the data at one time, X_i , on the values at another time, X_{i+r} . The normalized autocorrelation function, R_{xr} , is defined in series form as

$$R_{xr} = \frac{1}{N-r} \sum_{i=1}^{N-r} X_i X_{i+r} / \frac{1}{N} \sum_{i=1}^N X_i X_i, r = 0, 1, 2 \dots m \quad (2)$$

where:

- $X_i = X(i \Delta t)$
- $r = \text{lag number}$
- $N = \text{total number of dynamic data points}$
- $m = \text{number of lags.}$

The lag time, Δt , is inversely proportional to the rate at which the data is digitized. A typical autocorrelogram of the digitized data exhibits the features of a sine wave plus random noise. A second order least square function is fit to the data in the second positive peak of the autocorrelogram. The inverse of the time at which this least square function is a maximum is equal to the frequency, f , of the time-dependent data.

The phase difference of the pressure disturbance along the airfoil chord in relation to the airfoil motion is calculated through the cross-correlation function. This function, for two sets of data, X_i , Y_i , describes the dependence of the values of one set of data on the other. The normalized cross-correlation function, R_{xyr} , is defined as:

$$R_{xyr} = \frac{1}{N-r} \sum_{i=1}^{N-r} X_i Y_{i+r} / \frac{1}{N} \sum_{i=1}^N X_i Y_i, r = -m, \dots -1, 0, 1, \dots \quad (3)$$

where the variables are defined analogous to those in Equation (2).

As in the frequency calculation, a second order least square function is fit to the data in the first positive peak of the cross-correlogram. The time, t_p , at which this least square function is a maximum is analytically determined. The phase difference, in degrees, is calculated as

$$\theta_p = t_p f 360 \quad (4)$$

where f is the frequency calculated for the airfoil motion from the strain gage data, utilizing Equation (2).

Two sources of phase relation discrepancy are inherent in the electronic data acquisition system and correlation computation. The analog-digital (A/D) converter-multiplexer unit does not permit data to be digitized simultaneously on all channels. Consequently, an inherent phase shift is introduced into the physical data when the cross-correlation function operates on the raw digitized data. This phase shift, for the sinusoidal data in this experiment, is directly proportional to the "cut rate" of the multiplexer, as shown in Equation (5):

$$\theta_s = f_x (K_y - K_x) 360/R_a \quad (5)$$

where θ_s is the AD phase shift inherent in the computation between channels K_y and K_x , representing the respective data, Y_i and X_i . The frequency, f_x , corresponds to the disturbance in channel K_x , and R_a is the rate at which the data were being digitized.

Prior to acquiring data the electronic data acquisition system is calibrated for phase shift, θ_a , using the A/D converter and the computation described in the foregoing. Therefore, the phase difference of the pressure disturbance along the airfoil surface in relation to the airfoil motion is

$$\theta_{xy} = \theta_p - \theta_s - \theta_a \quad (6)$$

This computational procedure results in a valid on-line data analysis system and provides the experimentalist with meaningful information with which to make judicious decisions during the test. All analyzed results are stored on a magnetic disk for further examination.

RESULTS

The procedure followed in this experiment included first obtaining a periodic steady-state cascade flow field, as determined from the schlieren flow visualization and the sidewall static pressures immediately upstream of the leading edge of each airfoil in the cascade. Figure 8 presents a schlieren photograph which typifies the periodic steady-state cascade flow field established at the inlet Mach number of 1.40 and a cascade static pressure ratio of unity. As indicated, the bow shock intersects the suction surface of the adjacent airfoil near the trailing edge, with both the reflection of this shock and the trailing edge wake shock from the adjacent airfoil intersecting the pressure surface near mid-chord. A comparison of this overall cascade steady flow field, as characterized by the location of the shock waves, with that predicted by the analysis of reference 18, is presented in Figure 9. As can be seen, the correlation between the experimentally determined shock waves and those indicated by the predicted constant pressure lines is quite good.

With the steady-state periodicity established and the cascade performance determined, the airfoil cascade was harmonically oscillated in a translation mode at a reduced frequency value equal to 0.41. Specified interblade phase angles were investigated and at selected points, the cascade static pressure ratio increased from the nominal 1.00:1 to 1.30:1. Fundamental time-variant data were then obtained and analyzed. These unique translation mode data were then correlated with predictions obtained from the current state-of-the-art cascade analysis of reference 2. This analysis assumes small perturbations which are generated by oscillating zero thickness flat plate cascaded airfoils in a uniform inviscid steady flow field and includes the effect of variable blade-to-blade amplitude of oscillation, accomplished through input of the measured amplitudes into the analysis.

These unique chordwise pressure and suction surface translation mode data together with the corresponding predictions are presented in the form of an aerodynamic phase lag as referenced to the motion of the instrumented airfoil (the center airfoil in the cascade), and the unsteady pressure coefficient, C_p . These results for interblade phase angles between -180° and $+3^\circ$ at a cascade static pressure ratio

equal to 1.00:1 are presented in Figures 10 through 14 and for interblade phase angles between -180° and $+45^\circ$ at a 1.30:1 static pressure ratio in Figures 15 through 19.

The time-variant suction surface data are seen to generally exhibit very good correlation with the predictions. The aerodynamic phase lag and unsteady pressure coefficient data are both nearly constant in the chordwise direction, with the theory predicting an approximate 60° greater lag than characteristic of the data. As the effects of increased cascade static pressure ratio are largely taken up in the trailing edge wave system, only the trailing edge of the suction surface should be affected. Indeed this is the case, as evidenced through comparison of the 1.00:1 and 1.30:1 pressure ratio suction surface data at corresponding interblade phase angle values, e.g. Figures 10 and 16, 13 and 18, and 14 and 19. As seen from these figures, only the suction surface phase lag and dynamic pressure coefficient data near to the trailing edge are affected as the pressure ratio is increased. However, the 1.00:1 suction surface phase lag data appears much more regular in the chordwise direction than does the corresponding 1.30:1 data.

The time-variant pressure surface data also generally exhibit very good correlation with the theoretical predictions. Both the aerodynamic phase lag and dynamic pressure coefficient data and prediction remain nearly constant in the chordwise direction between the leading edge and the mid-chord region shock wave intersection location on this surface. The theory predicts this intersection location to be at approximately 70% of the chord, with the 1.00:1 pressure ratio data indicating the presence of a shock in the region between the 60% and 75% chord transducer locations. Comparison of the 1.00:1 and the 1.30:1 pressure ratio data indicates that the effect of increasing the back pressure is to move the shock intersection location forward on the pressure surface such that at the higher pressure ratio it lies between the 40% and 60% chord transducer locations.

An interesting trend can also be noted in the aerodynamic phase lag data-theory correlation on the pressure surface in the region between the leading edge and the shock intersection for both values of the pressure ratio which were investigated. In particular, in this region, as the interblade phase angle is decreased and attains larger negative values, the phase lag data decreases as compared to the prediction, with the best data-theory correlation obtained at a 0° interblade phase angle value.

SUMMARY AND CONCLUSIONS

An unsteady cascade experiment directed at providing fundamental translation mode aerodynamic data for the first time has been described. This data was obtained at a realistic value of the reduced frequency and is necessary for the verification and/or direction of refinements to the basic analytical model of unstalled flutter in fans and compressors. In particular, a unique dynamically instrumented classical airfoil cascade fabricated from graphite/epoxy composite material was investigated at an inlet Mach number of 1.40 over a range of interblade phase angles for two levels of aerodynamic loading. This time-variant data was then correlated with corresponding predictions obtained from a state-of-the-art unsteady cascade analysis.

The data generally exhibited very good correlation with the prediction on both the pressure and suction surfaces. The predicted suction surface phase lag was increased on the order of 60° as compared to the data, although in excellent agreement trendwise. Also, the mid-chord region pressure surface shock wave intersection location was in general agreement with the prediction for the lower pressure ratio data, but not for the higher pressure ratio as the theory does not include the effect of back pressure. Also, in the region between the leading edge and the mid-chord region shock intersection location on the pressure surface, decreasing the interblade phase angle toward large negative values resulted in decreasing values of the phase lag data as compared to the prediction, with the best correlation obtained at the 0° interblade phase angle value.

REFERENCES

1. Verdon, J. M., "The Unsteady Aerodynamics of a Finite Supersonic Cascade with Subsonic Axial Flow", Journal of Applied Mechanics, September 1973.
2. Caruthers, J. E., "Theoretical Analysis of Unsteady Supersonic Flow Around Harmonically Oscillating Turbofan Cascades", Ph.D. Thesis, Georgia Tech, September 1976.
3. Brix, C. W., Jr. and Platzer, M. F., "Theoretical Investigation of Supersonic Flow Past Oscillating Cascades with Subsonic Leading Edge Locus", AIAA Paper No. 74-14, 1974.
4. Nagashima, T. and Whitehead, D. S., "Aerodynamic Forces and Moments for Vibrating Supersonic Cascade Blades", CUED/A-Turbo/TR59, 1974.
5. Yates, J. E., "Analysis of Supersonic Unsteady Cascades with the Method of Characteristics", AFFDL-TR-75-159, December 1975.

6. Kurosaka, M., "On the Unsteady Supersonic Cascade with a Subsonic Leading Edge — An Exact First Order Theory", ASME Journal of Engineering for Power, January 1974.
7. Kurosaka, M., "Supersonic Cascade Study", Work Currently Performed for the Air Force Office of Scientific Research.
8. Sisto, F. and Ni, R. H., "Numerical Computation of Non-stationary Aerodynamics of Flat Plate Cascades in Compressible Flow", ASME Journal of Engineering for Power, Vol. 98, No. 2, April 1976.
9. Verdon, J. M. and McCune, J. E., "Unsteady Supersonic Cascade in Subsonic Axial Flow", AIAA Journal, Vol. 13, No. 2, February 1975.
10. Verdon, J. M., "Further Developments in the Aerodynamic Analysis of Unsteady Supersonic Cascades", ASME Paper No. 77-GT-44, 45, 1977.
11. Goldstein, M. E., "Cascade With Subsonic Leading Edge Locus", AIAA Journal, Vol. 13, No. 8, August 1975.
12. Adamczyk, J. J. and Goldstein, M. E., "Unsteady Flow in a Supersonic Cascade with Subsonic Leading-Edge Locus", (to be published).
13. Novick, A. S., Jay, R. L., Sinnet, G. T., and Fleeter, S., "An Experimental Investigation of Unsteady Airfoil Motion in a Supersonic Stream", Unsteady Aerodynamics Vol. I and II, Edited by R. B. Kinney, Proceedings of a Symposium held at the University of Arizona, March 1975.
14. Fleeter, S., Novick, A. S., Riffel, R. E., and Caruthers, J. E., "An Experimental Investigation of the Unsteady Aerodynamics in a Controlled Oscillating Cascade", ASME Journal of Engineering for Power, Vol. 99, No. 1, January 1977.
15. Fleeter, S., and Riffel, R. E., "Aerodynamic Phenomena in an Oscillating Transonic MCA Airfoil Cascade Including Loading Effects", AGARD Conference on Unsteady Aerodynamics, AGARD CPP-227, September 1977.
16. Fleeter, S., McClure, R. B., Holtman, R. L., and Sinnet, G. T., "A Unique Supersonic Inlet Unsteady Aerodynamic Cascade Experiment", AIAA Paper No. 74-622, 1974.
17. Fleeter, S., McClure, R. B., Holtman, R. L., and Sinnet, G. T., "Supersonic Inlet Torsional Cascade Flutter", AIAA Journal of Aircraft, 1975.
18. Delaney, R. A. and Kavanagh, P., "Transonic Flow Analysis in Axial-Flow Turbomachinery Cascades by a Time-Dependent Method of Characteristics". ASME Paper No. 75-GT-8, ASME Transactions, Journal of Engineering for Power.

ACKNOWLEDGEMENTS

This research was supported, in part, by the Office of Naval Research, Power Branch, under Contract N00014-72-C-0351. The authors are also grateful to Ms. Barbara Townsend for her valuable assistance and to Ms. Harlene Clark for preparing this manuscript.

TABLE I. CASCADE PHYSICAL PARAMETERS

CHORD	3.00 IN. (7.62 CM.)
SOLIDITY	1.231
SETTING ANGLE	61.5° (1.07 RADIANS)
MAXIMUM THICKNESS/CHORD	0.029
LEADING EDGE WEDGE ANGLE	3.317° (0.058 RADIANS)
TRAILING EDGE WEDGE ANGLE	3.317° (0.058 RADIANS)
LEADING EDGE RADIUS/CHORD	0.0026

TABLE II. PERCENT CHORD LOCATIONS OF THE AIRFOIL
SURFACE DYNAMIC PRESSURE TRANSDUCERS

15.
25.
40.
60.
75.
85.

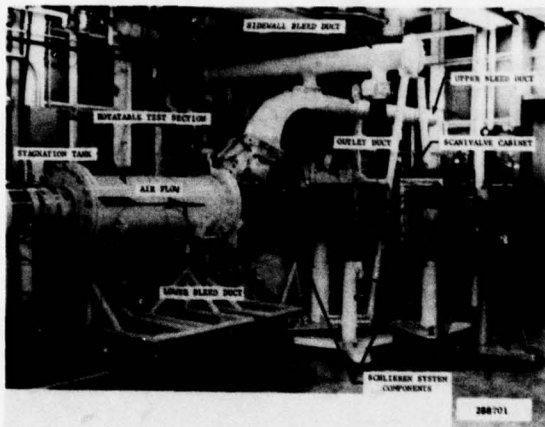


Figure 1. Rectilinear Cascade Facility

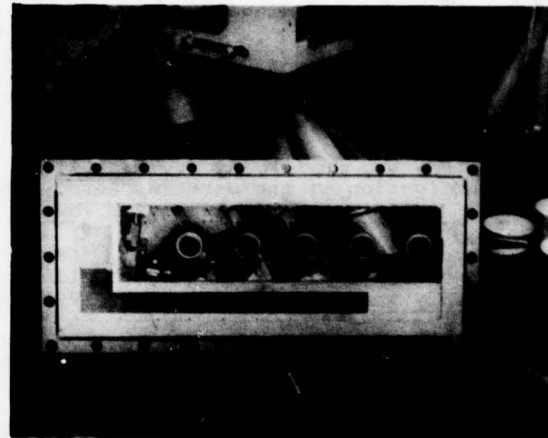


Figure 3. Cascade Inlet Sidewall Bleed Strip

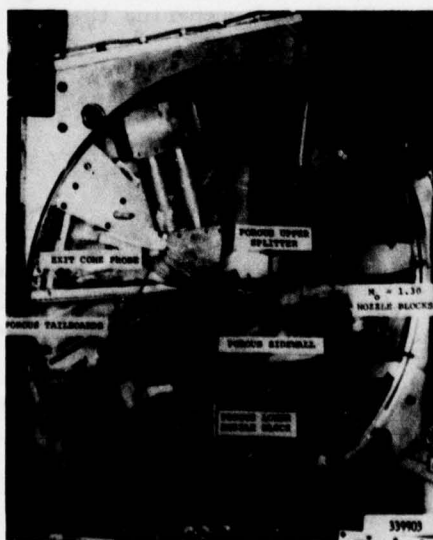
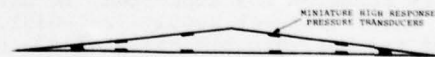


Figure 2. View of Cascade Test Section



330808

Figure 4. Schematic of Airfoil Profile

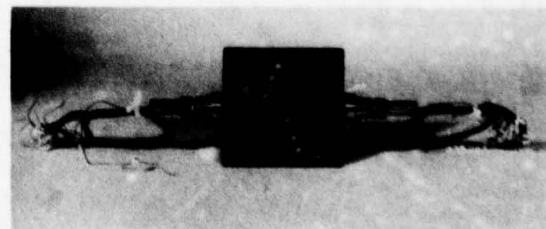


Figure 5. Dynamically Instrumented Airfoil

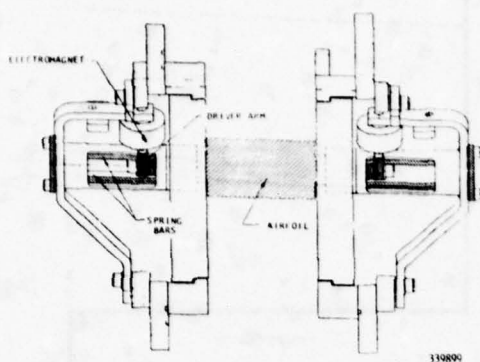


Figure 6. Schematic of Translation Mode Drive System

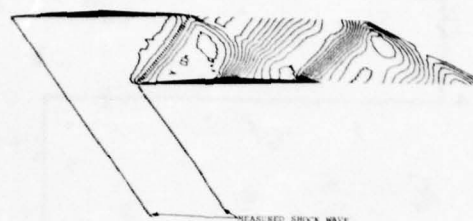


Figure 9. Comparison of Experimental and Predicted Overall Cascade Flow Field

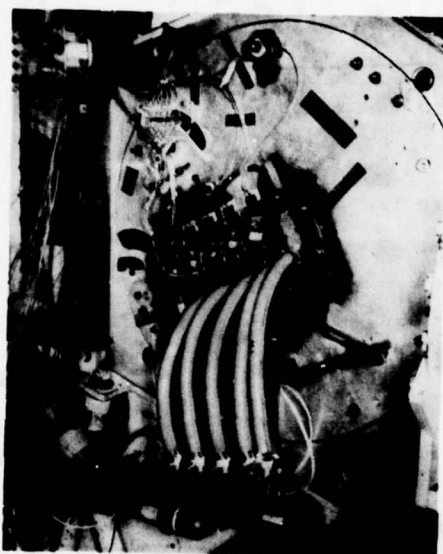


Figure 7. Translation Mode Cascade Drive System as Installed in Test Section

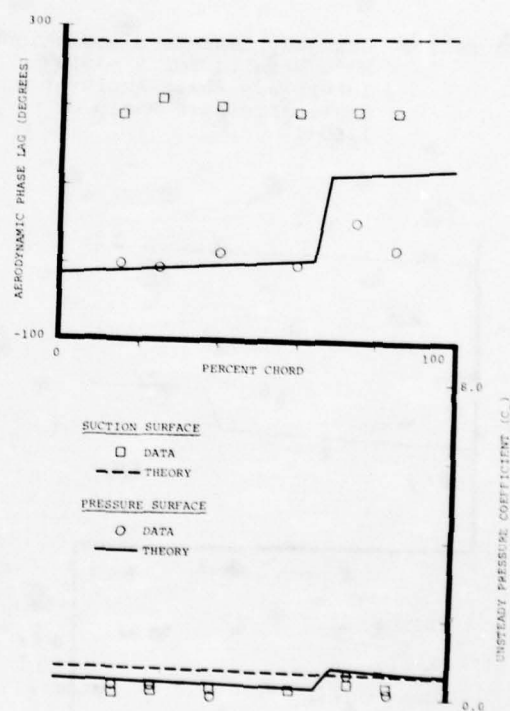


Figure 10. Unsteady Cascade Translation Mode Results for a 2.9° Inter-blade Phase Angle at a Static Pressure Ratio of 1.00:1

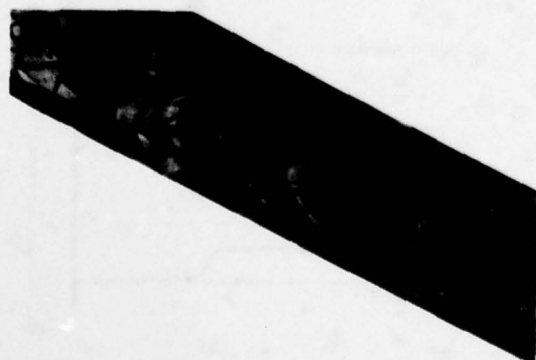


Figure 8. Periodic Steady-State Flow Field at the Inlet Mach Number of 1.40 and a Static Pressure Ratio Value of Unity

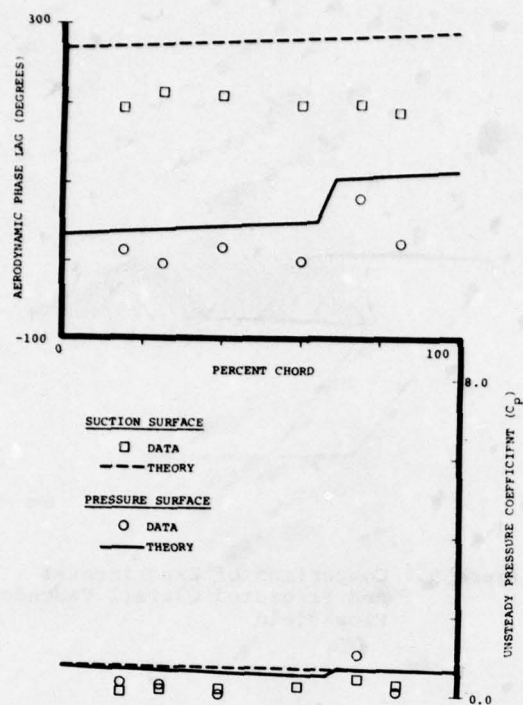


Figure 11. Unsteady Cascade Translation Mode Results for a -35.0° Interblade Phase Angle at a Static Pressure Ratio of 1.00:1

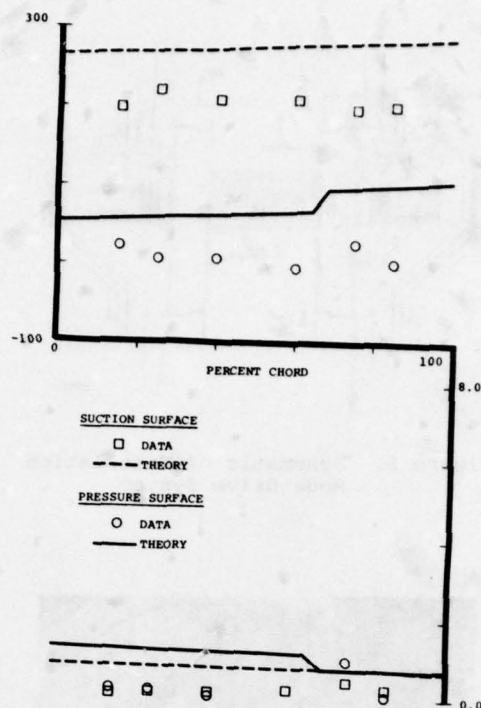


Figure 13. Unsteady Cascade Translation Mode Results for a -90.0° Interblade Phase Angle at a Static Pressure Ratio of 1.00:1

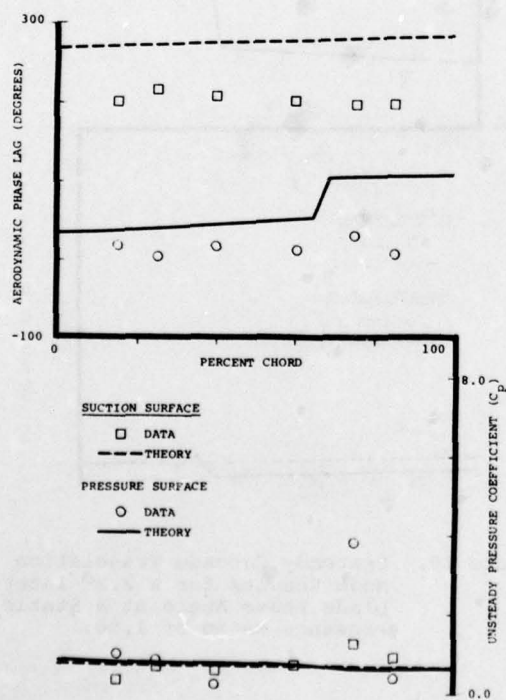


Figure 12. Unsteady Cascade Translation Mode Results for a -41.0° Interblade Phase Angle at a Static Pressure Ratio of 1.00:1

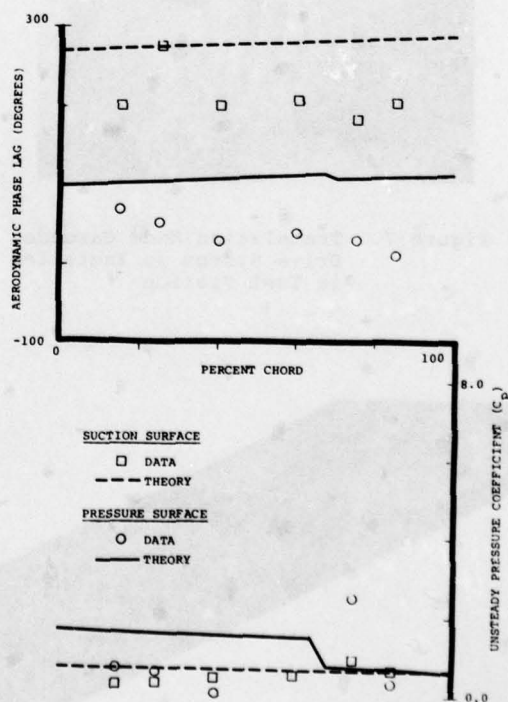


Figure 14. Unsteady Cascade Translation Mode Results for a -178.0° Interblade Phase Angle at a Static Pressure Ratio of 1.00:1

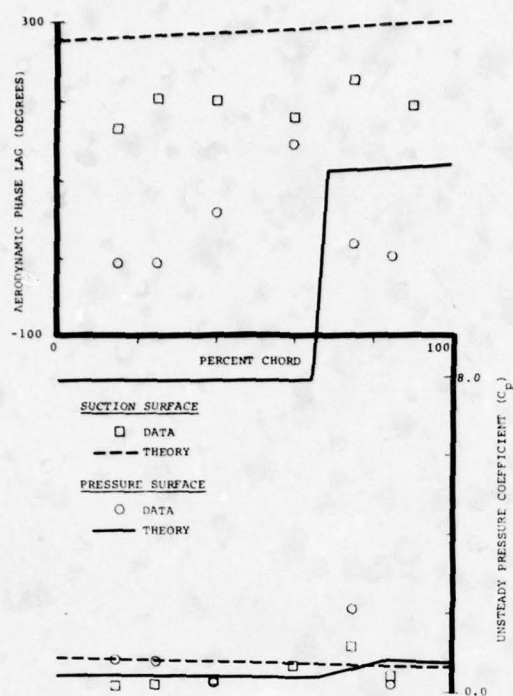


Figure 15. Unsteady Cascade Translation Mode Results for a 45.0° Interblade Phase Angle at a Static Pressure Ratio of 1.30:1

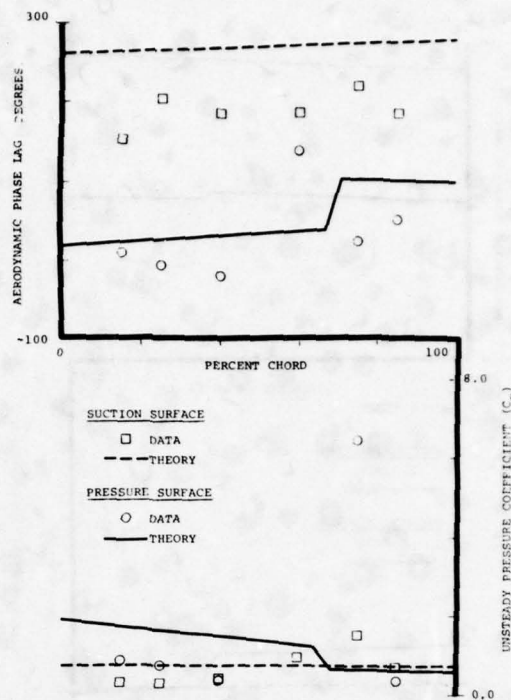


Figure 17. Unsteady Cascade Translation Mode Results for a -64.0° Interblade Phase Angle at a Static Pressure Ratio of 1.30:1

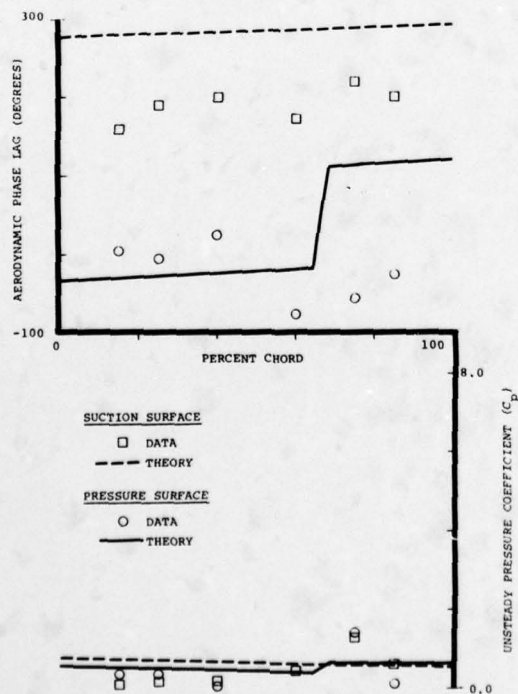


Figure 16. Unsteady Cascade Translation Mode Results for a 0.0° Interblade Phase Angle at a Static Pressure Ratio of 1.30:1

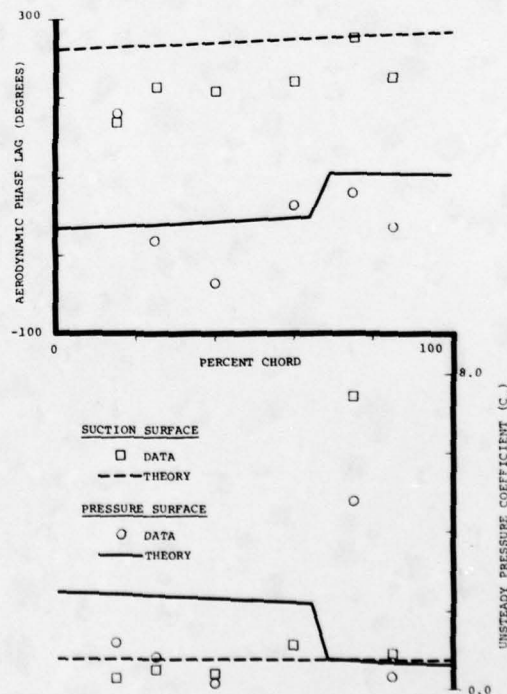


Figure 18. Unsteady Cascade Translation Mode Results for a -90.0° Interblade Phase Angle at a Static Pressure Ratio of 1.30:1

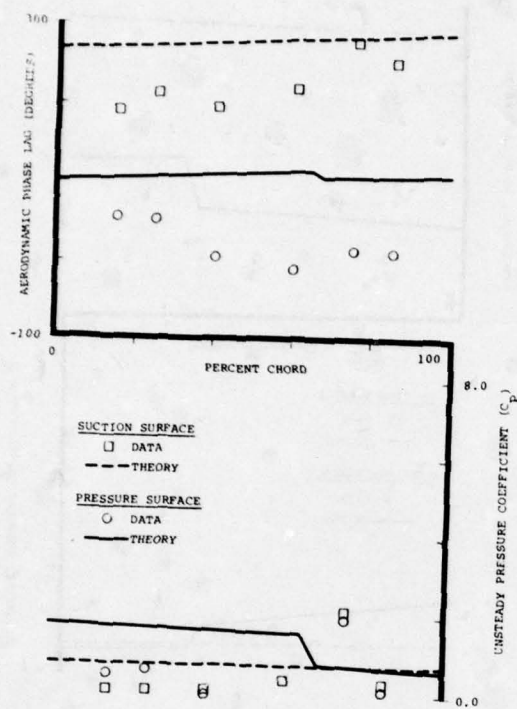


Figure 19. Unsteady Cascade Translation Mode Results for a -180.0° Interblade Phase Angle at a Static Pressure Ratio of 1.30:1

DISCUSSION

D.G.Halliwell, UK

- (1) I would agree that phase angle measurement is vastly more difficult than unsteady amplitude. Your biggest phase discrepancy relative to theory is in the high pressure ratio case. Have you used one of the strong shock theories to improve the prediction?
- (2) Has DDAD any experience in this field on a rotating machine?

Author's Reply

- (1) No, we haven't. We have only used a small perturbation, flat plate model (Reference 2) which does consider variations in the blade-to-blade amplitude of oscillation but has only an acoustic approximation to the shock waves.
- (2) No. We have been limited to cascades.

J.Dunham, UK

When the amplitude of the flutter is small, is the amplitude of shock wave movement also small? Does your theory model the existence of the shock waves and their movement?

Author's Reply

With regard to our unsteady cascade experiments, small blade oscillatory amplitudes result in small motion of the bow shock. However, the in passage shock system can exhibit large motions. For example, in the case of a torsionally oscillating cascade, we have observed that for interblade phase angles on the order of 180° , the in passage shocks move over a large percentage of the airfoil chord even though the oscillatory amplitude is relatively small (approximately $\pm 0.2^\circ$).

The small perturbation unsteady flat plate cascade analysis used for the data-theory correlation (Reference No.2) involves an acoustic approximation to the shock wave and does not consider their movement.

SUPERSONIC UNSTALLED FLUTTER

by

J.J.Adamczyk, M.E.Goldstein and M.J.Hartmann
National Aeronautics and Space Administration
Lewis Research Center
Cleveland, Ohio 44135

SUMMARY

Recently two flutter analyses have been developed at NASA Lewis Research Center to predict the onset of supersonic unstalled flutter of a cascade of two-dimensional airfoils. The first of these analyses the onset of supersonic flutter at low levels of aerodynamic loading (i.e., backpressure), while the second examines the occurrence of supersonic flutter at moderate levels of aerodynamic loading. Both of these analyses are based on the linearized unsteady inviscid equations of gas dynamics to model the flow field surrounding the cascade. The details of the development of the solution to each of these models have been published. The objective of the present paper is to utilize these analyses in a parametric study to show the effects of cascade geometry, inlet Mach number, and backpressure on the onset of single and multi degree of freedom unstalled supersonic flutter. Several of the results from this study are correlated against experimental qualitative observation to validate the models.

INTRODUCTION

The problem of flutter has long plagued the development of high speed compressor fan stages. The solution to this problem is often costly both in terms of time and money. For this reason engine manufacturers as well as government agencies are currently supporting numerous research programs in an attempt to better define regions of flutter instability and solutions to the problem. To date their research activities have uncovered two regions of the operating map of fan stages where flutter can be encountered at high speeds. These regions are shown schematically on the performance map of a typical high speed fan stage in Figure 1. Region I, the zone of moderate to high backpressure supersonic flutter can extend from the stall line of the fan down to its operating line. Experimental evidence of this flutter mode is presented in Reference 1.

Region II, the zone of low backpressure supersonic flutter can extend from wide open discharge to slightly below the operating line of the stage. Numerous analytical as well as experimental papers have appeared in the open literature which document the existence of this flutter mode (see References 2 to 4). Recently NASA Lewis Research Center has developed analytical analyses for both of these flutter zones. In Reference 5 an analysis is developed for the region of moderate to high backpressure flutter, while Reference 6 deals with the problem of low backpressure supersonic flutter. Both of these analyses are based on the linearized unsteady inviscid two-dimensional equations of gas dynamics to describe the flow field surrounding an infinite cascade of oscillating thin airfoils in a supersonic stream. The details of the mathematical development of these models will not be presented in the present paper. The objective of the present paper is to utilize these analyses in a parametric study to show the effects of cascade geometry, inlet Mach number, reduced frequency, and backpressure on supersonic flutter. Several of the results from this study are correlated against experimental qualitative observation to validate the models.

MODEL FORMULATION

The present analyses represents an incremental annulus of a fan stage as an infinite two-dimensional cascade of thin airfoils. In both analyses the steady relative flow approaching the cascade is assumed to be supersonic, with a subsonic axial velocity component, and satisfies the Kantrowitz unique incidence relationship. This flow configuration causes the weak oblique leading edge shock wave to propagate upstream of the cascade. At moderate to high pressures it is assumed that the steady pressure rise across the cascade is produced by a system of normal shock waves lying within the cascade passages. Downstream of the shock waves the steady flow is uniform and subsonic. Figure 2 shows a sketch of this steady flow configuration. As the operating point of the fan at high speeds is moved towards wide open discharge, the system of nearly normal in passage shock waves in the tip region is transformed into a series of weak oblique shock waves (see Figure 2). The flow downstream of these waves is supersonic. Since these waves are weak and the blade sections are

AD-A070 950

ADVISORY GROUP FOR AEROSPACE RESEARCH AND DEVELOPMENT--ETC F/G 21/5
STRESSES, VIBRATIONS, STRUCTURAL INTEGRATION AND ENGINE INTEGRI--ETC(U)
APR 79

UNCLASSIFIED

AGARD-CP-248

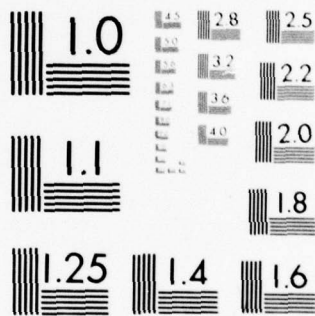
NL

6 OF 6

AD
A070950



END
DATE
FILMED
8-79
DDC



thin the steady flow deviates only slightly from a uniform flow at wide open discharge. In both analyses it is assumed that the blade motion results in a small perturbation to a steady two-dimensional base flow solution. At moderate to high backpressure the base flow, as described above, has a normal shock within the cascade passage with a uniform stream approaching and leaving the shock. At wide open discharge the base flow is assumed to be a uniform stream. This assumption according to linear theory uncouples the unsteady flow problem from its steady state counterpart. The motion of the airfoils in both analyses is restricted to simple harmonic motion in time, at a constant interblade phase angle between adjacent airfoils. The governing equations employed in the analyses are the linearized unsteady two-dimensional inviscid equations for a non-conducting gas. The change of the unsteady flow variables across the in passage shock wave are governed by the first order perturbed Rankine-Hugoniot shock relationships. The solution to both problems was obtained by analytical means the details of which can be found in References 5 and 6. These solutions resulted in accurate and efficient computational algorithms for computing the unsteady aerodynamic loading induced by the cascade motion, including the limiting case of a free stream Mach number of 1.

PARAMETRIC STUDY

The work done by the gas stream on the cascade over a cycle of motion is a direct measurement of the susceptibility of the cascade to flutter. If the sign of the work is negative, the cascade is doing work on the gas stream. Under these conditions any small unsupported motion imparted to the cascade will decay in time, hence the system is stable. If however, the sign of the work is positive the gas stream is doing work on the cascade. If this work is not dissipated by the internal mechanical damping any small unsupported motion imparted to the cascade will grow in time, causing the system to fail.

For a single degree of freedom pitching or plunging motion the nondimensional work done by the gas stream on an airfoil in the cascade is (see Reference 7)

$$W = \alpha_0 \pi \operatorname{Im}\{C_M\} \quad (1)$$

for pitching motion and

$$W = h_0 \pi \operatorname{Im}\{C_L\} \quad (2)$$

for plunging motion, where the symbol $\operatorname{Im}\{\}$ denotes the imaginary part of the bracketed quantity. The variables appearing in these two equations are C_M , C_L , α_0 , and h_0 , which are the complex moment coefficient about the pitching axes, the complex lift coefficient, the amplitude of the pitching oscillation, and the amplitude of the plunging oscillation, respectively. There will be a tendency for single degree of freedom flutter to occur in either the pitching or plunging mode whenever the imaginary part of the complex moment or lift coefficient becomes positive. For two-degree of freedom coupled flutter the nondimensional work done by the gas stream on an airfoil in the cascade is

$$W = -\alpha_0 \pi \sin \gamma \operatorname{Real}\{C_M\} + h_0 \pi \operatorname{Im}\{C_L\} + \alpha_0 \pi \cos \gamma \operatorname{Im}\{C_M\} \quad (3)$$

where the symbol $\operatorname{Real}\{\}$ denotes the real part of the complex bracketed quantity and γ is the phase angle at an instant in time between the pitching and plunging motion of an airfoil. Unlike single degree of flutter whose onset is independent of the amplitude of the airfoil motion the onset of coupled flutter as shown by Equation (3) is strongly dependent on the ratio of the pitch to plunge amplitudes and their associated phase shift γ .

Computations were performed based on the theory of References 5 and 6 to determine the effect of backpressure, inlet Mach number, reduced frequency, cascade solidity, and stagger angle on the nondimensional aerodynamic work for single degree of freedom pitching and plunging motion and for coupled pitching and plunging motion. These results are shown plotted as a function of the phase angle between two adjacent airfoils (i.e., interblade phase angle) at all times.

SINGLE DEGREE OF FREEDOM FLUTTER

The geometry of the cascade assumed in this study is, solidity 1.3, stagger angle 60° unless otherwise noted. Pitching axis location is assumed to lie at mid-chord. Figures 3 to 7 show graphs of the work per cycle for a cascade undergoing simple harmonic pitching motion at moderate to high backpressures. The in passage normal shock wave is assumed to lie slightly upstream of the passage entrance. Results are shown in Figures 3 to 5 for inlet Mach numbers of 1.2, 1.4, and 1.6, respectively. The parameter varied in each of these figures is the reduced frequency based on semichord from a value of 0.25 to 1.0. Recalling that positive work per cycle implies instability provided the effect of mechanical damping is neglected, Figures 3 to 5 show that for Mach numbers between 1.2 and 1.6 single degree of freedom pitching (i.e., torsional) flutter can exist for reduced frequencies less than 0.25 at moderate to high backpressures. At Mach numbers above 1.2 this mode of flutter exists for reduced frequencies above 0.25 but ceases to exist at reduced frequencies greater than 0.5. The effects of cascade solidity and stagger angle on torsional flutter at moderate to high backpressures are shown in Figures 6 and 7. These results were computed based on solidities of 1.2 and 1.4 and stagger angles of 50° and 70° . The reduced frequency and inlet Mach number were held constant at 0.5 and 1.4. Although

Figures 6 and 7 show no region of instability they do show that reducing the solidity and decreasing the stagger angle have a slight stabilizing effect on single degree of freedom torsional flutter at moderate to high backpressures.

The nondimensional work per cycle for a cascade pitching about mid-chord at low backpressures is shown in Figures 8 to 12. The cascade geometry assumed in the computation of these results is identical to that assumed for the previous results unless otherwise noted. Figures 8 to 10 show the effect of Mach number and reduced frequency. From these results it appears that single degree of freedom torsional flutter will not exist at low backpressures at reduced frequencies in excess of 0.50. This reduced frequency limit is greater than the corresponding limit established from the previous set of results for moderate to high backpressure cascade operation. This implies that a cascade operating with a finite backpressure across it will be less susceptible to torsional flutter than a cascade operating at low back pressures. This backpressurizing phenomenon has been observed in fans where it causes the torsional flutter boundary to bend back as the pressure ratio across the fan is raised (see Figure 1). The effects of cascade solidity and stagger angle on the work per cycle for torsional oscillation at low backpressures are shown in Figures 11 and 12. The values of the parameters used in these computations are identical to those used previously in computing the results in Figures 6 and 7. These results like their counterparts for moderate to high backpressure show that reducing the stagger angle and reducing the cascade solidity have a slight stabilizing effect on torsional flutter at low backpressures.

The work per cycle for a cascade undergoing simple harmonic plunging motion at moderate to high backpressures is shown in Figures 13 to 17. Figures 13 to 15 show the effects of reduced frequency and Mach number. These results imply that the work per cycle will remain negative over all values of interblade phase angle provided the reduced frequency is slightly greater than 0.20 for inlet Mach numbers up to 1.6. As the inlet Mach number is reduced from 1.6 the transition reduced frequency decreases to approximately 0.15 at Mach number 1.2. The effects of solidity and stagger angle on the work per cycle are shown in Figures 16 and 17. Increasing the solidity slightly enhances the stability of the system, while increasing the stagger has a destabilizing effect.

The results for plunging motion at low backpressure are not presented because they showed that the work per cycle always remained negative. Thus the theory of Reference 6 predicts that flutter in a pure plunging mode cannot occur at low backpressures. However, the results presented in Figures 13 to 17 which were based on the theory of Reference 5 show that single degree of freedom bending flutter can occur at moderate to high backpressures. Thus it can be concluded that backpressuring tends to induce bending flutter. Experimental evidence to support this observation is provided in Reference 1.

COUPLED FLUTTER

Carta⁸ showed the existence of coupled flutter in compressor rotors. Unlike coupled flutter in fixed wing aircraft where the coupling between the bending and torsional mode is due to the aerodynamic forces, the coupling in compressor rotors is caused by mechanical restraining forces associated with part span shrouds and flexible disks. Carta in his analysis assumed the motion of the rotor disk to be

$$S = Ae^{-i(\omega t - (2\pi n/N)(r/p))}$$

where A is the amplitude of the motion, t is time, ω is the circular frequency, n is an integer, N is the number of rotor blades, p is the pitch chord ratio, and r the peripheral distance around the wheel. If the rotor blades are rigidly fixed to the deforming disk the plunging and pitching amplitude of a blade section at a given radial location are

$$h_0 = A \cos \delta$$

$$\alpha_0 = \frac{2\pi n A}{Np} e^{i\pi/2}$$

respectively, where δ is the local stagger angle of the blade sections. The non-dimensional aerodynamic work per cycle associated with this motion is

$$W = A\pi \cos \delta \left\{ \text{Im } C_L - \frac{2\pi n}{pN \cos \delta} \text{Real } C_M \right\}$$

where the integer n can take on both positive and negative values corresponding to either a backward or forward traveling wave along the disk rim. The lift and moment coefficients appearing in this equation are to be evaluated at an interblade phase angle of

$$\sigma = \frac{2\pi n}{N}$$

Computations were performed to assess the influence of the twist bend coupling ratio

$$\epsilon = \frac{2\pi n}{Np \cos \delta}$$

inlet Mach number and reduced frequency on the aerodynamic work per cycle at low and high backpressures. The results for moderate to high backpressures are shown plotted as a function of the harmonic number n for specified values of reduced frequency and inlet Mach number in Figures 18 to 20. The cascade solidity and stagger angle are 1.3 and 60° , respectively. These results show that for n negative and large the gas stream is supplying energy to the cascade, while for positive values of n the energy flow is generally from the cascade to the gas stream. Hence, the vibrational waves traveling in the direction of rotation appear to be less stable than those traveling in the opposite direction. For small absolute values of n and for reduced frequencies greater than 0.25 the work per cycle remains negative for Mach numbers greater than 1.2. Since the twist bend coupling parameter ϵ is directly proportional to n it is seen that an effective means of suppressing coupled flutter is by mechanically controlling the ratio of twist to bend in the lower order vibrational modes. These results also show that increasing reduced frequency has a stabilizing effect on coupled flutter but not to the extent it does for single degree of freedom flutter.

The effect of lowering the backpressure across the cascade on the work per cycle is shown in Figures 21 to 23. The trends of these results are quite similar to those for moderate to high backpressure. Increasing reduced frequency and limiting the ratio of twist bend coupling suppresses coupled flutter at low backpressure, as it did at high to moderate backpressures. From these results it appears that proper choice of these two parameters can prevent coupled flutter from occurring over the entire high speed operating angle of a fan or compressor stage.

CONCLUSIONS

The results of numerous calculation based on the theory of References 5 and 6 has been presented to show the effect of inlet Mach number, cascade geometry, reduced frequency, and backpressure on the susceptibility of a cascade to single- and multi-degree of freedom flutter. It was shown that increasing reduced frequency and backpressure had a stabilizing effect on single degree of freedom torsional flutter. It was also shown that single degree of freedom bending flutter could occur at moderate to high backpressure if the reduced frequency was below 0.25. For a coupled vibrational mode it was shown that the occurrence of flutter could be prevented over the entire high speed operating range of a fan stage by mechanically controlling the ratio of twist bend coupling and reduced frequency. These stability trends are consistent with experimental rig observations.

A detailed experimental verification of the theories of References 5 and 6 is necessary. One suitable approach would be to utilize a high speed wind tunnel with a linear cascade in which the airfoils are driven in a prescribed mode and operated over a range of back pressures. Measured surface pressure distributions could then be correlated against predicted results to establish the model validity or the need for additional model refinements.

REFERENCES

1. Ruggeri, R.S.
Benser, W.A. *Performance of Highly Loaded Two-Stage Axial-Flow Fan*. NASA TM X-3076, 1974.
2. Kurosaka, M. *On the Unsteady Supersonic Cascade with a Subsonic Leading Edge - An Exact First Order Theory: Parts 1 and 2*. J. Eng. Power, Vol.96, No.1, pp.13-31, January 1974.
3. Verdon, J.M. *Further Developments in the Aerodynamic Analysis of Unsteady Supersonic Cascades Parts 1 and 2*. ASME Paper 77-GT-44 and 77-GT-45, March 1977.
4. Snyder, L.E.
Commerford, G.L. *Supersonic Unstalled Flutter in Fan Rotors: Analytical Experimental Results*. J. Eng. Power, Vol.96, No.4, pp.379-386, October 1974.
5. Goldstein, M.E.
Braun, W.
Adamczyk, J.J. *Unsteady Flow in a Supersonic Cascade with Strong In-Passage Shocks*. J. Fluid Mech., Vol.83, Part III, pp.569-604, 1977.
6. Adamczyk, J.J.
Goldstein, M.E. *Unsteady Flow in a Supersonic Cascade with Subsonic Leading Edge Locus*. To be published in the AIAA Journal.
7. Fung, Yuan-cheng *An Introduction to the Theory of Elasticity*. Wiley, New York, pp.166-168, 1955.
8. Carta, F.O. *Coupled Blade-Disk-Shroud Flutter Instabilities in Turbojet Engine Rotors*. J. Eng. Power, Vol.89, No.3, pp.419-426, July 1967.

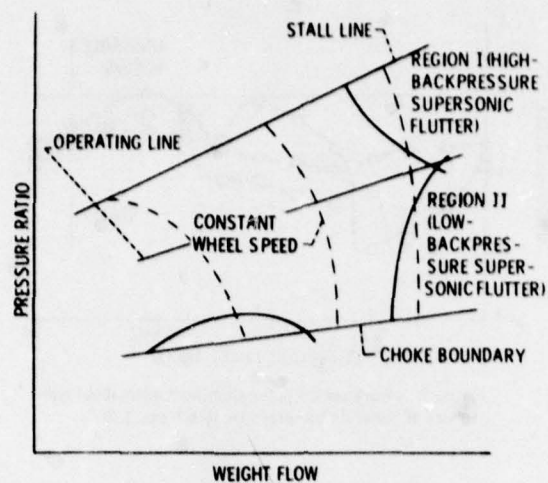


Figure 1. - Compressor performance and stability map.

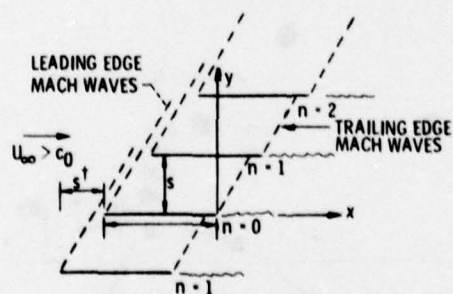
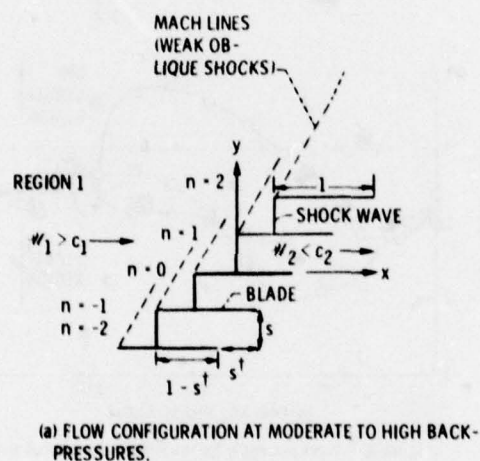


Figure 2.

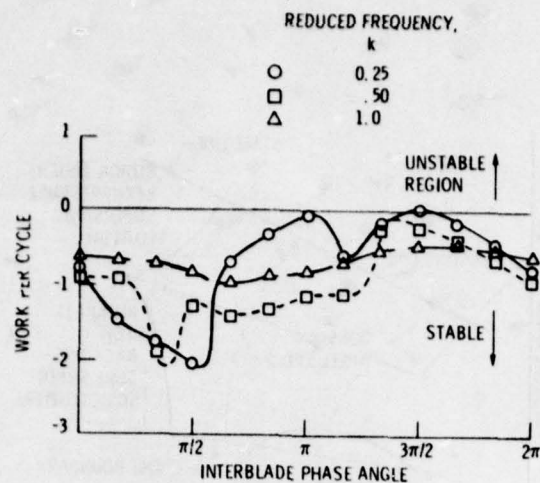


Figure 3. - Work per cycle for pitching motion about mid-chord at moderate backpressure (Mach no. 1.2).

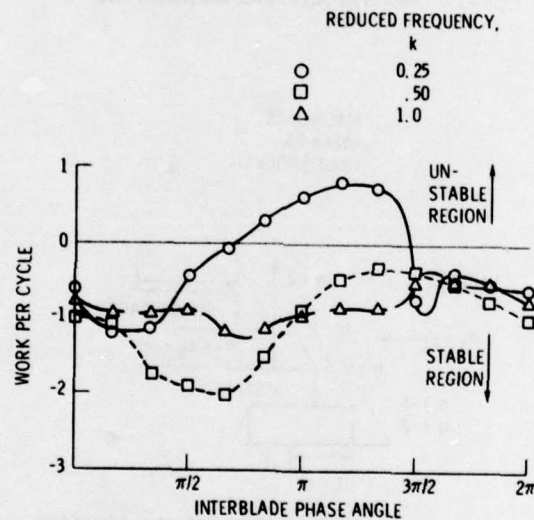


Figure 4. - Work per cycle for pitching motion about mid-chord at moderate backpressure (Mach no. 1.4).

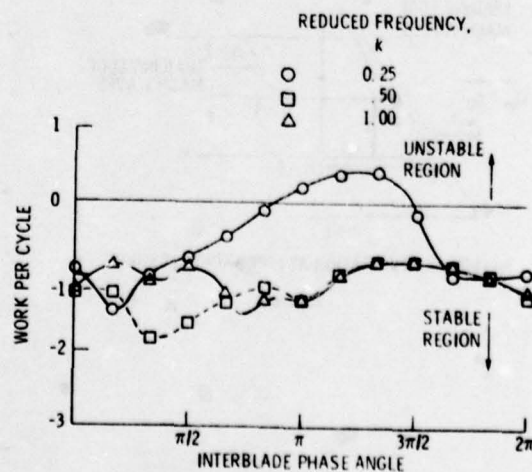


Figure 5. - Work per cycle for pitching motion about mid-chord at moderate backpressure (Mach no. 1.6).

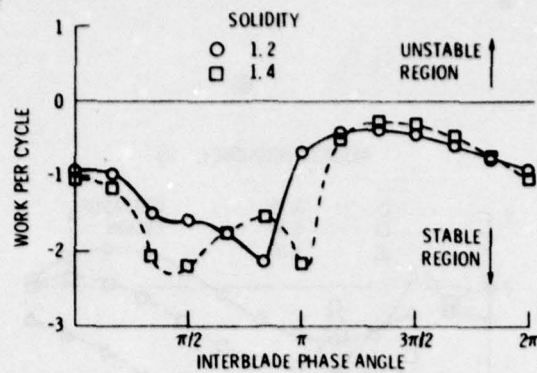


Figure 6. - The effect of solidity on the work per cycle for pitching motion at moderate backpressure.

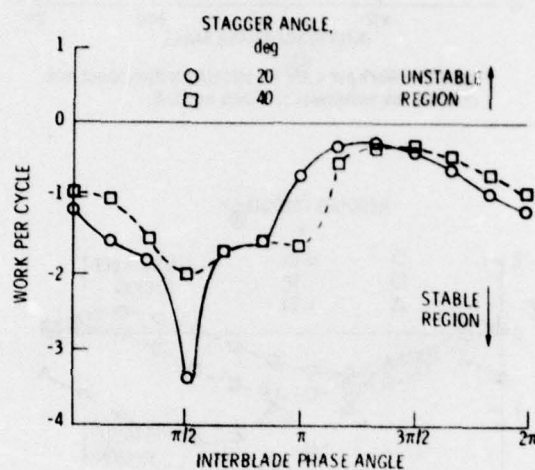


Figure 7. - The effect of stagger angle on the work per cycle for pitching motion at moderate backpressure.

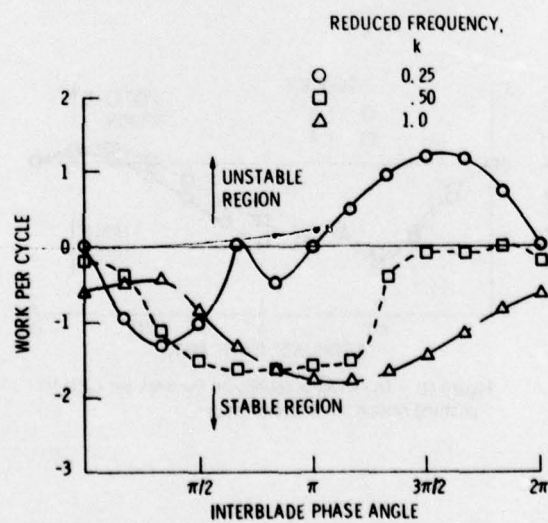


Figure 8. - Work per cycle for pitching motion about mid-chord at low backpressure (Mach no. 1.2).

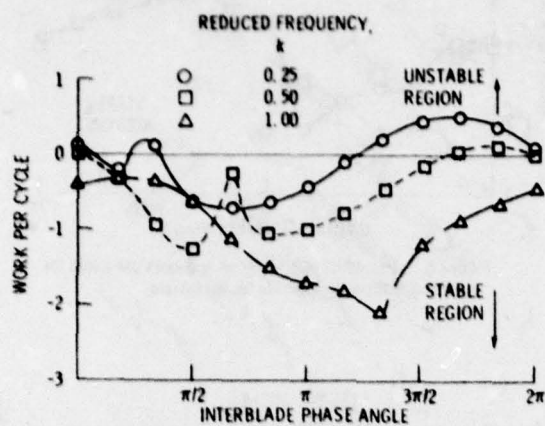


Figure 9. - Work per cycle for pitching motion about mid-chord at low backpressure (Mach no. 1.4).

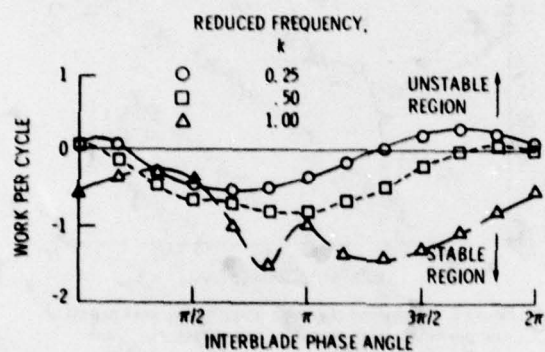


Figure 10. - Work per cycle for pitching motion about mid-chord at low backpressure (Mach no. 1.6).

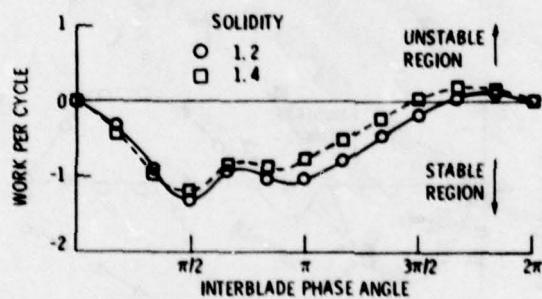


Figure 11. - The effect of solidity on the work per cycle for pitching motion at low backpressure.

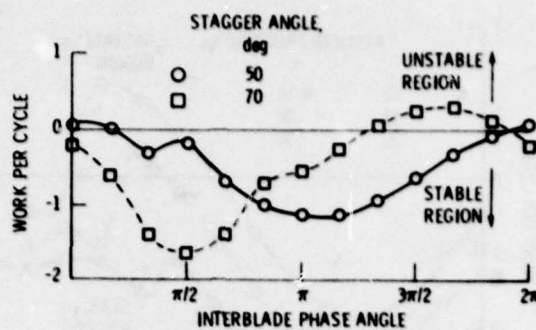


Figure 12. - The effect of stagger angle on the work per cycle for pitching motion at low backpressure.

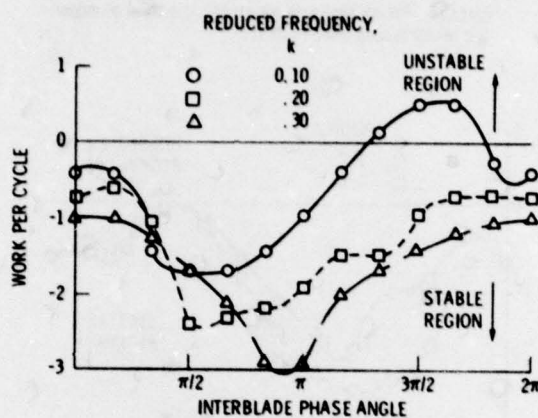


Figure 13. - Work per cycle for plunging motion at moderate backpressure (Mach no. 1.2).

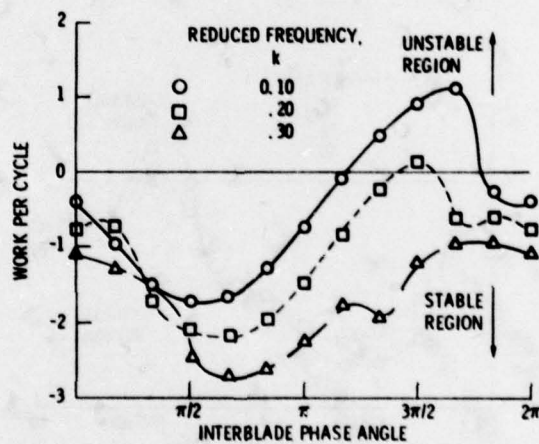


Figure 14. - Work per cycle for plunging motion at moderate backpressure (Mach no. 1.4).

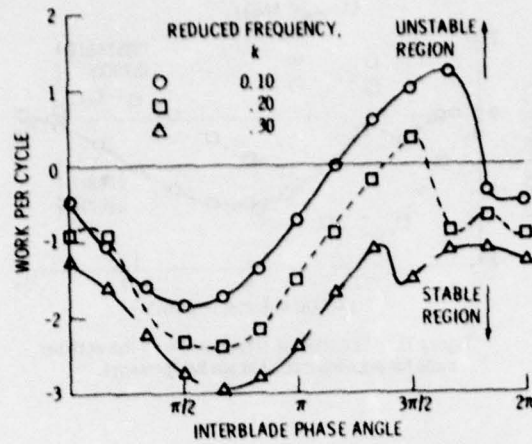


Figure 15. - Work per cycle for plunging motion at moderate backpressure (Mach no. 1.6).

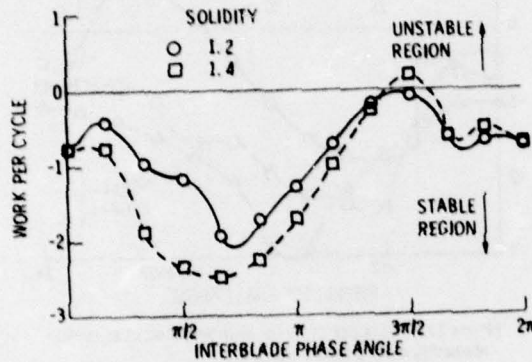


Figure 16. - The effect of solidity on the work per cycle for plunging motion at moderate backpressure.

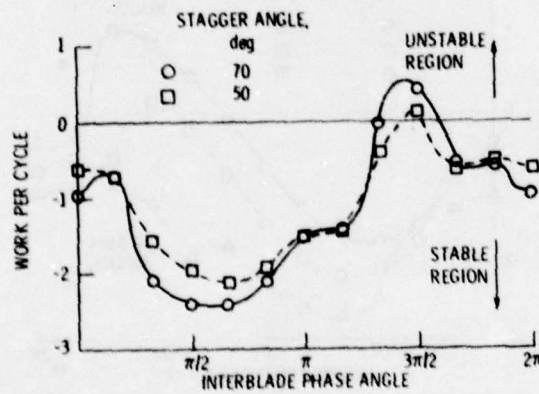


Figure 17. - The effect of stagger angle on the work per cycle at moderate backpressure.

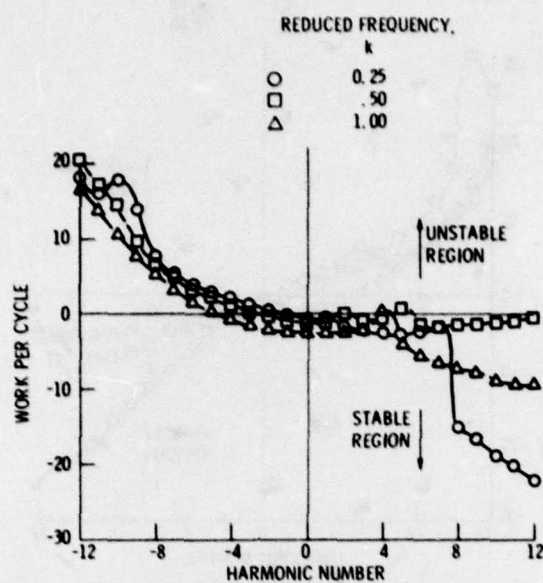


Figure 18. - Work per cycle for coupled motion at moderate backpressure (Mach no. 1.2).

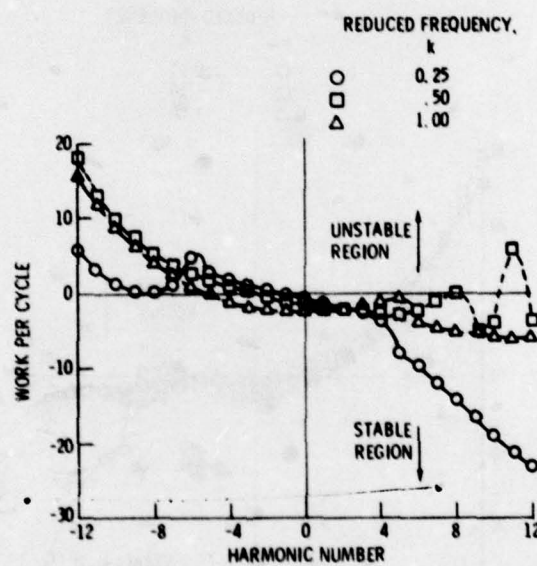


Figure 19. - Work per cycle for coupled flutter at moderate backpressure (Mach no. 1.4).

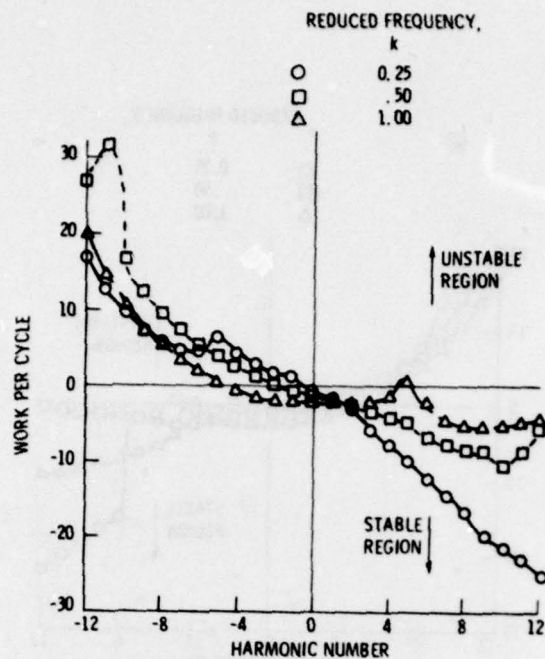


Figure 20. - Work per cycle for coupled motion at moderate backpressure (Mach no. 1.6).

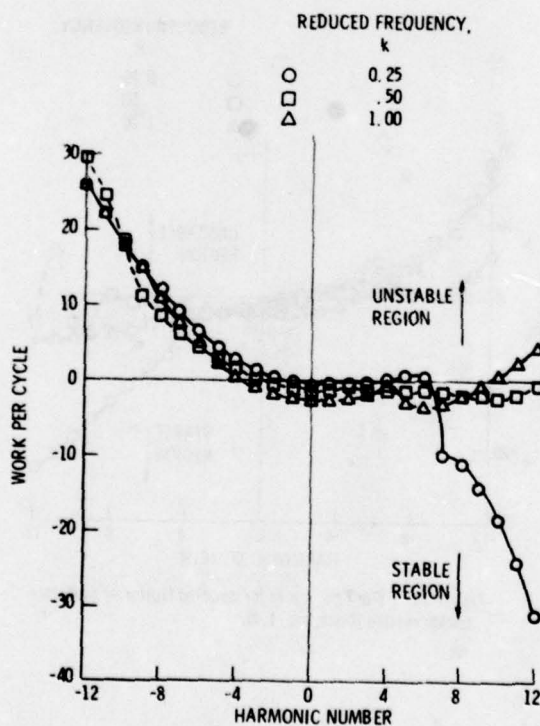


Figure 21. - Work per cycle for coupled motion at low backpressure (Mach no. 1.2).

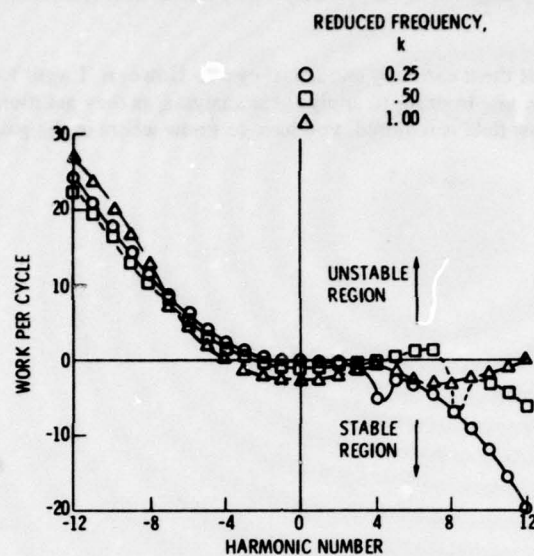


Figure 22. - Work per cycle for coupled motion at low back-pressure (Mach no. 1.4).

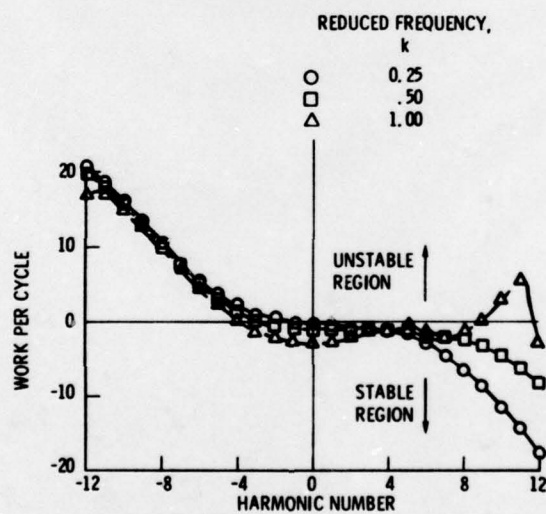


Figure 23. - Work per cycle for coupled motion at low back-pressure (Mach no. 1.6).

DISCUSSION

D.G. Halliwell, UK

I think this is a very useful and interesting study. My question concerns the coupled flutter case. A change in Mach number from 1.2 to 1.6 represents a speed increase of over 30%.

Reduced frequency also changes with speed but the curves are very close together. For the above change in speed one would expect a very large change in stability. Why do the curves not reflect this?

Author's Reply

I guess probably if you look at them carefully enough, they do. However, I want to point out that we assume the shock was at the leading edge. In order to apply these analyses, as they get more sophisticated, detailed information on the steady flow field is required, you have to know where in the passage the shock lies and what his configuration is like.


REPORT DOCUMENTATION PAGE			
1. Recipient's Reference	2. Originator's Reference AGARD-CP-248	3. Further Reference ISBN 92-835-0235-3	4. Security Classification of Document UNCLASSIFIED
5. Originator	Advisory Group for Aerospace Research and Development North Atlantic Treaty Organization 7 rue Ancelle, 92200 Neuilly sur Seine, France		
6. Title	STRESSES, VIBRATIONS, STRUCTURAL INTEGRATION AND ENGINE INTEGRITY (INCLUDING AEROELASTICITY AND FLUTTER)		
7. Presented at	the 52nd Symposium of the AGARD PEP, held in Cleveland, Ohio, USA, October 1978.		
8. Author(s)/Editor(s) Various			9. Date April 1979
10. Author's/Editor's Address Various			11. Pages 510
12. Distribution Statement	This document is distributed in accordance with AGARD policies and regulations, which are outlined on the Outside Back Covers of all AGARD publications.		
13. Keywords/Descriptors			
Stress analysis Aeroelasticity Flutter Dynamic structural analysis		Vibration Aircraft engines Life (durability)	
14. Abstract			
<p>These Conference Proceedings contain 33 papers presented at the 52nd Symposium of the AGARD Propulsion and Energetics Panel, held at Cleveland, Ohio, USA, on 23-28 October 1978.</p> <p>The papers were grouped into eight sessions covering the following topics: Experimental Stress Analysis; Stress Analysis Techniques, Life Prediction; Engine Structural Integrity, Vibration and Containment; Engine-Airframe Integration/Compatibility; Aeroelasticity and Flutter. The discussions after each presentation are included in the Conference Proceedings.</p> <p>The meeting covered engine development, engine-aircraft integration and engine operation. It led into the over-riding concern of the current aircraft engine systems: the durability and life management of aircraft gas turbine engines. The papers of this Symposium are all connected with this, most of them address real engines, but only few actually show failed engine parts. Some correlations between analysis and test or field experience are included.</p>			

<p>AGARD Conference Proceedings No.248 Advisory Group for Aerospace Research and Development, NATO STRESSES, VIBRATIONS, STRUCTURAL INTEGRATION AND ENGINE INTEGRITY (INCLUDING AEROELASTICITY AND FLUTTER) Published April 1979 510 pages</p> <p>These Conference Proceedings contain 33 papers presented at the 52nd Symposium of the AGARD Propulsion and Energetics Panel, held at Cleveland, Ohio, USA, on 23-28 October 1978.</p> <p>The papers were grouped into eight sessions covering the following topics: Experimental Stress Analysis; P.T.O.</p>	<p>AGARD-CP-248</p> <p>Stress analysis Aeroelasticity Flutter Dynamic structural analysis Vibration Aircraft engines Life (durability)</p>	<p>AGARD Conference Proceedings No.248 Advisory Group for Aerospace Research and Development, NATO STRESSES, VIBRATIONS, STRUCTURAL INTEGRATION AND ENGINE INTEGRITY (INCLUDING AEROELASTICITY AND FLUTTER) Published April 1979 510 pages</p> <p>These Conference Proceedings contain 33 papers presented at the 52nd Symposium of the AGARD Propulsion and Energetics Panel, held at Cleveland, Ohio, USA, on 23-28 October 1978.</p> <p>The papers were grouped into eight sessions covering the following topics: Experimental Stress Analysis; P.T.O.</p>	<p>AGARD-CP-248</p> <p>Stress analysis Aeroelasticity Flutter Dynamic structural analysis Vibration Aircraft engines Life (durability)</p>
<p>AGARD Conference Proceedings No.248 Advisory Group for Aerospace Research and Development, NATO STRESSES, VIBRATIONS, STRUCTURAL INTEGRATION AND ENGINE INTEGRITY (INCLUDING AEROELASTICITY AND FLUTTER) Published April 1979 510 pages</p> <p>These Conference Proceedings contain 33 papers presented at the 52nd Symposium of the AGARD Propulsion and Energetics Panel, held at Cleveland, Ohio, USA, on 23-28 October 1978.</p> <p>The papers were grouped into eight sessions covering the following topics: Experimental Stress Analysis; P.T.O.</p>	<p>AGARD-CP-248</p> <p>Stress analysis Aeroelasticity Flutter Dynamic structural analysis Vibration Aircraft engines Life (durability)</p>	<p>AGARD Conference Proceedings No.248 Advisory Group for Aerospace Research and Development, NATO STRESSES, VIBRATIONS, STRUCTURAL INTEGRATION AND ENGINE INTEGRITY (INCLUDING AEROELASTICITY AND FLUTTER) Published April 1979 510 pages</p> <p>These Conference Proceedings contain 33 papers presented at the 52nd Symposium of the AGARD Propulsion and Energetics Panel, held at Cleveland, Ohio, USA, on 23-28 October 1978.</p> <p>The papers were grouped into eight sessions covering the following topics: Experimental Stress Analysis; P.T.O.</p>	<p>AGARD-CP-248</p> <p>Stress analysis Aeroelasticity Flutter Dynamic structural analysis Vibration Aircraft engines Life (durability)</p>

<p>Stress Analysis Techniques, Life Prediction; Engine Structural Integrity, Vibration and Containment; Engine-Airframe Integration/Compatibility; Aeroelasticity and Flutter. The discussions after each presentation are included in the Conference Proceedings.</p> <p>The meeting covered engine development, engine-aircraft integration and engine operation. It led into the over-riding concern of the current aircraft engine systems: the durability and life management of aircraft gas turbine engines. The papers of this Symposium are all connected with this, most of them address real engines, but only few actually show failed engine parts. Some correlations between analysis and test or field experience are included.</p> <p>ISBN 92-835-0235-3</p>	<p>Stress Analysis Techniques, Life Prediction; Engine Structural Integrity, Vibration and Containment; Engine-Airframe Integration/Compatibility; Aeroelasticity and Flutter. The discussions after each presentation are included in the Conference Proceedings.</p> <p>The meeting covered engine development, engine-aircraft integration and engine operation. It led into the over-riding concern of the current aircraft engine systems: the durability and life management of aircraft gas turbine engines. The papers of this Symposium are all connected with this, most of them address real engines, but only few actually show failed engine parts. Some correlations between analysis and test or field experience are included.</p> <p>ISBN 92-835-0235-3</p>
<p>Stress Analysis Techniques, Life Prediction; Engine Structural Integrity, Vibration and Containment; Engine-Airframe Integration/Compatibility; Aeroelasticity and Flutter. The discussions after each presentation are included in the Conference Proceedings.</p> <p>The meeting covered engine development, engine-aircraft integration and engine operation. It led into the over-riding concern of the current aircraft engine systems: the durability and life management of aircraft gas turbine engines. The papers of this Symposium are all connected with this, most of them address real engines, but only few actually show failed engine parts. Some correlations between analysis and test or field experience are included.</p> <p>ISBN 92-835-0235-3</p>	<p>Stress Analysis Techniques, Life Prediction; Engine Structural Integrity, Vibration and Containment; Engine-Airframe Integration/Compatibility; Aeroelasticity and Flutter. The discussions after each presentation are included in the Conference Proceedings.</p> <p>The meeting covered engine development, engine-aircraft integration and engine operation. It led into the over-riding concern of the current aircraft engine systems: the durability and life management of aircraft gas turbine engines. The papers of this Symposium are all connected with this, most of them address real engines, but only few actually show failed engine parts. Some correlations between analysis and test or field experience are included.</p> <p>ISBN 92-835-0235-3</p>

B723
4

AGARD

NATO  OTAN

7 RUE ANCELLE · 92200 NEUILLY-SUR-SEINE
FRANCE

Telephone 745.08.10 · Telex 610176

DISTRIBUTION OF UNCLASSIFIED
AGARD PUBLICATIONS

AGARD does NOT hold stocks of AGARD publications at the above address for general distribution. Initial distribution of AGARD publications is made to AGARD Member Nations through the following National Distribution Centres. Further copies are sometimes available from these Centres, but if not may be purchased in Microfiche or Photocopy form from the Purchase Agencies listed below.

NATIONAL DISTRIBUTION CENTRES

BELGIUM

Coordonnateur AGARD - VSL
Etat-Major de la Force Aérienne
Quartier Reine Elisabeth
Rue d'Evere, 1140 Bruxelles

CANADA

Defence Scientific Information Service
Department of National Defence
Ottawa, Ontario K1A 0Z2

DENMARK

Danish Defence Research Board
Østerbrogades Kaserne
Copenhagen Ø

FRANCE

O.N.E.R.A. (Direction)
29 Avenue de la Division Leclerc
92 Châtillon sous Bagneux

GERMANY

Zentralstelle für Luft- und Raumfahrt-
dokumentation und -information
c/o Fachinformationszentrum Energie,
Physik, Mathematik GmbH
Kernforschungszentrum
7514 Eggenstein-Leopoldshafen 2

GREECE

Hellenic Air Force General Staff
Research and Development Directorate
Holargos, Athens, Greece

ICELAND

Director of Aviation
c/o Flugrad
Reykjavik

ITALY

Aeronautica Militare
Ufficio del Delegato Nazionale all'AGARD
3, Piazzale Adenauer
Roma/EUR

LUXEMBOURG

See Belgium

NETHERLANDS

Netherlands Delegation to AGARD
National Aerospace Laboratory, NLR
P.O. Box 126
Delft

NORWAY

Norwegian Defence Research Establishment
Main Library
P.O. Box 25
N-2007 Kjeller

PORTUGAL

Direcção do Serviço de Material
da Força Aérea
Rua da Escola Politecnica 42
Lisboa
Attn: AGARD National Delegate

TURKEY

Department of Research and Development (ARGE)
Ministry of National Defence, Ankara

UNITED KINGDOM

Defence Research Information Centre
Station Square House
St. Mary Cray
Orpington, Kent BR5 3RE

UNITED STATES

National Aeronautics and Space Administration (NASA)
Langley Field, Virginia 23365
Attn: Report Distribution and Storage Unit

THE UNITED STATES NATIONAL DISTRIBUTION CENTRE (NASA) DOES NOT HOLD
STOCKS OF AGARD PUBLICATIONS, AND APPLICATIONS FOR COPIES SHOULD BE MADE
DIRECT TO THE NATIONAL TECHNICAL INFORMATION SERVICE (NTIS) AT THE ADDRESS BELOW.

PURCHASE AGENCIES

Microfiche or Photocopy

National Technical
Information Service (NTIS)
5285 Port Royal Road
Springfield
Virginia 22161, USA

Microfiche

Space Documentation Service
European Space Agency
10, rue Mario Nikis
75015 Paris, France

Microfiche

Technology Reports
Centre (DTI)
Station Square House
St. Mary Cray
Orpington, Kent BR5 3RE
England

Requests for microfiche or photocopies of AGARD documents should include the AGARD serial number, title, author or editor, and publication date. Requests to NTIS should include the NASA accession report number. Full bibliographical references and abstracts of AGARD publications are given in the following journals:

Scientific and Technical Aerospace Reports (STAR)
published by NASA Scientific and Technical
Information Facility
Post Office Box 8757
Baltimore/Washington International Airport
Maryland 21240, USA

Government Reports Announcements (GRA)
published by the National Technical
Information Services, Springfield
Virginia 22161, USA

